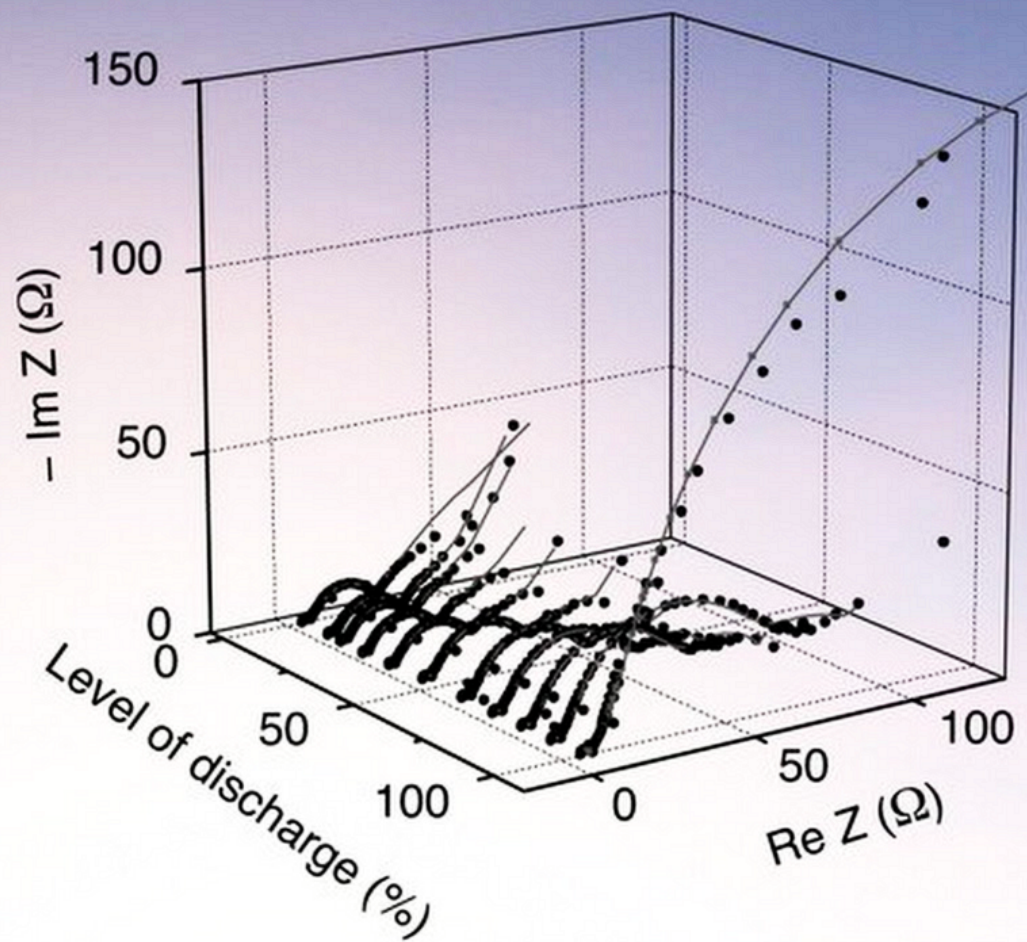


Edited By
Evgenij Barsoukov and J. Ross Macdonald

Impedance Spectroscopy

Theory, Experiment, and Applications

Third Edition



IMPEDANCE SPECTROSCOPY

IMPEDANCE SPECTROSCOPY

Theory, Experiment, and Applications

Third Edition

Edited by
Dr. Evgenij Barsoukov

Head of Algorithm Development
Battery Management Systems
Texas Instruments Inc.
Dallas, TX, USA

Dr. J. Ross Macdonald
(William R. Kenan, Jr., Professor of Physics, Emeritus)
Department of Physics and Astronomy
University of North Carolina
Chapel Hill, NC, USA

WILEY

This edition first published 2018
© 2018 John Wiley & Sons, Inc.
Second edition: 2005, John Wiley & Sons, Inc.

All rights reserved. No part of this publication may be reproduced, stored in a retrieval system, or transmitted, in any form or by any means, electronic, mechanical, photocopying, recording or otherwise, except as permitted by law. Advice on how to obtain permission to reuse material from this title is available at <http://www.wiley.com/go/permissions>.

The right of **Evgenij Barsoukov** and **J. Ross Macdonald** to be identified as the editors of the editorial material in this work has been asserted in accordance with law.

Registered Office(s)
John Wiley & Sons, Inc., 111 River Street, Hoboken, NJ 07030, USA

Editorial Office
111 River Street, Hoboken, NJ 07030, USA

For details of our global editorial offices, customer services, and more information about Wiley products visit us at www.wiley.com.

Wiley also publishes its books in a variety of electronic formats and by print-on-demand. Some content that appears in standard print versions of this book may not be available in other formats.

Limit of Liability/Disclaimer of Warranty

In view of ongoing research, equipment modifications, changes in governmental regulations, and the constant flow of information relating to the use of experimental reagents, equipment, and devices, the reader is urged to review and evaluate the information provided in the package insert or instructions for each chemical, piece of equipment, reagent, or device for, among other things, any changes in the instructions or indication of usage and for added warnings and precautions. While the publisher and authors have used their best efforts in preparing this work, they make no representations or warranties with respect to the accuracy or completeness of the contents of this work and specifically disclaim all warranties, including without limitation any implied warranties of merchantability or fitness for a particular purpose. No warranty may be created or extended by sales representatives, written sales materials or promotional statements for this work. The fact that an organization, website, or product is referred to in this work as a citation and/or potential source of further information does not mean that the publisher and authors endorse the information or services the organization, website, or product may provide or recommendations it may make. This work is sold with the understanding that the publisher is not engaged in rendering professional services. The advice and strategies contained herein may not be suitable for your situation. You should consult with a specialist where appropriate. Further, readers should be aware that websites listed in this work may have changed or disappeared between when this work was written and when it is read. Neither the publisher nor authors shall be liable for any loss of profit or any other commercial damages, including but not limited to special, incidental, consequential, or other damages.

Library of Congress Cataloging-in-Publication Data

Names: Barsoukov, Evgenij, editor. | Macdonald, J. Ross (James Ross), 1923– editor.
Title: Impedance spectroscopy : theory, experiment, and applications.
Description: Third edition / edited by Evgenij Barsoukov (head of algorithm development, Battery Management Systems, Texas Instruments Inc. Dallas, Texas). J. Ross Macdonald (professor of physics, Department of Physics and Astronomy, University of North Carolina, Chapel Hill, NC, USA). | Hoboken, NJ : Wiley, 2018. | Includes bibliographical references and index. | Identifiers: LCCN 2017055303 (print) | LCCN 2017060301 (ebook) | ISBN 9781119333173 (pdf) | ISBN 9781119333180 (epub) | ISBN 9781119074083 (cloth)
Subjects: LCSH: Impedance spectroscopy—Textbooks. | Impedance spectroscopy—Experiments. | Electrochemical analysis—Experiments.
Classification: LCC QD116.I57 (ebook) | LCC QD116.I57 I47 2018 (print) | DDC 543/.6—dc23
LC record available at <https://lccn.loc.gov/2017055303>

Cover image: © Art Stocker/Shutterstock; © Evgenij Barsoukov, 2017
Cover design by Wiley

Set in 10/12pt Palatino by SPi Global, Pondicherry, India

Contents

Preface to the Third Edition xi

Preface to the Second Edition xiii

Preface to the First Edition xv

Contributors to the Third Edition xvii

Chapter 1 Fundamentals of Impedance Spectroscopy	1
J. Ross Macdonald and William B. Johnson	1

1.1 Background, Basic Definitions, and History 1

- 1.1.1 The Importance of Interfaces 1
- 1.1.2 The Basic Impedance Spectroscopy Experiment 2
- 1.1.3 Response to a Small-Signal Stimulus in the Frequency Domain 3
- 1.1.4 Impedance-Related Functions 5
- 1.1.5 Early History 6

1.2 Advantages and Limitations 7

- 1.2.1 Differences between Solid-State and Aqueous Electrochemistry 9

1.3 Elementary Analysis of Impedance Spectra 10

- 1.3.1 Physical Models for Equivalent Circuit Elements 10
- 1.3.2 Simple RC Circuits 11
- 1.3.3 Analysis of Single Impedance Arcs 12

1.4 Selected Applications of IS 16

Chapter 2 Theory	21
Ian D. Raistrick, J. Ross Macdonald, and Donald R. Franceschetti	21

2.1 The Electrical Analogs of Physical and Chemical Processes 21

- 2.1.1 Introduction 21
- 2.1.2 The Electrical Properties of Bulk Homogeneous Phases 23
 - 2.1.2.1 Introduction 23
 - 2.1.2.2 Dielectric Relaxation in Materials with a Single Time Constant 23
 - 2.1.2.3 Distributions of Relaxation Times 27
 - 2.1.2.4 Conductivity and Diffusion in Electrolytes 34
 - 2.1.2.5 Conductivity and Diffusion: A Statistical Description 36
 - 2.1.2.6 Migration in the Absence of Concentration Gradients 38
 - 2.1.2.7 Transport in Disordered Media 40
- 2.1.3 Mass and Charge Transport in the Presence of Concentration Gradients 45
 - 2.1.3.1 Diffusion 45
 - 2.1.3.2 Mixed Electronic–Ionic Conductors 49

2.1.4	2.1.3.3 Concentration Polarization 50 Interfaces and Boundary Conditions 51 2.1.4.1 Reversible and Irreversible Interfaces 51 2.1.4.2 Polarizable Electrodes 52 2.1.4.3 Adsorption at the Electrode–Electrolyte Interface 54 2.1.4.4 Charge Transfer at the Electrode–Electrolyte Interface 56
2.1.5	Grain Boundary Effects 60
2.1.6	Current Distribution: Porous and Rough Electrodes—The Effect of Geometry 62 2.1.6.1 Current Distribution Problems 62 2.1.6.2 Rough and Porous Electrodes 63
2.2	Physical and Electrochemical Models 67
2.2.1	The Modeling of Electrochemical Systems 67
2.2.2	Equivalent Circuits 67 2.2.2.1 Unification of Immittance Responses 67 2.2.2.2 Distributed Circuit Elements 69 2.2.2.3 Ambiguous Circuits 75
2.2.3	Modeling Results 79 2.2.3.1 Introduction 79 2.2.3.2 Supported Situations 80 2.2.3.3 Unsupported Situations: Theoretical Models 84 2.2.3.4 Equivalent Network Models 96 2.2.3.5 Unsupported Situations: Empirical and Semiempirical Models 97

Chapter 3 Measuring Techniques and Data Analysis	107
Michael C. H. McKubre, Digby D. Macdonald, Brian Sayers, and J. Ross Macdonald	107

3.1	Impedance Measurement Techniques 107
3.1.1	Introduction 107
3.1.2	Frequency Domain Methods 108 3.1.2.1 Audio Frequency Bridges 108 3.1.2.2 Transformer Ratio Arm Bridges 110 3.1.2.3 Berberian–Cole Bridge 112 3.1.2.4 Considerations of Potentiostatic Control 115 3.1.2.5 Oscilloscopic Methods for Direct Measurement 116 3.1.2.6 Phase-Sensitive Detection for Direct Measurement 118 3.1.2.7 Automated Frequency Response Analysis 119 3.1.2.8 Automated Impedance Analyzers 122 3.1.2.9 The Use of Kramers–Kronig Transforms 124 3.1.2.10 Spectrum Analyzers 126
3.1.3	Time-Domain Methods 128 3.1.3.1 Introduction 128 3.1.3.2 Analog-to-Digital Conversion 129 3.1.3.3 Computer Interfacing 133 3.1.3.4 Digital Signal Processing 135
3.1.4	Conclusions 138
3.2	Commercially Available Impedance Measurement Systems 139
3.2.1	General Measurement Techniques 139 3.2.1.1 Current-to-Voltage (I–E) Conversion Techniques 139 3.2.1.2 Measurements Using 2-, 3-, or 4-Terminal Techniques 144 3.2.1.3 Measurement Resolution and Accuracy 146

	3.2.1.4	Single Sine and FFT Measurement Techniques	148
3.2.2	Electrochemical Impedance Measurement Systems 152		
	3.2.2.1	System Configuration	152
	3.2.2.2	Why Use a Potentiostat?	152
	3.2.2.3	Multi-electrode Techniques	153
	3.2.2.4	Effects of Connections and Input Impedance	154
	3.2.2.5	Verification of Measurement Performance	155
	3.2.2.6	Floating Measurement Techniques	156
	3.2.2.7	Multichannel Techniques	157
3.2.3	Materials Impedance Measurement Systems 157		
	3.2.3.1	System Configuration	157
	3.2.3.2	Measurement of Low Impedance Materials	158
	3.2.3.3	Measurement of High Impedance Materials	158
	3.2.3.4	Reference Techniques	159
	3.2.3.5	Normalization Techniques	159
	3.2.3.6	High Voltage Measurement Techniques	160
	3.2.3.7	Temperature Control	160
	3.2.3.8	Sample Holder Considerations	161
3.3	Data Analysis	161	
3.3.1	Data Presentation and Adjustment 161		
	3.3.1.1	Previous Approaches	161
	3.3.1.2	Three-Dimensional Perspective Plotting	162
	3.3.1.3	Treatment of Anomalies	164
3.3.2	Data Analysis Methods 166		
	3.3.2.1	Simple Methods	166
	3.3.2.2	Complex Nonlinear Least Squares	167
	3.3.2.3	Weighting	168
	3.3.2.4	Which Impedance-Related Function to Fit?	169
	3.3.2.5	The Question of "What to Fit" Revisited	169
	3.3.2.6	Deconvolution Approaches	169
	3.3.2.7	Examples of CNLS Fitting	170
	3.3.2.8	Summary and Simple Characterization Example	172

Chapter 4 | Applications of Impedance Spectroscopy**175**

4.1	Characterization of Materials	175
	N. Bonanos, B. C. H. Steele, and E. P. Butler	175
4.1.1	Microstructural Models for Impedance Spectra of Materials 175	
	4.1.1.1	Introduction 175
	4.1.1.2	Layer Models 176
	4.1.1.3	Effective Medium Models 183
	4.1.1.4	Modeling of Composite Electrodes 191
4.1.2	Experimental Techniques 194	
	4.1.2.1	Introduction 194
	4.1.2.2	Measurement Systems 195
	4.1.2.3	Sample Preparation: Electrodes 199
	4.1.2.4	Problems Associated with the Measurement of Electrode Properties 201
4.1.3	Interpretation of the Impedance Spectra of Ionic Conductors and Interfaces 203	
	4.1.3.1	Introduction 203
	4.1.3.2	Characterization of Grain Boundaries by IS 204

4.1.3.3	Characterization of Two-Phase Dispersions by IS	215
4.1.3.4	Impedance Spectra of Unusual Two-Phase Systems	218
4.1.3.5	Impedance Spectra of Composite Electrodes	219
4.1.3.6	Closing Remarks	224
4.2	Characterization of the Electrical Response of Wide-Range-Resistivity Ionic and Dielectric Solid Materials by Immittance Spectroscopy	224
J. Ross Macdonald 224		
4.2.1	Introduction	224
4.2.2	Types of Dispersive Response Models: Strengths and Weaknesses	225
4.2.2.1	Overview	225
4.2.2.2	Variable-Slope Models	226
4.2.2.3	Composite Models	227
4.2.3	Illustration of Typical Data Fitting Results for an Ionic Conductor	233
4.2.4	Utility and Importance of Poisson–Nernst–Planck (PNP) Fitting Models	239
4.2.4.1	Introduction	239
4.2.4.2	Selective History of PNP Work	240
4.2.4.3	Exact PNP Responses at All Four Immittance Levels	243
4.3	Solid-State Devices	247
William B. Johnson, Wayne L. Worrell, Gunnar A. Niklasson, Sara Malmgren, Maria Strømme, and S. K. Sundaram 247		
4.3.1	Electrolyte–Insulator–Semiconductor (EIS) Sensors	248
4.3.2	Solid Electrolyte Chemical Sensors	254
4.3.3	Photoelectrochemical Solar Cells	258
4.3.4	Impedance Response of Electrochromic Materials and Devices	263
4.3.4.1	Introduction	263
4.3.4.2	Materials	265
4.3.4.3	Theoretical Background	266
4.3.4.4	Experimental Results on Single Materials	270
4.3.4.5	Experimental Results on Electrochromic Devices	280
4.3.4.6	Conclusions and Outlook	280
4.3.5	Fast Processes in Gigahertz–Terahertz Region in Disordered Materials	281
4.3.5.1	Introduction	281
4.3.5.2	Lunkenheimer–Loidl Plot and Scaling of the Processes	282
4.3.5.3	Dynamic Processes	285
4.3.5.4	Final Remarks	292
4.4	Corrosion of Materials	292
Michael C. H. McKubre, Digby D. Macdonald, and George R. Engelhardt 292		
4.4.1	Introduction	292
4.4.2	Fundamentals	293
4.4.3	Measurement of Corrosion Rate	293
4.4.4	Harmonic Analysis	297

4.4.5	Kramers–Kronig Transforms	303
4.4.6	Corrosion Mechanisms	306
4.4.6.1	Active Dissolution	306
4.4.6.2	Active–Passive Transition	308
4.4.6.3	The Passive State	312
4.4.7	Reaction Mechanism Analysis of Passive Metals	324
4.4.7.1	The Point Defect Model	324
4.4.7.2	Prediction of Defect Distributions	334
4.4.7.3	Optimization of the PDM on the Impedance Data	335
4.4.7.4	Sensitivity Analysis	339
4.4.7.5	Extraction of PDM Parameters from EIS Data	343
4.4.7.6	Simplified Method for Expressing the Impedance of a Stationary Barrier Layer	349
4.4.7.7	Comparison of Simplified Model with Experiment	355
4.4.7.8	Summary and Conclusions	359
4.4.8	Equivalent Circuit Analysis	360
4.4.8.1	Coatings	365
4.4.9	Other Impedance Techniques	366
4.4.9.1	Electrochemical Hydrodynamic Impedance (EHI)	366
4.4.9.2	Fracture Transfer Function (FTF)	368
4.4.9.3	Electrochemical Mechanical Impedance	370
4.5	Electrochemical Power Sources	373
	Evgenij Barsoukov, Brian E. Conway, Wendy G. Pell, and Norbert Wagner	373
4.5.1	Special Aspects of Impedance Modeling of Power Sources	373
4.5.1.1	Intrinsic Relation between Impedance Properties and Power Source Performance	373
4.5.1.2	Linear Time-Domain Modeling Based on Impedance Models: Laplace Transform	374
4.5.1.3	Expressing Electrochemical Model Parameters in Electrical Terms, Limiting Resistances, and Capacitances of Distributed Elements	376
4.5.1.4	Discretization of Distributed Elements, Augmenting Equivalent Circuits	379
4.5.1.5	Nonlinear Time-Domain Modeling of Power Sources Based on Impedance Models	381
4.5.1.6	Special Kinds of Impedance Measurement Possible with Power Sources: Passive Load Excitation and Load Interrupt	384
4.5.2	Batteries	386
4.5.2.1	Generic Approach to Battery Impedance Modeling	386
4.5.2.2	Lead–Acid Batteries	396
4.5.2.3	Nickel–Cadmium Batteries	398
4.5.2.4	Nickel–Metal Hydride Batteries	399
4.5.2.5	Li-ion Batteries	400
4.5.3	Nonideal Behavior Developed in Porous Electrode Supercapacitors	406
4.5.3.1	Introduction	406
4.5.3.2	Equivalent Circuits and Representation of Electrochemical Capacitor Behavior	409
4.5.3.3	Impedance and Voltammetry Behavior of Brush Electrode Models of Porous Electrodes	417
4.5.3.4	Deviations from Ideality	421

4.5.4	Fuel Cells	424
4.5.4.1	Introduction	424
4.5.4.2	Alkaline Fuel Cells (AFCs)	437
4.5.4.3	Polymer Electrolyte Fuel Cells (PEFCs)	443
4.5.4.4	The Solid Oxide Fuel Cells (SOFCs)	454

4.6 Dielectric Relaxation Spectroscopy 459

C. M. Roland 459

4.6.1	Introduction	459
4.6.2	Dielectric Relaxation	460
4.6.2.1	Ion Conductivity	462
4.6.2.2	Dielectric Modulus	467
4.6.2.3	Use of Impedance Function in Dielectric Relaxation Experiments	467
4.6.2.4	Summary	472

4.7 Electrical Structure of Biological Cells and Tissues: Impedance Spectroscopy, Stereology, and Singular Perturbation Theory 472

Robert S. Eisenberg 472

4.7.1	Impedance Spectroscopy of Biological Structures Is a Platform Resting on Four Pillars	474
4.7.1.1	Anatomical Measurements	474
4.7.1.2	Impedance Measurements	475
4.7.1.3	Measurement Difficulties	476
4.7.1.4	Future Measurements	476
4.7.1.5	Interpreting Impedance Spectroscopy	477
4.7.1.6	Fitting Data	477
4.7.1.7	Results	477
4.7.1.8	Future Perspectives	478

Acronym and Model Definitions 479**References 481****Index 517**

Preface to the Third Edition

Previous editions of this book have been used by generations of researchers as primary reference on impedance spectroscopy. This third extended edition updates the book to include the results of the last 10 years of research as well as to add new areas that are now extensively using impedance spectroscopy.

Changes have most affected Section 3.2 where a completely new overview of commercial impedance systems is provided and Section 4.2.4, which includes completely new section dedicated to Poisson–Nernst–Planck (PNP) fitting models. Significant additions have been done to Section 4.3.4 that covers impedance response of electrochromic materials and devices and Section 4.3.5 that covers fast processes in gigahertz–terahertz region in disordered materials. A new Section 4.4.7 is now covering in detail reaction mechanism analysis of passive metals. Chapters on electrochemical power sources, supercapacitors, and fuel cells have been significantly refreshed and augmented with new materials.

Two completely new topics have been added to the book, with Section 4.6 covering dielectric relaxation spectroscopy of polymers and Section 4.7 on impedance spectroscopy of electrical structure of biological cells and tissues. Authors are confident that with these updates and additions, this book will give a solid foundation for anyone entering the field of impedance spectroscopy and will serve as a trusted reference to those already well on the way.

October 2016

EVGENIJ BARSOUKOV
Dallas, Texas

Preface to the Second Edition

The principal audience that will benefit from this book are M.Sc. and Ph.D. students with specialization in physical chemistry, electrochemistry, or physics, as well as researchers and engineers in the field of electrochemistry, particularly in areas of semiconductors, solid electrolytes, corrosion, solid state devices, and electrochemical power sources. Impedance spectroscopy has firmly established itself as one of the most informative and irreplaceable investigation methods in these areas of research. In addition, the book provides a valuable source of information and resource for established researchers and engineers working in one or more of the said fields.

The book should enable understanding of the method of impedance spectroscopy in general, as well as detailed guidance in its application in all mentioned areas. It is the only book in existence that brings expert reviews of all main areas of impedance applications together. This book covers all subjects needed by a researcher to identify whether impedance spectroscopy may be a solution to his/her particular needs and to explain how to set up experiments and how to analyze their results. It includes both theoretical considerations and the know-how needed to begin work immediately. For most subjects covered, theoretical considerations dealing with modeling, equivalent circuits, and equations in the complex domain are provided. Best measurement methods for particular systems are discussed, and sources of errors are identified along with suggestions for improvement. The extensive references to scientific literature provided in the book will give a solid foundation in the state of the art, leading to fast growth from a qualified beginner to an expert.

The previous edition of this book became a standard textbook on impedance spectroscopy. This second extended edition updates the book to include the results of the last two decades of research and adds new areas where impedance spectroscopy has gained importance. Most notably, it includes completely new chapters on batteries, supercapacitors, fuel cells and photochromic materials. A new chapter on commercially available measurements systems reflects the reality of impedance spectroscopy as a mainstream research tool.

July 2004

EVGENIJ BARSOUKOV
Dallas, Texas

Preface to the First Edition

Impedance spectroscopy (IS) appears destined to play an important role in fundamental and applied electrochemistry and materials science in the coming years. In a number of respects, it is the method of choice for characterizing the electrical behavior of systems in which the overall system behavior is determined by a number of strongly coupled processes, each proceeding at a different rate. With the current availability of commercially made, high-quality impedance bridges, and automatic measuring equipment covering the millihertz to megahertz frequency range, it appears certain that impedance studies will become increasingly popular as more and more electrochemists, materials scientists, and engineers understand the theoretical basis for impedance spectroscopy and gain skill in the interpretation of impedance data.

This book is intended to serve as a reference and/or textbook on the topic of IS, with special emphasis on its application to solid materials. The goal was to produce a text that would be useful to both the novice and the expert in IS. To this end, the book is organized so that each individual chapter stands on its own. It is intended to be useful to the materials scientist or electrochemist, student, or professional, who is planning an IS study of a solid-state system and who may have had little previous experience with impedance measurements. Such a reader will find an outline of basic theory, various applications of IS, and a discussion of experimental methods and data analysis, with examples and appropriate references. It is hoped that the more advanced reader will also find this book valuable as a review and summary of the literature up to the time of writing, with a discussion of current theoretical and experimental issues. A considerable amount of the material in the book is applicable not only to solid ionic systems but also to the electrical response of liquid electrolytes as well as to solid ones, to electronic as well as to ionic conductors, and even to dielectric response.

The novice should begin by reading Chapter 1, which presents a broad overview of the subject and provides the background necessary to appreciate the power of the technique. He/she might then proceed to Chapter 4, where many different applications of the technique are presented. The emphasis in this chapter is on presenting specific applications of IS rather than extensive reviews; details of how and why the technique is useful in each area are presented. To gain a fuller appreciation of IS, the reader could then proceed to Chapters 2 and 3, which present the theory and measuring and analysis techniques.

For someone already familiar with IS, this text will also be useful. For those familiar with one application of the technique, the book will provide both a convenient source for the theory of IS, as well as illustrations of applications in areas possibly unfamiliar to the reader. For the theorist who has studied IS, the applications discussed in Chapter 4 pose questions the experimentalist would like answered; for the experimentalist, Chapters 2 and 3 offer different (and better!) methods to analyze IS data. All readers should benefit from the presentation of theory, experimental data, and analysis methods in one source. It is our hope that this widened perspective of the field will lead to a more enlightened and therefore broadened use of IS.

In format and approach, the present book is intended to fall somewhere between the single-author (or few-author) text and the "monograph" of many authors and as many chapters. Although the final version is the product of 10 authors' labors, considerable effort has been made to divide the writing tasks so as to produce a unified presentation with consistent notation and terminology and a minimum of repetition. To help reduce repetition, all authors had available to them copies of Sections 1.1–1.3, 2.2,

and 3.2 at the beginning of their writing of the other sections. We believe that whatever repetition remains is evidence of the current importance to IS of some subjects, and we feel that the discussion of these subjects herein from several different viewpoints is worthwhile and will be helpful to the readers of the volume.

March 1987

J. ROSS MACDONALD
Chapel Hill, North Carolina

Contributors to the Third Edition

Dr. Evgenij Barsoukov
Head of Algorithm Development
Battery Management Systems
Texas Instruments Inc.
Dallas, TX, USA

Prof. N. Bonanos
Senior Research Scientist
Materials Research Department
Risø National Laboratory
Roskilde, Denmark

E. P. Butler
ALCAN International Ltd.
Banbury Laboratories
Banbury, TN, USA

Prof. Brian E. Conway
Department of Chemistry
University of Ottawa
Ottawa, Ontario, Canada

Robert S. Eisenberg
Bard Endowed Professor and Chairman
Department of Molecular Biophysics & Physiology
Rush University
Chicago, IL, USA

George R. Engelhardt
Senior Corrosion Scientist
OLI Systems, Inc.
Cedar Knolls, NJ, USA

Prof. Donald R. Franceschetti
Department of Physics
The University of Memphis
Memphis, TN, USA

Dr. William B. Johnson
W. L. Gore & Associates
Elkton, MD, USA

Prof. Digby D. Macdonald
Department of Nuclear Engineering
University of California at Berkeley
Berkeley, CA, USA

Dr. Sara Malmgren
Swedish Energy Agency,
Eskilstuna, Sweden

Dr. J. Ross Macdonald
(William R. Kenan, Jr., Professor of Physics,
Emeritus)
Department of Physics and Astronomy
University of North Carolina
Chapel Hill, NC, USA

Dr. Michael C. H. McKubre
Director, SRI International
Menlo Park, CA, USA

Prof. Gunnar A. Niklasson
Department of Engineering Sciences
The Ångstrom Laboratory
Uppsala University
Uppsala, Sweden

Dr. Wendy G. Pell
Department of Chemistry
University of Ottawa
Ottawa, Ontario, Canada

Ian D. Raistrick
Los Alamos National Laboratory
Los Alamos, NM, USA

C. M. Roland
Naval Research Lab
Washington, DC, USA

Brian Sayers
Product Manager, Solartron Analytical
Hampshire, UK

B. C. H. Steele
Department of Metallurgy and Materials Science
Imperial College of Science and Technology
London, UK

Maria Strømme
Professor of Nanotechnology
Head Nanotechnology and Functional
Materials Division
The Ångström Laboratory
Uppsala University
Uppsala, Sweden

S. K. Sundaram
Inamori Professor of MSE
Kazuo Inamori School of Engineering
New York State College of Ceramics
Alfred University
Alfred, NY, USA

Dr. Norbert Wagner
Deutsches Zentrum für Luft- und Raumfahrt e.V.
(German Aerospace Center)
Institut für Technische Thermodynamik
Stuttgart, Germany

Wayne L. Worrell
Department of Materials Science and Engineering
University of Pennsylvania
Philadelphia, PA, USA

Fundamentals of Impedance Spectroscopy

J. Ross Macdonald¹ and William B. Johnson²

¹(William R. Kenan, Jr., Professor of Physics, Emeritus), Department of Physics and Astronomy, University of North Carolina, Chapel Hill, NC, USA

²W. L. Gore & Associates, Elkton, MD, USA

1.1 BACKGROUND, BASIC DEFINITIONS, AND HISTORY

1.1.1 The Importance of Interfaces

Since the end of World War II, we have witnessed the development of solid-state batteries as rechargeable energy storage devices with high power density; a revolution in high-temperature electrochemical sensors in environmental, industrial, and energy efficiency control; and the introduction of fuel cells to avoid the Carnot inefficiency inherent in noncatalytic energy conversion. The trend away from corrosive aqueous solutions and toward solid-state technology was inevitable in electrochemical energy engineering, if only for convenience and safety in bulk handling. As a consequence, the characterization of systems with solid-solid or solid-liquid interfaces, often involving solid ionic conductors and frequently operating well above room temperature, has become a major concern of electrochemists and materials scientists.

At an interface, physical properties—crystallographic, mechanical, compositional, and, particularly, electrical—change precipitously, and heterogeneous charge distributions (polarizations) reduce the overall electrical conductivity of a system. Proliferation of interfaces is a distinguishing feature of solid-state electrolytic cells, where not only is the junction between electrode and electrolyte considerably more complex than in aqueous cells but also the solid electrolyte is commonly polycrystalline. Each interface will polarize in its unique way when the system is subjected to an applied potential difference. The rate at which a polarized region will change when the applied voltage is reversed is characteristic of the type of interface: slow for chemical reactions at the triple-phase contacts between atmosphere, electrode, and electrolyte, appreciably faster across grain boundaries in the polycrystalline electrolyte. The emphasis in electrochemistry has consequently shifted from a time/concentration dependency to frequency-related phenomena, a trend toward small-signal alternating current (ac) studies. Electrical double layers and their inherent capacitive reactances are characterized by their relaxation times or more realistically by the distribution of their relaxation times. The electrical response of a heterogeneous cell can vary substantially depending on the species of charge present, the microstructure of the electrolyte, and the texture and nature of the electrodes.

Impedance spectroscopy (IS) is a relatively new and powerful method of characterizing many of the electrical properties of materials and their interfaces with electronically conducting electrodes. It may be used to investigate the dynamics of bound or mobile charge in the bulk or interfacial regions of

any kind of solid or liquid material: ionic, semiconducting, mixed electronic–ionic, and even insulators (dielectrics). Although we shall primarily concentrate in this monograph on solid electrolyte materials—amorphous, polycrystalline, and single crystal in form—and on solid metallic electrodes, reference will be made, where appropriate, to fused salts and aqueous electrolytes and to liquid metal and high-molarity aqueous electrodes as well. We shall refer to the experimental cell as an electrode–material system. Similarly, although much of the present work will deal with measurements at room temperature and above, a few references to the use of IS well below room temperature will also be included. A list of acronym and model definitions appears at the end of this work.

In this chapter we aim to provide a working background for the practical materials scientist or engineer who wishes to apply IS as a method of analysis without needing to become a knowledgeable electrochemist. In contrast to the subsequent chapters, the emphasis here will be on practical, empirical interpretations of materials problems, based on somewhat oversimplified electrochemical models. We shall thus describe approximate methods of data analysis of IS results for simple solid-state electrolyte situations in this chapter and discuss more detailed methods and analyses later. Although we shall concentrate on intrinsically conductive systems, most of the IS measurement techniques, data presentation methods, and analysis functions and methods discussed herein apply directly to lossy dielectric materials as well.

1.1.2 The Basic Impedance Spectroscopy Experiment

Electrical measurements to evaluate the electrochemical behavior of electrode and/or electrolyte materials are usually made with cells having two identical electrodes applied to the faces of a sample in the form of a cylinder or parallelepiped. However, if devices such as chemical sensors or living cells are investigated, this simple symmetrical geometry is often not feasible. Vacuum, a neutral atmosphere such as argon, or an oxidizing atmosphere is variously used. The general approach is to apply an electrical stimulus (a known voltage or current) to the electrodes and observe the response (the resulting current or voltage). It is virtually always assumed that the properties of the electrode–material system are time invariant and it is one of the basic purposes of IS to determine these properties, their interrelations, and their dependences on such controllable variables as temperature, oxygen partial pressure, applied hydrostatic pressure, and applied static voltage or current bias.

A multitude of fundamental microscopic processes take place throughout the cell when it is electrically stimulated and, in concert, lead to the overall electrical response. These include the transport of electrons through the electronic conductors, the transfer of electrons at the electrode–electrolyte interfaces to or from charged or uncharged atomic species that originate from the cell materials and its atmospheric environment (oxidation or reduction reactions), and the flow of charged atoms or atom agglomerates via defects in the electrolyte. The flow rate of charged particles (current) depends on the ohmic resistance of the electrodes and the electrolyte and on the reaction rates at the electrode–electrolyte interfaces. The flow may be further impeded by band structure anomalies at any grain boundaries present (particularly if second phases are present in these regions) and by point defects in the bulk of all materials. We shall usually assume that the electrode–electrolyte interfaces are perfectly smooth, with a simple crystallographic orientation. In reality of course, they are jagged, full of structural defects and electrical short and open circuits, and they often contain a host of adsorbed and included foreign chemical species that influence the local electric field.

There are three different types of electrical stimuli that are used in IS. First, in transient measurements a step function of voltage [$V(t) = V_0$ for $t > 0$, $V(t) = 0$ for $t < 0$] may be applied at $t = 0$ to the system, and the resulting time-varying current $i(t)$ measured. The ratio $V_0/i(t)$, often called the indicial impedance or the time-varying resistance, measures the impedance resulting from the step function voltage perturbation at the electrochemical interface. This quantity, although easily defined, is not the usual impedance referred to in IS. Rather, such time-varying results are generally Fourier or Laplace transformed into the frequency domain, yielding a frequency-dependent impedance. If a Fourier transform is used, a distortion arising because of the non-periodicity of excitation should be corrected by using windowing. Such transformation is only valid when $|V_0|$ is sufficiently small that system response is linear. The advantages of this approach are that it is experimentally easily accomplished and that

the independent variable, voltage, controls the rate of the electrochemical reaction at the interface. Disadvantages include the need to perform integral transformation of the results and the fact that the signal-to-noise ratio differs between different frequencies, so the impedance may not be well determined over the desired frequency range.

Second, a signal $v(t)$ composed of random (white) noise may be applied to the interface and measure the resulting current. Again, one generally Fourier transforms the results to pass into the frequency domain and obtain an impedance. This approach offers the advantage of fast data collection because only one signal is applied to the interface for a short time. The technique has the disadvantages of requiring true white noise and then the need to carry out a Fourier analysis. Often a microcomputer is used for both the generation of white noise and the subsequent analysis. Using a sum of well-defined sine waves as excitation instead of white noise offers the advantage of a better signal-to-noise ratio for each desired frequency and the ability to analyze the linearity of system response.

Third, the most common and standard one is to measure impedance by applying a single-frequency voltage or current to the interface and measuring the phase shift and amplitude, or real and imaginary parts, of the resulting current at that frequency using either analog circuit or FFT analysis of the response. Commercial instruments (see Section 3.2) are available, which measure the impedance as a function of frequency automatically in the frequency ranges of about 1 mHz to 1 MHz and which are easily interfaced to laboratory microcomputers. The advantages of this approach are the availability of these instruments and the ease of their use, as well as the fact that the experimentalist can achieve a better signal-to-noise ratio in the frequency range of most interest.

In addition to these three approaches, one can combine them to generate other types of stimuli. The most important of these, ac polarography, combines the first and third techniques by simultaneously applying a linearly varying unipolar transient signal and a much smaller single-frequency sinusoidal signal (Smith [1966]).

Any intrinsic property that influences the conductivity of an electrode–material system, or an external stimulus, can be studied by IS. The parameters derived from an IS spectrum fall generally into two categories: (i) those pertinent only to the material itself, such as conductivity, dielectric constant, mobilities of charges, equilibrium concentrations of the charged species, and bulk generation–recombination rates, and (ii) those pertinent to an electrode–material interface, such as adsorption–reaction rate constants, capacitance of the interface region, and diffusion coefficient of neutral species in the electrode itself.

It is useful and not surprising that modern advances in electronic automation have included IS. Sophisticated automatic experimental equipment has been developed to measure and analyze the frequency response to a small-amplitude ac signal between about 10^{-4} and $>10^6$ Hz, interfacing its results to computers and their peripherals (see Section 3.1). A revolution in the automation of an otherwise difficult measuring technique has moved IS out of the academic laboratory and has begun to make it a technique of importance in the areas of industrial quality control of paints, emulsions, electroplating, thin-film technology, materials fabrication, mechanical performance of engines, corrosion, and so on.

Although this book has a strong physicochemical bias, the use of IS to investigate polarization across biological cell membranes has been pursued by many investigators since 1925. Details and discussion of the historical background of this important branch of IS are given in the books of Cole [1972] and Schanne and Ruiz-Ceretti [1978].

1.1.3 Response to a Small-Signal Stimulus in the Frequency Domain

A monochromatic signal $v(t) = V_m \sin(\omega t)$, involving the single-frequency $\nu \equiv \omega/2\pi$, is applied to a cell, and the resulting steady-state current $i(t) = I_m \sin(\omega t + \theta)$ measured. Here θ is the phase difference between the voltage and the current; it is zero for purely resistive behavior. The relation between system properties and response to periodic voltage or current excitation is very complex in the time domain. In general, the solution of a system of differential equations is required. Response of capacitive and inductive elements is given as $i(t) = [dv(t)/dt]C$ and $v(t) = [di(t)/dt]L$ correspondingly, and combination of many such elements can produce an intractable complex problem.

Fortunately, the use of Fourier transformation allows one to simplify significantly the mathematical treatment of this system. The aforementioned differential equations can be transformed into $I(j\omega) = C\cdot\omega\cdot j\cdot V(j\omega)$ and $I(j\omega) = V(j\omega)/(L\cdot\omega\cdot j)$. Here $j \equiv \sqrt{-1}$, which is also often denoted in the literature as “*i*.” For the case of sine-wave excitation as aforementioned, Fourier transforms of voltage and current $V(j\omega)$ and $I(j\omega)$ become $V_m\pi$ and $I_m\pi\cdot\exp(\theta j)$, respectively. It can be easily seen that in frequency domain voltage/current relations can be rearranged to a form similar to Ohm’s law for dc current: $I(j\omega) = V(j\omega)/Z(j\omega)$ where for capacitance the complex quantity $Z(j\omega)$ is $1/(C\cdot\omega\cdot j)$ and for inductance $Z(j\omega)$ is $L\cdot\omega\cdot j$. The complex quantity $Z(j\omega)$ is defined as the “impedance function,” and its value at a particular frequency is “impedance” of the electric circuit. For simplicity, $Z(j\omega)$ is usually written as just $Z(\omega)$. Because of this Ohm’s law-like relationship between complex current and voltage, the impedance of a circuit with multiple elements is calculated using the same rules as with multiple resistors, which greatly simplifies calculations.

Impedance may be defined not only for discrete systems but also for arbitrary distributed systems as the Fourier transform of the differential equation, defining the voltage response divided by the Fourier transform of the periodic current excitation: $Z(j\omega) = F\{v(t)\}/F\{i(t)\}$. Here the $F\{\}$ operator denotes a Fourier transform. However, Fourier transformation only reduces differential equations to simple Ohm’s law-like form under conditions of linearity, causality, and stationarity of the system; therefore impedance is properly defined only for systems satisfying these conditions.

The concept of electrical impedance was first introduced by Oliver Heaviside in the 1880s and was soon developed in terms of vector diagrams and complex representation by A. E. Kennelly and especially C. P. Steinmetz. Impedance is a more general concept than resistance because it takes phase differences into account, and it has become a fundamental and essential concept in electrical engineering. IS is thus just a specific branch of the tree of electrical measurements. The magnitude and direction of a planar vector in a right-hand orthogonal system of axes can be expressed by the vector sum of the components a and b along the axes, that is, by the complex number $Z = a + jb$. The imaginary number $j \equiv \sqrt{-1} \equiv \exp(j\pi/2)$ indicates an anticlockwise rotation by $\pi/2$ relative to the x -axis. Thus, the real part of Z , a , is in the direction of the real axis x , and the imaginary part b is along the y -axis. An impedance $Z(\omega) = Z' + jZ''$ is such a vector quantity and may be plotted in the plane with either rectangular or polar coordinates, as shown in Figure 1.1.1. Here the two rectangular coordinate values are clearly

$$\text{Re}(Z) \equiv Z' = |Z| \cos(\theta) \quad \text{and} \quad \text{Im}(Z) \equiv Z'' = |Z| \sin(\theta) \quad (1)$$

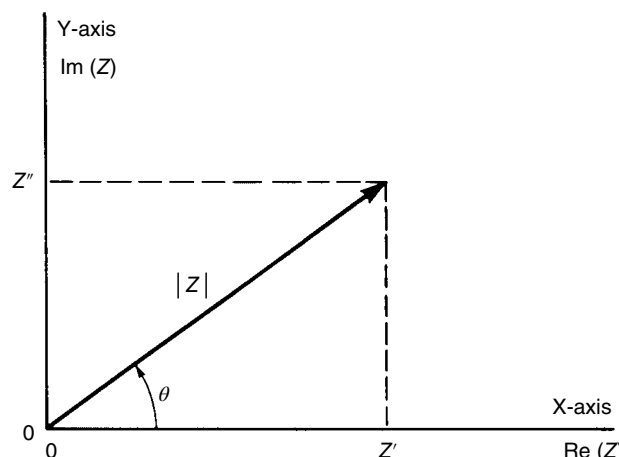


FIGURE 1.1.1 The impedance Z plotted as a planar vector using rectangular and polar coordinates.

with the phase angle

$$\theta = \tan^{-1} \left(\frac{Z''}{Z'} \right) \quad (2)$$

and the modulus

$$|Z| = \left[(Z')^2 + (Z'')^2 \right]^{1/2} \quad (3)$$

This defines the Argand diagram or complex plane, widely used in both mathematics and electrical engineering. In polar form, Z may now be written as $Z(\omega) = |Z| \exp(j\theta)$, which may be converted to rectangular form through the use of the Euler relation $\exp(j\theta) = \cos(\theta) + j \sin(\theta)$. It will be noticed that the original time variations of the applied voltage and the resulting current have disappeared and the impedance is time invariant (provided the system itself is time invariant).

In general, Z is frequency dependent, as defined previously. Conventional IS consists of the (nowadays often automated) measurement of Z as a function of ν or ω over a wide frequency range. It is from the resulting structure of the $Z(\omega)$ versus ω response that one derives information about the electrical properties of the full electrode–material system.

For nonlinear systems, that is, most real electrode–material systems, IS measurements in either the time or the frequency domain are useful and meaningful in general only for signals of magnitude such that the overall electrode–material system response is electrically linear. This requires that the response to the sum of two separate input-measuring signals applied simultaneously be the sum of the responses of the signals applied separately. A corollary is that the application of a monochromatic signal, one involving $\sin(\omega t)$, results in no, or at least negligible, generation of harmonics in the output, that is, components with frequencies $n\nu$ for $n = 2, 3, \dots$. Both solid and liquid electrochemical systems tend to show strong nonlinear behavior, especially in their interfacial response, when applied voltages or currents are large. But so long as the applied potential difference (p.d.) amplitude V_m is less than the thermal voltage, $V_T \equiv RT/F \equiv kT/e$, about 25 mV at 25°C, it can be shown that the basic differential equations that govern the response of the system become linear to an excellent approximation. Here k is Boltzmann's constant, T the absolute temperature, e the proton charge, R the gas constant, and F the faraday. Thus if the applied amplitude V_m is appreciably less than V_T , the system will respond linearly. Note that in the linear regime, it is immaterial as far as the determination of $Z(\omega)$ is concerned whether a known $\nu(\omega t)$ is applied and the current measured or a known $i(\omega t)$ applied and the resulting voltage across the cell measured. When the system is nonlinear, this reciprocity no longer holds.

1.1.4 Impedance-Related Functions

The impedance has frequently been designated as the ac impedance or the complex impedance. Both these modifiers are redundant and should be omitted. Impedance without a modifier always means impedance applied in the frequency domain and usually measured with a monochromatic signal. Even when impedance values are derived by Fourier transformation from the time domain, the impedance is still defined for a set of individual frequencies and is thus an ac impedance in character.

Impedance is by definition a complex quantity and is only real when $\theta = 0$ and thus $Z(\omega) = Z'(\omega)$, that is, for purely resistive behavior. In this case the impedance is completely frequency independent. When Z' is found to be a variable function of frequency, the Kronig–Kramers (Hilbert integral transform) relations (Macdonald and Brachman [1956]), which holistically connect real and imaginary parts with each other, ensure that Z'' (and θ) cannot be zero over all frequencies but must vary with frequency as well. Thus it is only when $Z(\omega) = Z'$, independent of frequency, so $Z' = R$, an ordinary linear resistance, that $Z(\omega)$ is purely real.

There are several other measured or derived quantities related to impedance that often play important roles in IS. All of them may be generically called immittances. First is the admittance,

TABLE 1.1.1 Relations between the Four Basic Immittance Functions

	M	Z	Y	ϵ
M	M	μZ	μY^{-1}	ϵ^{-1}
Z	$\mu^{-1}M$	Z	Y^{-1}	$\mu^{-1}\epsilon^{-1}$
Y	μM^{-1}	Z^{-1}	Y	$\mu\epsilon$
ϵ	M^{-1}	$\mu^{-1}Z^{-1}$	$\mu^{-1}Y$	ϵ

$\mu \equiv j\omega C_c$, where C_c is the capacitance of the empty cell.

$Y \equiv Z^{-1} \equiv Y' + jY''$. In the complex domain where ν , i , and Z are all taken complex, we can write $\nu = Zi$ or alternatively $i = Y\nu$. It is also customary in IS to express Z and Y in terms of resistive and capacitance components as $Z = R_s(\omega) - jX_s(\omega)$ and $Y = G_p(\omega) + jB_p(\omega)$, where the reactance $X_s \equiv [\omega C_s(\omega)]^{-1}$ and the susceptance $B_p \equiv \omega C_p(\omega)$. Here the subscripts s and p stand for "series" and "parallel."

The other two quantities are usually defined as the modulus function $M = j\omega C_c Z = M' + jM''$ and the complex dielectric constant or dielectric permittivity $\epsilon = M^{-1} \equiv Y/(j\omega C_c) \equiv \epsilon' - j\epsilon''$. In these expressions $C_c \equiv \epsilon_0 A_c / l$ is the capacitance of the empty measuring cell of electrode area A_c and electrode separation length l . The quantity ϵ_0 is the dielectric permittivity of free space, 8.854×10^{-12} F/m. The dielectric constant ϵ is often written elsewhere as ϵ^* or $\hat{\epsilon}$ to denote its complex character. Here we shall reserve the superscript asterisk to denote complex conjugation; thus $Z^* = Z' - jZ''$. The interrelations between the four immittance functions are summarized in Table 1.1.1.

The modulus function $M = \epsilon^{-1}$ was apparently first introduced by Schrama [1957] and has been used appreciably by McCrum *et al.* [1967], Macedo *et al.* [1972b], and Hodge *et al.* [1975, 1976]. The use of the complex dielectric constant goes back much further but was particularly popularized by the work of Cole and Cole [1941], who were the first to plot ϵ in the complex plane.

Some authors have used the designation *modulus spectroscopy* to denote small-signal measurement of M versus ν or ω . Clearly, one could also define admittance and dielectric permittivity spectroscopy. The latter is just another way of referring to ordinary dielectric constant and loss measurements. Here we shall take the general term *IS* to include all these other very closely related approaches. Thus IS also stands for *immittance spectroscopy*. The measurement and use of the complex $\epsilon(\omega)$ function is particularly appropriate for dielectric materials, those with very low or vanishing conductivity, but all four functions are valuable in IS, particularly because of their different dependence on and weighting with frequency.

1.1.5 Early History

IS is particularly characterized by the measurement and analysis of some or all of the four impedance-related functions Z , Y , M , and ϵ , and the plotting of these functions in the complex plane. Such plotting can, as we shall see, be very helpful in interpreting the small-signal AC response of the electrode-material system being investigated. Historically, the use of Z and Y in analyzing the response of electrical circuits made up of lumped (ideal) elements (R , L , and C) goes back to the beginning of the discipline of electrical engineering. An important milestone for the analysis of real systems, that is, ones distributed in space, was the plotting by Cole and Cole [1941] of ϵ' and ϵ'' for dielectric systems in the complex plane, now known as a Cole–Cole plot, an adaption at the dielectric constant level of the circle diagram of electrical engineering (Carter [1925]), exemplified by the Smith–Chart impedance diagram (Smith [1939, 1944]). Further, Z and Y have been widely used in theoretical treatments of semiconductor and ionic systems and devices since at least 1947 (see, e.g., Randles [1947], Jaffé [1952], Chang and Jaffé [1952], Macdonald [1953a], and Friauf [1954]). Complex plane plots have sometimes been called Nyquist diagrams. This is a misnomer, however, since Nyquist diagrams refer to transfer function (three- or four-terminal) response, while conventional complex plane plots involve only two-terminal input immittances.

On the experimental side, one should mention the early work of Randles and Somerton [1952] on fast reactions in supported electrolytes; no complex plane plotting appeared here. But complex plane plotting of G_p/ω versus C_p was used by Macdonald [1955] for experimental results on photoconducting alkali halide single crystals. Apparently the first plotting of impedance in the impedance plane for aqueous electrolytes was that of Sluyters [1960] (theory) and Sluyters and Oomen [1960] (experiment). The use of admittance plane plotting for accurate conductivity determination of solid electrolytes was introduced by Bauerle [1969], the first important paper to deal with IS for ionic solids directly. Since then, there have been many pertinent theoretical and experimental papers dealing with IS and complex plane plots. Many of them will be cited later, and we conclude this short survey of early history pertinent to IS with the mention of three valuable reviews: Sluyters-Rehbach and Sluyters [1970], Armstrong *et al.* [1978], and Archer and Armstrong [1980]. The first and second of these deal almost entirely with liquid electrolytes but are nevertheless somewhat pertinent to IS for solids.

1.2 ADVANTAGES AND LIMITATIONS

Although we believe that the importance of IS is demonstrated throughout this monograph by its usefulness in the various applications discussed, it is of some value to summarize the matter briefly here. IS is becoming a popular analytical tool in materials research and development because it involves a relatively simple electrical measurement that can readily be automated and whose results may often be correlated with many complex materials variables: from mass transport, rates of chemical reactions, corrosion, and dielectric properties, to defects, microstructure, and compositional influences on the conductance of solids. IS can predict aspects of the performance of chemical sensors and fuel cells, and it has been used extensively to investigate membrane behavior in living cells. It is useful as an empirical quality control procedure, yet it can contribute to the interpretation of fundamental electrochemical and electronic processes.

A flow diagram of a general characterization procedure using IS is presented in Figure 1.2.1. Here CNLS stands for complex nonlinear least squares fitting (see Section 3.2.2). Experimentally obtained impedance data for a given electrode–materials system may be analyzed by using an exact mathematical model based on a plausible physical theory that predicts theoretical impedance $Z_t(\omega)$ or by a relatively empirical equivalent circuit whose impedance predictions may be denoted by $Z_{ec}(\omega)$. In case either of the relatively empirical equivalent circuit or of the exact mathematical model, the parameters can be estimated and the experimental $Z_e(\omega)$ data compared with either the predicted equivalent circuit impedance $Z_{ec}(\omega)$ or the theoretical impedance $Z_t(\omega)$. Such fitting is most accurately accomplished by the CNLS method described and illustrated in Section 3.2.2.

An analysis of the charge transport processes likely to be present in an experimental cell (the physical model) will often suggest an equivalent circuit of ideal resistors and capacitors (even inductors or negative capacitors in some instances) and may account adequately for the observed IS response. For example, Schouler *et al.* [1983] found that the effects of densification by sintering a polycrystalline electrolyte will reduce the magnitude of the resistance across the grain boundaries and simultaneously decrease the surface area associated with the interface capacitance. These components will clearly be electrically in parallel in this situation. Their combination will be in series with other similar subcircuits representing such processes as the ionization of oxygen at the electrodes.

In another example, the oxidation–reduction reaction for the Zn^{2+} couple in an aqueous solution with a dropping mercury electrode (Sluyters and Oomen [1960]) can be represented by a reaction resistance R_R , arising from the transfer of electrons between the electrode and the solution, in parallel with a capacitor C_R associated with the space-charge diffuse double layer near the electrode surface. It is not difficult to calculate the theoretical impedance for such a circuit in terms of the parameters R_R and C_R . From an analysis of the parameter values in a plausible equivalent circuit as the experimental conditions are changed, the materials system can be characterized by analysis of its observed impedance response, leading to estimates of its microscopic parameters such as charge mobilities, concentrations, and electron transfer reaction rates.

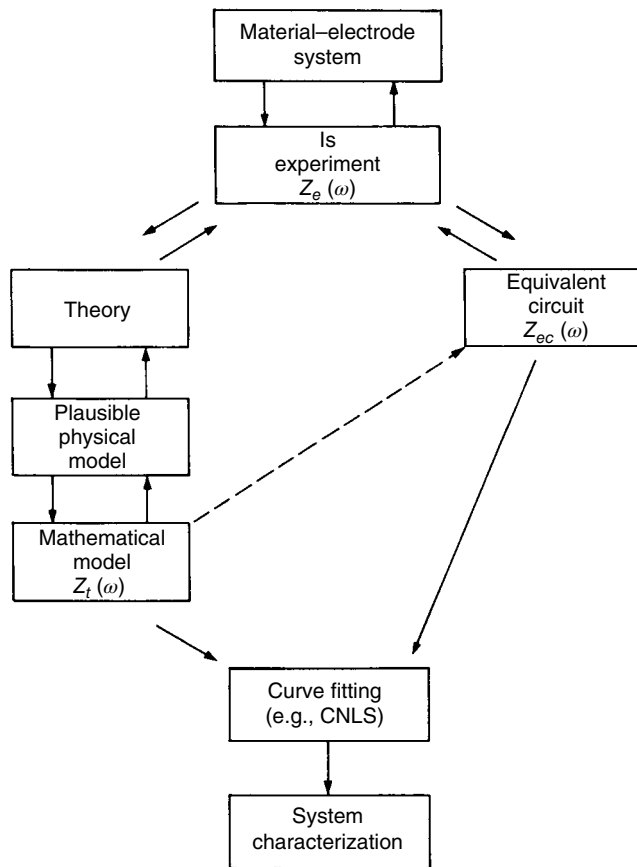


FIGURE 1.2.1 Flow diagram for the measurement and characterization of a material-electrode system.

The disadvantages of IS are primarily associated with possible ambiguities in interpretation. An important complication of analyses based on an equivalent circuit (e.g., Bauerle [1969]) is that ordinary ideal circuit elements represent ideal lumped-constant properties. Inevitably, all electrolytic cells are distributed in space, and their microscopic properties may be also independently distributed. Under these conditions, ideal circuit elements may be inadequate to describe the electrical response. Thus, it is often found that $Z_e(\omega)$ cannot be well approximated by the impedance of an equivalent circuit involving only a finite number of ordinary lumped-constant elements. It has been observed by many in the field that the use of distributed impedance elements (e.g., constant-phase elements (CPEs) (see Section 2.2.2.2)) in the equivalent circuit greatly aids the process of fitting observed impedance data for a cell with distributed properties.

There is a further serious potential problem with equivalent circuit analysis, not shared by the direct comparison with $Z_t(\omega)$ of a theoretical model: what specific equivalent circuit out of an infinity of possibilities should be used if one is necessary? An equivalent circuit involving three or more circuit elements can often be rearranged in various ways and still yield exactly the same $Z_{ec}(\omega)$. For the different interconnections, the values of the elements will have to be different to yield the same $Z_{ec}(\omega)$ for all ω , but an essential ambiguity is present. An example is presented in Figure 1.2.2. In these circuits the impedance Z_i is arbitrary and may be made up of either lumped elements, distributed elements, or a combination of these types. Examples of other circuits that demonstrate this type of ambiguity will be presented in Section 2.2.2.3. Which one of two or more circuits that all yield exactly the same $Z_{ec}(\omega)$ for all ω should be used for physicochemical analysis and interpretation? This question cannot be answered for a single set of $Z_e(\omega)$ data alone. An approach to its solution can only be made by employing

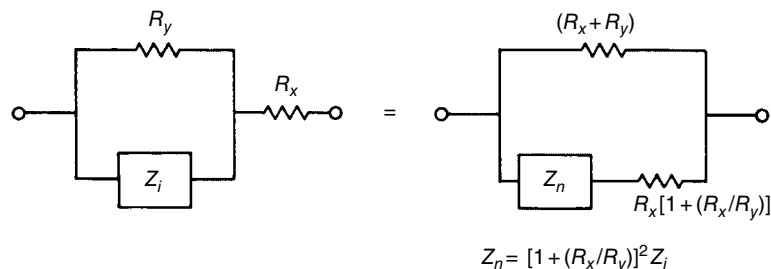


FIGURE 1.2.2 An example of different circuits with the same overall impedance at all frequencies.

physical intuition and by carrying out several $Z_e(\omega)$ sets of measurements with different conditions, as discussed in Section 2.2.2.3.

1.2.1 Differences between Solid-State and Aqueous Electrochemistry

The electrochemist who works with aqueous electrolytes has available to him/her at least one major stratagem not accessible to those who work with solid electrolytes. If he/she is interested in the interfacial behavior of a particular charged species, he/she is usually free to add to the solution an excess of a second electrolyte, the ions of which are neither adsorbed nor react at the interface but which by sheer numbers are able to screen the interior of the electrolyte from any electric field and cause nearly all the potential drop to occur within a few angstroms of the interface. The investigator is thus (at least by assumption) freed from having to take into account the effect of a nonuniform electric field on the transport of the electroactive species through the bulk electrolyte and need not (again by assumption) puzzle over the fraction of the applied signal that directly governs the exchange of ions or electrons between the electrode surface and the adjacent layer of electrolyte. The added electrolyte species that thus simplifies the interpretation of the experimental results is termed the *indifferent* or *supporting electrolyte*, and systems thus prepared are termed *supported systems*. Solid electrolytes must necessarily be treated as unsupported systems, even though they may display some electrical characteristics usually associated with supported ones. The distinction between unsupported and supported situations is a crucial one for the interpretation of IS results.

It is thus unfortunate that there has been a tendency among some workers in the solid electrolyte field to take over many of the relatively simple theoretical results derived for supported conditions and use them uncritically in unsupported situations, where the supported models and formulas rarely apply adequately. For example, the expression for the Warburg impedance for a redox reaction in a supported situation is often employed in the analysis of data on unsupported situations where the parameters involved are quite different (see, e.g., Sections 2.2.3.2 and 2.2.3.3).

There are a few other important distinctions between solid and liquid electrolytes. While liquid electrolytes and many solid electrolytes have negligible electronic conductivity, quite a number of solid electrolytes can exhibit substantial electronic conductivity, especially for small deviations from strict stoichiometric composition. Solid electrolytes may be amorphous, polycrystalline, or single crystal, and charges of one sign may be essentially immobile (except possibly for high temperatures and over long time spans). On the other hand, all dissociated charges in a liquid electrolyte or fused salt are mobile, although the ratio between the mobilities of positive and negative charges may differ appreciably from unity. Further, in solid electrolytes, mobile ions are considered to be able to move as close to an electrode as permitted by ion-size steric considerations. But in liquid electrolytes, a compact inner or Stern layer composed of solvent molecules, for example, H_2O , immediately next to the electrode, is usually present. This layer may often be entirely devoid of ions and only has some in it when the ions are specifically adsorbed at the electrode or react there. Thus capacitative effects in electrode interface regions can be considerably different between solid and liquid electrolyte systems.

1.3 ELEMENTARY ANALYSIS OF IMPEDANCE SPECTRA

1.3.1 Physical Models for Equivalent Circuit Elements

A detailed physicoelectrical model of all the processes that might occur in investigations on an electrode–material system may be unavailable, premature, or perhaps too complicated to warrant its initial use. One then tries to show that the experimental impedance data $Z_e(\omega)$ may be well approximated by the impedance $Z_{ec}(\omega)$ of an equivalent circuit made up of ideal resistors, capacitors, perhaps inductances, and possibly various distributed circuit elements. In such a circuit a resistance represents a conductive path, and a given resistor in the circuit might account for the bulk conductivity of the material or even the chemical step associated with an electrode reaction (see, e.g., Randles [1947] or Armstrong *et al.* [1978]). Similarly, capacitances and inductances will be generally associated with space-charge polarization regions and with specific adsorption and electrocrystallization processes at an electrode. It should be pointed out that ordinary circuit elements, such as resistors and capacitors, are always considered as lumped-constant quantities that involve ideal properties. But all real resistors are of finite size and are thus disturbed in space; they therefore always involve some inductance, capacitance, and time delay of response as well as resistance. These residual properties are unimportant over wide frequency ranges and therefore usually allow a physical resistor to be well approximated in an equivalent circuit by an ideal resistance, one which exhibits only resistance over all frequencies and yields an immediate rather than a delayed response to an electrical stimulus.

The physical interpretation of the distributed elements in an equivalent circuit is somewhat more elusive. They are, however, essential in understanding and interpreting most impedance spectra. There are two types of distributions with which we need to be concerned. Both are related, but in different ways, to the finite spatial extension of any real system. The first is associated directly with nonlocal processes, such as diffusion, which can occur even in a completely homogeneous material, one whose physical properties, such as charge mobilities, are the same everywhere. The other type, exemplified by the CPE, arises because microscopic material properties are themselves often distributed. For example, the solid electrode–solid electrolyte interface on the microscopic level is not the often presumed smooth and uniform surface. It contains a large number of surface defects such as kinks, jags, and ledges, local charge inhomogeneities, two- and three-phase regions, adsorbed species, and variations in composition and stoichiometry. Reaction resistance and capacitance contributions differ with electrode position and vary over a certain range around a mean, but only their average effects over the entire electrode surface can be observed. The macroscopic impedance that depends, for example, on the reaction rate distribution across such an interface is measured as an average over the entire electrode. We account for such averaging in our usual one-dimensional treatments (with the dimension of interest perpendicular to the electrodes) by assuming that pertinent material properties are continuously distributed over a given range from minimum to maximum values. For example, when a given time constant, associated with an interface or bulk processes, is thermally activated with a distribution of activation energies, one passes from a simple ideal resistor and capacitor in parallel or series to a distributed impedance element, for example, the CPE, which exhibits more complicated frequency response than a simple undistributed RC time constant process (Macdonald [1984, 1985a, c, d], McCann and Badwal [1982]).

Similar property distributions occur throughout the frequency spectrum. The classical example for dielectric liquids at high frequencies is the bulk relaxation of dipoles present in a pseudoviscous liquid. Such behavior was represented by Cole and Cole [1941] by a modification of the Debye expression for the complex dielectric constant and was the first distribution involving the important CPE, defined in Section 2.1.2.3. In normalized form the complex dielectric constant for the Cole–Cole distribution may be written as

$$\frac{\epsilon - \epsilon_\infty}{\epsilon_s - \epsilon_\infty} = \left[1 + (j\omega\tau_0)^{1-\alpha} \right]^{-1} \quad (1)$$

where ϵ is the dielectric constant, ϵ_s and ϵ_∞ the static and high-frequency-limiting dielectric constants, τ_0 the mean relaxation time, and α a parameter describing the width of the material property distribution (in this case a distribution of dielectric relaxation times in frequency space).

1.3.2 Simple RC Circuits

Figure 1.3.1 shows two RC circuits common in IS and typical Z and Y complex plane responses for them. The response of Figure 1.3.1a is often present (if not always measured) in IS results for solids and liquids. Any electrode–material system in a measuring cell has a geometrical capacitance $C_g \equiv C_\infty = C_1$ and a bulk resistance $R_b \equiv R_\infty = R_1$ parallel with it. These elements lead to the time constant $\tau_D = R_\infty C_\infty$, the dielectric relaxation time of the basic material. Usually, τ_D is the smallest time constant of interest in IS experiments. It is often so small ($< 10^{-7}$ s) that for the highest angular frequency applied, ω_{\max} , the condition $\omega_{\max} \tau_D \ll 1$ is satisfied and little or nothing of the impedance plane curve of Figure 1.3.1b is seen. It should be noted, however, that lowering the temperature will often increase τ_D and bring the bulk arc within the range of measurement. Since the peak frequency of the complete semicircle in Figure 1.3.1b, ω_p , satisfies $\omega_p \tau_D = 1$, it is only when $\omega_{\max} \tau_D \gg 1$ that nearly the full curve in Figure 1.3.1b is obtained. Although the bulk resistance is often not appreciably distributed, particularly for single crystals, when it is actually distributed, the response of the circuit often leads to a partial semicircle in the Z plane, one whose center lies below the real axis, instead of a full semicircle with its center on the real axis. Since this distributed-element situation is frequently found for processes in the $\omega \ll \tau_D^{-1}$ frequency range, however, we shall examine in detail one simple representation of it shortly.

Besides $R_1 = R_\infty$ and $C_1 = C_\infty$, one often finds parallel R_1, C_1 response associated with a heterogeneous electrode reaction. For such a case we would set $R_1 = R_R$ and $C_1 = C_R$, where R_R is a reaction

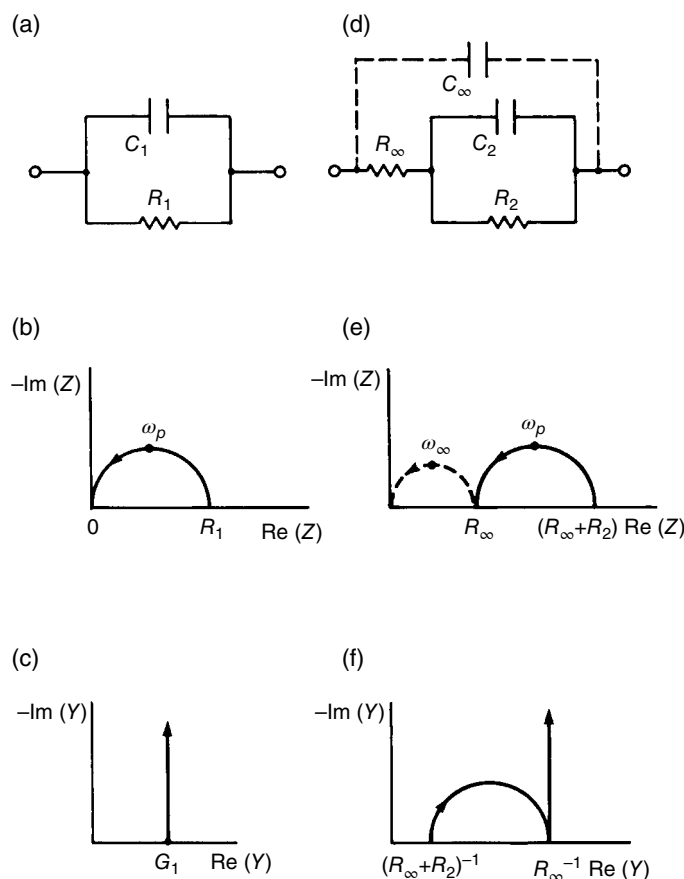


FIGURE 1.3.1 (a) and (d) show two common RC circuits, (b) and (e) show their impedance plane plots, and (c) and (f) show their admittance plane plots. Arrows indicate the direction of increasing frequency.

resistance and C_R is the diffuse double-layer capacitance of the polarization region near the electrode in simplest cases. The circuit of Figure 1.3.1d combines the aforementioned possibilities when $R_2 = R_R$ and $C_2 = C_R$. The results shown in Figure 1.3.1e and f are appropriate for the well-separated time constants, $R_\infty R_\infty \ll R_2 C_2$. It is also possible that a parallel RC combination can result from specific adsorption at an electrode, possibly associated with delayed reaction processes. The response arising from R_∞ and C_∞ in Figure 1.3.1e is shown dotted to remind one that it often occurs in too high a frequency region to be easily observed. Incidentally, we shall always assume that the capacitance and resistance of leads to the measuring cell have been subtracted out (e.g., by using the results of a preliminary calibration of the system with the cell empty or shorted) so that we always deal only with the response of the material-electrode system alone.

In the complex plane plots, the arrows show the direction of increasing frequency. Further, $G_1 \equiv R_1^{-1}$, $G_\infty \equiv R_\infty^{-1}$, $G_2 \equiv R_2^{-1}$. Because IS results usually involve capacitance and rarely involve inductance, it has become customary to plot impedance in the $-\text{Im}(Z)$, $\text{Re}(Z)$ plane rather than the $\text{Im}(Z)$, $\text{Re}(Z)$ plane, thereby ensuring that the vast majority of all curves fall in the first quadrant, as in Figure 1.3.1b. This procedure is also equivalent to plotting $Z^* = Z' - iZ''$ rather than Z , so we can alternatively label the ordinate $\text{Im}(Z^*)$ instead of $-\text{Im}(Z)$. Both choices will be used in the rest of this work.

The admittance of the parallel RC circuit of Figure 1.3.1a is just the sum of the admittances of the two elements, that is,

$$Y_a = G_1 + j\omega C_1 \quad (2)$$

It immediately follows that

$$Z_a = Y_a^{-1} = \frac{R_1}{R_1 Y_a} = \frac{R_1}{1 + j\omega R_1 C_1} \quad (3)$$

This result can be rationalized by multiplying $[1 - j\omega R_1 C_1]$, the complex conjugate of $[1 + j\omega R_1 C_1]$, to both numerator and denominator. The response of the Figure 1.3.1a circuit is particularly simple when it is plotted in the Y plane, as in Figure 1.3.1c. To obtain the overall admittance of the Figure 1.3.1d circuit, it is simplest to add R_∞ to the expression for Z_a previously mentioned with $R_1 \rightarrow R_2$ and $C_1 \rightarrow C_2$, convert the result to an admittance by inversion, and then add the $j\omega C_\infty$ admittance. The result is

$$Y_d = j\omega C_\infty + \frac{1 + j\omega R_2 C_2}{(R_2 + R_\infty) + j\omega C_2 R_2 R_\infty}. \quad (4)$$

Although complex plane data plots, such as those in Figure 1.3.1b, c, e, and f in which frequency is an implicit variable, can show response patterns that are often very useful in identifying the physicochemical processes involved in the electrical response of the electrode–material system, the absence of explicit frequency-dependent information is frequently a considerable drawback. Even when frequency values are shown explicitly in such two-dimensional (2D) plots, it is usually found that with either equal intervals in frequency or equal frequency ratios, the frequency points fall very nonlinearly along the curves. The availability of computerized plotting procedures makes the plotting of all relevant information in a single graph relatively simple. For example, three-dimensional (3D) perspective plotting, as introduced by Macdonald *et al.* [1981], displays the frequency dependence along a new $\log(v)$ axis perpendicular to the complex plane (see Section 3.2). For multi-time-constant response in particular, this method is particularly appropriate. The full response information can alternately be plotted with orthographic rather than perspective viewing.

1.3.3 Analysis of Single Impedance Arcs

Analysis of experimental data that yield a full semicircular arc in the complex plane, such as that in Figure 1.3.1b, can provide estimates of the parameters R_1 and C_1 and hence lead to quantitative estimates

of conductivity, faradic reaction rates, relaxation times, and interfacial capacitance (see detailed discussion in Section 2.2.3.3). In practice, however, experimental data are only rarely found to yield a full semicircle with its center on the real axis of the complex plane. There are three common perturbations that may still lead to at least part of a semicircular arc in the complex plane:

1. The arc does not pass through the origin, either because there are other arcs appearing at higher frequencies or because $R_\infty > 0$.
2. The center of an experimental arc is frequently displaced below the real axis because of the presence of distributed elements in the material-electrode system. Similar displacements may also be observed in any of the other complex planes plots (Y , M , or ϵ). The relaxation time τ is then not single-valued but is distributed continuously or discretely around a mean, $\tau_m = \omega_m^{-1}$. The angle θ by which such a semicircular arc is depressed below the real axis is related to the width of the relaxation time distribution and as such is an important parameter.
3. Arcs can be substantially distorted by other relaxations whose mean time constants are within two orders of magnitude or less of that for the arc under consideration. Many of the spectra shown in following chapters involve overlapping arcs.

We shall begin by considering simple approximate analysis methods of data yielding a single, possibly depressed, arc. Suppose that IS data plotted in the impedance plane (actually the Z^* plane) show typical depressed circular arc behavior, such as that depicted in Figure 1.3.2. Here we have included R_∞ but shall initially ignore any effect of C_∞ . We have defined some new quantities in this figure that will be used in the analysis to yield estimates of the parameters R_∞ , $R_R \equiv R_0 - R_\infty$, τ_R , and the fractional exponent ψ_{ZC} , parameters that fully characterize the data when they are well represented by the distributed-element ZARC impedance expression (see Section 2.2.2.2):

$$Z - R_\infty \equiv Z_{ZARC} \equiv (R_0 - R_\infty) I_Z \quad (5)$$

where

$$I_Z \equiv [1 + (j\omega\tau_R)^{\psi_{ZC}}]^{-1} \equiv [1 + (js)^{\psi_{ZC}}]^{-1} \quad (6)$$

Here $s \equiv \omega\tau_R$ is a normalized frequency variable and I_Z is the normalized, dimensionless form of Z_{ZARC} . Notice that it is exactly the same as the similarly normalized Cole-Cole dielectric response

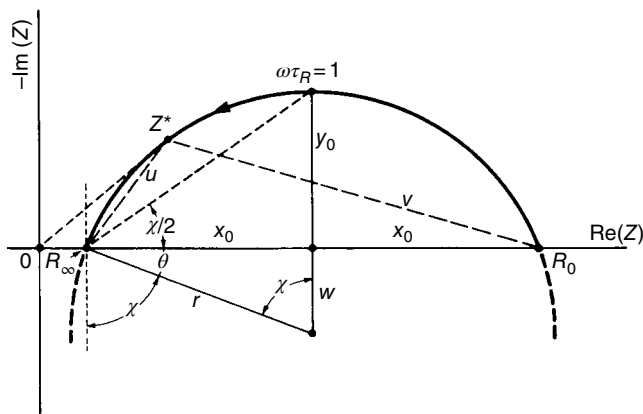


FIGURE 1.3.2 Impedance plane plot for a depressed circular arc showing definitions of quantities used in its analysis.

function of Eq. (1) when we set $\psi_{ZC} = 1 - \alpha$. We can also alternatively write the ZARC impedance as the combination of the resistance R_R in parallel with the CPE impedance Z_{CPE} (see Section 2.2.2.2). The CPE admittance is (Macdonald [1984])

$$Y_{CPE} = Z_{CPE}^{-1} \equiv A_0(j\omega)^{\psi_{ZC}} \equiv (j\omega\tau_R)^{\psi_{ZC}} \quad (7)$$

Then Eq. (5) may be expressed as

$$Z_{ZARC} = \frac{R_R}{1 + B_0(j\omega)^{\psi_{ZC}}}, \quad (8)$$

where $B_0 \equiv \tau_R^{\psi_{ZC}} \equiv R_R A_0$. The fractional exponent ψ_{ZC} satisfies $0 \leq \psi_{ZC} \leq 1$.

Let us start by considering two easy-to-use approximate methods of estimating the parameters, methods often adequate for initial approximate characterization of the response. The estimates obtained by these approaches may also be used as initial values for the more complicated and much more accurate CNLS method described and illustrated in Section 3.2.2. Note that the single $R_R C_R$ situation, where $\theta = 0$ and $\psi_{ZC} = 1$, is included in the analysis described in the succeeding text.

From the Figure 1.3.2, $-Z''$ reaches its maximum value, y_0 , when $\omega = \omega_m = \tau_R^{-1}$ and thus $s = 1$. At this point the half-width of the arc on the real axis is $Z' - R_\infty = x_0 \equiv R_R/2$. Now from the data, the complex plane plot, and estimated values of x_0 , y_0 , and ω_m , one can immediately obtain estimates of R_∞ , R_0 , R_R , and τ_R . In order to obtain θ , one must, of course, find the direction of the circle center. The easiest graphical method is to draw on the Z^* plane plot several lines perpendicular to the semicircle; the center will be defined by their intersection. Two other more accurate approaches will be described in the succeeding text. Incidentally, when there is more than one arc present and there is some overlap that distorts the right, lower-frequency side of the arc, the present methods can still be used without appreciable loss of accuracy, provided overlap distortion is only significant for $\omega < \omega_m$, that is, on the right side of the center of the left arc. Then all parameters should be estimated from the left side of the arc, that is, for $\omega \geq \omega_m$. A similar approach may be used when data are available only for $\omega \leq \omega_m$. From Figure 1.3.2 and Eq. (5), we readily find that $\theta = \pi/2 - \chi \equiv (\pi/2)(1 - \psi_{ZC})$; thus when $\psi_{ZC} = 1$ there is no depression and one has simple single-time-constant ($\tau_R \equiv R_R C_R$) Debye response with $A_0 \equiv C_R$. When $\psi_{ZC} < 1$, $\tau_R = (R_R A_0)^{1/\psi_{ZC}}$, but an ideal C_R capacitor cannot be directly defined, reflecting the distributed nature of the response.

The rest of the analysis proceeds as follows. First, one may obtain an estimate of ψ_{ZC} from the θ value using $\psi_{ZC} = 1 - 2\theta/\pi$. But a superior alternative to first obtaining θ by finding the circle center approximately is to use the values of x_0 and y_0 defined on the Figure 1.3.2. For simplicity, it will be convenient to define

$$q \equiv (\omega\tau_R)^{\psi_{ZC}} \equiv (s)^{\psi_{ZC}} \quad (9)$$

$$\chi \equiv \frac{\pi}{2} - \theta \equiv \frac{\pi}{2}\psi_{ZC} \quad (10)$$

and note that

$$x_0 \equiv \frac{R_0 - R_\infty}{2} \equiv \frac{R_R}{2} \quad (11)$$

We may now rewrite Eq. (6) for I_Z as

$$I_Z(q, \chi) = \frac{[1 + q \cos(\chi)] - jq \sin(\chi)}{1 + 2q \cos(\chi) + q^2} \quad (12)$$

For $q = 1$, the peak point, one finds

$$I_Z(1, \chi) = 0.5 \left[1 - j \tan\left(\frac{\chi}{2}\right) \right] \quad (13)$$

Let us further define for later use the quantity

$$\psi_J \equiv \tan\left(\frac{\chi}{2}\right) = \tan\left(\frac{\pi\psi_{ZC}}{4}\right) \quad (14)$$

Now in general from Eq. (12), we may write

$$-\frac{I''_Z}{I'_Z} = \frac{q \sin(\chi)}{1 + q \cos(\chi)} \quad (15)$$

which becomes, for $q = 1$,

$$\left. -\frac{I''_Z}{I'_Z} \right|_{q=1} = \frac{y_0}{x_0} = \tan\left(\frac{\chi}{2}\right) \equiv \psi_J \quad (16)$$

Thus from knowledge of y_0 and x_0 , one can immediately calculate χ , ψ_J , ψ_{ZC} , and θ . For completeness, it is worth giving expressions for w and r that follow from the Figure 1.3.2. One finds

$$w = x_0 \operatorname{ctn}(\chi) = x_0 \tan(\theta) = x_0 \frac{1 - \psi_J^2}{2\psi_J} \quad (17)$$

and

$$r - y_0 + w = x_0 \csc(\chi) = x_0 \sec(\theta) = x_0 \frac{1 + \psi_J^2}{2\psi_J} \quad (18)$$

Another method of obtaining ψ_{ZC} and θ is to first estimate R_∞ and plot $(Z - R_\infty)^{-1}$ in the Y plane. Then a spur inclined at the angle $[(\pi/2) - \theta] = \chi$ will appear whose $\omega \rightarrow 0$ intercept is $(R_0 - R_\infty)^{-1}$. A good estimate of ψ_{ZC} may be obtained from the χ value when the spur is indeed a straight line. Now at $\omega = \omega_m$, it turns out that $B_0 \omega_m^{\psi_{ZC}} = 1$. Thus one may obtain an estimate of B_0 from $\omega_m^{-\psi_{ZC}}$. Then $\tau_R = B_0^{1/\psi_{ZC}} = \omega_m^{-1}$ and $A_0 = R_R^{-1} B_0$. Thus all the parameters of interest have then been estimated.

The aforementioned simple methods of estimating ψ_{ZC} depend only on the determination of x_0 and y_0 from the impedance complex plane arc or on the use of a few points in the admittance plane. Although they are often adequate for initial investigation, it is worth mentioning a relatively simple alternative procedure that can be used to test the appropriateness of Eqs. (5) and (6) and obtain the parameter estimates of interest. Consider the point Z^* on the arc of Figure 1.3.2, a point marking a specific value of Z . It follows from this figure and Eq. (5) that $Z^* - R_\infty = (R_0 - R_\infty) I_Z^* \equiv u$ and $R_0 - Z^* = (R_0 - R_\infty)(1 - I_Z^*) \equiv v$. Therefore,

$$\ln\left|\frac{v}{u}\right| = \ln\left|(I_Z^*)^{-1} - 1\right| = \ln(q) = \psi_{ZC}[\ln(\omega) + \ln(\tau_R)] \quad (19)$$

If one assumes that R_0 and R_∞ may be determined adequately from the complex plane plot—not always a valid assumption—then v and u may be calculated from experimental Z data for a variety of frequencies. A plot of $\ln|v/u|$ versus $\ln(\omega)$ will yield a straight line with a slope of ψ_{ZC} and an intercept of $\psi_{ZC} \ln(\tau_R)$, provided Eq. (19) holds. Ordinary linear least squares fitting may then be used to obtain estimates of ψ_{ZC} and $\ln(\tau_R)$.

Although a more complicated nonlinear least squares procedure has been described by Tsai and Whitmore [1982], which allows analysis of two arcs with some overlap, approximate analysis of two or more arcs without much overlap does not require this approach, and CNLS fitting is more appropriate for one or more arcs with or without appreciable overlap when accurate results are needed. In this section we have discussed some simple methods of obtaining approximate estimates of some equivalent

circuit parameters, particularly those related to the common symmetrical depressed arc, the ZARC. An important aspect of material–electrode characterization is the identification of derived parameters with specific physicochemical processes in the system. This matter is discussed in detail in Sections 2.2 and 3.2 and will not be repeated here. Until such identification has been made, however, one cannot relate the parameter estimates, such as R_R , C_R , and ψ_{ZC} , to specific microscopic quantities of interest such as mobilities, reaction rates, and activation energies. It is this final step, however, yielding estimates of parameters immediately involved in the elemental processes occurring in the electrode–material system, which is the heart of characterization and an important part of IS.

1.4 SELECTED APPLICATIONS OF IS

In this section two applications will be presented, illustrating the power of the IS technique when it is applied to two very diverse areas, aqueous electrochemistry and fast ion transport in solids. These particular examples were chosen because of their historical importance and because the analysis in each case is particularly simple. Additional techniques and applications of IS to more complicated systems will be presented in Chapter 4 as well as throughout the text.

The first experimental use of complex plane analysis in aqueous electrochemistry was performed in 1960 (Sluyters and Oomen [1960]). This study is a classic illustration of the ability of IS to establish kinetic parameters in an aqueous electrochemical system. Using a standard hanging mercury drop cell, the impedance response of the $Zn(Hg)/Zn^{2+}$ couple in a $1\text{ M NaClO}_4 + 10^{-3}\text{ M HClO}_4$ electrolyte was examined at 298 K. For this couple, the reaction rate is such that in the frequency range of 20 Hz to 20 kHz, the kinetics of charge transfer is slower than ion diffusion in the electrolyte. The results (Figure 1.4.1) show a single semicircle characteristic of kinetic control by an electrochemical charge transfer step at the electrode–electrolyte interface. The physical model appropriate to this system is the same as that presented in Figure 1.3.1d. The semicircle beginning at the origin in Figure 1.3.1e is not observed in Figure 1.4.1 because the frequency range was limited to below 20 kHz. Thus, in Figure 1.4.1, R_∞ is the solution resistance, R_2 is the charge transfer resistance, and C_2 is the double-layer capacitance.

By solving the standard current–potential equation for an electrochemical reaction (see, e.g., Bard and Faulkner [1980]) under the conditions of kinetic control (i.e., the rate of charge transfer is much

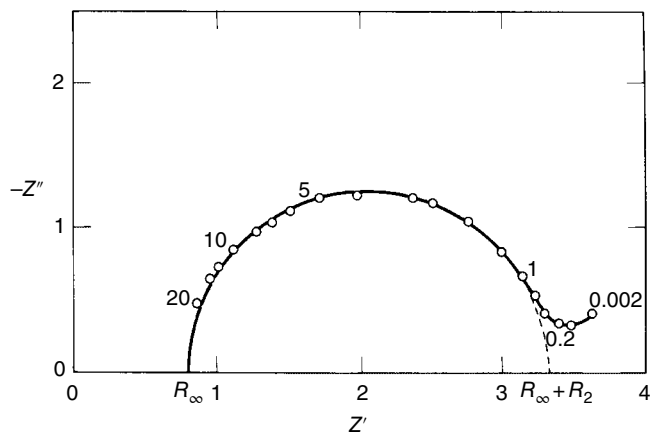


FIGURE 1.4.1 The impedance results of a $Zn(Hg)/Zn^{2+}$ couple in $1\text{ M NaClO}_4 + 10^{-3}\text{ M HClO}_4$ with $C_{Zn} = 8 \times 10^{-6}$ moles/cm³ and $C_{Zn^{2+}} = 8 \times 10^{-6}$. The numbers represent the frequency in kilohertz; the axes are in arbitrary scale units.
Source: Sluyters 1960. Reproduced with permission of John Wiley & Sons, Inc.

slower than diffusive processes in the system), the value of R_2 can be evaluated. For a known concentration of Zn at the amalgam–electrolyte interface, $C_{\text{Zn}(\text{Hg})}$, and a known concentration of Zn^{2+} at the electrolyte–electrode interface, $C_{\text{Zn}^{2+}}$, the value of R_2 is given by Eq. (1):

$$R_2 = \frac{RT}{n^2 F^2 k (C_{\text{Zn}^{2+}})^\alpha (C_{\text{Zn}(\text{Hg})})^{1-\alpha}} \quad (1)$$

where n is the number of electrons transferred, F is Faraday's constant, k is the rate constant for the electrochemical charge transfer reaction, α is the electrochemical transfer coefficient, R is the ideal gas constant, and T is the absolute temperature. When the concentration of Zn in the amalgam is equal to the concentration of Zn ions in the solution, then the rate constant k can be determined. Results at several different equal concentrations of Zn and Zn^{2+} (Table 1.4.1) gave a mean value of $k = 3.26 \times 10^3$ cm/s. By using different concentrations of Zn and Zn^{2+} , the transfer coefficient α (Tables 1.4.2 and 1.4.3)

TABLE 1.4.1 Calculation of Rate Constant of $\text{Zn}(\text{Hg})/\text{Zn}^{2+}$ Couple

$C_{\text{Zn}} = C_{\text{Zn}^{2+}}$ (mol/cm ³)	R_2 ($\Omega\text{-cm}^2$)	$R_2 \times C_{\text{Zn}}$ (mol· Ω /cm)	k (cm/s) ^a
2×10^{-6}	10.17	20.3×10^{-6}	
4	4.95	19.8	
5	4.26	21.3	
8	2.41	19.3	$3.26 \times 10^{-3} \pm 3.6\%$
10	2.13	21.3	
16	1.27	20.3	
16	1.28	20.5	

^aCalculated from the average value of $R_2 \times C_{\text{Zn}} = 20.4 \times 10^{-6}$ by $k = (R_2 C_{\text{Zn}} n^2 F^2)^{-1} RT$ according to Eq. (1).
Source: Sluyters and Oomen [1960].

TABLE 1.4.2 Calculation of Transfer Coefficient α of $\text{Zn}(\text{Hg})/\text{Zn}^{2+}$ Couple

C_{Zn} (mol/cm ³)	$C_{\text{Zn}^{2+}}$ (mol/cm ³)	R_2 ($\Omega\text{-cm}^2$)	$\log R_2$	$-\log C_{\text{Zn}^{2+}}$	α^a
16×16^{-6}	16×10^{-6}	1.28	0.107	4.796	
16	8	2.00	0.301	5.097	0.70
16	4	3.29	0.517	5.398	
16	2	5.37	0.730	5.699	

^aFrom slope of $-\log C_{\text{Zn}^{2+}}$ versus $\log R_2$ plot.
Source: Sluyters and Oomen [1960].

TABLE 1.4.3 Calculation of Transfer Coefficient $1 - \alpha$ of $\text{Zn}(\text{Hg})/\text{Zn}^{2+}$ Couple

$C_{\text{Zn}^{2+}}$ (mol/cm ³)	C_{Zn} (mol/cm ³)	R_2 ($\Omega\text{-cm}^2$)	$\log R_2$	$-\log C_{\text{Zn}}$	$1 - \alpha^a$
16×10^{-6}	16×10^{-6}	1.28	0.107	4.796	
16×10^{-6}	8	1.56	0.193	5.097	0.29
16×10^{-6}	4	1.93	0.286	5.398	

^aFrom slope of $-\log C_{\text{Zn}}$ versus $\log R_2$ plot.
Source: Sluyters and Oomen [1960].

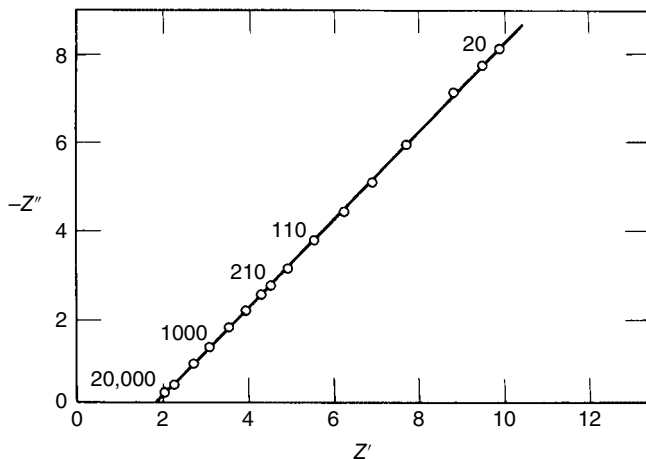


FIGURE 1.4.2 The impedance results of a $\text{Hg}_2^{2+}/\text{Hg}$ couple in 1 M HClO_4 electrolyte with $C_{\text{Hg}^{2+}} = 2 \times 10^{-6} \text{ mol/cm}^3$. The numbers represent the frequency in kilohertz; the axes are in arbitrary scale units. Source: Sluyters 1960. Reproduced with permission of John Wiley & Sons, Inc.

was found to be 0.70. In addition, the value of the double-layer capacitance could be easily determined in each of the experiments.

In a similar experiment, the Hg/Hg^{2+} reaction in 1 M HClO_4 has also been investigated (Sluyters and Oomen [1960]) using IS in the frequency range of 20 Hz to 20 kHz and for concentrations between 2×10^{-6} and $10 \times 10^{-6} \text{ mol/cm}^3 \text{ Hg}^{2+}$. The results (Figure 1.4.2) show linear behavior in the complex plane with an angle of 45° to the real axis. Such a response is indicative of a distributed element as discussed in the previous section. In this case, the system is under diffusion control as the kinetics of the charge transfer at the electrode-electrolyte interface is much faster than the diffusion of the Hg^{2+} ions in the solution. Solution of the diffusion equation with the appropriate boundary conditions under a small AC perturbation gives the diffusional contribution to the impedance in the complex plane as (see Chapter 2 for a detailed discussion)

$$W = \sigma\omega^{-1/2} - j\sigma\omega^{-1/2} \quad (2)$$

where the impedance W is generally called the Warburg impedance, ω is the angular frequency, j is equal to $(-1)^{1/2}$, and σ is a constant given by

$$\sigma = \frac{RT}{n^2 F^2 \sqrt{2}} \left[\frac{1}{C_{\text{Hg}_2^{2+}} (D_{\text{Hg}_2^{2+}})^{1/2}} + \frac{1}{[C_{\text{Hg}} (D_{\text{Hg}})^{1/2}]} \right] \quad (3)$$

where $D_{\text{Hg}_2^{2+}}$ and D_{Hg} are the diffusivity of mercurous ions in solution and mercury in amalgam, respectively, and the other terms are defined as aforementioned. This impedance is to be added (see Sluyters [1960] and the discussion in Chapter 2) in series with R_2 of Figure 1.3.1d. When the impedance of this circuit is plotted in the complex plane, one obtains a semicircle combined with a straight line at an angle of 45° to the real axis. The line, when extended to the real axis, has an intercept of $R_\infty + R_2 - 2\sigma C_{\text{dl}}$. If $2\sigma C_{\text{dl}}$ is small, as in the present case, the semicircle is suppressed and the product of the imaginary part of W , $\text{Im}(W)$, and $\omega^{1/2}$ will be equal to σ at all frequencies.

The experimental results in Figure 1.4.2 are thus consistent with a system under diffusion control. The diffusivity of Hg_2^{2+} ions in solution can be easily calculated (Table 1.4.4) at several different concentrations of Hg_2^{2+} in the solution from the value of σ . No further information can be obtained from this

TABLE 1.4.4 Calculation of Diffusion Coefficient of Hg²⁺ in 1 N NaClO₄

$C_{\text{Hg}_2^{2+}}$ (mol/cm ³)	σ ($\Omega \cdot \text{s}^{-1}/^2\text{cm}^2$) ^a	$D_{\text{Hg}_2^{2+}}$ (cm ² /s) ^b	$R_\infty + R_2$ ($\Omega \cdot \text{cm}^2$)
10×10^{-6}	2.09	0.241×10^{-5}	0.190
5	4.10	0.251	0.188
4	4.99	0.264	0.188
3	6.60	0.268	0.195
2	9.73	0.277	0.193

Source: Sluyters and Oomen [1960].

^a $\sigma = \text{Im}(W)_w^{1/2}$ was found to be independent of frequency within 2%.

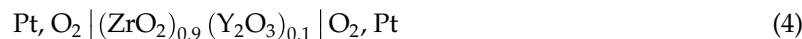
^b $D = [RT(\sigma n^2 F^2 \sqrt{2} C_{\text{Hg}_2^{2+}} C_{\text{Hg}_2^{2+}})^{-1}]^2$ according to Eq. (3) with $1/[C_{\text{Hg}}(D_{\text{Hg}})^{-1/2}] \ll 1/[C_{\text{Hg}_2^{2+}}(D_{\text{Hg}_2^{2+}})^{1/2}]$, as is the case here with a pure Hg electrode.

data because the time constant associated with the kinetics is too fast to be measured at frequencies below 20 kHz.

The frequency range chosen in the aforementioned experiments was dictated by the limited electronics available in 1960 and the cumbersome experimental approach associated with it, which required that the impedance be measured independently at each frequency. The introduction of automated impedance analysis instruments removes this restriction and allows the experimenter to choose the most appropriate frequency range for a given experiment. This choice should be determined by the nature of the interfaces in the experiment and the time constants that are associated with them. For example, corrosion studies, which often involve a slow aqueous diffusion process, generally have relatively large time constants (on the order of 0.1 – 10 s), and thus most impedance studies of corroding systems use frequencies between a few millihertz and 100 kHz. On the other hand, studies of solid ionic conductors require higher frequencies to measure the time constant associated with ionic motion (milli- to microseconds), which is generally smaller than those found in aqueous diffusion processes. Thus, frequencies between a few hertz and 15 MHz are most appropriate here.

That is not to say that the frequency range should always be restricted based upon predetermined expectations. In the aforementioned studies, a wider frequency range would probably have allowed a determination of additional information. For the Zn/Zn²⁺ couple, lower frequencies would have allowed the measurement of the diffusivity of zinc ions in the solution. For the study of the Hg/Hg²⁺ couple, the kinetics of the electrochemical reaction at the interface could have been explored by using higher frequencies. Nevertheless, an understanding of the relationship between the time constant in an experiment and the frequencies with which to measure it provides an intelligent starting point in the choice of the most appropriate frequency range.

Another example that illustrates the utility of IS to solid-state chemists is the application of impedance analysis to zirconia–yttria solid electrolytes (Bauerle [1969]). At elevated temperatures solid solution zirconia–yttria compounds are known to be oxygen-ion conductors, which function by transport of oxygen ions through vacancies introduced by the dopant yttria. By examining cells of the form



using IS, admittance plots were obtained (Figure 1.4.3a). The equivalent circuit proposed to fit this data is shown in Figure 1.4.3b. By a careful examination of the effect of the electrode-area-to-sample-length ratio and by measuring the DC conductivity of the samples, the high-frequency semicircle (the one on the right in Figure 1.4.3a) was ascribed to bulk electrolyte behavior, while the low-frequency semicircle (on the left in Figure 1.4.3a) corresponded to the electrode polarization. In the terminology of Figure 1.4.3b, R_1 and C_1 correspond to electrode polarization phenomena, while R_2 , R_3 , and C_2 describe processes that occur in the bulk of the electrolyte specimen. Furthermore, by varying temperature, oxygen partial pressure, and electrode preparation, the role of each component in the overall conduction

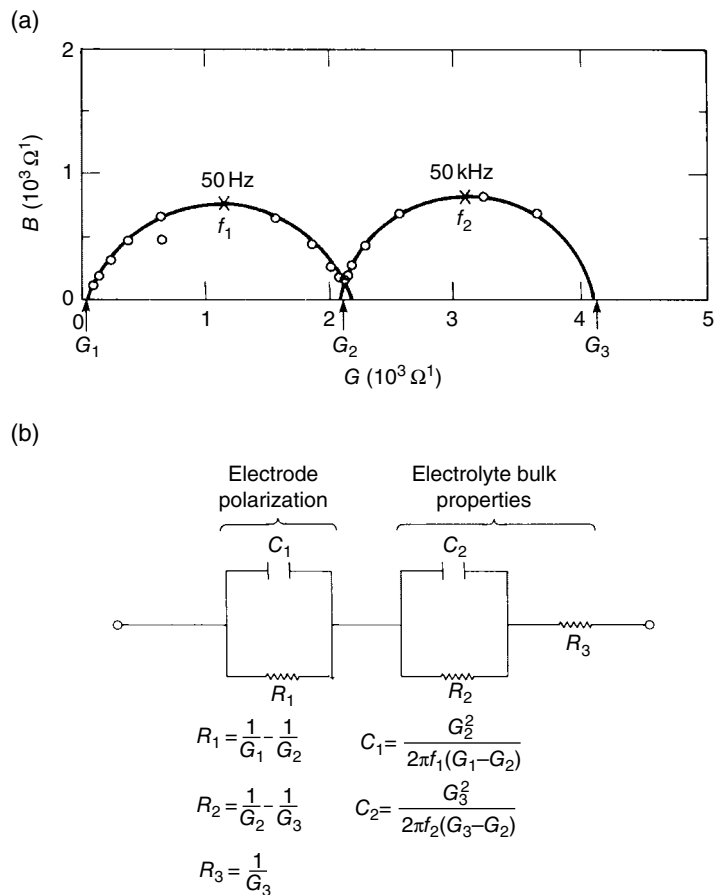
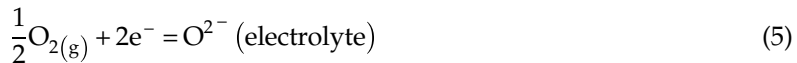


FIGURE 1.4.3 (a) Admittance behavior of the electrochemical cell given in 1.4.4 at 873 K for a specimen with naturally porous electrodes (sputtered Pt). (b) The equivalent circuit for the behavior in part a showing the two impedance elements associated with each semicircle. Source: Bauerle 1969. Reproduced with permission of Elsevier.

mechanism was determined. In particular, R_1 represents an effective resistance for the electrode reaction:



where C_1 is the double-layer capacitance of the electrode; R_2 is a “constriction” or intergranular resistance corresponding to resistance of conduction across two different grains, primarily due to impurities located there; C_2 is the capacity across the intergranular region; and R_3 is the resistance to conduction within the grains. Electron microprobe studies supported the theory of impurities at the grain boundary. Thus, in a system as electrochemically complex as this, with many different effects interacting, one can still obtain fundamental information about processes occurring at each interface and in the bulk specimen.

This second study illustrates a very important point about IS. Although it is an extremely powerful technique in its own right, the analysis of complicated systems must be correlated with other experimental information to verify that the chosen circuit is physically reasonable. Furthermore, agreement between independently determined experimental values and those determined in a fitting procedure of the complex plane results can only strengthen the IS results and thus should never be overlooked.

Theory

Ian D. Raistrick,¹ J. Ross Macdonald,² and Donald R. Franceschetti³

¹Los Alamos National Laboratory, Los Alamos, NM, USA

²(William R. Kenan, Jr., Professor of Physics, Emeritus), Department of Physics and Astronomy, University of North Carolina, Chapel Hill, NC, USA

³Department of Physics, The University of Memphis, Memphis, TN, USA

2.1 THE ELECTRICAL ANALOGS OF PHYSICAL AND CHEMICAL PROCESSES

2.1.1 Introduction

One of the most attractive aspects of impedance spectroscopy (IS) as a tool for investigating the electrical and electrochemical properties of materials and systems is the direct connection that often exists between the behavior of a real system and that of an idealized model circuit consisting discrete electrical components. The investigator typically compares or fits the impedance data to an equivalent circuit, which is representative of the physical processes taking place in the system under investigation. The main objective of the present section is to define and discuss the analogies between circuit elements and electrochemical processes, so that the results of data fitting can be more easily converted into physical understanding. Such a close connection exists between electrochemistry and the behavior of idealized circuit elements is not surprising, since the fundamental laws that connect charge and potential and that define the properties of linear systems are unchanged in passing from electronic to ionic materials.

There are, however, dangers in the indiscriminate use of analogies to describe electrochemical systems. The first point to be made is that equivalent circuits are seldom unique. Only the simplest circuits can be unambiguous in their description of experimental data; in complex situations, choices based upon other physical data are often necessary. It should also be remembered that electrolytes, interfaces, and so on are only *approximately* modeled by idealized circuit elements over a limited range of experimental conditions. One general condition, which will be assumed through much of this volume, is that we are dealing with small signals; that is, linear behavior is implied. The impedance is supposed to be independent of the amplitude of the applied signal or at least approach a constant finite limit as the amplitude of the signal is decreased. Electrochemical systems, of course, can be highly nonlinear, and response to large signals includes rectification and higher harmonic generation. In Section 2.1.4 we discuss the linearization of interfacial kinetics to produce a charge transfer resistance. Interfacial capacitances are also voltage dependent, and mass transport will also be nonlinear if diffusion coefficients or thermodynamic terms, present in the diffusion expression, are a function of concentration (see Section 2.1.3.2). The use of small signals, however, is in general a distinct advantage of the impedance approach as compared with cyclic voltammetry, for example, where the wealth of information contained in a single experiment may prove too difficult to deconvolute. Usually, the voltage dependence of the electrochemical parameters is rather slow, and a linear expansion of the ac, in terms of the variation of the perturbed

concentrations, is well justified. Higher-order effects are not discussed in this chapter, but a discussion of electrochemical applications may be found in the review by Sluyters-Rehbach and Sluyters [1984].

Two other limitations on the exact correspondence between equivalent circuits and electrochemical systems are also addressed. The first of these is the effect of geometry on the current distribution. The effect of this on the frequency dispersion of the impedance is only beginning to be explored by those interested in impedance methods and will prove to be important as the technique is extended to more complex geometries and small structures. A number of problems where current distribution is undoubtedly important, for example, in the behavior of polycrystalline solid electrolytes and the effect of roughness on interfacial impedance, have recently been considered by Fleig and Maier [1996].

A further limitation is the often observed anomalous frequency dependence of both bulk and interface parameters. Several electrochemical properties, for example, conductivity and interface capacitance, are predicted to be independent of frequency, whereas, in fact, they often show significant deviations from this behavior. This type of phenomenon has achieved recognition only since the application of ac techniques to a wide variety of problems, since a small degree of frequency dispersion is difficult to recognize in transient (time domain) experiments. Although good parameterization of this frequency dispersion has been achieved, and certain general or "universal" forms suggested, a universally accepted microscopic description has not yet emerged. Some of the aspects of this phenomenology are discussed in Sections 2.1.2.3 and 2.1.2.7, and we have brought together some of the various attempts that have appeared in a wide variety of fields to deal with this problem.

The general approach adopted in this section is to treat bulk and interfacial phenomena separately. First the electrical properties of homogeneous phases are discussed. There are two aspects to this treatment, relating respectively to dielectric relaxation and long-range direct current (dc) conductivity.

Although the well-established measurement of dielectric loss is not, in its narrowest sense, strictly IS, a discussion of relaxation behavior is central to the family of techniques that use the interaction of a time-varying electromagnetic signal with a material to deduce microscopic detail. The generalization of the treatment of systems with a single relaxation time (Debye behavior) to those with multiple relaxations or distributions of relaxation times is discussed in Section 2.1.2.3. Recently, the application of impedance methods to disordered, condensed phases, such as organic polymers and glasses, warrants a general appreciation of the concepts involved. Dielectric loss measurements are also important and are used extensively to study the energetics of relaxations of complex ionic defects, such as those found in the fluorite family of materials.

The determination of dc ionic conductivity is perhaps the most widespread and also the simplest application of IS. By using ac methods, electrode polarization can be *correctly* eliminated from an electrochemical system, and other sources of spurious frequency dispersion, such as grain boundary effects, may also be removed under certain circumstances. Electrodes may be inert foreign metals, thus eliminating the need for demonstrating the reversibility of parent-metal electrodes.

Conductivity is of course closely related to diffusion in a concentration gradient, and IS has been used to determine diffusion coefficients in a variety of electrochemical systems, including membranes, thin oxide films, and alloys. In materials exhibiting a degree of disorder, perhaps in the hopping distance or in the depths of the potential wells, *simple* random walk treatments of the statistics are no longer adequate; some modern approaches to such problems are introduced in Section 2.1.2.7.

The aforementioned sections deal with bulk phenomena. The other important area about which IS gives important information is that of the electrochemical interface. This is usually a junction between an electronic and an ionic conductor; electrochemical devices utilize the charge transfer that occurs at this interface. The kinetics of this process as well as the electrical nature of the interface region are discussed in Section 2.1.4.

The emphasis of this section is on solid systems; therefore, several important aspects of electrical response appropriate to liquid electrochemistry are either neglected or given little emphasis. Examples are the omission of convection in the treatment of mass transport and the related neglect of ac impedance at a rotating disk electrode. Similarly, porous electrodes are not discussed, although related "rough" electrodes are briefly considered. Complex electrochemical mechanisms at solid-solid interfaces have

been hardly mentioned in the literature; the treatment of the topic here reflects that. However, some attempt has been made to give a sufficiently general approach to interface kinetics and the development of expressions for the faradic impedance so that solid-state scientists may be aware of the advanced state of development of the theory used by aqueous electrochemists.

2.1.2 The Electrical Properties of Bulk Homogeneous Phases

2.1.2.1 *Introduction*

In this section we are concerned with the electrical response of solids with a uniform composition. Mass and charge transport in the presence of concentration gradients are discussed in Section 2.1.3.

On the time scale of interest to electrochemists (i.e., $\gtrsim 1 \mu\text{s}$), an electric field can interact with a solid in two principal ways: the reorientation of defects having electric dipole moments (usually complex defects) and the translational motion of charge carriers (usually simple defects such as vacancies, ionic interstitials, and defect electronic species).

The first interaction leads to a displacement current,

$$i = \frac{d\mathbf{D}}{dt} \quad (1)$$

where \mathbf{D} is the electric displacement (defined as the total charge density on the electrodes),

$$\mathbf{D} = \epsilon_0 \mathbf{E} + \mathbf{P} \quad (2)$$

where \mathbf{E} is the electric field, ϵ_0 is the permittivity of free space, and \mathbf{P} is the polarization of the dielectric material.

The second type of interaction leads to a purely real (dc) conductivity σ :

$$i = \sigma \mathbf{E} \quad (3)$$

We therefore deal first with the phenomenon of dielectric relaxation in materials with a single time constant and an absence of conductivity and later with materials that show long-range conductivity. As we are primarily concerned with developing the electrical analogs of these processes, little consideration is given to the characteristics of individual defects or materials. Similarly, the thermodynamics of the formation of defects, which determines their concentration, is also ignored.

2.1.2.2 *Dielectric Relaxation in Materials with a Single Time Constant*

When an electric field \mathbf{E} is applied to an insulating material, the resulting polarization \mathbf{P} may be divided into two parts according to the time constant of the response:

1. An almost instantaneous polarization due to the displacement of the electrons with respect to the nuclei. This defines the high-frequency dielectric constant ϵ_∞ related to the refractive index:

$$\epsilon_\infty - 1 = \frac{\mathbf{P}_\infty}{\mathbf{E}\epsilon_0} \quad (4)$$

The time constant of this process is about 10^{-16} s and therefore occurs in the UV region of the electromagnetic spectrum. Ionic vibrations have a time constant that usually occurs in the infrared and are also therefore instantaneous as far as electrochemical experiments are concerned.

2. A time-dependent polarization $\mathbf{P}'(t)$ due to the orientation of dipoles in the electric field. If the field remains in place for an infinitely long time, the resulting total polarization \mathbf{P}_s defines the static dielectric constant ϵ_s :

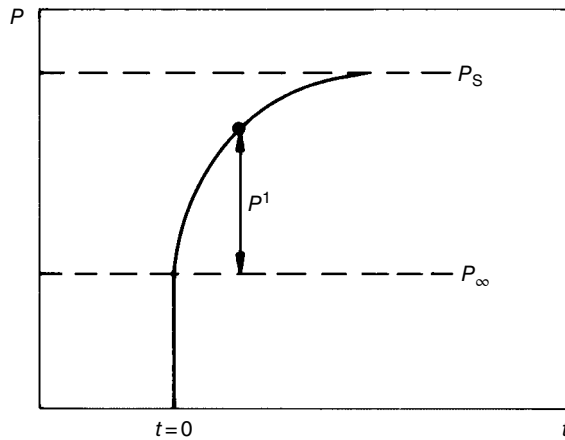


FIGURE 2.1.1 Time dependence of the polarization P after the application of an electric field to an insulator at $t = 0$.

$$\epsilon_s - 1 = \frac{P_s}{E\epsilon_0} \quad (5)$$

$$P_s = P_\infty + P' (t = \infty) \quad (6)$$

The simplest assumption allowing calculation of the properties of such a system is that $\mathbf{P}'(t)$ is governed by first-order kinetics, that is, a single relaxation time τ , such that

$$\frac{\tau d\mathbf{P}'(t)}{dt} = \mathbf{P}_s - \mathbf{P} \quad (7)$$

In other words, the rate at which \mathbf{P} approaches \mathbf{P}_s is proportional to the difference between them. Referring to Figure 2.1.1, on application of a unit step voltage $u_0(t)$,

$$\mathbf{P} = \mathbf{P}_\infty u_0(t) + \mathbf{P}'(t) \quad (8)$$

If we take the Laplace transforms of the last two equations and solve for $\{\mathbf{P}\}$, we obtain

$$\{\mathbf{P}\} = \frac{\mathbf{P}_\infty}{(p + \omega_0)} + \frac{\omega_0 \mathbf{P}_s}{p(p + \omega_0)} \quad (9)$$

where $\{\mathbf{P}\}$ is the Laplace transform of the polarization and $\omega_0 = \tau^{-1}$ and p is the complex frequency variable.

The current density is obtained using the relation

$$\{i\} = p\{\mathbf{P}\} - \mathbf{P}(t = 0) \quad (10)$$

or by differentiating in the time domain to give

$$\{i\} = \mathbf{P}_\infty + (\mathbf{P}_s - \mathbf{P}_\infty) \frac{\omega_0}{(p + \omega_0)} \quad (11)$$

and therefore

$$i(t) = \mathbf{P}_\infty \delta(t) + (\mathbf{P}_s - \mathbf{P}_\infty) \tau^{-1} \exp\left(\frac{-t}{\tau}\right) \quad (12)$$

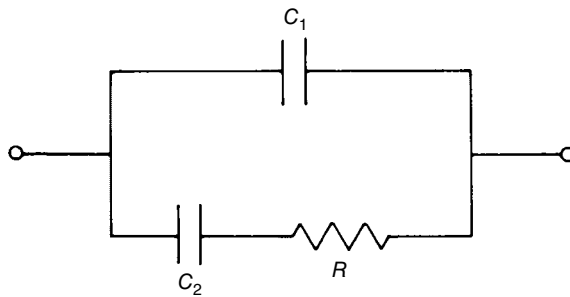


FIGURE 2.1.2 The Debye equivalent circuit.

This is the same result as that obtained for the circuit of Figure 2.1.2, with the identities

$$\begin{aligned}\tau &= RC_2 \\ C_2 &= (\epsilon_s - \epsilon_\infty) \epsilon_0 \\ C_1 &= \epsilon_\infty \epsilon_0\end{aligned}\quad (13)$$

The admittance due the relaxation process is, since $\{\mathbf{E}\} = 1/p$,

$$Y^* = \frac{\{i\}}{\{\mathbf{E}\}} = \epsilon_\infty \epsilon_0 p + (\epsilon_s \cdot \epsilon_\infty) \epsilon_0 \frac{\omega_0 p}{(p + \omega_0)} \quad (14)$$

or, separating the real and imaginary parts ($p = j\omega$),

$$Y^* = \frac{\omega^2 R C_2}{1 + \omega^2 R^2 C_2^2} + j \frac{\omega C_2}{1 + \omega^2 R^2 C_2^2} + j \omega C_1 \quad (15)$$

The expression may be rewritten in terms of the complex dielectric constant $\epsilon^* = Y^*/j\omega\epsilon_0$:

$$\epsilon^* - \epsilon_\infty = \frac{\epsilon_s - \epsilon_\infty}{1 + \omega^2 \tau^2} - j \frac{\omega \tau (\epsilon_s - \epsilon_\infty)}{1 + \omega^2 \tau^2} \quad (16)$$

The real and imaginary parts of this expression are the Debye dispersion relations, which have remained the basic model of dielectric relaxation since their inception (Debye [1929]). They are plotted against one another in Figure 2.1.3 and in Figure 2.1.4 are separately plotted against the normalized frequency ω/ω_0 in Figure 2.1.4. The dielectric loss peak ϵ'' , which corresponds to the real part of the admittance, has been widely used in solid-state measurement for the characterization of relaxation processes. As will be seen later, the equivalent circuit of Figure 2.1.2 is also used in the interpretation of ac impedance data for solid electrolyte systems even though the physical phenomena describing the relaxation processes, that is, conductivity and space-charge accumulation and depletion, are quite different.

The principal difference between a dielectric loss experiment and an impedance spectrum is that the former usually utilizes temperature as the independent variable and measurements are made at several fixed frequencies. A typical example of the use of dielectric loss measurements to obtain data about the relaxations of defects in crystalline solids is the recent paper by Wapenaar *et al.* [1982], who studied LaF₃-doped BaF₂. Two main types of relaxation are found in this material, corresponding to dipole moments caused by association of substitutional lanthanum with an interstitial fluorine along the <100> and <111> crystal axes, respectively. Loss peaks are seen at low levels of doping corresponding to both defects. Calculation of the respective dipole moments allows calculation of the concentration of defects from the strengths of the losses (i.e., from the associated values of C_2).

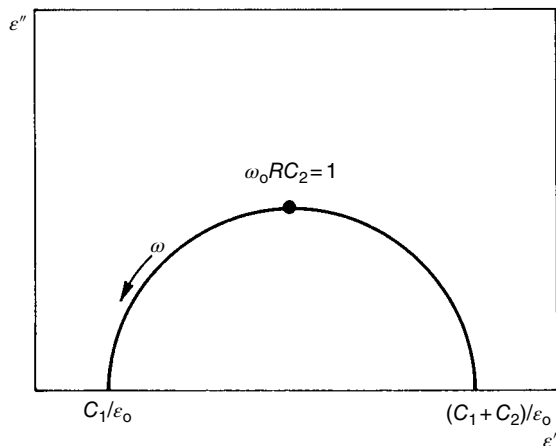


FIGURE 2.1.3 Nyquist plot of the frequency dependence of the complex permittivity modeled by the circuit of Figure 2.1.2.

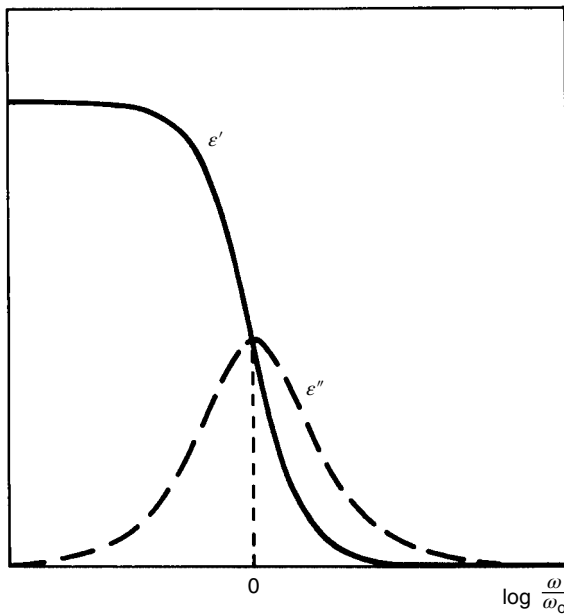


FIGURE 2.1.4 Real and imaginary parts of the complex permittivity as a function of normalized radial frequency.

In practice, very few systems obey the Debye equations with accuracy; an extensive literature exists on the real properties of dielectric materials. It is often found, especially in disordered materials (e.g., glasses and amorphous thin films), that the Debye peak is considerably broadened over its theoretical half-width of $\log[(2 + \sqrt{3})/(2 - \sqrt{3})]$ decades. A number of empirical relaxation functions have been proposed to parameterize the observations, usually interpreted in terms of a distribution of relaxation times. This theme is discussed in the next section.

2.1.2.3 Distributions of Relaxation Times

The Debye dispersion relations were derived previously for a process with a single relaxation time. Figure 2.1.4 showed that the dielectric loss function ϵ'' corresponding to this situation is symmetric about a central frequency, with a characteristic shape and width. The current flow in such a material, after the imposition of a voltage step function, decays exponentially with time. In view of the observations mentioned at the end of the previous section, attempts have been made to extend the Debye model by including processes with more than one relaxation time. By choosing a distribution of relaxation times with appropriate strengths and frequencies, it should prove possible to parameterize the broad response of many dielectric materials. The distribution of relaxation times has also been suggested as the origin of the "constant phase elements" (CPEs) that are often seen in impedance studies of solid electrolytes and the solid-solid interface. In this section, some of the main features of this line of reasoning are presented. The dielectric literature in this area is extensive; no attempt is made here to be comprehensive.

Assuming linear relaxation processes of the type modeled by the series—RC—branch, the principle of superposition allows the dielectric function $\epsilon^* - \epsilon_\infty$ to be generalized:

$$\epsilon^* - \epsilon_\infty = \int_0^\infty \frac{(\epsilon_s - \epsilon_\infty)G(\tau)d\tau}{1 + p\tau} \quad (17)$$

where p is the complex frequency variable and $G(\tau)$ represents a distribution of relaxation times. The distribution should be normalizable,

$$\int_0^\infty G(\tau)d\tau = 1 \quad (18)$$

and should have upper and lower limits. Here $G(\tau)$ represents the fraction of the total dispersion $(\epsilon_s - \epsilon_\infty)$, which is contributed by processes having relaxation times between τ and $\tau + d\tau$.

Now ϵ^* may be divided into real and imaginary parts corresponding to the frequency $j\omega$:

$$\epsilon' - \epsilon_\infty = \int_0^\infty \frac{G(\tau)(\epsilon_s - \epsilon_\infty)d\tau}{1 + (\omega\tau)^2} \quad (19)$$

$$\epsilon'' = \int_0^\infty \frac{\omega\tau G(\tau)(\epsilon_s - \epsilon_\infty)d\tau}{1 + (\omega\tau)^2} \quad (20)$$

Kirkwood and Fuoss [1941] first showed that $G(\tau)$ could be recovered by integration from a set of ϵ'' values. A general treatment has been given by Macdonald and Brachman [1956], who provided a useful set of relations between the various functions used to describe networks and systems as well as between responses to various types of input.

Using the notation of those authors, the network function is defined as

$$Q(p) = \int_0^\infty \frac{G(\tau)d\tau}{1 + p\tau} \quad (21)$$

where $Q(p)$ corresponds to $(\epsilon^* - \epsilon_\infty)/(\epsilon_s - \epsilon_\infty)$.

The admittance is related to $Q(p)$:

$$Y(p) = pQ(p) \quad (22)$$

The step function response $A(t)$ and the impulse response $B(t)$ are

$$A(t) = L^{-1}[Q(p)] \quad (23)$$

$$B(t) = L^{-1}[Y(p)] \quad (24)$$

where L^{-1} is the inverse Laplace transform operator.

It was shown that $G(\tau)$ was derivable from these quantities through the relations

$$\tau G(\tau) = D(\lambda) = L^{-1}L^{-1}Q(p) \quad (25)$$

or

$$D(\lambda) = L^{-1}A(t), \quad (26)$$

where $D(\lambda)$ is a distribution function of the new variable $\lambda = \tau^{-1}$. Other relationships may also be derived. The authors give useful examples of various types of network functions and derived distributions. The simplest is

$$G(\tau) = \delta(\tau - \tau_0) \quad (27)$$

which corresponds to a single relaxation time and leads to the simple Debye dispersion equations. Rewriting $G(\tau)$ in terms of λ ,

$$D(\lambda) = \tau G(\tau) = \tau \delta(\tau - \tau_0) \quad (28)$$

and therefore

$$\begin{aligned} D(\lambda) &= \lambda^{-1} \delta(\lambda^{-1} - \lambda_0^{-1}) \\ &= \lambda_0 \delta(\lambda - \lambda_0) \end{aligned} \quad (29)$$

Hence,

$$A(t) = L\{D(\lambda)\} \quad (30)$$

$$= \lambda_0 \exp(-\lambda_0 t) \quad (31)$$

$$= \left(\frac{1}{\tau_0}\right) \exp\left(\frac{-t}{\tau_0}\right) \quad (32)$$

and

$$Q(p) = \frac{1}{1 + \tau_0 p} \quad (33)$$

Observed relaxation times may occur over many orders of magnitude, and it seems reasonable that such a range of variation would, for a thermally activated process of the type

$$\tau = \tau^* \exp\left(\frac{E^*}{kT}\right) \quad (34)$$

correspond to a distribution of activation energies rather than to a distribution of τ^* . We may therefore define a distribution $K(E^*)$ such that

$$K(E^*) dE^* = G(\tau) d\tau \quad (35)$$

Evidently, from Eq. (34)

$$K(E^*) = \left(\frac{\tau}{kT}\right) G(\tau) \quad (36)$$

Macdonald [1962] has pointed out that if $K(E^*)$ is independent of T , then $G(\tau)$ cannot be so independent. Both the midpoint τ_0 and the width of the distribution will change with temperature. Not all of the $G(\tau)$ proposed in the literature are consistent with this postulate. See Section 2.2.3.4 for further discussion of activation energy distributions.

Van Weperen *et al.* [1977] noted that in fluorite structure materials, the dielectric and ionic thermo-current peaks broadened with increasing concentration of dipoles (see, e.g., Johnson *et al.* [1969]) and developed a theory of dipole-dipole interactions, which predicted an almost Gaussian distribution of activation energies:

$$K(E^*) = \frac{1}{\sigma\sqrt{(2\pi)}} \exp\left[-\frac{(E^* - E_0^*)^2}{2\sigma^2}\right] \quad (37)$$

The corresponding distribution of τ is lognormal, while the Wagner distribution is

$$G(\tau) = \frac{b}{\tau\sqrt{\pi}} \exp\left[-b^2\left(\ln\frac{\tau}{\tau_0}\right)^2\right] \quad (38)$$

where $\sigma = kT/b\sqrt{2}$; σ^2 is the variance of the $K(E^*)$. If $K(E^*)$ is to be invariant with T , then b should be proportional to T .

The importance of this distribution, apart from being well defined in a physical sense, is its behavior for large σ , that is, wide distributions. As b becomes small, $G(\tau)$ becomes proportional to $1/\tau$, and $A(t)$, the current response to a unit step function, becomes proportional to $1/t$. The power spectrum may mimic $1/f$ behavior over several decades, and the dielectric function will show a very gradual frequency dispersion.

One of the most widely used distributions is that proposed by Cole and Cole [1941] to describe the occurrence of depressed semicircular arcs in the $\epsilon'' - \epsilon'$ plots obtained for a wide variety of polar liquids and solids. The dielectric constant behavior was described by the equation

$$\epsilon^* - \epsilon_\infty \frac{(\epsilon_s - \epsilon_\infty)}{\left[1 + (j\omega\tau_0)^{1-\alpha}\right]} \quad (39)$$

where $\alpha\pi/2$ is the angle between the real axis and the line to the center of the circle from the high-frequency intercept. Now ϵ^* may be separated into real and imaginary parts:

$$\frac{\epsilon' - \epsilon_\infty}{\epsilon_s - \epsilon_\infty} = \frac{1}{2} \left[1 - \frac{\sinh(1-\alpha)x}{\cosh(1-\alpha)x + \cos\alpha\pi/2} \right] \quad (40)$$

$$\frac{\epsilon''}{\epsilon_s - \epsilon_\infty} = \frac{1}{2} \frac{\cos\alpha\pi/2}{\cosh(1-\alpha)x + \sin\alpha\pi/2} \quad (41)$$

where $x = \log\omega\tau_0$. These expressions reduce to the Debye relationships for $\alpha \rightarrow 0$. The derived distribution function of time constants is

$$G(\tau) = \frac{1}{2\pi\tau} \frac{\sin\alpha\pi}{\cosh(1-\alpha)\log(\tau/\tau_0) - \cos\alpha\pi} \quad (42)$$

from which the distribution of activation energies would be, using Eq. (36),

$$K(E^*) = \frac{1}{2\pi kT} \frac{\sin \alpha \pi}{\cosh(1-\alpha)(E^* - E_0^*)/kT - \cos \alpha \pi} \quad (43)$$

Unlike the Wagner distribution, $K(E^*)$ cannot be rendered temperature independent except in limiting cases where $\alpha \rightarrow 0$ or 1. The Cole–Cole distribution, like the lognormal distribution, is symmetrical with respect to a central frequency or relaxation time. The distribution of time constants is plotted as a function of the variable $s \equiv \log(\tau/\tau_0)$ in Figure 2.1.5, and the complex plane plots for various values of α are given in Figure 2.1.6.

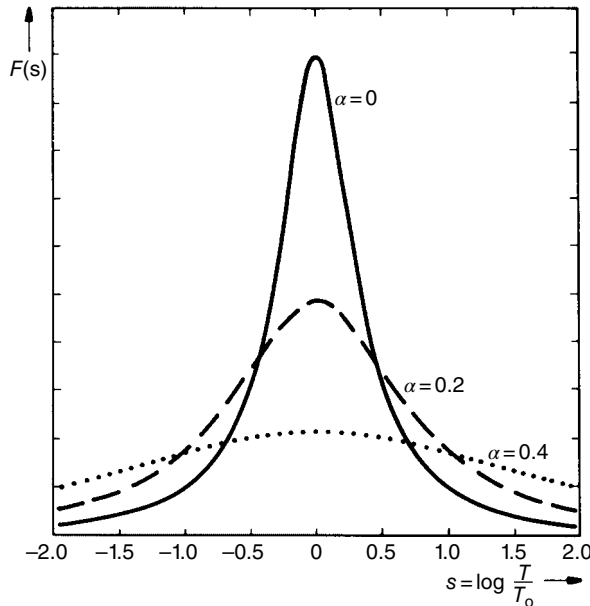


FIGURE 2.1.5 The distribution function $F(s)$ associated with the Cole–Cole distribution of relaxation times [Eq. (42)] for different values of α .

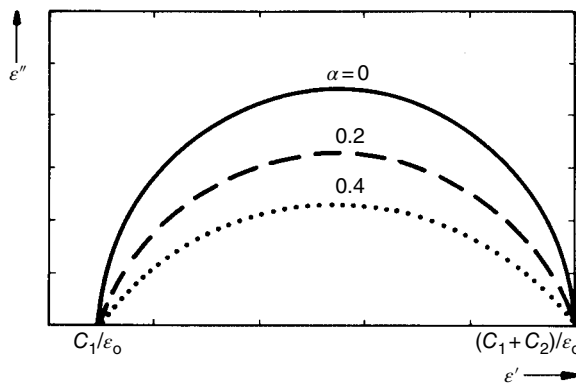


FIGURE 2.1.6 Complex permittivity associated with the Cole–Cole expression [Eq. (39)].

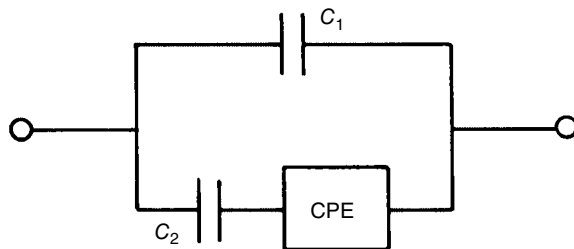


FIGURE 2.1.7 The analog of Figure 2.1.2, which models the electrical response associated with the Cole–Cole expression.

As was pointed out by Cole and Cole, dielectric response corresponding to the function of Eq. (39) may be decomposed into the circuit shown in Figure 2.1.7, which contains a CPE. The CPE is an empirical impedance function of the type

$$Z_{\text{CPE}}^* = A(j\omega)^{-\alpha} \quad (44)$$

which has proved of considerable value in data fitting. The admittance of this circuit may be expressed as

$$Y^* = j\omega C_1 + \frac{j\omega C_2}{[1 + C_2 A(j\omega)^{1-\alpha}]} \quad (45)$$

Dividing by $j\omega\epsilon_0$ and comparing with Eq. (39), we find that

$$A = \frac{\tau_0^{1-\alpha}}{(\epsilon_s - \epsilon_\infty)\epsilon_0} \quad (46)$$

It is interesting to enquire about the distribution of relaxation times implied by the presence of Z_{CPE}^* alone. If

$$Z_{\text{CPE}}^* = Ap^{-\alpha} \quad (47)$$

then the admittance is

$$Y(p) = A^{-1}p^\alpha \quad (48)$$

Therefore,

$$A(t) = L^{-1}\{A^{-1}p^{\alpha-1}\} \quad (49)$$

$$= \frac{A^{-1}t^{-\alpha}}{\Gamma(1-\alpha)} \quad (50)$$

where Γ is the gamma function. And

$$D(\lambda) = \frac{A^{-1}\lambda^{\alpha-1}}{\Gamma(1-\alpha)\Gamma(\alpha)} \quad (51)$$

or

$$G(\tau) = \frac{\sin \alpha\pi}{\pi} \cdot A^{-1} \tau^{-\alpha} \quad (52)$$

Thus, the distribution of relaxation times is proportional to $1/\tau^\alpha$. It has often been pointed out that this distribution is nonnormalizable. Physical acceptability may be restored by truncating the distribution at upper and lower limits of τ . The resulting distribution has been discussed by Matsumoto and Higasi [1962].

Assuming an expression for τ of the form given by Eq. (34), we find a distribution of activation energies:

$$K(E^*) \propto \exp \left[\frac{(1-\alpha)E^*}{kT} \right] \quad (53)$$

The important point to be made here is that the assumption of (i) an exponential distribution of activation energies and (ii) an exponential form for τ leads directly to CPE behavior. The exponential distribution of activation energies has been further discussed by Macdonald [1963]. See also Section 2.2.3.4.

Two other distribution functions are mentioned by Kirkwood and Fuoss [1941] and Davidson and Cole [1951] (see also Davidson [1961]).

The first of these is symmetric and is again based on an extension of the Debye theory functions. In the Debye theory,

$$\frac{\epsilon''}{\epsilon''_{\max}} = \operatorname{sech} x \quad (54)$$

where $x = \log(\omega/\omega_0)$. Instead of this, Kirkwood and Fuoss wrote

$$\frac{\epsilon''}{\epsilon''_{\max}} = \operatorname{sech} \alpha x \quad (55)$$

which leads to a distribution of the form

$$G(s) = \frac{2}{\pi} \cdot \frac{\cos(\alpha\pi/2)\cosh\alpha s}{\cos^2(\alpha\pi/2) + \sinh^2\alpha s} \quad (56)$$

where s is again equivalent to $\log(\tau/\tau_0)$.

The Davidson–Cole equation

$$\frac{\epsilon^* - \epsilon_\infty}{\epsilon_s - \epsilon_\infty} = \frac{1}{(1 + j\omega\tau_0)^\beta} \quad (57)$$

leads to a skewed arc in the $\epsilon'' - \epsilon'$ plane. It is a semicircle at low frequency, but asymptotic to $\beta\pi/2$ at high frequencies (Figure 2.1.8).

The real and imaginary parts are

$$\epsilon' - \epsilon_\infty = (\epsilon_s - \epsilon_\infty) \cos \beta y (\cos y)^\beta \quad (58)$$

$$\epsilon'' = (\epsilon_s - \epsilon_\infty) \sin \beta y (\cos y)^\beta \quad (59)$$

where $y = \tan^{-1}\omega\tau_0$.

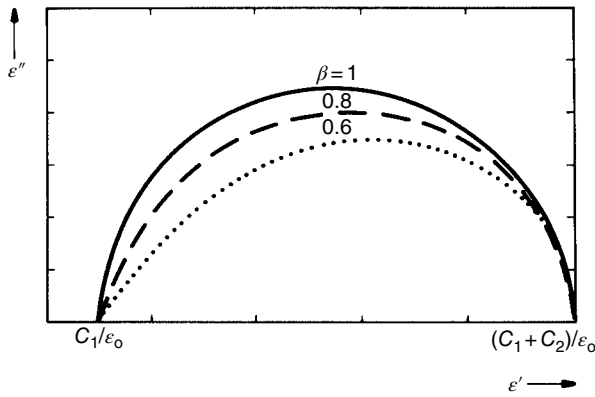


FIGURE 2.1.8 Complex permittivity associated with the Cole–Davidson expression [Eq. (57)].

The current response to the application of a step function potential difference is

$$i(t) = \mathbf{P}_\infty \delta(t) + \frac{\mathbf{P}_s - \mathbf{P}_\infty}{\tau_0 \Gamma(\beta)} \left(\frac{t}{\tau_0} \right)^{\beta-1} \exp - \left(\frac{t}{\tau_0} \right) \quad (60)$$

which may be compared with the equivalent Cole–Cole expression

$$i(t) = \mathbf{P}_\infty \delta(t) + \frac{\mathbf{P}_s - \mathbf{P}_\infty}{\tau_0 \Gamma(1+\alpha)} \left(\frac{t}{\tau_0} \right)^{(1+\alpha)} \quad (61)$$

and the Debye expression [Eq. (12)].

The distribution of relaxation times is highly asymmetric:

$$G(\tau) = \begin{cases} \frac{\sin \beta \pi}{\pi} \left(\frac{\tau}{\tau_0 - \tau} \right)^\beta, & \tau < \tau_0 \\ 0, & \tau > \tau_0 \end{cases} \quad (62)$$

Thus, the distribution ends abruptly at its most probable value.

A further generalization of the Debye approach was made by Williams and Watts [1970] and Williams *et al.* [1970] who introduced the use of the following fractional exponential form to describe the decay of polarization after the removal of a constant field:

$$\phi(t) = \frac{\mathbf{P}(t)}{\mathbf{P}_s - \mathbf{P}_\infty} = \exp - \left(\frac{t}{\tau} \right)^\alpha, \quad 0 < \alpha < 1 \quad (63)$$

neglecting the instantaneous drop in polarization. The equivalent Debye expression has $\alpha = 1$.

Thus,

$$A(t) = -\frac{d\phi}{dt} = \left(\frac{\alpha t^{\alpha-1}}{t^\alpha} \right) \exp - \left(\frac{t}{\tau} \right)^\alpha \quad (64)$$

The Laplace transform of $A(t)$, that is, $Q(p)$, may be evaluated by series expansions, although care is needed because of slow convergence for certain ranges of α (Williams *et al.* [1970]). For the particular case of $\alpha = 1/2$, an analytical expression is easily derived:

$$Q(p) = \frac{\sqrt{\pi}}{2\sqrt{\tau_0}} \exp \frac{1}{\tau_0} \operatorname{erfc} \frac{1}{\sqrt{(\tau_0 p)}} \quad (65)$$

The inverse Laplace transform of functions of this type, which gives the distribution of relaxation times, is given by Montroll and Bendler [1984]. A simple expression for $\alpha=1/2$ may be derived:

$$G(\tau) = \frac{1}{2\sqrt{(\pi t\tau_0)}} \exp\left(-\frac{t}{4\tau_0}\right) \quad (66)$$

Like the Cole–Davidson function, the Williams–Watts approach gives asymmetric plots in the complex ϵ^* plane. A detailed comparison of these two forms has been made by Lindsey and Patterson [1980].

Interest in the Williams–Watts approach has arisen, not only because of its empirical success in fitting dielectric data but also because of its relation to certain types of diffusion and random walk problems. The mechanistic relation between diffusion and relaxation was introduced by Glarum [1960], who suggested a process in which a mobile defect enabled a “frozen in” dipole to relax. Further aspects of random walk processes and their relation to CEPs and other empirical functions are discussed in a later section.

2.1.2.4 Conductivity and Diffusion in Electrolytes

In the previous sections the expressions for the admittance of materials were developed on the assumption that they had no dc conductivity (Ibl [1983a], Newman [1973]). The real part of the admittance arose from the dissipative process of dipole reorientation. Energy was absorbed by the system when the orientation of dipoles was changed with respect to the electric field vector.

Dissipation may also occur by mass transport of particles in the bulk of the phase. Work must be done against the frictional forces of the medium through which the particle moves. In solids, migration and diffusion are usually important; in liquids and membranes, hydrodynamic mass transport must also be considered.

A convenient starting point for discussion of transport properties in electrolytes is a consideration of the physical laws that connect charge and electric potential. In a medium of uniform dielectric constant, we may write Poisson’s equation, which connects the gradient of the electric field with the charge density:

$$\nabla^2\Phi = -\frac{\rho}{\epsilon_s\epsilon_0} \quad (67)$$

Here Φ is the electric potential. The charge density ρ is equal to the sum over the local concentrations of species multiplied by their charges:

$$\rho = F\sum z_i c_i \quad (68)$$

Because of the magnitude of the constant F/ϵ_0 , very large electric fields result from very small deviations from electroneutrality. It is, therefore, a very good approximation to write for the interior of an electrolyte:

$$\sum z_i c_i = 0 \quad (69)$$

provided the separation of the electrodes is not too small.

In other words, except for the smallest systems, the bulk of the electrolyte is electrically neutral. This situation is generally otherwise at interfaces where there exists the possibility of large electric fields. It also follows that, in general, Laplace’s equation

$$\nabla^2\Phi = 0 \quad (70)$$

is a good approximation in the electrolyte bulk.

A second basic equation expresses the conservation of mass in the system:

$$\frac{\partial c_i}{\partial t} = -\nabla \cdot j_i + R_i \quad (71)$$

This equation states that the rate of accumulation of a species i in a given volume element is equal to the negative of the divergence of the flux plus any terms that lead to the production or deletion of i , such as chemical reactions or recombination in the bulk of the material.

Third, we can write an equation for the electric current density in terms of the fluxes of changed species:

$$i = F \sum z_i j_i \quad (72)$$

We now need an expression for the flux of species i in terms of the forces acting on the particles. The assumption that is usually made is that a particle has a characteristic mobility u_i , which is the proportionality constant between its velocity and the force causing it to move. The driving force is supposed to be the gradient in electrochemical potential η_i of the species, so that when the mobility is multiplied by the driving force and the concentration, we obtain the flux of i :

$$j_i = -c_i u_i \nabla \eta_i \quad (73)$$

The problem with this equation lies in the formulation of the force term. In general, a particle may move in response to gradients in the electrochemical potentials of other species, leading to cross-terms in the flux equation. In principle, the presence of cross-terms will occur whenever a component is present whose chemical potential may vary independently of that of species i . Thus, the motion of i may depend not only on $\nabla \eta_i$ but also on $\nabla \eta_j$ if η_j is independent of η_i (i.e., it is not coupled through a Gibbs–Duhem relation). The flux equation may therefore be generalized as

$$j_i = -c_i u_i \left[\nabla \eta_i + \sum_j \alpha_{ij} \nabla \eta_j \right] \quad (74)$$

where α_{ij} are the coefficients expressing the influence of $\nabla \eta_j$ on i .

It may be shown that this equation is equivalent to the phenomenological equations derived from irreversible thermodynamics, as well as the multicomponent diffusion equations derived from the Stefan–Maxwell equations, which were first used to describe diffusion in multicomponent gases.

Further development of transport theory involves solution of Eqs. (71) and (73), subject to the appropriate initial and boundary conditions to give currents, concentration profiles, and so on.

The simplest approach, often adopted in practice, particularly in solution electrochemistry, may be termed dilute solution approximation. We can write, for the gradient in electrochemical potential for a dilute solution,

$$\nabla \eta_i = \frac{RT \nabla c_i}{c_i} + z_i F \nabla \Phi \quad (75)$$

Thus,

$$j_i = -RT u_i \nabla c_i - z_i F c_i u_i \nabla \Phi \quad (76)$$

The quantity $RT u_i$ is called the diffusion coefficient (Nernst–Einstein relation)

$$j_i = -D_i \nabla c_i - z_i F c_i u_i \nabla \Phi \quad (77)$$

and the current density is given by the expression

$$i = -F \Sigma z_i \nabla c_i D_i - F^2 \Sigma z_i^2 c_i u_i \nabla \Phi \quad (78)$$

Substituting Eq. (77) into Eq. (71), we obtain

$$\frac{\partial c_i}{\partial t} = z_i F \nabla \cdot (u_i c_i \nabla \Phi) + \nabla \cdot (D_i \nabla c_i) + R_i \quad (79)$$

or, in one dimension,

$$\frac{\partial c_i}{\partial t} = z_i F u_i \frac{\partial c_i}{\partial x} \mathbf{E} + D_i \frac{\partial^2 c_i}{\partial x^2} + R_i \quad (80)$$

if we assume $\partial \mathbf{E} / \partial x = 0$, that is, electroneutrality. This is the classical Nernst–Planck equation.

Instead of assuming dilute or ideal behavior, it is possible to write

$$\nabla \eta_i = \nabla \mu_i + z_i F \nabla \Phi \quad (81)$$

$$j_i = -c_i u_i \nabla \mu_i - z_i F c_i u_i \nabla \Phi \quad (82)$$

$$= -\frac{D_k c_i \nabla \mu_i}{RT} - z_i F c_i u_i \nabla \Phi \quad (83)$$

Here D_k is known as the component diffusion coefficient. The importance of this definition lies in the fact that Nernst–Einstein proportionality between a diffusion coefficient and a mobility has been retained, even though the condition of ideality has been relaxed. This is important since the apparent violation of the Nernst–Einstein equation in nonideal solutions is not a failure of the proportionality between mobility and mean displacement; it is a weakness in the method of formulating the driving force for diffusion in terms of a concentration gradient (Fick’s law) rather than in terms of an activity or chemical potential gradient.

2.1.2.5 Conductivity and Diffusion: A Statistical Description

In the previous section, the Nernst–Planck equation was developed from the macroscopic flux density and mass conservation equations [Eqs. (71) and (73), respectively]. The same equation can also be derived by statistical methods, which describe the probability of finding a particle within a volume region at a time t , given an initial distribution and a set of jump probabilities. For the simplest case, in one dimension, with equal probabilities of the particle making a jump to the right or to the left, the time evolution of an initial delta function in concentration at $x = 0$ is Gaussian:

$$n(x, t) \Delta x = \frac{1}{2 \sqrt{(\pi D t)}} \exp\left(\frac{-x^2}{4 D t}\right) \Delta x \quad (84)$$

where D , the diffusion coefficient, is equal to $v l^2 / 2$, where v is the number of steps of length l the particle makes per unit time. Another assumption involved in the use of the statistical arguments that led to this equation is that the jumps are statistically independent. $n(x, t)$ is plotted for several different times in Figure 2.1.9. The total area under the curve is constant.

The mean displacement of the particles is zero:

$$\langle x \rangle = \int x n(x, t) dx = 0 \quad (85)$$

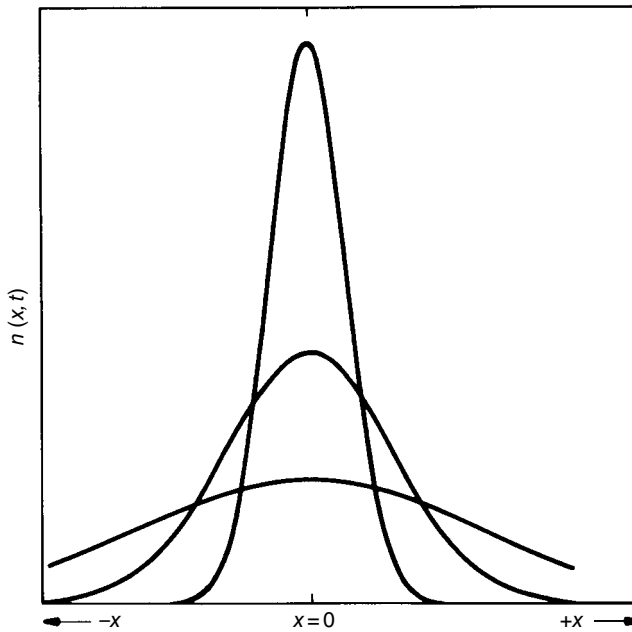


FIGURE 2.1.9 The Gaussian or normal distribution function $n(x, t)$ plotted as a function of distance from the origin for different times.

as long as the jump probabilities are symmetrical. The second moment is

$$\langle x \rangle^2 = \int x^2 n(x, t) dx = 2Dt \quad (86)$$

The probability density $n(x, t)$, given by Eq. (84), is a solution of the diffusion equation

$$\frac{\partial n(x, t)}{\partial t} = \frac{D \partial^2 n(x, t)}{\partial x^2} \quad (87)$$

This is identical to the Nernst–Planck Eq. (80) in the absence of an electric field term and a generation–recombination term.

If the jump probabilities are not symmetrical—for example, in the presence of an electric field—then $\langle x \rangle$ is no longer equal to zero and the probability distribution is

$$n(x, t) \Delta t = \frac{1}{2\sqrt{\pi Dt}} \exp \left[\frac{(-x - \langle \nu \rangle t)^2}{4Dt} \right] \Delta x \quad (88)$$

Here $\langle \nu \rangle$ is the mean drift velocity $\langle x \rangle/t$. The mean drift velocity per unit field is the drift mobility b_i , and the conductivity σ_i is defined by

$$\sigma_i = b_i c_i z_i F \quad (89)$$

$$= \frac{\langle \nu \rangle c_i z_i F}{E} \quad (90)$$

Note that b_i is equal to $z_i F u_i$.

Now $n(x, t)$ from Eq. (88) is the solution to Eq. (80) with R_i set to zero and describes a propagating Gaussian packet. The ratio of the dispersion $\sqrt{(\langle x^2 \rangle - \langle x \rangle^2)}$ to distance traveled is inversely proportional to the square root of time.

A more general approach via the master equation, leading to Fokker–Planck equations, may also be followed and may be found in texts on statistical physics (see, e.g., Reichl [1980]).

The type of diffusion discussed here may be termed “normal” or “Gaussian” diffusion. It arises simply from the statistics of a process with two possible outcomes, which is attempted a very large number of times. In Section 2.1.2.7, the statistical basis of diffusion is enlarged to include random walks in continuous rather than discrete time and also situations where different distributions of jump distances occur.

2.1.2.6 Migration in the Absence of Concentration Gradients

Under certain circumstances, the passage of electric current through an electrolyte does not lead to a concentration gradient, and Eq. (78) becomes

$$i = -F^2 \sum c_i z_i^2 u_i \nabla \Phi \quad (91)$$

The term $F^2 \sum c_i z_i^2 u_i$ is called the conductivity σ , and under these conditions Ohm’s law is obeyed by the electrolyte. Examples of this behavior are found where only one electrolyte species is mobile, for example, in a solid electrolyte, with reversible electrodes (see Section 2.1.3) or at high frequencies where several carriers may move, but where neither electrode nor concentration polarizations have time to build up.

For a simple hopping conductivity process, in the absence of long-range interactions, the conductivity is expected to be independent of frequency. Here, a single particle is presumed to move along an infinite lattice of identical potential wells (Figure 2.1.10a). This might be contrasted with the case of a single particle hopping backward and forward in double well, where the low-frequency conductivity is zero and a Debye-like transition region is followed by a constant high-frequency conductivity (Figure 2.1.10b).

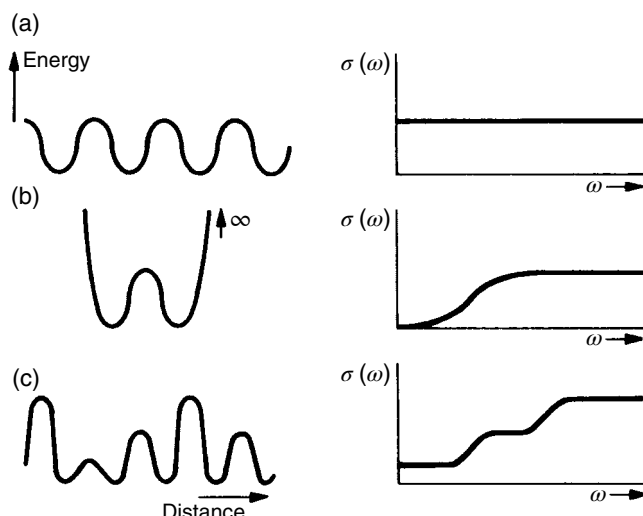


FIGURE 2.1.10 Frequency dependence of the hopping conductivity for different potential energy profiles: (a) Periodic constant activation energy, (b) a single bi-well, and (c) a potential profile with multiple activation energies.

Apart from the most dilute solutions, however, we do expect interactions between unassociated defect species, and in general this will lead to a frequency-dependent conductivity. This has been recognized for many years by electrochemists (Onsager [1926, 1927], Debye and Falkenhagen [1928]). The form of the frequency dependence, however, is of considerable interest.

Following the work of Jonscher (see, e.g., Jonscher [1977, 1980]), who showed that a large number of different types of conductors exhibited a frequency dispersion of the CPE type, the presence of interactions has been highlighted to explain the observed frequency dispersion in the conductivity of a number of solid electrolytes by Almond, West, and coworkers (Almond *et al.* [1982, 1983, 1984], Almond and West [1983a, b]). These authors expressed the real part of the ionic conductivity of a number of materials by an expression of the type

$$\sigma(\omega) = \sigma_0 + A\omega^n \quad (92)$$

where σ_0 is a "dc" or frequency-independent part, and the second term is of the CPE type. Making use of Jonscher's empirical expressions, Eq. (92) was rewritten:

$$\sigma(\omega) = K\omega_p + K\omega_p^{1-n}\omega^n \quad (93)$$

where ω_p is the hopping frequency and K depends on the concentration of the mobile charge carriers. The high-temperature limiting value for ω_p should be equal to the attempt frequency, which is independently accessible using IR spectroscopy. For the case of sodium beta-alumina, good agreement was found. Once ω_p is known, then the carrier concentration and activation entropy can also be deduced. For the case of beta-alumina, the hopping rate calculation has been confirmed by mechanical relaxation measurements. In a number of materials, however, including β'' -alumina, the low-frequency region is not independent of frequency, and a second CPE term must be included. The work of Almond and West is also discussed, beginning at Eq. (78) of Section 2.2.3.4.

According to Jonscher, the origin of the frequency dependence of the conductivity was due to relaxation of the ionic atmosphere after the movement of the particle. This idea, and the earlier concepts of Debye, Onsager, and Falkenhagen, has been developed into a quantitative model suitable for solids by Funke [1986]. It is assumed that immediately after an ion hops to a new site (a new minimum in lattice potential energy), it is still displaced from the true minimum in potential energy, which includes a contribution from other mobile defects. At long times the defect cloud relaxes, until the true minimum coincides with the lattice site. The model predicts upper- and lower-frequency-limiting conductivities and a region in between power-law (CPE) behavior.

In general, both conductivity and dipolar relaxation processes may be present in the same material, and the total conductivity is given by

$$\sigma_{\Sigma} = \sigma + j\epsilon_0\epsilon^*\omega \quad (94)$$

where ϵ^* is given by Eq. (16)

The equivalent circuit for such a combination of processes is shown in Figure 2.1.11. An—RC—series combination will be present for each relaxation process present in the material. The dielectric loss peaks will be superimposed on a background loss due to the long-range conductivity process. Due to interactions, for example, dipole-dipole, or lattice relaxations, as discussed previously, a distribution of relaxation times is to be expected, and Wapenaar and Schoonman [1981] have included Cole-Cole branches (series—CZ_{CPE}—combinations) rather than Debye branches to fit data on Ba_{1-x}La_xF_{2+x} fluorite structure solid solutions. Recently, the impedance spectra of doped tynorite materials have been investigated by Roos *et al.* [1984], who again found excellent agreement between data and a circuit, which included Cole-Cole branches. However, the activation energies were not consistent with a simple dielectric relaxation, and a model in which conducting species move between inequivalent sites has been developed (Franceschetti and Shipe [1984]). The motion of the defect species may involve several distinguishable jump processes, each governed by a different activation energy. The interpretation of the

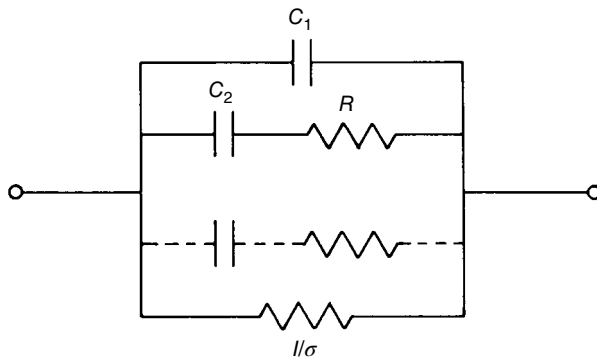


FIGURE 2.1.11 An equivalent circuit that models the behavior of a material, which has both long-range conductivity (σ) and a number of discrete relaxation processes.

relaxation branches in the circuit is that they describe a polarization arising from the inequalities in jump probabilities.

The important point to be emphasized here is that although for a single jump frequency, in the absence of interactions, no particular structure is expected in the conductivity or dielectric constant at that frequency, a more complex model that incorporates several jump frequencies (Figure 2.1.10c) indicates that frequency dispersion is expected in this range. Although the model of Franceschetti and Shipe was developed for the tysonite structure, a more general treatment for a small number of sub-lattices has been independently given (Wong and Brodwin [1980]) and confirms the main conclusions. As the number of possible jump frequencies increases, it is apparent that generalization of the model will eventually describe conductivity and diffusion in disordered materials, that is, in materials in which the jump probabilities are described by random variables.

2.1.2.7 Transport in Disordered Media

In a previous section, reference was made to the random walk problem (Weiss and Rubin [1983], Montroll and Schlesinger [1984]) and its application to diffusion in solids. Implicit in these methods are the assumptions that particles hop with a fixed jump distance (e.g., between neighboring sites on a lattice) and, less obviously, that jumps take place at fixed equal intervals of time (discrete time random walks). In addition, the processes are Markovian, that is, the particles are without memory: the probability of a given jump is independent of the previous history of the particle. These assumptions force normal or Gaussian diffusion. Thus, the diffusion coefficient and conductivity are independent of time.

In recent years more complex types of transport processes have been investigated, and from the point of view of solid-state science, considerable interest is attached to the study of transport in disordered materials. In glasses, for example, a distribution of jump distances and activation energies is expected for ionic transport. In crystalline materials, the best ionic conductors are those that exhibit considerable disorder of the mobile ion sublattice. At interfaces, minority carrier diffusion and discharge (e.g., electrons and holes) will take place in a random environment of mobile ions. In polycrystalline materials the lattice structure and transport processes are expected to be strongly perturbed near a grain boundary.

In general, the study of transport processes in disordered media has its widest application to electronic materials, such as amorphous semiconductors, and very little attention has been given to its application to ionic conductors. The purpose of this section is to discuss briefly the effect of disorder on diffusion process and to point out the principles involved in some of the newly developing approaches. One of the important conclusions to be drawn is that frequency-dependent transport properties are predicted to be of the form exhibited by the CPE if certain statistical properties of the distribution functions

associated with time or distance are fulfilled. If these functions exhibit anomalously long tails, such that certain moments are not finite, then power-law frequency dispersion of the transport properties is observed. However, if these moments are finite, then Gaussian diffusion, at least as limiting behavior, is inevitable.

Although the general problem of a random walk on a random lattice is difficult, there has been considerable success in approaching this problem from the point of view of the continuous time random walk (CTRW), which was first proposed by Montroll and Weiss [1965]. In this approach, the walk is supposed to take place on a regular lattice; disorder is introduced by defining a distribution of waiting or residence times for a particle on a site. In a disordered material there will be a distribution of energy barriers. It therefore seems reasonable that a particle in a deep well will spend more time there than will a particle in a shallow well. The waiting time distribution function $\psi(t)$ therefore describes the probability for an event to happen at a time t after a previous event. The original $\psi(t)$ of Montroll and Weiss was generalized to a position-dependent $\psi(r, t)$ by Scher and Lax [1973a]. The application of the approach to electronic transport in amorphous semiconductors has been discussed in several papers (Scher and Lax [1973b], Scher and Montroll [1975], Pfister and Scher [1978]).

There is a qualitative difference in transport properties depending on the nature of $\psi(t)$. If $\psi(t)$ is such that the time between hops has finite first moment, that is, a mean residence time $\langle t \rangle$ can be defined, then classical diffusion is observed. An example would be

$$\psi(t) = \lambda \exp(-\lambda t) \quad (95)$$

where the mean waiting time is $1/\lambda$. If, on the other hand, $\int t \psi dt$ diverges, then non-Gaussian or "dispersive" transport is seen. Of particular interest in this respect are $\psi(t)$ with long time tails:

$$\psi(t) = \frac{\alpha A t^{-1-\alpha}}{\Gamma(1-\alpha)}, \quad 0 < \alpha < 1 \quad (96)$$

In other words, the hopping probability is a slowly decaying function of time. Under these conditions, the dispersion of the concentration, $\langle x^2(t) \rangle$, becomes proportional to t^α , and the diffusion coefficient

$$D(t) = \left(\frac{1}{2\Delta} \right) \frac{d\langle x^2 \rangle}{dt} \quad (97)$$

and conductivity become time dependent, with a power-law dependence on frequency and time. Here Δ is the dimensionality of the system.

The physical origin of a power-law distribution function for waiting times might arise from an exponential distribution of activation energies. Suppose the distribution function of activation energies was of the form

$$K(E^*) = \frac{K_0 \exp(-E^*)}{E_0^*} \quad (98)$$

Then, if the waiting time were proportional to the exponential of the activation energy, the distribution of waiting times would have a power-law dependence on time, as required by Eq. (96).

The concepts of the CTRW approach have been applied to ionic conductivity in glasses by Abéard and Baumard [1984]. In an alkali silicate glass, it is usually assumed that only a small number of the alkali metal ions are mobile, and the remainder is associated with nonbridging oxygens, which forms dipoles that may reorient in the presence of an electric field. Interpretation of the complex impedance or dielectric constant of these glasses therefore is usually made in terms of a distribution of these relaxation times, in the manner discussed in the previous section. Abéard and Baumard, however, suggest that a more appropriate approach is to consider all alkali ions mobile, but with a distribution of activation energies associated with the potential wells in which they are situated. There is, therefore, a

distribution of waiting times, which leads to the observed frequency dependence of the real part of the conductivity.

An interesting extension of the dispersive transport model is its application to dielectric relaxation. As mentioned earlier, Glarum [1960] proposed that “frozen in” polarizations could be relaxed when a defect (e.g., a mobile charge carrier) approached them. Bordewijk (1975) extended the model and showed that in one-dimensional transport, a Williams–Watts dielectric relaxation function with $\alpha=1/2$ resulted, but normal Debye relaxation was predicted in three dimensions ($\alpha=1$). Schlesinger and Montroll [1984] have shown that if diffusion of the mobile defect is restricted to a CTRW with a long-time-tailed $\psi(t)$, then a Williams–Watts dielectric function for the relaxation of the dipoles is expected. The relaxation process is treated as a diffusion-controlled chemical reaction.

The essentially different nature of transport processes with $\psi(t) \propto t^{-(1-\alpha)}$ should be stressed. Processes with this type of waiting time distribution function show an absence of scale. They exhibit very sporadic behavior. Long dormancies are followed by bursts of activity. They have been described as *fractal time* processes (Schlesinger [1984]). *Fractal space* processes, in which the absence of scale is present in the spatial aspects of the transport, are considered later in this section.

A different approach to transport in disordered systems has been developed by considering the excitation dynamics of random one-dimensional chains (Alexander *et al.* [1981]). Such a system may be represented by a master equation of the form

$$\frac{dP_n}{dt} = w_{n,n-1}(P_{n-1} - P_n) + W_{n,n+1}(P_{n+1} - P_n) \quad (99)$$

where the P 's are the amplitude of the excitations (site occupancies) and the W 's are the transition probabilities between the nodes or sites, n , and so on. This equation is obviously a discrete form of the diffusion equation, with the W 's stochastic variables described by a distribution function. The electrical analog to this equation is the random transmission line, described by the equation

$$\frac{C_n dP_n}{dt} = W_{n,n-1}(P_{n-1} - P_n) + W_{n,n+1}(P_{n+1} - P_n) \quad (100)$$

Here the C 's are the random capacitances, the W 's are the random conductances, and the P 's are the node potentials.

Alexander *et al.* [1981] have obtained solutions to this type of equation for various types of distribution functions of W for an initial delta function input in P . In particular, they considered distribution functions for which a mean transition rate $\langle W \rangle$ could be defined and functions that were of the form

$$\rho(W) = \rho_0(T)W^{-\alpha(T)} \quad (101)$$

where no mean transition rate exists. This is similar to the distribution function of waiting times for a CTRW defined in Eq. (96), and the arguments suggesting its use are essentially the same. The transition rate is an exponential function of activation energies, and the activation energies are supposed to be exponentially distributed, leading to a power-law form for the distribution of transition rates. A similar argument can be used if a distribution of jump distances is assumed, that is, configurational disorder rather than randomness in the activation energies is assumed.

As for the case of the CTRW method, qualitatively different solutions are obtained depending on whether a mean transition rate can be defined or not. In the former case, the system behaves as if it were ordered with a single transition rate [$\rho(W) = \delta(W - W_{av})$], even though the W 's are random variables. These systems exhibit a frequency-independent low-frequency conductivity.

For power-law distributions, however, the low-frequency conductivity tends to the form

$$\sigma(\omega) \propto (-j\omega)^{\alpha/(2-\alpha)} \quad (102)$$

as $\omega \rightarrow 0$. There may also be a situation in which a crossover between the two distributions occurs as a function of time, in which case the mean square particle displacement is given by

$$\langle x^2 \rangle = 2D_0t + Bt^{1-s} \quad (103)$$

and the real part of the conductivity is

$$\sigma'(\omega) = \sigma(0) + A\omega^s \quad (104)$$

Thus, at low frequencies a constant conductivity would be seen, but at higher frequencies a power-law contribution enters. In these equations, D_0 is the limiting diffusion coefficient and A and B are thermally activated constants.

Experimental observations of the frequency dependence of the conductivity in the one-dimensional ionic conductor potassium hollandite (Bernasconi *et al.* [1979]) show a pronounced power-law dependence, as predicted by the model. It was proposed that the transport process in this material was limited by random barrier heights caused by the presence of impurities.

In the previous paragraphs it was pointed out that a discrete time random walk, or a CTRW with a finite first moment for the waiting time distribution, on a lattice with a fixed jump distance led to a Gaussian diffusion process with a probability density given by Eq. (84). The spatial Fourier transform of this equation is

$$\mathbf{n}(q, t) = \exp(-Dtq^2) \quad (105)$$

Disorder was introduced into this system by postulating a distribution of waiting times. A complementary extension of the theory may be made by considering a distribution of jump distances. It may be shown that, as a consequence of the central limit theorem, provided the single-step probability density function has a finite second moment, Gaussian diffusion is guaranteed. If this condition is not satisfied, however, then Eq. (105) must be replaced by

$$\mathbf{n}(q, t) = \exp(-At|q|^\mu) \quad (106)$$

where μ lies between 0 and 2. This distribution function is known as a Levy or stable distribution. This distribution is a solution of the equation

$$\frac{\partial \mathbf{n}(q, t)}{\partial t} = -A|q|^\mu \mathbf{n}(q, t) \quad (107)$$

which is, of course, the Fourier transform of the diffusion equation when $\mu = 2$. A number of authors have considered the type of random walk process, defined by the Levy distribution (Hughes *et al.* [1981]). A particle executes a walk, which may be transient and clustered. In other words, not all regions of space are visited by the walker, and a hierarchy of clusters is developed. The clusters may be self-similar, and Mandelbrot [1983] has stressed the fractal nature of walks with this distribution.

Other workers have also considered transport on a self-similar geometry through the connection with percolation. Close to a percolation threshold, the conductivity and dielectric constant behave with a power-law exponent in the concentration of one of the components, and the percolating cluster at the threshold has been identified as a fractal object. The temporal behavior of the diffusion process close to the percolation threshold has also been considered (Gefen *et al.* [1983]), and, using scaling arguments, it has been shown that the mean square displacement is

$$\langle r(t)^2 \rangle = at^\theta \quad (108)$$

where a and θ are constants, leading to a time- and frequency-dependent diffusion coefficient and conductivity. Experimental verification of this power-law dependence has been obtained for two-dimensional (2-D) percolation in thin gold films (Laibowitz and Gefen [1984]).

An alternative approach, used to describe the properties of ionically conducting glasses, is conceptually closely related to the earlier discussion of transport properties in materials with a small number of sublattices for the conducting species.

It has been recognized for a considerable time that if the translational invariance of the conductivity activation energy barriers is lost, then the dielectric and conductivity properties become frequency dependent. (See Figure 2.1.10c). For a material with no dipolar relaxation processes (i.e., ϵ_s is not a function of time), but with a conductivity σ_0 , then Eq. (94) becomes

$$Y^* = \sigma_0 + j\omega\epsilon_s\epsilon_0 \quad (109)$$

The equivalent circuit is simply a parallel—RC—combination, and thus

$$\epsilon^* = \epsilon_s - \frac{j\sigma_0}{\omega\epsilon_0} \quad (110)$$

Macedo *et al.* [1972b] defined the *conductivity relaxation time*:

$$\tau_\sigma = \frac{\epsilon_0\epsilon_s}{\sigma_0} \quad (111)$$

Hence

$$\epsilon^* = \epsilon_s - \frac{je_s}{\omega\tau_\sigma} \quad (112)$$

Macedo and others (Hodge *et al.* [1975, 1976]) have stressed the electric modulus formalism ($M^* = 1/\epsilon^*$) for dealing with conducting materials, for the reason that it emphasizes bulk properties at the expense of interfacial polarization. Equation (112) transforms to

$$M^* = M_s \frac{j\omega\tau_\sigma}{1 + j\omega\tau_\sigma} \quad (113)$$

where $M_s = 1/\epsilon_s$.

For a material with a single relaxation time τ_σ , a plot of M'' versus $\log(f)$ shows a maximum, in just the same way that ϵ'' shows a maximum for a dielectric relaxation process. Glassy conductors, however, often show broad and asymmetric modulus spectra, and, in complete analogy to the discussion of Section 2.1.2.3, Macedo *et al.* [1972a] introduced a distribution function of conductivity relaxation times $G(\tau_\sigma)$ such that

$$M^* = M_s \int_0^\infty G(\tau_\sigma) \frac{j\omega\tau_\sigma}{1 + j\omega\tau_\sigma} d\tau_\sigma \quad (114)$$

They were able to fit experimental modulus data for a calcium–potassium nitrate melt and a lithium aluminosilicate glass using a double lognormal distribution function.

The decay function for the electric field after the imposition of a charge on the electrodes

$$\phi'(t) = \frac{\mathbf{E}(t)}{\mathbf{E}(t=0)} \quad (115)$$

may also be defined, in analogy to the decay of polarization function [Eq. (63)]. For a single relaxation time,

$$\phi'(t) = \exp\left(-\frac{t}{\tau_\sigma}\right) \quad (116)$$

The modulus is related to ϕ' through the expression

$$\frac{M^*}{M_s} = 1 - \left\{ \left(-\frac{d\phi'}{dt} \right) \right\} \quad (117)$$

where, as usual, { } denote a Laplace transform.

Moynihan *et al.* [1973] used the Williams–Watts form of ϕ' ,

$$\phi'(t) = \exp \left[- \left(\frac{t}{\tau_\sigma} \right)^\beta \right], \quad 0 < \beta \leq 1 \quad (118)$$

to obtain a much better fit to the same glass data mentioned previously. The same function has also been recently used to analyze modulus data for lithium phosphate glasses (Martin and Angell [1986]), where it was found that the parameter β was largely independent of temperature but the distribution broadened with increasing alkali content.

2.1.3 Mass and Charge Transport in the Presence of Concentration Gradients

2.1.3.1 Diffusion

In the absence of an electric field and terms in R_i , Eq. (30) reduces to

$$\frac{\partial c_i}{\partial t} = -\nabla \cdot j_i \quad (119)$$

$$= \nabla \cdot (D_i \nabla c_i) \quad (120)$$

In one dimension, for constant D_i ,

$$\frac{\partial c_i}{\partial t} = \frac{D_i \partial^2 c_i}{\partial x^2} \quad (121)$$

This equation has been introduced from two points of view. In the macroscopic approach it was assumed that the flux or diffusion current is proportional to a concentration gradient or a chemical potential gradient and also satisfies a continuity equation. The generalizations of and justifications for this approach lie at the basis of nonequilibrium thermodynamics; as such, they are independent of the atomistic nature of the processes involved.

On the other hand, in the atomistic approach, the time-dependent configurations of the system are determined from the probabilities of the elementary atomic process. The random walk approach calculates the probability of finding the system in a certain state after a certain time, given an initial distribution of particles. It is then possible to show that the distributions are solutions of the diffusion equation.

It was shown in Section 2.1.2.4 that the general flux equations (e.g., the Nernst–Planck equation) contain, in addition to the diffusion terms, a contribution from migration, that is, the movement of charged particles under the influence of an electric field. Under certain circumstances, it is quite possible to carry out experiments in which the field is negligibly small compared with the concentration or activity driving force.

In aqueous electrochemistry this situation is usually achieved by the use of a supporting electrolyte. This is an inactive salt that is added to the solution in high concentration to increase the conductivity enough that the migration term in Eq. (78) or Eq. (82) becomes very small. In solid-state electrochemistry, it is difficult to achieve the same effect in such a simple way. The movement of a minority charge carrier, either electronic or ionic, in a good solid electrolyte is an analogous situation. This result is exploited in the Wagner [1933] asymmetric polarization experiment in which the partial conductivity of electronic

species in a solid electrolyte is measured, assuming that the driving force for electronic conductivity is an activity gradient rather than an electric field. In the next section, another example, that of chemical diffusion in a majority electronic carrier, is discussed in more detail. It is worth mentioning that local electric fields arising from the coupled motion of two charged species through an approximate electroneutrality condition are not necessarily absent from the equations of this section. This local field may be present and profoundly affect the diffusion of species, without any net average field across the bulk of a sample leading to a migration process. In this section, it is assumed that a field that leads to a migration current is absent, but local fields, such as those present in neutral electrolyte diffusion or ambipolar diffusion, may be present.

The purposes of this section is to discuss the electrical analogs of diffusion processes in the absence of migration and to present suitable electrical equivalent circuits for analysis of data obtained under these circumstances.

From the point of view of IS, solutions of the diffusion equation are required in the frequency domain. The Laplace transform of Eq. (121) is an ordinary differential equation:

$$p\{c\} - c(t=0) = \frac{Dd^2\{c\}}{dx^2} \quad (122)$$

where p is the complex frequency variable:

$$p = \sigma + j\omega \quad (123)$$

This transformation of a partial differential equation into an ordinary differential equation illustrates a general advantage of working in the frequency domain. Solutions are of the form

$$\{\Delta c\} = A\exp(-\alpha x) + B\exp(\alpha x) \quad (124)$$

where $\{\Delta c\}$ is the Laplace transform of the excess concentration

$$\Delta c = c(x, t) - c(x, 0) \quad (125)$$

and $\alpha = \sqrt{(p/D)}$. Here A and B are constants to be determined by the boundary conditions. Experimentally, one boundary is usually the interface between the electrode and the electrolyte ($x = 0$). Consider the case of semi-infinite diffusion into the electrode:

$$\Delta c \rightarrow 0 \text{ as } x \rightarrow \infty$$

and therefore $B = 0$.

At $x = 0$ (the electrode-electrolyte interface), the solution is

$$\{\Delta c\}_{x=0} = \frac{\{\Delta i\}}{zF\sqrt{(pD)}} \quad (126)$$

where Δi is the ac current, which is equal to $-zFDd\Delta c/dx$. To calculate the impedance, we need a relationship between $\Delta c_{x=0}$ and Δv , the ac component of the voltage. For small perturbations around equilibrium, we may write

$$\frac{\Delta v}{\Delta c} = \frac{dE}{dc} \quad (127)$$

where (dE/dc) represents the change in electrode potential with concentration, which may be developed from a model (e.g., ideal solution assumptions) or from a separate thermodynamic measurement. For an

ideal solution $dE/dc = RT/zFc$. For small-signal conditions, the perturbation may also be expanded around a steady-state dc potential, in which case the surface concentrations due to dc must also be calculated from a steady-state flux equation.

Taking the Laplace transform of Eq. (127) and substituting into Eq. (126) gives

$$Z^*(p) = \frac{\{\Delta v_{x=0}\}}{\{\Delta i\}} = \frac{dE/dc}{zF\sqrt{(pD)}} \quad (128)$$

Setting $\sigma=0$ and separating the real and imaginary parts gives

$$Z^*(j\omega) = \frac{(dE/dc)(\omega^{-0.5} - j\omega^{-0.5})}{zF\sqrt{(2D)}} \quad (129)$$

The complex impedance is therefore inversely proportional to the square root of frequency. In the complex plane it is a straight line inclined at $\pi/4$ to the real axis.

Equation (121) has analogies in both heat conduction and electrical circuit theory. Consider the semi-infinite transmission line composed only of resistors and capacitors (Figure 2.1.12). If r is the resistance per unit length and c is the capacitance per unit length, then

$$I = -\frac{\partial V/\partial x}{r} \quad (130)$$

$$\frac{\partial V}{\partial t} = -\frac{\partial I/\partial x}{c} \quad (131)$$

Differentiating Eq. (130) and combining the two equations gives

$$\frac{\partial V}{\partial t} = \frac{\partial^2 V/\partial x^2}{rc} \quad (132)$$

The analogy with diffusion may be made more specific if we compare the appropriate driving forces and fluxes. The electric potential difference V in the transmission line case is analogous to the electrochemical potential difference in the case of diffusion. Thus,

$$\frac{\partial V}{\partial x} \equiv \frac{RT}{zF} \cdot \frac{1}{c} \cdot \frac{\partial c}{\partial x} \quad (133)$$

for an ideal solution (the case for which Fick's law is least ambiguously valid). The reciprocal of the resistance per unit length is analogous to cDF^2z^2/RT , and the capacitance per unit length is analogous to z^2F^2c/RT .

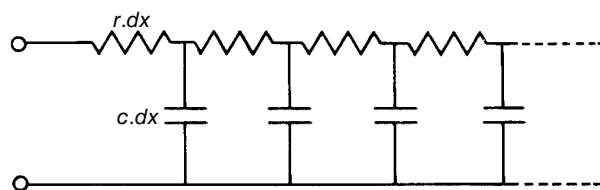


FIGURE 2.1.12 A resistive-capacitive transmission line that describes the behavior of a semi-infinite diffusion process.

Thus the reciprocal of the rc product plays the role of the diffusion coefficient. The impedance of the transmission line is

$$Z_R = \sqrt{\frac{r}{pc}} \quad (134)$$

which is exactly the same form as Eq. (129) if appropriate substitutions are made. For a nonideal solution, RT/zFc may be replaced by (dE/dc) .

So far, only semi-infinite boundary conditions have been considered. For many problems, however, thin samples dictate the use of finite-length boundary conditions. A reflective boundary $dc/dx = 0$ has been considered by Ho *et al.* [1980] and the impedance derived for this case:

$$Z(j\omega) = \frac{dE}{dc} \cdot \frac{1}{zF} \cdot \frac{\coth l\sqrt{(j\omega/D)}}{\sqrt{(j\omega D)}} \quad (135)$$

The equivalent circuit analog of this situation is a finite-length transmission line terminated with an open circuit. A constant activity or concentration is also a common condition for the interface removed from $x = 0$. In this case the finite-length transmission line would be terminated in a resistance, and the impedance is given by the expression

$$Z(j\omega) = \frac{dE}{dc} \cdot \frac{1}{zF} \cdot \frac{\tanh l\sqrt{(j\omega/D)}}{\sqrt{(j\omega D)}} \quad (136)$$

The complex plane representations of these two impedance behaviors are shown in Figure 2.1.13.

In this section the following principal assumptions were made. First, it was assumed that the surface concentrations and potentials were given by their equilibrium or dc steady-state values. In other words, there was supposed to be no barrier preventing or slowing down the transfer of matter across the electrode–electrolyte interface. In general, of course, this will not be true, and the impedance associated with the interface forms a very important aspect of IS as applied to electrochemical situations. This is in

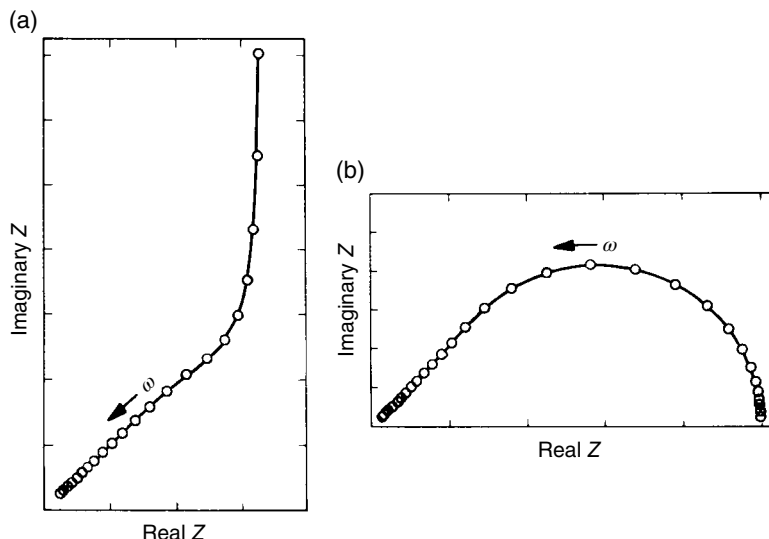


FIGURE 2.1.13 Complex plane representations of the impedance due to a finite-length diffusion process with (a) reflective and (b) transmissive boundary conditions at $x = 1$.

contrast to applications where the only interest lies in bulk effects. The interfacial impedance, due to both the storage and the dissipation of energy, will be addressed in Section 2.1.4.

Second, although the form of the diffusion equation was derived from ideal solution theory, it will be seen in the next section that the form of the equation may be retained, even though the dilute solution assumptions are relaxed, through definition of a chemical diffusion coefficient.

2.1.3.2 Mixed Electronic-Ionic Conductors

It was seen in the previous paragraphs that the presence of a supporting electrolyte leads to a situation in which a charged species may diffuse in an essentially field-free environment. Under these circumstances, Fick's law of diffusion may be solved for the appropriate boundary conditions, and the electrical response of the system may be modeled by a transmission line composed of distributed elements. Although such situations are very common in aqueous electrochemistry, the analogous situation in solids, where a minority ion diffuses in a solid supporting electrolyte, occurs infrequently.

More interesting is the commonly encountered situation where an ion diffuses in a majority electronic conductor. Thus, diffusion in metallic and semiconducting alloys or of inserted species in transition-metal oxides and chalcogenides falls into this category. Many electrode reactions are of this type. Lithium diffusion in β -LiAl and other alloys is of interest in negative electrode reactions for advanced lithium batteries; hydrogen and lithium diffusion in oxides (e.g., V_6O_{13}) and sulfides (e.g., TiS_2) is of importance as positive electrode reactions for batteries and electrochromic devices.

In materials of this type, the diffusion process may be regarded as involving a neutral atomic species, or as a coupled process in which an ionic and electronic species move together. In the simplest case, where the electronic partial conductivity is much greater than the ionic, the flux equation for a neutral species may be written as

$$j = -c^* u \frac{d\mu^*}{dx} = -c^* u RT \frac{d \log a^*}{dx} = -c^* D_k \frac{d \log a^*}{dx} \quad (137)$$

Here we cannot assume ideal or dilute solution behavior since the mobile species activity may vary widely especially if the electron activity changes rapidly over the stoichiometric domain of the phase of interest. After rearrangement we obtain the equation

$$j = -D_k \frac{d \log a^*}{d \log c^*} \cdot \frac{dc^*}{dx} = -D_k \left[1 + \frac{d \log \gamma^*}{d \log c^*} \right] \frac{dc^*}{dx} \quad (138)$$

which is equivalent of Fick's law if we write

$$D_c = D_k \left[1 + \frac{d \log \gamma^*}{d \log c^*} \right] \quad (139)$$

Here u is the mobility, μ the chemical potential, and γ the activity coefficient of the mobile species. The “*” denotes that the relations are written for a neutral species. Now D_k is the component diffusion coefficient, which, as pointed out in Section 2.1.2.4, obeys the Nernst-Einstein relation:

$$D_k = uRT \quad (140)$$

for all situations, irrespective of ideality assumptions.

The term in square brackets in Eq. (138) expresses the variation of activity coefficient of the *neutral* species with concentration. Thus, in addition to the statistical contribution to diffusion, expressed by the familiar gradient-in-concentration term, there is a chemical driving force due to the variation of free energy with composition and hence position. The term in square brackets is known as the thermodynamic enhancement factor and was identified by Darken [1948]. The diffusion coefficient D_c is known

as the chemical diffusion coefficient, and its use is appropriate whenever diffusion takes place in an appreciable concentration gradient and when ideal solution laws cannot be applied to the solute. The concept was extended by Wagner [1953], and a recent general treatment has been given by Weppner and Huggins [1977]. The more general approach involves elimination of the field term from simultaneous equations of the type

$$j_i = -RTu_i \left[\frac{d \log a_i}{d \log c_i} \frac{dc_i}{dx} + \frac{z_i F c_i}{RT} \frac{d\Phi}{dx} \right] \quad (141)$$

written for ionic and electronic species. The result is a general equation:

$$j_i = -D_{k_i} \left[\frac{(1-t_i)d \log a_i^*}{d \log c_i^*} - \sum_{j \neq i, e, h} t_j \frac{z_i}{z_j} \frac{d \log a_j^*}{d \log c_i^*} \right] \frac{dc_i}{dx} \quad (142)$$

valid for general transference numbers and thermodynamic parameters. For small-signal conditions (constant enhancement factor over the concentration range of the experiment), the diffusion equations are still of the Fick's law type and therefore lead to $\sqrt{\omega}$ dependence of the admittance (Warburg behavior).

In recent years, cells of the type



(where M is a mixed conducting host material for the inserted lithium) have been used to investigate the diffusion of Li in a number of alloys and oxides using ac impedance methods. The boundary condition at the electrolyte-electrode interface is a sinusoidally varying chemical potential of (neutral) lithium. It is important to recognize that the potential difference applied across a cell determines the activity of the electroactive species at the point at which the conductivity of the system changes from being predominantly ionic to being predominantly electronic. In this kind of experiment, the thermodynamic enhancement factor is conveniently determined *in situ* by measuring the dependence of equilibrium cell potential on electrode composition.

For thin samples, the second boundary condition may be modified to include either transmissive or reflective interfaces, as discussed in Section 2.1.3.1.

2.1.3.3 Concentration Polarization

The situation is often encountered where, upon the passage of current through an electrochemical cell, only one of the mobile species is discharged at the electrodes. Examples are (i) the use of a liquid or polymeric electrolyte, where both ions are mobile, and yet where only one is able to participate in the electrode reaction, and (ii) a mixed conducting solid in which current is passed by electrons but in which cations also have a significant transport number.

Consider a system consisting of a binary, unsupported electrolyte between electrodes that are reversible only to the cation. The cell is initially at equilibrium (no net currents are passing). At very short times after the imposition of a potential difference, the concentrations of all species in the bulk of the electrolyte are uniform, and the ions move in response to the applied field. The current is determined by the uniform electrolyte conductivity:

$$i = -F^2 \Sigma c_i z_i^2 u_i \frac{d\Phi}{dx} \quad (143)$$

At long times, on the other hand, the flux of the blocked anion falls to zero, and a constant flux of cations passes through the system. In order to maintain electroneutrality, there must also be a gradient in

anion concentration and hence in electric potential, which just balances the gradient in anion chemical potential:

$$\frac{d\Phi}{dx} = -\frac{1}{z_- F} \frac{d\mu_-}{dx} \quad (144)$$

Thus, there is effectively a gradient in the concentration of neutral species across the cell, and therefore we must include in the total potential difference a Nernstian term, which is equal to the potential difference that would exist immediately after the interruption of current flow, but before the reestablishment of uniform concentration profiles. The other contribution to the potential difference, that which is due to the flow of current itself, is a term arising from the gradient in conductivity due to the variations in concentration. This of course arises from differences in the mobility of the two species. It must be distinguished from the ohmic term present at very short times (high frequencies) due to the initially uniform conductivity of the electrolyte. The concentration polarization is therefore the additional polarization that is present due to concentration gradients caused by the current flow; this is compared with the ohmic polarization that would be present if the current flow (and distribution) were the same but the concentration gradients were absent.

Substitution of the condition (144) into the flux equation for cations

$$j_+ = -c_+ u_+ RT \frac{d \log c_+}{dx} - c_+ u_+ F \frac{d\Phi}{dx} \quad (145)$$

(assuming ideal solutions) gives the steady-state cation current

$$i_+ = -2u_+ RT \frac{dc^*}{dx} \quad (146)$$

The ohmic potential difference may then be found by integration of Eq. (144) across the cell using this flux equation. Since the current is constant, the concentration profile must also be uniform. The Nernstian term may be included as the potential of a concentration cell with the same concentration profile. It is possible to show that the ratio of the steady-state resistance to the high-frequency resistance depends on the transference numbers of the ions.

At large potentials this model predicts a limiting current density at which point the concentration at one of the electrodes has fallen to zero. For example, in a solid or polymeric electrolyte, with plane parallel electrodes and an initial uniform concentration of c ,

$$i_L = \frac{4c^* D_+ F}{l} \quad (147)$$

where l is the thickness of the electrolyte.

It is therefore apparent that in passing from high to low frequency in a system of this kind, there is an additional impedance due to concentration polarization. Macdonald and Hull [1984] considered this effect on the electrical response of this type of system. Under many circumstances, the presence of concentration polarization might be confused with an interface impedance. At different ratios of mobilities of anions and cations, either diffusion-like response (finite-length transmission line behavior) or parallel capacitive-resistive behavior may appear. Ac impedance methods have been used to determine ionic transference numbers in polymeric electrolytes using this principle (Sorensen and Jacobsen [1982]).

2.1.4 Interfaces and Boundary Conditions

2.1.4.1 Reversible and Irreversible Interfaces

Although it is quite reasonable to discuss the bulk properties of homogeneous phases in isolation, it is seldom possible in electrochemical situations to neglect the interfaces, since potentials and fluxes are

usually measured or defined at junctions between ionically and electronically conducting phases. In general, two extreme types of interface are recognized.

The first type is an interface that is reversible to the species under consideration. The term *reversible* implies certain thermodynamic and kinetic properties. Thermodynamically, it means that an equilibrium relation of the type

$${}^1\Delta^2\eta_i = 0 \quad (148)$$

may be written for the i th species, which applies to points immediately on each side of the interface in phases 1 and 2. Here, η is the electrochemical potential. Thus, a clean interface between a parent-metal M and a binary M^+ conducting solid electrolyte is thermodynamically reversible; the activities of M , M^+ , and e^- are all equal across the interface.

Kinetically, the term is less well defined and depends more explicitly on the nature of the experiment. In practice, it means that the exchange current density (the microscopic flux crossing the interface equally in both directions at equilibrium) is very much greater than the net current density crossing the interface during the experiment or the measuring process. At appreciable current densities, however, the net current density may eventually exceed the exchange current density; interface kinetics then become important.

In the electrochemical literature it is useful to refer to a reversible interface or interfacial reaction as one whose potential is determined only by the thermodynamic potentials of the various electroactive species at the electrode surface. In other words, it is only necessary to take into account mass transport to and from the interface, and not the inherent heterogeneous kinetics of the interfacial reaction itself, when discussing the rate of the charge transfer reaction. This nomenclature has two principal disadvantages. First, it neglects the fact that mass transport to the interface, whether migration or diffusion, is inherently an irreversible or dissipative process in a thermodynamic sense. Second, it neglects the time dependence of the system. At short times the rate may be largely determined by interfacial reaction rates; at long times it may be determined by mass transport processes. This is particularly clear when ac experiments are performed; steady states may be achieved in the frequency domain that correspond to transient conditions in the time domain.

An interface may be reversible to one species, but blocking to others. In addition, in multicomponent systems, a reversible electrode may not necessarily define the thermodynamic potentials of all components present at the interface.

An electrode that is reversible to electrons but irreversible to ions is a common situation in both aqueous and solid-state electrochemistry. For determinations of *ionic* conductivity in electrolytes, this type of electrode has proved useful, because the concentrations of majority ionic species do not depend critically on the imposition of a well-defined thermodynamic activity of the electroactive neutral species. Measurements with two irreversible electrodes of a nonreactive metal are then permissible; numerous examples are found in the solid electrolyte literature. Minority electronic transport, however, typically depends very strongly on the activity of neutral components, and care must be taken to utilize thermodynamically meaningful experiments to determine minority conductivities. Asymmetric cells using one reversible electrode and one irreversible electrode are then appropriate but have actually been little explored using ac impedance methods.

A real electrode with some degree of reversibility will therefore allow a steady-state current to pass; in the sense that such a current obeys Faraday's laws, it is termed a *faradic current*. A completely polarizable electrode passes no faradic current. In transient or ac experiment, however, a polarizable electrode and a reversible electrode both pass a nonfaradic current, corresponding to charging or discharging of the interface capacitance and perhaps changes in the nature and concentration of any adsorbed species. The distinction between the two types of current is important in developing expressions for the impedance of the electrode-electrolyte interface.

2.1.4.2 Polarizable Electrodes

Within the voltage limits set by the thermodynamic stability range of the electrolyte, foreign metal electrodes may sometimes be regarded as ideally polarizable or blocking. The metal electrodes must not

react with the electrolyte, and for the moment adsorption and underpotential deposition will be neglected. From an electrochemical point of view, this is the simplest type of interface and has furnished much of the information we have about the electrified interface.

Depending on the initial positions of the Fermi levels of the electrolyte and electrode, a small amount of charge flows in one direction or the other, and a field is created on the electrolyte side of the contact. The mobile charges in the electrolyte distribute themselves over this field; the charge density of the metal is confined to the surface of the electrode. The excess charge density at any point within the electrolyte is given by Boltzmann statistics,

$$\begin{aligned}\rho(x) &= \sum z_i F c_i \\ &= \sum z_i F c_i^0 \exp\left(\frac{-z_i F \Phi}{RT}\right)\end{aligned}\quad (149)$$

and the relationship between charge and potential is given by the Poisson's equation, and thus

$$\frac{d^2\Phi}{dx^2} = \frac{-1}{\epsilon \epsilon_0} \sum z_i F c_i^0 \exp\left(\frac{-z_i F \Phi}{RT}\right) \quad (150)$$

Solution of this equation leads to the space-charge (diffuse double-layer) capacitance. For a symmetrical ($z_+ = z_-$) electrolyte,

$$C_d = \left[\frac{2z^2 F^2 \epsilon \epsilon_0 c_i^0}{RT} \right]^{1/2} \cosh\left(\frac{z F \Phi_0}{2RT}\right) \quad (151)$$

where Φ_0 is the potential at $x = 0$ (measured relative to $\Phi = 0$ at $x = \infty$). The diffuse double layer therefore behaves as a simple parallel plate capacitor. The perturbation in concentration due to the electric field extends into the electrolyte a distance on the order of the Debye length L_D :

$$L_D = \left[\frac{RT \epsilon \epsilon_0}{2z^2 F^2 c_i^0} \right]^{1/2} \quad (152)$$

Thus, the higher the concentration of the electrolyte, the thinner the diffuse double layer. In addition to the use of Boltzmann statistics, the model has assumed the following:

- a. Point charges, and hence no limit on the distance of closest approach to the interface
- b. A uniform dielectric constant
- c. A sharp boundary between the metal and the electrolyte, that is, the electronic wave functions do not extend beyond the geometrical plane of the interface
- d. No screening effects such as those found in the Debye-Hückel theory of electrolytes

At some potential, the situation will occur where there is no excess charge on either side of the interface and the concentration profiles are flat. This point is known as the potential of zero charge.

Up to now no real distinction has been made between solid and liquid electrolytes. In an extrinsically conducting solid, the complementary charge carrier will be absent; therefore, it will not be included in the distribution. However, the theory is basically equally applicable to solids, molten salts, and polar solvent electrolytes.

In the presence of a polar solvent molecule such as water, considerable attention has been focused on the role of the solvent. Since the dipole moment is free to rotate in the presence of an electric field, it is reasonable that in a layer of water close to the interface, there will be a net dipolar orientation and the water will not exhibit its normal dielectric constant. In addition, hydrated ions will not be able to

approach indefinitely close to the interface. Thus, up to a monolayer of charge will exist at a distance of closest approach to the electrode; this distance is determined by the size of the (hydrated) ion. Beyond this inner layer, the diffuse layer will extend back into the solution. The interface therefore behaves as two capacitors in series: an inner (Stern) layer and an outer (Gouy–Chapman) layer. The model takes into account both the dipolar nature of the solvent and some of the finite-size effects.

In a solid, of course, there is no solvent. However, we still expect an inner-layer capacitance, since there is still a finite distance of closest approach of the ions to the interface. Therefore,

$$C_i = \frac{\epsilon \epsilon_0}{d} \quad (153)$$

where C_i is the capacitance per unit area. If d is of the order of a few angstroms and ϵ is of order 1, then C_i should lie between 1 and $10 \mu\text{F}/\text{cm}^2$. We also expect it to be independent, or a slowly varying function, of interfacial potential difference. Since C_d , however, depends exponentially on voltage, we expect it to become large quickly, and therefore C_i will dominate the interface capacitance except when it is close to the potential of zero charge.

There are few experimental studies of the solid electrolyte–solid electrode interface carried out in such a way that meaningful potential capacitance data can be obtained. This would involve the asymmetric cell type of arrangement, for example,



where the thermodynamic quantities of the electrolyte are fixed at the inert metal–electrolyte interface by the application of a potential difference. Some studies of this type have been performed, but there seems to be few instances of the observation of a well-defined diffuse double-layer capacitance. Most of the experiments were, however, performed on highly conducting materials, which would be expected to have very thin diffuse double layers.

A possible exception to this is the study of the graphite–AgBr interface (Kimura *et al.* [1975]), where a broad minimum in capacitance was found at potentials somewhat positive of the Ag–AgBr electrode potential at temperatures between 219 and 395°C. The minimum was somewhat broader than expected from the theoretical model, but of the correct order of magnitude. On the other hand, a similar experiment by Armstrong and Mason [1973] showed no particular minimum in capacitance at a similar temperature.

More often, the double-layer capacitance for the silver conductors seems to show a small potential dependence, more easily interpreted, at least qualitatively, in terms of an inner-layer phenomenon.

The experimental study of the solid–solid interface is complicated by a further problem. It is often (perhaps usually) observed that instead of a purely capacitive behavior, the interface shows significant frequency dispersion. Several authors have found excellent agreement of this behavior with the dispersion shown by the CPE (Bottelberghs and Broers [1976], Raistrick *et al.* [1977]). Although the amount of frequency dispersion is influenced by electrode roughness and other aspects of the quality of the interface (i.e., nonuniform current distribution), these are evidently not the only contributions to the observation of CPE behavior. Although no well-defined microscopic theory of the CPE has emerged, this empirically important aspect of both interface and bulk behavior is discussed further in this section and in Section 2.2. As is true for the case of the potential dependence of the capacitance, there have been too few studies of the frequency dispersion of the interface. It should be mentioned that the microscopically smooth liquid metal–aqueous electrolyte interfaces apparently do not show frequency dispersion of the capacitance if the systems are quite pure.

2.1.4.3 Adsorption at the Electrode–Electrolyte Interface

In the previous section, the distance of closest approach of ions to a planar electrode–electrolyte interface was discussed. In solid electrolyte systems, this distance is assumed to be approximately the radius of the mobile ion. In the presence of a polar solvent, the hydration sheath of the ion and the solvent layer

adjacent to the metal are also important. The only forces acting on the interface have been assumed to be electrostatic in origin. These forces orient the solvent dipoles and determine the distribution of ions with distance from the interface.

It is possible, however, that an ion can interact chemically with the electrode material. If this happens, the ion may break through the solvent layers or, as in the case of the solid, become displaced from a normal lattice site. This possibility is known as specific adsorption. In aqueous electrochemistry the locus of the centers of the specifically adsorbed ions is known as the inner Helmholtz plane. Neutral molecules may also adsorb and hence affect the faradic current, for example, by blockage of the reaction sites. Neutral molecule effects have not been studied in the case of solid systems and will therefore not be considered further.

In order to include adsorption in a discussion of the electrical response, it is necessary to know the relationship between the surface concentration of the adsorbed species and the concentration in the electrolyte just outside the double layer. This last concentration can then be related to the bulk or average concentration through appropriate diffusion equations.

For a neutral molecule, potential dependence will still be expected, since at large potential differences the force acting on the dipole of a polar solvent will be sufficient to compete with all but the strongest adsorption bonds.

A simple isotherm, due originally to Langmuir, assumes that the free energy of adsorption ΔG_i^0 is the same all over the surface and that interactions between adsorbed species are neglected. Under these conditions, the surface concentration Γ_i is related to the surface concentration at full coverage Γ_0 by the expression

$$\frac{\Gamma}{\Gamma_0 - \Gamma} = \frac{\theta}{1-\theta} = a_i^b \exp\left(\frac{-\Delta G_i^0}{RT}\right) \exp\left(\frac{-\Phi z_i F}{RT}\right) \quad (154)$$

where a_i^b is the bulk activity of i .

The capacitance associated with the adsorption can be obtained by differentiation of the charge due to the adsorbed species

$$q = \theta q_i \quad (155)$$

where q_i is the charge corresponding to one monolayer:

$$C = \frac{dq}{d\Phi} = \left(\frac{dq}{d\theta}\right) \left(\frac{d\theta}{d\Phi}\right) = q_i \left(\frac{z_i F}{RT}\right) \theta(1-\theta) \quad (156)$$

Various attempts have been made to include interactions between adsorbed species. As pointed out by Conway *et al.* [1984], the correct way to handle interactions is to include the appropriate pairwise or long-range interaction term into the partition function, which allows calculation of the Helmholtz free energy and the chemical potential. These quantities are a function of θ due to (i) the configurational term, as included in the Langmuir case, and (ii) the interaction or deviation from ideality.

As an example, Frumkin's isotherm may be derived by assuming a pairwise interaction of the form

$$U(\theta) = \frac{r\theta^2}{2} \quad (157)$$

where r is positive for a repulsive interaction and negative for an attractive force. This leads to

$$\frac{\theta}{1-\theta} = a_i^b \exp\left(\frac{-\Delta G_i^0 - r\theta}{RT}\right) \exp\left(\frac{-\Phi z_i F}{RT}\right) \quad (158)$$

This yields a capacitance of the form

$$C(\theta) = q_i \left(\frac{z_i F}{RT} \right) \cdot \frac{\theta(1-\theta)}{1 + r\theta(1-\theta)} \quad (159)$$

Comparing this expression with Eq. (156) indicates that the new capacitance expression can be expressed as a "Langmuir" capacitance in series with an "interaction" capacitance:

$$C(\theta) = (C_L^{-1} + C_I^{-1})^{-1} \quad (160)$$

Other expressions for different forms of the interaction term have been given by Conway *et al.* [1984].

The Temkin isotherm attempts to account for heterogeneity of the electrode surface by making the energy of adsorption vary linearly with coverage, which gives

$$\exp(r\theta) = K a_i^b \exp\left(\frac{z_i F \Phi}{RT}\right) \quad (161)$$

and

$$C(\theta) = q_1 \left(\frac{z_i F}{RT} \right) \cdot \frac{1}{r} \quad (162)$$

The rates of adsorption are usually rapid, and hence the kinetics is determined by other electrochemical or chemical steps and mass transport. Armstrong has pointed out that in solid electrolyte systems, where the interfacial potential difference cannot be varied independently of the concentration of the mobile species, the adsorption of that species cannot be controlled by a diffusional process.

Raleigh [1976] has put forward a model of competitive chemisorption of anions and cations in silver halides that leads to a broad maximum in capacitance at the potential of zero charge, in agreement with observations on some of these compounds. This approach is greatly extended in Macdonald *et al.* [1980a].

The kinetics of complex electrochemical reactions in the presence of adsorbed intermediates and its effect on the impedance of the interface is discussed in Section 2.1.4.4.

2.1.4.4 Charge Transfer at the Electrode–Electrolyte Interface

The rate of heterogeneous charge transfer reaction

$$O + ne = R \quad (163)$$

is given by the expression

$$-i_F = nF[k_f c_O - k_b c_R] \quad (164)$$

where i_F is the faradic current density, $k_{f,b}$ are the forward and reverse rate constants, and $C_{O,R}$ are the concentrations of the reactants and products at the interface at time t .

The current, in general, is composed of a steady state or dc part determined by the mean dc potential E and the mean dc concentrations at the interface, c_O and c_R , and an ac part, Δi_F , determined by the ac perturbing potential ΔE and the fluctuating concentrations Δc_i . The faradic impedance is given by the ratio of the Laplace transforms of the ac parts of the voltage and current

$$Z_F = \frac{\{\Delta E\}}{\{\Delta i_F\}} \quad (165)$$

Because charge transfer is involved, the presence of an electric field at the interface affects the energies of the various species differently as they approach the interfacial region. In other words, the activation energy barrier for the reaction depends on the potential difference across the interface. It is convenient to express the potential dependence of the rate constants in the following manner:

$$k_f = k_0 \exp \left[-\frac{\alpha nF}{RT} (E - E^0) \right] \quad (166)$$

$$k_b = k_0 \exp \left[\frac{(1-\alpha)nF}{RT} (E - E^0) \right] \quad (167)$$

where k_0 is the rate constant at the formal electrode potential E^0 and α is the apparent cathodic transfer coefficient. Hence

$$\frac{k_f}{k_b} = \exp \frac{nF}{RT} (E - E^0) \quad (168)$$

Generally, we can express Δi_F as an expansion of the ac parts of the concentrations and electrode potential:

$$\Delta i_F = \sum \left(\frac{\partial i_F}{\partial c_i} \right) \Delta c_i + \left(\frac{\partial i_F}{\partial E} \right) \Delta E + \text{higher-order terms} \quad (169)$$

Neglecting all but the first-order terms (linearization) and solving for ΔE ,

$$-\Delta E = \frac{1}{\partial i_F / \partial E} \left[\sum \left(\frac{\partial i_F}{\partial c_i} \right) \Delta c_i - \Delta i_F \right] \quad (170)$$

and hence

$$Z_F = \frac{1}{\partial i_F / \partial E} \left[1 - \sum \left(\frac{\partial i_F}{\partial c_i} \right) \frac{\{\Delta c_i\}}{\{\Delta i_F\}} \right] \quad (171)$$

The first term is the *charge transfer resistance*; the second term contains the influence of the ac part of the mass transport on the impedance. Here $\{\Delta c_i\}/\{\Delta i_F\}$ can be expressed as a solution of the diffusion equation. For example, for semi-infinite diffusion to a plane, we can use Eq. (126):

$$\frac{\{\Delta c_i\}}{\{\Delta i_F\}} = \frac{1}{nF \sqrt{(pD_i)}} \quad (172)$$

The coefficients in parentheses may be evaluated from the rate expressions discussed previously:

$$\left(\frac{\partial i_F}{\partial E} \right) = k_f \frac{n^2 F^2}{RT} \left[\alpha c_O + (1-\alpha)c_R \exp \frac{nF}{RT} (E - E^0) \right] \quad (173)$$

and

$$-\left(\frac{\partial i_F}{\partial c_O} \right) = nFk_f; -\left(\frac{\partial i_F}{\partial c_R} \right) = -nFk_f \exp \frac{nF}{RT} (E - E^0) \quad (174)$$

Here c_O and c_R are determined by the solution of the appropriate dc mass transport equations. The coefficients may then be substituted into Eq. (166) to give the overall faradic impedance.

At the equilibrium potential E_r , the net current is zero; therefore, c_O and c_R are equal to their bulk values c_O^* and c_R^* and are related through the Nernst equation

$$\frac{c_O^*}{c_R^*} = \exp \frac{nF}{RT} (E_r - E^0) \quad (175)$$

Under these circumstances, the coefficient $(\partial i_F / \partial E)$ simplifies to give

$$\frac{\partial i_F}{\partial E} = \frac{n^2 F^2}{RT} k^0 \exp \left[-\frac{\alpha nF}{RT} (E_r - E^0) c_O^* \right] \quad (176)$$

and the charge transfer resistance is

$$r_{ct} = \frac{RT}{nF i_0} \quad (177)$$

where the exchange current density is

$$\begin{aligned} i_0 &= nFk^0 c_O^* \exp \left[-\alpha \left(\frac{nF}{RT} \right) (E_r - E^0) \right] \\ &= nFk^0 c_O^{*(1-\alpha)} c_R^{\alpha} \end{aligned} \quad (178)$$

When mass transport to the electrode is unimportant, substitution of Eq. (178) into Eq. (164) gives the Butler–Volmer equation:

$$-i_F = i_0 \left[\exp \frac{nF}{RT} \alpha (E - E_r) - \exp \frac{nF}{RT} (1 - \alpha) (E - E_r) \right] \quad (179)$$

When E is sufficiently far removed from E_r , the current in one direction may be neglected, leading to the Tafel relation:

$$E - E_r = a + b \log i \quad (180)$$

It should be emphasized that the development of the expressions for charge transfer kinetics given here is not completely general. It rests on the assumptions of absolute rate theory. More general treatments have been given in the literature where no a priori assumption of the form of the dependence of the rate constants on potential is made (Birke [1971], Holub *et al.* [1967]). A point that arises from these more general treatments is worth pursuing here. For the case of semi-infinite diffusion to a planar interface, the faradic impedance may be written in the form

$$Z_F = r_{ct} + (\sigma_O + \sigma_R) \left(\frac{1}{\sqrt{\omega}} \right) (1 - j) \quad (181)$$

where r_{ct} is given by the inverse of Eq. (168) and σ are of the form

$$\sigma_O = \frac{RT}{n^2 F^2 \sqrt{2}} \cdot \frac{1/\sqrt{D_O}}{\alpha c_O + (1 - \alpha) c_R \exp(nF/RT)(E - E^0)} \quad (182)$$

and

$$\sigma_R = \frac{RT}{n^2 F^2 \sqrt{2}} \cdot \frac{(1/\sqrt{D_R}) \exp(nF/RT)(E - E^0)}{\alpha c_O + (1 - \alpha) C_R \exp(nF/RT)(E - E^0)} \quad (183)$$

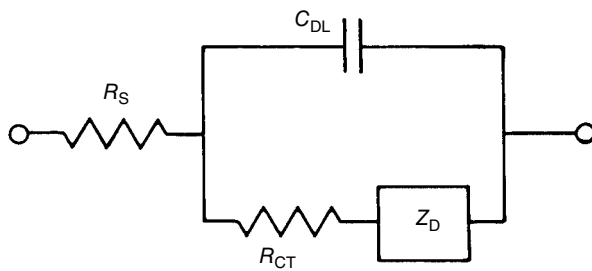


FIGURE 2.1.14 The Randles equivalent circuit, which describes the response of a single-step charge transfer process with diffusion of reactants and/or products to the interface.

The terms in $\sigma_i/\sqrt{\omega}$ correspond to the normal Warburg impedance; they do not contain the heterogeneous rate constants. The more general treatments, however, indicate that the Warburg impedance does in general contain coefficients that depend on the rate constants and their potential dependence. It is only on the basis of absolute rate theory that these coefficients cancel out of the final expression.

The complete equivalent circuit for a single-step charge transfer reaction in the presence of diffusion is given in Figure 2.1.14. The electrolyte resistance and double-layer capacitance have also been added to this figure.

A second aspect of the theory developed in this section is the assumption that the faradic current is decoupled from the nonfaradic current. In other words, the impedance due to the double-layer capacitance is included afterward and placed in parallel to the faradic impedance, since

$$i = i_F + i_{NF} \quad (184)$$

In general, however,

$$i_{NF} = \left(\frac{dq}{dt} \right) = \left(\frac{\partial q}{\partial E} \right) \left(\frac{\partial E}{\partial t} \right) + \sum \left(\frac{\partial q}{\partial c_i} \right) \frac{\partial \Delta c_i}{\partial t} \quad (185)$$

where the summation extends over all species, including O and R . Thus, the nonfaradic component is coupled to the faradic current unless experimental steps are taken to decouple them. This is usually achieved by making the concentration of electroactive ions very small compared with the inactive charge carriers, which do most of the double-layer charging.

In solid electrolytes, however, the unsupported electroactive species is often the sole charge carrier. It is thus impossible to change the interfacial potential difference without changing the concentration of ions in the double-layer region. This means, of course, that the normal Warburg impedance is not seen, but it also means that there is a coupling between the faradic current and the double-layer charging.

This has been recognized by Armstrong [1974], who has proposed the rate equation

$$i = i_0 \left[1 + \frac{C_{dl}(E - E_r)}{|q_-| - \Delta E C_{dl}} \right] \exp \frac{nF}{RT} \alpha(E - E_r) \quad (186)$$

for metal deposition from a solid electrolyte. Here, ΔE is the difference between E and the potential of zero charge, q_- is the charge density of anions in the inner layer, and C_{dl} is taken independent of voltage.

The treatment given previously for a single-step charge transfer reaction may be readily extended to more complex reaction schemes. For a multistep reaction, the partial currents of the individual steps must be appropriately coupled, and the mass transport relations defined for each step.

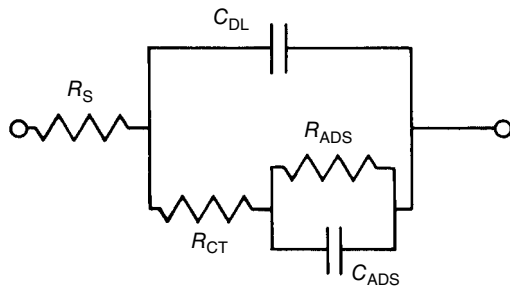


FIGURE 2.1.15 An equivalent circuit that describes the electrical response of an electrochemical reaction with a strongly adsorbed intermediate.

For example, for a surface-adsorbed species, intermediate in a two-step reaction, there will be an additional relationship of the type

$$\frac{d\Gamma}{dt} = \frac{\Delta i_F^1}{n_1 F} - \frac{\Delta i_F^2}{n_2 F} \quad (187)$$

where Γ is the surface concentration of the adsorbed intermediate produced by reaction 1 and removed by reaction 2. This case is of considerable importance in aqueous electrochemistry. The form of the impedance and the expected equivalent circuits have been discussed by Gerischer and Mehl [1955], Armstrong and Henderson [1972], Grahame [1952], and Epelboim and Keddam [1970]. In the absence of mass transport control, the equivalent circuit is of the form shown in Figure 2.1.15. Here R_{CT} is a charge transfer resistance, and R_{ADS} and C_{ADS} are components that contain the contribution of the surface concentration (converge) of the adsorbed intermediate and the rate of adsorption or desorption, respectively. Under certain circumstances R_{ADS} and C_{ADS} can become negative, leading to the appearance of inductive behavior in the impedance spectrum.

As applications of IS to very complex reactions in the solid state have not yet been made, further development of the theory of the faradic impedance seems unwarranted here. The linear operator approach to calculating the impedance of the systems is due to Rangarajan [1974] and is well described in the recent review of Sluyters-Rehbach and Sluyters [1984].

2.1.5 Grain Boundary Effects

It was suggested earlier that the electrical analog of an isotropic, homogeneous, ionically conducting solid is a pure resistance in parallel with a high-frequency ideal capacitor. This model assumes the absence of electrode polarization and of relaxation processes within the crystal that would lead to additional parallel branches in the equivalent circuit. This model is generally accepted, and several studies of single-crystal materials have demonstrated its validity.

Many solids are, however, studied in polycrystalline form, either because they are only available as such or because this is the manner in which they will be utilized. Polycrystalline materials usually have less than theoretical density (voidage) and misorientated grains (important in anisotropic materials). In the simplest case, these effects would lead to purely geometric reductions in the conductivity with respect to the single crystal. In addition, impurities may be present as a second phase at the grain boundaries. Because of the importance of ac IS as a tool for measuring ionic conductivity, there have been several studies of the effect of polycrystallinity on the impedance of solid electrolytes.

The problem was first attacked in a modern manner by Bauerle [1969], whose paper was the first application of IS to solid electrolytes. He studied both high-purity and "impure" polycrystalline zirconia. Bauerle found that the presence of a second phase at the grain boundaries in dense material led to the introduction of a second time constant in the equivalent circuit. This additional impedance was

absent in the very high-purity material. Bauerle envisaged the ionically insulating second phase as introducing a constriction in the area of contact between the grains of the highly conducting phase. Beekmans and Heyne [1976] found similar behavior in calcia-stabilized zirconia and suggested as well that a distribution of time constants for the grain boundary behavior was appropriate rather than the single—RC—time constant as was suggested by Bauerle.

Later, it became apparent that a second phase need not be present in polycrystalline materials for the grain boundaries to make a contribution to the impedance of the system. There have been several studies of the impedance of polycrystalline sodium β -alumina, a very nonisotropic solid electrolyte. Hooper [1977] systematically studied the relationship between single-crystal and polycrystalline material and showed that it was possible to extract “true” bulk values from polycrystalline samples. This intragrain conductivity had the same activation energy as the single-crystal material; there still was, however, a relatively small difference between the absolute conductivity values, probably mostly due to the geometric effects introduced by the anisotropy of the material, and preferential orientation in the pressed samples. Grain boundary (intergrain) conductivity had greater activation energy and disappeared at high temperatures.

There have also been several studies of the more isotropically conducting materials based on the Li_4SiO_4 and γ -II Li_3PO_4 (“LISICON”) structures (Ho [1980], Bruce and West [1983]). Ho varied the density of polycrystalline $\text{Li}_{4+y}\text{Si}_{1-y}\text{Al}_y\text{O}_4$ from nearly the theoretical density down to about 60% of theoretical density. At the highest densities, only a single circular arc was seen in the impedance plots, but at lower densities two arcs became apparent. The resistance associated with the lower-frequency arc exhibited higher activation energy than that associated with the higher-frequency arc, which was attributed to intergrain impedance. As with Hooper’s study of β -alumina, this contribution disappeared at higher temperatures. Ho’s study and the 1976 work of Raistrick *et al.* [1976] on other polycrystalline aluminosilicates noted, however, that except for the very densest of materials, polycrystalline samples always showed some anomalous frequency dispersion. The circuit element now often known as a CPE was introduced to fit the data:

$$Y_{\text{CPE}}^* = A(j\omega)^\alpha \quad (188)$$

Each of the circular arcs found in the polycrystalline materials was of the form shown in Figure 2.1.16. It seems that polycrystallinity introduces anomalous frequency dispersion into the bulk impedance behavior before a second and separate contribution from an intergrain impedance appears. A recent study by Bruce and West [1983] of polycrystalline LISICON essentially reached the same conclusions. Unlike Ho, however, the same activation energy was found for both inter- and intragrain resistances. This suggests that essentially the same physical processes are involved and that the authors attributed the intergrain impedance to a constriction effect, like that proposed by Bauerle. Bruce and West, however, attributed the constriction to the smaller area of contact between grains rather than

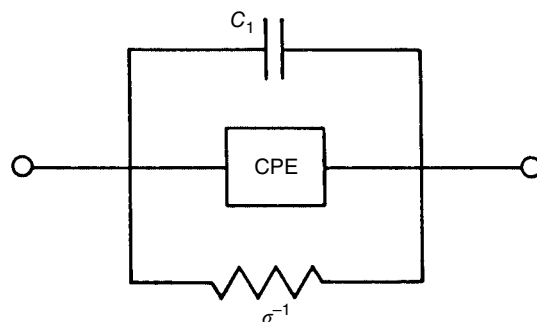


FIGURE 2.1.16 An equivalent circuit that describes the electrical response of polycrystalline solid electrolytes.

to the presence of an ionically insulating second phase. A recent investigation of the effect of a single-grain boundary on the response of an otherwise single-crystal CaO-doped CeO₂ specimen also found two semicircles in the impedance plane (El Adham and Hammou [1983]). Depending on the presence or absence of CaO enrichment at the grain boundary, a different activation energy was present for the resistance associated with the boundary. A detailed modeling of the properties of a constriction resistance of this type should be possible, but does not yet appear to have been carried out. It is also possible that close to a grain boundary, the transport properties of the crystal are controlled by imperfections, expected to be present there in higher concentration than that in the center of a grain, leading to an additional contribution to the intergrain impedance. This idea is very close to the observation of conductivity enhancement due to heterogeneous doping of solid electrolytes. Here, a second insoluble, nonconducting phase is introduced into the solid electrolyte as finely dispersed particles. The internal space charge created at the phase boundaries may lead to a significant increase in the concentration of mobile defects. A detailed impedance study of such a system would be of considerable interest, but does not yet appear to have been carried out.

2.1.6 Current Distribution: Porous and Rough Electrodes—The Effect of Geometry

2.1.6.1 Current Distribution Problems

It was pointed out in Section 2.1.2.4 that in most electrochemical systems, including those situations in which there is a concentration gradient but in which regions close to interfaces between different phases are excluded, electroneutrality is a reasonable assumption (Ibl [1983b]). Under these circumstances, the potential variation is given by Laplace's equation:

$$\nabla^2 \Phi = 0 \quad (189)$$

In principle, this equation may be solved subject to the following boundary conditions:

$$\Phi = \text{constant} \text{ (conducting boundary)}$$

$$\frac{\partial \Phi}{\partial n} = \text{constant} \text{ (insulating boundary)}$$

where n is normal to the boundary.

The potential and current distributions derived from these boundary conditions are called the *primary distribution*. They depend only on the geometry of the system. For very simple geometries, analytical solutions to Laplace's equation have been found. In recent years, numerical solutions have often become the preferred method, and both finite difference and finite element methods, as well as techniques based on Green's function methods, are valuable. Equation (189) corresponds to steady temperature in heat conduction problems; a useful discussion is found in Carslaw and Jaeger [1959].

Often, in solid-state experiments, the most common experimental arrangement is the most satisfactory from a primary current distribution point of view. The electrodes completely cover the ends of the electrolyte, and there is no spreading of the current lines. The current distribution should, however, be considered whenever more complex geometries are involved or the placement of a reference electrode is in question.

The real importance of current distribution problems in impedance measurements, however, lies in the fact that the distribution is frequency dependent. This arises because of the influence of interfacial polarization combined with the geometrical aspects of the arrangement.

The electrode–electrolyte interface is not an equipotential surface. This is because the interfacial potential difference is typically a function of the local current density. Thus, even for a purely resistive interface impedance—*independent* of local current density—there is a smoothing effect on the current distribution in the system. The greater the current density at a particular point, the greater the potential

drop across the interface, which in turn tends to lower the local current density. The tendency is therefore to make a uniform current distribution. The magnitude of the smoothing depends on the relative magnitudes of the interface and bulk impedances, as well as the geometry of the system. The current distribution in the presence of interfacial polarization (but neglecting mass transport effects) is called the *secondary distribution*.

In general, interfacial impedance is partly capacitive as well as resistive in nature. At high frequencies, the capacitance short-circuits the interface, and the primary distribution is observed for the ac part of the current. As the frequency is lowered, the interface impedance increases, causing a changeover to the secondary distribution. Of necessity, this effect leads to a frequency dependence of the equivalent circuit parameters that describe the system. Of course, if the primary distribution is uniform, there will be no frequency dispersion arising from this source.

The question of the frequency dependence of the current distribution and its effect on the measured impedance of a solid-state electrochemical system has been hardly considered, although it is important in discussing the impedance of, for example, porous gas electrodes on anion conductors, of rough electrodes (discussed below), and also perhaps of polycrystalline materials. In aqueous electrochemical situations, the effects have been considered with respect to the rotating disk electrode, where there may be severe current distribution problems.

2.1.6.2 Rough and Porous Electrodes

It is recognized that porosity or roughness of the electrode surface could be expected to lead to a frequency dispersion of the interfacial impedance even in the absence of detailed considerations of the current distribution problems as outlined previously.

A simple approach to the problem of porous and rough interfaces is based on the use of transmission line analogies (de Levie [1967]). Consider a cylindrical pore in a conducting electrode. If the series resistance of the electrolyte per unit length is r and the interfacial capacitance per unit length is c , then the pore behaves as a transmission line and has an impedance given by Eq. (135). This approach can be extended to more complex situations, which include pores of finite depth, nonuniform pores, and situations where the interfacial capacitance is replaced by a complex faradic admittance, corresponding to an electrochemical reaction taking place down the depth of the pore. It is also possible to include finite electrode resistance.

In order to describe a rough electrode, de Levie [1965] suggested a model based on the V-shaped groove shown in Figure 2.1.17. It was assumed that the double-layer capacitance was uniform over the true surface of the electrode and that the current lines were perpendicular to the *macroscopic* surface of the electrode. The impedance of the groove is then analogous to a transmission line in which the components are a function of the distance into the groove. The transmission line equation may be

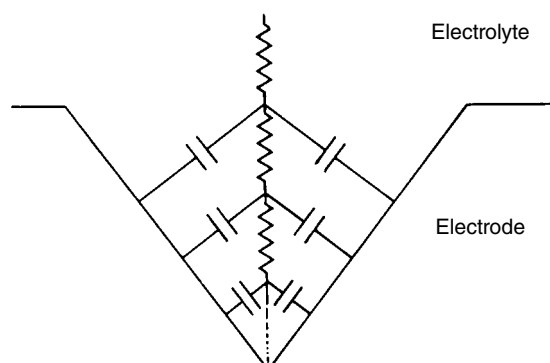


FIGURE 2.1.17 Transmission line model for a V-shaped groove in an electrode surface.

readily modified for the present case, where r and c are functions of x , which is the distance down the line:

$$I = -[1/r(x)]\partial V/\partial x \quad (190)$$

$$\frac{\partial V}{\partial t} = -[1/c(x)]\partial I/\partial x \quad (191)$$

On combining these equations, we obtain

$$-c(x)\frac{\partial V}{\partial t} = \frac{1}{r(x)^2} \cdot \left[\frac{\partial V}{\partial x} \frac{\partial r(x)}{\partial x} - r(x) \frac{\partial^2 V}{\partial x^2} \right] \quad (192)$$

The Laplace transform of this equation is, like the diffusion equation, an ordinary differential equation:

$$r^2 \frac{d^2\{V\}}{dx^2} - r \frac{dr}{dx} \cdot \frac{d\{V\}}{dx} - r^3 c p\{V\} = 0 \quad (193)$$

For r and c simple functions of x , the equation becomes a modified Bessel equation and may be solved analytically. For example, in the case of the groove geometry, as considered by de Levie,

$$Z = \frac{(\rho / \tan \beta) I_0(\lambda)}{\lambda I_1(\lambda)} \quad (194)$$

where Z is the impedance, 2β is the angle at the apex of the groove, ρ is the specific solution resistivity, and λ is $2\sqrt{(\rho l p k / \sin \beta)}$; k is the interface capacitance per unit area. In the limit of low and high frequency, the phase angle of the impedance changes from $\pi/2$ to $\pi/4$.

Using this approach, a number of different geometries can be analyzed (Keiser *et al.* [1976]). The interface impedance, considered in the aforementioned example to be a pure capacitance, could be generalized to include both real and imaginary components, for example, a Warburg impedance. In general, however, ρ and k would become functions of distance into the groove if significant diffusional effects were included in the calculation, and the diffusion layer thickness, relative to the thickness of the surface features, becomes important.

As pointed out by de Levie, however, the most important weakness in the model is the assumption that the current distribution is normal to the macroscopic surface, that is, a neglect of the true current distribution. For a rough surface, the lines of electric force do not converge evenly on the surface. The double layer will therefore be charged unevenly, and the admittance will be time and frequency dependent.

The tangential components of the interface charging were recognized and included in a qualitative model by Scheider [1975], who suggested the use of branched transmission lines to model the effects of uneven surface topology. The suggestion was significant in that transmission lines of this type do represent a circuit that, unlike the unbranched transmission line of de Levie, agrees with experimental observations of the impedance at rough electrodes.

The basic type of line suggested by Scheider is shown in Figure 2.1.18 for a single type of branching. In general, both the series (as shown) and the parallel components of a simple—RC—line may be replaced by other transmission lines, which may themselves be branched. The degree of branching may be unlimited. Let the series impedance per unit length be z and the parallel admittance per unit length be y (Figure 2.1.19). In addition, let all the z and all the y be independent of distance down the line. Using the continued-fraction approach to write the total impedance Z_T ,

$$Z_T = \frac{1}{y + \frac{1}{z + \frac{1}{y + \dots}}} \quad (195)$$

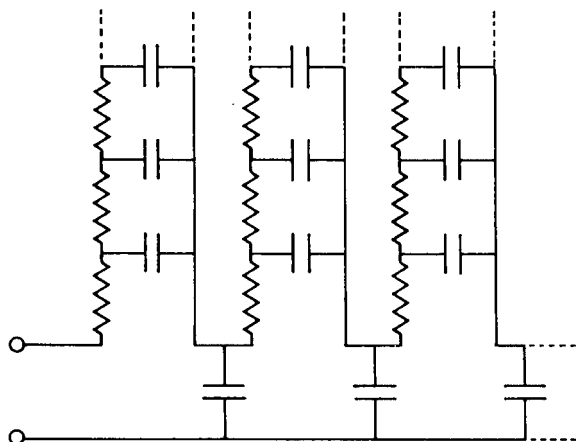


FIGURE 2.1.18 A branched transmission line circuit that shows CPE behavior.

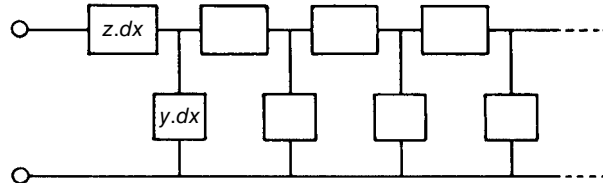


FIGURE 2.1.19 A generalized transmission line where z and y are, respectively, the series impedance and interfacial admittance per unit length.

For an infinite line,

$$Z_T = \frac{1}{y + \frac{1}{z + Z_T}} \quad (196)$$

or

$$Z_T = -\frac{z}{2} + \sqrt{\frac{z^2}{4} + \frac{z}{y}} \quad (197)$$

In the limit of $dx \rightarrow 0$, $z, y \rightarrow 0$ but z/y is finite. Therefore,

$$Z_T = \sqrt{\frac{z}{y}} \quad (198)$$

Suppose if z represents a transmission line $z = A(j\omega)^{-1/2}$ and y is a pure capacitance $y = j\omega C$, then

$$Z_T = \sqrt{\left(\frac{A}{C}\right)(j\omega)^{-3/4}} \quad (199)$$

Evidently, a first-order branching of the series component leads to an impedance with a phase angle of $(3/4)\pi/2$.

In fact, the value of the frequency exponents is limited only by the degree of branching of the circuit. The interval between frequency exponents is

$$\left[\frac{1}{2}\right]^{\theta+1}$$

where θ is the order of the branching. The frequency dependence is determined by the branching type and not by the magnitude of the components.

The important feature of these lines is that they produce a constant phase angle, like a Warburg impedance, but with the phase angle not restricted to $\pi/4$. This is exactly the behavior often found at the electrode-electrolyte interface and has been termed a CPE. It appears to be true that roughness is an important contributing factor to the observed frequency dispersion. Scheider's model, however, remains qualitative, and the microscopic link between the topology and the circuit is absent.

In general, a transmission line with nonuniform components, such as that described by Eq. (192), does not lead to CPE behavior. Schrama [1957] has shown that for lines with a particular type of non-uniformity, CPE behavior is predicted. This relationship is, for a discrete—RC—line,

$$R_k = \frac{2\Gamma(1-\alpha)}{\Gamma(\alpha)} \cdot \frac{\Gamma(\alpha+\kappa)}{\Gamma(1-\alpha+\kappa)} \cdot h^\alpha \quad (200)$$

$$C_k = (2\kappa+1) \frac{\Gamma(\alpha)}{\Gamma(1-\alpha)} \cdot \frac{\Gamma(1-\alpha+\kappa)}{\Gamma(1+\alpha+\kappa)} \cdot h^{1-\alpha} \quad (201)$$

where h is a positive real number. Schrama suggested an interpretation in terms of nonuniform diffusion (NUD) coefficients and driving forces.

Recently it has been shown (Liu [1985]) that at a fractal interface, a nonuniform transmission line will model the electrical response. The fractal geometry assumed was that of the triadic bar of Cantor, illustrated schematically in Figure 2.1.20a. The equivalent circuit corresponding to such an interface is shown in Figure 2.1.20b. It is evident that the circuit may be folded over into an—RC—transmission line with the resistance and capacitance per unit length related to one another in a specific manner.

The possible relationship between CPE behavior and a fractal interface geometry has also been emphasized by Le Mehaute [1984] and Le Mehaute and Crepy [1983].

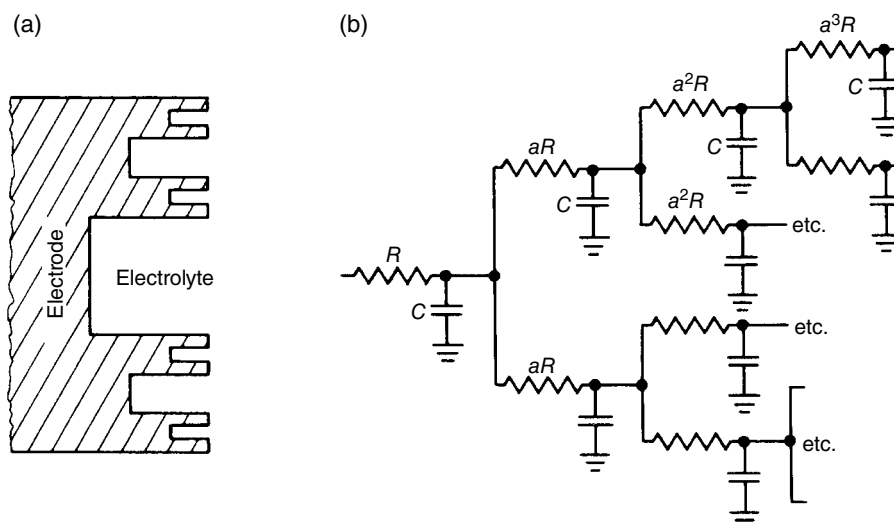


FIGURE 2.1.20 (a) Formal model for a fractal electrode-electrolyte interface and (b) an equivalent circuit that models the double-layer charging behavior.

This section was written by Ian D. Raistrick. The US government retains a royalty-free license to reproduce or reuse this material for in-house or governmental purpose.

2.2 PHYSICAL AND ELECTROCHEMICAL MODELS

2.2.1 The Modeling of Electrochemical Systems

Numerous theoretical models have been developed to explain and predict the behavior of electrochemical systems and to guide the design of systems with desired characteristics. The models that have been developed thus far fall generally into three broad categories, corresponding to three different levels of description of the system. From a practical standpoint, no one group of models is more important than another: the models that may be helpful to a materials scientist in fabricating a new solid electrolyte may provide no assistance at all to the engineer attempting to design a portable power source, which meets rigid cost and performance specifications.

At the most fundamental level of description are atomistic or microscopic models that attempt to provide an accurate description of the motions of individual charge-carrying particles in the system. At the least detailed level are the equivalent circuit models, in which hypothetical electrical circuits, consisting of elements with well-defined electrical properties, are used to describe the response of the system to a range of possible signals. Such models are of special interest in IS, since the frequency-response behavior of linear electrical circuits is now extremely well understood. An important variant of the equivalent circuit is the equivalent electrical network, composed of simple circuit elements of differential size. An introduction to equivalent circuit models is provided in Section 2.2.2. The electrical network approach is discussed in Section 2.2.3.4. The level intermediate between equivalent circuits or networks and microscopic models might be termed the *continuum level*, as the bulk regions of the electrodes and electrolyte are regarded as continuous media. The transport of mobile species is thus assumed to be governed by differential equations, and the transfer of charge across interfaces obeys rate laws that serve as boundary conditions for these equations. The parameters of the continuum model can be regarded as averages of the parameters appearing in an atomistic model. As can be seen in Section 2.2.3, the continuum parameters can usually be related to the parameters of an equivalent circuit model, and the analysis of the continuum model can thus guide in the construction of an appropriate equivalent circuit.

2.2.2 Equivalent Circuits

2.2.2.1 Unification of Immittance Responses

For a long time dimensionless normalization has been used in the dielectric constant measurement area of IS. As in Eq. (1) in Section 1.3, one supposes that there exist a low-frequency limiting value of the dielectric constant, ϵ_s , and a high-frequency limiting value, ϵ_∞ . In the latter case there may be even higher-frequency dispersions than that whose limit is ϵ_∞ , but in ordinary IS it is usually sufficient to establish (or assume) that $\epsilon = \epsilon_\infty$ over a wide range of high frequencies, and primary attention is directed to the response in the frequency region between $\epsilon = \epsilon_s$ and ϵ_∞ . Then the normalized response may be written as

$$k \equiv \frac{\epsilon - \epsilon_\infty}{\epsilon_s - \epsilon_\infty} \quad (1)$$

where $k \rightarrow 1$ as $v \rightarrow 0$ and $k \rightarrow 0$ as $v \rightarrow \infty$ (or to the region where $\epsilon \rightarrow \epsilon_\infty$). The function k is a normalized immittance, defined at the dielectric constant level.

For solid electrolytes one usually is concerned with intrinsically conducting systems rather than with intrinsically nonconducting (dielectric) ones. It is then appropriate and usual to consider basic system response at the impedance rather than the complex dielectric constant level. Then if one assumes

that the overall impedance of the system, Z_z , approaches R_0 at sufficiently low frequencies and R_∞ at sufficiently high ones, one can form the normalized dimensionless quantity

$$I_Z \equiv \frac{Z_z - R_\infty}{R_0 - R_\infty} \quad (2)$$

in analogy to Eq. (1). We have given a specific expression for I_z in Eq. (6) of Section 1.3. Again, $I_z \rightarrow 1$ as $v \rightarrow 0$ and $I_z \rightarrow 0$ as $v \rightarrow \infty$.

Since Eqs. (1) and (2) are similar in form, we can combine them in the single expression

$$I_k = \frac{U_k - U_{k\infty}}{U_{k0} - U_{k\infty}} \quad (3)$$

where $k = \epsilon$ or Z , $U_\epsilon = \epsilon^* = \epsilon' + j\epsilon''$ and $U_Z = Z = Z' + jZ''$. As before, U_{k0} and $U_{k\infty}$ are, respectively, the low- and high-frequency limiting real values of U_k . We actually use ϵ^* rather than ϵ here so that the imaginary parts of I_ϵ and I_z may be defined with the same sign.

Now as already mentioned in Section 1.3, the I_Z of that section's Eq. (6) is of just the same form as the well-known Cole–Cole dielectric dispersion response function (Cole and Cole [1941]). In its normalized form, the same I_k function can thus apply at either the impedance or the complex dielectric constant level. We may generalize this result (Macdonald [1985a, c, d]) by asserting that *any* IS response function that can be normalized as in Eq. (3) may be used at either the complex dielectric constant level or at the impedance level. It is very important to note that when the same function (with possibly different parameter values) is applied at both the complex dielectric constant and the impedance levels, it defines different systems at these levels. This matter is discussed in more detail in Macdonald [1985c]. Thus a theoretical derivation of response at one level automatically yields a response of the same kind for the other level but applying a different type of system. When the form of Eq. (3) is used to discuss bulk properties, we will use I_ρ for the complex frequency-dependent resistivity and I_σ for the complex frequency-dependent conductivity.

The aforementioned results allow us to use a single general $I(\omega)$ function to represent normalized response at either the ϵ or Z system levels. When the k subscript of I_k is omitted, it will be understood to be general in this sense. The use of the general normalized immittance response function I allows one to subsume two kinds of systems and response with a single function and will be so employed in the next section. Table 2.2.1 shows how I_k , for $k = Z$ or ϵ , is related for the various immittance levels to the specific conductive and dielectric systems functions. Here, as before, $\mu \equiv j\omega C_C$. Alternatively, to maintain dimensionless quantities at all levels, one might replace μ by $j\omega\tau \equiv js$, where τ is a specific relaxation time and $s \equiv \omega\tau$. Note that all functions are simply related to I . Let us illustrate these relations with a specific example. Take, for concreteness, $I_k = F_k(\psi_{kC}, s)$, the specific response function of Eq. (6) in Section 1.3. Then we can write

$$\epsilon_\epsilon = \epsilon_\infty + (\epsilon_s - \epsilon_\infty) F_\epsilon(\psi_{\epsilon C}, s) \quad (4)$$

TABLE 2.2.1 Relations between the General, Unified Immittance Function I and Specific System Functions

Conductive system ($k = Z$)	General system normalized	Dielectric system ($k = \epsilon$)
M	μI_k	Y
Z	I_k	ϵ
Y	I_k^{-1}	M
ϵ	$(\mu I_k)^{-1}$	Z

Note: Here $\mu \equiv j\omega C_C$.

$$Y_\epsilon = i\omega C_C \epsilon_\epsilon \quad (5)$$

$$Z_\epsilon = \{i\omega C_C [\epsilon_\infty + (\epsilon_s - \epsilon_\infty) F_\epsilon(\psi_{\epsilon C}, s)]\}^{-1} \quad (6)$$

and

$$Z_Z = R_\infty + (R_0 - R_\infty) F_Z(\psi_{ZC}, s) \quad (7)$$

$$Y_Z = Z_Z^{-1} \quad (8)$$

$$\epsilon_Z = \{i\omega C_C [R_\infty + (R_0 - R_\infty) F_Z(\psi_{ZC}, s)]\}^{-1} \quad (9)$$

We have used specific subscripts here to designate which type of system is involved. Now when one compares, say, Eqs. (6) and (7), both at the impedance level but for different types of systems, or Eqs. (4) and (9), both at the complex dielectric constant level, one sees that although the normalized expressions for I_z and I_ϵ are of exactly the same form, Z_ϵ and Z_Z as well as ϵ_ϵ and ϵ_Z yield very different frequency response. The main unification produced by the introduction of the general $I \equiv I_k$ is a single function allowed to represent typical normalized response of either a conductive ($k = Z$) or a dielectric ($k = \epsilon$) system.

2.2.2.2 Distributed Circuit Elements

Diffusion-Related Elements. Although we usually employ ideal resistors, capacitors, and inductances in an equivalent circuit, actual real elements only approximate ideality over a limited frequency range. Thus an actual resistor always exhibits some capacitance and inductance as well and, in fact, acts somewhat like a transmission line, so that its response to an electrical stimulus (output) is always delayed compared with its input. All real elements are actually distributed because they extend over a finite region of space rather than being localized at a point. Nevertheless, for equivalent circuits that are not applied at very high frequencies (say, over 10^7 or 10^8 Hz), it will usually be an adequate approximation to incorporate some ideal, lumped-constant resistors, capacitors, and possibly inductances.

But an electrolytic cell or dielectric test sample is always finite in extent, and its electrical response often exhibits two generic types of distributed response, requiring the appearance of distributed elements in the equivalent circuit used to fit IS data. The first type, that discussed previously, appears just because of the finite extent of the system, even when all system properties are homogeneous and space invariant. Diffusion can lead to a distributed circuit element (the analog of a finite-length transmission line) of this type. When a circuit element is distributed, it is found that its impedance cannot be exactly expressed as the combination of a finite number of ideal circuit elements, except possibly in certain limiting cases.

The second generic type of distributed response is quite different from the first, although it is also associated with finite extension in space. In all ordinary IS experiments, one uses electrodes of macroscopic dimensions. Therefore, the total macroscopic current flowing in response to an applied static potential difference is the sum of a very large number of microscopic current filaments originating and ending at the electrodes. If the electrodes are rough and/or the bulk properties of the material are inhomogeneous, the individual contributions to the total current will all be different and the distribution in electrode surface or bulk properties will lead to a distributed resistance (many different elemental resistances) or conductance.

The situation is even more complicated when small-signal frequency and time dependence are considered. Consider a material involving ion-hopping conduction. The immediate microscopic surroundings of different ions may be different at a given instant either because of inhomogeneous material properties or because the dynamic relaxation of the positions of atoms surrounding an ion has progressed a different amount for different ions. The result may be described in terms of a distribution of relaxation times, which, for example, might be associated with a distribution of hopping barrier height activation energies. Such a distribution of relaxation times will lead to frequency-dependent

effects, which may, at least approximately, often be described through the use of certain simple distributed circuit examples.

The first distributed element introduced into electrochemistry was the infinite-length Warburg [1899] impedance, often termed *the* Warburg impedance by those possibly unaware of the more general finite-length Warburg solution. The infinite-length Warburg impedance is obtained from the solution of Fick's second law, the diffusion equation, for one-dimensional diffusion of a particle in a semi-infinite space, a situation mathematically analogous to wave transmission on a semi-infinite distributed RC transmission line (see, e.g., Franceschetti and Macdonald [1979c]). Diffusion of atomic oxygen in an infinitely thick electrode might be described by this impedance, an impedance that we shall designate $Z_{W\infty}$ (see succeeding text). But real physical situations never involve infinite lengths (although this limit may sometimes be a useful one to consider). The solution for the diffusion of particles in a finite-length region (equivalent to a finite-length short-terminated transmission line) appears first to have been presented by Llopis and Colom [1958], for the *supported* situation, where the finite length considered was the thickness of the Nernst diffusion layer, appropriate for a stirred electrolyte or a rotating electrode. But particles diffusing in an electrode of thickness l_e or in an electrolytic cell of unstirred liquid or in solid material are free to move through the entire available region l_e or l . Thus it is reasonable to take the finite-length region where diffusion occurs as l or l_e in the case of present interest. General Warburg response for charge motion in a finite-length region of an *unsupported* electrolyte appears in the first exact solution of this problem (Macdonald [1953b]). It was identified and discussed in a later work (Macdonald [1971a, b, 1974a, b], Macdonald and Franceschetti [1978]). These results, particularly appropriate for solid electrolytes, will be discussed later in Section 2.2.3.3. Here it is sufficient to give the expression for Z_W for an uncharged particle diffusing in a finite-length region of length l_e , which might be the thickness of an electrode (Franceschetti and Macdonald [1979c]), and show how it reduces to $Z_{W\infty}$ as $l_e \rightarrow \infty$. The result may be written as

$$Z_W \equiv R_{D0} \left[\frac{\tanh(\sqrt{js})}{\sqrt{js}} \right] \quad (10)$$

where $s \equiv l_e^2(\omega/D)$ and D is the diffusion coefficient of the diffusing particle. Here the diffusion resistance R_{D0} is the $\omega \rightarrow 0$ limit of $Z_W(\omega)$. It may be expressed in a form involving various rate constants if so desired (Macdonald and Franceschetti [1978], Franceschetti [1981]). Series expansion readily shows that when $s \ll 3$, Z_W is well approximated by R_{D0} in parallel with a capacitance C_{D0} , where

$$C_{D0} \equiv \frac{l_e^2}{3DR_{D0}} \quad (11)$$

When plotted in the complex plane, Z_W leads to an initial straight-line region with $\theta = 45^\circ$: it reaches a peak value of $-Z''_w = 0.417 R_{D0}$ at $s = 2.53$ and then begins to decrease toward the real axis, finally approaching it vertically, as required by the limiting R_{D0} and C_{D0} in parallel.

When $s \gg 3$, the tanh term approaches unity and Z_W approaches $Z_{W\infty}$, given by

$$Z_{W\infty} = \frac{R_{D0}}{\sqrt{js}} = \left(\frac{R_{D0}}{l_e} \right) \left(\frac{2\omega}{D} \right)^{-1/2} (1-j) \quad (12)$$

clearly showing the 45° response of $Z_{W\infty}$. Let us define the frequency-dependent diffusion length as $l_D \equiv \sqrt{D/\omega}$; then $s \equiv (l_e/l_D)^2$. It is obvious that when $l_D \ll l_e$, for example, at high frequencies, $Z_{W\infty}$ response is found: the diffusion length is then much less than the entire region available for diffusion. But when l_D begins to approach l_e , $Z_{W\infty}$ response is no longer appropriate since diffusion begins to be limited and $Z_{W\infty}$ must then be replaced with Z_W . In fact, it is always reasonable and appropriate to use Z_W . The quantity Z_W will always be referred to as the Warburg or diffusion impedance in this work. Finally, the resistance R_{D0} is proportional to l_e and is thus extensive. Equation (11) also shows that

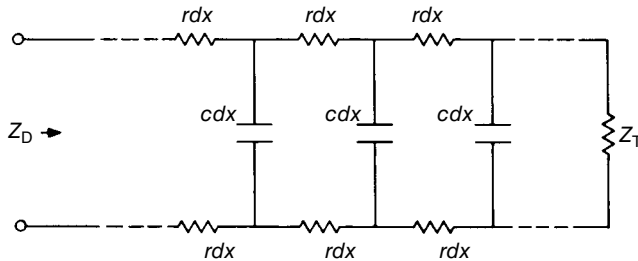


FIGURE 2.2.1 Uniform continuous transmission line involving series resistance of $2r$ per unit length and shunt capacitance of c per unit length, terminated by an impedance Z_T . When $Z_T = 0$, $Z_D = Z_W$, and when $Z_T = \infty$, $Z_D = Z_{DOC}$.

C_{D0} is also extensive (but proportional to l_e rather than to l_e^{-1} as in an ordinary plane parallel capacitance). Thus Warburg response becomes extensive and depends on electrode separation at sufficiently low frequencies. But as Eq. (12) shows, $Z_{W\infty}$ is entirely intensive since (R_{D0}/l_e) is itself intensive. One way of identifying Warburg response is to validate the transition from intensive to extensive behavior using measurements with two or more different values of l_e .

The Warburg impedance Z_W is the diffusion analog of the impedance of a finite-length, uniformly distributed RC transmission line (see Figure 2.2.1), which is short at the far end, equivalent in the diffusion case to unhindered disappearance of the diffusing particles at $x = l_e$. But this special situation, while common, by no means includes all cases of interest. An expression for the impedance Z_D of the finite-length diffusion problem with more general conditions at the far end has been presented by Franceschetti and Macdonald [1979c]. It is recommended that the general Z_D be used initially in an equivalent circuit representation and for fitting unless and until it can be established that $Z_D \cong Z_W$.

Although we shall not discuss the general $Z_D(\omega)$ further here, there is one additional specific case that follows from it and deserves mention. Suppose that the finite-length transmission line analog is open circuited (see Franceschetti and Macdonald [1979c]). Then no direct current can flow in the actual system, as it could with Z_W (but not $Z_{W\infty}$), and the concentration of the diffusing particle increases at the far end of the diffusion region where complete blocking occurs. The final low-frequency behavior of the open-circuit impedance, Z_{DOC} , is thus capacitive. Its representation at the dielectric constant level is

$$\epsilon \equiv \frac{Y}{j\epsilon C_C} = \left(\frac{C_{D0C}}{C_C} \right) \left[\frac{\tanh \sqrt{js}}{\sqrt{js}} \right] \quad (13)$$

Thus, the process leads to the limiting capacitance C_{D0C} as $\omega \rightarrow 0$: further, the frequency response at this level is exactly the same as that for Z_W at the impedance level [see Eq. (10)] and thus involves an initial straight line at $\theta = 45^\circ$. At the impedance level, $Z_{DOC} \equiv (j\omega C_C \epsilon)^{-1}$ is given by

$$Z_{DOC} = \left(\frac{\tau_{D0C}}{C_{D0C}} \right) \left[\frac{\operatorname{ctnh}(\sqrt{js})}{\sqrt{js}} \right] \quad (14)$$

where we have written $s \equiv \omega \tau_{D0C}$ so that $\tau_{D0C} \equiv l_e^2/D$. The appearance of response of the present type has been found in electrochromic thin films (see Glarum and Marshall [1980], Ho *et al.* [1980], Franceschetti and Macdonald [1982]). Equations (10) and (13) show immediately that the general I_k function associated with shorted or open-circuited diffusion is just

$$I_k = \frac{\tanh(\sqrt{js})}{\sqrt{js}} \quad (15)$$

A distributed element that shares some features with Z_W , Eq. (14), is the Gerischer impedance:

$$Z_G(\omega) = \frac{Z_{G0}}{\sqrt{k+j\omega}}. \quad (16)$$

This arises when an electroactive species undergoes a chemical reaction in the bulk (Gerischer [1951], Sluyters-Rehbach and Sluyters [1970, 1984], Boukamp and Bouwmeester [2003]). The Gerischer function is indistinguishable from the finite-length Warburg in the high-frequency limit, and like it, it yields purely resistive behavior in the low-frequency limit but differs from it in its detailed frequency dependence, yielding, for example, an arc closer to the real axis in the Z plane. Like the infinite-length Warburg, the Gerischer impedance is representable by a semi-infinite transmission line with a series resistance per unit length but with a parallel resistance added to the transmission line capacitance per unit length. A related result describing the diffusion of an electroactive species that is trapped at fixed sites was developed by Franceschetti [1984].

The somewhat similar function

$$Z_L(\omega) = \frac{Z_{L0}}{\sqrt{k+j\omega}} \tanh\left(\sqrt{k+j\omega}\right) \quad (17)$$

was found by Lorenz [1954] for an electrode reaction in which atoms are added to a ledge on a crystalline electrode. This function was proposed by Franceschetti and Macdonald [1979a] based on a treatment by Wang and Nowick [1979] involving oxygen diffusion along strip-like electrode contacts with an oxygen-conducting electrolyte. Franceschetti and Ross [1989] extended this result to circular electrode contacts, obtaining an impedance function in terms of cylindrical Bessel functions of $(k+j\omega)^{1/2}$.

The Constant Phase Element and Its Simple Combinations. Although Warburg and open-ended diffusion effects frequently appear in supported situations and sometimes in unsupported ones and exhibit characteristic $\theta = 45^\circ$ lines in the Z^* or ϵ plane, one often finds approximate straight-line behavior over a limited frequency range with $\theta \neq 45^\circ$ (e.g., McCann and Badwal [1982]). Then the frequency response of Z' and Z'' is no longer proportional to $\omega^{-1/2}$, but to some other power of ω . To describe such response, it is convenient to write, as in Eq. (7) in Section 1.3, at the admittance level,

$$Y_{CPE} = A_0(j\omega)^\psi = A_0\omega^\psi \left[\cos\left(\frac{\psi\pi}{2}\right) + j \sin\left(\frac{\psi\pi}{2}\right) \right] \quad (18)$$

where A_0 and ψ are frequency-independent parameters that usually depend on temperature and $0 \leq \psi \leq 1$. This admittance has been designated the CPE admittance because its characteristic feature, and that of Z_{CPE} as well, is a phase angle independent of frequency. Although a slightly more general form $a_0(j\omega t)^\psi$ may be written, the combination $(a_0 t)^\psi$ cannot be resolved into its parts using single-temperature frequency response measurements and fitting. The parameter A_0 will be intensive for interface processes and may be extensive for bulk ones. Unlike the finite-length Warburg impedance, the CPE exhibits no transition from intensive to extensive behavior as the frequency decreases. Note that a resistance R_∞ in series with $Z_{CPE} = Y_{CPE}^{-1}$ yields an inclined spur (straight line) in the Z plane, with an $\omega \rightarrow \infty$ intercept of R_∞ .

The importance of constant phase response was probably first emphasized by Fricke [1932]; the CPE was explicitly mentioned by Cole and Cole [1941], and its importance and ubiquity have been independently emphasized in recent times by Jonscher [1974, 1975a, b, 1980, 1983]. Some discussion of its history, relation to physical processes, and applicability has been given by Macdonald [1984]. Note that it describes an ideal capacitor for $\psi = 1$ and an ideal resistor for $\psi = 0$. It is generally thought to arise, when $\psi \neq 0$ or 1, from the presence of inhomogeneities in the electrode–material system, and it can be described in terms of a (nonnormalizable) distribution of relaxation times (Macdonald and Brachman [1956]), or it may arise from NUD whose electrical analog is an inhomogeneously distributed RC transmission line (Schrama [1957]).

Although CPE-like response appears in the majority of experimental data on solid and liquid electrolytes, it is always well approximated only over a finite range of frequency. In fact, the CPE cannot be applied for all frequencies and becomes physically unrealizable for sufficiently low or high frequencies (Macdonald [1984, 1985b, c, d]). Although many response theories lead to the CPE type of response for a finite frequency range, they must deviate from such response at the frequency extremes in order to yield realistic, physically realizable response. Because of the lack of full physical realizability, the CPE, as in Eq. (18), cannot be normalized in the usual I_k fashion. For example, the $\omega \rightarrow 0$ limits of neither ε_{CPE} nor Z_{CPE} exist. With this understood, we shall nevertheless write a unified expression for the CPE, taking it to represent just a dimensionless form of either ε or Z . Then we have

$$I_{\text{CPE}k} = B_k(j\omega)^{-\psi_k} \equiv (js)^{-\psi_k} \quad (19)$$

where B_k is a frequency-independent constant and the second form is less general than the first (Macdonald [1984]). For $k = Z$, one usually sets $\psi_Z = n$ and for $k = \varepsilon$, $\psi_\varepsilon = 1 - n$, where as usual $0 \leq n \leq 1$. These choices ensure that at the admittance level, for either $k = \varepsilon$ or $k = Z$, the fractional exponent ψ in Eq. (18) is just n .

There are three important subcircuits, shown in Figure 2.2.2, which consist of the CPE in conjunction with other circuit elements. Although they can always be treated by considering the CPE contribution separately, their wide use as combined elements and their historical importance justify their separate discussion as compound circuit elements and our assignment of specific designations to them. Further, it has not usually been recognized how such compound expressions can involve individual CPEs. The first subcircuit, that in Figure 2.2.2a, the εARC , yields a depressed symmetrical semicircular arc in the complex ε plane; the second, shown in Figure 2.2.2b, the $Z\text{ARC}$ or $Z\text{C}$, yields an arc in the Z plane; and the third, the $Y\text{ARC}$, leads to an arc in the Y plane. The depression of the arc of course depends on the CPE parameter ψ or n . We have already discussed in Section 1.3 the $Z\text{ARC}$ and simple ways of analyzing data exhibiting it. The same methods apply to depressed arcs in any complex plane.

The circuit shown in Figure 2.2.2a is just that originally proposed by Cole and Cole [1941] for dielectric systems. It yields capacitances C_0 in the $\omega \rightarrow 0$ limit and C_∞ in the $\omega \rightarrow \infty$ limit. When one uses the Eq. (18) definition of the CPE admittance, it leads to the following expression for ε :

$$\varepsilon = \varepsilon_\varepsilon = \varepsilon_\infty + \frac{\varepsilon_s - \varepsilon_\infty}{1 + (j\omega\tau)^{\psi_\varepsilon}} \quad (20)$$

where $\varepsilon_\infty \equiv C_\infty/C_C$, $\varepsilon_s \equiv C_0/C_C$, $\tau \equiv [(C_0 - C_\infty)/A_0]^{1/\psi_\varepsilon}$ and $\psi_\varepsilon \equiv 1 - \psi$. Cole and Cole related Eq. (20) to a particular distribution of relaxation times, and it has been widely used with $\psi_\varepsilon \equiv 1 - \alpha$ for the interpretation of IS results for dielectric and low conductivity liquid and solid materials. Clearly when $0 < \psi_\varepsilon < 1$,

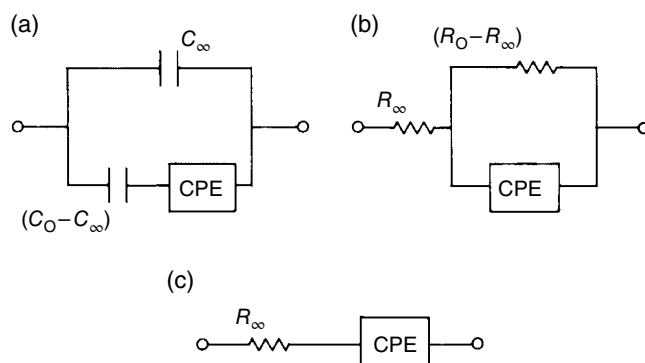


FIGURE 2.2.2 Three compound circuits involving the CPE:
(a) the εARC , (b) the $Z\text{ARC}$, and (c) the $Y\text{ARC}$.

Eq. (20) leads to a depressed arc in the complex ϵ plane. For $\psi_\epsilon = 1$, it yields a single relaxation constant Debye curve, a full semicircle.

In terms of the original CPE parameters of Eq. (18), the ϵ ARC admittance of Figure 2.2.2a may be written as

$$Y_\epsilon = Y_{\epsilon\text{ARC}} = j\omega \left[C_\infty + \frac{C_0 - C_\infty}{1 + [(C_0 - C_\infty)/A_0](j\omega)^{1-\psi}} \right] \quad (21)$$

For simplicity we shall usually ignore C_∞ in the definition of ϵ ARC; it may readily be included when needed. The ϵ ARC circuit element will, in fact, often appear in solid electrolyte equivalent circuits with C_∞ zero (or appearing elsewhere in the overall circuit). Then it is clear that the ϵ ARC function of Eq. (21) may be considered to represent a distributed (complex) capacitor. When $\psi = 0$, it involves an ordinary capacitor C_0 and resistor A_0^{-1} in series, and when $\psi = 1$, it involves C_0 in series with the capacitor A_0 . These results are consistent with the behavior of the CPE alone. The CPE reduces to an ideal capacitor for $\psi = 1$ and to a resistor for $\psi = 0$. A recent example of the use of the ϵ ARC function for the analysis of a polycrystalline sample is provided by the work of Casciola and Fabiani [1983].

It was independently suggested some time ago (Ravaire and Souquet [1973], Sandifer and Buck [1974], Macdonald [1976b]) that the following impedance form might be used to describe the depressed arcs that often appear when impedance data on solids is plotted in the Z^* plane, namely,

$$Z_Z = Z_{Z\text{ARC}} = \frac{R_0}{1 + (j\omega\tau)^{1-\alpha}} \quad (22)$$

where no R_∞ is included and $0 \leq \alpha \leq 1$. When R_∞ is included, one can write

$$Z_Z = R_\infty + \frac{R_0 - R_\infty}{1 + (j\omega\tau)^{\psi_z}} \quad (23)$$

which is just the impedance of the Figure 2.2.2b circuit with $\psi = \psi_Z$. This is an exact analog, at the impedance level, of the Cole–Cole complex dielectric constant expression of Eq. (20). Although the two forms may be described in terms of the same formal distribution of relaxation times, this distribution applies at different response levels for the two cases and thus describes a quite different system behavior (Macdonald and Brachman [1956], Macdonald [1985a, b, c]). Now it is clear that Eq. (22), which applies when $R_\infty = 0$ or is neglected, may be rewritten as

$$Z_Z = \frac{R_0}{1 + A(j\omega)^{\psi_z}} \quad (24)$$

involving the parameter $A \equiv \tau^{\psi_z}$. Now the parallel combination of a resistance R_0 and a CPE with parameter A_0 , as in Figure 2.2.2b, yields just

$$Z_Z = \frac{R_0}{1 + A_0 R_0 (j\omega)^{\psi_z}} \quad (25)$$

equivalent to the result in Eq. (24) if $A = A_0 R_0$ or $\tau = (A_0 R_0)^{1/\psi_z}$.

The foregoing results and the definition of I_k of Eq. (3) lead immediately to

$$I_k = [1 + (js)^{\psi_k}]^{-1} \quad (26)$$

where, as usual, $s \equiv \omega\tau$ (see the discussion in the last section). Since one obtains the ZARC function and the Cole–Cole equation when $k = Z$ and $k = \epsilon$, respectively, we suggest that the general normalized

response function of Eq. (26) be designated the ZC function. Again it is most appropriate to take $\psi_Z = \psi = \alpha$ and $\psi_\epsilon = 1 - \alpha$. Although CNLS fitting of data with either a CPE and R in parallel, as in Eq. (25), or the unified expression of Eq. (26), involving τ , will yield exactly the same fit, the two approaches involve different parameterizations (R_0, A_0 , and ψ_Z or R_0, τ , and ψ_Z). One or the other will generally yield smaller estimated standard errors for A_0 or τ and less correlation of one of these quantities with the other parameters. That choice should be used. Analysis of Na β -alumina data (Macdonald and Cook [1985]) gave better results, for example, with the τ parameterization.

It has already been mentioned that the series combination of a resistance R_∞ and a CPE as in Figure 2.2.2c leads to a depressed arc in the Y plane. Since such arcs are also often encountered experimentally, it is reasonable to define them as YARCs, for which the admittance may be written as

$$Y_{\text{YARC}} = \frac{G_\infty}{1 + (R_\infty A_0)^{-1} (j\omega)^{-\psi}} \quad (27)$$

where $G_\infty \equiv 1/R_\infty$. The similarity to Eq. (25) is obvious, although frequency increases along the ZARC and the YARC in opposite directions, as usual for Z - and Y -plane plots. Although it is possible to define a dimensionless function like I_k , which can represent either Y -system or M -system response, just as I_k represents either conductive or dielectric system response, the matter will not be pursued here. In fact, a single dimensionless function with superscript $k = \epsilon, Y, Z$, or M may be used to represent response of any of the four different immittance-level systems if the normalization is properly defined at each level.

It is worth mentioning that although Eqs. (20)–(27) may be interpreted as involving NUD (Schrama [1957]) either in bulk or at an interface, another allied but somewhat different approach that also leads to Eq. (22) has recently been proposed (Le Mehaute and Crepy [1983]) without reference to its earlier history and use. This theory involves mass transfer at a fractal interface, one with apparent fractal dimensionality d , with $d = \psi^{-1} = (1 - \alpha)^{-1}$. A more solidly based treatment of a fractal interface has been published by Liu [1985]. Unfortunately, neither of these approaches provides a quantitative interpretation in terms of microscopic parameters of why ψ , determined from data fitting on solids or liquids, often depends appreciably on temperature.

The aforementioned results show that the $\psi_\epsilon = 1 - \alpha$ parameter that appears in the ϵ ARC Cole–Cole function, Eq. (20), associated with a CPE and ideal capacitor in series, and the ψ s appearing in the ZARC and YARC functions, Eqs. (25) and (27), associated with a CPE and resistor in parallel or in series, may all be interpreted as the ψ of a CPE. The ψ values estimated from fitting with these forms are thus comparable. Although the CPE has sometimes been found in equivalent circuit data fitting to appear separately and not directly in any of the aforementioned compound forms (e.g., Macdonald *et al.* [1982a]), its presence as a direct part of the ϵ ARC, ZARC, and YARC functions, ones that have long been used in the interpretation of a wide variety of IS data on dielectric and conduction materials, underlines the wide usefulness of the CPE.

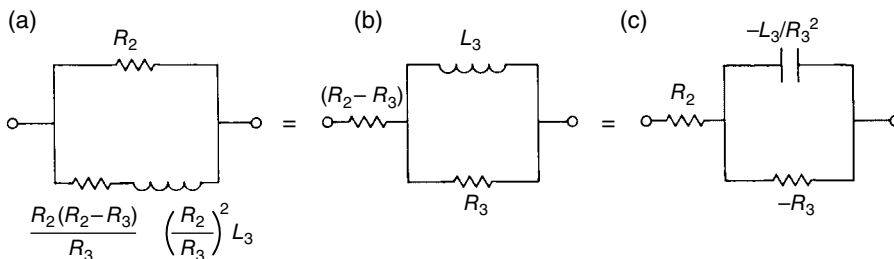
As already mentioned, the lack of any physically based relation for the temperature dependence of the CPE and CPE-like fractional exponent ψ (or n or α) is an important weakness in the theories that lead to frequency response with such exponents. A new theory that involves a distribution of activation energies and does predict temperature dependence for ψ often in agreement with experiment (Macdonald [1985a, c, d]) will be discussed in Section 2.2.3.5, along with some empirical frequency-response relations suggested by Jonscher. We summarize the various distributed elements (simple and compound) discussed in this section in Table 2.2.2.

2.2.2.3 Ambiguous Circuits

Let us now further consider the inherent ambiguity of equivalent circuit fitting. One example of two different equivalent circuits having the same overall impedance at all frequencies has already been presented in Figure 1.2.2. Incidentally, if we change all the resistors in both circuits to capacitors, we have another instance of the same kind of ambiguity. Another series of circuits that may all have the same impedance is shown in Figure 2.2.3 (see Franceschetti and Macdonald [1977]). Here we have again given

TABLE 2.2.2 Some Distributed Elements and Their Descriptions at the Impedance Level

Symbol	Name and description	Defining equation
Z_W	Finite-length Warburg diffusion	(10)
$Z_{W\infty}$	Infinite-length Warburg diffusion	(12)
Z_D	Diffusion with general boundary conditions	—
Z_{DOC}	Open-circuit (blocked) diffusion	(14)
Z_{CPE}	Constant phase element	(18), (19)
$Z_{\epsilon\text{ARC}}$	Depressed semicircle in complex dielectric constant plane (see Figure 2.2.2a)	(20), (21)
$Z_{Z\text{ARC}}$	Depressed semicircle in impedance plane (see Figure 2.2.2b)	(22), (23)
Z_{ZC}	ZC element, general form of ϵARC and $Z\text{ARC}$	(26)
$Z_{Y\text{ARC}}$	Depressed semicircle in admittance plane (see Figure 2.2.2c)	(27)

**FIGURE 2.2.3** Three circuits having the same impedance at all frequencies.

the actual relations between the various components. Some adsorption models (see later) yield inductive-type behavior and a resulting arc that falls below the real axis in the Z^* plane. Sometimes the apparent inductance can be very large. But it is only an apparent inductance since real inductance requires storage of energy in a magnetic field and there is no appreciable ac magnetic field energy present in low current IS measurements. The actual situation involves an inductive type of phase shift, but rather than represent it by the inductive circuits of Figure 2.2.3a and b, which gives a somewhat misleading picture of the process, we recommend following earlier work (e.g., Franceschetti and Macdonald [1977]) and using circuit (c), which involves both a negative differential capacitor and a negative differential resistor. Since adsorption often can be represented electrically by a positive resistor and capacitor in the (c) type of circuit, continuity is served by allowing both these elements to become negative when appropriate. It is then unnecessary to pass from an ordinary RC circuit to an LC one as adsorption changes; instead the R and C can just go from positive values to negative ones.

Figure 2.2.4 presents three more electrical circuits often encountered in IS work. They exhibit three time constants ($N = 3$) and can all yield the same impedance for all frequencies when their elements are properly related. All three circuits yield three distinct arcs in the Z^* plane when the three time constants are well separated. Starting from the Voigt circuit with only two time constants, one can find relatively simple algebraic formulas yielding expressions for the elements in the other two $N = 2$ circuits, which ensure that the impedance is the same (Novoseleskii *et al.* [1972]), but such simple relations do not always exist when one starts with another of the circuits or when there are three or more time constants present. In practice, however, the detailed relations between the elements are not particularly important when CNLS fitting procedures are available. First, parameter estimates for any of the circuits may be obtained by such fitting and those for the different circuits compared. Incidentally, the degree of fit is completely independent of which of the three circuits is employed. Second, when the time constants are separated by factors of 100 or more, the R 's and C 's of, say, the top and bottom circuits closely approach each other. It is particularly when this condition is not satisfied, however, that CNLS fitting is necessary to resolve the overlapping arcs in the Z^* plane.

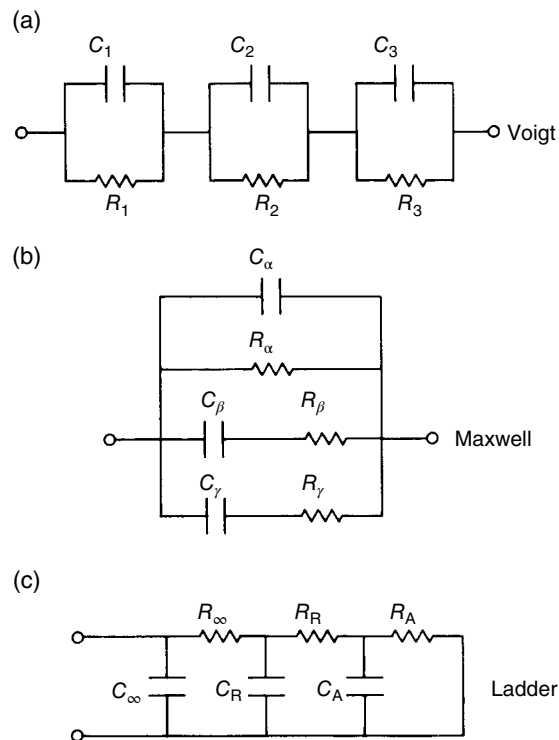


FIGURE 2.2.4 Three further circuits that can have the same impedance at all frequencies when the parameters of the circuit are properly interrelated.

But CNLS fitting is not always available or may not be justified for preliminary fits. When $N = 2$ in the circuits of Figure 2.2.4, several of the relations between the circuit elements of the three types of circuits can prove very useful in graphical fits. These relationships are summarized in the appendix at the end of this section. Once the parameters of a particular $N = 2$ circuit have been graphically estimated from impedance spectra, estimates of the parameters of the other two circuits may be obtained using these relations, avoiding the need for graphical fitting of the other circuits. Indeed, the equivalence relations are the easiest way to obtain the parameters of the ladder network (Figure 2.2.4c), which cannot be well estimated from either an impedance or admittance plot but require a laborious process involving more than one type of plot (de Levie and Vukadin [1975]). It is simple to fit to the $N = 2$ circuit of Figure 2.2.4a or b and transform to the ladder representation. Further, the equivalence relations may be useful when no IS data are available, but circuit element estimates are, as in published work of others.

Since all three of the Figure 2.2.4 circuits are equivalent as far as fitting is concerned, how does one choose between them, particularly in cases when element estimates for the different circuits are quite different? First, one may use continuity and knowledge of the physical processes involved, as in the aforementioned brief discussion of inductive-like effects in adsorption. Second, one may be able to compare the circuits with the predictions of a physical model—one which yields simpler expressions for the elements of one of the circuits than for the others. This has been done for the unsupported conduction case (Franceschetti and Macdonald [1977]), and the work showed that in the case of charge of a single-sign mobile, the ladder circuit was much superior to others (see Section 2.2.2.3).

Finally, one should apply the criterion of simplicity. Given equally good fits, the circuit with the smallest number of elements should be used. Second, when electrode separation l , temperature T , or possibly oxygen partial pressure $p(\text{O}_2)$ (see, e.g., Verkerk and Burggraaf [1983], Badwal [1984]) is changed, one expects some or all of the fitting parameters to change. But that circuit in which the changes are least, simplest, and/or closest to theoretical expectations should certainly generally be preferred. By

carrying out CNLS fitting with several different but plausible circuits, such as those in Figure 2.2.4, for various l , T , and/or $p(\text{O}_2)$ conditions, one can often reach an unambiguous choice of the “best” fitting circuit (out of those considered) to use. Since various processes occur in often widely separated different frequency regions, it should be emphasized that IS measurements must include such regions to allow identification and analysis of the individual processes present. Generally, then, as wide a frequency span as possible should be covered by the experimental measurements.

Appendix. This appendix summarizes the relations between the elements of the three circuits of Figure 2.2.4 when $N = 2$. Here the subscripts a and b are used in place of the α and β of Figure 2.2.4:

a. Voigt → Maxwell

$$C_a = \frac{C_1 C_2}{C_1 + C_2} \quad (\text{A1})$$

$$C_b = \frac{(R_1 C_1 - R_2 C_2)^2}{(C_1 + C_2)(R_1 + R_2)^2} \quad (\text{A2})$$

$$R_a = R_1 + R_2 \quad (\text{A3})$$

$$R_b = \frac{R_1 R_2 (R_1 + R_2)(C_1 + C_2)^2}{(R_1 C_1 - R_2 C_2)^2} \quad (\text{A4})$$

b. Maxwell → Voigt

$$C_{1,2} = 2C_a \left(1 \mp \frac{R_b/R_a - C_a/C_b + 1}{k^{1/2}} \right)^{-1} \quad (\text{A5})$$

$$R_{1,2} = \frac{R_a}{2} \left(1 \pm \frac{C_a/C_b - R_b/R_a + 1}{k^{1/2}} \right) \quad (\text{A6})$$

where

$$k = \left(\frac{C_a}{C_b} + \frac{R_b}{R_a} + 1 \right)^2 - 4 \frac{C_a R_b}{C_b R_a} \quad (\text{A7})$$

Here $R_{1,2}$ and $C_{1,2}$ are defined such that $R_1 C_1 > R_2 C_2$.

c. Maxwell → Ladder

$$C_\infty = C_a \quad (\text{A8})$$

$$R_\infty = \frac{R_a R_b}{R_a + R_b} \quad (\text{A9})$$

$$C_R = C_b \left(\frac{R_a + R_b}{R_a} \right)^2 \quad (\text{A10})$$

$$R_R = \frac{R_a^2}{R_a + R_b} \quad (\text{A11})$$

d. Ladder → Maxwell

$$C_a = C_\infty \quad (\text{A12})$$

$$R_a = R_\infty + R_R \quad (\text{A13})$$

$$C_b = \left(\frac{R_R}{R_\infty + R_R} \right)^2 C_R \quad (\text{A14})$$

$$R_b = \frac{R_\infty}{R_R} (R_\infty + R_R) \quad (\text{A15})$$

2.2.3 Modeling Results

2.2.3.1 Introduction

In any modeling situation one must first specify the physical conditions considered. Is the system in equilibrium or in a steady state? What species of mobile and immobile charges are present? Is the material between the electrodes homogeneous (liquid or single crystal) or not (amorphous or polycrystalline)? In the polycrystalline case, what boundary conditions should be used at the interfaces between crystallites? In all cases, what kind of electrodes are assumed, and thus what are the appropriate boundary conditions at the electrode–material interfaces?

Perhaps the most general problem one would like to solve in the present area, a sufficiently general situation that would include almost all simpler ones of interest, is the following: a biased situation with applied dc p.d. of arbitrary size and a small-signal ac p.d. also applied, an arbitrary number of charged species (but not exceeding, say, six) with arbitrary mobilities and bulk concentrations present, general interactions (e.g., generation/recombination) possible between the various positive and negative charged species, arbitrary (i.e., general) blocking–nonblocking reaction–adsorption conditions for each of the mobile species at the electrode interfaces, and separate treatments of homogeneous and polycrystalline situations. One would like to calculate the dc I over a wide range of applied potential difference and, at any given applied steady-state potential difference, calculate the impedance as a function of frequency.

Unfortunately, this general problem, which usually involves an inhomogeneous distribution of charge within the material, has not been solved. The situation is highly nonlinear and, although the many coupled differential equations and boundary conditions that could be used to specify it mathematically could, in principle, be solved with a large computer, only purely numerical results depending on a very large number of input parameter values (e.g., mobilities, equilibrium concentrations) would be obtained. Of course even such a general, and almost useless, solution would still be approximate since the equations used would themselves still be approximations to the actual physical situation.

Thus far, only much simpler idealizations of the general problem have been solved, and in Section 2.2.3.3 we shall discuss some of their results. When the simpler solutions are thought to be adequate, they may be used to analyze experimental data and obtain estimates of such interesting quantities as electrode charge transfer reaction rate. Many of the simpler solutions can be represented exactly or approximately by an equivalent circuit, but some yield only a complicated expression for $Z(\omega)$, which cannot always be so represented in a useful manner.

Solutions for unbiased, flat-band situations (i.e., where there are no intrinsic space-charge layers at the boundaries) are simplest, and only these will be discussed in the succeeding text, except when otherwise noted. We shall present a brief discussion of the supported situation, primarily appropriate for liquids and mixed conductors, and devote more space to results for unsupported materials, since most solid electrolytes involve unsupported ionic conduction under conditions of primary interest. For simplicity, theoretical results for flux, currents, impedances, and other circuit elements will be given in specific form, per unit of electrode area A_c , so this area will not appear directly in the formulas.

The possible behaviors of an electrode–electrolyte interface are variously discussed in the literature in terms of polarizability, blocking or nonblocking character, and reversibility, with usage differing somewhat from one author to another. For clarity and precision we shall use the term *polarizability* to denote the electrical behavior of the electrode–electrolyte interface and the terms *blocking* (or *nonblocking*) and *reversibility* to describe the electrochemical character of the interface. An electrode–electrolyte

interface is nonpolarizable if the potential drop across the interface is independent of the current through the interface. It is partially polarizable if the interfacial potential difference is dependent on the current and completely polarizable if it completely prohibits the flow of (faradic) current. An interface is blocking with respect to a given charge-carrying species in the electrolyte if that species cannot cross the interface or exchange charge (in the form of electrons) with the electrode; otherwise it is nonblocking with respect to the given species. A nonblocking interface is generally thermodynamically reversible since, in thermal equilibrium, the electrochemical potential of the species involved in the interfacial charge transfer will obey an equilibrium relation. The interface is kinetically reversible if the rate of the electrode charge transfer reaction is rapid enough that the equilibrium relation is maintained in the immediate vicinity of the interface as current passes through the system.

The polarization of an electrode–electrolyte interface can result either from the slowness of the electrode reaction, as in the case of nonblocking but kinetically nonreversible electrodes, or from any factor that limits the transport of any of the species participating in the electrode reaction, for example, slow diffusion of the reactant or product species away from the interface or the generation or consumption of one of the species by a slow chemical reaction in the electrolyte.

We shall be concerned primarily with the behavior of ionic charge carriers at the interface, and the electrode–electrolyte combinations to be encountered will fall into two general groups: parent-atom electrodes and redox electrodes. In parent-atom electrodes, charge can cross the interface in ionic form. Electrodes of this type include parent-metal electrodes such as Ag in the solid-state cell $\text{Ag} \mid \text{AgCl} \mid \text{Ag}$, in which the electrode serves both as a source of ions and as an electronic conductor, and parent-nonmetal electrodes, as in the cell $\text{Br}_2(\text{Pt}) \mid \text{AgBr} \mid \text{Br}_2(\text{Pt})$, in which an inert metal phase must be present to serve as the electronic conductor. In redox electrodes, charge crosses the interface in the form of electrons, and the reaction may be written in the form



where k_f and k_b are forward and reverse reaction rate constants, respectively. Both Ox and Red are usually soluble in the electrolyte, but if $z = n_e$, the Red species is uncharged, and if it is a gas, it may evolve at an electrode and/or diffuse into the electrode, especially if the electrode is somewhat porous. The admittance behavior of more complex electrode reactions (in aqueous electrolytes) than those mentioned previously has been discussed by Seralathan and de Levie [1987] and is not considered herein.

Finally, while still dealing with interface effects, it is worth stating one of the most important equations of reaction rate electrochemistry, the Butler–Volmer equation (see Vetter [1967], Franceschetti [1982]). Written in terms of flux for a simple redox reaction, it is

$$J \equiv \left(\frac{I}{nF} \right) = \left\{ k_f^0 c_{\text{Red}}^H \exp \left[\left(\frac{nF}{RT} \right) \alpha \eta_{\text{MH}} \right] - k_b^0 c_{\text{Ox}}^H \exp \left[- \left(\frac{nF}{RT} \right) (1-\alpha) \eta_{\text{MH}} \right] \right\} \quad (29)$$

Here n is the number of moles of electrons involved in the reaction, the rate constants have been assumed to be thermally activated, and k_f^0 and k_b^0 are potential-independent rate constant parameters. The potential-dependent concentrations c_{Red} and c_{Ox} are evaluated at their points of closest approach to the electrode, taken here as the outer Helmholtz plane. Further, α is here a dimensionless symmetry factor often assumed to be 0.5 (the symmetrical barrier case), and η_{MH} is the charge transfer overvoltage effective in driving the reaction away from equilibrium (for $\eta_{\text{MH}} = 0$, $J = 0$). The Butler–Volmer equation is usually a good approximation for both biased and unbiased conditions.

2.2.3.2 Supported Situations

Half-Cells The concept of a supported electrolyte has proven quite valuable in solution electrochemistry by allowing great theoretical simplification at (usually) only a small cost in accuracy. The several

(often implicit) assumptions made in treating the electrolyte in a given cell as supported, however, deserve careful attention as they generally do not apply in the case of solid-state electrochemical systems. It should also be noted that it is usually possible in solution electrochemistry to use a large, essentially kinetically reversible counter electrode so that all but a negligible fraction of the applied potential difference falls across the electrode–electrolyte interface of interest. In its simplest form, the supported approach assumes that all the potential difference in the system falls across the compact double layer—approximately one solvent molecule diameter in thickness—at this electrode and the approach of the electroactive species to the boundary of the compact layer, the outer Helmholtz plane, occurs purely by diffusion. Corrections for the buildup of space charge near the interface (the diffuse double layer) and the ohmic drop across the electrolyte are then made in piecewise fashion as needed. In solid-state electrochemistry, one is usually concerned with measurements on a cell with an unsupported electrolyte and identical plane parallel electrodes. The impedance of such a cell will be twice that of its two half-cells. Although most solid electrolytes are essentially unsupported for temperatures of interest, Archer and Armstrong [1980] have suggested that when a solid electrolyte contains immobile anions and two different species of cations of similar mobilities, if one of the ionic species is present in much higher bulk concentration than the other, it can act as support for the other species of mobile ion—a supported case. Also, mixed electronic–ionic conduction can sometimes lead to supported conditions. Thus the supported situation may even be of some direct interest for solid electrolytes.

A symmetrical full cell with identical electrodes, no intrinsic space-charge layers, and zero potential drop across the compact double layers is mathematically equivalent to two half-cells in series since the concentrations of the diffusing species will be zero in the center. In this one case the normalized impedance of the half-cell is the same as that of the full cell. For identical and kinetically reversible redox electrodes and both oxidized and reduced species mobile in the supported electrolyte, a complete solution, neglecting compact-layer capacitance, has been obtained by Sluyters [1963]. This solution, derived and presented as real functions, is highly complicated in appearance. Macdonald [1971a] pointed out that the Sluyters result simplifies greatly when the impedance is written in complex variable form. Franceschetti [1987] treated the same situation allowing for a finite charge transfer rate and a compact-layer capacitance and in the process found Sluyters result as the sum of two finite-length Warburg elements. In the same paper Franceschetti found an impedance for a supported system with two dissimilar electrodes of the parent-metal type (perhaps a pure metal and an amalgam). The resulting equivalent circuit requires an inductive element and three lengths of transmission line, one of which includes an inductive series reactance. Let us now consider only infinitesimal deviations from zero bias equilibrium conditions and assume that the equilibrium distribution of all charges is constant throughout the material, so for equilibrium there is no polarization, and electroneutrality applies everywhere. Solution of Fick's laws of diffusion under supported small-signal ac conditions for a simple one-step reaction (single reacting charged species) (Randles [1947], Sluyters-Rehbach and Sluyters [1970], Armstrong *et al.* [1978], Franceschetti [1982]) leads to the equivalent circuit of Figure 2.2.5. This circuit may be taken to apply to a half-cell of infinite extent to the right of the electrode. It thus does not include any bulk or solution resistance R_∞ , which would depend on the finite extent of an actual cell. It does include an infinite-length Warburg impedance, the charge transfer reaction resistance R_R , the capacitance associated with it (C_R)

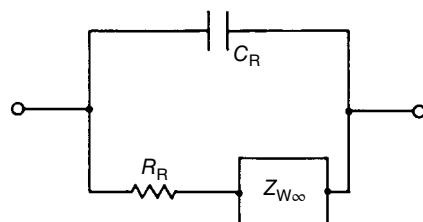


FIGURE 2.2.5 Equivalent circuit for a single electrode and its interface under supported conditions.

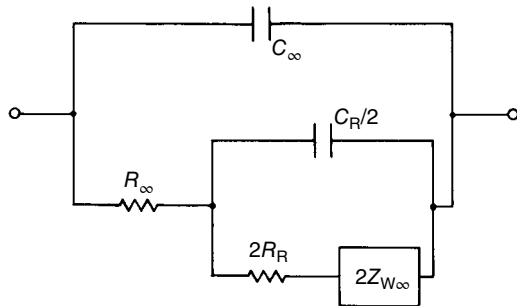


FIGURE 2.2.6 Equivalent circuit for a full cell with two identical electrodes under supported conditions. This circuit only applies when $Z_W \cong Z_{W\infty}$.

and the diffuse double-layer capacitance, sometimes denoted C_{dl} . This circuit, with the addition of a bulk or solution resistance in series with it, is customarily known as the *Randles circuit*. Appreciable discussion of the circuit from an electrochemical viewpoint appears in Macdonald [1971a].

Full-Cell Results. We can generalize the circuit of Figure 2.2.5 to a full-cell situation with identical electrodes as long as Z_W is well approximated by $Z_{W\infty}$, that is, as long as the diffusion length is much smaller than l . One then obtains two contributions to the impedance of the Figure 2.2.5 type, one associated with each electrode. Since the electrodes are taken identical, the two intensive impedances are identical and may be combined to yield a result of twice the individual impedances. When we additionally add a geometrical capacitance $C_g \equiv C_\infty$ and the bulk or solution resistance R_∞ , we obtain the circuit of Figure 2.2.6.

Although we will always refer to actual circuit elements in an equivalent circuit, we shall, for simplicity, give expressions for these elements per unit area. We shall not, however, usually distinguish between a quantity and its per unit area-specific form, so, for example, a capacitance unit area will still be referred to as a *capacitance*. If the separation of the electrodes is l , the geometrical capacitance (per unit area) is given by

$$C_\infty = \frac{\epsilon \epsilon_0}{l} \quad (30)$$

where ϵ is the effective dielectric constant of the electrolyte. It is customary to omit C_∞ in supported situations since IS measurements on liquids rarely extend to high enough frequencies for it to affect the overall impedance appreciably. This is not always the case for solid electrolytes where impedance contributions from other elements may be high, especially at low temperatures.

Now ionic conduction in a full cell actually occurs in a region of length $l_{eff} = l - 2l_H$, where l_H is the effective thickness of the inner region, next to the electrode, into which ions cannot fully penetrate. Because of the finite size of ions, the minimum steric but not necessarily electrical value of l_H is an ionic radius. Except for unrealistically thin cells, the distinction between l_{eff} and l is not important for most circuit elements and will usually be neglected hereafter. It should be mentioned, however, that in the study of thin (sometimes monomolecular) membranes in the biological field, using high-molarity liquid electrolyte electrodes, the distinction may be important. We may now write the expression for R_∞ as

$$R_\infty = \left(\frac{l}{F} \right) \left(\sum_{i=1}^m z_i \mu_i c_i^0 \right)^{-1} \quad (31)$$

where z_i and μ_i are the valence numbers and mobilities of the m charged species of bulk concentration c_i^0 present in the electrolyte. We have followed an earlier work in assigning the ∞ subscripts to C_∞ and R_∞ herein since these elements lead to the semicircle in the complex impedance plane, which occurs at

higher frequencies than do any other impedance plane structures. This semicircle peaks at $\omega = \tau_D^{-1}$, where $\tau_D = R_\infty C_\infty$ is the dielectric relaxation time of the material, an intensive quantity.

An important quantity in solid and liquid electrolytes is the Debye length L_D , given by

$$L_D = \left[(\epsilon \epsilon_0 RT)^{-1} F^2 \sum_{i=1}^{m'} z_i^2 c_i^0 \right]^{-1/2} \quad (32)$$

where the sum includes mobile charge species only. The Debye length is a measure of the distance in the electrolyte over which a small perturbation in potential or electric field decays. Such a perturbation creates a region of space charge where electroneutrality no longer holds. This region extends only over a few Debye lengths.

The Gouy–Chapman diffuse double-layer differential capacitance C_R that is associated with the charge transfer reaction resistance R_R appearing in Figure 2.2.6 is given by

$$C_R = \frac{\epsilon \epsilon_0}{L_D} \quad (33)$$

in the absence of bias. An expression taking dc bias into account appears in Macdonald [1954], and a further generalization taking finite-ion-size effects into account as well by means of a lattice gas treatment is presented in Macdonald *et al.* [1980b] (see also Franceschetti [1982]).

The supported electrolyte half-cell reaction resistance R_R may be written in the general form

$$R_R = \left(\frac{RT}{n^2 F^2} \right) (k_i^0 c_i^0)^{-1} \quad (34)$$

where k_i^0 and c_i^0 depend on the specific type of reaction considered. For the parent-metal electrode situation, $M|M^{2+}$, where M denotes the metal electrode, $k_i^0 = k_b^0$, a potential-independent Butler–Volmer-type reaction rate parameter, and $c_i^0 = c_{M+}^0$, the bulk equilibrium concentration of the reacting cation. Similarly for a redox situation one finds (Vetter [1967], Gabrielli [1981]) $k_i^0 c_i^0 = (I_0/nF) = k_f^0 c_{\text{Red}}^0 = k_b^0 c_{\text{Ox}}^0$, where I_0 is the exchange current, a measure of the rates at which oxidation and reduction processes occur in equilibrium. It is the common magnitude of the equal and opposite electrical currents associated with oxidation and with reduction (no net current in equilibrium). A more complicated expression for R_R and for infinite-length Warburg impedance under steady-state conditions where the dc bias is nonzero has been given by Sluyters-Rehbach and Sluyters [1970].

Diffusion Effects. Next consider small-signal unbiased diffusion effects. We initially discuss the parent-ion equal electrode situation for simplicity. The problem with applying the circuit of Figure 2.2.6 to the supported full-cell situation at low frequencies is that C_R remains an intensive quantity associated with an interface region but $2Z_{W\infty} \rightarrow Z_D$, some new diffusion impedance, and becomes extensive at low enough frequencies. It is then not correct to continue to allow the element $C_R/2$ to bridge the series combination of $2R_\infty$ and $2Z_{W\infty}$. In fact, at sufficiently low frequencies where the diffusion effects are extensive, there can only be a single diffusion impedance Z_D for the entire cell. At sufficiently high frequencies Z_D will be well approximated by $Z_{W\infty}$, but the full cell then exhibits an effective diffusion impedance of $2Z_{W\infty}$, not $Z_{W\infty}$, as shown in Figure 2.2.6. There is thus a transition region in frequency as the frequency is decreased in which the effective diffusion impedance goes from $2Z_{W\infty}$ to $Z_D = Z_W$, not $2Z_W$, and the $C_R/2$ connection shown in Figure 2.2.6 is also no longer entirely applicable. Let us therefore first consider at sufficiently low frequencies that the extensive Z_D is present and the admittance of $C_R/2$ is negligible. We can then consider Z_D alone and its transition to $Z_{W\infty}$. We shall start with the expressions (Franceschetti [1981]) appropriate for Z_D in the parent-metal electrode and redox cases.

In the parent-metal electrode case, take the diffusion coefficient of the metal ion M^{z+} as D_M . Then one finds

$$Z_D = Z_W = \left[\frac{RT}{(zF)^2} \right] \left[\frac{l}{D_M c_{M^+}^0} \right] \left[\frac{\tanh \sqrt{j\omega l^2/D_M}}{\sqrt{j\omega l^2/D_M}} \right] \quad (35)$$

which should be compared with the result in Eq. (10). Now when $(\omega l^2/D_M) \gg 3$, $Z_W \rightarrow Z_{W\infty}$ and one obtains

$$Z_{W\infty} = \frac{RT/(zF)^2}{(c_{M^+}^0)(j\omega D_M)^{1/2}} \quad (36)$$

The situation is somewhat more complicated in the redox case because of the presence of the two charged species in the electrolyte [unless $(z - n_e) = 0$]. Then one finds

$$Z_D = Z_{W,\text{Ox}} + Z_{W,\text{Red}}$$

where

$$Z_{W,\text{Ox}} = \left[\frac{RT}{(nF)^2} \right] \left[\frac{l}{D_{\text{Ox}} c_{\text{Ox}}^0} \right] \left[\frac{\tanh \sqrt{j\omega l^2/D_{\text{Ox}}}}{\sqrt{j\omega l^2/D_{\text{Ox}}}} \right] \quad (37)$$

$$Z_{W,\text{Red}} = \left[\frac{RT}{(nF)^2} \right] \left[\frac{l}{D_{\text{Red}} c_{\text{Red}}^0} \right] \left[\frac{\tanh \sqrt{j\omega l^2/D_{\text{Red}}}}{\sqrt{j\omega l^2/D_{\text{Red}}}} \right] \quad (38)$$

and D_{Ox} and D_{Red} are the relevant diffusion coefficients and all concentrations are those in the bulk. When both tanh terms are well approximated by unity, the expression for Z_D reduces to

$$Z_D = Z_{W\infty,\text{Ox}} + Z_{W\infty,\text{Red}} \equiv Z_{W\infty} = \left[\frac{RT}{(nF)^2} \right] \left[(D_{\text{Ox}} (c_{\text{Ox}}^0)^2)^{-1/2} + (D_{\text{Red}} (c_{\text{Red}}^0)^2)^{-1/2} \right] (j\omega)^{-1/2} \quad (39)$$

the classical result (Armstrong *et al.* [1978], Gabrielli [1981]). The aforementioned results show that we may expect to find two finite-length Warburg in series (and generally displaced in frequency) at sufficiently low frequencies. It is worth again emphasizing that although it will be the $Z_{W\infty}$ of Eq. (39), which appears in the half-cell circuit, it is $2Z_{W\infty}$ that appears for the full cell under supported conditions at sufficiently high frequencies.

We have attempted to give supported results in a form appropriate for comparison with unsupported ones by considering full-cell conditions. The transition problems discussed previously only occur for unstirred (liquid) electrolytes or for solid electrolytes. When a stirred solution or rotating electrode with laminar flow is employed, the l that appears in Z_D and Z_W expressions is replaced by δ_N , where δ_N is the thickness of the Nernst diffusion layer. It decreases as the frequency of rotation of a rotating electrode increases, and the experiment is always carried out for conditions where $\delta_N \ll l$.

2.2.3.3 Unsupported Situations: Theoretical Models

Introduction. We shall discuss results for unsupported situations under two categories: (i) those that follow directly or indirectly from exact solutions of the small-signal differential equations of charge motion in the material-electrode system and (ii) those that largely arise from empirical analysis of data and often use such ubiquitous distributed elements as CPEs. The first category deals with more idealized

situations than the second, but generally leads to more detailed results and to more specific relations between macroscopic equivalent circuit elements and microscopic processes occurring in the system. At the present early stage of theoretical analysis of real systems, both approaches have important roles to play.

Most theories of charge transport and interfacial charge transfer in unsupported situations involve a model that assumes a homogeneous material, for example, a single crystal. Here we shall initially discuss the electrical response following from the application of a small-signal ac potential difference to homogeneous materials without applied dc bias or built-in Frenkel space-charge layers and with identical plane parallel electrodes—the idealized full-cell situation. Theoretical results are only available so far for conditions where there may be a single species of mobile positive charge and a single species of mobile negative charge present with electroneutrality in the bulk. Results for polycrystalline materials and for homogeneous ones with Frenkel layers or applied dc bias will be discussed later on.

We shall start with a discussion of the exact results obtained from the solution of the most general model yet considered, but one that is still appreciably idealized (Macdonald and Franceschetti [1978]). Then work relaxing some of the idealizations will be discussed. Some of the present results have been included in the solid electrolyte reviews of Archer and Armstrong [1980] and by Franceschetti [1982]. The model of Macdonald and Franceschetti involves mobile positive and negative charges, which may arise from three sources: the partial or full dissociation of (i) neutral intrinsic centers, (ii) neutral donor centers, and (iii) neutral acceptor centers. The model is general enough to include disordered sublattice materials and single crystals with Schottky or Frenkel disorder. Arbitrary amounts of generation/recombination are allowed. After dissociation of a neutral center, the resulting positive and negative charges are taken to have arbitrary mobilities, so, for example, a donor center might dissociate to yield an immobile positive charge and a mobile negative charge. We shall denote the mobility ratio for negative and positive charges as $\mu_m \equiv \mu_n/\mu_p$. Although the present model also allows arbitrary valence numbers for the mobile charged species, we shall primarily restrict attention here to the usual univalent case.

Boundary Conditions: Adsorption–Reaction Effects. The Macdonald–Franceschetti model involves relatively general boundary conditions at the electrodes and so includes the possibility of charge transfer reactions and specific adsorption. Because of its generality, however, the model prediction for $Z_t(\omega)$ is very complicated and, in general, cannot be well represented by even a complicated equivalent circuit. The $Z_t(\omega)$ expression may, however, be used directly in CNLS fitting. Here, for simplicity, we shall consider only those specific situations where an approximate equivalent circuit is applicable. Idealizations involved in the model include the usual assumption of diffusion coefficients independent of field and position, the use of the simplified Chang–Jaffé [1952] boundary conditions, and the omission of all inner layer and finite-ion-size effects. Some rectification of the latter two idealizations will be discussed later.

The Chang–Jaffé boundary conditions involve the physical assumption that the current arising from the reaction of a charge carrier of a given species is proportional to the excess concentration of that species at the interface, say, a negatively charged species,

$$I_n = -z_n e k_n (n - n^0) \quad (40)$$

where z_n is the valence number of the charge carrier, k_n is a reaction rate parameter at the reaction plane, and n^0 is the bulk concentration of the species. The Chang–Jaffé conditions, as compared to the Butler–Volmer equation, are unrealistic in two important respects: there is a complete neglect of the finite size of the charge carriers (i.e., the compact double layer) and it is assumed that the charge transfer rate does not depend at all on the local concentration of the electrode reaction products. These deficiencies are not, however, nearly as limiting as one might at first expect. The neglect of the compact double layer introduces only a small error (which becomes zero at zero frequency) in many solid-state situations (Randles [1947], Franceschetti and Macdonald [1977]). The accumulation of the electrode reaction product can be neglected when (i) the product species is a metal atom that is rapidly incorporated into a parent-metal electrode, (ii) the product is a gas atom that equilibrates very rapidly with the ambient

atmosphere, or (iii) the product species is soluble in the electrolyte or electrode and diffuses away from the interface very quickly. If the accumulation of the product species is not eliminated by one of these processes, but the transport of the product is governed by diffusion and therefore is independent of the electric field, it may be incorporated into the Chang–Jaffé boundary condition through the artifice of a complex, frequency-dependent reaction rate constant as described in the succeeding text.

It proves convenient in the theoretical work to use the dimensionless Chang–Jaffé rate parameters

$$\rho_n = \left(\frac{l}{2}\right) \left(\frac{k_n}{D_n}\right) \quad (41)$$

and

$$\rho_p = \left(\frac{l}{2}\right) \left(\frac{k_p}{D_p}\right) \quad (42)$$

where the k 's are effective rate constants and the D 's the diffusion coefficients of the negative and positive species. These parameters have in some previous work been given in terms of the alternate equivalent quantities $\rho_n = \rho_2 = r_2/2 = r_n/2$ and $\rho_p = \rho_1 = r_1/2 = r_p/2$. Clearly when $\rho_n = 0$ the electrode is completely blocking for the negative species, and for $\rho_n = \infty$ it is completely nonblocking and nonpolarized.

Now since to a good approximation specific adsorption of an ion at an electrode and then a reaction of the adsorbed ion to form a neutral species occur at very nearly the same point in space, one might expect that these sequential interface processes would be largely decoupled from bulk and double-layer effects that occur elsewhere in the system. Lányi [1975] introduced the concept of frequency-dependent complex rate constants, and they have been found very useful in allowing reaction–adsorption effects to be included in a very simple way (Macdonald [1976a], Franceschetti and Macdonald [1977]). In essence, if a $Z_t(\omega)$ solution has been found for a certain situation involving the presence of real, frequency-independent ρ_n and ρ_p boundary parameters, one only needs to change them to complex frequency-dependent quantities to automatically include adsorption effects. No other parts of the solution are affected. As an example, suppose that a negative carrier is adsorbed and the adsorbed species then reacts to form a neutral species whose concentration remains, or is held, constant. One finds that the real ρ_n originally present in the solution need only be replaced by

$$\rho_n = \frac{\rho_{n0} + j(\omega\tau_D)\xi_{na}\rho_{n\infty}}{1 + j(\omega\tau_D)\xi_{na}} \quad (43)$$

where ρ_{n0} and $\rho_{n\infty}$ are the $\omega \rightarrow 0$ and $\omega \rightarrow \infty$ limits of $\rho_n : \xi_{na} \equiv \tau_{na}/\tau_D$ where τ_{na} is the adsorption relaxation time. In this case $\rho_{n\infty}$ is the rate constant for the first step in the adsorption–reaction sequence in which charge is exchanged between the electrolyte and the adsorbed layer, and ρ_{n0} is a function of both $\rho_{n\infty}$ and the rate constant for the second step in the process, in which charge is exchanged between the adsorbed layer and the electrode. For the case of pure adsorption, ρ_{n0} is zero and ρ_n becomes zero at $\omega \rightarrow 0$. In the limit in which the second (reaction) step is much faster than the initial (adsorption) step, the adsorbed layer becomes inconsequential, $\tau_{na} \rightarrow 0$, $\rho_{n0} \rightarrow \rho_{n\infty}$, and $\rho_{n\infty}$ becomes real and frequency independent. The quantities ρ_{n0} and $\rho_{n\infty}$ or, equivalently, k_{n0} and $k_{n\infty}$ may be expressed in terms of partial derivatives with respect to various surface concentrations of the small-signal boundary conditions written in terms of current (Franceschetti and Macdonald [1977]). Derivative definitions of this form that depend on Taylor series expansions, appropriate for small-signal conditions, were developed earlier by Armstrong and Henderson [1972], for example. See also Armstrong *et al.* [1978].

The rate-limiting diffusion of an electrode reaction can also be incorporated into the Chang–Jaffé boundary conditions by a similar approach. In this case, assuming, for example, diffusion through a semi-infinite electrode, the result obtained is

$$\rho_n = \frac{\rho_{n\infty} \sqrt{i\omega D}}{\rho'_n + \sqrt{i\omega D}} \quad (44)$$

where, as before, $\rho_{n\infty}$ is the $\omega \rightarrow \infty$ limit of ρ_n , ρ'_n is a rate parameter for the inverse electrode reaction, and D is the diffusion coefficient of the reaction product. For sufficiently large D , diffusion becomes undetectable and $\rho_n = \rho_{n\infty}$. Various adsorption–reaction–diffusion sequences have been considered by Franceschetti and Macdonald [1979c, 1982] and Franceschetti [1982, 1984].

DC Response. Before passing to the uni-univalent case, which we will consider in detail, let us consider the full dc resistance of the system for arbitrary valence numbers, but only for two (or possibly one) species of mobile charge with equilibrium bulk concentrations n^0 and p^0 , valence numbers z_n and z_p , and electrical mobilities μ_n and μ_p . Then electroneutrality in the bulk leads to $z_n n^0 = z_p p^0$. The bulk conductance G_∞ may be expressed as

$$G_\infty = R_\infty^{-1} = G_{\infty n} + G_{\infty p} \quad (45)$$

where

$$G_{\infty n} = \frac{F}{l} (z_n \mu_n n^0) \quad (46)$$

and

$$G_{\infty p} = \frac{F}{l} (z_p \mu_p p^0) \quad (47)$$

Let us further define the conductivity fractions (or bulk transport numbers) $\varepsilon_n \equiv G_{\infty n}/G_\infty$ and $\varepsilon_p \equiv G_{\infty p}/G_\infty$. These quantities may be written in the simple forms

$$\varepsilon_n = (1 + \pi_m^{-1}) - 1 \quad (48)$$

and

$$\varepsilon_p = (1 + \pi_m)^{-1} \quad (49)$$

under intrinsic conditions, the only case to be considered in detail here. Finally, define the Debye length when only one species of charge is mobile as L_{D1} . The important quantities $M \equiv (l/2)/L_D$ and $M_1 \equiv (l/2)/L_{D1}$ then measure the number of Debye lengths in a half-cell (half a symmetrical cell of full electrode separation l). In the present case where L_D and M refer to a single species of positive and a single species of negative charge mobile, $L_{D1} = \sqrt{2}L_D$.

Let us (apparently arbitrarily) now define the small-signal half-cell adsorption–reaction impedances associated with the positively and negatively charged species as

$$Z_{Rn} \equiv \frac{RT}{z_n^2 F^2 k_n n^0} \quad (50)$$

and

$$Z_{Rp} \equiv \frac{RT}{z_p^2 F^2 k_p p^0} \quad (51)$$

where the k 's may be complex. Using the Einstein relation $D_j = (RT/F)(\mu_j/z_j)$ for the $j = n$ and p species, one readily finds that ρ_j may be written as $(l/2)(F/RT)(z_j k_j / \mu_j)$, so if ρ_j is complex, so is k_j . Note that the $\omega \rightarrow 0$ limits of Z_{Rn} and Z_{Rp} are

$$R_{\Theta n} \equiv \frac{RT}{z_n^2 F^2 k_{n0} n^0} \quad (52)$$

and

$$R_{\theta p} \equiv \frac{RT}{z_p^2 F^2 k_{p0} p^0} \quad (53)$$

where k_{n0} and k_{p0} are related as aforementioned to ρ_{n0} and ρ_{p0} .

Now it is often useful to consider normalized quantities in theoretical analysis or even in an equivalent circuit or three-dimensional (3-D) plot. We shall, when desirable, normalize impedances with the bulk resistance R_∞ , so $Z_N \equiv Z/R_\infty$, and capacitances with C_∞ , so $C_N \equiv C/C_\infty$. The normalized expressions for some of the circuit elements defined previously simplify considerably and are

$$G_{\infty nN} \equiv \frac{G_{\infty n}}{G_\infty} = \varepsilon_n \quad (54)$$

$$G_{\infty pN} \equiv \frac{G_{\infty p}}{G_\infty} = \varepsilon_p \quad (55)$$

$$G_{\theta nN} \equiv \frac{R_\infty}{R_{\theta n}} = 2\varepsilon_n \rho_{n0} \quad (56)$$

and

$$G_{\theta pN} \equiv \frac{R_\infty}{R_{\theta p}} = 2\varepsilon_p \rho_{p0} \quad (57)$$

We are now finally in a good position to write down the expression for the full-cell complete dc resistance following from the present model, $R_D \equiv Z_t(\omega \rightarrow 0)$. We write it here as R_D or R_{DN} rather than R_0 to agree with earlier usage. The exact R_D result applies for arbitrary valences for the mobile charged species, arbitrary mobilities, intrinsic, extrinsic, or intrinsic and extrinsic conduction, and any dissociation–recombination conditions. In unnormalized form it is just

$$R_D \equiv G_D^{-1} = (G_n + G_p)^{-1} \quad (58)$$

where

$$G_n \equiv (R_{\infty n} + 2R_{\theta n})^{-1} \quad (59)$$

and

$$G_p \equiv (R_{\infty p} + 2R_{\theta p})^{-1} \quad (60)$$

These results show that the total dc conductance is made up of a branch G_n , involving negative charge carrier effects only, in parallel with a similar branch involving only positive carrier effects. Each individual branch involves a bulk resistive contribution and two equal adsorption–reaction resistances, one associated with each electrode. The expression for R_D in normalized form, R_{DN} (see, e.g., Franceschetti and Macdonald [1977]), is even simpler, namely,

$$R_{DN} = \left(\frac{\varepsilon_n}{1 + \rho_{n0}^{-1}} + \frac{\varepsilon_p}{1 + \rho_{p0}^{-1}} \right)^{-1} \quad (61)$$

Note that when $\rho_{n0} = \rho_{p0} = \infty$, one obtains $R_{DN} = (\varepsilon_n + \varepsilon_p)^{-1} \equiv 1$, so $R_D = R_\infty$, ohmic behavior and thus not very interesting. Of course in the completely blocking $\rho_{n0} = \rho_{p0} = 0$ case, $R_{DN} = \infty$. To set a scale, it is

interesting to note that when $\rho_{n0} = \rho_{p0} = 1$, $R_{DN} = 2$ and adsorption–reaction effects have contributed an additional R_∞ resistance to R_D . In general, when $\rho_{p0} = \rho_{n0} \equiv \rho_e$, then $R_{DN} = 1 + \rho_e^{-1}$, a result entirely independent of mobilities and π_m , except indirectly through R_∞ and ρ_e themselves.

Adsorption–Reaction and Reaction–Diffusion Predictions. Next, in order to investigate adsorption and reaction effects more fully, let us consider Z_{Rn} and Z_{Rp} in normalized form. It is straightforward to show that

$$Z_{RnN} = (2\epsilon_n \rho_n)^{-1} = \frac{\rho_{n0} R_{\theta nN}}{\rho_n} \quad (62)$$

and

$$Z_{RpN} = (2\epsilon_p \rho_p)^{-1} = \frac{\rho_{p0} R_{\theta pN}}{\rho_p} \quad (63)$$

If we now substitute the complex ρ_n from Eq. (43) into Eq. (62) and a similar expression for ρ_p into Eq. (63), we readily find that the resulting impedances each lead to a simple ladder network whose hierarchical form is consonant with the sequential processes: adsorption then reaction. But for the full cell, there are two identical interface impedances in series. The circuit for a half-cell with total impedance Z_{Rn} is shown in Figure 2.2.7a. The full-cell impedance is just $2Z_{Rn}$. The normalized elements of Figure 2.2.7a are readily found to be given by

$$R_{RnN} = (\epsilon_n \rho_{n\infty})^{-1} \quad (64)$$

$$R_{AnN} = \frac{\rho_{nm}}{\epsilon_n \rho_{n0} \rho_{n\infty}} \quad (65)$$

and

$$C_{AnN} = \frac{\xi_n \epsilon_n \rho_{n\infty}^2}{\rho_{nm}} \quad (66)$$

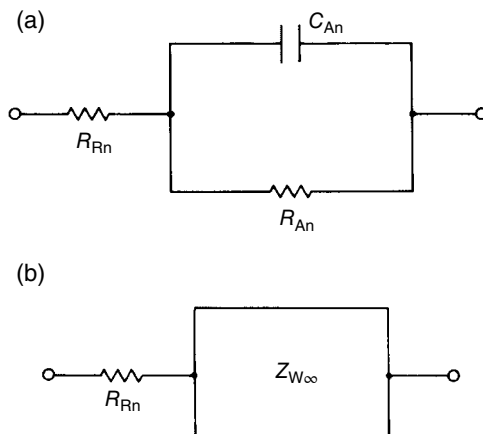


FIGURE 2.2.7 (a) Equivalent circuit for two identical simple electrode adsorption–reaction processes in series, one at each electrode, with negative charge carriers reacting. Unsupported conditions.
(b) Equivalent circuit for two identical reaction–diffusion processes with negative charge carriers reacting. Unsupported conditions.

where $\rho_{nm} \equiv \rho_{n\infty} - \rho_{n0}$. All the elements in the circuit of Figure 2.2.7 are intensive, as they should be for interface effects. The normalized dc resistance of the circuit is just

$$2Z_{RnN}(\omega \rightarrow 0) = R_{RnN} + R_{AnN} = (\epsilon_n \rho_{n0})^{-1} \equiv 2R_{\theta nN} \quad (67)$$

which is as expected. Note that since ρ_{nm} may be either positive or negative, R_{An} and C_{An} , specific adsorption elements, have the same sign and also may be positive or negative, in agreement with earlier discussion. In the absence of the adsorption step, $2Z_{Rn} = R_{Rn}$, the reaction resistance (for two electrodes), since R_{An} is then zero and C_{An} infinite. See Figure 4.3.25 for some of the complex plane shapes that follow from the present approach.

In like manner, if we substitute the complex ρ_n from Eq. (44) into Eq. (62), we obtain the circuit shown in Figure 2.2.7b, appropriate for a reaction-diffusion sequence without an intermediate adsorption stage. Here R_{RnN} is given by Eq. (64) as before and

$$Z_{WN} = \frac{\rho'_n}{\epsilon_n \rho_{n\infty} \sqrt{i\omega D}} \quad (68)$$

Theoretical Results for Various Cases of Interest. Thus far we have only considered some exact $\omega \rightarrow 0$ results and typical adsorption-reaction interface frequency response for a half-cell or full cell. Let us now turn to further predictions of the complete full-cell model (Macdonald and Franceschetti [1978]), predictions derived from its specific analytical results in several simplified cases and from a large amount of CNLS fitting of various equivalent circuits to the exact model predictions (see, e.g., Franceschetti and Macdonald [1977], Macdonald *et al.* [1977], Macdonald and Franceschetti [1979a], Macdonald and Hull [1984]). For simplicity, we consider only the uni-univalent case ($z_n = z_p = 1$), intrinsic conduction, and $M \gg 1$. The latter condition excludes the behavior of very thin layers and membranes, but their response has been discussed in the literature. Let us define cases of interest by their $[\rho_p, \rho_n, \pi_m]$ values. Actual values of ρ_p and ρ_n cited in this way will always be real, but when the symbols are used, they may include complex cases. Because the electrodes are taken identical, ρ_n and ρ_p values apply to both electrodes.

Little has been done on the $[\rho_e, \rho_e, \pi_m]$ case, where the normalized reaction rates (but not necessarily k_n and k_p) are equal and nonzero. Although this is a situation of small experimental interest except for $\rho_e \leq 0$, a formal expression for its admittance has been given (Macdonald and Franceschetti [1978]) but does not lead to a useful approximate equivalent circuit representation except when $\pi_m = 1$. When $\rho_e = 0$ as well, there is no finite-length Warburg present. Because of its complexity, model predictions for the general $[\rho_p, \rho_n, \pi_m]$ case with both ρ_p and ρ_n values nonzero and noninfinite have been little explored, although it has been found that for a nonzero ρ_n value, say, and even for $\pi_m = 1$, as ρ_p increases from zero toward ρ_n , a finite-length Warburg arc that appears in the impedance plane rapidly decreases in size (Macdonald [1975]). Note that when a diffusion arc is present, one finds (Macdonald [1974b]) that $C_p(\omega)$, the total frequency-dependent parallel capacitance associated with Y , exhibits $\omega^{-3/2}$ and $\omega^{-1/2}$ dependence, quite different from ω^{-2} simple Debye response, yet frequently observed experimentally.

The situation of most experimental interest, especially for solid electrolytes, is defined by $[0, \rho_n, \pi_m]$ or, equivalently, $[\rho_p, 0, \pi_m]$. Thus only one species of charge carrier discharges, but both positive and negative ones may be mobile. The equivalent circuit we believe to be most appropriate in this case is presented in Figure 2.2.8. First, we see the usual elements C_∞ , R_∞ , R_R , C_A , and R_A already discussed. For this $[0, \rho_n, \pi_m]$ situation, R_R , R_A , and C_A are given by just the unnormalized forms of R_{RnN} , R_{AnN} , and C_{AnN} presented in Eqs. (64)–(66). The additional elements Z_{De} , Z_W , C_R , and $R_{R\infty}$ that appear in the circuit require discussion. But first it should be emphasized that much theoretical analysis and fitting of theory to different equivalent circuits makes it quite clear that the hierarchical ladder-network form of this circuit is far more appropriate than either the series Voigt or the parallel Maxwell form. The ladder network, which leads to a continued-fraction expression for the total impedance, ensures that the $R_\infty C_\infty$ arc in the impedance plane will occur at the highest frequencies, followed (with or without overlap) by a

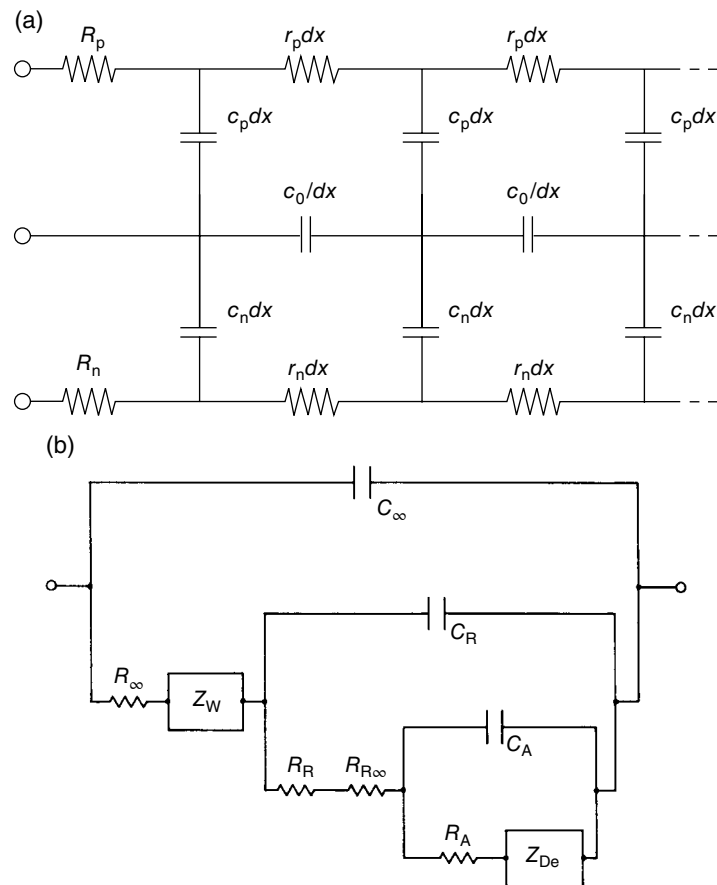


FIGURE 2.2.8 (a) Transmission line representation of Nernst–Planck–Poisson equation system for a binary electrolyte. R_p and R_n are charge transfer resistances for positive and negative charge species at the electrode, respectively. (b) General approximate equivalent circuit (full cell, unsupported) for the $[0, \rho_n, \pi_m]$ cases applying to a homogeneous liquid or solid material.

$R_R C_R$ arc and then $R_A C_A$ arc as the frequency decreases. The Voigt circuit, for example, imposes no such requirements. The diffusion arc(s) may actually occur in any frequency range for the present circuit but is usually found at the right of the diagram, the lowest-frequency region.

The element Z_{De} is a general diffusion impedance added to account for possible diffusion of uncharged reactants such as oxygen atoms (but not parent-electrode atoms) in the electrodes (for the present full-cell situation, it accounts of course for diffusion in both electrodes). When $\rho_n \equiv 0$, it should not appear. In most cases of interest, it will probably be best represented by a finite-length Warburg impedance, so $Z_{De} = Z_{We}$. One might at first be surprised to find Z_{De} in series with the adsorption-related resistance R_A rather than in series with C_∞ and R_∞ . Although the diffusion process in the electrode does occur after the charge carrier has been transported through the electrolyte, it has only a negligible effect on the potential difference across the electrode, which is essentially zero for a metallic electrode. Rather, it contributes to the interfacial impedance by hindering the discharge of the adsorbed species. If adsorption does not occur to any significant extent, then $C_A \rightarrow 0$, $R_A \rightarrow 0$, and Z_{De} is in series with R_R .

The next new element is a finite-length Warburg impedance Z_W , associated with diffusion of charged particles within the electrolyte. It is primarily present in low-frequency regions where the more mobile or more abundant charged species have time in a half-cycle to rearrange positions so

as to screen the less mobile or less abundant charges from the electric field, leaving diffusion as the primary conduction method for such low frequencies. Since this diffusional process occurs in the electrolyte bulk, Z_W is placed in series with R_∞ . For the present situation, the diffusion impedance is well approximated by

$$Z_{WN} = \frac{Z_W}{R_\infty} = \pi_m^{-1} \left[\left(\tanh \left((j\Omega H_N^2)^{1/2} \right) \right) / (j\Omega H_N^2)^{1/2} \right] \quad (69)$$

except when $\rho_n = 0$ and $\pi_m = 1$ simultaneously, a situation where $Z_W = 0$. Here $\Omega \equiv \omega\tau_D \equiv \omega R_\infty C_\infty$. The quantity H_N is found to be

$$H_N = \frac{M_e}{2} (\pi_m^{-1} + 2 + \pi_m)^{1/2} \quad (70)$$

We defined $M_e \equiv l/2L_{De}$, where L_{De} in the present case is given by

$$L_{De} = \left(\frac{\epsilon\epsilon_0 RT}{8\pi F^2 q n^0} \right)^{1/2} \quad (71)$$

and q takes intrinsic generation/recombination into account and is actually frequency dependent and complex in the exact theory. Here it will be sufficient to take $q = 1$ when charges of both sign are mobile and usually take $q = 0.5$ when only one species is mobile (see later discussion). Then L_{De} equals either L_D or L_{D1} . Note that when $\pi_m = 1$, $H_N = M_e$. Alternatively, when $\pi_m \rightarrow 0$ because $\mu_n \rightarrow 0$, there will be no dc path through the circuit and $Z_W \rightarrow \infty$.

The appearance of a Warburg impedance—generally associated with a diffusion process—arising from the motion of charged particles in an unsupported system has been the source of some confusion. A discussion and comparison of the various sources of finite-length Warburg impedances in both supported and unsupported systems can be found in Franceschetti *et al.* [1991]. The essential point is that the appearance of Warburg behavior in itself is not necessarily a signature of mobile neutral species coupled to the electrode reaction.

It should be mentioned that when the product of a reaction at the electrode is neutral, it may possibly diffuse back into the electrolyte as well as into the electrode (Franceschetti [1981]). Then another Z_W appears in series with R_R . How can one distinguish between up to three different Z_W s, all effectively in series with R_∞ ? By changes in the electrode thickness l_e and the separation of the electrodes l , one should be able to identify a given Z_W arc as arising from diffusion in one or the other region. One can then decide whether a Z_W that depends on l involves charged or uncharged species by changing (if possible) the equilibrium concentration of the neutral species in the electrolyte, either directly or by changing the composition or pressure of the ambient atmosphere. Of course, in most experimental situations, only a single Z_W arc appears in the very low-frequency region (or measurements do not extend to low enough frequencies to show others). As we shall see subsequently, a single Z_W can only arise from neutral-species diffusion if $\mu_n = 0$ and $\mu_n \neq 0$, so $\pi_m = \infty$, the one-mobile case. Similar results appear for $\mu_n = 0$ and $\mu_p \neq 0$.

The next element requiring discussion is C_R , the reaction capacitance, arising from the series combination of equal diffuse double-layer capacitance effects at each electrode. It is usually very well approximated by

$$C_{RN} \equiv \frac{C_R}{C_\infty} = M_e \operatorname{ctnh}(M_e) - 1 \quad (72)$$

essentially equal to M_e in the present $M \gg 1$ case, but note that $C_R + C_\infty = C_\infty M_e \operatorname{ctnh}(M_e)$. When $M_e \gg 1$, the usual situation, this full-cell result is just half of the conventional diffuse double-layer capacitance, an intensive quantity, given in Eq. (33) for the supported half-cell situation.

Now what about the remaining element, $R_{R\infty}$? In the present case, Eq. (61) leads to $R_{DN} = \epsilon_n^{-1} [1 + \rho_{n0}^{-1}] = 1 + \pi_m^{-1} + [\epsilon_n \rho_{n0}]^{-1}$, an exact result. But on omitting Z_{De} , the circuit of Figure 2.2.8b leads to $R_{DN} = R_{\infty N} + Z_{WN0} + (R_{RN} + R_{AN}) + R_{R\infty N} = 1 + \pi_m^{-1} + (\epsilon_n \rho_{n0})^{-1} + R_{R\infty N}$. Thus $R_{R\infty}$ must actually be zero, at least in the $\omega \rightarrow 0$ limit, unless expressions for one or more of the other parameters are incorrect in this limit. Macdonald and Hull [1984] found that even when $R_A = 0$ and $R_R = 0$ (taking $\rho_n = \rho_{n\infty} = \infty$), a circuit similar to the present one with the present Z_W could be best fitted to the exact $[0, \infty, \pi_m]$ case with a nonzero $R_{R\infty}$ approximately given by

$$R_{R\infty N} = 2M^{-1}(\pi_m^{-1} - 1) \quad (73)$$

for $\pi_m \leq 1$ and by zero for $\pi_m \geq 1$. Thus even in the absence of a normal reaction resistance, CNLS fitting of exact data leads to a nonzero apparent reaction resistance. For large M it is only of importance when π_m is very small (a high resistance case), since when $R_{R\infty} < 0.01 R_\infty$, its effect will be essentially negligible and difficult to resolve even with CNLS fitting. Note also that $R_{R\infty N}$ will always be appreciably smaller than $Z_{WN0} = \pi_m^{-1}$ for $M \gg 1$. Nevertheless, the presence of this element in the circuit and the natural tendency to consider the measured $R_R + R_{R\infty}$ as "the" reaction resistance can lead to incorrect estimates of the rate parameter unless the presence of $R_{R\infty}$ is explicitly recognized (Macdonald and Hull [1984]). The fact that $R_{R\infty}$ should not actually appear at $\omega = 0$, yet is needed in the fitting circuit, is an indication of some inappropriateness in the fitting circuit itself. But for the present it seems the best circuit available.

Let us continue to ignore Z_{De} and investigate two simpler cases. First consider the important completely blocking case $[0, 0, \pi_m]$ where $R_R = \infty$. There is still a Warburg impedance present in general, but it can only contribute to making the normally vertical spur present at low frequencies in the impedance plane and associated with complete blocking show less than vertical behavior over a finite frequency range. But an inadequacy of the present expression for Z_W appears when $\pi_m = 1$; then the exact solution leads to no Z_W , but Eq. (69) still yields a nonzero Z_W . The special $[0, 0, 1]$ case must therefore be handled separately until a more complete expression for Z_W is found or unless direct CNLS comparison between data and model predictions is employed.

The Case of Charge of Only a Single-Sign Mobile. The remaining one-mobile case, $[0, \rho_n, \infty]$, is of particular interest for solid electrolytes with only a single species-of-charge (here negative charge) mobile. This situation is the most usual one for solid electrolytes, although it should be realized that it is always something of an approximation. At nonzero temperature both positive and negative charge species present in a solid material or a fused salt are mobile, although their mobility ratio, $\pi_m \equiv \mu_n/\mu_p$, may be either very large or very small. The relatively immobile species may have so low a mobility at a given temperature that motion of this species is negligible during a half-cycle of the lowest frequency applied. Then the one-mobile approximation will be a good one. Although we have taken ρ_p as zero in the aforementioned case designation, its value is immaterial since the positive charges are taken immobile ($\mu_p = 0$) and cannot react at an electrode. In the present case all the ϵ_n 's that appear in the defining equations are unity and all π_m^{-1} 's zero. Therefore, as Eq. (69) shows, $Z_W = 0$, and no charged-particle Warburg arc is present, and the only Warburg diffusion response possible must arise from diffusion of neutral particles in the electrodes or the bulk of the material. The exact theoretical results show that in the present case the circuit of Figure 2.2.8b (with $R_{R\infty} = 0$) is completely applicable with all frequency-independent elements given exactly by their values following from the foregoing expressions except that for C_{RN} . When $Z_{De} = 0$ and the time constants are well separated, so that $R_A C_A \gg R_R C_R \gg R_\infty C_\infty$, the circuit of Figure 2.2.8b leads to just three distinct arcs in the Z^* plane.

It is in the partially dissociated one-mobile case that generation/recombination can play a role of some importance (e.g., Macdonald [1953b], Macdonald and Franceschetti [1978]). We have already mentioned that the L_{De} that appears in the equation for C_{RN} should usually be taken as L_{D1} ($q = 0.5$) in the one-mobile case. This choice is particularly relevant for fully dissociated charges, such as those that might arise from the complete ionization of immobile donors. But in the partly dissociated situation, appropriate for intrinsic conduction, generation/recombination can lead to an effective mobility for the immobile charge species (except at dc). Then over some region of frequency, as v decreases,

$L_{D\text{e}}$ changes from L_{D1} to L_D because of the frequency dependence of q . Thus, although the formal expression for C_{RN} given previously remains valid for the one-mobile case, one must consider the physical situation to decide whether to use L_{D1} or L_D in M_e . Alternatively, it is more accurate to use the full frequency-dependent expression for q as a part of the definition of C_{RN} in this case. Then CNLS fitting can, in principle, lead to information about the degree of dissociation of intrinsic centers and the associated generation/recombination parameters. Such a procedure would only be justified, however, for excellent data. It was originally thought (Macdonald [1976b]) that generation/recombination might lead to a separate semicircle in the impedance plane, but a later work (Macdonald *et al.* [1977]) suggests that it does not for ionic conduction. Thus its effects for the one-mobile case are entirely restricted to C_R only and are relatively small even there. Note that in the two-mobile case, as long as the mobilities are not greatly different, effective mobilization, arising from generation/recombination, of the species with the smaller mobility will still lead to negligible effects.

Some Results for More General and Realistic Situations. Next let us consider the removal of some of the approximations inherent in the foregoing model. For the small-signal flat-band case, it turns out that the half-cell reaction resistance in the supported case, Eq. (34), derived using the Butler–Volmer equation, and the half-cell reaction resistance in the unsupported case, R_{0n} , Eq. (52), which followed from use of the Chang–Jaffé boundary equations, are essentially identical (Macdonald [1974a, b]). Furthermore, Franceschetti and Macdonald [1977] and Macdonald and Franceschetti [1979a] later showed that the calculation of the reaction resistance in either the unsupported or supported case gave the same result (because of compensating errors) whether Chang–Jaffé or Butler–Volmer equations were employed, provided, however, that any inner- or compact-layer capacitance C_C present was much larger than the diffuse double-layer capacitance. In addition, a method of transforming an unsupported small-signal impedance solution based on Chang–Jaffé boundary conditions to one employing Butler–Volmer, or even more general boundary equations, was developed. This method obviates the difficult task of solving the small-signal equations ab initio with the new boundary conditions.

There are plausible physical reasons to prefer Butler–Volmer to Chang–Jaffé conditions, especially when a compact layer is present, since the Butler–Volmer equations can account for the p.d. across this layer. Macdonald and Franceschetti [1979a] therefore studied how, for the $[0, \rho_{n0}, \infty]$ case without adsorption, C_R and R_R are changed from the results given here to new values when Butler–Volmer, or even more general boundary conditions, are used instead of Chang–Jaffé conditions and a compact layer of arbitrary constant capacitance was assumed present as well. Theoretical results were given, and CNLS fitting of such results to an equivalent circuit were carried out in order to find the simplest adequate modifications needed. This approach not only allowed $\omega \rightarrow 0$ modifications to appear but yielded information on changes in the interface impedance over all ω values of interest arising from the presence of C_C and the more general boundary conditions.

Results found from the aforementioned approach were surprisingly simple. The present expression for R_{0N} or R_{0nN} (with $\epsilon_n = 1$) was shown to hold exactly in the Butler–Volmer case, independent of the size of C_{cN} . A simple expression for a new effective full-cell C_R , say, C_{Re} , was found in the Butler–Volmer case, namely,

$$C_{ReN} = C_{RN} - (C_{RN} + 1 + \rho_{n0})^2 / (C_{RN} + 1 + C_{cN}) \quad (74)$$

Now in the usual $M \gg 1$ case where $C_{RN} \gg 1 + \rho_{n0}$, this result reduces to just $C_{ReN}^{-1} \cong C_{RN}^{-1} + C_{cN}^{-1}$, a series combination of the original C_R and the compact-layer capacitance C_c . However, this is just the $\omega \rightarrow 0$ result always used in the supported case! Although these results were derived for the $[0, \rho_{n0}, \infty]$ case without adsorption, they should hold quite adequately for the nonadsorption $[0, \rho_{n0}, \pi_m]$ case as well.

When adsorption is present and the effects of a compact layer are included as well, it has been shown (Macdonald *et al.* [1980a]) that in the $[0, 0, \infty]$ case, the $\omega \rightarrow 0$ expression for the total differential capacitance is more complicated than just C_{Re} and C_A in parallel. One needs first to separate C_C into two series parts so $C_C^{-1} = C_\alpha^{-1} + C_\beta^{-1}$, where C_α is the capacitance between the electrode and the charge centroids of

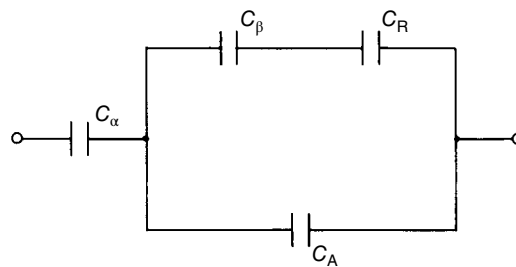


FIGURE 2.2.9 Circuit for the total interface differential capacitance in the $(0, 0, \infty)$ case without adsorption for $\omega \rightarrow 0$.

the adsorbed ions (at the inner Helmholtz plane) and C_β is that from this plane to the outer Helmholtz plane, where the diffuse layer of charge begins. Then one obtains the circuit of Figure 2.2.9, which reduces to the aforementioned result for C_{Re} when $C_\alpha = \infty$. When $C_\alpha < \infty$, it is not clear how R_R should be added to this circuit since it should bridge C_α and still be in series with C_A . For most solid electrolyte situations, however, it will usually be an adequate approximation to take $C_\alpha = \infty$ in fact and to put R_R in series with C_A , returning to the usual form of the interface part of the circuit (see Figure 2.2.8). First, there is the probability of the electron wave function spilling out from the surface of a metal electrode and reducing the effective thickness of C_α toward zero (Kornyshev *et al.* [1982]). Second, for solid materials there will be no inner uncharged layer of solvent material, as in liquid electrolyte situations. This means that the plane marking the beginning of the diffuse layer is nearly as close to the electrode as the plane where adsorption occurs; when $C_{\alpha N} \rightarrow \infty$ or it is very large, C_{BN} will also be extremely large and may often be neglected compared with C_R , so $C_{Re} \cong C_R$. Incidentally, in the presence of dc bias, C_R (and C_A) are both functions of the effective overpotential and can increase greatly over their flat-band values under some conditions. They are limited in maximum value, however, because of the finite size of ions (Macdonald *et al.* [1980a]). When one finds experimentally that C_{Re} is nearly independent of applied dc bias and temperature, it is likely that it is dominated by C_C rather than C_R .

Now let us briefly consider some results for the non-flat-band case without adsorption (Franceschetti and Macdonald [1979a, b, 1980]). Both transient response and biased small-signal frequency-response results have been obtained using computer simulation, that is, numerical solution of coupled sets of partial or ordinary second-order differential equations describing the model. Chang-Jaffé and Butler-Volmer boundary conditions were both employed. Here we shall discuss only the frequency-response results. First, the response of cells with $(0, 0, \pi_m)$ conditions at the left electrode and (∞, ∞, π_m) conditions at the right one was considered, leading to essentially half-cell conditions. The dc bias was assumed to arise from either built-in Frenkel space-charge regions or an actual applied p.d. No dc flowed in these completely blocking situations. Second, results were obtained for the full-cell system with $(0, 0, \pi_m)$ conditions at each electrode. Many complex plane Z and Y plots were presented to show how arcs and spurs varied with applied bias. More importantly, it was found that the equivalent circuit of Figure 2.2.8b with $Z_{De} = 0$, $\rho_{n0} = 0$, and no adsorption applied quite well, not only for zero bias (flat band) but also for either polarity of applied bias up to the maximum magnitude applied of about $15 (RT/F)$, sufficient bias to make the system very nonlinear. There are no R_A and R_R elements present under these conditions, but Z_W did appear for $\pi_m \neq 1$ and for $\pi_m \neq \infty$ conditions. It is impractical to summarize here all the results found and reported, but the dependences of C_R and the components of Z_W generally varied with bias in reasonable and expected ways. The bulk parameters R_∞ and C_∞ showed negligible variation with bias.

Later, large-bias frequency-response results were obtained for one-mobile partially blocking situations with no adsorption and with either $(\rho_{p0}, - , 0)$ for the left electrode and $(\infty, - , 0)$ for the right (half-cell conditions) or $(\rho_{p0}, - , 0)$ for both. Then a dc can flow, and steady-state current-voltage curves for Chang-Jaffé conditions were compared with those for Butler-Volmer ones. Appreciable differences occurred for biases bigger in magnitude than (RT/F) . As expected, no diffusion effects were present in the response.

The circuit of Figure 2.2.8b was again found adequate to describe the response, here with $Z_{De} = 0$, $R_A = 0$, and $Z_W = 0$. For Chang–Jaffé conditions $R_{\infty N}$ remained very close to its expected unity value and $C_{\infty N}$ was held fixed at unity, but for Butler–Volmer conditions, $R_{\infty N}$ and $C_{\infty N}$ were somewhat bias dependent and differed from unity. The dependences of R_R and C_R on bias were in accord with predictions based on the buildup of charge accumulation or depletion regions near the partly blocking electrodes, and it was found that C_{RN} was smaller in the Butler–Volmer case, because of compact-layer effects, than in the Chang–Jaffé one. For the same reason R_{RN} was less bias dependent for Butler–Volmer than for Chang–Jaffé.

The foregoing results show the wide scope of the Figure 2.2.8b general circuit. It applies with good approximation for both flat-band small-signal conditions and under equilibrium or nonequilibrium biased conditions, provided its elements are properly interpreted to account for the presence or absence of a compact layer and the appropriate type of boundary conditions.

Thus far we have dealt with either half-cells, where the right half-cell boundary involves nonpolarizing ohmic boundary conditions (∞, ∞, π_m) and the left involves conditions such as $(0, \rho_n, \pi_m)$ or with full cells with identical boundary conditions at each electrode. Another interesting full-cell case is that of crossed reactions where the left electrode involves $(0, \rho_n, \pi_m)$ and the right $(\rho_p, 0, \pi_m)$. Different electrodes are used, so charge of one sign reacts at one electrode and that of the other sign at the other electrode. This double-injection model cannot pass dc and has been analyzed by Glarum and Marshall [1980]. Although their solution is rather complicated, it reduces under conditions of interest ($\pi_m \ll 1$) to just the Z_{DOC} impedance of Section 2.2.2.2, that for an open-circuited transmission line. As already noted, it leads to an ordinary finite-length Warburg arc in the ϵ , not the Z , complex plane. Glarum and Marshall have used this result with some success in analyzing data for iridium oxide thin films (see also Franceschetti and Macdonald [1982]). It is therefore likely that a modification of the general Figure 2.2.8b circuit, useful in some $R_D = 0$ situations, would be to replace Z_W by Z_{DOC} . In fact, the most general modification would be to replace Z_W by Z_D , allowing the possibility of any kind of uniform transmission line-like behavior.

2.2.3.4 Equivalent Network Models

Sah [1970] introduced the use of networks of electrical elements of infinitesimal size to describe charge carrier motion and generation/recombination in semiconductors. Barker [1975] noted that the Nernst–Planck–Poisson equation system for an unsupported binary electrolyte could be represented by a three-rail transmission line (Figure 2.2.8a), in which a central conductor with a fixed capacitive reactance per unit length is connected by shunt capacitances to two resistive rails representing the individual ion conductivities. Electrical potentials measured between points on the central rail correspond to electrostatic potential differences between the corresponding points in the cell, while potentials computed for the resistive rails correspond to differences in electrochemical potential. This idea was further developed by Brumleve and Buck [1978] and by Franceschetti [1984] who noted that nothing in principle prevents extension of the model to 2-D or 3-D systems.

Most recently, the electrical network formalism has been used extensively by Jamnik, Maier, and their collaborators (Jamnik *et al.* [1999], Jamnik and Maier, [2001], Jamnik [2003]), whose work has highlighted the utility of the models for qualitative reasoning about phenomena occurring in systems with a mixed ionic and electronic conducting electrolyte (MIEC) and electrodes nearly blocking for one species. These workers highlight the fact that the capacitors connecting the ionic rails to the central rail representing bulk dielectric behavior are in fact chemical, rather than electrostatic capacitances related to the derivative of chemical potential with respect to ionic concentration. In modeling mixed conductors with a large enough electrode separation to have bulk electroneutrality, Jamnik *et al.* [1999] and Jamnik and Maier [2001] obtained informative approximate results by eliminating the central or displacement rail in Figure 2.2.8a and replacing it with a geometric capacitance in parallel with the transmission line. In particular, they are able to model the transition between a “nearly single-carrier system” not exhibiting a Warburg region and a two-carrier system exhibiting a Warburg. Jamnik [2003] describes the use of the model to describe multiphase systems and to model grain boundary effects.

While electrical networks offer a number of useful features, as a guide to qualitative reasoning about electrochemical systems and as a means of shedding light on the origin of the elements appearing in “lumped” circuits, it should be remembered that they are simply a graphical representation for what amounts to a finite difference representation of the underlying Nernst–Planck, Poisson, Maxwell, and Diffusion equations. Fleig and Maier [1997] have made use of this direct computational approach to study the effects of partial contact with a real electrode, while Maier *et al.* [2000] have used it to study the effective rate constant for structured arrays of contact points or strips.

2.2.3.5 Unsupported Situations: Empirical and Semiempirical Models

In this section, we shall first discuss some ways in which the theoretical model results and equivalent circuits of the last section may be modified to attempt to account for less ideal conditions than assumed in the theory, conditions often appreciably closer to those found in real material–electrode systems. Then we shall discuss empirical and semiempirical models that may be useful as elements in equivalent circuits used for fitting real IS data.

Possible Circuit and Model Modifications. Further modifications of the Figure 2.2.8b equivalent circuit are often necessary, especially for polycrystalline material. One frequently finds experimentally that one or more of the $R_\infty C_\infty$, $R_R C_R$, or $R_A C_A$ semicircles in the complex plane are depressed, so their centers lie below the real axis. It is more probable for the $R_R C_R$ arc to show such depression than the bulk $R_\infty C_\infty$ one for single-crystal material. Such depression may be interpreted in terms of a distribution of relaxation times, possibly arising in the case of the $R_R C_R$ arc from electrode surface roughness and/or porosity (see, e.g., de Levie [1967], Franklin [1975]). Although the exact small-signal solution with identical electrodes actually leads to some arc depression when π_m is very different from unity (Macdonald [1974b]), the amount of depression possible from widely different positive and negative charge mobilities is insufficient to explain most experimental depressions.

In the absence of a fully adequate microscopic theory leading to arc depression in the impedance plane, it has become customary to use the ZARC function defined in Section 2.2.2.2 to describe the depression analytically. This function involves either a resistance and a CPE in parallel or a unified impedance as in Eqs. (23) and (25). For describing depressed arcs in the ϵ plane, the ϵ ARC (Cole–Cole) function also defined in Section 2.2.2.2 has long been used. Note that the CPE that appears in both the ZARC and the ϵ ARC may be associated with a nonuniform transmission line and NUD in a region of infinite extent, but the CPE has not been generalized so far to the finite-length diffusion regime. When an adequate expression is available, it will represent a more complex process than ordinary finite-length (uniform) diffusion, for example, Z_W , a subset of such generalized CPE response. Although this process would be appropriate for distributed (nonuniform) bulk response, since it would change from intensive to extensive behavior with decreasing frequency as Z_W does, the ordinary CPE, which can be taken either intensive or extensive, seems more appropriate for intensive interface processes. Whenever a straight-line spur in the impedance of plane is found with an angle from the real axis different from $\pi/4$, the CPE should replace Z_W .

Although there is no complete derivation of a generalized CPE yet available, which arises from NUD in a finite-length region, one may heuristically modify the CPE and Warburg diffusion expressions in such a way as to generalize them both. The result is

$$Z_{\text{NUD}} = R_0 \tanh \left(\frac{A_0 R_0 (j\omega)^\psi}{A_0 R_0 (j\omega)^\psi} \right) \quad (75)$$

where R_0 , which might be R_∞ for bulk behavior, is taken extensive and we require $0 < \psi < 1$. For $\psi = 0.5$, this expression reduces to just Z_W when one takes $A_0 = l_e / R_0 \sqrt{D}$. For $A_0 R_0 \omega^\psi \gg 1$, $Z_{\text{NUD}} \cong Z_{\text{CPE}}$. Further, for any ψ , $Z_{\text{NUD}} \rightarrow R_0$, an extensive quantity, when $A_0 R_0 \omega^\psi \ll 1$, and, for $\psi < 1$, to $[A_0 (j\omega)^\psi]^{-1}$ for $A_0 R_0 \omega^\psi \gg 1$. This result is intensive, as it should be if A_0 is taken intensive, as it is in the Warburg limit. Note that while both the ZARC impedance and Z_{NUD} involve $R_0 A_0$, they will have somewhat different shapes at

the lowest frequencies where they approach the real axis. Further, the present expression for Z_{NUD} is just an empirical stopgap result and is probably most useful for $0 < \psi \leq 0.6$. We shall denote this heuristic generalization as the generalized finite-length Warburg model (GFW).

The fact that the current ungeneralized CPE has no dc path (while a generalized one would) can lead to problems in using the CPE in hierarchical circuits such as that of Figure 2.2.8. Whenever it seems appropriate to replace an ordinary capacitor in the circuit by a CPE, no problem arises. But one cannot replace a resistor needed as part of a dc path by a CPE and still maintain the dc path; all one can do is put a CPE in parallel with the resistor, producing a ZARC function, or perhaps to use Z_{NUD} . But there is a problem in using such elements in hierarchical circuits. Although the real and imaginary parts of, say, a ZARC function could be separated, and the imaginary part used in place of an ideal capacitor in an hierarchical circuit and the real part in place of an ideal resistor, there is no physical justification for such separation.

In the polycrystalline case, one must consider the processes that occur within an individual single-crystal grain and what happens at the grain boundaries, taking into account that there is almost certainly a distribution of grain sizes and orientations present. Since the response is a 3-D average of the response of a great many interacting grains, one expects that the bulk response for composite materials will both be more complicated than the $R_\infty C_\infty$ semicircle expected for a perfect homogeneous material and may often be described by a distribution of relaxation times, either discrete or continuous. Since one usually finds that it is experimentally impossible to distinguish results arising from a continuous distribution and its approximation by, say, 10 or more discrete relaxations, it is often easiest to use the continuous distributions, since many less parameters need be specified. For the distorted and displaced arcs, which are usually seen in the impedance plane for composite materials such as ceramics, it of course makes no difference in which order the elements representing this overall bulk response appear in the equivalent circuit (Voigt, not hierarchical connection), and it has also been customary to try to represent the response by one or more ZARC functions in series. No charged-particle Warburg response will be present if charge of only a single sign is mobile.

Although it does not seem reasonable to build a hierarchical ladder-network circuit using the separated real and imaginary parts of a distributed element such as the ZARC, we can still achieve considerable generality and flexibility if we form a circuit using *only* unified distributed elements as in the three-level circuit of Figure 2.2.10. Here DE represents a general distributed element, one like the ZARC, which can well approximate either an ideal resistor or an ideal capacitor in limiting cases of its fractional frequency dependence exponent ψ . Thus, in Figure 2.2.10, the odd-numbered DEs could, in the limit, be taken as capacitors, and the even-numbered ones as resistors. In practical cases, however, one would often find it necessary to choose some of the DEs as nonideal distributed elements. Note that if the electrodes were nonblocking, one would need to ensure a dc path through the circuit by, for example, taking

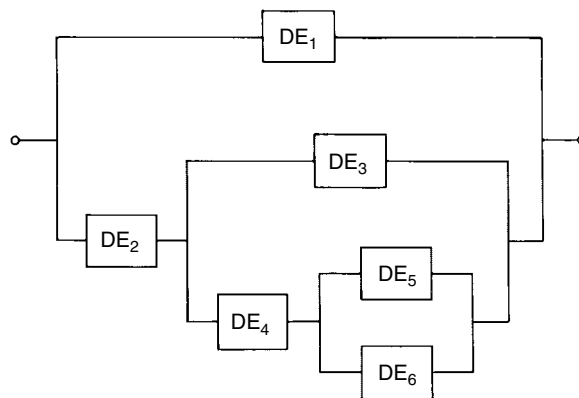


FIGURE 2.2.10 General equivalent circuit showing hierarchical structure and involving general distributed elements.

the even-numbered DEs as resistors, ZARCs, or some other unitary or composite nonblocking distributed element.

Further Empirical and Semiempirical Models. Although various empirical distributed-element models have already been discussed, particularly in Section 2.2.2.2, the subject is by no means exhausted. Here we briefly mention and discuss various old and new elements that may sometimes be of use in a fitting circuit such as that of Figure 2.2.10. Complex plane plots of IS data by no means always yield perfect or depressed semicircular arcs; often the arc is unsymmetric and cannot be well approximated by the ZC. An unsymmetrical impedance plane arc usually exhibits a peak at low frequencies and CPE-like response at sufficiently high frequencies. The reverse behavior is not, however, unknown (Badwal [1984]). An expression originally proposed in the dielectric field by Davidson and Cole [1951] yields ordinary asymmetric behavior. Its I_k generalization is

$$I_k = [1 + js]^{-\psi_k} \quad (76)$$

with $s \equiv \omega\tau$ and $0 \leq \psi_k \leq 1$, and it reduces to symmetric Debye response for $\psi_k = 1$. This model will be denoted by DC. A further empirical dielectric-area approach, due to Kohlrausch [1854] and Williams and Watts [1970], yields transient response of the fractional exponential form $\exp(-t/\tau_0)^\psi$, with $0 < \psi \leq 1$. Only complicated series expressions and tables exist for its small-signal response, but it yields frequency domain response generally rather similar to that of Eq. (76). It will be denoted by WW. See Macdonald and Hurt [1986] for an accurate WW fitting method.

Jonscher [1974, 1975a, b, 1980, 1983], in an extensive series of papers, has also worked primarily in the dielectric area, independently emphasized the importance and ubiquity of constant phase response, and proposed and demonstrated the utility of three different empirical frequency-response functions in IS data fitting. These three equations, termed *universal dielectric response* by Jonscher, were originally expressed in terms of the imaginary part of the complex dielectric susceptibility, χ'' . They may alternatively be expressed, of course, in terms of ϵ'' or Y' . Further, they may all be generalized to the I_k'' ($k = \epsilon$ or Z) representation. Finally, it has been found (Macdonald [1985d]) that two of them may be written in full complex form, not just as I_k'' .

The three generalized Jonscher equations may be expressed as

$$I_k = B_{k0}(j\omega)^{-\psi_k} \quad (77)$$

$$I_k = B_{k1}[(j\omega\tau_{k1})^{-\psi_{k1}} + (j\omega\tau_{k2})^{-\psi_{k2}}] \quad (78)$$

and

$$I_k'' = -B_{k2} \left[\left(\frac{\omega}{\omega_{kp}} \right)^{-\psi_{k3}} + \left(\frac{\omega}{\omega_{kp}} \right)^{-\psi_{k4}} \right]^{-1} \quad (79)$$

It is clear the Eq. (77) is just the CPE and Eq. (78) is a combination of two CPEs (in parallel for $k = \epsilon$ and in series of $k = Z$). Of course, the ω_{kp} of Eq. (79), which denotes a peak frequency, could be replaced by $\tau_{kp} \equiv \tau_{kp}^{-1}$. The possible range of all the exponents is $(0, 1)$. In Jonscher's $k = \epsilon$ "universal dielectric response" case, one has $\psi_\epsilon = 1 - n$, $\psi_{\epsilon 1} = 1 - n_1$, $\psi_{\epsilon 2} = 1 - n_2$, $\psi_{\epsilon 3} = m$, and $\psi_{\epsilon 4} = 1 - n$. If we further choose $\psi_Z = n$, $\psi_{Z1} = n_1$, and $\psi_{Z2} = n_2$, Eqs. (77) and (78) yield the same frequency dependence exponents at the admittance level when a single term dominates. For example, Eq. (77) yields $Y_\epsilon \propto (j\omega)^n$ and $Y_Z \propto (j\omega)^n$ for the aforementioned choices. We shall term Eq. (78) the *generalized second Jonscher equation* (GJ2) and Eq. (79) the *generalized third Jonscher equation* (GJ3).

The minus sign in Eq. (79) arises because we have defined I_k with a plus sign as $I_k = I_k' + iI_k''$. When $\omega = \omega_{kp}$ in Eq. (79), $|I_k''|$ reaches a maximum. Further, when $\psi_{k3} = \psi_{k4}$, this equation reduces to the long-known Fuoss-Kirkwood [1941] form, yielding a symmetrical curve for $-I''$ versus $\log(\omega/\omega_{kp})$. We shall denote this special form of the GJ3 as the GFKJ equation. Although no fully complex general expression

consistent with Eq. (79) is available, when $\psi_k \equiv \psi_{k3} = \psi_{k4}$ complex forms have been given for various fractional values of ψ_k . Jonscher and his collaborators have shown that the χ'' forms of Eqs. (77)–(79) can fit a great deal of dielectric and conductive-system data. Unfortunately, the fits never used CNLS, and no ordinary nonlinear least squares fits of χ'' giving fitted parameter estimates and standard deviation estimates have been presented. Further recent discussion of “universal dielectric response” appears in Macdonald [1985d].

Almond *et al.* [1982], Bruce *et al.* [1982], and Almond and West [1983b] specialized the χ'' form of Jonscher's Eq. (78) for hopping conduction situations to obtain

$$\sigma(\omega) = k \left(\omega_p + \omega_p^{1-n} \omega^n \right) \quad (80)$$

where $\sigma(\omega)$ is the ac conductivity, K is a temperature-dependent constant, and ω_p is the thermally activated ionic hopping frequency v_H . Now Eq. (80) may be rewritten at the Y level as

$$Y'(\omega) = G_0 \left[1 + \left(\frac{\omega}{\omega_p} \right)^n \right] \quad (81)$$

Next, generalization of Eq. (81) to the complex plane yields

$$Y(\omega) = G_0 [1 + (j\omega\tau_0)^n] \quad (82)$$

which is fully consistent with Eq. (81) when

$$\omega_p = \left\{ \tau_0 \left[\cos \left(\frac{n\pi}{2} \right) \right]^{1/n} \right\}^{-1} \quad (83)$$

or, equivalently,

$$\tau_0 \equiv \omega_0^{-1} = \frac{[\cos(n\pi/2)]^{-1/n}}{\omega_p} \quad (84)$$

Finally, Eq. (82) yields

$$Z = \frac{R_0}{1 + (j\omega\tau_0)^n} \quad (85)$$

where $R_0 = G_0^{-1}$. This expression is just the long-known ZARC [compare Eq. (22)]. Thus, it appears that the principal new element in the Almond–West work is the identification of ω_p as the hopping frequency. This interesting suggestion has been examined at some length recently (Macdonald and Cook [1985]), with the conclusion that the case is not proven so far. If, in fact, the hopping frequency v_H is directly involved in the ZARC when it is applied to hopping conduction situations, it seems most plausible that $v_H = \omega_0 = \tau_0^{-1}$, or perhaps $\omega_0/2\pi$, rather than ω_p . Equation (83) shows that $\omega_p \rightarrow \infty$ as $n \rightarrow 1$, an unlikely result and one avoided by the choice of ω_0 instead.

Several of the empirical model responses discussed previously have been given a more theoretical basis (see Macdonald [1985c, d] for references), but they still suffer from two important weaknesses. They do not generally lead to physically realistic response at both high- and low-frequency extremes, and they do not lead to any predictions for possible temperature dependence of the fractional exponent(s) ψ . A semiempirical theory whose frequency-response results are briefly discussed in the succeeding text does, however, avoid these weaknesses. Since any real material will have largest (τ_∞) and smallest (τ_0) response times, response at longer (shorter) times than those materials will be determined by these limiting responses (for a single type of physical process). But such single time

constant behavior leads to frequency response proportional to ω for $\omega \ll \tau_{\infty}^{-1}$ and to ω^{-1} for $\omega \gg \tau_0^{-1}$. Although simple Debye behavior with $\tau_0 = \tau_{\infty} = \tau$ also leads to limiting $\omega^{\pm 1}$ response, here τ_0 and τ_{∞} may differ greatly, and for the range $\tau_{\infty}^{-1} < \omega < \tau_0^{-1}$, non-Debye fractional exponent response may appear and usually does so.

Note that CPE response fails the aforementioned test of physical realism at both frequency extremes and so does ZC response for $\psi < 1$. On the other hand, Davidson–Cole low-frequency-limiting response is realistic, but not its high-frequency-limiting response. One might reasonably ask, if all these models are not entirely physically realistic, why are they discussed and used for fitting? The reason is that it is rare for a single-response process, say, which is associated with an electrode reaction (R_R and C_R in the ideal nondistributed case), to be so isolated in its frequency range that one can follow its response alone to very high or low (relative) frequencies. Because of the usual presence of other processes yielding response near or even overlapping in frequency that of the process of immediate concern, one cannot usually follow the response of the process in question very far into its wings where $\omega^{\pm 1}$ limiting response finally must appear. Further, one usually finds that experimental limitations preclude measuring far into the high-frequency wing of the lowest-frequency process present. In essence, what we cannot measure does not matter—at least until we can measure it! Nevertheless, a theoretical model that does incorporate proper limiting behavior is clearly superior in that respect to one that does not.

Although dielectric response data often leads to temperature-independent ψ 's (so that the time–temperature superposition law holds), this is by no means always the case (Jonscher [1983]). Further, conductive-system response, as in ionic hopping conductors, often leads to appreciable temperature dependence of ψ . Surprisingly, ψ_e and ψ_Z temperature responses, when apparent, are usually found to be quite different, with ψ_e increasing with increasing temperature and ψ_Z decreasing.

In recent years several variations of the Kohlrausch–Williams–Watts model have been produced, and attention has been drawn to a nearly constant component of bulk dielectric response in low conductivity electrolytes. This work is outlined in Section 4.2.

Fitting Ambiguity and a New Semiempirical Model. Although all the models we have discussed in this section and in Section 2.2.2.2 are distinct and separate, and although they may be associated with different physical processes, it turns out that there is a high degree of practical fitting ambiguity between most of them. Response differences between several unsymmetric models with the same ψ value are demonstrated in Figure 2.2.11. Here Debye response is included for comparison, and DAE₁ (which involves the parameter ϕ rather than ψ) refers to the semiempirical distribution-of-activation-energies model discussed in the succeeding text. But the situation is different when “data” derived from one model involving a given ψ , say, ψ_a , are fitted by CNLS to another model, yielding a ψ estimate for this

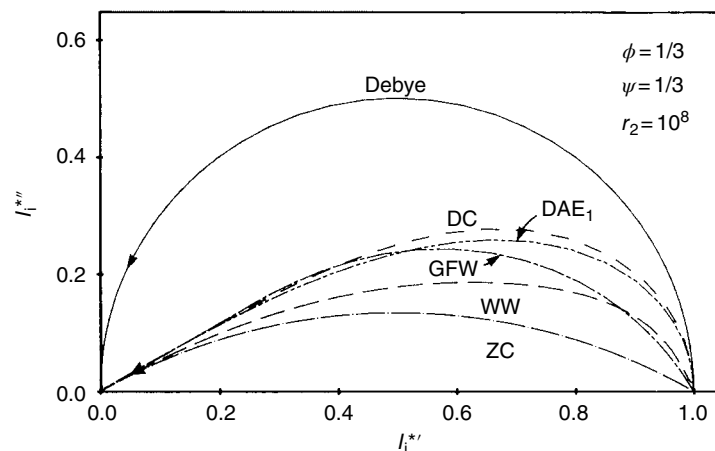


FIGURE 2.2.11 Complex plane response of the normalized I_i^* response of various distributed models.

model, say, ψ_b . It turns out, as we shall demonstrate in the succeeding text (see also Macdonald [1985d]), that when ψ_a and ψ_b are allowed to be different, one model can often fit another within 1% or so (usually better than most experimental data are known) over quite wide frequency and magnitude ranges. When such ambiguity is present, as it usually is for practical less-than-perfect data, it will often be easiest to fit with the simplest model, whether or not it is physically reasonable for the material-electrode system considered, and then relate the fitting results to a more appropriate, but more complex, model.

Such a more complex model is the DAE, involving an exponential density distribution of activation energies. Its rationale and results are described in detail in Macdonald [1963, 1985c, d]. Let us distinguish three forms of it. First is DAE₁, which involves a single exponential density distribution and leads to unsymmetrical response (Macdonald [1985c]). Second is DAE₂, which involves two joined complementary exponential distributions and leads to symmetric behavior in the complex plane. Finally, the general DAE involves two joined noncomplementary exponential distributions and spans the range of shapes from DAE₁ to DAE₂ (Macdonald [1985d]). Of course, the DAE is most generally given in normalized I_k form.

Although the frequency response of the DAE model can only be expressed in integral form (associated with a hypergeometric function) for arbitrary ϕ , relatively simple closed-form response has been given for many values of ϕ . Such closed-form, discrete- ϕ response is useless, however, for accurate CNLS fitting using this model. Therefore, the full-integral DAE model and nearly all of the other distributed-element models discussed so far have been built into the general CNLS fitting program, LEVM/LEVMW, available for free from Dr. J. R. Macdonald and Solartron Inc. [2003]. Thus, any of the models can be used to fit experimental frequency-response data or "data" derived from another model.

Some of the model-fitting ambiguity mentioned previously is demonstrated in the next figures. Further discussion of DAE-Jonscher ambiguity appears in Macdonald [1985d]. First, it is worthwhile to categorize the models discussed by their complex plane symmetry as in Table 2.2.3. The symmetric and asymmetric curves give closed arcs in the complex I_k plane, but the CPE and GJ2 yield only open spurs in this plane (and, as mentioned earlier, cannot be normalized in the usual I_k way). The fitting ambiguity with which we are concerned here applies only within a given column in Table 2.2.3. We cannot expect to get a good fit of asymmetric WW data, for example, with a symmetric model such as the ZC. Note that all models will generally show some region of frequency where CPE-like response appears. In this region, the CPE model is clearly sufficient. It is not this ambiguity with which we are concerned but rather with the holistic response, that which includes regions beyond and below that where CPE response alone dominates.

We have found that any symmetric model in Table 2.2.3 can be very well fitted by any other symmetric model. Figures 2.2.12 and 2.2.13 show 2-D plots obtained from full CNLS fitting of the DAE₂ and ZC models to GFKJ model "data" for several different ψ values. The fits are so good that only with extremely accurate experimental data (better than those usually available) could one decide unambiguously between any of the three symmetric models on the basis of CNLS fitting alone. Further, the DAE has been found to yield a very good fit of the GJ2 model as well (Macdonald [1985d]).

Figures 2.2.12 and 2.2.13 of course do not show frequency response explicitly. It is found to agree exceptionally well also at each point, at least until one moves far away from the peak frequency. Some

TABLE 2.2.3 Summary of Main Models Discussed, Showing Their Symmetry Characteristics in the Complex Plane

Symmetric	Asymmetric	General
ZC	DC	CPE
GFKJ	GFW	GJ2
DAE ₂	WW	DAE
		DAE ₁

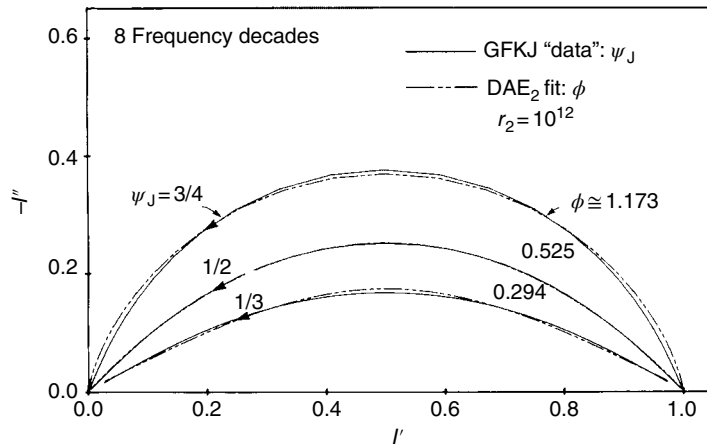


FIGURE 2.2.12 Complex plane comparisons of the response of the GFKJ and DAE₂ models when the DAE₂ is fitted to GFKJ response with CNLS.

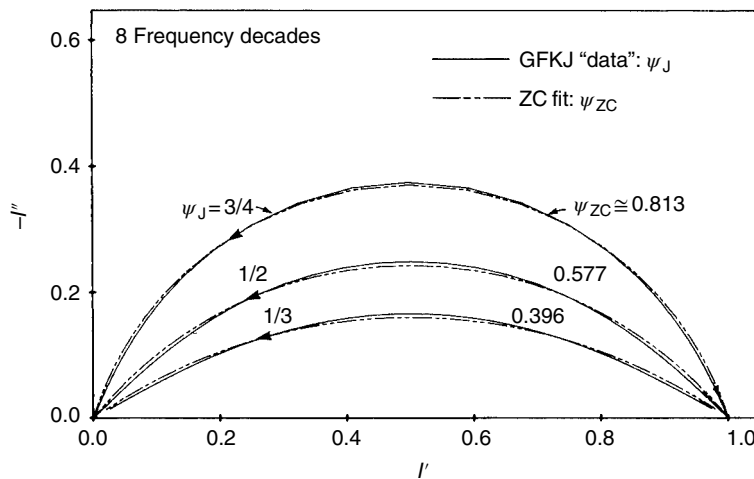


FIGURE 2.2.13 Complex plane comparisons of the response of the GFKJ and ZC models when the ZC is fitted to GFKJ response with CNLS.

results for DAE₂ fitting to GFKJ data for $\psi_J = \frac{1}{3}$ are shown in Figure 2.2.14. The unity weighting used in Figures 2.2.12 and 2.2.13 yields a better fit near the peak, and proportional weighting (see Section 3.2.2) leads to better agreement in the skirts of the curve. Here $s \equiv \omega\tau_0$ is a normalized frequency variable (Macdonald [1985c, d]).

The situation is somewhat less ambiguous for the special asymmetric models of Table 2.2.3. Although the DC and DAE₁ models can well fit each other, neither one can fit WW model response adequately over a wide ψ_i range. For $0.7 \leq \psi_{WW} \leq 1$, the DAE₁ can fit WW results quite well, but better fits are obtained for this region and below using the general DAE model to fit WW "data." Figure 2.2.15 shows the results of such CNLS fitting plotted in the complex plane, and Figure 2.2.16 shows them with 3-D plotting (see Section 3.2.1). Again the fits are so close that only with superb data could one unambiguously discriminate between the two models. One reason to prefer the various DAE models to the others, however, is that the former yields explicit temperature dependences for the ϕ_i 's that enter the

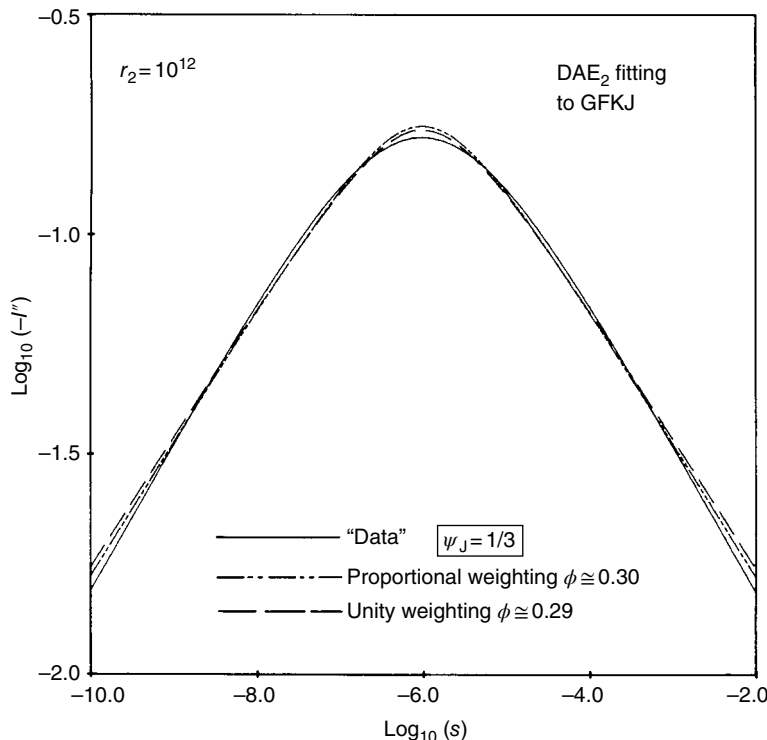


FIGURE 2.2.14 Frequency-response curves comparing the results of fitting the DAE₂ model to GFKJ "data." The logarithm of $-I''$ is plotted versus the logarithm of a normalized frequency variable s .

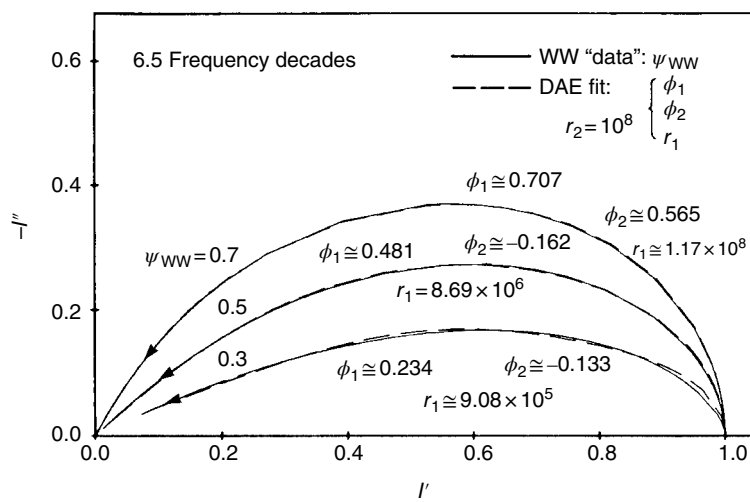


FIGURE 2.2.15 Complex plane comparisons of the response of the WW and DAE models when the DAE is fitted to WW response with CNLS.

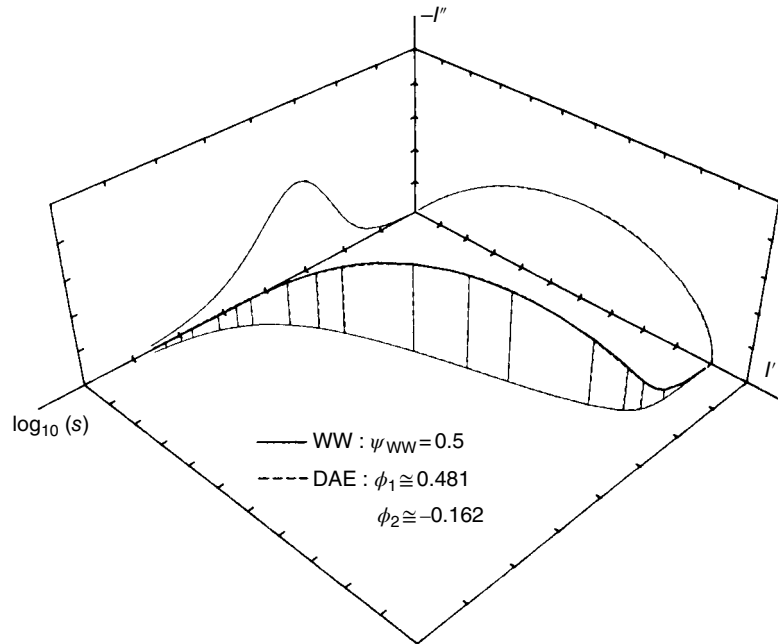


FIGURE 2.2.16 Three-dimensional plot with perspective showing the excellent agreement between WW “data” and the results of fitting these data with the DAE model.

model, while no such ψ_i temperature dependence is a part of the other models. When the actual fractional frequency-response exponents observed in a set of experimental data are found to vary with temperature, as they often do for both conductive and dielectric systems, it is thus natural to try DAE fitting and see if the ϕ_i estimates found depend on temperature in one of the ways predicted by the theory (Macdonald [1985c, d]). If such agreement is established, much can be learned about the detailed response of the system. Finally, it should be mentioned that the exponential DAE model has recently been simplified and its predictions compared with those of a symmetric or asymmetric Gaussian DAE model (D.D. Macdonald [1987a]). Again fitting ambiguity is sometimes found.

Measuring Techniques and Data Analysis

Michael C. H. McKubre,¹ Digby D. Macdonald,² Brian Sayers,³ and J. Ross Macdonald⁴

¹SRI International, Menlo Park, CA, USA

²Department of Nuclear Engineering, University of California at Berkeley, Berkeley, CA, USA

³Solartron Analytical, Hampshire, UK

⁴(William R. Kenan, Jr., Professor of Physics, Emeritus), Department of Physics and Astronomy, University of North Carolina, Chapel Hill, NC, USA

3.1 IMPEDANCE MEASUREMENT TECHNIQUES

3.1.1 Introduction

Until the advent of digital computers, all electrochemical studies involved the processing and analysis of analog signals in either the time domain or the frequency domain. Typical examples of analog signal analysis include the use of ac-coupled bridges and of Lissajous figures for determining interfacial impedance. In both instances, the desired information (e.g., balance of a bridge) is obtained in purely analog format, and no need exists for converting signals into digital form.

When describing analog instrumental methods, it is convenient to classify techniques according to the type of excitation functions employed particularly with respect to the independent variable. For example, frequency domain impedance measurements are carried out using a small-amplitude sinusoidal excitation with frequency as the independent variable. Alternatively, the perturbation and response may be recorded in the time domain with time as the independent variable, and the impedance as a function of frequency can then be extracted by time-to-frequency conversion techniques such as Laplace or Fourier transformation. Time-domain methods characteristically use digital processing techniques; frequency domain methods have traditionally used analog techniques although digital processing is becoming common in synthesis and analysis of sinusoidal signals.

The application of a sine-wave excitation to a system under test often is the easiest method of determining the system transfer function. Here we are concerned with measuring or inferring a transfer function for an electrochemical cell as a first step in determining reaction mechanistic and kinetic parameters (Macdonald [1977], Gabrielli [1981], Macdonald and McKubre [1981, 1982]).

By way of review, the transfer function of a system can be determined as the output divided by the input:

$$G(j\omega) = \frac{X_{\text{out}}(j\omega)}{X_{\text{in}}(j\omega)} \quad (1)$$

For the special case where the output signal is the system voltage and the input (or excitation function) is the current, the transfer function is the system impedance:

$$G(j\omega) = \frac{E(j\omega)}{I(j\omega)} = Z(j\omega) \quad (2)$$

Since the output may be changed in both amplitude and phase with respect to the input, we must express the impedance as a complex number:

$$Z(j\omega) = Z' + jZ'' \quad (3)$$

where primed and double-primed variables refer to inphase and quadrature components, respectively.

It is important to note that we are using the formalism of linear systems analysis; that is, Eq. (2) is considered to hold independently of the magnitude of the input perturbation. Electrochemical systems do not, in general, have linear current–voltage characteristics. However, since any continuous, differentiable function can be considered linear for limitingly small input perturbation amplitudes (Taylor expansion), this presents more of a practical problem than a theoretical one.

In the following section we present a number of standard methods of measuring a system impedance or a frequency domain transfer function. In applying any of the methods described, the perturbation must be of a sufficiently small magnitude that the response is linear. Although the condition of linearity may be decided from theoretical considerations (Bertocci [1979], McKubre [1981, 1983], McKubre and Syrett [1986]), the most practical method is to increase the input signal to the maximum value at which the response is independent of the excitation function amplitude.

3.1.2 Frequency Domain Methods

3.1.2.1 Audio Frequency Bridges

In the past, impedance measurements using reactively substituted Wheatstone bridges at audio frequencies have been the easiest to accomplish. Consequently, great emphasis has been placed historically on electrochemical processes having characteristic impedance spectra in the audio frequency range 20–20 000 Hz, namely, double-layer capacitive and moderately fast reaction kinetic effects at plane parallel electrodes.

The mathematics and methodology of such measurements are well understood (Hague [1957], Armstrong *et al.* [1968]). However, considerable use still may be made of passive audio frequency bridge measurements in this age of active circuitry principally in high-precision applications. Following a brief review of bridge circuits, we will restrict our discussion to the limitations imposed by the use of each type of bridge, since these will influence the point at which an experimentalist will select a more complex measuring device.

Figure 3.1.1 shows schematically the familiar representation of an audio frequency bridge adapted for use with an imposed direct current (dc) potential. The condition of balance for the bridge shown is

$$Z_x = \left(\frac{R_1}{R_2} \right) Z_s \quad (4)$$

where subscripts x and s refer to unknown and standard impedances, respectively. A variety of RCL combinations are possible for Z_s ; in the commonly used Wien bridge (Hague [1957]), Z_s takes the form of series variable resistance and capacitance standards, which are adjusted alternately until the real and imaginary components of the voltage at the null detector simultaneously are zero. For this null condition the real and imaginary components of the unknown impedance may be calculated as

$$Z'_x = \left(\frac{R_1}{R_2} \right) R_s \quad (5)$$

$$Z''_x = \frac{(R_1/R_2)}{\omega C_s} \quad (6)$$

The form of Eqs. (5) and (6) has led to the widespread and unfortunate practice of tabulating and plotting measured impedance data in terms of the complex pair $(R_s, j/\omega C_s)$ even when a Wien bridge has not been used. The impedance notation (Z', jZ'') is significantly less ambiguous and will be used here.

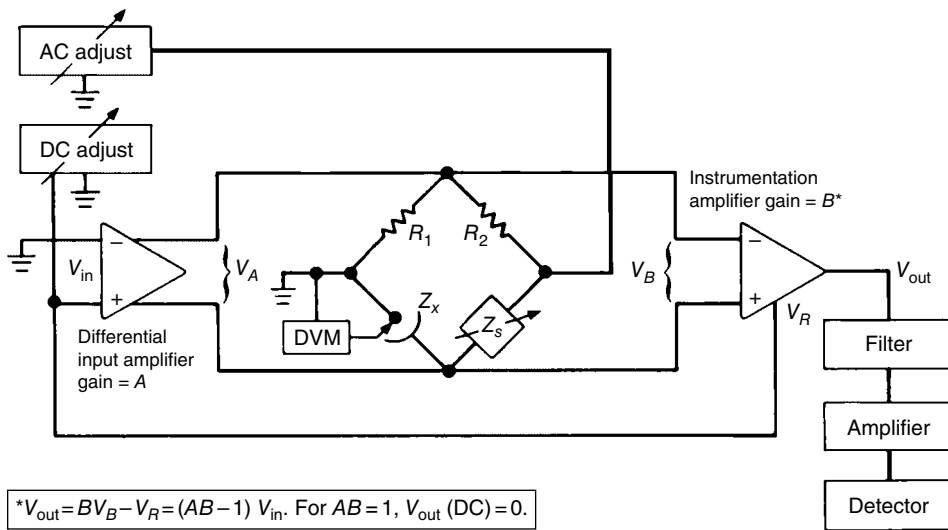


FIGURE 3.1.1 Audio frequency bridge modified to include working electrode dc potential control.

High-Frequency Limitations. The upper operating limit is imposed primarily by reactivity and nonlinearity of available resistive standards (chiefly inductive effects) and the effects of stray capacitive shunts. By using a Wagner earth (Hague [1957], Armstrong *et al.* [1968]), the latter effect can often be reduced sufficiently to allow sensible measurements at frequencies up to 10^5 Hz. However, the importance of Wagner earthing varies greatly with the magnitude of the impedance being measured (Hague [1957]). In general, elimination of stray capacitance is most important at high frequencies when measuring small capacitances or large resistances (i.e., for small-area electrodes).

Low-Frequency Limitations. The null detection system traditionally used with an audio frequency bridge consists of an amplifier, filter, and ac voltmeter. This combination imposes three limitations at low frequencies:

- Null detection with a magnitude voltmeter or oscilloscope is most sensitive when the resistive and reactive components of the unknown impedance are of the same magnitude, since the total bridge out-of-balance signal contains terms proportional to each. For an impedance bridge used to measure the electrical properties of electrochemical cells, this fact imposes a limit on accuracy at low frequencies since the reactive terms, which are primarily capacitive, dominate the cell admittance with decreasing frequency. Increasing the gain to observe the resistive component more precisely results in saturation of the detection system with the reactive out-of-balance signal.
- A significant source of noise at the detector may result from harmonic distortion originating in the oscillator or caused by nonlinearity in the system under test or in subsequent amplifiers. In such cases, the signal at balance consists mainly of the second harmonic. At high frequencies, this signal can be removed effectively by appropriate signal conditioning with bandpass, low-pass, or notch filters (McKubre and Macdonald [1984]). At low frequencies, however, analog filters of bandwidth less than 10 Hz are less easy to construct and control.
- Another major source of noise at low frequencies is mains pickup. This may amount to hundreds of millivolts superimposed on the test signal unless major efforts are made at shielding and ground loop suppression. Usually, unless an adequate notch filter is used in addition, the experimentalist must be satisfied with reduced precision at frequencies below about 100 Hz.

These three effects can be reduced to a large extent by using a phase-sensitive detector (PSD) to measure separately the real and imaginary components of the bridge out-of-balance signal. By separate

amplification of the inphase and quadrature components, differential sensitivities in excess of 100 : 1 can be attained. The advantages and limitations conferred by the use of PSDs are described in Section 3.1.2.6.

In normal operation, a PSD is completely insensitive to the second harmonic, but most commercial instruments have the additional facility of being able to select a reference signal at twice the fundamental frequency. By this means the extent of second harmonic distortion can be measured. This distortion often reflects not an error signal (i.e., noise), but an expected response induced by nonlinearity of the system under test (McKubre [1981, 1983], McKubre and Syrett [1986]).

In addition, and unlike traditional bandpass filters, a PSD has a bandpass characteristic with bandwidth that decreases with decreasing frequency, and frequently can be used within ± 5 Hz of 50- or 60-Hz mains pickup.

When phase-sensitive null detection is used, the practical low-frequency limit becomes a function of the particular form of bridge chosen. For the Wien bridge, this limit is imposed by the selection of suitably large adjustable capacitance standards at frequencies below 20 Hz.

Limitations of Imposed Potential. A considerable limitation on the use of this form of bridge is that it necessitates the use of a two-terminal cell. Although it is often possible to construct a cell in which the working electrode (WE) impedance greatly exceeds that of the counter electrode, potentiostatic conditions cannot be established adequately with this type of bridge. Closely associated with this limitation is the fact that in normal use, the cell current and voltage vary with the settings of the resistive and reactive standards.

In electrochemical applications, these combined limitations may be severe. Figure 3.1.1 shows one of a variety of possible methods by which an imposed WE dc potential can be adjusted to the desired value without influencing the detector circuit. The method shown can be used at frequencies less than the normal operating frequency limit of ac-coupled amplifiers.

3.1.2.2 Transformer Ratio Arm Bridges

The high-frequency limitation imposed on the operation of reactively substituted Wheatstone bridges by unavoidable stray capacitances prompted the development of the transformer ratio arm bridge (Calvert [1948]). By substituting a transformer for orthodox ratio arms, a bridge was produced for which the impedance ratio is proportional to the square of the number of turns and was capable of accepting heavy capacitive loads with virtually no effect on the voltage ratio.

The operation of a transformer ratio arm bridge is shown schematically in Figure 3.1.2. Briefly, voltage 180° out of phase is fed from the secondary winding of the input “voltage” transformer to the cell or unknown impedance and to resistance and capacitance standards. The “arms” of the bridge consist of a series of ratio taps of the primary windings of an output “current” transformer. The standard and unknown impedances are connected to the output transformer in such a way that a detector null is achieved when the sum of the flux induced by the unknown and standard currents in the output transformer is zero. In this condition

$$\frac{r_1}{Z_x} = \frac{r_2}{R} + j\omega Cr_3 \quad (7)$$

for all V_{in} , where r_1 , r_2 , and r_3 are ratios (usually decade) separately selected.

The advantages of using this type of bridge are as follows:

- Error resulting from the impurity of standard variables can be virtually eliminated. Because ratios are selectable over a wide range (usually 1000 : 1), standards can be small. Also, with decade-spaced transformer ratios, standards need be variable only over a range of about 11 : 1. Consequently, standards can be used to closely approximate ideality (e.g., air-gap capacitors and nonreactively wound metal resistance), wherein one standard can be used to measure a wide impedance range.

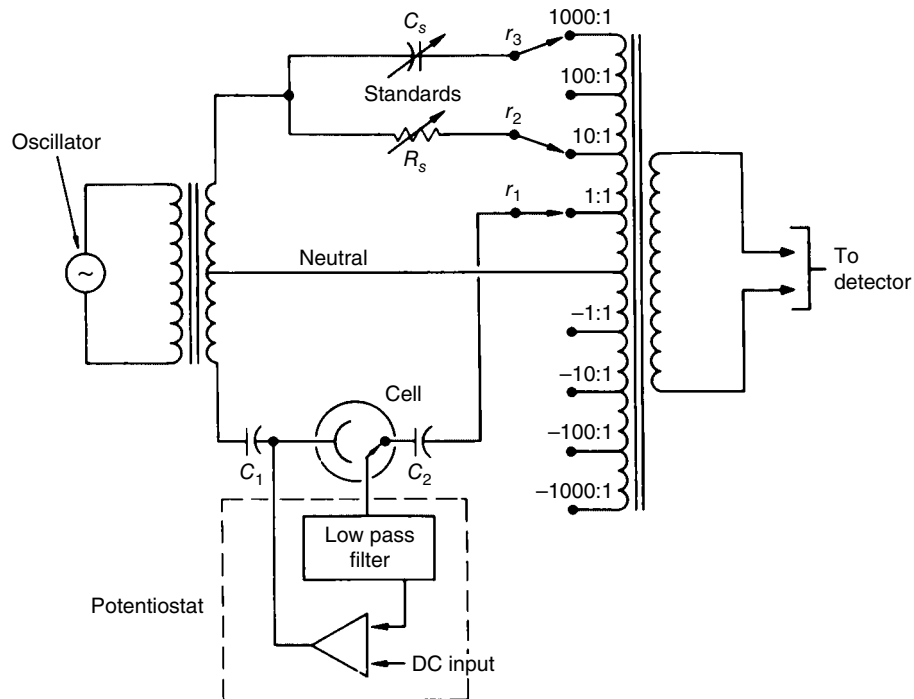


FIGURE 3.1.2 Transformer ratio arm bridge with dc potentiostatic control.

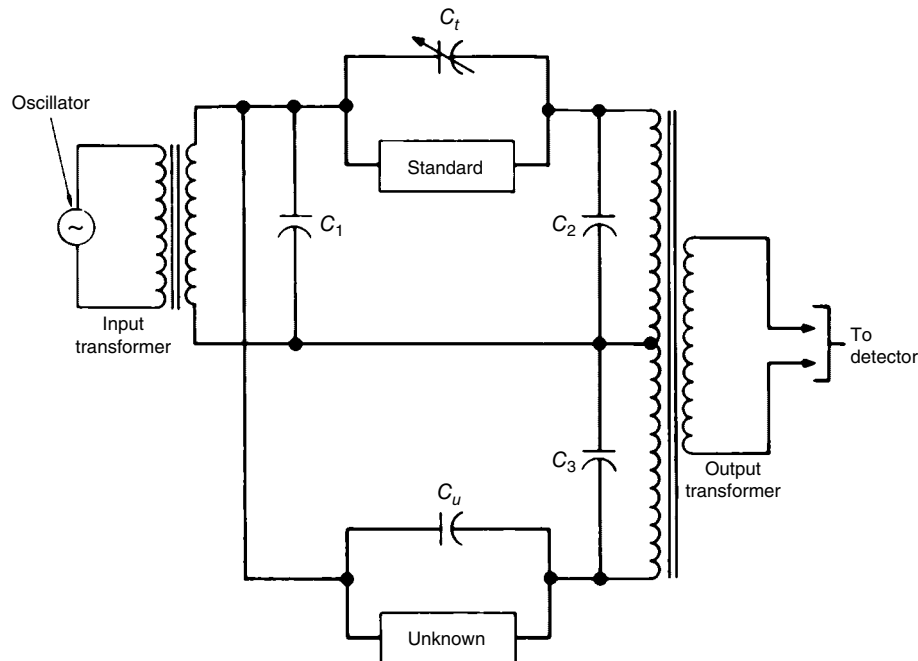


FIGURE 3.1.3 The effect of stray capacitances in the transformer ratio arm bridge.

- By the use of precision transformers as ratio arms, one can obtain highly accurate ratio values that are essentially independent of frequency well into the megahertz range.
- The bridge is highly insensitive to the presence of stray capacitance. Figure 3.1.3 shows the reason: C_1 , C_2 , and C_3 can cause no measurement error— C_1 because it merely produces a reactive

potential drop that is common to the unknown and standard circuits and C_2 and C_3 because at balance no potential drop appears across them. Now C_u represents the capacitance across the unknown terminals, and its effect is canceled by trimming capacitor C_t on the standard side. Here C_t is adjusted at each measurement frequency by disconnecting the standard and balancing the bridge. Similarly, effects of the stray capacitances to earth virtually disappear if the neutral terminal is grounded (Calvert [1948]; see also Figure 3.1.2).

- Impedances may be measured in all four quadrants by selecting positive or negative ratios. Of particular importance is the use of pure capacitive standards to measure unknowns with a positive (inductive) reactance.

High-Frequency Limitations. In normal use for electrochemical cells, the effective upper operating limit is imposed by effects external to the bridge. These effects, which have been described in detail by Armstrong *et al.* [1968], consist primarily of transmission line effects in connecting cables, the effect of residual series inductance in leads and the cell, and (normally desired) impedance dispersion effects of solid electrodes. In the latter group, edge effects (Sluyters-Rehbach and Sluyters [1970]) and transmission line effects due to surface roughness (de Levie [1963, 1965, 1967]) become dominant with increasing frequency. In electrochemical systems for which the interfacial impedance is the desired parameter, measurement precision becomes limited by the dominance of the uncompensated electrolyte resistance in the total measured impedance. This effect has prompted the use of very small electrodes for which the ratio of uncompensated resistance to interfacial impedance is reduced (Zeuthen [1978]).

Series leakage inductances in the transformers within the bridge result in an impedance measurement error that is proportional to frequency. This effect has been examined by Calvert [1948] but is seldom likely to impose high-frequency limitations in electrochemical applications.

Low-Frequency Limitations. The use of input and output transformers results in cell current and voltage and thus detector signals that decrease with decreasing frequency. This effect becomes apparent only at low audio frequencies and imposes a practical lower limit of the order of 100–200 Hz with commercial bridges.

Limitations of Potential Control. The limitations of potential control for a transformer ratio arm bridge are similar to those imposed in classical bridge measurement. That is, it is not possible to apply the ac potential via a reference electrode (RE) and potentiostat circuit only to the interface of interest. The measured impedance necessarily includes series terms associated with the lead and electrolyte resistance and the counter electrode (CE) impedance.

Dc potentials can be applied to the interface of interest by using a circuit of the form shown within the dashed lines in Figure 3.1.2, since at moderate frequencies the low-pass filter will not observe the ac component. However, dc must be excluded from the bridge windings by the use of blocking capacitors C_1 and C_2 . The impedance of these also will be included in the measured “cell” impedance.

3.1.2.3 Berberian–Cole Bridge

An active null admittance measuring instrument that incorporates many of the advantages of the transformer ratio arm technique, while obviating many of the disadvantage of passive bridges, has been reported by Berberian and Cole [1969]. Figure 3.1.4 shows a form of this bridge modified to measure impedance and to remove some of the limitations of the earlier instrument (McKubre [1976]).

The basic operation is as follows. R_1 and C are the external variable decade standards, while R' and R'' are internal and fixed. With reference to Figure 3.1.4, at all times,

$$i_1 + i_2 + i_3 = 0 \quad (8)$$

$$i_1 = \frac{AV_A}{R_1} \quad (V_A = IZ) \quad (9)$$

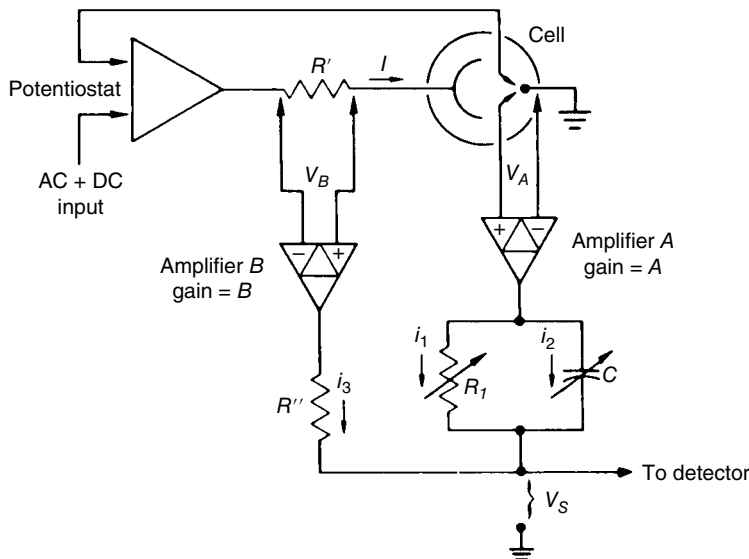


FIGURE 3.1.4 Modified Berberian–Cole bridge shown as a three-terminal interfacial-impedance-measuring system, with potentiostatic control of the working electrode.

$$i_2 = AV_A(j\omega C) \quad (V_A = IZ) \quad (10)$$

$$i_3 = \frac{BV_B}{R'} \quad (V_B = -IR') \quad (11)$$

where Z is the impedance between the WE and the RE and I is the current flowing through the cells. Therefore, for the condition of balance at the summing point,

$$\frac{BIR'}{R''} = \frac{AIZ}{R_1} + AIZ(j\omega C) \quad (12)$$

Removing I and solving for the unknown impedance yields

$$Z = \frac{BR'R_1(1-j\omega R_1 C)}{AR'' 1 + \omega^2 R_1^2 C^2} \quad (13)$$

The advantages of this method apply principally at low (audio and subaudio) frequencies. It is important to note that the device shown schematically in Figure 3.1.4 is a bridge only in the sense that external variables are adjusted to produce an output null.

The principal advantages of the Cole–Berberian bridge are as follows:

- Because of the use of buffer amplifiers, null adjustment does not vary the potential across (or current through) the unknown impedance, as is the case for classical and transformer ratio bridge measurement.
- Measurements can be made on two, three, or four terminal cells, allowing the isolation of the impedance component of interest from the total cell impedance. This is not possible with a passive bridge, and it is frequently infeasible to construct a cell for which the impedance of interest is much greater than all series terms. This is particularly difficult when measuring the impedance of an electrode of large area, when measuring impedance in a highly resistive electrolyte, or when the impedance of interest is that of a highly conductive electrolyte.

- Measurements can be made effectively down to 0 Hz. Because the bridge shown in Figure 3.1.4 is direct coupled, the low-frequency limits are those of the null detection system and the patience of the experimenter.
- Measurements can be made in the presence of a dc bias under potentiostatic control, without the use of blocking capacitors.
- Impedance can be measured over an extremely wide range, from below $10^{-3} \Omega$ to over $10^9 \Omega$.
- Error resulting from the impurity of standards can be virtually eliminated because standards can be selected according to ideality, not magnitude of the components.
- By using differential gain for the real and reactive standards, a suitable range of measurement can be selected for each impedance component separately. This feature is incorporated in Figure 3.1.5.
- Impedances may be measured in all four quadrants (RC , $-RC$, RL , $-RL$) using resistance and capacitance standards alone.

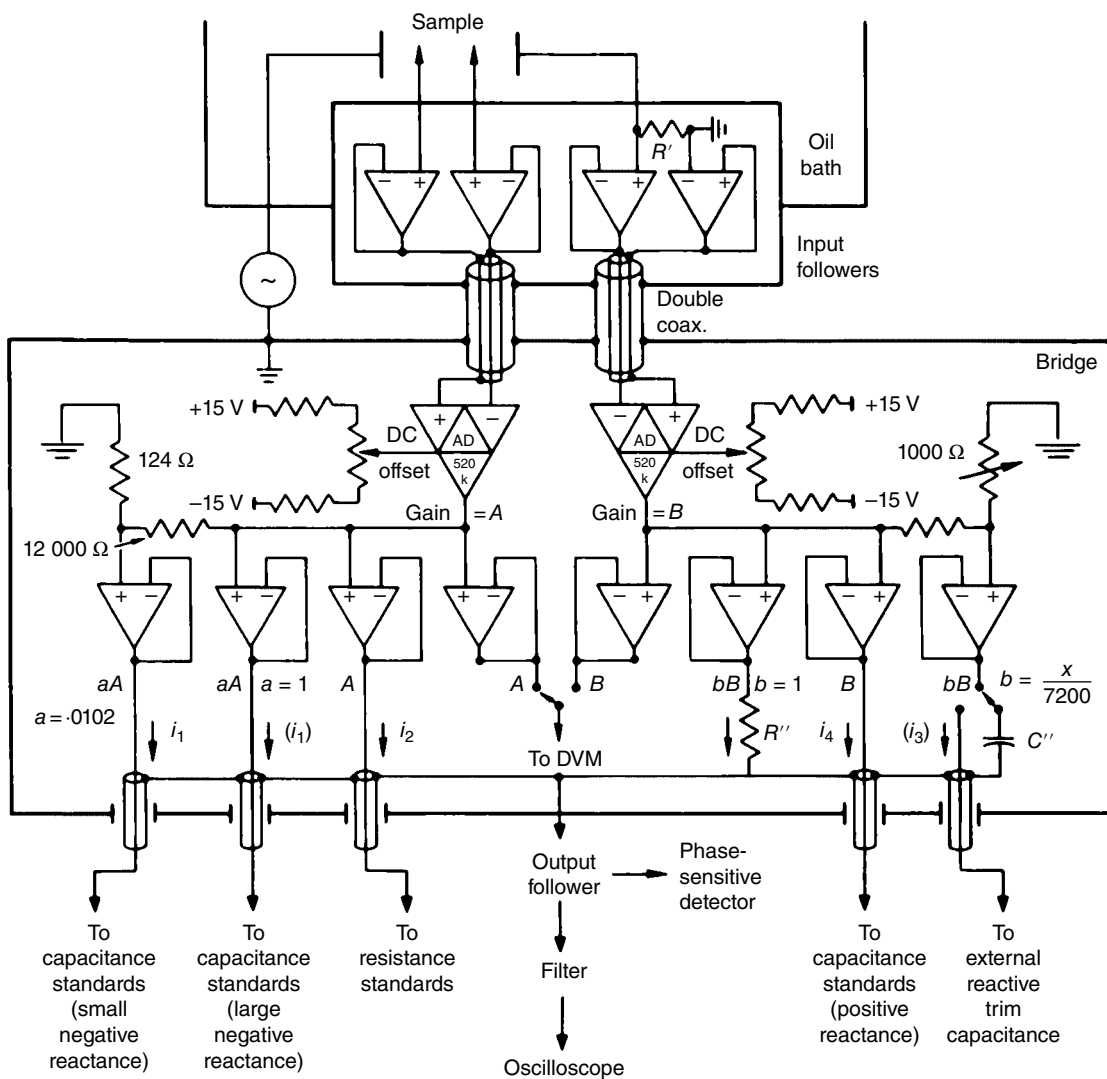


FIGURE 3.1.5 Schematic diagram of a working (modified) Berberian–Cole bridge shown as a four-terminal impedance-measuring system.

Because the gains of amplifiers A and B perform the same function as the ratios in a transformer ratio arm bridge, the two techniques have many features in common.

High-Frequency Limitations. Inaccuracies at high frequencies can occur because of errors in the gain functions A and B with decreasing amplifier open-loop gain (McKubre and Macdonald [1984]). Figure 3.1.5 shows, schematically, a practical bridge of the Berberian–Cole type. Gain errors in the voltage followers are negligible, and, since amplifiers A and B are identical devices and their gains appear as a ratio in Eq. (13), inaccuracies in this term are partially compensated. Nevertheless, the upper operating frequency limit for the bridge shown in Figure 3.1.5 is about 10 kHz, depending somewhat on the magnitude of the unknown impedance. This device is capable of 0.01% measurement accuracy for both impedance components between 1.0 Hz and 1 kHz and 0.1% accuracy in the peripheral decades (0.1–1.0 Hz, 1–10 kHz).

Low-Frequency Limitations. As stated previously, the low-frequency operating limit is imposed by the detection system. At frequencies down to 0.5 Hz, a two-component PSD performs an ideal null detection function (McKubre [1976]). At frequencies below 0.1 Hz, a low-pass filter and oscilloscope or picoammeter can be used (Berberian and Cole [1969]).

Potential Control. Although it is possible to impose ac potentiostatic control at the interface of interest, the presence of a dc bias will result in a signal in the active bridge circuits. Dc offset must be adjusted to near zero to prevent overloading in subsequent gain stages. For a cell under dc potentiostatic control, this requirement may necessitate frequent offset adjustment of the current amplifier B.

3.1.2.4 Considerations of Potentiostatic Control

An essential element of electrode kinetics is the characteristic dependence of electrode reaction rate of the electrode potential. Thus, for many electrode studies, the use of the potentiostatic control is the most convenient method of obtaining relevant kinetic and mechanistic parameters. A limitation of passive bridge methods in general is their inflexibility with regard to potential control, so that in many cases, the experimenter must forgo the advantages of simplicity and sensitivity associated with bridge measurement to impose ac and/or dc potentiostatic control at a single interface. The “direct” methods permit effective potential control while retaining the relative simplicity of operation of many of the bridge techniques.

If the cell current and voltage are measured with regard to their magnitude and phase relations, the impedance can be determined directly from Eq. (2). Figure 3.1.6 shows, in simplified form, a circuit that allows the direct measurement of impedance under potentiostatic control.

It is necessary at the outset to separate phase shifts associated with the cell impedance from those attributable to the potentiostat control loop. Commercial potentiostats normally are optimized for fast step response, and the potentiostatting function becomes substantially in error for sinusoidal inputs, with increasing frequency. Analyses have been performed of the frequency-dependent errors introduced by the potentiostatting function for a variety of potentiostats with varying loads (Brown *et al.* [1968], McKubre and Macdonald [1984]). However, the fidelity of the potentiostatting function with respect to an ac test signal superimposed on a dc control level is seldom of significance *provided that*

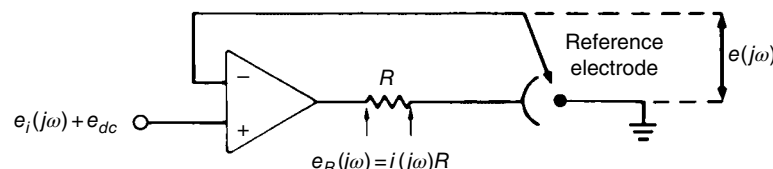


FIGURE 3.1.6 Direct measurement of interfacial impedance under ac and dc potentiostatic control.

the system under test is linear (the fundamental assumption of the use of ac methods in electrochemical kinetic studies) and that the ac voltage is measured directly as the potential difference between the working and a suitably placed RE, *not* at the input to the potentiostat.

In fact, the so-called high-speed potentiostats are often undesirable for use in high-frequency impedance measurements at an electrode–aqueous electrolyte interface. The reactive impedance at such an interface reduces to that of the double-layer capacitance at limiting high frequencies. Thus, one may have 3 A/cm^2 of out-of-phase current flowing at 10^6 Hz to an electrode with $50 \mu\text{F/cm}^2$ of double-layer capacitance if the potentiostat is able to maintain a 10-mV ac perturbation at that frequency. Such high current densities may result in severe nonlinearities, and one often will prefer the reduced amplitude and phase shift of a narrow-bandwidth potentiostat when the voltage is measured at the point of interest (e , not e_i , in Figure 3.1.6).

3.1.2.5 Oscilloscopic Methods for Direct Measurement

By recording $e(j\omega)$ and $i(j\omega)$ (as the voltage drop across a series resistance R_s ; see Figure 3.1.6) with a twin-beam oscilloscope, the magnitude of the impedance can be calculated from the ratio of the two peak-to-peak voltages and the directly observed phase angle. Figure 3.1.7 shows the oscilloscope traces for $e(j\omega)$ and $e_R(j\omega)$ that result from the imposition of a sine wave between the working and REs.

The real and imaginary components can be calculated (with reference to Figure 3.1.7) as

$$|Z| = \frac{R_s |e(j\omega)|}{|e_R(j\omega)|} \quad (14)$$

$$Z' = |Z| \cos(\phi) \quad (15)$$

$$Z'' = |Z| \sin(\phi) \quad (16)$$

The time base of available storage oscilloscopes limits low-frequency measurements to about 10^{-2} Hz . High-frequency limitations are imposed by effects external to the oscilloscope, principally stray

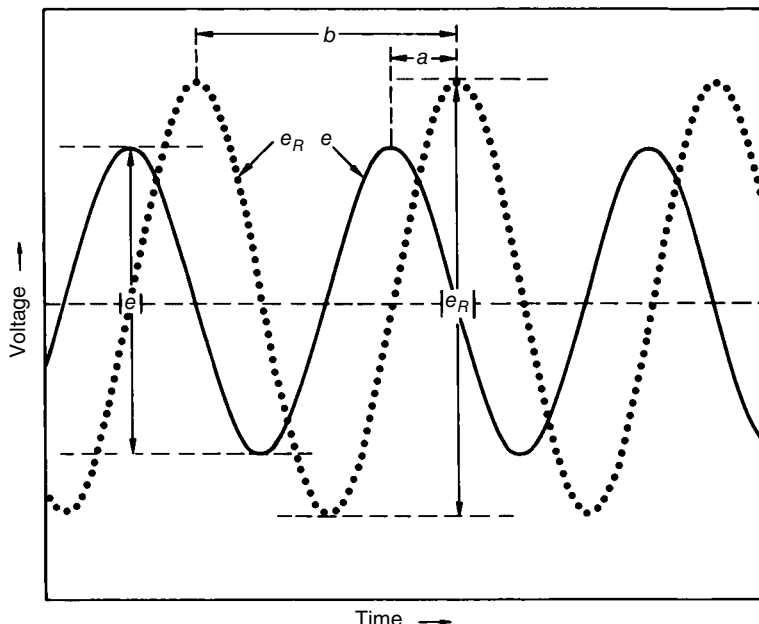


FIGURE 3.1.7 The direct measurement of impedance using a twin-beam oscilloscope.

capacitance and transmission line effects in the leads and cell. Measurements can often be made at frequencies above 10^5 Hz.

The primary limitation of this technique is precision. Oscilloscope linearity is seldom better than 1%, and it is difficult to measure phase angles directly with a precision of better than 2° . Measurements usually can be accomplished with an uncertainty in Z' and Z'' of $\pm 3\%$ of $|Z|$.

A single-beam oscilloscope or an "X-Y" recorder also can be used to measure impedance parameters directly by the method of Lissajous figures.

Elimination of t between expressions for e and i of the form

$$e = |e|\sin(\omega t)$$

$$i = |i|\sin(\omega t + \phi)$$

leads to an equation in the form of an ellipse when e and i are plotted orthogonally (e applied to the "X" plates and i applied to the "Y" plates), and the components of the impedance can be calculated from the dimensions of the ellipse. With reference to Figure 3.1.8,

$$|Z| = \frac{\Delta e}{\Delta i} \quad (17)$$

$$\sin(\phi) = \frac{\Delta i'}{\Delta i} = \frac{\alpha\beta}{\Delta i \Delta e} \quad (18)$$

where Z' and Z'' can be calculated from Eqs. (15) and (16).

Limitations of oscilloscopic recording are essentially those of precision as described previously for two-channel measurement. However, since time is not an explicit variable, time base limitations do not apply when recording Lissajous figures. Low-frequency limitations are imposed by electrochemical instabilities in the system under test and electrical instabilities (particularly dc offset drift) in the attendant circuitry. Electromechanically "X-Y" recording can be used to achieve a precision better than 1% of $|Z|$ at frequencies from 1 Hz to below 10^{-3} Hz.

Considerable caution is necessary when applying this last method. Electrochemical systems are susceptible to external noise pickup. The use of high gain, without appropriate electrical filtering, to amplify low-level sine-wave voltage and current perturbations may result in severe errors in the dimensions of the ellipse traced on an electromechanical "X-Y" plotter because the mechanical damping of the plotter

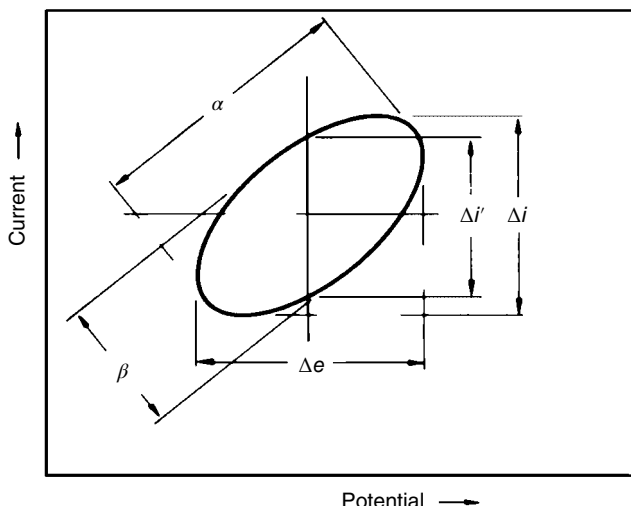


FIGURE 3.1.8 Lissajous figure for the evaluation of impedance.

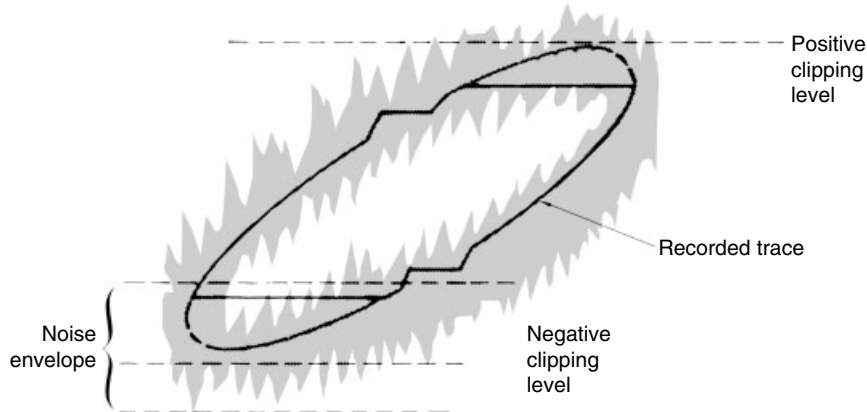


FIGURE 3.1.9 The errors in electromechanical Lissajous figure recording due to the presence of input noise.

may disguise the fact that the input amplifiers are overloaded by the “high”-frequency (>10 Hz) noise envelope. This effect is shown schematically in Figure 3.1.9 for 50- or 60-Hz mains pickup in the “Y” amplifier. Errors may, of course, occur in both channels. This phenomenon often is reflected as skewing or tracking of the recorded ellipse but may result in a stable erroneous trace. To prevent errors in the calculated impedance values, appropriate electronic low-pass or notch (50- or 60-Hz mains pickup) filtering must be used at an early stage of amplification.

3.1.2.6 Phase-Sensitive Detection for Direct Measurement

The real and imaginary components of a voltage can be measured directly with respect to a reference signal with a PSD. Because of the requirements for linearity, small input signals must be used to measure electrochemical impedances, and noise problems often make it impractical to use either e or e_R (Figure 3.1.6) as a reference signal. Accordingly, e and e_R must be measured alternately in terms of a coherent reference signal of arbitrary phase and the impedance determined from the complex quotient:

$$Z = \frac{e}{e_R} R = \frac{(e' + j e'')}{(e'_R + j e''_R)} R \quad (19)$$

To understand the advantages inherent in this method, it is appropriate to discuss briefly the detection technique.

Phase-sensitive detection may be accomplished by the sequential operation of multiplexing and time-averaging circuits. The multiplexer serves effectively to multiply the input sine wave e_i with a reference square wave e_{ref} . We can represent e_{ref} in terms of its Fourier components:

$$e_{\text{ref}} = \frac{4}{\pi} \left[\sin(\omega_r t) + \frac{1}{3} \sin(3\omega_r t) + \frac{1}{5} \sin(5\omega_r t) + \dots \right] \quad (20)$$

and the input sine wave can be written as $e_i = |A^0| \sin(\omega_i t + \phi)$, where $|A^0|$ is the input signal amplitude, ω is the angular frequency, and subscripts r and i refer to the reference and input signals.

The multiplexer output will be

$$\begin{aligned} e_{\text{mpx}} = e_{\text{ref}} e_i &= \frac{2|A^0|}{\pi} \{ \cos[(\omega_i - \omega_r)t + \phi] \\ &+ \frac{1}{3} \cos[(\omega_i - 3\omega_r)t + \phi] - \frac{1}{3} \cos[(\omega_i + 3\omega_r)t + \phi] + \dots \} \end{aligned} \quad (21)$$

In normal practice, ω_r and ω_i are derived from a common source (i.e., $\omega_r = \omega_i$), and the multiplexer output is

$$e_{\text{mpx}} = \frac{2|A^0|}{\pi} \left[\cos(\phi) - \cos(2\omega_r t + \phi) + \frac{1}{3} \cos(-2\omega_r t + \phi) - \frac{1}{3} \cos(4\omega_r t + \phi) + \dots \right] \quad (22)$$

Only the first term in Eq. (22) is time independent and, when applied to the time-averaging circuit, will result in a nonzero output:

$$e_{\text{out}} = \frac{2}{\pi} |A^0| \cos(\phi) \quad (23)$$

This is obviously a phase-sensitive dc output voltage, which is a maximum at $\phi = 0$.

The PSD output is frequency selective since the time average of Eq. (21) for $\omega_r \neq \omega_i$ is zero. The important exception to this statement is for $\omega_i = 3\omega_r, 5\omega_r, 7\omega_r$, and so forth. That is, a PSD responds to odd-order harmonics of the input signal. This contribution diminishes with the order of the harmonic.

Time averaging may be accomplished by analog or digital means. In the vast majority of commercial instruments, an analog low-pass smoothing circuit is used with a front-panel-adjustable time constant. This arrangement offers the advantage of simplicity and flexibility in high-frequency operation. The upper frequency limit is commonly 10^5 Hz. The low-frequency limit of analog time-averaging devices is imposed by the practical details of low-pass filter design (Sallen and Key [1955]) smoothing capacitor ideality, current leakage in buffer amplifiers, and external asynchronous (nonrandom) noise effects. The low-frequency limit of commercial instruments is commonly in the range 0.5–10 Hz. Impedance usually can be measured with 0.1% precision in both components over the specified frequency range.

By using digital integration methods, the low-frequency response can be extended to below 10^{-3} Hz. In this method, the average is taken digitally over an integral number of cycles (McKubre and Hills [1979] A Digitally Demodulated Synchronous Detector for Fast, High Precision Impedance Measurement, unpublished work). At very low frequencies, information relating to e and i taken over a single cycle can be used to calculate the real and imaginary impedance components with a precision of 0.1%.

3.1.2.7 Automated Frequency Response Analysis

In general, direct methods can be used to acquire impedance data significantly more rapidly than bridge methods. This is particularly true for digitally demodulated PSDs, for which only a single cycle is required. Nevertheless, in unstable systems, such as rapidly corroding specimens, acquisition rate is an important consideration, and a major criticism of PSD methods is that these must be performed frequency by frequency. Fortunately, this often is not a serious hindrance when such equipment is automated. In the past decade, a number of experimenters have used automated “FRAs” as digitally demodulated, stepped-frequency impedance meters. Typical of this class are the Solartron 1170 and 1250 series frequency response analyzers (FRAs).

FRAs determine the impedance by correlating the cell response $S(t)$ with two synchronous reference signals, one of which is in phase with the sine-wave perturbation and the other shifted 90° in phase (Armstrong *et al.* [1968, 1977], Gabrielli and Keddam [1974], Gabrielli [1981]). A typical FRA is shown schematically in Figure 3.1.10. The sine-wave perturbation function $P(t)$ applied to the cell may be represented as

$$P(t) = P^0 \sin(\omega t) \quad (24)$$

where P^0 is the amplitude and ω is the frequency. Likewise, the cell response may be written as

$$S(t) = P^0 |Z(\omega)| \sin[\omega t + \phi(\omega)] + \sum_m A_m \sin(m\omega t - \phi_m) + N(t) \quad (25)$$

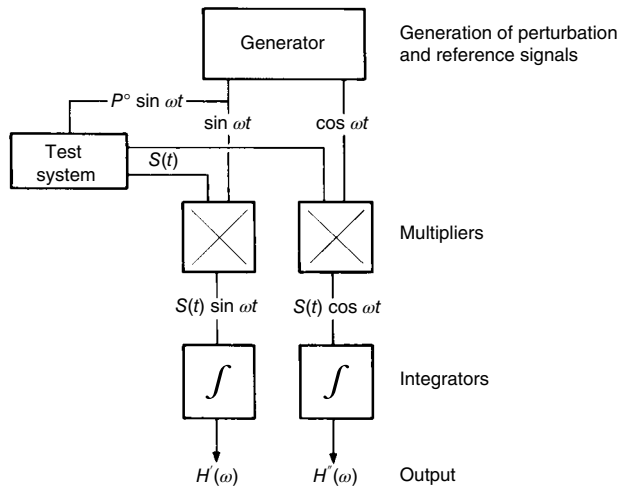


FIGURE 3.1.10 Schematic of transfer function analyzer.

where $|Z(\omega)|e^{j\phi(\omega)}$ is the transfer function of the cell and the first term on the right side of Eq. (25) is the fundamental component. However, because of the nonlinear nature of electrochemical systems, the response will also contain harmonics. Also, electrochemical studies are normally carried out in environments electronically “cluttered” by signals due principally to pickup from main power sources. The harmonic and noise contents of the cell response are represented by the second and third terms, respectively, on the right side of Eq. (25).

The real and imaginary components of the impedance are given by the integrals:

$$H'(\omega) = \frac{1}{T} \int_0^T S(t) \sin(\omega t) dt \quad (26)$$

$$H''(\omega) = \frac{1}{T} \int_0^T S(t) \cos(\omega t) dt \quad (27)$$

Substituting Eqs. (26) and (27) into Eqs. (24) and (25), we obtain

$$\begin{aligned} H'(\omega) &= P^0 |Z(\omega)| \int_0^T \sin[\omega t + \phi(\omega)] \sin(\omega t) dt \\ &+ \frac{1}{T} \int_0^T \sum_m A_m \sin(m\omega t - \phi_m) \sin(\tau t) dt \\ &+ \frac{1}{T} \int_0^T N(t) \sin(\omega t) dt \end{aligned} \quad (28)$$

$$\begin{aligned} H''(\omega) &= P^0 |Z(\omega)| \int_0^T \sin[\omega t + \phi(\omega)] \cos(\omega t) dt \\ &+ \frac{1}{T} \int_0^T \sum_m A_m \sin(m\omega t - \phi_m) \cos(\tau t) dt \\ &+ \frac{1}{T} \int_0^T N(t) \cos(\omega t) dt \end{aligned} \quad (29)$$

If the noise is completely random (i.e., asynchronous), then the last integrals in Eqs. (28) and (29) are equal to zero provided that they are carried out over infinite time. If the integration is carried

out over N_f periods of the sinusoidal perturbation, the equivalent filter selectively is given by (Gabrielli [1981])

$$\frac{\Delta f}{f_1} = \frac{1}{N_f} \quad (30)$$

where f_1 is the center frequency in hertz and Δf is the bandwidth. For example, if the integration is carried out over 10 periods, then at $f_1 = 1000$ Hz and 1 Hz, Δf is 100 Hz and 0.1 Hz, respectively. On the other hand, if the integration is carried out over 100 periods, the bandwidths are reduced to 10 Hz and 0.01 Hz. Clearly, the ability of a transfer function analyzer to reject asynchronous noise improves greatly as the number of periods over which the integration performed is increased. However, the price is an excessively long data acquisition time, during which the stability condition may be violated (see Section 3.1.2.3). Figure 3.1.11 shows the transfer function of an FRA as a function of the number of integration cycles performed.

As far as the harmonics are concerned, the integrals in Eqs. (28) and (29) may be expanded to read

$$\int_0^T \sin(m\omega t - \phi_m) \sin(\omega t) dt = \cos(\phi_m) \int_0^T \sin(\omega t) \sin(m\omega t) dt \\ - \sin(\phi_m) \int_0^T \sin(\omega t) \cos(m\omega t) dt \quad (31)$$

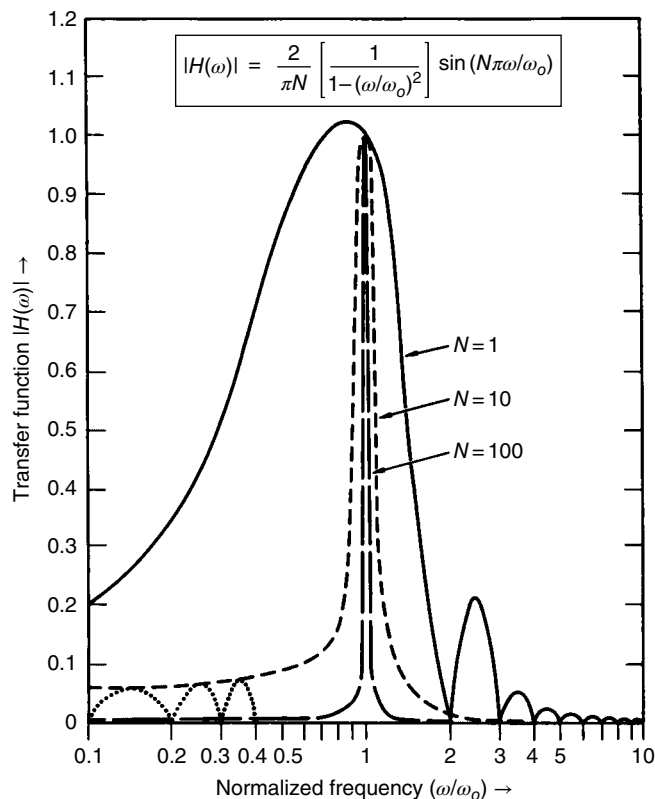


FIGURE 3.1.11 Frequency response analyzer transfer function vs. normalized frequency, as a function of number of integration cycles.

$$\int_0^T \sin(m\omega t - \phi_m) \cos(\omega t) dt = \cos(\phi_m) \int_0^T \cos(\omega t) \sin(m\omega t) dt \\ - \sin(\phi_m) \int_0^T \cos(\omega t) \cos(m\omega t) dt \quad (32)$$

Also noting that

$$\int_0^{k\pi T} \sin(nx) \sin(mx) dx = \begin{cases} 0 & \text{if } m, n \text{ integers, } m \neq n \\ k\pi/2 & \text{if } m, n \text{ integers, } m = n \end{cases} \quad (33)$$

$$\int_0^{k\pi T} \sin(nx) \cos(mx) dx = \begin{cases} 0 & \text{if } m, n \text{ integers, } m + n \text{ even} \\ 2kn/(m^2 - n^2) & \text{if } m, n \text{ integers, } m + n \text{ odd} \end{cases} \quad (34)$$

Then the integrals involving the harmonics in Eqs. (31) and (32) are identically equal to zero provided that the integrals are carried out over multiples of 2π . Accordingly, FRAs effectively reject the harmonics. Application of the previous identities to the fundamental components in Eqs. (28) and (29) therefore yields the real and imaginary outputs from the integrators as

$$H'(\omega) = P|Z(\omega)| \cos[\phi(\omega)] \quad (35)$$

$$H''(\omega) = P|Z(\omega)| \sin[\phi(\omega)] \quad (36)$$

which may be scaled to give directly the real and imaginary components of the cell impedance.

FRAs are also readily used to determine the harmonics contained within the output from the cell. This is done by multiplying the reference signal to the multipliers (but not to the cell) by the harmonic coefficient (2 for the second harmonic, 3 for the third, and so forth). The ability of FRAs to characterize the harmonics provides a powerful tool for investigating nonlinear systems—a topic that is now being actively developed (McKubre [1983]).

FRAs provide a very convenient, high-precision, wide-bandwidth method of measuring impedances in electrochemical systems. Commercial instruments are available that provide up to $4\frac{1}{2}$ digits of precision in the real and imaginary components, in frequency ranges covering 10^{-4} to 10^6 Hz. These are direct-measuring devices and therefore are not susceptible to limitations on imposed potentiostat control.

The primary limitation is one of cost. The basic FRA may cost on the order of \$20 000 (1986), and an additional investment for microcomputer and data storage facility is necessary to accommodate the higher rates of data collection made possible by the use of an FRA. A more subtle difficulty often occurs, as these devices are capable of operating with $4\frac{1}{2}$ digits of precision (the data dutifully recorded by the microcomputer) whether or not the instrument is connected correctly, or at all, to the electrochemical cell. Considerable familiarity with electrical systems is necessary in order to get accurate impedance data, particularly at higher frequencies. It is highly desirable that an oscilloscope be used in parallel with the two input channels of an FRA in order to monitor continuously the form of the input and output signals.

3.1.2.8 Automated Impedance Analyzers

There are a number of automated and semiautomated “impedance analyzers” on the market. Although these are intended primarily for network and network component analysis, they have a limited applicability for measurements in electrochemical systems.

Generally, this class of ac analyzer operates with a so-called auto balance bridge. The desired signal (comprising both ac and dc components) is applied to the unknown impedance as is shown in Figure 3.1.12a. The current follower effectively constrains all the current flowing through the unknown

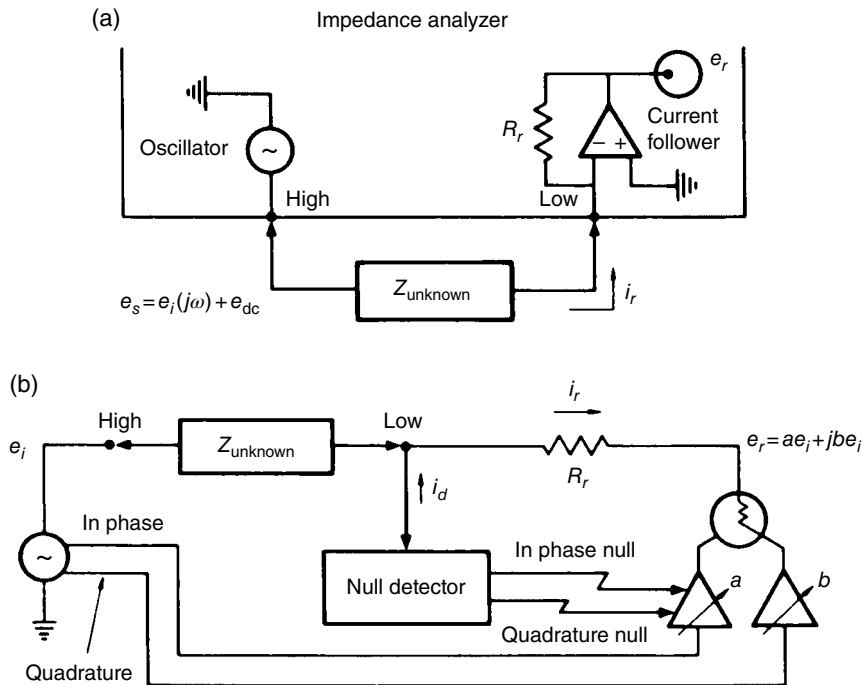


FIGURE 3.1.12 Direct measurement of impedance using an impedance analyzer. (a) Electrical connections (b) auto-balance bridge operation.

impedance i_r to flow through the range resistor R_r , presenting a virtual ground at the terminal marked "low" (for a further description of the use of current followers, see McKubre and Macdonald [1984]). For this condition the impedance can be measured as

$$Z_{\text{unknown}} = R_r \frac{e_i}{e_r} \quad (37)$$

The complex ratio e_i/e_r is measured in a manner very similar to that described in Sections 3.1.2.2 and 3.1.2.3 for transformer ratio and Berberian–Cole bridge circuits, in which inphase and quadrature fractions of the input signal are summed with the unknown output signal (current) until the result is zero. One method of accomplishing this is shown in Figure 3.1.12b. The oscillator that produces the input perturbation signal e_i also outputs inphase and quadrature (90° out of phase) reference signals that are proportional in amplitude to e_i . These are fed to a summing circuit and summed with the unknown current until the current to the detector, i_d , is zero. At this condition the low-potential terminal is at ground voltage, and

$$Z_i = \frac{R_r}{a+jb} \quad (38)$$

Thus, the unknown impedance can be determined directly from the value of the range resistor, R_r , and the attenuation factors a and b imposed by the null detector to achieve the null condition.

The advantages of this method are that relatively high speed and high precision are attainable. Being a null method, the effects of stray capacitances are somewhat reduced, although, unlike in a "true" bridge, currents do flow through the unknown impedance at the null condition. This method is usable up to very high frequencies (tens or hundreds of megahertz), well beyond the range of interest in aqueous electrochemistry.

The intrinsic disadvantage of this method is its two-terminal nature: the facts that a dc potential cannot be applied to the electrode of interest with respect to a suitable RE and that the potential e_i across

the specimen varies during the balance procedure. Since the inphase and quadrature null signals usually are derived from a PSD, instruments of this type are limited at low frequencies to approximately 1 Hz due to the instability of analog filters with longer time constants.

3.1.2.9 The Use of Kramers–Kronig Transforms

The use of a frequency domain transformation first described by Kramers [1929b] and Kronig [1926] offers a relatively simple method of obtaining complex impedance spectra using one or two ac multimeters. More importantly, retrospective use of Kramers–Kronig (KK) transforms allows a check to be made on the validity of an impedance data set obtained for linear system over a wide range of frequencies. Macdonald and Urquidi-Macdonald [1985] recently have applied this technique to electrochemical and corrosion impedance systems.

The KK transforms of interest in analyzing corrosion and electrochemical systems are

$$Z'(\omega) - Z'(\infty) = \left(\frac{2}{\pi} \right) \int_0^\infty \frac{x Z''(x) - \omega Z''(\omega)}{x^2 - \omega^2} dx \quad (39)$$

$$Z'(\omega) - Z'(0) = \left(\frac{2\omega}{\pi} \right) \int_0^\infty \left[\left(\frac{\infty}{x} \right) Z''(x) - Z''(\omega) \right] \frac{1}{x^2 - \omega^2} dx \quad (40)$$

$$Z''(\omega) = - \left(\frac{2\omega}{\pi} \right) \int_0^\infty \frac{Z'(x) - Z'(\omega)}{x^2 - \omega^2} dx \quad (41)$$

$$\phi(\omega) = \left(\frac{2\omega}{\pi} \right) \int_0^\infty \frac{\log|Z(x)|}{x^2 - \omega^2} dx \quad (42)$$

$$R_p = \left(\frac{2}{\pi} \right) \int_0^\infty \frac{Z''(x)}{x} dx \quad (43)$$

These equations show that the real component of the impedance can be calculated from the imaginary component and vice versa, the phase angle $\phi(\omega)$ can be computed from the magnitude of the impedance, and the polarization resistance (R_p) can be extracted from the imaginary component [Eq. (43)] in addition to being derived directly from the real component of the impedance:

$$R_p = Z'(0) - Z'(\infty) \quad (44)$$

The use of these expressions to validate impedance data will not be discussed in detail here (see Section 3.1.3.4 and Macdonald and Urquidi-Macdonald [1985], Urquidi-Macdonald *et al.* [1986]). Instead, we note that if the magnitude of the impedance is measured over an effectively infinite bandwidth, then the real and imaginary components can be calculated. These data are then used to compute the polarization resistance directly from Eq. (44) and indirectly from the imaginary component according to Eq. (43). The application of this latter method to calculating R_p in concentrated potassium hydroxide solution at 25°C is shown in Figures 3.1.13 and 3.1.14. In the first figure, the complex plane diagram for this system is shown, illustrating the inductive behavior at low frequencies and the extrapolation to the real axis to determine $Z'(0)$ and $Z'(\infty)$. In the second figure, the imaginary component is plotted as a function of $\log x$, together with a fitted polynomial:

$$Z''(x) = \sum_{k=0}^n a_k x^k \quad (45)$$

which is then used to evaluate the integral in Eq. (40). This procedure yields a value for R_p of 82.4 Ω, compared with 90 ± 5 Ω determined from the real components. This difference is insignificant from a

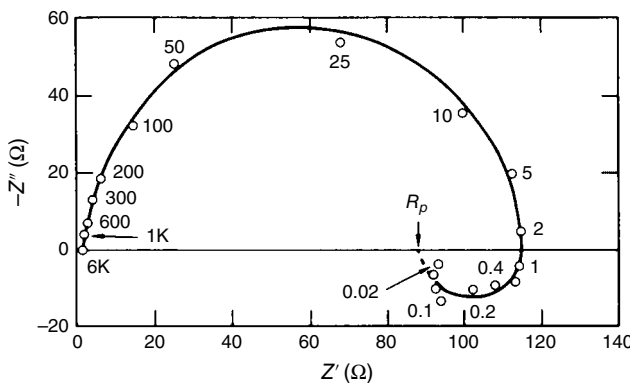


FIGURE 3.1.13 Impedance diagram for Al-0.1 P-0.1 In-0.2 Ga-0.01 T1 alloy in 4 M KOH at 25°C and at the open-circuit potential (-1.760 V vs. Hg/HgO). The parameter is frequency in Hz.

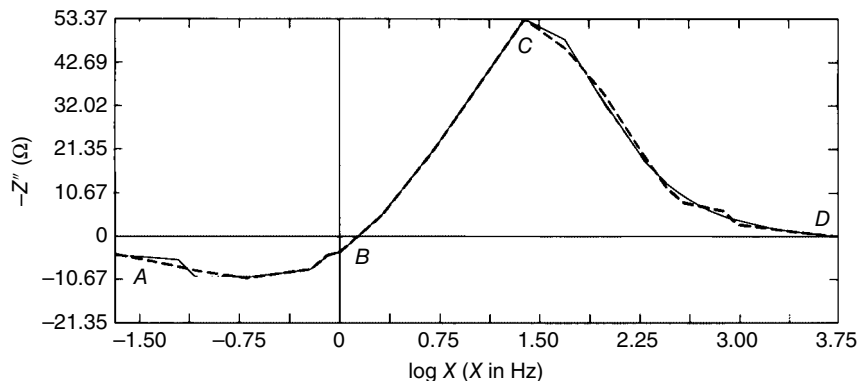


FIGURE 3.1.14 Plot of Z'' versus $\log X$ (X in Hz) for Al-0.1 P-0.1 In-0.2 Ga-0.1 alloy in 4 M KOH at 25°C under open-circuit conditions ($E = -1.76$ V vs. Hg/HgO). Dashed line = polynomial fit [Eq. (45)], solid line = experimental data.

corrosion-monitoring viewpoint; it probably arises from changes in the interface during the period of data acquisition.

As indicated earlier, KK transforms not only can be used to check a data set for internal consistency but also provide a simple method of obtaining impedance data. Briefly, the magnitude of an unknown impedance is often very easily measured as the scalar ratio of the magnitudes of the voltage across, and current passing through, the unknown element. It is considerably more difficult to measure the phase information, but this can be calculated from the impedance magnitude spectrum using the appropriate KK transformation.

A circuit to allow the measurement of an unknown impedance magnitude spectrum is shown schematically in Figure 3.1.15; although a two-terminal configuration is shown, there is no reason that this method cannot be applied with potentiostatic control. To obtain an impedance magnitude spectrum, the frequency of the ac oscillator is simply stepped or swept through the desired frequency range, the ac voltage and current recorded, and the ratio taken as a function of frequency. Since a machine transformation is necessary to obtain the phase spectrum (which can be used in conjunction with the magnitude information to yield the real and imaginary components in Cartesian coordinates), the most practical implementation of this method is to use a computer interfaced with, for example, an IEEE-488 controlled

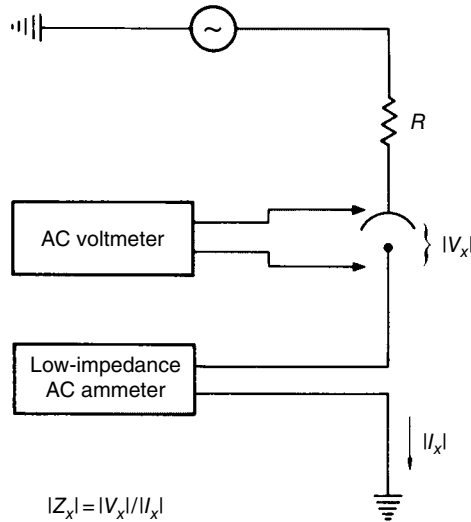


FIGURE 3.1.15 Circuit to obtain an impedance magnitude spectrum.

oscillator and multimeters to output frequencies and record the current and voltage information directly (see Section 3.1.2.5 for a description of the IEEE-488 interface).

The major advantages of this method are simplicity and low cost; a practical system can be configured for under \$5000 if a microcomputer is used to synthesize the sine wave. Since ac amp/voltmeters operate basically as dc devices (following a rectifying front end), they can operate to very high frequencies, and reliable measurements can be made well into the megahertz frequency range, the high-frequency limitation usually depending only on stray capacitances and transmission line effects external to the measurement circuit.

Practical limitations are imposed at low frequencies, however, where the rectification-smoothing function necessary to transduce the ac voltage magnitude to a dc level becomes inaccurate. Ac voltmeters typically become seriously in error at frequencies below 20 Hz. To obtain an accurate KK transform, it is necessary to extend the measurement frequency range significantly beyond the limits of frequency needed to elucidate the equivalent circuit under test. Thus, the method described here is not appropriate for aqueous electrochemical systems for which the diffusional impedance is prominent. This method can be useful for systems in which the lowest frequency of interest is greater than 50 Hz or so, as is usually the case for solid ionic conductors, oxide films, and semiconductor surfaces.

A more subtle limitation is imposed by the use of the method described here in that all of the four assumptions implied in the use of KK transforms are subsumed when the magnitude-to-phase transformation is made. That is, the unknown impedance is given the properties of linearity, invariance, and causality whether or not they apply, and there is no independent check of this assumption. In current practice, this limitation is not very severe since experimenters frequently report and draw conclusions from impedance data sets, normally derived, which have not been subjected to the scrutiny of the KK rules or other simple tests of experimental validity.

3.1.2.10 Spectrum Analyzers

Spectrum analyzers are instruments that are optimized to characterize signals in the frequency domain; the requirements of signal analysis are subtly different from those of linear network analysis, the former requiring low noise and low distortion over a wide range of frequencies (bandwidth), while the latter being optimized to give accurate amplitude and phase measurements over a wide range of input–output voltages (dynamic range). Nevertheless, spectrum analyzers can be used to measure impedances rapidly at audio and higher frequencies, using a variety of input excitation functions. In this section we will

describe the functioning of the three major classes of spectrum analyzer: parallel filter, swept filter, and dynamic.

The classical function of a spectrum analyzer is to measure the power (or amplitude) of a signal at a number of discrete points, or in discrete frequency bands, within a defined frequency range. Normally, the frequency bands are linearly or, more commonly, logarithmically spaced within the spectrum of interest. A very simple method to accomplish this goal is to apply the unknown signal to a parallel array of filters, each tuned to pass a defined (and narrow) frequency band. If these bandpass filters are arranged to be uniformly spaced with minimal overlap, as shown in Figure 3.1.16a, then the output of one or more voltmeters applied sequentially or simultaneously to the parallel array of "N" filters will be an "N"-point analog of the input frequency spectrum. The advantages of this method are simplicity and speed. If, however, a highly accurate analog of the spectrum is needed, then a large number of closely spaced narrow-bandwidth filters are required. As the bandwidth is reduced, such filters become expensive and unstable, and the cost of such an analyzer becomes greater as the resolution is increased.

One way to avoid the need for a large number of expensive filters is to use only one filter and to sweep it slowly through the frequency range of interest. If, as in Figure 3.1.16b, the output of the filter is plotted against the frequency to which it is tuned, then one obtains a record of the spectrum of the input signal. This swept analysis technique is commonly used in radio frequency and microwave spectrum analysis. However, the filter has a finite response time, and the narrower the bandwidth of the filter, the longer it takes to respond. To avoid amplitude errors, one must sweep the filter slowly through the frequency range of interest, and the advantage of speed afforded by spectrum analyzers is compromised.

There is a basic trade-off between parallel- and swept-filter spectrum analyzers. The parallel-filter analyzer is fast but has limited resolution and is expensive. The swept-filter analyzer can be cheaper and have higher resolution, but the measurement takes longer (especially at high resolution). Furthermore, since the swept-filter analyzer does not observe all frequencies simultaneously, it cannot be used to analyze transient events.

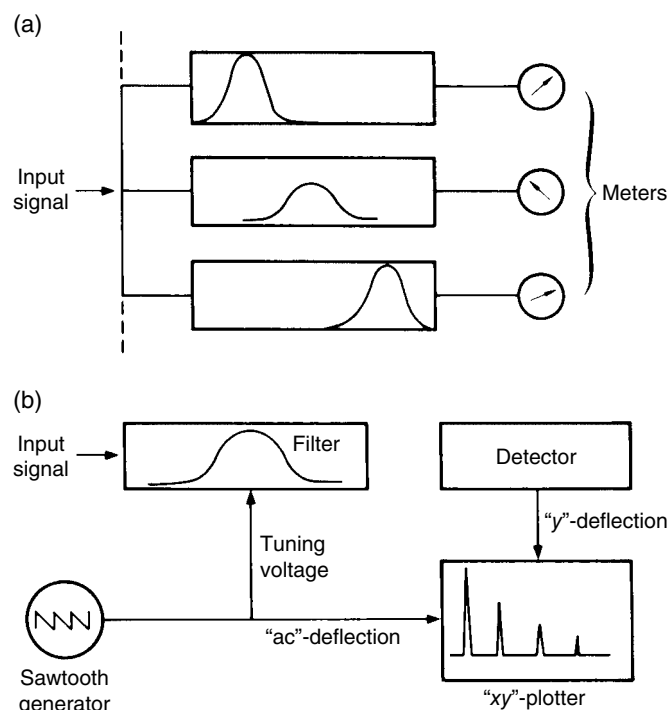


FIGURE 3.1.16 Spectrum analyzers. (a) Parallel-filter analyzer (b) Swept-filter analyzer.

A disadvantage common to both classes of spectrum analyzer discussed so far is that they do not measure absolute amplitudes accurately and phase at all. Although this last limitation can be circumvented by the use of KK transformations (see Section 3.1.2.9), these instruments generally are poor choices for linear circuit (ac impedance) analysis.

In recent years, another kind of analyzer has been developed that offers the best features of parallel- and swept-filter spectrum analyzers. The so-called dynamic signal analyzers use analog-to-digital (A/D) conversion followed by frequency-to-time-domain transformation, usually using hard-wired computational machines, to mimic the function of a parallel-filter analyzer with hundreds of filters and yet are cost-competitive with swept-filter analyzers. In addition, dynamic spectrum analyzers are capable of measuring amplitude *and* phase accurately; these are basically time-domain instruments, and their function will be discussed in Section 3.1.2.7.

3.1.3 Time-Domain Methods

3.1.3.1 Introduction

With the advent of high-speed digital computers, a clear trend toward digital signal processing has become apparent. The advantage of digital over analog data processing is purely mathematical; a far wider range of mathematical computations can be performed in the digital mode than on analog signals. Digital signal processing using hard-wired devices has also expanded rapidly over the past decade and is likely to find even more application in the years to come.

Since the world of electrochemistry is an analog one, the use of digital computation methods must be preceded by A/D conversion. One of the most important experimental aspects of this process is the method by which the computer interacts with the analog experiment: the computer interface. Having achieved the digital state, the range of computational algorithms used to extract ac impedance information is very diverse. Although a thorough discussion of these topics is beyond the scope of this chapter, in this section we discuss briefly the techniques that are now in common use for A/D conversion, computer interfacing, and digital signal processing, with reference to the measurement of the ac impedance parameters.

From the definitions given in Section 4.3.2, it is apparent that the interfacial impedance can be calculated from the perturbation and response in the time domain, in which the excitation can be any arbitrary function of time. In principle, any one of several linear integral transforms can be used (Macdonald and McKubre [1981]) to convert from the time domain into the frequency domain, but the two most commonly used are the Laplace and Fourier transforms:

$$F(s) = \int_0^{\infty} F(t)e^{-st}dt \quad (46)$$

$$F(j\omega) = \frac{1}{\sqrt{2\pi}} \int_{-\infty}^{\infty} F(t)e^{-j\omega t}dt \quad (47)$$

where s is the Laplace frequency. Noting that $s = \sigma + j\omega$, Eq. (46) leads to

$$F(j\omega) = \int_0^{\infty} F(t)e^{-j\omega t}dt \quad (48)$$

which is referred to as a single-sided Fourier transform. By transforming the time-domain voltage [$E(t)$] and current [$I(t)$] to yield the frequency domain quantities [$E(j\omega)$ and $I(j\omega)$], the impedance may be calculated as

$$Z(\omega) = \frac{E(j\omega)}{I(j\omega)} \cdot \frac{I^*(j\omega)}{I^*(j\omega)} \quad (49)$$

where $I^*(j\omega)$ is the complex conjugate of $I(j\omega)$.

As noted previously, any arbitrary time-domain excitation can be used to measure the system impedance provided that the excitation is applied and the response recorded over a sufficiently long time to complete the transforms over the desired frequency band. Thus, potential and current steps and various noise excitations have been extensively used (Smith [1966, 1971, 1976], Pilla [1970, 1972, 1975], Doblhofer and Pilla [1971], Creason and Smith [1972, 1973], Sierra-Alcazar [1976]), particularly in the field of ac polarography. More recently, these same methods have been applied in corrosion science (Pound and Macdonald [1985], Smyrl [1985a, b], Smyrl and Stephenson [1985]) to obtain impedance spectra, but more importantly to estimate polarization resistance for rapidly corroding systems. In the work of Pound and Macdonald [1985], various time-to-frequency transformation techniques were evaluated, including the discrete Fourier transform, the fast Fourier transform (FFT), the Laplace transform, and an algorithm that duplicates the mathematical operation of an FRA (see Section 3.1.2.7). All these techniques involve the recording of the perturbation and response in digital form in the time domain before signal processing in either software or hardware. Regardless of the mode of processing, the accuracy of transformation depends critically on acquiring data records having the desired characteristics of length and sampling frequency.

3.1.3.2 Analog-to-Digital Conversion

The conversion of analog signals into digital form, and ultimately into binary word representation, is now a common practice in electrochemistry, particularly for interfacing analog instruments, such as potentiostats, with digital recording and processing equipment (e.g., computers). The essential operation desired is to convert the value of an analog signal into a binary word whose magnitude is proportional to the signal being sampled. This process involves two operations: sampling and quantization. The first involves momentarily “freezing” the analog signal in time to produce a discrete value. This value is then converted to its binary representation during the “quantization” step after which the cycle is repeated.

Sampling is normally achieved by using “sample and hold” amplifiers of the type shown schematically in Figure 3.1.17. In this circuit, a signal to the analog switch (e.g., 4066 CMOS) connects the analog input to the amplifier. Provided that the capacitance to ground is sufficiently small, the capacitor will charge to the analog input voltage with good fidelity. Removal of the control signal effectively disconnects the input from the capacitor so that the analog output assumes the value of the input at the instant the switch was opened. This cycle is then repeated, with the sample rate being determined by the control signal from the clock; it is necessary in the case of A/D conversion, however, that the hold time be sufficiently long for the quantization step to generate an accurate digital representation of the analog input.

A number of quantization techniques are available, and the selection of the optimum analog-to-digital converter (ADC) for a particular application is properly based on considerations of resolution (precision), accuracy (initial and drift with time and temperature), ease of interfacing, cost, and convenience (availability, size, and power requirements). To select an ADC, it is useful to understand exactly what types are available and how they work. The listing in Table 3.1.1, although far from complete, does include the most popular ADCs, especially those currently produced in an integrated circuit form.

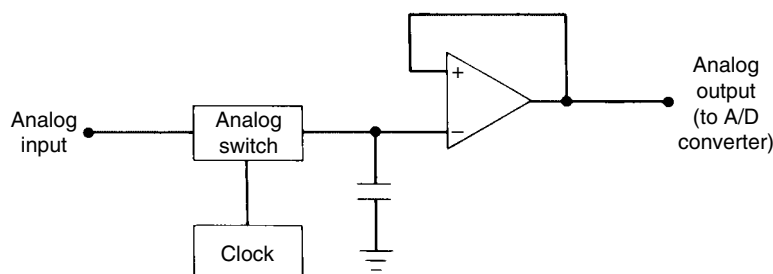
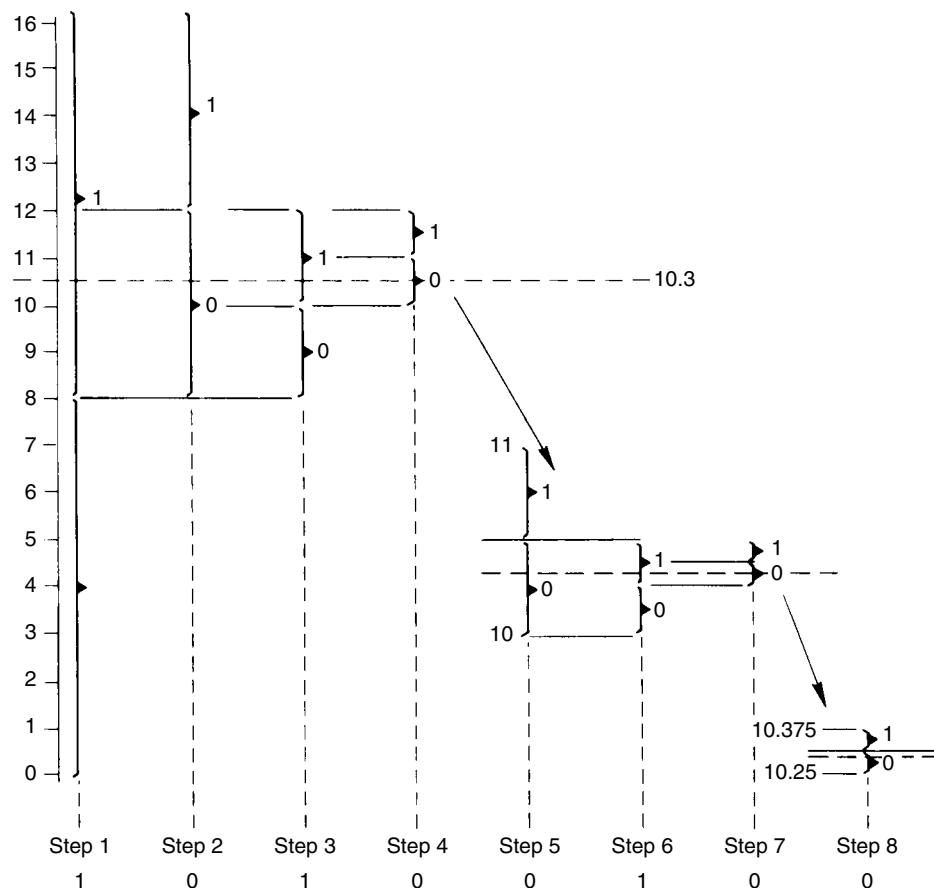


FIGURE 3.1.17 Schematic diagram of a sample-and-hold amplifier.

TABLE 3.1.1 Property of Common Analog-to-Digital Converters

Type	Advantages	Disadvantages	Typical Uses
Successive approximation	High speed Flexibility High accuracy Low cost	Precision expensive Susceptible to noise Low speed	Multiplexing 100 Hz to 1 MHz/channel
Integrating	Low sensitivity to noise		DC—100 Hz Digital voltmeters
Tracking (counter-comparator)	High tracking speed	Susceptible to noise	DC—100 Hz
Multicomparator (flash)	High speed High resolution	Expensive	1 MHz and up
Voltage-frequency converter	Fast response Continuous output	Moderate precision	Telemetry

**FIGURE 3.1.18** Successive-approximation conversion of an analog signal to its 8-bit binary representation. Analog input = 10.3 V, equivalent binary output = 1010.0100 \equiv 10.25.

We will discuss here only successive-approximation and integration ADCs in detail. The tracking A/D and voltage-to-frequency converter can be looked on as variations of the successive-approximation and the integration design techniques; in these types, the digital data is available on a virtually continuous basis.

The principle of the successive-approximation technique is shown in Figure 3.1.18. In this particular example we wish to convert the analog input voltage (10.3 V) into its floating point, 8-bit binary form to

the nearest 0.0625 V. The process involves eight successive steps, in which the field is divided into halves and a bit of 1 or 0 is assigned to each step, depending on which half of each field the analog value lies. For example, in the first step, 10.3 lies between 8 and 16, so that 1 is assigned as the most significant bit. However, in the second conversion step, the analog input lies in the 8–12 field rather than in the upper half (12–16), so that 0 is assigned to the second most significant bit. This process is repeated until the desired precision is achieved. Clearly, only n steps are required to quantize an unknown voltage into its $\{A\}_n$ binary form.

A block diagram of a successive-approximation ADC is shown in Figure 3.1.19. The circuit converts each successive approximation into an analog signal Y , which is equivalent to the center of each division shown in Figure 3.1.18. The analog input (A) is then compared with Y in the following cycle; if A is greater than Y , the comparator swings to positive saturation and a “1” is loaded into the register.

The principal advantage of the successive-approximation technique is high speed, and conversion rates in the megahertz range are possible. The principal disadvantages are limited accuracy and precision. Accuracy is limited because, as with all wide-bandwidth (high-speed) devices, the technique is very susceptible to external noise sources, and a noise spike coinciding with any of the more significant bit conversions can result in large errors; to some extent this difficulty can be removed by averaging multiple conversions at the expense of speed. The precision is limited by the number of bits converted. Thus a 16-bit ADC (8, 10, 12, 14, and 16 bits are commonly used) will have a minimum uncertainty of 1 part in 2^{16} or 0.0015% and can achieve that level of precision only if the voltage being measured is close to the ADC maximum. However, even when using a 2-V device, the sensitivity of one 16-bit ADC is 0.03 mV, which is adequate for most electrochemical measurements.

A second A/D conversion technique offers greater immunity to noise and almost unlimited precision, as well as reducing the need for sample-and-hold circuitry at the signal input. The concept of the “dual-slope” or up/down integrating ADC is simple. A current proportional to the input signal charges a capacitor for a fixed length of time; the capacitor is then discharged by a current proportional to a reference voltage until the starting point is crossed. Figure 3.1.20 shows a schematic representation of the implementation of this technique. The input voltage e_i is applied to the input resistor R_i . With the switches in position 1, op amp OA1 forces a current $I_i = e_i/R_i$ to charge the plates of capacitor C . Thus, with the switches in position 1, and after time t_i , the output voltage e_o will be given by

$$e_o = e_{\text{initial}} + \frac{1}{RC} \int_0^{T_i} e_i dt \quad (50)$$

where e_{initial} is the output at $t = 0$. For simplicity, if the initial voltage is zero and the integral is replaced by the average in the input time window, \bar{e}_i ,

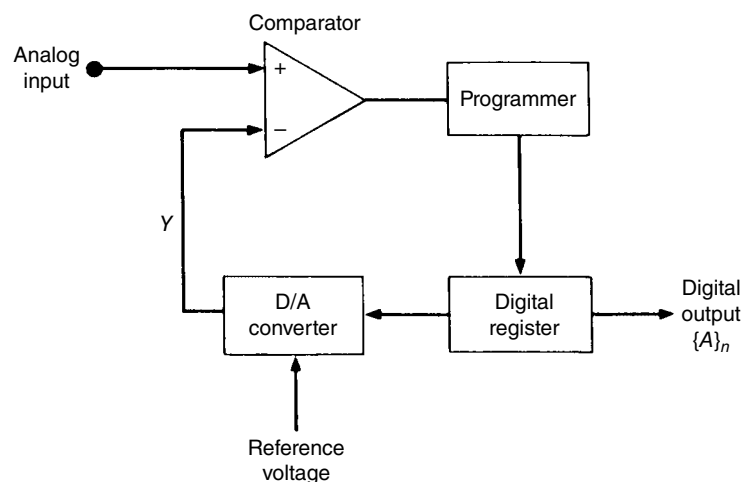


FIGURE 3.1.19 Schematic diagram of a successive-approximation A/D converter.

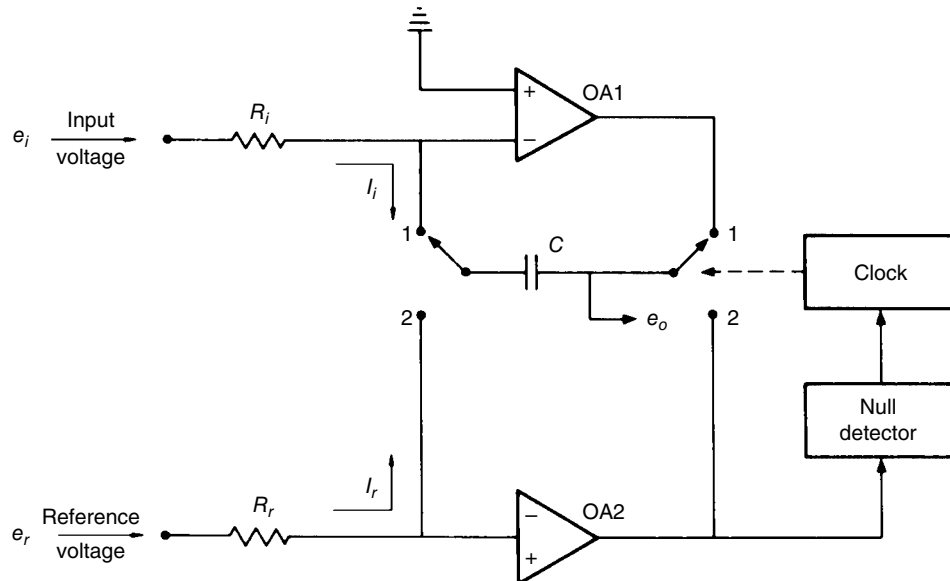


FIGURE 3.1.20 Schematic diagram of an up/down integrating D/D converter.

$$e_o = \frac{\bar{e}_i t_i}{R_i C} \quad (51)$$

After an accurately clocked interval t_i , the clock sets the switches to position 2, and the negative reference current is applied to discharge the capacitor. Thus,

$$e_o = \frac{\bar{e}_i t_i}{R_i C} - \frac{e_r t}{R_r C} \quad (52)$$

and at the condition of null, when $e_o = 0$,

$$e_i = \frac{R_i t}{R_r t_i} e_s \quad (53)$$

and the averaged input voltage can be calculated very precisely from the accurately known values of resistances and time.

Although quality components (especially the capacitor) must be used for reasonable accuracy, only the reference need be an expensive, high-quality component. Speed is an obvious limitation because of the long count time required. (e.g., one must count to 2000 and effectively do 1000 successive comparison tests at the null detector to achieve 3-digit or 10-bit resolution.)

Dual-slope integration has many advantages. Conversion accuracy is independent of both the capacitor value and the clock frequency, because they affect both the upslope and the downramp in the same ratio. The averaging mode and the fixed averaging period also grant excellent immunity to noise, and an integrating ADC has “infinite” normal mode rejection at frequencies that are integral multiples of $1/t_i$. In practical terms, if the ADC is set to integrate over exactly n cycles of some extraneous and periodic noise source (e.g., main frequency), then the integral will be zero, as if the spurious signal had been completely filtered out at the input.

Throughput rate of dual-slope converters is limited to somewhat less than $\frac{1}{2}t_i$ conversions per second; the sample time t_i is determined by the fundamental frequency to be rejected. For example, if one wishes to reject 60 Hz and its harmonics, the minimum integration time is 10.167 ms, and the maximum conversion rate is somewhat less than 30 Hz.

3.1.3.3 Computer Interfacing

The details of computer interfacing are so intimately connected to the details of programming itself that a discussion of arbitrary, low-level interfacing is best suited to a treatise on software than to one on hardware. Interfaces that operate at a high level, with their details of operation obscured to the user by a "driver" program, however, are of significant importance to the experimenter interested in the implementation of ac methods. Most common among the high-level interfacing systems is the general-purpose interface bus (GPIB), also known as the IEEE-488 (or IEC-625 or HPIB*). This interface standard is becoming capable of almost universally connecting computers with digital multimeters, transient recorders, and Fourier analyzers—in short, with all those tools needed to implement the ac impedance method in the time domain.

IEEE standard 488-1978 interface represents a highly flexible, moderate-speed system that is well suited to general laboratory use. The IEEE-488 interface bus (IB) consists of 16 signal lines. Eight lines are used for data, five for bus management, and three are used to establish a temporary communication link, or "handshake," between two devices that are properly attached to the bus. Because there are eight data lines, an 8-bit byte can be communicated in each handshake cycle. Thus 16-bit, 24-bit, etc. words (either instructions or data) can be communicated with sequential handshake cycles. This method is often referred to as "bit parallel, byte serial" transmission (Colloms [1983]).

A very large number of devices can be connected simultaneously to the interface bus. Each device is given a unique address, which is used in establishing a handshake. Handshake is used to ensure that data is transferred from a source to one or more designated acceptors. Figure 3.1.21 shows a portion of the bus structure, and Figure 3.1.22 shows the handshake sequence in detail. The three signals used for handshake are data valid (DAV), not ready for data (NFRD), and no data accepted (NDAC). The DAV line is driven by the sender, while the NFRD and NDAC lines are driven by the receiver. The handshake procedure ensures that all listeners are ready to receive data, that the data on the eight data lines is valid, and that the data has been accepted by all listeners. Data will be sent only as fast as it can be accepted by the slowest receiver.

The IEEE-488 IB is designed to interface with the four major types of devices shown in Figure 3.1.21. A master or controller sends commands over the bus using the bus control (uniline) and data lines (multiline). Normally, one controller is present (e.g., a computer or microprocessor), but if more are present, only one may exercise control at any time. A controller issues a system initiation command, interface clear (IFC), and designates which devices are talkers and which are listeners. The controller has complete

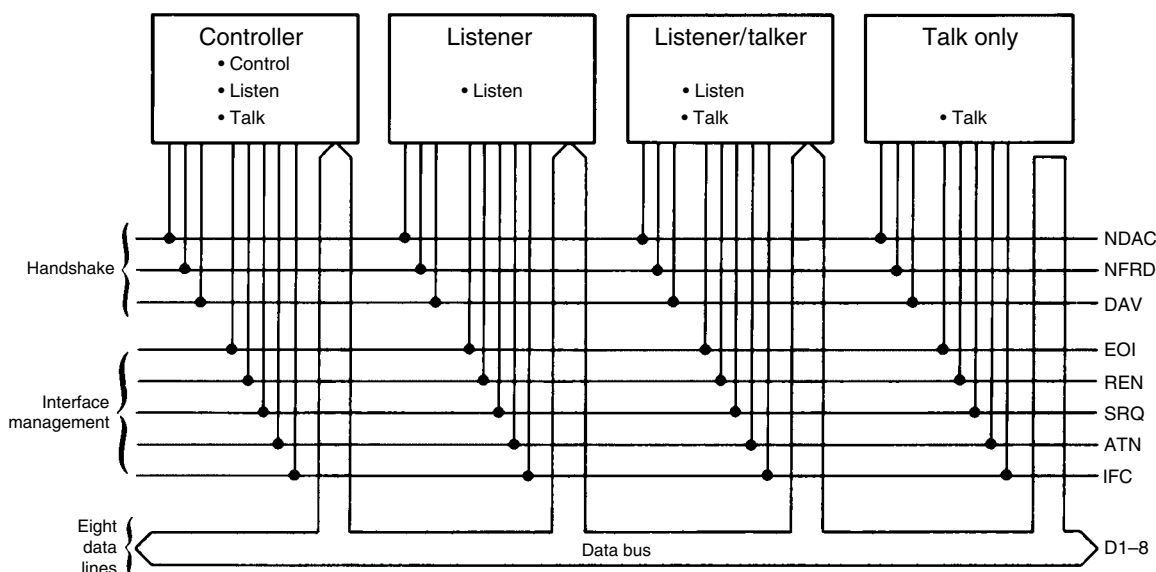


FIGURE 3.1.21 A section of an IEEE-488 interface bus, showing the major classes of user devices.

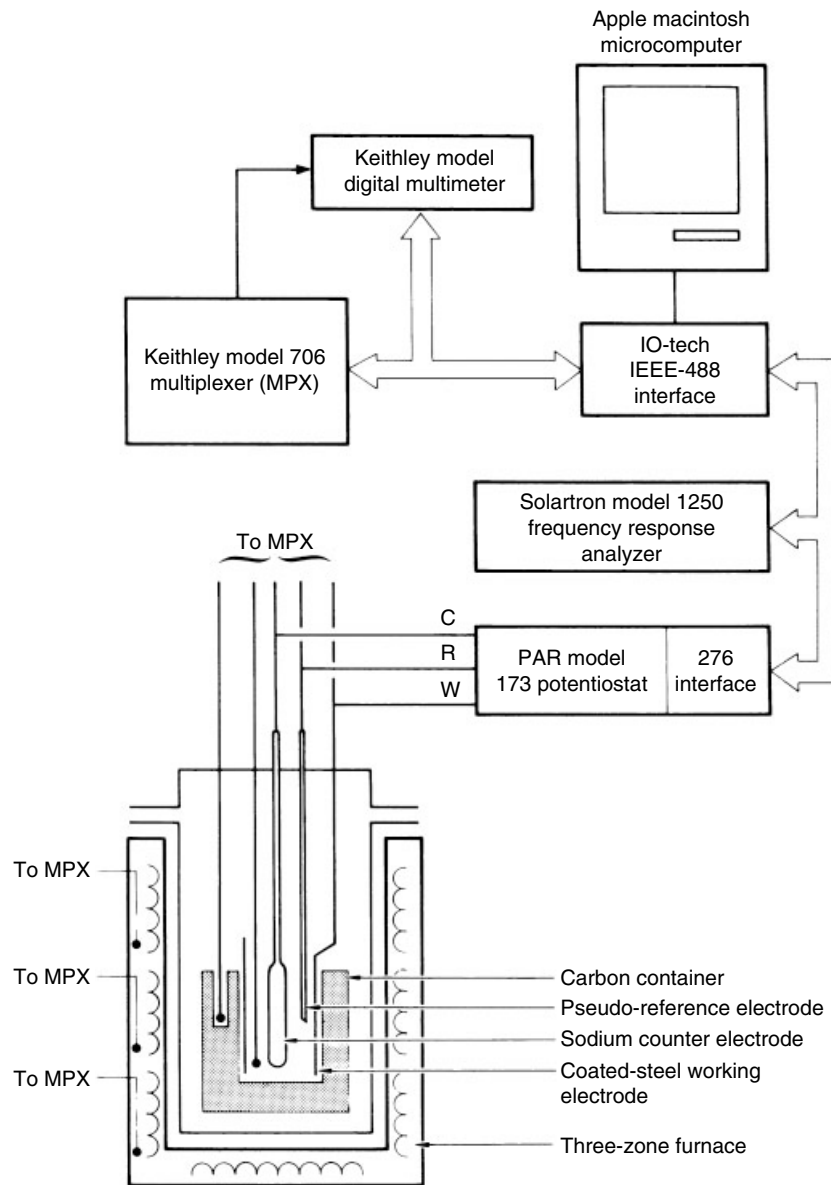


FIGURE 3.1.22 Use of the IEEE-488 interface for dc and ac measurement and control.

control of the attention line (ATN). When ATN is “true,” the controller is issuing messages or commands.

A listener receives data over the IB, following an acceptor handshake. Addressed listeners respond to controller commands. Listen-only devices are intended for use in a circuit with no controller. An example of a listener might be a digitally controlled analog potentiostat.

A talker is a device capable of sending data over the IB to a controller or listener. An unaddressed talk-only device, such as a digital voltmeter, may represent a problem in a circuit with a controller, since this device may continue talking when the controller requires attention (ATN “true”), resulting in a garbled message.

Most commercial devices intended for use with an IEEE-488 IB are combined talker listeners, capable of receiving instructions, setting the data collection mode and experimental conditions, and returning data to the controller.

IEEE-488 systems of considerable complexity have been developed for electrochemical data acquisition and experimental control. One such system, shown in Figure 3.1.22, uses a microcomputer to monitor temperature and dc signals with an IEEE-488 multiplexer and multimeter to control and IEEE-488 potentiostat and to output and input data for an IEEE-488 FRA, in order to measure impedances in a sodium/sodium-polysulfide cell at elevated temperatures (McKubre and Sierra-Alcazar [1985]).

3.1.3.4 Digital Signal Processing

In principle, any one of several integral transforms can be used to convert data collected in the time domain into the frequency domain for subsequent analysis. Because of the similarity of the various transformation techniques, it is convenient first to discuss briefly the interrelationships of the various transform functions.

The general linear integral transformation of a function $F(t)$ with respect to a kernel $K(t, q)$ is given as (Bohn [1963], Crain [1970])

$$\bar{F}(q) = \alpha \int_a^b K(t, q) F(t) dt \quad (54)$$

where a and b define the transform interval and q is the transformation variable. The kernels and the limits of integration frequently adopted for the transforms of interest are summarized in Table 3.1.2. It is clear that the methods are very closely related. In particular, the reader will note that the imaginary axis Laplace transformation

$$\tilde{F}(j\omega) = \int_0^\infty F(t) e^{-j\omega t} dt \quad (55)$$

is in fact a single-sided Fourier transform. Also, since the form of the Laplace variable ($s = \sigma + j\omega$) dictates that both frequency domain and transient responses can be obtained, it is clear that the Fourier transform is a special case of the more general Laplace transform. The remaining linear transform of interest, the "Z" transform, to our knowledge has not been used for the analysis of interfacial impedance. Accordingly, this transform will not be considered in this discussion.

In this chapter, we are concerned with machine implementation of transform techniques, either software or hardware, to obtain data in a form convenient for ac impedance analysis. In recent years, the advent of hard-wired (dedicated) Fourier transform units (Reichl [1977]) and the FFT algorithm, or FFT (Cooley and Tukey [1965], Hartwell [1971]), has concentrated practical interest almost exclusively on the Fourier transform.

Again, in the formalism of linear systems analysis, the transfer function is the mathematical description of the relationship between any two signals. In the special case where the signals of interest are the input (current excitation) and output (voltage response) of a linear electrical system, the transfer function is equivalent to the system impedance.

TABLE 3.1.2 Linear Integral Transforms

Transform	Kernel $K(t, q)$	α	a	b
Laplace	e^{-st}	1	0	∞
Fourier				
Infinite	$e^{-j\omega t}$	1	$-\infty$	$+\infty$
Infinite	$e^{-j\omega t}$	$\frac{1}{2\pi}$	$-\infty$	$+\infty$
Single-sided	$e^{-j\omega t}$	1	0	$+\infty$
Segment	$e^{-j\omega t}$	1	0	$+\infty$

Mathematically,

$$G(j\omega) = \frac{E(j\omega)}{I(j\omega)} = \frac{\tilde{F}[E(t)]}{\tilde{F}[I(t)]} = Z(j\omega) \quad (56)$$

where $G(j\omega)$ is the system transfer function, \tilde{F} denoting the Fourier transform, E is the system voltage, and I is the current. The variable $j\omega$ indicates that this is a complex frequency domain parameter, and t indicates a time-domain parameter. Equation (56) indicates that the ratio of the Fourier transforms of the measured time-domain voltage and current is equal to the impedance.

Obviously, two stages of data manipulation are required to obtain $Z(j\omega)$ as a function of frequency from the response of the system to an arbitrary time-domain perturbation: first, the input and response functions must be sampled and recorded in the time window of interest and then the transform of each must be computed and the complex ratio calculated. In hard-wired Fourier transform units, the acquisition subsystem is an integral part of the unit, and this function normally can be ignored. If the experimenter is using a computer or microcomputer to perform these functions, the concepts of A/D conversion and computer interfacing (described briefly in Sections 3.1.2.4 and 3.1.2.5) must be used.

With either hard-wired or software-programmed logic, the most common method of obtaining $\tilde{F}[E(t)]$ and $\tilde{F}[I(t)]$ uses the FFT algorithm first devised by Cooley and Tukey [1965] as a method for obtaining a discrete digital approximation of the infinite Fourier transformation from a finite data record. The digital nature of the transformation, however, and the finite length of the time record result in a number of properties of the FFT that must be recognized in order to minimize distortion of the derived impedance data (Creason and Smith [1972, 1973], Smith [1976]).

The FFT algorithms demand that the time record contain 2^n words, where n is an integer. This requirement is easily satisfied by simply adjusting the digitizing sampling rate and/or the length of the record. However, the sampling theorem states that the highest-frequency component that can be completely characterized in terms of amplitude and phase must have a frequency of less than half the sampling rate. On the other hand, the lowest frequency that is accessible is the reciprocal of the total sampling period. These limitations are readily illustrated by considering a standard FFT array of 1024 words. If this array is collected over 0.7 s, the lowest frequency is 1.43 Hz, whereas the highest frequency is $0.5 \times (1024/0.7) = 731.4$ Hz. Clearly, somewhat less than three decades of frequency are accessible from a single 1024-point FFT. This may be construed as a serious limitation of the FFT algorithm, but it is possible to apply the transformation to successive segments, thereby extending the total frequency range to many orders of magnitude.

The finite length of the data record may cause broadening of the Fourier spectrum relative to the actual spectrum. The phenomenon, which is frequently referred to as "leakage," may be minimized (but not eliminated) by increasing the length of the time record as much as possible or by modifying the way in which the time record is truncated. Also, the leakage error can be reduced to zero if the waveform is periodic within the time record since the components whose frequencies match those computed are not subjected to leakage error.

Another source of error is due to a phenomenon known as "aliasing," which arises because of the discrete nature of the data record. In this case, the error is induced by components whose frequencies are greater than the $\frac{1}{2}$ sampling rate maximum imposed by the sampling theorem. These higher-frequency components are incorrectly included as lower-frequency components when executing the FFT. Aliasing is easily avoided by simply ensuring that the data sampling frequency is greater than twice the highest frequency in the exciting waveform. This can be achieved by using a low-pass filter to remove the unwanted high-frequency components, leading to the use of bandwidth-limited excitation.

A number of other operational problems exist when using the FFT algorithm. The most important of these, as far as electrochemistry is concerned, is due to the inherently nonlinear nature of the system. When Eq. (56) is used to measure the impedance with an arbitrary time-domain input function (i.e., not a single-frequency sinusoidal perturbation), then the Fourier analysis will incorrectly ascribe the harmonic responses due to system nonlinearity to input signal components, which may or may not be

present at higher frequencies. As a consequence, the "measured" impedance spectrum may be seriously in error.

Up to this point we have described methods in which impedance is measured in terms of a transfer function of the form given by Eq. (56). For frequency domain methods, the transfer function is determined as the ratio of frequency-domain voltage and current and for time-domain methods as the ratio of the Fourier or Laplace transforms of the time-dependent variables. We will now describe methods by which the transfer function can be determined from the power spectra of the excitation and response.

In addition to Eq. (56), the transfer function $G(j\omega)$ can be calculated for the cross-power spectra of the input and the output, which in turn can be calculated from the linear spectra of the input and output. Thus

$$G(j\omega) = \frac{P_{yx}(j\omega)}{P_{xx}(j\omega)} = \frac{S_y(j\omega) S_x^*(j\omega)}{S_x(j\omega) S_x^*(j\omega)} \quad (57)$$

where $P_{yx}(j\omega)$ is the average cross-power spectrum of the input and output; $P_{xx}(j\omega)$ is the average power spectrum of the input; $S_x(j\omega)$ and $S_y(j\omega)$ are the linear spectra of the input and output, respectively; and $*$ denotes the complex conjugate.

By invoking the equivalence of Eqs. (56) and (57), it is apparent that the information required to calculate the operational impedance is contained in the input and output linear magnitude spectra S_x and S_y . In practice these are cumbersome and faster to compute and can be applied to measurements to which linear magnitude spectra cannot (Roth [1970]).

Calculations of power spectra are most conveniently performed via the correlation functions. The auto- and cross-correlation functions for time-domain input $[x(t)]$ and output $[y(t)]$ functions are

$$R_{xx} = \frac{1}{T} \int_0^T x(t)x(t+\tau)dt \quad (58)$$

$$R_{xy} = \frac{1}{T} \int_0^T x(t)y(t+\tau)dt \quad (59)$$

where T is the time interval over which the correlation is required and τ is a time displacement or delay. In essence, the correlation function yields a time-averaged quantity having greatly improved signal-to-noise characteristics. The value of self- and autocorrelation before transformation is therefore clear.

The significance of the correlation functions in transfer function analysis becomes apparent from the following equations:

$$P_{xx}(\omega) = \tilde{F}[R_{xx}(t)] \quad (60)$$

$$P_{yx}(\omega) = \tilde{F}[R_{yx}(t)] \quad (61)$$

Thus, it is possible to calculate the frequency domain power spectra [and hence $Z(\omega)$] from the Fourier-transformed auto- and cross-correlation functions. The application of correlation techniques for the determination of electrochemical impedance data has been used by Blanc *et al.* [1975], Barker [1969], and Bindra *et al.* [1973], using both random noise input functions and internally generated noise.

A number of significant advantages are inherent in this method:

- The correlation technique is an averaging method and thus affords the same type of insensitivity to asynchronous system noise as phase-sensitive detection.
- In common with other transform methods, $G(j\omega)$ is determined for all frequencies simultaneously and in the time required for the lowest frequency alone by conventional methods. Thus,

impedance can be measured down to relatively low frequencies in time-varying systems, and impedance parameters can be measured as a function of time in, for example, a rapidly corroding environment.

- Correlation analysis can be performed on internally generated noise in the complete absence of an external excitation function. Because the ionic events that produce this noise are not synchronized to an external trigger, the correlation function in this case contains no phase information but may be considered analogous to the magnitude of the impedance. This technique is potentially an extremely powerful one, allowing equilibrium and steady state conditions to be approached very closely.
- The coherence function provides an internal check on the validity of the measurement. In this regard, it is important to note that methods, which determine impedance as the ratio of the imposed input to the observed output, do so without regard to the degree of causality between the two signals. Thus, for example, in a system exposed to mains noise or containing electrolyte pumped in an oscillatory or peristaltic fashion, a component of the output signal power results from frequencies characteristic of the environment or system, but not of the applied input. Another frequent cause of error in a measured electrochemical impedance is nonlinearity of the interfacial reaction impedance at large perturbations. Thus excitation at frequency ω_0 results in harmonic distortion and a component of output power at frequencies $2\omega_0$, $3\omega_0$, and so on, which may invalidate the "impedance" measured at these frequencies.

The coherence function $\gamma_{xy}^2(\omega)$ can be calculated to determine the validity of a transfer function measurement if the extent of extraneous input and nonlinearity is not known. This function is defined as

$$\gamma_{xy}^2(\omega) = \frac{\overline{P_{xy}(\omega)^2}}{\overline{P_{xx}(\omega)}\overline{P_{yy}(\omega)}} \quad (62)$$

where bars denote average quantities and P_{yy} is the auto power spectrum of the output signal $y(t)$. Coherence function values range between 0 and 1. A coherence value of 1 means there is only one input and the system is linear.

The primary limitation of this method of impedance measurement is cost.

3.1.4 Conclusions

In an age of computerized instrumentation, ac impedance and other measurement results are often presented to the user with four or more digits of precision, with little reminder of the intrinsic limitations of the measurement or computational techniques used. Even when considerable care is given to the electrical connections of the system under test and to analysis of subsequently produced data, the operation of the instrument is often transparent to the user. Since the choice of analyzer may determine acquisition precision, time, and other important parameters of data collection, it is of some value to the careful experimenter to understand as fully as possible the method of operation of the impedance analyzer. It is hoped that this chapter is useful in contributing to this understanding.

As a final note of caution, even carefully performed experiments may be subject to systematic error; the system under test may be intrinsically nonlinear or it may be subject to periodic oscillations, to drift with time, or to other extraneous effects. The results of such perturbations may not be obvious to the experimenter, even when the input and output waveforms are closely monitored with an oscilloscope. It is therefore desirable that impedance data be screened routinely for systematic error. Two screening methods, the KK integrals and the coherence function, have been described in this chapter, and their use is recommended.

This section was written by Michael C. H. McKubre and Digby D. Macdonald.

3.2 COMMERCIALLY AVAILABLE IMPEDANCE MEASUREMENT SYSTEMS

3.2.1 General Measurement Techniques

This section presents ideas and techniques that are applied in the latest generation of commercially available equipment to the impedance measurement of many types of cells/samples including conductors at one extreme and dielectric/insulator materials at the other. These general measurement topics are equally applicable to electrochemical (where samples are typically tested in electrolytes) and to solid-state materials measurements. Subjects covered include 2/3/4 terminal sample connections, current-to-voltage (I-E) conversion techniques and architectures, measurement accuracy/resolution, and single/multi-sine/harmonic measurements.

Section 3.2.2 focuses more specifically on additional measurement techniques that are suited to electrochemical applications, while Section 3.2.3 on techniques used in materials applications.

3.2.1.1 Current-to-Voltage (I-E) Conversion Techniques

Impedance characterization involves accurate measurement of voltage and current over as wide a frequency range as possible: the ratio of the two being the impedance of the sample under test. Usually current is the more difficult to measure, and this requires careful application of I-E conversion techniques.

Two techniques are widely used in electrochemical and materials test systems to measure the *current* that passes through the sample—shunt (passive) and virtual earth (active) I-E conversion. Once the current has been converted into a voltage using one of these techniques, it can then be transformed into a digital signal using an ADC. The digital signal is a mathematical representation of the current passing through the sample that is processed to produce the final measured result. Processing can include calibration to correct systematic measurement errors, notch, or specialized filtering to remove 50/60 Hz power interference, low-pass filtering to remove higher frequency noise and interference, and signal averaging to further reduce noise or emphasize measured characteristics that are of interest. The starting point however is the I-E converter, and each method of conversion has advantages and disadvantages that will be described in this section.

Current measurement circuits typically need to cover a very wide range of current, from amps or higher, down to pico-amps or even lower, to femto-amps. This is typically achieved by having multiple switched measurement ranges that are decades apart, for example, 1 A, 100 mA, 10 mA, and so on. Usually the software/firmware provides facilities that allow the user to set particular ranges or select auto-range mode where the system makes the ranging decisions. In any case, multiple ranges need to be accommodated in the design of the I-E conversion circuit for measurement of most practical cells and samples. As an example dielectric materials are capacitive in nature that produce an impedance response that decreases by one decade for every decade increase in test frequency, so multiple ranges are needed to test over a reasonable range of frequency.

Passive I-E Converters. Passive I-E converters use a reference resistor (Z_{Ref}) connected in series with the measured sample to produce a voltage proportional to the current passing through the sample. The sample current is then calculated by dividing the voltage V_{out} by the reference resistance Z_{Ref} . In practice several switched reference resistors are used to measure current over a wide range. Typically an amplifier is used to produce the final voltage output that is measured by the ADC and is subsequently divided by the reference to obtain the sample current as in Figure 3.2.1.

Advantages	Relatively straightforward calibration for dc and ac measurements
Disadvantages	The reference resistors produce a voltage drop that appears in series with the cell/sample that is being measured. This results in the following <ul style="list-style-type: none">• Loss of polarization/compliance voltage range• The cell experiences voltage steps at current range changes• Stray impedances that can drive leakage currents

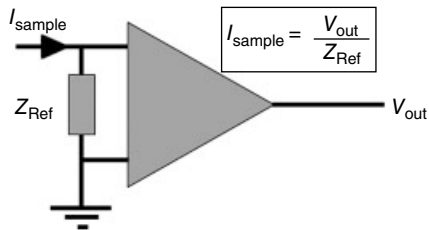


FIGURE 3.2.1 Passive I-E converter.

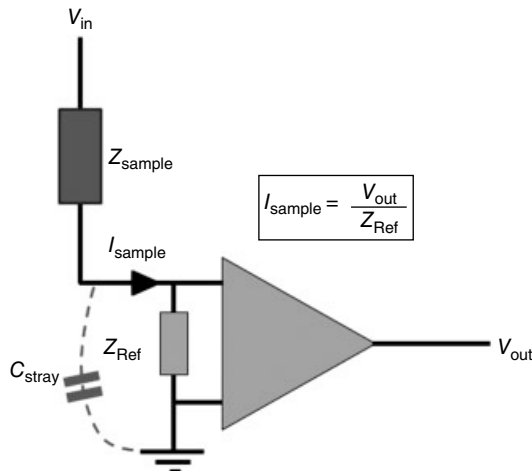


FIGURE 3.2.2 Passive I-E converter on low side of sample/cell.

The polarization/compliance issue mentioned previously is undesirable as often the whole voltage range of the system is needed for use of the cell/sample that is being tested, having a voltage drop associated with the measurement electronics reduces the measurement range of the equipment.

Other disadvantages depend on where the passive I-E converter is positioned in the system. There are two choices: the I-E converter appears either on the *low side* of the sample Figure 3.2.2 or on the *high side* as in Figure 3.2.3.

If the passive converter is positioned on the *low side* of the sample (i.e., the converter is closer to ground potential than the sample/cell), there will be a disturbance to the cell each time there is a range change, as the voltage across the shunt reference resistor Z_{Ref} changes whenever a new range (reference resistor) is selected. The cell base voltage changes for each current range change. Cell disturbances are not desirable as the cell can take some time to settle after each change. The fact that the shunt method develops a voltage other than zero on the base of the cell can cause some of the current that passed through the cell to leak to earth via stray impedances such as cable capacitance (C_{stray} in Figure 3.2.2), instead of being measured, leading to systematic measurement errors.

If the passive converter is instead positioned on the *high side* of the cell (Figure 3.2.3), the cell base voltage is now held at ground potential (no jumps at range changes), but there is still a disturbance to the cell as the voltage across Z_{Ref} changes at each current range change point, and there is still the issue of loss of compliance range as was discussed earlier.

Current measurement errors also occur as the current that was measured through the shunt Z_{Ref} does not all go through the sample, leading to systematic measurement errors. Leakage current from cable capacitance becomes more significant as the voltage at the high side of the cell includes the sample/cell voltage itself, which drives more of the measured current to ground via stray impedance. In addition,

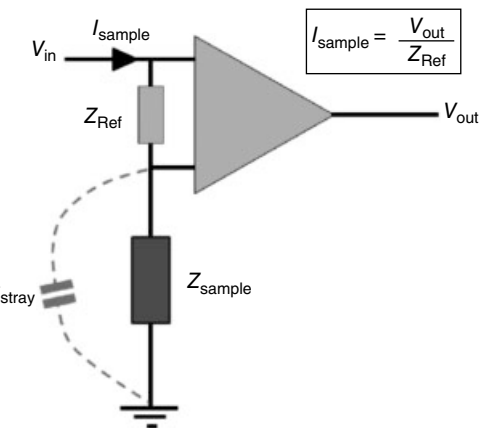


FIGURE 3.2.3 Passive I-E converter on high side of sample/cell.

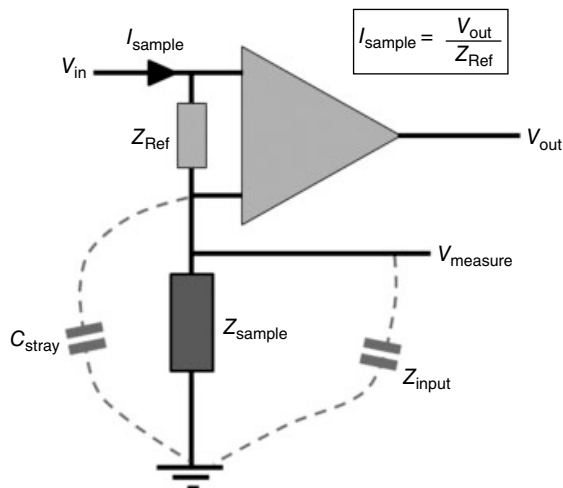


FIGURE 3.2.4 Passive I-E converter input impedance.

some of the measured current will leak into the voltage measurement input (V_{measure}) circuit. Even where extremely high input impedance is quoted in the Tohm range, that will certainly not be the case at high frequency as input capacitance becomes more dominant as the frequency increases, which dramatically lowers the input impedance of the voltage measurement circuit. So in addition to the desired current path through the sample, there are stray current paths that produce current measurement errors. These are due to the cable capacitance C_{stray} and input impedance Z_{input} stray current paths that produce current measurement errors. The I-E converter will also experience “common-mode” rejection errors as it has nonzero voltage on its low input (Figure 3.2.4).

All measured current that does not actually pass through the sample contributes to measurement error of the sample current and therefore error in the sample impedance.

Active I-E Converters. What alternative techniques are available? Virtual earth techniques as exemplified in Figure 3.2.5 have been used for many years that eliminate a lot of the errors, which are seen from passive (shunt) measurement systems.

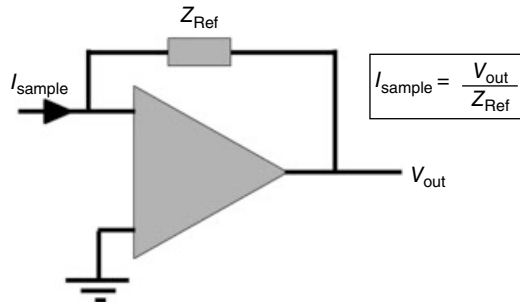


FIGURE 3.2.5 Virtual earth current measurement.

The virtual earth measurement technique does not introduce a voltage drop in series with the sample as the amplifier works to keep the voltages on both of its inputs the same, so an immediate advantage is the possibility to apply the full polarization/compliance range of the system across the sample without any loss of range due to the current measurement circuit.

Advantages	<p>There is no voltage drop in series with the cell/sample that is being measured. This results in the following</p> <ul style="list-style-type: none"> • Full polarization/compliance range being available for the cell • Minimal disturbance to the cell at range changes • Much less issues with leakage currents
Disadvantages	More complicated impedance calibration

As with the passive I-E technique, there are alternate positions for the active I-E that can either appear on the high or low side of the cell/sample. We will discuss positioning on the *high side* first. As mentioned previously, whether used on high or low side, the full compliance/polarization range of the instrument is available for the cell/sample. Instruments are available that use virtual earth techniques even up to 100 V for use with battery/fuel cell stacks, and that full range of voltage can be applied to the cell.

However when applied on the *high side* (Figure 3.2.6), there can still be issues with stray current. Great care needs to be taken to ensure that current that has been measured actually does pass through the sample and does not leak to earth either via stray capacitance or through the voltage reference input impedance as was seen for the case of *high side* passive current measurement. Also there will be common mode rejection issues in this *high side* configuration as the voltage of the amplifier low input is nonzero.

To avoid stray current leakage, the virtual earth technique is typically used for *low side* measurement. In this case the virtual earth (active) circuit appears between the sample and ground (Figure 3.2.7).

The low side of the sample is maintained at virtual earth potential by the action of the amplifier circuit, so this avoids the key disadvantages of the shunt technique when used on the low side of the sample—the cell is at zero base voltage, no disturbance at range changes, and no loss of polarization/compliance range. As the name implies, the sample is held at virtual earth potential so there is also no voltage present to drive leakage current to ground, and no issue with common-mode rejection. All of the current that passes through the sample is measured by the current measurement circuit.

As can be seen, the virtual earth technique provides many advantages for current measurement. What are the disadvantages? Calibration is more difficult as the response from a virtual earth circuit is fully predictable but requires more comprehensive modeling than that of the shunt measurement circuit. Calibration involves careful characterization of the active I-E converter output using multiple samples and multiple frequency points on each range—a time-consuming and costly process. For best impedance performance every system built must be *uniquely calibrated* (no use of generic or approximate

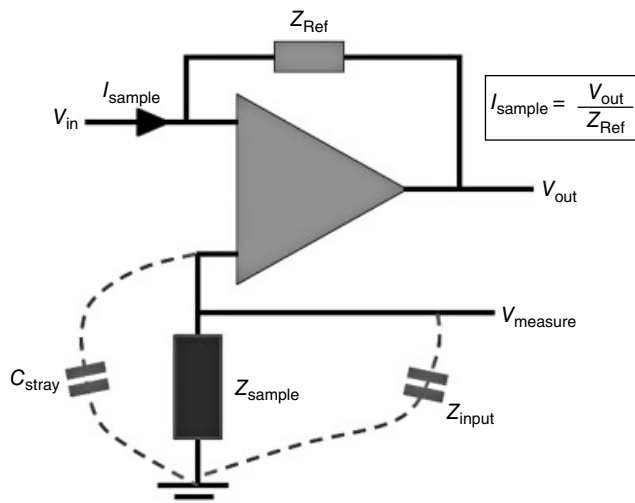


FIGURE 3.2.6 Virtual earth high side current measurement.

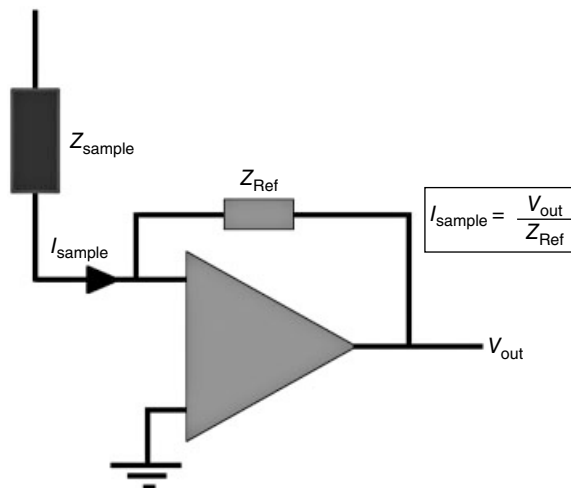


FIGURE 3.2.7 Virtual earth low side current measurement.

calibration techniques). With care the active I-E technique provides the best measurement performance available and is exclusively used by highly acclaimed brands throughout the industry.

High Impedance Measurements and the Effect of Input Impedance. As discussed previously, the only way to use shunt measurement while minimizing disturbance to the cell base voltage is to apply the technique on the high side of the sample. However, we saw that this has disadvantages that some of the measured current does not follow the path through the sample but instead goes to ground via cable leakage, or leakage into the voltage measurement system (despite the apparent very high $T\Omega$ input impedance). This is due in both cases to capacitance when measuring sample impedance at high frequency where input capacitance and cable capacitance dominates over the high input resistance and cable insulation resistance.

For example, if the input impedance of the instrument is 10 pF capacitance in parallel with $1\text{ T}\Omega$ resistance, the input impedance is actually really only $16\text{ k}\Omega$ at 1 MHz . If the *high side* shunt

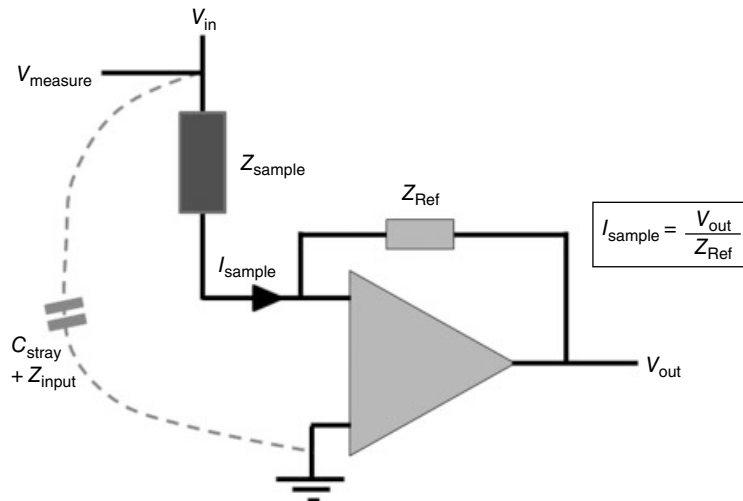


FIGURE 3.2.8 Virtual earth low side current measurement (plus strays).

measurement technique is used to measure a dielectric or insulator sample at high frequency, the measured current will be much higher (due to current leakage) than the actual current through the sample, and the measured sample impedance will be badly affected.

We have seen that the use of virtual earth techniques allows positioning of the current measurement on the *low side* of the sample/cell impedance avoiding current leakage and common mode rejection effects. One benefit of this system is that *ultrahigh impedance voltage measurement inputs are not needed* (which in any case as we have seen cannot be achieved at high frequency due to stray capacitance). In the virtual earth case, *all* of the current that passes through the sample goes into the current measurement circuit. There is no leakage of current between the sample and the virtual earth measurement as this point is at ground potential (Figure 3.2.8).

There are still parallel current paths that go from the high side of the sample into the voltage reference input and also to ground via cable capacitance, but these current paths are *in parallel* and therefore do not affect the sample current that is measured accurately by the virtual earth. The parallel current path also does not affect the measured voltage, so impedance measurements are accurate.

3.2.1.2 Measurements Using 2-, 3-, or 4-Terminal Techniques

Most modern impedance measurement systems provide at least four connections to the cell. These connections typically consist of a generator output, current measurement input, and at least two voltage measurement inputs. These can be configured in different ways depending on the impedance of the cell/sample that is to be measured.

Two-Terminal (2T) Measurement. Two-terminal (2T) measurement technique is used for testing *high impedance* cells/samples where the impedance of the sample is much higher than the impedance of the connection cables. It is apparent from the 2T connection diagram later that the voltage measurement includes the voltage drop of the cables that connect to the sample. For the measurement of high impedance samples such as dielectrics, insulators, and high impedance coatings, the error introduced by the relatively small cable impedance can be ignored, especially if sample/reference measurement technique (see Section 3.2.3.4) is used to compensate for cable capacitance at high frequency (Figure 3.2.9).

For high impedance samples, the use of four-terminal (4T) connections for measurement can add error due to the voltage measurement connection to the low side of the sample (see Figure 3.2.10) that

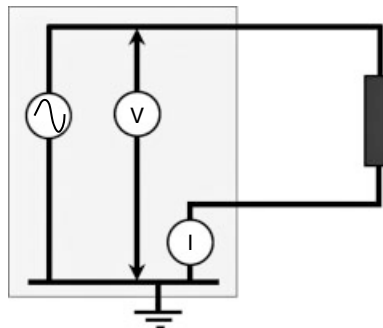


FIGURE 3.2.9 2T measurement connections.

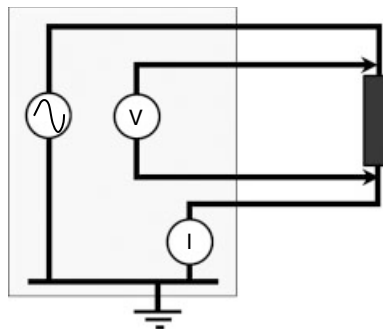


FIGURE 3.2.10 4T measurement connections.

provides a stray current path for current that passed through the sample to bypass the current measurement circuit, so 2T is usually preferred.

Four-Terminal (4T) Measurement. 4T measurement capability is extremely important when measuring low impedance samples such as batteries, fuel cells, ultra-capacitors, and conductive materials. In this case, the impedance of the connection cables may well be of the same order of magnitude or even larger than the impedance of the cell itself and will cause inaccurate measurement of the cell impedance if 4T connections are not used. Care should be taken to position the voltage measurement cables as close as possible to the sample to avoid adding cable or contact impedance to that of the sample. Screw connections are recommended to get the best contact quality. Example of such connection is given in Figure 3.2.10.

If 2T (or three-terminal (3T)) connections are used for this type of measurement, the instrumentation will be unable to differentiate between the impedance of the cables and impedance of the cell, and this can produce large measurement errors. The 4T technique ensures that the voltage drop measured by the instrument is measured across the cell only and does not include the voltage drop in the current carrying CE and WE cables, therefore providing accurate measurement of the cell voltage.

The voltage measurement inputs have very high input impedance compared with the current-measuring circuit, so all of the current is measured correctly at the I-E converter.

Where the cell voltage is measured using 4T connections and is combined with accurate measurement of the current flowing through the cell, it becomes possible to characterize extremely low impedance test cells in the sub-mΩ range, which is very much needed in today's rapidly developing energy market. Example of low noise 100 μΩ 4T results is given in Figure 3.2.11.

Three-Terminal (3T) Measurement. The 3T technique is mostly used for corrosion and general electrochemical measurements where an RE senses the voltage in solution close to the sample that is being

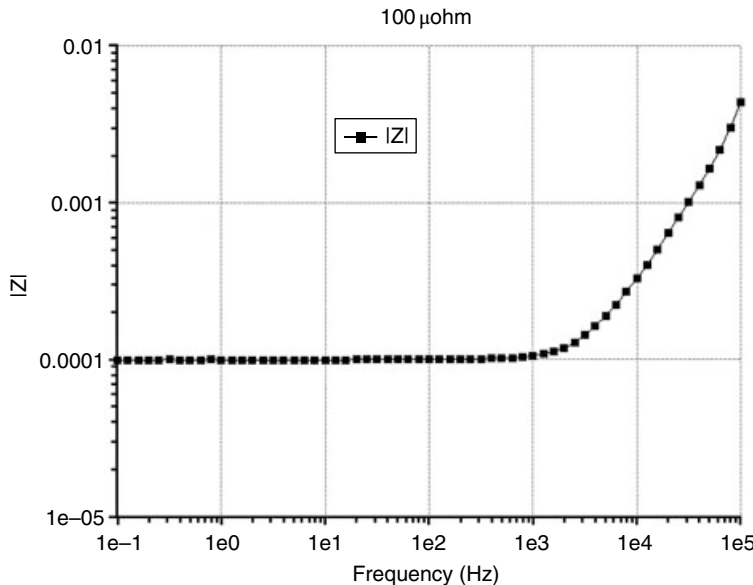


FIGURE 3.2.11 Example low noise 100 $\mu\Omega$ 4T results.

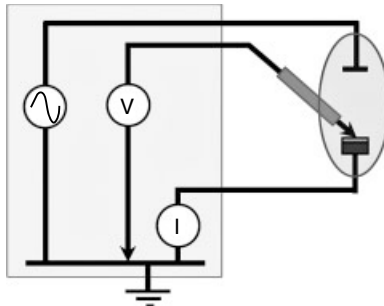


FIGURE 3.2.12 3T measurement connections.

tested. As usual there is a generator (known as CE) providing current to the cell, a current measurement electrode (known as WE) that measures the current through the cell, and a connection for the use of a standard reference electrode within the cell (known as RE). Note that as with the 2T technique, the low side voltage measurement is connected to the other side of the current measurement circuit away from the cell, so that leakage paths are not introduced into the measurements.

It is important to realize that since the measurement of the differential voltage across the cell also includes the voltage drop in the WE connection cable, the 3T connection system can give measurement errors when measuring low impedance cells such as batteries and fuel cells (Figure 3.2.12). The 4T measurement technique is preferred for low impedance samples.

3.2.1.3 Measurement Resolution and Accuracy

Frequency resolution is an important parameter for some applications, and this is a function of the design of the waveform synthesizer in the FRA or spectrum analyzer. Using state-of-the-art techniques, it is possible to design very high-resolution waveform synthesizers that are able to provide 26-bit, or even higher, frequency resolution (i.e., 1 in 67 000 000). Using these waveform generator techniques,

very fine frequency sweeps with as little as 100 mHz steps can be achieved at 1 MHz (this is essential when testing highly resonant samples such as crystals, e.g., in piezoelectric or in quartz crystal microbalance QCM applications). Of course it is important that the analyzers are also able to measure at such fine increments of frequency, and this is part of the overall system design.

Frequency accuracy, as opposed to resolution, depends on the stability of the onboard frequency reference that is usually a crystal oscillator, and these are usually stable at 10 ppm if the temperature is held stable (in a typical laboratory measurement environment). For more precise applications some instruments allow a very accurate external frequency reference to be used.

Impedance measurement accuracy depends on the measurement of ac voltage and current through the cell. The 4T measurement technique is extremely important for the measurement of low impedance devices and 2T equally as important for dielectrics as explained earlier. Other considerations are the number of voltage and current ranges that are available in the impedance analyzer system, the bandwidth of the measurement circuits (this is dependent on the range selection), the availability of bias rejection, and the measurement accuracy of the FRA.

Usually measurement of ac voltage is not so much of a problem, and bandwidths of 1 MHz and beyond can fairly easily be achieved with careful design. Current measurement however usually presents much more difficulty. It is therefore extremely important to check the specified bandwidth of the potentiostat for the particular measurement that is required. The bandwidth of any potentiostat will tend to be widest in its mid-impedance range (probably when measuring cells of around 1 k Ω impedance); see typical contour plot in Figure 3.2.13.

For measurements on batteries and fuel cells, however, the impedance being measured is very much lower (typically lower than 15L ~1 Ω and even down to milliohms). In this case, since the cell impedance is low, the potentiostat is usually measuring on one of its high current ranges (current through the cell = applied voltage/cell impedance), which usually has lower frequency bandwidth. This can also be seen on the example contour; a cell with 100 m Ω impedance can be measured to just over 10 kHz at highest accuracy and up to 100 kHz with slightly lower accuracy. Power boosters can usually be added to systems to increase accuracy for extreme low impedance devices by increasing the cell current to compensate and produce a measurable voltage.

At the other end of the impedance scale, when measuring high impedance samples such as for dielectrics, insulators, or anticorrosion coatings, the impedance measurement system is usually

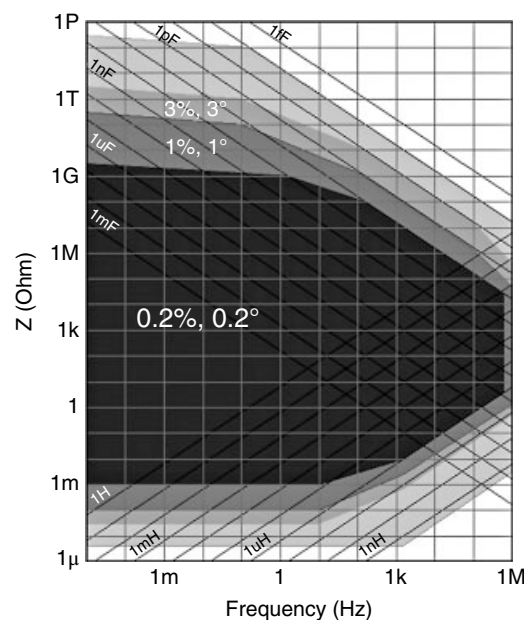


FIGURE 3.2.13 Example accuracy contour.

operating on a low current range where again the bandwidth is limited compared with the mid-impedance range bandwidth. This can be seen by following the high impedance lines on the contour plot and seeing where they intersect with various constant capacitance lines that indicate the bandwidth of various ranges (e.g., diagonal 1 pF line). It is very important therefore to study and understand impedance measurement specifications (accuracy contours) that are provided by instrument manufacturers and select instrumentation that is appropriate for the measurements to be performed.

It is not sufficient to only consider the bandwidth of an electrometer (the voltage measurement circuits); the whole system especially including the bandwidth of the current measurement system should be considered for the specific cells that are likely to be tested (the accuracy contour is a far better indication of performance than a single specification on electrometer bandwidth). Wherever possible, the instruments should be tested on the actual cells to be analyzed to make sure that they are able to make the required measurements.

3.2.1.4 Single Sine and FFT Measurement Techniques

Single sine and FFT measurement techniques are widely used for the impedance analysis of electrochemical cells. In terms of accuracy the single sine frequency response analysis technique (sometimes referred to as single sine correlation) is unsurpassed. This technique involves applying a pure sinusoidal voltage or current waveform to the cell at a particular frequency and then calculating the impedance of the cell at that frequency from the measured ac voltage across the cell and ac passing through the cell. This measurement process is repeated at a number of frequencies in order to fully characterize the cell impedance across the frequency range of interest.

The FFT technique provides an alternative method for measuring the impedance of the cell by applying a stimulus waveform containing multiple frequency components (e.g., multi-sine, random noise, or step/pulse waveforms) and then calculating the impedance from the measured voltage and current time-domain waveforms. This process involves performing FFT computations to transform the measured time-domain results into the frequency domain. Single sine and multi-sine techniques are examined in more detail, and the advantages/disadvantages of each technique are assessed later in this section.

For the single sine analysis technique as applied to electrochemical applications, a low amplitude sinusoidal stimulus is typically used (usually around 10 mV) in order to operate within a linear region on the cell. This is very important since the nonlinear nature of electrochemical cells can lead to impedance measurement inaccuracies when using higher amplitude signals. For materials applications higher signal levels can sometimes be used, but this depends on the linearity of the material.

Figure 3.2.14 shows what would happen if a sine-wave stimulus of too high amplitude was used to make measurements on a cell or sample, which has a nonlinear voltage versus current response curve.

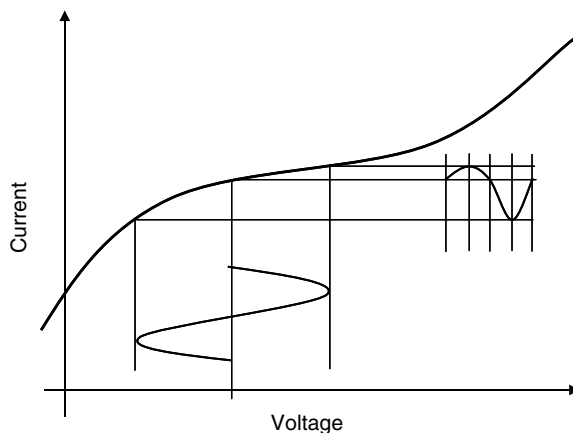


FIGURE 3.2.14 Non-linear electrochemical cells.

The resulting ac waveform in this case is heavily distorted (certainly not a pure sine wave), giving rise to additional frequency components (harmonic distortion). Since the single sine correlation technique applies a single frequency sine wave and measures only at the same frequency, the effect of harmonic distortion introduced by measurement of cells in a nonlinear regime is minimized. However, in order to obtain accurate impedance results, it is *essential* to operate within a linear regime on the cell by using a low enough amplitude ac stimulus. As will be seen later in this section, the FFT (or harmonic analysis) can be used to provide useful information about whether the measurement results are obtained in a linear or nonlinear measurement regime and can also give important information about the noise content of the measured signals.

The process of signal integration is used to reject harmonics and noise from the measurements. Even measurement of one cycle of the waveform to be analyzed provides rejection of all harmonic frequencies, as can be seen from the upper trace ($N = 1$) in Figure 3.2.15. Additional cycles can be averaged to provide rejection of noise and sub-harmonics from the waveform as shown by the other two traces that show the improved rejection of spurious signals for 10 and 100 cycles of integration. Refer to Section 3.1.2.7 for more information about the single sine correlation process.

For a complete impedance characterization of the cell, the frequency of the stimulus sine wave is swept across the frequency range of interest, and measurements are taken at each frequency point. FRAs give very accurate measurements but are limited in their measurement speed due to having to sweep the measurement frequency. This has limited their use for measurements on fast changing systems. However, with the increased use of digital signal processor (DSP) technology, this is becoming less of a limitation for the technique with very fast frequency sweeps now being available, at least at the high frequency end of the spectrum. At low frequency the measurement time is limited by the necessity to measure at least one cycle of the waveform (e.g., at 1 mHz, a single measurement takes 1000 s).

The use of FFT spectral analysis can be the perfect complement to the single sine analysis technique. The FFT can perform very fast measurements since it is not necessary to sweep the stimulus frequency in order to measure multiple frequencies. With the introduction of DSP technology, very fast measurements at multiple frequencies can be performed. Typically a multi-sine stimulus waveform is constructed, which includes a number of discrete frequency components added in such a way that the crest factor (spikiness) of the final waveform is kept as low as possible. This is important as large peaks in the multi-sine waveform may lead to harmonic distortion. The crest factor of the waveform is

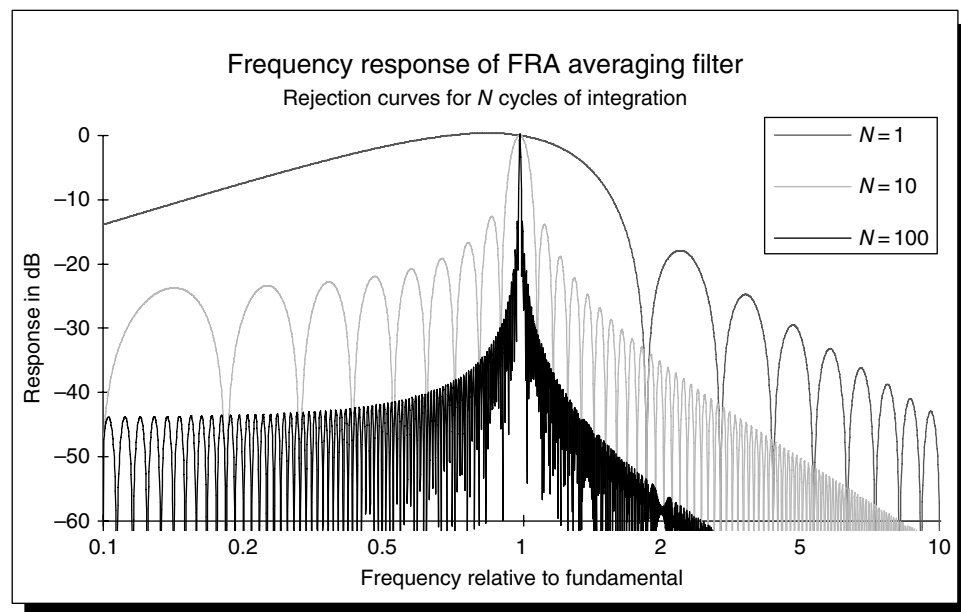


FIGURE 3.2.15 Single sine correlation (rejection of noise and harmonics).

optimized by adjusting the phase of each sinusoidal component relative to the others until the waveform is as smooth as possible and is free from large spikes.

The resulting multi-sine waveform is applied to the cell, and measurements of ac voltage and current are taken over a user-defined whole number of cycles of the lowest frequency present in the stimulus waveform. Since the stimulus waveform contains multiple frequencies, the measured waveforms will also contain the same frequencies. The FFT algorithm computes the results from all frequencies simultaneously, producing an impedance spectrum. The advantages for FFT analysis are fast multifrequency analysis, fewer problems when measuring time-variant systems (since measurements can be very fast—depending on the lowest frequency to be analyzed), and a consistent set of data since all frequencies are measured at the same time.

The choice of frequencies that are included in the multi-sine stimulus waveform is an interesting area for discussion. In the case where all frequencies are stimulated in the applied multi-sine waveform, the FFT analysis is not able to differentiate between signals that are the response of the cell to the same frequency in the stimulus waveform or signals that are simply harmonics of other frequencies due to nonlinearity of the cell, and this can lead to poor results. Of course it is essential to operate in a linear regime on the cell, and if that rule is observed the FFT impedance results can be much improved as harmonic frequencies due to distortion will not be present. However, if all frequencies are used in the stimulus waveform in order to keep the overall signal level low to operate in a linear regime on the cell, the amplitude of each frequency will need to be very low, leading to possible additional problems with noisy results.

Much improved measurement can be obtained by reducing the number of stimulus frequencies in the multi-sine waveform. Some commercially available analyzers either have a preprogrammed list of frequencies or allow the multi-sine frequencies to be selected by the user. In this case, many frequencies in the FFT analysis band are deliberately not stimulated. The applied multi-sine frequencies are usually chosen so that each stimulus frequency is not coincident with the *main* harmonics of lower frequencies. In this case the *main* components of harmonic distortion from each frequency in the stimulus waveform do not interfere with other stimulus frequencies (though of course it is not possible to avoid all significant harmonic frequencies). Without doubt, the impedance results from this approach are much improved compared with those obtained by the method where *all* frequencies are stimulated.

It is also possible (and this is a major benefit of the FFT or harmonic analysis approach) by measuring the results at the non-stimulated frequencies to investigate whether the cell is operating in a linear regime or is badly affected by noise. If the non-stimulated frequencies are showing a significant response, then it is necessary to adjust the experimental conditions, for instance, by reducing the applied ac level until the non-stimulated responses are sufficiently low (or in the case of noise where *all* non-stimulated frequencies are affected, it may be necessary to increase the stimulus level while ensuring that the cell remains in a linear regime by checking that the main harmonics remain low).

In addition, the fact that fewer frequencies are contributing to the multi-sine stimulus waveform allows a much higher amplitude signal to be used at each frequency while keeping the overall waveform amplitude within the linear regime of the cell. Typically 10–15 frequencies may be selected (usually with an approximately logarithmic relationship) for each decade, leading to perhaps 50 frequencies being stimulated across the entire measurement frequency band while analyzing several thousand frequencies using the FFT algorithm to check for nonlinearity or noise and then focusing on the 50 original frequencies to provide the impedance response. This approach can lead to good quality impedance data while utilizing the advantage of the FFT measurement speed.

Another possible problem area that should be discussed for the FFT approach is that of dynamic range. As all frequencies are measured at the same time, there can be problems with dynamic range especially when measuring over several decades of frequency. This can be seen when using an FFT-based instrument to measure the impedance of a capacitor over a wide range of frequency. Since the impedance of a capacitive sample changes by an order of magnitude for every decade of frequency, the current measurement input needs to be able to resolve the wide range of current levels that are present at the same time. This can be a problem for measurement on corrosion coatings or dielectric samples, for example, which may cover a very wide range of impedance when tested over several decades of

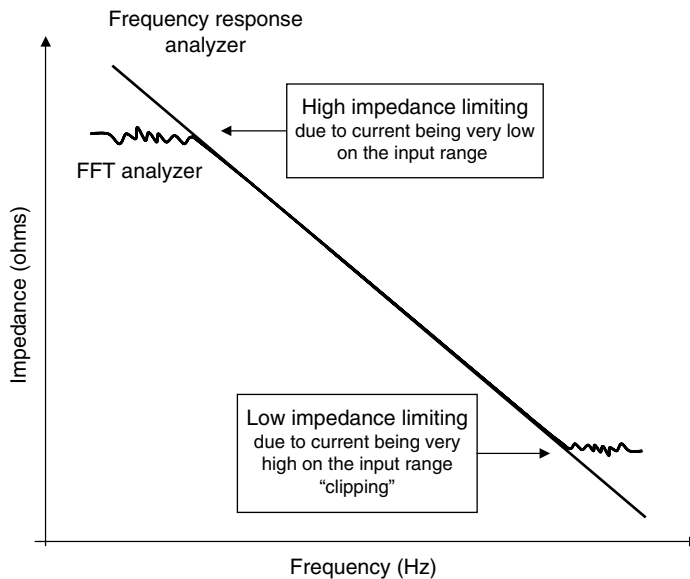


FIGURE 3.2.16 FFT analyzer versus frequency response analyzer.

frequency. In other applications the range of impedance being measured may not be as large, and the dynamic range issue may not be a significant problem.

In the case of a capacitive sample, the problem is to measure the high current signal present at the high-frequency end of the spectrum where the capacitor is low impedance at the same time as measuring the low current signal at the low frequency end of the spectrum where the capacitor is high impedance. If many decades of frequency are being analyzed at the same time, then the high frequency current component may be some orders of magnitude bigger than the low frequency current component. This may give rise to noisy or “limited” measurements at the low frequency end of the spectrum and “clipping” at the high frequency end of the spectrum (Figure 3.2.16). This problem may be avoided by running several FFTs in sequence each on different input ranges over different bands of frequency and then patching the results together, though this reduces the speed of measurement, and the results are no longer simultaneous. There may also be steps seen at the edges of each frequency band as the integration time may be different in each case. The single sine technique does not suffer from this limitation since optimum voltage, and current ranges can be automatically selected at each frequency in the sweep.

Great care must also be exercised in the acquisition of data that is to be used for FFT analysis. In order to avoid problems with aliasing of frequencies (see Section 3.1.3.4 Digital Signal Processing for a discussion of this problem), it is essential to apply rigorous analog and digital filtering techniques, and the measurement sample rate must be sufficiently high (at least 2 times the maximum frequency of interest); otherwise, out-of-band signals (aliases) may appear in the analysis frequency range.

Sub-sampling (sometimes called under-sampling) techniques are sometimes used where the sample rate is many times lower than the frequency that is to be analyzed. This technique is not suited to FFT analysis as unwanted alias frequencies can easily appear in the analysis and lead to misinterpretation of data.

In summary, the single sine analysis technique is a pure technique that results in very stable, repeatable measurements and is able to reject noise and distortion from the cell. Speed improvements for this technique are available due to the introduction of DSP-based FRAs. The FFT technique is complementary to the single sine technique and gives very fast impedance results that are less affected by time variant cells and can give information about cell nonlinearity. However, if not applied with care, the FFT can sometimes be more susceptible to nonlinear effects, alias frequencies, noisy results, or dynamic range limitations. Systems that offer both techniques throughout the full frequency range of the instrumentation are able to extract the maximum information from test cells.

3.2.2 Electrochemical Impedance Measurement Systems

Electrochemical impedance tests usually investigate the interface between an electrode material and a solution (e.g., corrosion tests may investigate different coated metals in a salt solution, while battery/fuel cell tests may investigate different electrode materials in an electrolyte). Electrochemical impedance tests provide complementary information to that obtained from dc electrochemical techniques such as cyclic voltammetry, pulse voltammetry, ohmic drop analysis, and chronoamperometry.

3.2.2.1 System Configuration

Electrochemical impedance measurement systems used for the analysis of the ac properties of electrochemical cells typically consist of a potentiostat (sometimes called an electrochemical interface) together with an FRA or a spectrum analyzer or even a combination of the two. The potentiostat provides buffered connections to the cell under investigation together with circuitry for applying a controlled voltage or current stimulus and for the measurement of the dc properties of the cell. The FRA is connected through the potentiostat to the cell, and therefore the bandwidth of the potentiostat is a very important consideration for accurate high frequency analysis.

A PC running application software is typically used to provide control of the instrumentation, storage of data, and display of graphical results and detailed analysis functions (including access to equivalent circuit fitting and data analysis programs such as LEVM—refer to Section 3.3 Data Analysis). The instruments are connected to the PC via a standard interface such as GPIB (IEEE-488), USB, Ethernet, serial port (RS232), parallel port, or in some cases via a proprietary interface. The USB and Ethernet approaches are gaining popularity due to the low cost of connection to the PC (these interfaces are available in most PCs as standard or can easily be added at very low cost). High data transfer rates are available via Ethernet and USB. Ethernet also provides the possibility of distributing instrumentation and control PCs throughout a factory or laboratory, allowing data to be easily analyzed in a more comfortable environment well away from the corrosive chemicals and noisy equipment that may be associated with the experiment.

3.2.2.2 Why Use a Potentiostat?

The potentiostat is a very important part of an electrochemical impedance test system. The potentiostat consists of the following elements:

- A power amplifier that can supply or take power from a cell, for instance, when charging or discharging a battery or fuel cell
- One or more high input impedance voltage measurement reference inputs, usually connected to the cell via a standard RE
- A current measurement input connected to the WE on the cell
- A control loop that maintains the required voltage across the cell (when operating in potentiostatic control mode) or current through the cell (when operating in galvanostatic mode)
- Connections to an FRA to allow impedance analysis of the cell
- Bias rejection to allow the ac to be measured on a more sensitive range

One important capability of the potentiostat is to maintain the required dc conditions on the cell, while the FRA is performing the impedance (ac) analysis. The actual dc conditions required depend on the application. For tests on fuel cells, it may be necessary to set up a particular steady-state dc to investigate the impedance of the cell under load conditions. In other cases it may be necessary to run the impedance test at the “open-circuit” potential of the electrochemical cell, in which case the open-circuit voltage is measured and then held on the cell while the impedance test progresses (Figure 3.2.17). In other cases it may be required to impose a particular dc potential offset relative to the open-circuit potential of the cell to investigate the impedance under conditions that encourage a

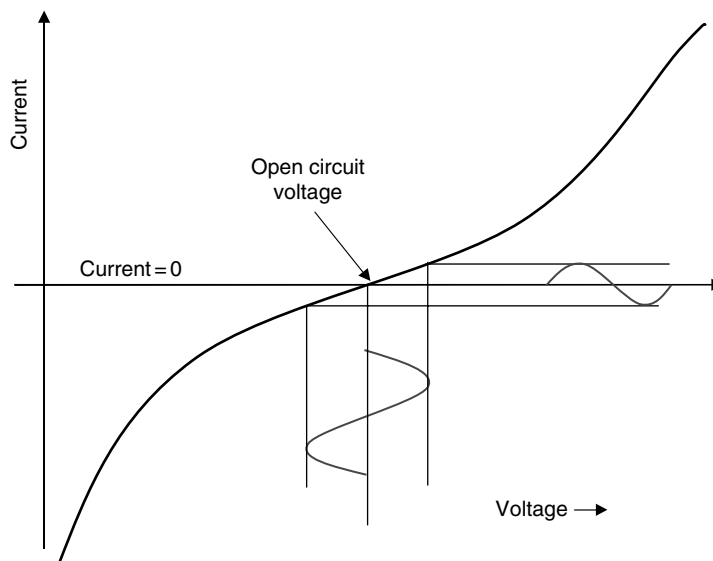


FIGURE 3.2.17 Setting up the DC conditions on the cell for an impedance test.

particular form of corrosion to take place. Whenever running impedance tests, it is very important to operate in a linear regime and under conditions of stability on the cell. If the cell changes significantly during the time taken to run the impedance test, the results taken at the start of the test (usually the high frequency part of the sweep) may not be consistent with the results at the end of the test (usually the low frequency data). This can cause strange impedance artifacts that, if the reason is not known, may easily lead to misinterpretation of the data. A simple test for stability is to repeat the impedance test to see if the results are consistent.

3.2.2.3 Multi-electrode Techniques

Some commercially available electrochemical impedance test systems have the ability to measure not only the overall impedance of a complete electrochemical cell but also the impedance contribution of various component parts of the cell, allowing, for example, direct comparison of different anode or cathode materials in a battery. Multi-electrode measurement techniques may also be used to investigate individual cells in a battery or fuel cell stack.

It is important to realize that some systems may only provide the use of auxiliary electrodes for dc voltage measurement (it is not possible to use these particular systems for the measurement of impedance from the auxiliary electrodes). Careful selection of equipment is therefore important if it is necessary to measure the impedance of parts of cells in this way.

For anode/cathode investigations on batteries or fuel cells, it is necessary to have extra connections built into the cell itself to allow connection to the auxiliary voltage inputs on the instrumentation. This provides separate measurement of the ac voltage drop across the anode, cathode, and separators. With modern measurement equipment, it is becoming possible to make simultaneous measurements of the overall battery impedance and of the individual electrodes within the cell using single sine or FFT techniques, as shown in Figure 3.2.18.

By combining ac voltage measurements from the auxiliary voltage inputs together with the measurement of the ac through the whole cell, it is possible to measure the impedance contribution of the anode, cathode, and impedance of the whole cell. By overlaying the results it is easy to see the contribution to the overall cell impedance that is made by the anode and cathode. Measurements from the main and auxiliary channels can be made simultaneously to ensure that the results represent a consistent data set.

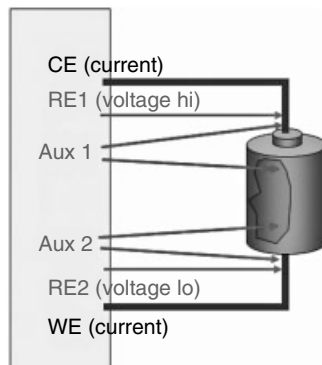


FIGURE 3.2.18 Auxiliary voltage measurements (measurement of electrodes in a cell).

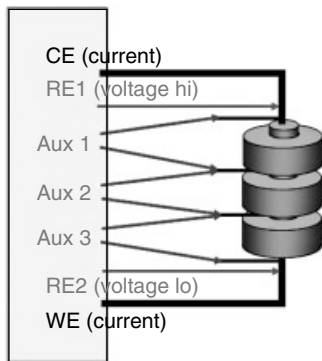


FIGURE 3.2.19 Auxiliary voltage measurements (measurement of individual cells in a battery).

For measurements of individual cells in a battery or fuel cell stack, the main channel connections are placed across the whole stack with the auxiliary electrodes connected across each individual cell allowing the overall impedance and the impedance of each cell to be investigated (Figure 3.2.19). This method of obtaining individual cell impedance measurements from the auxiliary voltage input signals, in combination with the charge/discharge facilities provided by the potentiostat for the standard cycling of the cells, provides early detection of bad cells in a stack. Power boosters and high voltage auxiliary channels can be added to investigate high voltage stacks.

3.2.2.4 Effects of Connections and Input Impedance

Connections to electrochemical cells are usually made via a potentiostat/galvanostat. There are particularly critical points on the cell where great care needs to be taken in the method of connection. Usually the CE is where the stimulus waveform is applied to the cell, and this is not a particularly critical part of the system; however, the points where voltage and current are measured are vital to the accuracy of the results.

In the case of voltage measurement as we saw earlier, it is critical that current that has passed through the cell does not “leak” into the voltage inputs since this can lead to errors in both current and voltage measurements. For this reason the reference inputs usually consist of very high input impedance and low capacitance buffer amplifiers. The method of connection of the voltage

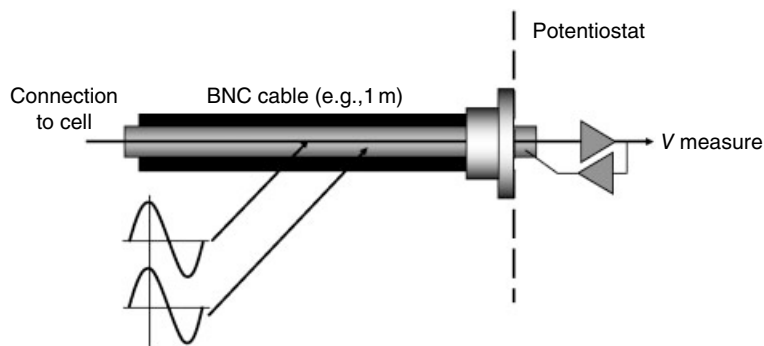


FIGURE 3.2.20 Driven shields (zero voltage drop between cable inner and shield).

measurement circuits to the point of interest in the cell is also critical. Typically potentiostats provide either “driven shield” voltage measurement connections to the cell or external voltage-follower buffer amplifiers (sometimes referred to as electrometers) that are positioned close to the measurement points in the cell. Using the latter technique, it is necessary to position electronics close to the cell that can be a disadvantage when performing temperature tests on the cell since the electronics may also be subject to temperature variations, which can lead to measurement errors or in extreme cases may damage the electronics. If however tests are only being performed at room temperature, this technique gives good results.

Using the driven shield technique, all of the electronics is positioned inside the potentiostat avoiding any problems of cell temperature affecting the measurement electronics. The driven shield technique ensures that whatever voltage signal is seen at the measurement point within the cell is accurately reproduced on the shield of the connection cable so that the voltage difference between the cable inner and shield is permanently maintained at zero volts (Figure 3.2.20). Therefore there is zero current flow between cable inner and shield. Using this technique, a cable that has a real capacitance of around 100 pF/m actually exhibits very low capacitance of the order of a few pF/m that allows accurate high frequency ac voltage measurements to be made on the cell.

For very sensitive measurements on very low impedance (or very high impedance) cells, it may be necessary to shield the cell from external interference using a Faraday cage that is connected to the instrument ground, and it may also be necessary to take particular care regarding the placement of cables to avoid electrical interference and cross-talk between cables.

3.2.2.5 Verification of Measurement Performance

Usually equipment manufacturers supply a known test circuit to verify the performance of the equipment. The test circuit is typically a combination of resistors and capacitors that give a known impedance frequency response curve. Of course this only tests the particular voltage and current ranges that are appropriate for the circuit in the test box. It may well be the case that a particular system performs well for that level of impedance but has problems when measuring other cells. Batteries are difficult to simulate in a test box since they often have very low impedance and also have a dc cell voltage. The impedance response of the battery also changes dramatically at different stages of partial charge/discharge, so it is difficult to investigate the performance of the equipment for these tests. However, tests can be performed on accurate low value resistors or large capacitors to simulate different aspects of the battery in a more controlled way and gain an insight into the measurement performance of the system. Of course the voltage/current rating of the components must be compatible with the tests that are to be performed; otherwise, result accuracy could be affected or the test component may fail or even explode.

Other tests that are of great value are to check the stability and linearity of the cell under the imposed test conditions. The stability may easily be checked by repeating the impedance tests on the same cell

within a short period of time and in the same environmental conditions to check if the impedance results are repeatable and stable. If this is not done, time can be wasted in trying to interpret artifacts that are simply due to an unstable cell. In addition, it is very important to test for cell linearity by referring to the tests using harmonic or FFT analysis that were suggested earlier.

3.2.2.6 Floating Measurement Techniques

Most modern potentiostats allow measurements on grounded devices such as pipelines, metal storage tanks, and even laboratory tests using grounded autoclaves or similar devices. For measurements to be properly made under these difficult conditions, it is necessary for the instrumentation to have “floating” measurement capability. In this case, the internal circuitry in the potentiostat is referred to an internal floating ground rather than actual ground. For measurements on grounded structures (refer to Figure 3.2.21), the instrument is set to “floating” measurement mode (usually by software control or by a manual switch on the unit), and the CE is connected directly to the grounded structure, while the WE that measures current flowing through the structure is allowed to “float” to the required voltage under the control of the potentiostat. In this case the whole structure becomes a large CE that supplies the required test current to the WE where it is accurately measured. The WE is controlled by the potentiostat and floats to an offset voltage relative to the grounded CE in order to supply the required current (if operating in current controlled mode) or offset potential (when operating in voltage controlled mode). In the case of a non-floating measurement system, where CE is instead set to a particular voltage relative to ground while the WE is held close to ground potential (non-floating), much of the current supplied by the CE goes directly to ground via the structure under test, completely avoiding (short circuiting) the WE current measurement input and leading to very high current levels and overloads in the system. The floating measurement capability is therefore extremely important for some applications.

Floating measurements are also used to avoid ground loops where equipment and test cell are grounded at different points, leading to noise and interference in the measurements. If the cell is grounded but the equipment is floating, then this problem can be avoided.

It has been known for earth connections to be removed from non-floating systems to convert them into floating systems. This is a very dangerous practice and is not recommended from the safety point of view since the whole equipment could become “live,” which could lead to injury or fatalities.

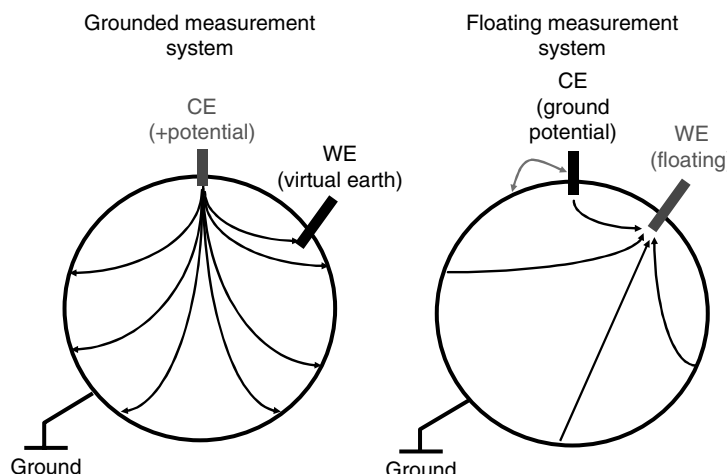


FIGURE 3.2.21 Grounded and floating measurement systems.

3.2.2.7 Multichannel Techniques

There are many applications where multichannel impedance measurement systems are particularly useful. The throughput of testing in a laboratory can be increased either by the use of multiplexed systems where multiple cells are connected and are automatically tested in sequence by, for example, a potentiostat and FRA or by the use of true parallel measurement systems where each cell has access to its own potentiostat and FRA. The parallel system of course is the more efficient method since all cells can be tested simultaneously; however, the equipment required for this is more expensive since there are separate potentiostats and FRAs on every channel. The introduction of multichannel systems however has seen a reduction in cost of these parallel measurement systems since the PC, software, power supplies, communications, and casework are shared between a number of channels in the system.

Multichannel systems also allow more advanced tests to be performed, for example, testing a segmented fuel cell where one electrode has been partitioned to investigate different electrode materials or to do impedance mapping of the fuel cell electrode. Different materials can also be simultaneously screened in a common corrosive environment using a multichannel potentiostat system with several WEs, one CE and an RE.

Multichannel potentiostats can often be connected in parallel to provide tests on high power devices when needed while allowing the flexibility to be used as a multichannel system on lower power devices by reconfiguring the connections to the cells.

3.2.3 Materials Impedance Measurement Systems

Whereas electrochemical tests usually investigate the interface between electrode material and solution (e.g., a metal in salt solution for corrosion tests or an electrode in an electrolyte for battery tests), materials impedance tests tend to focus on the properties of the material in isolation and the electrodes are simply a method for providing electrical contact to the material. The material under investigation might be a solid (ferroelectric, piezoelectric, ceramic, polymer, semiconductor, OLED, etc.) or a liquid (e.g., liquid crystal materials, oils, gels, pharmaceutical products, etc.).

The impedance of the material may need to be investigated as a function of applied dc voltage, for example, semiconductors are very low impedance (conductors) in their ON state and extremely high impedance (dielectrics) in their OFF state. It is important to characterize such devices at a range of points in their polarization profile to investigate trap states, charge carrier mobility, and ON/OFF thresholds.

In other cases the impedance properties of the material may be under investigation as a function of temperature (e.g., ceramic materials in high-temperature fuel cells or satellite materials over a wide range of temperature), and materials that are used in insulator applications are investigated using impedance techniques close to their breakdown potential by the use of high voltage amplifiers.

3.2.3.1 System Configuration

Typical commercially available materials impedance test systems consist of either a self-contained impedance analyzer that is capable of measuring the ac voltage drop across a material and the ac current through the sample. For very high impedance materials, a more specialized system made up of a very sensitive ultrahigh resolution I-E converter interface unit connected to a frequency response or impedance analyzer is required. The measurement principles are the same in both cases: an ac stimulus signal is applied to the sample under test, the ac voltage and current are both measured, and the impedance of the sample is obtained. A PC is used to control the instrumentation and collect impedance results for storage on disk and for display in graphical form. Equivalent circuit fitting routines such as LEVM are widely used for further analysis of the impedance results.

Self-contained impedance analyzers are usually connected to the sample using 2T or 4T techniques depending on the impedance of the sample to be measured. Specialized sample holders are available from various manufacturers that can be used for measurements of liquid and solid materials samples. Self-contained impedance analyzers usually cover measurements of medium to low impedance samples (100 M Ω to 10 m Ω being a typical measurement range). Ultra-sensitive amplifiers are often added to the

system for the investigation of very high impedance materials, and these typically offer an impedance range of tens of ohms to over $10^{14} \Omega$. The frequency range of medium frequency impedance analyzers and FRAs is typically from tens of μHz to tens of MHz. RF impedance analyzers are also available to extend the frequency range up to tens of GHz using waveguide sample measurement techniques. The latest-generation systems allow impedance and time-domain measurements to be combined, for example, using pulses, to activate charge carriers followed by impedance/capacitance to obtain mobility measurements to characterize the charge carriers.

3.2.3.2 Measurement of Low Impedance Materials

The same arguments apply to testing low impedance materials as those for testing low impedance electrochemical cells. It is very important to use 4T test techniques to ensure that the impedance of the connection cables does not invalidate the measurement of the material itself. Typically a stand-alone 4T impedance analyzer is used for this type of measurement. A Faraday cage may also be required to screen very low impedance samples against interference since the voltage levels measured on low impedance samples is often very small (maybe in the millivolt region).

3.2.3.3 Measurement of High Impedance Materials

For measurement of high impedance insulator or dielectric materials, 2T test connections to the sample are generally used. This is because the impedance of the sample is much greater than the impedance of the test cables; therefore, any errors introduced by the cables are unlikely to significantly affect the sample measurement results. This is true at low frequency in particular, but at high frequency specialist techniques are often needed to minimize errors due to cables, and these will be discussed later in this section.

It is important in many applications to have very sensitive current measurement capability for measurements at low frequency ($<1 \text{ Hz}$) where the impedance of many materials becomes very high. This is especially true for ceramic and other insulator materials.

For the measurement of high impedance (or ultrahigh impedance insulator) materials, it is often necessary to add a specialized materials test interface into the system (Figure 3.2.22). The impedance interface typically comprises a very sensitive virtual earth I-E converter capable of resolving current in the sub pico-amp region ($<10^{-12} \text{ A}$). This type of measurement system is able to measure very high impedance (insulator) materials in the range up to $100 \text{ T}\Omega$ ($10^{14} \Omega$), allowing characterization of ceramic, polymer, and ferroelectric materials. The interface is connected to a frequency response or impedance analyzer that provides the analysis of the ac voltage across the material and the signal output of the I-E

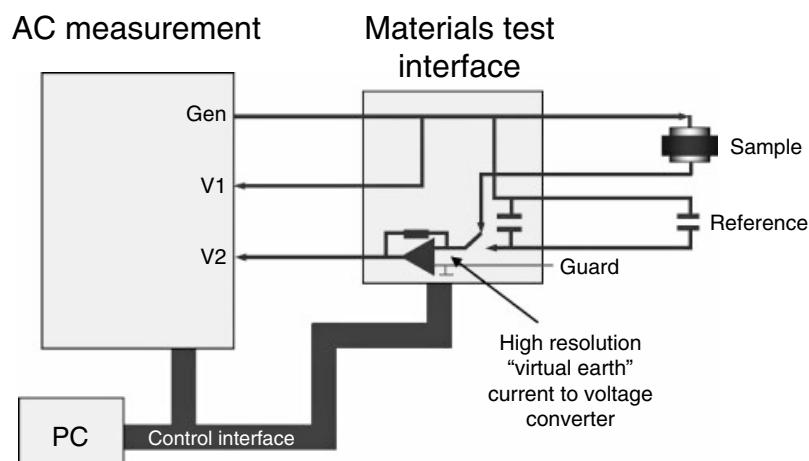


FIGURE 3.2.22 Connection of AC measurement unit and materials test interface.

converter, which is proportional to the current flowing through the sample. The impedance of the sample can then be calculated. For measurement of ultrahigh impedance samples, a Faraday cage is again recommended in order to screen the sample from interference. The Faraday cage can usually be connected to the screen of one of the sample connection cables since this is usually connected to earth inside the instrument.

3.2.3.4 Reference Techniques

Impedance tests on materials are often performed over a wider frequency range than those on electrochemical cells. In particular, measurements at the high frequency end of the spectrum ($>1\text{ MHz}$) are more difficult to perform with high accuracy, and measurement errors due to cables and instrumentation become more pronounced in this frequency range, requiring specialized reference and normalization techniques to be used to reduce or eliminate these effects and obtain accurate and repeatable results.

Impedance interfaces often provide the facility for automatically switching between measurements of the sample to be measured and measurements of a low loss calibrated reference capacitor (see Figure 3.2.22). An ideal reference capacitor would have a completely "flat" response (constant capacitance) across the entire frequency range. This "ideal" capacitor cannot be achieved in reality since there will always be some parallel resistance in the capacitor even though this can in practice be an extremely high value. However, the difference between an ideal and non-ideal capacitor is sufficiently small for most purposes, and the reference capacitor is a very useful tool that can be used to quantify errors due to cables and instrument measurement errors. The deviation of the capacitor from its ideal response due to cables and measurement errors is measured and recorded, and this deviation is used to apply a correction to the measured results from the material under test.

Materials test interfaces often have a selection of reference capacitors available inside the unit that can be automatically switched to match a wide range of different materials samples. Measurement is usually taken of the sample and then the closest available reference capacitor (of similar capacitance value) is chosen for the reference measurement. In this case the measurements can be taken on the same voltage, and current ranges and any errors due to instrumentation or connection cables can be virtually eliminated.

The internal reference capacitors can even be changed automatically as the sweep progresses to provide the best reference capacitance matching when measuring dispersive materials where the measured capacitance of the material changes significantly during the sweep.

Usually external reference capacitors can be connected to the interface, allowing an ultra-stable reference to be used if one is available. This also provides the best matching of cable errors since the same type of connection cables can be used on the sample and on the reference. The reference technique is especially useful when using external amplifiers for high voltage tests though the reference capacitor must be chosen with care to withstand the applied voltage level.

3.2.3.5 Normalization Techniques

An alternative technique is to use normalization to improve measurement accuracy. In this case the capacitance of the sample is measured across the range of frequency of interest. A capacitance value is then chosen to most closely match the measured capacitance of the sample. The sample is removed from the sample holder, converting it into an empty cell (air) capacitor, and the spacing of the sample holder electrodes is adjusted until the same capacitance value is measured. The same frequency sweep is then performed on the "empty cell" recording results at the same list of frequencies as the original sweep on the sample and also recording the dimensions of the empty cell. The "empty cell" results may then be used to normalize the measured results from the sample.

The "empty cell" measurement may only need to be taken once if a series of samples of similar capacitance are required to be measured, saving valuable test time.

3.2.3.6 High Voltage Measurement Techniques

High voltage amplifiers are sometimes added to materials test systems to allow impedance testing at close to the dielectric breakdown of the material under test. Amplifiers can provide ac or dc stimulus signals at well beyond 1 kV. Care must be taken to attenuate the signals back down to within the measurement voltage range of the equipment in order to avoid damage to the instrumentation. Usually current limited power supplies are required to ensure that high current does not enter the equipment especially in the case when the sample breaks down.

3.2.3.7 Temperature Control

Some impedance test systems provide integrated temperature control capability that is included to characterize the way that materials change with temperature. There are a wide range of temperature controllers available from various manufacturers, and these can often be coupled with furnaces for very high-temperature tests to $>1000^{\circ}\text{C}$ or with nitrogen or helium cryostats for low-temperature testing of the sample. Cryostats and furnaces provide closed loop control of temperature using temperature sensors positioned close to the sample. The temperature controller compares the temperature being reported by the sensor with the required temperature and automatically adjusts the power supplied to a heater coil in order to achieve the desired sample temperature (Figure 3.2.23).

In the case of cryostats, liquid nitrogen or helium is used to cool the sample, and a heater coil is used to raise the temperature of the sample relative to the base temperature that would otherwise be set by the nitrogen or helium. It is preferable that the cryogen does not come into contact with the sample to ensure that there is no contamination or condensation on the sample, which may in some cases affect the measurement results (can cause bubbling of the sample surface). It is also preferable for the sample chamber not to be filled with air to avoid possible oxidation problems. For the previous reasons it is often the case that the sample chamber in the cryostat is filled with an inert gas that inhibits oxidation.

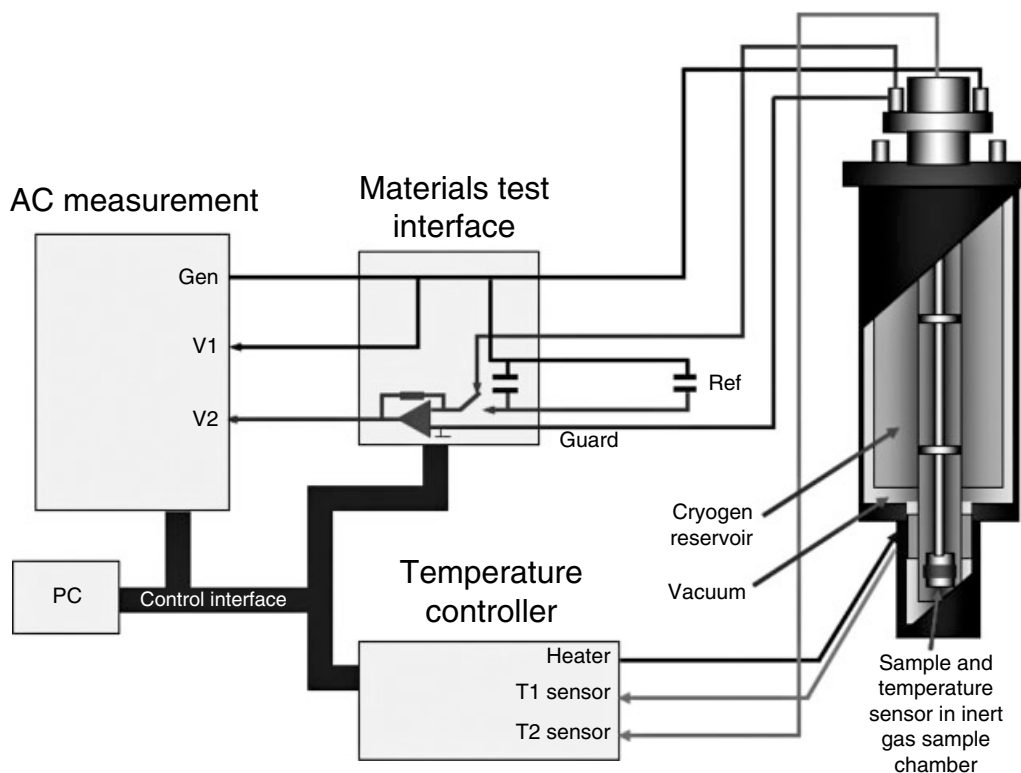


FIGURE 3.2.23 Cryostat measurement set-up.

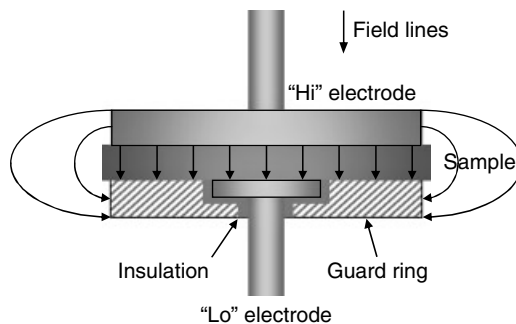


FIGURE 3.2.24 Sample holder with guard ring.

There are often two temperature sensors in the system; one is positioned close to the heater coil and provides very stable control of temperature since there is immediate feedback of any temperature changes in the coil. The other is positioned close to the sample in order to provide an accurate record of the actual sample temperature (this may be slightly different from the heater coil temperature).

3.2.3.8 Sample Holder Considerations

The sample holder is also a very important part of a materials impedance measurement system. Fringing and stray capacitance effects can easily give measurement errors if inappropriate sample holders are used. Tests on dielectric (or high impedance) materials are often performed using 2T connections, and for the most accurate results, sample holders that have guard electrodes are used in order to minimize fringing effects. Ideally, field lines should be parallel throughout the sample for accurate measurements, but Figure 3.2.12 shows how the field lines at the edge of the sample become distorted leading to measurement errors. For this reason, sample holders have been specifically developed that provide an earthed guard ring surrounding the actual measurement electrode (Figure 3.2.24). The central electrode is connected to the instrument current measurement input, while the guard ring is connected to the shield of the current measurement input that is typically connected to earth inside the instrument. The current measurement circuit uses a "virtual earth" I-E converter, which maintains the central electrode on the sample holder close to earth potential, while the guard electrode is connected to actual earth. Since there is no potential difference between the guard and the measurement electrode, the field lines are kept parallel and evenly distributed throughout the part of the sample that is to be measured. The current that passes through the edge of the sample that experiences fringing and stray capacitance effects simply goes direct to earth and is not measured, giving very accurate measurement of current through the central part of the sample. A general rule is that the width of the guard ring should be at least two times the thickness of the material in order to avoid fringing problems.

The same techniques can be applied to liquid sample holders and also to sample holders that are used in high- or low-temperature tests as part of a furnace/cryostat system.

3.3 DATA ANALYSIS

3.3.1 Data Presentation and Adjustment

3.3.1.1 Previous Approaches

In this section we shall first summarize a number of previous methods of data presentation and then illustrate preferred methods. A common method of showing data has been to plot the imaginary parts (or sometimes their logarithms when they show considerable variation) of such quantities as Z , Y , M , or ϵ versus ν or $\log(\nu)$. More rarely, real parts have been plotted versus ν . Such plotting of the individual parts

of Z or M data has itself been termed *impedance* or *modulus spectroscopy* (e.g., see Hodge *et al.* [1976], Almond and West [1983b]). As mentioned earlier, however, we believe that this approach represents only a part of the umbrella term *impedance spectroscopy* and that complex plane and 3-D plots can much better show full-function frequency dependence and interrelationships of real and imaginary parts.

Let us consider some of the previous plots qualitatively for the simplest possible cases: a resistor R in parallel or in series with a capacitor C . Let the single time constant $\tau \equiv RC$ and define the Debye function $D(\omega\tau) = D' - jD'' = [1 + j\omega\tau]^{-1}$, which leads to a semicircle in the complex plane. $D'' = (\omega\tau)/[1 + (\omega\tau)^2]$. A plot of this functions versus ω yields a peak at $\omega_m = \tau^{-1}$ and an eventual drop-off proportional to ω at $\omega \ll \omega_m$ and to ω^{-1} at $\omega \gg \omega_m$. Thus the final slopes of $\log(D'')$ versus $\log(\omega\tau)$ are +1 and -1. It is easy to show that for the parallel connection, $Z = RD(\omega\tau)$, $-Z'' = RD''(\omega\tau)$, $M = (C_c/C)(j\omega\tau)D(\omega\tau)$, and $M'' = (C_c/C)D''(\omega\tau)$. For the series connection, one finds $Y = (j\omega C)D(\omega\tau)$, $Y'' = GD''(\omega\tau)$, $\epsilon = (C/C_c)D(\omega\tau)$, and $\epsilon'' = (C/C_c)D''(\omega\tau)$. These results demonstrate that under different conditions $-Z''$, M'' , Y'' , and ϵ'' all exhibit $D''(\omega\tau)$ response. Further, in some sense the pairs Z and $M = (j\omega C_c)Z$ and ϵ and $Y = (j\omega C_c)\epsilon$ are closely related. Real materials often do not lead to IS results of the simple $D(\omega\tau)$ semicircle form, however, but frequently involve a distorted or depressed semicircle in the complex plane that may arise from not one but several relaxation times or from a continuous distribution of relaxation times. Under such conditions, curves of $-Z''$ versus ν , for example, are often appreciably broader than that following from $D(\omega\tau)$.

It has been customary in much past work to plot $-Z''$ or M'' versus ν and either to not give estimates of parameters, such as R and C , leading to the response or to estimate them roughly by graphical means. It is often found that the frequency at the peak, ω_m , is at least approximately thermally activated. But this frequency involves both R and C , quantities that may be separately and differently thermally activated. Thus instead of using the composite quantity ω_m , which may be hard to interpret properly, we believe it to be far preferable to find estimates of all the parameters entering into an equivalent circuit for the situation. As we shall see, such estimates can best be obtained from CNLS fitting.

One other type of plotting has been very common in the dielectric field in earlier years, namely, plotting of $\tan(\delta)$ versus ν , where $\delta = -\theta = \tan^{-1}(\epsilon''/\epsilon')$. Thus $\tan(\delta) = \epsilon''/\epsilon'$. Since energy loss is proportional to ϵ'' and energy storage to ϵ' , δ is often termed the *loss angle*. When ϵ is given by Eq. (18) in Section 2.2 with $\psi_\epsilon = 1$, so there is only a single time constant, and $D(\omega\tau)$ response is involved, the simplest case of interest, one readily finds that

$$\tan(\delta) = \frac{(\epsilon_s - \epsilon_\infty)(\omega\tau)}{\epsilon_s + \epsilon_\infty(\omega\tau)^2} \quad (1)$$

which again gives a Debye-type peaked curve, with maximum value $(\epsilon_s - \epsilon_\infty)/[2\sqrt{\epsilon_s\epsilon_\infty}]$ occurring at $\omega\tau = \sqrt{\epsilon_s/\epsilon_\infty}$. But here again there is no longer any good reason to plot $\tan(\delta)$ versus ν when much more about the total response can be learned from a 3-D plot of ϵ or Y . Incidentally, the use of $\tan(\delta)$ plots is entirely absent from a recent compendium of dielectric theory and behavior (Böttcher and Borde-wijk [1978]).

3.3.1.2 Three-Dimensional Perspective Plotting

It should be clear from the previous discussion that we strongly believe that all IS data should be examined and presented using three-dimensional perspective plotting. One then automatically obtains the plots of real and imaginary parts as projections in the coordinate planes, a normal complex plane plot in the real-imaginary plane and an overall 3-D curve showing the response in proper 3-D perspective. Sometimes when the variation of the quantity plotted is extreme, it is desirable to replace the real and imaginary axes by $\log(\text{real})$ and $\log(\text{imaginary})$ axes.

A typical simple circuit is shown at the top of Figure 3.3.1, and 3-D plots for its impedance response appear in the middle and bottom of the figure. The two 3-D graphs are for different viewing angles. Note that a $\log(\text{frequency})$ axis has been added at right angles to the ordinary $-\text{Im}(Z)$, $\text{Re}(Z)$ complex plane plot, allowing frequency response to appear explicitly. We shall sometimes use f and sometimes ν to

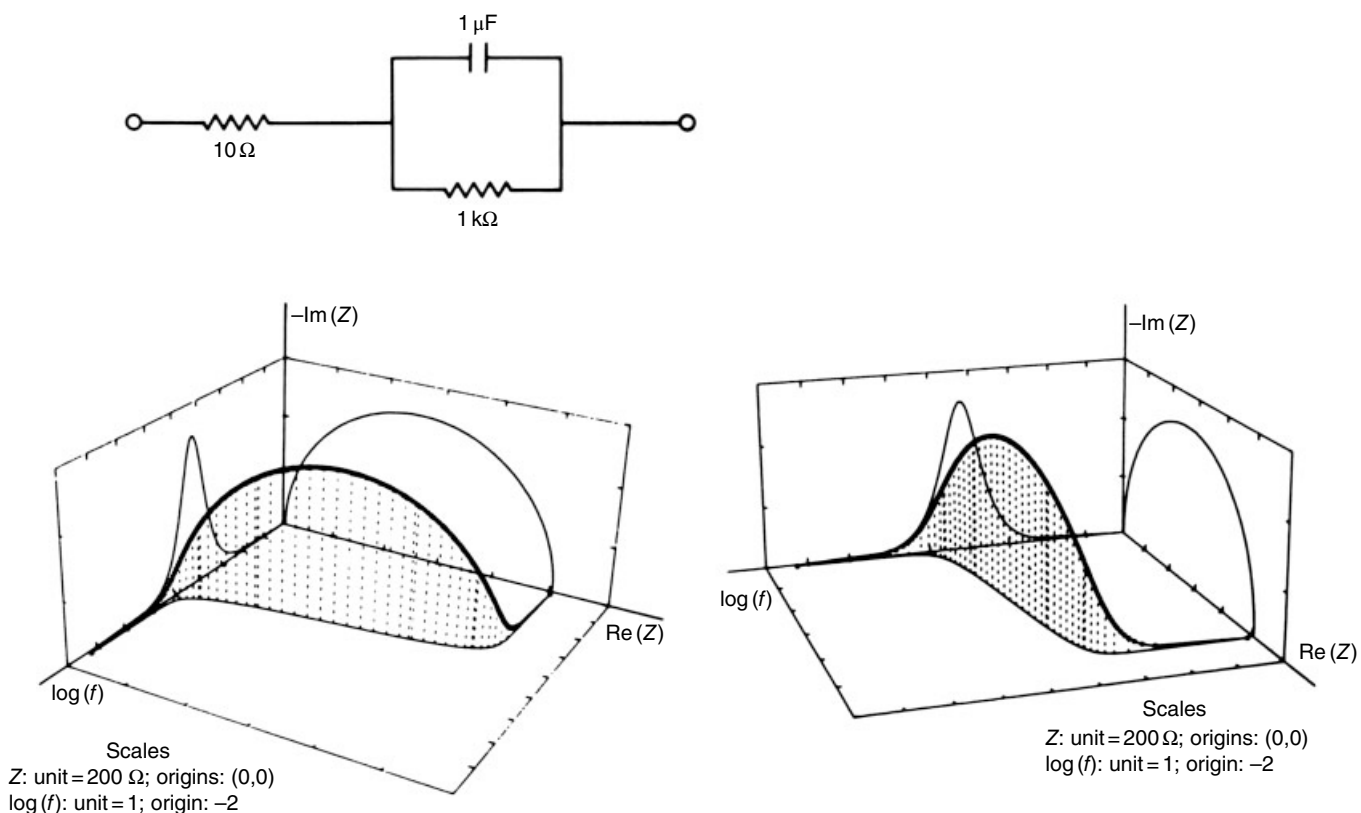


FIGURE 3.3.1 A simple circuit and 3-D plots of its impedance response. The 3-D plots are for different viewpoints.
Source: Macdonald *et al.* [1981]. Reproduced with permission of Elsevier.

indicate frequency in the succeeding graphs. The heavy curve in Figure 3.3.1 is the 3-D response line, its vertical projections to the $\log(f)$ - $\text{Re}(Z)$ plane are shown dotted, and the curve in the complex plane plot is actually a semicircle here.

There is an alternative to the usual 3-D plotting of Z in rectangular form which we have been discussing. Instead, we may express a quantity such as Z or M in polar form, involving, say, $|M|$ and θ . If one defines the three axes in a 3-D plot as $(X, Y, Z) = (\theta, |M|, \log(\nu))$, one will obtain a different looking 3-D plot and different projection curves. If the $|M|$ axis is replaced by $\log |M|$, one even has a 3-D Bode plot. Note that $\ln(M) = \ln[|M| \exp(j\theta)] = \ln |M| + j\theta$, a complex number, so the $\ln |M|, \theta$ plane is a consistent complex plane, whereas that involving M and θ is not since M and θ do not form the parts of a complex number. Thus, there is some reason to prefer the second of these approaches to the first. The use of the projection curves $\ln |Z|$ versus ν and θ versus ν has been proposed and encouraged recently by Cahan and Chen [1982]. Although there may be instances where both the standard rectangular and polar 3-D representations are worthwhile plotting and examining, we believe that the standard rectangular one with either real and imaginary axes or log axes is usually quite sufficient and shows the entire frequency response of the function considered in a way that yields projection curves of the kind, which have been widely used in the past and about which there exists a larger body of interpretative knowledge.

There still remains the problem of which ones of the four functions Z, M, Y , and ε to plot in 3-D. Certainly, one should always plot that one of these, which was directly measured. If, in addition, all four are plotted and examined, a good general rule, emphasis should be put on the one (or ones) that show the most detail and cover the entire frequency range with best resolution.

We shall illustrate the previous by showing results for IS impedance data for a single-crystal Na β -alumina with blocking gold electrodes, measured at $T = 83$ K. These data (Almond and West

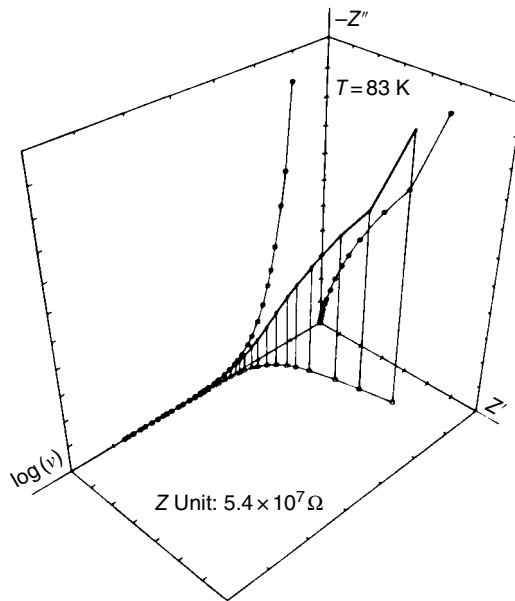


FIGURE 3.3.2 A 3-D plot of the impedance- $\log(\nu)$ response of single-crystal Na β -alumina at $T=83$ K.
Source: Macdonald and Cook [1985]. Reproduced with permission of Elsevier.

[1981], Bruce *et al.* [1982]) were kindly provided by Dr. West [West 1983], private communication to Macdonald]. This set, and data for eight higher temperatures, have recently been reanalyzed with CNLS fitting (Macdonald and Cook [1984, 1985]).

Figure 3.3.2 shows a 3-D impedance plot of the data, using straight lines between data points. Solid dots are employed for the data points themselves and open circles for their projections in the three planes. The $\log(\nu)$ scale starts at 1 here, and in the succeeding plots, and its scale interval (between tick-marks) is always also 1. The zero points of $-Z''$ and Z' occur at the origin. Three important conclusions may be drawn from these results. First, it is clear that much of the higher-frequency data are too small to be adequately resolved in this plot. Second, it seems likely that the lowest-frequency point is in error. Third, although this anomaly shows up clearly in the 3-D curve and in the complex plane curve, it is entirely absent from the $-Z''$ versus $\log(\nu)$ and the Z' versus $\log(\nu)$ projection curves. Were these the only curves plotted, as would often be the case in the absence of 3-D plotting, the anomaly would not be discovered. More 3-D plots are presented in Section 3.2.3.5.

3.3.1.3 Treatment of Anomalies

What should one do about anomalies of this kind, points that do not seem to lie close to a smooth curve? First, if the experiment can be repeated, that should be done, and averaged or best data used. In this instance, measurement at a few more frequencies between the present lowest and next lowest point would yield intermediate points, which would help clarify whether the last point is badly off or not. If the experiment cannot be repeated, then outliers of appreciable magnitude, such as the lowest-frequency point in the present plot, should be omitted (or weighted very low) in subsequent CNLS fitting.

Figure 3.3.3 presents a 3-D log-impedance plot of the same data. It has the virtue of allowing all the data to appear with the same relative resolution, but it clearly reduces anomalies. Although we could show the higher-frequency data alone on a separate regular 3-D plot to achieve better resolution, it turns

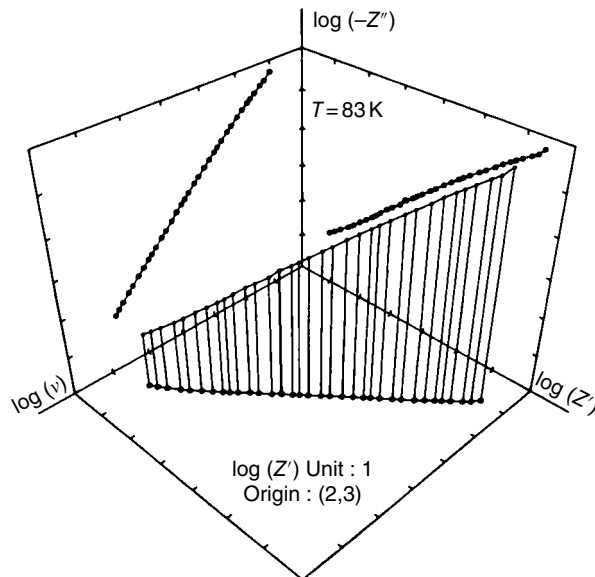


FIGURE 3.3.3 A 3-D plot of the same data as that of Figure 3.2.2, but with logarithmic transformation of the impedance. *Source:* Macdonald and Cook [1984]. Reproduced with permission of Elsevier.

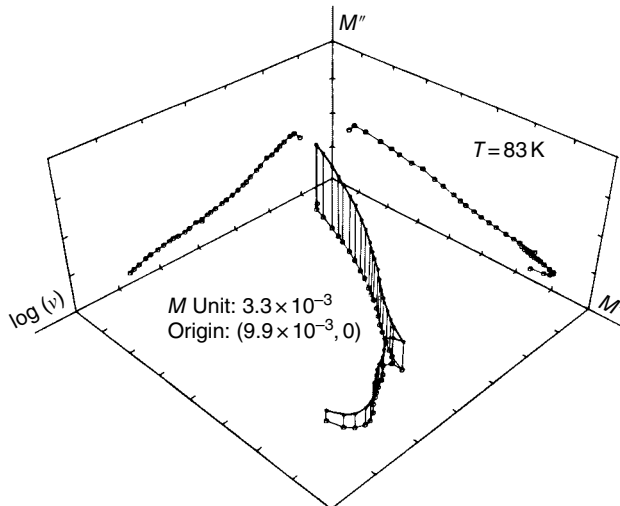


FIGURE 3.3.4 A 3-D modulus function plot of the $\text{Na } \beta\text{-alumina}$, $T = 83\text{ K}$ data. Here $M = j\omega C_c Z$. *Source:* Macdonald and Cook [1985]. Reproduced with permission of Elsevier.

out for the present data that a 3-D M plot (Figure 3.3.4) covers the full data range with adequate resolution. Here we see two more important anomalous regions not apparent on the earlier curves or in the papers of Almond and West. The one in the middle arises (West [1983], private communication to Macdonald) from overlapping data taken with two different measuring devices, which evidently gave inconsistent results in their regions of overlap. This anomaly only shows up clearly in the 3-D curve and in the M' versus $\log(v)$ curve. It was apparently not recognized until the present 3-D M plotting was carried out (Macdonald and Cook [1984]). In this instance, the plot shows that it would certainly

have been desirable to recalibrate the measuring instruments and repeat the experiment. Also, there is a probable anomaly for the highest-frequency three points. Although M plots emphasize high frequencies as compared with Z plots, there is no physical reason to believe that M' should begin to decrease at high frequencies (Macdonald and Cook [1984]), and it would be difficult to justify putting in elements in a fitting equivalent circuit that would cause it to do so. Therefore, in subsequent CNLS fitting of these data, at least the highest-frequency three points should be omitted.

Thus far we have recommended that when appreciable outliers or other anomalies appear in IS data, the experiment be repeated one or more times, or, when this is impractical, particularly anomalous points be omitted. But there is one further procedure that has often been found useful in other areas and could be applied here as well. This procedure is smoothing; it should, however, only be carried out after the averaging and pruning mentioned previously. All IS frequency data curves should, ideally, follow smooth curves with no abrupt changes in slope, except at possibly sharp cusps where two arcs join each other in the complex plane (see, e.g., Figure 1.3.1e). Even here no sharp change is present unless the processes represented by the two arcs occur in widely separated frequency regions, and even then it is not present in the 3-D curve itself.

When large anomalies have been eliminated, it is still often valuable to reduce the remaining smaller deviations (noise, experimental error) from a smooth curve by smoothing. The resulting smoothed data will then generally lead to more accurate estimates of the parameters involved in a CNLS fitting. There are many methods available for smoothing. We suggest that the holistic approach of smoothing using B-splines calculated by a least squares approximation would be particularly appropriate for the type of complex data obtained in IS (see de Boor [1978]). Unfortunately it does not yet seem practical to apply this procedure to both real and imaginary parts simultaneously, as would certainly be most appropriate; instead, one would smooth, say, Z' versus ν [or possible $\log(\nu)$] and Z'' versus ν results separately and then recombine the results to obtain $Z(\omega)$. This procedure would have another virtue. Besides producing an analytic approximation to the Z data, it would yield $\partial Z / \partial \nu$ results with no further calculation. These results, now expressed in analytic form, in turn would simplify CNLS fitting of the smoothed $Z(\omega)$ data to a specific model or equivalent circuit. Much work still remains to be done to develop this approach, which could, in fact, be incorporated as an optional initial part of a CNLS fitting program. It may sometimes prove useful, when major anomalies (which cannot be directly remedied) appear more evident in M or Y 3-D plots than in the Z plot, to carry out the actual smoothing on the transformed data and then convert the smoothed Z for use in CNLS fitting.

3.3.2 Data Analysis Methods

3.3.2.1 Simple Methods

When nonoverlapping semicircular arcs appear in, say, the impedance plane, one can directly estimate the associated R and C values from the left and right intercepts of the arc with the real axis and the value of ω at the peak of the arc, $\omega_m = (RC)^{-1}$. This procedure is quite adequate for initial estimates, but it yields no uncertainty measures for the parameters and does not check that the frequency response along the arc is consonant with that for an R and C in parallel. Further, experimental arcs rarely approximate exact semicircles well. There have been many graphical methods proposed for the analysis of impedance and dielectric data (e.g., Cole and Cole [1941], Vetter [1967], Macdonald [1974a, b], Böttcher and Bordewijk [1978]). These methods often consist of plotting some function of the data versus some function of frequency with the expectation of obtaining a straight line whose parameters may be related to the desired parameters of the equivalent circuit. Although these parameters may be estimated from the straight line by ordinary least squares fitting, this is not usually necessary if the estimates are to be used as initial values in subsequent CNLS fitting. Often subtraction of the effects of some estimated parameters is used to help in the estimation of further parameters. But subtractive methods are notoriously inaccurate. Again, all quantities are usually estimated without using all the available data simultaneously and without yielding uncertainties.

An improved geometrical, iterated–subtractive curve fitting method for resolving two or more overlapping arcs (which may be depressed) has been described by Kleitz and Kennedy [1979] and has been

further developed and automated by Tsai and Whitmore [1982]. An algebraic method of estimating parameters for systems that exhibit pseudoinductance (i.e., negative capacitance and resistance) and lead to an arc in the first quadrant of the impedance plane followed by an arc in the fourth quadrant has been proposed by Macdonald [1978c] (see also Macdonald and Franceschetti [1979b]). Finally, a sophisticated least squares method for finding the best circle through a set of data points in the plane appears in Macdonald *et al.* [1982b]. For obtaining initial parameter estimates, the simple methods described in Section 1.3 are usually sufficient.

3.3.2.2 Complex Nonlinear Least Squares

None of the previous methods uses all the data simultaneously, and they are often restricted to the analysis of limited situations (e.g., two possibly overlapping arcs). Nevertheless, when applicable, these methods are useful for initial exploration of the data and for initial parameter estimates for use in CNLS fitting. The much more general and powerful method of complex nonlinear least squares was first applied to IS in the work of Macdonald and Garber [1977], and further discussion of the method and demonstrations of its high resolving power and accuracy appears in Macdonald *et al.* [1982b]. The very flexible and general computer program for weighted CNLS fitting described herein is available at nominal cost from Macdonald. Later, a somewhat similar CNLS program was developed by Tsai and Whitmore [1982], but it does not include the very important feature of allowing arbitrary or analytical weighting of the data and has no built-in procedure for avoiding or recognizing local minima in the sum of squares to be minimized.

Why should one be interested in using complex nonlinear least squares fitting? After all, as already mentioned, the KK relations (Macdonald and Brachman [1956]) ensure that if one knows the real or imaginary part of a minimum-phase function over all frequencies, one can calculate the value of the other part at any frequency. This may suggest to the reader that ordinary nonlinear least squares fitting of data for either the real or imaginary part versus ν should be sufficient. But we never have data over all frequencies, and all experimental data are contaminated with error. Thus, application of the KK relations to the real or imaginary part of actual experimental data often does not allow the measured values of the other part (which contain errors) to be calculated very closely. It therefore appears reasonable to attempt to fit all of the data simultaneously to a given model, a model that involves a set P of unknown parameters (e.g., circuit elements), which may enter nonlinearly in the formula for the measured function of frequency, impedance, admittance, and so on. Although the real and imaginary parts of this physically realizable function are connected in a holistic, averaged way with each other through the KK relations, it is usually a good approximation to assume that the random (nonsystematic) errors in each of these quantities are uncorrelated with each other. Since practical fitting models nearly always are minimum phase and thus satisfy the KK relations, the achievement of a good CNLS fit of data to the model automatically ensures that the KK relations hold, and it is thus unnecessary to carry out the lengthy integrations necessary to check KK satisfaction directly. When no appropriate mathematical model is available, however, CNLS fitting cannot be used. In such cases, KK analysis turns out to be particularly useful, as demonstrated in the discussion of Section 4.3.5.

Complex nonlinear least squares avoids most of the weaknesses of earlier methods since it fits all the data simultaneously and thus yields parameter estimates associated with *all*, rather than half, the data. In addition, it provides uncertainty estimates for all estimated parameters, showing which ones are important and which are unimportant in the model or equivalent circuit used for fitting; and finally, it allows one to fit a very complex model, one having 5, 10, or even more unknown (free) parameters. None of the other methods can do this adequately, especially when several of the time constants of the model are close together.

Here, we shall briefly describe a slightly more general fitting method than ordinary weighted CNLS, but for simplicity we shall still refer to it as CNLS. Consider a theoretical model expression $f_t(\omega; P)$, which is a function of both angular frequency ω and a set of model parameters P . Consider $i = 1, 2, \dots, k$ data points associated with ω_i . We need not specify the number of parameters here, but we do assume that they enter f_t nonlinearly in general. Now suppose that f_t is separated into two parts, $f_t^a(\omega; P)$ and $f_t^b(\omega; P)$,

which both depend on the same set of parameters. For $f_t(\omega; \mathbf{P}) = Z_t(\omega; \mathbf{P})$, for example, the two parts might be $f_t^a = Z'_t$ and $f_t^b = Z''_t$ or $f_t^a = |Z_t|$ and $f_t^b = \theta$, where θ is the phase angle of Z_t . The least squares procedure involves minimizing the sum of squares function:

$$S = \sum_{i=1}^k \left\{ w_i^a [f_{ei}^a - f_t^a(\omega_i; \mathbf{P})]^2 + w_i^b [f_{ei}^b - f_t^b(\omega_i; \mathbf{P})]^2 \right\} \quad (2)$$

where w_i^a and w_i^b are the weights associated with the i th data point and f_{ei}^a and f_{ei}^b are experimental data values. When, say, $f_t^b(\omega; \mathbf{P}) \equiv 0$, the procedure reduces to ordinary nonlinear least squares.

Since the previous generalization of the ordinary nonlinear least squares method is so minor, it is a simple matter to modify a standard nonlinear least squares program to implement Eq. (2). In any *non-linear* least squares procedure, however, there is a problem of ensuring that the minimum found in parameter space is the absolute minimum. This problem, which may become serious when the number of free parameters is large, has been attacked in the work of Macdonald *et al.* [1982b] by using two programs in series. The first does not require inversion of the system matrix and thus nearly always converges. The second program, which uses the results of the first as input, does not usually converge, however, unless it can find a set of parameter values that lead to an absolute minimum in S or at least a good local minimum. The first program often helps it to do so. In spite of the power of this serial method, the achievement of an absolute minimum, giving the least squares estimates of the parameters as well as their uncertainty estimates (standard deviation estimates), is always simplified and facilitated by using the best available estimates of the parameter values as input to the first program. Some of the simpler analysis methods mentioned previously are often useful in providing such initial estimates.

The procedure described previously is not really a CNLS approach unless f^a and f^b are the real and imaginary parts of a complex variable. But as we have seen, $|Z|$ and θ are not, although $\ln|Z|$ and θ and Z' and Z'' are. Since we sometimes are interested in fitting data in the $|Z|, \theta$ form rather than $\ln|Z|, \theta$, this distinction is worth making, although it makes no formal difference in the minimization of Eq. (2).

3.3.2.3 Weighting

The problem of what weights to use is not always an entirely well-defined one. The simplest choice, termed *unweighted* or *unity-weighted*, is to set all w_i^a and w_i^b values equal to unity. But if values of f_e^a and f_e^b vary over several orders of magnitude, as is often the case, only the larger values will contribute appreciably to the sum S , resulting in poor parameter estimates. A reasonable procedure, when it can be done, is to replicate the experiment 5 or 10 times and determine the w_t from the standard deviations from the mean for each point. The general relations to use are $w_i^a = (\sigma_i^a)^{-2}$ and $w_i^b = (\sigma_i^b)^{-2}$, where the σ 's are the experimental standard deviations.

When replication is impractical and there is no direct information on the best individual w_i to employ, it has usually proved most satisfactory to assume that the relative errors of the measured quantities are constant. This approach has been termed proportional or P weighting. It is equivalent to setting

$$\sigma_i^a - g f_{ei}^a \text{ and } \sigma_i^b - g f_{ei}^b \quad (3)$$

where g is a proportionality constant that is usually taken to be unity and whose value makes no difference in the parameter estimates. Here P weighting is particularly needed when the data exhibit large variation. In the Z case, S would become

$$S = S_Z = \sum_{i=1}^k \left\{ \left[\frac{Z'_{ei} - Z'_t(\omega_i; \mathbf{P})}{Z'_{ei}} \right]^2 + \left[\frac{Z''_{ei} - Z''_t(\omega_i; \mathbf{P})}{Z''_{ei}} \right]^2 \right\} \quad (4)$$

An alternative choice, which yields nearly the same parameter estimates if the relative errors are small (i.e., the squared terms previously), is to take $\sigma_i^a = g f_t^a(\omega_i; \mathbf{P})$ and $\sigma_i^b = g f_i^b(\omega; \mathbf{P})$.

3.3.2.4 Which Impedance-Related Function to Fit?

The next problem is which function Z , Y , M , or e to fit. The answer is that it is most sensible from a statistical point of view to fit the data in measured rather than transformed form. Suppose that Z is measured in rectangular form. When both Z and the associated $Y = Z^{-1}$ data are separately fitted with P weighting, it is found that there are often significant differences between the parameter estimates obtained from the two fits. This is not unexpected; the operation of taking an inverse (complex or not) on data with errors generally introduces a bias in the fitted results; it is for this reason that the directly measured results should be fitted directly.

In most automated measurements the rectangular components are measured directly, but sometimes the modulus and phase angle are directly obtained. These are the two quantities, $f_e^a = |f_e|$ and $f_e^b = \theta_e = \arg(f_e)$, which would then appear in Eq. (2) for S . Again in the absence of measured uncertainties, P weighting would usually be most appropriate. In this case $\sigma_i^a = g |f_{ei}|$ and $\sigma_i^b = g \theta_{ei}$. It is worth mentioning that it has sometimes been suggested that with data in rectangular form, a modified P weighting be used in which $\sigma_i^a = \sigma_i^b = g |f_{ei}|$. Such weighting leads to parameter estimates from Z and Y fitting that are generally much closer together than those obtained with ordinary P weighting. Thus with this weighting it makes no significant difference whether the data are fitted to the model in Z or Y form. Since, however, this weighting seems physically unrealistic and blurs a distinction that we in fact expect, it seems to have little to recommend it. Further, when ordinary P weighting is used for fitting of data in either rectangular or polar form, it is easy to show that the ω factors occurring in M or e cancel out of the S function; thus fitting of Z and M then yields exactly the same set of parameter estimates and relative fitting residuals, and fitting of Y and e also yields the same set of parameter estimates and relative residuals. Of course, the Z and Y sets will be different unless the data are exact for the model considered. Thus when P weighting is employed, one should fit to Z or Y depending on which was measured directly and should fit in rectangular or polar form, again depending on which form is directly measured.

3.3.2.5 The Question of "What to Fit" Revisited

The remaining problem is what equivalent circuit or equation to fit by CNLS (see Sections 2.2.2.3 and 2.2.3.4). If it is expected that the data arise from an experiment described by a known analytic model, then of course fitting to the $Z(\omega)$ or $Y(\omega)$ predictions of this model would be appropriate. In the more usual case where a complete, appropriate model is unknown, the first step is to examine 3-D plots of the data and attempt to identify the effects of specific processes appearing in different frequency regions. An equivalent circuit may then be put together to try to describe these processes and their interactions (see Sections 2.2.3.3 and 2.2.3.4). When CNLS fitting with this circuit is then carried out, one would hope to find little evidence of systematic error (leading to large, serially correlated residuals), small relative standard errors for all free parameters, and small relative residuals for the data points, so the overall standard deviation of the fit, s_f , is small. If relative standard deviations of the parameters are of the order of 30% or more, the associated parameters are not well determined by the data and should be removed from the equivalent circuit. Generally, one would keep modifying the equivalent circuit and doing CNLS fitting until the previous criteria are as well satisfied as possible under the general criterion of using as simple an equivalent circuit with as few individual elements as practical.

3.3.2.6 Deconvolution Approaches

There is an alternative sometimes worth trying to some of the previous trial-and-error procedure. Suppose that the impedance plane plot shows a wide arc that is not exactly a displaced semicircle. It might possibly be best described by several discrete time constants not too far apart (e.g., Armstrong

et al. [1974], Badwal and de Bruin [1978]) or by a continuous distribution of time constant. In the first case, the equivalent circuit would involve several individual parallel RC's in series, and in the second it might involve one or more ZARC functions (CPE and R in parallel) in series. Although the best of these choices could be discovered by carrying out several CNLS fits, a more direct method would first be to use deconvolution of the $Z''(\omega)$ data to find an estimate of the distribution function of time constants implicit in the data (see Colonomos and Gordon [1979], Franklin and de Bruin [1983]). Such a distribution, if sufficiently accurate, will separate out the various time constants present, even if they are completely invisible in 3-D plots and by the width of the individual relaxations apparent in the distribution suggest whether they may be best described by discrete circuit elements or by continuous distributions in the frequency domain. From the values of relaxation time τ where relaxation peaks occur, τ_p , one may also calculate the approximate frequency region $\omega_p = \tau_p^{-1}$ where the relaxation produces its maximum effect. These results may then be used to construct an appropriate equivalent circuit and estimate initial values of the parameters for subsequent CNLS fitting.

The basic equations for obtaining the distribution of relaxation times, $g_z(\tau)$, at, say, the impedance level, start with defining the relation (Macdonald and Brachman [1956]):

$$Z(\omega) = R_0 \int_0^\infty \frac{g_z(\tau) dt}{1 + j\omega\tau} \quad (5)$$

where R_0 is the $\omega \rightarrow 0$ value of $Z(\omega)$. This relation can be put in convolution form by several transformations. Let us use normalized quantities and pick some frequency ω_0 that is approximately the central value of all frequencies measured. Let $\omega_0 \equiv 2\pi\nu_0$, $\tau_0 \equiv \omega_0^{-1}$, $\omega\tau_0 \equiv \exp(-z)$, $\tau \equiv \tau_0 \exp(s)$, and $G_z(s) \equiv \tau g_z(\tau)$. We have here introduced the new logarithmic variables s and z . Then Eq. (5) becomes

$$Z(z) = R_0 \int_{-\infty}^{\infty} \frac{G_z(s) ds}{1 + j\exp[-(z-s)]} \quad (6)$$

This equation may now be separated into real and imaginary parts, each giving an independent expression involving $G_z(s)$, the desired quantity. Although both may be used, the imaginary part of Z generally shows more structure than the real part, and it is customary to calculate $G_z(s)$ from Z'' data rather than from Z' data. The expression for Z'' following from Eq. (6) is

$$Z''(z) = -\left(\frac{R_0}{2}\right) \int_{-\infty}^{\infty} G_z(s) \operatorname{sech}(z-s) ds \quad (7)$$

now in standard convolution form. The process of deconvolution to find $G_z(s)$ and thus $g_z(\tau)$ is generally a complicated one but can be carried out by computer when needed. Two different methods are described by Franklin and de Bruin [1983] and Colonomos and Gordon [1979].

3.3.2.7 Examples of CNLS Fitting

As a first example of CNLS fitting, the circuit shown in Figure 3.3.5 was constructed with lumped elements whose values were measured on an impedance bridge (top figures) (see Macdonald *et al.* [1982b]). This circuit leads to very little structure in either the Z or Y 3-D plots shown in Figures 3.3.6 and 3.3.7. The bottom numbers shown for each element in Figure 3.3.5 are the CNLS Y -fitting values estimated from all the data; they are probably more accurate than the nominal values. Clearly the resolution and accuracy are very good here in spite of the appearance of little structure in the 3-D plots. But this was a situation where the proper circuit was initially known.

Figure 3.3.8 shows the results of fitting impedance data for β -PbF₂ at 474 K (Macdonald *et al.* [1982b]) with CNLS to the circuit at the top of the figure. Initially the form of the circuit that would best fit the data was unknown, so several different ones were tried. The use of a CPE in the circuit, as shown, allowed quite a good fit to the data to be obtained and led to well-determined parameter estimates. The

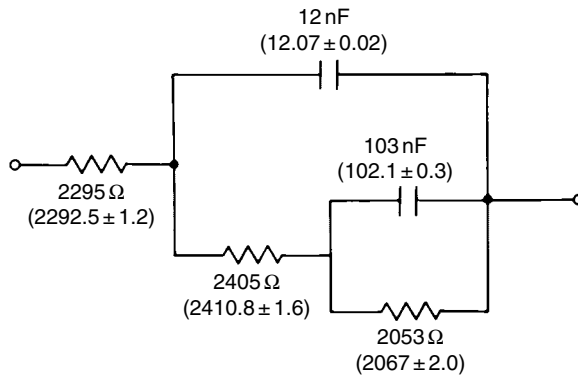


FIGURE 3.3.5 Test circuit involving lumped circuit elements. Nominal values are the numbers on top, while those in parentheses are CNLS estimates. Source: Macdonald *et al.* [1981]. Reproduced with permission of Elsevier.

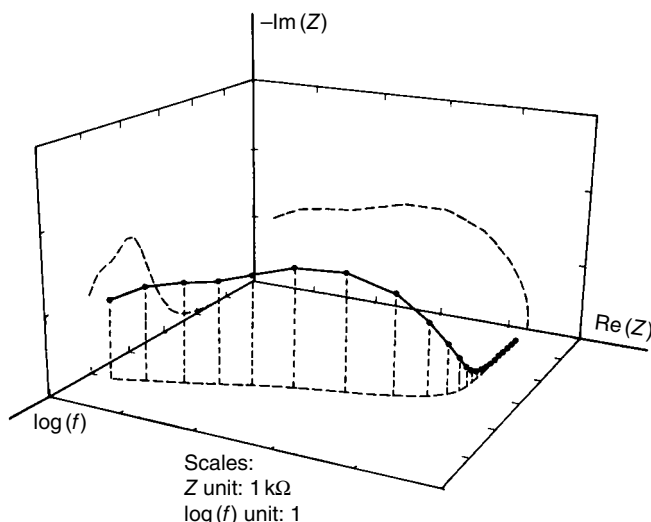


FIGURE 3.3.6 Perspective 3-D plot of the Z response of the circuit of Figure 3.2.5. Source: Macdonald *et al.* [1981]. Reproduced with permission of Elsevier.

deviations between the dotted and dashed projection lines at the lowest frequencies show that the fit is not perfect in this region, however.

Finally, Figure 3.3.8 shows a 3-D log-impedance plot for the same data shown in Figure 3.3.3. Here the fit (dotted curves) appears to agree very well indeed with the data, but an M plot (as in Figure 3.3.4) showing both data and fit predictions shows regions of appreciable disagreement (Macdonald and Cook [1984, 1985]). Since it has become customary to plot curves such as $\log(-Z'')$ versus ν or $\log(\nu)$ and $\log(Z')$ versus ν or $\log(\nu)$ when data variation is large and to compare data and fitted results in this form, we wish to warn that this is often insufficient; discrepancies of some importance may be obscured by the logarithmic transformation. Even though several 3-D plots with different scales may be required to show data of wide variability plotted linearly, it is generally a good idea to examine them all when data and predicted values are to be compared. Regions of discrepancy then yield immediate information about

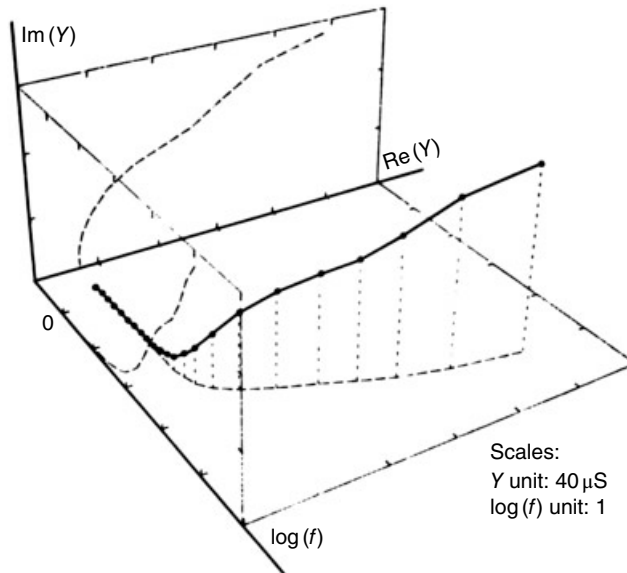


FIGURE 3.3.7 Perspective 3-D plot of the Y response of the circuit of Figure 3.2.5. Source: Macdonald *et al.* [1981]. Reproduced with permission of Elsevier.

needed modifications in the fitting circuit. Finally, although the idea has not been much exploited as yet, it is a simple matter to plot relative residuals themselves in 3-D. For Z data one would plot $(-Z_e'' + Z_t'')/(Z_e'')$ on the vertical axis and $(-Z_e' - Z_t')/Z_e'$ on the horizontal real axis and employ the usual $\log(\nu)$ axis. For P weighting, one would expect the resulting 3-D curve to be well bounded (magnitudes of most residuals comparable), but the plot should clearly show any regions of correlated residuals, indicating the presence of systematic errors and the need for improving the fitting circuit.

3.3.2.8 Summary and Simple Characterization Example

In the IS field, workers ordinarily spend much time and effort in preparing materials and measuring them under closely controlled conditions. But frequently their subsequent attention to data analysis is quite inadequate and does not do justice to the work done. Although some kind of a data presentation is usually included, it is rare when it incorporates sufficient plots to resolve all the data well and show its shapes for different kinds of plots. We have tried herein to illustrate some of the virtues of 3-D perspective plotting and strongly urge its increased use in the IS field.

Even in the rare cases where the data are presented adequately, one often finds either no discussion of an appropriate model or equivalent circuit or just the statement that the data fit a given equivalent circuit without either a comparison of the original data and the circuit predictions or a listing of estimates of the values of the parameters in the equivalent circuit. In most cases where such a listing is included, the estimates have been obtained by approximate methods, and the reader is given no measure of their accuracy and applicability. Finally, even when an equivalent circuit is presented and used, one rarely finds any discussion of why it is the most appropriate circuit to use or any comparison with other possible fitting circuits.

In summary, we first advocate 3-D plotting of data in various forms, followed by data adjustment and smoothing when warranted. Then crude approximate analysis methods may be employed to estimate initial values of the parameters, which enter into an equivalent circuit thought appropriate. Next, CNLS fitting with weighting should be carried out using this and any other possibly likely allied circuits in order to find the simplest and best-fitting one. Then the data and the fitting results should be compared in 3-D and the final parameter estimates and their estimated standard deviations presented.

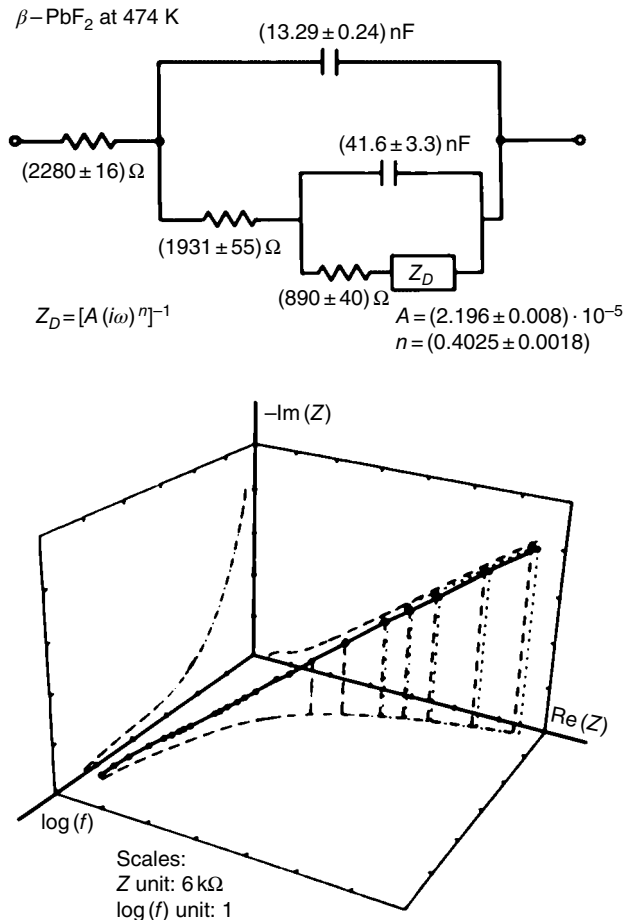


FIGURE 3.3.8 At the top is a circuit used to fit $\beta\text{-PbF}_2$ data at 474 K. Parameter values and their standard deviations estimated from CNLS fitting are shown. The bottom part shows a 3-D perspective plot of the Z data (solid line and short dashes) and predicted values and curves (long dashes). Source: Macdonald *et al.* [1981]. Reproduced with permission of Elsevier.

Even when all the previous procedures have been completely carried out, there is a final stage of analysis that should always be included when possible. This stage is the essence of characterization: the passage from good equivalent-circuit macroscopic element estimates to estimates of microscopic parameter values. It is, of course, unnecessary if one is fitting data directly to an impedance function involving microscopic parameters. But in the more usual case of fitting to an equivalent circuit, this stage is the heart of the whole enterprise. A general approach to such macroscopic-microscopic transformation for unsupported systems has been outlined in detail in Macdonald and Franceschetti [1978], and the method is illustrated in, for example, Macdonald *et al.* [1982a] and Macdonald and Cook [1984, 1985].

Here we shall illustrate the method for a simple unsupported situation, which where the equivalent circuit of Figure 2.2.8 applies with only C_∞ , R_∞ , C_R , and R_R present. Assume that univalent charge of only a single sign, say, positive, is mobile and the partially blocking electrodes are identical with known spacing l . The equations presented in Section 2.2.3 become (per unit area)

$$C_\infty = \frac{\epsilon\epsilon_0}{l} \quad (8)$$

$$R_\infty = \frac{l}{F\mu_p c_p^0} \quad (9)$$

$$C_R = \left(\frac{\epsilon \epsilon_0 F^2 c_p^0}{RT} \right)^{1/2} \quad (10)$$

and

$$R_R = \frac{RT}{F^2 c_p^0 k_p^0} \quad (11)$$

Assume that either ϵ , the bulk dielectric constant, is known or C_∞ has been determined from CNLS fitting of the data. In either case, $\epsilon \epsilon_0$ can be obtained and used in Eq. (10) to obtain from the C_R estimated value an estimate of c_p^0 , the bulk concentration of the mobile positive charge carriers. Then this value of c_p^0 may be used in Eq. (9) along with the estimated value of R_∞ to obtain an estimate of μ_p , the mobility of the positive charges. Finally, the c_p^0 estimate may be used in Eq. (11) in conjunction with the R_R estimate to calculate k_p^0 , the effective reaction rate for the reacting positive charges. Thus from the four macroscopic estimates C_∞ , R_∞ , C_R , and R_R , one obtains estimates of the four microscopic quantities ϵ , c_p^0 , μ_p , and k_p^0 . These values and their dependences on controllable variables such as ambient temperature should then finally lead to valuable insight into the electrical behavior of the material-electrode system.

Applications of Impedance Spectroscopy

4.1 CHARACTERIZATION OF MATERIALS

N. Bonanos,¹ B. C. H. Steele,² and E. P. Butler³

¹Senior Research Scientist, Materials Research Department, Risø National Laboratory, Roskilde, Denmark

²Department of Metallurgy and Material Science, Imperial College of Science and Technology, London, England

³ALCAN International Ltd., Banbury Laboratories, Banbury, TN, USA

4.1.1 Microstructural Models for Impedance Spectra of Materials

4.1.1.1 Introduction

In polycrystalline solids, transport properties are strongly affected by microstructure, and impedance spectra usually contain features that can be directly related to microstructure. This is clearly illustrated in ceramic electrolytes such as zirconia and β -alumina. Much work on correlating microstructure and electrical properties can be directly traced to the pioneering study of Bauerle [1969]. The main purpose of this research effort has often been to optimize electrical conductivity for use in solid-state electrochemical devices, such as solid oxide fuel cells (SOFCs) and sensors. In parallel, impedance spectroscopy (IS) has been developed as a technique for the study of materials not intended for electrical applications, where transport properties are incidental to the main application, for example, structural ceramics. In this section we discuss microstructural models describing grains and grain boundaries of differing phase composition, suspensions of one phase within another, and porosity, while in Section 4.1.3, we give examples of the combined use of IS and electron microscopy. With the two techniques combined, it is possible to derive information of microstructural relevance that is not accessible using one of the techniques alone.

The electrical properties of heterogeneous media have been modeled for over 100 years. Meredith and Tobias [1962], Mitoff [1968], and McLachlan *et al.* [1990] have given clear accounts of their scope and validity. However since these articles cover the case where conductivity or permittivity is real, which normally means direct current (dc) conductivity or permittivity of loss-free dielectrics, these properties are not directly applicable to IS. Ac properties have been discussed by Wimmer *et al.* [1974] with special

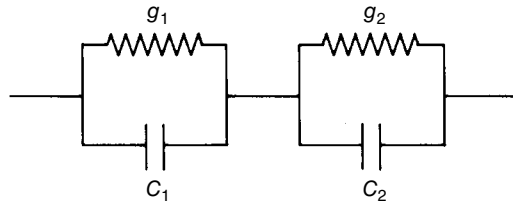


FIGURE 4.1.1 Circuit equivalent of a two-phase microstructure.

reference to ceramics. The literature on dielectric properties has been reviewed by van Beek [1965], while models that include the effects of the interfacial double layer have been described by Dukhin and Shilov [1974]. Sihvola [1999] has recently produced a comprehensive survey of the properties of mixed phase systems with an excellent coverage of the historical and theoretical background.

As this section emphasizes material properties, the results are presented in terms of bulk intensive quantities, such as the complex conductivity ψ , the complex resistivity ρ , the permittivity ϵ , and the modulus M . A further distinction is made between two kinds of properties, both bulk intensive: (i) macroscopic properties, such as the resistivity of a sample due to grain boundaries (after correction for length/area), which are directly measurable, and (ii) microscopic properties, such as the resistivity of the grain boundary phase, which can only be estimated with the help of a microstructural model. The macroscopic quantities are represented by Latin symbols, while the microscopic ones by Greek symbols.

The quantity used for expressing models of this type is the complex conductivity, defined as

$$\psi_i = \sigma_i + j\omega\epsilon_i \quad (1)$$

where σ_i is the dc conductivity and ϵ_i is the permittivity of phase i . The role of the model is to provide a hypothetical microstructure, for which the total complex conductivity, ψ_t , may be calculated. Having obtained $\psi_t = \psi_t(\omega)$, this may be converted to another representation, such as the complex resistivity $\rho \equiv \psi^{-1}$. In many cases, it is possible to find an equivalent circuit that represents the model. This has the advantage that the circuit parameters can be estimated from the impedance spectrum. Equation (1) is equivalent to assigning a Voigt element to each phase. As will be shown in the following text, some of the models for two-phase microstructures are equivalent to a circuit consisting of two elements in a series (Figure 4.1.1), while others predict a more complex behavior. The models fall into two types: layer models and effective medium models.

4.1.1.2 Layer Models

The earliest model used to describe the electrical properties of a two-phase mixture is the *series layer model* (Maxwell [1881]) shown microstructurally in Figure 4.1.2a. The two phases are assumed to be stacked in layers parallel to the measurement electrodes, with total thicknesses of each phase proportional to the volume fractions x_1 and x_2 . The series layer model is described by the equation

$$\psi_t^{-1} = x_1\psi_1^{-1} + x_2\psi_2^{-1} \quad (2)$$

or, in terms of the complex resistivities,

$$\rho_t = x_1\rho_1 + x_2\rho_2 \quad (2a)$$

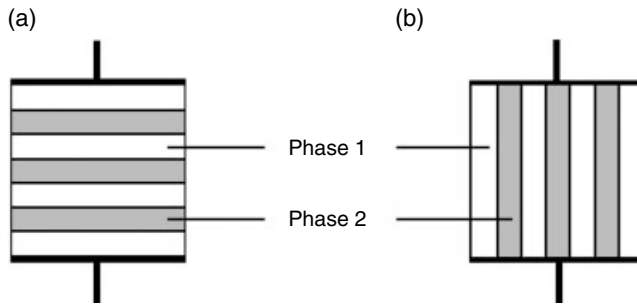


FIGURE 4.1.2 Hypothetical two-phase microstructures described by simple layer models: (a) series layer model; (b) parallel layer model.

which expresses a linear mixing rule. The series layer model is equivalent to the circuit in Figure 4.1.1, in which

$$\begin{aligned} g_1 &= \frac{\sigma_1}{x_1}, & g_2 &= \frac{\sigma_2}{x_2} \\ c_1 &= \frac{\varepsilon_1}{x_1}, & c_2 &= \frac{\varepsilon_2}{x_2} \end{aligned} \quad (3)$$

The impedance and modulus spectra for this model in general consist of two semicircles whose diameters are g_1^{-1} , g_2^{-1} in the impedance and c_1^{-1} , c_2^{-1} in the modulus spectra. The time constants of the two phases are defined as $\tau_1 = c_1/g_1$ and $\tau_2 = c_2/g_2$. If these time constants differ as a result of differences in c , then the arcs will be well resolved in the impedance spectrum. If they differ as a result of g , they will be resolved in the modulus spectrum (Hodge *et al.* [1976]). In practice good resolution is not obtained in both Z and M spectra.

It is interesting to compare the series model (Figure 4.1.2a) with the corresponding parallel model (Figure 4.1.2b), in which the layers are stacked across the electrodes. For the *parallel layer model*, the complex conductivity follows a linear mixing rule,

$$\psi_t = x_1\psi_1 + x_2\psi_2 \quad (4)$$

The equivalent circuit would be that in Figure 4.1.3a with values

$$\begin{aligned} g_1 &= x_1\sigma_1, & g_2 &= x_2\sigma_2 \\ c_1 &= x_1\varepsilon_1, & c_2 &= x_2\varepsilon_2 \end{aligned} \quad (5)$$

The behavior of this circuit differs qualitatively from the previous one, because conductances g_1 , g_2 and capacitances c_1 , c_2 are in parallel. Thus the circuit is equivalent to that in Figure 4.1.3b. This circuit shows only one relaxation. For the microstructure of Figure 4.1.2b, the individual relaxations cannot be resolved by any method, graphical, CNLS, or other. Although at first glance this model would appear to be as plausible as the series layer model, it fails to describe the behavior of grain boundaries in ceramics.

A third model, originally suggested by Beekmans and Heyne [1976], has been termed the *brick layer model* (van Dijk and Burggraaf [1981], Verkerk *et al.* [1982]). It is more realistic, treating the microstructure as an array of cubic grains, separated by flat grain boundaries, as shown in Figure 4.1.4a. The grains have a side D and the grain boundaries a thickness d , where $d \ll D$, and so the volume fraction of the grain boundary phase is $3d/D$. The current flow is assumed to be one-dimensional, and curvature of the current paths at the corners of the grains is neglected. In this case the two paths available to the current are either through grains *and* across grain boundaries or along grain boundaries, as depicted in the

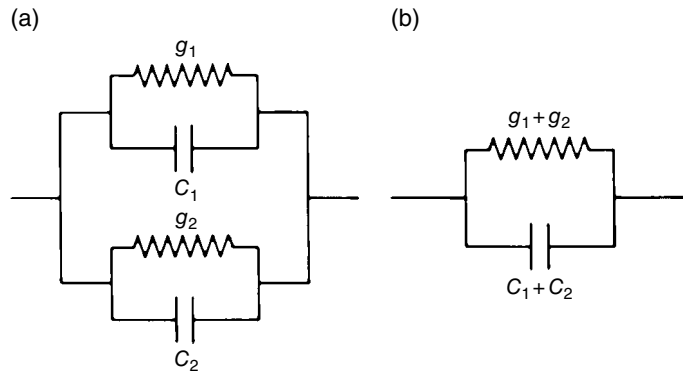


FIGURE 4.1.3 Circuit equivalent of the parallel layer model.
Two parallel connected Voigt elements (a) transform to a single Voigt element (b).

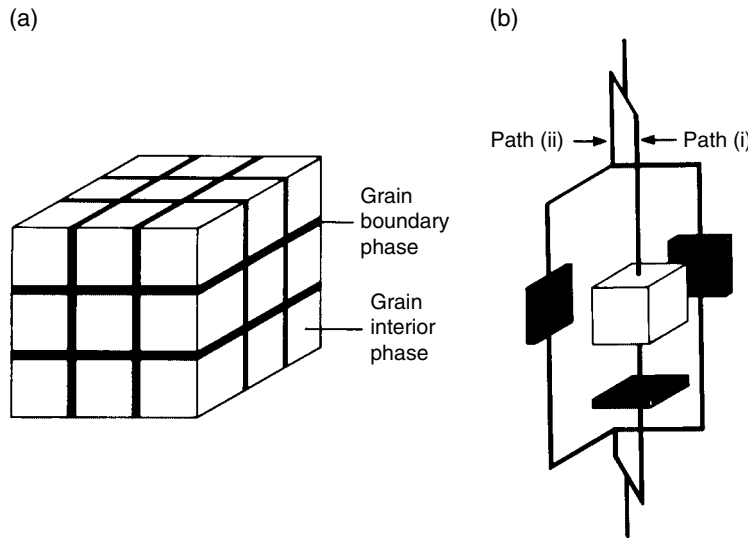


FIGURE 4.1.4 Brick layer model for a two-phase ceramic. (a) Overall view, showing array of cubic grains, separated by flat grain boundaries. (b) Exploded view of a single cell, showing parallel electrical paths: (i) through grains and grain boundaries and (ii) along grain boundaries.

exploded diagram shown in Figure 4.1.4b. Depending on the relative magnitudes of σ_{gi} and σ_{gb} , one of the two paths will normally dominate.

Case (i): $\sigma_{gi} \gg \sigma_{gb}$. Conduction along the grain boundaries is negligible, while conduction through the grains and across grain boundaries dominates. The behavior can be described in terms of complex resistivity,

$$\rho_t = \rho_{gi} + \frac{1}{3}x_{gb}\rho_{gb} \quad (6a)$$

or, for consistency with the rest of this section, in terms of the complex conductivity:

$$\psi_t = \left(\psi_{gi}^{-1} + \frac{1}{3}x_{gb}\psi_{gb}^{-1} \right)^{-1} \quad (6b)$$

Case (ii): $\sigma_{gi} \ll \sigma_{gb}$. Conduction along the grain boundaries is dominant:

$$\psi_t = \psi_{gi} + \frac{2}{3}x_{gb}\psi_{gb} \quad (7)$$

Case (iii): general. According to Näge [1984], the two paths (i) and (ii) may be combined into a network describing the polycrystalline properties for all ratios of σ_{gi}/σ_{gb} . Using our own notation this means

$$\psi_t = \left(\psi_{gi}^{-1} + \frac{x_{gb}}{3}\psi_{gb}^{-1} \right)^{-1} + \frac{2}{3}x_{gb}\psi_{gb} \quad (8)$$

We examine each case separately.

Case (i). For $\sigma_{gi} \gg \sigma_{gb}$, the brick layer model is equivalent to the series layer model but with one-third weighting of the grain boundary resistance. This reflects the fact that grain boundaries in only one of the three orientations (i.e., normal to the current) have a blocking effect. The circuit equivalent of the brick layer model is, therefore, that in Figure 4.1.1 with parameters

$$\begin{aligned} g_{gi} &= \sigma_{gi}, & c_{gi} &= \epsilon_{gi} \\ g_{gb} &= \frac{3\sigma_{gb}}{x_{gb}}, & c_{gb} &= \frac{3\epsilon_{gb}}{x_{gb}} \end{aligned} \quad (9)$$

A useful expression can be derived from these equations,

$$x_{gb} = 3 \frac{c_{gi} \epsilon_{gb}}{c_{gb} \epsilon_{gi}} \quad (10)$$

or, expressed in terms of grain size D and the grain boundary thickness d ,

$$\frac{d}{D} = \frac{c_{gi} \epsilon_{gb}}{c_{gb} \epsilon_{gi}} \quad (11)$$

By making the assumption $\epsilon_{gb} = \epsilon_{gi}$, the thickness or volume fraction of the grain boundary phase can be estimated, if the grain size is known. This applies only when the boundary capacitance arises from the presence of a second phase, which, as explained later, is not always the case. Often one refers loosely to g_{gi} and g_{gb} as grain interior and grain boundary conductivities. A more appropriate term would be *macroscopic* conductivities, as they are corrected for the macroscopic shape of the sample (length/area). For the brick layer model, and for $d \ll D$, g_{gi} is indeed the microscopic conductivity of the grain interior. By contrast, g_{gb} is usually 100–1000 times higher than σ_{gb} because x_{gb} is small. Therefore, although we can have $g_{gb} > g_{gi}$, this should not be taken to imply $\sigma_{gb} > \sigma_{gi}$.

Case (ii). When the current is mainly carried along grain boundaries, the brick layer model is equivalent to the parallel layer model (Figure 4.1.2a), but with two-thirds weighting on the grain boundary conductance term. A ceramic sample will then show a single arc in the impedance or modulus spectrum revealing little or nothing about its microstructure.

Case (iii). Näge's [1984] model combines the two extremes in one expression and is valid at high or low conductivity ratios, as it reduces to the expressions given for cases (i) and (ii). We have reservations about using this model over the entire range of σ_{gi}/σ_{gb} , since the assumption of current flowing via separate pathways is not tenable when $\sigma_{gb} \cong \sigma_{gi}$.

Thus it is possible, on the basis of the impedance spectrum alone, to differentiate between two situations: conducting grains with blocking grain boundaries or poorly conducting grains with highly conducting grain boundaries.

Blocking of Ions: Easy Paths. The brick layer model assumed the grain boundary region separating the grains to be continuous. However, it is often observed that the activation energies for the two conductivities, g_{gb} and g_{gi} , are equal or very similar. This led Bauerle [1969] to suggest, in connection with zirconia ceramics, that there were regions of the grain boundary where good intergranular contact was established; these are called *easy paths* (Figure 4.1.5a). The circuit chosen by Bauerle (Figure 4.1.5b) expresses the idea that mobile species (oxide ions) are sequentially blocked at grain interiors and grain boundaries. g_{ep} is the conduction through easy paths. Since $\epsilon_{gb} \cong \epsilon_{gi}$, the small intergranular contact areas do not affect c_{gb} . A slightly different model, proposed by Schouler [1979] (Figure 4.1.5c), divides the ionic current into two paths, one of which (g_b , C_b) is blocked capacitively, while the other (g_a) is not. The proportion of blocked ionic current is then given by

$$\beta = \frac{g_b}{g_a + g_b} \quad (12)$$

The same ratio β could be expressed in terms of a series model as

$$\beta = \frac{r_{gb}}{r_{gi} + r_{gb}} \quad (13)$$

Both models explain the identical activation energies of r_{gi} and r_{gb} , and, as they are equivalent (see Chapter 1), there is no *a priori* reason to prefer one over the other. One might prefer to visualize constriction resistances according to Bauerle [1969], when the grain boundary coverage is known to be high, or partial blocking according to Schouler [1979], when the grain boundary coverage is low, in the form of isolated islands.

Effect of Space Charge. As mentioned earlier, grain boundary effects arise not only from the presence of second phases. The electrical behavior of interfacial regions often differs from that of the grain interior due to space charge effects, studied by Maier and coworkers. Maier [1986] has shown that the conductance of a polycrystal contains three components: that of the grain interior (gi), the grain core (gc), and a region next to the grain boundary, dominated by space charge (sc). The space charge extends over a length, λ , from the core, known as the Debye length. For the simplest case, a pair of defects with the same charge, the Debye length is given by the expression

$$\lambda = \sqrt{\frac{\kappa \epsilon_0 R T}{2c_\infty z^2 F^2}} \quad (14)$$

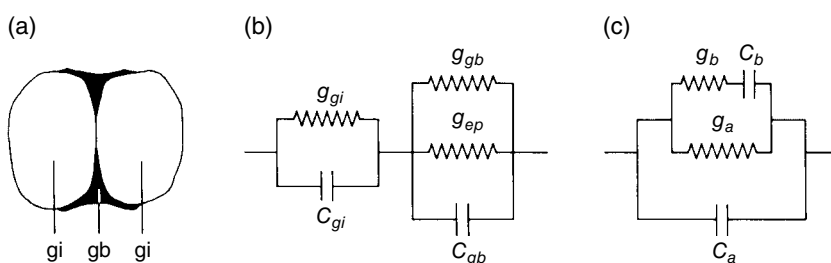


FIGURE 4.1.5 Easy path model for a two-phase ceramic: (a) Schematic representation of grains separated by a discontinuous grain boundary phase. (b) Series circuit equivalent according to Bauerle [1969]. (c) Parallel circuit equivalent according to Schouler [1979]. Source: Adapted from Schouler 1979.

where

- κ is the dielectric constant of the medium
- z is the number of charges on the defect
- c_∞ is the molar concentration of defect far from the interface
- ϵ_0, R, T , and F have their usual meanings

In the Debye model, the defect concentration is an analytic function of the distance from the boundary and, therefore, so is the conductivity, assuming that the mobility is constant. The defect concentration depends on the difference in local free energy between a defect at the boundary and a defect in the bulk and is parameterized by a quantity in the range -1 to 1 , describing the sign and strength of the effect. Figure 4.1.6a shows a defect concentration profile, in which the concentration is normalized with respect to the bulk concentration and the distance from the interface is normalized with respect to the Debye length.

For current perpendicular to a grain boundary, the following expression holds for the impedance¹:

$$Z^\perp = Z_{gi}^\perp + Z_{gc}^\perp + \Delta Z_{sc}^\perp \quad (15)$$

While for the current parallel to a grain boundary, a related admittance expression is derived:

$$Y^{\parallel} = Y_{gi}^{\parallel} + Y_{gc}^{\parallel} + \Delta Y_{sc}^{\parallel} \quad (16)$$

Both terms prefixed by Δ in these equations can be obtained by integrating the relevant concentration profiles over the distance from the grain boundary core. By considering a system composed of square grains (Figure 4.1.6b) and summing the contributions of the perpendicular and parallel paths (while neglecting the squared term in x_{gb}), the following expression is derived for the complex conductivity¹:

$$\psi_t = \frac{\psi_{gi}\psi_{gb}^\perp + \frac{2}{3}x_{gb}\psi_{gb}^{\parallel}\psi_{gb}^\perp}{\psi_{gb}^\perp + \frac{1}{3}x_{gb}\psi_{gi}} \quad (17)$$

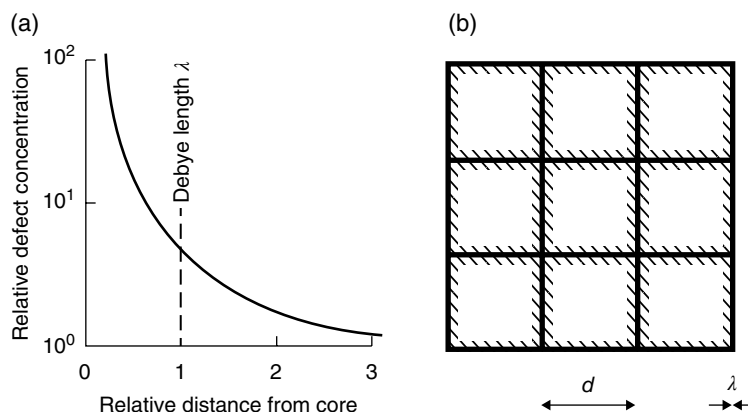


FIGURE 4.1.6 (a) Defect concentration profile near an interface, according to the Debye model. (b) Model microstructure for a polycrystalline solid, after Maier [1986]. Source: Maier 1986. Reproduced with permission of German Bunsen Society.

¹ The notation used in this expression has been altered for consistency with the rest of the section.

where x_{gb} refers to the combined volume fraction of the core and space charge region, that is, $x_{gb} = x_{gc} + x_{sc}$. This is equivalent to Eq. (8), rewritten so as to distinguish between parallel and perpendicular paths and after the squared term in x_{gb} has been removed, namely,

$$\psi_t = \left(\psi_{gi}^{-1} + \frac{1}{3}x_{gb}\psi_{gb}^{\perp-1} \right)^{-1} + \frac{2}{3}x_{gb}\psi_{gb}^{\parallel} \quad (18)$$

A salient point in this work is that, by specifying a variation in conductivity with distance from the grain boundary core, conductivity profiles in both orientations can be integrated, and a phenomenological description obtained is consistent with the brick layer model. On one hand, this is encouraging, because it shows that the simple brick layer model is able to reproduce some of the more subtle effects in ceramics. On the other hand, it suggests that conventional studies of ceramics, especially those of pure ceramics with low grain boundary phase content, may completely miss the effect of the space charge layer. A recommendation arising from the aforementioned is that several ceramic samples should be prepared with the same composition and with the widest possible range of grain sizes. However, it must also be recognized that this recommendation cannot always be turned into practice.

The aforementioned treatment assumes that the defects are mobile and distributed in response to the thermodynamic driving force. It should be mentioned that this is not always the case: ceramics often contain defects frozen in from higher temperature treatment (e.g., sintering), in which case some of the defect concentrations will be fixed. The two cases, respectively, known as the Debye and Schottky cases, produce different interfacial properties, including different characteristic lengths. For a concise discussion of the two cases, see Maier [1996]. Further relevant information can be found in Kim *et al.* [2003] and Maier [2004].

Effects of Grain Shape and the Presence of Distributed Easy Paths. Fleig and Maier [1998] have approached the question of grain boundary impedance by finite element modeling. They have modeled various periodic grain structures with grains of different shapes and aspect ratios and a realistic microstructure, consisting of about 40 grains. They have compared the results to the predictions of the brick layer model. The modeling results published so far cover only two-dimensional systems. Figure 4.1.7 shows two model structures comprising grains of high symmetry and the resulting impedance spectra, together with the spectrum for the brick layer case. For these examples, and for the realistic microstructure (not shown), the discrepancy from the brick layer model in terms of r_{gb} was of the order of 5%. For another case, namely, of a serrated grain structure, where grain boundaries intersected the current lines at an angle, the macroscopic grain boundary conductivity varied with the slope angle α as follows²:

$$g_{gb} = \frac{d}{D} \sigma_{gb} \sin \alpha \quad (19)$$

This differs from the brick layer model, for which the sine term is absent. This should be expected, since for this model, $\alpha = 90^\circ$. Note that the previous relation holds even when the serrations are on a much smaller scale than that of the grains. Fleig and Maier [1998] also explored the effect of a specific serrated microstructure on the temperature dependence of the macroscopic grain boundary conductivity. They assumed activation energies of 1.0 and 0.5 eV for σ_{gi} and σ_{gb} , respectively, fed these values into the model and observed that ΔH_{gb} was slightly different from $\Delta H_{\sigma_{gb}}$. In the temperature region near the point where $g_{gi} = g_{gb}$, ΔH_{gb} increased to 0.6 eV; outside this region, it returned to the expected value of 0.5 eV. Fleig [2000] examined the spatial distribution of easy paths in grain boundaries and found that conduction across the boundary was significantly greater with many small paths than with a single large one *when these paths occupied the same total grain boundary area*. Fleig [2002] examined a large number of computer-generated realistic microstructures and confirmed that deviations from the brick layer model

²This has been converted to our preferred notation.

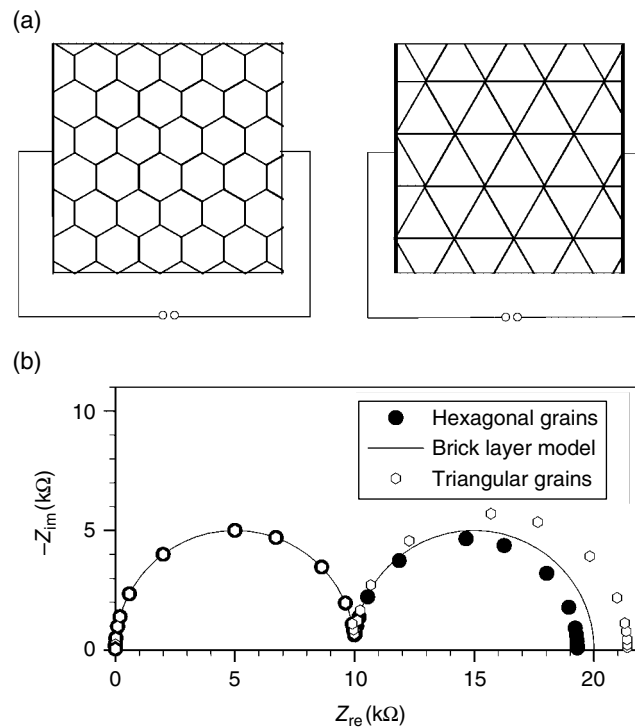


FIGURE 4.1.7 (a) Model grain boundary structures and the impedance spectra resulting from finite element modeling of these structures. (b) The spectrum for the square, brick layer case is shown for comparison, after Fleig and Maier [1998]. Source: Fleig 1998. Reproduced with permission of The Electrochemical Society.

were usually less than 10% and noted that the grain boundary relaxation frequency for the model reflected the correct input value.

The work demonstrates that the layer model is acceptable, provided the grain size distribution is narrow and the grain shape is roughly isotropic. In the case of grain boundary blocking with easy paths, the grain boundary conduction not only is directly proportional to the area of the easy path contacts but also depends on their spatial distribution. Regarding the effect of space charges, we conclude that, in general, simple studies will miss these effects, although some help could be provided by studying ceramics with a range of grain sizes.

4.1.1.3 Effective Medium Models

The Maxwell-Wagner Model. The layer models presented so far have the advantage of clarity but have been derived under unrealistic assumptions concerning the current distribution. Alternative models have been developed, which take into account the real current distributions, based on the *effective medium technique*. This may be briefly described as follows: One imagines a continuous medium (the effective medium) of conductivity ψ_{eff} . A portion of this is removed and replaced by an equal portion of the heterogeneous system consisting of two (or more) phases. By applying the constraint that the current distribution in the effective medium is not altered by this operation, an expression is derived for ψ_{eff} . The total conductivity of the two-phase system ψ_t is then equal to ψ_{eff} . It should be noted that this approach makes certain implicit assumptions about the microstructure, especially regarding the

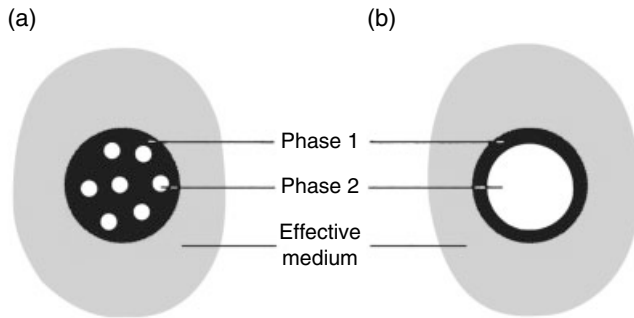


FIGURE 4.1.8 Hypothetical microstructures that may be described by the effective medium model: (a) Continuous matrix of phase 1 containing a dilute dispersion of spheres of phase 2. (b) A grain boundary shell of phase 1 surrounding a spherical grain of phase 2.

continuity of the constituent phases. Figure 4.1.8 shows two possible microstructures with a continuous phase 1 and a discontinuous phase 2.

The first exact expression of this type was derived by Maxwell [1881] for the dc conductivity of a dispersion of spheres in a continuous medium. Maxwell Garnett [1904] derived a similar expression for dielectric and optical properties. Wagner [1914] extended Maxwell's model to the complex domain, and this model has thereafter been known as the Maxwell-Wagner model.³ It gives the following expression for complex conductivity:

$$\psi_t = \psi_1 \frac{2\psi_1 + \psi_2 - 2x_2(\psi_1 - \psi_2)}{2\psi_1 + \psi_2 + x_2(\psi_1 - \psi_2)} \quad (20)$$

Despite its complexity compared to expressions derived from layer models, this expression has proven to be versatile in describing the impedance spectra of heterogeneous media. It is assumed that distortions to the electric field caused by the particle are local, that is, neighboring particles experience a uniform field. This has traditionally been taken to mean that the suspension must be dilute in phase 2.⁴ An embodiment of this model is shown in Figure 4.1.8a, in which the system consists of spheres suspended in a continuous medium. Simulated complex resistivity and modulus spectra are given in Figure 4.1.9a and b for $x_2 = 0.25$ and for phases having conductivities $\sigma_2 \gg \sigma_1$ and identical permittivities. In this case, the relaxations of the two phases are best resolved in the modulus plot.

Brailsford and Hohnke [1983] have applied the Maxwell-Wagner model to grain boundaries in two-phase systems. Their microstructural model, shown in Figure 4.1.8b, consists of a spherical grain of radius r_2 surrounded by a shell of outer radius r_1 , which represents the grain boundary and has a volume fraction $x_1 = 1 - (r_2/r_1)^3$. The authors observe that for $x_1 \rightarrow 0$ and $\psi_2 \ll \psi_1$, the effective medium model becomes identical to case (i) of the brick layer model, namely, Eq. (6). Further, we have found that for $x \rightarrow 0$ and $\psi_1 \gg \psi_2$, it reduces to case (ii) of the brick layer model, namely, Eq. (7).⁵

The assumed conditions of a low grain boundary phase volume fraction and high grain boundary conductivity are realistic as far as ceramic electrolytes are concerned. It is therefore encouraging to see

³ There is much confusion regarding the name that should be attributed to this expression. Garnett's given names were James Clerk Maxwell, but he appears to have incorporated the last one into his surname. Furthermore, while K.W. Wagner extended Maxwell's formula to the complex variable, the term Maxwell-Wagner is also associated with a slightly different phenomenon of interfacial polarization. We have used the term to describe Eq. (20) following the practice of Fricke [1953].

⁴ The maximum volume fraction x_2 for which Eq. (20) is valid has not been accurately specified, with values as low as 0.1 and as high as 0.5 having been proposed. A sensible upper bound might be 0.30 since, above this, the system approaches the percolation limit for spherical particles. On the other hand, in the following paragraph, we mention a case where the model is valid for $x_2 \cong 1$.

⁵ For consistency with the rest of the section, we have used different subscripts than have Brailsford and Hohnke.

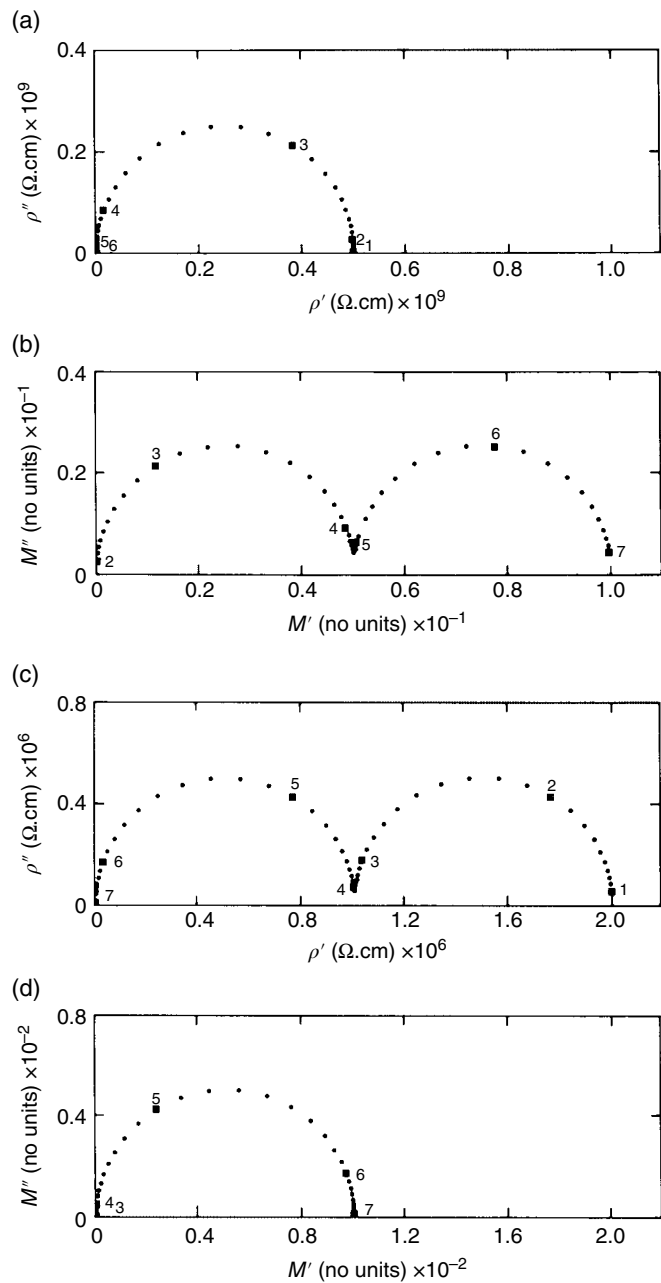


FIGURE 4.1.9 Simulated impedance and modulus spectra for a two-phase microstructure, based on the effective medium model. Values of the input parameters are given in Table 4.1.1. (a, b) Spectra for a matrix of phase 1 containing 25% by volume of spheres of phase 2. Resolution is achieved in the modulus spectrum (b), but not the impedance spectrum (a). (c, d) Spectra for a spherical grain of phase 2 surrounded by a grain boundary shell of phase 1. The ratio of shell thickness to sphere radius is 10^{-3} . Resolution is achieved in the impedance spectrum (c), but not the modulus spectrum (d).

TABLE 4.1.1 Input Parameters Used to Calculate the Spectra Shown in Figure 4.1.9

Volume fraction x_2	σ_1 S/cm	σ_2 S/cm	ϵ_1 F/cm	ϵ_2 F/cm	Figure
0.25	10^{-9}	10^{-6}	8.85×10^{-13}	8.85×10^{-13}	(a, b)
0.997	10^{-9}	10^{-6}	8.85×10^{-13}	8.85×10^{-13}	(c, d)

Note: The permittivities ϵ_1, ϵ_2 correspond to a dielectric constant of 10.

that models derived from two different grain geometries give the same results under these conditions. This suggests that the estimation of grain boundary properties from electrical circuit parameters should be subject to a relatively small error as a result of assumptions about the shape of the grains, if they are isotropic.

Simulated complex resistivity and modulus spectra based on Eq. (20) for the blocking grain boundary situation (Figure 4.1.8b) are shown in Figure 4.1.9c and d. It is evident that for the parameters chosen ($\sigma_1 \gg \sigma_2$), either the impedance or the modulus spectra resolve the microstructural components. For an appreciable volume fraction of high conductivity suspended phase (Figure 4.1.8a), the modulus spectrum is preferable. For the situation with a low volume fraction of continuous grain boundary phase (Figure 4.1.8b), the impedance or complex resistivity spectra give a good resolution.

Brailsford and Hohnke [1983] make two further observations regarding porosity for the case $\sigma_{gi} \ll \sigma_{gb}$. If the volume fraction of pores is x_p , then for intragranular pores,

$$g_{gi} = \frac{\sigma_{gi}}{1 + (3/2)x_p} \quad (21)$$

The same amount of porosity distributed intergranularly has a larger effect on the grain boundary conductivity, highlighting the importance of the spatial distribution of pores:

$$g_{gb} = \frac{3\sigma_{gb}}{x_{gb} + (3/2)x_p} \quad (22)$$

Comparing the last two equations to Eq. (9) shows that the presence of pores modifies the impedance spectra (complex conductivity spectra) by altering the diameters of the grain interior or grain boundary arc. Nevertheless, in neither of these cases do pores introduce a new arc or other feature in the impedance spectrum. Thus, stating that the effect of pores can be seen on the impedance spectrum does not imply that from an empirical impedance spectrum, the degree or type of porosity can be established. This deduction could only be made if the electrical properties σ, ϵ were known beforehand for both the grain and grain boundary phases, a condition that is unlikely to be fulfilled.

Inspection of Figure 4.1.9 suggests that Eq. (20) generates spectra that are similar to those of simple RC circuits. This is indeed the case. In fact, Bonanos and Lilley [1981] showed that the Maxwell–Wagner model is formally identical to the two-element circuit in Figure 4.1.1, but with values of g_1, g_2, c_1 , and c_2 that can be expressed as rather complicated functions of $\sigma_1, \sigma_2, \epsilon_1, \epsilon_2$, and x_2 (Table 4.1.1).

The Fricke Model for Two-Phase Dispersions. Expressions similar to those of Maxwell have been derived for ellipsoidal particles of random orientation (Fricke [1932]) and for aligned ellipsoidal particles (Fricke [1953]). The expressions contain form factors that depend on the axial ratio of the ellipsoids and their orientation with respect to the electric field. The case of random orientation is the most interesting, as it describes a realistic ceramic microstructure and results in the following equation:

$$\psi_t = \psi_2 + \frac{(\psi_1 - \psi_2)(1 - x_2)}{1 + (x_2/3) \sum_{n=1}^3 (\psi_1 - \psi_2)/(\phi_n \psi_1 + \psi_2)} \quad (23)$$

where

ψ_t = complex conductivity of the dispersion

ψ_1, ψ_2 = complex conductivities of the matrix and the dispersed phase, respectively

x_2 = volume fraction of the dispersed phase

$\phi_{1,2,3}$ = form factors that depend on the axial ratios of the ellipsoidal particles, defined by the semi-axes a, b, c , where $a \geq b \geq c$

Selected values of ϕ are given in Table 4.1.2. A simulated modulus spectrum for Eq. (23) is shown in Figure 4.1.10. The parameters used to generate this are listed in Table 4.1.3. A plot of complex resistivity (not shown) displays only the low-frequency arc, with a very small distortion at high frequency.

For the parameters chosen, there are two readily resolvable arcs in the modulus spectrum (Figure 4.1.10). The low-frequency arc corresponds to the low conductivity continuous phase and is apparently a perfect semicircle with its center on the real axis. The high-frequency arc corresponds to the discontinuous phase and is composed of three relaxations corresponding to the three possible orientations of the ellipsoids. In Figure 4.1.10 these are not well resolved but cause the arc to be non-ideal. The two-phase dispersion can be represented by either of the two circuits in Figure 4.1.11; the values shown in Table 4.1.4 are the results of NLLS fits to the spectrum.

The Bruggeman Effective Medium Models. Bruggeman [1935] is credited with two very significant contributions to the modeling of two-phase systems, generally known as the Bruggeman asymmetric and symmetric models.⁶ The asymmetric model is an extension of the Maxwell-Wagner model to high volume fractions of discontinuous phase. This model treats the discontinuous phase as embedded in a medium that is itself modified by the presence of the discontinuous phase. Using the same notation as before, the Bruggeman asymmetric model is described by Eq. (24).

$$\frac{\psi_1}{\psi_t} \left(\frac{\psi_t - \psi_2}{\psi_1 - \psi_2} \right)^3 = (1 - x_2)^3 \quad (24)$$

Since this expression has an excellent pedigree and is explicit in the volume fraction x_2 , it has often been used to estimate the phase volume fractions of composite conductors or dielectrics where the

TABLE 4.1.2 Selection of form Factors According to Fricke [1953] for Use in Eq. (23)

a/b	b/c	ϕ_1	ϕ_2	ϕ_3	Particle shape
1	1	2.00	2.00	2.00	Spherical
1	2	4.79	1.42	1.42	
1	4	12.2	1.16	1.16	Spheroidal
1	6	21.6	1.09	1.09	
2	2	7.9	2.50	0.66	Ellipsoidal
2	6	20.7	6.9	0.209	

Source: Fricke 1953. Reproduced with permission of American Chemical Society.

Note: These factors have been calculated from the axial ratios of the ellipsoidal particles a, b, c , where $a \geq b \geq c$.

⁶ As is common in this area, these expressions have been credited to several sources. For example, the symmetrical Bruggeman formula is also known as the Polder-van Santen formula. It has also been attributed to Landauer [1978], who pointed out the percolation aspect. For a more complete discussion of the equations and their nomenclature, the reader is referred to Sihvola [1999].

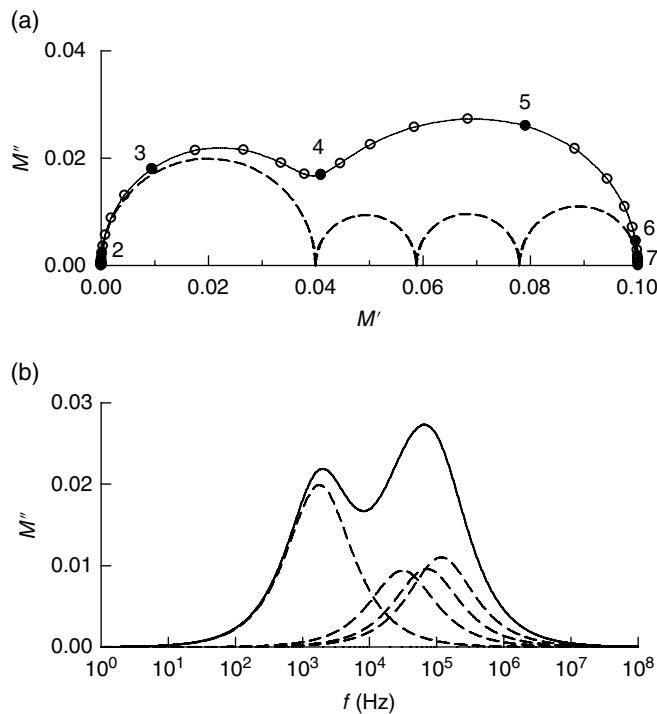


FIGURE 4.1.10 Simulated impedance and modulus spectra for two-phase microstructure comprising a matrix of phase 1 with randomly oriented ellipsoids of phase 2 at a volume fraction of 0.25. (a) Modulus spectrum resolving two arcs. (b) Imaginary modulus spectrum, showing peaks relating to the three principal orientations of the ellipsoids. The input parameters are given in Table 4.1.3.

TABLE 4.1.3 Input Parameters Used for the Simulation Shown in Figure 4.1.10, according to the Fricke [1953] model for ellipsoids

Conductivities (S/cm)	$\sigma_1 = 10^{-8}, \sigma_2 = 10^{-6}$
Permittivities (F/cm)	$\epsilon_1 = \epsilon_2 = 8.85 \times 10^{-13}$
Ratios of ellipsoid semiaxes	$a/b = 2, b/c = 2$
Form factors	$\phi_1 = 7.90, \phi_2 = 2.50, \phi_3 = 0.66$
Volume fraction of suspended phase	$x_2 = 0.25$

Source: Fricke 1953. Reproduced with permission of American Chemical Society.

conductivity and permittivity, respectively, are real. The expression has not been often used with complex variables, no doubt, because it is implicit in ψ_t and, therefore, difficult to evaluate. Tuncer *et al.* [2001, 2002] have used a numerical solution, while Sihvola [1999] has given a series expansion that can be used for complex variables. An extended version of the series is given hereafter (Sihvola [2003] private communication).

$$\begin{aligned} \psi_t = & \psi_1 + 3\psi_1 r x_2 + 3\psi_1 r^2 \frac{\psi_1 + 2\psi_2}{\psi_2 + 2\psi_1} x_2^2 + 2\psi_1 r^4 \frac{\psi_1 + 5\psi_2}{\psi_2 + 2\psi_1} x_2^3 \\ & + 3\psi_1 r^4 \frac{5\psi_2^3 - 21\psi_1\psi_2^2 + 6\psi_2\psi_1^2 + \psi_1^3}{(\psi_2 + 2\psi_1)^3} x_2^4 \dots \end{aligned} \quad (25a)$$

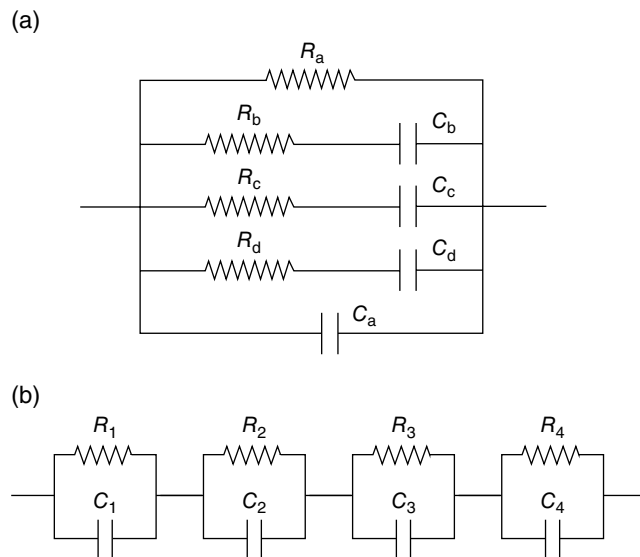


FIGURE 4.1.11 Two equivalent circuits for a matrix of phase 1 containing randomly oriented ellipsoids of phase 2 according to model proposed by Fricke [1953]: (a) parallel circuit and (b) series circuit. Source: Fricke 1953. Reprinted with permission of American Chemical Society.

TABLE 4.1.4 Parameter Values for the Circuits Shown in Figure 4.1.11, Obtained by NLLS Fitting to the Spectrum of Figure 4.1.10

Element	r_i ($\Omega \text{ cm}$)	c_i (F/cm)	f_i (Hz)	Element	r_i ($\Omega \text{ cm}$)	c_i (F/cm)	f_i (Hz)
a	4.2×10^7	8.9×10^{-13}	4.3×10^3	1	4.0×10^7	2.2×10^{-12}	1.8×10^3
b	9.8×10^6	8.3×10^{-13}	2.0×10^4	2	1.1×10^6	4.7×10^{-12}	3.1×10^4
c	2.0×10^7	7.8×10^{-14}	1.0×10^5	3	4.8×10^5	4.6×10^{-12}	7.2×10^4
d	1.2×10^7	2.4×10^{-13}	5.5×10^4	4	3.4×10^5	4.0×10^{-12}	1.2×10^5

Note: The products $f_a f_b f_c f_d$ and $f_1 f_2 f_3 f_4$ are equal.

where

$$r = \frac{\psi_2 - \psi_1}{\psi_2 + 2\psi_1} \quad (25b)$$

Evaluation of this expression generates a spectrum rather similar to that for the Maxwell–Wagner model but with a different weighting of the two phases. Figure 4.1.12 shows a modulus spectrum for the same input parameters as those that were used to produce the spectrum in Figure 4.1.9b.

The symmetric Bruggeman model does not make a distinction between continuous and discontinuous phases, and, therefore, the relevant expression is symmetrical in ψ_1, ψ_2 . It seems to have been first applied to the complex variable by Landauer [1978]. Coverdale *et al.* [1995] give an in-depth discussion of its relevance to impedance spectra of composite materials. The symmetric Bruggeman model is described by Eq. (26):

$$\psi_m = \frac{1}{4} \left\{ q + (q^2 + 8\psi_1\psi_2)^{\frac{1}{2}} \right\} \quad (26a)$$

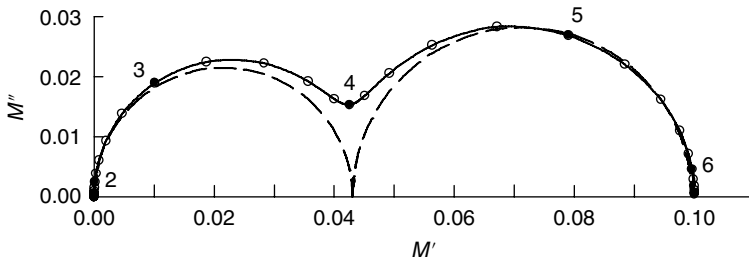


FIGURE 4.1.12 Modulus spectrum for the Bruggeman asymmetric dispersed phase model (Eq. 19), using $\sigma_1 = 1 \times 10^{-8} \text{ S/cm}$, $\sigma_2 = 1 \times 10^{-6} \text{ S/cm}$, $\kappa_1 = \kappa_2 = 10$, and $x_2 = 0.25$. This calculation was made by solving Eq. (24) numerically in the complex domain. Labels indicate $\log(f)$.

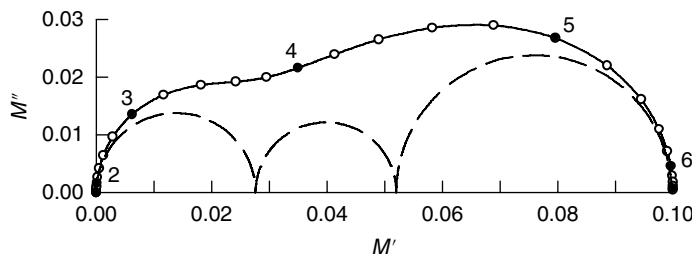


FIGURE 4.1.13 Modulus spectrum for the Bruggeman symmetric model (Eq. 20) for dispersed phases using the same input parameters as were used for Figure 4.1.12. Labels indicate $\log(f)$.

where

$$q = (3x_1 - 1) \psi_1 + (3x_2 - 1) \psi_2 \quad (26b)$$

and

$$x_1 + x_2 = 1 \quad (26c)$$

While the model was originally based on effective medium considerations, it is instructive that Kirkpatrick [1973] was able to derive an identical expression using a discrete resistor network. For an application to mixed conductors, see Wu and Liu [1997].

Figure 4.1.13 shows a modulus spectrum generated using Eq. (26) with the same input parameters as those in the previous figure. Unlike the case of the Maxwell-Wagner model, the spectrum cannot be reproduced by a simple RC circuit (the dashed arcs shown in the figure give only an approximate fit). Equation (26) has the important property that, as the volume fraction of the high conductivity phase approaches $1/3$, its effect becomes dominant, as can be easily verified by substituting two unequal values of (real) dc conductivity. Thus the model provides an elementary and very economical description of phase percolation.

Finite Element Modeling of Mixed Phase Systems. Another approach to the problem is to generate lattices populated with phases of different dielectric constant/conductivity and to compute their properties by the method of finite elements. Tuncer *et al.* [2001, 2002] have pursued this for a variety of pseudorandom and periodic lattices and compared the results obtained with the predictions of

mathematically precise models, including the Bruggeman symmetric model and others presented in this section. The articles are a good introduction to the literature on mixed phases as well as covering computational aspects of the subject.⁷

Non-ideal Behavior. The previous examples illustrate the way in which microstructural features affect the impedance spectra. This should not, however, be taken to mean that non-ideal behavior (i.e., departure from a single arc centered on the real axis of Z or M) necessarily implies phase heterogeneity. The assumption that σ and κ are frequency independent is not justified for real materials; see, for example, Jonscher [1975c, 1983]. Frequency-dependent conductivity can be caused by factors other than microstructure, even for ceramics such as zirconia (Abélard and Baumard [1982]). However, the resulting non-idealities are, in general, less prominent than the microstructural effects discussed here. The examples also illustrate the importance of choosing the right representation. In cases where grain boundary effects are dominant, the impedance spectrum is the best starting point, while for mixtures of phases with different conductivities, the modulus is more useful. In the author's opinion, the value of the modulus representation has been often underrated, and investigators are urged to use it more extensively, where mixed phases are concerned.

4.1.1.4 Modeling of Composite Electrodes

In the models discussed previously, the constituent phases have different values of conductivity, but the conductivities are of the same type, that is, they are both ionic or both electronic, therefore, no special conditions apply at the boundaries between the phases. Examples of systems where this situation holds are polyphase zirconia ceramics (oxide ion conductors), discussed in Section 4.1.3, and PTCR materials (electronic conductors).

There are, however, a number of important systems where this situation does not hold, for example, ceramic–metal composites and ceramic composites of electronic and ionic conductors, used as electrodes in SOFCs. Composite electrodes are important in an SOFC, as they provide the contact area necessary for the electrode processes to occur.⁸ This is usually visualized as the three-phase boundary (TPB), the boundary line where electronic conductor, ionic conductor, and pores meet. A composite cathode is shown schematically in Figure 4.1.14, after Costamagna *et al.* [1998]. The processes occurring in a composite electrode are briefly as follows:

- Electron transport from the electronic current collector to the TPB
- Electrochemical reaction at the TPB and gas diffusion in the pores
- Ion transport from TPB to the electrolyte, via the ionic conductor

These reactions generate electrochemical impedances due to charge transfer, gas- or solid-state diffusion, and so on. Since these impedances appear specifically at the boundaries between dissimilar phases, the composites cannot be fully described by simple effective medium models, even if these impedances are approximated by linear resistive elements. As pointed out by several authors, in the mixture of electronic and ionic phases, there are clusters connected to (i) both current collector and electrolyte, (ii) only to the electrode, and (iii) isolated clusters. This is illustrated in Figure 4.1.15a for a composite of three phases, an electronic conductor (40%), an ionic conductor (40%), and pores (20%), arranged in a hexagonal lattice and assigned pseudorandomly. Clusters of type (i) and (ii) are labeled.

Kenjo *et al.* [1991] have described composite electrodes using the finite-length pore model shown in Figure 4.1.15b. The electronic and ionic conductor paths run in parallel, with pores providing access to the gas phase via the electrolyte, which is unrealistic, but may not be of any great consequence.

⁷Tuncer *et al.* [2001, 2002] displayed the results in the spectrum of complex dielectric susceptibility, χ , defined by the relation $\chi \equiv \kappa - 1$, rather than the modulus ($M \equiv \kappa^{-1}$), adopted in this section.

⁸The electronic conductors commonly used for SOFCs are lanthanum strontium manganite (LSM) for cathodes and nickel metal for anodes. The anodes are prepared *in situ* by reduction of a nickel oxide/electrolyte composite.

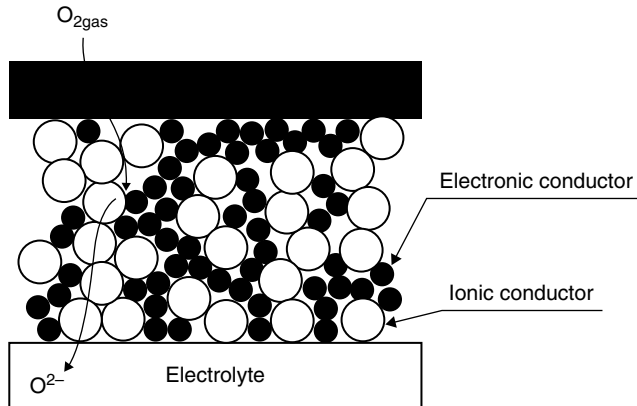


FIGURE 4.1.14 Schematic diagram of composite cathode, after Costamagna *et al.* [1998]. Source: Costamagna 1998. Reprinted with permission of Elsevier.

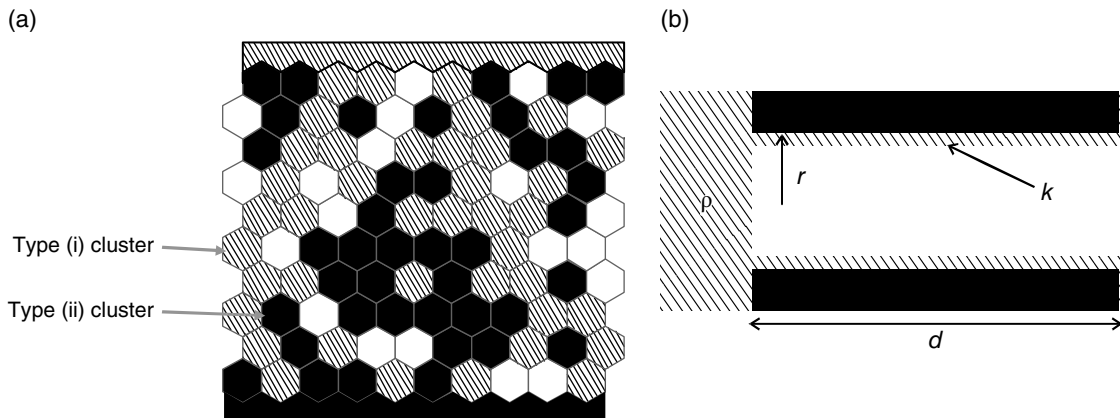


FIGURE 4.1.15 Visualization of a composite electrode with electronic conductor (black), ionic conductor (hatched), and pores (blank). (a) As a composite consisting of three phases with different types of clusters (see text). (b) As a finite-length pore with electronic and ionic conductor paths running in parallel.

Essentially, the composite is regarded as consisting of type (i) clusters only. For this model, the polarization resistance is given by Eq. (27),

$$R_p = \sqrt{\frac{\rho k r}{2}} \coth \sqrt{\frac{2d^2 \rho}{kr}} \quad (27)$$

where ρ is the electrolyte resistivity, k is the contact resistance, d is the pore length, and r is the pore radius. The resistivity of the electrode material is taken as zero.⁹ R_p increases with the pore radius and decreases with the pore length, to an asymptotic value of $\sqrt{\rho k r / 2}$. The pore radius and pore length in Figure 4.1.15b roughly correspond to the electrode thickness and particle size in Figure 4.1.15a. It is not clear how the volume fractions of the electrode and electrolyte materials could be built into this

⁹ In the previous expression, ρ is in Ωcm and k in Ωcm^2 . Kenjo *et al.* [1991] have mainly used an alternative definition for k , which contains the factor $r/2$ and, therefore, has units of Ωcm^3 .

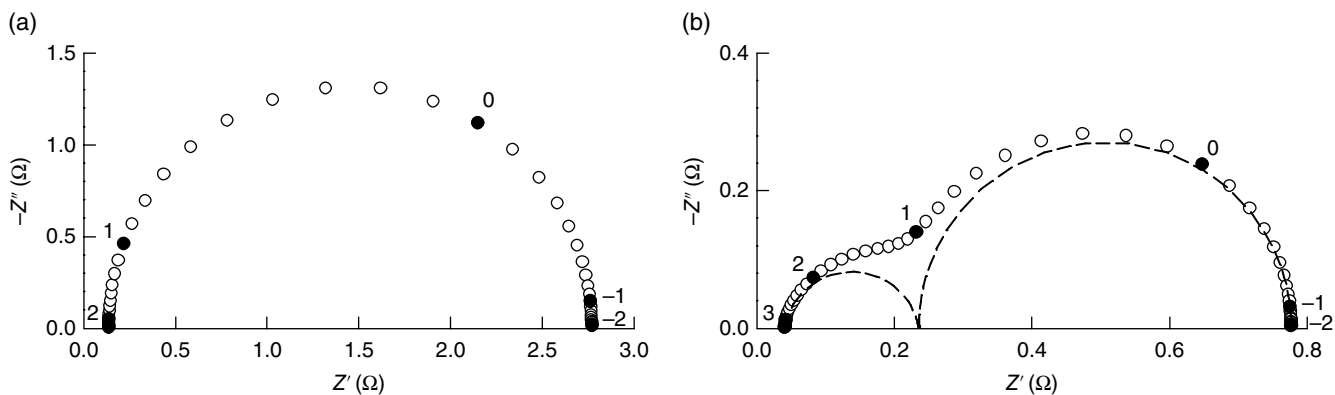


FIGURE 4.1.16 Impedance spectra of an electrode with two volume fractions, ϕ , of the electrode phase, for the case where the contact impedances contain only charge transfer resistance and double-layer capacitance: (a) $\phi = 0$ (single phase electrode) and (b) $\phi = 0.3$ (composite electrode). For details of the simulation, see Sunde [2000]. The labels show the logarithm of the normalized frequency. Source: Sunde 2000. Reprinted with permission of Springer.

model. Kenjo *et al.* [1991] treated only for the dc case but, if an interfacial capacitance were to be included, the model would become equivalent to a Gerischer impedance.

A refinement of the previous approach is to treat the composite as a quasi-homogeneous system with specific electronic/ionic conductivities and gas diffusion properties, with the electrochemical reaction distributed uniformly over its volume. The problem has been solved in one dimension by Costamagna *et al.* [1998], but their solution applies to the steady state and is not relevant to the present discussion, which concentrates on the frequency domain. Furthermore, intuition would suggest that a one-dimensional model would not completely describe a system as complex as that depicted in Figure 4.1.14.

There seems to be no alternative to the generation of stochastic composite structures and their solution by computer methods. In a series of papers, Sunde has treated the bulk resistivity and polarization resistance for the steady-state (Sunde [1996a, b]) and the electrode impedance in the frequency domain (Sunde [1997, 2000]). Although this work focused on nickel/zirconia anodes, the methodology is equally valid for other composite electrodes. The first step was to use the Monte Carlo method to generate pseudorandom packings of spherical electrode and electrolyte particles and identify neighbors. Contacts between dissimilar phases were assigned electrochemical impedances describing charge transfer, double-layer capacitance, reactant adsorption, and so on, while contacts between similar phases were taken to be purely ohmic.¹⁰

The simplest case is illustrated here, where the contact impedances contained terms for charge transfer and double-layer capacitance. Figure 4.1.16 shows impedance spectra for such an electrode for two volume fractions, ϕ , of the electrode phase. In the first case ($\phi = 0$), which describes a single-phase electrode, the spectrum corresponds to a summation of many RC elements in parallel. In the second case ($\phi = 0.3$), which describes a composite electrode, a new arc appears at the high-frequency end of the spectrum. For the simulation in hand, the high-frequency arc can be fitted to a ZARC ($n \approx 0.9$), while the low-frequency arc corresponds closely to a parallel RC element ($n = 1$). Note that in the case of $\phi = 0.3$, the polarization resistance ($Z_{f \rightarrow 0} - Z_{f \rightarrow \infty}$) decreases by a factor of about four, which elegantly illustrates the technological importance of composite electrodes in SOFCs.

¹⁰ It is important to distinguish between the bulk resistivity of the composite, which arises when it is contacted via two electronic conductors, and the electrode impedance, which arises when it is placed between an ionic and an electronic conductor, as in SOFCs.

The presence of a new feature may be qualitatively explained in terms of the three types of clusters mentioned previously. It is suggested that at low frequency only clusters of types (i) and (ii) are active, while at high frequency, the double-layer capacitance reduces the magnitude of the contact impedance, and type (iii) clusters progressively "switch in," producing a second arc. The degree of overlap of the arcs depends on the volume fraction of the electrode phase, an effect for which Sunde provides a tentative explanation: at low volume fractions, where the overall impedance is dominated by the electrolyte, type (iii) clusters have a significant effect and generate a well resolved arc, while at higher volume fractions, where the electrode phase is near or above percolation, the effect amounts only to a distortion of the original electrode arc.

A valuable property of such modeling experiments is that all currents and potentials are stored and available for further analysis. An elegant way of visualizing the function of the composite electrode would be to sum the partial electronic and ionic currents at various depths within the composite electrode and plot them as a function of position. The partial currents could be used to identify the region of maximum charge transfer in the composite.

4.1.2 Experimental Techniques

4.1.2.1 Introduction

A wide range of materials can be usefully characterized by IS, namely, electrical and structural ceramics, magnetic ferrites, semiconductors, membranes, polymeric materials, and protective paint films. The measurement techniques used to characterize materials are generally simpler than those used for electrode processes. Impedance spectra are usually independent of applied potential (both ac amplitude and dc bias) up to potentials of 1 V or more. Consequently, it is unnecessary to fix the potential of electrodes, as is the case with potentiostatic experiments, and two-electrode symmetrical cells are commonly used.

Considerations of Frequency and Impedance Range. As discussed in Section 4.1.3, the frequency range to be chosen depends on the relaxation frequencies f_n of phases present in the sample under study and also on the microstructure. The highest relaxation frequency is normally that of the grain interior relaxation and is given by $f_{gi} = \sigma_{gi}/(2\pi\epsilon_{gi})$, corresponding to the apex of the grain interior impedance arc. Conductivities vary enormously from one material to another, and with temperature for any one material. By contrast, the dielectric constants of most compounds, apart from ferroelectrics, lie within the range of 5–100. Taking a dielectric constant 30 as typical (this is close to the value for cubic zirconia), the relationship between conductivity and relaxation frequency is illustrated in Figure 4.1.17.

Impedance analyzers have maximum frequencies of 10–100 MHz, but operation at these frequencies requires samples to be contacted with very short leads. If the samples are placed in a furnace or cryostat, leads of 10–100 cm in length are required, and this limits the maximum operating frequencies to a few MHz. At the low-frequency end, a practical limit is set by the measurement time: one cycle at 10^{-4} Hz has a duration of about 3 h. This frequency range is shown in the upper shaded region of Figure 4.1.17. Based on a dielectric constant of 30, the usable frequency range corresponds to a range of 10^{-4} to 10^{-15} S/cm for the conductivity. A further lower bound for the conductivity is set by the resolution of the impedance analyzer, which is typically approximately 10^{-8} S. For a sample of aspect ratio 0.1 cm^{-1} , this would correspond to a conductivity approximately 10^{-9} S/cm, while for samples of lower aspect ratio, the lower conductivity bound is increased proportionally. For example, it is possible to obtain the spectra of grain boundary layers in ceramics even though these layers have microscopic conductivities as low as

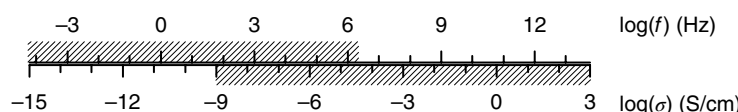


FIGURE 4.1.17 Relationship between relaxation frequency and conductivity and for a solid having a dielectric constant of 30.

10^{-12} S/cm, because they are very thin. The lower shaded region in Figure 4.1.17 shows the range of bulk conductivity for which impedance spectra can be obtained using generally available impedance measurement systems.

4.1.2.2 Measurement Systems

Most of the measurement equipment required for impedance studies can be bought off the shelf and fall under three categories:

1. Frequency response analyzers (FRAs)
2. Component analyzers, impedance analyzers, and ac bridges
3. Potentiostats, galvanostats, and general electrochemical interfaces

Frequency Response Analyzers. These instruments are designed to measure a voltage ratio, rather than impedance, but can be adapted to measure impedance by the addition of auxiliary components—in the simplest case, a standard resistor. A detailed account of the circuitry, which was included in the first edition of this volume, would be out of place today; here it will be dealt with in brief, to illustrate the principles involved.

FRA generates a sinusoidal voltage of variable frequency and amplitude and measures the in-phase and out-of-phase components of the voltage at two inputs, "X" and "Y." The voltages are expressed as complex quantities $V_X = V'_X + jV''_X$ and $V_Y = V'_Y + jV''_Y$. The simplest circuit for measurement of impedance uses the standard resistor in a voltage divider configuration, shown in Figure 4.1.18. In this case, input "X" is used to measure the generator output and input "Y" to measure the midpoint of the divider. The unknown impedance is then given by

$$Z_u = \frac{V_Y}{V_X - V_Y} Z_s \quad (28)$$

The main disadvantage of this configuration is that input "Y" is connected in parallel to the sample. The inputs of the FRA have a finite impedance, Z_{in} , typically $1\text{ M}\Omega$ in parallel with $30\text{--}50\text{ pF}$ and, unless $Z_s \ll Z_{in}$, this leads to an error in Z_u . The problem can be reduced by placing fast unity-gain amplifiers (buffers) at the FRA inputs. The situation can also be helped by interchanging the standard and the unknown, so that the input impedance of "Y" appears across the standard. If the standard resistance is made small, the effect of Z_{in} is minimized. This, however, adds complexity and results in a low voltage signal at "Y."

An alternative approach that eliminates the aforementioned problems uses the active current-to-voltage converter shown in Figure 4.1.19, with the standard resistor placed in the feedback loop of a fast operational amplifier. The amplifier delivers an output, such that the junction "T" in the diagram is maintained at ground potential (*virtual ground*). Consequently, any stray conductance/capacitance from "T" to ground is excluded from the measurement. Since the effect of capacitances has been

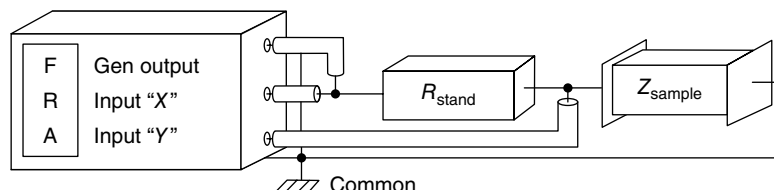


FIGURE 4.1.18 Impedance adaptor for frequency response analyzer (FRA) based on voltage divider network.

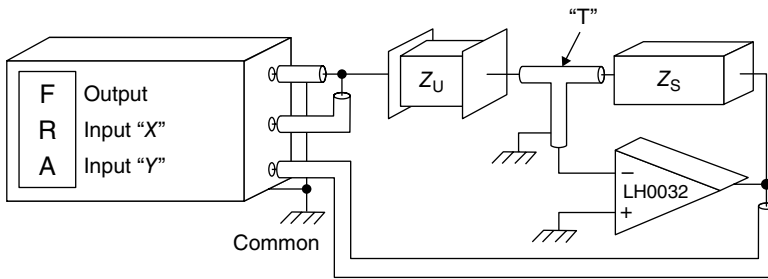


FIGURE 4.1.19 Impedance adaptor for frequency response analyzer (FRA) incorporating a current-to-voltage converter.

eliminated, the leads to the sample can be screened, reducing the effect of electrical noise. In the configuration, the unknown impedance is given by

$$Z_u = -\frac{V_X}{V_Y} Z_s \quad (29)$$

The complex quotient V_X/V_Y is computed by the impedance analyzer. Normally, Z_s is a pure resistor, in which case, Z_u has a simple relationship to this quotient. In principle, any circuit of well-defined impedance may be used (e.g., parallel RC combination), bearing in mind, of course, that the multiplication of V_X/V_Y and Z_s must be performed in the complex domain. It is good practice to select a standard resistor of magnitude comparable to the real part of the unknown. Obviously, a trial measurement is needed in order to select the standard resistor.

The frequency range of an active current-to-voltage converter is limited mainly by the gain and phase performance of the operational amplifier, which falls at high frequencies. An analysis of this effect (T. Goldrick [1982], unpublished work) shows that, for certain simplifying assumptions, the apparent impedance Z_m is related to the standard and unknown as follows:

$$Z_m = Z_u + j \frac{f}{f_o} (Z_s + Z_u) \quad (30)$$

where f is the measurement frequency and f_o is the frequency at which the open-loop gain of the amplifier falls to unity. This formula can be rewritten as

$$Z_m = Z_u + j 2\pi f L_s \quad (31)$$

where

$$L_s = \frac{Z_s + Z_u}{2\pi f_o} \quad (32)$$

For the case where the standard and unknown resistances are both real, the introduced error is equivalent to that of an inductor in series with the unknown. The pseudo-inductance will, of course, appear in addition to any physical inductance introduced by the leads.

Impedance Analyzers. Component analyzers, impedance analyzers, and ac bridges have built-in current-measuring circuits, which are designed to minimize the aforementioned problems. These instruments are usually configured for a four-wire connection, which minimizes stray series resistance and inductance, the dominant source of error for low impedance samples.

Impedance analyzers do not have the capability of controlling the potential with respect to a reference electrode—this requires the use of electrochemical interfaces, as described in Section 3.2. They can, nevertheless, be used to measure electrochemical cells under current load. In the configuration of Figure 4.1.20, the ac generated by an impedance analyzer in galvanostatic mode is added to the (higher) dc generated by an external galvanostat (S. Højgaard Jensen [2003], unpublished work). This configuration takes advantage of the superior high-frequency performance of the impedance analyzer, as compared to an electrochemical interface, which is essential for separating the series electrolyte resistance and electrode polarization effects.

While commercial measurement systems generally perform better than the improvised impedance adaptors described in Figures 4.1.18 and 4.1.19, they are not immune to errors, especially at the extremes of their specified range. The burden of obtaining error-free data cannot be carried wholly by the manufacturers, who may have designed the instrument for a different application than the one it is used for.

Measurement Rigs. Important considerations in the design of a rig for IS of materials are (i) provision of a controlled temperature and chemical environment for the sample and (ii) provision of the best possible electrical path to the sample.

The importance of temperature control is illustrated by considering a sample with an activation energy of 1 eV for the conductivity: at 800°C a change of 1°C would produce a change of 1% in conductivity. At 300°C, the same error would produce a change of 3.5%. A temperature stability of 1°C or better can be easily achieved with present-day three-term controllers, but this alone is not sufficient to ensure good temperature control: temperature gradients in the rig must be kept to a minimum and the temperature sensor must be in thermal contact with the sample.

The inner assembly of a general-purpose conductivity rig is shown in Figure 4.1.21. It is based on a ceramic “shoe” that slides over a ceramic supporting tube. A spring-loaded harness of Nichrome or Kanthal wire provides a load of approximately 20 g on the contacts. Contact is made with the sample via a platinum foil on either side. For situations where the electrode response is to be measured, the sample can be contacted by means of “castellated” alumina pellets, (Figure 4.1.22) wrapped in platinum mesh. This allows good contact while providing the gas with access to the electrodes. A four-wire configuration is recommended for this cell, as it reduces the magnitude of the series stray resistance and stray inductance.

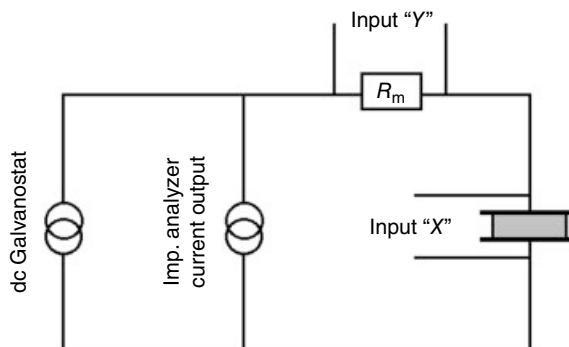


FIGURE 4.1.20 Measurement on an electrochemical cell under load. The dc generated by the external galvanostat is added to the ac generated by the impedance analyzer. The measurement resistor R_m is a low inductance, metal strip resistor, rated to the necessary dc current. Source: Reproduced with kind permission of S. Højgaard Jensen 2003.

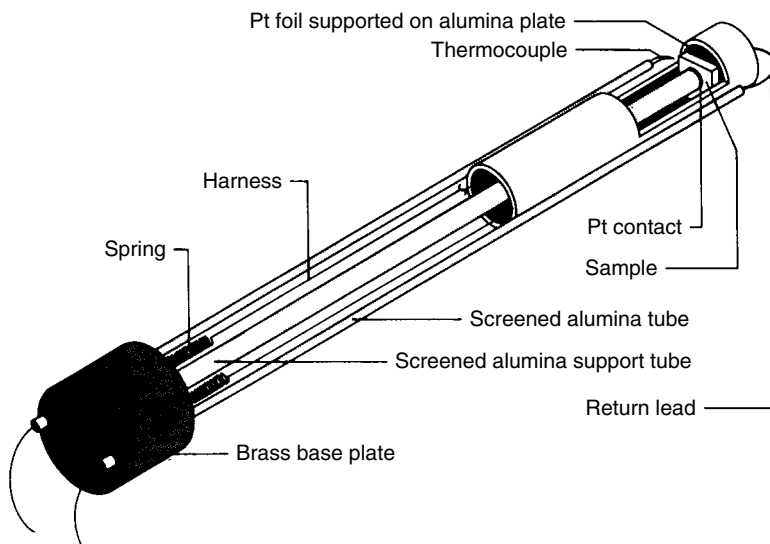


FIGURE 4.1.21 Rig used for the characterization of ceramic samples.

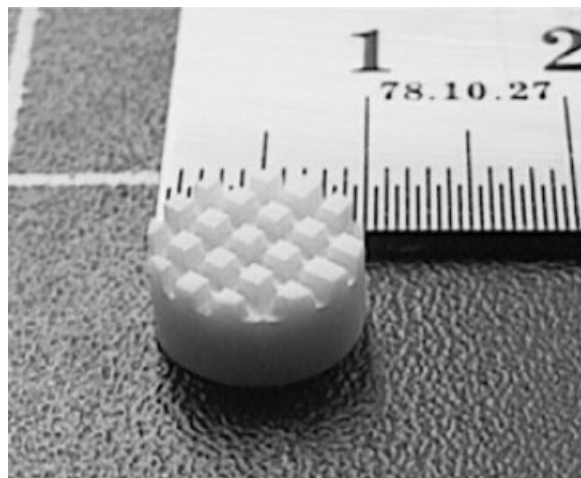


FIGURE 4.1.22 Castellated pellet used to support platinum mesh in impedance measurement rig.

Measurement Errors and Their Correction. One of the major sources of error is uncompensated or stray components. The components can be effectively connected in parallel or in series with the sample. The most important parallel component is stray capacitance, C_{sp} . In the first place, this can be minimized by screening leads within a short distance from the sample and grounding metal parts of the measurement cell. C_{sp} cannot be estimated by a measurement on the empty cell; without a sample, the capacitance of the air gap remains. Instead, the unknown is replaced with a sample of known dielectric constant and shape, and the calculated capacitance is subtracted from the measured one to give C_{sp} . Correction for the stray capacitance can then be made by subtracting $2\pi f C_{sp}$ from the imaginary part of the measured admittance. In a well-designed cell, the stray parallel conductance G_{sp} should be negligible. In cases where G_{sp} is significant, it is less straightforward to correct it after the measurement, as G_{sp} varies with the measurement conditions more strongly than C_{sp} does.

The series stray components are the inductance L_{ss} and resistance R_{ss} . Both of these can be kept low by using a four-wire connection. While the resistance can usually be eliminated, the inductance cannot; it

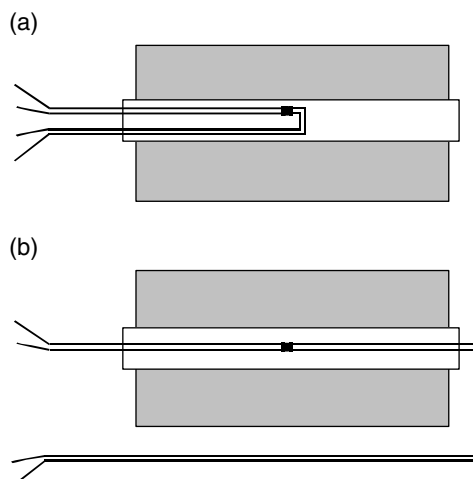


FIGURE 4.1.23 Two possible wiring configurations for a tube furnace. Configuration (b) produces an inductance that many times greater than that of (a) and should be avoided.

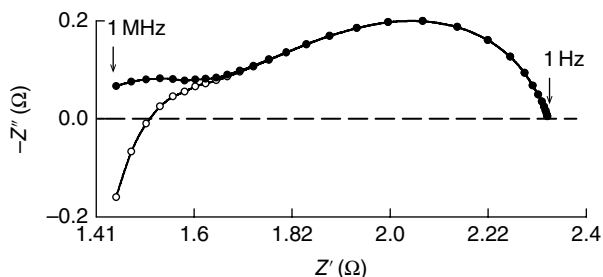


FIGURE 4.1.24 Effect of inductance error on the impedance spectrum of a symmetrical cell. Open symbols: raw data. Closed symbols: data corrected for stray inductance of 36×10^{-9} H. The sample is a YSZ tape of area 0.21 cm^2 with an LSM composite cathode on both sides, measured in air, 850°C .

depends on the length of leads and their positioning. Figure 4.1.23 shows two wiring configurations that could be used with a tube furnace. Configuration (b) produces an inductance that is 10–20 times greater than (a) and should be avoided at all cost (Primdahl and Hendriksen [1996]). The components R_{ss} and L_{ss} are measured with the cell shorted at the sample position. Correction for the series stray components is made by subtracting R_{ss} from the real part of the impedance and $2\pi f L_{ss}$ from the imaginary part. The effect of correction for inductance is shown in Figure 4.1.24 for a symmetrical cathode sample described in Section 4.1.3. The design of cells and correction of measurement errors have been further discussed by Bonanos *et al.* [2012].

4.1.2.3 Sample Preparation: Electrodes

The impedance of a sample is the product of the complex resistivity and the length over area ratio, l/A ; therefore samples should be prepared with parallel faces and a well-defined cross section. For

measurement of grain interior properties, surface finish is not critical, as this only affects the electrode impedance (Armstrong *et al.* [1973]). If the grain boundary and electrode arcs overlap, their resolution can be improved by polishing before applying the electrodes. Electrodes are applied by painting, vacuum evaporation, or sputtering. The types of electrodes commonly used are described in the following text.

Precious metal paints, also known as pastes or dags, are good general-purpose electrodes for IS studies. The most commonly used precious metal paints are platinum, palladium, gold, and silver, all of which are commercially available. Nickel and other transition metals are not generally available as paints. It is the case of platinum, as certain commercial products contain inorganic fluxes or glass to assist sintering, and these are best avoided, as they lead to high electrode impedances. Flux-free platinum paints are preferable, as long as the samples can tolerate the curing temperatures of over 1000°C that these products require. If high-temperature, oxidizing conditions are not part of the study, carbon paints can be used; moreover, water-based formulations should be used if the samples are sensitive to organic solvents.

Silver and gold, which have relatively high vapor pressures, can be easily applied by vacuum evaporation, while metals of lower vapor pressure, such as platinum, palladium, and stainless steel, can be deposited by radio frequency (RF) sputtering; in this case, however, the film thicknesses are limited to about 100 nm. Before electrode deposition, the samples must be cleaned and heat treated. Failure to remove surface impurities will result in loss of adhesion when samples are subsequently heated during the measurement.

The choice of electrodes also depends on the temperature of the investigation and the type of conductivity that is being investigated. Platinum and gold electrodes perform well at high temperatures, but at temperatures below 600°C, they are relatively blocking to oxygen. If the measurement temperature is lower than this, silver electrodes are preferable, as they generally have lower electrode impedances. Figure 4.1.25 shows impedance spectra for yttria-stabilized zirconia (an oxide ion conductor) with platinum and silver electrodes, at 300°C. The electrode impedances are considerably lower for the silver electrodes.

The preparation of electrodes is only the first step toward a successful experiment. The measurement system must also be kept free of elements such as silicon or phosphorus, which, under high-temperature-reducing conditions, form volatile compounds that attack the electrodes, for example, platinum, to produce brittle and poorly conducting compounds.

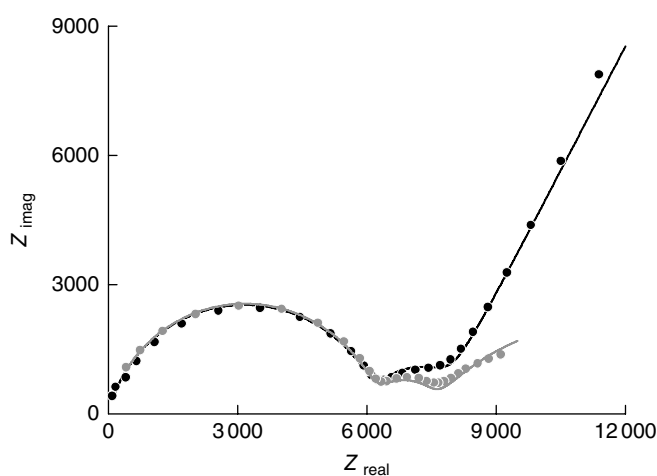


FIGURE 4.1.25 Impedance spectra for yttria-stabilized zirconia oxide ion conductor with platinum and silver electrodes, at 300°C. The electrode impedances are lower for the silver.

4.1.2.4 Problems Associated with the Measurement of Electrode Properties

In the work discussed so far, the main objective was to characterize the bulk properties; the electrodes were there only to make this measurement possible. In other situations, the bulk properties are already known, and the objective is to characterize the electrodes; this applies, for example, in the development of electrodes for SOFCs. In SOFCs, the current-potential characteristics of the electrodes are often found to be linear, and the steady-state properties of the electrodes can be adequately represented by a linear polarization resistance, R_p . The characterization of electrodes in these systems can be performed in one of two ways.

1. On symmetrical cells equipped with two nominally identical electrodes, using a small ac signal, at zero dc polarization. In this case, the electrode polarization obtained from the impedance plot must be divided by two, since it is caused by the two electrodes in series. The measurement is simple and can be performed with an impedance analyzer.
2. On three-electrode cells, that is, cells equipped with working electrode (WE), counter electrode (CE), and reference electrode (RE) under potentiostatic or galvanostatic control. In this case, the small ac signal is superimposed on a dc polarization. The measurement requires an electrochemical interface (potentiostat or galvanostat) coupled to an FRA (see Section 3.2).

While the latter case offers greater flexibility, it is also susceptible to rather subtle errors, which arise from the positioning of the RE in relation to the WE. These errors need to be considered, if reliable electrode performance is to be obtained on solid electrolyte cells. With liquid electrolytes, the RE can be made as small as necessary and placed as close to the WE as required. With solids, the electrode must be located on the electrolyte surface or, if the electrolyte thickness permits, in a suitably fashioned recess (see Figure 4.1.26b). Here, the discussion is confined to the planar geometry shown in Figure 4.1.26a.

The problem arises because of nonuniform current distribution at the WE, or more precisely, different nonuniform current distributions in the case of $f \rightarrow \infty$ and $f \rightarrow 0$. If the cell could be constructed so that the current density was uniform over the WE, the measurement would yield the correct value of R_p . However, any misalignment of the WE and CE produces a distortion in the equipotential lines, of the type shown in Figure 4.1.27. Accordingly, an RE placed at the side of the WE will not be intersected by the equipotential passing through the midpoint of the electrolyte, but will read a potential either too high or too low. At $f \rightarrow 0$ the electrode impedance is equal to R_p , while at $f \rightarrow \infty$, the electrode impedance is negligible, due to the displacement current flowing through the double-layer capacitance. The different

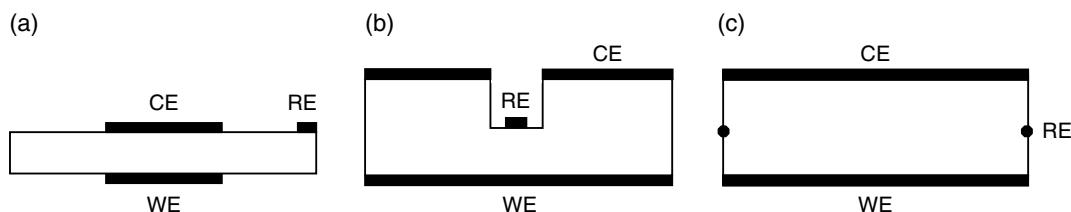


FIGURE 4.1.26 Commonly used geometries of three-electrode solid electrolyte cells.

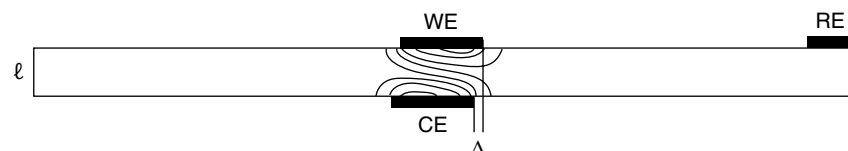


FIGURE 4.1.27 Distortion in the equipotential lines due to misalignment of the CE and WE in a thin electrolyte cell.

current distributions obtained in the two cases will cause a shift of the equipotential lines. This will interfere with the correct estimation of R_p when this is obtained using the expression $R_p = |Z_{f \rightarrow 0}| - |Z_{f \rightarrow \infty}|$ (see also Section 4.4.3).

The error has been analyzed by Winkler *et al.* [1998] using finite element modeling in the real domain (see also Primdahl and Hendriksen [1996]). The total current and RE potential were calculated for the low- and high-frequency limits and used to estimate the apparent value of R_p . The resulting error is plotted in Figure 4.1.28 as a function of the displacement between WE and CE, based on realistic values of electrolyte conductivity and polarization resistance of the electrodes and a value of 9×10^{-3} for the ratio of electrolyte thickness/electrode width. The figure shows that a displacement of one electrolyte thickness can produce an error of over 50%, for input parameters typical of SOFCs at operating temperature. Since electrolytes have thicknesses of 150 μm or less, it is clear that the construction of a fully reliable three-electrode cell in the planar geometry is technically impossible. It was further shown that, even with perfectly aligned electrodes, the errors arise if the R_p of the WE and CE do not match, although these are more difficult to explain in brief. Since the simulation covered only the extrema of frequency, the shape of the electrode arc could not be reconstructed from this analysis.

A recent and authoritative analysis of these features has been written by Adler [2002], who described the thin electrolyte case using finite element analysis in the complex domain. This revealed distortions of the electrode arc, both as a result of electrode displacement and a result of mismatch in the polarization resistances of the WE and CE. Figure 4.1.29 shows simulated spectra for perfectly aligned electrodes and for a displacement of one electrolyte thickness. Regarding the sign and magnitude of the errors, his conclusions are in agreement with those expressed previously. Adler [2002] also modeled the case of R_p mismatch between CE and WE and showed that the resulting plots have unusual reentrant shapes that cannot be explained with RC elements with positive component values.

Errors in three-electrode cells are also well covered in a series of papers by Hsieh and coauthors [1996a, b, 1997] and by Reinhardt and Göpel [1998] who showed distortions in the three-electrode spectra, produced by a size mismatch between WE and CE. From the aforementioned and from our practical

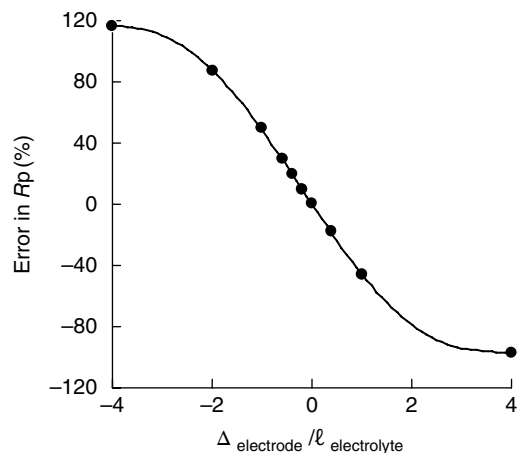


FIGURE 4.1.28 Error in the apparent polarization resistance due to the relative displacement of WE and CE in a planar cell. The error is calculated for an electrolyte resistivity of $10 \Omega \text{ cm}$ and a polarization resistance $0.16 \Omega \text{ cm}^2$ for both the WE and CE. A positive displacement is defined as a displacement of the WE in the direction of the RE, as in Figure 4.1.27. Source: Winkler 1998. Reproduced with permission of The Electrochemical Society.

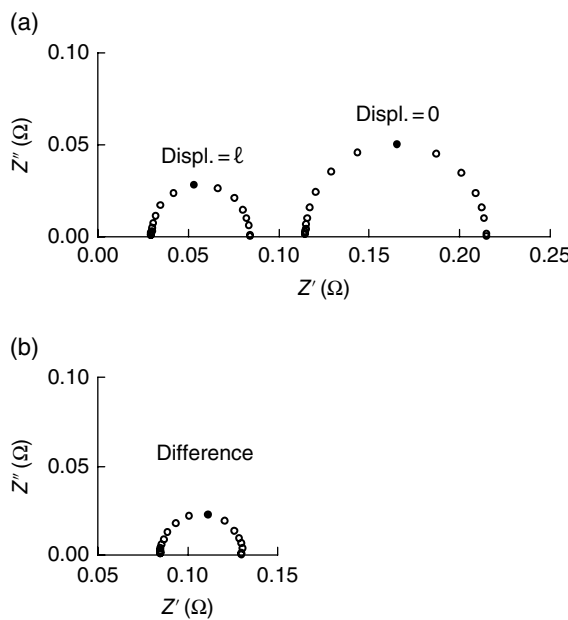


FIGURE 4.1.29 Distortion of the electrode arc in a thin electrolyte cell due to displacement of the WE. (a) No displacement and displacement from the RE by one electrolyte thickness. (b) Difference between the two spectra. For details, see Adler [2002]. Solid data markers show the angular frequencies, ω , of 1 s^{-1} . Source: Adler 2002. Reproduced with permission of The Electrochemical Society.

experience, we conclude that thin electrolyte cells are not suitable for use in three-electrode measurements. Instead we recommend using symmetric cells, because this will restrict the impedance measurements to open-circuit conditions only.

4.1.3 Interpretation of the Impedance Spectra of Ionic Conductors and Interfaces

4.1.3.1 Introduction

This section covers the interpretation of experimental impedance spectra of two-phase ceramics, solid electrolytes, and their electrode interfaces. Examples are given from the authors' work and from the literature, with preference to cases where the original data were available. Many of the examples refer to zirconia ceramics, since these materials give well-resolved spectra and exhibit interesting polymorphic phenomena, as well as the ionic conductivity that underlies their use in SOFCs and other electrochemical devices. In many of these examples, spectra are presented for temperatures well below normal operating temperatures of the materials, in order to bring the spectral features into the instrumental frequency range (see Figure 4.1.10).

Microstructural Aspects of Zirconia Ceramics. ZrO_2 is polymorphic and can have one of three crystal structures: monoclinic (*m*) at ambient temperatures, tetragonal (*t*) at $1170\text{--}2370^\circ\text{C}$, and cubic (*c*) between 2370°C and its melting point of 2700°C . On cooling from the temperatures of $1300\text{--}1800^\circ\text{C}$ normally used for sintering ceramics, ZrO_2 adopts the monoclinic structure. The transformation from *t* to *m* is accompanied by a significant volume change; as a result, pure ZrO_2 is unsuitable for the preparation of ceramics. The effect can be suppressed by doping with oxides such as CaO , MgO , and Y_2O_3 .

(Subbarao [1981], Subbarao and Maiti [1984]), with which it forms extensive solid solutions. At dopant concentrations of approximately 10 mol %, the solid solutions have a cubic structure and are called *fully stabilized zirconia* (FSZ). At 2–6 mol % Y_2O_3 , their structure remains tetragonal, provided the grain size is around 500 nm or less (Gupta *et al.* [1977]) and the materials are sometimes referred to as *tetragonal zirconia polycrystals* (TZPs). These systems can be sintered at lower temperatures than cubic zirconia and have a very high mechanical strength and toughness. Intermediate level of stabilizer results in a *c* matrix, with a fine dispersion of *t* and/or *m* precipitates (Kobayashi *et. al.* [1981]), which is termed *partially stabilized zirconia* (PSZ). The *t* precipitates have the property of transforming to *m* under the influence of a stress field and in doing so retard the propagation of cracks; the effect is known as *transformation toughening* (Garvie *et al.* [1975]).

When elements of valence 2 or 3 are introduced into zirconia, they occupy Zr^{4+} lattice sites, generating vacancies at oxygen sites. These provide zirconia its well-known ionic conductivity, leading to its use in high-temperature electrochemical cells (Steele [1976], Steele *et al.* [1981], Subbarao and Maiti [1984]). FSZ is mainly used for electrochemical application and PSZ mainly for structural applications, while TZP is used both as a solid electrolyte and a structural ceramic.

Bauerle's Circuit Equivalent. The use of IS for the characterization of ceramic solid electrolytes became routine after Bauerle [1969] showed that, for stabilized zirconia with platinum electrodes, the polarizations of the grain interiors, grain boundaries, and electrode–electrolyte interface could be resolved in the admittance plane. He presented a circuit equivalent for this arrangement that has since been applied to many other systems (Figure 4.1.30) with RC elements corresponding to grain interiors (gi), grain boundaries (gb), and electrode (e) connected in series.¹¹ The estimation of the circuit parameters was not straightforward due to Bauerle's choice of the admittance plane. Subsequent workers have generally used the impedance plane, where a direct relationship exists between the spectrum and the circuit (Armstrong *et al.* [1974], Schouler *et al.* [1981]). Examples of admittance and impedance spectra for a sample of ZrO_2 , mole % Y_2O_3 at 240°C, are given in Figure 4.1.31a and b. A simulated impedance plot is shown in Figure 4.1.31c using the parameters given in Table 4.1.5. The agreement between experiment and simulation is satisfactory for the grain interior and grain boundary arcs both in shape and distribution of frequencies, indicating that the circuit is adequate for representing the salient features of the frequency response.

4.1.3.2 Characterization of Grain Boundaries by IS

Understanding the origin of polarizations in ceramics is important, not only to optimize the electrical conductivity but also to achieve a better understanding of the microstructure, that in turn influences other properties, such as the mechanical strength. The fabrication of ceramics may involve adding small

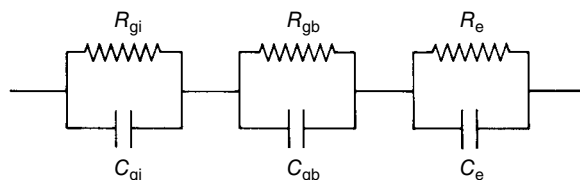


FIGURE 4.1.30 Circuit equivalent for a ceramic electrolyte according to Bauerle [1969] and modeling the impedance of the grain interiors (gi), grain boundaries (gb), and electrode (e). Source: Bauerle 1969. Reproduced with permission of Elsevier.

¹¹ The circuit shown in Figure 4.1.18 contains an extra capacitor for the grain interior element, not included by Bauerle, because the grain interior relaxation lay above the frequency range covered.

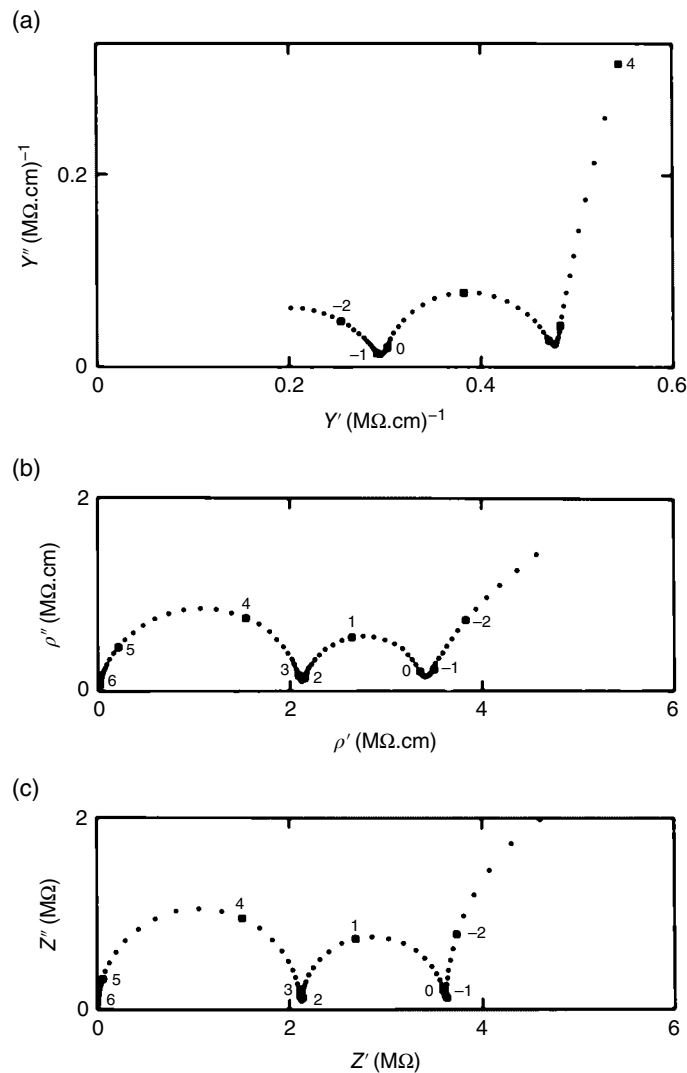


FIGURE 4.1.31 Comparison of admittance and impedance spectra for a zirconia solid electrolyte (ZrO_2 : 6 mol % Y_2O_3) at 240°C: (a) Experimental admittance spectrum. (b) Experimental impedance spectrum. (c) Simulated impedance spectrum, using the circuit of Figure 4.1.18 and parameter values given in Table 4.1.4.

TABLE 4.1.5 Circuit Parameters Used to Generate the Impedance Spectrum of Figure 4.1.31c

$C_{gi} = 4.8 \text{ pF}$	$C_{gb} = 1.7 \text{ nF}$	$C_e = 2.0 \mu\text{F}$
$R_{gi} = 2.1 \text{ M}\Omega$	$R_{gb} = 1.5 \text{ M}\Omega$	$R_e = 5.0 \text{ M}\Omega$

amounts of impurities that form liquids at the sintering temperature. In zirconia ceramics, trace amounts of silica and alumina fulfill this function, even if not added deliberately. On cooling, aluminosilicate phases, both amorphous and crystalline, form at the grain boundaries, with adverse effects on the ionic conductivity, as shown by Bauerle [1969], Schouler *et al.* [1973], Schouler [1979], Kleitz *et al.* [1981], and Bernard [1981]. Noting that small additions of Al_2O_3 could reduce the grain boundary resistance, Drennan and Butler [1982] suggested that the Al_2O_3 particles scavenge SiO_2 to form discrete particles of $\text{Al}_6\text{Si}_2\text{O}_{13}$ (mullite). Subsequent grain boundary migration during grain growth leaves these particles in the interior of the grains, where their influence on the ionic conductivity is smaller. This effect is in accordance with Eqs. (21) and (22), describing the effect of high-resistivity inclusions on the resistivity of ceramics.

Microstructure–Grain Boundary Property Correlations. The way in which the grain boundary structure affects the impedance spectrum is illustrated by comparing 3 mol % Y_2O_3 tetragonal and 6 mol % mainly cubic ceramics. Figure 4.1.32a shows a transmission electron micrograph of the 3 mol % specimen. The grain boundary phases were continuous with a thickness of 10 nm or less; from images obtained at lower magnifications, the grain size was estimated as 0.5–1 μm . Selected area diffraction patterns (SADPs) showed the grain boundary films to be amorphous, and energy-dispersive X-ray

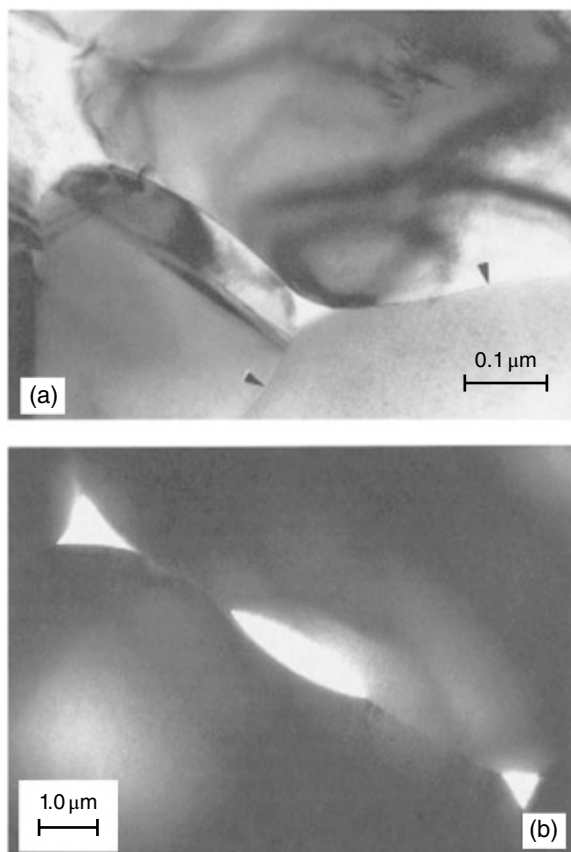


FIGURE 4.1.32 Transmission electron micrographs of two zirconia ceramics: (a) Tetragonal zirconia ceramic (ZrO_2 : 3 mol % Y_2O_3) showing thin, continuous grain boundary phase (arrowed). (b) Partially stabilized ceramic (ZrO_2 : 6 mol % Y_2O_3) showing discrete, lenticular grain boundary phase.

microanalysis detected SiO_2 , Al_2O_3 , and Y_2O_3 at levels of 65, 20, and 70 wt %, respectively (Butler and Bonanos [1985]). Figure 4.1.32b shows a transmission electron micrograph of the 6 mol % specimen with a size of approximately 10 μm . Pockets of second phase are seen along the grain boundaries—their lenticular shape indicates that they originate from non-wetting liquid phases present at high temperatures. Selected area electron diffraction analysis shows both crystalline and amorphous grain boundary phases; both are discrete, allowing partial intergranular contact.

While high-resolution transmission electron microscopy (TEM) is a powerful technique, it samples only a tiny fraction of the grain boundary area, potentially allowing some grain boundary defects to be missed. A definitive statement as to the absence of grain boundary phases cannot be made—the phases could be too thin or too sparse to detect. For electrically conducting materials, IS averages over the entire sample and thus provides a valuable complement to TEM.

Impedance spectra of the two zirconia ceramics at 300°C are shown in Figure 4.1.33. Both systems exhibit a Bauerle-type behavior. The spectrum of the 3 mol % material (Figure 4.1.34a) is dominated by a grain boundary arc due to the presence of a continuous grain boundary phase. In the 6 mol % material (Figure 4.1.34b), the grain boundary arc is relatively small. It seems that this material has been optimized for electrical conductivity and that the grain boundary resistance has been reduced by making the grain boundary phases discrete.

Further indirect information about the topology of the grain boundary phases can be obtained from the temperature dependence of the quantities r_{gi} and r_{gb} . In crystalline ionic conductors in the extrinsic region, the conductivity is thermally activated and described by

$$\sigma = \left(\frac{\sigma_0}{T}\right) \exp\left(\frac{-\Delta H_m}{kT}\right) \quad (33)$$

where ΔH_m is the activation enthalpy for migration. The Arrhenius plot linearizes this equation and ΔH_m is obtained from its slope. Arrhenius plots of r_{gi} and r_{gb} for the TZP and FSZ ceramics (Figure 4.1.22) are linear over the temperature range examined (200–500°C). In the tetragonal ceramic

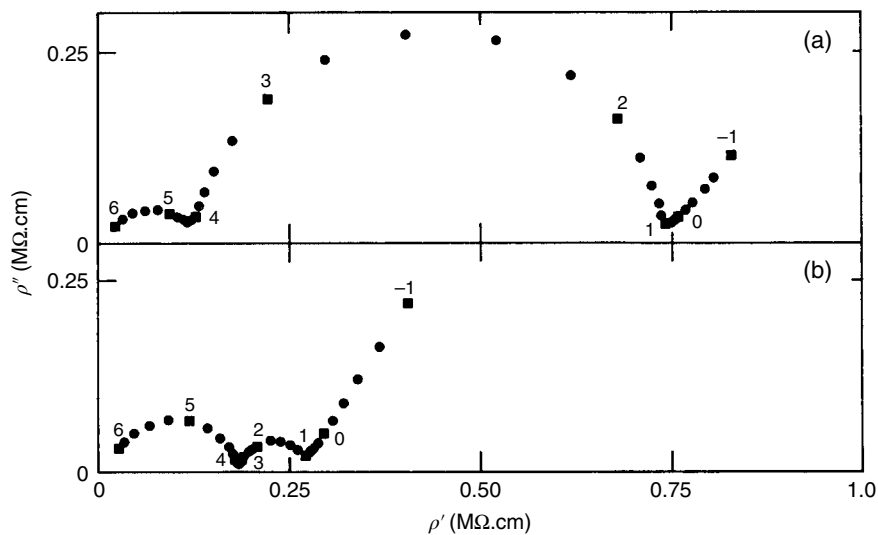


FIGURE 4.1.33 Impedance spectra for two zirconia ceramics, obtained at 300°C using sputtered platinum electrodes: (a) Tetragonal zirconia ceramic (ZrO_2 : 3 mol % Y_2O_3) with large grain boundary arc due to continuous grain boundary phase. (b) Partially stabilized ceramic (ZrO_2 : 6 mol % Y_2O_3) with small grain boundary arc due to discrete grain boundary phase.

Source: From Bonanos 1985.

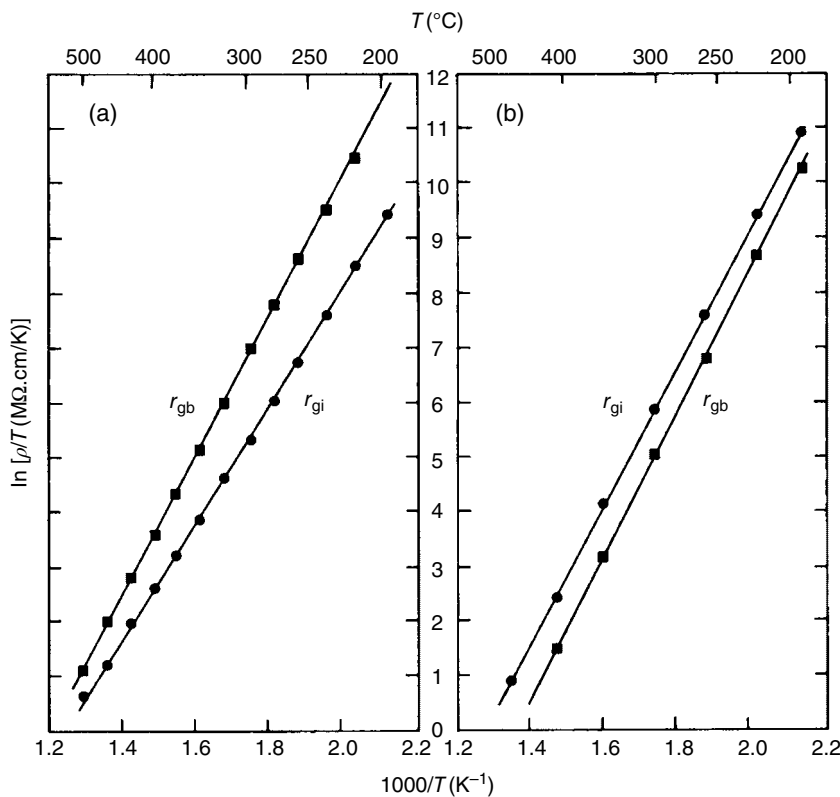


FIGURE 4.1.34 Arrhenius plots of the grain interior and grain boundary resistivities for two zirconia ceramics: (a) Tetragonal zirconia ceramic (ZrO_2 : 3 mol % Y_2O_3) in which the lines have different slopes, as expected from the brick layer model. (b) Partially stabilized ceramic (ZrO_2 : 6 mol % Y_2O_3) in which the slopes of the lines are similar, as expected for discrete grain boundary phase. Source: From Bonanos 1985.

TABLE 4.1.6 Activation Energies for Conduction for Three $\text{ZrO}_2:\text{Y}_2\text{O}_3$ Ceramics of Different Composition and Structure

Sample	Composition	Structure	ΔH_{gi} (eV)	ΔH_{gb} (eV)
Y-TZP	3.0 mol % Y_2O_3	Tetragonal	0.92	1.09
Y-PSZ	4.7 mol % Y_2O_3	Cubic + tetragonal	1.07	1.15
Y-PSZ	6.0 mol % Y_2O_3	Cubic + tetragonal	1.07	1.12

(Figure 4.1.22a), the slopes are different (higher for r_{gb}), as expected on the basis of the brick layer model without easy paths. For the mainly cubic ceramic (Figure 4.1.22b), the slopes are quite similar, suggesting that a partial blocking model is more appropriate to this material. The conclusions based on analysis of the impedance spectra support TEM studies in assigning specific microstructural models to each ceramic. Table 4.1.6 gives the activation enthalpies for the two materials and for a third PSZ ceramic, intended for electrical applications.

The treatment of the capacitive elements of the circuit equivalent differs according to which model applies. For the brick layer tetragonal ceramic, the grain boundary capacitance can be used to calculate the grain boundary thickness using Eq. (11). Not having any information on the dielectric constants of

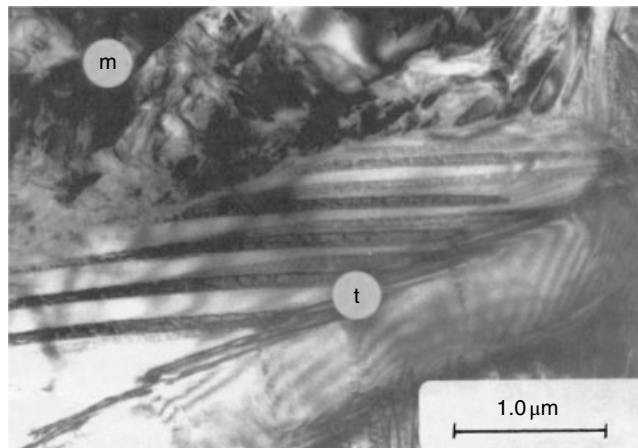


FIGURE 4.1.35 Transmission electron micrograph of a single crystal (ZrO_2 : 2.2 mol % Y_2O_3), showing separate regions of monoclinic (*m*) and tetragonal (*t*) phases. The micrograph was obtained at 1 MV.

Source: From Bonanos 1985.

the grain boundary phase, we assume $\varepsilon_{gi} = \varepsilon_{gb}$,¹² and calculate a grain boundary thickness of 4 nm, compatible with the 10 nm estimated from the electron micrograph.

For the mainly cubic 6 mol % material, this type of calculation is inappropriate, since the grain boundary phases are discontinuous. Instead, one can use Eq. (13) (partially blocked transport) to calculate a blocking coefficient β . A value of 0.3 is found, implying grain boundary coverage of 30% in second phase. This seems to be in accord with the appearance of the boundaries in Figure 4.1.20 and in other micrographs examined. Thus, for the two zirconia ceramics, TEM and IS give compatible information regarding the dimensions and continuity of the grain boundary phases.

Materials with No Grain Boundary Impedance Arc. Single crystals are an obvious example of such materials. Single crystals of stabilized zirconia are grown commercially for artificial gems by a process known as *skull melting*. Bonanos and Butler [1985] characterized crystals of $\text{ZrO}_2\text{:Y}_2\text{O}_3$ (2.2 and 3.4 mol %) by X-ray diffraction, TEM, and IS. Transmission electron micrographs of the 2.2 mol % crystal (Figure 4.1.35) showed striated areas characterized by a reorientation of the crystals known as *twinning*. SADP of these areas revealed the presence of both *m* and *t* phases. The *t* phase was similar in morphology to a non-transformable phase *t* observed by Lanteri *et al.* [1983] in crystals of similar composition. In the 3.4 mol % crystal, only the *t* phase was observed.

The impedance spectra of the two crystals are shown in Figure 4.1.36. For the 2.2 mol % crystal (Figure 4.1.24a), the spectrum shows a large, distorted grain interior arc and an electrode arc. The depressed arc is due to the combination of tetragonal and monoclinic phases; indeed, it appears to be composed of two poorly resolved arcs. The 3.4 mol % crystal displays one high-frequency arc due to the *t* phase. The resistivity of $0.10 \text{ M}\Omega \text{ cm}$ is close to the value of $0.13 \text{ M}\Omega \text{ cm}$ measured for 3 mol % Y-TZP. The two spectra illustrate the sensitivity of IS toward phase composition and lend confidence to its use in investigating relatively complex microstructures.

Although the three-arc response is observed in most crystalline solid electrolytes, cases are known where the grain boundary arc is absent or at least too small to be seen. Figure 4.1.37 shows the impedance spectrum of $\text{ZrO}_2:(\text{Y}_2\text{O}_3 + \text{MgO})$ measured by Slotwinski, Bonanos, and Butler [1985]. The large arc with ρ'_{\max} of about 10 kHz can be identified as a bulk property from the fact that it passes through the origin and from the associated capacitance of about 4 pF/cm. The abnormally small grain boundary arc

¹² The error introduced by this assumption is smaller than the spread in the distribution of grain size, that is, about a factor of two.

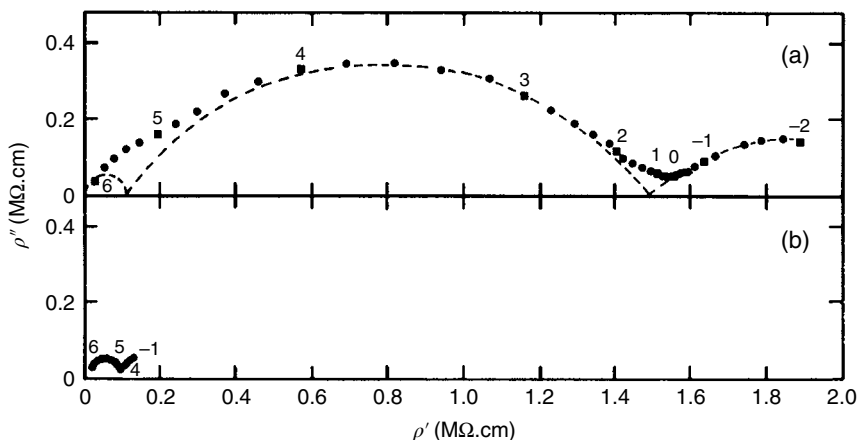


FIGURE 4.1.36 Comparison of the impedance spectra obtained at 300°C for two zirconia- yttria single crystals. (a) Tetragonal + monoclinic single crystal (ZrO_2 : 2.2 mol % Y_2O_3) showing large bulk arc. (b) Fully tetragonal single crystal (ZrO_2 : 3.4 mol % Y_2O_3) showing small bulk arc.

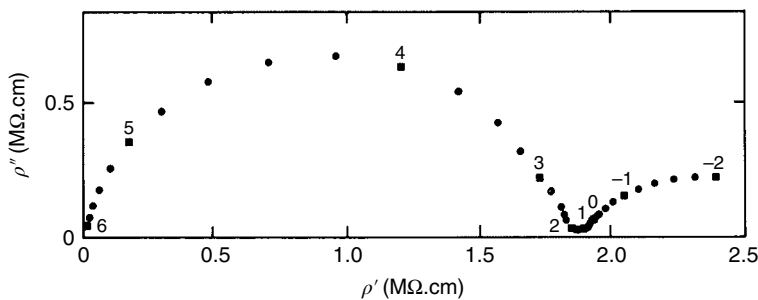


FIGURE 4.1.37 Impedance spectrum for a partially stabilized zirconia ceramic of composition ZrO_2 : (7.0 mol % MgO + 1.5 mol % Y_2O_3), obtained at 300°C, not resolving a grain boundary arc. Source: Slotwinski 1985. Reprinted with permission of Springer.

was explained by reference to a transmission electron micrograph (Figure 4.1.38). Unlike other zirconia-based systems, in $\text{ZrO}_2:(\text{Y}_2\text{O}_3 + \text{MgO})$ there are finely twinned crystallites along substantial lengths of grain boundary. Selective area electron diffraction patterns of this phase showed a tetragonal symmetry, resembling the patterns of the *t* phase, which has a relatively high ionic conductivity. It is suggested that *t*-phase dispersed along the grain boundary area effectively short-circuits the grain boundary impedance.

Another example of a ceramic lacking a grain boundary response is found in dense $\text{Bi}_2\text{O}_3:\text{Er}_2\text{O}_3$ ceramics (C. P. Tavares and Bonanos [1984], unpublished work). Figure 4.1.39 shows the impedance spectrum of a pellet of Bi_2O_3 (17 mol % Er_2O_3). Here, the absence of grain boundary impedance can be by the absence of grain boundary phases altogether. Unlike zirconia, bismuth oxide has a considerable solid solubility for silica and alumina, common impurities in ceramics, and, therefore, they would not be expected to segregate during sintering and subsequent cooling.

Effect of Anisotropy in Grain Shape and Conductivity. In the ceramics discussed so far, the shape and conductivity of the grains were isotropic. This is not, however, a rule for ceramics. Two examples are given for materials whose conduction or grain structure is anisotropic.

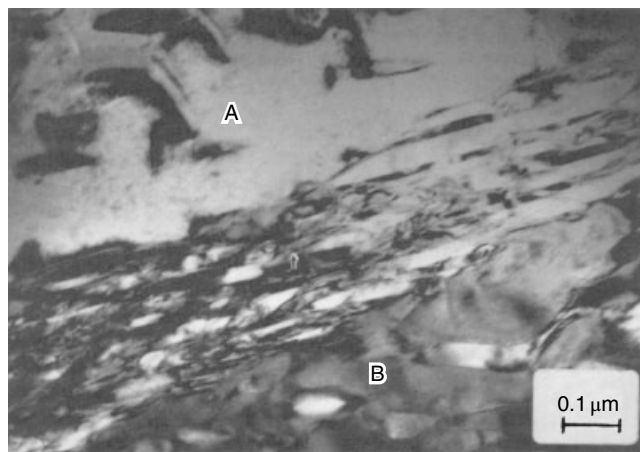


FIGURE 4.1.38 Transmission electron micrograph of partially stabilized zirconia ceramic ZrO_2 : (7.0 mol % MgO + 1.5 mol % Y_2O_3) showing two grains (labeled A, B) and the intervening tetragonal grain boundary phase (arrowed).
Source: Slotwinski 1985. Reprinted with permission of Springer.

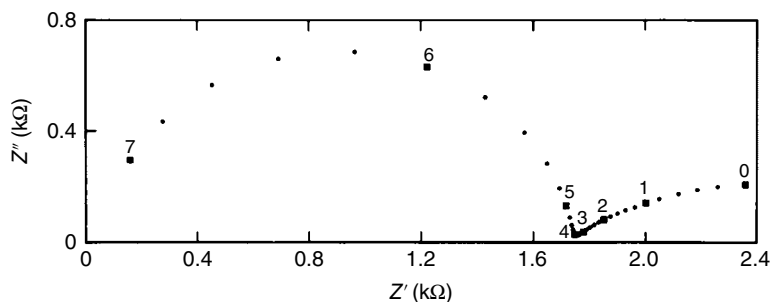


FIGURE 4.1.39 Impedance spectrum obtained at 300°C for a pellet of Bi_2O_3 : 17 mol % Er_2O_3 showing no grain boundary arc. (The pellet was supplied by Dr. C. P. Tavares of Basic Volume Ltd., London, England.)

The first example concerns the polymorphic compound Bi_2UO_6 that, at ambient temperature, has a monoclinic structure, which transforms to triclinic at approximately 730°C. The monoclinic structure comprises layers of U–O and double Bi–O layers and may be regarded as a superstructure of fluorite. Bonanos [1989] identified Bi_2UO_6 as an oxide ion conductor and, based on IS, reported grain interior conductivities of 5×10^{-4} at 200°C and 10^{-1} S/cm at 400°C. An impedance spectrum is shown in Figure 4.1.40 for 200°C. The large grain boundary arc (an order of magnitude larger than the grain interior arc) might suggest the presence of second phase at grain boundaries. However, high-resolution TEM (Figure 4.1.41) showed the grain boundaries to be free of second phases to a scale of a few nm. To reconcile these observations, Bonanos [1989] suggested that the grain boundary impedance arose because of the random orientation of grains having two-dimensional conductivity. In a subsequent structural/electrical study of this system, Vannier *et al.* [1999] reported the total conductivity as $2 \times 10^{-2} \text{ S/cm}$ at 400°C. However, since the grain interior arc was not resolved, the exceptionally high value of σ_{gi} claimed by Bonanos was neither confirmed nor refuted.

Sodium-conducting β -alumina ceramics are another example of anisotropic materials; they consist of elongated grains in which the Na^+ ions migrate along specific crystallographic planes. Early studies

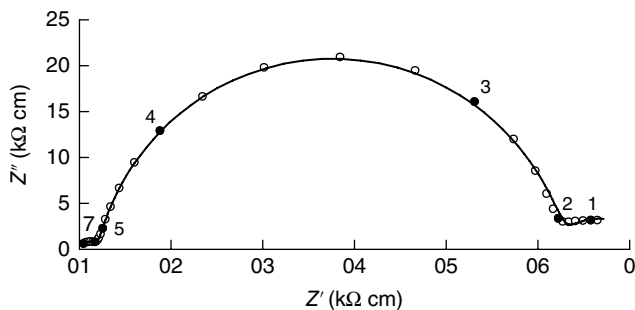


FIGURE 4.1.40 Complex resistivity spectrum for Bi_2UO_6 at 200°C (air, Ag electrodes).

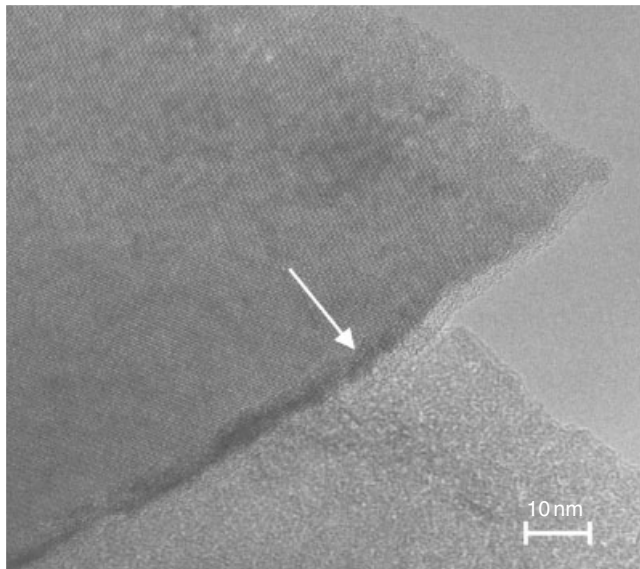


FIGURE 4.1.41 High resolution transmission electron micrograph of a grain boundary Bi_2UO_6 . Source: White 1989. Reproduced with the permission of Elsevier.

by Whittingham and Huggins [1971] and by Powers and Mitoff [1975] established activation energies of 0.2 for the grain interior and 0.4 eV for the grain boundary conductivities. Lilley and Strutt [1979] performed IS over the temperature range -135 to 400°C . Figure 4.1.41a reveals a large grain boundary resistance at -135°C ,¹³ which was interpreted as due to two-dimensional conductivity of grains in random orientation. Arrhenius plots of the conductivities (Figure 4.1.41b) fell into two regions: a low-temperature region, where the activation energies were identical at 0.18 eV, and a high-temperature region, where the grain boundary activation energy was 0.45 eV. According to Lilley and Strutt, at low temperatures, the grain boundary conduction was dominated by easy paths (Figure 4.1.42a) while, at high temperatures, transports through the grain boundary overtook the easy path mechanism. If this interpretation is correct, a transition between easy path and true grain boundary conduction in the same system would be a clear indication that IS can reveal in-depth information, when performed over the

¹³The experimental conditions were chosen to allow resolution of the grain interior arc over the widest possible temperature range. The conductivity of $5 \times 10^{-3} \text{ S/cm}$ at ambient temperature corresponds to a relaxation frequency of the order of 10^8 Hz .

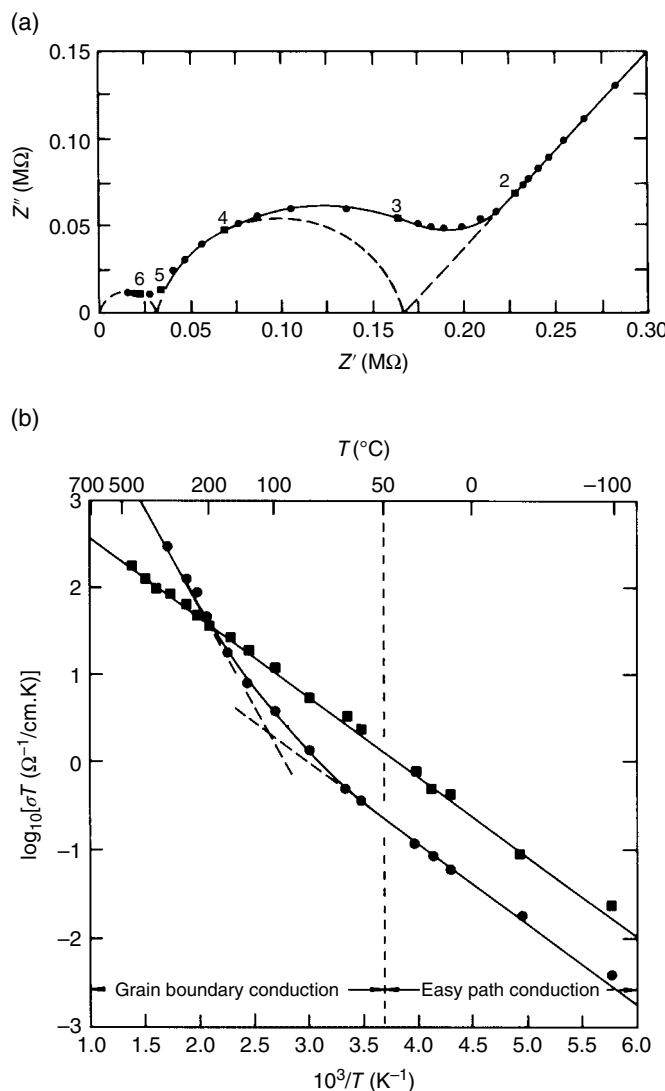


FIGURE 4.1.42 Application of impedance spectroscopy to a study of sodium β -alumina by Lilley and Strutt [1979]: (a) Impedance spectrum obtained at -135°C using evaporated gold blocking electrodes. (b) Arrhenius plot of σ_{gi} and σ_{gb} showing transition between grain boundary and easy path conduction. Source: Lilley 1979. Reproduced with permission of John Wiley & Sons.

necessary range of frequency and temperature. Table 4.1.7 gives the capacitance values reported by these authors.

In a contemporaneous TEM/IS study of the same system, De Jonghe [1979] concluded that a simple RC network was unsuitable for describing the varying cross section and orientation of the grains in ceramics. As an alternative, he proposed a circuit having a series-parallel configuration (Figure 4.1.43b). De Jonghe simulated the effect of grain boundary blocking by varying the grain boundary parameters r_i , c_i along the branches while holding r_{gi} constant. By assigning activation energies 0.17 and 0.35 eV to the microscopic parameters $\Delta H_{r_{gi}}$ and $\Delta H_{r_{gb}}$, he simulated a range of temperatures and compared the macroscopic values of r_{gb} , c_{gb} with those obtained by a parallel summation of the r_i , c_i branches. The macroscopic values deviated from the microscopic values at all but the lowest temperatures; moreover the

TABLE 4.1.7 Capacitance Values for β -Alumina at Various Temperatures, as Determined by Lilley and Strutt [1979]

Temperature (K)	C_{gi} (F)	C_{gb} (F)	C_{el} (F)
138	4×10^{-12}	7×10^{-10}	1.5×10^{-7}
149	—	8×10^{-10}	1.5×10^{-7}
371	—	8×10^{-10}	1.0×10^{-7}
652	—	—	0.8×10^{-7}

Source: Lilley 1979. Reprinted with permission of John Wiley & Sons.

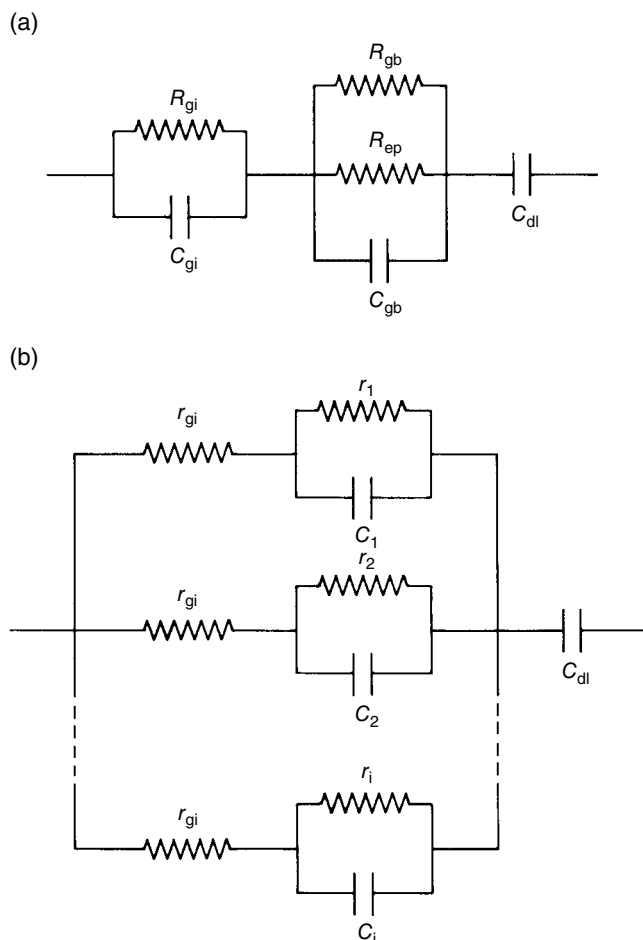


FIGURE 4.1.43 Circuits proposed for modeling the impedance spectrum of polycrystalline sodium β -alumina: (a) Easy path model according to Lilley and Strutt [1979]. Source: Lilley 1979. Reproduced with permission of John Wiley & Sons. (b) Multi-element model according to De Jonghe [1979]. Source: Jonghe 1979. Reproduced with permission of Springer.

apparent grain boundary capacitance increased with temperature. De Jonghe concluded that, for systems with shape-significant grain anisotropy, the information obtained by IS was of limited fundamental value. He also stressed the difficulty in interpreting c_{gb} in microstructures with discontinuous grain boundary phases.

While De Jonghe's cautionary advice is worth heeding, the actual trend in C_{gb} predicted by his model is not mirrored in the results of Lilley and Strutt [1979] (Table 4.1.7); the capacitances were found to be constant over the temperature range studied. Accordingly, the De Jonghe model may be regarded as a worst-case analysis of a complex microstructure with grain anisotropy.

While the first edition contained a defense of IS against the previous and other criticisms, such a discussion would be less relevant today, in view of the advancement in finite element simulations (see Coverdale *et al.* [1995], Fleig [2000, 2002], Tuncer *et al.* [2001, 2002]).

4.1.3.3 Characterization of Two-Phase Dispersions by IS

In the systems discussed so far, the continuous phase was concentrated in grain boundary regions, such that its blocking properties were noticeable, even at low volume fraction. This subsection covers two-phase dispersions, where the volume fractions of continuous and discontinuous phase are closer, for example, 0.70 and 0.30. Two examples are discussed, one where the time constants of the phases are well resolved and another where they are not.

Characterization of a Two-Phase Alkali Halide System. Alkali halide crystals have been studied as model systems for defect aggregation and solid-state precipitation. In the NaCl/CdCl₂ system, crystals grown from the melt contain a phase of composition CdNa₆Cl₈, *Suzuki phase*, in which 12.5% of the cation sites are vacant. This phase has a higher Na⁺ conductivity than the matrix in which it forms. A transmission electron micrograph of a crystal with Suzuki phase precipitates is shown in Figure 4.1.44. The volume fraction of the dispersed phase in this system is about 0.28.

Impedance spectra of such crystals, reported by Bonanos and Lilley [1981], displayed only bulk and electrode arcs. The same data plotted in the modulus plane (Figure 4.1.45) revealed two overlapping arcs: a low-frequency arc ascribed to the matrix and a high-frequency one ascribed to the dispersed

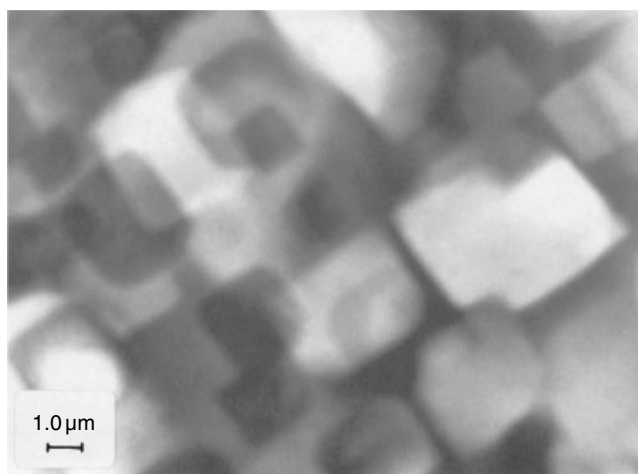


FIGURE 4.1.44 Transmission electron micrograph of a NaCl:CdCl₂ single crystal with precipitates of the Suzuki phase CdNa₆Cl₈. The micrograph was taken by A. L. Guererro and E. P. Butler at a voltage of 1 MV, at liquid helium temperature. Source: Bonanos 1981. Reproduce with permission of Elsevier.

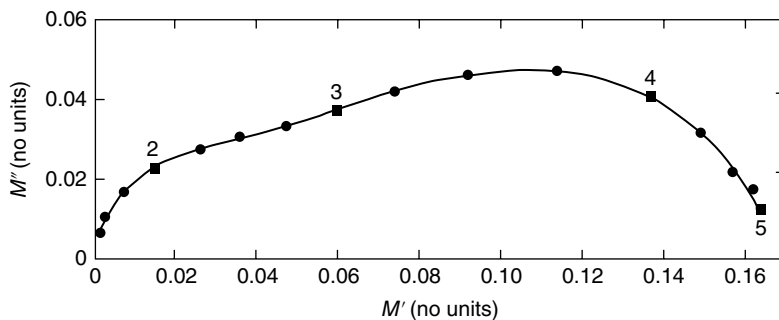


FIGURE 4.1.45 Modulus spectrum obtained at 150°C for a single crystal of NaCl:CdCl₂, of which a micrographs is shown in Figure 4.1.28. Source: Bonanos 1981. Reproduce with permission of Elsevier.

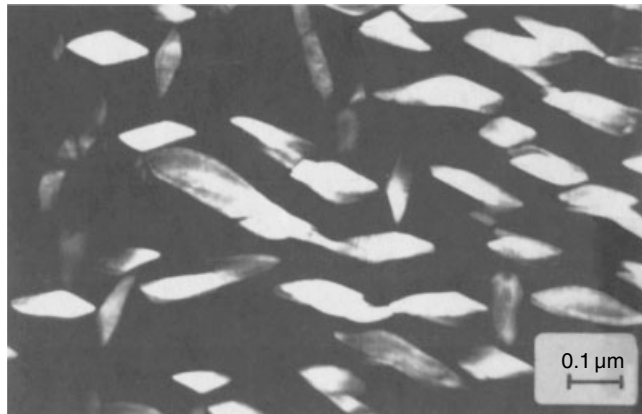


FIGURE 4.1.46 Transmission electron micrograph of grain interior of a partially stabilized zirconia ceramic ZrO₂: (7.0 mol % MgO + 1.5 mol % Y₂O₃), aged for 40 h at 1400°C. Bright areas correspond to the tetragonal phase.

phase. Using the Maxwell-Wagner effective medium relation (Eq. 20), the modulus spectra were modeled and the microscopic conductivities of the two phases were evaluated for several volume fractions of dispersed phase. The ionic conductivity of the dispersed phase was similar to that determined on polycrystalline samples.

In the aforementioned system, the analysis was possible because the relaxation frequencies of the matrix and dispersed phases differed by a factor of about 30. In other cases, it is impossible to identify the relaxations of individual phases due to proximity of the time constants. Even in these cases, the IS in conjunction with microstructural characterization can be used to glean information regarding the conductivities of individual phases. This is illustrated hereafter.

Resistivity Analysis in Polyphase Ceramics. As mentioned earlier, the grains in PSZ consist of a matrix of cubic zirconia with a fine dispersion of tetragonal particles. Figure 4.1.46 shows the microstructure of ZrO₂ (Y₂O₃ + MgO) PSZ. The appearance of the elongated particles, distributed equally along three normal axes, is reminiscent of the Fricke model for a dispersion of ellipsoids (Section 4.1.1). The simulated spectrum for this model (Figure 4.1.10) indicates that (depending on the symmetry of the precipitates) up to four different relaxations could arise within the grain interior, in addition to that of the grain boundary. Prolonged heat treatment (aging) of PSZ ceramics at high temperature is known to cause

transformation of the precipitates from t to m , with a small increase in size but with no significant change in shape or chemical composition. Since the c , t , and m phases have different conductivities, these microstructural changes should be reflected in the electrical properties.

This approach has been used by Bonanos *et al.* [1984a] to study PSZ of composition ZrO_2 with 8 mol % CaO (Ca-PSZ). XRD and TEM showed the $t \rightarrow m$ transformation to be complete after 20 h of heat treatment at 1400°C , while quantitative X-ray diffraction analysis gave a value of 0.3 for the volume fraction of the t component. Electron microscopy showed the t particles to be ellipsoidal, with axial ratios a/b and b/c of approximately 2, for which Table 4.1.2 gives the corresponding form factors $\phi_1 = 7.9$, $\phi_2 = 2.5$, and $\phi_3 = 0.66$. In short the parameters ϕ_i and x_2 in Eq. (23) are given, and the only remaining variables are the complex conductivities ρ_1 , ρ_2 , and ρ_t .

Figure 4.1.47 shows impedance spectra for Ca-PSZ after aging at 1400°C for different times. Distinct relaxations of the matrix and dispersed phases are not resolved in these spectra, which are of a simple Bauerle type, nor are they resolved in the corresponding modulus spectra (not shown), presumably due to the proximity of the relaxation frequencies. Thus, multi-element circuits (Figure 4.1.9) cannot be used to represent these data, and the grain interior response must be approximated by a single RC element. Nevertheless, Eq. (23) can be used to interpret the dc conductivity of the grain interiors σ_{gi} (for convenience, the inverse, r_{gi} , was used).

From a microstructural analysis and from the evolution of r_{gi} , aging was found to occur in three stages.

Stage I: An increase in volume fraction of t phase, resulting in a sharp fall in r_{gi} since $\sigma_t > \sigma_c$ (Figure 4.1.47a to 4.1.47b).

Stage II: A period of precipitate growth at constant volume fraction with no change in r_{gi} .

Stage III: A transformation of the precipitates from t to m without change in the chemical composition of the matrix or the precipitates (Figure 4.1.47b and c), with no change in σ_c .

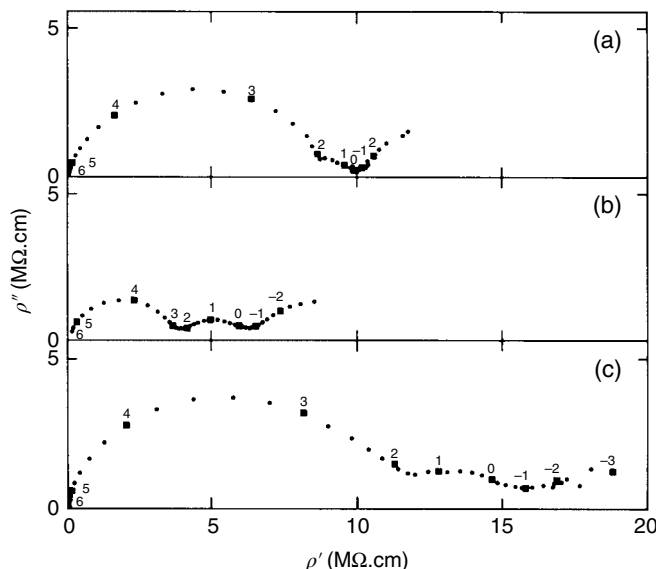


FIGURE 4.1.47 Impedance spectra obtained at 300°C for partially stabilized zirconia ceramics (ZrO_2 : 8 mol % CaO): (a) as fired; (b) aged for 15 h at 1400°C ; (c) aged for 30 h at 1400°C . Source: Bonanos 1984. Reproduced with permission of Springer.

A numerical analysis of the conductivity changes during these transitions showed that physically consistent solutions to Eq. (23) could be obtained only for $\sigma_t > \sigma_c > \sigma_m$ and allowed an estimation of σ_t and σ_c to within an order of magnitude. Since CaO-stabilized TZP were not available at the time of that paper (and to the author's knowledge have not been prepared since), the analysis of a polyphase material was the only way of accessing the conductivity of this system.

The Significance of Grain Boundary Phases Placed in Context. While grain boundary phases have a dominant effect on the impedance spectrum, it should be remembered that, even in the absence of second phases, the electrical properties of interfacial regions differ from those of the interior, as illustrated by the space charge effects discussed in Section 4.1.1. Dopants segregated to interfaces during high-temperature processing and frozen in during later cooling also modify the electrical resistance of the interfaces. Finally, unlike bulk properties, which are invariably linear, the grain boundaries in oxide semiconductors often have non-ohmic characteristics, which form the basis for positive temperature coefficient resistors (PTCRs) (Levinson [1981]). Interfacial segregation and space charges in ionic conductors have been discussed by Heyne [1983], Burggraaf *et al.* [1985], and Steele and Butler [1985] to explain the appearance of grain boundary-like arcs in nominally pure ceramics. In many situations, second phases, segregation, and space charges all together contribute to a rich variety of electrical behavior.

4.1.3.4 Impedance Spectra of Unusual Two-Phase Systems

In a volume such as this, most examples are unavoidably drawn from systems that are fairly well understood. As a counterbalance, two examples are mentioned that are, in some way, unusual.

The first example concerns a composite of $(\text{Sc}_2\text{O}_3 + \text{Y}_2\text{O}_3)$ stabilized ZrO_2 , a pure ionic conductor, and $\text{La}_{0.85}\text{Sr}_{0.15}\text{Mn}_{1.10}\text{O}_\xi$, a pure electronic conductor, at a volume fraction 0.30 for the latter. Figure 4.1.48 shows an impedance spectrum obtained under ambient conditions. It resembles that of a classical solid electrolyte, with a "bulk" resistivity of $5 \times 10^6 \Omega \text{ cm}$ and a "bulk" capacitance of $4 \times 10^{-12} \text{ F/cm}$.

The "grain boundary" and "electrode" features are associated with Warburg components of $3 \times 10^{-8} \text{ S/cm/s}^2$ and $1.3 \times 10^{-5} \text{ S/cm}^2/\text{s}^2$, respectively. The known properties of the zirconia phase do not, however, fit such an interpretation: the resistivity, extrapolated from higher temperature, is at least $10^{12} \Omega \text{ cm}$. This would suggest that the enhanced bulk conductivity is due to the presence of a high conductivity phase close to the percolation threshold. Unfortunately, the effective medium models presented in Section 4.1.1 cannot be used to describe this composite, as they apply to phases

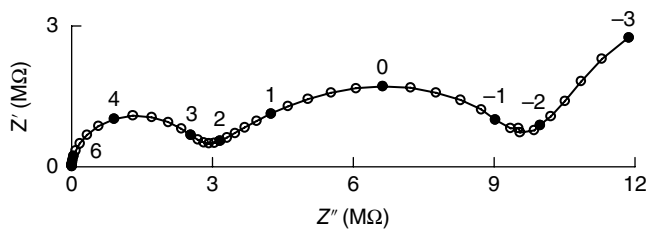


FIGURE 4.1.48 Impedance spectrum at ambient conditions for a composite of $(\text{Sc}_2\text{O}_3 + \text{Y}_2\text{O}_3)$ stabilized ZrO_2 and $\text{La}_{0.85}\text{Sr}_{0.15}\text{Mn}_{1.10}\text{O}_\xi$ at a volume fraction 0.30. The spectrum resembles that of a classical solid electrolyte, but the "bulk conductivity" exceeds the expected value by a factor of 10^6 .

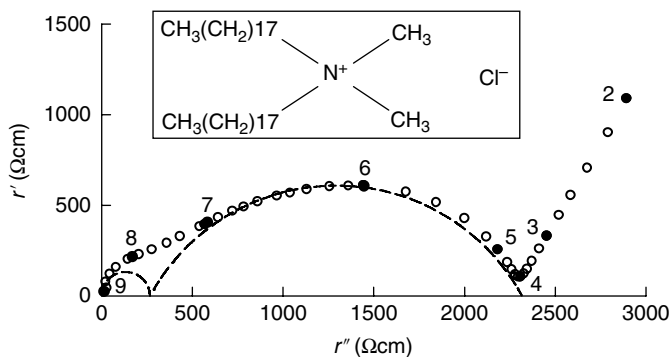


FIGURE 4.1.49 Impedance spectrum of dihydrogenated tallow dimethylammonium chloride (see inset), obtained at ambient temperature in a coaxial cell with gold electrodes. Labels indicate $\log(f)$.

of the same type of conductivity, that is, they do not include any charge transfer impedances at the interfaces between ionic and electronic conductor.

The second example is a concentrated aqueous dispersion of dihydrogenated tallow dimethylammonium chloride (DHTDMAC), a lamellar liquid crystal commonly used in fabric conditioners. Figure 4.1.49 shows an impedance spectrum obtained at ambient temperature in the frequency range 10^2 – 10^9 Hz. It shows two overlapping arcs with capacitance/CPE elements of 8×10^{-12} F/cm and 8×10^{-9} S/cm/s². Despite the superficial similarity of the spectra with the grain/grain boundary spectra of solids, the substance is actually a viscous liquid consisting of spherical aggregates called *liposomes*. These are made up of thick regions of aqueous phase separated by thinner bi-layers of DHTDMAC (see, e.g., Clint [1992]). One may imagine that the bulk arc is due to the conductive aqueous regions and the grain boundary-like arc is due to the resistive bi-layers. Thus, while it is often said that IS resolves the grain boundary properties in ceramics, it would be more correct to say that this spectrum is sensitive to structure, be that the structure of a solid or a liquid.

Acknowledgments

The authors wish to thank R. K. Slotwinski for providing some of the data presented here and for producing the diagrams, Dr. E. Lilley for providing data on β -alumina ceramics, and Dr. C. P. Tavares for supplying a sample of $\text{Bi}_2\text{O}_3:\text{Er}$. They are also grateful for many useful discussions with other members of the Wolfson Unit for Solid State Ionics at Imperial College, United Kingdom, and Risø National Laboratory, Denmark. Much of the work in developing the measurement system described in Section 4.1.2 is credited to C. D. Waters, Sihvola, Ringgaard, Sunde, Maier, Fleig, Tuncer, Goldrick, and StuAdler.

This section was written by N. Bonanos, B. C. H. Steele, and E. P. Butler.

4.1.3.5 Impedance Spectra of Composite Electrodes

Electrode impedances appear over a small space scale, characteristic of atomic dimensions, and as a result their spectra differ from those of bulk materials in several ways listed in the following text. This section presents two examples of composite cathodes for SOFCs. For these systems, the most commonly used cathode material and solid electrolyte are LSM and YSZ, respectively.

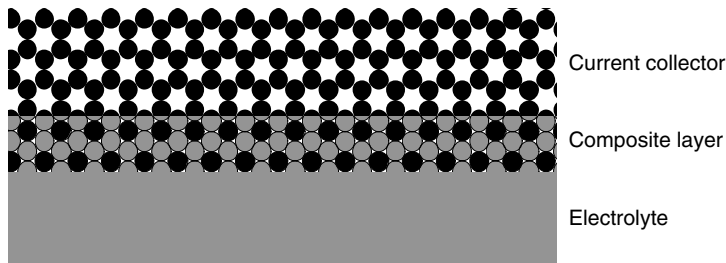


FIGURE 4.1.50 Composite electrode, consisting of a mixture of ionically and electronically conducting phases, with porous current-collecting layer.

- a. Their properties are dependent on both the electrolyte and the electrode material and on the microstructure (grain size, porosity, etc.).
- b. The associated capacitances are of the order of 10^{-6} F/cm^2 or more when they arise from processes other than charge storage at the double layer.
- c. Their impedances are in general nonlinear, that is, dependent on the amplitude of the applied ac signal and the dc bias. Measurements are usually performed at small signal amplitudes in order to stay within the linear regime.
- d. Electrode reactions usually involve a gas phase, and, therefore, electrochemical impedances will depend on the gas composition and transport within this phase.
- e. As stated in Section 4.1.3, measurements on cells with REs are subject to substantial errors, in the case of thin electrolyte cells.

Figure 4.1.50 shows the structure of a composite electrode. The composite is made of a mixture of electrolyte and electronically conducting phases and has a thickness of 5–50 μm . Since this layer usually has insufficient in-plane electronic conductivity for current collection, it is covered with a current-collecting layer of porous electronic conductor. This can be made of the same substance as the electronic component of the composite or another substance of high electronic conductivity. For laboratory testing, precious metal pastes are convenient for this purpose. The thickness of the current-collecting layer is typically in the region of 50 μm .

The impedance spectra of composite cathodes reveal several processes, not all of which are fully resolved in the impedance spectrum. Some of the processes are observed also in point contact electrodes, while some are specific to the composite electrode.¹⁴ Jørgensen and Mogensen [2001] have surveyed the dominant impedance arcs of composite cathodes (not including the electrolyte series resistance) and have classified them as follows, in descending order of their relaxation frequency:

- A and B. Geometrical impedances, that is, conductivity relaxations, related to the microstructure of the composite. Their activation energies are about 1 eV, similar to those of the grain or grain boundary conductivities and are independent of the oxygen partial pressure (P_{O_2}). One or both of these arcs may be absent in some composite cathodes, and neither of them is observed with point contact electrodes.
- C. This arc is ascribed to the main cathodic process, namely, adsorption and dissociation of oxygen molecules on the surface of the electrode material. Activation energies are in the range 1.8–2.0 eV, and it is dependent on P_{O_2} with a power law $(P_{\text{O}_2})^q$, with q in the range –0.14 to –0.50. The

¹⁴ Point contact electrodes are made by contacting a point of electrode material on a dense electrolyte. They are simpler than composite cathodes due to (i) their well-defined geometry, allowing the estimation of the three-phase boundary length, and (ii) the absence of complex diffusional processes.

associated capacitances are in the region 10^{-4} to 10^{-1} F/cm². This feature is observed in composite cathodes and point contact electrodes alike.

- D. Gas phase diffusional impedance. This arc is observed mainly in high performance cathodes and increases with cathodic polarization (negative applied potential). The observed impedance is in accordance with the presence of a stagnant gas layer close to the electrode surface. This arc may be difficult to observe due to overlap with C.
- E. Inductive loop. It is not entirely clear whether this arc represents a new feature or is a manifestation of an activation process within arc C. The feature seems to be variable, even for nominally identical samples and is observed with point contact electrodes. It is ascribed to adsorbed oxygen intermediates or segregation of chemical species at the three-phase boundary.

The previous classification implicitly assumes an equivalent circuit composed of ZARC elements. There are, however, alternatives, namely, the Gerischer¹⁵ element, as used by Holtappels *et al.* [1998]. This is illustrated in Figure 4.1.51 for the spectrum of a composite cathode at 850°C. In Figure 4.1.51a the electrode response is simulated using a circuit with three ZARC elements, while in Figure 4.1.51b one of the ZARCs is replaced by a Gerischer element. There is no appreciable difference in the goodness of fit, as judged by the solid lines; moreover, the χ^2 values in both cases were about 6×10^{-6} , and the estimation of the polarization resistance differs by only 2%.¹⁶

The ability of two different circuits to model the same data set has both positive and negative implications. On one hand, it facilitates the process of electrode development, since the values of the polarization resistance estimated by different investigators can be compared, even if they were not based on

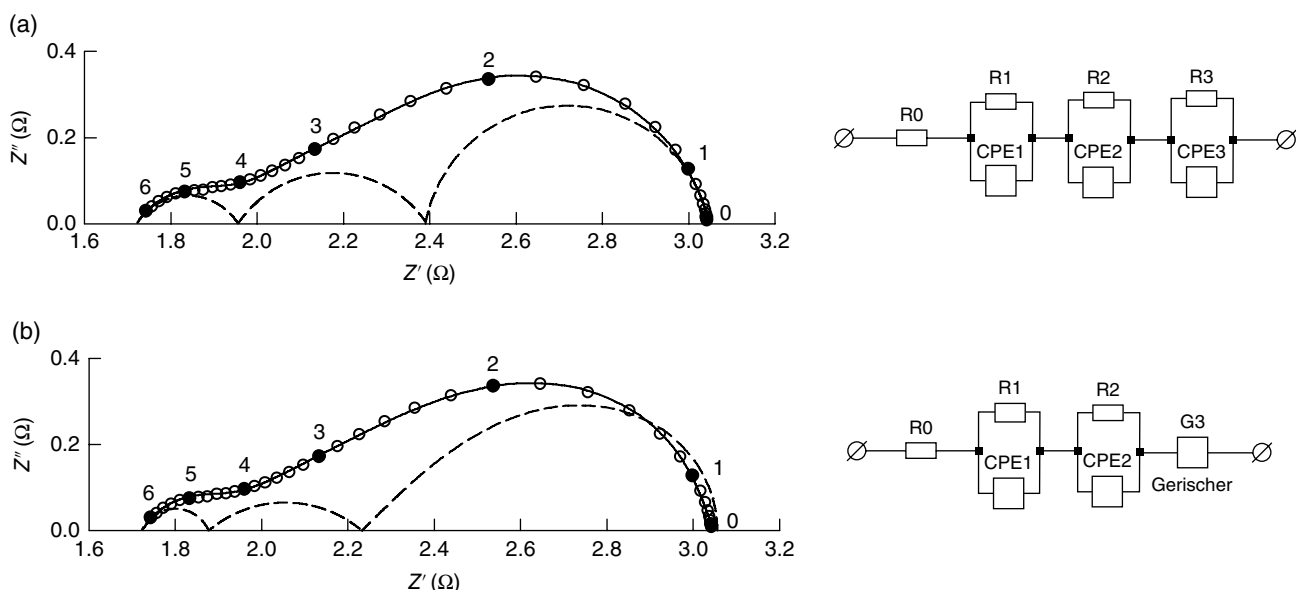


FIGURE 4.1.51 Impedance spectrum of a symmetrical cell with composite cathode on both sides, fitted to two different circuits. The solid lines show the total fit, while the dashed lines show the impedances of the individual elements. The composite layer consists of ZrO_2 (8 mol % Y_2O_3) and $\text{La}_{0.85}\text{Sr}_{0.15}\text{Mn}_{1.10}\text{O}_\xi$ in equal proportions and the current collector is porous platinum paste. The measurement was made in air, at 850°C. The data were corrected for the series inductance of the measurement rig, determined in short circuit.

¹⁵For the definition of this element see Section 2.2.2.2.

¹⁶The circuit containing the Gerischer element is not able fully to reproduce the spectrum at the low-frequency end, although in the data of Holtappels *et al.* [1998], this problem did not arise.

exactly the same circuit. On the other hand, it complicates the interpretation of the spectral features in terms of mechanisms, because arcs cannot be paired to processes on a one-to-one basis. It is therefore essential that a fundamental investigation covers the widest possible range of experimental conditions (viz., temperature, gas composition), including conditions that are far from those of the planned application, so that all the electrode processes “get a chance to make their appearance” in the impedance spectrum.

Another example concerns functionally graded cathodes, consisting of five layers of YSZ/LSM with increasing LSM content (20–100%) (Holtappels and Bagger [2002]). The cathodes were prepared on both sides of a YSZ tape (thickness ~150 µm), characterized by IS, and found to have a very high performance, with polarization resistances of $100 \text{ m}\Omega \text{ cm}^2$ or less at 850°C (see also spectrum in Figure 4.1.24). Close examination of the results revealed that the electrolyte resistance associated with the cathodes was higher, by about $50 \text{ m}\Omega \text{ cm}^2$, than that expected from the known conductivity of the electrolyte; this was attributed to the resistance of the YSZ-rich layer adjacent to the electrolyte. To investigate this further, impedance studies were performed at temperatures below the operating temperature (Bonanos *et al.* [2002]).

Figure 4.1.52 shows impedance spectra at two temperatures, with simulated data for a circuit based on four ZARCs (for Figure 4.1.52a one of the ZARCs is replaced by a resistor). By starting at low temperatures and using the parameters estimated at one temperature as initial guesses for the next one, convergence was obtained in all cases.

The spectra illustrate the difficulty in estimating R_0 . At 700°C (Figure 4.1.52a), the arc R_1Q_1 is very flat. The simulation suggests that this arc should intersect the real axis at 10^8 Hz , which is outside the

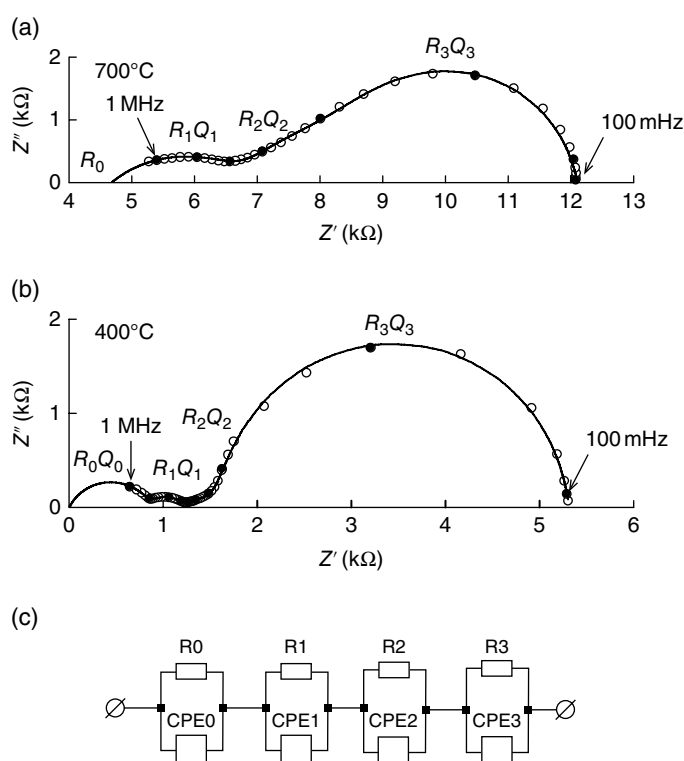


FIGURE 4.1.52 (a, b) Impedance spectra of cathode consisting of five layers of YSZ/LSM, with graded thickness and composition. The cathodes were prepared on both sides of a YSZ tape. The measurements were performed in air. Source: From Bonanos 2002, p 578ff.

frequency range used. The spectrum at 400°C, however, falsifies this expectation: rather than approaching the real axis, the spectrum develops into a new, high-frequency arc, R_0Q_0 . This development could not have been observed in the spectrum obtained at high temperature, graphically, or by CNLS fitting. The frequency range is simply too limited to reveal this arc.

The temperature dependence of the resistors R_0 – R_3 is shown in Figure 4.1.53; for convenience, R_0 , R_1 , and R_2 and R_3 are shown separately. The plots for R_0 and R_1 (Figure 4.1.53a) have significant curvature in opposite directions. This is certainly due to a systematic error in the resolution, because their sum, $R_0 + R_1$, gives a good straight line with an activation energy of 0.96 eV, the value expected for YSZ.¹⁷ This leads to the conclusion that R_0 and R_1 are both manifestations of the electrolyte resistance but that they cannot be resolved completely in the impedance spectra, even at low temperatures. This may be qualitatively described as a “smearing out” of the electrode–electrolyte interface due to the graded nature of this system. The corresponding plots for R_2 and R_3 are shown in Figure 4.1.53b. The Arrhenius plots are curved, as observed for two-layer composite cathodes (Juhl *et al.* [1996]). As with the cases of R_0 and R_1 , the sum $R_2 + R_3$ gives a better straight line (activation energy of 1.25 eV), than either R_2 or R_3 , suggesting that these processes too may be not be fully separable. It was also found that R_0 and R_1 showed negligible variation with oxygen partial pressure, as expected for ionic conduction in the YSZ fraction, while R_2 and R_3 showed power law dependence.

The problems of resolution described previously are explained by the proximity of characteristic time constants, rather than experimental error. The problem is fundamental to the material and could not be solved using another technique, such as current interrupt. The understanding of a system with four relaxation frequencies but only two temperature dependences seems to need a more advanced model than that afforded by an electrical circuit.

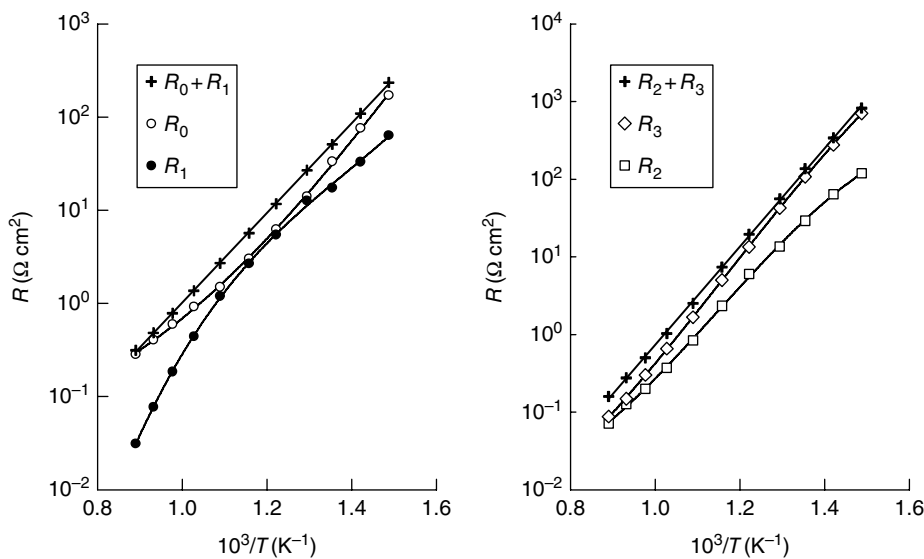


FIGURE 4.1.53 Temperature dependence of the resistive elements obtained by fitting the circuit of Figure 4.1.52c to the data of a multilayer composite cathode. (a) R_0 and R_1 ; (b) R_2 and R_3 . The plots for R_0 and R_1 curve in opposite directions, indicating a systematic error of resolution, while their sum gives a straight line. This may be due to a “smearing out” of the electrode–electrolyte interface in the graded structure. The corresponding plots for R_2 and R_3 also show a (slightly) greater curvature than their sum. The activation energies for $(R_0 + R_1)$ and $(R_2 + R_3)$ are 0.96 and 1.25 eV, corresponding to electrolyte and electrode processes, respectively.

¹⁷ Estimated from $\ln[(R_0 + R_1)/T]$ versus T^{-1} .

4.1.3.6 Closing Remarks

The work presented here has covered three main aspects of IS, namely, modeling, experimental techniques, and application of the technique to systems with complex microstructures. Since it is not possible to summarize this work in a paragraph, we will draw attention to three themes that recur in this section.

- Choice of appropriate model: IS is not a technique that can or should be applied without prior knowledge of the system. Impedance spectra must be interpreted in the context of a model, be this a simple brick layer model for a ceramic or an advanced one based on electrode kinetics. When used in conjunction with electron microscopy, IS provides information about structure and especially grain boundary structure. The microstructural information and the models that are derived from this are what make the conclusions of IS valid, precise, and unequivocal.
- Choice of equipment and experimental conditions: The instrumental frequency range needs to cover the dominant relaxations of the system. In this connection, it is as important to choose the temperature of the system as it is to choose the right instrument. It is also important to make the measurements over a range of conditions considerably wider than those expected in operation.
- Choice of formalism: The formalism (Z , M , etc.) should be chosen to make the correspondence between measured spectrum and model as simple as possible. In cases where grain boundaries or electrodes are blocking, the preferred choice will normally be the impedance formalism—in other cases, others will be better. It is advisable to examine data in more than one formalism.

Acknowledgments

The following are warmly thanked: E. Lilley, R.K. Slotwinski, S. Sunde, J. Fleig, and S.B. Adler for providing original data from experiments and simulations, A. Sihvola and T. Goldrick for mathematical analysis, E. Ringgaard and J. Maier for critical comments, and C.P. Tavares for supplying a sample of $\text{Bi}_2\text{O}_3:\text{Er}$. Work on measurement systems is credited to C. D. Waters and J. Poulsen.

Countless discussions with members of the Wolfson Unit for Solid State Ionics, Imperial College, London (1979–1984), and the Fuel Cells Group, Materials Research Department, Risø National Laboratory, Denmark, have indirectly contributed. This section was written by N. Bonanos, B. C. H. Steele, and E. P. Butler and revised by N. Bonanos. The revised section is now dedicated to the memory of B. C. H. Steele.

4.2 CHARACTERIZATION OF THE ELECTRICAL RESPONSE OF WIDE-RANGE-RESISTIVITY IONIC AND DIELECTRIC SOLID MATERIALS BY IMMITTANCE SPECTROSCOPY

J. Ross Macdonald

(William R. Kenan, Jr., Professor of Physics, Emeritus) Department of Physics and Astronomy,
University of North Carolina, Chapel Hill, NC, USA

4.2.1 Introduction

For at least several decades, the effects of charged-particle motion in doped semiconductors, amorphous materials, polycrystals, single crystals, inorganic glasses, and polymers have been of much interest to both experimentalists and theorists. In fact, Phillips [1994] has characterized the problem of relaxation in complex disordered systems as the most important unsolved problem in physics! For ionically

conducting materials such as solid electrolytes, the dynamics of the mobile ions have been usually investigated by analyzing the frequency response of the material over a wide range of frequencies, sometimes as wide or wider than 10^{-5} to 10^{12} Hz. Such investigations thus usually involve immittance spectroscopy measurements and techniques. In this section, the main emphasis is on ionic conductors because of their technological importance in such areas as batteries, fuel cells, electrochromic displays, energy storage in capacitors, sensors, and even bionics. Because the electrical response of ionic conductors is rarely of simple Debye relaxation character except in limiting cases, one must be concerned with its generalization: dispersive response. A recent summary and discussion of electrochemical impedance spectroscopy appear in Barsoukov and Macdonald [2012] (see also Bonanos *et al.* [2012]).

Conductive-system dispersive response may be associated with a distribution of relaxation times (DRTs) at the complex resistivity level, as in the work of Moynihan *et al.* [1973] based on the assumption of stretched-exponential response in the time domain [Eq. (118), Section 2.1.2.7], work that led to the widely used original modulus formalism (OMF) for data fitting and analysis. In contrast, dielectric dispersive response may be characterized by a distribution of dielectric relaxation times defined at the complex dielectric constant or permittivity level (Macdonald [1995]). Its history, summarized in the monograph of Böttcher and Bordewijk [1978], began more than a hundred years ago. Until relatively recently, however, these two types of dispersive response were not usually distinguished, and conductive-system dispersive response was often analyzed as if it were of dielectric character, even when this was not the case. In this section, material parameters will be expressed in specific form appropriate to the level concerned.

Conductive-system dispersion (CSD) usually involves thermally activated conduction extending to zero frequency plus an always present bulk dielectric constant, $\epsilon_{D\infty}$, usually taken to be frequency independent in the experimental range. Dielectric-system dispersion (DSD) often involves dielectric-level response with only weak temperature dependence, and it may or may not involve a non-negligible frequency-independent leakage resistivity, $\rho_{C\infty} = \rho_{dc} \equiv \rho_0 \equiv 1/\sigma_0$. There may be cases where separate processes lead to the simultaneous presence within an experimental frequency range of both types of dispersion, but this is rare for most solid electrolytes. Further complications are present when conduction involves both mobile ionic and electronic charges, neither of whose effects are negligible (Jamnik [2003]). Here only ionic, dipolar, and vibronic effects will be further considered, with the main emphasis on conductive rather than on dielectric dispersion.

Since conductive-system dispersive response may be transformed and shown graphically at the complex dielectric level, and dielectric dispersion may be presented at the complex resistivity level, frequency-response data alone may be insufficient to allow positive identification of which type of process is present since there may be great similarity between the peaked dispersion curves that appear in plots of $\rho''(\omega)$ and of $\epsilon''(\omega)$ or of $\epsilon''_s(\omega) \equiv \epsilon''(\omega) - (\sigma_0 - \omega\epsilon_V)$. Here, ϵ_V is the permittivity of vacuum. This quantity has usually been designated as ϵ_0 , as in other parts of this book. Its designation here as ϵ_V avoids ambiguity and allows clear distinction between it and $\epsilon(0) = \epsilon'(0) \equiv \epsilon_0$, the usage in the present section.

Even complex nonlinear least squares (CNLS) data fitting at a specific temperature may not always allow unambiguous discrimination between CSD and DSD responses. But if data are available over a range of temperatures, discrimination is straightforward. Then, one generally finds that ρ_0/T (or ρ_0) and τ_o , the characteristic relaxation time of a model exhibiting thermally activated CSD, involve the same activation enthalpy (usually termed the activation energy) (e.g., Macdonald [2002a]). This is an effective quantity when the process considered involves a distribution of activation energies. Dielectric dispersion response may not be thermally activated, but when it is, τ_o certainly does not have the same activation energy as that of an independent leakage resistivity ρ_0 . A detailed study of discrimination between the two types of dispersion appears in Macdonald [1999a].

4.2.2 Types of Dispersive Response Models: Strengths and Weaknesses

4.2.2.1 Overview

Conductive-system dispersive response involving mobile charge may be conceptually associated with the effects of three processes. These are (i) electrode effects, which are particularly important at low frequencies (see Section 2.2.3.1) but may not be negligible at very high ones (Macdonald [2002a, b]);

(ii) ionic hopping effects, usually significant at mid-range frequencies (Macdonald [2002a, b]); and
 (iii) nearly constant loss (NCL) effects primarily evident at sufficiently low temperatures over the usual frequency range or at high frequencies for higher temperatures (Ngai [1999], Macdonald [2002c, 2003b], Ngai and León [2002]).

Three different kinds of models have been proposed for describing these responses. A summary of some of the pertinent history of attempts to characterize the situation appears in Roling *et al.* [2001]. We shall consider here only models for the aforementioned behaviors that may be associated with mobile charge effects. The first and most desirable would be a fully microscopic model that accounted for all the aforementioned processes, since they are all directly or indirectly associated with mobile charge in conductive-system materials. Unfortunately, this many-body problem involving all interactions is currently insoluble.

A second approach involves approximate microscopic models whose log–log $\sigma'(\omega)$ slope continuously increases toward a value of unity until a high-frequency plateau is reached. No account of electrode effects is included in these approaches. In most other models, the high-frequency slope is related to a model parameter and quickly increases to a constant value less than unity as the frequency increases and before a final plateau begins to appear (Macdonald [1997b, 2002d]).

The third approach involves a composite model involving separate parts: one accounting for ionic hopping; a parallel contribution representing the effect of the endemic bulk dielectric constant, $\epsilon_{D\infty}$, possibly a part describing NCL; and finally a series response model to account for electrode effects. For fitting most limited-range data, only two or three of these parts are usually required, and excellent data fits are generally found using appropriate models. We shall therefore consider some composite models in detail.

It is noteworthy that most comparisons and fits of models to experimental data deal with only $\sigma'(\omega)$ response. An advantage of this procedure is that $\sigma'(\omega)$ and $\epsilon''(\omega) \equiv \sigma'(\omega)/\omega\epsilon_V$ are the only ones of the eight real and imaginary parts of the four immittance levels that are independent of the presence of $\epsilon_{D\infty}$: $\sigma'(\omega)$ fitting is thus simpler than fitting with any of the four complex immittance-level responses or with the six other real and imaginary parts. Such an approach does not allow estimation of $\epsilon_{D\infty}$, however, and it forfeits not only the error averaging inherent in CNLS fitting but also the latter's test for the applicability of the Kronig–Kramers (KK) transformations.

The following discussion does not include consideration of all reasonable models that have been proposed and used for conductive-system fitting, but considers only some widely used ones and ones of particular theoretical importance.

4.2.2.2 Variable-Slope Models

The Mismatch and Relaxation Model. Although some apparent theoretical defects inherent in the mismatch-and-relaxation model of Funke [1998] have been pointed out (Macdonald [1999b]), they have neither been explicitly recognized nor directly resolved. A recent empirical modification of this approach (Funke *et al.* [2002]) seems, however, to avoid some of the problems of the earlier work. Further, new work of Funke and Banhatti [2004] corrects further weakness in the model although it still contains some empirical elements and thus cannot be considered a full microscopic response model.

The Symmetric Hopping Model. This model (Dyre and Schröder [2000]) ignores Coulomb interactions, claims to be of universal character in the extreme disorder limit, and yields response rather similar to that of the mismatch-and-relaxation model. Of the several approximate but specific microscopic hopping realizations of the microscopic model considered by Dyre and Schröder, the diffusion-cluster-approximation one led to best results, although it involves low-frequency-limiting response in disagreement with the physically realistic dependencies of the real and imaginary parts of the ac conductivity on ω^2 and ω , respectively (Odagaki and Lax [1980], Macdonald [1996, 1997b, 2001a]). The mathematical complexities of both the mismatch-and-relaxation model and the diffusion-cluster-approximation one make data fitting and the estimation of values of model parameters difficult, and thus no CNLS fitting of data to estimate such parameters seems to have been published so far.

Comparisons of the variable-slope models with real-part conductivity data have rarely involved responses with a variation of $\sigma'(\omega)/\sigma_0$ greater than three decades starting from a low-frequency experimental value of this ratio of nearly unity (Macdonald and Ahmad [2007]), and even for such a limited range they usually show increasing disagreement with experiment toward the high end of this ratio where the relative frequency is large. In contrast, the results of a PK1-model (defined in the next section) fit of accurate synthetic data calculated for the microscopic diffusion-cluster hopping model and involving a range of $\sigma'(\omega)/\sigma_0$ greater than seven decades yielded a value of S_F , the relative standard deviation of the fit, of less than 0.01 and showed no deviation between $\sigma'(\omega)/\sigma_0$ data and fit points on a log–log plot, as well as no apparent slope variation (Macdonald [2001b]).

It is therefore clear that since the variable-slope models have not been compared with experimental data that would allow discrimination between their predictions and those of simpler composite models, the variable-slope approaches, while of theoretical interest, are currently less appropriate for data fitting and analysis than simpler and well-fitting composite models.

4.2.2.3 Composite Models

The ZC Power-Law Model. Although we discuss some single dispersive response models here, in practice they must always take account of $\epsilon_{D\infty}$ and of possibly some other effects as well and so the overall model is always composite. A frequently used fitting model is the ZARC one of Eq. (22), Section 2.2. It is now more often designated as the ZC, and, when written at the complex conductivity level, it may be expressed as $\sigma_{ZC}(\omega) = \sigma_0[1 + (i\omega\tau_{ZC})^{\gamma_{ZC}}]$, where $0 < \gamma_{ZC} \leq 1$. The exponent γ_{ZC} has often been written as n and is the high-frequency-limiting log–log slope of the model. It has usually been found to have a value in the range $0.6 \leq \gamma_{ZC} \leq 0.7$.

The real part of the ZC model has been termed Jonscher or universal dynamic response, but the word “universal” is inappropriate since CNLS fits with the ZC or with its $\sigma'_{ZC}(\omega)$ part have been shown to be much poorer than those with other composite models (Macdonald [2000b, 2003a]). Finally, the identification of τ_{ZC} , or its real-part-fitting counterpart, as the inverse of the hopping radial frequency of the charge carriers has also been shown to be unsuitable (Macdonald [2003a]), and a more appropriate choice, the CK1 model, is discussed later.

OMF and CMF Kohlrausch Response Models. Consider now the general definition of the I_k normalized frequency-response quantity of Eq. (3), Section 2.2, with $k = D, 0$, and 1 . For $k = D$, U_k in that equation is the complex dielectric constant, $\epsilon(\omega)$, and for the other two values, U_k is the complex resistivity, $\rho(\omega)$. Now I_k may be calculated from either a distribution of relaxations times or from a temporal correlation function (see Macdonald [1996, 2002d] and Section 2.1.2.3). Although the $\rho_{0\infty}$ and $\rho_{1\infty}$ quantities entering into the definition of U_0 and U_1 are usually either zero or negligibly small, they may be large enough to affect the frequency response of the model at very large frequencies (Macdonald [2002d]). They will be taken zero for most of the present work. Then it follows that we may write $\rho_0(\omega) = \rho_0 I_0(\omega)$ and $\rho_1(\omega) = \rho_0 I_1(\omega)$, where we ignore the distinction between ρ_{00} and ρ_{01} .

The stretched-exponential temporal response of Eq. (63), Section 2.1, a versatile and theoretically plausible correlation function, is one whose corresponding frequency behavior is now called Kohlrausch–Williams–Watts (KWW) or just Kohlrausch [1854] model response, denoted here by Kk. It is also now customary to replace the α of the stretched-exponential equation by β or β_k , with $k = D$ or 0 . The $k = D$ choice may be related to KD-model dispersive frequency response involving a distribution of dielectric relaxation (properly “retardation”) times, and the $k = 0$ and 1 choices to two different distributions of resistivity relaxation times and thus to K0 and K1-model responses, respectively. Note that the β_1 parameter of the important K1 model is not directly related to stretched-exponential temporal response, as are the other Kk models, but the DRTs of the K0 and K1 models are closely related (Macdonald [1997a, 2000a]). Further, although the KD and K0 models are identical in form, they apply at different immittance levels and so represent distinct response behaviors.

No closed-form expressions are available for the frequency responses of the Kk models for arbitrary β_k values, but algorithms for calculating such responses and for fitting data with them are included in the

free LEVM CNLS fitting program (Macdonald and Potter [1987], Macdonald [2000a]) and are very accurate for $0.3 \leq \beta_k \leq 0.7$ and somewhat less accurate outside this range. Further, LEVM also includes closed-form exact-response expressions for the choices $\beta_k = 1/3$ and $1/2$.

Although defects in the 1973 OMF K1-model approach of Moynihan and associates [1973] have been pointed out for the last 10 years, papers continue to be published that use the OMF and ignore criticisms of it. It is therefore worthwhile to discuss it and its corrected version, the CMF, in order to make the issues involved clear to the reader, who can then make an informed choice between the two approaches. Although they both use the K1 response model, the OMF and CMF approaches are nevertheless crucially different.

Since the OMF response model was originally derived at the modulus level, let us begin by writing for the K0 model, $M_0(\omega) = i\omega\epsilon_V\rho_0 I_0(\omega)$. The OMF analysis (Moynihan *et al.* [1973]) led to the following result for the $M_1(\omega)$ response of the K1-model in terms of $I_0(\omega)$:

$$M_1(\omega) = i\omega\epsilon_V\rho_0 I_1(\omega) = \frac{1 - I_{01}(\omega)}{\epsilon_Z}, \quad (1)$$

where ϵ_Z was defined as $\epsilon_{D\infty}$, now written by supporters of the OMF as ϵ_∞ . The subscript 01 is used here to indicate that $I_{01}(\omega)$ is just $I_0(\omega)$ in form but involves β_1 rather than β_0 .

The OMF K1 model of Eq. (1), derived from a purely conductive-system correlation function, improperly mixes together conductive-system and dielectric-system responses through its identification of ϵ_Z as $\epsilon_{D\infty}$. This identification leads to a world of problems (e.g., see Macdonald [1996, 2002a, 2004, 2009]), vitiating this approach and implying that the OMF should be replaced by the CMF or by a superior model.

The CMF correction is simple: ϵ_Z in Eq. (1) is defined as the limiting dielectric constant $\epsilon_{C1\infty} = \epsilon_{C1}(\infty)$, a purely conductive-system nonzero quantity associated only with charge carrier motion and defined later. Except for the explicit introduction of ϵ_Z , the essence of the 1973 OMF derivation of Eq. (1) appeared in the earlier work of Macdonald and Barlow [1963]. Incidentally, for the K0 model, $\epsilon_{CO\infty} \equiv \epsilon_{CO}(\infty) = 0$. For both the K0 and CMF K1 models, one therefore needs to account for the endemic presence of $\epsilon_{D\infty}$ by including a free dielectric-constant fitting parameter, ϵ_x , in the composite fitting model, now designated the CK0 model for K0 response and the CK1 for the CMF K1 situation. Then for the K0 model $\epsilon_\infty = \epsilon_x$, and for the CK1 $\epsilon_\infty = \epsilon_{C1\infty} + \epsilon_{D\infty}$. The separate existence of $\epsilon_{C1\infty}$ is not recognized by users of the OMF. Note that CK0 and CK1 fits of the same data lead to nearly the same estimates of ϵ_∞ .

It has sometimes been found useful to replace the ideal capacitance represented by $\epsilon_x = \epsilon_{D\infty}$ by a parallel constant phase element (PCPE) $\epsilon_{PC}(\omega) \equiv A_{PC}(i\omega)^{-\gamma_{PC}}$, with $0 \leq \gamma_{PC} < 1$, reducing to a nearly ideal capacitance when $\gamma_{PC} \ll 1$ so that $A_{PC} \cong \epsilon_{D\infty}$. The resulting composite model has been designated the PK1. A series CPE (SCPE), $\sigma_{SC}(\omega) \equiv \epsilon_V A_{SC}(i\omega)^{\gamma_{SC}}$ with $0 \leq \gamma_{SC} \leq 1$, has often been found satisfactory for modeling electrode effects, and it represents the effect at the complex resistivity level of a completely blocking series capacitance when $\gamma_{SC} = 1$. When SCPE response is combined with that of the CK1, the result is written as the CK1S model. For the data fitting described in the next section, it turns out that a more complicated model is needed there to represent electrode effects more exactly.

The OMF K1 was derived by considering electric field decay at constant dielectric displacement and is thus a macroscopic response model. It has been shown, however, that the CMF K1, with $\epsilon_Z = \epsilon_{C1\infty}$, is completely isomorphic in form with the famous stochastic-transport microscopic analysis of Scher and Lax [1973a], a continuous-time random-walk hopping model. The extended version of this model (Macdonald [2002d]) leads to response of exactly the form shown in Eq. (1), involving a quantity equivalent to $I_{01}(\omega)$ derived by Fourier transform from an initially unspecified correlation function associated with a waiting time distribution for hopping. It is the specific stretched-exponential choice for this function that leads to explicit K1 response. These considerations show that the K1 may be derived by considering either macroscopic or microscopic processes, and such generality possibly accounts for the ability of the CK1 to fit a variety of conductive-system frequency-response data exceptionally well (e.g., Macdonald [2000b, 2002a, 2003a]).

The OMF expression for $\varepsilon_Z = \varepsilon_\infty$ may be written (Macdonald [1996, 2001c, 2002d]) as

$$\varepsilon_\infty = \frac{\sigma_0 \langle \tau \rangle_{01}}{\varepsilon_V} = \varepsilon_{\text{Ma}} \langle x \rangle_{01} = \varepsilon_{\text{Ma}} \beta_{1O}^{-1} \Gamma(\beta_{1O}^{-1}), \quad (2)$$

where the averages are over the resistivity DRT for the K1 model and the OMF β_1 is designated as β_{1O} to distinguish it from that of the CMF, β_{1C} . Here the Maxwell quantity ε_{Ma} is

$$\varepsilon_{\text{Ma}} \equiv \frac{\sigma_0 \tau_o}{\varepsilon_V} \quad (3)$$

$x \equiv \tau / \tau_o$; and τ_o denotes the characteristic relaxation time of the K1 model, and it will be used for other models as well. The part of Eq. (2) involving the gamma function is only appropriate in the absence of cutoff of the K1 DRTs (Macdonald [1996]).

In contrast, for the CMF K1 dispersion model, $\varepsilon_Z = \varepsilon_{C1\infty}$, where

$$\varepsilon_{C1\infty} = \frac{\varepsilon_{\text{Ma}}}{\langle x^{-1} \rangle_1} = \frac{\varepsilon_{\text{Ma}}}{\langle x \rangle_{01}} = \varepsilon_{\text{Ma}} \beta_{1C}^{-1} \Gamma(\beta_{1C}^{-1}) = \frac{[\gamma N(qd)^2 / (6k_B \varepsilon_V)]}{T} = \frac{A}{T} \quad (4)$$

and N is the maximum mobile charge number density; γ is the fraction of charge carriers of charge q that are mobile; and d is the rms single-hop distance for the hopping entity. The high-frequency-limiting effective dielectric constant, $\varepsilon_{C1\infty}$, associated entirely with mobile charge effects, is likely to arise from the short-range vibrational and librational motion of caged ions.

Comparison of CMF equations with those of the Scher–Lax hopping model (Macdonald [2002d]) shows that the K1 mean relaxation time, $\langle \tau \rangle_{01} \equiv \tau_o \langle x \rangle_{01}$, is identical with the mean hopping time of the microscopic model, also defined as the mean waiting time for a hop. The term involving N in Eq. (4), not included in the OMF, is fully consistent with the Scher–Lax model predictions. In practice, fits of the same data with the OMF K1 and with the CK1 of the CMF approach lead to very different estimates of τ_o and of β_{1O} and β_{1C} .

We expect that the quantities in the square brackets of Eq. (4) are usually temperature independent, so the fitting parameter A is then itself independent of temperature. It follows that in the usual case where τ_o is thermally activated, $T\sigma_0$ is activated with the same activation energy (Macdonald [2002a]). The presence of the N term of Eq. (4) shows that as the ionic concentration approaches zero, $\varepsilon_{C1\infty} \rightarrow 0$ and so $\varepsilon_\infty \rightarrow \varepsilon_{D\infty}$, requiring that $\varepsilon_{\text{Ma}} \rightarrow 0$ as well, in accordance with CMF fit results. The situation is different for the OMF expression of Eq. (2), however. In this case, OMF fits show that both ε_∞ and ε_{Ma} approach the same constant value, that of $\varepsilon_{D\infty}$. There is then no dispersion, and the response reduces to that of single-time-constant Debye behavior.

Fits of frequency-response data for a variety of materials, temperatures, and concentrations lead to β_{1C} estimates all very close to 1/3. But OMF fits, particularly of data in $M''(\omega)$ form, the usual OMF approach, invariably yield appreciably larger values of β_{1O} , ones that approach unity as the ionic concentration decreases or as the temperature increases. Such dependence led most users of the OMF to conclude that the correlation between charge carriers decreased as β_{1O} increased. But constancy of β_{1C} and the lack of Coulomb interactions in the well-fitting CMF microscopic model fail to support this supposition. For most data, it has been found that CK1 fits are superior to CK0 fits of the same data, but even in situations where these fits are comparable, CK1 ones are preferable to CK0 ones because $\beta_{1C} \cong 1/3$ estimates are virtually independent of temperature and ionic concentration, while CK0 β_0 estimates depend strongly on these variables (Macdonald [2002a, 2003a]).

Note that OMF data fitting with LEVM leads to estimates of the free parameters ρ_0 , τ_o , and β_{1O} , and ε_∞ may then be calculated using Eq. (2). When β_{1C} is taken constant at the value of 1/3, CMF fits yield estimates of ρ_0 , τ_o , and $\varepsilon_x \cong \varepsilon_{D\infty}$, and $\varepsilon_{C1\infty}$ may then be calculated using Eq. (4), with $\varepsilon_{C1\infty} = 6\varepsilon_{\text{Ma}}$ for this value of β_{1C} . Although ρ_0 estimates are usually nearly the same for the two types of fits of the same data, as are also calculated values of ε_∞ , β_{1O} is always appreciably larger than 1/3, and CMF τ_o estimates are generally at least an order of magnitude smaller than those from OMF fits.

When the OMF approach is used to fit experimental data, a fatal flaw appears, one that invalidates any conclusions based on such fitting results. For good data, all CMF fits yield closely the same estimates of τ_o and β_{1C} , independent of the immittance level for the data. This is not the case, however, for OMF fits. They lead to inconsistent results such that fits of the data in $M(\omega)$ or $M''(\omega)$ form yield characteristically large values of β_{1O} , usually falling in the range $0.45 \leq \beta_{1O} \leq 0.55$ for mid-range temperatures and concentrations, while fits of the same data in $\sigma'(\omega)$ form yield values close to $1/3$. As mentioned earlier, since $\varepsilon_{D\infty}$ has no effect on $\sigma'(\omega)$ response, K1 and CK1 fits at this level must yield the same estimates, and OMF and CMF fits are then equivalent. A table of such comparisons and further discussion of OMF problems appear in Macdonald [2004] and make it evident that the OMF treatment of $\varepsilon_{D\infty}$ as an intrinsic part of the K1 dispersive conductive-system model is incorrect.

Coupling and Cutoff Models. The Ngai coupling model (Ngai [1979, 1998]), discussed in Macdonald [1998, 2005b], has been used in many conductive-system data analyses by Ngai and his associates. It assumes that for times longer than t_c , a temperature insensitive crossover time of the order of 1 ps, the temporal response of the system is of stretched-exponential character, and for shorter times it is of ordinary exponential character. In its applications to frequency-response behavior, the coupling model has made use of OMF estimates of β_{1O} , although the frequency-response model directly corresponding to stretched-exponential behavior is the K0, not the K1, and generally $\beta_{1O} \neq \beta_0$.

A superior alternative, the cutoff model, avoids this inconsistency, makes no use of the OMF, and is based on a cutoff of the K1 DRTs at $\tau = t_c$. It does not involve the OMF assumption that the correlation between charge carriers decreases as β_{1O} increases for response at frequencies below $\omega_c = 1/t_c$, and it properly undergoes a transition to simple Debye response for frequencies greater than ω_c . Further, as shown in Macdonald [2005b], it leads not only to a smoother frequency-response transition around $\omega = \omega_c$ but also to satisfaction of the physical requirement that the K1 $\tau_o(T)$ never decreases below t_c as the measurement temperature becomes high. This requirement is not met by the $\tau_o(T)$ of the coupling model approach, suggesting that it should be superceded by the cutoff model. Both the coupling model and the cutoff one lead to non-Arrhenius behavior of $\sigma_0(T)$, with a transition from a low-temperature Arrhenius activation energy to a smaller apparent energy at high temperatures (León *et al.* [1998], Macdonald [1998, 2005b]).

Rationalization of the Barton, Nakajima, and Namikawa Relation. The Barton [1966], Nakajima [1972], and Namikawa [1975] empirical relation, usually designated by BNN, has played a useful role for some time in the analysis of dispersed frequency-response data (e.g., Dyre [1988], Macdonald [1996], Dyre and Schröder [2000], Porto *et al.* [2000]). It involves a loosely defined parameter, p , expected to be of order 1, and Nakajima and Namikawa believed that it arose from correlation between electrical conduction and dielectric polarization, apparently because it involved both measured dc conductivity and a dielectric strength quantity $\Delta\epsilon$.

But as we have seen, for a conductive system, both σ_0 and $\Delta\epsilon = \epsilon'(0) - \epsilon'(\infty) = \epsilon_0 - \epsilon_\infty$ may arise entirely from mobile charge effects and not involve bulk dielectric effects at all. Then $\Delta\epsilon = \Delta\epsilon_{C1} \equiv \epsilon_{C10} - \epsilon_{C1\infty}$ for the CK1 model, and $\Delta\epsilon = \Delta\epsilon_{C0} \equiv \epsilon_{C00}$ for the CK0 one. It was indeed pointed out by Macdonald [1996] that the K1 conducting-system model could lead to a quantitative value for p , one that depended on the value of β_{1C} .

Here it is shown that the BNN expression is most reasonably interpreted as arising entirely from charge motion, and if the K1 fit value of $\beta_{1C} = 1/3$ is a universal value, then the value of p is fully defined and the BNN equation is just a natural consequence of the apparent universal applicability or quasi-universality of the conductive-system CK1 model with $\beta_{1C} = 1/3$. For ion-conducting homogeneous glasses and single crystals, it has been shown theoretically in two independent ways that $1/3$ is the only possible value of β_{1C} and that the resulting high-frequency-limiting-response power-law exponent is $2/3$ (Macdonald and Phillips [2004], Macdonald [2005a]). Consistent with these results, it follows that CK0-model fits of such response lead to $\beta_0 = 2/3$.

The BNN equation may be expressed as

$$\Delta\epsilon = p^{-1} \left(\frac{\sigma_0}{\epsilon_V \omega_p} \right) = p^{-1} \left(\frac{\tau_p}{\tau_o} \right) \epsilon_{Ma} = p^{-1} \left(\frac{\nu_o}{\nu_p} \right) \epsilon_{Ma} \quad (5)$$

Here as usual, τ_o is the characteristic response time of a fitting model such as the CK1. Further, $\omega_p \equiv 2\pi\nu_p = 1/\tau_p$, where ν_p is the frequency at the peak of the dielectric loss curve, $\epsilon_s''(\nu)$, and $\nu_o \geq \nu_p$. For $\beta_{1C} = 1/3$, the K1 model leads to $\epsilon_{C1\infty} = 6\epsilon_{Ma}$ and to $\epsilon_{C10} = 60\epsilon_{Ma}$ (Macdonald [2001c]). Therefore, $\Delta\epsilon = 54\epsilon_{Ma}$, and one may write for this situation, $p = (\nu_o/\nu_p)/54$.

Sidebottom [1999] noted the similarity between the BNN equation and a scaling factor he proposed. This similarity arises because his result, appropriate for situations where the model shape is temperature independent, the situation for the CK1 model with a constant $\beta_{1C} = 1/3$ value, is a simplification of scaling factors associated with K0 and K1 models with variable β_k , as discussed in Macdonald [2001c]. Of course with accurate CNLS fitting, scaling is unnecessary. The success of the Sidebottom scaling approach is further indirect evidence of the widespread applicability of the CMF CK1 model with fixed $\beta_{1C} = 1/3$.

From nearly exact calculations of K1-model $\epsilon_s''(\omega)$ synthetic data derived from the parameter estimates of experimental-data fits of the next section, with the electrode contributions present or removed, one finds that the ν_o/ν_p ratio is about 95 and 89, respectively, leading to p estimates of about 1.77 and 1.65. The 1.65 value is the appropriate one for K1-alone response and is universal to the degree that Eqs. (1) and (4) are applicable and $\beta_{1C} = 1/3$. Although many data fits suggest that this value of β_{1C} is a constant for CK1 fits, one would expect that as $\beta_{1C} \rightarrow 1$, p should also approach unity in the limit, and, for example, when $\beta_{1C} = 0.5$, one obtains $p \approx 1.27$.

Over the years since the introduction of the BNN equation, published p values have mostly fallen in the range of 0.5–10 but are often close to unity. Accurate estimation of p directly from experimental data is uncertain when electrode effects are significant and/or when the data range is too small to lead to good estimates of ϵ_0 and ϵ_∞ . It is therefore appropriate to calculate p values from parameter values estimated from data fitting.

Although Hunt [1992] concluded that p cannot have a universal value, the present 1.65 value is consistent with most of the many BNN-related p estimates for experimental data presented by Dyre and Schröder [2000] in their figure 3, ones mostly slightly larger than unity. Such agreement is further evidence of the appropriateness of the CK1 model for many different materials. Earlier, Dyre [1988] quoted an estimate of p for a CTRW model different from the present Scher–Lax K1 one of only 0.42, while for their microscopic symmetric hopping model, Dyre and Schröder [2000] listed a value of 1.5 ± 0.4 . The present results show that if CMF fitting is used, there is no need for the BNN since it is an automatic consequence of the applicability of such fitting. When CK1 CNLS fit parameters are available, however, the BNN equation with $p = 1.65$ may be used to obtain an accurate estimate of ν_p for the conducting-system part of the data alone.

Finally, Porto *et al.* [2000] have recently suggested that the BNN relation cannot apply for an appreciable range of concentrations because data fits show that $\Delta\epsilon$ does not scale as N/T . But Eq. (4) shows that for the CMF K1 model, $\epsilon_{C1\infty}$ does indeed scale in this fashion and involves d^2 as well. Further, at constant β_{1C} , ϵ_{C10} and thus $\Delta\epsilon$ also do so (Macdonald [2001c, 2002a]). Therefore, this criticism does not seem appropriate. To test the matter, estimates of p were calculated from CK1 CNLS fits of $x_c \text{K}_2\text{O} \cdot (1-x_c) \text{GeO}_2$ germanate glasses with the relative ionic concentration, x_c , equal to 0.2 and 0.02, data kindly provided by Drs. Jain and Krishnaswami [1998]. The p estimates were 1.64 and 1.65, respectively, thus well verifying the appropriateness of the BNN equation over a considerable concentration variation.

Nearly Constant Loss Models. NCL is evidenced by a power-law dependence of $\sigma'(\omega)$ on frequency with an exponent very close to unity, leading to $\epsilon_s''(\omega)$ loss response that varies only slightly over a substantial frequency range. It may appear directly at low temperatures or may contribute significantly to $\sigma(\omega)$ response at the high end of the measured frequency range. In the first case, NCL is dominant and

thermally activated hopping response is completely negligible (Macdonald [2001a, 2003b]). In the second case, hopping is dominant over most of the frequency range.

Excellent reviews and discussions of NCL behavior in ionically conducting glasses appear in Ngai [1999] and Roling *et al.* [2001]. Although most authors believe that NCL arises from the restricted motion of caged ions or groups of atomic species, very few quantitative NCL models have been proposed. An important early composite one may be written as $\sigma'(\omega) = \sigma_0[1 + (\omega\tau_0)^n] + A\omega^s$, with $0 < n \leq 1$ and $s \approx 1$ (Lee *et al.* [1991], Nowick *et al.* [1998]). The first term represents universal dynamic response, as discussed earlier, and constant loss occurs when $s = 1$, not a viable situation for a finite frequency range.

Although this composite model implies the additivity of hopping and NCL effects, the appropriateness of such additivity has been challenged by León *et al.* [2001] and Rivera *et al.* [2002]. They suggested an alternate serial (not series) picture in which NCL ceases to exist when hopping begins and ions begin to exit their cages. This is not a quantitative model, and their work dealt primarily with $\sigma'(\omega)$ response. Fitting of both synthetic and experimental complex data provides strong evidence, however, that additivity should not be rejected, and analysis using a quantitative complex model such as the PK1 suggests that hopping and NCL effects can exist simultaneously in a crossover region of finite length (Macdonald [2001a, b, c, 2002a]). Here, the parts of the model are in parallel electrically and additivity is ensured. The PCPE part of the expression models NCL behavior and can extend over an unrestricted frequency range.

Although a PCPE may be used to model NCL data with equal slopes for both $\epsilon'(\omega)$ and $\epsilon''_s(\omega)$ since they both involve the same $\gamma_{PC} \ll 1$ exponent, some data may be better represented by such power-law response for $\epsilon'(\omega)$ but by a function that yields a very close approximation to constant loss for the $\epsilon''_s(\omega)$ part of the response (Nowick *et al.* [1998]). In the absence of hopping, just the series combination of an ideal capacitor and a CPE can yield such behavior with very NCL over several decades of frequency (Macdonald [2001a]).

It was first shown in 2002 that the CPK1 composite model, where both C and a PCPE are in parallel with K1, could be used to represent frequency-independent undispersed $\epsilon_{D\infty}$ behavior, hopping behavior, and NCL (Macdonald [2002a]). This work, in turn, suggested that the model could be made more physically plausible by an effective medium approach, one that might be able to represent both kinds of NCL behavior, as well as possibly non-negligible hopping effects. The resulting effective medium model, the EMK1, indeed met this objective well (Macdonald [2003b]). It is based on the assumption of a background involving a constant $\epsilon_{D\infty}$ term and a volume fraction, η , of "inclusions" associated with ions vibrating over a limited region and represented by a PCPE. Thus, even in the absence of the K1 part, $\epsilon_{EM}(\omega)$ is complex.

The EMK1 model, unlike the CPK1 one, leads to physically plausible low-frequency-limiting slopes for $\epsilon(\omega)$ and other immittance functions, as well as equal or superior fits to those of the CPK1. As a first approximation, η is set equal to the relative ionic concentration, x_c . Synthetic data for $\epsilon''_{EM}(\omega)$ extending over many decades of frequency and for a wide range of η values showed that although there is no finite range of exact constant loss behavior, such response is well approximated for η near 0.25. In addition, when the response is approximated by a power-law model, the resulting very small exponent may be either positive for $\eta \ll 1$ or negative for $\eta \geq 0.25$ over the higher-frequency region of the response.

There are two important questions arising from the present model discussions. First, a microscopic model that leads to $\beta_{1C} \cong 1/3$ needs to be developed, and second, a microscopic model is also needed that yields response like the present effective medium model and takes explicit account of the detailed interactions, electromagnetic and otherwise, between vibrating ions and bulk dipoles.

Poisson–Nernst–Planck (PNP) Models. These models, like most of those currently used for fitting experimental data involving mobile charges, are continuum ones, but this limitation is nearly always unimportant for data fitting. The Poisson–Nernst–Planck (PNP)-model data fitting is particularly useful because it can lead to estimates of the values of most, if not all, of the physically significant parameters involved with and to the data set analyzed, not possible with empirical and most other models.

The PNP model with complete blocking of mobile charges at the electrodes was derived and discussed in Macdonald [1953] and has been much used and expanded since then, as summarized in the following. (See Barbero and Alexe-Ionescu [2005].) The CJPNP model (Macdonald and Franceschetti

[1978]; see especially Eq. (B38) and Section 2.1.4 of the present book) involves Chang–Jaffe (CJ) boundary conditions. The ECJPNP, also discussed there, further extends the boundary conditions to include specific adsorption as well as electrode reactions. The PNPA model (Macdonald [2010], Macdonald *et al.* [2011]) generalizes the ordinary PNP model involving ordinary diffusion of the mobile charges to anomalous diffusion and involves a fractional parameter that is unity for the PNP.

Since 2009 many publications dealing with various aspects of the PNP model have appeared. (See especially Evangelista *et al.* [2011, 2013], Macdonald [2009, 2010, 2011, 2012b, 2013].) The Macdonald [2013] publication is an extensive summary of the background and virtues of the PNP-model fitting approach. It lists the many physically significant parameters whose values may be estimated from such fitting of experimental data.

In addition, this publication includes frequency-response figures that compare PNP and PNPA, PNPA and CJPNPA, and CJPNPA and DCDCJPNPA responses for each of the four immittance levels. The DCDCJPNPA is a composite model involving CJPNPA response in parallel with that of the DCD model. Here DCD is the designation of the Davidson–Cole empirical model included to represent possible dielectric dispersion effects, often needed for good fitting of wide-range frequency-response experimental results. The free LEVM CNLS computer fitting program includes in its Circuit H a section called FITTESTS that includes many PNP-related LEVM input files that may be used in fitting new data, including one named DCDCJPNPAEXACTZN. The publications of J. R. Macdonald and the LEVM program are all available at <http://jrossmacdonald.com>.

4.2.3 Illustration of Typical Data Fitting Results for an Ionic Conductor

CNLS fitting has been little used by most workers who have analyzed frequency-response data for ionic conductors. The majority of published work deals primarily with either $\sigma'(\nu)$ or $M''(\nu)$ response, but not usually with both or with simultaneous fitting of real and imaginary parts of an immittance data set. An apparent advantage of the fitting and analysis of $\sigma'(\nu)$ data alone is that it and its direct transform, $\epsilon''(\omega) \equiv \sigma'(\omega)/\omega\epsilon_0$, are the only immittance-level parts that include no effects from $\epsilon_{D\infty}$, as already mentioned in Section 4.2.2.1. But much more can generally be learned by considering full complex response at other immittance levels. Here we will only deal with data that do not extend to high enough frequencies or low enough temperatures to require an NCL contribution.

It is therefore worthwhile to illustrate, for a typical data set, the usefulness of CNLS fitting and of various plots of the results. For generality, the data set selected is one for which both bulk dispersion and electrode effects are non-negligible. It was kindly provided by Dr. Carlos León and involves the fast ionic conductor $\text{Li}_{0.5}\text{La}_{0.5}\text{LiO}_3$, measured at $T = 225$ K (León *et al.* [1998]). This set is designated hereafter as LLTO.5. Fitting was carried out using the O circuit of the LEVM program. To allow independent work with this data set, its full LEVM input file, 225Z36EL, has been included in the LEVM FITTESTS folder of test files for the O circuit.

Figure 4.2.1 shows the full O circuit. For LEVM, only those circuit elements that are given nonzero values are used in fitting. Here “DE” designates a distributed circuit element, one that can be selected from a large number of different elements available in LEVM. DED involves a dielectric distributed element, such as the DSD, a dielectric-system dispersive element. Similarly, DEC designates a conductive distributed element, such as the CSD. In LEVM, the series inductance shown in the figure may be replaced by a short circuit, a resistor, or a capacitance, C_S .

Since it was initially established that the LLTO.5 data sets for different temperatures involved thermally activated response and were therefore of CSD character, we begin by carrying out CMF fits of the $T = 225$ K data. The bulk response was thus represented by the K1 model in the DEC part of the circuit. It involves the parameters ρ_0 , τ_o , and β_{1C} , but, as usual, a β_{1C} value of 1/3 yielded best results. Therefore, this value was taken as fixed for all the present fits. When the CMF CK1 model was employed, $\epsilon_{D\infty}$ was represented by the C_∞ element of the circuit. As usual, R_∞ was found to contribute nothing to the fits and was thus not used thereafter.

For blocking electrodes the simplest element to represent their effect is a series capacitance, C_S , but electrode processes are generally too complicated for adequate representation by a single capacitance. The next level of complexity, often found adequate, is to use a SCPE in the DE₃ position of the circuit.

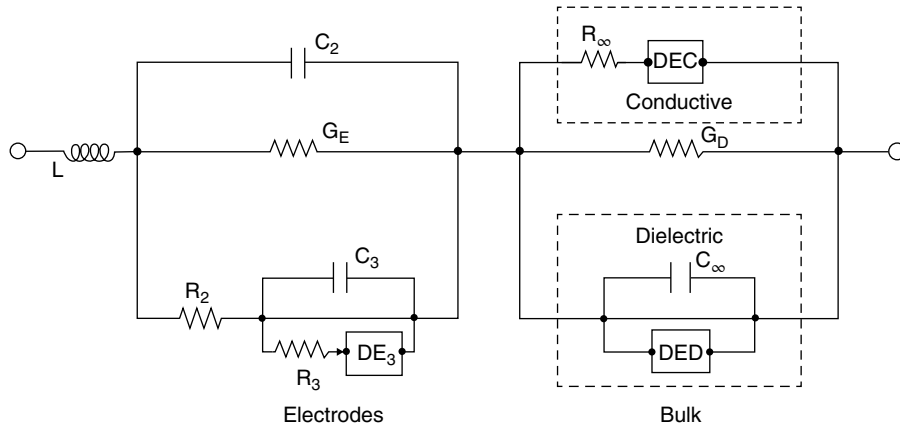


FIGURE 4.2.1 The LEVM fitting circuit O. It may be used as shown for fitting immittance data in raw or specific form. The DE blocks may each be selected as any one of the many available distributed-circuit-element response models.

A recent analysis of the use of a CPE for modeling electrode behavior appears in Bisquert *et al.* [1998]. For the present data, for which electrode effects are far from negligible, it was found that they were best represented by an SCPE in parallel with the C_3 capacitance of the circuit, all in series with C_S , involving a total of four free fitting parameters. The full CK1 model including these free electrode-related parameters is termed the CK1EL and involves a total of seven free parameters.

The CK1EL CNLS fit of the data at the complex resistivity level using LEVM with proportional weighting led to the estimates $\epsilon_{D\infty} \cong 83.08$, $\rho_0 \cong 1.78 \times 10^5 \Omega\text{-cm}$, and $\tau_0 \cong 4.488 \times 10^{-8} \text{ s}$. In addition, the estimate for the γ_{SC} parameter of the SCPE was about 0.641. The fit also led to the estimates $\epsilon_0 = 254$, $\epsilon_{C10} \cong 171$, $\epsilon_{C1\infty} \cong 17.1$, $\epsilon_\infty \cong 100$, and $\Delta\epsilon = \Delta\epsilon_{C1} \cong 154$. Exactly the same parameter values were obtained for proportional-weighting fitting at the complex modulus level. The relative standard deviation of the overall fit, S_F , was 0.0072, indicating an excellent result.

When electrode effects were represented only by an SCPE, the CK1S model, S_F increased appreciably to 0.015. This fit led to a larger γ_{SC} estimate of about 0.897 and to the slightly different estimates for $\epsilon_{D\infty}$, ϵ_0 , ϵ_{C10} , $\epsilon_{C1\infty}$, ϵ_∞ , and $\Delta\epsilon$ of about 79, 254, 175, 17.5, 97, and 157, respectively. In the limit of low frequencies, the four-parameter model for electrode behavior is dominated by the blocking capacitor, C_S . Its value, expressed in dielectric-constant form, was more than 30 times larger than the CK1EL estimate of ϵ_0 .

Figure 4.2.2 presents a three-dimensional (3-D) log-log-log plot of complex resistivity data as well as fit points for the CK1EL model fit. The projections in the three planes involve only the data. The 3-D line shows every other one of the data points and every fourth fit point. Since the open-circle fit points enclose their corresponding data points symmetrically, no deviations are evident. The projection lines at the two back planes clearly show the transition to electrode-related power-law behavior toward the low end of the frequency scale. Space restrictions preclude presentation here of the three other 3-D imittance plots.

Figure 4.2.3 shows the behavior of the real and imaginary parts of the complex modulus. In addition to the CK1EL-fit lines, those for the CK1 and K1 parts of the model are also shown. They were calculated using in LEVM the appropriate parameter values found from the full CK1EL fit, and thus they are virtually exact representations of the model behavior for these values. The present M' results show that electrode effects are dominant at low frequencies and have only a minor effect at the high-frequency end of the data range. As one would expect, the difference between the CK1 and K1 results, associated entirely with $\epsilon_{D\infty}$, becomes great at the high-frequency end.

It is often been stated that a virtue of plotting and analyzing data in M'' form is the resulting suppression of electrode effects. The present results demonstrate such suppression near the M'' peak, but it clearly diminishes as the frequency departs from the peak value. Further, since the same parameter

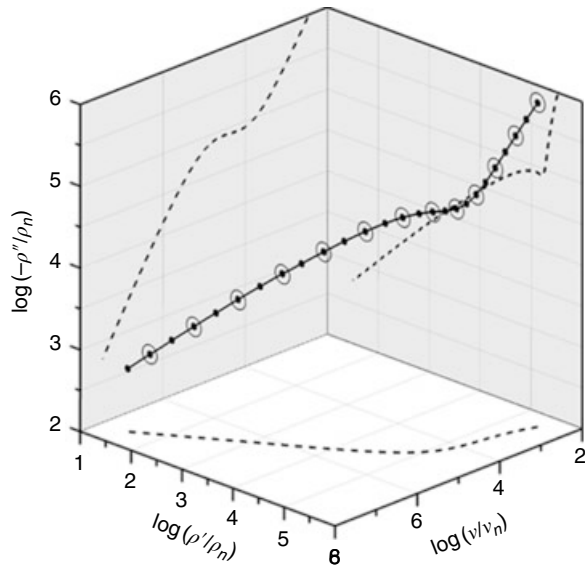


FIGURE 4.2.2 3-D log-log-log plot, with planar projections. Lines and solid circles show the data, and open circles identify points from CK1EL-model CNLS fitting of the data (denoted LLTO.5 hereafter) at the complex resistivity level.

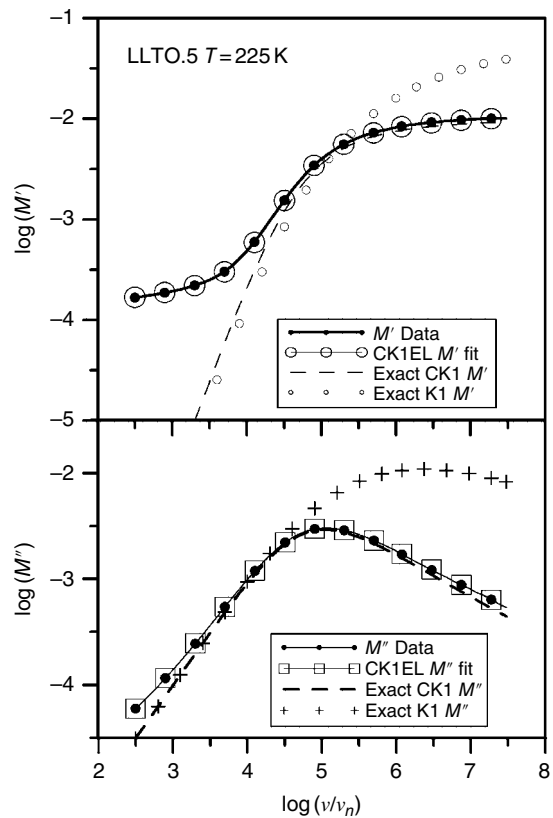


FIGURE 4.2.3 Log-log complex modulus data and fit results for $M'(\omega)$ and $M''(\omega)$ obtained from fitting the $M(\omega)$ complex data with the CK1EL model. In addition, predictions for the CK1 and K1 parts of the full model are shown.

estimates are obtained for both $\rho(\omega)$ and $M(\omega)$ fits when proportional weighting is employed, the suppression is graphical but not significant for least squares fitting. Finally, it is evident that the peak of the OMF K1 M'' curve appears at much higher frequencies than that of the CMF CK1 one and the breadth of the K1 curve at half height is also much larger. This difference is associated with the CK1 value of β_1 of 1/3 and a value greater than 0.5 found for OMF fitting of the $M(\omega)$ data, as expected from the discussion in Section 4.2.2.

Figure 4.2.4 compares $\sigma'(\omega)$ data and CK1EL fit values, as well as individual contributions to the full model. For this immittance level, there is no effect from $\epsilon_{D\infty}$, so here CK1EL and K1EL fit results are equivalent. The CK1SG results were obtained by first setting the G_D parameter of the Figure 4.2.1 circuit to $-\sigma_0$. This, together with the K1 parameter estimates obtained from the CK1EL fit, was then used in LEVM to calculate the resulting exact response of the combination and thus to eliminate the effect of σ_0 . It is evident that, as expected, the high-frequency end of the range $\sigma'(\omega)$ response is nearly entirely associated with the ac part of the K1 model, with only a small contribution from electrode effects apparent. Further, the data curve shows that no accurate value of σ_0 could be directly estimated from it, making it essential that all fits should account for electrode effects.

Rather than present $\sigma''(\omega)$ fitting results, it is appropriate to show those for the corresponding $\epsilon'(\omega)$, related to $\sigma''(\omega)$ by a factor of $1/\epsilon_V\omega$. Such results are presented in the top part of Figure 4.2.5. It is clear that the $\epsilon'(\omega)$ data curve alone does not allow one to obtain a reasonable estimate of ϵ_0 from it. Removal of the electrode effects obtained from the full CK1EL fit leads to the low- and high-frequency plateau values ϵ_0 and ϵ_∞ , respectively, while subsequent removal of $\epsilon_{D\infty}$ leads to the limiting conductive-system K1-model quantities ϵ_{C10} and $\epsilon_{C1\infty}$. It is again evident that electrode effects play a minor but not completely negligible role at high frequencies. The bottom part of the present figure shows $\epsilon''(\omega)$ results, where again $\epsilon_{D\infty}$ plays no role. The frequency at the peak of the CK1SG curve, that for $\epsilon''_S(\omega)$, is shown by ν_p and is needed for the calculation of the BNN quantity p .

Finally, Figure 4.2.6 shows a linear-scale complex-resistivity-plane plot. Here, to allow greater resolution, lower-frequency points than those shown have been omitted. The results indicate that electrode effects remain important over most of the frequency range, even near the highest frequencies. Comparison of corresponding data and fit points shows some very minor discrepancies for the spur part of the response, ones that are too small to be evident in log-log plots. The low-frequency end of the CK1-only

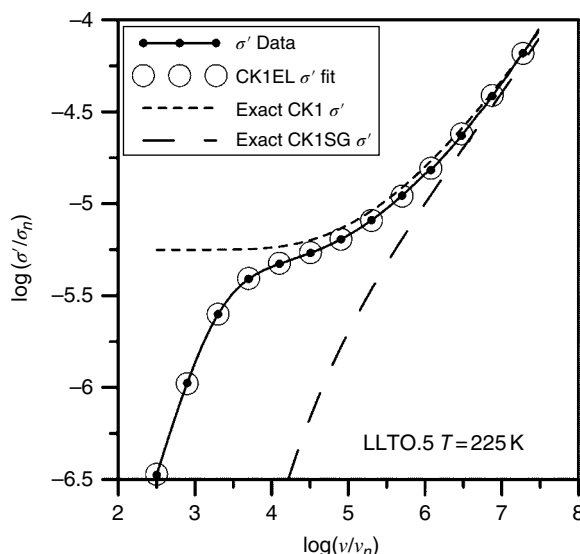


FIGURE 4.2.4 Log-log $\sigma'(\omega)$ data and fit results from CNLS fitting as in Figure 4.2.3. The CK1SG results eliminate both electrode effects and those of σ_0 .

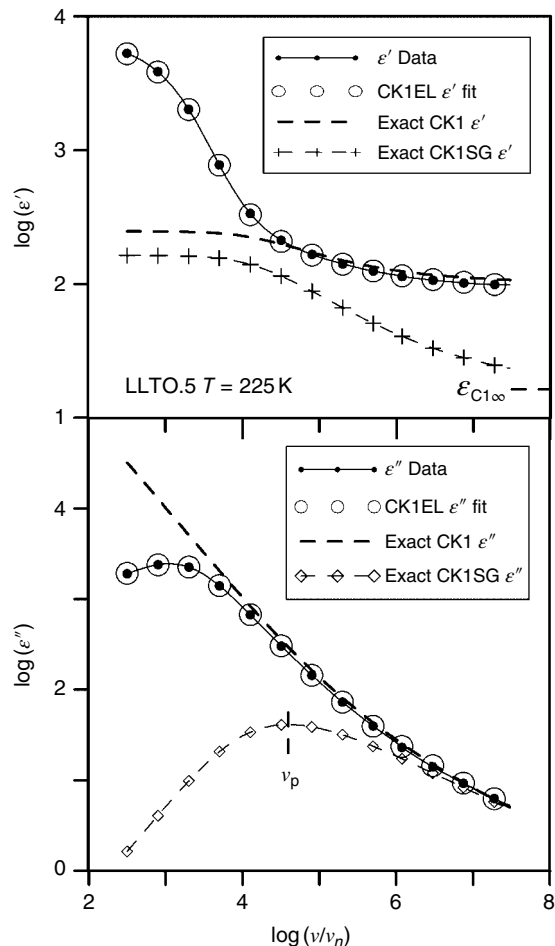


FIGURE 4.2.5 Log-log $\epsilon(\omega)$ data and fit results from CNLS fitting as in Figure 4.2.3. The exact CK1 response is that without electrode effects, and the K1 response eliminates the effect of $\epsilon_{D\infty}$ as well and shows the approach of the data toward the limiting $\epsilon_{C1\infty}$ value. The peak of the CK1SG $\epsilon''_s(\omega)$ curve is denoted by ν_p .

part of the response approaches the axis at 90° as it should and defines the value of ρ_0 . It is important to note that extrapolation of the electrode spur line down to the ρ' axis leads directly to an excellent estimate of ρ_0 . This can be useful when the temperature is so high that little or none of the bulk arc is included in the measurement range and CNLS fitting may not have been carried out. However, such extrapolation fails for mixed ionic and electronic conduction situations.

In a full data analysis, one would first determine the most appropriate model and then use it to carry out fits for each different temperature available. Here, only partial results for fits of the present $T = 225$ K data with a few other models will be discussed. First, S_F values for CNLS proportional-weighting fits with the CK0EL, OMF K1EL, and “DSD” EDAEEL models were all close to 0.007, excellent fits. Here, the EDAE model involves an exponential distribution of activation energies fitted at the complex dielectric level and assuming DSD. Since the fits were all comparable, selection of a best model must depend on other criteria.

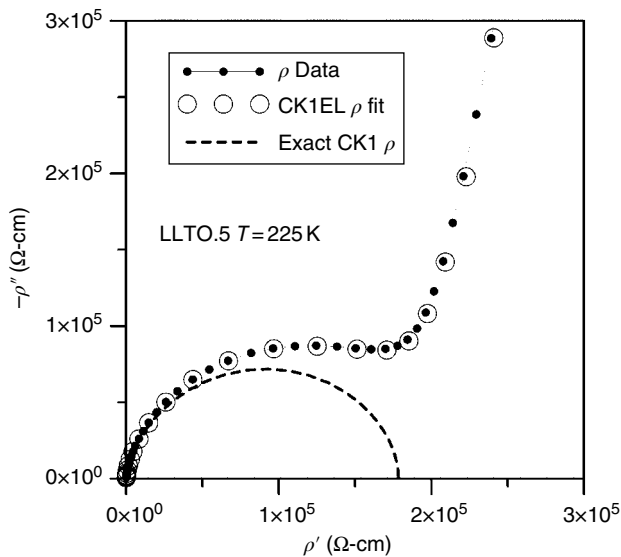


FIGURE 4.2.6 $\rho(\omega)$ data and fit results from CNLS fitting as in Figure 4.2.2. These complex plane results demonstrate clearly the dominance of electrode effects up to quite high frequencies.

The CK0EL model led to CNLS estimates of ϵ_0 , $\epsilon_{C10} = \Delta\epsilon$, and ϵ_∞ of about 255, 145, and 97, respectively. Since this model always involves $\epsilon_{C0\infty} = 0$, it does not yield a separate estimate of $\epsilon_{D\infty}$, but its β_0 and γ_{SC} estimates were about 0.487 and 0.635, respectively. Note that with $\beta_{1C} = 1/3$, $\beta_0 + \beta_{1C} \neq 1$ here. Even when the CK1EL and CK0EL models yield comparable fits and nearly the same estimates for some common parameters, the former, with fixed $\beta_1 = 1/3$, should be preferred because it yields not only a comparable fit with fewer free parameters but because it also leads to separate estimates of both $\epsilon_{C1\infty}$ and $\epsilon_{D\infty}$.

For the OMF K1EL model, ϵ_0 , ϵ_{C10} , $\Delta\epsilon$, and $\epsilon_\infty = \epsilon_{C1\infty}$ values were all calculated from the CNLS fit parameters, leading to estimates were about 233, 118, and 115, respectively. They thus agree less well with the CK1EL and CK0EL fit results. The aforementioned $M(\omega)$ fit results used proportional weighting, but $M''(\omega)$ NLS fits with either proportional or unity weighting led to closely similar estimates. The β_{10} and γ_{SC} values estimated for these fits were about 0.604 and 0.607, respectively. Finally, an OMF K1EL fit of the $\sigma'(\omega)$ part of the data, with electrode parameters fixed at their K1EL $M(\omega)$ -fit values, led to ϵ_0 , $\Delta\epsilon$, and ϵ_∞ estimates of about 175, 156, and 18.5, respectively. The last value is clearly an estimate of the CK1 $\epsilon_{C1\infty}$ quantity here. Further, the β_{10} estimate was 0.338, very close to the fixed value of 1/3 for the CK1EL fitting. The stark inconsistency between the OMF $M(\omega)$ and $\sigma'(\omega)\beta_{10}$ estimates, also observed in all other such published comparisons, is a clear indication of the failure of the OMF to take proper account of $\epsilon_{D\infty}$. Therefore, it is a particularly inappropriate fitting model and should not be used.

Although the present data involve CSD rather than DSD behavior, it is of interest to fit at the dielectric level with a DSD model, one that involves a ρ_0 parameter separate from the dispersion model. The asymmetric EDAE model, available in LEVM, is appropriate for this situation and involves the bulk parameters $\Delta\epsilon$, ϵ_∞ , τ_o , and γ_E , where γ_E falls in the range $0 \leq \gamma_E \leq 1$. CNLS fitting using the EDAEEL model with proportional weighting led to estimates of the aforementioned quantities of 131, 109, 9.11×10^{-6} s, and 0.473, respectively. The prediction for ϵ_0 is therefore 240 and the estimate for ρ_0 was 1.73×10^6 $\Omega\text{-cm}$.

The standard deviations of parameters common to both the CK1EL and EDAEEL fits were appreciably larger for the latter than for the former even though their overall S_F values were nearly the same.

Not only does the EDAEEL model involve two more free parameters than does the CK1EL one, but its separate treatment of ρ_0 is inappropriate for a CSD situation. The present results clearly indicate that for the LLT0.5 CSD data, and probably for most such data, the CK1 model with $\beta_1 = 1/3$ is the most appropriate bulk fitting and analysis model. Its BNN p value was found to be 1.65, as is that for the EDAE fit, and that for the K0 was about 1.33.

4.2.4 Utility and Importance of Poisson–Nernst–Planck (PNP) Fitting Models

4.2.4.1 Introduction

This work describes in detail some IS models for the fitting and analysis of conductive-system models involving diffusive mobile charges. Although all fitting models are necessarily approximate and Feynman rightly said, “Experiment is the sole judge of scientific truth,” one should also consider Bohr’s statement: “Science is not a means of obtaining absolute truth. The real test of a scientific theory is not whether it is ‘true’ but whether it works.”

Here we consider models that work in the sense that they well describe and interpret IS frequency-response data for a variety of conducting materials. But as Macdonald [2006] has rightly pointed out, one can divide such models into two classes: analog ones, usually instantiated as electrical equivalent circuits that are often only required to fit the data well, and physical ones that additionally account for the physicochemical processes present in the material, particularly those occurring at the interfaces between the electrodes and the material considered. To be useful, all models must satisfy the KK relations, but even then ambiguity is often present for the first class since more than one different circuit may be found to fit the data equally well. Even the physically relevant PNP model, although unique, involves some ambiguity in the interpretation of its physically relevant estimated parameters (see Macdonald [2012b, #256].)

Because many PNP publications cited here are by J. R. Macdonald and coauthors, and all are available from his website (<http://jrossmacdonald.com>), their citations here include their numbers in the full serial listing there. In addition, for brevity J. R. Macdonald citations will often just list a number such as the #256 earlier. Further, much of the following discussion is included in the comprehensive paper Macdonald [2013, #260].

The distinction between the two classes may become blurred when a model of interest includes not only some of the R, L, and C elements of ordinary circuit theory but also one or more distributed circuit elements (DCEs), such as a transmission line. They may then require an infinite number of such non-distributed elements to fully describe their response only with such elements. But useful DCEs, often the result of solution of physically relevant differential equations, may involve such functions as power laws and hyperbolic tangents and so are readily expressed in simple closed form.

Most useful IS models involve explicitly or implicitly a high-frequency-limiting real resistance and a real capacitance (or resistivity, ρ_∞ , and dielectric constant, ϵ_∞ , for data in specific form) as well one or more DCEs. Since these high-frequency-limiting bulk parameters are physically significant, the physical significance of any other parameters also present, such as DCEs, determines the class into which the resulting composite model falls. For simplicity, we shall often use just PNP to implicitly include both these limiting elements and the PNP DCE, one that is highly physically significant for appropriate IS data. Further, PNP will often be used as a general term that includes the anomalous-diffusion (PNPA) model.

The next section provides a short review of theoretical and experimental work involving the PNP approach, and the following one shows exact responses of progressively more complicated PNP models for all four IS immittance levels. Finally, it is worth emphasizing that the paper Macdonald [2013, #260] illustrates PNP response that involves adsorption and adsorption–reaction electrode processes and shows to what degree the various PNP-model responses can be well fitted by other more common but less physically germane continuum, discrete, and empirical models, thus considerably expanding the range of usefulness and applicability of the PNP models.

4.2.4.2 Selective History of PNP Work

The purpose of this section is to provide a history of the development of the small-signal PNP diffusion model for the analysis of IS data of nonbiological materials, especially emphasizing work where it has been used in analyzing experimental IS frequency-response data. This model is particularly important because when it is employed to analyze such immittance data, preferably using full CNLS fitting, as in the LEVMW computer program (available free at <http://jrossmacdonald.com>, Macdonald and Potter [1987, #179], Macdonald [2000a, #220]), it can lead to estimates of many more physically relevant electrical parameters than any other available IS model.

Here we shall consider small-signal sinusoidal immittance data in specific form and initially deal with the important one-mobile situation, where charges of only a single sign are mobile and thus may be free to be adsorbed or react at identical plane parallel electrodes separated by a distance L . In general, however, for the binary electrolyte situation generally considered in the PNP area, charge carriers of both signs may be mobile with a mobility ratio, $\Pi_m \equiv \mu_n/\mu_p$, of the mobilities of the negative to positive species of charge, and Π_m will not always be effectively infinite or zero. Another important parameter of the present PNP model is $M \equiv L/(2L_D)$, where L_D is the Debye length. In most experimental situations $M \gg 1$ and the $\tanh(M)$ diffusion-related function is then well approximated by unity. Further, for simplicity, we shall here consider a material containing neutral entities that may partly or fully dissociate into positive and negative, possibly mobile, charged species of equal concentration and unity valence numbers and may be either completely blocked at the electrodes or may be adsorbed and/or react at the electrodes.

Although the PNP diffusion model is a mean-field, conductive-system, effective medium continuum one that considers point charges inside a nondispersive dielectric medium, it may nevertheless well fit many situations involving real charges hopping in a diffusive manner between sites separated by random barriers, as demonstrated later. Further, it can lead to estimates of neutral-species concentration, N_0 , equal concentrations of mobile positive and negative charges, c_0 , mobilities and diffusion constants of mobile species, dissociation and recombination parameters, and three reaction and adsorption parameters for each of the two species of mobile charge. Of course, for most data not all of these many parameters will be found to be simultaneously relevant.

Although the Nernst–Planck and even Poisson equations have been used to describe and analyze electrochemical response for a century or more, they originally considered the possible presence of dc applied potentials (e.g., G. Jaffé [1952], S. Mafé *et al.* [1986]) and did not ensure that the Poisson equation applied correctly everywhere. This latter work did not, however, refer to the earlier PNP numerical analysis of Macdonald and Franceschetti [1978, #126], which included dc bias and proper satisfaction of the Poisson equation. Even the no-bias small-signal treatment of H. Chang and G. Jaffé [1952] did not require the Poisson equation to apply everywhere between the electrodes, and it was not until the publication of the Macdonald [1953, #11] small-signal PNP paper that it was properly required to do so. An extension of this work, including dc bias, was given by Franceschetti and Macdonald [1979a, #131]. Many no-bias small-signal extensions and generalizations of the #11 work have been published by these authors, especially Macdonald [1974a, #100] and Macdonald and Franceschetti [1978, #124]. A valuable summary of the applicability of PNP models for supported and unsupported electrochemical cells was later published by Franceschetti *et al.* [1991, #188].

A remarkable precursor of the PNP approach was the semi-infinite Warburg [1899] diffusion impedance, a CPE with a fractional exponent slope parameter, ψ_W , of 0.5, resulting in a slope of -0.5 in a log-log impedance-level plot. It was later generalized for a finite length and then involved a tanh response function involving the same value of ψ_W . In turn, an expression with ψ_W not restricted to a value of 0.5 was proposed by Macdonald [1985c, #169] but not explicitly identified as involving anomalous diffusion. Later J. Bisquert and A. Compte [2001] independently introduced such an anomalous-diffusion generalization, but it is important to emphasize that none of these diffusion expressions required the satisfaction of the Poisson equation between two electrodes separated by a finite length of the material of interest, and so none of them is a proper solution of the full PNP equations for such a situation. Proper PNP impedance expressions for complete blocking of mobile charges of both signs and blocking of charge of one sign and no blocking for the other are presented in Macdonald [1971b, #92] and are appreciably more complicated than just the finite-length Warburg expression.

Unfortunately, the PNP model was not often used to fit appropriate data in the period from 1953 to 2010, even though it was available from about 1992 onward as a fitting model in the LEVM computer program and its current windows version, LEVMW, Circuit H. However, Klein *et al.* [2006] used a simplified, $M \gg 1$, approximate version of the one-mobile, fully dissociated PNP model (of actual dielectric-level Debye form) to allow estimation of mobile ion concentrations and their mobilities for three different polymers over a range of temperature. These results are discussed in Macdonald [2010, #252], where also several one-mobile full PNP models were used to fit IS data for a hydrogel with LEVMW and theoretical PNPA and generation–recombination (GR) effects were demonstrated therein. The PNP-model parameter ψ_A is fixed at unity for the ordinary-diffusion PNP model, and for the anomalous-diffusion PNPA one, $0 < \psi_A < 1$. The ψ_A parameter was denoted ψ in #252–254 and is different from the ψ of #124, one that did not define a fractional exponent.

Three interesting possibilities that can lead to possibly well-separated low-frequency plateaus in plots of the real part of the resistivity versus frequency are electrode reactions at electrodes that are not fully blocking for one or both species of mobile charge, some GR values that effectively mobilize the immobile species of charge, and the presence of actual different mobilities of the two species. Results for the two last possibilities are illustrated in figure 4 of #252.

Also in the #252 work complex plane, exact normalized dielectric-level plots were compared with “ordinary” diffusion (finite-length Warburg diffusion but erroneously identified in the caption of figure 1 as infinite-length Warburg diffusion), Debye response, the interface part of PNP response, and the full PNP response. The Warburg and PNP interface responses are similar but differ appreciably at low frequencies, and the full PNP conductive-system response is almost indistinguishable from the Debye relaxation response, a matter discussed later here in more detail.

In Macdonald *et al.* [2011, #253], two generalizations of the PNP model to PNPA ones were compared, and the one discussed in #252 and instantiated in the LEVMW PNPA fitting model used in that work was shown to be superior by comparing composite model fits of IS data for a hydrogel, for the polymer LiTFSI, and for single-crystal $\text{CaCu}_3\text{Ti}_4\text{O}_{12}$ (CCTO), an electronic conductor. Various different suggested boundary conditions appropriate for incomplete blocking of mobile charges at the electrodes and incorporated in the PNP differential equations were next compared in Macdonald [2011, #254].

The original CJ boundary conditions used in the PNP model, the CJPNP one, do not take account of the Stern inner layer of double layers at the electrodes as does the Butler–Volmer (BV) model. Nevertheless, over the full frequency range for $M \gg 1$, a condition nearly always satisfied in fits of actual data, the CJ and BV conditions were found to be equivalent. Even when a Stern capacitance parameter was added in series with the CJPNP model, its value could not be estimated from CJPNP fits of experimental data.

Also in #254 the response of the CJPNP model was compared with a somewhat different model, the GPNP one, that accounts for partial or no blocking by the addition of a real dc conductance G or conductivity, $\sigma_p \equiv \sigma(0)$, in parallel with the PNP model. The GPNP model fits exact CJPNP data perfectly, but it leads to different estimates of the PNP parameters than the CJPNP ones. However, the σ_p value estimated from a GPNP fit may be used with the value of ρ_∞ to accurately estimate the value of the CJPNP dimensionless reaction rate parameter, denoted in earlier work by the symbol ρ_2 for one-mobile situations involving mobile negative charges. These matters are further discussed in 254, and the results of CJPNPA one-mobile fits of CCTO data at 80 and 140 K were compared there to investigate possible temperature dependence of the reaction rate.

The paper by Evangelista *et al.* [2011, #255] considered further PNPA extensions, including memory effects associated with fractional-time diffusion equation of distributed order, leading to suggestive results that, however, have not been used so far for analysis of actual experimental data. Contemporaneously, Evangelista *et al.* [2011] discussed one- and two-mobile, fully dissociated PNP situations in detail and presented expressions for the values of the two real-impedance plateaus that may appear in the two-mobile case, as well as expressions for the frequencies associated with these plateaus.

In Macdonald [2012b, #256], the Barbero work was further discussed, and epsilon-level, rho-level, and sigma-level immittance results for $\log_{10}(\Pi_m)$ mobility-ratio values of 0, 5, and 38 were presented. This paper also identified an ambiguity that can appear in the interpretation of the results of all model fitting of IS data, as well as several other ambiguities specific to PNP models because of their ability to

estimate more physically significant parameters than others. One of the latter arises because one-mobile situations and equal-mobility $\log_{10}(\Pi_m) = 0$ two-mobile ones lead to the same response shapes but with a few parameter values different by small factors, so their fit results cannot be distinguished without external knowledge. Examples of this ambiguity are presented for the $\log_{10}(\Pi_m)$ values of 0 and 38 for the real-epsilon and the real-rho responses of figures 1a and 3a of Macdonald [2012b].

It is worth mentioning that in actuality there are no physical one-mobile PNP situations because potential wells and barriers that restrict the free motion of the less mobile of the two charge species present are never infinite, and eventually some of these charges become free to diffuse/hop. But the fixed $\log_{10}(\Pi_m) = 38$ choice used here is a good proxy for actual one-mobile behavior because the effects of the resulting small but nonzero mobility of the less mobile species appear at such low frequencies and long times that they fall very far outside the practical range of measurement.

de Paula *et al.* [2012] recently presented a theoretical PNP treatment of adsorption, generation, and recombination of ions. The adsorption part of the analysis was based on a Langmuir approximation and was said to involve a set of equations different from those appearing in #124 and earlier work that involved complex electrode rate constants that generalized the original CJ boundary conditions to account for the simultaneous presence of either or both faradaic reactions and specific adsorption. These general small-signal boundary conditions are designated here as ECJ ones, and some of their consequences are presented later in the present work. The authors of the de Paula paper concluded with the hope that their results would be useful because they showed general response results for "a set of fundamental equations characterizing a continuum diffusional model."

Although the de Paula adsorption boundary equations were overtly different from those in #124, Eq. (38), which also included both reaction and specific adsorption effects, they have been shown, as discussed later, to lead to identical adsorption results. Because the #124 ECJ boundary conditions agree with the basic BV ones and, for adsorption, have been shown to encompass Langmuir behavior as well (#113, #122, #126, and #134), possible agreement or disagreement between theoretical ECJ analysis and its adsorption predictions and the adsorption analysis and results of the de Paula work seemed worth pursuing. Therefore, the exact numerical results calculated from the latter approach and presented in its graphs were sent by the corresponding author of that work, Professor L. R. Evangelista, to the present author. They were all then fitted to the PNP model using the LEVMW program with proportional weighting, and "exact" agreement to about thirteen decimal places resulted. Thus, all of the de Paula results are fully consistent with those predicted by the earlier theory, but the work does usefully show some response behaviors not previously depicted.

The GR part of the de Paula *et al.* [2012] analysis is consonant with that in papers #11 and #124, but it did not refer to the detailed PNP GR results of #252. Those GR results in the de Paula work that did not include adsorption, for example, the data for the red lines in figures 1 and 2, were also fitted exactly using the $\log_{10}(\Pi_m) = 38$ one-mobile PNP model. But an additional fit of the same data with the mobility ratio free to vary led to a two-mobile estimate of $\Pi_m \approx 742 \pm 12$, with a small value of the relative standard deviation of the fit residuals, S_F , of about 0.002. In addition, the GR parameter values and that of N_0 were quite different from the one-mobile fit ones.

Although this two-mobile fit was not exact, it was sufficiently good that, had it and the one-mobile one been used with experimental data containing some random errors (real-life situations where S_F is usually no smaller than 0.01), it would have been impossible to choose between the two fits without additional knowledge of the material involved. As one might expect, PNP-model fitting evidently does not allow one to necessarily discriminate between effective motion of an otherwise immobile charged species associated with GR or actual mobility of that species. In fact, for the present two-mobile fit situation, both mechanisms contribute to the response since a second plateau still appears when the two-mobile GR parameter values are used even with the one-mobile Π_m condition.

Diffusion-related studies published by others before 2010 did not usually require satisfaction of the Poisson equation, evidently because of unawareness of the earlier PNP work in the field. In addition, these theoretical results were generally not compared with experiment and were not full PNP treatments. But the three papers, namely, Santoro *et al.* [2011], Lenzi *et al.* [2011], and Ciuchi *et al.* [2012], dealt with some aspects of anomalous adsorption and do satisfy the Poisson requirement. The first of these did not include experimental-data fitting, introduced an undefined parameter N , and assumed *equal*

values of the diffusion coefficients of positive and negative ions, unlikely in practice except as a proxy for one-mobile behavior, as discussed in #256.

The Santoro work provided some plots of the real and imaginary parts of the impedance calculated from a fractional anomalous-diffusion equation but does not mention its limitations, as discussed in #253 and above. The parameter N is evidently the present N_0 with the unstated assumption of full dissociation, so it also denotes the equal concentrations of the mobile ions. The same impedance equation was used in the Ciuchi paper to fit some data for liquid-crystalline electrochemical cells. Its fit results are significantly different, however, from those for the smectic liquid crystal material included in table 1 of the slightly earlier #256 publication. Finally, the second paper usefully cites many references to ordinary or anomalous diffusion in many different materials and uses a PNPA model to analyze IS data for deionized water with electrode boundary condition stated to encompass adsorption and reaction. It did, not, however, cite the earlier results of #124 that also do so. It too seems to assume complete dissociation of the unidentified mobile ions (of equal assumed mobility) present in the water, and it led to estimated values of both N and diffusion coefficients for two different electrode materials.

All three of the aforementioned publications and most earlier theoretical, diffusion-related ones present plots of the real and imaginary parts of the impedance and do not usually show corresponding results for the admittance and dielectric levels. This is unfortunate since real-part impedance plots may involve two, or possibly even three, low-frequency plateaus. But it is only at the admittance or conductivity level that one may unambiguously identify an approach to dc response if mobile charges are present, adsorb, and/or react at the electrodes and if the data extend to sufficiently low frequencies. Even dispersive pure dielectric materials inherently involve a low-frequency real-part impedance plateau [#239].

Therefore, although many of the second real-part plateaus that appear for experimental data at frequencies lower than the ordinary bulk one may be associated with power-law anomalous-diffusion effects, the approach to an actual final low-frequency plateau value requires the additional presence of unequal mobilities, or GR effects, and/or adsorption or reaction processes. Full ECJPNPA fits with free GR parameters and with a possibly free mobility-ratio parameter are generally needed in general to identify and distinguish between the two or three real-impedance plateau processes that may appear in principle. Unfortunately, none of the 2011–2012 papers mentioned earlier carried out such full fits, and so they did not lead to unambiguous identifications of the processes leading to their experimental results. A virtue of dealing as herein with experimental data transformed to specific form rather than with raw data is that it is then simple to show specific results for all four immittance levels that usually allow separate identification of bulk and interface (sometimes called electrode) effects. The results of the next sections further clarify these matters.

4.2.4.3 Exact PNP Responses at All Four Immittance Levels

In paper #256 two separate types of PNP response are defined: type A is that with small dissociation, so $c_0 \ll N_0$, while these concentrations are equal for type B. Although type A response is common for solids, type B may be found for mobile impurity ions in a dielectric material. In this section, we progressively show how exact type A one-mobile PNP responses at all four immittance levels change as more and more physical processes and parameters are added to the model. Thus, we compare by pairs PNP and PNPA, PNPA and CJPNA, and CJPNA and DCDCJPNA. Here the DCDCJPNA model is that of a dielectric-level Davidson–Cole one in parallel with the CJPNA.

The Circuit H PNP model available in LEVMW and used to calculate the present results includes the following possibly free parameters for data: N_0 , Π_m , $k_{gr}\xi$, R_1 , C_1 , ρ_{20} , and ψ_A . For the full CJPNA model, several other possibly free reaction and adsorption parameters are also available. Here, the k_{gr} and ξ parameters are GR related, with $k_{gr} \equiv k_g/k_r$ and $\xi \equiv \tau_{GR}/\tau_D$, where k_g and k_r are the generation and recombination parameters of papers 124 and #252. Further, τ_{GR} and τ_D are the recombination reaction time and the Debye relaxation time, respectively, and ρ_{20} is the dimensionless reaction rate for the mobile negative charge species, named ρ_2 in published work.

For the present results, all in specific form, $R_1 = \rho_\infty$, $C_1 = \epsilon_V \epsilon_\infty$, and $\tau_D = R_1 C_1$, where ϵ_V is the permittivity of vacuum, 8.8542×10^{-14} F/cm. Other parameters held fixed are T , the absolute temperature, L , A , and Π_Z , where A is the area of an electrode and Π_Z , here unity, is the ratio of the valence numbers of the negative to positive charges, both of concentration c_0 . From the values of the fixed and estimated parameters of a fit, LEVMW also calculates values of the indirect quantities defined earlier, as well as ϵ_∞ , M , and mobilities and diffusion coefficients, and the Debye length. Note that, for example, in the present one-mobile case with negative charges mobile, $\sigma_\infty \equiv (1/\rho_\infty) \equiv (e\mu_n c_0)(1 + \Pi_m^{-1})$. Although the full frequency-response expression for the CJPNPA model instantiated in LEVMW is too long to list here, the one-mobile CJPNP response formula appears in Eq. (7) of 254 for small dissociation conditions. In the zero-frequency limit, it leads to $\rho'(0)/\rho_\infty = 1 + (\rho_{20})^{-1}$.

To obtain DCDCJPNPA composite model parameters of experimental relevance, I combined and modified unpublished fit results for a smectic liquid crystal that showed both dielectric dispersion, represented by the DCD part of the model, and mobile charge associated with small dissociation of a neutral center, somewhat similar to that found from PNPA fits of CCTO material in publications #253, #254, and #256. Some values found for the latter were modified to yield much smaller diffusion coefficients than those for CCTO in order to represent the motion of mobile ions rather than that of electrons. Fixed values of $T = 305.6$ K and $L = 0.01$ cm were used, as well as $\Pi_m = 10^{38}$. Other PNP and CJPNPA direct-parameter rounded values were $N_0 = 4.305 \times 10^{21}$ cm $^{-3}$, $k_{gr} = 4.305 \times 10^5$ cm $^{-3}$, $\xi = 10^{35}$, $R_1 = 5.925 \times 10^7$ Ω·cm, $C_1 = 2.877 \times 10^{-13}$ F/cm, $\rho_{20} = 0.01$, and $\psi_A = 1$ or 0.9. Relevant rounded calculated values were $c_0 = 4.305 \times 10^{13}$ cm $^{-3}$, $\epsilon_\infty = 3.25$, $M = 151$, $k_g = 5.87 \times 10^{-39}$ s $^{-1}$, $k_r = 1.36 \times 10^{-44}$ cm 3 /s, $\tau_D = 1.70 \times 10^{-5}$ s, $\tau_{GR} = 1.70 \times 10^{30}$ s, and $L_D = 2.34 \times 10^{-5}$ cm. Here $M = M_1$ is the one-mobile value and k_2 . For the DCD model the parameter values were $\Delta\epsilon_D \equiv \epsilon_0 - \epsilon_\infty = 11.09$, $\tau_{DCD} = 4.03 \times 10^{-8}$ s, and $\gamma_{DCD} = 0.963$. The very large value of τ_{GR} used here ensures that type A behavior remains relevant even at the lowest applied frequencies.

The low-frequency-limiting PNP plateau value of $\epsilon_0 = \epsilon'(0)$ is $\epsilon_\infty M_1 = 490.2$, and so $\Delta\epsilon_D = (M_1 - 1)\epsilon_\infty$. Therefore, $\rho_\infty = (\tau_D/\epsilon_V \epsilon_\infty) = (M_1 \tau_D / \epsilon_V \epsilon_0)$, the value of the low-frequency ρ' plateau. The often-used empirical BNN equation, involving a parameter p with a value often near unity, has been discussed for several different conductive-system fitting models in #251. It may be written as $\sigma_0 = p \epsilon_V \Delta\epsilon \omega_p$, where $\omega_p = 2\pi\nu_p$ is the angular frequency of the peak of the $|\epsilon''(\omega)|$ loss curve. Although the PNP model without electrode reactions involves complete blocking and so its σ_0 is zero, to obtain an effective estimate of p for the PNP model, let us replace σ_0 in the BNN relation by $1/\rho_\infty$, write the result as an equation for ρ_∞ , and set it equal to the aforementioned PNP expression for ρ_∞ . Then solving for p yields $p = (\epsilon_0/\Delta\epsilon)/(M_1 \tau_D \omega_p)$. Finally, define $\omega_{PNP} \equiv 2\pi\nu_{PNP} \equiv 1/M_1 \tau_D$; then it follows that $p = \{M_1/(M_1 - 1)\}(\nu_{PNP}/\nu_p)$. For the present PNP data, the first quotient is 1.00662 and the second is $(61.8926/62.0995) = 0.99667$. Thus the effective BNN value for the PNP model is here about 1.003, indistinguishable from unity in experimental situations.

Figures 4.2.7 and 4.2.8 show how PNP responses change to PNPA ones at all four immittance levels when the value of ψ_A is reduced from 1 to 0.9. We see that the major changes occur in the low-frequency responses of ρ' and σ' with the appearance of CPE-like behavior. This behavior, *per se*, is actually unrealistic since it continues unabated with no approach to plateaus in the low-frequency limit. In actuality, however, any of four different processes mentioned in the last section lead to such plateaus, and for real data one or more of them is always present even when their effects occur at frequencies below the range of measurement.

Figures 4.2.9 and 4.2.10, demonstrating the change from PNPA responses to CJPNPA ones, illustrate the appearance of such plateaus as PNPA complete blocking of mobile charges at the electrodes changes to partial blocking involving CJ boundary conditions. Note, however, that no approach to a plateau in ϵ' is evident. It is particularly important that of the four processes mentioned earlier, it is only the presence of partial or no blocking of charges at the electrode interface that leads to a final low-frequency-limiting dc plateau in σ' . For both PNP and PNPA, $\sigma_\infty = 1/\rho_\infty$.

Figures 4.2.11 and 4.2.12 demonstrate the change from CJPNPA responses to DCDCJPNPA ones. The dielectric-level Davidson–Cole model, the DCD, has been found useful for fitting the IS data for

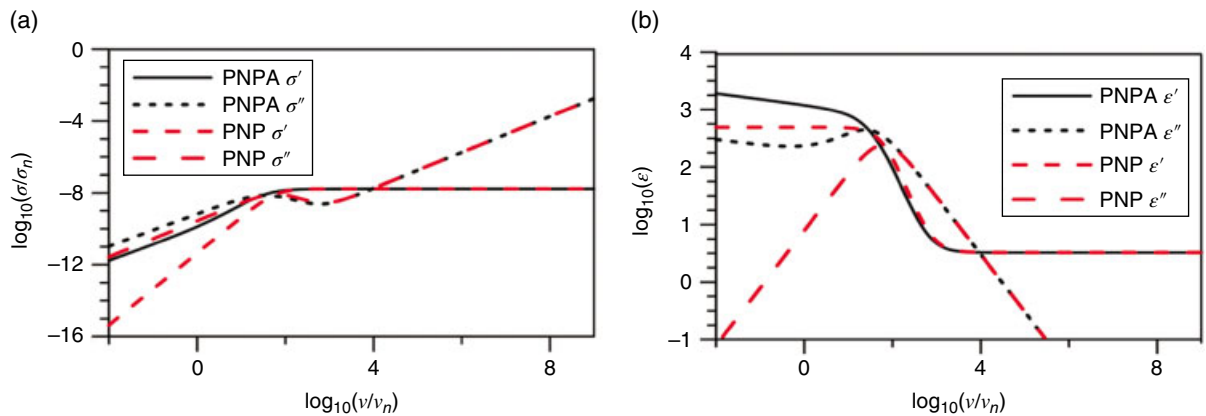


FIGURE 4.2.7 Comparison of log–log PNP and PNPA responses at the (a) σ and (b) ϵ immittance levels. Here and elsewhere $\sigma_n = 1 \text{ S/cm}$ and $v_n = 1 \text{ Hz}$.

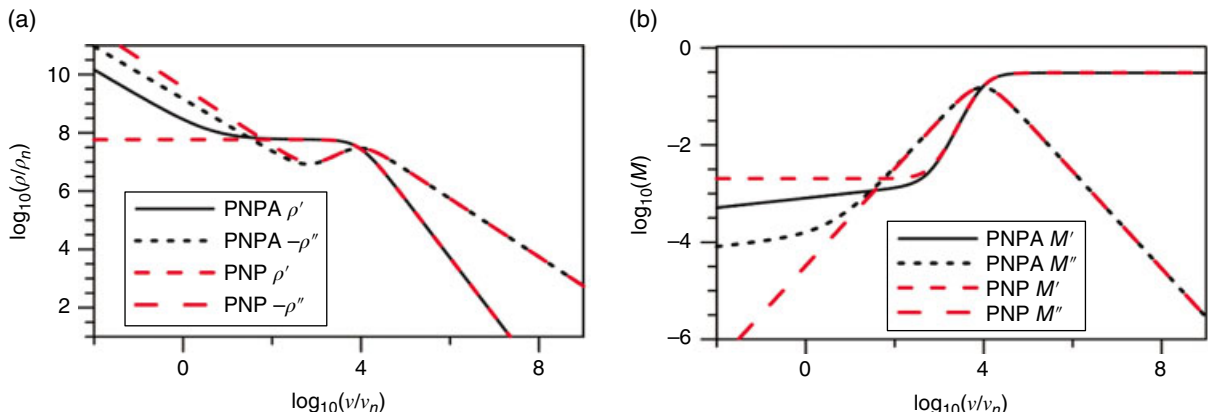


FIGURE 4.2.8 Comparison of log–log PNP and PNPA responses at the (a) ρ and (b) M immittance levels. Here and elsewhere $\rho_n = 1 \Omega\text{-cm}$.

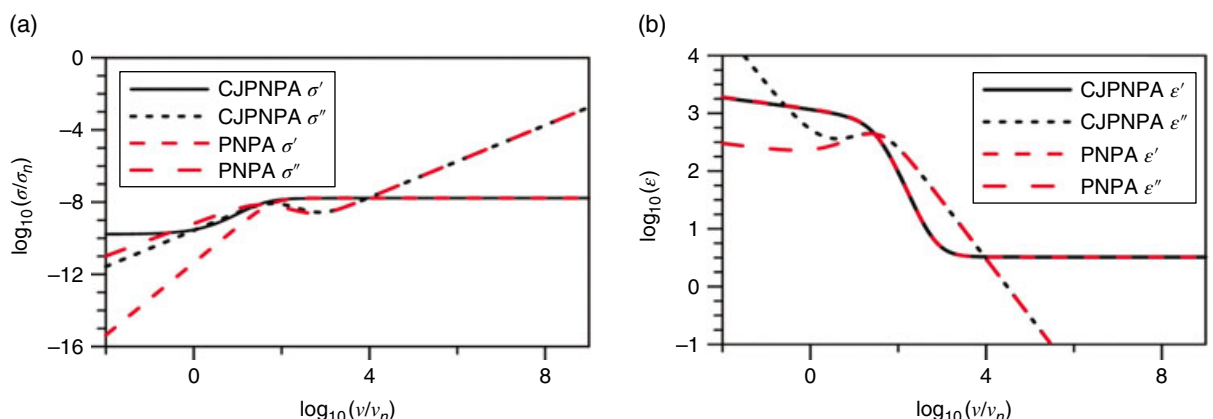


FIGURE 4.2.9 Comparison of log–log PNPA and CJPNPA responses at the (a) σ and (b) ϵ immittance levels.

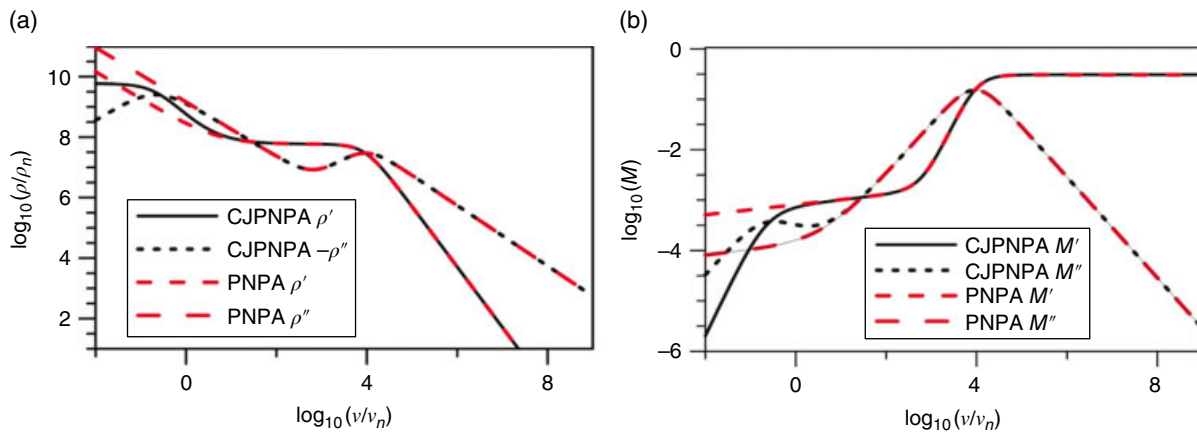


FIGURE 4.2.10 Comparison of log-log PNPA and CJPNA responses at the (a) ρ and (b) M immittance levels.

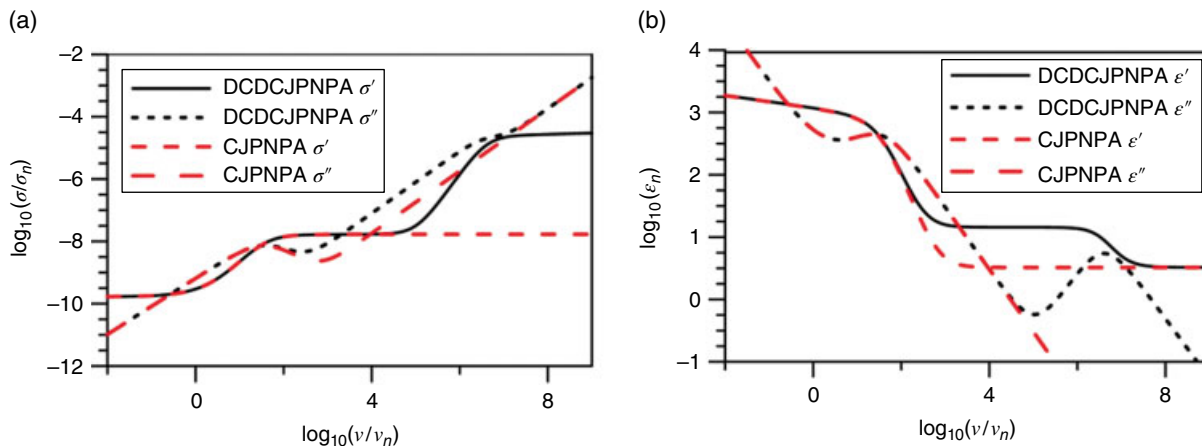


FIGURE 4.2.11 Comparison of log-log CJPNA and DCDCJPNA responses at the (a) σ and (b) ϵ immittance levels.

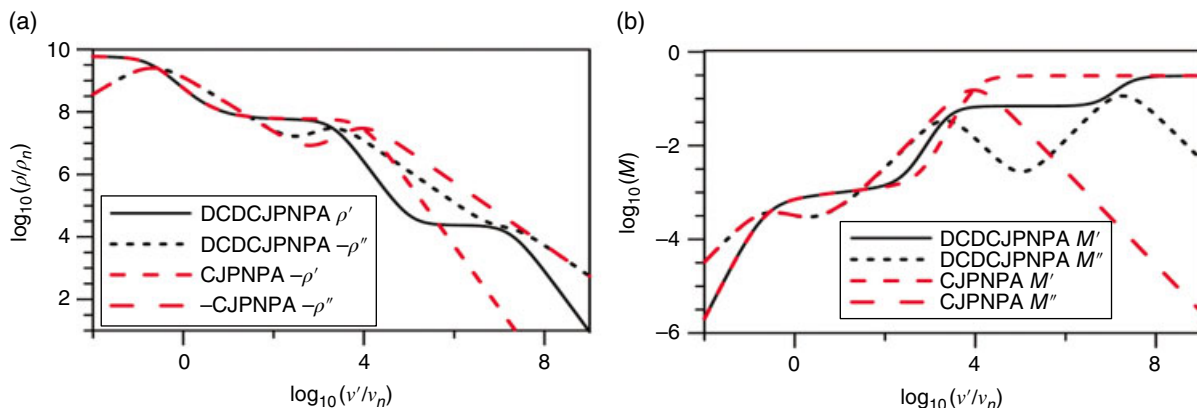


FIGURE 4.2.12 Comparison of log-log CJPNA and DCDCJPNA responses at the (a) ρ and (b) M immittance levels.

a variety of materials, but it is often more appropriate for the higher-frequency parts of the response and another model needs to be used to represent electrode effects. Here we use the CJPNA model to account for such interfacial effects. It is interesting, however, that in the absence of anomalous diffusion, the ε_0 values for the PNP, CJPNP, and DCDCJPNP models are about 490.2, 480.6, and 491.7, respectively, with the difference between the last two values being just that of $\Delta\varepsilon_D$. The inclusion of the DCD as part of the full composite model produces further important changes above 10^4 Hz as shown in Figures 4.2.11 and 4.2.12.

4.3 SOLID-STATE DEVICES

William B. Johnson,¹ Wayne L. Worrell,² Gunnar A. Niklasson,³
Sara Malmgren,⁴ Maria Strømme,⁵ and S. K. Sundaram⁶

¹W. L. Gore & Associates, Elkton, MD, USA

²Department of Materials Science and Engineering, University of Pennsylvania, Philadelphia, PA, USA

³Department of Engineering Sciences, The Ångstrom Laboratory, Uppsala University, Uppsala, Sweden

⁴Swedish Energy Agency, Eskilstuna, Sweden

⁵Nanotechnology and Functional Materials Division, The Ångström Laboratory, Uppsala University, Uppsala, Sweden

⁶Kazuo Inamori School of Engineering, New York State College of Ceramics, Alfred University, Alfred, NY, USA

In this section examples of several different applications of IS will be presented. Four different devices have been chosen: solid electrolyte chemical sensors (SECSs), secondary (rechargeable) batteries, photoelectrochemical devices, and semiconductor–insulator–electrolyte sensors. In each subsection one selected application of IS will be briefly summarized to indicate the utility of this technique in determining the parameters important to that device. These sections are not intended to provide an extensive review of the area, but rather to show the power of the technique to solid-state researchers. Thus this section is not a description of every device to which IS has been applied. Devices not discussed here that have been studied using IS include, among others, ion-selective membranes (Sandifer and Buck [1974], Buck [1980, 1982]) and high-temperature steam electrolyzers (Schouler *et al.* [1981]).

Before beginning a detailed discussion, it will be helpful to indicate the advantages and limitations that IS has in general application. Particularly desirable features of IS inherent to each specific applications will be discussed in the following subsections. The most important advantage is the ability to determine all of the time constants associated with a given interface in one experiment. That means that it is possible to determine diffusive, electrochemical, and chemical rate constants for a process from a single impedance spectrum. Further, the impedance is measured with a small ac signal, and a dc bias voltage can be superimposed with the ac signal so that the impedance and the rate information can be determined under various conditions. Such potential control is particularly important for electrochemical systems because the applied potential influences the rate of electron transfer at the interface. By measuring the impedance in such systems as a function of applied potential (i.e., dc bias), it is possible to determine the importance of the electrochemical reaction step to the overall rate of the reaction.

Although the equipment necessary to measure impedance spectra is readily available from many different suppliers, it remains expensive (\$15 000–20 000 in 1985) even before the purchase of the nearly mandatory computer required for control and data analysis. Another disadvantage of IS is that very careful cell design is required to minimize stray capacitances and inductances. In addition to requiring three-electrode cell arrangements, as with all electrochemical systems, lead effects, including length, shielding, and the nature of all electrical contacts leading to and from the sample, must be considered.

Ideally, the impedance of the cell should be measured under the actual experimental conditions but in the absence of the sample. These results can be used to verify or correct the experimental results. However, it is usually sufficient to minimize the stray impedances so that their values are negligible in comparison with the sample impedances.

A final drawback of the technique is the cumbersome data analysis that is required to obtain the desired physical quantities from the impedance spectra. A model electrical circuit that approximates the physical process being examined must be formulated. The model parameters are then obtained by determining parameter values that give the best fit to the impedance data. Finally, the model must be correlated with the physical system to establish the reliability of the model and to establish that the model values determined from the fit are physically reasonable. If not, the model may have to be modified and the entire analysis process repeated. In Chapter 3 there is a detailed discussion of this entire procedure. Clearly the required analysis is not always straightforward and is usually quite involved.

4.3.1 Electrolyte–Insulator–Semiconductor (EIS) Sensors

Electrolyte–insulator–semiconductor (EIS) sensors are one of a larger class of chemically sensitive electronic devices (Zemel in Janata and Huber [1985]) that meld integrated circuit technology with traditional chemical sensor technology. The EIS device is composed of a doped semiconductor, normally Si, acting as a substrate for a thin insulating layer, normally an oxide or nitride, which can be immersed in an electrolyte containing a fixed concentration of an ionic species to be measured. General reviews of the construction (Huber in Janata and Huber [1985]), thermodynamics (Janata in Janata and Huber [1985]), and operation (Abe *et al.* [1979], Lauks and Zemel [1979], Bergveld and De Rooij [1981]) of such devices are available. Only a brief overview of the area will be given here so that those unfamiliar with these devices will be able to appreciate the application of IS described in the following text.

A schematic of a typical EIS sensor is shown in Figure 4.3.1a. The operation of the sensor can easily be understood by considering the solid-state analog of it, the metal–oxide–semiconductor (MOS) capacitor shown in Figure 4.3.1b. In the MOS device the capacitance is controlled by applying an external voltage between the gate and substrate. When there is a negative voltage relative to a p-type substrate, the capacitance will be large because the holes in the substrate will be attracted to the insulator–semiconductor interface, giving rise to a wider region of dielectric material through which charge is separated. If the gate voltage is increased toward zero, the space-charge layer in the capacitor will become narrower so the capacitance will decrease. As the voltage goes positive, the space-charge layer in the semiconductor becomes narrower until it eventually disappears, and electrons build up at the surface of the semiconductor, forming what is normally called an *inversion layer*. This process is shown schematically in Figure 4.3.1c. For an n-type substrate, the capacitance curve is inverted (Figure 4.3.1d), as when $V_G < 0$, an inversion layer forms (holes at surface of n-type Si) and when $V_G > 0$, there is a wider space-charge layer.

The EIS functions in exactly the same fashion except the gate is formed by an RE in solution rather than a metal contact. The ability of the EIS to respond to ions in solution results from a modification of the electric charge distribution at the insulator–liquid and/or the insulator–semiconductor interface. Thus, at a given value of the reference potential, the capacitance of the device will change depending on the ionic concentration in the solution. For example, for the simple device shown in Figure 4.3.1a, it has been shown that the capacitance will respond to a change in pH in the solution (Bergveld [1970], Siu and Cobbald [1979], Bousse [1982], Leroy *et al.* [1982], Bousse and Bergveld [1983], among others).

One real advantage of these sensors lies in the fact that an ion-selective membrane can act as a gate directly on a field effect transistor (FET) (Janata and Huber [1985]). These ion-selective field effect transistors (ISFET, shown schematically in Figure 4.3.2a) again are the analog of a solid-state device, the metal–oxide–semiconductor field effect transistor (MOSFET) (Figure 2.2.2b).

A MOSFET operates by controlling the concentration of charge carriers in p-type substrate between two n-type regions, called the source and the drain. When the gate is negatively biased with

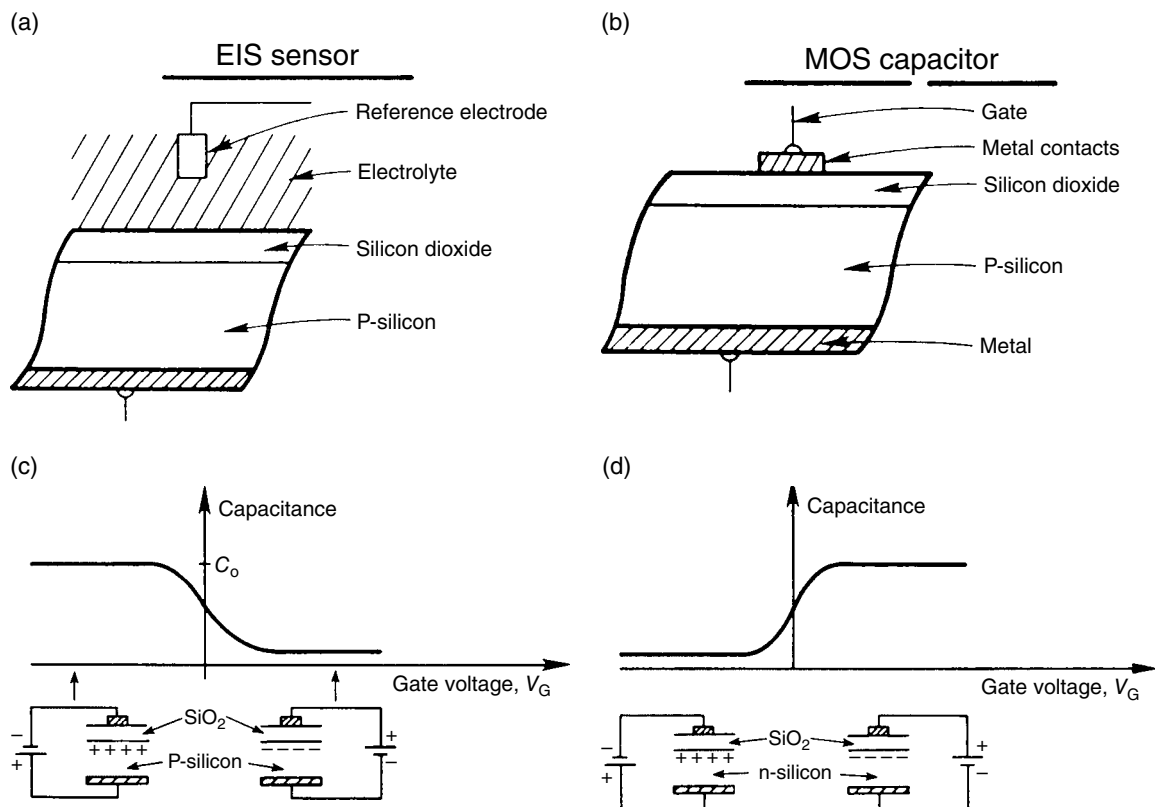


FIGURE 4.3.1 A schematic of a typical (a) EIS sensor and (b) an analogous MOS capacitor. (c) The capacitance of a MOS capacitor as a function of gate voltage for a p-type substrate and (d) the equivalent response for an n-type substrate.

respect to the substrate, the region between the two n-type regions below the gate has no free electrons and the conductivity between the source and drain is very low. But as the voltage is increased until it becomes positive, at some point an inversion layer will form, so there will be electrons available to form a channel. The conductivity between the source and drain will then increase. If there is a drain voltage supplied in this case, then a drain current can exist. At a given gate voltage, as the drain voltage is increased, the drain current will saturate because the inversion layer is no longer of uniform thickness and becomes pinched off at the drain end. The transfer curve shown in Figure 4.3.2c results. As before, the ISFET operates in the same fashion except that an ion-selective membrane and RE operate as a gate.

Although the impedance characteristics of the MOS devices are reasonably well understood (Nicollian and Goetzberger [1967], Nicollian and Brew [1982]), IS has not been applied nearly as widely to the EIS or ISFET devices. In this section the IS results of one of the simplest EIS devices, the Si– SiO_2 –electrolyte pH sensor (Barabash and Cobbold [1982], Bousse and Bergveld [1983], Diot *et al.* [1985]), will be used to illustrate the relative advantages of the technique.

An equivalent circuit for an EIS device has been derived (Bousse and Bergveld [1983], adapted by Diot *et al.* [1985]). From left to right in Figure 4.3.3a, it consists of the RE impedance Z_{ref} ; the electrolyte solution resistance R_s ; the electrolyte–insulator interface impedance, which is composed of the double-layer capacitance C_{dl} ; a diffusion impedance associated with the ionic species in solution (hydrogen ions for pH sensor), Z_w ; and the SiO_2 –electrolyte interface capacitance C_a ; the insulator capacitance C_i ; and the semiconductor–insulator interface impedance, which is composed of the space-charge capacitance in the semiconductor, C_{sc} , as well as a capacitance and resistance, C_{it} and R_{it} , respectively, associated with the interface states at this interface. At high frequency the electrolyte–insulator impedance is small

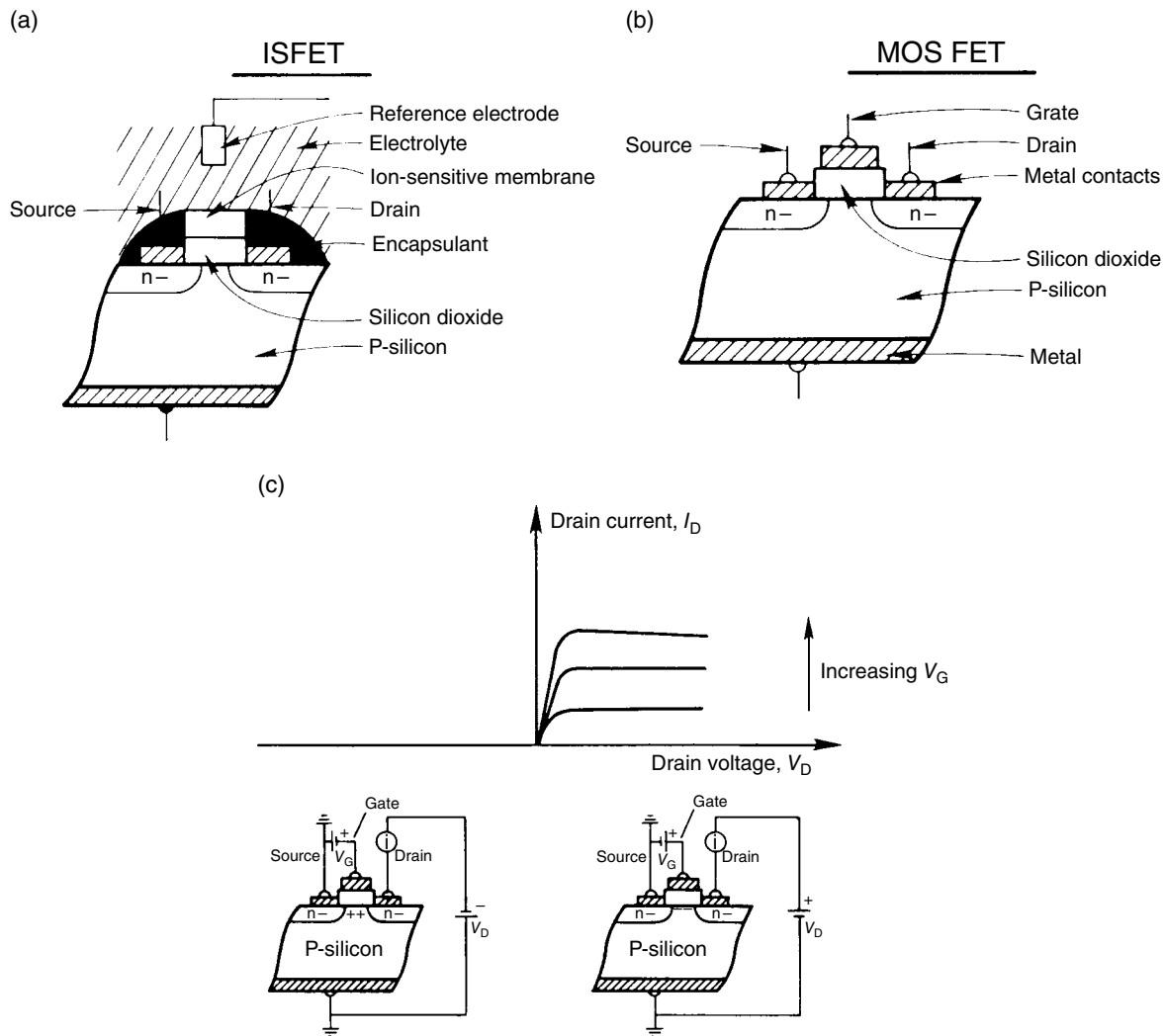


FIGURE 4.3.2 A schematic of a typical (a) ISFET device and (b) the analogous MOSFET device. (c) The current in the drain circuit as a function of the drain voltage at various different gate voltages. When the gate voltage is negative (left portion of figure), the $n-p-n$ junction will not conduct and there will be negligible drain current.

with respect to C_i , as is the impedance of the RE, so the equivalent circuit reduces to that shown in Figure 4.3.3b, where C_p represents the combined response of the C_{sc} and C_{it} .

In the EIS structure the value of C_p depends upon the biasing of the device as described in Figure 4.3.1. In forward bias, C_p will be large with respect to C_i because an accumulation layer exists in the semiconductor (Figure 4.3.1d, $V_G < 0$). In this case, the measured capacitance at high frequency, which is a series combination of C_{sc} and C_i , reduces to $C_i(1/C_i + 1/C_{sc} \cong 1/C_i)$, which is independent of applied potential. By evaluating the relative voltage in the space-charge layer and the oxide (Diot *et al.* [1985], Sze [1985]), it can be shown that

$$E - E_{fb} = eN_D \epsilon_0 \epsilon_i \left[\left(\frac{C_i}{C} \right)^2 - 1 \right] / 2C_i^2 \quad (1)$$

where E is the applied potential, E_{fb} is the flat-band potential, e is the charge on an electron, N_D is the doping level, ϵ_0 and ϵ_i are the vacuum permittivity and relative dielectric constant, respectively, C_i is the

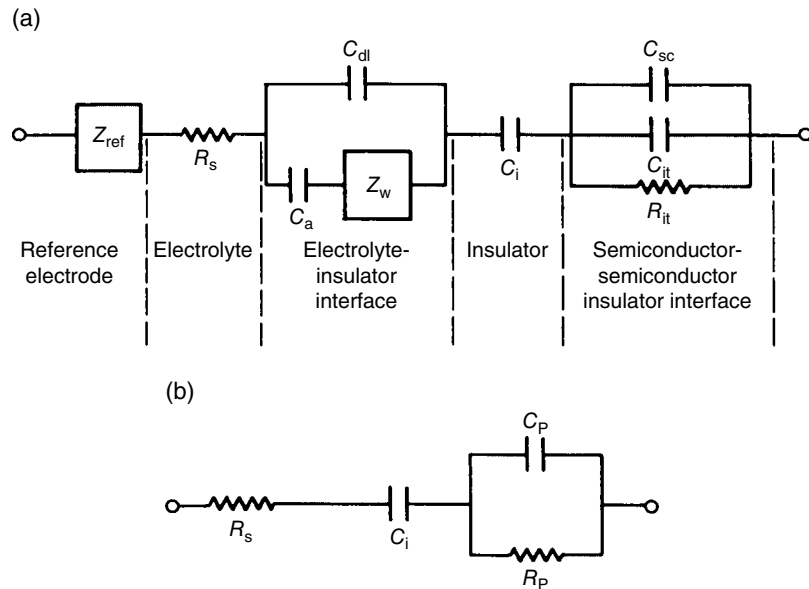


FIGURE 4.3.3 (a) The equivalent circuit of EIS sensor shown in Figure 4.3.1a (after Bousse and Bergveld [1983]). (b) The reduced equivalent circuit for an MIS where the reference electrode–electrolyte interface impedances are small. Here R_p and C_p are the equivalent R and C elements associated with the combined impedance of the semiconductor and semiconductor–insulator interface. Source: Diot 1985. Reproduced with permission of Elsevier.

insulator layer capacitance, and C is the total measured capacitance. The value of C varies with applied potential because the semiconductor capacitance, C_{sc} , depends on E through the surface voltage ψ_s (see following text). Thus, the values of N_D and E_{fb} can be determined from the slope and intercept, respectively, of the linear portion of a plot of E versus $(C_i/C)^2 - 1$. An example of such a result is shown in Figure 4.3.4.

Additional information about the semiconductor can be obtained from the interface capacitance C_{it} , which arises because each interface state stores a charge. A surface potential C_{it} can be defined as the potential at the semiconductor–insulator interface that causes the center of the band gap of the semiconductor [the Fermi level of the intrinsic material, $(E_f)_i$] to shift to a new value (Figure 4.3.5). This surface potential arises whenever the applied potential causes charge to build up at the interface. For example, for an n-type material, when $E = E_f - (E_f)_{\text{ref}}$ is very much less than zero, $(E_f)_i$ will cross E_f as shown in Figure 4.3.5, leading to an accumulation of holes at the interface, that is, inversion as described earlier for the MOS devices. Now ψ_s can be calculated from the capacitance data described earlier by means of (Nicollian and Goetzberger [1967])

$$\psi_s = \int_{E_{\text{fb}}}^E (1 - CC_i^{-1}) dE \quad (2)$$

Thus, the important electrical characteristics of the semiconductor can be determined.

Further information about the interface states can also be extracted from the impedance data. From measured values of the total conductance G and capacitance C , the interface conductance can be calculated at any given potential after correcting for the solution resistance according to (Diot *et al.* [1985])

$$\frac{G_p}{\omega} = \frac{C_i^2 G}{\omega [(G/\omega)^2 + (C_i - C)^2]} \quad (3)$$

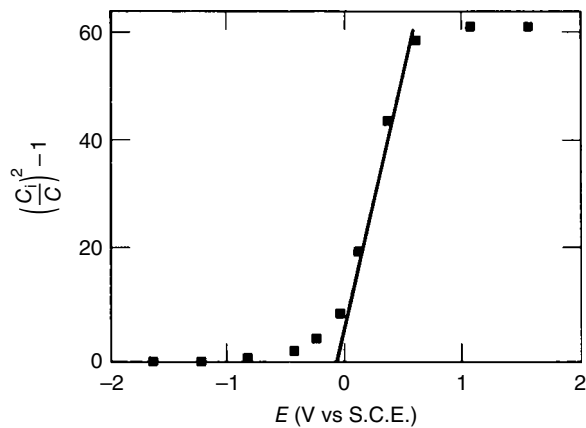


FIGURE 4.3.4 A plot of $(C_i/C)^2 - 1$ for n-type Si/SO₂ EIS, where C_i is the insulator capacitance derived from high-frequency data and C is the total capacitance of the system. The oxide thickness is 94 nm and pH = 2.5. The values of the doping density N_d and the flat-band potential E_{fb} calculated from the linear portion of the curve are $2.2 \times 10^{20} \text{ m}^{-3}$ and -0.06 V, respectively
Source: Diot 1985. Reproduced with permission of Elsevier.

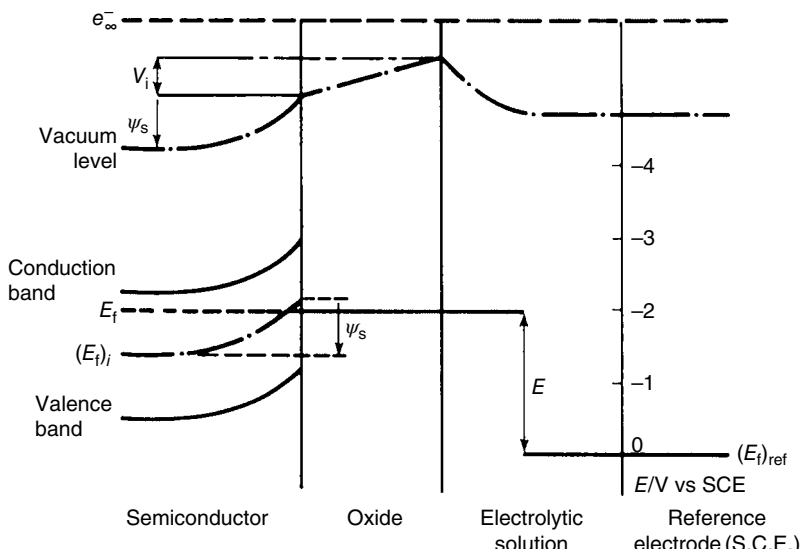


FIGURE 4.3.5 A simplified energy band diagram of an n-type EIS device that has an applied voltage E such that the semiconductor oxide interface is in the inversion regime [shown by crossing of E_f and $(E_f)_i$], leading to a buildup of holes at the interface. Two energy scales are shown—one referenced to an electron at infinity (e^-_∞) and the other referenced to the saturated calomel electrode (SCE). The surface potential ψ_s , the voltage drop across the insulator, V_i , and the Fermi levels of the reference electrode, the semiconductor under an applied voltage E , and the intrinsic semiconductor [$(E_f)_{ref}$, E_f , and $(E_f)_i$ respectively] are all shown.
Source: Diot 1985. Reproduced with permission of Elsevier.

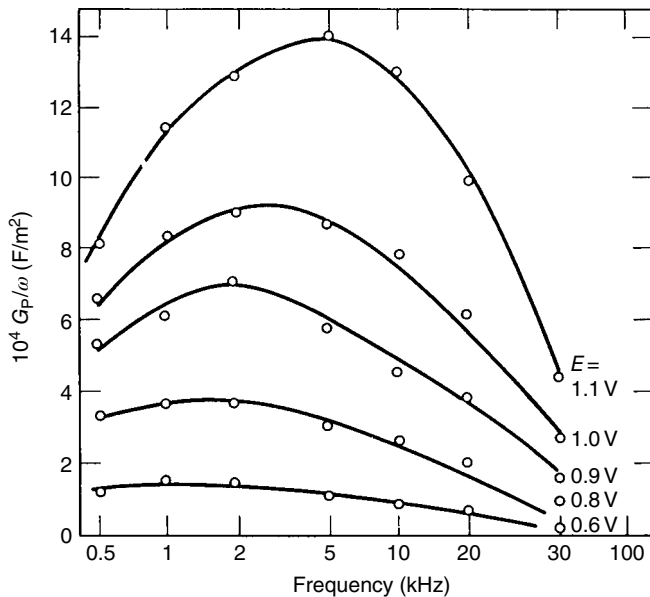


FIGURE 4.3.6 Plot of G_p/ω versus frequency for a p-type Si/SiO₂ EIS at pH = 4.0 with doping density $N_A = 5.0 \times 10^{21} \text{ m}^{-3}$ and oxide thickness of 60 nm. Here G_p is the total equivalent conductance associated with the semiconductor–semiconductor interface as described in Figure 4.3.3b.

Source: Diot 1985. Reproduced with permission of Elsevier.

The insulator capacitance can be determined as described earlier. Thus, at any given reference potential, the surface conductance G_p can be determined as a function of frequency. An example for typical results (Diot *et al.* [1985]) of a Si–SiO₂–electrolyte EIS is shown in Figure 4.3.6. Alternatively, G_p/ω can be calculated as the reference potential is swept and then converted to the representation in Figure 4.3.6.

Using these data, it is possible to calculate the number of interface states N_{it} at the semiconductor–insulator interface. In addition, a characteristic time constant τ_{it} associated with these states can be calculated. It is the time constant associated with the exponential decay of the interface states back to equilibrium after a perturbation. Qualitatively, when a small ac potential applied to the system swings in one direction, the electrons will be promoted from the interface states into unoccupied states in the silicon band and then demoted back to them as it swings in the other sense. The characteristic time for the electrons (in an n-type material) to decay back to the equilibrium configuration is τ_{it} .

The interface conductance can be understood, then, simply as the energy loss associated with this RC circuit such that $R_{it}C_{it} = \tau_{it}$ or $G_{it} = C_{it}/\tau_{it}$. The loss will be a maximum when the applied frequency reaches resonance with the characteristic time. In that case, G_p/ω will reach a maximum value. For the case of weak inversion in the semiconductor, the maximum will occur when $\omega\tau_{it} = 1$ and $(G_p/\omega)_{\max}$ will equal $C_{it}/2$. The number of interface states N_{it} is given by C_{it}/e .

Using the techniques earlier, the effect of pH in the electrolyte has been exemplified on the Si–SiO₂–electrolyte EIS to ascertain the nature of the interaction between the hydrogen ions and the device (Bousse and Bergveld [1983]; Diot *et al.* [1985]). One immediate advantage of IS appears in the ability to measure very-low-interface state concentrations, lower than $10^{15} \text{ m}^{-2}(\text{eV})^{-1}$ (Diot *et al.* [1985]). Plots of the N_{it} (calculated as described earlier) versus the surface potential [calculated from Eq. (2)] have also been made as a function of pH and show that the effect of pH is very small (Figure 4.3.7). This implies that the SiO₂–electrolyte interface is the one responsible for the change in potential of the device, not the SiO₂–Si interface (Diot *et al.* [1985]). Based upon a similar conclusion, a theoretical model that depends

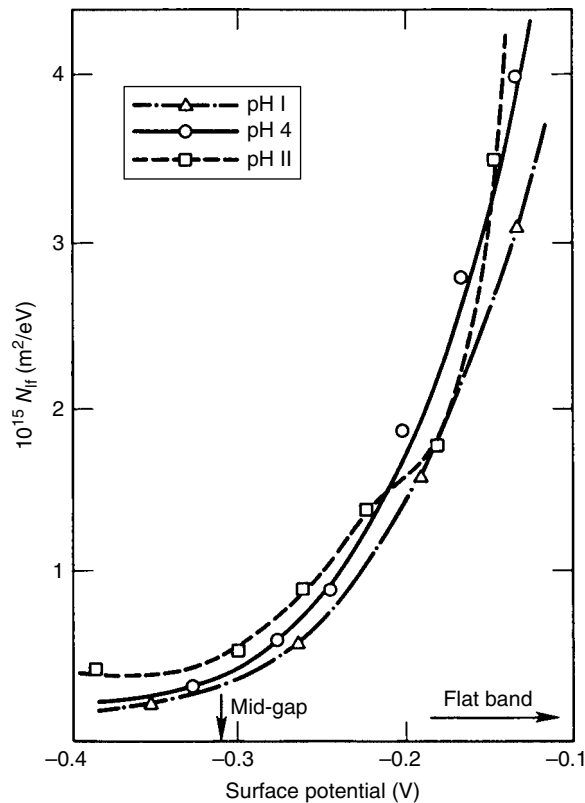


FIGURE 4.3.7 The number of interface states N_{it} as a function of surface potential ψ_s at three different pH values for a p-type Si/SiO₂ EIS (doping density $N_A = 4 \times 10^{-21} \text{ m}^{-3}$ and oxide thickness of 92.5 nm). Source: Diot 1985. Reproduced with permission of Elsevier.

only on the sensitivity of the SiO₂ to the ionic concentration in the electrolyte has been used to successfully model the Si–SiO₂–electrolyte capacitance as a function of pH (Bousse and Bergveld [1983]). In addition, the general shape of Figure 4.3.7 is identical to that observed in MOS devices, thus reinforcing the contention that MOS and EIS devices function in exactly the same manner. Measurements of τ_{it} (Diot *et al.* [1985]) are also consistent with this supposition.

To reiterate, IS can be used to determine the important semiconductor electrical characteristics [E_{fb} and N_d (or N_a)], the insulator characteristics (C_i), and the nature of the semiconductor–insulator interface states (N_{it} and ψ_s). The technique is quite sensitive, allowing interface state concentration measurements below $10^{15} \text{ m}^{-2}(\text{eV})^{-1}$. Results from several different studies (Barabash and Cobbold [1982], Diot *et al.* [1985]) verify that the EIS device behavior is identical to that of the MOS device except that the metal gate is replaced by an electrolyte containing an RE. Finally, and most importantly to device operation, in the Si–SiO₂–electrolyte device, the electrolyte–insulator interface is shown (Bousse and Bergveld [1983], Diot *et al.* [1985]) to be the one that responds to changes in pH rather than the Si–SiO₂ interface. A major advantage of IS is its ability to gather such detailed interfacial information that is not easily accessible with other measurement techniques.

4.3.2 Solid Electrolyte Chemical Sensors

The role of IS in the development and characterization of SECSs is rapidly expanding. SECSs are electrochemical cells designed to measure the concentration or pressure of chemical species in gases or

fluids. IS is emerging as an extremely useful technique to investigate the critical parameters that determine the electrolyte and electrode performances in these sensors.

The most successful SECSs are those that use zirconia-based electrolytes to measure oxygen concentrations. The three most common applications of these electrolytes are to measure oxygen concentrations of steel melts and in combustion gas environments and to control the air-fuel ratio in automobile engines. In the latter two applications, there is increasing interest in lowering the sensor temperature below 600°C, the current minimum temperature of operation because of low ionic conductivity, and slow charge transfer reactions at electrode-electrolyte interfaces.

An excellent example of the advantages and limitations of IS is the recent use of this technique to examine the effect of various electrode materials on the properties of zirconia-based oxygen sensors at temperatures below 600°C (Matsui [1981], Badwal [1983], Mizusaki *et al.* [1983], Badwal *et al.* [1984]). The most common electrode material is platinum. However, the charge transfer reaction (I) at the electrode-electrolyte interface is restricted to regions at or near lines of three-phase (gas-electrode-electrolyte) contact:



Because of this, a finely dispersed porous electrode (PE) structure is formed on the electrolyte surface to maximize the regions of three-phase contact. However, an optimum pore structure is very difficult to maintain due to electrode sintering upon exposure to elevated temperatures.

Several authors (e.g., Matsui [1981], Badwal [1983], Mizusaki *et al.* [1983], Badwal *et al.* [1984]) have used IS to investigate the effects of different electrode materials and their pretreatment temperatures upon oxygen sensor performance at low temperatures. It is particularly interesting to compare the properties of gold and silver electrodes with the commonly used platinum electrodes. A typical impedance spectrum of a zirconia-based oxygen sensor at 500 °C is characterized by two semicircles, as shown in Figure 4.3.8 (Matsui [1981]). The semicircle in the low-frequency range shows a characteristic distortion

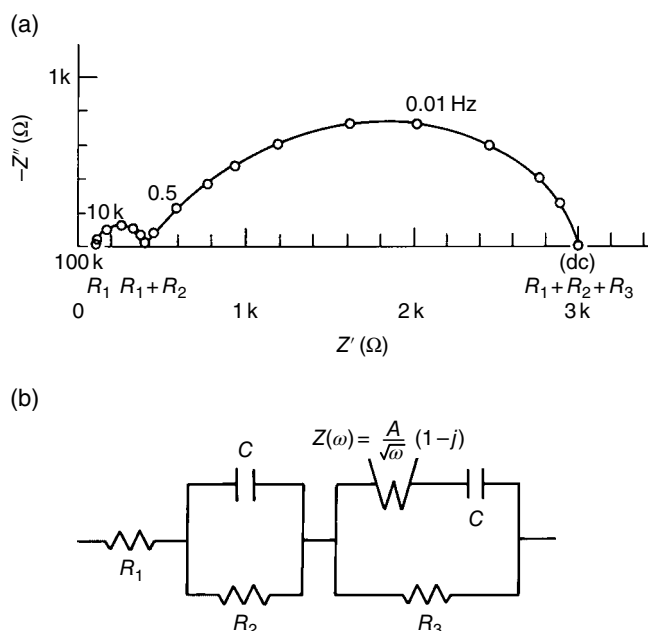


FIGURE 4.3.8 (a) Impedance response for a Pt/yttria-stabilized zirconia electrolyte with additives/Pt cell at 500°C and (b) the corresponding equivalent circuit. Source: Matsui 1981. Reproduced with permission of Elsevier.

depending largely on the electrode material and preparation. The intersection of the low-frequency semicircle at the extreme right side of the abscissa (3000Ω) is determined by the resistance arising from the oxygen electrode reaction (I) and is represented in the equivalent circuit by R_3 . The values of R_1 and R_2 in Figure 4.3.8 represent the bulk and grain boundary resistance, respectively. As shown in Figure 4.3.8, the centers of the semicircle are usually below the real axis. In general this may result from two factors as described in Section 1.3, a constant phase element (CPE) such as that arising either from diffusion (the Warburg impedance) or from a distribution of time constants around an ideal value.

Oxygen sensor electrodes can experience temperatures as high as 900°C during cell preparation because of the necessity to remove organic impurities in the platinum paste electrodes and/or to ensure adherent platinum films on the zirconia electrolyte. The exposure time and temperature can affect and significantly increase the electrode impedance due to a reduction in the three-phase contact regions for reaction (I), which is caused by sintering of the finely dispersed PE at high temperatures. Thus, oxygen cells with similar platinum paste electrodes but having different exposure times and temperatures will exhibit different complex impedance spectra and electrode resistances. The IS data can therefore be used to optimize the sintering times and temperature to provide an electrode with better properties.

The electrode preparation technique is another important factor in determining the electrode resistance. For example, the difference between porous platinum electrodes prepared from a platinum paste (A) and a sputtering technique (B) is shown in Figure 4.3.9 (Mizusaki *et al.* [1983]), which shows only the low-frequency part of the complex impedance spectrum. Although both cells were held at 900°C for 50 h in 1 atm oxygen, the resistance of the sputtered platinum electrode is less than that of the one prepared from platinum paste. However, the resistance of the oxide ($\text{U}_{0.5}\text{Sc}_{0.5}\text{O}_{2+x}$) electrode (C) is about an order of magnitude less than that of the platinum electrodes. These oxide electrodes significantly decrease the electrode resistance by increasing the interfacial area for charge transfer reaction (I). Both oxygen ions and electrons are mobile in these electrodes (Badwal *et al.* [1984]), and reaction (I) can occur over the entire gas-electrode interfacial area. Scanning electron micrographs of the three electrodes shown in Figure 4.3.9, taken before and after heating at 900°C , clearly indicate substantial sintering of the platinum electrodes, while only small morphological changes are observed with the oxide electrodes (Badwal [1983]).

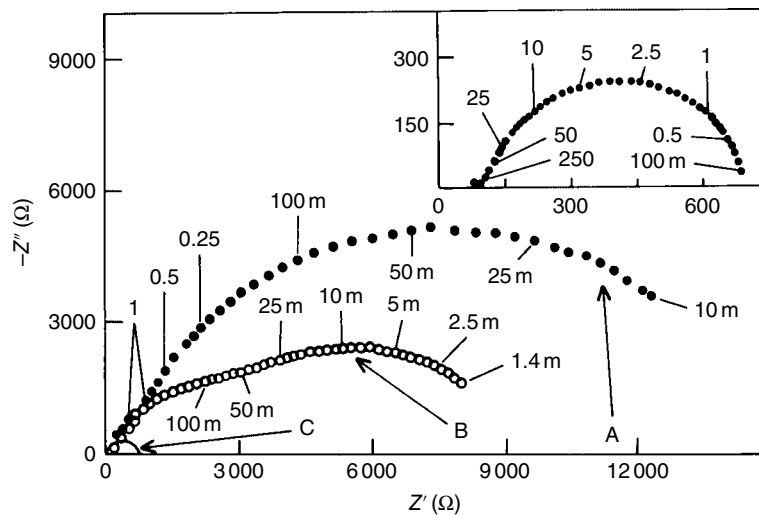


FIGURE 4.3.9 Complex impedance response for (A) 6082 Pt paste electrodes, (B) sputtered Pt electrodes $0.9 \mu\text{m}$ thick, and (C) $\text{U}_{0.5}\text{Sc}_{0.5}\text{O}_{2+x}$ electrodes (also inset on enlarged scale) at 600°C in 100% oxygen.

All cells were given a prior heat treatment at 900°C for 50 h. Numbers on the arcs are frequencies in hertz. Source: Badwal 1983. Reproduced with permission of Elsevier.

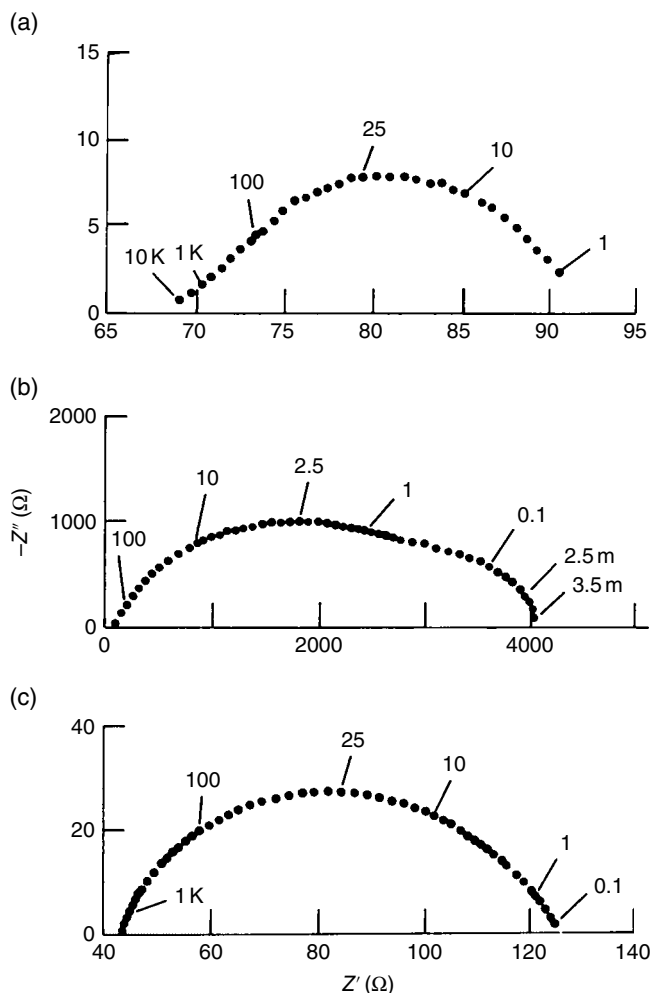


FIGURE 4.3.10 Complex impedance response at 600°C in 1 atm of oxygen after heating at 600°C for 50 h for the cells (a) Ag/yttria-stabilized zirconia/Au, (b) Au/yttria-stabilized zirconia/Au, and (c) Pt/yttria-stabilized zirconia/Pt. The numbers on the arcs are frequencies in hertz. Source: Badwal 1984. Reproduced with permission of Elsevier.

The impedance spectra (only the low-frequency region) for three noble metals (Ag, Au, Pt) electrodes are shown in Figure 4.3.10 (Badwal *et al.* [1984]). The results clearly indicate a significant difference between the silver and the gold electrode resistance in an oxygen sensor cell at 600°C. Although the resistance of the silver electrode is only slightly smaller than that of the platinum electrode, the resistance of the latter electrode significantly increases upon exposure to high temperatures. These sintering effects are not as severe for the silver electrodes because the appreciable solubility of oxygen in silver enables reaction (I) to occur over the entire electrode–electrolyte interfacial area rather than only at or near the three-phase contact region, as in the case with the platinum and gold electrodes.

Figure 4.3.10 clearly indicates that silver is a better electrode material in low-temperature oxygen sensors. However, significant volatility and microstructural changes of silver can occur at elevated temperatures, particularly at or above 900°C (Badwal *et al.* [1984]). Silver has been combined with platinum to form a Pt–Ag electrode, which possibly could exhibit the advantages of both metals. As shown in Figure 4.3.11 (Matsui [1981]), a Pt–Ag electrode (circles with centers) does have a significantly lower

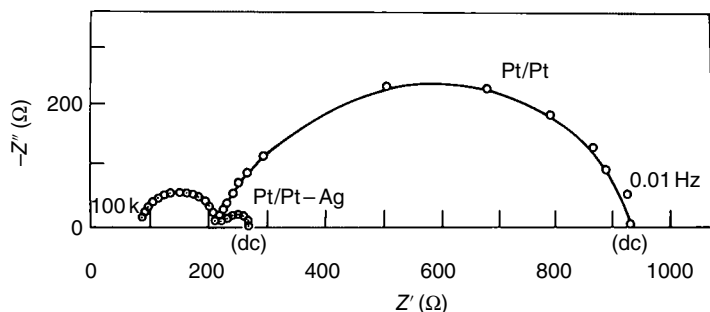


FIGURE 4.3.11 The impedance response for two kinds of electrodes using a tube of yttria-stabilized zirconia as the electrolyte. The arcs in the high-frequency range coincide, but the low-frequency arcs show a significantly lower resistance for the Pt/Ag electrode. Source: Matsui 1981. Reproduced with permission of Elsevier.

resistance than that of the platinum one (open circles). The impedance spectra shown in Figure 4.3.11 and zirconia-cell results at 300 °C indicate that the Pt–Ag electrode could be a very useful electrode in a low-temperature oxygen sensor (Matsui [1981]).

The use of impedance spectra to determine the optimum electrode materials and preparation procedures for low-temperature oxygen sensors is only one example of the application of this technique in solid electrolyte sensors. For example, impedance spectra have already been used to examine the properties of zirconia stabilizers such as yttria and calcia in low-temperature zirconia electrolyte oxygen sensors (Badwal [1983]). The use of this technique in the development and characterization of other solid-state sensors should increase significantly in the next few years.

4.3.3 Photoelectrochemical Solar Cells

Photoelectrochemical solar cells (PESCs) are devices that harness light energy and convert it into electrical or chemical energy by means of an electrochemical reaction at an interface. A general review of the electrochemistry of these devices can be found in most electrochemistry texts (e.g., Bard and Faulkner [1980]), but a cursory description will be given here for those unfamiliar with these devices. Most PESCs are composed of a semiconductor–electrolyte interface with an appropriate redox couple in solution. For an n-type semiconductor, when light with energy greater than the band gap strikes the interface, photons are absorbed and electron–hole pairs are created in the semiconductor. Some of these electron–hole pairs will simply recombine in the bulk, dissipating their energy thermally by the creation of phonons, by photon emission, and so on. However, some proportion of the holes created at the interface will be available to oxidize the reduced species in solution, liberating an electron in the semiconductor that can flow in the external circuit. This photocurrent is absent in the dark where the concentration of holes is very low, so no reaction with the species in the solution is possible. The behavior of p-type semiconductors under irradiation is analogous; however, in this case electrons assist a reduction process in the solution and a current is produced by holes in the semiconductor.

In practice, the electrochemical behavior of semiconductor–electrolyte interfaces is far more complex than that described earlier (for a good review, see Boddy [1965]). One of the complications arises because the semiconductor surface at the electrolyte–semiconductor interface is not equivalent to that in the bulk. In particular, the energy states localized at the surface for holes and/or electrons are different than those present in the bulk. These surface states may arise in several ways, for example, through pretreatment (etching, polishing, etc.) of the semiconductor surface before immersion in the electrolyte. The surface states can be detrimental to the PESC efficiency if they increase the recombination of the electron–hole pairs in the semiconductor, thus reducing the number of holes (electrons for p-type material) available for chemical reaction with the redox species in solution.

Another complication arises because the semiconductor may chemically or electrochemically react with the electrolyte after immersion, leaving a layer on the surface of the semiconductor that has different electrical or electrochemical characteristics (e.g., an insulating layer) from the semiconductor. Because the photocurrent under illumination is very sensitive to the semiconductor–electrolyte interface, these surface perturbations not only change the electrochemical behavior but also, in extreme cases, completely inhibit the photoresponse.

IS offers an excellent tool to examine the existence of surface states or other modifications of the ideal semiconductor–electrolyte interface. The general response of such interfaces was reviewed as early as 1965 (Boddy [1965]), but detailed studies of the response of PESCs are fairly recent. Dutoit *et al.* [1975] found that the capacitance of these interfaces at a given dc potential was dependent on the measuring frequency for CdSe, CdS, and TiO₂ in several different aqueous and nonaqueous electrolytes. Tomkiewicz [1979] and McCann and Badwal [1982] have made more thorough investigations of the impedance response of several different technologically important semiconductor–electrolyte interfaces. The capacitance of a semiconductor–electrolyte junction has also been measured as a function of incident wavelength and used to characterize energy levels in semiconductors (Haak *et al.* [1982], Haak and Tenth [1984]). One particular study (Shen *et al.* [1986a]) will be examined in more detail here to illustrate the kinds of effects that can be resolved using IS.

The impedance response of *n*-CuInSe₂ in polyiodide solutions has recently been used to understand the behavior of this material in a PESC (Shen *et al.* [1986b]). Typical current–potential response curves for *n*-CuInSe₂–polyiodide solutions are given in Figure 4.3.12 (Shen *et al.* [1986b]) in which the effect of

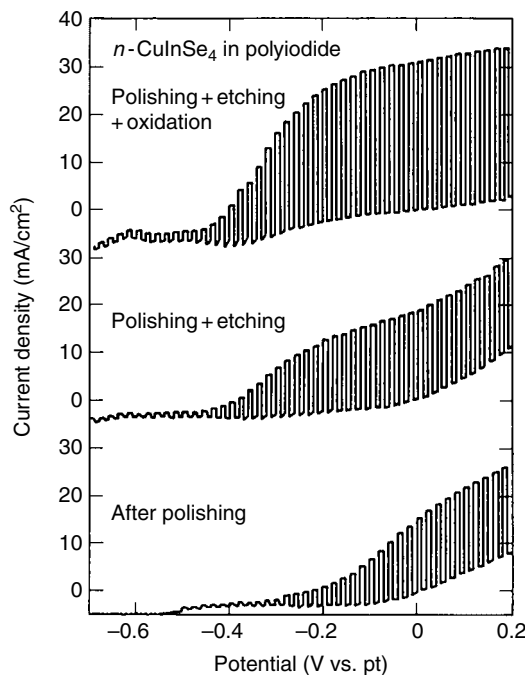


FIGURE 4.3.12 The effect of surface preparation of the current–potential response curves of *n*-CuInSe₂ in a solution of 6 M KI + 0.1 M InI₃ + 0.0125 M I₂ at pH 6.0. The square-wave response results from using a chopped white light source of intensity 100 mW/cm². Etching was in a 2% Br₂–methanol solution for 60 s; oxidation was for 2 h at 150°C. Source: Shen 1986. Reproduced with permission of The Electrochemical Society.

various pretreatments is shown. Polishing + etching or polishing + etching + oxidation significantly improves the photoresponse over simple polishing. For example, from Figure 4.3.15 at -0.2 V versus Pt, the photocurrent increases by approximately a factor of two after each additional pretreatment. IS was used in combination with electroreflectance (Shen *et al.* [1986a]) to understand this behavior.

The impedance response obtained for polished + etched crystals and polished + etched + oxidized crystals (Figure 4.3.13a and b, respectively) show qualitatively different behavior, the principal one being the addition of at least one more time constant in the oxidized case as manifested by (at least) one additional peak in the imaginary part in Figure 4.3.13b. Such behavior is reasonable since there is an additional interface between the oxide and semiconductor.

Using the equivalent circuits shown in Figure 4.3.16a and b, the high-frequency data were analyzed to determine the capacitance associated with the two fastest time constants in the polished + etched

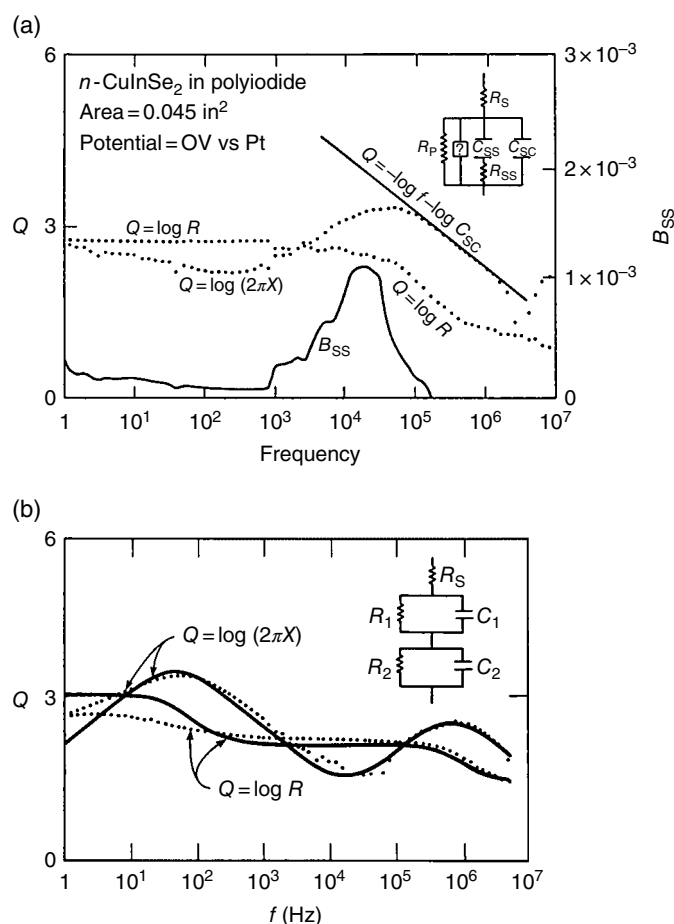


FIGURE 4.3.13 The impedance response and equivalent circuit of $n\text{-CuInSe}_2$ in the same solution as described in Figure 4.2.15 for: (a) Polished + etched sample. B_{ss} is the imaginary portion of the measured admittance less ωC_{sc} . The value of C_{sc} is calculated from the linear part of the high-frequency portion of the imaginary response of the impedance. The low-frequency response was not analyzed. (b) Polished + etched + oxidized sample. The solid line is a theoretical fit assuming the equivalent circuit shown. Source: Shen 1986. Reproduced with permission of The Electrochemical Society.

material and the fastest time constant in polished + etched + oxidized material. The low-frequency data were not analyzed because their physical interpretation was not clear. For the data shown in Figure 4.3.16a and b, the fastest time constant has been associated with the space-charge layer in the semiconductor (C_{SC} in Figure 4.3.16a and C_1 in Figure 4.3.16b). In the polished + etched material, the next fastest is that associated with surface states on the semiconductor-electrolyte interface. It was assumed that the surface states are characterized by one time constant that does not significantly overlap with the time constants of any other states. It has been pointed out (McCann and Badwal [1982]) that should there be overlap of states with time constants close to one another, the time constants become essentially continuous, and a frequency-dependent resistance and capacitance must be used to model the interface. Here, though, the essential features of the interface appear to be adequately described without resorting to such elements.

In the case of the polished + etched + oxidized sample, C_1 was associated with the space-charge layer capacitance. No further data were used. Thus, C_1 is representative of the change in capacitance of the space-charge layer from the presence of the oxide layer.

Analyzing the effect of applied potential on the capacitance arising from the surface states, C_{ss} , in the polished + etched material (Figure 4.3.14) led to the conclusion that there were two surface states: one centered 0.17 eV below the conduction band [$-0.69 - (-0.72)$ in Figure 4.3.17] and the other at 0.45 eV below the conduction band. Assuming a Gaussian distribution of surface states (Tomkiewicz [1979]), the area density of both states was calculated to be less than 1% of a monolayer. Thus, it was concluded that one major effect of etching was to remove most of the surface states. This conclusion is consistent with electroreflectance results (Shen *et al.* [1986a]) on the same system that show that in unetched samples the surface states pin the Fermi level, while after etching the surface states are nearly completely removed.

To determine the effect of oxidation, a Mott-Schottky plot of the space-charge capacitance before and after oxidation was compared. In these plots, which were originally derived for a metal-semiconductor interface (Mott [1939], Schottky [1939, 1942]) but hold equally well for the metal-electrolyte interface, a linear relationship is predicted between the applied potential and one over the square of the capacitance arising from the space-charge layer in the semiconductor. The slope is

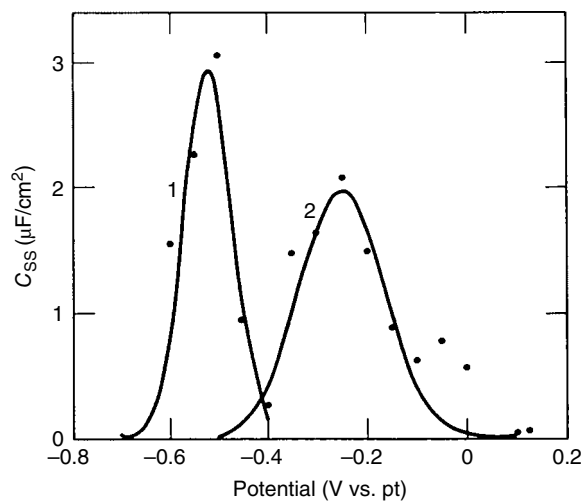


FIGURE 4.3.14 The variation of the capacitance associated with the surface states C_{ss} as a function of potential. The solid lines are a theoretical fit to two Gaussian line shapes as described in text. Source: Shen 1986. Reproduced with permission of The Electrochemical Society.

inversely proportional to the effective donor or acceptor concentration in the semiconductor. For the semiconductor-electrolyte interface (Bard and Faulkner [1980]),

$$\frac{1}{C_{sc}^2} = \frac{2}{e\epsilon_0\epsilon N_d} \left(-\Delta\phi - \frac{kT}{e} \right) \quad (4)$$

where $\Delta\phi$ is the difference between the applied potential and the flat-band potential $E - E_{fb}$, C_{sc} is the space-charge capacitance, ϵ is the dielectric constant, ϵ_0 is the permittivity of free space, k is Boltzmann's constant, T is absolute temperature, and N_d is the concentration of donors or acceptors. For the n -CuInSe₂ electrode, the Mott-Schottky plot (Figure 4.3.15) shows that the polish + etch + oxidation procedure does not change the flat-band potential, but the effective doping level decreases by nearly one order of magnitude from that observed in the polished + etched material.

Several conclusions can be drawn from these data. First, the oxidation produced a layer that does not alter the electrical characteristics of the semiconductor since the flat-band potential did not change. Second, the oxide layer decreases the doping level, thus increasing the width of the space-charge layer. This wider layer in turn leads to higher photocurrent because most of the light is absorbed within the space-charge layer so that recombination of charge carriers in the bulk is reduced. Finally, by applying a simple model of photoresponse, Tomkiewicz [1979] determined that surface recombination arises from the surface state at 0.17 eV below the conduction band. Electroreflectance measurements (Shen *et al.*

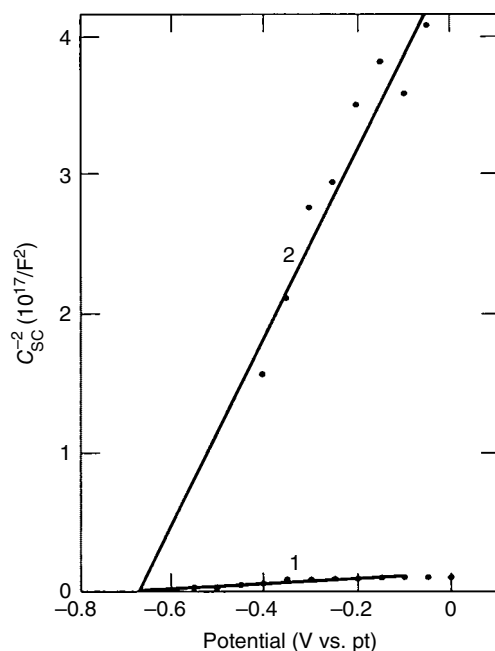


FIGURE 4.3.15 Mott-Schottky plots of the space-charge capacitance C_{sc} (curve 1) as derived from data like those shown in Figure 4.2.9a and the capacitance associated with the high-frequency response, C_1 (curve 2) derived from data like those shown in Figure 4.2.9b. The flat-band potential is the same in both cases (0.69 V), but the doping level, as calculated from the slope of the lines, is an order of magnitude lower for curve 2 (polished + etched + oxidized sample) than for curve 1 (polished + etched sample).
Source: Shen 1986. Reproduced with permission of The Electrochemical Society.

[1986a]) are consistent with this conclusion. Thus, the improved response caused by etching can be explained by the decrease in density of these surface states observed in the impedance results after etching.

Several key features of this study should be emphasized. IS clearly can be used to successfully model a semiconductor–electrolyte interface in a PESC. The ability to probe the physics of this interface using IS while controlling the applied potential can allow significant insight into the important parameters of the device. In particular, the surface states at the semiconductor–electrolyte interface may be determined, as can their relative importance after several different pretreatments or in different cell configurations. The electrical characteristics of the interface, for example, the flat-band potential and the space-charge capacitance, can also be determined.

The work described earlier also shows that it is not always necessary to analyze the entire frequency spectrum (i.e., determine the complete equivalent circuit) of a cell in order to obtain significant insights into its operation if it is possible to associate a particular region of the spectrum with a meaningful physical quantity. In the case of the semiconductor–electrolyte interface described earlier, a strong theoretical background describing the expected behavior along with other experimental findings (electroreflectance, current–potential curves) on the system permitted such a limited but meaningful analysis. Further, a more detailed analysis of the results would probably have led to a more complete description of the operation of the PESC. This fact was recognized by the authors themselves (Shen *et al.* [1986b]). Although a limited analysis may allow significant insights, it should be made with extreme caution, as the results could lead to erroneous conclusions. A complete detailed analysis of the entire frequency spectrum is far preferable and leads to a more complete understanding of the device operation.

4.3.4 Impedance Response of Electrochromic Materials and Devices

4.3.4.1 Introduction

Electrochromic materials have the ability to change their optical properties in response to an electrical field. The optical properties and hence the color can be altered gradually and reversibly, that is, the original state is recovered if the polarity of the applied voltage is reversed. For practical use, the electrochromic material must be incorporated in a system, or a device, with contacts connected to an external circuit including a voltage source. Depending on the intended application for the device, at least one of the contacts must exhibit a high optical transmittance. Research on electrochromic materials became widespread around 1970, due to a widely cited paper by Deb [1969]. The aim of the early work was to develop devices for display technology. However, it has been realized that electrochromic devices are of interest for a wide range of applications, a number of commercial activities have been started during the last decades (Lampert [2003, 2004], Pittaluga [2014]), and today industrial production is being implemented by several actors (Granqvist [2014]). The potentially most important application seems to be energy-efficient windows with variable solar and luminous transmittance; they are able to reduce the influx of solar energy into a building. This will lead to large reductions in the need for cooling and air conditioning in warm and temperate climates (Azens and Granqvist [2003], Pittaluga [2014]). Overheating and reduced comfort is often a problem in modern buildings because windows and glass façades allow too much solar energy to penetrate into buildings. Research on electrochromic materials and devices is extensive and has been reviewed several times. A number of review papers (Granqvist [1995, 2000, 2014], Niklasson and Granqvist [2007]) give a comprehensive picture of the research field.

In this section we concentrate on inorganic electrochromic materials and devices that use this class of materials. The electrochromic effect is caused by simultaneous ion and electron insertion into the materials. Figure 4.3.16 shows a schematic picture of an electrochromic device. It consists of five layers interfaced between two substrates, or alternatively deposited on a single substrate. We consider first the configuration with two substrates. They are coated by a transparent conducting layer and then by an electrochromic layer. The two sides of the device are subsequently laminated by an ion conductor, preferably a polymer. The electrochromic layers are chosen to be complementary. One of them is cathodic

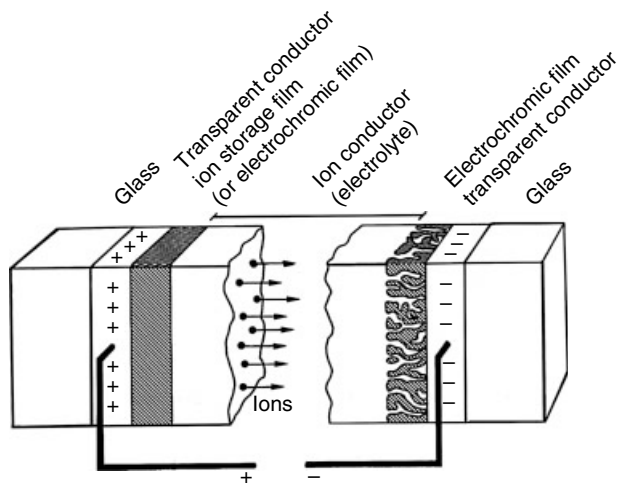


FIGURE 4.3.16 Schematic illustration of an electrochromic device.

(i.e., it colors under cation/electron insertion) and the other is anodic (coloring under cation/electron extraction). This means that both will color upon the application of a voltage between the transparent contacts and both will bleach when the polarity is reversed. One of the electrochromic layers may be replaced by an ion storage layer, which can accommodate inserted ions and electrons without changing its optical properties. The alternative design, the so-called all-thin-film (ATF) device consists of five layers consecutively deposited on one substrate. The material requirements are similar for this kind of device, except for the ion conductor, which in this case has to be an inorganic thin film.

Optical properties together with ion and electron transport are the physical properties of electrochromic materials that are of importance for the performance of a device. The requirements on the optical behavior can be summarized as follows: one of the electrochromic materials should change color upon ion/electron insertion, while the other electrochromic material should show complementary behavior, that is, change color upon ion/electron extraction, or remain optically invariant during the whole intercalation–deintercalation cycle. The ion conductor should be transparent. Inorganic electrochromic materials mostly belong to the class of wide band-gap transition metal oxides. Coloration occurs as the Fermi level moves from a position in the band gap into the conduction or valence band. In most cases the absorption process is due to electronic transitions between localized states. Hence it is important to study the electronic density of states (DOS) of the material in order to assess the number and energies of possible optical transitions.

The requirements on the electrical properties are somewhat more complex. A good electrochromic material should be a relatively fast mixed ionic and electronic conductor. Since the optical modulation is a consequence of changing the number of electrons in the material, and because of the requirement of charge neutrality, charges of opposite signs must be able to move. The ion conductor, on the other hand, should ideally not conduct electrons at all, in order to prevent the device from short-circuiting. When investigating the ability of a material to act as one of the layers in an electrochromic device, it is thus important to extract information about the electronic conductivity as well as the ion diffusion coefficient, the latter one usually being rate limiting. Furthermore, the energy barriers felt by the ions when moving between the ion conductor and the electrochromic layers should be as low as possible.

IS is widely recognized as a versatile technique to obtain detailed information on ion and electron transport. It can give information on the electrochemical properties of the ion conductor (electrolyte)–electrode interface and the ion diffusion coefficient in the electrode as well as on the electronic DOS, which is of obvious importance for electrochromic coatings. The first studies of the electrochemical impedance of electrochromic coatings in contact with a liquid electrolyte appeared around 1980. Measurements on Li-intercalated tungsten oxide films were carried out by Ho *et al.* [1980]. They

developed a basic model of the impedance response and showed that it can be represented by the Randles equivalent circuit (see Section 2.1.4.4, p. 56). A similar circuit was used by Glarum and Marshall [1980] in an early work on iridium oxide films. The determination of the circuit elements from experimental data yielded information on the ion diffusion in the coating, as well as the properties of the electrolyte–film interface. The work of Ho *et al.* [1980] was generalized by Franceschetti and Macdonald [1982], who introduced an additional adsorption process. It was assumed that an ion combines with an electron from the conduction band of the coating to form an adsorbed intermediate species before insertion into the electrochromic film. This process leads, under certain conditions, to the occurrence of two semicircles at high frequencies in complex impedance (Z) plots. Unfortunately, this theory has rarely been used in the field of electrochromic materials (Pyun *et al.* [1996]), and the occurrence of two semicircles in the Z plots has sometimes been ascribed to electron injection at the back contact of the film (Yoshiike *et al.* [1984]). The basic Randles circuit has later been generalized in order to incorporate effects of anomalous diffusion (Bisquert and Compte [2001]), as well as ion diffusion coupled with trapping (Bisquert [2002], Bisquert and Vikhrenko [2002], Diard and Montella [2003]) and reaction processes (Fabregat-Santiago *et al.* [2001]). A systematic approach for deriving generalized equivalent circuits for mixed conductors from the basic transport equations has been established by Jamnik and Maier [2001]. The case of a mixed conductor with one electrode blocking to ions and the other blocking to electrons (Jamnik [2003]) is of obvious relevance for electrochromic materials. In the following text we will use generalized Randles circuits to illustrate how basic information on the properties of electrochromic materials can be extracted from impedance spectra.

4.3.4.2 Materials

Cathodic Electrochromic Materials. Amorphous tungsten oxide is a widely studied cathodic electrochromic material. The history of induced color changes in tungsten oxides dates back to the days of Berzelius in the early nineteenth century, while electrochemical studies were initiated around 1930, as discussed by Granqvist [1995]. The optical properties of WO_3 switch from a transparent state to a colored blue state upon insertion of small cations like H^+ , Li^+ , and Na^+ . The coloration is actually due to simultaneous insertion of charge-balancing electrons into the conduction band from the transparent contact to the external circuit. Electronic transitions between localized states give rise to intervalence transfer absorption (Faughnan *et al.* [1975]). On the other hand, polycrystalline tungsten oxide switches from a transparent state to a near-infrared (IR) absorbing one and then to an IR reflecting state upon ion/electron insertion (Larsson *et al.* [2003]). The reflecting state is due to free electrons in the conduction band. Published research on tungsten oxide coatings is very extensive; see, for example, the reviews of Granqvist [1995, 2000] and the review on charge transport by Monk [1999]. Most electrochromic devices employ tungsten oxide as a cathodic material, and no serious contenders have appeared despite long-standing efforts.

Titanium dioxide exhibits optical properties very similar to those of tungsten oxide (Sorar *et al.* [2013]). Electrons in the conduction band become localized by the electron–phonon interaction and give rise to polaron absorption. Coatings of titanium oxide are less stable in an electrochromic device than films of tungsten oxide and have therefore not been used so much in practical devices.

Anodic Electrochromic Materials. The most commonly used anodic electrochromic materials are nickel oxide (Svensson and Granqvist [1986]) and iridium oxide (Gottesfeld *et al.* [1978]). They switch from a transparent state to a colored one upon extraction of positive ions. Charge-balancing electrons are simultaneously extracted from the valence band. The films are very probably a mixture of oxide and hydroxide components in the bleached state. Due to the high cost of iridium, the use of nickel oxide is favored for large-scale applications. Nickel oxide-based films display large optical modulation in KOH electrolyte, and in this case protons appear to be the active ionic species (Avendano *et al.* [2005]). During coloration the films are partially transformed to the oxygen-rich compounds NiOOH and Ni_2O_3 , which are both strongly absorbing at visible wavelengths. Intercalation of Li ions into nickel oxide films is of major interest for device applications. However, in this case the change of the optical absorption in the films is quite moderate. This is because the charge insertion capacity for Li ions is low, and recent studies

suggest that surface adsorption of positive and/or negative ions from the electrolyte (Boschloo and Hagfeldt [2001], Mihelcic *et al.* [2014]), rather than Li intercalation, is the main mechanism causing the electrochromic response.

Transition metal oxides that do not change their transparency, or color very little, under ion/electron insertion and extraction can be used as a CE in electrochromic devices employing tungsten oxide as a cathodic material. A particular interest has been devoted to oxides based on vanadium pentoxide and cerium oxide. Pure V₂O₅ as well as mixtures of vanadium and titanium oxide are of interest for device applications (Burdis *et al.* [1998]). Cerium-based mixed oxides, in particular cerium-zirconium oxide (Veszelei *et al.* [1999]), exhibit less optical absorption, but the stability is not sufficient for many applications.

Ionic Conductors. As mentioned earlier, the ion conductor used in electrochromic devices can be of two types, namely, a polymer electrolyte or an inorganic thin film. A large number of polymer electrolytes, protonic as well as lithium conducting, have been tested in electrochromic devices. A review of results for devices, using a polymer electrolyte, was given in Granqvist [2000]; see also references therein. In good polymer electrolytes the dc conductivity is usually dominating the impedance response for frequencies below the MHz range. At higher frequencies an ion pair relaxation, as well as relaxations due to segmental motions of the polymer chains, is present. The dielectric properties of polymer electrolytes constitute a large field of research, and a treatment is outside the scope of this review. Reviews have been given by Bruce [1987] and Greenbaum *et al.* [1990].

Inorganic ion conductors are found among the transition metal oxides, as well as among lithiated metal oxides and fluorides. We refer to Granqvist [2000], and references given therein, for data on devices that have used inorganic ion conductors. Among the transition metal oxides, tantalum pentoxide has been used in window devices close to the commercial stage (O'Brien *et al.* [1999]). Both tantalum and zirconium oxides exhibit reasonable proton and lithium ion conductivities (Jonsson *et al.* [1999], Frenning *et al.* [2001]).

4.3.4.3 Theoretical Background

In this section, we discuss how IS can be used to extract quantities necessary for the evaluation of the viability of a material as a component in an electrochromic device. In electrochemical three-electrode IS, the film under study is backed by an electronic conductor, which is connected to a CE and a RE via an outer circuit. The film is immersed into an electrolyte containing ions that will be intercalated into the film. The ac potential is superimposed on an equilibrium potential, U_{Eq} , applied between the film, which acts as the WE, and the RE, while the current is measured between the film and the CE. The equilibrium potential decreases as more cations are inserted (or anions are extracted) into the film. The extraction of cations (or insertion of anions) is accompanied by an increasing equilibrium potential. Electrochromic materials typically display a stable operating range at U_{Eq} 's in the range of 2–4 V versus the Li/Li⁺ electrode. Ion conductor materials should not be possible to intercalate at the operating potentials of the electrochromic materials. For example, significant intercalation starts at about 2 V versus LiLi⁺ in tantalum and zirconium oxide films.

In the first subsection we discuss how the electronic DOS can be obtained from the so-called chemical capacitance by using IS. In the second subsection we will show how data obtained from electrochemical three-electrode IS can be used to obtain information about the chemical diffusion coefficient, D , as well as about energy barriers at the interfaces. In the third subsection the determination of ion density and mobility of ion conductors will be in focus.

The Electrochemical Density of States. It has been shown that measurements of intercalated charge as a function of U_{Eq} can give information on the electronic DOS of electrochromic materials (Strømme *et al.* [2004], Niklasson *et al.* [2006]). This indicates that the DOS of the electrons is much broader than the energy distribution of the intercalated ionic species. Provided that the rigid band approximation holds during the intercalation process, measuring the charge inserted or extracted at each potential will give an image of the electronic DOS. The DOS in regions up to 2 eV from the Fermi level can be measured by

electrochemical techniques, so-called intercalation spectroscopy (Strømme *et al.* [2004]). The intercalation of monovalent cations M^+ with charge-balancing electrons e^- into the WE material S may be represented schematically as



where x denotes the fraction of intercalated ion/electron pairs per formula unit of S. When the WE is inserted into the electrolyte, it attains an OCP, which gives the position of the Fermi level of the WE relative to the Li/Li⁺ potential of the RE. As x changes, the potential will decrease or increase, depending on whether electrons are inserted or extracted. In intercalation spectroscopy, the derivative dx/dE gives a normalized number of charges inserted per energy (E) interval and is denoted the “electrochemical density of states” (EDOS). The energy is as usual related to the potential scale by $E = -eU_{Eq}$.

IS can be used to obtain the EDOS, and in this case we are interested in the asymptotic low-frequency capacitance, which gives information on the charge storage capacity of the material. The chemical capacitance per unit volume is formally proportional to the derivative of the density of charge carriers with respect to their chemical potential (Jamnik and Maier [2001]). In the present case the charge carriers in the electrochromic film are ions and electrons, and therefore the chemical capacitance has contributions from both species. The ionic and electronic chemical capacitances can be regarded as connected in series (Jamnik and Maier [2001]). Neglecting a possible capacitance due to trapping processes (Bisquert [2003a], Diard and Montella [2003]), the chemical capacitance per volume can be written as (Bisquert [2003a], Jamnik [2003])

$$C_{ch} = e^2 \frac{dN}{dE}, \quad (6)$$

where dN/dE is the number of ion/electron species inserted per unit energy. By dividing with the number of formula units of the host material, we obtain the EDOS per formula unit, dx/dE .

Determination of Physical Parameters from Extended Randles Circuits. Electrochemical three-electrode impedance spectra taken on electrochromic materials can very often be fitted to a Randles equivalent circuit (Randles [1947]) (see Figure 2.1.14). In this circuit R_s denotes the resistance of the electrolyte, R_{ct} is the charge transfer resistance associated with ion injection from the electrolyte into the electrochromic film, and Z_D is a Warburg diffusion impedance of either semi-infinite or finite-length type (Ho *et al.* [1980]). The double-layer capacitance C_{dl} is often replaced by a CPE describing the distributed capacitance of the electrochemical double layer between the electrolyte and the film. The impedance of a CPE can be written as

$$Z_{CPE} = \frac{1}{q(i\omega)^m}, \quad (7)$$

where q is a parameter with the dimension Fs^{m-1} and m is a positive number between zero and unity. It has been shown that the exponent m in Eq. (7) can, at least in certain cases, be directly associated with the fractal dimension of the electrochromic film surface (Strømme Mattsson *et al.* [1996a]). To distinguish between different CPEs, we will use subscripts on the parameters q and m ; hence the subscript “DL” will be used for the double-layer CPE.

The diffusion element can be generalized in various ways, as mentioned in the Introduction. It can be represented by the transmission line in Figure 4.3.17, where χ_m and ζ_m are general impedance elements. Transmission line representations of ordinary diffusion were discussed earlier in Sections 2.1.3.1 and 2.2.2.2; in this case χ_m is a resistance per unit length and ζ_m the impedance corresponding to a capacitance per unit length. Various generalizations can be obtained by replacing these with different combinations of circuit elements. The termination of the transmission line is determined by the electrical properties of the interface between the electrochromic film and the transparent contact. Usually

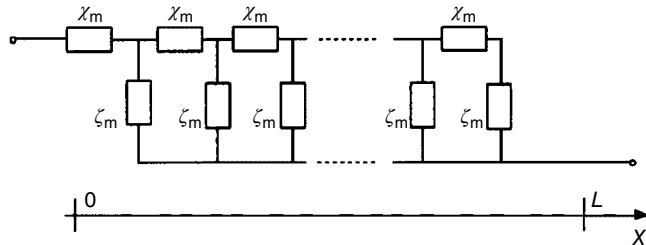


FIGURE 4.3.17 The diffusion impedance in an extended Randles equivalent circuit is represented by the shown transmission line.

ions are blocked by this interface and this corresponds to an open-circuit termination. In the case of ordinary diffusion, the impedance Z_D is then given by Eq. (135) in Section 2.1.3.1. Another model with a CPE termination (Bisquert *et al.* [1998]) could be relevant to take into account effects of ion diffusion toward a rough or fractal interface.

The general expression for the impedance of the transmission line in Figure 4.3.17, with open-circuit termination, becomes (Bisquert and Compte [2001])

$$Z(\omega) = (\zeta_m \chi_m)^{1/2} \coth \left[L \left(\frac{\chi_m}{\zeta_m} \right)^{1/2} \right], \quad (8)$$

where L is the film thickness. By anomalous diffusion we understand cases where the frequency dependence of the Warburg element Z_D departs from the characteristic behavior of ordinary diffusion. There exist two different anomalous-diffusion models denoted AD1a and AD1b, which are of interest for electrochromic materials. In the case of AD1a, χ_m is a resistance per unit length (denoted r), and ζ_m is the impedance length of a CPE (Eq. (7) with subscript a), while in the case of AD1b, χ_m is the impedance per unit length of a CPE (Eq. (7) with subscript b) and ζ_m denotes the impedance of a capacitance per unit length (denoted c) (Bisquert and Compte [2001]). An interesting feature of the AD1a model is that it is derived from a generalized continuity equation wherein the number of diffusing ions is not conserved. This model is therefore suitable for describing the multiple-trapping regime (Bisquert [2003b]) and probably also situations where intercalation displays a degree of irreversibility.

A number of other models have been suggested to take into account trapping of the intercalated charge or alternatively chemical reactions in the electrochromic film. Diffusion combined with trapping/reactions can be modeled by an extension of the ordinary-diffusion model (Fabregat-Santiago *et al.* [2001], Bisquert [2002], Bisquert and Vikhrenko [2002]). The equivalent circuit of Figure 4.3.17 can still be used, but now χ_m is a resistance per unit length, and ζ_m is replaced by a parallel combination of a capacitance with either a resistance, a resistance/capacitance series combination, or a CPE. It has also been observed that the addition of a side reaction resistor in parallel to the diffusion element sometimes improves fitting to experimental spectra in the low-frequency region (Backholm *et al.* [2008]).

Fitting an impedance spectrum to the extended Randles circuit is a convenient way of obtaining the properties of the electrolyte-film interface (from R_{ct} and CPE_{dl}) as well as the chemical diffusion coefficient, which gives a measure of the speed with which the intercalated ion/electron couple moves. The determination of the diffusion coefficient from the AD1 models needs special considerations. Because of the presence of powers of frequency in the CPE expressions, the diffusion coefficient appearing in the fractional diffusion equations of Bisquert and Compte [2001] will not have the usual units of m^2/s . However, as shown elsewhere (Backholm *et al.* [2008]), it is possible to define effective diffusion coefficients in

these cases, which have the same correct dimensionality as for ordinary diffusion. For the AD1a model it is found that

$$D_{\text{eff}} = L^{2-2/m_a} (rq_a)^{-1/m_a}, \quad (9)$$

and for the AD1b model we obtain the related relation

$$D_{\text{eff}} = L^{2-2/(1-m_b)} \left(\frac{q_b}{c} \right)^{1/(1-m_b)} \quad (10)$$

The chemical capacitance is easily obtained for the ordinary-diffusion and AD1b models, since they exhibit a capacitive response in the low-frequency limit. In the AD1b model the chemical capacitance can be calculated from

$$C_{\text{ch}} = Lc = \frac{L}{i\omega\zeta_m}, \quad (11)$$

where we also indicate the relation with the impedance length, ζ_m . For the AD1a model ζ_m is a frequency-dependent CPE, and the low-frequency asymptotic response is not purely capacitive. We suggest to approximate $(\omega\zeta_m)$ by the amplitude of its imaginary part, which is a reasonable approximation at least in cases where the CPE exponent has values close to a capacitive response.

Determination of Ion Density and Mobility. In this section we present methods to obtain the ion density and mobility from two-electrode IS measurements with ion-blocking contacts. We concentrate on applications to inorganic and polymer electrolytes, where it is of interest to investigate not only the conductivity of the ions but also their density, n , and mobility, μ . In principle it is possible to determine both parameters, provided that electrode polarization (space-charge effects) dominates the impedance response of the layer under investigation. The frequency dependence of the impedance due to space-charge relaxation in ion-conducting solids was first theoretically described by Macdonald [1953]. A number of further developments of this theory have been discussed in a recent review (Macdonald [2013]). The theory has also been extended to situations involving anomalous diffusion (Macdonald *et al.* [2011]). For the present purposes, we make use of a simple approximation developed for singly charged positive ions moving under the influence of relatively low applied voltages (Schütt and Gerdes [1992a, b]). This model is valid at low frequencies when the film thickness is much larger than the Debye screening length; the effective dielectric permittivity is given by (Schütt and Gerdes [1992b])

$$\epsilon(\omega) = \epsilon_s' \left(1 + \frac{\delta - 1}{1 + i\omega\delta\tau} \right), \quad (12)$$

which is recognized as a Debye relaxation with a space-charge relaxation time $\tau_{sc} = \delta\tau$. This relaxation can be observed at frequencies below those of bulk relaxation processes. In Eq. (12), ϵ_s' is the real part of the bulk relative permittivity for frequencies $\omega \ll \tau$. Also, $\delta = d/(2L)$, where d is the film thickness, $L = \sqrt{D\tau}$ the Debye screening length, D the diffusion coefficient of the moving ions, and $\tau = \epsilon_0\epsilon_s'/\sigma_{dc}$ the bulk electrical relaxation time. The density and mobility of the moving ions can be obtained from the high-frequency part of ϵ immediately below the frequency range of bulk polarization (ϵ_s'), by picking a frequency ω_X , where $\epsilon'(\omega_X) = X\epsilon_s'$. Provided that the approximation $1 + (\omega_X\tau\delta)^2 \approx (\omega_X\tau\delta)^2$ holds, the ion density is obtained by using the Nernst–Einstein relation ($D = \mu kT/e$, where kT is the thermal energy and e the unit charge) as

$$n = \left(\frac{\sigma_{dc}}{\sqrt{(X-1)\epsilon_0\epsilon_s'\omega_X}} \right)^4 \frac{\epsilon_0\epsilon_s' kT}{e^2 d^2}, \quad (13)$$

and μ is then straightforwardly obtained from

$$\sigma_{dc} = ne\mu. \quad (14)$$

There also exist other methods to obtain values of the Debye length from experimental data. (i) Klein *et al.* [2006] have shown that the loss tangent, that is, the ratio between the imaginary and real parts of the capacitance, displays a pronounced maximum at a frequency, $\omega_{max} = 1/(\tau\sqrt{\delta})$. (ii) The ratio between the asymptotic low-frequency capacitance, $\epsilon(0)$, and ϵ'_s directly gives δ . This simple method is complicated by the fact that the space-charge relaxation is very seldom ideal. If L is known, the ion density can be obtained from

$$n = \frac{\epsilon_b \epsilon_v kT}{L^2 e^2}, \quad (15)$$

and the mobility from Eq. (14) as before (Niklasson [2008]). The methods discussed earlier have been found to be very useful for analyzing ion density and mobility in cases of ion-conducting polymers (Niklasson [2008]), cellulose gels (Gråsjö *et al.* [2008]), the mesoporous magnesium carbonate material "Upsalite" (Pochard *et al.* [2014]), and suspensions of biological cells (Jönsson *et al.* [2006]). It should be noted that all these cases involve relatively low ion concentrations, that is, below 10^{19} cm^{-3} .

The case of two mobile ion species has been studied by Macdonald [1974b] and by Lelidis and Barbero [2005]. The single mobile ion case cannot be distinguished from the case where both kinds of ion have the same diffusion coefficient. When the ions exhibit significantly different diffusion coefficients, the impedance response changes so that two capacitance plateaus occur at low frequencies and two conductance plateaus can be seen instead of a single bulk conductance.

We now discuss some limitations of the theoretical framework introduced earlier. Firstly, it cannot account for the experimentally found dependence of the dielectric permittivity on electrode material (Serghei *et al.* [2009]). Secondly, the validity of the model for very high ion concentrations is in question. It is not clear how the Debye length should be interpreted when it becomes smaller than a nm and approaches ion-ion distances and eventually ion diameters. An analysis of the dielectric permittivity of special types of polymer electrolyte (Klein *et al.* [2006]) found out surprisingly low ion concentrations (<0.1% of the ions introduced into the polymer) together with mobilities that are unusually large for this kind of materials. Similar values were obtained by Macdonald *et al.* [2011] in a reanalysis of data on a LiTFSI polyethylenimine electrolyte (Bayrak Pehlivan *et al.* [2010]). This issue obviously merits a more detailed study in the future.

An alternative method to obtain ion concentration and mobility is to use transient current measurements. We will not go into details but give only a few references to theoretical work (Greeuw and Hoenders [1984], Frenning and Strømme [2001]). It should be noted that the same model can be used to extract a value of the mobility of Li ions intercalated from an electrolyte into an electrochromic film under the application of a potential step (Strømme Mattsson *et al.* [1999b], Strømme Mattsson [2000]). Models for IS response and transient currents can be extended in order to analyze a full three-layered device (Frenning *et al.* [2003]).

4.3.4.4 Experimental Results on Single Materials

In this section we present examples of experimental data obtained by IS on electrochromic materials and inorganic ion conductors. Most of our examples pertain to tungsten oxide, since this is the most studied material. We also review the application of IS to other frequently used electrochromic materials. We will present results from intercalation of Li^+ ions in different oxides. In most cases metallic Li foils were used as CEs and REs in an electrolyte consisting of 1M LiClO_4 in propylene carbonate.

Cathodic Electrochromic Materials: Tungsten Oxide. Figure 4.3.18 shows electrochemical impedance spectra on both amorphous and crystalline Li containing WO_3 films together with fits to the Randles

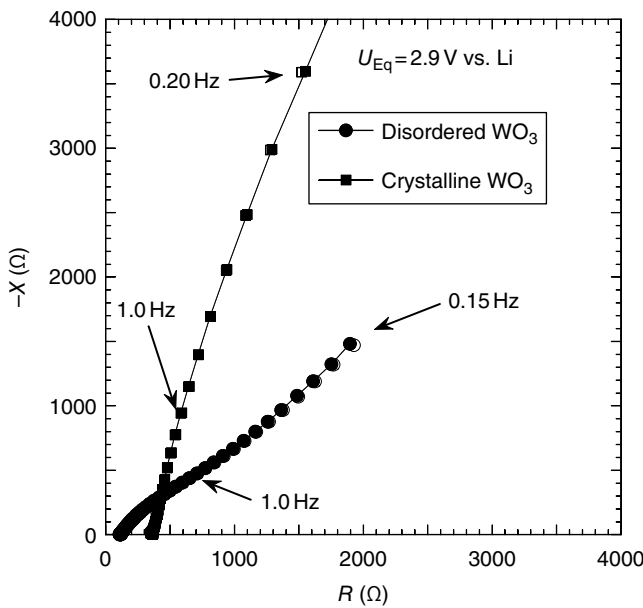


FIGURE 4.3.18 Electrochemical three-electrode impedance complex plane plots for the real (R) and the imaginary (X) parts of the impedance of crystalline (filled squares) and disordered (filled circles) WO_3 recorded at 2.9 V versus Li [Strømme Mattsson (2000)]. This equilibrium potential corresponds to ~ 0.004 Li/W atom ratio for the crystalline film and 0.03 Li/W for the amorphous one [Strømme Mattsson (2000)]. Included in the figure are also fits (open squares for crystalline and open circles for disordered WO_3) to a Randles circuit with a finite-length ordinary-diffusion element. Explicit frequency readings are shown at a few selected data points. Source: Strømme 2000. Reproduced with permission of Elsevier.

circuit (Strømme Mattsson [2000]). In the case of the crystalline film, only a part of the semicircle due to C_{dl} and R_{ct} can be observed. Impedance spectra were taken at several equilibrium potentials, and in all cases the impedance response corresponded to that of the Randles circuit with Z_{D} appropriate for ordinary semi-infinite diffusion. Figure 4.3.19 shows the obtained charge transfer resistance; associated with the barrier the Li ions have to pass to enter the WO_3 films. The results were discussed in more detail by Strømme Mattsson [2000], where information about the film preparation and the measurement conditions were also given. As is obvious also from Figure 4.3.18, the charge transfer resistance is much larger for the crystalline sample than for the disordered one.

In the following, we will focus on amorphous WO_3 films, as these absorb at visible wavelengths more efficiently than crystalline WO_3 in the colored state (Niklasson and Granqvist [2007]) and therefore are more interesting for smart window applications. Anomalous-diffusion models were found to accurately model the impedance response in this case; the thin-film deposition and measurement results were discussed by Niklasson *et al.* [2010]. The open-circuit voltage was about 3.2–3.3 V versus Li/Li⁺, and the potential drops as Li ions are intercalated into the film. Figure 4.3.20 shows impedance spectra recorded at different potentials versus Li/Li⁺ for amorphous tungsten oxide films produced with an O₂/Ar gas ratio of 0.16 during sputter deposition. Similar spectra were obtained for films deposited using other oxygen contents during the sputtering process. The oxygen content probably affects the stoichiometry of the films, but differences were too small to be readily detectable and the evidence point to a composition of WO_y with $y = 3.0 \pm 0.15$. For the spectrum acquired at 1.0 V, that is, at the highest degree of intercalation, the slope at the right-hand side to the semicircular part of the graph is clearly < 0.5 , and a “knee” where the slope approximately doubles can be observed. These characteristics are typical for the

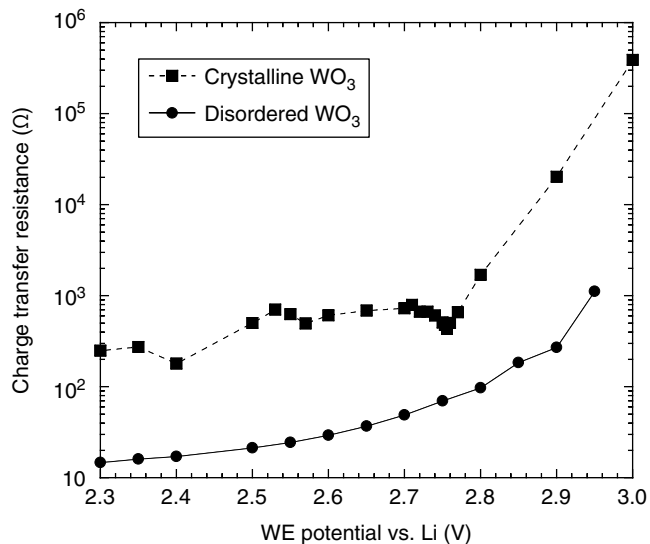


FIGURE 4.3.19 Charge transfer resistance for Li-ion intercalation into WO_3 . Data are obtained by electrochemical impedance spectroscopy from fits of the type shown in Figure 4.3.18.

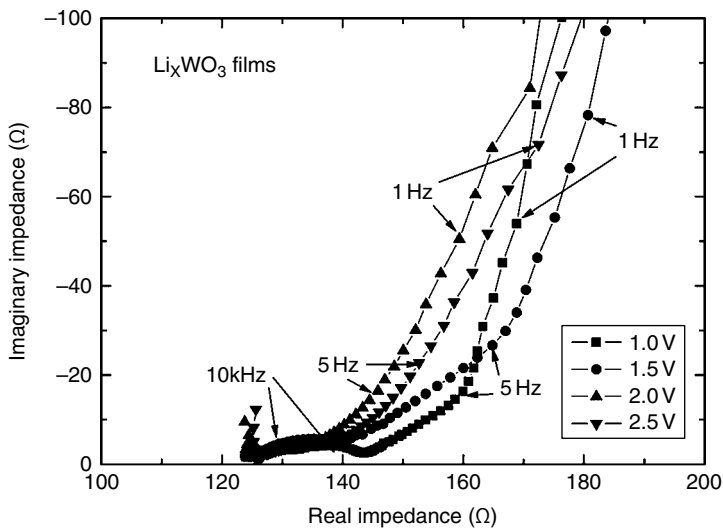


FIGURE 4.3.20 Electrochemical three-electrode impedance complex plane plot for the real part as a function of the imaginary part of the impedance of a Li-intercalated amorphous tungsten oxide film sputtered at an O_2/Ar ratio of 0.16. Spectra were taken at different potentials versus Li/Li^+ , as given in the inset.

AD1a model. The AD1b model on the other hand produces spectra with a slope >0.5 in the diffusion-dominated part of the spectra, as observed in spectra acquired at potentials above 2 V. The impedance spectrum taken at 1.5 V seems to exhibit an intermediate behavior. These features can be used as a rule of thumb to check which diffusion model that should be appropriate for a given set of data. However it is

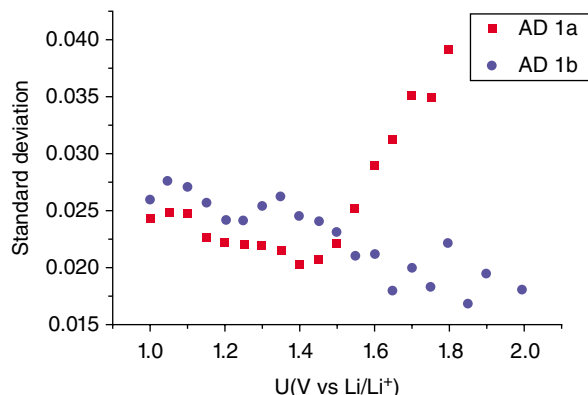


FIGURE 4.3.21 Standard deviation of two anomalous-diffusion model fits to experimental impedance spectroscopy data for the film considered in Figure 4.3.20 as a function of potential versus Li/Li⁺.

important to point out that the rule is not rigorous and must be validated by actual fitting of the models to the data.

Therefore the standard deviation of fits to Randles equivalent circuits using either of the two anomalous-diffusion models for the Warburg element was compared, as shown in Figure 4.3.21 for one of our samples. It was shown that the AD1b model gave the best fits to spectra acquired during the initial intercalation stages (i.e., at high potentials vs. Li/Li⁺), while fits to the AD1a model produced lower standard deviation values at low potentials. The limit between the ranges of validity of the two models was in the range of ~1.5–1.8 V versus Li/Li⁺ for different samples. It is also seen that it is not easy to discriminate between the two models in the low potential region. The number of diffusing particles is conserved in the AD1b model, and it should be expected to apply at potentials above ~2 V versus Li/Li⁺ where intercalation is reversible. The number of diffusing particles is not conserved in the AD1a model, and therefore it is interesting to note that during intercalation of ions into amorphous tungsten oxide films at potentials below 2 V versus Li/Li⁺, irreversibility appears and it is not possible to extract all ions that have been inserted into the film. The irreversibility observed is probably associated with the formation of Li compounds in the film (Bressers and Meulenkamp [1998], Li and Fu [2010]).

Figure 4.3.22 shows a complex capacitance plot of the same data that were discussed in Figure 4.3.20 (Niklasson *et al.* [2010]). The capacitance representation emphasizes the low-frequency region. It is clearly seen that it is possible to estimate a chemical capacitance by extrapolating the semicircular part of the data to low frequencies, that is, to the right in the figure. The resulting EDOS obtained from fits to the spectra in Figure 4.3.22 using the AD1b model for potentials >1.5 V and the AD1a model for the lower potentials are shown in Figure 4.3.23 (Niklasson *et al.* [2010]). The EDOS is compared with band structure calculations of the DOS for monoclinic crystalline WO₃ (Strømme *et al.* [2004]). To facilitate comparison between experimental and theoretical data, the zero of the energy scale has been put at the conduction band edge. In Figure 4.3.23, it is shown that the shape of the computed DOS and the experimental EDOS diverges at ~1.3 eV above the measured conduction band edge, corresponding to ~2 eV versus Li/Li⁺. As the intercalation proceeds further, the EDOS decreases, while the DOS obtained from band structure calculations continues to increase. This discrepancy seems to be related to effects of irreversibility, probably arising from complex reactions between WO₃ and Li (Li and Fu [2010], Yoon *et al.* [2014]) in this potential range. If reactions forming species such as Li₂O in the samples occur at low potentials, discrepancies from DOS calculations for pure tungsten oxide would indeed be expected.

The magnitude of the EDOS obtained from IS is much lower than the calculated DOS. This may be attributed to kinetic effects, that is, that the ions do not have time to penetrate the whole film during the time duration of the experiment. Alternatively, the low-frequency capacitance seen in Figure 4.3.22

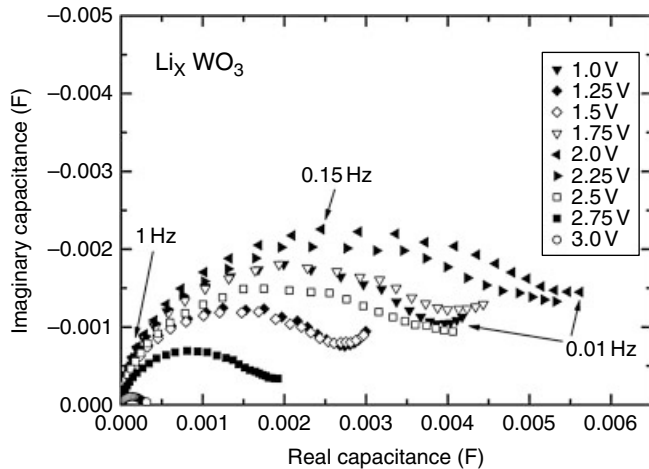


FIGURE 4.3.22 Complex plane capacitance plot for the real part as a function of the imaginary part of the capacitance of a Li-intercalated amorphous tungsten oxide film sputtered at an O₂/Ar ratio of 0.16. Spectra were taken at different potentials versus Li/Li⁺, as given in the figure.

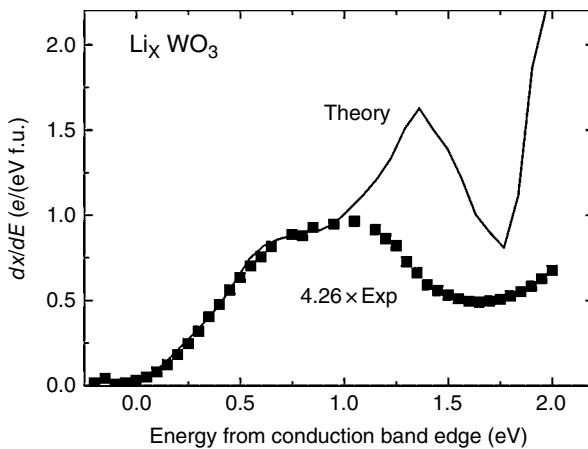


FIGURE 4.3.23 Electrochemical density of states as a function of energy from the conduction band edge for the amorphous tungsten oxide film considered in Figure 4.3.22. Experimental data are depicted by squares and have been multiplied with a factor of 4.26. The computed electronic density of states for monoclinic WO₃ is shown for comparison. Source: Strømme 2004. Reproduced with permission of American Physical Society.

might be a trapping capacitance (Bisquert [2003a]) and not the real asymptotic chemical capacitance. Interestingly, analogous experiments with proton intercalation using films prepared at identical conditions gave a smaller DOS/EDOS factor, namely, 1.5 (Niklasson *et al.* [2010]), instead of 4.26 as for the Li-intercalation case in Figure 4.3.23.

Figure 4.3.24 shows effective diffusion coefficients obtained from fitting EIS data to the anomalous-diffusion models for samples deposited at different O₂/Ar ratios. As Li ions are intercalated into the

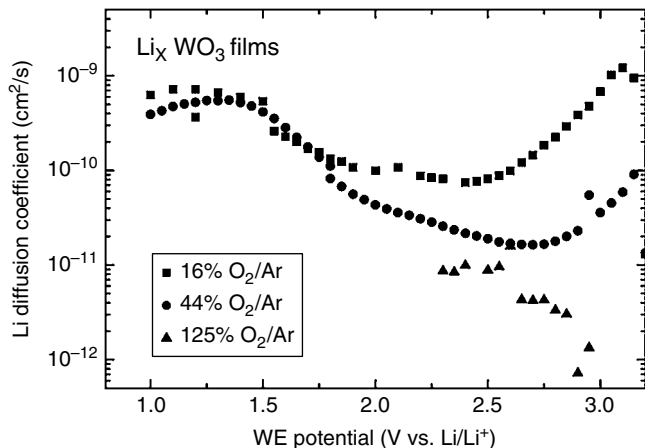


FIGURE 4.3.24 Effective Li diffusion coefficients as a function of potential versus Li/Li⁺ are shown for three amorphous tungsten oxide films deposited at different O₂/Ar gas ratios, as given in the inset. Impedance spectroscopy data were given in Figure 4.3.18 for the 125% O₂/Ar film and in Figure 4.3.20 for the 16% O₂/Ar ratio films.

film, the figure shows that the diffusion coefficient first decreases and subsequently increases to a maximum just below 1.5 V, that is, fairly close to the potential where lithium oxide can be expected to form (Bressers and Meulenkamp [1998]).

The diffusion coefficients obtained in the present work are higher than those obtained for the disordered film of Figure 4.3.18, deposited at the O₂/Ar ratio of 1.25 (Strømme Mattsson [2000]), for which the ordinary-diffusion model was used. The values of D vary in a wide range between 10⁻¹² and 10⁻⁹ cm²/s. It is observed that the O₂/Ar ratio present during sputtering appears to influence the diffusion coefficient; lower oxygen content consistently gives higher Li diffusion coefficients. For comparison, the chemical diffusion coefficient from IS measurements on crystalline WO₃ films (see Figure 4.3.18) and the average diffusion coefficient from transient current measurements are presented in Figure 4.3.25. The minima in the diffusion coefficient are due to phase changes in the crystalline structure. There is a significant difference in the information obtained from the IS and the transient current measurements, where the latter ones do not reveal the phase changes.

Tungsten trioxide is a widely studied electrochromic material and the impedance response has been measured several times. The results are consistent in that they can invariably be fitted to a Randles circuit, but details in the spectra vary. In particular values of the ion diffusion coefficient and the other circuit parameters depend not only on the crystallinity but also on the deposition method and deposition conditions of the films. Since tungsten oxide easily becomes nonstoichiometric when deposited as a thin film, probably also the stoichiometry plays a role. Data have been presented for films produced by thermal evaporation (Ho *et al.* [1980], Bohnke and Bohnke [1990], Lee *et al.* [2000, 2001]), electron-beam evaporation (Yoshiike *et al.* [1984]), sputtering (Pyun and Bae [1996]), sol-gel deposition (Wang and Bell [1999], Sharma *et al.* [2002]), and various other techniques (Bohnke and Bohnke [1988]). The data presented here are in general agreement with other studies of sputtered films, as well as with the detailed study of Lee *et al.* [2000, 2001]. Recent studies have fitted experimental data for amorphous (Fabregat-Santiago *et al.* [2001]) and crystalline WO₃ (Bobics *et al.* [2008]) to Randles circuits with Warburg elements obtained from coupled diffusion-trapping models, with good agreement. Garcia-Canadas *et al.* [2004] studied the chemical capacitance as well as the diffusion coefficient of films deposited by electron-beam evaporation and found that to a good approximation $C_{ch} \sim x^{0.65}$ and $D \sim 1/x$. In recent years there has emerged an interest in the electrochromic properties of mixed transition metal oxides. Impedance studies of pure and Ni-doped tungsten oxide films produced by sputtering were

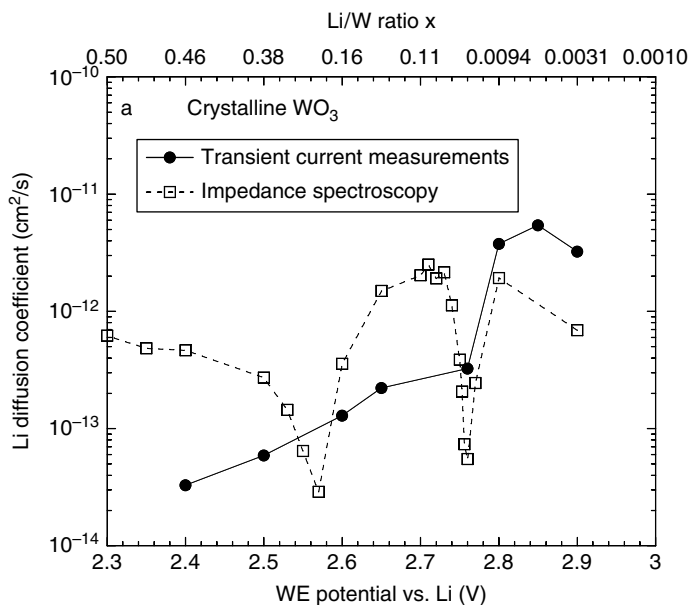


FIGURE 4.3.25 Diffusion coefficients for Li in crystalline WO_3 as obtained from electrochemical transient current measurements and from electrochemical impedance spectroscopy (Strømme Mattsson [2000]). The diffusion coefficient obtained by impedance spectroscopy is the chemical diffusion coefficient relevant for a specific composition (specified on the upper x -axis), while that obtained from the current measurements is an average diffusion coefficient for all compositions lower than the composition value specified on the upper x -axis. Source: Strømme 2000. Reproduced with permission of Elsevier.

carried out by Green *et al.* [2012]. The experimental data were fitted with anomalous-diffusion models, the chemical capacitance increased, and the diffusion coefficient decreased as a function of x . In addition the charge transfer resistance was much larger at the bleached state in the case of Ni-WO_3 .

Cathodic Electrochromic Materials: Titanium Oxide. We now present data on fluorinated titanium oxide films in order to highlight the information that can be obtained from the temperature dependence of impedance spectra. Figure 4.3.26 shows two electrochemical three-electrode impedance spectra taken at different temperatures on a heavily intercalated Li containing fluorine-doped Ti oxide (Strømme Mattsson *et al.* [1997]). The impedance response corresponds to the Randles circuit with a $Z_{\tilde{D}}$ of finite-length type. (Details about the film preparation and the measurement conditions can be found in papers of Strømme Mattsson *et al.* [1996b, 1997].) The high-frequency semicircle clearly has a center below the real axis; hence it is appropriate to use a CPE for C_{dl} . The low-frequency response is a model case of a Warburg ordinary-diffusion element of finite-length type. The impedance spectra taken at different temperatures and different Li compositions (equilibrium potentials) were fitted to the Randles circuit with excellent agreement. By this procedure, the results for the circuit elements, displayed in Figure 4.3.27, were obtained (Strømme Mattsson *et al.* [1996b]).

Figure 4.3.27a shows that both the charge transfer resistance and its activation energy decrease with decreasing equilibrium potential (increasing ion content in the film). These quantities are associated with the barrier that the Li ions have to traverse to enter the film. The more Li ions in the film, the easier it gets for additional ions to enter. From the way the activation energy changes, one can also draw conclusions about the symmetry properties of the energy barrier (Strømme Mattsson *et al.* [1996b]). From Figure 4.3.27b we observe that the power-law parameter m_{DL} is rather independent of temperature

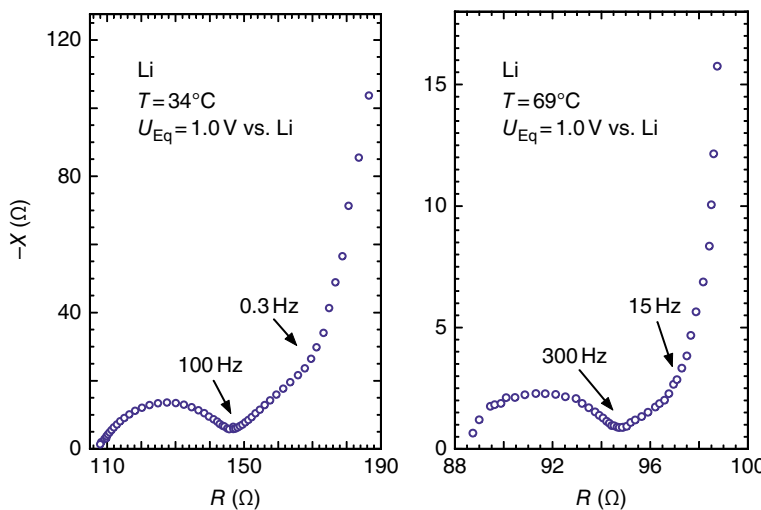


FIGURE 4.3.26 Electrochemical three-electrode impedance complex plane plots for the real (R) and the imaginary (X) parts of the impedance of fluorine-doped Ti oxide films recorded at the displayed temperatures at an equilibrium potential of 1.0 V versus a Li reference electrode (corresponding to ~0.85 Li/Ti unit) (Strømme Mattsson *et al.* [1997]). Explicit frequency readings are shown at a few selected data points. Source: Strømme 2000. Reproduced with permission of Elsevier.

and Li-ion composition (equilibrium potential). This is in accordance with the fact that the distributed capacitance exponent described by this parameter only depends on the surface geometry (Strømme Mattsson *et al.* [1996a]). Finally, Figure 4.3.27c shows that the chemical diffusion process is thermally activated with the activation energy virtually independent of Li-ion content (equilibrium potential). The value of ~0.5 eV is comparable with that of Li-ion diffusion in amorphous WO_3 films (Nagai *et al.* [1986]), but somewhat higher than the activation energy for proton diffusion (Randin and Viennet [1982]). The activation energy being independent of the Li content in the film indicates that the ions move unaffected by each other so that they are only influenced by their surroundings. In fact, it was shown (Strømme Mattsson *et al.* [1996b]) that the obtained activation energy for diffusion gave a Li-ion “jump length” corresponding to the distance between neighboring cells in the anatase structure of the nanocrystallites (Strømme Mattsson *et al.* [1996b]) in the films under study.

Counter Electrode Materials. The anodic electrochromic materials and ion storage materials have not been so widely studied by IS as the cathodic electrochromic materials discussed earlier. In general, the main features of the impedance spectra are similar to those shown earlier. The impedance response of nickel oxide films with protons (Gorenstein *et al.* [1990]) as well as lithium ions (Decker *et al.* [1992], Artuso *et al.* [2002]) as the intercalated species has been studied. The spectra of films intercalated by protons can be fitted by a Randles circuit, with a finite-length Warburg element (Gorenstein *et al.* [1990]). The charge transfer resistance decreases, and the low-frequency-limiting capacitance as well as the diffusion impedance both increase with increasing equilibrium potential, that is, during proton extraction. The ion diffusion is thus slowed down as the hydrated nickel oxide colors. Sputtered mixed Ni–V oxide films exhibited diffusion coefficients in a Li electrolyte in the range between 10^{-12} and $10^{-11} \text{ cm}^2/\text{s}$ (Artuso *et al.* [2002]). Impedance data for iridium oxide films have also been modeled within the framework of a Randles circuit (Glarum and Marshall [1980]). Frequently more complex equivalent circuits were necessary, especially for iridium oxide films obtained by (electro)chemical techniques (Terezo *et al.* [2001], Sziraki and Bobics [2002]). The situation appears to be more clear for sputtered films (Pauporté and Durand [2000], Backholm *et al.* [2008]). In these cases Randles circuits with ordinary-diffusion and

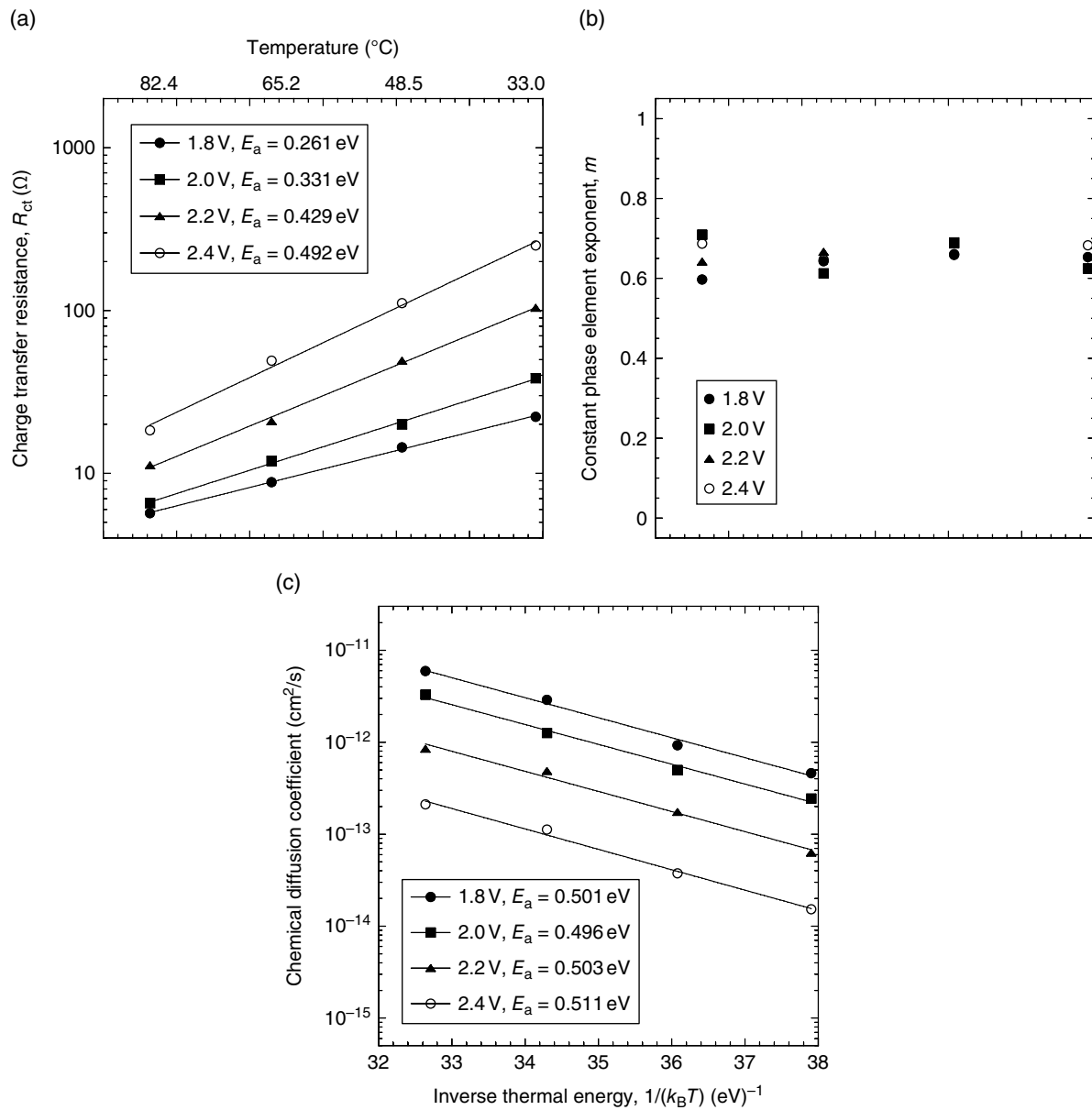


FIGURE 4.3.27 Magnitude of the charge transfer resistance R_{ct} (a), double-layer CPE exponent m (b), and Li diffusion coefficient D (c) for Li ions in fluorine-doped Ti oxide versus inverse thermal energy (Strømme Mattsson *et al.* [1996b]). Data were obtained from fits of impedance spectra of the type shown in Figure 4.3.26 to a Randles circuit, using a finite-length ordinary-diffusion element. The displayed activation energies E_a in part (a) and (c) were obtained from exponential fits (lines) to the individual data points. Source: Strømme 2000. Reproduced with permission of Elsevier.

AD1b elements were used, together with a parallel resistance to account for possible side reactions in the electrochemical cell. Reported diffusion coefficients vary very much for sputtered iridium oxide (Pauporté and Durand [2000], Backholm *et al.* [2008]). Backholm *et al.* [2008] found qualitative agreement between the experimental EDOS and the theoretical DOS of IrO_2 for both iridium and mixed iridium-tantalum oxide films. In a detailed study of lithium intercalation into vanadium oxide films (Bae and Pyun [1995]), the impedance spectra were interpreted with the extended Randles circuit of Franceschetti and Macdonald [1982].

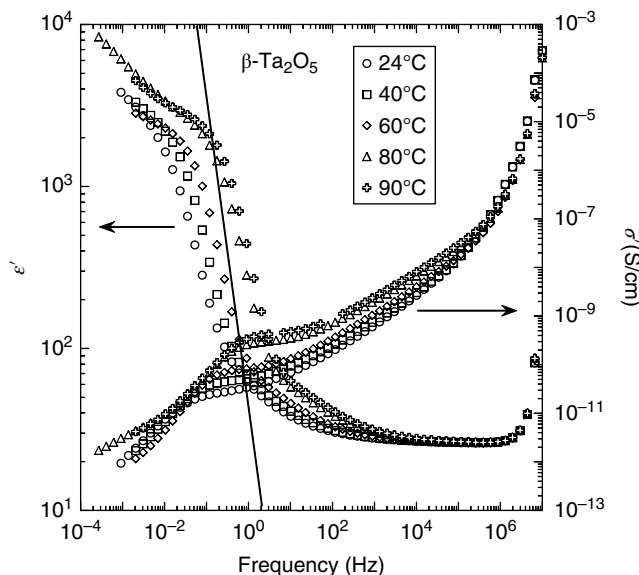


FIGURE 4.3.28 Real parts of the dielectric permittivity (ϵ') and the ac conductivity (σ') as a function of frequency for a $\beta\text{-Ta}_2\text{O}_5$ sample (Strømme Mattsson et al. [1999a]). The measurements were performed at the displayed temperatures. Included in the figure is also a straight line with a slope of ω^{-2} .

Inorganic Thin-Film Ion Conductors. We now discuss the determination of ion concentration and mobility from the impedance response of thin tantalum pentoxide films. Such films are very interesting as an ion conductor, in particular because it is possible to make the electronic leakage current very low. We also make some comments on ZrO_2 .

Figure 4.3.28 shows a series of two-electrode IS measurements on a proton containing crystalline $\beta\text{-Ta}_2\text{O}_5$ sample (Strømme Mattsson et al. [1999a]). The data are presented in terms of the real parts of the dielectric permittivity (ϵ') and the ac conductivity (σ'). The measurements were performed at temperatures between 24 and 90°C. It was found that the dc conduction process has an activation energy of 0.42 eV, with the room temperature value of σ_{dc} being 25.3 pS/cm (Strømme Mattsson et al. [1999a]).

The behavior of both ϵ' and σ' in the frequency region between 10^{-2} and 10^2 Hz clearly shows a space-charge limited response (Schütt and Gerdts [1992a]). A straight line with a slope of ω^{-2} is included in the figure to show that the Schütt and Gerdts model may be used to extract approximate values of n and μ . We observe that ϵ' , when its magnitude is slightly below 10^3 , is approximately parallel to the line. The somewhat smaller slope of ϵ' as compared with the line can partly be attributed to surface roughness of the Ta_2O_5 samples (Schütt and Gerdts [1992a]) and partly to the fact that the factor $(\omega_X \tau \delta)^2$ is only ~ 5 (as can be deduced from the calculations as follows). Applying Eq. (13) to the room temperature ϵ' and using an X value of $941/\epsilon'_s = 36.4$ ($\epsilon'_s = \epsilon_\infty = 25.8$), which corresponds to a ω_X value of $0.0235 \text{ Hz} \times 2\pi = 0.148 \text{ s}^{-1}$, gives the proton density in the sample as $n \approx 3.5 \times 10^{17} \text{ protons/cm}^3$. Further, Eq. (14) gives the proton mobility as $\mu \approx 4.5 \times 10^{-10} \text{ cm}^2/\text{Vs}$. These numbers imply that $(\omega_X \tau \delta)^2 \approx 5$ and that the relation $1 + (\omega_X \tau \delta)^2 \approx (\omega_X \tau \delta)^2$ required for the validity of Eq. (13) is not completely satisfied. The obtained proton density and mobility must therefore be considered as rough order of magnitude estimates. An independent determination of n and μ can be obtained from transient current measurements (Strømme Mattsson et al. [1999a]). This procedure gives $n \approx 1.3 \times 10^{17} \text{ protons/cm}^3$ and $\mu \approx 5.5 \times 10^{-10} \text{ cm}^2/\text{Vs}$, which corresponds very well to, and hence verifies, the parameters obtained from the space-charge limited impedance response.

It has been shown that Li ions and their charge-balancing electrons enter the $\beta\text{-Ta}_2\text{O}_5$ at a higher energy than that for intercalation into, for example, WO_3 (Strømme Mattsson and Niklasson [1999]). This finding, together with the fact that Li ions in tantalum oxide thin films can exhibit mobilities of the order of $10^{-9} \text{ cm}^2/\text{Vs}$ (Frenning *et al.* [2001]), makes the Ta oxide potentially very interesting as a Li-ion conductor in a WO_3 -based electrochromic device.

Electrochemical three-electrode IS has been performed for proton intercalation on sputtered ZrO_2 by Jonsson *et al.* [1999]. The data can be fitted very well to the Randles equivalent circuit. The charge transfer resistance was found to be very high at low intercalation levels and then drops several orders of magnitude at medium intercalation levels. The reason for the high R_{ct} could be a layer grown on the surface of the film that slows down the transport of ions from the electrolyte into the film. The diffusion coefficient was determined to be in the range of 10^{-13} to $10^{-12} \text{ cm}^2/\text{s}$, which is much lower than in Ta_2O_5 .

4.3.4.5 Experimental Results on Electrochromic Devices

IS has been carried out on devices with WO_3 as the cathodic electrochromic layer, CEs of nickel oxide, iridium oxide, polyaniline or Prussian blue, and polymer electrolytes (Katsume *et al.* [1986], Friestad *et al.* [1997], Chen [2013]). The equivalent circuit for a whole device becomes very complicated and there is no detailed agreement on how to construct it. In the works quoted earlier, simplified Randles-type circuits were used for the two electrochromic layers or else only interface properties were considered. The ion conductor has been modeled by a pure resistance, a simplified Randles circuit, or even neglected. Extraction of device parameters from the data fitting was reported. However, it is clear that it is difficult to distinguish the contributions from the different layers in a device, in particular if the interfacial impedances, ion diffusion impedances, and so on, are of the same order of magnitude. For quality control of electrochromic devices, IS is a very time-consuming process, since a spectrum down to low frequencies should be taken at a number of equilibrium potentials.

Transient current measurements have been performed on laminated devices (Jonsson *et al.* [2004]) as well as on ATF devices (Frenning *et al.* [2003]). The laminated electrochromic devices consisted of cathodic tungsten oxide and anodic nickel oxide films that were laminated with a layer of polymer electrolyte, namely, PEO-LiTFSI (polyethylene glycol mixed with lithium trifluoromethanesulfonate). Both Li ions from the electrolyte and protons, probably introduced into the films during deposition, may act as charge carriers in this type of device. Very different responses were obtained depending on the direction of the electric field, that is, in which direction the charge carriers were moving. The ATF devices consisted of nanocrystalline thin films of hydrated NiO and ZrO_2 as well as amorphous WO_3 . The main charge carriers were protons, probably introduced into the nickel oxide during deposition. When protons were transported from the NiO layer into the WO_3 layer in the coloration process, a peak was observed at about 3000 s. When the protons were transported in the opposite direction, a much smeared-out peak was seen at about 10,000 s. Subsequently, the current decreased, because the ions arrived at a blocking electrode. The peak was modeled by Frenning *et al.* [2003], and its position corresponds to an ion mobility of the same order of magnitude as in a ZrO_2 film. The initial transient current response of the two types of device is similar although the response is slower in the all-solid-state device. In both devices the ion transport is markedly quicker from WO_3 into NiO than in the opposite direction. Pronounced peaks and shoulders are only present when ions are transported from the NiO layer toward the WO_3 layer. The asymmetric behavior indicates that barriers of different magnitude are present at the interfaces between the oxide layers and that these barriers strongly affect the electrochromic response.

IS seems also to be of large interest as a nondestructive tool for studies of aging of electrochromic devices. Initial steps in this direction have been taken and the impedance response of tungsten oxide films during repeated cycling has been studied (Pehlivan *et al.* [2010]).

4.3.4.6 Conclusions and Outlook

Today there exists a good understanding of the impedance response of electrochromic materials. Experiments on oxide electrodes deposited onto an electron-conducting substrate and immersed in an electrolyte, invariably show the characteristic behavior of extended Randles circuits. By fitting the data to the

equivalent circuit, detailed information on chemical capacitances and ion diffusion coefficients in the oxide film, as well as processes occurring at the interfaces, can be obtained. The chemical capacitance can give important information on the electronic DOS of the electrochromic film. We have reviewed a number of investigations of transition metal oxides. In the search for improved electrochromic materials, mixed oxide films are gaining increased attention, and it is expected that more IS work will be carried out on these materials in the future.

Some details of the Randles circuit require further study. First, the double-layer capacitance is in many cases more properly modeled with a CPE. This gives information on the mesoscopic structure of the oxide–electrolyte interface. Frequently the diffusion impedance exhibits a power-law behavior, a so-called anomalous diffusion. The physics behind the AD models needs to be further elucidated, especially their relation to diffusion-trapping models. Because models for the Warburg diffusion element are becoming more complicated, more fitting parameters are introduced and to distinguish between different models will require very high quality data in an extended frequency range. In the low-frequency range further studies are needed to clarify the nature of the low-frequency capacitance. How can we distinguish between chemical and trapping capacitances?

In order to further improve our understanding of electrochromic systems, it seems necessary to make use of other spectroscopy techniques. A scheme for combining IS with color impedance (ac colorimetry) and mass impedance (ac electrogravimetry) has been described by Agrisuelas *et al.* [2009]. To investigate the color impedance, an ac signal is applied to the electrochromic film, and the resulting transmittance modulation is measured. This method should give information not only on the ion transport but also on the kinetics of the coloration, which is an electronic process. Initial work has been reported on WO_3 (Gabrielli *et al.* [1994], Kim *et al.* [1997], Garcia-Belmonte *et al.* [2004], Bueno *et al.* [2008]) and NiO (Cordoba-Torresi *et al.* [1990]) films. It appears that the color impedance exhibits a similar low-frequency relaxation behavior as the electrical impedance in a significant range of frequencies (Garcia-Belmonte *et al.* [2004], Bueno *et al.* [2008]). This may indicate that chemical diffusion is the rate-limiting step in the coloration process. In mass impedance the changes in the mass of the films are measured by an electrochemical quartz crystal microbalance. These techniques will certainly open up interesting possibilities for more detailed studies of electrochromic coloration and charge intercalation processes.

4.3.5 Fast Processes in Gigahertz–Terahertz Region in Disordered Materials

4.3.5.1 Introduction

Glasses and ionic conductors are some examples of a wide range of disordered materials. These materials behave similarly over a broad dynamic range of frequencies from terahertz (THz) to below gigahertz (GHz) in the electromagnetic spectrum. The complex conductivity $\sigma^* = \sigma' + i\sigma''$ and dielectric permittivity $\epsilon^* = \epsilon' + i\epsilon''$ are generally used to describe this behavior. The $\sigma'(\nu)$ and the dielectric loss $\epsilon''(\nu)$ are related by $\sigma' = 2\pi\epsilon''\epsilon_0$ (ϵ_0 is the permittivity of free space). It was Jonscher [1977] who first demonstrated that the disordered materials followed a “universal dielectric response” (UDR) at $\nu < \text{GHz}$. This follows a sublinear power law in the frequency-dependent conductivity, $\sigma'(\nu)$. In addition, linear or even superlinear increase of $\sigma'(\nu)$ had been detected under specific conditions, for example, at higher frequencies (Wong and Angell [1976], Lee *et al.* [1991], Le Stanguennec and Elliott [1994], Cramer *et al.* [1995a], Sidebottom *et al.* [1995], Lunkenheimer *et al.* [1996], Lunkenheimer *et al.* [1997], Dyre and Schröder [2000], Lunkenheimer *et al.* [2000], Lee and Stutzmann [2001], Roling *et al.* [2001], Helgren *et al.* [2002], Lunkenheimer *et al.* [2002]).

The behavior of the disordered materials in the region between GHz to THz is one of the least investigated areas of research. Lunkenheimer and Loidl [2003a] addressed this gap in the GHz–THz region and showed that a sublinear–superlinear power-law (SLPL) behavior is common to all classes of disordered materials. This chapter is inspired by the extensive work of Lunkenheimer and Loidl and other researchers cited in this chapter. The focus of this chapter is on a supercooled liquid transitioning into a glass at low temperatures, which is a classical disordered material. In this chapter, the Lunkenheimer–Loidl plot is presented and discussed, followed by brief descriptions of specific features of the plot, the

excess wing, $\epsilon''(\nu)$ -minimum, and boson peak. For the benefit of the readers, a summary of selected works on a model material, glycerol, is presented in this chapter.

4.3.5.2 Lunkenhimer–Loidl Plot and Scaling of the Processes

A molecule rattling inside a cage of its neighbors is the simple depiction of a glass. This motion leads to a fast secondary β -relaxation over 10^{-10} to 10^{-12} s. An Arrhenius-type temperature dependence describes this motion:

$$v(T) = v_\infty \exp\left(\frac{E_A}{k_B T}\right). \quad (16)$$

where v_∞ is the relaxation rate in the high-temperature limit, E_A the activation energy, and k_B the Boltzmann constant. The relaxation is about $\tau_\infty \equiv 10^{-13}$ s as one approaches the high-temperature limit. This corresponds to the local orientational fluctuations with viscosity approaching values of about 10^{-2} to 10^{-1} poise.

An empirical Vogel–Fulcher–Tammann (VFT) equation describes the temperature dependence of viscosity and the relaxation time (Vogel [1921], Fulcher [1925], Tammann and Hesse [1926]):

$$v(T) = \frac{1}{2\pi\tau(T)} = v_\infty \exp\left[\frac{-DT_0}{T-T_0}\right] \quad (17)$$

where $v_\infty = (2\pi\tau_\infty)^{-1}$, D is a constant, and T_0 or ideal glass transition temperature is the Vogel temperature. Temperature dependence of the $v(T)$ of “fragile” materials deviates from Arrhenius-type behavior, while that of “strong” materials is close to the behavior. The parameter D is a quantity of fragility of materials (Angell [1985]). At $T = T_0$, the divergence of Eq. (17) is attributed to Kauzmann paradox (Angell [1985]) occurring in the entropy measurement (Kauzmann [1942, 1948], Zallen [1983], Johari [2000a, b]). The Gibbs–DiMarzio model (Gibbs and DiMarzio [1958a]) resolves the Kauzmann paradox by a phase transition. The VFT equation describes a correlated motion of the molecule within the cage, corresponding to dynamic glass transition or α -relaxation (Gibbs and DiMarzio [1958b], Adam and Gibbs [1965]). A boson peak is in the THz regime (Karpov *et al.* [1983], Malinovsky *et al.* [1987], Buchenau *et al.* [1992], Elliott [1992], Schirmacher *et al.* [1998]). As one approaches ultraslow relaxation rates, clusters begin to fluctuate (Fischer [1993], Patkowski *et al.* [2000]). These assignments and interpretations continue to attract further research, disagreements, and revision.

Figure 4.3.29 shows the schematics of these processes (Kremer and Schönhals [2003a]). A simple double minimum potential can be used to describe various features. Angell [1997], Stillinger [1995], and Debenedetti and Stillinger [2001] have shown that the same simple double minimum potential can be used for glass-forming systems using the landscape model.

The mode-coupling theory (MCT) of the glass transition uses a generalized nonlinear oscillator equation (Bengtzelius *et al.* [1984], Leutheuser [1984], Götze [1985], Götze and Sjogren [1992]):

$$\frac{d^2\phi_q(t)}{dt^2} + \Omega^2\phi_q(t) + \zeta\frac{d\phi_q(t)}{dt} + \Omega^2 \int_0^t m_q(t-\tau)\frac{d\phi_q(\tau)}{d\tau} d\tau = 0 \quad (18)$$

where the normalized density correlation function $\phi(t)_q$ is defined as

$$\phi(t)_q = \frac{\langle \Delta\rho_q(t)\Delta\rho_q(0) \rangle}{\langle \Delta\rho_q^2 \rangle} \quad (19)$$

where $\Delta\rho_q(t)$ are density fluctuations at a wave vector q , Ω is a macroscopic oscillator frequency, and ζ denotes a frictional contribution.

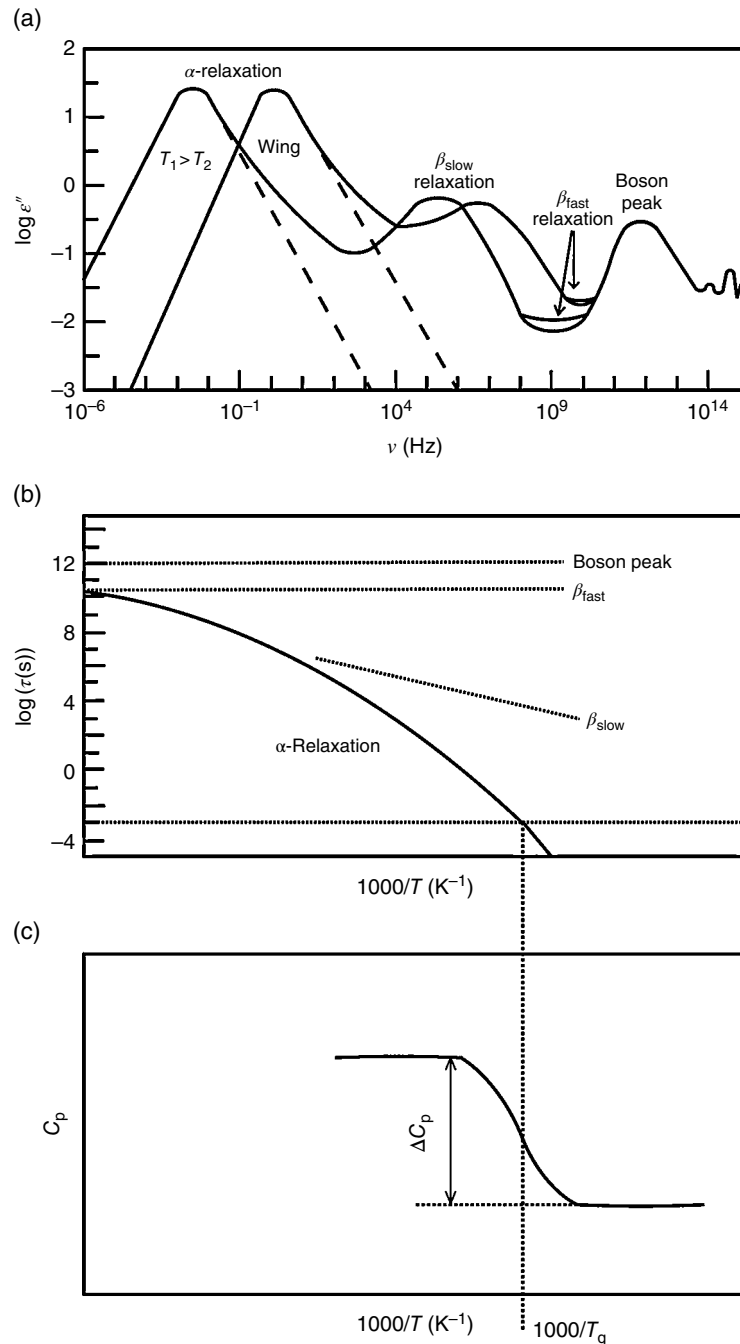


FIGURE 4.3.29 (a) Lunkhenheimer and Loidl plots for two temperatures, T_1 and T_2 . (b) Relaxation rate versus inverse temperature of different processes shown in (a). (c) Specific heat at constant pressure versus inverse temperature for a specific cooling rate. Source: Kremer 2003 a. Reproduced with permission of Springer.

The first three terms in Eq. (18) correspond to a damped harmonic oscillator. The fourth term contains a memory function, $m_q(t-\tau)$, which is due to a depiction of a hard-sphere system interacting only by elastic scattering. The integral term comes from the internal frictional losses of the correlated motions within the cage. The faster contribution corresponds to a β -relaxation, while the slower one, a

α -relaxation. The relaxation time diverges at a critical temperature T_c , and a phase transition from an ergodic ($T > T_c$) to a nonergodic ($T < T_c$) state occurs. In its idealized version of the MCT, for $T > T_c$, the relaxation time of τ_α of the α -relaxation scales as follows:

$$\tau_\alpha \sim \eta \sim \left[\frac{T_c}{T - T_c} \right]^\gamma \quad (20)$$

where γ is a constant. The relaxation function of the α -relaxation can be described as

$$\phi_q(t) \sim \exp \left[- \left(\frac{t}{\tau_\alpha} \right)^{\beta_{KWW}} \right] \quad (21)$$

with $0 < \beta_{KWW} \leq 1$ (KWW), where ϕ_q is the amplitude of the α -relaxation. For $T > T_c$, the relaxation time distribution should be temperature independent. Above and close to the critical temperature T_c , the minimum of the susceptibility ϵ''_{\min} , ω_{\min} between the α -relaxation and the β -relaxation, should follow a power law:

$$\epsilon''_{\min} \sim \left[\frac{T - T_c}{T_c} \right]^{\frac{1}{2}} \quad (22)$$

The scaling of these processes follows a master function:

$$\epsilon''(\omega) = \frac{\epsilon''_{\min}}{a + b} \left[b \left(\frac{\omega}{\omega_{\min}} \right)^a + a \left(\frac{\omega_{\min}}{\omega} \right)^b \right] \quad (23)$$

The exponents a and b in equation are related as follows:

$$\frac{\Gamma^2(1+b)}{\Gamma(1+2b)} = \lambda = \frac{\Gamma^2(1+a)}{\Gamma(1+2a)} \quad (24)$$

where Γ is the Γ -function. These exponents are related to each other as follows:

$$\omega_{\min} \sim \left[\frac{T - T_c}{T_c} \right]^{\frac{1}{2a}} \quad (25)$$

$$\omega_{\max} \sim \left[\frac{T - T_c}{T_c} \right]^{\left(\frac{1}{2a} + \frac{1}{2b} \right)} \quad (26)$$

Derivatives of the relaxation rate with the respect to $1/T$ capture the dynamic glass transition spanning across microscopic (10^{-11} s) and ultraslow fluctuations (10^6 s). Equations (27)–(29) show the temperature dependence of the derivatives of the Arrhenius equation (16), VFT equation (17), and MCT equation (22), respectively:

$$\frac{d \log \nu}{d(1/T)} = \frac{-E_A}{k_B} \cdot \log e \quad (27)$$

$$\frac{d \log \nu}{d(1/T)} = -(DT_0) \left(1 - \frac{T_0}{T} \right)^{-2} \log e \quad (28)$$

$$\frac{d \log \nu}{d(1/T)} = \frac{\gamma \cdot \log e}{(T_c/T^2) - (1/T)} \quad (29)$$

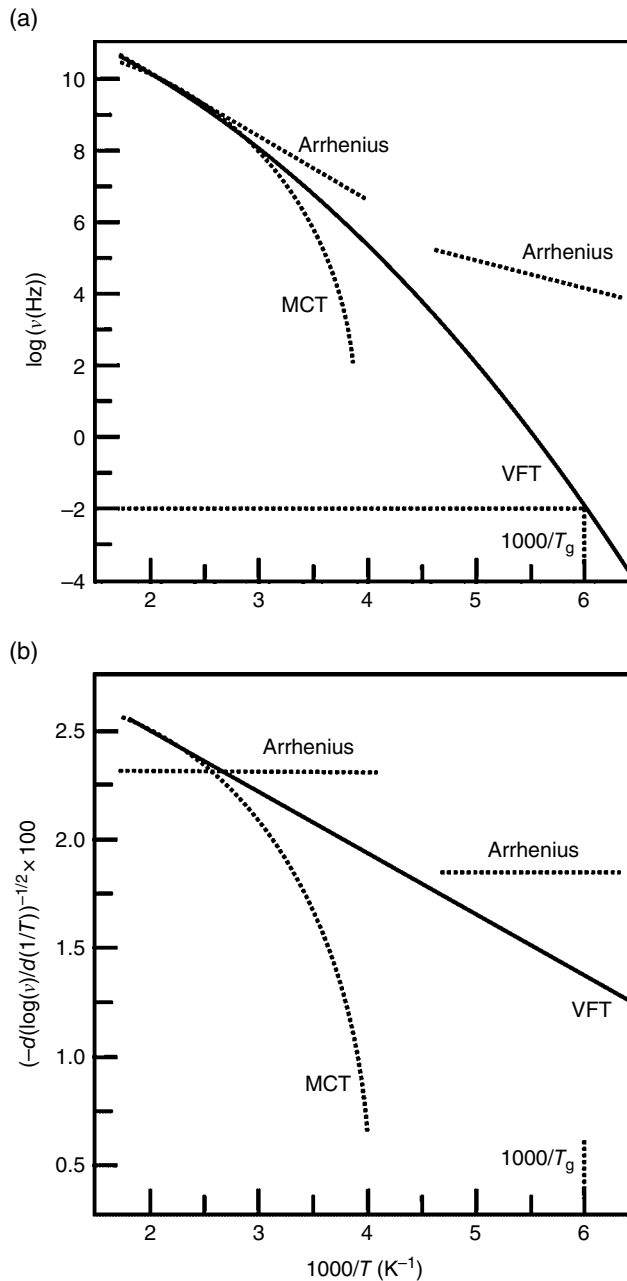


FIGURE 4.3.30 Scaling behaviors: (a) predicted by Eqs. (16) (Arrhenius), (17) (VFT), and (20) (the MCT); (b) differential quotient $(-\frac{d}{d}(\log(\nu))/d(1/T))^{-1/2} \times 100$ for the behaviors shown in (a). Source: Kremer 2003 a. Reproduced with permission of Springer.

Figure 4.3.30 shows the plots of temperature dependence of the derivatives. For detailed discussion of the scaling, the readers are referred to Kremer [2003a], cited in this chapter.

4.3.5.3 Dynamic Processes

In the Lunkenheimer and Loidl plot (Figure 4.3.29a), the α -process is responsible for the loss peak at $v_p \approx v_\tau = 1/(2\pi(\tau_\alpha))$. The plot shows various different processes universal to glasses over a wide frequency

range of about 19 decades. At frequencies some decades above ν_p , the empirical functions break down. An “excess wing” shows up (Figure 4.3.29a), which can be described by a second power law, $\epsilon'' \sim \nu^{-b}$ with $b < \beta$, in addition to the power law $\nu^{-\beta}$, commonly found at $\nu > \nu_p$. All these features under various conditions and materials can be collapsed into a single master curve as a part of the α -relaxation via Nagel scaling (Dixon *et al.* [1990]).

Figure 4.3.29a shows a slow β -relaxation in a glass-forming material. Johari [2000a, b] has demonstrated that these secondary relaxation processes are a rather universal property of glass formers including simple molecular glass formers, called the Johari–Goldstein β -relaxations (Dixon *et al.* [1990], Kudlik *et al.* [1999]). A “type A” glass former shows an excess wing without a β -process. A “type B” glass former shows a β -process only. This classification is oversimplified and does not fit some materials. The excess wing is simply the high-frequency side of a β -peak, dominated by the α -peak (Schneider *et al.* [2000]).

The boson peak appears in the THz region (Petry and Wuttke [1995], Rössler *et al.* [1997]), which is a universal feature of glass-forming materials (Angell *et al.* [1969], Strom *et al.* [1974], Wong and Angell [1976], Strom and Taylor [1977], Zallen [1983], Liu and Angell [1990], Cole and Tombari [1991], Zarzycki [1991], Perova and Vij [1996], Schneider *et al.* [1998], Perova *et al.* [1999], Schneider *et al.* [1999]). This is related to the imaginary part of the susceptibility via $\chi'' = \epsilon'' \sim S_v$ (Lovesey [1984]) and also the corresponding peak in $\chi''(\nu)$. Dipolar liquids (Chantry and Gebbie [1965]) show an IR absorption peak in the THz region, termed Poley absorption (Poley [1955], Vij and Hufnagel [1985]) interpreted in terms of vibrational motions of the dipoles (Hill [1963], Coffey *et al.* [1987]). Between the α -peak and the boson peak, a minimum in $\chi''(\nu)$ must exist. Several experimental results support these interpretations. This is schematically shown as the hatched area in Figure 4.3.29a.

Figures 4.3.31–4.3.38 are adapted from the excellent overview of these processes by Lunkhenheimer and Loidl [2003b]. Figure 4.3.31 shows the dielectric spectra for a model material, glycerol ($T_g \approx 85$ K), with the α -peak situated at a low frequency near T_g , shifting to higher frequencies with increasing temperature. With a fragility (m) of 53, glycerol (Bohmer *et al.* [1993]) is strong in terms of fragility. The spectra of $\epsilon''(\nu)$ in Figure 4.3.31b follow the Lunkhenheimer and Loidl plot (Figure 4.3.29a). These spectra exhibit asymmetrically shaped α -relaxation peaks, accompanied by relaxation steps in $\epsilon'(\nu)$ as seen in Figure 4.3.31a. The regime around ν_p can be described by the Cole–Davidson (CD) function, as shown by the lines in Figure 4.3.31. At frequencies $\nu > \nu_p$, $\epsilon''(\nu)$ follows a power law $\epsilon'' \sim \nu^{-\beta}$. At higher frequencies, deviations from this power law occur. At $T \geq 273$ K for glycerol, $\epsilon''(\nu)$ shows a smooth transition into a minimum. At lower temperatures, an excess wing develops showing up as a second power law, ν^{-b} with $b < \beta$ before the minimum region is reached. A peak appears in the THz region, whose frequency and amplitude depend on temperature. A steplike decrease appears near 1 THz (Figure 4.3.31a). Additional resonance-like features appear around 10 THz, due to the onset of the intramolecular excitations (Du *et al.* [1994], Wuttke *et al.* [1994], Wuttke *et al.* [2000]).

The Excess Wing. Nagel scaling can be applied to the $\epsilon''(\nu)$ -curves for different temperatures and different materials, including the wing, by plotting $Y = w^{-1} \log_{10}[\epsilon'' \nu_p / (\Delta \epsilon \nu)]$ versus $X = w^{-1}(1 + w^{-1}) \log_{10}(\nu / \nu_p)$. Here w denotes the half-width of the loss peak, normalized to that of the Debye peak, ν_p is the peak frequency, and $\Delta \epsilon$ is the relaxation strength. Nagel scaling is generally phenomenological in nature. Nevertheless, the Nagel scaling works well in many materials. Figure 4.3.32 shows that the Nagel scaling is applied to glycerol. Small deviations from the master curve have been reported for low values of X (Menon and Nagel [1991, 1993], Schönhals *et al.* [1993], Kudlik *et al.* [1996], Leheny *et al.* [1996]). Figure 4.3.32 reveals a good scaling up to $X \approx 9$ with small deviation for higher X values, as shown in the inset.

A constant loss should be reached near the Vogel–Fulcher temperature T_{VF} (Menon and Nagel [1995], Leheny and Nagel [1997]) by a low-temperature extrapolation of $w(T)$ and $b(T)$ curves of various glass formers. Figure 4.3.33 shows the data for glycerol. The exponent b is obtained from fits with a phenomenological ansatz comprising a sum of two power laws go the high-frequency wing of the α -peak and some additional contributions for the $\epsilon''(\nu)$ -minimum. The crosses show the results reported by Leheny and Nagel [1997]. The solid lines demonstrate possible low-temperature extrapolations of $b(T)$. The dashed lines indicate T_{VF} . The inset shows the prefactor of the power law $c_b \nu^{-b}$ used for the

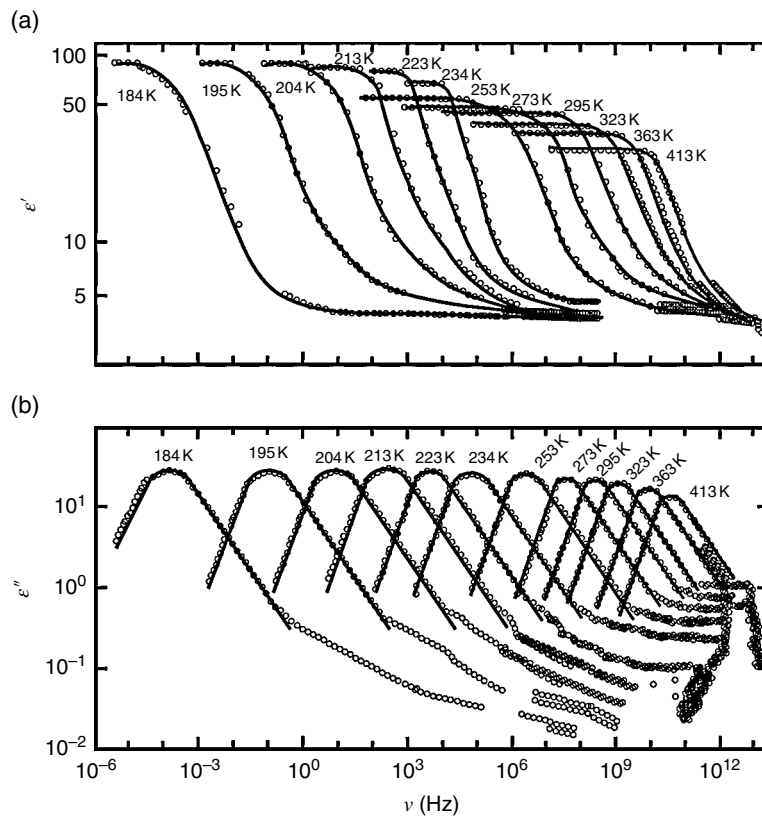


FIGURE 4.3.31 (a) Real and (b) imaginary parts of the dielectric permittivity versus frequency of glycerol over a temperature range of 184–413 K. The lines are fits of the appropriate region near ν_p with the CD function performed simultaneously on real and imaginary parts.
Source: Lunkenheimer 2003 b. Reproduced with permission of Springer.

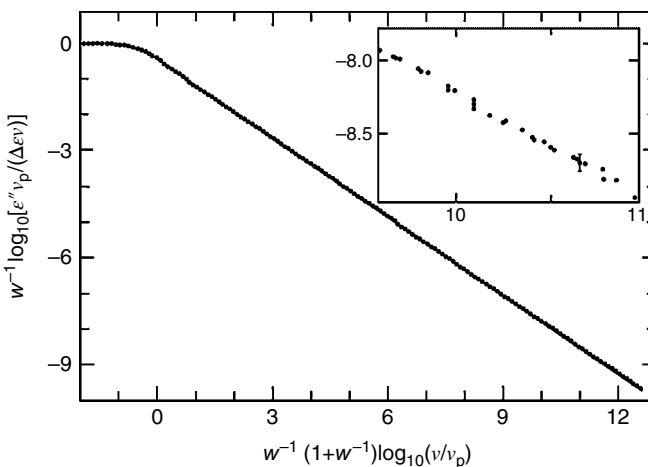


FIGURE 4.3.32 Dielectric loss of glycerol at 195, 223, and 363 K. The inset shows a closer view of the high-frequency region.
Source: Lunkenheimer 2003 b. Reproduced with permission of Springer.

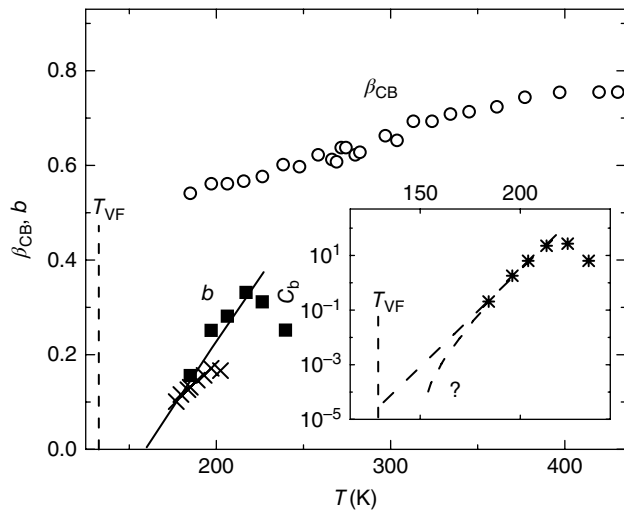


FIGURE 4.3.33 α -Peak width parameter β_{CB} (circles) and the excess-wing exponent b (squares) versus temperature for glycerol. Source: Lunkenheimer 2003 b. Reproduced with permission of Springer.

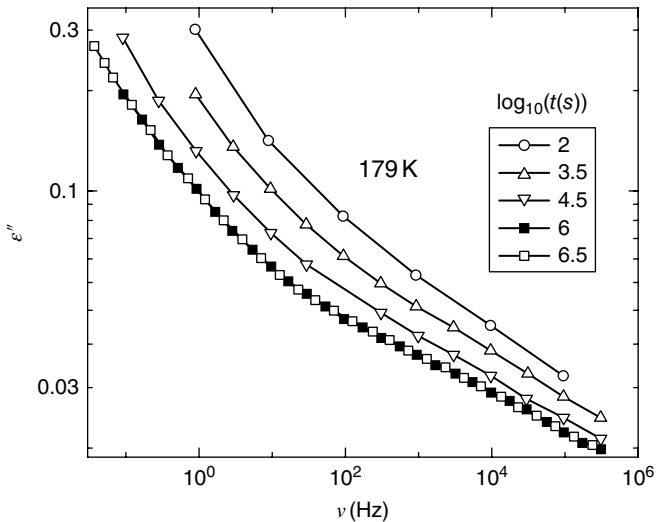


FIGURE 4.3.34 Dielectric loss versus frequency of glycerol for different aging times, t Schneider *et al.* [2000]. The lines connect the symbols for $t \leq 10^6$ s. The spectra for the maximum aging time of $10^{6.5}$ s have been taken in an extended frequency range. Source: Lunkenheimer 2003 b. Reproduced with permission of Springer.

description of the excess wing. The dotted lines in the inset demonstrate that a nonzero of c_b at T_{VF} is not conclusive (Lunkenheimer *et al.* [1999]).

Figure 4.3.34 shows loss spectra for glycerol at a temperature below T_g (179 K) for different times after reaching this temperature (Schneider *et al.* [2000]). The excess wing has developed into a shoulder after the maximum aging times of five weeks. A β -relaxation is responsible for the excess wing in glycerol. Then the excess wing develops into a shoulder due to a β -relaxation on aging.

The $\epsilon''(\nu)$ -Minimum. A $\epsilon''(\nu)$ -minimum of glass-forming materials exists in the GHz–THz range. This region can be described as a simple crossover from the α -peak or the excess wing to the boson peak. Therefore, the following ansatz with $b < 1$ and $n \geq 1$ can be used:

$$\epsilon'' = c_b \nu^{-b} + c_n \nu^n \quad (30)$$

Figure 4.3.35 shows the $\epsilon''(\nu)$ -minimum analyzed using Eq. (30) with smallest value of $n = 1$ for glycerol. Within idealized MCT, the minimum region can be approximated by the sum of two power laws:

$$\epsilon''(\omega) = \frac{\epsilon''_{\min}}{a+b} \left[a \left(\frac{\nu}{\nu_{\min}} \right)^{-b} + b \left(\frac{\nu}{\nu_{\min}} \right)^a \right] \quad (31)$$

The solid lines are first with the MCT prediction (Eq. (31) with $a = 0.325$ and $b = 0.63$). For the lowest temperatures, the increase toward the boson peak approaches power laws $\epsilon'' \sim \nu^3$, as indicated by the dashed lines. The inset demonstrates that the simple superposition ansatz (Eq. (30)) is not sufficient to explain the shallow minimum.

Dielectric spectroscopy and KK relation can be used to calculate both $\epsilon'(\nu)$ and $\epsilon''(\nu)$. The $\epsilon'(\nu)$ adds more insight to high-frequency dynamics. From the idealized MCT prediction,

$$\epsilon' = f_e + \frac{\epsilon}{a+b} \left[a \cot \left(\frac{b\pi}{2} \right) \left(\frac{\nu}{\nu_{\min}} \right)^{-b} - b \cot \left(\frac{a\pi}{2} \right) \left(\frac{\nu}{\nu_{\min}} \right)^a \right] \quad (32)$$

where f_e is a constant. MCT also predicts a critical temperature dependence of the $\epsilon''(\nu)$ -minimum near T_c . For $T > T_c$,

$$\nu_{\min} \sim (T - T_c)^{1/2a} \quad (33)$$

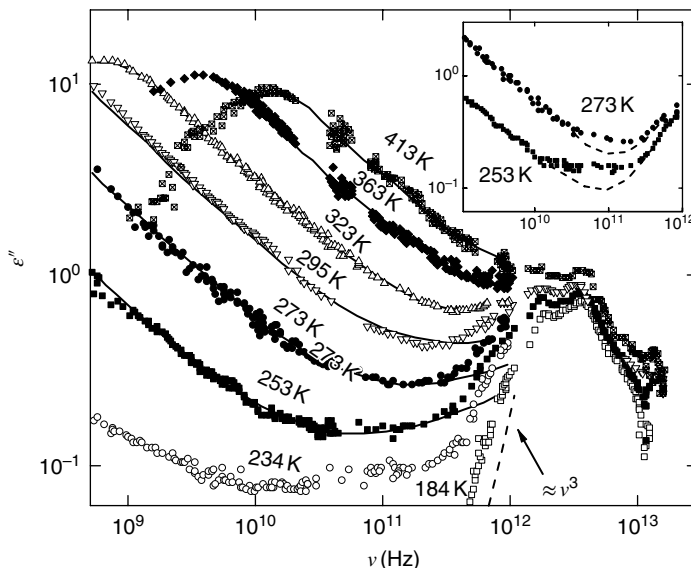


FIGURE 4.3.35 Dielectric loss versus frequency of glycerol in the minimum and boson peak region. Source: Lunkhenheimer 2003 b. Reproduced with permission of Springer.

$$\epsilon_{min} \sim (T - T_c)^{1/2} \quad (34)$$

$$\nu_\tau \sim (T - T_c)^\gamma \text{ with } \gamma = \frac{1}{2a} + \frac{1}{2b} \quad (35)$$

Figure 4.3.36 shows the frequency dependence of ϵ' for the high-frequency region in glycerol. The solid lines are fits with the MCT prediction (Eq. (32)) with f_e the only free parameters. The other parameters used for fitting are from the fits of $\epsilon''(\nu)$.

Figure 4.3.37 shows the temperature dependence of ϵ''_{min} , ν_{min}^{2a} , and $\nu_\tau^{1/\gamma}$ for glycerol. Fitting the MCT predictions (Eqs. (33)–(35)) to the data yields straight lines. Note extrapolation of all three quantities to a T_c of 262 K shown as solid lines and also the deviation from the straight line fit for temperatures near T_c . This is attributed to a smearing out of the critical behavior due to hopping processes, which is expected to show up as a “knee” (though not seen in Figure 4.3.36) in $\epsilon''(\nu)$ at T_c .

Figure 4.3.38 shows that experimental scattering measurements can be used to verify the dielectric susceptibility (χ''). The solid lines show the light scattering results (Du *et al.* [1994], Wuttke *et al.* [1994], Leheny *et al.* [1996]), and the open circles, the neutron scattering results. Note that the light and neutron scattering datasets have been vertically shifted to give a comparable intensity of the α -peak. The dielectric and light scattering results show a α -peak, a minimum, and a boson peak. In the case of the dielectric results, the ratio of the boson peak and α -peak amplitudes is much smaller than for the scattering results. These results clearly demonstrate that the MCT predictions can be experimentally verified.

The Boson Peak. Figure 4.3.35 shows a double-peak structure in the boson peak region, with peaks located at about 1.8 and 3.5 THz. The far-infrared (FIR) absorbance data by Perova and Vij [1996] have shown a double peak as well and also the “fine structure” above about 5 THz. Figure 4.3.38 shows the same double peak. At the low-frequency side of the boson peak, two regimes are identified. A shallow increase in $\epsilon''(\nu)$ just above ν_{min} is observed. The critical law of MCT at higher temperatures can describe this behavior. But at higher frequencies, a steep increase is observed on approaching $\epsilon'' \sim \nu^3$ for $T \rightarrow T_g$, shown as dashed line in Figure 4.3.35.

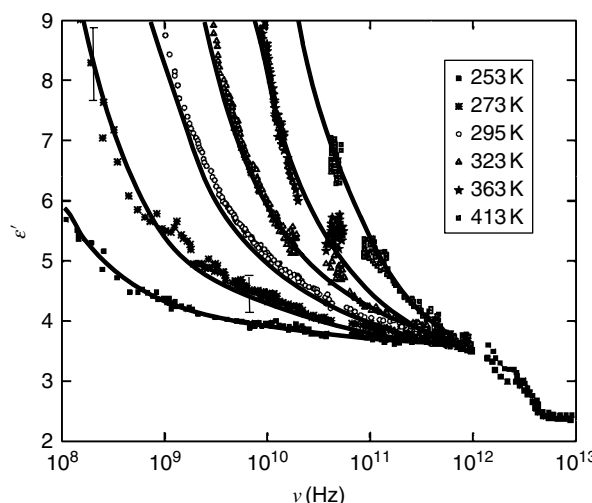


FIGURE 4.3.36 $\epsilon'(\nu)$ versus frequency of glycerol for different temperatures. Source: Lunkhenheimer 2003 b. Reproduced with permission of Springer.

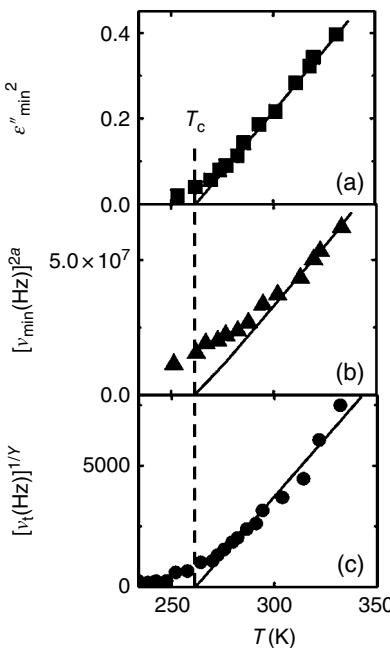


FIGURE 4.3.37 Temperature dependence of (a) the amplitude, (b) the position ν_{\min} of the $\epsilon''(\nu)$ -minimum, and (c) the α -relaxation rate ν_r of glycerol. Source: Lunkenheimer 2003 b. Reproduced with permission of Springer.

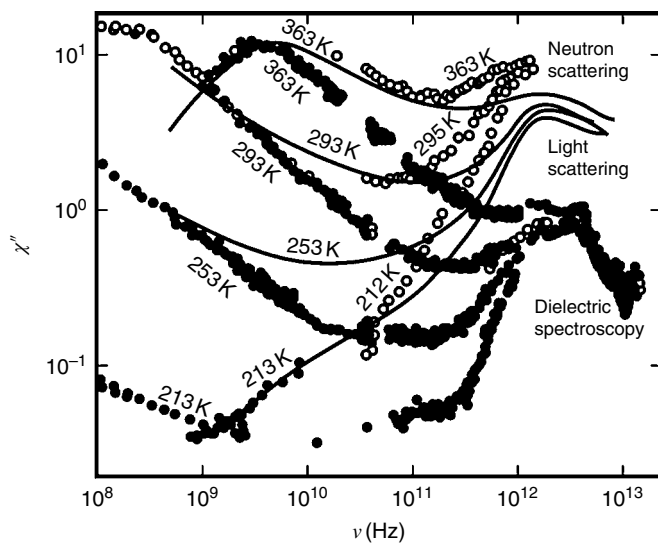


FIGURE 4.3.38 Frequency dependence of the imaginary part of the susceptibility of glycerol obtained from different experimental methods. Source: Lunkenheimer 2003 b. Reproduced with permission of Springer.

4.3.5.4 Final Remarks

This chapter presents some glimpses of various features and processes over 19 decades of frequencies particularly in the GHz-THz frequency region. In summary, this field continues to excite and intrigue researchers. For detailed in-depth discussion of several models and results on several different materials, the readers are referred to Lunkenheimer and Loidl [2003b], Richert and Blumen [1994], and recent three-part review, Capaccioli *et al.* [2015] and Ngai *et al.* [2015a, b].

Novel tools are being used in advancing the fundamental understanding of the disordered materials. For example, Ponga *et al.* [2015] have used picosecond photoacoustics (BPA) to investigate the energy dispersion and mode attenuation of the vibrational excitations of indomethacin (IMC) in the frequency range 10–20 GHz and inelastic X-ray scattering (IXS) to study of the high-frequency limit (THz). These results show that the state of the glass can be identified fully by the fictive temperature (T_f) and temperature of measurement (T). The sound velocity jump at T_f can be used to calculate the nonergodicity parameter and thus the relaxation time. Another tool is THz time-domain spectroscopy (Sibik and Zeitler [2016]), which allows direct measurement of real and imaginary parts of dielectric and optical properties. Continued active research in this area shows promise for fundamental advancements in the theory of the glass transition process.

Acknowledgments

The author thanks graduate students Braeden Clark, Priyatham Tumurugoti, and Ruhil Dongol in the Sundaram Group for their help in preparing the illustrations. The author acknowledges Kyocera Corporation, Japan, for the support of Inamori Professorship. He also appreciates the inspiration and support from Dr. James Ross Macdonald.

4.4 CORROSION OF MATERIALS

Michael C. H. McKubre,¹ Digby D. Macdonald,² and George R. Engelhardt³

¹SRI International, Menlo Park, CA, USA

²Department of Nuclear Engineering, University of California at Berkeley, Berkeley, CA, USA

³OLI Systems, Inc., Cedar Knolls, NJ, USA

4.4.1 Introduction

Corrosion is defined as the spontaneous degradation of a reactive material by an aggressive environment, and, at least in the case of metals in condensed media, it occurs by the simultaneous occurrence of at least one anodic (metal oxidation) and one cathodic (e.g., reduction of dissolved oxygen) reaction. Because these partial reactions are charge transfer processes, corrosion phenomena are essentially electrochemical in nature. Accordingly, it is not surprising that electrochemical techniques have been used extensively in the study of corrosion phenomena, both to determine the corrosion rate and to define degradation mechanisms.

Of all of the electrochemical techniques that are available, IS promises to be the most valuable because of its ability, in a single experiment, to detect interfacial relaxations covering a wide range of relaxation times. The application of this technique in corrosion science became possible in the practical sense only within the past decade, with the advent of techniques for measuring transfer functions at subhertz frequencies (see Section 3.1.3). Instruments and techniques are now available for measuring

interfacial impedances at frequencies down to the 10^{-3} to 10^{-4} Hz region, where relaxations involving adsorbed intermediates and diffusing species appear.

Over this same period, considerable development has taken place in the theoretical treatment of the impedance properties of corroding interfaces (Macdonald and McKubre [1981]). These theoretical developments have been especially important, since they serve to enhance the quantitative nature of the technique. Indeed, IS has emerged as probably the most powerful technique currently available for identifying corrosion reaction mechanisms, and methods are now being developed to extract kinetic parameters (rate constants, transfer coefficients) for multistep reaction schemes.

In this section, we review the application of IS to the study of corrosion phenomena. Emphasis is placed on illustrating how the method is applied to identify the different processes that occur at a corroding interface. We also review the use of impedance measurements for measuring corrosion rate, since this was the initial application of the technique in corrosion science and engineering. The use of IS to analyze other cause-and-effect phenomena of interest in corrosion science, including electrochemical hydrodynamic, fracture, and electrochemical mechanical processes, is also discussed.

4.4.2 Fundamentals

The response of any physical system to a perturbation of arbitrary form may be described by a transfer function:

$$H(s) = \frac{\bar{V}(s)}{\bar{I}(s)} \quad (1)$$

where s is the Laplace frequency and $\bar{V}(s)$ and $\bar{I}(s)$ are the Laplace transforms of the time-dependent voltage and current, respectively (Goldman [1950]). In terms of the steady-state sinusoidal frequency domain, the transfer function becomes

$$H(j\omega) = \frac{F[V(t)]}{F[I(t)]} = \frac{V(j\omega)}{I(j\omega)} \quad (2)$$

where F signifies the Fourier transform and $V(j\omega)$ and $I(j\omega)$ are the sinusoidal voltage and current, respectively. Provided that the system is linear, that causality is obeyed, and that the interface is stable over the time of sampling (see later), the transfer function may be identified as an impedance $Z(j\omega)$. Because they are vector quantities, $H(j\omega)$ and $Z(j\omega)$ are complex numbers containing both magnitude and phase information. From a theoretical viewpoint, the impedance (or, more generally, the transfer function) is one of the most important quantities that can be measured in electrochemistry and corrosion science. This is because, if it is sampled over an infinite bandwidth, it contains all the information that can be obtained from the system by purely electrical means.

An important requirement for a valid impedance function is that the system be linear. Theoretically, this implies that the real and imaginary components transform correctly according to the KK relationships (discussed later in this section). Practically, linearity is indicated by the impedance being independent of the magnitude of the perturbation, a condition that is easily (although seldom) tested experimentally.

4.4.3 Measurement of Corrosion Rate

The Stern–Geary equation provides a direct relationship between the steady-state corrosion current and the “dc” resistance across the interface (Stern and Geary [1957]):

$$i_{\text{corr}} = \left[\frac{\beta_a \beta_c}{2.303(\beta_a + \beta_c)} \right] \left(\frac{1}{R_p} \right) \quad (3)$$

where β_a and β_c are the Tafel constants for the anodic and cathodic partial reactions, respectively, and R_p is the polarization resistance (Mansfeld [1976]). Because corroding interfaces are inherently reactive by

nature, owing to the presence of capacitive, psuedoinductive, and diffusional impedance terms, it is evident that the polarization resistance is given only by the difference of the measured impedance at sufficiently low and high frequencies:

$$R_p = |Z(j\omega)|_{\omega \rightarrow 0} - |Z(j\omega)|_{\omega \rightarrow \infty} \quad (4)$$

Measurement of the series resistance at the high-frequency limit normally presents few problems, because $Z(j\omega)$ becomes nonreactive at frequencies as low as 10 kHz, in most cases. On the other hand, in the low-frequency region, reactance is commonly observed at frequencies in the vicinity of 10^{-3} Hz, so that special precautions must be adopted to obtain reliable data (Syrett and Macdonald [1979]). The need for these precautions is independent of the form of the perturbation applied to the interface. Accordingly, they apply equally well to the use of potential or current steps and triangular and sinusoidal voltage perturbations in the measurement of the polarization resistance, as well as to the determination of "steady-state" current–voltage curves. Practically, therefore, it is necessary to use a sufficiently low-frequency (sinusoidal perturbation), low-voltage scan rate (small-amplitude cyclic voltammetry (SACV)) or to wait a long enough time (potential or current step perturbation) before acquiring the response data (e.g., current) for calculating the polarization resistance.

The problem of acquiring impedances at sufficiently low frequencies is amply demonstrated by the data (Syrett and Macdonald [1979]) for 90 : 10 Cu/Ni alloy corroding in flowing seawater (Figure 4.4.1). Thus, for an exposure time of 22 h, the impedance function can be defined over the entire bandwidth, and an accurate value for R_p may be obtained by probing the interface at frequencies above 0.01 Hz. On the other hand, at much longer exposure times, frequencies as low as 0.0005 Hz are not sufficient to completely define the interfacial impedance, and considerable extrapolation is required to acquire a value for R_p .

It is important to emphasize again that, because time-domain functions can be synthesized as linear combinations of sinusoidal (sine and cosine) components (Fourier synthesis), this problem is not limited to IS. Thus, failure to use a sufficiently low sweep rate in the case of SACV will also introduce significant error (Figure 4.4.2), depending upon which resistance is considered as being the parameter of interest (R_d or R_{app} ; Figure 4.4.3; Macdonald [1978a]). Interestingly, our experience in using a variety of electrochemical monitoring techniques indicates that SACV is superior, in many respects, to IS for determining the polarization resistance. Thus, quite reliable values for R_p for systems as reactive as that shown in Figure 4.4.1 generally can be obtained using a single voltage sweep rate of 0.1 mV/s, which is quite accessible using standard electrochemical instrumentation.

Because most impedance measurements are made sequentially at discrete frequencies, the total data acquisition time can be expressed as

$$T = \sum_i \frac{n_i}{f_i} \quad (5)$$

where n_i is the number of cycles at frequency f_i . The minimum acquisition time is obtained by setting $n_i = 1$. Therefore,

$$T_{\min} = \sum_i \frac{1}{f_i} \quad (6)$$

and it is apparent that the minimum acquisition time is dominated by the low-frequency components. For example, the impedance data shown in Figure 4.4.1, for an exposure period of 164 h, required an acquisition time of more than 1 h. This contrasts with an acquisition time of 100 s required to obtain a reliable value for R_p using SACV with a voltage sweep rate of 0.1 mV/s and a peak-to-peak amplitude for the triangular voltage excitation of 5 mV. Because SACV does not readily yield the mechanistic information afforded by IS, the two methods are best regarded as being complementary in nature.

According to Fourier's theorem, all small-amplitude techniques must yield identical results (i.e., the same interfacial impedance), regardless of the form of the excitation. This is clearly the case for

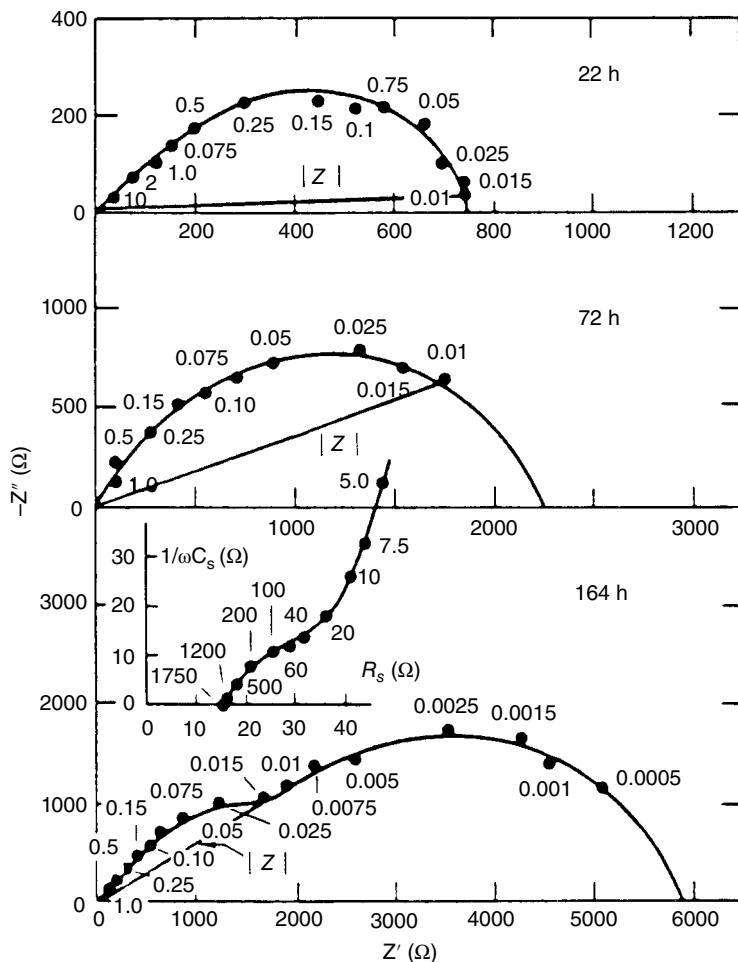


FIGURE 4.4.1 Complex plane impedance diagrams for 90 : 10 Cu/Ni alloy in flowing seawater as a function of exposure time. Flow velocity = 1.62 m/s, $[O_2] = 0.045 \text{ mg/L}$, specimen area = 11.05 cm^2 , $T = 26^\circ\text{C}$; exposure time = 50 h. Source: From B. C. Syrett and D.D. Macdonald 1979. Numbers next to each point to frequency in hertz.

the system discussed earlier, as shown in Figure 4.4.4. In this figure, polarization resistance data, obtained using the impedance spectroscopic, potential step, and SACV techniques, are plotted as a function of time for two copper–nickel alloys exposed to flowing seawater (Syrett and Macdonald [1979]). The fact that the polarization resistance data are independent of the technique used for their measurement implies that the experimenter has the freedom to tailor a perturbation for the measurement of interfacial impedance in order to achieve some desired experimental goal. One implementation of this concept is the application of a large number of sine-wave voltage signals simultaneously, so that the total data acquisition time is determined only by the lowest frequency and not by the summation embodied in Eq. (5). These “structured noise” techniques are now being actively developed for corrosion-monitoring purposes.

The structured noise method stem from the elegant work of Smith and coworkers (Smith [1966]), who developed a multifrequency technique for ac polarography. Subsequently, structured noise techniques have been used in corrosion studies by Smyrl and coworkers (Smyrl [1985a, b], Smyrl and Stephenson [1985], Pound and Macdonald [1985]). In all cases, the perturbation applied to the system is of the form

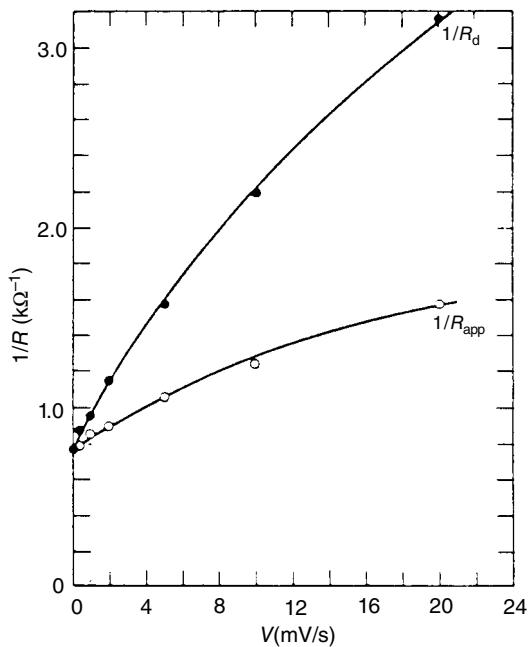


FIGURE 4.4.2 Plots of $1/R_d$ and $1/R_{\text{app}}$ as measured using SACV for 90 : 10 Cu/Ni in flowing seawater. Flow velocity = 1.62 m/s, $[\text{O}_2] = 0.045 \text{ mg/L}$, $T = 26^\circ\text{C}$, and exposure time = 50 h. Source: Macdonald 1978 a. Reproduced with permission of The Electrochemical Society.

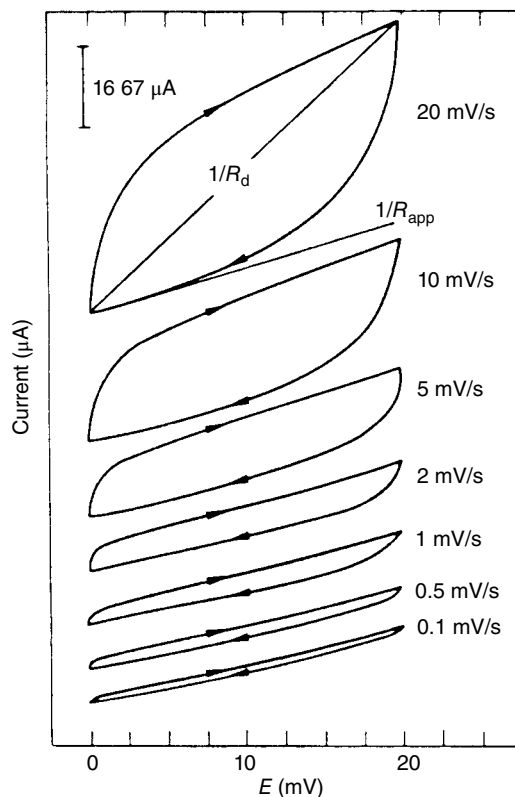


FIGURE 4.4.3 Small-amplitude cyclic voltammograms for 90 : 10 Cu/Ni alloy in flowing seawater. Experimental conditions are as listed in Figure 4.4.1. Source: Macdonald 1978 a. Reproduced with permission of The Electrochemical Society.

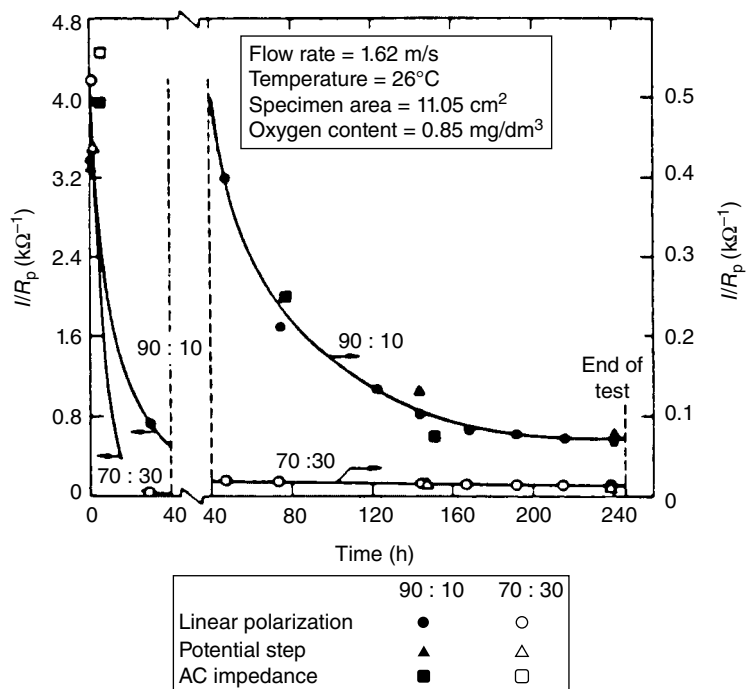


FIGURE 4.4.4 Corrosion rate (as I/R_p) versus time for 90 : 10 Cu/Ni and 70 : 30 Cu/Ni in flowing seawater having an oxygen content of 0.85 mg/dm^3 . Source: From B. C. Syrett and D.D. Macdonald 1979. Numbers next to each point to frequency in hertz.

$$V(t) = \sum_i a_i \sin(\omega_i t + \phi_i) \quad (7)$$

where a_i is the amplitude, ω_i is the frequency, and ϕ_i is the phase. If these parameters are selected in a completely random fashion, the signal is referred to as *white noise*. However, because corroding interfaces are inherently nonlinear, considerable advantages exist in choosing values for a_i , ω_i , and ϕ_i such that certain experimental problems are avoided. For example, nonlinearity produces harmonics of $2\omega_i$, $3\omega_i$, ..., $n\omega_i$ in response to a perturbation at the fundamental frequency ω_i . Because the amplitude of a harmonic decreases rapidly with increasing n , harmonic intrusion may be avoided by ensuring that $\omega_j \neq n\omega_i$ ($n = 2, 3, \dots$) or may at least be minimized by requiring that $n > 3$. Also, the power applied to the interface, which is proportional to the square of the amplitude of each component, may be tailored by choosing appropriate values for a_i . Regardless of the exact form of the perturbation employed, the impedance data are extracted from the perturbation and the response by Fourier or Laplace transformation (Pound and Macdonald [1985], Smyrl [1985a, b]). As an example of this technique, we show the data of Pound and Macdonald [1985] for carbon steel in acidified brine (Figure 4.4.5). The structured noise data are compared with those obtained using a frequency-by-frequency correlation technique (FRA). Clearly, the structured noise data are considerably more scattered than are those obtained by the correlation method, but that is compensated for by the reduction in the data acquisition time.

4.4.4 Harmonic Analysis

The derivation leading to the Stern–Geary relationship [Eq. (3)] assumes that the corroding electrode responds linearly to the imposed electrical perturbation; that is, doubling the perturbing voltage amplitude results in a double current response (but an unchanged impedance). Since physical variables in all

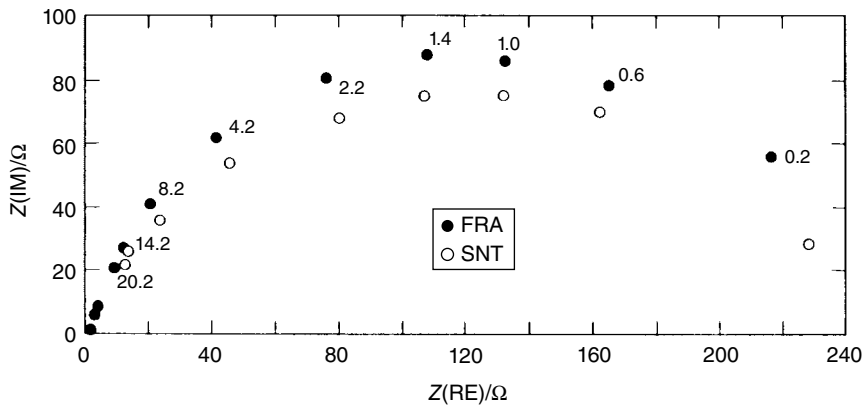


FIGURE 4.4.5 Nyquist plot of impedance data for 1018 steel in HCl-acidified 3% NaCl (pH = 3). Exposure time = 28 h, $E_{corr} = -0.682$ V (SCE).

physically realizable systems must have a finite first derivative, it is always possible to achieve linear conditions by applying a perturbation of limitingly small amplitude.

The nonlinearity of the current–voltage relationship in corroding systems provides an opportunity to determine corrosion rates without the need to measure independently the Tafel constants. The reason is that the electrical perturbation, which is imposed on the system at a frequency of f , in a nonlinear system results in a response at $2f$, $3f$, $4f$, and so on, in addition to a dc component (Kruger [1903], Mooring and Kies [1977], Bertocci [1979], Bertocci and Mullen [1981], McKubre [1983], McKubre and Macdonald [1984]). Neither the fundamental response (f_0) nor the total power response ($\sum_{h=0}^{\infty} hf$) can be analyzed to determine uniquely the corrosion rate (as opposed to the polarization resistance). Nevertheless, an analysis of the harmonic responses can be used to determine the unknown parameters in Eq. (3) and thus to measure corrosion rates in systems for which the Tafel coefficients are not known or at potentials removed from the free corrosion potential V_{fc} , for example, under conditions of an applied cathodic protection potential.

The origin of the harmonic response is shown schematically in Figure 4.4.6a for an input voltage sine wave at frequency f , superimposed on a current–voltage curve of the form

$$I = I_{fc} \{ \exp[\beta_a(V - V_{fc})] - \exp[-\beta_c(V - V_{fc})] \} \quad (8)$$

where β_a and β_c are the forward anodic and reverse cathodic Tafel coefficients, respectively, and I_{fc} is the free corrosion current flux, defined at the free corrosion potential (V_{fc}) as

$$I_{fc} = I_a = -I_c \quad (\text{at } V_{fc}) \quad (9)$$

Figure 4.4.6a shows a perturbing voltage sinusoid reflected about the dc current–voltage response curve at V_{fc} and at some positive bias. In the linear region, this reflection results in an undistorted current response, with V/I being a constant (equal to the dc corrosion resistance).

The expected response in the time domain is shown schematically in Figure 4.4.6b. The output is generally shifted in phase with respect to the input due to reactive terms associated with diffusional and capacitive processes. The extent of the distortion in the nonlinear region can be quantified by performing a Fourier series analysis. As indicated in Figure 4.4.6c, when a sinusoidal perturbation of moderate amplitude is applied to a corroding electrode, the response will consist of components at the same frequency (generally shifted in phase with respect to the input), as well as terms at integral multiples of the input frequency (the harmonics). Unless the input excitation is symmetric about V_{fc} , then the output also will show a dc offset that we term the *zeroth harmonic*. An offset is shown even for a symmetric

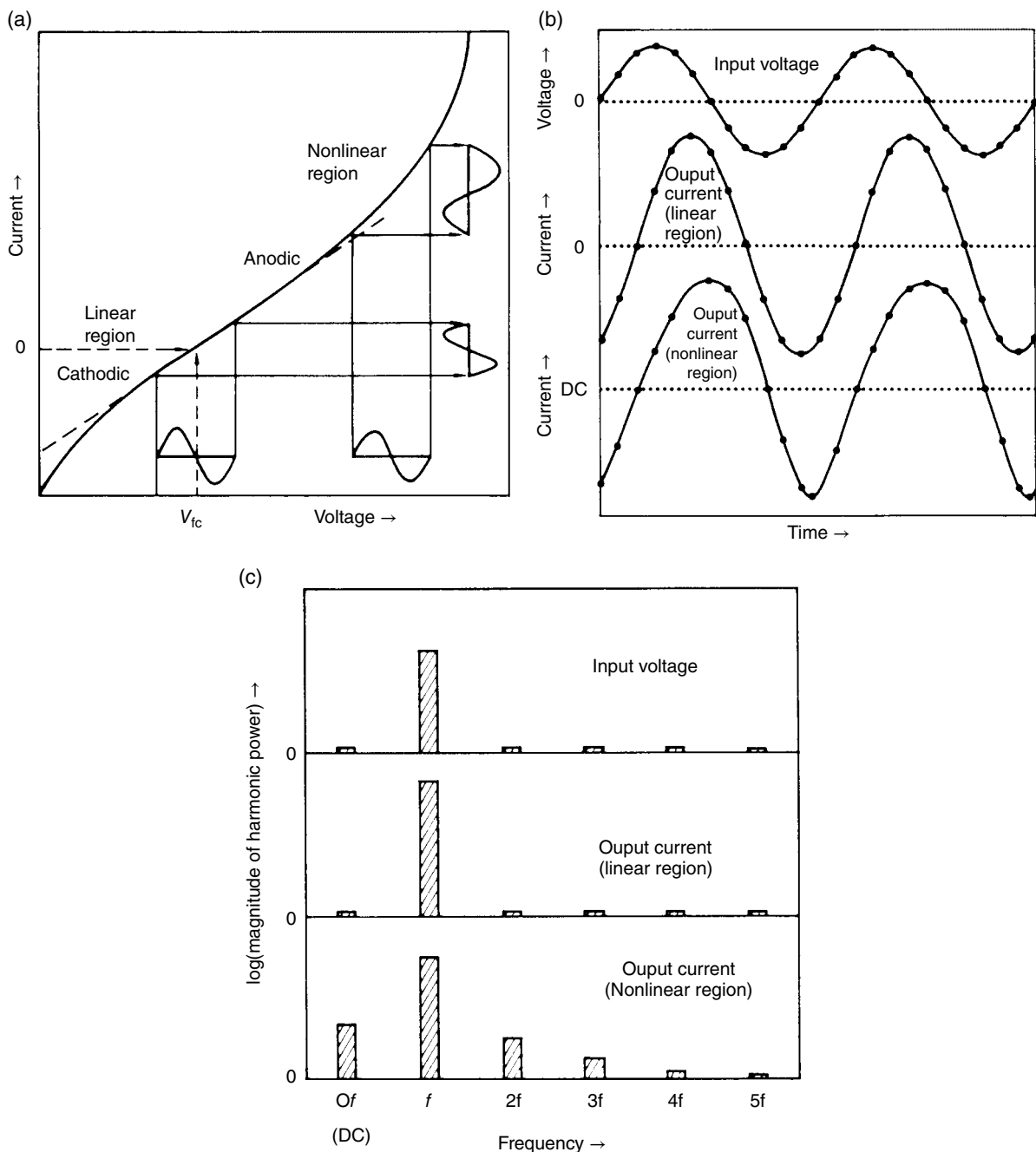


FIGURE 4.4.6 (a) The source of a harmonic response: reflection of an input sine wave on a nonlinear current-voltage curve. (b) The source of a harmonic response. Time-domain representation of input and output waveforms. (c) The source of a harmonic response: frequency domain representation of input and output waveforms.

perturbation if the I/V curves are not symmetrical—this is the basis of the faradic rectification effect. These harmonic response terms contain information sufficient to completely specify the current-voltage curve, in principle, at any dc voltage and thus to monitor the instantaneous corrosion rate even in the presence of an applied cathodic polarization.

The analysis of the harmonic response of a system of a sinusoidal current or voltage perturbation has received periodic attention in the electrochemical literature since the pioneering work of Warburg [1899] and Kruger [1903]. This effect has been studied as faradic rectification (Oldham [1957], Barker [1958], Barker *et al.* [1958], Delahay *et al.* [1960], Iami and Delahay [1962], Bauer [1964]) and faradic distortion (Delahay [1954], Breyer and Bauer [1964], Smith [1966]), and the results of this form of analysis have been applied to the development of ac polarography (Mooring and Kies [1977]). More recently, Bertocci [1979], Bertocci and Mullen [1981], and others (Chin and Venkatesh [1979]) have investigated the effect of large-amplitude perturbations in increasing the corrosion rates of electrical conduit materials (so-called ac corrosion).

The theoretical treatments referenced earlier all suffer from a major deficiency. The nonlinear term of interest in corrosion (the electron transfer process) is contained within a circuit comprising other linear (electrolyte resistance) and nonlinear (double-layer capacitance and diffusional impedance) terms. Since the voltage dropped across nonlinear circuit elements cannot be considered to linearly superimpose, we cannot use the equivalent circuit method to isolate the impedance terms of interest. Properly, one must solve for the system as a whole, including diffusional and double-layer terms, and identify the harmonic components associated with the faradic process of interest.

The simplified theoretical treatment presented here is similar in form to that described previously (Rangarajan [1975], Callow *et al.* [1976], Ramamurthy and Rangarajan [1977], Rao and Mishra [1977], Bertocci [1979], Devay and Meszaros [1980], Hladky *et al.* [1980], Bertocci and Mullen [1981], Devay and Meszaros [1982]; Gill *et al.* [1983]; McKubre [1983]).

We are interested in the current response of an electrode to a voltage perturbation of the form

$$V = V_0 + v \sin(\omega t) \quad (10)$$

Substituting Eq. (10) into Eq. (8) yields

$$I = I_{fc} \langle \exp\{\beta_a[\eta + v \sin(\omega t)]\} - \exp\{-\beta_c[\eta + v \sin(\omega t)]\} \rangle \quad (11)$$

where

$$\eta = V_0 - V_{fc} \quad (12)$$

One can make the substitution (Bauer [1964], Abramowitz and Stegun [1965])

$$\exp[z \sin(x)] = J_0(z) + 2 \sum_{k=0}^{\infty} (-1)^k J_{2k+1}(z) \sin[(2k+1)x] + 2 \sum_{k=1}^{\infty} (-1)^k J_{2k}(z) \cos(kx) \quad (13)$$

where $J_n(z)$ is a modified Bessel function of order n . The value of $J_n(z)$ can be calculated by means of the expression

$$J_n(z) = \left(\frac{z}{2}\right)^n \sum_{k=0}^{\infty} \left[\frac{(z/2)^{2k}}{k!(n+k)!} \right] \quad (14)$$

The first term in Eq. (13) represents the expected dc response (zeroth harmonic or faradic rectification component) attributable to an ac perturbation. The second term gives the odd-order harmonic response, and the last term gives the even harmonics. In the limit as $v \rightarrow 0$, all response functions except the fundamental disappear, and for $\eta = 0$ we obtain the familiar expression for the Stern and Geary [1957] relationship:

$$\frac{dI_{fc}}{dV} = \frac{1}{R_p} = \frac{2.303 I_{fc} (\beta_a + \beta_c)}{\beta_a \beta_c} \quad (15)$$

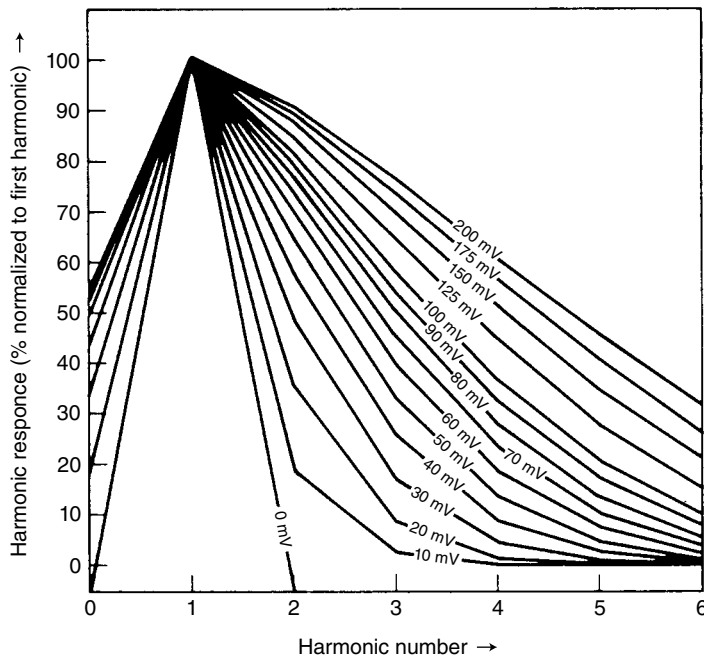


FIGURE 4.4.7 The effect of ac amplitude on the magnitude of the harmonic response for a two-electron process.

Under all other conditions, the faradic current must be represented by a Fourier series of harmonic responses, as indicated by Eqs. (12)–(14).

Substituting Eqs. (13) and (14) into Eq. (11), we obtain an equation of the form

$$\frac{I}{I_{fc}} = [\exp(\beta_a \eta)] ({}_0 C^+ + {}_1 C^+ + {}_2 C^+ + {}_3 C^+ + \dots) - [\exp(-\beta_c \eta)] ({}_0 C^- + {}_1 C^- + {}_2 C^- + {}_3 C^- + \dots) \quad (16)$$

where the harmonic series of constants C^\pm are $\exp[\pm v \sin(\omega t)]$ evaluated according to Eq. (13) and pre-subscripts are used to denote the harmonic number.

Figures 4.4.7 and 4.4.8 demonstrate the influence of various corrosion parameters on the expected harmonic response, calculated from Eq. (16). Figure 4.4.7 shows the effect of the ac amplitude (v) on the magnitude of the response at large overvoltages; the responses are normalized by that at the first harmonic. Clearly, the application of perturbation levels as low as 50 mV can result in significant powers of the harmonic response at $0f$, $2f$, and $3f$.

The effect of dc potential and Tafel coefficient on the harmonic response is shown in Figure 4.4.8. The power of the current response normalized by the free corrosion current (I_{fc}), shown on a log-linear scale, parallels that of the dc current response with constant ratio between the harmonics. For the symmetric case, shown in Figure 4.4.6a, the minimum in harmonic response occurs at the free corrosion potential. However, as the ratio of the reverse cathodic to forward anodic Tafel coefficients is increased, the potential at which the response is a minimum for each harmonic is increased. This phenomenon is shown in Figure 4.4.8 and has been suggested as the basis for a corrosion monitor (Gill *et al.* [1983]).

Precise measurements of the current responses at each of a number of harmonics can be used, in conjunction with Eq. (16), to evaluate the unknown terms in Eq. (11). A complete description of the faradic current–voltage response is sufficient to define the anodic partial current (the corrosion rate)

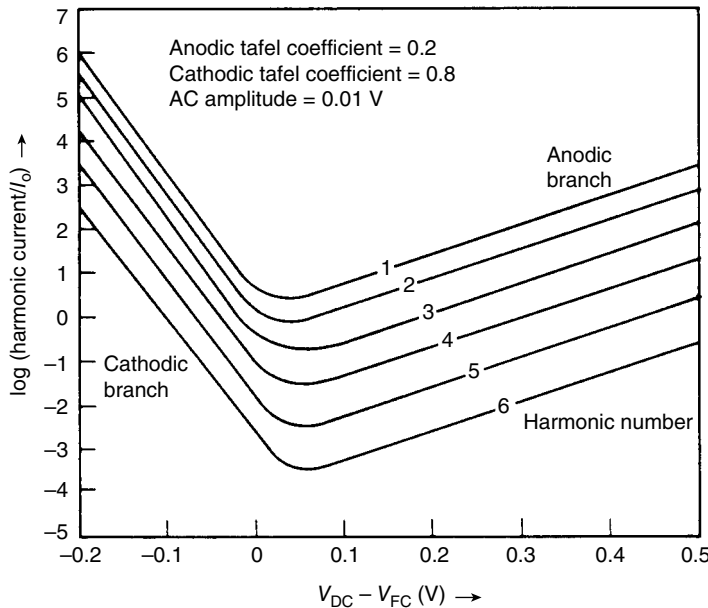


FIGURE 4.4.8 The effect of dc applied potential on the harmonic response for an asymmetric corrosion process.

at any potential; the parameters needed are the forward and reverse Tafel coefficients, the free corrosion current, and the free corrosion potential.

In applying the harmonic method to corrosion rate monitoring, three major sources of interferences must be overcome. A major source of error is due to the presence of an uncompensated series electrolyte resistance. The harmonic current responses due to the corrosion process are transformed by such a resistance into a voltage that appears as an input perturbation at the harmonic frequency, leading to an erroneous harmonic current response. A second source of error appears at large values of anodic or cathodic polarization, where the measured dc (and thus low-frequency impedance) response may be largely dominated by diffusional processes. Since the genesis of the harmonic response is considered to be in the faradic processes, it is necessary to deconvolve the diffusional from the charge transfer impedance terms. A practical, although approximate, solution to the problem of uncompensated resistance and diffusional impedance is to completely determine the equivalent circuit for the corroding electrode by performing the impedance (fundamental or harmonic) study over a wide range of frequencies and mathematically correcting the data set retrospectively (McKubre and Syrett [1986]).

A more insidious problem is the limitation on precision imposed by the vanishingly small magnitude of the anodic (corrosion) component compared with the cathodic partial current at large values of cathodic bias, due to the exponential form of the current–voltage relationships for the anodic and cathodic half-reactions.

Methods by which these limitations can be minimized and the parameters of interest calculated are described by McKubre and Syrett [1986]. The ratio of the harmonic admittance to the fundamental admittance (both corrected as described earlier) is used to evaluate the desired corrosion parameters. Equation (15) can be expressed in the more appropriate form by noting that

$$\frac{nY}{mY} = \frac{nI}{1V} \cdot \frac{1V}{mI} = \frac{nI}{I_{fc}} \cdot \frac{I_{fc}}{mI} \quad (17)$$

$$\frac{0Y}{1Y} = \frac{[\exp(\beta_a \eta)](0C^+) - [\exp(-\beta_c \eta)](0C^-)}{[\exp(\beta_a \eta)](1C^+) - [\exp(-\beta_c \eta)](1C^-)} \quad (18)$$

$$\frac{2Y}{1Y} = \frac{[\exp(\beta_a\eta)](2C^+) - [\exp(-\beta_c\eta)](2C^-)}{[\exp(\beta_a\eta)](1C^+) - [\exp(-\beta_c\eta)](1C^-)} \quad (19)$$

$$\frac{3Y}{1Y} = \frac{[\exp(\beta_a\eta)](3C^+) - [\exp(-\beta_c\eta)](3C^-)}{[\exp(\beta_a\eta)](1C^+) - [\exp(-\beta_c\eta)](1C^-)} \quad (20)$$

The constants ${}_hC^\pm$ can be evaluated using Eqs. (17) and (18); the unknown parameters η , β_a , β_c are calculated from the best fit of the measured admittance ratios to this system of equations.

4.4.5 Kramers–Kronig Transforms

At this point it is fitting to ask the question: "How do I know that my impedance data are correct?" This question is particularly pertinent in view of the rapid expansion in the use of IS over the past decade and because more complex electrochemical and corroding systems are being probed. These give rise to a variety of impedance spectra in the complex plane, including those that exhibit pseudoinductance and intersecting loops in the Nyquist domain. By merely inspecting the experimental data, it is not possible to ascertain whether or not the data are valid or have been distorted by some experimental artifact. However, this problem can be addressed by using the KK transforms (Kronig [1926], Kramers [1929b], Bode [1945], Macdonald and Brachman [1956], Tyagai and Kolbasov [1972], Van Meirhaeghe *et al.* [1976]), as recently described by Macdonald and Urquidi-Macdonald [1985] and Urquidi-Macdonald *et al.* [1986].

The derivation of the KK transforms (Bode [1945]) is based on the fulfillment of four general conditions of the system:

1. *Causality.* The response of the system is due only to the perturbation applied and does not contain significant components from spurious sources.
2. *Linearity.* The perturbation/response of the system is described by a set of linear differential laws. Practically, this condition requires that the impedance be independent of the magnitude of the perturbation.
3. *Stability.* The system must be stable in the sense that it returns to its original state after the perturbation is removed.
4. The impedance must be finite-valued at $\omega \rightarrow 0$ and $\omega \rightarrow \infty$ and must be a continuous and finite-valued function at all intermediate frequencies.

If the aforementioned conditions are satisfied, the KK transforms are purely a mathematical result and do not reflect any other physical property or condition of the system.

These transforms have been used extensively in the analysis of electrical circuits (Bode [1945]), but only rarely in the case of electrochemical systems (Tyagai and Kolbasov [1972], Van Meirhaeghe *et al.* [1976]).

The KK transforms may be stated as follows:

$$Z'(\omega) - Z'(\infty) = \left(\frac{2}{\pi}\right) \int_0^\infty \frac{xZ''(x) - \omega Z''(\omega)}{x^2 - \omega^2} dx \quad (21)$$

$$Z'(\omega) - Z'(0) = \left(\frac{2\omega}{\pi}\right) \int_0^\infty \left[\left(\frac{\omega}{x}\right) Z''(x) - Z''(\omega) \right] \cdot \frac{1}{x^2 - \omega^2} dx \quad (22)$$

$$Z''(\omega) = - \left(\frac{2\omega}{\pi}\right) \int_0^\infty \frac{Z'(x) - Z'(\omega)}{x^2 - \omega^2} dx \quad (23)$$

$$\phi(\omega) = \left(\frac{2\omega}{\pi}\right) \int_0^\infty \frac{\ln|Z(x)|}{x^2 - \omega^2} dx \quad (24)$$

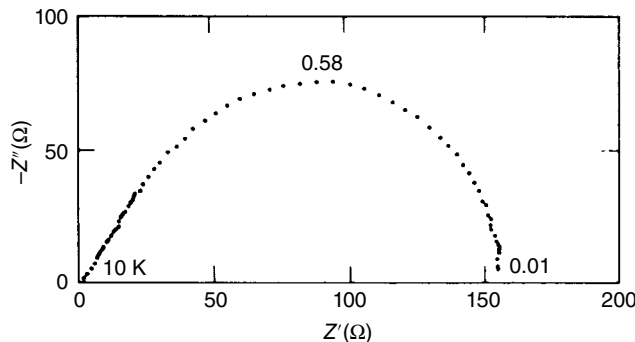


FIGURE 4.4.9 Complex plane impedance plot for TiO_2 -coated carbon steel in HCl/KCl solution ($\text{pH} = 2$) at 25°C . The parameter is frequency in hertz. Source: Macdonald 1985. Reproduced with permission of The Electrochemical Society.

where $\phi(\omega)$ is the phase angle, Z' and Z'' are the real and imaginary components of the impedance, respectively, and ω and χ are frequencies. Therefore, according to Eq. (4), the polarization resistance simply becomes

$$R_p = \left(\frac{2}{\pi} \right) \int_0^{\infty} \left[\frac{Z''(x)}{x} \right] dx \approx \left(\frac{2}{\pi} \right) \int_{\chi_{\min}}^{\chi_{\max}} \left[\frac{Z''(x)}{x} \right] dx \quad (25)$$

where χ_{\max} and χ_{\min} are the maximum and minimum frequencies selected such that the error introduced by evaluating the integral over a finite bandwidth, rather than over an infinite bandwidth, is negligible.

To illustrate the application of the KK transformation method for validating polarization resistance measurements in particular and for verifying impedance data in general, we consider the case of TiO_2 -coated carbon steel corroding in HCl/KCl solution ($\text{pH} = 2$) at 25°C (McKubre [1985], unpublished work). The complex plane diagram for this case is shown in Figure 4.4.9, illustrating that at high frequencies the locus of points is linear but that at low frequencies the locus curls over to intersect the real axis. Application of Eq. (25) predicts a polarization resistance of $158.2\ \Omega$ compared with a value of $157.1\ \Omega$ calculated from the high- and low-frequency intercepts on the real axis (Macdonald and Urquidi-Macdonald [1985]).

By using the full set of transforms, as expressed by Eqs. (21)–(24), it is possible to transform the real component into the imaginary component and vice versa (Macdonald and Urquidi-Macdonald [1985], Urquidi-Macdonald *et al.* [1986]). These transforms therefore represent powerful criteria for assessing the validity of experimental impedance data. The application of these transforms to the case of TiO_2 -coated carbon steel is shown in Figures 4.4.10 and 4.4.11. The accuracy of the transform was assessed by first analyzing synthetic impedance data calculated from an equivalent electrical circuit (EEC). An average error between the “experimental” and “transformed” data of less than 1% was obtained. In this case, the residual error may be attributed to the algorithm used for evaluating the integrals in Eqs. (21)–(23). A similar level of precision was observed on transforming McKubre’s (McKubre [1985], unpublished work) extensive data set for TiO_2 -coated carbon steel in HCl/KCl (Macdonald and Urquidi-Macdonald [1985], Urquidi-Macdonald *et al.* [1986]). Not all impedance data are found to transform as well as those for the EEC and the TiO_2 -coated carbon steel system referred to earlier. For example, Urquidi-Macdonald *et al.* [1986] recently applied the KK transforms (21)–(23) to the case of an aluminum alloy corroding in 4-M KOH at temperatures between 25 and 60°C and found that significant errors occurred in the transforms that could be attributed to interfacial instability as reflected in the high corrosion rate.

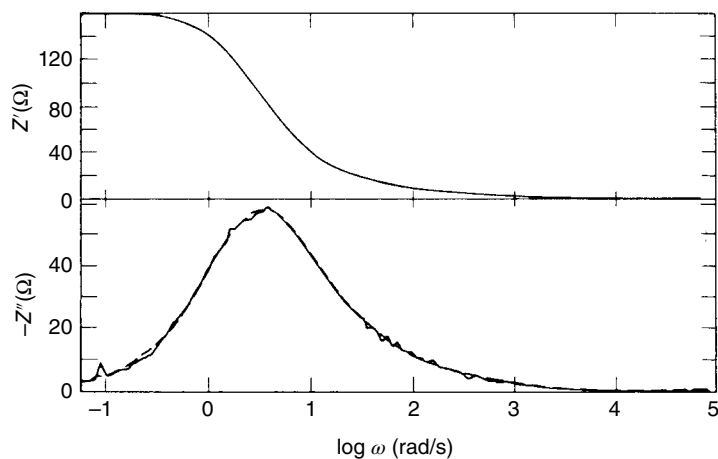


FIGURE 4.4.10 Kramers–Kronig transforms of impedance data for TiO_2 -coated carbon steel in HCl/KCl solution ($\text{pH}=2$) at 25°C : (a) Real impedance component versus $\log \omega$. (b) Comparison of the experimental imaginary impedance component (---) with $Z''(\omega)$ data (—) obtained by KK transformation of the real component.
Source: Macdonald 1985. Reproduced with permission of The Electrochemical Society.

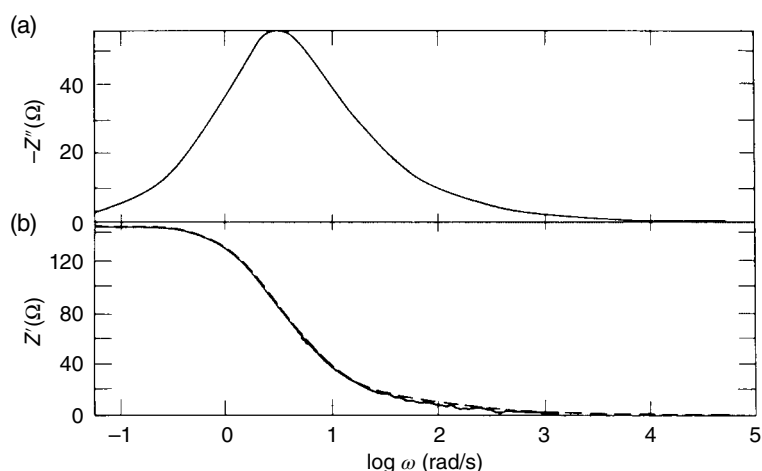


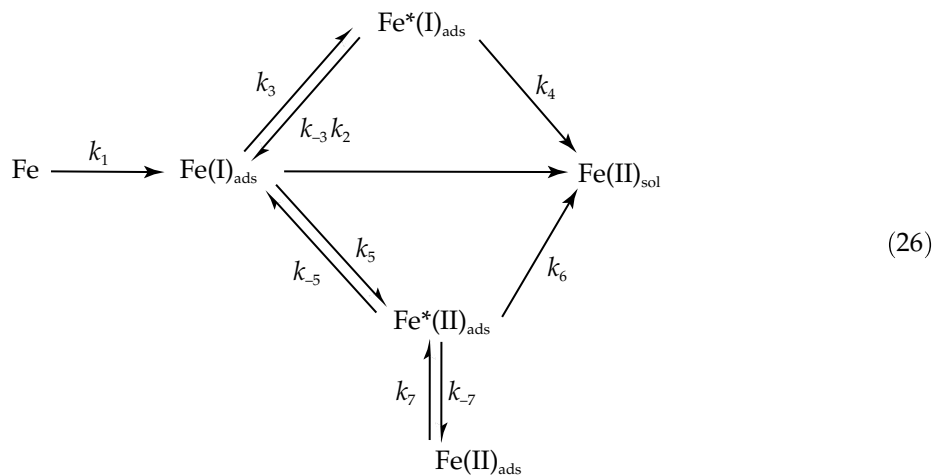
FIGURE 4.4.11 Kramers–Kronig transforms of impedance data for TiO_2 -coated carbon steel in HCl/KCl solution ($\text{pH}=2$) at 25°C : (a) Imaginary impedance component versus $\log \omega$. (b) Comparison of the experimental real impedance component (---) with $Z'(\omega)$ data (—) obtained by KK transformation of the imaginary component. Source: Macdonald and Urquidi-Macdonald [1985]. Reproduced with permission of The Electrochemical Society.

4.4.6 Corrosion Mechanisms

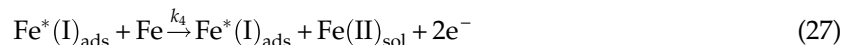
4.4.6.1 Active Dissolution

IS has been applied extensively in the analysis of the mechanism of corrosion of iron and other metals in aqueous solutions. Typical work of this kind is that reported by Keddam *et al.* [1981], who sought to distinguish between various mechanisms that had been proposed for the electrodissolution of iron in acidified sodium sulfate solutions. Since this particular study provides an excellent review of how IS is used to discern reaction mechanism, the essential features of the analysis are described in the following text.

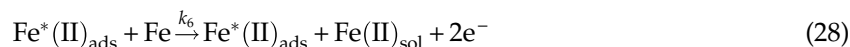
As the result of analyzing a large number of possible mechanisms for the dissolution of iron, Keddam *et al.* [1981] concluded that the most viable mechanism for this reaction involves three intermediate species:



in which steps 4 and 6 are written in complete form as



and



In setting up the reaction model for this case, Keddam *et al.* assumed that the elementary steps obey Tafel's law, that the transfer coefficient (α) has a value between 0 and 1 and is independent of potential, and that the coverage by adsorbed species obeys the Langmuir isotherm. Designating the fractional coverages by the species $\text{Fe}(\text{I})_{\text{ads}}$, $\text{Fe}^*(\text{I})_{\text{ads}}$, and $\text{Fe}^*(\text{II})_{\text{ads}}$ to be θ_1 , θ_2 , and θ_3 , respectively, and that of the passivating species $\text{Fe}(\text{II})_{\text{ads}}$ as θ_4 , and assuming no overlap, then the current flowing across the interface may be expressed as

$$I = F[k_1\Sigma + (k_2 + k_5)\theta_1 + 2k_4\theta_2 + (2k_6 - k_{-5})\theta_3] \quad (29)$$

where

$$\Sigma = 1 - \theta_1 - \theta_2 - \theta_3 - \theta_4 \quad (30)$$

and k_i is the rate constant for the i th step defined by

$$k_i = k_{o,i} \exp\left(\frac{z\alpha F}{RT} \cdot E\right) \quad (31)$$

Mass balance relationships involving the adsorbed species results in the following expressions for the time dependencies of θ_1 , θ_2 , θ_3 , and θ_4 :

$$\beta_1 \frac{d\theta_1}{dt} = k_1 \Sigma - (k_2 + k_3 + k_5)\theta_1 + k_{-3}\theta_2 + k_{-5}\theta_3 \quad (32)$$

$$\beta_2 \frac{d\theta_2}{dt} = k_3\theta_1 = k_{-3}\theta_2 \quad (33)$$

$$\beta_3 \frac{d\theta_3}{dt} = k_5\theta_1 - (k_{-5} + k_7)\theta_3 + k_{-7}\theta_4 \quad (34)$$

$$\beta_4 \frac{d\theta_4}{dt} = k_7\theta_3 - k_{-7}\theta_4 \quad (35)$$

where β is a constant that links the surface fractions to surface concentrations ($\text{mole}/\text{cm}^{-2}$). The value for β is $\sim 10^{-8} \text{ mole}/\text{cm}^2$, which corresponds to about one monolayer. The steady state is characterized by $d\theta_i/dt = 0$, in which case

$$\bar{\theta}_1 = \frac{k_1 k_{-3} k_{-5} k_{-7}}{D} \quad (36)$$

$$\bar{\theta}_2 = \frac{k_1 k_{-3} k_{-5} k_{-7}}{D} \quad (37)$$

$$\bar{\theta}_3 = \frac{k_1 k_{-3} k_5 k_{-7}}{D} \quad (38)$$

$$\bar{\theta}_4 = \frac{k_1 k_{-3} k_5 k_7}{D} \quad (39)$$

where

$$D = k_1 k_{-3} k_5 k_7 + \{k_1 [k_3 k_{-5} + k_{-3} (k_5 + k_{-5})] + k_2 k_{-3} k_{-5}\} k_{-7} \quad (40)$$

and hence the steady-state current becomes

$$\bar{I} = 2F(k_2 \bar{\theta}_1 + k_4 \bar{\theta}_2 + k_6 \bar{\theta}_3) \quad (41)$$

In order to derive the faradic impedance (Z_F), we note that for sinusoidal variations in the potential and in the surface coverages of reaction intermediates we may write

$$\delta E = |\delta E| e^{j\omega t} \quad (42)$$

$$\delta \theta_i = |\delta \theta_i| e^{j\omega t} \quad (43)$$

$$j = \sqrt{-1} \quad (44)$$

Thus, from Eq. (41) and defining Z_F as

$$Z_F = \frac{\delta E}{\delta I} \quad (45)$$

we obtain the following expression for the faradic impedance:

$$\frac{1}{Z_F} = \frac{1}{RT} - F(k_1 - k_2 - k_5) \frac{d\theta_1}{dE} + (k_1 - 2k_4) \frac{d\theta_2}{dE} + (k_1 + k_{-5} - 2k_6) \frac{d\theta_3}{dE} + k_1 \frac{d\theta_4}{dE} \quad (46)$$

where

$$\frac{1}{RT} = F[(b_1 + b_2)k_2\bar{\theta}_1 + 2b_4k_4\bar{\theta}_2 + [(b_5 + b_{-5})k_{-5} + 2b_6k_6]\bar{\theta}_3] \quad (47)$$

$$b_i = \frac{\alpha_i F}{RT} \quad (48)$$

The faradic impedance is readily obtained by first deriving expressions for $d\theta_i/dt$. This is done by taking the total differentials of Eqs. (32)–(35). For example, in the case of Eq. (33), we write

$$\delta\left(\beta_2 \frac{d\theta_2}{dt}\right) = k_3\delta\theta_1 + \theta_1\delta k_3 - k_{-3}\delta\theta_2 - \theta_2\delta k_{-3} \quad (49)$$

Since

$$\delta\left(\beta_2 \frac{d\theta_2}{dt}\right) = \beta_2 \frac{d(\delta\theta_2)}{dt} = \beta_2 j\omega \delta\theta_2 \quad (50)$$

and

$$\delta k_i = b_i k_i \delta E \quad (51)$$

we obtain

$$(k_{-3} + j\omega\beta_2) \frac{\delta\theta_{-2}}{\delta E} - k_3 \frac{\delta\theta_1}{\delta E} - \theta_1 b_3 k_3 + \theta_2 b_{-3} k_{-3} = 0 \quad (52)$$

Additional linear simultaneous equations may be generated from Eqs. (32), (34), and (35), and the set may be solved for $\delta\theta_1/\delta E$, $\delta\theta_2/\delta E$, $\delta\theta_3/\delta E$, and $\delta\theta_4/\delta E$. These values are then substituted into Eq. (46) to calculate the faradaic impedance, which in turn yields the interfacial impedance as

$$Z_T = \frac{Z_F}{1 + j\omega C_{dl} Z_F} \quad (53)$$

where C_{dl} is the double-layer capacitance.

Experimental and simulated [Eq. (29)] steady-state current–voltage curves for iron in $\text{Na}_2\text{SO}_4\text{--H}_2\text{SO}_4$ solutions as a function of pH are shown in Figure 4.4.12, and simulated and experimental complex plane impedance diagrams at various points on these curves are shown in Figures 4.4.13 and 4.4.14, respectively (Keddam *et al.* [1981]). The close agreement between the steady-state polarization curves is immediately apparent, even to the extent that the inflection in the curve for pH 4 is accurately reproduced. Examination of the impedance diagrams in Figures 4.4.13 and 4.4.14 show that the mechanism selected by Keddam *et al.* [1981] is capable of reproducing the essential features of the diagrams, including the number and type of relaxations, but not the details. However, the latter depend strongly upon the values selected for the rate constants and are also probably affected by the isotherm selected for describing the adsorption of intermediate species onto the surface.

4.4.6.2 Active–Passive Transition

The sudden transition of a metal–solution interface from a state of active dissolution to the passive state is a phenomenon of great scientific and technological interest. This transition has been attributed to the formation of either a monolayer (or less) of adsorbed oxygen on the surface or to the coverage of the

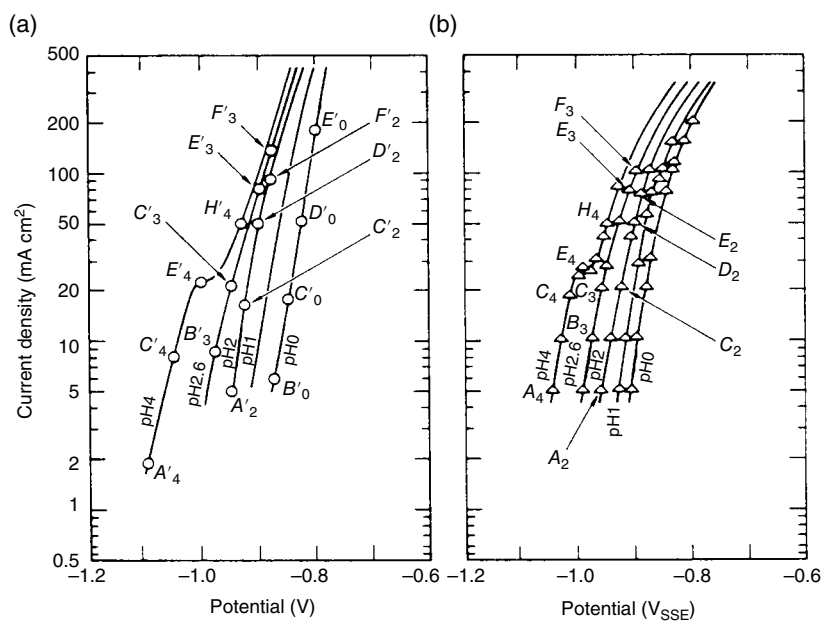


FIGURE 4.4.12 Steady-state polarization curves for iron in $\text{NaSO}_4\text{-H}_2\text{SO}_4$ solutions according to Keddam *et al.* [1981]. (a) Simulated curves and (b) experimental data. Rotating disk electrode (rotating speed = 1600 rpm, diameter = 3 mm), $T = 25 \pm 0.2^\circ\text{C}$. Source: Keddam 1981. Reproduced with permission of The Electrochemical Society.

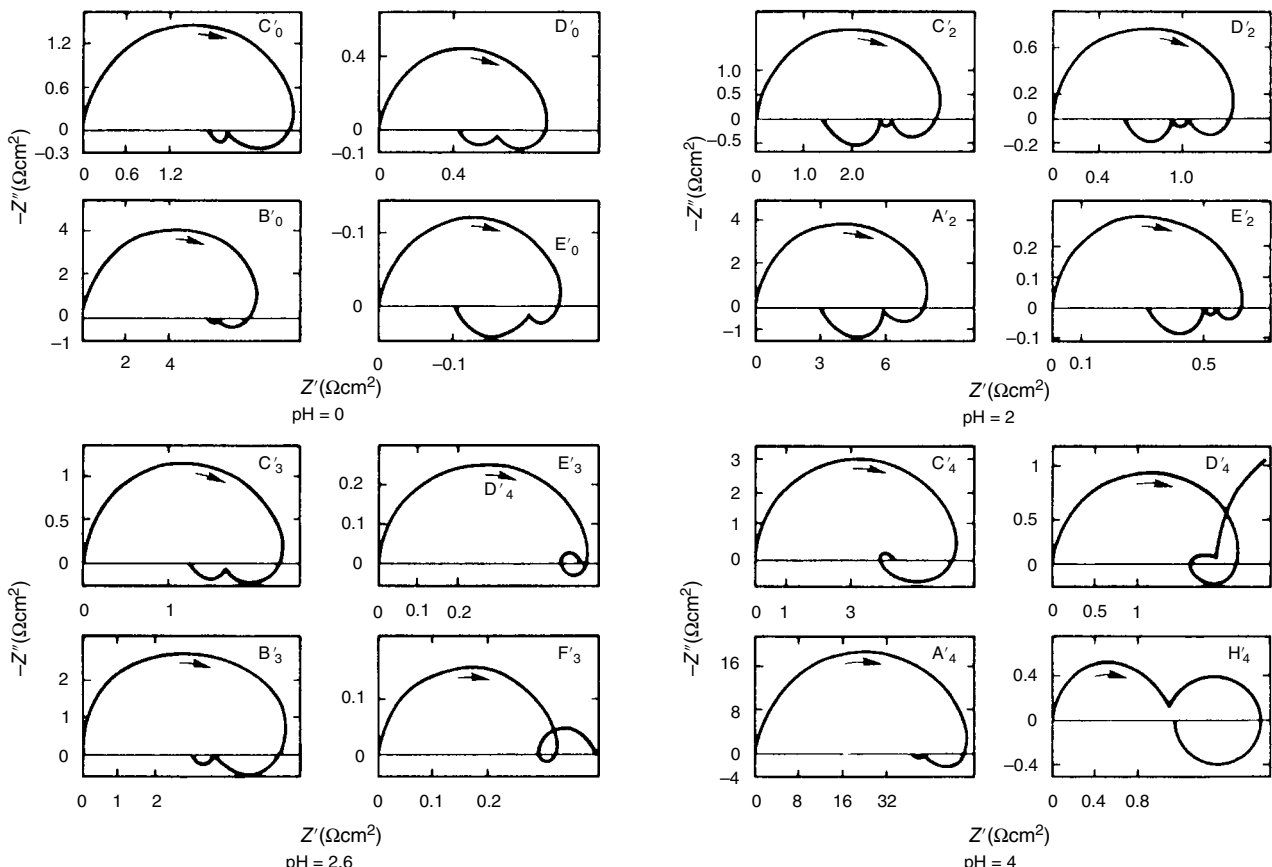


FIGURE 4.4.13 Simulated complex plane impedance diagrams for the electrodissolution of iron in sulfate media as a function of pH according to Keddam *et al.* [1981]. The potentials for which the diagrams are calculated are shown in Figure 4.4.12. The arrows indicate the direction of decreasing frequency. Source: Keddam 1981. Reproduced with permission of The Electrochemical Society.

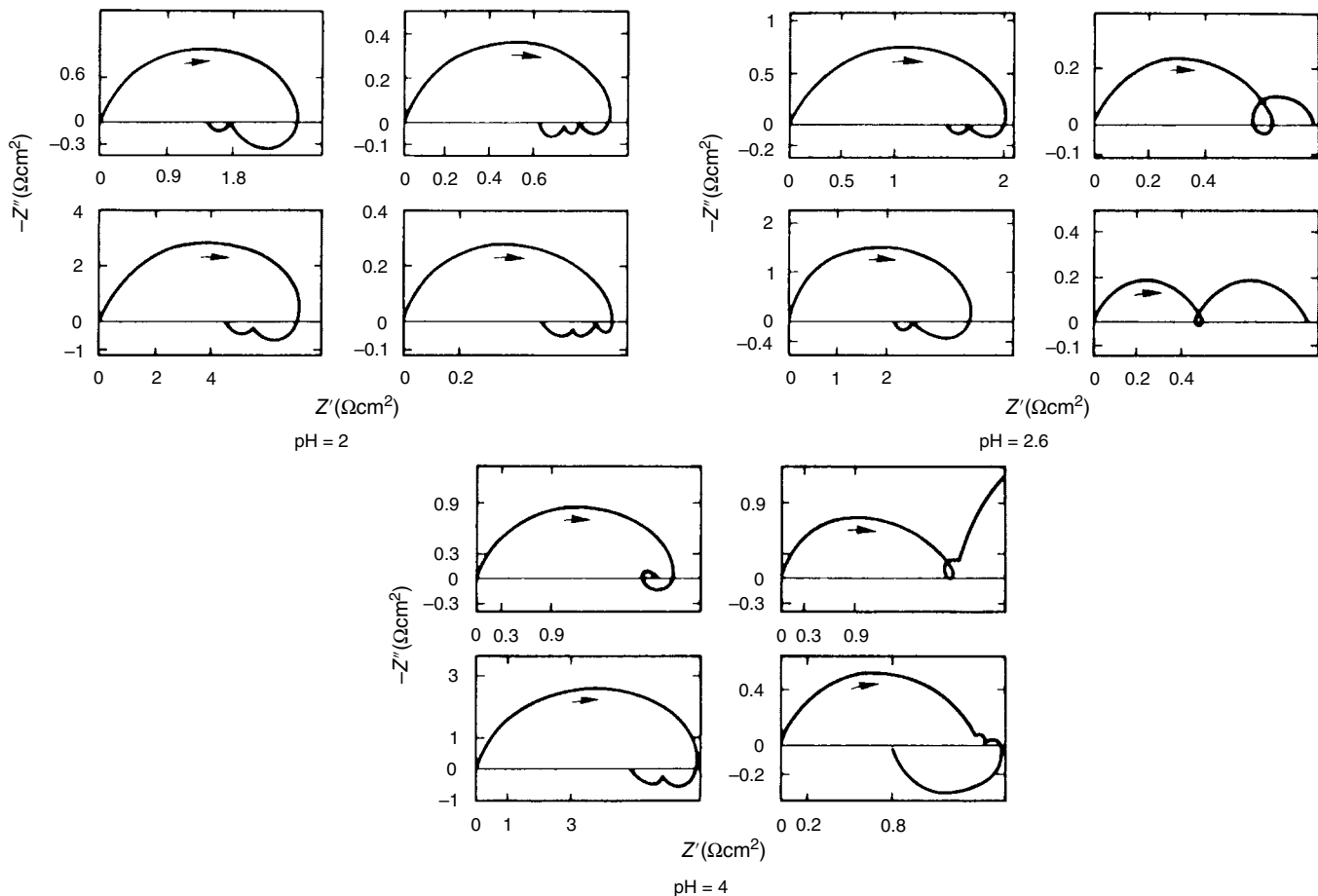


FIGURE 4.4.14 Experimental complex plane impedance diagrams for iron in sulfate media as a function of pH according to Keddam *et al.* [1981]. The potentials at which the diagrams were measured are shown in Figure 4.4.12. The arrows indicate the direction of decreasing frequency. Source: Keddam 1981. Reproduced with permission of The Electrochemical Society.

surface by a three-dimensional corrosion product film. In either case, the reactive metal is shielded from the aqueous environment, and the current drops sharply to a low value that is determined by the movement of ions or vacancies across the film.

The changes that typically occur in the complex plane impedance diagram on increasing the potential through an active-to-passive transition are shown in Figure 4.4.15 (Keddam *et al.* [1984]). At point A, the high-frequency arm of the impedance is typical of a resistive-capacitive system, but the impedance locus terminates in a negative resistance as $\omega \rightarrow 0$. This, of course, is consistent with the negative slope of the steady-state polarization curve. At higher potentials, the high-frequency locus is again dominated by an apparent resistive-capacitance response (see Section 4.4.6.2), but the low-frequency arm is not observed to terminate at the real axis in this case because of the very high value for the polarization resistance (horizontal I vs. E curve). The origin of the negative resistance can be accounted for theoretically (Keddam *et al.* [1984]) in terms of an increasing coverage of the surface by an adsorbed intermediate as the potential is increased. Thus, the low-frequency loop exhibited in Figure 4.4.15a is due to relaxations involving these surface species.

Epelboin and coworkers [1972] and Diard and LeGorre [1979] have recognized a serious shortcoming of classical potentiostatic methods for investigating the active-to-passive transition. The problem arises because a potentiostat has a load line of negative slope in I versus E plane and hence is incapable

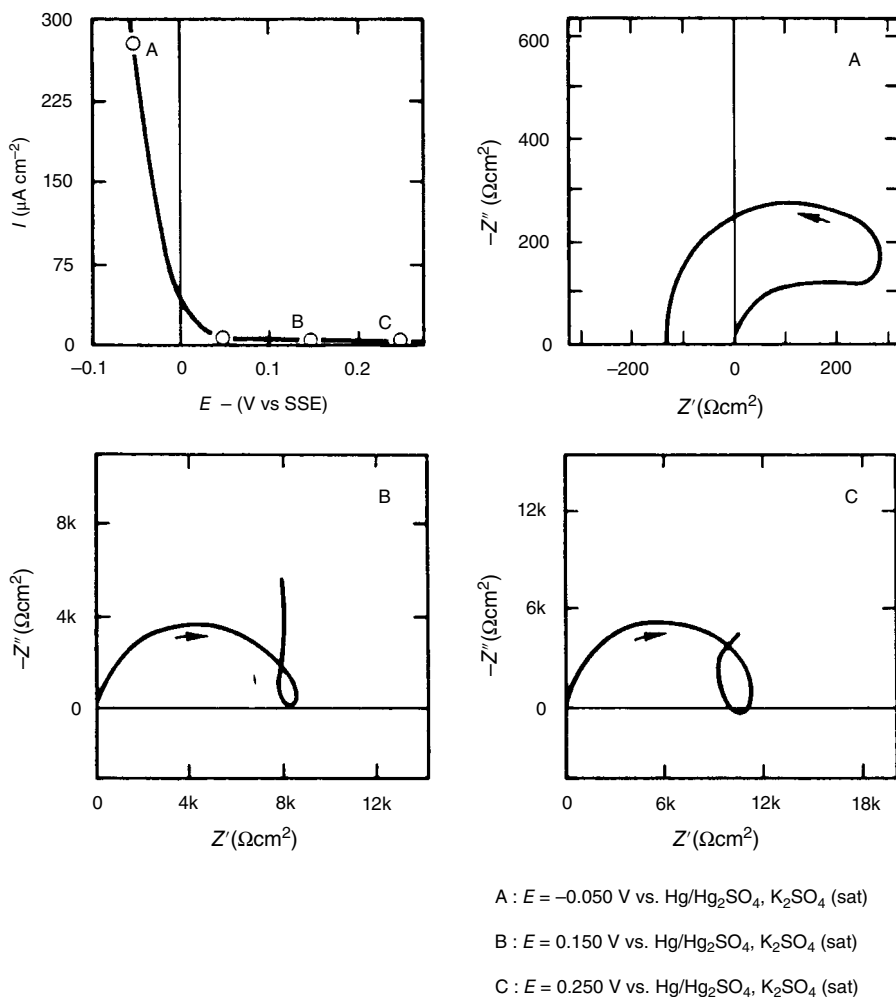


FIGURE 4.4.15 Steady-state polarization curve and complex plane impedance diagrams at selected potentials through the active-to-passive transition for iron in 1 M H_2SO_4 as reported by Keddam *et al.* [1984]. The arrows indicate the direction of decreasing frequency. Source: Keddam 1981. Reproduced with permission of The Electrochemical Society.

of effectively defining the current–voltage characteristics of a metal–solution interface in the active-to-passive transition region. To overcome this limitation of potentiostatic control, Epelboim *et al.* [1972, 1975] and Diard and LeGorrec [1979] devised potential control instruments having negative output impedances, which are characterized by load lines having positive (and controllable) slopes. These negative impedance converters (NICs) have allowed “Z-shaped” active-to-passive transitions to be studied and the impedance characteristics to be determined, as shown by the data plotted in Figure 4.4.16. In contrast to the case shown in Figure 4.4.15a, the active-to-passive transition shown in Figure 4.4.16, as determined using a NIC, exhibits a change in the sign of dI/dE from negative to positive to negative as the current decreases from the active to the passive state. This change in sign, as reflected in the shape of the Z-shaped polarization curves, has been explained by Epelboim *et al.* [1975] in terms of coupling between mass transfer and surface reactions, although other explanations have also been advanced (Law and Newman [1979]).

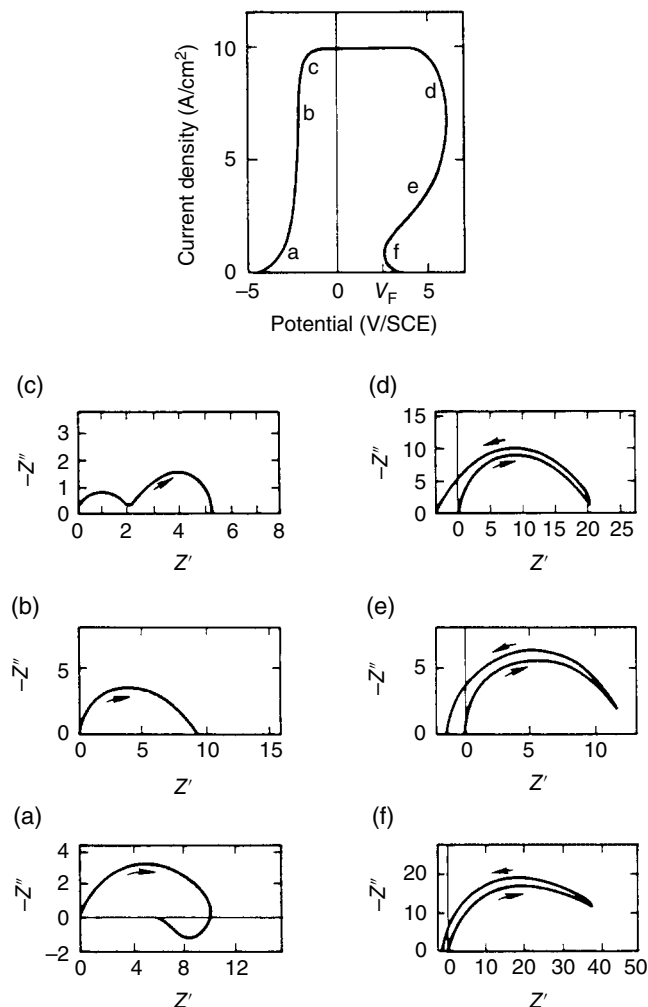


FIGURE 4.4.16 Impedance spectra for iron in 1 M H₂SO₄ at various potentials within the active dissolution and active-to-passive transition regions as determined using a negative impedance converter (NIC). Impedance values are given in ohms (electrode diameter = 0.5 cm), and the arrows indicate the direction of decreasing frequency.
Source: Epelboin 1975. Reproduced with permission of Elsevier.

4.4.6.3 The Passive State

The phenomenon of passivity is enormously important in corrosion science and engineering, since it is responsible for the relatively low corrosion rates that are observed for most engineering metals and alloys. It is not surprising, therefore, that passivity has been studied extensively using a wide variety of techniques, including IS. A brief account of these impedance studies is given later.

In discussing this subject it is convenient to delineate the processes that occur at the film/solution (f/s) interface and those that take place within a passive film (Figure 4.4.17). In the first case, the processes are essentially ion exchange phenomena with the possibility of solution phase transport, whereas the second processes involve only transport. The movement of charged species within the film (anion vacancies V_o^- and cation vacancies $V_M^{x'}$) occurs, however, under the influence of both concentration and

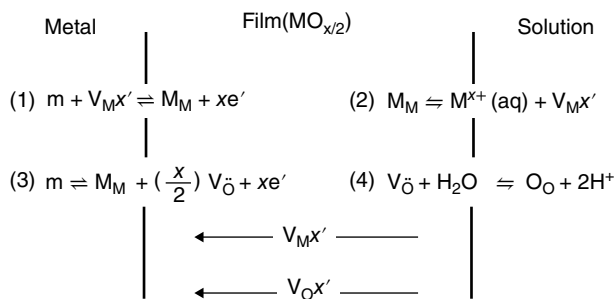


FIGURE 4.4.17 Schematic of physicochemical processes that occur within a passive film according to the point defect model. Here m , metal atom, M_M , metal cation in cation site, O_O , oxygen ion in anion site, $V_M^{X'}$, cation vacancy, and $V_O \ddot{O}$, anion vacancy. During film growth, cation vacancies are produced at the film/solution interface but are consumed at the metal/film interface. Likewise, anion vacancies are formed at the metal/film interface but are consumed at the film/solution interface. Consequently, the fluxes of cation vacancies and anion vacancies are in the directions indicated.

electrical potential gradients, with the electrical effects probably dominating, at least in the case of thin films. Accordingly, any analysis of the impedance characteristic of passive films must consider electromigration as well as diffusional transport.

The total impedance of the system of interphases shown in Figure 4.4.17 may be written as

$$Z_T = Z_{m/f} + Z_f + Z_{f/s} \quad (54)$$

where $Z_{m/f}$, Z_f , and $Z_{f/s}$ are the impedances associated with the metal/film (m/f) interface, the film, and the f/s interface, respectively. Because the elements are connected in series, the largest impedance will dominate the total impedance of the system. However, the impedance elements are frequency dependent, so that each of the elements may dominate over different frequency ranges.

Metal/Film Interface. According to Armstrong and Edmondson [1973], the impedance of the m/f interface can be described in terms of a capacitance (C'_∞) in parallel with two charge transfer resistances: one for the transfer of electrons (R_e) and the other for the transfer of cations (R_c) from the metal to the film. Accordingly,

$$Z_{m/f} = \frac{R_e R_c (R_e + R_c)}{(R_e + R_c)^2 + \omega^2 C'^2 R_e^2 R_c^2} - j \frac{\omega C R_e^2 R_c^2}{(R_e + R_c)^2 + \omega^2 C'^2 R_e^2 R_c^2} \quad (55)$$

For most systems, particularly for diffuse metal oxide junctions, we assume that the resistance to the movement of electrons across the interface is small compared with the resistance to the movement of cations, so that

$$R_e \ll R_c \quad (56)$$

In this case, Eq. (55) reduces to

$$Z_{m/f} = \frac{R_e}{1 + \omega^2 C'^2 R_c^2} - j \frac{\omega C R_c^2}{1 + \omega^2 C'^2 R_e^2} \quad (57)$$

Furthermore, the capacitance associated with this interface is probably that due to the space charge layer within the oxide. Therefore, over the frequency range of most interest to corrosion scientists (10^{-4} to 10^4 Hz), $1/CR_e \gg \omega$ so that

$$Z_{m/f} \sim R_e \quad (58)$$

Accordingly, under these conditions, the impedance of the m/f interface is likely to appear as a (small) frequency-independent resistance due to the transfer of electrons between the two phases.

The Film. A quantitative analysis of the impedance of a passive film has been reported by Chao *et al.* [1982], and the essential features of this treatment are reproduced here. The treatment is based upon their previously proposed (Chao *et al.* [1981], Lin *et al.* [1981]) point defect model (PDM) for the growth and breakdown of passive films, the essential features of which are depicted in Figure 4.4.17.

In this model, it is assumed that the total current that is detected in an external circuit upon application of a voltage is the sum of four components: (i) electronic current due to the transport of electrons (e'), (ii) electronic current due to the flow of electron holes (h'), (iii) ionic current due to the transport of anion vacancies ($V_O^{x'}$), and (iv) ionic current due to the movement of cation vacancies ($V_M^{x'}$):

$$I = I_{e'} + I_{h'} + I_{V_O} + I_{V_M} \quad (59)$$

Therefore,

$$\frac{1}{Z_f} = \frac{1}{Z_e} + \frac{1}{Z_h} + \frac{1}{Z_0} + \frac{1}{Z_M} \quad (60)$$

The total impedance of the film is therefore described in terms of the transport of vacancies in parallel with the electron and hole resistances, provided that electron or hole exchange processes do not occur at the f/s interface. This situation exists in the absence of any redox couples in the solution.

The movement of anion and cation vacancies within the film under the influence of concentration (C) and electrical potential (ϕ) gradients is determined by Fick's second law:

$$\frac{\partial C}{\partial t} = D \frac{\partial^2 C}{\partial x^2} - DqK \frac{\partial C}{\partial x} \quad (61)$$

where

$$K = \frac{\epsilon F}{RT} \quad (62)$$

$$\epsilon = -\frac{d\phi}{dx} \quad (63)$$

Here q is the charge on the moving species ($-\chi$ for cation vacancies and +2 for oxygen vacancies for an oxide film of stoichiometry $MO_{\chi/2}$), D is the diffusivity, and F , R , and T have their usual meanings. The current observed in an external conductor due to the movement of the vacancies is given by Fick's first law, as applied to the m/f interface:

$$I = qFJ = qF \left(-D \frac{\partial C}{\partial x} + DqKC \right)_{m/f} \quad (64)$$

According to the PDM, and under conditions where the various equations can be linearized with respect to the applied ac voltage (V_{ac}), the concentration of vacancies at the m/f and f/s interfaces may be expressed as (Chao *et al.* [1982])

$$C_{V_0}(m/f) = [C_{V_0}(m/f)]_{dc} \cdot \frac{2F(1-\alpha)}{RT} \cdot V_{ac} \quad (65)$$

$$C_{V_M}(m/f) = [C_{V_M}(m/f)]_{dc} \cdot \frac{\chi F(\alpha-1)}{RT} \cdot V_{ac} \quad (66)$$

$$C_{V_0}(f/s) = [C_{V_0}(f/s)]_{dc} \cdot \frac{2F\alpha}{RT} \cdot V_{ac} \quad (67)$$

$$C_{V_M}(f/s) = [C_{V_M}(f/s)]_{dc} \cdot \frac{\chi F\alpha}{RT} \cdot V_{ac} \quad (68)$$

where the quantities in square brackets are constants, which are related to the thermodynamic parameters for the interfacial reactions shown in Figure 4.4.17.

The set of Eqs. (61)–(68) is readily solved by Laplace transformation to yield the impedance

$$Z_f(j\omega) = \frac{\bar{V}_{ac}}{\bar{I}_{ac}}, \quad s = j\omega, \quad j = \sqrt{-1} \quad (69)$$

where s is the Laplace frequency. The impedance so calculated is found to have the form

$$Z_T = \left(\frac{\sigma_M \sigma_0}{\sigma_M + \sigma_0} \right) \omega^{-1/2} (1-j) \quad (70)$$

where σ_0 and σ_M are given by

$$\sigma_0 = \frac{RT}{F^2(32D)^{1/2} \{ [C_{V_0}(m/f)]_{dc} (1-\alpha) \}} \quad (71)$$

$$\sigma_M = \frac{RT}{F^2(2x^4 D)^{1/2} \{ (\alpha-1) [C_{V_M}(m/f)]_{dc} \}} \quad (72)$$

The reader will recognize Eq. (70) as being of the form of a Warburg impedance for two parallel moving species. Two limiting cases may be defined: (i) movement of cations vacancies alone ($\sigma_0 \gg \sigma_M, Z_T \rightarrow Z_0$) and (ii) movement of anion vacancies alone ($\sigma_M \gg \sigma_0, Z_T \rightarrow Z_M$). Accordingly,

$$Z_T = \sigma_M \omega^{-1/2} (1-j) \quad (\text{cation vacancies}) \quad (73)$$

$$Z_T = \sigma_0 \omega^{-1/2} (1-j) \quad (\text{anion vacancies}) \quad (74)$$

Substitution of the appropriate expression for $[C_{V_0}(m/f)]_{dc}$ into Eq. (71) yields the Warburg coefficients for the movement of oxygen ion vacancies as

$$\sigma_0 = \frac{1}{I_{dc}} \left(\frac{D_0}{2} \right)^{1/2} \cdot \frac{\epsilon}{1-\alpha} \quad (75)$$

The form of the equation for σ_0 is particularly interesting, because it suggests that if the electric field strength (ϵ) and α are constants (as assumed in the PDM), then the product $\sigma_0 I_{dc}$ should be independent of the applied voltage across the system and the thickness of the film.

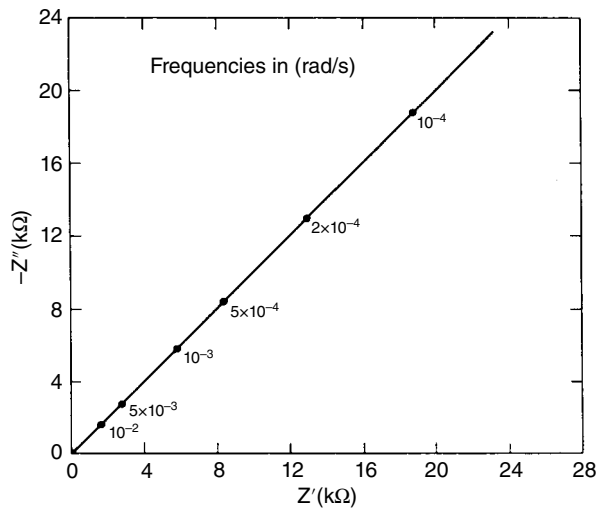


FIGURE 4.4.18 Complex impedance plane predicted by Eq. (74): $D_0 = 10^{-21} \text{ cm}^2/\text{s}$, $I_{dc} = 1 \mu\text{A}/\text{cm}^2$, $\epsilon = 10^6 \text{ V/cm}$, $\alpha = 0.88$, and area = 1 cm^2 .

A plot of $-Z''$ versus Z' for selected values of the various parameters contained in Eq. (74) is shown in Figure 4.4.18. As expected, the impedance locus is a straight line when

$$\epsilon > D \left(\frac{F^2 \epsilon^2}{R^2 T^2} \right) \quad (76)$$

However, for sufficiently low frequencies (Chao *et al.* [1982]), the impedance is predicted to intercept the real axis at a value of

$$R_{\omega=0} = \frac{RT}{4F^2 DK \{ 2[C_{V_0}(\text{m/f})]_{dc}(1-\alpha) - A' \}} \quad (77)$$

where

$$A' = A \left(\frac{RT}{F\bar{V}_{ac}} \right) \quad (78)$$

with

$$A = - \left(\frac{F\bar{V}_{ac}}{RT} \right) \cdot \frac{[C_{V_0}(\text{f/s})]_{dc}\alpha + [C_{V_0}(\text{m/f})]_{dc}(1-\alpha)\exp[KL - (K^2 + s/DL)^{1/2}]}{\exp(KL)\sinh[(K^2 + s/DL^{1/2})]} \quad (79)$$

These equations show that the most critical parameters in determining the value of $R_{\omega=0}$ is the diffusivity of oxygen vacancies ($D \equiv D_0$) and the film thickness L ; $R_{\omega=0}$ increases roughly exponentially with L and with $1/D$. Similar arguments can be made in the case of the transport of cation vacancies across a passive film.

The diagnostic features of this analysis have been used by Chao *et al.* [1982] in their investigation of the growth of passive films on nickel and Type 304 stainless steel in borate and phosphate buffer solutions. Typical complex plane and Randles's plane plots for nickel in 0.1N Na₂HPO₄ (pH = 9.1) and in 0.15N H₃BO₃/0.15N Na₂B₄O₇ (pH = 8.7) solutions are shown in Figures 4.4.19 and 4.4.20. The data

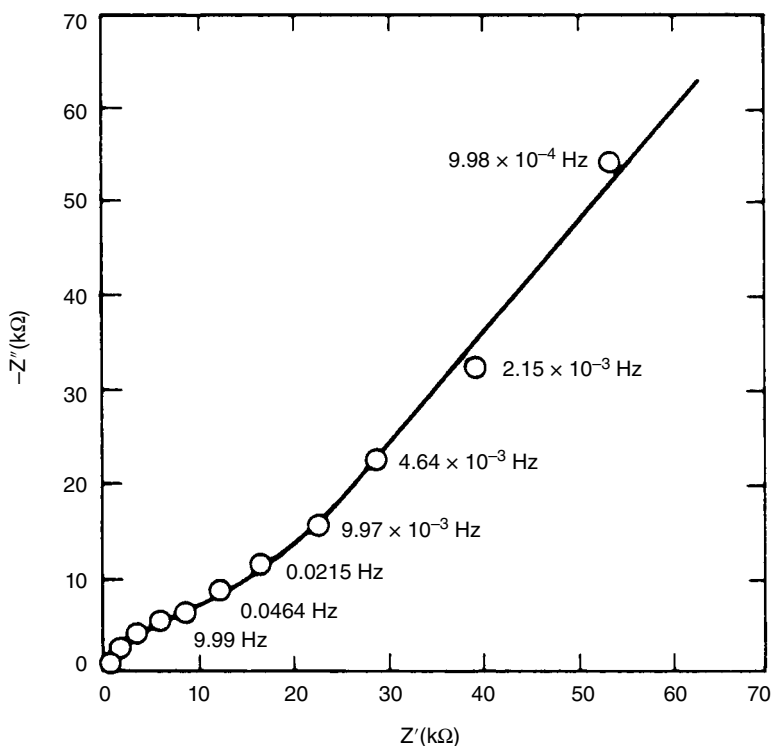


FIGURE 4.4.19 Complex plane impedance plot for Ni(111) in phosphate buffer ($[\text{PO}_4] = 0.1 \text{ M}$) at 25°C . $E = 0.1 \text{ V}$ (SCE), $\text{pH} = 10$. The frequency at which each point was measured is indicated. Electrode area = 0.998 cm^2 .

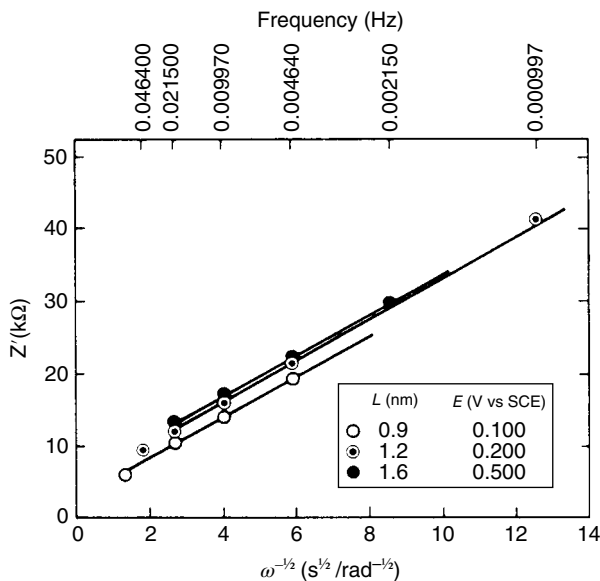


FIGURE 4.4.20 Randles plot of Z' versus $\omega^{-1/2}$ for Ni(111) passivated in 0.1 M phosphate solution ($\text{pH} = 9$). L = film thickness measured ellipsometrically. Electrode area = 0.998 cm^2 .

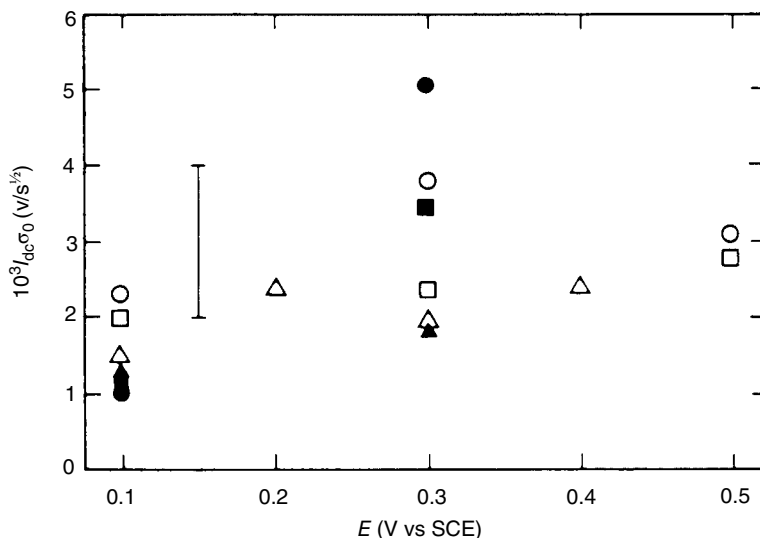


FIGURE 4.4.21 Plot of $I_{dc}\sigma_0$ versus potential for Ni(111) in phosphate buffers ($[PO_4] = 0.1$ M) as a function of pH. Open circles = pH 7, closed circles = pH 8, open squares = pH 9, closed squares = pH 10, open triangles = pH 11, and closed triangles = pH 12. $T = 25^\circ\text{C}$, I = estimated error for each point, and electrode area = 0.998 cm^2 .

shown in Figure 4.4.19 reveal a linear impedance locus at low frequencies, with a partially resolved semicircle at high frequencies. This latter characteristic is attributed to relaxations occurring at the f/s interface, as discussed later. The Randles plots shown in Figure 4.4.20 provide further evidence for the low-frequency Warburg response predicted by Eqs. (73) and (74). These plots also show that the experimentally measured Warburg coefficient $\sigma = dZ'/d\omega^{-1/2}$ is independent of the film thickness (as measured ellipsometrically) and of the applied voltage. Furthermore, the values of σ obtained for the phosphate ($23.1\text{ k}\Omega/\text{s}^{1/2}$) and borate ($8.53\text{ k}\Omega/\text{s}^{1/2}$) environments differ by nearly the factor of 3, as do the passive currents. This is predicted by Eqs. (75) and (76), assuming that negligible differences exist between the passive films formed in these two solutions.

A more extensive impedance analysis of passive films formed on nickel in borate buffer solution has been reported by Liang *et al.* [1984]. In this study, impedance data were obtained for passive nickel over a wide range of applied potential and pH (Figure 4.4.21), and these data serve as a good test of the constancy of σI_{dc} , as predicted by Eqs. (75) and (76). The data (Figure 4.4.21) show that this product is indeed constant, within experimental error, thereby supporting the original hypothesis of the PDM that the electric field strength is independent of film thickness and applied voltage.

An important application of the data shown in Figure 4.4.21 and of the equation for the Warburg coefficient [Eq. (75)] is in the calculation of the diffusivity for anion vacancies within the film. In the case of passive polycrystalline nickel in borate and phosphate buffer solutions, Chao *et al.* [1982] computed a value of $1.3 \times 10^{-21}\text{ cm}^2/\text{s}$ for the diffusivity of oxygen ion vacancies. In a later study by Liang *et al.* [1984], a somewhat higher (and possibly more reliable) value of $1.5 \times 10^{-19}\text{ cm}^2/\text{s}$ for this same quantity was calculated from the data shown in Figure 4.4.21 for passive films formed on single-crystal nickel (100) in borate buffer solution. The principal problem with these calculations lies in the accurate measurement of the passive current I_{dc} . Experience shows that this quantity can vary over several orders of magnitude depending upon how the surface is prepared, the method by which it is measured (potentiostatic vs. potentiodynamic techniques), and possibly the means by which the passive film is formed. Nevertheless, the values for D_0 given earlier are consistent with data extrapolated from high temperatures for a variety of oxides, and they appear to be eminently reasonable from a physicochemical viewpoint (Chao *et al.* [1982]).

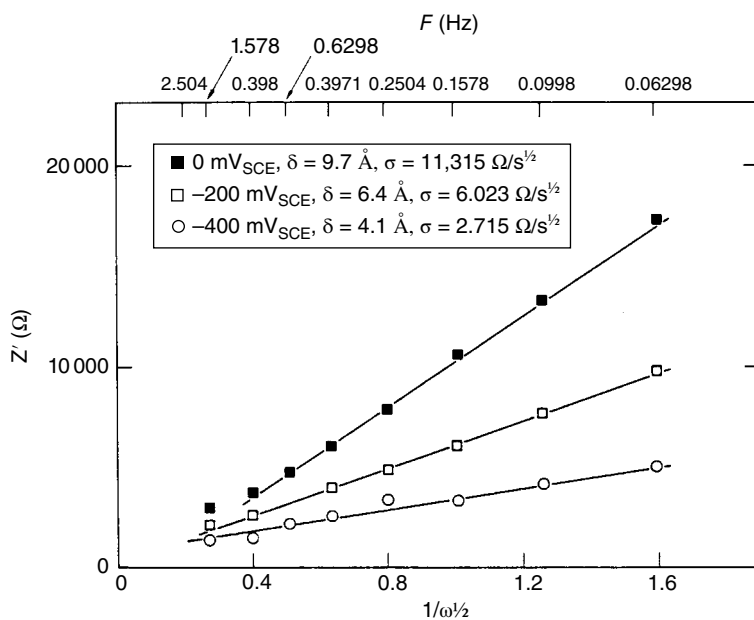


FIGURE 4.4.22 Dependence of Z' on $\omega^{-1/2}$ for Type 304SS passivated in 0.1N Na_2HPO_4 solution (pH 9.1). Source: Chao 1982. Reproduced with permission of The Electrochemical Society.

The data shown in Figure 4.4.22 for Type 304 stainless steel appear to contradict the findings reported earlier for nickel. However, as noted by Chao *et al.* [1982], the potential-dependent and film-thickness-dependent Warburg coefficient can be accounted for by the fact that the composition of the passive film also changes with potential. A study of passive films on Fe-25 Ni-XCr alloys by Silverman *et al.* [1982] indicated that the quantity $\varepsilon/(1-\alpha)$ changes very little as the Fe/Cr ratio is varied over a wide range, but diffusivity data for oxygen ion vacancies in iron and chromium oxides at elevated temperatures vary by many orders of magnitude and in a manner that provides a qualitative explanation of the Randles plots shown in Figure 4.4.22.

Film/Solution Interface. The most comprehensive treatment of the impedance characteristics of the f/s interface of a passive film is that reported by Armstrong and Edmondson [1973]. Their treatment essentially considers the ion exchange properties of an interface (Figure 4.4.23) by addressing the movement of anions and cations between the film surface and the solution as the applied potential is modulated over a wide frequency range.

Armstrong and Edmondson [1973] begin their analysis by noting that the time dependence of the excess of cations over anions in the surface layer (Figure 4.4.23) is given as

$$\frac{d\Gamma}{dt} = V_1 + V_2 - V_3 - V_4 \quad (80)$$

in which rates V_1 , V_2 , V_3 , and V_4 can be expanded linearly as Taylor series in applied potential and excess cation concentration. Therefore,

$$V_i = V_{io} + \left(\frac{\partial V_i}{\partial E} \right)_\Gamma \Delta E e^{j\omega t} + \left(\frac{\partial V_i}{\partial \Gamma} \right)_E \Delta \Gamma e^{j\omega t}, \quad i = 1 - 4 \quad (81)$$

Equations (80) and (81) may be combined to yield

$$\Delta \Gamma = \frac{\left[\left(\frac{\partial V_1}{\partial E} \right)_\Gamma + \left(\frac{\partial V_2}{\partial E} \right)_\Gamma - \left(\frac{\partial V_3}{\partial E} \right)_\Gamma - \left(\frac{\partial V_4}{\partial E} \right)_\Gamma \right] \Delta E}{j\omega - \left(\frac{\partial V_1}{\partial \Gamma} \right)_E - \left(\frac{\partial V_2}{\partial \Gamma} \right)_E + \left(\frac{\partial V_3}{\partial \Gamma} \right)_E + \left(\frac{\partial V_4}{\partial \Gamma} \right)_E} \quad (82)$$

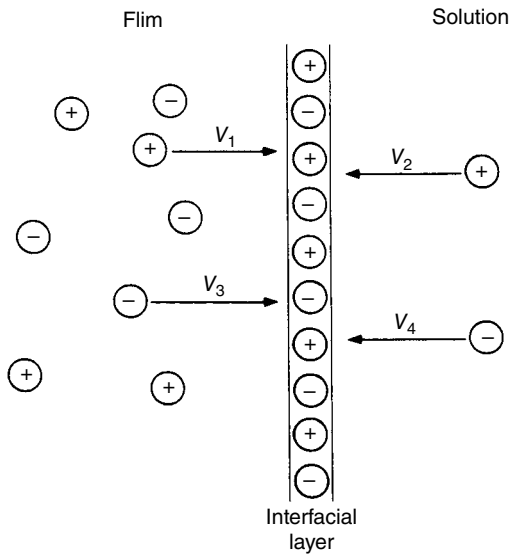


FIGURE 4.4.23 Model of film/solution interface according to Armstrong and Edmondson [1973].
Source: Armstrong 1973. Reproduced with permission of Elsevier.

If the number of electrons that flow through an external circuit upon the transfer of one species in reaction i (Figure 4.4.23) is n_i , then the faradic admittance of the f/s interface is

$$Y_{f/s} = \frac{n_1 F V_1 + n_2 F V_2 + n_3 F V_3 + n_4 F V_4}{\Delta E \exp(j\omega t)} \quad (83)$$

which upon substitution of Eq. (81) becomes

$$Y_{f/s} = \sum_{i=1}^4 n_i F \left(\frac{\partial V_i}{\partial E} \right)_\Gamma + \Delta \Gamma \sum_{i=1}^4 n_i F \left(\frac{\partial V_i}{\partial \Gamma} \right)_E \quad (84)$$

where $\Delta \Gamma$ is given by Eq. (82). According to Armstrong and Edmondson [1973], it is convenient to define infinite-frequency charge transfer resistances as

$$\frac{1}{R_{\infty 1}} = n_1 F \left(\frac{\partial V_1}{\partial E} \right)_\Gamma + n_2 F \left(\frac{\partial V_2}{\partial E} \right)_\Gamma \quad (85)$$

$$\frac{1}{R_{\infty 2}} = n_3 F \left(\frac{\partial V_3}{\partial E} \right)_\Gamma + n_4 F \left(\frac{\partial V_4}{\partial E} \right)_\Gamma \quad (86)$$

and resistances at zero frequency as

$$\begin{aligned} \frac{1}{R_{01}} &= \left[\left(\frac{\partial V_1}{\partial E} \right)_\Gamma + \left(\frac{\partial V_2}{\partial E} \right)_\Gamma - \left(\frac{\partial V_3}{\partial E} \right)_\Gamma - \left(\frac{\partial V_4}{\partial E} \right)_\Gamma \right] \\ &\cdot \left[n_1 F \left(\frac{\partial V_1}{\partial \Gamma} \right)_E + n_2 F \left(\frac{\partial V_2}{\partial \Gamma} \right)_E \right] / k \end{aligned} \quad (87)$$

$$\frac{1}{R_{02}} = \left[\left(\frac{\partial V_1}{\partial E} \right)_{\Gamma} + \left(\frac{\partial V_2}{\partial E} \right)_{\Gamma} - \left(\frac{\partial V_3}{\partial E} \right)_{\Gamma} - \left(\frac{\partial V_4}{\partial E} \right)_{\Gamma} \right] \\ \cdot \left[n_3 F \left(\frac{\partial V_3}{\partial \Gamma} \right)_E + n_4 F \left(\frac{\partial V_4}{\partial \Gamma} \right)_E \right] / k \quad (88)$$

where k defines the relaxation time τ as

$$\tau = \frac{1}{k} \quad (89)$$

with

$$k = \left(\frac{\partial V_3}{\partial \Gamma} \right)_E + \left(\frac{\partial V_4}{\partial \Gamma} \right)_E - \left(\frac{\partial V_1}{\partial \Gamma} \right)_E - \left(\frac{\partial V_2}{\partial \Gamma} \right)_E \quad (90)$$

Accordingly, the faradic admittance becomes

$$Y_{f/s} = \frac{1}{R_{\infty 1}} + \frac{1}{R_{\infty 2}} + \frac{k}{k+j\omega} \cdot \left(\frac{1}{R_{01}} + \frac{1}{R_{02}} \right) \quad (91)$$

However, Armstrong and Edmondson [1973] claim that, in most cases, oxygen will be in equilibrium between the interface and the solution, a condition that can only be satisfied if $R_{\infty 2} = -R_{02}$. Thus, Eq. (91) becomes

$$Y_{f/s} = \frac{1}{R_{\infty 1}} + \frac{k}{k+j\omega} \cdot \frac{1}{R_{01}} + \frac{1}{R_{\infty 2}} \cdot \frac{j\omega}{k+j\omega} \quad (92)$$

and the total interfacial impedance is written as

$$Z_{f/s} = \frac{1}{Y_{f/s} + j\omega C_{\infty}} \quad (93)$$

where C_{∞} is the double-layer capacitance. The complex plane impedance loci that can be generated by Eq. (93) according to the relative values of k and ω have been explored by Armstrong and Edmondson [1973], and their results are summarized as follows:

1. Large $k(k \gg \omega)$. In this case, Eq. (92) reduces to

$$Y_{f/s} = \frac{1}{R_{\infty 1}} + \frac{1}{R_{01}} + \frac{j\omega}{kR_{\infty 2}} \quad (94)$$

and the impedance locus takes the form of a single semicircle in the complex plane (Figure 4.4.24) resulting from a resistance $R_{\infty 1}R_{01}/(R_{\infty 1} + R_{01})$ in parallel with the capacitance $C_{\infty} + kR_{\infty 2}$.

2. Small $k(k \ll \omega)$, in which case Eq. (92) becomes

$$Y_{f/s} = \frac{1}{R_{\infty 1}} + \frac{1}{R_{\infty 2}} - \frac{jk}{\omega R_{01}} \quad (95)$$

indicating that two semicircles will appear in the complex plane according to the relative values of A and B :

$$A = \frac{R_{\infty 1}R_{01}}{R_{\infty 1} + R_{01}} \quad (96)$$

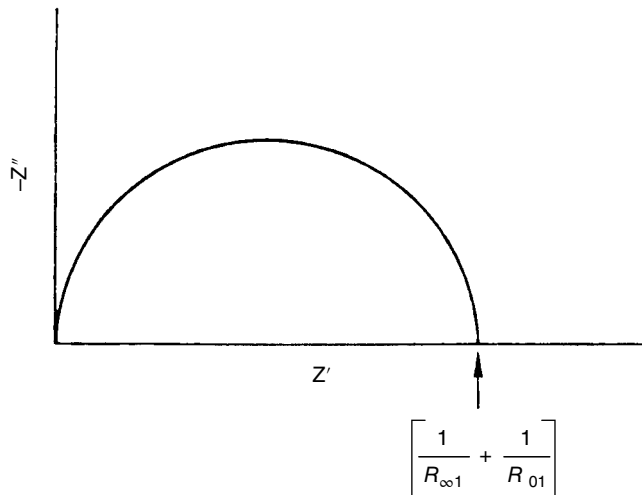


FIGURE 4.4.24 Film/solution interface according to Eq. (89) for large k . Source: Armstrong 1973. Reproduced with permission of Elsevier.

$$B = \frac{R_{\infty 1} R_{\infty 2}}{R_{\infty 1} + R_{\infty 2}} \quad (97)$$

Thus, for $A > B > 0$ and $B > A > 0$, the complex plane impedance loci shown in Figures 4.4.25a and b are obtained, whereas for $B > 0 > A$ that shown in Figure 4.4.25c results. The latter case occurs because R_{01} may be positive or negative, depending upon the relative values of the differentials contained in Eq. (87). Provided that R_{01} is negative, but that $|R_{\infty 1}| > |R_{01}|$, second-quadrant behavior at low frequencies is predicted, terminating in a negative resistance at $\omega \rightarrow 0$. The low-frequency inductive response predicted in the second case ($B > A > 0$) is also of considerable practical and theoretical interest, because fourth-quadrant behavior is frequently observed experimentally.

At this point it is worthwhile pausing to consider the properties of the total impedance of the interphase system consisting of the m/f interface, the film, and the f/s interface. According to Eq. (54) and subsequent expressions for $Z_{m/f}$, Z_f , and $Z_{f/s}$, the total impedance becomes

$$Z_T = R_e + W + \frac{X}{X^2 + Y^2} - j \left(W + \frac{Y}{X^2 + Y^2} \right) \quad (98)$$

$$W = \frac{\sigma_M \sigma_0 \omega^{-1/2}}{\sigma_M + \sigma_0} \quad (99)$$

$$X = \frac{1}{R_{\infty 1}} + \frac{1}{k^2 + \omega^2} \left(\frac{\omega^2}{R_{\infty 2}} + \frac{k^2}{R_{01}} \right) \quad (100)$$

$$Y = \frac{\omega k}{k^2 + \omega^2} \left(\frac{1}{R_{\infty 2}} - \frac{1}{R_{01}} \right) + \omega C_\infty \quad (101)$$

These rather complicated expressions predict that a variety of impedance loci in the complex plane might be observed, depending upon the frequency range employed and the relative values of the parameters contained in Eqs. (98)–(101).

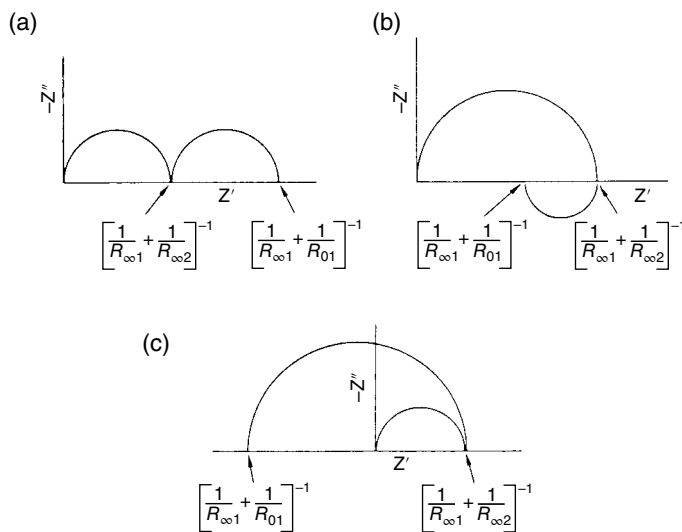


FIGURE 4.4.25 Complex plane impedance diagrams for film/solution interface according to Eq. (93) for small k .
Source: Armstrong 1973. Reproduced with permission of Elsevier.

By way of illustration, we calculate complex impedance diagrams for the case of a passive film in which only anion vacancies are mobile and for which k [Eq. (90)] is large. Thus, for $k \gg \omega$, $\sigma_M \gg \sigma_0$, and assuming that no redox reactions occur at the f/s interface, then the total impedance becomes

$$Z_t = \left(\frac{a}{a^2 + \omega^2 b^2} + \sigma_0 \omega^{-1/2} \right) - j \left(\frac{\omega b}{a^2 + \omega^2 b^2} + \sigma_0 \omega^{-1/2} \right) \quad (102)$$

where

$$a = \frac{1}{R_{\infty 1}} + \frac{1}{R_{01}} \quad (103)$$

$$b = C_{\infty} + \frac{1}{kR_{\infty 2}} \quad (104)$$

Impedance diagrams for a passive film, computed using Eq. (102), are displayed in Figure 4.4.26. These diagrams show a partially resolved semicircle at high frequencies and a low-frequency Warburg response. These same general features are exhibited by the impedance data for passive Ni(III) in phosphate buffer solution, as shown in Figure 4.4.19. The calculated impedance spectra (Figure 4.4.26) show that as the kinetics of the interfacial ion exchange processes become slower (increasing R_{01}), the impedance becomes increasingly dominated by the nondiffusional component. In the limit of sufficiently slow interfacial reactions but fast transport of vacancies across the film, the impedance locus takes the form of a semicircle, which is similar to that expected for a purely capacitive (dielectric) response.

A major shortcoming of the theory developed earlier is that the various processes (e.g., ion exchange and vacancy transport) are assumed to be uncoupled. More realistically, the kinetic expression given by Eq. (80), for example, should be employed as a boundary condition for the solution of Eq. (61). In this way, coupling, which is expected to become most apparent at intermediate frequencies where the vacancy transport and ion exchange processes are of comparable importance, may be a significant factor in determining the impedance spectrum. Such coupling is included in the approach described in Section 2.2.3.3.

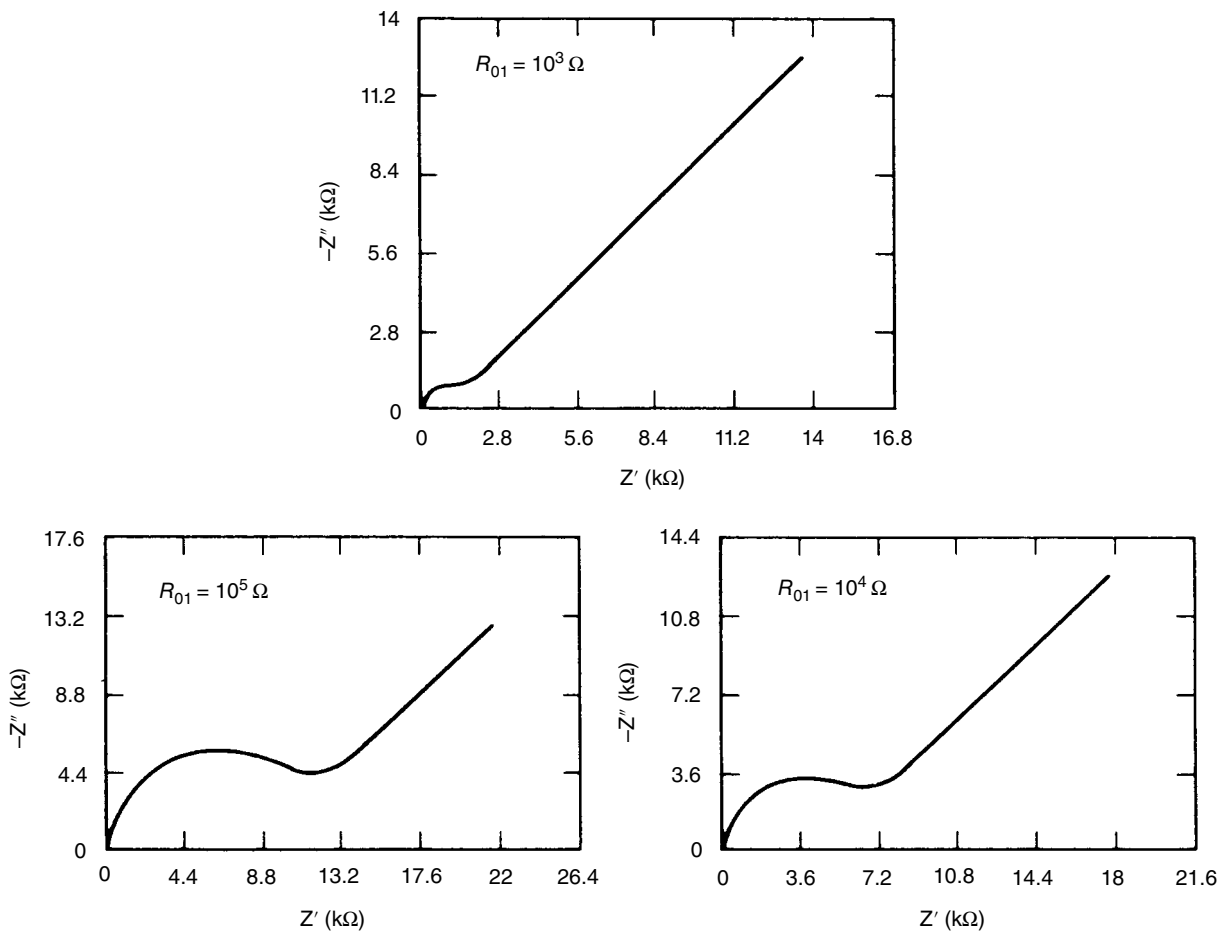


FIGURE 4.4.26 Theoretical complex plane impedance diagrams for a passive film according to Eq. (102). $C_\infty = 5 \times 10^{-5} \text{ F}$, $R_{\infty 1} = 10^4 \Omega$, $R_{\infty 2} = 1 \Omega$, $\sigma_0 = 10^3 \Omega/\text{s}^{1/2}$.

4.4.7 Reaction Mechanism Analysis of Passive Metals

Passivity, in which a reactive metal possesses kinetic stability in a corrosive environment, due to the formation of a thin oxide film on the surface that separates the reactive metal from the environment, is recognized as being one of the most important of all natural phenomena, because it is responsible for our reactive metal-based civilization (Macdonald [1999a]). Thus, our civilization is based upon the building of machines from reactive metals (e.g., Fe, Al, Cr, Ni, Cu, Ti, Zr, and so forth) that often require extremely small dimensional tolerances. Any change in dimension, due to corrosion, for example, will often render the machine nonfunctional and hence to fail. This section describes the use of electrochemical impedance spectroscopy (EIS) to explore the phenomenon of passivity and to ultimately indicate how the passive state may be engineered to achieve even greater corrosion resistance and stability.

4.4.7.1 The Point Defect Model

The PDM was developed by Macdonald and coworkers as a mechanistically based model that could be evaluated analytically against experiment, in order that it might be used to deterministically predict the accumulation of corrosion damage in practical systems (Macdonald [1992, 1999a, 2012a]). The PDM,

which is now highly developed and which has accounted for all of the known phenomena associated with the passive state, at least those known to the author, forms the analytical basis for interpreting EIS data for the passive state. Thus, the author is not aware of any known conflicts with experiment. Indeed, the model has predicted new phenomena that have subsequently been observed, including the photo-inhibition of passivity breakdown (PIPБ) (Lenhart *et al.* [1987], Alkire *et al.* [1996], Breslin *et al.* [1997b]) and resistive depassivation (Macdonald [2010]). It also provides a theoretical basis for designing new alloys from first principles (Macdonald [1985a]). The PDM has been previously used to interpret electrochemical impedance data by optimizing the model on frequency dispersions of the experimental real and imaginary impedance, with considerable success (Ai *et al.* [2008], Ling *et al.* [2013], Lu *et al.* [2013], Macdonald [2013], Sharifi-Asl *et al.* [2013a], Taylor *et al.* [2013]). This model assumes that the impedance due to the transport of point defects in the barrier layer is separable from the impedance due to the point defect generation/annihilation reactions occurring at the barrier layer interfaces. This assumption is justified by the fact that when deriving the impedance function, the concentration of oxygen vacancies does not appear in the expression for the passive current density, because the interfacial reactions are considered to be irreversible and because the annihilation of oxygen vacancies by injection of oxide ions from water does not result in the generation of electron current.

The PDM postulates that the passive film that forms on a metal surface is a bilayer structure comprising a point defective oxide, sulfide, or hydride barrier layer that grows directly into the metal, with an outer layer forming by hydrolysis and precipitation of cations that are transmitted through the barrier layer and ejected at the barrier layer/outer layer (bl/ol) interface and/or by the dissolution of the barrier layer at the same location (Macdonald [1992, 1999a, 2012a]). The point defects that are considered in the model are cation and oxygen/sulfide/hydride vacancies, as the case may be, and metal interstitials; oxygen/sulfide interstitials are not considered, because they are too large to move through most oxide/sulfide lattices except possibly at very high temperatures, but the PDM possibly should be extended to incorporate hydrogen interstitials.

The physicochemical basis of the PDM is shown in Figure 4.4.27 (Macdonald [1992, 1999a, 2012a]). Briefly, the model postulates that defect generation and annihilation reactions occur at the metal/barrier layer (m/bl) and the bl/ol interfaces and stipulates that these reactions essentially establish the high point defect concentrations in the barrier layer (10^{20} – 10^{22} cm $^{-3}$) that are observed

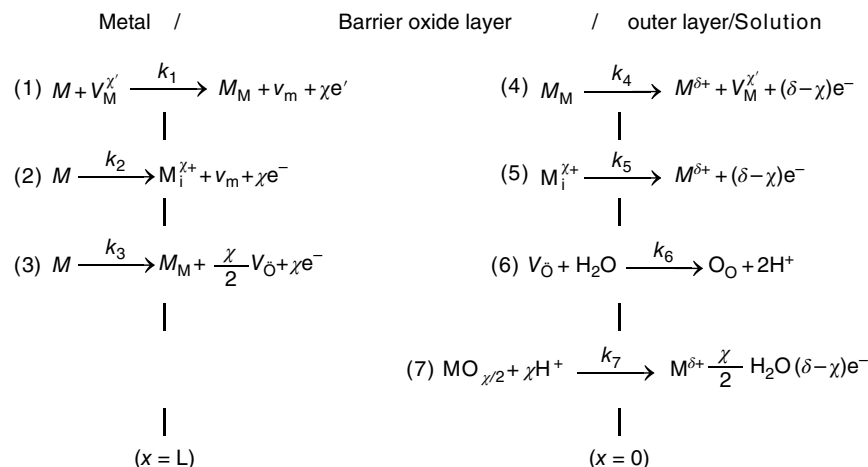


FIGURE 4.4.27 Interfacial defect generation/annihilation reactions that are postulated by the point defect model to occur in the growth of the anodic barrier oxide layer of the passive film on a metal. m , metal atom; $M_i^{\chi+}$, interstitial cation; M_M , metal cation on the metal sublattice of the barrier layer; $M^{\delta+}$, metal cation in solution; O_O , oxygen anion on the oxygen sublattice of the barrier layer; $V_M^{\chi'}$, cation vacancy on the metal sublattice of the barrier layer.

TABLE 4.4.1 Rate Constants for the Reactions That Annihilate and Generate Point Defects in the Barrier Layer of the Passive Film at the m/bl Interface [Reactions (1)–(3)] and at the bl/s Interface [Reactions (4)–(7)], Figure 4.4.27, and for Dissolution of the Barrier Layer [Reaction (7)]

Reaction	$a_i (V^{-1})$	$b_i (cm^{-1})$	c_i	Units of k_i^0
(1) $m + V_M^{\chi'} \rightarrow^{k_1} M_M + v_m + \chi e'$	$\alpha_1(1-\alpha)\chi\gamma$	$-\alpha_1\chi K$	$-\alpha_1\beta\chi\gamma$	s^{-1}
(2) $m \rightarrow^{k_2} M_i^{\chi'} + v_m + \chi e'$	$\alpha_2(1-\alpha)\chi\gamma$	$-\alpha_2\chi K$	$-\alpha_2\beta\chi\gamma$	$mol/cm^2 s$
(3) $m \rightarrow^{k_3} M_M + \frac{\chi}{2}V_{\dot{O}} + \chi e'$	$\alpha_3(1-\alpha)\chi\gamma$	$-\alpha_3\chi K$	$-\alpha_3\beta\chi\gamma$	$mol/cm^2 s$
(4) $M_M \rightarrow^{k_4} M^{\delta+} + (\delta-\chi)e'$	$\alpha_4\alpha\delta\gamma$		$\alpha_4\beta\delta\gamma$	$mol/cm^2 s$
(5) $M_i^{\chi'} \rightarrow^{k_5} M^{\delta+} + (\delta-\chi)e'$	$\alpha_5\alpha\delta\gamma$		$\alpha_5\beta\delta\gamma$	cm/s
(6) $V_{\dot{O}} + H_2O \rightarrow^{k_6} O_O + 2H^+$	$2\alpha_6\alpha\gamma$		$\alpha_6\beta\delta\gamma$	cm/s
(7) $MO_{\chi/2} + \chi H^+ \rightarrow^{k_7} M^{\delta+} + \frac{\chi}{2}H_2O + (\delta-\chi)e'$	$\alpha_7\alpha(\delta-\chi)\gamma$		$\alpha_7(\delta-\chi)\beta\gamma$	$mol/cm^2 s$

Note: $k_i = k_i^0 e^{a_i V} e^{b_i L} e^{c_i pH}$, where $K = \epsilon\gamma$, ϵ is the electric field strength within the barrier layer and $\gamma = F/RT$.

experimentally by Mott–Schottky analysis. Analytical expressions for the rate constants, as derived by the method of partial charges, are summarized in Table 4.4.1.

The passive current density, I , is given by the expression

$$I = F \{ \chi k_1 C_v^L + \chi k_2 + \chi k_3 + (\delta-\chi)k_4 + (\delta-\chi)k_5 C_i^0 + (\delta-\chi)k_7 \} \quad (105)$$

The concentration of H^+ ions is considered to be constant (a well-buffered solution) and included within the definition of k_7 ; that is, $k_7 = k_7^0 (C_{H^+}/C_{H^+}^0)^n$, where $C_{H^+}^0$ is the standard state concentration (105 m), k_7^0 is the standard rate constant for barrier layer dissolution, and n is the kinetic order of dissolution [Reaction (111), Figure 4.4.27] with respect to the proton concentration at the barrier layer/solution (bl/s) interface. The rate constants, as summarized in Table 4.4.1, may be written as

$$k_j = k_j^0 \exp [a_j(V - R_{ol}I) + b_j L] \quad j = 1, 2, 3 \quad (106)$$

$$k_j = k_j^0 \exp [a_j(V - R_{ol}I)] \quad j = 4, 5 \quad (107)$$

and

$$k_7 = k_7^0 \exp [a_7(V - R_{ol}I)] \left(\frac{C_{H^+}}{C_{H^+}^0} \right)^n \quad (108)$$

where a correction has been made for the IR potential drop across the outer layer. This correction is necessary, because the voltage that is measured or controlled with respect to an RE is that just outside of the outer layer whereas that which affects barrier layer growth is that at the bl/ol interface. Note that, in these expressions, R_{ol} is the specific resistance of the outer layer (units of $\Omega \cdot cm^2$) and I is the current density (A/cm^2). Note also that the rate constants for the reactions occurring at the bl/ol interface [Reactions (4), (5), and (7)] do not depend upon the thickness of the barrier layer, but that those that occur at the m/bl interface do depend upon L (Macdonald [1992, 1999a, 2012a]).

Let us assume that potential that is applied at the position of a Luggin probe just outside of the outer layer/solution (ol/s) interface varies sinusoidally according to the expression

$$V = \bar{V} + \delta V = \bar{V} + \Delta V e^{j\omega t} \quad (109)$$

The bar refers to the value of the parameter value under steady-state conditions. Accordingly, in the linear case, the other variables are assumed to also vary sinusoidally as follows:

$$I = \bar{I} + \delta I = \bar{I} + \Delta I e^{j\omega t} \quad (110)$$

$$L = \bar{L} + \delta L = \bar{L} + \Delta L e^{j\omega t} \quad (111)$$

$$C_i^0 = \bar{C}_i^0 + \delta C_i^0 = \bar{C}_i^0 + \Delta C_i^0 e^{j\omega t} \quad (112)$$

$$C_v^L = \bar{C}_v^L + \delta C_{V_M}^L = \bar{C}_v^L + \Delta C_v^L e^{j\omega t} \quad (113)$$

$$C_o^L = \bar{C}_o^L + \delta C_o^L = \bar{C}_o^L + \Delta C_o^L e^{j\omega t} \quad (114)$$

where C_i^0 , C_v^0 , and C_o^L are the concentrations of metal interstitials, metal vacancies, and oxygen vacancies, respectively, at the bl/ol interface (superscript "0") and at the m/bl interface (superscript "L"). The quantities, ΔL , ΔC_i^0 , ΔC_v^L , and ΔC_o^L are the amplitudes in the sinusoidal variations in those same variables, while ΔV is the amplitude of the applied voltage perturbation, all at the angular frequency, ω .

Our task is to calculate the admittance, which is defined as

$$Y_F = \frac{\delta I}{\delta V} = \frac{\Delta I}{\Delta V} \quad (115)$$

which, in the linear approximation, yields

$$Y_F = \left(\frac{dI}{dV} \right)_{V=\bar{V}} \quad (116)$$

It follows from the aforementioned equations that the current density I is a function of the potential at the bl/ol interface and that the local potential is defined as

$$U = V - R_{ol} I \quad (117)$$

Accordingly

$$Y_F = \left(\frac{dI}{dV} \right)_{V=\bar{V}} = \left(\frac{dI}{dU} \right)_{U=\bar{U}} \left(\frac{dU}{dV} \right)_{V=\bar{V}} = \left(\frac{dI}{dU} \right)_{U=\bar{U}} \left(1 - R_{ol} \left(\frac{dI}{dV} \right)_{V=\bar{V}} \right), \quad (118)$$

that is,

$$Y_F = \frac{Y_F^0}{1 + R_{ol} Y_F^0} \quad (119)$$

where

$$Y_F^0 = \left(\frac{dI}{dU} \right)_{U=\bar{U}} \quad (120)$$

is the admittance calculated in the absence of the outer layer, assuming that the potential at the bl/ol interface is \bar{U} under steady-state conditions. It is evident that $Y_F \rightarrow Y_F^0$ at $R_{ol} \rightarrow 0$ and $Y_F \rightarrow 1/R_{ol}$ for $R_{ol} \rightarrow \infty$.

The values of \bar{U} and other steady-state parameters can be easily calculated. Assuming some arbitrary value of \bar{U} , we can immediately calculate \bar{k}_i , $i = 4, 5, 7$ from Eq. (107). From the condition of change in thickness of the barrier layer, which is written as

$$\frac{dL}{dt} = \Omega k_3 - \Omega k_7 \quad (121)$$

we have $\bar{k}_3 = \bar{k}_7$, which after some algebraic manipulation yields the steady-state thickness as

$$\begin{aligned} \bar{L} = & \frac{1}{\epsilon} \left[1 - \alpha - \frac{\alpha \alpha_7}{\alpha_3} \left(\frac{\delta}{\chi} - 1 \right) \right] V + \frac{1}{\epsilon} \left\{ \frac{2.303n}{\alpha_3 \chi \gamma} - \beta \left[\frac{\alpha_7}{\alpha_3} \left(\frac{\delta}{\chi} - 1 \right) + 1 \right] \right\} \text{pH} \\ & + \frac{1}{\alpha_3 \chi K} \ln \left(\frac{k_3^0}{k_7^0} \right) \end{aligned} \quad (122)$$

Subsequently, the values \bar{k}_i $i = 1, 2, 3$ can be readily calculated by using Eq. (106).

The values of the steady-state concentrations, \bar{C}_i^0 , \bar{C}_v^L , and \bar{C}_o^L , can be found from the equating the fluxes for each species at the m/bl and bl/ol interfaces to yield

$$\bar{C}_i^0 = \frac{\bar{k}_2^0}{\bar{k}_5^0} \quad (123)$$

$$\bar{C}_v^L = \frac{\bar{k}_4^0}{\bar{k}_1^0} \quad (124)$$

and

$$\bar{C}_o^L = \frac{\bar{k}_3^0}{\bar{k}_6^0}, \quad (125)$$

respectively.

Finally, we calculate the values of

$$\bar{I} = F \{ \chi \bar{k}_1 \bar{C}_v^L + \chi \bar{k}_2 + \chi \bar{k}_3 + (\delta - \chi) \bar{k}_4 + (\delta - \chi) \bar{k}_5 \bar{C}_i^0 + (\delta - \chi) \bar{k}_7 \} \quad (126)$$

and

$$\bar{V} = \bar{U} + R_{\text{ol}} \bar{I}, \quad (127)$$

that is, we can calculate the steady-state current density $\bar{I}(\bar{V})$. In solving for the admittance in the absence and presence of the outer layer, we will choose the value at which \bar{V} is equal to a prescribed value. Essentially, the task is reduced to solving the equation $\bar{V} = \bar{U} + R_{\text{ol}} \bar{I}(\bar{U})$ for the unknown value \bar{U} at the bl/ol interface.

An important finding of this analysis is that if we have code for calculating the admittance of the system in the absence of the outer layer, Y_F^0 , we can calculate the admittance in the presence of the outer layer Y_F by using Eq. (119), assuming that Y_F^0 is calculated at the steady-state applied potential that equals \bar{U} (but not \bar{V}).

Calculation of Y_F^0

We have in the linear approximation

$$\delta k_i = \bar{k}_i [a_i \delta U + b_i \delta L] \quad i = 1, 2, 3 \quad (128)$$

and

$$\delta k_i = \bar{k}_i a_i \delta U \quad i = 4, 5, 7 \quad (129)$$

By taking the total differential of Eq. (105), the linear approximation of the variation in the current is obtained as

$$\delta I = I_V \delta U + I_L \delta L + I_v^L \delta C_v^L + I_i^0 \delta C_i^0 \quad (130)$$

where

$$I_U = F \{ \chi a_1 \bar{k}_1 \bar{C}_v^L + \chi \bar{k}_2 a_2 + \chi \bar{k}_3 a_3 + (\delta - \chi) \bar{k}_4 a_4 + (\delta - \chi) \bar{k}_5 a_5 \bar{C}_i^0 + (\delta - \chi) \bar{k}_7 a_7 \} \quad (131)$$

$$I_L = F \{ \chi b_1 \bar{k}_1 \bar{C}_e^L + \chi \bar{k}_2 b_2 + \chi \bar{k}_3 b_3 \} \quad (132)$$

$$I_v^L = F \chi \bar{k}_1 \quad (133)$$

and

$$I_i^0 = F(\delta - \chi) \bar{k}_5 \quad (134)$$

Taking into account Eqs. (109) and (120), we have

$$Y_F^0 = \frac{\delta I}{\delta U} = \frac{\Delta I}{\Delta U} = I_V + I_L \frac{\Delta L}{\Delta U} + I_v^L \Delta \frac{C_v^L}{\Delta U} + I_i^0 \Delta \frac{C_i^0}{\Delta U} \quad (135)$$

Here, it is assumed that $U = \bar{U} + \delta U = \bar{U} + \Delta U e^{j\omega t}$. We now calculate $\Delta L / \Delta U$, $\Delta C_v^L / \Delta U$, and $\Delta C_i^0 / \Delta U$. It is convenient to start from the expression for $\Delta L / \Delta U$, which is developed as follows. The rate of change of thickness of the barrier layer is described by Eq. (121). Accordingly, we write the total differential as

$$\frac{dL}{dt} = \frac{d\delta L}{dt} = j\omega \Delta L e^{j\omega t} = \Omega \delta k_3 - \Omega \delta k_7 = \Omega (\bar{k}_3 a_3 \delta U + \bar{k}_3 b_3 \delta L) - \Omega \bar{k}_7 a_7 \delta V \quad (136)$$

or

$$L_U \equiv \frac{\Delta L}{\Delta U} = \frac{\Omega (\bar{k}_3 a_3 - \bar{k}_7 a_7)}{j\omega - \Omega \bar{k}_3 b_3} \quad (137)$$

Note that this quantity is reactive; that is, it has a nonzero phase shift. However, numerical analysis shows that L_U is very small; hence, to a good approximation, the relaxation in the barrier layer thickness induced by the imposed sinusoidal variation in potential can be neglected. This issue is expanded upon later in this chapter.

Calculation of $\Delta \frac{C_i^0}{\Delta U}$

Flux density of interstitials is expressed as

$$J_i = -D_i \frac{\partial C_i}{\partial x} - \chi D_i K C_i \quad (138)$$

and the continuity equation is given by

$$\frac{\partial C_i}{\partial t} = D_i \frac{\partial^2 C_i}{\partial x^2} + \chi D_i K \frac{\partial C_i}{\partial x} \quad (139)$$

where $K = \epsilon\gamma$, ϵ is the electric field strength within the barrier layer, C_i and D_i are the concentration and diffusivity of metal interstitials in the barrier layer, respectively, and $\gamma = F/RT$. Accordingly, by taking the total differential, we have

$$\frac{\partial \delta C_i}{\partial t} = D_i \frac{\partial^2 \delta C_i}{\partial x^2} + \chi D_i K \frac{\partial \delta C_i}{\partial x} \quad (140)$$

or

$$j\omega \Delta C_i = \frac{d^2 \Delta C_i}{dx^2} + \chi D_i K \frac{d \Delta C_i}{dx} \quad (141)$$

The general solution of this second-order ordinary differential equation is

$$\Delta C_i = A e^{r_1 x} + B e^{r_2 x} \quad (142)$$

where

$$r_{1,2} = \frac{-\chi K \pm \sqrt{\chi^2 K^2 + 4j\omega/D_i}}{2} \quad (143)$$

In particular, the following solution

$$\Delta C_i = \Delta C_i^L - \Delta \frac{C_i^0 e^{r_2 L}}{e^{r_1 L} - e^{r_2 L}} e^{r_1 x} + \Delta C_i^0 e^{r_1 L} - \Delta \frac{C_i^L}{e^{r_1 L} - e^{r_2 L}} e^{r_2 x} \quad (144)$$

satisfies the boundary conditions

$$\Delta C_i = \Delta C_i^0 \text{ at } x = 0 \text{ and } \Delta C_i = \Delta C_i^L \text{ at } x = L.$$

The values ΔC_i^0 and ΔC_i^L can be found from the boundary conditions

$$-k_5 C_i^0 = -D_i \frac{d C_i}{d x} - \chi D_i K C_i \text{ at } x = 0 \quad (145)$$

and

$$-k_2 = -D_i \frac{d C_i}{d x} - \chi D_i K C_i \text{ at } x = L \quad (146)$$

or

$$-\bar{k}_5 (\bar{C}_i^0 a_5 \Delta U + \Delta \bar{C}_i^0) = -D_i \left(\frac{d \Delta C_i}{d x} \right)_{x=0} - \chi D_i K \Delta C_i^0 \text{ at } x = 0 \quad (147)$$

and

$$-\bar{k}_2 (a_2 \Delta U - b_2 \Delta L) = -D_i \left(\frac{d \Delta C_i}{d x} \right)_{x=L} - \chi D_i K \Delta C_i^L \text{ at } x = L \quad (148)$$

These equations yield two linear equations in the two unknown values, A and B :

$$\begin{aligned} a_{11}A + a_{12}B &= b_{1V} \Delta U \\ a_{21}A + a_{22}B &= b_{2V} \Delta U + b_{2L} \Delta L \end{aligned} \quad (149)$$

where

$$\begin{aligned} a_{11} &= (r_1 + \chi K)D_i - \bar{k}_5, \quad a_{12} = (r_2 + \chi K)D_i - \bar{k}_5, \\ a_{21} &= (r_1 + \chi K)D_i e^{r_1 L}, \quad a_{22} = (r_2 + \chi K)D_i e^{r_2 L} \end{aligned} \quad (150)$$

and

$$b_{1U} = \bar{k}_5 a_5 \bar{C}_i^0, \quad b_{2U} = \bar{k}_2 a_2, \quad b_{2L} = \bar{k}_2 b_2 \quad (151)$$

Accordingly, the amplitude in the sinusoidal variation of the concentration of interstitials in the barrier layer at the bl/ol interface, ΔC_i^0 , can be expressed in the form

$$\Delta C_i^0 = A + B = \Delta C_{iU}^0 \Delta U + \Delta C_{iL}^0 \Delta L \quad (152)$$

where

$$\Delta C_{iU}^0 = \frac{b_{1U}(a_{22} - a_{21}) + b_{2U}(a_{11} - a_{12})}{\det} \quad (153)$$

$$\Delta C_{iL}^0 = \frac{b_{2L}(a_{11} - a_{12})}{\det} \quad (154)$$

and

$$\det = a_{11}a_{22} - a_{12}a_{21} \quad (155)$$

Calculation of $\Delta \frac{C_v^L}{\Delta U}$

The flux density of cation vacancies, which carry a charge of $-\chi$, is written as

$$J_v = -D_v \frac{\partial C_v}{\partial x} + \chi D_M K C_v \quad (156)$$

Again, the continuity equation is expressed as

$$\frac{\partial C_v}{\partial t} = D_v \frac{\partial^2 C_v}{\partial x^2} - \chi D_v K \frac{\partial C_v}{\partial x}, \quad (157)$$

and taking the total differential yields

$$\frac{\partial \delta C_v}{\partial t} = D_v \frac{\partial^2 \delta C_v}{\partial x^2} - \chi D_v K \frac{\partial \delta C_v}{\partial x} \quad (158)$$

or

$$j\omega \Delta C_v = \frac{d^2 \Delta C_v}{dx^2} - \chi D_v K \frac{d \Delta C_v}{dx} \quad (159)$$

The general solution of this equation is written as

$$\Delta C_v = A e^{r_1 x} + B e^{r_2 x} \quad (160)$$

where

$$r_{1,2} = \frac{\chi K \pm \sqrt{\chi^2 K^2 + 4j\omega/D_v}}{2} \quad (161)$$

As before, the values ΔC_v^0 and ΔC_v^L can be found from the boundary conditions

$$k_4 = -D_v \left(\frac{\partial C_v}{\partial x} \right)_{x=0} + \chi D_v K C_v \text{ at } x=0 \quad (162)$$

and

$$k_1 C_v^L = -D_v \left(\frac{\partial C_v}{\partial x} \right)_{x=L} + \chi D_M K C_M \text{ at } x=L \quad (163)$$

or

$$\bar{k}_4 a_4 \Delta U = -D_v \left(\frac{\partial \Delta C_v}{\partial x} \right)_{x=0} + \chi D_v K \Delta C_v^0 \text{ at } x=0 \quad (164)$$

and

$$\bar{k}_1 \bar{C}_v^L (a_1 \Delta U + b_1 \Delta L) + \bar{k}_1 \Delta \bar{C}_v^L = -D_v \left(\frac{\partial \Delta C_i}{\partial x} \right)_{x=L} + \chi D_M K \Delta C_v^L \text{ at } x=L \quad (165)$$

These expressions yield two linear equations with two unknown values, A and B :

$$\begin{aligned} a_{11}A + a_{12}B &= b_{1V} \Delta U \\ a_{21}A + a_{22}B &= b_{2V} \Delta U + b_{2L} \Delta L \end{aligned} \quad (166)$$

where

$$\begin{aligned} a_{11} &= (r_1 - \chi K) D_v, \quad a_{12} = (r_2 - \chi K) D_v, \\ a_{21} &= [(r_1 - \chi K) D_v + \bar{k}_1] e^{r_1 L}, \quad a_{22} = [(r_2 - \chi K) D_v + \bar{k}_1] e^{r_2 L} \\ b_{1V} &= -\bar{k}_4 a_4, \quad b_{2V} = -\bar{k}_1 a_1 \bar{C}_v^L, \quad b_{2L} = -\bar{k}_1 \bar{C}_v^L b_1 \end{aligned} \quad (167)$$

Accordingly, we have

$$\Delta C_v^L = A e^{r_1 L} + B e^{r_2 L} = \Delta C_{vV}^L \Delta U + \Delta C_{vL}^L \Delta L \quad (168)$$

where

$$\Delta C_{vU}^L = \frac{(b_{1U} a_{22} - b_{2U} a_{12}) e^{r_1 L} + (b_{2U} a_{11} - b_{1U} a_{21}) e^{r_2 L}}{\det} \quad (169)$$

$$\Delta C_{vL}^L = \frac{b_{2L} a_{11} e^{r_2 L} - b_{1L} a_{12} e^{r_1 L}}{\det} \quad (170)$$

and

$$\det = a_{11} a_{22} - a_{12} a_{21} \quad (171)$$

Substituting Eqs. (152) and (168) into Eq. (135), we have the final result:

$$Y_F^0 = I_U + I_L L_U + I_v^L (\Delta C_{vU}^L + \Delta C_{vL}^L L_V) + I_i^0 (\Delta C_{iU}^0 + \Delta C_{iL}^0 L_V) \quad (172)$$

The relaxation of oxygen vacancies in the barrier layer is not included in Eq. (172), because, mathematically, it is formally equivalent to that for the metal interstitial, but with a charge of +2 instead of + χ , provided that $\chi = \delta$.

If $k_2 = 0$, corresponding to no transport of cation interstitials, we have

$$Y_F^0 = I_U + I_L L_U + I_v^L (\Delta C_{vU}^L + \Delta C_{vL}^L L_V) \quad (173)$$

This is the case for a cation vacancy-conducting passive films, such as $\text{Ni}_{1-x}\text{O}_{1-y}$ on Ni (Macdonald [1992, 1999a, 2012a]), where x and y are the fractional vacancies on the cation and anion (oxygen) sub-lattices, respectively. If, in addition, we can neglect changes in cation vacancies concentrations (e.g., due to a high applied perturbation frequency) or $\chi = \delta$, we have

$$Y_F^0 = I_U + I_L L_U \quad (174)$$

$$Y_F^0 = I_U + I_L \frac{\Omega(\bar{k}_3 a_3 - \bar{k}_7 a_7)}{j\omega + \Omega k_3 b_3} \quad (175)$$

where constants I_U and I_L are described by Eqs. (131) and (132).

The reader will note that the expression for the current Eq. (105) does not contain the concentration of oxygen vacancies. This is because Reaction (107) (Figure 4.4.27) for the generation of oxygen vacancies is considered to be irreversible and because Reaction (110) does not contribute to the electronic current. However, physically, the transport of oxygen vacancies across the barrier layer still occurs, but its omission in Eq. (192) is simply an artifact of considering Reaction (107) (Figure 4.4.27) to be irreversible, so that the reverse reaction, the rate of which does depend upon the concentration of oxygen vacancies at the metal/barrier layer, is not included in the expression for the net current. While this “irreversibility” assumption is reasonable for very reactive metals where the applied potential is much more negative than the oxide formation equilibrium potential, in a future, theoretical iteration, we will relax this irreversibility assumption for all reactions in the model, so that the PDM will be able to describe both the growth and reduction of the barrier layer. In the present theory, we simply add a Warburg impedance, Eq. (176), as indicated by the original PDM (Chao *et al.* [1981, 1982]) in series with the faradaic impedance given by the inverse of Y_F :

$$Z_W = \sigma \omega^{-1/2} - j\sigma \omega^{-1/2} \quad (176)$$

where σ is the Warburg coefficient and ω is the angular frequency. As previously shown Chao *et al.* [1982], the Warburg coefficient can be written as

$$\sigma = \frac{D^{1/2} \epsilon}{2^{1/2} (1-\alpha) I_{ss}} \quad (177)$$

where I_{ss} is the steady-state passive current density, ϵ is the electric field strength within the barrier layer, D is the defect diffusivity, and α is the polarizability of the bl/s interface. Parenthetically, the Warburg coefficient may be used to obtain the diffusivity of the defect within the barrier layer by rearranging Eq. (196) to yield

$$D = 2\sigma^2 (1-\alpha)^2 \frac{I_{ss}^2}{\epsilon^2} \quad (178)$$

4.4.7.2 Prediction of Defect Distributions

The electronic defect structure of the barrier layer, and hence its electronic character (whether p-type or n-type), is defined by the distributions of the defects across the layer. This is because cation vacancies are electron acceptors, which dope the barrier layer p-type, while cation interstitials and oxygen vacancies are electron donors, which hence dope the barrier layer n-type.

The differential equations that describe the defect distributions within the barrier layer in the steady state can be written as

$$\frac{\partial^2 C_v}{\partial x^2} - \chi K \frac{\partial C_v}{\partial x} = 0 \quad (179)$$

$$\frac{\partial^2 C_i}{\partial x^2} + \chi K \frac{\partial C_i}{\partial x} = 0 \quad (180)$$

and

$$\frac{\partial^2 C_o}{\partial x^2} + 2K \frac{\partial C_o}{\partial x} = 0 \quad (181)$$

for cation vacancies, cation interstitials, and oxygen vacancies, respectively. The general solutions for Eqs. (179)–(181) are

$$C_v(x) = \tilde{A} e^{\chi K x} + \tilde{B} \quad (182)$$

$$C_i(x) = \hat{A} e^{-\chi_i K x} + \hat{B} \quad (183)$$

and

$$C_o(x) = A e^{-2Kx} + B \quad (184)$$

The fluxes of cation vacancies, cation interstitials, and oxygen vacancies are now readily calculated from the aforementioned equations, and the fluxes, as given by the Nernst–Planck, are

$$J_v = -D_v \frac{\partial C_v(x)}{\partial x} + \chi K D_v C_v(x) \quad (185)$$

$$J_i = -D_i \frac{\partial C_i(x)}{\partial x} - \chi_i K D_i C_i(x) \quad (186)$$

$$J_o = -D_o \frac{\partial C_o(x)}{\partial x} - 2K D_o C_o(x) \quad (187)$$

Applying these three equations to the f/s interface ($x = 0$) and to the m/f interface ($x = L$), we obtain all of the unknowns constants as

$$B = \left(\frac{\chi}{2}\right) \left(\frac{k_3}{2KD_0}\right) \quad (188)$$

$$A = \left(\frac{\chi}{2}\right) \left(k_3 \left(\frac{1}{k_6} - \frac{1}{2KD_0}\right)\right) \quad (189)$$

$$\hat{B} = \frac{k_2}{\chi K D_i} \quad (190)$$

$$\hat{A} = k_2 \left(\frac{1}{k_5} - \frac{1}{\chi K D_i} \right) \quad (191)$$

$$\tilde{B} = \frac{k_1}{-\chi K D_v} \quad (192)$$

$$\tilde{A} = k_1 \left(\frac{1}{k_4} - \frac{1}{\chi K D_v} \right) \quad (193)$$

4.4.7.3 Optimization of the PDM on the Impedance Data

The Igor Pro (Version 6.2.1.0, ©1988–2010 WaveMetrics, Inc.) software and its genetic curve fitting package was used in this work for optimization (Sharifi-Asl *et al.* [2013]), so as to obtain values for the standard rate constants, k_i^{00} , and transfer coefficients, α_i , for the i elementary interfacial reactions, the polarizability of the barrier layer/outer layer interface (BOI), α , the electric field strength across barrier layer, ϵ , and other parameters as described in the following text. Optimization was carried out in five stages as shown in Figure 4.4.28.

Firstly, an optimization algorithm is designed to find the minimum or maximum of an objective function (e.g., in this case, the impedance of an interface measured as a function of frequency and as a function of system independent variables (<http://www.wavemetrics.com/products/igorpro/igor-pro.htm>)). Thus, optimization methods are employed to find a set of design parameters that can in some way be defined as “optimal” (e.g., yielding a minimum error). This might be the minimization or maximization of some system characteristic that is dependent on a quantity, x . As expected, an efficient and accurate solution to this problem depends not only on the size of the problem, in terms of the number of constraints and design variables, but also on characteristics of the objective function and any constraints. The genetic algorithm is a method for solving optimization problems that is based on and, indeed, emulates natural selection, the process that drives biological evolution. The genetic algorithm repeatedly modifies a population of individual solutions, and, at each step, the algorithm selects individuals at random from the current population to be parents and uses them to produce the children for the next generation. Over successive generations, the population “evolves” toward an optimal solution in a “survival of the fittest” process. Importantly, one can apply the genetic algorithm to solve a variety of optimization problems that are not well suited for standard optimization algorithms, including problems in which the objective function is discontinuous, non-differentiable, stochastic, or highly nonlinear. The genetic

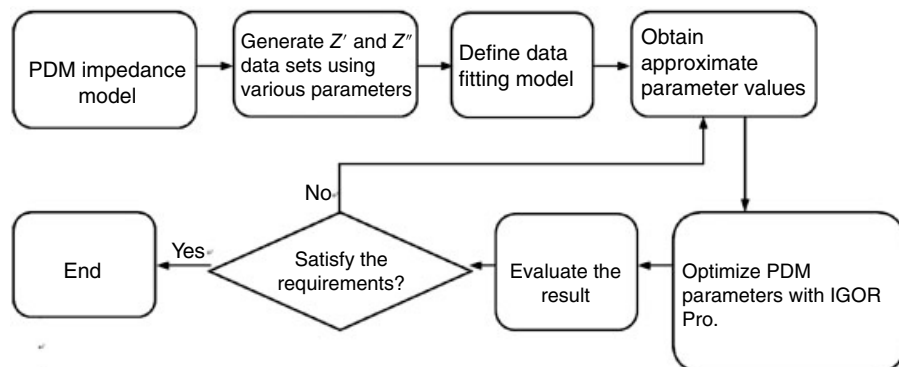


FIGURE 4.4.28 Flow chart of optimization of the point defect model on the experimental electrochemical impedance data for iron in contact with concrete pore water over extended periods.

TABLE 4.4.2 Comparison of the Method of Operation of the Standard and Genetic Algorithms for Optimizing Reaction Mechanisms on Experimental EIS Data

Standard algorithm	Genetic algorithm
Generates a single point at each iteration. The sequence of points approaches an optimal solution	Generates a population of points at each iteration. The population approaches an optimal solution
Selects the next point in the sequence by a deterministic computation	Selects the next population by computations that involve random choices

algorithm uses three main types of rules at each step to create the next generation from the current population:

- Selection rules select the individuals, called parents that breed the population of the next generation.
- Crossover rules combine two parents to form children for the next generation.
- Mutation rules apply random changes to individual parents to form children.

The genetic algorithm differs from a standard optimization algorithm in two main ways, as summarized in Table 4.4.2.

In applying the genetic algorithm to optimize the PDM on EIS data for passive metals (Figure 4.4.28), the total impedance model was decomposed into two parts: one for the real component and the other for the imaginary component. Secondly, the optimization model, together with the experimental impedance data upon which it is to be optimized, needs to be carefully defined in order to obtain optimal results. Thirdly, approximate parameter values are initially obtained by “manually optimizing” the model for $Z(\omega)$ on the experimental data. Fourthly, the parameter values are optimized using the Igor Pro algorithm, and, finally, the optimization results are evaluated. The optimization procedure ends if the result satisfies the following requirements simultaneously; if not, the procedure returns to the third stage and the model is optimized once again. These requirements include the following: (105) all the parameter values are physically reasonable and should exist within known bounds; (106) the calculated $Z'(\omega)$ and $Z''(\omega)$ should agree with their respective experimental results in both the Nyquist and Bode planes; (107) the parameters such as the polarizability of the barrier layer/outer layer interface, α , the electric field strength across barrier layer, ϵ , the standard rate constants, k_i^{00} , the transfer coefficients for the point defect generation and annihilation at the barrier layer interfaces, α_i (Figure 4.4.27), and the constant ϕ_{BOI}^0 should be approximately potential independent; and (108) the calculated current density and passive film thickness, as estimated from the parameter values obtained from the optimization, should be in reasonable agreement with the steady-state experimental values. It is important to note that the steady-state passive current density and barrier layer thickness are not employed in the optimization procedure, and, hence, these quantities represent legitimate evaluation criteria.

Typical experimental impedance spectra for the passive state on carbon steel in a highly alkaline solution [sat. $\text{Ca}(\text{OH})_2 + \text{NaOH}$, $\text{pH} = 13.5$]. $E = -0.07 \text{ V}_{\text{SHE}}$. $T = 80^\circ\text{C}$, and an exposure of 30 days is shown in Figure 4.4.29 in the form of Bode plots and Nyquist plots. Also plotted in this figure are impedance data calculated from the model described earlier using the optimized model parameters. In this figure, the simulated data are in good agreement with the experimental data, with the level of agreement being similar to that reported in other studies (Ai *et al.* [2008], Ling *et al.* [2013], Lu *et al.* [2013], Macdonald [2013], Sharifi-Asl *et al.* [2013a], Taylor *et al.* [2013]). Thus, the impedance model based on the PDM provides a reasonable account of the experimental data.

It is important to note, as was emphasized earlier, that the data satisfy the KK transforms (Kronig [1926], Kramers [1929], Macdonald [1985a], Macdonald [1986], unpublished research), demonstrating that the system complies with the constraints of linear systems theory (LST). The KK transformations

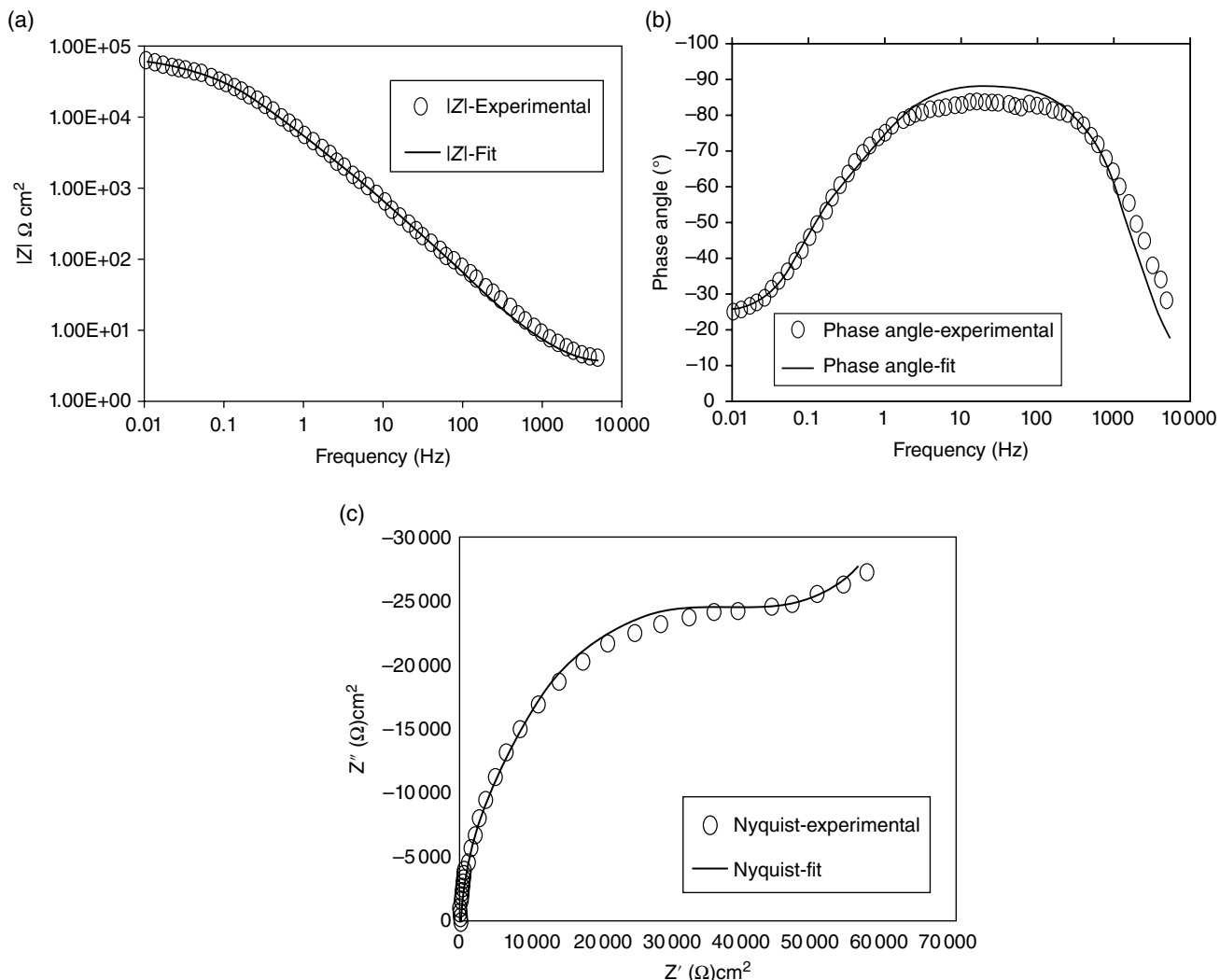


FIGURE 4.4.29 Impedance spectra for carbon steel in blank solution [sat. $\text{Ca}(\text{OH})_2 + \text{NaOH}$, pH = 13.5]. $E = -0.07 \text{ V}_{\text{SHE}}$. $T = 80^\circ\text{C}$, 30 days. (a) Bode plane, $\log |Z|$ versus f/Hz ; (b) Bode plane, phase angle versus f/Hz ; (c) Nyquist plane, $-Z''$ versus Z' .

mathematically relate the real and imaginary parts of any complex function; therefore, the transformations are often used, in order to investigate compliance of the system with the causality, stability, and linearity constraints of LST (Kronig [1926], Kramers [1929], Macdonald [1985a], Macdonald [1986], unpublished research). It should be noted that these transformations do not reflect any physical property or condition of the system under the study, but simply test the compliance of the system with LST. Figures 4.4.30 and 4.4.31 show examples of the validation of EIS data sets using the KK transforms. Thus, the KK transforms calculate the imaginary component from the real component and vice versa, and the calculated components are compared directly with the experimentally measured components, as shown in Figures 4.4.30 and 4.4.31. As observed, excellent agreement is obtained, demonstrating the compliance of the system with the constraints of LST.

The electrochemical reactions that occur at the m/f or f/s interfaces (Figure 4.4.27) contribute to the impedance of the system. Therefore, the total impedance of the system, which arises from the entire set of interfacial phenomena, includes two interfaces in series plus the resistance of the solution. Figure 4.4.32 shows the EEC for the metal/film/solution system that has been employed in the author's work to analyze the passivity of iron and carbon steel.

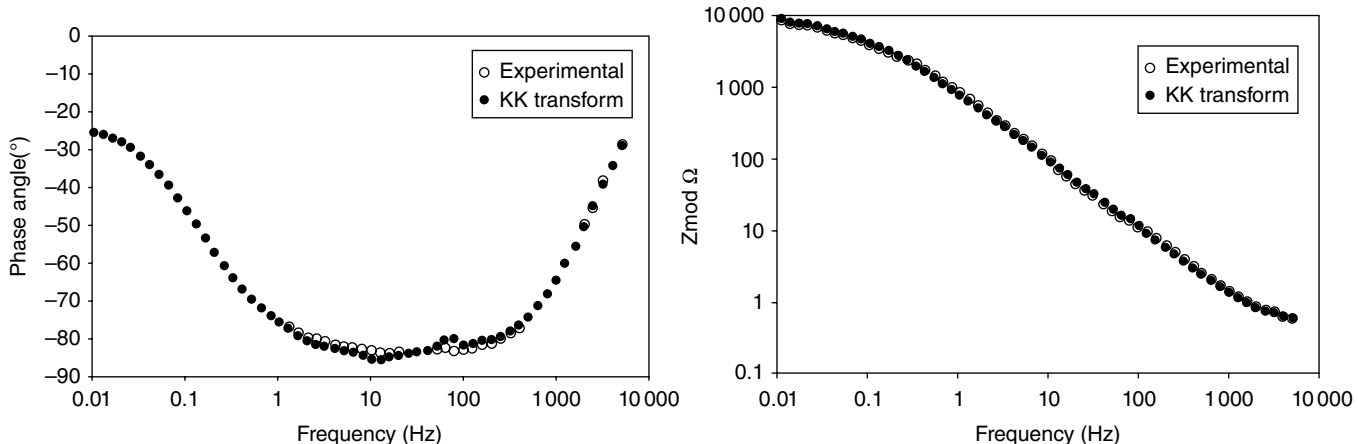


FIGURE 4.4.30 KK transforms of EIS data for carbon steel in a blank solution [sat. $\text{Ca}(\text{OH})_2 + \text{NaOH}$, pH = 13.5]. $E = -0.07 \text{ V}_{\text{SHE}}$. $T = 80^\circ\text{C}$, 30-day exposure.

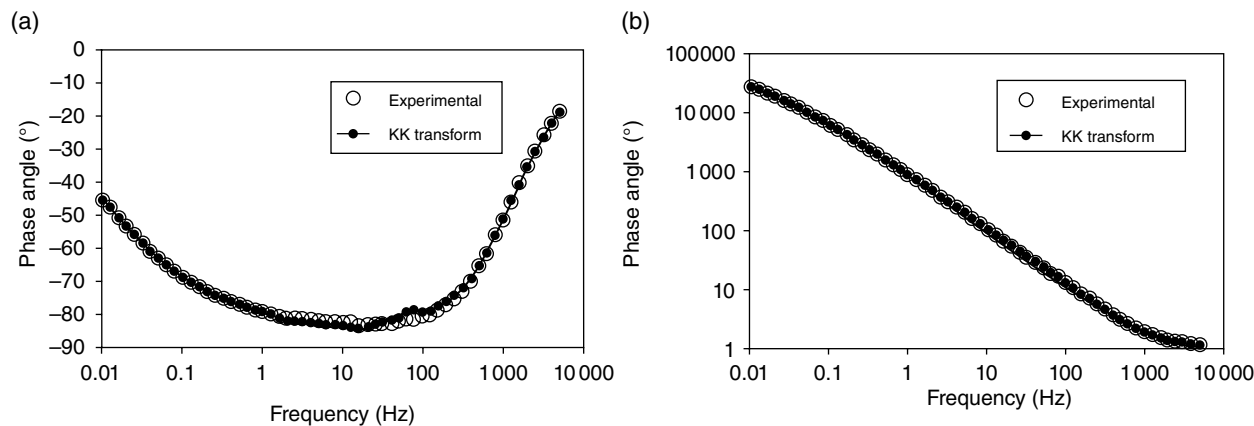


FIGURE 4.4.31 KK transforms of EIS data for carbon steel in a blank solution [sat. $\text{Ca}(\text{OH})_2 + \text{NaOH}$, pH = 13.5]. $E = -0.07 \text{ V}_{\text{SHE}}$. $T = 80^\circ\text{C}$, 99-day exposure.

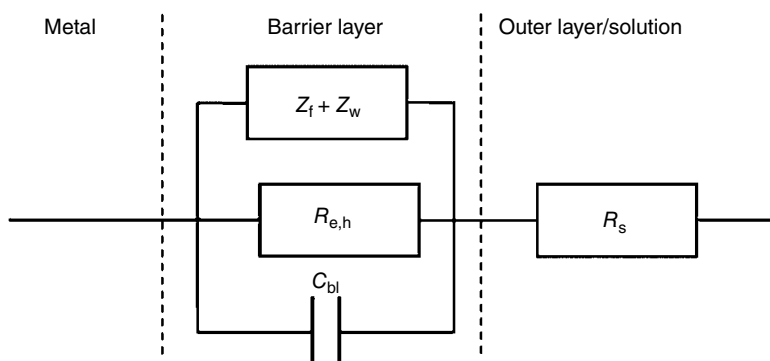


FIGURE 4.4.32 Equivalent electrical circuit describing the total impedance of the iron-concrete pore water interface.

The total impedance of the system is expressed by Eq. (194) as

$$Z = \left[j\omega c + \frac{1}{R_e} + \frac{1}{Z_f + Z_w} \right]^{-1} + R_s \quad (194)$$

where Z_f is the faradaic impedance associated with the reactions occurring at the m/f and f/s interfaces (Figure 4.4.27). Z_w is the Warburg impedance associated with the transport of metal interstitials and is expressed by Eq. (176), which is expressed here again as Eq. (195):

$$Z_w = \sigma_m \omega^{-1/2} - j\sigma_m \omega^{-1/2} \quad (195)$$

In Eq. (194), R_e is the resistance due to the transport of electronic defects such as electrons or holes and must be included under those circumstances where a cathodic reaction (e.g., hydrogen evolution and/or oxygen reduction), C_{bl} is the capacitance of the barrier layer, and R_s is the solution resistance.

4.4.7.4 Sensitivity Analysis

In order to determine the effect of different parameters on the overall impedance spectra, sensitivity analysis is mandatory in the analysis of EIS data. In Figures 4.4.33, 4.4.34, 4.4.35, 4.4.36, 4.4.37, 4.4.38, and 4.4.39, the typical effects of some of the important parameters are plotted in the Bode plane.

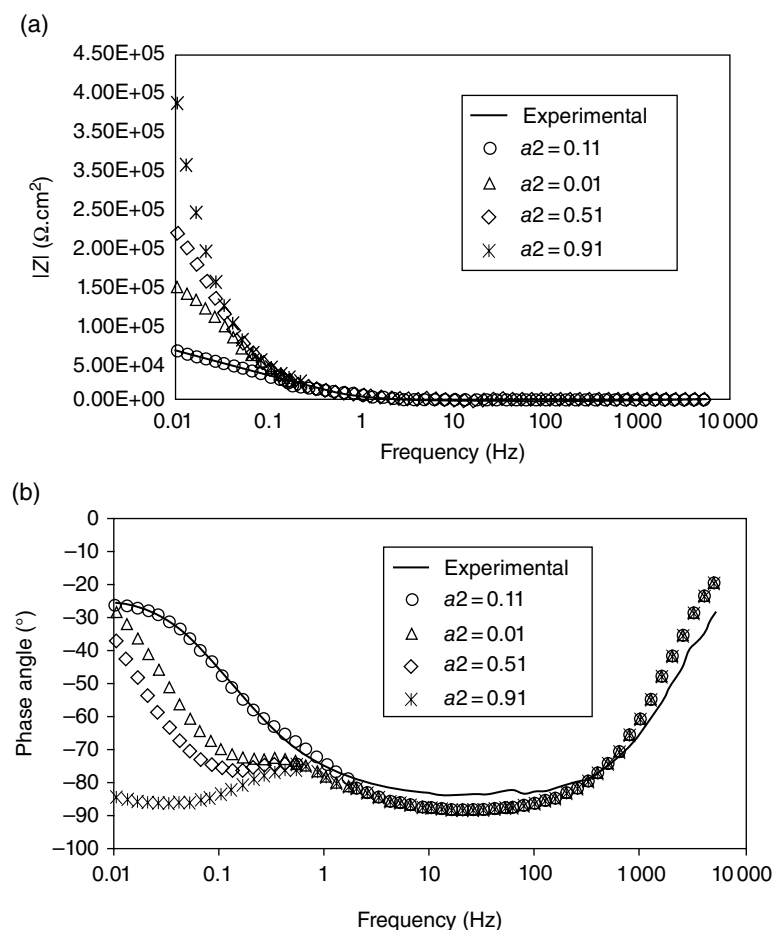


FIGURE 4.4.33 Sensitivity analysis showing the effect of α_2 on the calculated impedance.

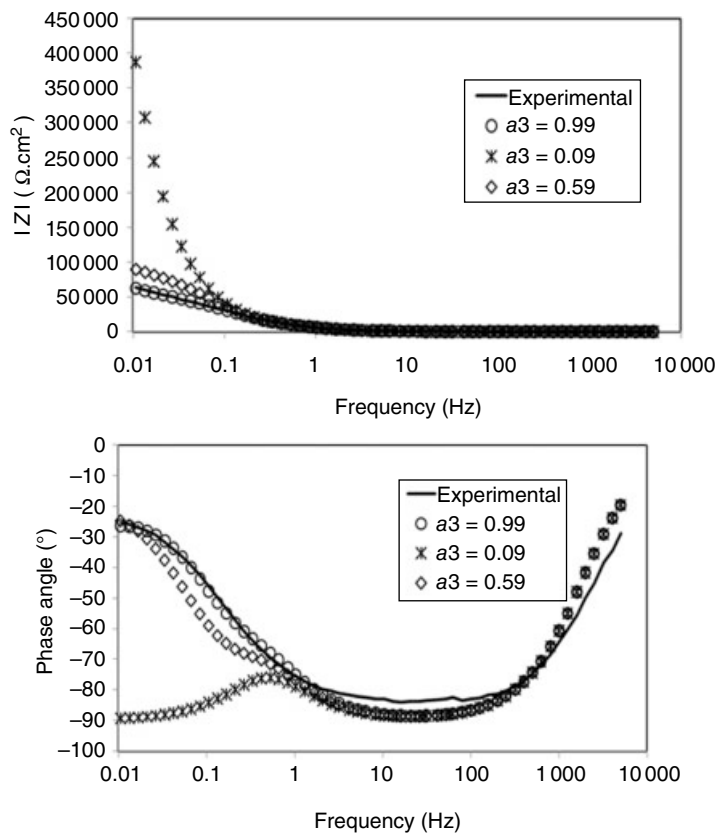


FIGURE 4.4.34 Sensitivity analysis showing the effect of α_3 on the calculated impedance.

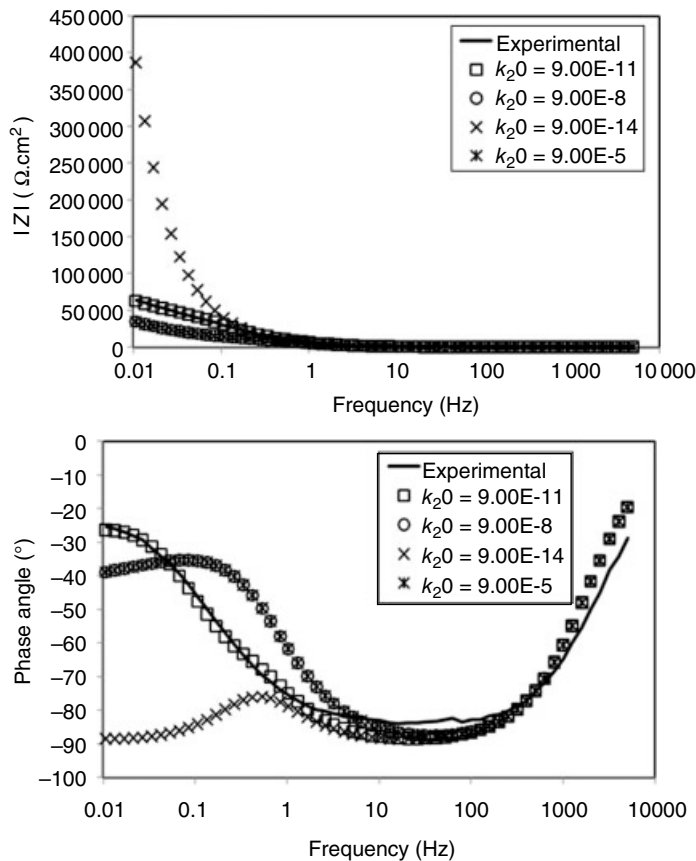


FIGURE 4.4.35 Sensitivity analysis showing the effect of k_2^0 on the calculated impedance.

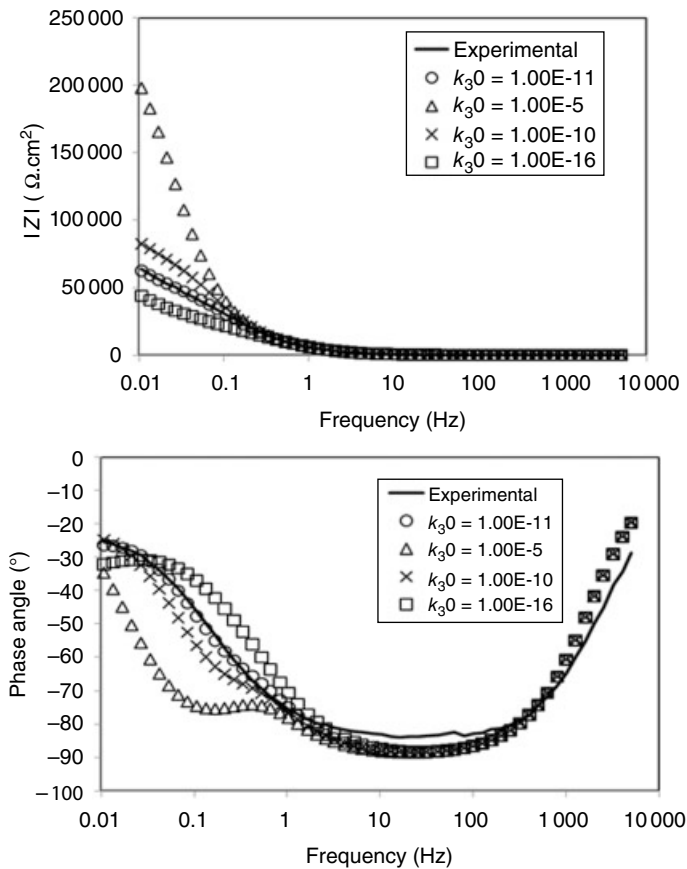


FIGURE 4.4.36 Sensitivity analysis showing the effect of k_3^0 on the calculated impedance.

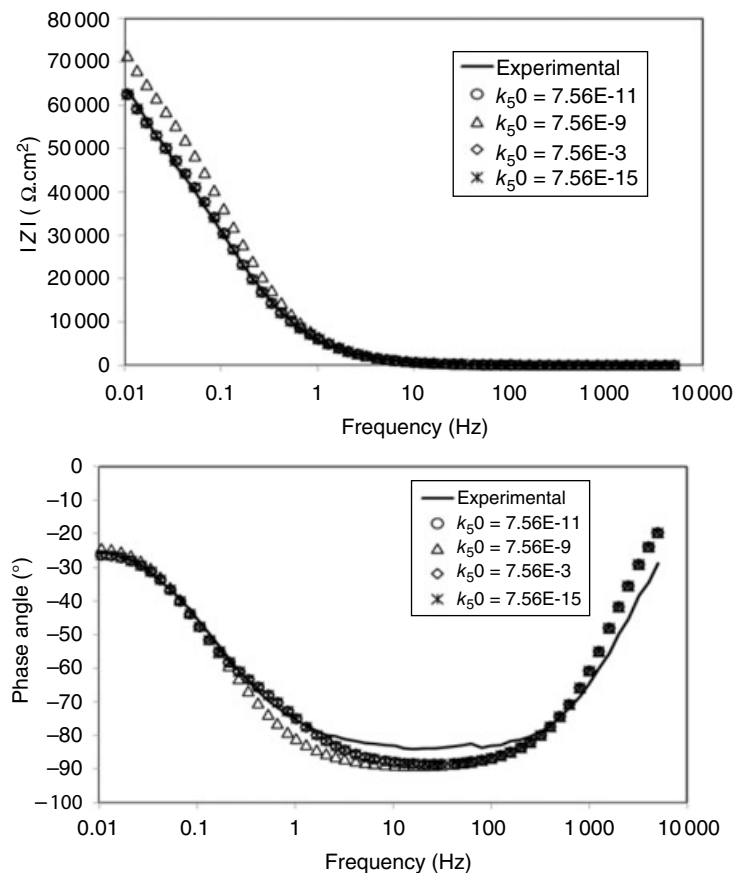


FIGURE 4.4.37 Sensitivity analysis showing the effect of k_5^0 on the calculated impedance.

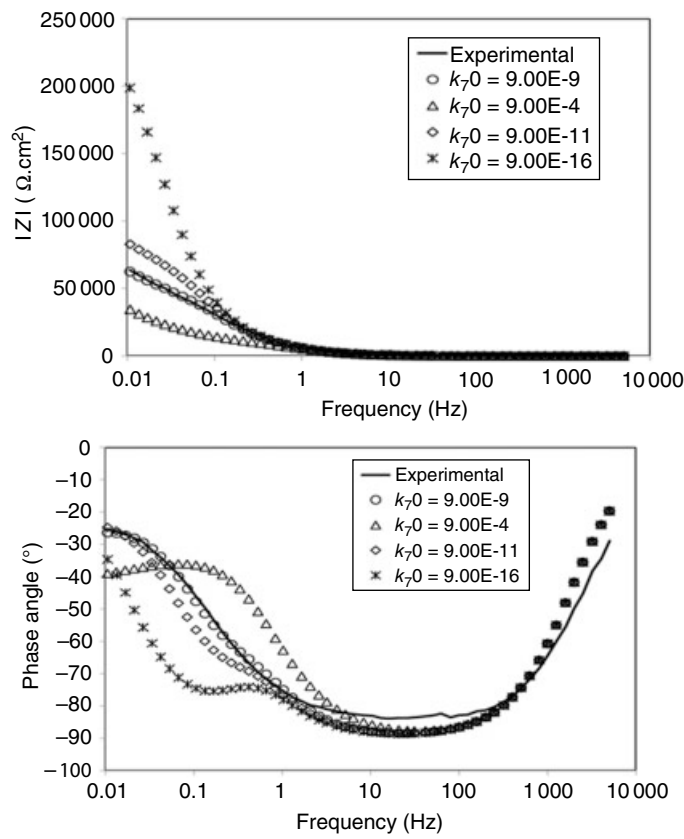


FIGURE 4.4.38 Sensitivity analysis showing the effect of k_7^0 on the calculated impedance.

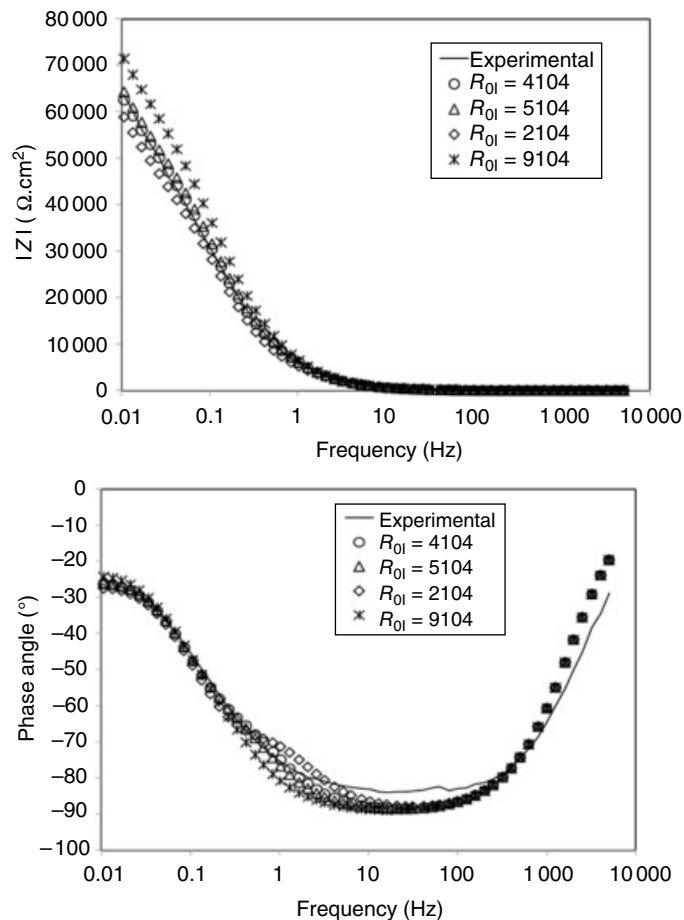


FIGURE 4.4.39 Sensitivity analysis showing the effect of R_{0l} on the calculated impedance.

In order to effectively analyze the results, the experimental impedance data are also included in these plots.

As it can be seen from the aforementioned plots, the kinetic parameters for Reactions (106), (107), and (111), but not Reaction (109), and the corresponding transfer coefficients, have a significant effect on the calculated impedance, particularly at low frequency where the impedance is most sensitive to kinetic effects (in contrast to high frequencies, where capacitive effects dominate). On the other hand, R_{ol} and k_5^{00} show no great effect on the calculated impedance. Regarding the outer layer resistance, it can impact the impedance only if its value is sufficiently high to modify the voltage sensed at the bl/ol (U) interface in comparison with the imposed voltage (V). This sensitivity analysis, therefore, emphasizes the need to obtain precise impedance data at very low frequencies at least to frequencies as low as 10^{-2} to 10^{-3} Hz in order to accurately determine values for the various kinetic parameters.

4.4.7.5 Extraction of PDM Parameters from EIS Data

The main task of the work described later was optimizing the parameters in the PDM on impedance data for iron in borate buffer solution as a function of applied potential and pH. Figures 4.4.40, 4.4.41, 4.4.42, and 4.4.43 display the optimized results as a function of potential for two different pH values, 8.15 and 10.0. The optimization of the PDM parameters makes it possible to assess, deterministically, the corrosion behavior of the iron in the solution of interest and to predict the corrosion rate more accurately. As can be seen in the following text, good optimization results were obtained for each potential and pH. The optimized parameter values involved in the PDM are listed in Tables 4.4.3 as a function of the applied potential and the pH of solution. Because the barrier layer displays no p-type electronic character whatsoever, the EIS data were interpreted in terms of a reduced reaction set (Figure 4.4.40) by omitting Reactions (105) and (108), as displayed in Figure 4.4.27. The rate constants (k_i), standard base rate constants (k_i^{00}), and the charge transfer coefficients (α_i) are related to the reactions shown in Figure 4.4.40, where “ i ” represents the reaction number in the figure (e.g., “ i ” = 3 is for Reaction (3) in the figure). It should be noted that all of the parameters in these tables have reasonable values with respect to the

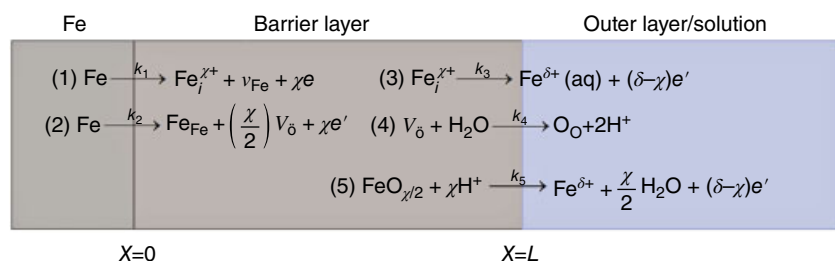


FIGURE 4.4.40 Reduced PDM for describing the growth and breakdown of the passive film on iron.

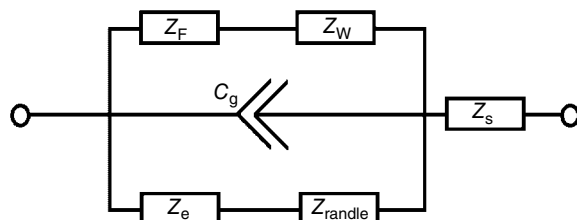


FIGURE 4.4.41 Electrical equivalent circuit employed in the analysis of the impedance of iron in borate buffer solution.

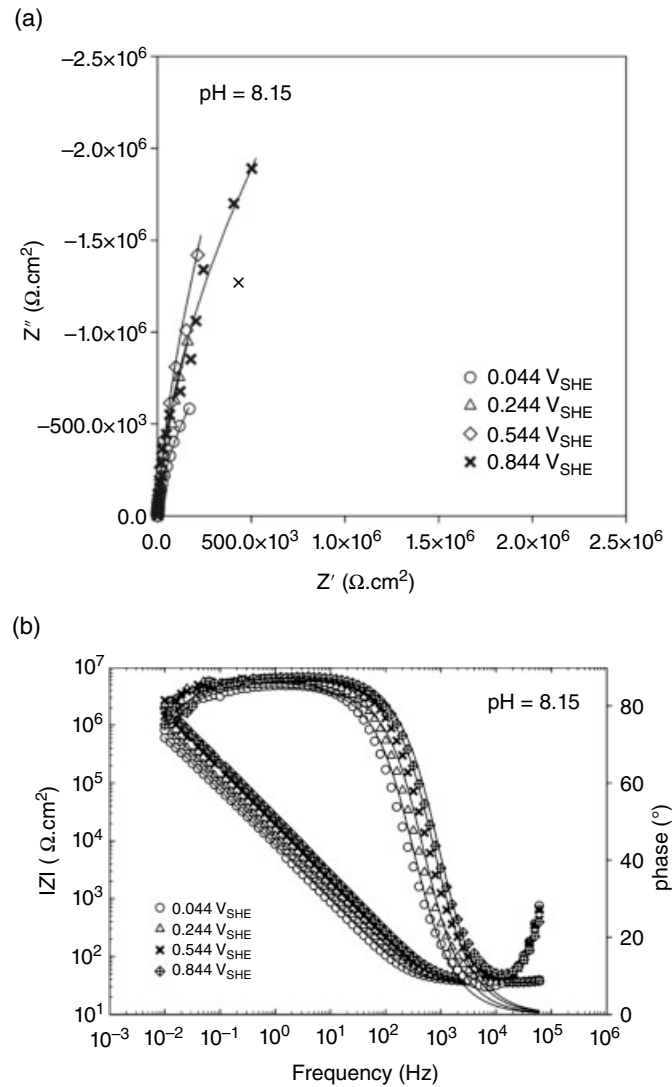


FIGURE 4.4.42 Experimental and simulated impedance spectra for iron in borate buffer solution ($0.3 \text{ M H}_3\text{BO}_3 + 0.075 \text{ M Na}_2\text{B}_4\text{O}_7$, as appropriate) + 0.001 M EDTA (ethylene-diaminetetraacetic acid, disodium salt), (a) Nyquist plane and (b) Bode plane for $\text{pH} = 8.15$, $T = 21^\circ\text{C}$, as a function of applied potential. The solid lines show the best optimization of the PDM on the experimental EIS data.

physico-electrochemistry of the system, which is one of the tests that is applied prior to accepting the data from optimization.

The EEC employed in the analysis is presented in Figure 4.4.41. The circuit incorporates a sub-circuit ($Z_{\text{randle}} + Z_e$) for representing the electronic impedance/cathodic reaction of the barrier layer, the faradaic impedance (Z_F) as derived earlier, a Warburg impedance describing the transport of the principal defect (Z_w), and a constant phase element (CPE) (C_g) representing the distributed capacitance of the barrier layer arising from the distribution in barrier layer thickness on the polycrystalline iron surface. Finally, the solution resistance between the f/s interface and the tip of the Luggin probe is designated R_s .

Examination of the impedance plots presented in Figures 4.4.42 and 4.4.43, as noted earlier, shows that the PDM represents the impedance of the interface quite accurately, except at very high frequency,

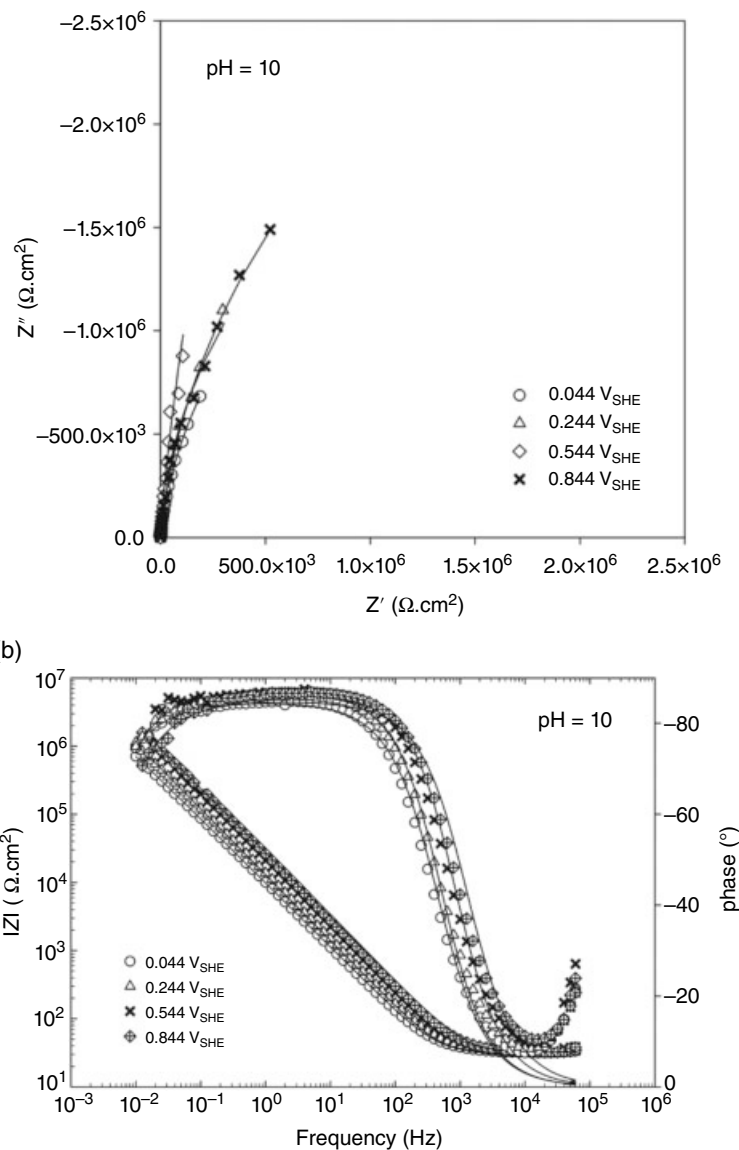


FIGURE 4.4.43 Experimental and simulated impedance spectra for iron in borate buffer solution ($0.3 \text{ M H}_3\text{BO}_3 + 0.075 \text{ M Na}_2\text{B}_4\text{O}_7$, as appropriate) + 0.001 M EDTA (ethylenediaminetetraacetic acid, disodium salt), (a) Nyquist plane and (b) Bode plane for $\text{pH} = 10.0$, $T = 21^\circ\text{C}$, as a function of applied potential. The solid lines show the best optimization of the PDM on the experimental EIS data.

where the impedance is entirely capacitive in nature. However, because the kinetics of processes involving point defects are manifest at low frequency ($f < 1 \text{ Hz}$), the high-frequency end on the spectrum is not of significant interest in this work, except, in as much, the high-frequency capacitance might be used to estimate barrier layer thickness. However, it is found that the high-frequency capacitance is not a strong function of frequency, so that the impact on the estimated barrier layer thickness is relatively minor.

In performing the optimization and to reduce the dimensionality of the problem, the values for certain parameters were either calculated (e.g., Ω from the molecular weight and density of maghemite, $\gamma\text{-Fe}_2\text{O}_3$) or were assumed, as indicated in the Table 4.4.3. The values of all other parameters were determined by optimization. The first thing to notice is that no rate constants are listed for Reactions (1) and

TABLE 4.4.3 Parameter Values as a Function of pH and Potential Obtained by Optimization of the PDM on the Experimental EIS Data for Iron in 0.3 M H₃BO₃ + 0.075 M Na₂B₄O₇ + 0.001 M EDTA (Ethylenediaminetetraacetic Acid, EDTA, Disodium Salt), at T = 21°C

pH = 8.15					
E_{app} (V _{SHE})	0.044	0.244	0.544	0.844	Average
Current density (A/cm ²)	1.28 × 10 ⁻⁶	1.81 × 10 ⁻⁶	5.20 × 10 ⁻⁷	4.75 × 10 ⁻⁷	-----
Thickness of barrier layer (nm)	0.86	1.00	1.57	1.73	-----
CPE-Y (S.s ^α /cm ²)	1.94 × 10 ⁻⁵	1.25 × 10 ⁻⁵	4.67 × 10 ⁻⁶	5.30 × 10 ⁻⁶	-----
CPE- $α$	0.94	0.95	0.94	0.96	-----
Electric field ($ε$)	3 × 10 ⁶	-----			
Warburg coefficient ($σ$)	1.97 × 10 ⁵	7.38 × 10 ⁵	1.61 × 10 ⁶	6.09 × 10 ⁵	-----
D_i (cm ² /s)	1.08 × 10 ⁻¹⁵	3.03 × 10 ⁻¹⁴	1.18 × 10 ⁻¹⁴	1.42 × 10 ⁻¹⁴	-----
Polarizability of the BOI ($α$)	0.724	0.724	0.724	0.724	0.724
Transfer coeff. reaction 1 ($α_1$)	0.01	0.003	0.02	0.01	0.01
Transfer coeff. reaction 2 ($α_2$)	0.19	0.17	0.18	0.17	0.17
k_1^0 (mol/cm ² /s)	3.88 × 10 ⁻¹²	5.95 × 10 ⁻¹²	1.68 × 10 ⁻¹²	1.54 × 10 ⁻¹²	3.2 × 10 ⁻¹²
k_2^0 (mol/cm ² /s)	4.98 × 10 ⁻¹⁶	4.47 × 10 ⁻¹⁶	8.85 × 10 ⁻¹⁶	5.03 × 10 ⁻¹⁶	5.8 × 10 ⁻¹⁶
k_5^0 (mol/cm ² /s)	5.52 × 10 ⁻¹²	6.68 × 10 ⁻¹²	1.99 × 10 ⁻¹²	2.49 × 10 ⁻¹²	5.5 × 10 ⁻¹²
k_1 (mol/cm ² /s)	4.41 × 10 ⁻¹²	6.26 × 10 ⁻¹²	1.80 × 10 ⁻¹²	1.64 × 10 ⁻¹²	-----
k_2 (mol/cm ² /s)	3.52 × 10 ⁻¹⁵	1.13 × 10 ⁻¹⁶	6.21 × 10 ⁻¹⁷	1.57 × 10 ⁻¹⁷	-----
k_5 (mol/cm ² /s)	5.58 × 10 ⁻¹²	8.20 × 10 ⁻¹²	2.99 × 10 ⁻¹²	5.52 × 10 ⁻¹²	-----
R_s (Ω.cm ²)	36	34.6	34.6	34.7	-----
$Φ_{f/s}^0$	-0.1	-0.1	-0.1	-0.1	-----
$β$	-0.03	-0.03	-0.03	-0.03	-----
C_{dl} (F/cm ⁻²)	1.16 × 10 ⁻⁶	1.63 × 10 ⁻⁶	4.25 × 10 ⁻⁶	1.26 × 10 ⁻⁶	-----
R_{ct} (Ω.cm ²)	3.46 × 10 ⁹	2.96 × 10 ⁹	3.86 × 10 ⁹	2.97 × 10 ⁹	-----
pH = 10					
E_{app} (V _{SHE})	0.044	0.244	0.544	0.844	Average
Current density (A/cm ²)	3.42 × 10 ⁻⁷	5.15 × 10 ⁻⁷	7.62 × 10 ⁻⁷	4.55 × 10 ⁻⁷	-----
Thickness of barrier layer (nm)	1.47	1.56	2.15	2.28	-----
CPE-Y (S.s ^α /cm ²)	1.79 × 10 ⁻⁵	1.21 × 10 ⁻⁵	7.60 × 10 ⁻⁶	6.15 × 10 ⁻⁶	-----
CPE- $α$	0.94	0.96	0.96	0.94	-----
Electric field ($ε$)	3 × 10 ⁶	-----			
Warburg coefficient ($σ$)	1.32 × 10 ⁵	7.54 × 10 ⁴	1.40 × 10 ⁵	1.35 × 10 ⁵	-----
D_i (cm ² /s)	3.47 × 10 ⁻¹⁷	2.55 × 10 ⁻¹⁷	1.94 × 10 ⁻¹⁶	6.42 × 10 ⁻¹⁷	-----
Polarizability of the BOI ($α$)	0.724	0.724	0.724	0.724	0.724
Transfer coeff. reaction 1 ($α_1$)	0.02	0.01	0.005	0.01	0.01
Transfer coeff. reaction 2 ($α_2$)	0.11	0.14	0.11	0.19	0.13
k_1^0 (mol/cm ² /s)	1.30 × 10 ⁻¹²	1.78 × 10 ⁻¹²	2.80 × 10 ⁻¹²	1.68 × 10 ⁻¹²	1.89 × 10 ⁻¹²
k_2^0 (mol/cm ² /s)	2.03 × 10 ⁻¹⁶	2.69 × 10 ⁻¹⁶	1.78 × 10 ⁻¹⁶	7.16 × 10 ⁻¹⁶	3.41 × 10 ⁻¹⁶
k_5^0 (mol/cm ² /s)	3.35 × 10 ⁻¹²	4.64 × 10 ⁻¹²	1.27 × 10 ⁻¹²	2.12 × 10 ⁻¹²	2.84 × 10 ⁻¹²
k_1 (mol/cm ² /s)	1.18 × 10 ⁻¹²	1.78 × 10 ⁻¹²	2.63 × 10 ⁻¹²	1.57 × 10 ⁻¹²	-----
k_2 (mol/cm ² /s)	1.13 × 10 ⁻¹⁶	8.49 × 10 ⁻¹⁷	6.80 × 10 ⁻¹⁸	1.08 × 10 ⁻¹⁸	-----
k_5 (mol/cm ² /s)	3.42 × 10 ⁻¹²	4.90 × 10 ⁻¹²	1.31 × 10 ⁻¹²	2.20 × 10 ⁻¹²	-----
R_s (Ω.cm ²)	31.5	31.5	34.6	32	-----
$Φ_{f/s}^0$	-0.1	-0.1	-0.1	-0.1	-----
$β$	-0.03	-0.03	-0.03	-0.03	-----
C_{dl} (F/cm ⁻²)	2.19 × 10 ⁻⁷	8.04 × 10 ⁻⁷	4.89 × 10 ⁻⁷	2.35 × 10 ⁻⁷	-----
R_{ct} (Ω.cm ²)	3.54 × 10 ⁹	3.22 × 10 ⁹	3.68 × 10 ⁹	3.76 × 10 ⁹	-----

(4), because the barrier layer on iron is an n-type semiconductor with no hint of p-type character. Accordingly, cation vacancies, which are electron acceptors, have no impact on the electronic character of the barrier layer and hence must be present at a level that is far below that of the principal donor. Thus, examination of the rate constants obtained by optimization reveals that cation interstitials are produced [Reaction (2)] at a rate that is about two orders in magnitude greater than the rate of generation of oxygen vacancies [Reaction (3)]. This comparison is possible, because both reactions are of the same kinetic order and the rate constants, therefore, have the same units. In other words the reaction involving iron interstitials dominates over that producing oxygen vacancies, due to the higher rate constant, and hence the principal defect in the barrier layer on iron is the metal interstitial, in agreement with the findings of Tony *et al.* (Engelhardt *et al.* [2016]).

The rate constant for the dissolution of the barrier layer, k_7 , has a value of about $3 \times 10^{-9} \text{ mol/cm}^2\text{s}$. Noting that the dissolution rate is defined as $\Omega k_7^0 (C_{\text{H}^+}/C_{\text{H}^+}^0)^n$ (cm/s) the dissolution rate is estimated to be $0.55 \times 10^{-11} \text{ cm/s}$ or $0.55 \times 10^{-4} \text{ nm/s}$ and $0.66 \times 10^{-12} \text{ cm/s}$ or $0.66 \times 10^{-5} \text{ nm/s}$ at $\text{pH} = 8.15$ and $\text{pH} = 10$, respectively. The value measured at $\text{pH} = 8.15$ using spectroscopic ellipsometry (Lu *et al.* [2013]) is about $3 \times 10^{-4} \text{ nm/s}$, which is in acceptable agreement, particularly when it is considered that the rate constants are probably no more accurate than an order of magnitude.

The impedance calculated ("simulated") from the optimized parameter values listed in Table 4.4.2 are compared with the experimentally measured impedance in Figures 4.4.40, 4.4.41, 4.4.42, and 4.4.43 in various formats (including in the Nyquist and Bode planes). Generally, excellent agreement is obtained with only minor differences being observed in the phase angle.

Figures 4.4.44 and 4.4.45 show a comparison between the experimental and calculated steady-state barrier layer thickness and current density, respectively, as a function of potential. It can be seen that there is a good agreement between the experimental and calculated steady-state current density values. The accuracy of the parameter values determined by optimization, in this case, is such that the uncertainty in the calculated current density is about a factor of three. Most importantly, the current density is found to be independent of potential as predicted by the PDM. Furthermore, the steady-state barrier layer thickness increases linearly with increasing potential, again as predicted by the PDM [Eq. (122)]. We conclude that the PDM can determine the oxide thickness and steady-state current density more precisely than any other proposed model for passivity of iron in mildly alkaline solutions. The steady-state current density can be used in order to calculate the rate of accumulation of general corrosion damage aqueous environments and predicts which reactions play an important role in the corrosion of carbon steel.

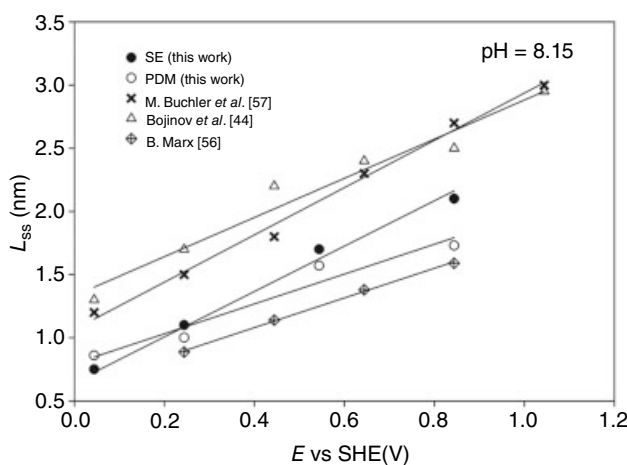


FIGURE 4.4.44 Comparison of barrier layer thickness on iron in borate buffer solution as a function of potential, as derived from the present EIS analysis with other data reported in the literature.

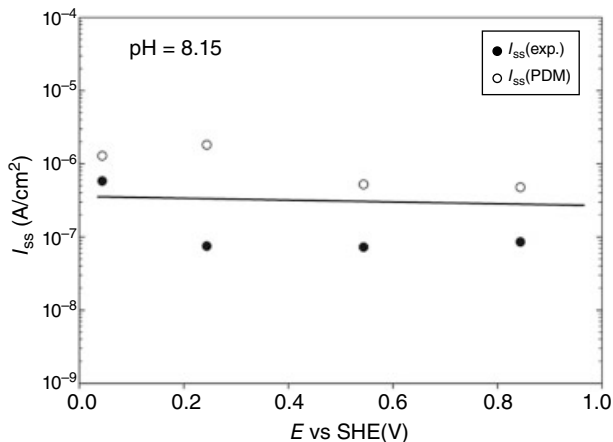


FIGURE 4.4.45 Comparison of steady-state passive current density for iron in borate buffer solution for $\text{pH} = 8.15$ as a function of potential.

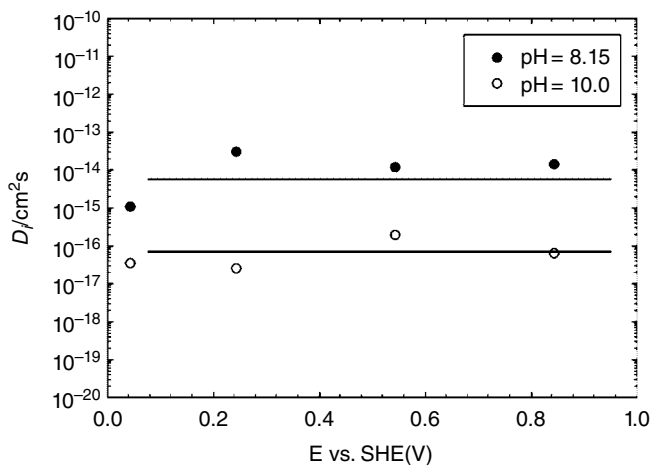


FIGURE 4.4.46 Calculated diffusivity of iron interstitials as a function of potential, $T = 22^\circ\text{C}$ (lines show the linear regressions).

Based upon the PDM, the metal interstitials generated at the m/f interface move toward the f/s interface and driving force for this transport phenomenon is primarily the electric field (ϵ) (migration) with the concentration gradient being important only in a narrow region close to the bl/s interface. The diffusivity of iron interstitials through the passive layers was calculated according to Eq. (198) (Kramers [1929b]) as a function of potential and plotted in Figure 4.4.46:

$$D_i = 2\sigma^2(105 - \alpha)^2 \frac{I_{ss}^2}{\epsilon^2} \quad (196)$$

It is evident that the diffusivity of iron interstitials is independent of potential, as is predicted by the PDM. However, there appears to be no rational explanation for the apparent dependence of the diffusivity on the pH, because the pH is, exclusively, a property of the solution and not of the barrier layer

bulk phase through which the defects migrate. On the other hand, it may be argued that the kinetics of the reactions that occur at the f/s interface are fundamentally dependent upon pH, although the reader will note that, in the theory developed earlier (Figure 4.4.27), the point defect generation and annihilation reactions are regarded as being irreversible. Finally, it may be argued that the two order of magnitude difference in D_i is within the uncertainty with which the diffusivity can be determined, particularly when recognized that it is “deeply buried” within the model.

4.4.7.6 Simplified Method for Expressing the Impedance of a Stationary Barrier Layer

It is well known that it is not uncommon in optimization to discover that the object function is not unimodal with a single minimum and, in nonlinear cases, it can be very difficult to find the global minimum (Press *et al.* [1992]). Accordingly, the genetic algorithm (or any other procedure, for that matter) cannot ensure that the best optimization values for the unknown parameters are found. In order to reduce the impact of the large dimensionality of the problem, in the following, we obtain simple closed analytical expressions for the steady-state passive corrosion current densities and faradaic resistance of the barrier layer on the basis of PDM. Along with the general case, we consider particular cases when the dominant transported species in the barrier layer is only one of the following defects: cation interstitials, cation vacancies, and anion vacancies. The method described in the following text will be especially suitable for describing the impedance of barrier layers at a sufficiently high potential that the current from any partial cathodic reaction is negligible (Engelhardt *et al.* [2016]).

Before describing this simplified model, we would like to remind a reader some assumptions that were adopted in developing the original version of the PDM (Lin *et al.* [1981], D. Macdonald [1992, 1999a, 2012a], Ling *et al.* [2013], Taylor *et al.* [2013]). These include the following: (i) the electric field strength, ϵ , does not depend on applied voltage and film thickness due to the buffering by electron–hole generation (Esaki tunneling), and (ii) the potential drop across the f/s interface, $\varphi_{f/s}$, can be expressed as a linear function of applied voltage, V , and pH (D. Macdonald *et al.* [1990], Lu *et al.* [2014]), that is,

$$\varphi_{f/s} = \alpha V + \beta \text{pH} + \varphi_{f/s}^0 \quad (197)$$

Accordingly, the potential drop across m/f interface can be presented as (Macdonald and Smedley [1990], Lu *et al.* [2014])

$$\varphi_{m/f} = (1 - \alpha)V - \beta \text{pH} - \varphi_{f/s}^0 - \varphi_R - \epsilon L \quad (198)$$

where φ_R is the potential of the RE against the vacuum (absolute) level and L is the film thickness. Here, it will be shown that some important conclusions can be drawn without Assumptions (197) and (198). However, also we emphasize that in order to obtain relationships between experimental observables (e.g., between barrier layer thickness and passive current density and the applied potential and pH), which allow the model to be evaluated against experiment, it is necessary to invoke Assumptions (197) and (198). The existence of outer layer is not considered here. However, the potential drop in the outer layer can be formally included into the value of φ_R .

For extending this analysis further, it is suitable to express rates of reactions in Figure 4.4.27 as functions of potential drops on f/s interface, $\varphi_{m/f}$, and potential drops on m/f interface, $\varphi_{m/f}$ (see Table 4.4.4).

The current density under steady-state conditions can be presented in the form

$$\bar{I} = \bar{I}_i + \bar{I}_v + \bar{I}_O \quad (199)$$

where $\bar{I}_i = \delta F \bar{k}_2$, $\bar{I}_v = \delta F \bar{k}_1$, and $\bar{I}_O = \delta F \bar{k}_7$ are the current densities due to the transport of cation interstitials, cation vacancies, and anion vacancies, respectively. Also, under steady state conditions, we have

$$\bar{k}_1 \bar{C}_v^L = \bar{k}_4, \quad \bar{k}_2 = \bar{k}_5 \bar{C}_i^0, \quad \text{and} \quad \bar{k}_3 = \bar{k}_7 \quad (200)$$

TABLE 4.4.4 Definition of the Rate Constants, k_i , for the Reactions Shown in Figure 4.4.27

Reaction number	Reaction rate constant	Units of k_i^0
1	$k_1^0 \exp\left(\frac{\chi\alpha_1 F \bar{\phi}_{m/f}}{RT}\right)$	cm/s
2	$k_2^0 \exp\left(\frac{\chi\alpha_2 F \bar{\phi}_{m/f}}{RT}\right)$	mol/cm ² /s
3	$k_3^0 \exp\left(\frac{\chi\alpha_3 F \bar{\phi}_{m/f}}{RT}\right)$	mol/cm ² /s
4	$k_4^0 \exp\left(\frac{\delta\alpha_4 F \bar{\phi}_{f/s}}{RT}\right)$	mol/cm ² /s
5	$k_5^0 \exp\left(\frac{\delta\alpha_5 F \bar{\phi}_{f/s}}{RT}\right)$	cm/s
6	$k_6^0 \exp\left(\frac{2\alpha_6 F \bar{\phi}_{f/s}}{RT}\right)$	cm/s
7	$k_7^0 * \exp\left(\frac{(\delta-\chi)\alpha_7 F \bar{\phi}_{f/s}}{RT}\right) \left(\frac{C_{H^+}}{C_{H^+}^0}\right)^n$	mol/cm ² /s

It is important to note that due to Condition (200), the potential drops across the m/f and f/s interfaces under steady-state conditions are not independent, but are connected by the relation

$$k_3^0 \exp\left(\frac{\chi\alpha_3 F \bar{\phi}_{m/f}}{RT}\right) = k_7^0 \exp\left(\frac{(\delta-\chi)\alpha_7 F \bar{\phi}_{f/s}}{RT}\right) = k_7^0 \exp\left(\frac{(\delta-\chi)\alpha_7 F \bar{\phi}_{f/s}}{RT}\right) \left(\frac{C_{H^+}}{C_{H^+}^0}\right)^n \quad (201)$$

and in the case of $\chi = \delta$, the potential drop across the m/f interface, $\bar{\phi}_{m/f}$, does not depend on applied voltage, V . In this case, the current densities of cation interstitials and oxygen vacancies also do not depend on applied voltage, V , and are described by the relations

$$\bar{I}_i = F\chi k_2^0 \left(\frac{k_7^0}{k_3^0}\right)^{\alpha_2/\alpha_3} = F\chi k_2^0 \left(\frac{k_7^0}{k_3^0} \left(\frac{C_{H^+}}{C_{H^+}^0}\right)^n\right)^{\alpha_2/\alpha_3} \quad (202)$$

$$\bar{I}_O = F\chi k_7^0 = F\chi k_7^0 \left(\frac{C_{H^+}}{C_{H^+}^0}\right)^n \quad (203)$$

Note that this conclusion has been made without taking into account Assumptions (197) and (198) when $\delta = \chi$. In all other cases (when $\delta \neq \chi$), \bar{I}_i , \bar{I}_v , and \bar{I}_O depend on V . The expressions of these values for all possible cases can be found in Table 4.4.6. Note that potential drops $\bar{\phi}_{m/f}$ and $\bar{\phi}_{f/s}$ that are in equations for the steady-state current densities in this table are functions of applied voltage, V , and can be considered as fitting parameters or can be described, for example, by Relations (197) and (198) with $V = \bar{V}$, if these relations are valid.

Assuming Arrhenius temperature dependencies

$$k_i^0 = k_i^{00} \exp\left(-\frac{E_{a,i}}{RT}\right) \quad i=2,3,7 \quad (204)$$

where $E_{a,i}$ is the activation energy for i th reaction, we can rewrite Eq. (202) in the form

$$\bar{I}_i = F\chi k^{00} \exp\left(-\frac{E_a}{RT}\right) \left(\frac{C_{H^+}}{C_{H^+}^0}\right)^m \quad (205)$$

where

$$k^{00} = k_2^0 \left(\frac{k_7^{0,*}}{k_3^0}\right)^{\alpha_2/\alpha_3}, \quad E_a = E_{a2} + (E_{a,7} - E_{a,3}) \frac{\alpha_2}{\alpha_3}, \quad m = n \frac{\alpha_2}{\alpha_3} \quad (206)$$

which can be easily fitted to experimental data when the current is transferred primarily by cation interstitials and $\delta = \chi$ (the case of carbon steel (Sharifi-Asl *et al.* [2013a])).

As usual, we assume that applied potential can be described by harmonic function in accordance with Eq. (109). In new variables, equation for the faradic admittance of barrier layer has the following form:

$$Y_f = \frac{\Delta I}{\Delta V} = F \left\{ \chi \bar{k}_1 \bar{C}_v^L g_1 + F\chi \bar{k}_1 \frac{\Delta C_v^L}{\Delta V} + \chi \bar{k}_2 g_2 + \chi \bar{k}_3 g_3 + (\delta - \chi) \bar{k}_4 g_4 + (\delta - \chi) \bar{k}_5 \bar{C}_i^0 g_5 + (\delta - \chi) k_5 \frac{\Delta C_i^0}{\Delta V} + (\delta - \chi) \bar{k}_7 g_7 \right\} \quad (207)$$

where

$$g_i = \frac{\chi F \alpha_i \xi}{RT} \quad (i=1-3), \quad g_i = \frac{\delta F \alpha_i \xi}{RT} \quad (i=4,5) \quad \text{and} \quad g_7 = \frac{(\delta - \chi) F \alpha_7 \xi}{RT} \quad (208)$$

and index “ i ” numerates heterogeneous reactions on Figure 4.4.27.

As mentioned earlier, the relaxation of the barrier layer thickness can be ignored, resulting in a substantial simplification of the expression for the faradaic admittance. The physical reason of this simplification is follows. In accordance with the assumptions of the PDM, in the absence of irradiation with super band-gap light, the only reason for the potential drop across the barrier layer, ϕ_f , oscillating upon the imposition of an oscillating voltage is the oscillation of the barrier layer thickness, L (because the electric field strength, ϵ , is assumed to be constant). However, the minimum experimentally observed change in L that is possible from an atomistic point of view is of the order of the thickness of a monolayer of the oxide, that is, of the order of the diameter of an iron cation ($d_{Fe} = 2.52 \times 10^{-8}$ cm). Accordingly, the minimum in the variation of the potential drop across the barrier layer, $\delta\phi_f$, that can cause the visible changes of the thickness of barrier layer is of the order of $d_{Fe}\epsilon$. By using $\epsilon = 3 \times 10^{-6}$ V/cm (Lin *et al.* [1981]), we estimate that $d_{Fe}\epsilon$ is of the order of 75 mV, which is much larger than the maximum amplitude of the applied modulated potential, δV (114 mV), used in the measurement of EIS data. Accordingly, we conclude that in normal EIS measurements, any changes in L with δV can be ignored and corresponding terms in Eq. (208) can be omitted.

The second important simplification is connected with the calculations of the values of $\Delta C_v^L / \Delta V$ and $\Delta C_i^0 / \Delta V$. Previously, these values were performed via solution of the equations of mass transfer. Numerical analysis shows that due to the high values of migration Peclet number (ratio of the intensity of migration to that of diffusion), migration dominates practically in all barrier layers with the exemption of a thin transient layer near the f/s interface, in the case of metal interstitials and oxygen vacancies, and in a very thin transient layer near the m/f interface in the case of cation vacancies (which are formally negatively charged species).

However, the thickness of the transient layers can be very small and in some cases much less than the thickness of a monolayer of the oxide of the barrier layer. Accordingly, the calculation loses validity from the point of view of atomistic theory, because the PDM is a continuum model. Under these conditions, in order to calculate, for example, $\Delta C_v^L / \Delta V$, we will use the following double barrier layer model

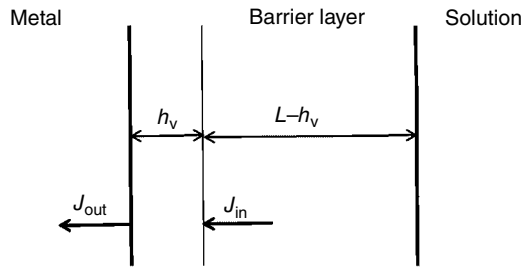


FIGURE 4.4.47 Scheme of the double structure of barrier layer.

(Figure 4.4.47). In Engelhardt *et al.* [2016], it was shown that the migration Peclet number (the ratio of the intensity of migration to that of diffusion) has the order of 10^3 . Accordingly, it is assumed that in the main part of the barrier layer, cation vacancies are transferred primarily by migration and the concentration of cation vacancies in the thin layer adjusted to the m/f interface is described by the following balance equation:

$$h_v \frac{\partial C_v^L}{\partial t} = J_{in} - J_{out} \quad (209)$$

Here, h_v is the thickness of the adjusted monolayer (it is of the order of the diameter of an Fe atom), and J_{in} and J_{out} are fluxes of cation vacancies into and out of the monolayer, respectively.

Mass transfer of the cation vacancies inside the main part of barrier layer is described by the equation

$$\frac{\partial C_v}{\partial t} = -U_v \frac{\partial C_v}{\partial x} \quad (210)$$

where U_v is migration rate of cation vacancies with the general solution

$$C_v = \theta(t - x/U_v) \quad (211)$$

where θ is the arbitrary function. Here it is assumed that, due to Esaki band-to-band tunneling (possibly via inter-band gap states, the electric field strength, ϵ , can be considered to be constant within barrier layer (Ahn *et al.* [2005], Lu *et al.* [2014])), and accordingly the migration rate U_v also can be considered as to be independent of the spatial coordinates.

Accordingly, the flux of the cation vacancies in the main part of the barrier layer is described by the equation

$$J(x, t) = k_4(t - x/U_v) \quad (212)$$

and

$$J_{in} = k_4 \left(t - \frac{L - h_v}{U_v} \right) = k_4(t - \tau) = \bar{k}_4 + \Delta \bar{k}_4 e^{j\omega(t - \tau_v)} = \bar{k}_4 + \bar{k}_4 g_4 \Delta V e^{j\omega(t - \tau_v)} \quad (213)$$

where

$$\tau_v = \frac{L - h_v}{U_v} \quad (214)$$

is the time required for cation vacancies to move from the f/s interface to the outer border of the adjusted m/f interface monolayer.

On the other hand

$$J_{\text{out}} = \bar{k}_1 \bar{C}_v^L + \Delta \bar{k}_1 \bar{C}_v^L e^{j\omega t} + \bar{k}_1 \Delta \bar{C}_v^L e^{j\omega t} = \bar{k}_4 + \bar{k}_1 g_1 \bar{C}_v^L \Delta V e^{j\omega t} + \bar{k}_1 \Delta \bar{C}_v^L e^{j\omega t}, \quad (215)$$

and Eq. (209) can be rewritten in the form

$$j\omega \Delta C_v^L = \bar{k}_4 g_4 \Delta V e^{-j\omega \tau} - \bar{k}_1 g_1 \bar{C}_v^L \Delta V - \bar{k}_1 \Delta C_v^L, \quad (216)$$

which yields

$$\frac{\Delta C_v^L}{\Delta V} = \frac{\bar{k}_4 g_4 e^{-j\omega \tau_v} - g_1}{\bar{k}_1 1 + j\omega h / \bar{k}_1} \quad (217)$$

By analogy it can be shown that

$$\frac{\Delta C_i^0}{\Delta V} = \frac{\bar{k}_2 g_2 e^{-j\omega \tau_i} - g_5}{\bar{k}_5 1 + j\omega h / \bar{k}_5} \quad (218)$$

where parameter

$$\tau_i = \frac{L - h_i}{U_i} \quad (219)$$

is also defined by analogy with Eq. (214).

Substituting Eqs. (217) and (218) into Eq. (207), we finally have

$$Y_f = \frac{1}{Z_f} = R_4^{-1} + (R_1 A_v)^{-1} + R_2^{-1} + (R_5 A_i)^{-1} + R_3^{-1} + R_7^{-1}, \quad (220)$$

that is, in general case, the impedance of barrier layer can be presented as a series of ohmic resistors R_4 , R_2 , R_3 , and R_7 and elements $R_1 A_v$ and $R_5 A_i$ where dimensionless parameters

$$A_v = 1 + \frac{(g_4/g_1)e^{-j\omega t_v} - 1}{1 + j\omega h_v / \bar{k}_1} \quad (221)$$

and

$$A_i = 1 + \frac{(g_2/g_5)e^{-j\omega t_i} - 1}{1 + j\omega h_i / \bar{k}_5} \quad (222)$$

depend on frequency. Parameters R_i ($i = 1-5, 7$) that have dimension Ωcm^2 can be found in Table 4.4.5. The physical meaning of parameters R_i is as follows: R_2 , R_3 , R_4 , and R_7 are the ohmic resistance of the corresponding reactions in Figure 4.4.27, R_1 is the ohmic resistance of Reaction (105) for $C_v^L = \text{const} = \bar{C}_v^L$, and R_5 is the ohmic resistance of Reaction (108) for $C_i^0 = \text{const} = \bar{C}_i^0$.

The faradaic resistances for all particular cases, along with the corresponding steady-state current densities, are shown in Table 4.4.6.

It is important to note that the potential drops $\phi_{m/f}$ and $\phi_{f/s}$ are considered here as independent variables that can be determined by optimization of the experimental EIS data. (In contrast, when Eqs. (197) and (198) are valid, the potential drops $\phi_{m/f}$ and $\phi_{f/s}$ are not independent but satisfy the

TABLE 4.4.5 Ohmic Resistances Due to the Reactions Shown in Figure 4.4.27 Assuming That Concentrations Are Time Independent and Are Equal Their Steady-State Values

<i>i</i>	R_i
1	$[F\chi\bar{k}_1\bar{C}_v^Lg_1]^{-1} = [(\chi/\delta)\bar{I}_vg_1]^{-1}$
2	$[F\chi\bar{k}_2g_2]^{-1} = [(\chi/\delta)\bar{I}_ig_2]^{-1}$
3	$[F\chi\bar{k}_3g_3]^{-1} = [(\chi/\delta)\bar{I}_og_3]^{-1}$
4	$[F(\delta-\chi)\bar{k}_4g_4]^{-1} = [(1-\chi/\delta)\bar{I}_vg_4]^{-1}$
5	$[F(\delta-\chi)\bar{k}_5\bar{C}_i^Lg_5]^{-1} = [(1-\chi/\delta)\bar{I}_ig_5]^{-1}$
7	$[F(\delta-\chi)\bar{k}_7g_7]^{-1} = [(1-\chi/\delta)\bar{I}_og_7]^{-1}$

TABLE 4.4.6 Faradaic Impedance Expressions for the Barrier Layer Due to Different Point Defects

δ	Main transport species	\bar{I}	Z_f
$\delta=\chi$	Cation interstitials	$F\chi k_2^0 \left(\frac{k_7^{*0}}{k_3^0} \left(\frac{C_{H^+}}{C_{H^+}^0} \right)^n \right)^{\alpha_2/\alpha_3}$	R_2
	Cation vacancies	$F\chi k_4^0 \exp\left(\frac{\alpha_4\chi F}{RT}\bar{\phi}_{f/s}\right)$	$R_1 A_v$
	Anion vacancies	$F\chi k_7^{*0} \left(\frac{C_{H^+}}{C_{H^+}^0} \right)^n$	R_3
$\delta>\chi$	Cation interstitials	$F\delta k_2^0 \exp\left(\frac{\alpha_1\chi F}{RT}\bar{\phi}_{m/f}\right)$	$[R_2^{-1} + (R_5 A_i)^{-1}]^{-1}$
	Cation vacancies	$F\delta k_4^0 \exp\left(\frac{\alpha_4\chi F}{RT}\bar{\phi}_{f/s}\right)$	$[R_4^{-1} + (R_1 A_v)^{-1}]^{-1}$
	Anion vacancies	$F\delta k_7^{*0} \exp\left(\frac{\alpha_7(\delta-\chi)F}{RT}\bar{\phi}_{f/s}\right) \left(\frac{C_{H^+}}{C_{H^+}^0} \right)^n$	$[R_3^{-1} + R_7^{-1}]^{-1}$

condition $\phi_{m/f} + \phi_{f/s} = V - \phi_R - \epsilon L$.) However, if the potential drop across the barrier layer, ϕ_f , does not depend on δV , the polarizabilities ξ and ζ are dependent and are related by the relation

$$\delta\phi_{m/f} + \delta\phi_{f/s} = \delta V \quad \text{or} \quad \xi + \zeta = 1 \quad (223)$$

because the contribution from δL can be ignored in the small-signal analysis and because $\delta\phi_R = 0$.

It must be also noted that, in the general case, the polarizabilities ξ and ζ may be functions (even nonlinear functions) of the applied voltage, V , and other parameters (e.g., temperature, pH, L , etc.). As follows from Eq. (223), only the sum of these values is constant (equals 1) at small values of applied voltage amplitude, δV . However, in the case when Eq. (197) and (198) are valid, we have

$$\xi = \alpha \quad \text{and} \quad \zeta = (105 - \alpha), \quad (224)$$

that is, polarizabilities ξ and ζ must be considered as constants, while the polarizability, α , in Eqs. (197) and (198) is assumed to be constant (independent of V , L , and pH).

4.4.7.7 Comparison of Simplified Model with Experiment

The impedance of passive iron (carbon steel) can be considered to be the simplest case from the point of view of an EEC that might be suggested for describing the experimental results. In this case, the barrier layer is an n-type semiconductor and the cation interstitial is the principal point defect in the lattice. We will assume that $\gamma\text{-Fe}_2\text{O}_3$ is the chemical structure of barrier layer and that the ejected cation at the bl/s interface is Fe^{3+} , that is, $\chi = \delta = 3$. In this case, the impedance of the barrier layer reduces to the faradaic resistance $Z_f = R_f = R_2$ (see Table 4.4.3). Accordingly, at sufficiently high applied voltage, where the influence of the cathodic reaction(s) is negligible, the equivalent circuit shown in Figure 4.4.48 is appropriate. If the transport by anion vacancies is not negligible, Z_f reduces to that of a parallel combination of the resistance R_2 and R_3 ; that is, $Z_f = R_f = R_2R_3/(R_2 + R_3)$.

Figure 4.4.49 shows EIS data collected for iron in borate buffer solution [0.3 M H_3BO_3 + 0.075 M $\text{Na}_2\text{B}_4\text{O}_7$ + 0.001 M EDTA, $\text{pH} = 8.5$, at $T = 21^\circ\text{C}$ (Sharifi-Asl *et al.* [2013b])]. As follows from Figure 4.4.48, the real and imaginary components of the impedance of the system are

$$Z_{\text{Re}} = \frac{R_f}{1 + R_f^2 \omega^2 C_g^2} + R_s \quad \text{and} \quad Z_{\text{Im}} = -\frac{R_f^2 \omega C_g}{1 + R_f^2 \omega^2 C_g^2} \quad (225)$$

The three unknown values, R_f , C_g , and R_s , are obtained from the requirement that the calculated values of Z_{Re} coincide with the measured values at two points, $\omega = \omega_{\text{min}}$ and $\omega = \omega_{\text{max}}$, and the calculated value of Z_{Im} coincides with the measured value at one point, $\omega = \omega_{\text{min}}$. Here, ω_{min} and ω_{max} are the minimum and maximum values of the frequency used in the measurements, respectively. The fitted parameters are shown in Table 4.4.7.

It must be noted that in the case of iron (but not in the cases of nickel and Alloy 316; see Figures 4.4.50, 4.4.51, and 4.4.53), a substantial discrepancy can be seen between the measured (extracted from Sharifi-Asl *et al.* [2013b]) and calculated phase angles at high frequencies. The same discrepancy was observed by comparing the experimental phase angle and the phase angle calculated on the basis of the non-simplified PDM model (compare Figures 4.4.43 and 4.4.49). In Ref. [12], it was stated that "the discrepancy at high frequencies arises from uncounted-for capacitance, which is not of primary interest of the study." For this same reason, we have not identified, in this review, the source of the additional capacitance.

As we can see from Table 4.4.7, the values of R_f are close to one another (except the case for $E = 0.044$), which confirms the results noted earlier. It can also be seen in Figure 4.4.31 that the comparison between calculated and experimental values are less satisfactory for the case of $E = 0.044 \text{ V}_{\text{SHE}}$. The possible explanation of this fact is that at the relatively low applied potential, $E = 0.044 \text{ V}_{\text{SHE}}$, cathodic reactions might play significant role by effectively reducing the observed value of R_f (by presenting two impedances in parallel), that is, the case $E = 0.044 \text{ V}_{\text{SHE}}$ cannot be described adequately by the single partial reaction model developed here. Thus, recently, a mixed potential model (MPM) (Lu *et al.* [2014]) comprising a passive anodic partial reaction that was represented by the PDM and a "fast" cathodic partial reaction of hydrogen evolution that was represented by the BV equation was used

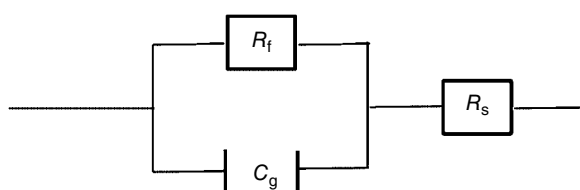


FIGURE 4.4.48 Simplified equivalent electrical equivalent circuit. $Z_f = R_f$, faradaic resistor, C_g is the capacity of barrier layer, and R_s is the resistance of the solution or/and outer barrier layer.

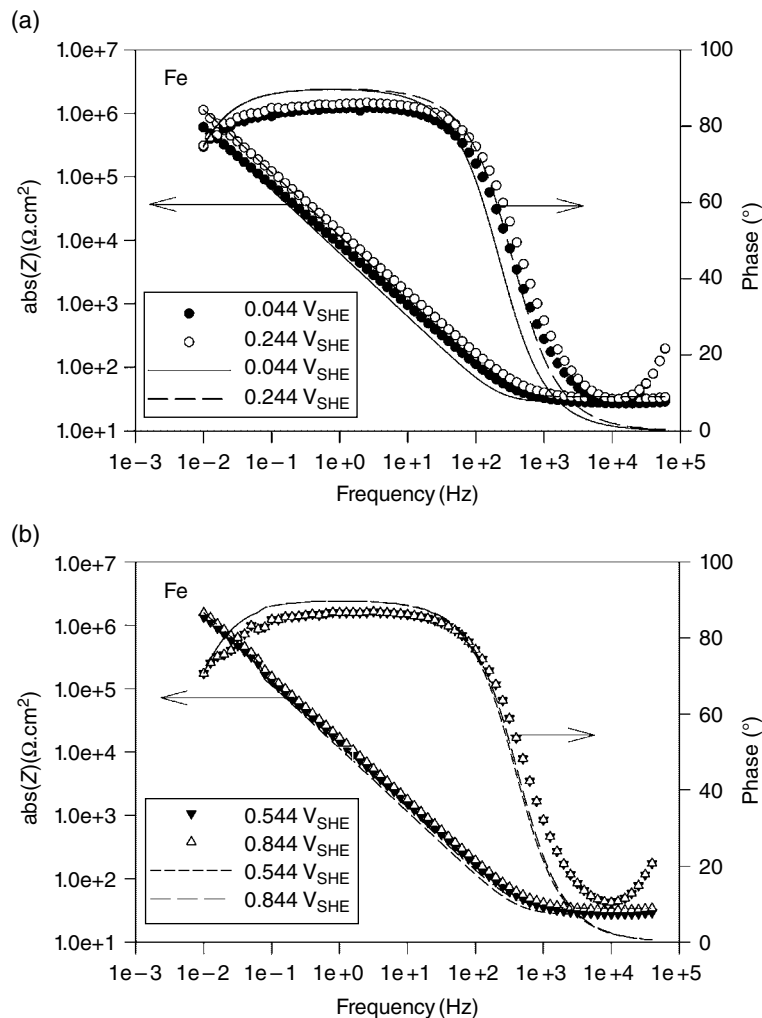


FIGURE 4.4.49 Experimental and simulated impedance spectra for corrosion of carbon steel in borate buffer solution ($0.3 \text{ M H}_3\text{BO}_3 + 0.075 \text{ M Na}_2\text{B}_4\text{O}_7 + 0.001 \text{ M EDTA}$) at $T = 21^\circ\text{C}$ and at different values of the applied potential: at $0.044 \text{ V}_{\text{SHE}}$ and $0.244 \text{ V}_{\text{SHE}}$ (a) and at $0.544 \text{ V}_{\text{SHE}}$ and $0.844 \text{ V}_{\text{SHE}}$ (b). The symbols are experimental data and the lines are the fit.

TABLE 4.4.7 Optimized Parameters for the Corrosion of Carbon Steel in Borate Buffer Solution

$E (\text{V}_{\text{SHE}})$	$R_f (\Omega \cdot \text{cm}^2)$	$C_g (\text{F cm}^2)$	$R_s (\Omega \cdot \text{cm}^2)$
0.044	2.86×10^6	2.52×10^{-5}	28.5
0.244	4.37×10^6	1.35×10^{-5}	34.0
0.544	4.09×10^6	0.880×10^{-5}	27.4
0.844	4.77×10^6	0.755×10^{-5}	34.0

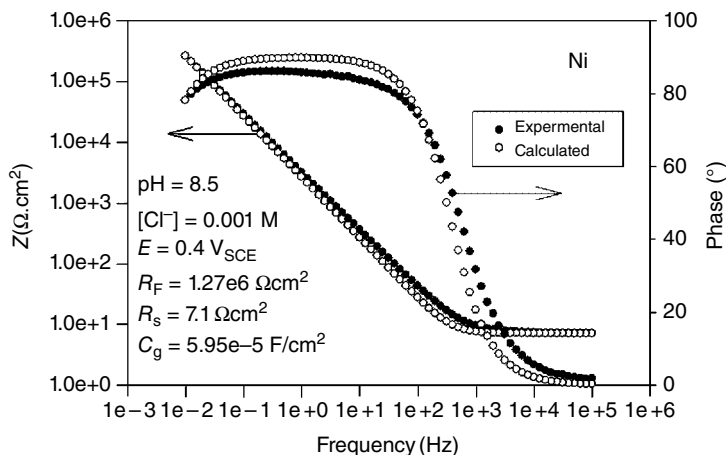


FIGURE 4.4.50 Experimental and simulated impedance spectra for corrosion of nickel in pH = 8.5 buffer solution with a chloride concentration 0.001 M.

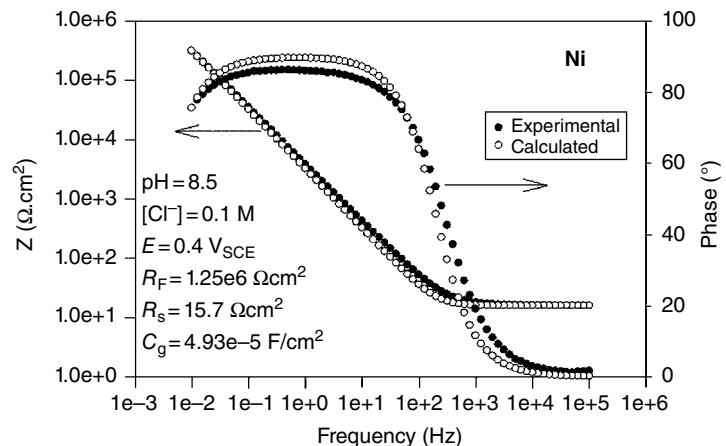


FIGURE 4.4.51 Experimental and simulated impedance spectra for corrosion of nickel in pH = 8.5 buffer solution with a chloride concentration 0.1 M.

in an MPM format to describe the impedance of passive carbon steel under highly anoxic conditions. This MPM accurately accounts for passive carbon steel under conditions where hydrogen evolution is significant and is the principal cathodic partial reaction that demonstrates the postulated impact of the additional partial reaction on the impedance of the interface. Parenthetically, we note that the successful application of the MPM required recognition of the fact that the partial cathodic reaction occurs upon the barrier layer, so that appropriate corrections had to be made for the quantum mechanical tunneling of charge carriers through the barrier layer.

It must be also noted that the parameters presented in Table 4.4.7 cannot be considered as the best-fit parameters in the usual sense. In this chapter, we have demonstrated that by using only three experimental points, this simplified method can yield acceptable estimations for R_f and C_g .

We now consider the case when the barrier layer is a p-type semiconductor, such as the case of passive Ni. In this case, $\chi = \delta = 2$. If we assume that the cation vacancy is the principal point defect in the barrier layer, then the impedance of the barrier reduces to $Z_f = R_1 A_v$ (see Table 4.4.6).

For $\omega \rightarrow 0$, we have the evident limit that $A_\nu \rightarrow g_4/g_1$ or $Z_{f,\nu} \rightarrow (g_4/g_1)R_1$, which corresponds to steady-state conditions. On the other hand, for $\omega \rightarrow \infty$ we have $\text{Re}(A_\nu) \rightarrow 1$ and $\text{Im}(A_\nu) \rightarrow 0$, that is, $Z_{f,\nu} \rightarrow R_1$. While the absolute value of the numerator of the ratio in the second term on the right side of Eq. (221) is of the order of 1, we can assume that $A_\nu \approx 1$ and $Z_{f,\nu}$ reduces to ohmic resistance, R_1 , for

$$\frac{\omega h_\nu}{\bar{k}_1} \gg 1 \quad (226)$$

Thus, for $f \geq 0.01$ Hz (≥ 0.0628 rad/s) and $h_\nu = 2.7 \times 10^{-8}$ cm (diameter of a Ni atom), the faradaic impedance does not depend on frequency for $\bar{k}_1 \ll 1.67 \times 10^{-9}$ cm/s. Figures 4.4.50 and 4.4.51 show that this is a good assumption for passive Ni under the conditions of the experiments that are described in Ahn *et al.* [2005]. It appears that R_f and C_g depend slightly on the concentrations of chloride.

For the case $\delta > \chi$, the faradaic impedance of the barrier layer may depend upon frequency because of the transport of metal interstitials. However, by analogy, we can conclude that this dependence will be negligible if

$$\frac{\omega h_i}{\bar{k}_5} \gg 1 \quad (227)$$

We may also conclude that if Conditions (226) and (227) are satisfied simultaneously, the faradaic resistance of the barrier layer reduces to a parallel combination of resistances and finally to the ohmic resistance:

$$R_f = \frac{1}{\sum_i (R_i)^{-1}} \quad (228)$$

By assuming that Conditions (226) and (227) hold, we compare the measured and calculated impedance data for the case of corrosion of Alloy 316 in 0.1 M NaCl, 25°C, pH = 4 solution buffered to keep a constant pH throughout the test, and with partial pressures of H₂S and CO₂ that were maintained constant at 20 psi (0.138 MPa) and 380 psi (106.62 MPa), respectively. These tests were performed in specially adapted benchtop autoclaves taking care that no crevices are possible within the WE, which might add artifacts to the measured data. However, the results of the optimization are not satisfactory (Figures 4.4.52 and 4.4.53).

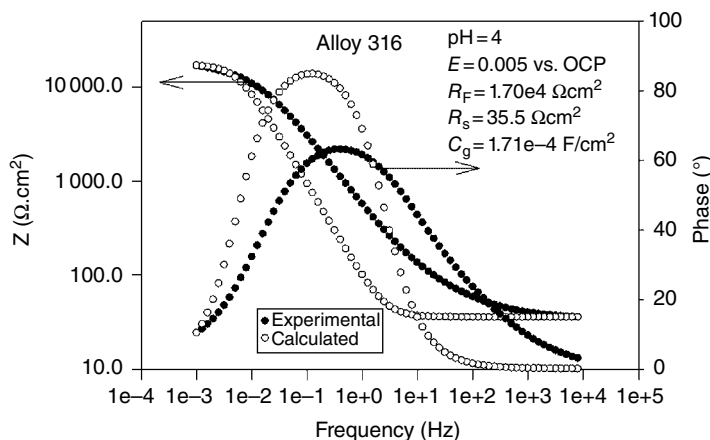


FIGURE 4.4.52 Experimental and simulated impedance spectra for the corrosion of Alloy 316 in 0.1 M NaCl, 25°C, pH = 4, and with partial pressures of 0.138 MPa H₂S and 2.62 MPa CO₂. Calculations were made in accordance with the simplified electrical equivalent circuit (Figure 4.4.48).

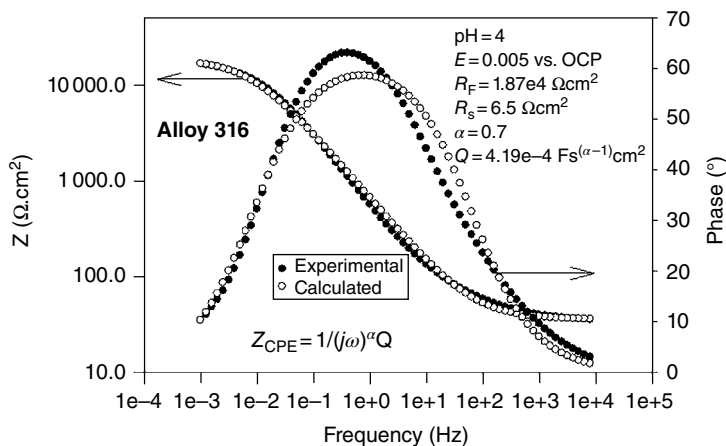


FIGURE 4.4.53 Experimental and simulated impedance spectra for corrosion of Alloy 316 in 0.1 M NaCl, 25°C, pH = 4, and with partial pressures of 0.138 MPa H₂S and 2.62 MPa CO₂. Here, the CPE element instead of capacitor is used in the simplified equivalent electrical circuit.

The optimization can be substantially improved if, instead of capacitor with the impedance $1/(\omega C_g)$ in the simplified equivalent circuit (Figure 4.4.49), a CPE (Orazem and Tribollet [2008]) with the impedance

$$Z_{\text{CPE}} = \frac{1}{(j\omega)^\alpha Q} \quad (229)$$

is employed (see Figure 4.4.34). Here, parameter Q has units of $\text{F}\cdot\text{s}^{(\alpha-1)}\text{cm}^2$. The reason for using a CPE instead of simple capacitor is not considered in this chapter, other than to note that polycrystalline surfaces are characterized by a distribution in barrier layer thickness and hence in geometric capacitance, due to the exposure of different grain faces, and this should be regarded as being a reasonable rationalization. Comprehensive results from EIS studies on Alloy 316 SS, along with the results for two other corrosion resistant alloys (Alloys 2205 and 625), in CO₂ + H₂S-containing environments (along with the possible explanation of using CPE instead of simple capacitors in equivalent circuits in these systems) will be published in a later chapter.

4.4.7.8 Summary and Conclusions

- The impedance of the barrier layers of passive films can be successfully described in terms of reaction mechanism analysis (RMA), in which the generation and annihilation of point defects at the interfaces are defined. Analytical expressions for the faradaic admittance are derived in which relations of the point defect concentrations and the thickness of the barrier layer are accounted for.
- Powerful optimization techniques, especially those that employ genetically inspired optimization algorithms, have been demonstrated to extract values for more than fifteen model parameters; this is possible because the impedance measured at each frequency is a separate experimental observation. Typically, the impedance is measured at more than fifty frequencies in any given experiment.
- The model parameters derived from the optimization successfully predict the steady-state thickness of the barrier layer and the steady-state passive current density, even though these quantities

were not employed in the optimization. However, the theory is complex and requires optimization skills that are beyond the average electrochemist. It is for this reason that a simplified treatment has been developed that is based upon the conclusion resulting from numerical analysis that the relaxation on the barrier layer thickness may be ignored.

- Thus, upon the basis of this assumption, closed analytical expressions for steady-state passive current densities have been obtained on the basis of the PDM for the simplified treatment without invoking an assumed relationship between the potential drop across the bl/s interface and the applied voltage and pH. It is shown that the current densities do not depend on the applied voltage only in the cases when the valence of the metal does not change ($\gamma = \delta$) and the principal transported point defect is the cation interstitial and/or the anion vacancy. In all other cases, some dependence of the passive current on applied voltage is predicted to be observed. These results are in agreement with previous findings obtained on the basis of the PDM.
- It was shown that both polarizabilities at the m/f and f/s interfaces may be considered to be dependent variables with their sum being equal to 1 under the usual EIS experimental conditions.
- Closed analytical expressions have been obtained for the faradaic impedance of the barrier layer, Z_f . In principle, these expressions allow us to only find exact combinations of unknown parameters by optimizing Z_f onto the experimental EIS data. However, by optimizing the PDM on synthetic EIS data, it has been demonstrated that the optimization returns the original parameter values, regardless of whether the parameters are contained within combinations.
- Clear criteria have been formulated for identifying the circumstances when the faradaic impedance of the barrier layer does not depend on frequency, that is, when Z_f reduces to an ohmic resistance.
- Comparison with experimental data show that in many cases (passive corrosion of carbon steel, Ni, and Alloy 316 SS), Z_f reduces to an ohmic resistance at frequencies that are usually used in EIS studies ($f > 10^{-3}$ to 10^{-2} Hz).
- It is shown that in the cases of Fe and Ni, the simplest EEC (parallel resistance and capacitor) adequately describes the EIS behavior of passive metals, but in the case of Alloy 316 SS, a CPE must be employed instead of the capacitor in the equivalent circuit in order to obtain a satisfactory optimization.
- However, we note that in order to relate the experimental observables (e.g., current and voltage), some assumption relating the voltage drop across the bl/s interface is ultimately necessary, as was invoked in the original PDM.

4.4.8 Equivalent Circuit Analysis

Because electrochemical impedance techniques have their genesis in electrical engineering, great emphasis has been placed in the past on identifying an equivalent “electrical circuit” for the interface. Although this exercise is useful, in that the equivalent circuit is capable of mimicking the behavior of the system, the circuits that often are adopted are too simplistic to be of any interpretive value. Thus, the impedance data plotted in Figure 4.4.9, for example, cannot be interpreted in terms of a simple RC circuit of the type shown in Figure 4.4.54, if for no other reason that the circuit does not delineate the partial anodic and cathodic reactions. Also, this circuit strictly yields a semicircle in the complex plane that is centered on the real axis, whereas the locus of the experimental data is clearly neither semicircular nor centered on the abscissa. Nevertheless, an equivalent circuit of the type shown in Figure 4.4.54 is frequently assumed, and values are often calculated for the various components. It is important to realize, however, that the choice of an “incorrect” equivalent circuit has no consequence for the measured polarization resistance or corrosion rate, since the resistance $|Z|_{\omega \rightarrow 0} - |Z|_{\omega \rightarrow \infty}$ is independent of the form of the reactive component.

The shape of the impedance locus plotted in Figure 4.4.9 suggests that a more appropriate equivalent circuit is an electrical transmission line of the type shown in Figure 4.4.55. Although extensive use

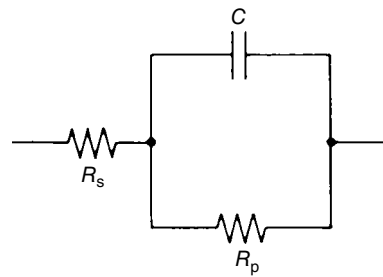


FIGURE 4.4.54 Simple electrical equivalent circuit for a corroding interface. Note that this circuit does not delineate the partial anodic or cathodic reactions.

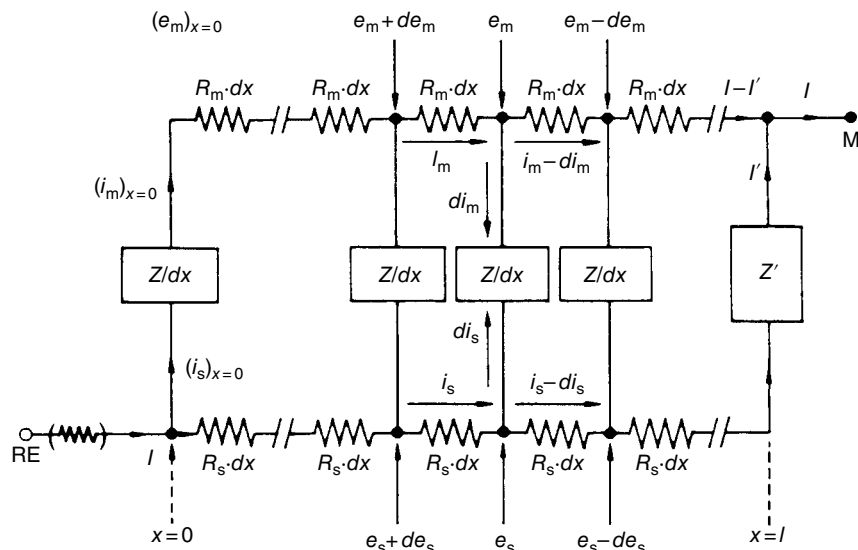


FIGURE 4.4.55 Discretized form of the transmission line model. e_m and e_s are the potentials in the magnetite and solution phases, respectively. Here i_m and i_s are the currents in the magnetite and solution phases, respectively; I and I' are the total current and the current flowing across the metal–solution interface and base of the pore, respectively; RE and M designate the reference electrode and metal (working electrode) locations, respectively. Source: Park 1983. Reproduced with permission of Elsevier.

has been made of transmission lines in the past (de Levie [1964, 1965, 1967], Atlung and Jacobsen [1976], McKubre [1976], Park and Macdonald [1983], Lenhart *et al.* [1984]) to model rough surfaces, PE, corroding interfaces, polarization in soils and clays, and coated surfaces, they have not been universally embraced by corrosion scientists and electrochemists. The particular transmission line shown in Figure 4.4.55 was developed by Park and Macdonald [1983] and by Lenhart *et al.* [1984] to model porous magnetite films on carbon steel in high-temperature chloride solutions and to describe the degradation of porous $\text{Ni}(\text{OH})_2\text{--NiOOH}$ battery electrodes in alkaline solution upon cyclic charging and discharging. We will discuss the first case in some detail, because it is a good example of how a transmission line can provide a physical picture of the processes that occur with a complex corrosion reaction.

The work of Park and Macdonald [1983] was performed in an attempt to understand the phenomenon of "denting" corrosion in pressurized water reactor (PWR) steam generators (Garnsey [1979]). Briefly, this phenomenon, which is represented schematically in Figure 4.4.56, occurs because of the rapid growth of magnetite in the crevice between an Inconel 600 steam generator tube and carbon steel support plate. The growing crystalline magnetite can deform or "dent" the tube and may result in leakage from the primary (radioactive) circuit to the secondary (nonradioactive) side via stress corrosion cracks that nucleate and grow in the highly stressed regions of the tubes. Previous work by Potter and Mann [1965], among others (see Park [1983]), had indicated that the growth of magnetite on carbon steel in simulated tube support plate crevice environments is kinetically linear; that is, the growing film offers no protection to the underlying metal. However, this conclusion was based on *ex situ* analyses of weight loss and film growth, neither of which yields real-time estimates of the rate of corrosion in the environment of interest.

In the work conducted by Park and Macdonald [1983], IS was used to measure the polarization resistance of corroding carbon steel in a variety of chloride (1 M)-containing solutions at temperatures from 200 to 270°C. Typical complex plane impedance spectra for one such system as a function of time are shown in Figure 4.4.57. In all cases (different exposure times), the impedance spectra are characteristic of a system that can be represented by an electrical transmission line. Also of interest is the observation (Park [1983]) that the inverse of the polarization resistance, which is proportional to the instantaneous corrosion rate, increases with increasing exposure time. Accordingly, the corrosion process is kinetically autocatalytic rather than being linear, as was previously reported. This autocatalytic behavior has been found for a wide range of solutions that simulate crevice environments, particularly those containing reducible cations, such as Cu²⁺, Ni²⁺, and Fe³⁺. The large amount of experimental polarization resistance data generated in the study showed that these reducible cations greatly accelerate the corrosion rate and yield autocatalytic behavior, with the effect lying in the order Cu²⁺ > Ni²⁺ > Fe³⁺. The enhanced rates were found to be far greater than could be accounted for by hydrolysis (to form H⁺) alone, and it was concluded that reduction of the foreign cations was largely responsible for the rapid corrosion of the steels. However, the autocatalytic nature of the reaction was also partly attributed to the buildup of chloride in the porous film. This buildup occurs for the reason of electrical neutrality, in response to the spatial separation of the anodic (iron dissolution at the bottom of the pores) and cathodic (H⁺ or cation reduction at the magnetite–solution interface) processes.

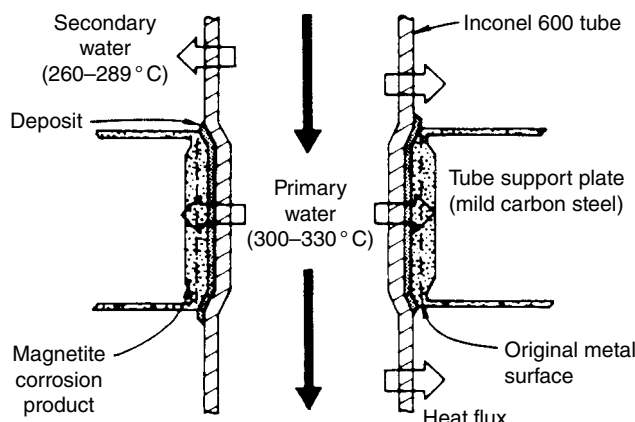


FIGURE 4.4.56 Schematic representation of denting corrosion in PWR steam generators.

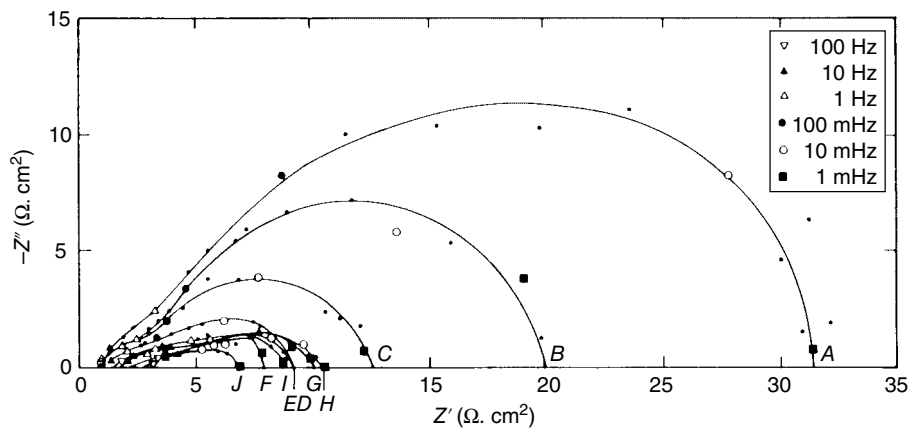


FIGURE 4.4.57 Impedance diagrams at the corrosion potential as a function of time for carbon steel exposed to a 0.997 M NaCl + 0.001 M FeCl₃ + 3500 ppb O₂ solution at 250°C. A = 11 h, B = 22 h, C = 35 h, D = 46 h, E = 58 h, F = 70 h, G = 86.5 h, H = 112 h, I = 136 h, and J = 216 h.

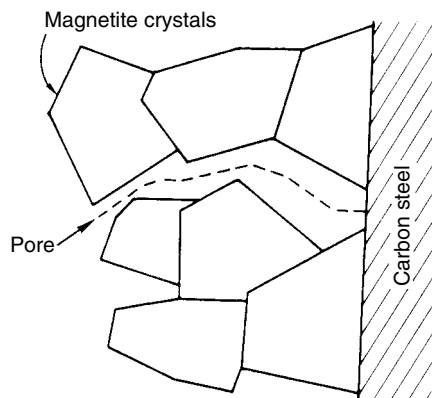


FIGURE 4.4.58 Schematic of fast growth of magnetite in acidic chloride solutions at elevated temperatures. Source: Park 1983. Reproduced with permission of Elsevier.

The model that was adopted to account for the fast growth of porous magnetite on carbon steel is shown schematically in Figure 4.4.58, and an ideal single pore is depicted in Figure 4.4.59. This single pore can be represented electrically by the continuous transmission line, as in Figure 4.4.60, and by the discretized transmission line shown in Figure 4.4.55, where Z is the impedance per unit length down the pore wall and Z' is the impedance of the metal–solution interface at the bottom of the pore. The impedance of a single pore is readily derived using Kirchhoff's equations to yield

$$Z_p = \frac{R_m R_s l}{R_m + R_s} + \frac{2\gamma^{1/2} R_m R_s + \gamma^{1/2} (R_m^2 + R_s^2) C + \delta R_s^2 S}{\gamma^{1/2} (R_m + R_s) (\gamma^{1/2} S + \delta C)} \quad (230)$$

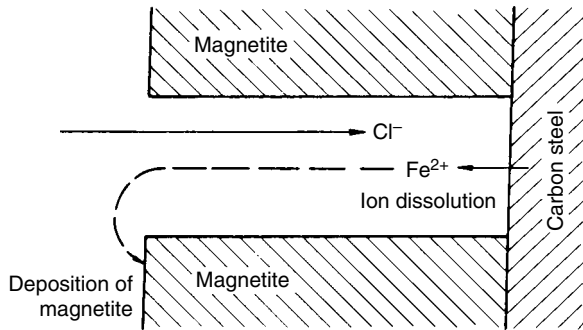


FIGURE 4.4.59 Ideal single-pore model for the growth of porous magnetite film in acidic chloride solutions at high temperature. Source: Park 1983. Reproduced with permission of Elsevier.

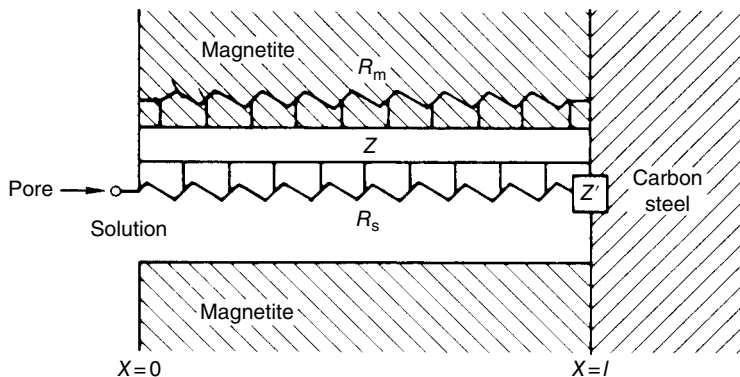


FIGURE 4.4.60 Transmission line model for a single one-dimensional pore: R_m , magnetite resistance per unit length of a pore; R_s , solution resistance unit length of a pore (Ω/cm); X , distance from the mouth of the pore along the pore axis (cm); Z , pore wall-solution interface impedance for unit length of a pore (Ω/cm); Z' , metal-solution interface impedance at the base of a pore (Ω). Source: Park 1983. Reproduced with permission of Elsevier.

where

$$\gamma = \frac{R_m + R_s}{Z} \quad (231)$$

$$\delta = \frac{R_m + R_s}{Z'} \quad (232)$$

$$C = \cosh(\gamma^{1/2}l) \quad (233)$$

$$S = \sinh(\gamma^{1/2}l) \quad (234)$$

Here R_m is the resistance of the magnetite per unit length of the pore, R_s is the corresponding quantity for the solution, and l is the length of the pore. For an oxide consisting of n independent parallel pores, the total impedance of the film then becomes

$$Z_T = \frac{Z_p}{n} \quad (235)$$

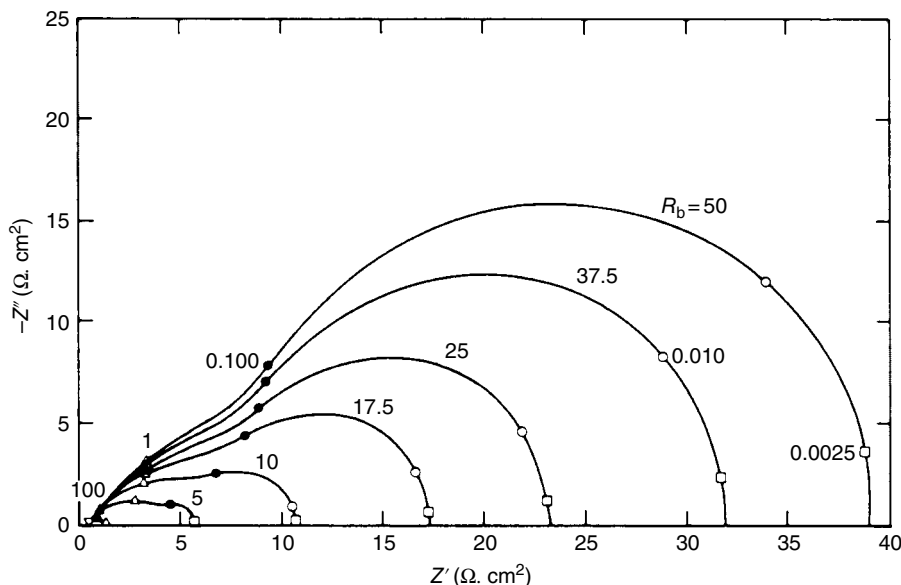


FIGURE 4.4.61 Calculated impedance spectra for a porous magnetite film on carbon steel in high-temperature aqueous sodium chloride solution as a function of the resistance at the base of the pore. N (no. of pores/cm 2) = 10^4 , ρ (solution) = $18.5\ \Omega\text{-cm}$, ρ (Fe_3O_4) = $116\ \Omega\text{-cm}$, θ (film porosity) = 0.01, L (film thickness) = 0.025 cm, R_W (pore wall-solution resistance) = $10^3\ \Omega\text{-cm}^2$, C_W (capacitance at pore wall-solution interface) = $2 \times 10^{-2}/\text{cm}^2$, and c_b (capacitance at pore base) = $7 \times 10^{-3}\ \text{F}/\text{cm}^2$.

To calculate the total impedance, it is necessary to assume models for the pore wall-solution and pore base-solution interfacial impedances (Z and Z' , respectively). In the simplest case, both interfaces are assumed to exist under charge transfer control, in which case Z and Z' can be represented by the equivalent circuit shown in Figure 4.4.54. Typical impedance spectra calculated for various values of the resistance at the pore base are shown in Figure 4.4.61. These theoretical curves generally exhibit the features displayed by the experimental data (Figure 4.4.57). Similar calculations have been carried out for porous films involving mass transfer control within the pores, and impedance spectra that compare well with experiment have again been generated (Park [1983], Park and Macdonald [1983]).

4.4.8.1 Coatings

An effective means of reducing the rate of corrosion of a metal is to protect the surface with a coating. However, coatings generally are not impervious to water or even ions, so that corrosion reactions still proceed at the metal-coating interface, albeit at a low rate. Because the rate of corrosion depends upon the transport of corrosive species through the film, in addition to the reactions occurring at the metal surface, it is evident that the overall process of attack is a very complicated one. It is therefore not surprising that coated metals have been studied using IS.

Perhaps one of the more extensive studies of this type is that reported by Mansfeld *et al.* [1982]. These workers evaluated polybutadiene coatings on carbon steel and aluminum alloys that had been subjected to different surface treatments, including phosphating for the steel and exposure to a conversion coating in the case of the aluminum alloys. Typical Bode plots ($\log |Z|$ and θ vs. $\log \omega$) for 1010 carbon steel that had been degreased, phosphated, and then coated with polybutadiene ($8 \pm 2\ \mu\text{m}$ thick), are shown in Figure 4.4.62 for two times after exposure to 0.5-N NaCl solution at ambient temperature. The low-frequency behavior of the phase angle ($\sim\pi/8$) suggests the existence of a transport process through the coating that is best described in terms of a transmission line (see earlier discussion in this section).

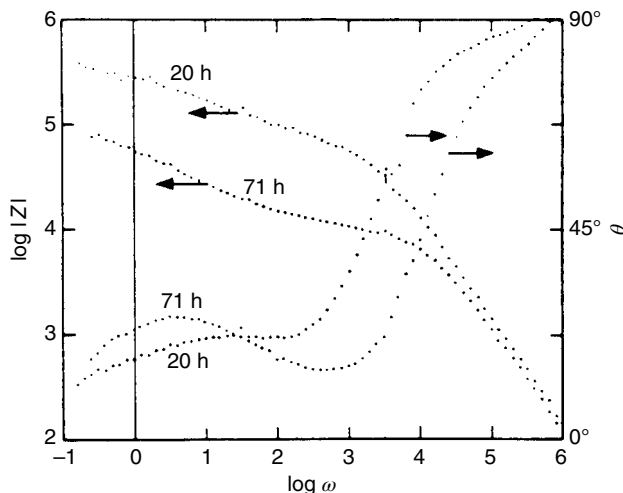


FIGURE 4.4.62 Bode plots for phosphated and coated 1010 carbon steel in 0.5N NaCl solution. Source: From Mansfield 1982.

However, the authors chose to analyze their data in terms of a classical Randles-type EEC containing a normal semi-infinite Warburg diffusional impedance element. Randles plots were then used to evaluate Warburg coefficients (σ), and polarization resistances (R_p) were calculated directly from the impedance magnitude at $\omega \rightarrow 0$ and $\omega \rightarrow \infty$ [Eq. (4)]. The R_p and σ parameters are plotted in Figure 4.4.63 as a function of time for a variety of surface pretreatments (including phosphating), as listed in Table 4.4.1. Both parameters are observed to decrease with time after an initial increase, at least in the case of R_p . The simultaneous decrease in R_p and σ was rationalized in terms of a model involving the development of ionically conducting paths through the polybutadiene coating as the corrosion reaction proceeds at the metal-coating interface.

4.4.9 Other Impedance Techniques

In keeping with the theme established at the beginning of this section that impedance techniques can be used to analyze many cause-and-effect phenomena, a number of other transfer functions have been defined. Three such functions—electrochemical hydrodynamic impedance (EHI), fracture transfer function (FTF), and electrochemical mechanical impedance (EMI)—are discussed briefly in the following text.

4.4.9.1 Electrochemical Hydrodynamic Impedance (EHI)

In the EHI technique (Deslouis *et al.* [1980, 1982], Bonnel *et al.* [1983]), the rate of mass transport of reactants to, or products from, an electrochemical interface is modulated (sine wave), and the response current or potential is monitored at constant potential or constant current, respectively, depending upon whether the transfer function is determined potentiostatically or galvanostatically. Experimentally, the transfer function is most easily evaluated using a rotating disk electrode, because of the ease with which the rotational velocity can be modulated. For a fast redox reaction occurring at the surface of a disk, the potentiostatic and galvanostatic electrochemical hydrodynamic admittances are given as follows:

$$Y_{\text{HD}}^I = \left(\frac{\delta I}{\delta \Omega} \right)_V = -\frac{3}{2\Omega_0} \exp(-0.26pj) \cdot \frac{C_\infty - C_0}{1.288} \cdot \frac{3^{1/3}}{\delta} \cdot \frac{K_1(s)}{Ai(s)} \cdot D \cdot \frac{Z_D}{Z} \quad (236)$$

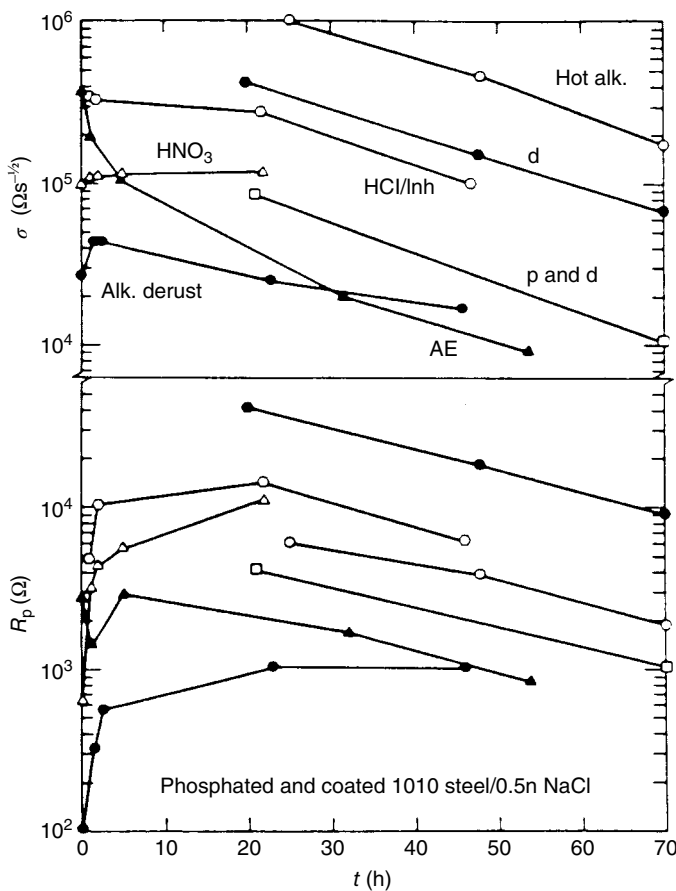


FIGURE 4.4.63 Time dependence of resistance R_p and Warburg coefficient σ for different surface pretreatment procedures applied to 1010 carbon steel. Source: From Mansfield 1982.

$$Y_{\text{HD}}^V = \left(\frac{\delta V}{\delta \Omega} \right)_I = -\frac{3}{2\Omega_0} \exp(-0.26pj) \cdot \frac{C_\infty - C_0}{1.288} \cdot \frac{K_1(s)}{Ai'(s)} \cdot R_T(k_f - k_b) \quad (237)$$

where Ω_0 is the mean angular velocity of the disk, $p = \omega/\Omega_0$, ω is the modulation frequency, $Ai(s)$ and $Ai'(s)$ are the Airy function of the first kind and its first derivative, $s = 1.56 j p Sc^{1/3}$, Sc (Schmidt number) = v/D , v is the kinematic viscosity, D is the diffusivity, $j = \sqrt{-1}$, Z_D is the diffusion impedance, R_T = the charge transfer resistance, k_f and k_b are the forward and backward rate constants for the redox reaction, Z is the overall impedance, and $K_1(s)$ is given by

$$K_1(s) = - \sum_0^\infty \frac{s^n}{n!} \int_0^\infty \frac{\delta^n Ai}{\delta \xi^n} \left[\xi_2 \exp\left(-\frac{\xi^3}{6}\right) + \xi^4 \rho_0(\xi) \exp\left(\frac{\xi^3}{6}\right) \right] d\xi \quad (238)$$

The application of EHI analysis to a corroding system has been described by Bonnel *et al.* [1983] in their recent study of the corrosion of carbon steel in neutral chloride solutions. An example of their data is shown in Figure 4.4.64 for carbon steel soon after immersion into air-saturated 3% NaCl solution. The steel surface is believed to be free of solid corrosion products under these conditions. The best fit of

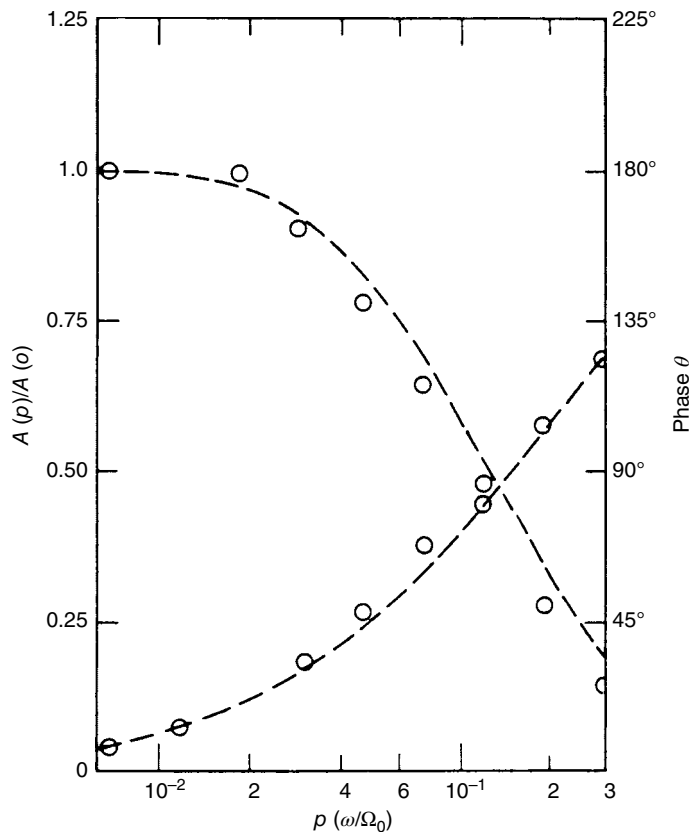


FIGURE 4.4.64 Bode plots of the reduced EHI modulus and phase angle as a function of reduced frequency (ω/Ω_0) for carbon steel in 3% NaCl solution. The EHI was measured in the galvanostatic mode [Eq. (112)] at a mean rotational velocity (Ω_0) of 1000 rpm and at $I=0$ (open-circuit conditions). Source: Bonnel 1983. Reproduced with permission of The Electrochemical Society.

Eq. (237) to the experimental data shown in Figure 4.4.64 (broken line) is found for $Sc = 615$ and $D(O_2) = 1.63 \times 10^{-5} \text{ cm}^2/\text{s}$. The value for the diffusivity of oxygen was found to be consistent with the steady-state current–voltage curve obtained for this system. A significant advantage claimed for the EHI technique is that it may be used to detect the presence of a porous corrosion product film on a corroding surface (Bonnel *et al.* [1983]), but in general the analysis is complicated, and the method has yet to demonstrate any clear advantages over more conventional techniques for examining coupled mass transfer–charge transfer phenomena.

4.4.9.2 Fracture Transfer Function (FTF)

Recently, Chung and Macdonald [1981] defined a transfer function for the propagation of a crack through an elastic–plastic material under transient loading conditions. Designating the stress intensity as $K_I(t)$ and the instantaneous crack velocity as $da(t)/dt$ (both time-dependent quantities), the FTF may be defined as

$$\bar{H}_F(s) = \frac{\mathcal{E}[K_I - K_{ISCC}]}{\mathcal{E}[da(t)/dt]} \quad (239)$$

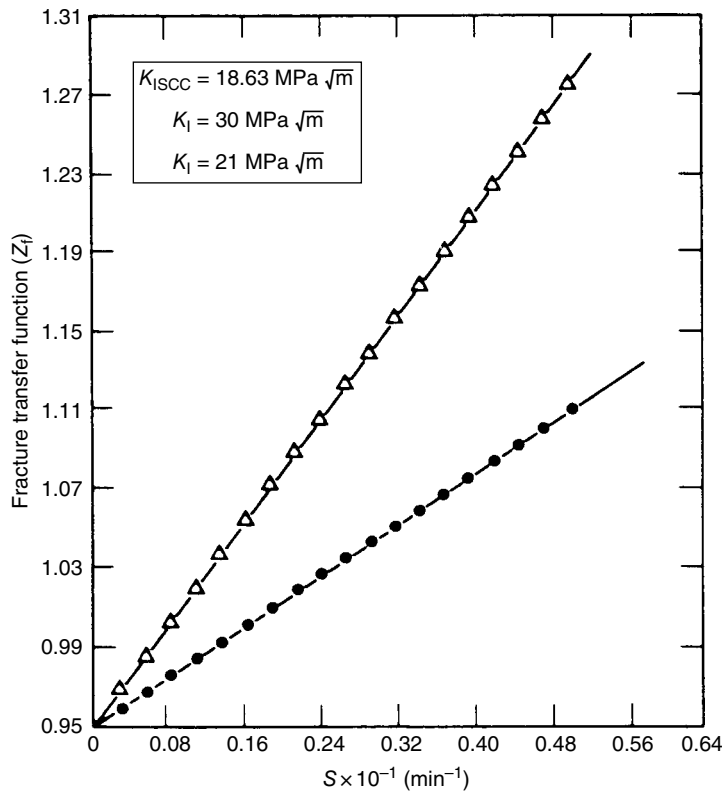


FIGURE 4.4.65 Fracture transfer function versus Laplace frequency.

where K_{ISCC} is the critical stress intensity for slow crack growth and \mathcal{L} designates the Laplace transform. The transfer function $\bar{H}_F(s)$ is a function of the Laplace frequency s .

Application of this analysis to transient crack growth data for AISI 4340 steel in 3% NaCl solution (Chung [1983]) is shown in Figure 4.4.65. It is seen that the transfer function $\bar{H}_F(s)$ increases linearly with the Laplace frequency s . Accordingly, the electrical analog for crack propagation is simply a resistance and inductance in series (Figure 4.4.66). However, the data shown in Figure 4.4.65 also reveal that the inductance, but not the resistance, is a function of the applied stress intensity; that is,

$$\bar{H}_F(s) = R + sL(K_I) \quad (240)$$

It is clear, therefore, that the system is nonlinear, so that $\bar{H}_F(s)$ is not expected to obey the KK transforms.

The parameter R provides a measure of the resistance to crack propagation, such that $1/R$ is proportional to the steady-state crack velocity. The R values obtained from the intercept at $s = 0$ indicate that the steady-state crack velocity is independent of stress intensity, a finding that is consistent with the fact that the applied stress intensity correlation for this system.

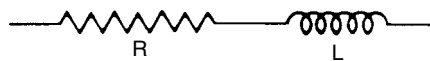


FIGURE 4.4.66 Series RL equivalent circuit used to represent the growth of a stress corrosion crack through AISI 4340 steel in 3% NaCl solution.

The inductance contained in the equivalent circuit shown in Figure 4.4.66 corresponds to an energy adsorption process, presumably due to the plastic deformation of the steel matrix in front of the crack tip. The size of the plastically deformed region, and hence the amount of energy deposited in the matrix in front of the crack tip, is known to increase with increasing K_I (Chung [1983]), and this accounts for the observed increase in $L(K_I)$.

4.4.9.3 Electrochemical Mechanical Impedance

Instead of the purely mechanical case discussed earlier, it is also possible to define an impedance in terms of the electrochemical response of a fractured specimen to a mechanical input that causes crack propagation.

One case in which this analysis can be usefully applied is that of the electrochemically assisted (stress corrosion) cracking of metals submerged in an electrolyte and subjected to a cyclic mechanical load or stress, corresponding to vibrational effects (Eiselstein *et al.* [1983, 1985]). With some simplification, crack growth due to cyclical film rupture at the growing crack tip, followed by metal dissolution, can be considered as described in the following text.

Figure 4.4.67 shows schematically the case of a crack growing into a metal under constant current but cyclic load conditions. The loading conditions can be controlled to achieve a sinusoidal variation in the crack opening displacement D :

$$D = \bar{D} + \tilde{d} \sin(\omega t) \quad (241)$$

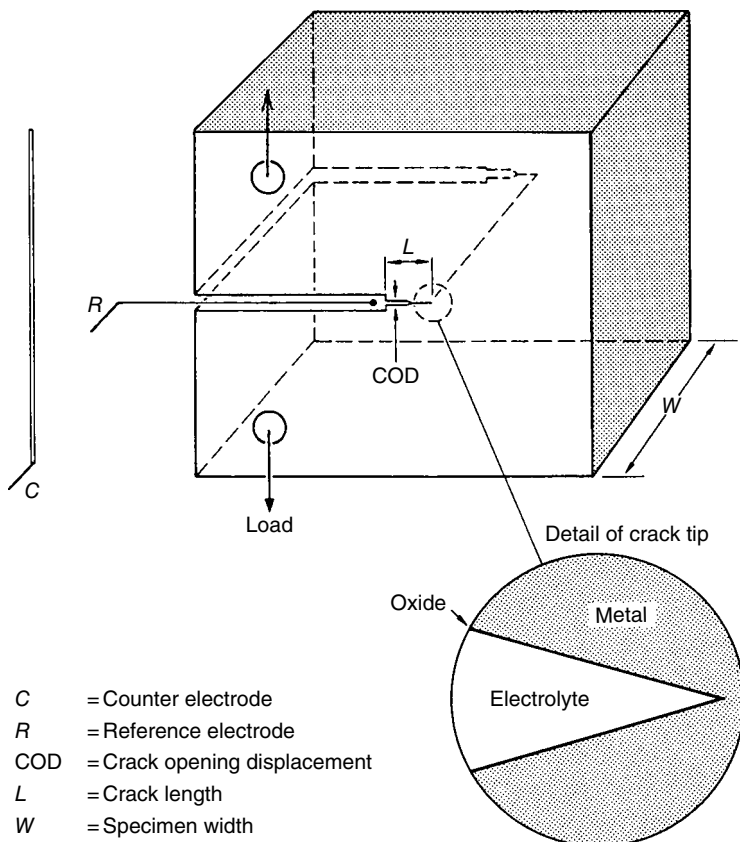
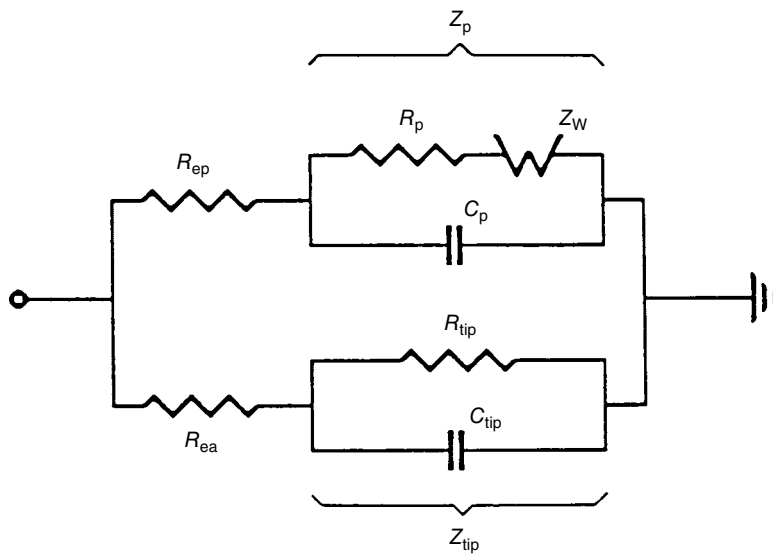


FIGURE 4.4.67 CT specimen geometry for determining the electrochemical mechanical impedance for the propagation of a crack.



- R_{ep} = Electrolyte resistance to crack walls
 R_p = Charge transfer resistance at passive walls
 C_p = Double layer capacitance at passive oxide
 Z_w = Diffusional impedance at passive walls
 Z_p = Interfacial impedance at passive walls
 R_{ea} = Electrolyte resistance to crack tip
 R_{tip} = Charge transfer resistance at exposed metal
 C_{tip} = Double layer capacitance at exposed metal
 Z_{tip} = Interfacial impedance to crack tip

FIGURE 4.4.68 Simplified equivalent circuit for a stress corrosion crack.

where \bar{D} is the mean crack opening and \tilde{d} the amplitude of the superimposed sinusoidal perturbation. Both \bar{D} and \tilde{d} will increase with crack length. To a first approximation, the area exposed at the crack tip can be considered to be proportional to the crack opening angle:

$$A = \gamma W \tan\left(\frac{D}{L}\right) \quad (242)$$

$$A \approx \gamma W \left(\frac{D}{L}\right) = \frac{\gamma W}{L} [\bar{D} + \tilde{d} \sin(\omega t)] \quad (243)$$

where γ is a proportionality constant determined by the mechanical properties of the metal and the oxide film (Eiselstein *et al.* [1985]) and W is the specimen width.

Figure 4.4.68 shows the approximate¹ equivalent circuit for the inside of the crack, with the impedance of the oxide-passivated walls appearing in parallel with the impedance element due to dissolution

¹ Because of the potential distribution along the crack, this equivalent circuit should more properly be represented as a nonuniform, finite transmission line for the oxide wall impedance, with the crack tip as a terminating impedance. Such a case is shown in Figure 4.4.60.

of exposed metal at the crack tip. The variation in crack opening displacement, described by Eq. (241), results in a sinusoidal perturbation at the exposed tip area such that

$$C_{\text{tip}} = C_{\text{tip}}^0 A \approx \frac{C_{\text{tip}}^0 \gamma W}{L} [\bar{D} + \tilde{d} \sin(\omega t)] \quad (244)$$

$$R_{\text{tip}} = \frac{R_{\text{tip}}^0}{A} \approx \frac{R_{\text{tip}}^0 L}{\gamma W [\bar{D} + \tilde{d} \sin(\omega t)]} \quad (245)$$

Without going through the algebra, for the equivalent circuit shown in Figure 4.4.68, we can obtain an expression for the EMI (Z_{em}) for this system, defined as the ratio of the ac voltage that appears at the RE to the crack opening displacement due to the sinusoidal load variation under dc galvanostatic conditions:

$$Z_{\text{em}} = \frac{\tilde{V}_{\text{ref}}}{\tilde{d}} = \bar{V}_{\text{tip}} [R_{e,p} + Z_p] \left[\frac{1}{R_{\text{tip}}^0} + j\omega C_{\text{tip}}^0 \right] \frac{\gamma W}{L} \quad (246)$$

Under optimal conditions, Z_{em} , measured over a range of frequencies can be used to deconvolve the equivalent circuit parameters in a manner analogous to that of electrochemical impedance analysis. The advantages of this method, in the example given, are that measurements can be made under dynamic load conditions and that the perturbation is imposed at the point of principal interest, the crack tip.

Figure 4.4.69 presents the real versus imaginary components of the EMI response measured for an HY80 steel specimen of geometry shown in Figure 4.4.67 immersed in 3.5 wt % NaCl. Due to the form of Eq. (246), these plots are somewhat more complex than a conventional Nyquist plot. Nevertheless, these data are amenable to standard methods of electrical analysis. We observe that the processes at the growing crack tip dominate at low frequencies and the properties of greatest interest, R_{tip} and C_{tip} , can be deconvolved at limitingly low frequencies.

Figure 4.4.70 shows the logarithm of the electrochemical mechanical admittance ($Y_{\text{em}} = 1/Z_{\text{em}}$) plotted versus log frequency, for a typical data set, as a function of the number of mechanical load cycles

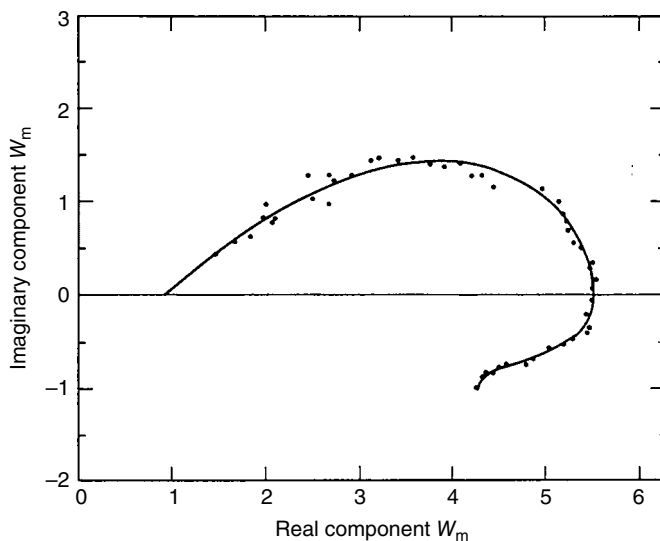


FIGURE 4.4.69 Complex plane plot of the electrochemical mechanical impedance for the propagation of a crack through HY80 steel in 3.5% NaCl solution at 25°C under sinusoidal loading conditions.

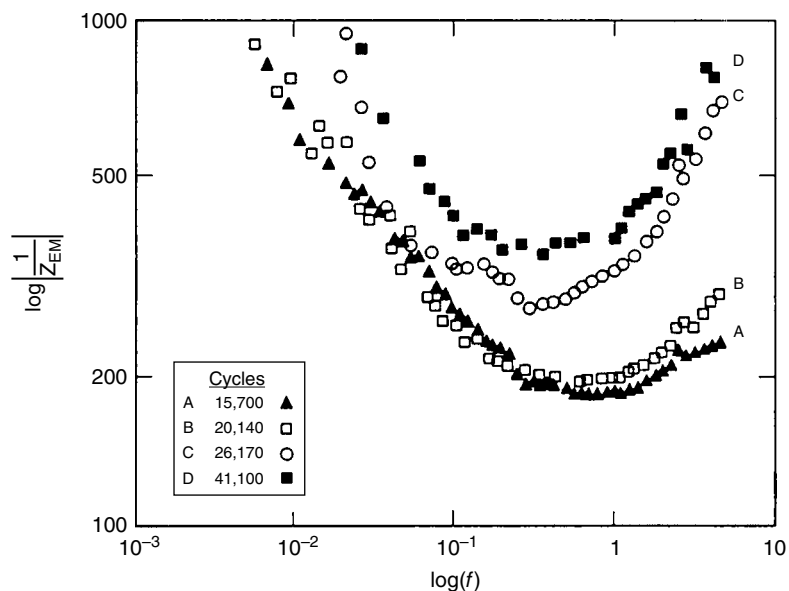


FIGURE 4.4.70 Log ($|1/Z_{em}|$) versus log (frequency) for an HY80 specimen of the geometry shown in Figure 4.4.65, exposed to 3.5 wt % NaCl at 25°C.

experienced by the specimen during crack growth. These data show some evolution in the crack tip parameters (the low-frequency descending portion of the curves), but considerably more changes appear in the crack wall impedance, reflecting the increased area with increasing crack length.

4.5 ELECTROCHEMICAL POWER SOURCES

Evgenij Barsoukov,¹ Brian E. Conway,² Wendy G. Pell,² and Norbert Wagner³

¹Head of Algorithm Development, Battery Management Systems, Texas Instruments Inc., Dallas, TX, USA

²Department of Chemistry, University of Ottawa, Ottawa, Ontario, Canada

³Deutsches Zentrum für Luft- und Raumfahrt e.V. (German Aerospace Center), Institut für Technische Thermodynamik, Stuttgart, Germany

4.5.1 Special Aspects of Impedance Modeling of Power Sources

4.5.1.1 Intrinsic Relation between Impedance Properties and Power Source Performance

It is widely recognized that apart from such characteristics as voltage and discharge capacity, internal energy losses constitute an important property of electrochemical power sources. There are multiple reasons for such losses. Usually both or one electrode of the power source is a porous layer of active material affixed on a surface of the current collector and in contact with a liquid or solid electrolyte. Electrodes are separated by a layer of electrolyte and in some cases an ionic conductive separator. If we trace the path of electric charge during charging or discharging, we will observe that it travels through an electronic pathway from one particle of active material to another, therefore experiencing ohmic

resistance. To pass from an electronic to an ionic conductive medium, charge has to cause electrochemical reaction at the surface of particles, which is an activated process and is therefore associated with energy loss described by the BV equation. For small voltages the current–voltage relationship at this boundary can be characterized using a charge transfer resistance R_{ct} . If charge passes for a prolonged time, the surface concentration of active materials decreases and has to be replenished by diffusion. The associated relationship with voltage is complex, but it can be said in general that diffusion-limited supply appears to an external observer as an additional time-dependent resistive term. After passing the boundary, charge then travels through an ionic pathway in the electrolyte, filling the pores and between electrodes. The voltage–current relationship there is also similar to ohmic at usual currents while becoming more complex at high currents.

These multiple resistive components will all degrade performance of the power source. IS helps in two different ways. First, it has the unique ability to separate different resistive contributions using only measurements at power source terminals. This allows researchers to identify the largest hindrance to high power capability of a power source and to investigate quantitatively how different steps help to eliminate it. Second, quantifying different components allows one to model power source current–voltage–time behavior. Older models of power sources assumed that all internal current hindrances could be represented by a single resistor in series with the voltage of the power source. For this approach no distinguishing of different components is needed, but only their sum is observed. However, limitations of such a model become apparent when the load on a power source is variable, as is now the case in most applications. The reason for failure of the simple model is the transient nature of voltage response of power source to applied load. Basically voltage does not drop immediately by an $I \cdot R$ value, where R is the sum of all resistive contributions, but drops by a time-dependent value that approaches $I \cdot R$ only at an infinite time. The only way to describe power capability of a power source at variable load is therefore to measure parameters describing all resistive and capacitive contributions to discharge hindrance and to use them in a physically relevant model to calculate the desired current–voltage–time relationship. IS does exactly this—it allows one both to test if a certain model is appropriate and to obtain parameters of this model for the particular power source.

4.5.1.2 Linear Time-Domain Modeling Based on Impedance Models: Laplace Transform

Electrochemical systems are in general nonlinear, which often makes analytical treatment of their kinetics prohibitively complex. Fortunately in many cases where small voltage changes are involved, a linear approximation, equivalent to representing the electrochemical system as an electric network made of ideal resistors, capacitors, and inductors, can be employed. The voltage response of resistances is not only linear but also time independent, and it follows Ohm's law, $i = V/R$, where R is not only independent of i and V but also independent of time. However, the current–voltage dependence of such elements as capacitors and inductors is time dependent and expressed by differential equations

$$i(t) = \left[\frac{dv(t)}{dt} \right] C, \quad v = \left[\frac{di(t)}{dt} \right] L \quad (1)$$

The reason why power sources exhibit transient voltage response and therefore deviate from Ohm's law is the presence of capacitive elements in parallel with resistive ones, for example, a double-layer capacitance in parallel with R_{ct} and pseudocapacitance associated with diffusion process in parallel with diffusion resistance.

Fortunately there is an indirect way to apply a treatment similar to Ohm's law to time-dependent systems. Linear differential equations have a very useful property to be transformed into linear equations, for example, to a form similar to that of Ohm's law, when subjected to Laplace transform, given in Eq. (2):

$$F(s) = \int_0^{\infty} e^{-s \cdot t} \cdot f(t) dt \quad (2)$$

Here s is a complex frequency in form of $\delta + \omega \cdot i$. For example, a differential equation describing the behavior of a capacitor C : $i(t) = dv(t)/dt \cdot C$, is transformed to $L[i(t)] = I(s)$ where $I(s) = C \cdot s \cdot V(s) - s \cdot v(0)$. I would like to emphasize here that due to advances in symbolic computing, both direct transform and inverse Laplace transform are no longer laborious table-searching procedures they used to be. Analytical software such as Maple or Mathematica can yield the Laplace transform (if it exists) of a function of almost any complexity in a matter of seconds, which makes this technique very convenient to use for any researcher. So, I encourage the reader not to be intimidated by Eq. (2), but get hold on some appropriate software and think Laplace transform as something easily done.

Now, as can be seen from the result earlier, the relationship between voltage and current in the Laplace domain does not involve differential equations and is therefore much more easy to solve for complex systems. Moreover, equations for a capacitor and an inductor can be formally represented in the same general form as that for resistors. Indeed, assuming that initial voltage on capacitor $v(0)$ is zero, we can rearrange the aforementioned equation as

$$I(s) = \frac{V(s)}{Z(s)} \text{ where } Z(s) = \frac{1}{C \cdot s} \quad (3)$$

Similarly, for an inductor $Z(s) = s \cdot L$. It can be seen that Eq. (3) has the same form as Ohm's law and the quantity $Z(s)$ plays the same role as resistance in Ohm's law. That allows to treat the voltage-current relationship for any network of capacitors, resistors, and inductors in the Laplace domain as if they all were resistors, only substituting the quantity $Z(s)$ instead of resistance for each element. For example, the Laplace current for a serially connected resistor R and a capacitor C will be $I(s) = V(s)/(Z(s) + R)$, which can be rearranged as

$$I(s) = \frac{V(s)}{1/C \cdot s + R} \quad (4)$$

Now, to find the current-voltage relationship in the time domain, we only need to substitute $V(s)$ for the particular excitation of interest and carry out the inverse Laplace transform for the entire equation. However, first we need to know how the particular excitation we want to apply looks in the Laplace domain. Here is an example how to do it for a voltage step. In the time domain it can be expressed as $v(t) = \text{Heaviside}(t) \cdot V_1$ where the function $\text{Heaviside}(t)$ takes a value 1 if $t > 0$ and 0 otherwise. V_1 is the value of voltage applied during the step. The Laplace transform of this function, $V(s) = L[\text{Heaviside}(t) \cdot V_1] = V_1/s$. To find the Laplace current of the aforementioned network to pulse excitation, we substitute this $V(s)$ into Eq. (4) and perform inverse Laplace transformation of the resulting equation. We obtain

$$i(t) = V_1 \cdot \exp\left(\frac{-t}{R \cdot C}\right) / R \quad (5)$$

You might note that neither impedance nor ac response was mentioned yet. The Laplace transform is handling a nonperiodic excitation (such as pulse); therefore the expression for $Z(s)$ is not identical to the impedance function of the same circuit. However, response to periodic excitation is related in elegant way with response to arbitrary excitation expressed in the Laplace domain. In Section 1.3 it is described how time-domain response to periodic excitation can be "folded" into the frequency domain by using Fourier transform where imaginary frequency is equal to the inverse period of the periodic excitation. Differential equations relating capacitor and inductor currents and voltages [Eq. (1)] are transformed to the frequency domain as $I(\omega \cdot i) = C \cdot \omega \cdot i \cdot V(\omega \cdot i)$ and $I(\omega \cdot i) = V(\omega \cdot i) / (L \cdot \omega \cdot i)$, which allows one, like in the case of the Laplace transform, to present it in a form similar to Ohm's law: $I(\omega \cdot i) = V(\omega \cdot i) / Z(\omega \cdot i)$ where the quantity $Z(\omega \cdot i)$ is called impedance and is given as $Z(\omega \cdot i) = 1 / (C \cdot \omega \cdot i)$ for a capacitor and $Z(\omega \cdot i) = L \cdot \omega \cdot i$ for an inductor.

By comparing $Z(\omega \cdot i)$ with the quantity $Z(s)$ in Eq. (3), obtained from the Laplace transform, we can see that they become identical if the real part, δ , in $s = \delta + \omega \cdot i$ is set to zero. Substituting instead of the complex $s = \delta + \omega \cdot i$ a purely imaginary frequency $s = \omega \cdot i$, we convert all expressions in the Laplace domain, which can be obtained, for example, by solving differential equations for a particular distributed system, as in Section 2.1.3, into impedance equations. Alternatively, all parameters of impedance functions (such as C and L in the previous example) obtained by fit of an experimental impedance spectrum can be substituted into Laplace-domain equations. Time-domain response to arbitrary (non-periodic) excitation can then be obtained by inverse Laplace transform as described earlier in this chapter.

4.5.1.3 Expressing Electrochemical Model Parameters in Electrical Terms, Limiting Resistances, and Capacitances of Distributed Elements

It is described in Section 2.2.2 how to express impedance functions for distributed systems in the form of a dimensionless function multiplied by a resistance factor. Dealing with dimensionless quantities simplifies theoretical analysis of particular impedance responses and is useful for comparing response of systems with different dimensions. However, properties of electrochemical power sources are often considered in the context of certain electrical device, and it is convenient when optimized parameters themselves have dimensions commonly used with electric elements, for example, ohm and farad. In some cases such usage has become common in electrochemistry, as is the case with expressing the impedance of the electrochemical double layer as charge transfer resistor [R_{ct}] in parallel with double-layer capacitance [C_{dl}], as shown in Section 1.3.2. By looking at the impedance plot in Figure 1.3.2, it is possible to estimate the approximate value of R_{ct} as the diameter of the semicircle in the complex plot. Moreover, if we would have an electrochemical power source with such an impedance (which is a good approximation with some fuel cells), we could immediately proceed from impedance analysis to modeling of this power source performance in the actual device by assigning the impedance model parameter R_{ct} as the internal resistance of the device. It is important to keep in mind that when moving to modeling of system performance under arbitrary loads or with changing state of charge (SOC), linearity assumptions will no longer hold. We would need to use parameters we obtained from low excitation impedance experiment (such as rate constant obtained from R_{ct}) and substitute them into full nonlinear equations of the system such as BV equation, which is valid for larger excitations. We would also not be able to use inverse Laplace transform to find time-domain response, but instead have to use a numerical solution of the system of nonlinear differential equations that govern the system.

In addition, not all impedance models are as simple as the aforementioned, mostly because multiple steps govern charge transfer kinetics and because electrochemical systems are distributed rather than discrete. In order to evaluate the relative importance of the contributions to the direct current (dc) resistance from different elements, we need to know how to characterize in electrical terms processes such as diffusion, which are commonly described in electrochemistry by specific physical quantities such as the diffusion coefficient. To achieve this, an impedance function for a particular process may be analyzed to find its limiting form at infinitely low and infinitely high frequencies. $\text{Lim } \{\underline{\omega} \rightarrow 0, \text{Re}[Z(\omega)]\}$ will be the equivalent of the dc resistance for this particular process. The limiting series capacitance of a power source may be obtained by analyzing $\text{Lim } \{\underline{\omega} \rightarrow 0, -1/\omega \text{Im}[Z(\omega)]\}$. Further, the impedance function may be rearranged in terms of these limiting quantities so that they can be directly obtained from fitting the experimental impedance spectrum.

We will exemplify this approach for the finite-length diffusion case. The impedance function for this case is described in Section 2.1.3, Eq. (135) for a reflective boundary and Eq. (136) for a transmissive one. The first case corresponds to diffusion into a layer of electrolyte or active material with limited thickness, often used to analyze the impedance of battery materials. The second case applies to diffusion through a membrane, important in fuel cell analysis. Before finding the limiting resistance, we need to make sure that impedance equation is not in normalized form, for example, produces unit ohm. Considering that dE/dc is the voltage change with volumetric concentration ($\text{volt} \cdot \text{mole}/\text{m}^3$), we need to divide it by

electrode area S so that Eqs. (135) and (136) involve the total impedance in ohms. Correspondingly modified equations are given as follows:

$$Z(\omega) = \frac{dE}{dc} \cdot \frac{1}{z \cdot F \cdot S} \cdot \frac{\coth\left(\sqrt{\frac{i \cdot \omega}{D}} \cdot l^2\right)}{\sqrt{i \cdot \omega \cdot D}} \quad (6)$$

$$Z(\omega) = \frac{dE}{dc} \cdot \frac{1}{z \cdot F \cdot S} \cdot \frac{\tanh\left(\sqrt{\frac{i \cdot \omega}{D}} \cdot l^2\right)}{\sqrt{i \cdot \omega \cdot D}} \quad (7)$$

Here D is the diffusion coefficient in m^2/s , z is the charge of diffusing ions, and l is the diffusion length.

On finding the real part from Eq. (6) and taking $\text{Lim}\{\underline{\omega} \rightarrow 0, \text{Re}[Z(\omega)]\}$, we obtain the limiting resistance

$$R_d = \frac{dE}{dc} \cdot \frac{1}{D \cdot S \cdot F \cdot z} \cdot \frac{1}{3} \quad (8)$$

The imaginary part of the impedance approaches infinity at zero frequency since its dependence on frequency approaches that of a series capacitor. Considering that the impedance of a such a capacitor is $Z(\omega) = 1/i \cdot \omega \cdot C$ and $\text{Im}[Z(\omega)] = -1/\omega \cdot C$, we can find the capacity knowing the imaginary part of the impedance to be $C = -1/\omega \cdot \text{Im}[Z(\omega)]$. To find the limiting capacity for reflective diffusion, we use this relation at the zero-frequency limit, $C = \text{Lim}\{\underline{\omega} \rightarrow 0, -1/\omega \cdot \text{Im}[Z(\omega)]\}$, where $Z(\omega)$ is given by Eq. (6). The resulting capacity is shown as follows:

$$C_d = \frac{l \cdot S \cdot F \cdot z}{dE/dc} \quad (9)$$

Figure 4.5.1 compares the impedance spectrum of reflective finite-length diffusion with the spectrum of its limiting equivalent circuit, a limiting resistance in series with a limiting capacitance. It can be seen that these responses approach each other as the frequency decreases.

The limiting equivalent circuit may be directly applied in analysis of power source performance because for evaluation of power sources, the dc response, which corresponds to the zero-frequency limit of the impedance spectrum, is of most importance. Conversion of Eqs. (8) and (9) allows one to find the ohmic characteristics of a given power source at dc. It also allows one to obtain a close initial guess for impedance fitting of the equivalent circuit by direct observation of the impedance plot. R_d will be the value on the right side of Re-axis, and C_d is found for the lowest-frequency point using the relation previously described. The values found can be used to find D and dE/dc or used as initial guesses for fitting. Alternatively, Eq. (6) can be rearranged in terms of limiting parameters, as shown as follows:

$$Z(\omega) = \sqrt{\frac{3R_d}{Cd \cdot i \cdot \omega}} \cdot \tanh\left(\sqrt{3 \cdot R_d \cdot C_d \cdot i \cdot \omega}\right) \quad (10)$$

Fitting experimental response to an equation expressed in electrical terms has the additional advantage that the errors in all parameters have electrical units, thus allowing one to evaluate their significance when used to model a particular electrical device. This way it can be easily seen which parameter becomes poorly defined in the fit from the point of view of its effect on the overall electric response.

If a system has more than one kinetic step, for example, a charge transfer reaction is followed by diffusion, treated first by Ho *et al.* [1980], the contributions of each kinetic step can be compared if all impedance equations are expressed in terms of their limiting resistances and capacitances. In this

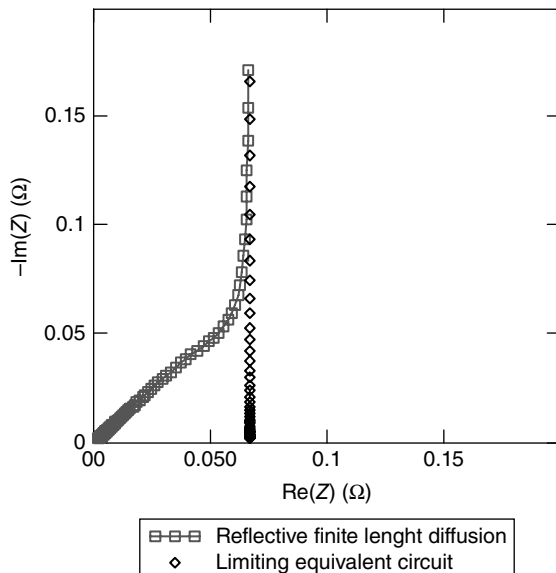


FIGURE 4.5.1 Reflective finite-length diffusion impedance spectrum.

example the equivalent circuit of a charge transfer reaction can be represented as R_{ct} in parallel with double-layer capacitance C_{dl} and its admittance as the sum of the admittances of the parallel elements. The limiting resistance of this equivalent circuit will be R_{ct} . The overall impedance of charge transfer resistance followed by diffusion is given by summing up impedances of these two serially connected equivalent circuits and considering the admittance of parallel capacitor:

$$Z(\omega) = \frac{1}{\frac{1}{R_{ct} + \sqrt{\frac{3 \cdot R_d}{C_d \cdot i \cdot \omega}} \cdot \coth(\sqrt{3 \cdot R_d \cdot C_d \cdot i \cdot \omega})} + i \cdot \omega \cdot C_{dl}} \quad (11)$$

The impedance spectrum of such a system is shown in Figure 4.5.2.

It can be seen that the semicircle due to the charge transfer on electrode–electrolyte boundary is followed by a 45° line, characteristic for diffusion, which changes to a vertical line due to the limited diffusion length and reflective boundary. The effective series resistance observed by applying dc to this circuit for a prolonged time is just a sum of R_{ct} and R_d . The relative “importance” of charge transfer and diffusion for the performance of this particular power source is simply quantified as the ratio between R_{ct} and R_d . In the previous example it is 0.1 and 0.2Ω . Thus for this case the diffusion is twice as important for the dc performance as the charge transfer. One caution about this approximation is that R_{ct} is constant only for small voltage excitations and will generally decrease at higher excitations, while R_d will remain constant. You would need to either use full nonlinear modeling of the system for given load using rate constant obtained from R_{ct} or make a correction of R_{ct} for a particular load of interest to make comparisons that are relevant for your applications.

If no parameter change is expected over the amount of passed charge, and only modeling of time-domain external voltage response is needed without attempting to analyze concentration gradients and other internal behavior, transfer function corresponding to the diffusion processes can be approximated either by large number of RC pairs in series or by more complex circuits that are chosen to be able match the $Z(\omega)$ function with minimal number of parameters. It has been shown by Tsividis and Milios [2013] that use of chain-corrected RC elements with unequal values requires drastically smaller number of elements compared with serially connected RC elements to represent accurately the same diffusion

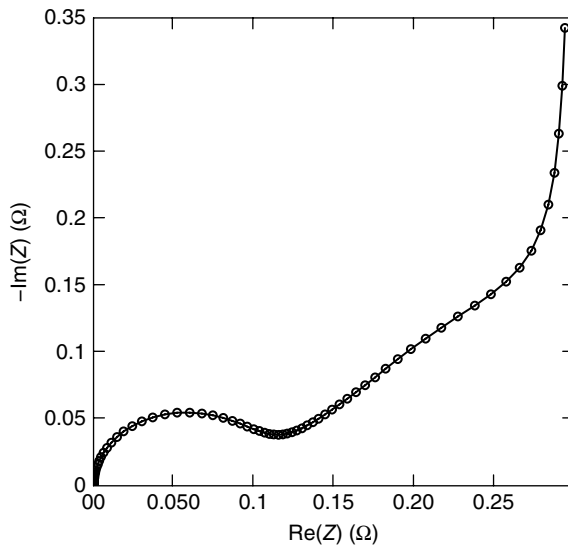


FIGURE 4.5.2 Diffusion impedance in series with surface impedance.

impedance. Note that such “transfer function match” does not allow to model the circuit when it becomes nonlinear, for example, over the range of inputs (e.g., charge) when parameters (resistors and capacitors) would become dependent on charge value. To model such systems, only circuits closely representing the true internal structure of the system, discussed in next chapter, are usable.

4.5.1.4 Discretization of Distributed Elements, Augmenting Equivalent Circuits

A description of the electrochemical kinetics of power sources requires treatment of two different kinds of processes. The first, intensive, can be thought of as localized, occurring in a specific volume negligible compared with volume of the entire system, such as charge transfer or double-layer capacitance. These processes are described by ordinary differential equations, and their equivalent circuits consist of basic building blocks representing losses and storage—resistors and capacitors. Once a system is represented as an equivalent circuit, additional complications can be easily taken into account. For example, nonlinearity can be introduced by making a resistor value dependent on current. Numerical solution for networks of nonlinear capacitors and resistors are straightforward with standard theoretical treatment and free computational tools (such as SPICE; Hageman [1993]) widely available.

Processes included in second class are extensive and so are distributed over a large volume, which can include the entire test system. Diffusion is one example of such a process. Because parameters describing such processes are different depending on position (e.g., concentration changes with distance from an electrode), two coordinates—time and space are needed for description and differential equations in partial derivatives—have to be employed. These can be analytically solved using the Laplace transform in many cases; however, sometimes only numerical solutions are possible, particularly if the system parameters are inhomogeneous or the system is nonlinear. One of the ways to obtain such numerical solutions involves subdividing the spatially distributed system into small “compartments,” each of them thought of as separate localized processes. This approach bridges the second type of systems with the first, because each of localized compartments can be represented as an equivalent circuit and the entire distributed process can be described as the response of a network of two- or three-dimensionally connected equivalent circuits of localized processes.

Section 2.1.3 shows how the process of diffusion in one dimension can be represented by a chain of resistors and capacitors, and Section 2.1.6 shows how PE can be represented by a similar network. While this approach is valid even for a distributed process with no boundary (like diffusion into infinite space),

discretization is even more important for the case where a distributed process is limited in space. In this case, a finite number of discrete elements can describe the system to arbitrary precision and can be used for numerical calculations, as treated in next chapter, even if no analytical solution is possible. Another convenience of discretizing a distributed process is the resulting ability to add additional “subprocesses” directly to the equivalent circuit rather than starting the derivation by formulating a new differential equation. For example, the equivalent network representing electric response of a pore is given in Figure 4.5.3.

Here ρ is the specific conductivity of the electrolyte in a pore (wall conductivity assumed infinite), and c is the specific capacity of the walls per unit length of the pore. Because we formulated the problem as electric network, we abstract from underlying physical meaning and seek a solution for input impedance in terms of complex specific impedances per unit length. Instead of ρ we will have the complex function $Z_{\text{trans}}(w)$, and instead of specific capacitance $c\Delta l$ we have specific surface impedance $Z_{\text{cross}}(w)$. The boundary condition at the side where a pore contacts the bulk solution can be considered as the termination impedance of the network, Z_t . For the case where parameters are constant along the length of the chain, the solution for the input impedance of a chain-connected network is found in the theory of electric networks (Zinke and Vlcek [1987]) as

$$Z(w) = Z_0(w) \cdot \frac{\frac{Z_t(w)}{Z_0(w)} - 1}{1 + \frac{Z_t(w)}{Z_0(w)} \cdot e^{-2 \cdot \gamma(w) \cdot l} + \frac{Z_0(w)}{Z_t(w)} + 1} \quad (12)$$

$$Z(w) = Z_0(w) \cdot \frac{1 - \frac{Z_0(w)}{Z_t(w)} \cdot e^{-2 \cdot \gamma(w) \cdot l}}{1 - \frac{Z_0(w)}{Z_t(w)} \cdot e^{-2 \cdot \gamma(w) \cdot l} + \frac{Z_0(w)}{Z_t(w)} + 1}$$

Here Z_0 is commonly called *the characteristic impedance* of the transmission line, and γ is its *propagation coefficient* defined as

$$Z_0 \equiv \sqrt{Z_{\text{trans}} \cdot Z_{\text{cross}}} \quad (13)$$

$$\gamma \equiv \sqrt{\frac{Z_{\text{trans}}}{Z_{\text{cross}}}}$$

For the case where parameters are changing along the chain, impedance does not have an analytical solution; however, approximate solution using a finite number of discrete elements can be obtained for arbitrary inhomogeneous chain network as described in Barsoukov [1996], p. 57.

In the case of homogeneous parameters and infinite terminating impedance (when pores are terminated by a wall), or when it is zero, as in the case of conduction through a membrane, this bulky equation reduces to simple and familiar equations. Note that these equations for conduction through a porous layer are mathematically identical to those for diffusion, given in Section 2.1.3.1:

$$Z(w) = Z_0 \cdot \coth(l \cdot \gamma \cdot (w)) \quad (14)$$

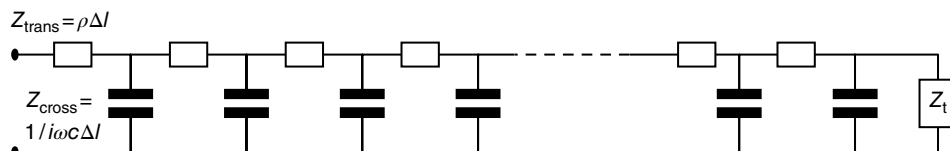


FIGURE 4.5.3 Discretization of a transmission line model of a porous electrode or diffusion process.

$$Z(w) = Z_0 \cdot \tanh(l \cdot \gamma \cdot (w)) \quad (15)$$

Formulating the problem in a discretized way allows us to extend it effortlessly to more complicated cases. Let us assume, for example, that in addition to double-layer capacitance, we will have an electrochemical reaction on the pore surface, as would be the case in a battery or fuel cell electrode. The equivalent circuit for the pore surface now will involve a capacitor in parallel with a charge transfer resistance, R_{ct} ; and the surface impedance Z_{cross} will be given as follows:

$$Z_{cross} = \frac{1}{(1/R_{ct}) + C \cdot \omega \cdot Ii} \quad (16)$$

To obtain the impedance of a PE with a reaction on its surface, we only need to substitute the aforementioned expression into Eq. (14). This relation will then be valid only at higher frequencies where diffusion can be neglected.

To extend the validity to lower frequencies, we can consider solid-state diffusion of reacted species into the bulk of the particles of the active material. The length of the diffusion path into a particle will be limited by the particle size, and finite-length reflective Warburg impedance can be used for its description. We simply need to add a finite-length Warburg impedance to R_{ct} in Eq. (16) to obtain the impedance of pore surface Z_{cross} , which was earlier derived in Eq. (11). Again, to obtain impedance for a PE with reaction and diffusion on the pore surface, we just need to substitute a new Z_{cross} into Eq. (14). This convenient approach of augmenting equivalent circuits with increasing complexity has been successfully applied to the analysis of conducting polymers (Fletcher [1992], Paasch *et al.* [1993], Popkirov *et al.* [1997]) but is also applicable for batteries (Barsoukov *et al.* [1998, 1999a]) and supercapacitors (Conway and Pell [2002]).

4.5.1.5 Nonlinear Time-Domain Modeling of Power Sources Based on Impedance Models

In Section 4.5.1.2 we discussed time-domain modeling based on an equivalent circuit used in impedance analysis. However, this is only possible for the case of small excitations, where all parameters can be assumed independent of the magnitude of the excitation (system is linear).

This is generally not the case over the operational range of power sources, for example, in the course of gradual discharge of a battery from full to empty, its impedance spectrum is changing significantly as shown in Figure 4.5.4 based on data from Barsoukov *et al.* [1999b].

Because of such large changes, any linear model would fail to describe the entire discharge process. The same conclusion applies in a lesser degree to supercapacitors, whose operational range of voltages is much smaller but still enough to cause significant change of electrochemical properties.

Another type of nonlinearity is dependence on load. Battery impedance has contributions from unrelated processes, which are affected by load in a different ways. Copper and aluminum current collectors give purely ohmic contribution, which is not affected by load except through temperature effect. The charge transfer resistance of the electrochemical reaction is governed by BV equation, which predicts linearity of voltage-current dependence only within a voltage change below 20 mV. If we map this excitation to a load typically experienced by notebook or cell phone type Li-ion battery, it corresponds to loads below 1/50C rate (means battery is fully discharged in 50 h). Normally these batteries operate at much higher rates of 1/10 and above. This means that the charge transfer resistance contribution will be rapidly decreasing as we go from extremely low rate where it is linear to the rates of interest, which is indeed observed. As can be seen in Figure 4.5.5b, with increasing rate of discharge from C/100, effective resistance quickly drops but stabilizes around C/10 and stays almost unchanged until C/2. Note that charge transfer resistance contribution is much higher in the phase transition regions, which can be used for phase detection in multiphase intercalation materials such as graphite.

The diffusion in the bulk of the particles remains largely a linear process during the entire range of excitation of interest from 50 to 1 h rate. The same is true to the contribution of the ionic resistance of electrolyte in the pores. The magnitude of these two effects is much larger than contribution of R_{ct}

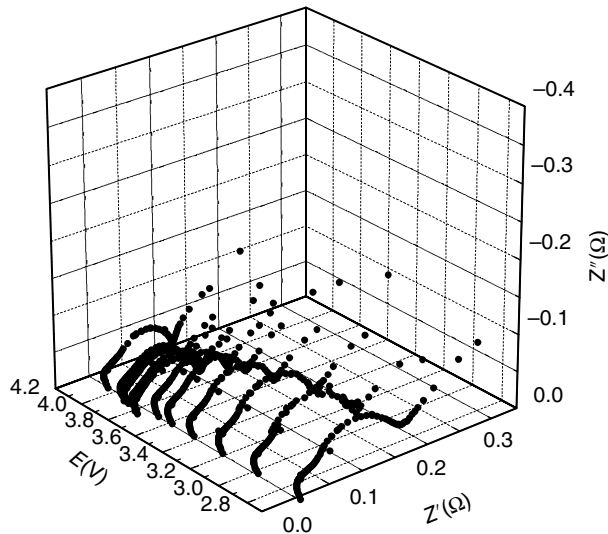


FIGURE 4.5.4 Impedance spectra of Sony 18650 Li-ion battery dependent on open-circuit voltage. Spectra are from 1 kHz to 1 mHz (frequency decreases from left to right).

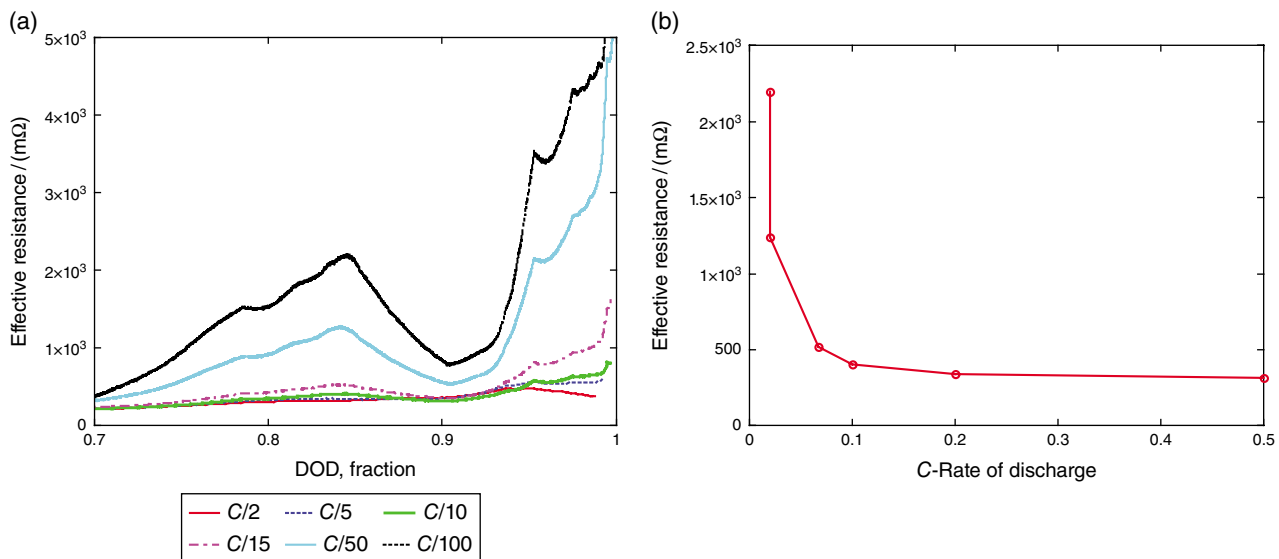


FIGURE 4.5.5 (a) Effective resistance of Li-ion battery measured by comparing voltage under different C-rate discharge loads with open-circuit voltage at given depth of discharge (DOD). Results are presented for C-rates from C/100 to C/2 and DOD range from 0.7 to 1 C rate means full discharge in 1 h. Resistance is normalized to 0°C temperature (b) R versus C rate at DOD of one of the graphite phase transitions (DOD = 0.85).

(i.e., quickly decreasing with rate) already at rates of $1/10C$ rate and higher. This creates a paradoxal but fortunat situation that overall impedance stays most constant in the range between $1/10$ rate and $1C$ rate, which is most commonly used in these battery applications, even though it is the region where R_{ct} contribution is completely nonlinear, just because this contribution basically disappears compared with diffusion and electrolyte resistance contributions. As you can see, the linearity of the overall response in particular rate region is strongly dependent on battery chemistry, and so considerations

in one particular chemistry cannot be extrapolated to other. For example, in lead–acid battery case, the response is highly nonlinear in the range of discharge rates common in actual applications (Mauracher and Karden [1997]).

Yet another type of nonlinearity observed in distributed system is due to the differences of the material state dependent on the distance from electrode. This occurs at high discharge rates in rechargeable batteries and results in “material blocking” or “starvation” of charge carriers. Areas near to electrode have higher “states of discharge” than less accessible areas, resulting in decrease of conductivity and increase of diffusion hindrance in these areas, thus preventing still available material from reacting. This inhomogeneity effect makes the apparent battery impedance at high discharge rate increase compared with lower rates. Note that BV and “blocking” effects change apparent impedance in opposite directions, so only complete nonlinear modeling can indicate which one will prevail in a particular material at a particular rate.

Fortunately, the formulation of an electrochemical model as a discretized equivalent circuit allows one to perform nonlinear modeling considering all this factors. Resistances and capacitances have to be made dependent on the SOC of the battery as well as other factors that can influence it, such as discharge rate and temperature. The dependence of parameters on the charge state can be obtained by fitting multiple impedance spectra measured at different SOC. Because “state of charge” is not an electric quantity that can be used in simulation of electric circuit behavior, parameter change can be represented as a function of open-circuit voltage instead. Open-circuit voltage is itself one of the simulation parameters and corresponds to the voltage at the largest series capacitor in a particular “chain” of the distributed circuit. In the case of a simple system with the equivalent circuit shown in Figure 4.5.3, the nonlinear circuit for time-domain modeling, where the number of discrete elements is chosen as $N = 8$, is given in Figure 4.5.6.

Here functions $R(v)$ and $C(v)$ can be obtained by piecewise linear interpolation of the dependence of R and C parameters obtained by fitting the experimental spectra at different voltages (such as in Figure 4.5.4) to the impedance function in Eq. (10). Any other suitable smooth interpolation can be used. The impedance function has to be expressed in terms of electric parameters, as described in Section 4.5.1.3. In discretized equivalent circuit, the values obtained from the fit have to be divided or multiplied by the number of chains, depending on series or parallel position of the electric element. So, for series resistors it has to be divided, and for parallel, multiplied. It should be considered that the low-frequency limit of $\text{Re}(Z)$, used as a fitting parameter in the equation, is not always a simple sum of the discrete elements that constitute a transmission line. In particular, in Eq. (10) the R_d is $1/3$ of the specific resistance multiplied by the transmission line length, as can be seen from Eq. (8). Therefore resistance of single chain will be $R_d \times 3/N$.

$V1\text{--}V8$ are voltages at the nodes with the given number. Note that this nonlinear equivalent circuit covers two types of nonlinearity—the one due to changing SOC (as voltage reflects SOC) and the one due to inhomogeneity—because SOC for calculation of parameters in each chain is not assumed to be the same everywhere along the transmission line, but is calculated at every node as a result of simulation. The nonlinearity due to the BV type of relation can also be introduced as, for example, dependence of R_{ct} value on voltage drop across it, shown in Eq. (17):

$$R_{ct}(V_{R_{ct}}) = \frac{V_{R_{ct}} \cdot R_{ct}}{K \cdot \left[e^{\frac{\beta \cdot V_{R_{ct}}}{K}} - e^{-(1-\beta) \cdot \frac{V_{R_{ct}}}{K}} \right]} \quad (17)$$

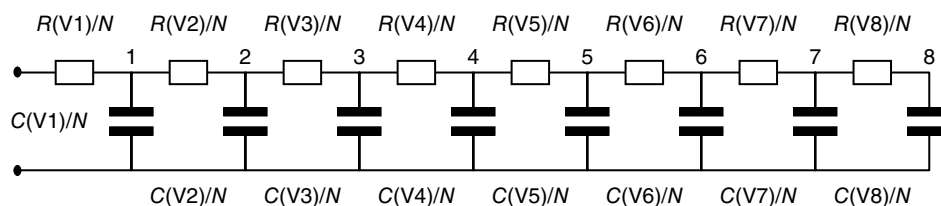


FIGURE 4.5.6 Discretized transmission line for nonlinear time-domain simulation.

Here $V_{R_{ct}}$ is the voltage across resistor, R_{ct} is the linearized value obtained from the fit of impedance spectra, K is RT/F , and β is the transfer coefficient, which can be assumed to have a value of 0.5. A more exact treatment allows one to derive a similar relationship using the Frumkin isotherm (Levi and Aurbach [1999]).

Methods to calculate time-dependent current–voltage response for circuits whose parameters depend on voltage or current are well developed in theoretical electronics, and free open-source tools for numerical calculations are available, such as general electronic circuit simulator SPICE (Hageman [1993]).

It is important to recognize that the aforementioned technique can only be used if actual physical model of the system is closely represented by the equivalent circuit used for nonlinear model. For correct nonlinear modeling it is *not enough if the impedance spectrum is closely fit by the circuit*. The set of circuits that is capable to create identical $Z(s)$ function is much larger than the set of nonlinear circuits that will produce an identical $V(t,I)$ behavior, because the values of the circuit elements (such as resistors and capacitors) depend on the voltages and currents at *each of these elements and not just the terminal voltage of the circuit as a whole*, and these in turn are dependent on the structure of the circuit.

4.5.1.6 Special Kinds of Impedance Measurement Possible with Power Sources: Passive Load Excitation and Load Interrupt

Impedance measurement techniques for most electrochemical systems are covered in detail in Chapter 3. One specific aspect of measurement on power sources arises from the special importance of low frequencies down to 1 mHz. Because of the very long time needed to collect each single low-frequency point, the system might change significantly in the course of measurement if frequencies are measured sequentially. Spectrum measurement time can be shortened up to order of magnitude by applying all frequencies of interest simultaneously and analyzing system response by FFT (Popkirov and Schindler [1992]). As an added bonus, nonlinearity of the response can be detected if additional frequencies appear in the response spectrum (Popkirov and Schindler [1994]). It is also possible to qualitatively discriminate between nonlinear, nonstationary, and noncausal distortions by analyzing response to wideband excitation signal as shown by Schoukens *et al.* [2001]. Another problem of impedance measurement on power sources is associated with using an external energy source to excite a voltage or current response of the system. Because electrochemical power sources are usually of very low resistance and always have voltage bias, an external power source needs quite a high power capability to achieve a response with an acceptable signal-to-noise ratio. For large power sources, such as cranking lead–acid batteries, there are few commercially available potentiostats/galvanostats available to support the needed excitation power. Fortunately, electrochemical power sources offer a unique opportunity to simplify the test setup, because they are energy sources themselves. Their impedance can be revealed by applying a varying load across their terminals and observing the transient voltage change. When the load variation is periodic, impedance can be found as $Z(w) = V^*(w)/I^*(w)$ where V^* and I^* are Fourier transforms of measured current and voltage. If excitation is nonperiodic, impedance can be found as $Z(s) = V(s)/I(s)$ where V and I are Laplace transforms of voltage and current, and only the imaginary part of s is substituted into the equation. There can be many different variations of this approach, reviewed in particular in Barsoukov *et al.* [2002]. In many cases, current measurement is not needed, as the applied load is known, so a test setup may consist of a digital voltmeter with data logging capability at a high rate and a low-pass filter set to $1/2$ of the sampling frequency.

The simplest method is “constant load.” It is accomplished by instantaneously connecting the terminals of a power source resting at a voltage V_0 to a resistor with a resistance value R , which will cause approximately a 20–40 mV voltage drop across the power source. The resistor should have a low thermal coefficient (such as constantan based) and appropriate power rating and cooling so that no extensive heating occurs. Voltage has to be sampled with a sampling interval at least twice shorter than the inverse of the maximum frequency, and the duration of sampling should be more or equal to the inverse of the minimum frequency needed to be measured (Nyquist theorem). Sampling points need not be equidistant in time. To save memory and even improve noise rejection, sampling with a logarithmically

increasing time between samples can be used. It is also necessary to use low-pass filtering at the frequency equal to half of the inverse of sampling interval to prevent aliasing.

To obtain impedance spectra, acquired arrays $v[i]$, $t[i]$ are used to estimate parameters of a differentiable interpolation function $v(t)$. These parameter values are then substituted into Laplace transform of this function, $V(s)$. To achieve maximum possible noise rejection, it is useful to employ a physically meaningful interpolation function for the particular system under test and to fit $v[i]$, $t[i]$ data to function to find its parameters. Most electric systems such function would be a sum of exponentials, proposed to use in such conversion by Macdonald [1993]. In this case $v(t)$ and its Laplace transform $V(s)$ are shown as follows:

$$v(t) = \sum_{i=0}^n k_i \cdot e^{\frac{-t}{\tau_i}} \quad (18)$$

$$v(s) = \sum_{i=0}^n \frac{k_i}{s + \frac{1}{\tau_i}} \quad (19)$$

The use of differentiable smoothing splines or even linear piecewise interpolation in conjunction with some noise-reduction method can also be practical if the nature of the system is not known. Once parameters of $V(s)$ are found by a fit of data to $v(t)$, the impedance spectrum in the frequency range defined by the sampling interval and duration of sampling can be obtained using Eq. (20). Fit can be performed either by linear regression with fixed values of time constants τ_i (e.g., logarithmically distributed from duration of sampling step to the duration of sampling period) or using nonlinear fit where both number and values of time constants are optimized to achieve statistically best description of data (Provencher [1976]):

$$Z(s) = \frac{V_0}{s} \cdot \frac{R}{V(s)} - R \quad (20)$$

Another similar method suitable for power sources testing is based on “current interrupt.” If the load is applied for long time, so that it can be assumed that system under test has stabilized and no longer changes in the time interval similar to needed measurement duration, the load is disconnected and sampling starts in the instant of disconnection. Acquired data values $v[i]$, $t[i]$ are again used in a fit to a selected carrier function $v(t)$ to obtain its parameters, which are then substituted into the equation of this function’s Laplace transform to obtain $V(s)$. The impedance function is then obtained as shown as follows:

$$Z(s) = \frac{s}{I} \cdot V(s) + \frac{1}{s \cdot C_{ser}} + R_{ser} \quad (21)$$

This method has the disadvantage that load application time prior to measurement is fixed. This can be inconvenient if a measurement has to be performed in a particular instant of time based on some other criteria, for example, we might want to limit maximum voltage drop between two measurements during the battery discharge. Variation of this method allows one to use excitation periods of arbitrary length, even much shorter ones than the subsequent sampling period during relaxation. Equation (19) should be modified in this case to correct for arbitrary excitation length pulse t_{pulse} as shown in Eq. (22) and then substituted into Eq. (21) to find the impedance

$$V(s) = \sum_{i=0}^n k_i \left/ \left(s + \frac{I}{\tau_i} \right) \cdot \left(e^{\frac{t_{pulse}}{\tau_i}} - 1 \right) \right. \quad (22)$$

For this method it is preferable to use an electronic load with constant current rather than a resistive load to make sure that current is unchanged during excitation pulse.

Note that the transient voltage curve after termination of discharge is not affected by serial capacitance and serial resistance. So these values have to be determined from other data. Serial capacitance C_{ser} can be determined from the voltage slope immediately prior to measurement as $I/dV/dt$ if discharge was much longer than the measurement time constant to reach saturation. For the case of short discharge pulse, open-circuit voltage before and after pulse/relaxation can be used as $C_{\text{ser}} = Q/dV$.

R_{ser} can be determined using last point of the discharge, V_{last} , as given in Eq. (23):

$$R_{\text{ser}} = \frac{V_{\text{last}}}{I} + \sum_{i=0}^n \left(k_i \cdot e^{-\frac{t_{\text{pulse}}}{\tau_i}} - k_i \right) - \frac{t_{\text{pulse}}}{C_{\text{ser}}} \quad (23)$$

4.5.2 Batteries

4.5.2.1 Generic Approach to Battery Impedance Modeling

Despite the large variety of existing battery chemistries, the basic design of batteries shares several common elements. All batteries have PE consisting particles of energy storing material and conductive additive hold together by polymeric binder. They also include an electrolyte and a separator preventing electric contact between opposite electrodes. Instead of focusing on particular chemical compositions, a general approach to battery kinetics can be based on analyzing the impedance of the aforementioned common components. This not only allows one to create a working kinetic model of the battery as a whole but also allows the evaluation of the effect of each component on material power capability and even comparison between different chemistries.

Figure 4.5.7 shows the kinetic steps that are common for most batteries, originally proposed for the Li-ion battery in Barsoukov *et al.* [2000]. These include (from the right) electronic conduction through the particles and ionic conduction through the electrolyte in cavities between particles. On the surface of each particle, charge transfer involves the resistance of an insulating layer and activated electron transfer resistance on the electronic-ionic conduction boundary. Further, ions have to diffuse into the bulk of particles via solid-state diffusion. Other subsequent processes such as the formation of new crystalline structures can also become limiting kinetic steps at frequencies below 1 mHz. Not indicated on the figure are conduction through the electrolyte and porous separator and conduction through wires, which both dominate high-frequency behavior above 10 kHz. The inductance of wires and electrode winding becomes a factor at even higher frequencies. In subsequent sections we will have a closer look at the impedance of all these components.

Impedance of Electrolyte and Membrane. The theoretical background of IS applied to liquid and solid electrolytes is covered in detail in Sections 2.1.2 and 2.1.3. In order to achieve high conductivity, batteries always use a large excess of conductive salts in liquid electrolytes. This allows them to be classified as “supported electrolytes” and to apply to them a simplified theoretical approach that assumes an absence of electric field in the bulk electrolyte and disregards the migration term in Eq. (78) of that chapter. In practice this means that we have to consider only the diffusion contribution to electrolyte impedance, while conduction and relaxation effects of bulk electrolyte are shifted to the high-frequency region and therefore appear as a series resistance contribution in impedance measurements in practical batteries. In order to measure electrolyte conduction and relaxation impedance excluding electrode effects, the four-electrode arrangement can be used, where two RE are placed in close proximity to two other electrodes that are unable to exchange ions with the electrolyte (such as Pt) in order to exclude diffusion contributions. Voltage response should then be measured differentially between the RE.

In the case of solid electrolytes, which are currently being tested but have not yet been used in commercial batteries, the situation is more complicated as they cannot be treated as being supported, and all relaxation, migration, and diffusion effects can overlap in the same frequency region. See Section 2.1.3 for the treatment of this case.

The diffusion impedance of a bulk electrolyte can be described by a finite-length Warburg impedance with transmissive boundary [Eq. (7)]. A transmissive boundary is appropriate because an ion

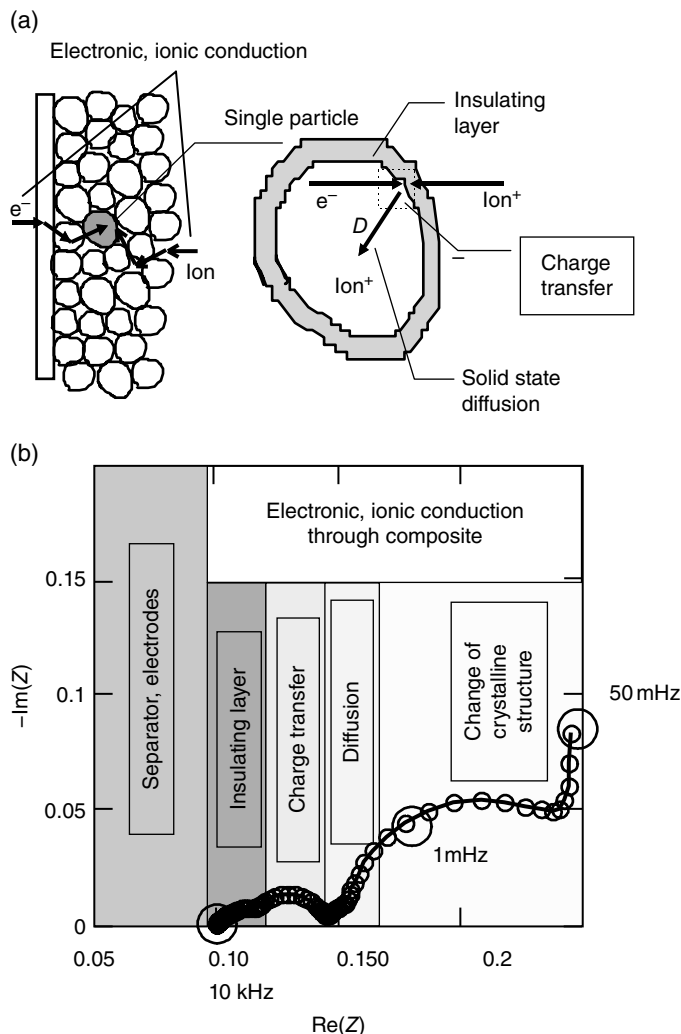


FIGURE 4.5.7 (a) Kinetic steps common in most batteries.
(b) Typical impedance spectra of intercalation material.

produced at the cathode is consumed at the anode and vice versa during battery electrochemical processes. A more precise treatment using Eq. (12) is one where electrodes and diffusion in the electrolyte between electrodes are represented by means of an ion-producing electrode in series with a transmission line, terminated with an electrode that consumes diffusing ions. In this case, the terminating impedance Z_t will be the impedance of this electrode. An alternative treatment of diffusion with imperfect boundary conditions is given in Franceschetti *et al.* [1991].

However because of the high concentration of the ions taking part in a charge/discharge reaction and the very thin electrolyte layer used in practical batteries, this impedance is negligible for most liquid electrolytes applied in practice, and its influence will only appear in the high-frequency region, or most commonly, as a *series resistance contribution*. On the other hand, in the case of gel electrolytes, the Warburg impedance of the electrolyte layer can be well resolved, especially if a thicker layer of electrolyte is used for research purposes (Qian *et al.* [2002]). The impedance spectrum of polymer and gel electrolytes appears as a depressed semicircle. Typical analysis of the spectrum in order to determine specific conductivity is given in Section 2.1.2.3, as devised by Cole and Cole [1941].

An important contribution of the electrolyte to overall battery impedance is that associated with electrolyte in the pores of the active material. Because the cross section of pores is much less than the

geometric dimensions of electrodes, even high-conductivity electrolyte leads to considerable resistance along the pores. Pores also have a significant surface capacitance, which makes the effect of the impedance of the electrolyte in pores appear over a wide frequency range. This effect will be discussed in detail in the section on PE.

Impedance of the Particle Surface. Electrochemical reactions, formation of a double layer, and adsorption all contribute to the particle surface impedance. Adsorbed species can diffuse inside the bulk of battery active material except for the case of metal anodes. Because of this, the impedance of the particle surface will involve a Warburg impedance element rather than a simple capacitor to represent adsorption (a model for metals can, however, use a capacitor instead of Z_w). The Randles [1947] equivalent circuit in Figure 4.5.8 encompasses all these steps. Note that in batteries active materials are not dissolved in the electrolyte, but are typically solid; therefore Z_w involves solid-state diffusion, as proposed by Ho *et al.* [1980], in contrast to diffusion in electrolyte originally discussed by Randles. The diffusion component will be discussed more in a later section on this subject.

On the surface of Li-ion anodes, the formation of an ionically conductive passivating layer, or SEI, has been observed (E. Peled [1983]). Other battery electrodes can also build up similar inactive layers due to different degradation reactions. Passivating layers, apart from their critical importance for preventing irreversible reactions in the battery, have measurable effects on the discharge kinetics and therefore can be analyzed by IS. The growth of such layers has been investigated by Barsoukov *et al.* [1998]. A simple model, treating surface impedance as the equivalent circuit in Figure 4.5.9, allowed the estimation of the dielectric constant, thickness, and ionic resistance of the layer.

In order to evaluate specific electrochemical characteristics, such as exchange current density $i_0 = R \cdot T / n \cdot F \cdot R_{ct} \cdot S$, estimation of the particles' surface area S is necessary. Note that the experimental estimation of the surface boundary between electronically and ionically conductive media in a composite material consisting of multiple particles has not been successful to date. BET surface area estimation usually tends to severely overestimate this surface area. It correlates well with irreversible capacity loss during first intercalation (Iijima *et al.* [1995]) but not with the surface impedance of materials (Aurbach *et al.*

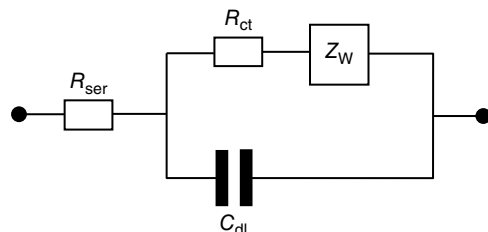


FIGURE 4.5.8 Randles equivalent circuit.

R_{ser} represents the series resistance, R_{ct} the charge transfer resistance of the electrochemical reaction, and Z_w solid-state diffusion and other subsequent reactions.

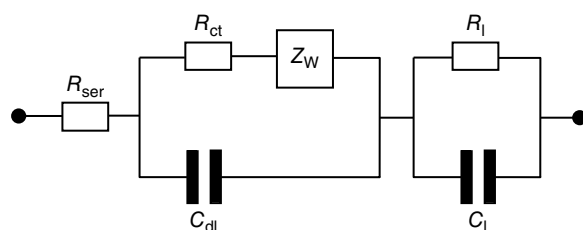


FIGURE 4.5.9 Equivalent circuit of particle surface impedance taking into account a passivating layer.

[2001]), which indicates that loosely electrically connected microparticles make a major contribution to BET surface area but not to the electrochemically active area. In order to estimate only the area that is electrically accessible and also to use the same value of S for both diffusion and surface kinetics, it is common to use a summary geometric area of the particles of the active material as an estimate for surface area. See further details in the section “Bringing It All Together.”

Diffusion. While an electron transfer reaction only occurs on a particle surface, most of the electrochemically active material resides in the bulk of the particles. Many electrochemically active substances are not suitable as battery materials, despite their promising specific capacity and voltage, because their crystals are too dense and so only the surface is active. An open crystalline structure, allowing ions to enter and leave the crystal, is a common characteristic of materials used in most modern batteries. Different from primary battery materials, such as MnO_2 , rechargeable battery materials should also be able to maintain and protect their crystalline structure from a change to dense form (collapse) and from dissolution. Cathode material in a Ni–Cd battery, both anode and cathode in Ni–MH and Li-ion one, follows this principle. The process of ion movement inside the crystals is controlled by solid-state diffusion. The aforementioned considerations make quantitative characterization of this process critical for determining suitability and improving the kinetics of battery materials.

Ions diffuse toward the center of particles; therefore their diffusion path is limited, for example, the boundary condition is reflective. Impedance analysis of the finite-length diffusion for different electrode geometries and boundary conditions is summarized by Jacobsen and West [1995]. Particle geometries occurring in battery materials are thin plate (planar), spherical, and cylindrical. The following are given equations for corresponding geometries, modified so that parameters are expressed in electrical terms:

For planar geometry, see Eq. (10).

For spherical geometry,

$$Z(s) = \frac{\tanh(\sqrt{3 \cdot C_d \cdot R_d \cdot s})}{\sqrt{\frac{3 \cdot C_d \cdot s}{R_d} - \frac{1}{R}} \cdot \tanh(\sqrt{3 \cdot C_d \cdot R_d \cdot s})} \quad (24)$$

Transformation from electrical unit parameters to electrochemical ones is given as

$$\frac{dE}{dc} = \frac{F \cdot n}{C_d} \cdot \frac{4}{3} \cdot \pi \cdot r^3 \quad D = \frac{r^2}{3 \cdot C_d \cdot R_d} \quad (25)$$

For cylindrical geometry,

$$Z(s) = \frac{I_0(\sqrt{2 \cdot R_d \cdot C_d \cdot s})}{(\sqrt{2 \cdot R_d \cdot C_d \cdot s}) \cdot I_1(\sqrt{2 \cdot R_d \cdot C_d \cdot s})} \cdot R_d \quad (26)$$

Here $I_0(x)$ and $I_1(x)$ are Bessel functions of the first kind, with 0 and 1 order correspondingly. Transformation from electrical unit parameters to electrochemical ones is given for this case as

$$\frac{dE}{dc} = \frac{F \cdot n \cdot \pi \cdot r^2 \cdot h}{C_d} \quad D = \frac{r^2}{2 \cdot C_d \cdot R_d} \quad (27)$$

Here r is the radius and h the length of the cylindrical rod. Equations (10) and (24)–(26) describe the impedance of a single particle. Obviously, a composite electrode consists of a huge number of such particles that are not in parallel or in series in the electrical sense, but are distributed as a chain network along the thickness of the composite. The way that impedances of single particles are combined into impedance of a whole electrode will be described in section “Bringing It All Together.”

Diffusion in solid-state materials when the activities of diffusing species are not concentration independent does not follow Fick’s law. The diffusion coefficient has to be modified by a *thermodynamic*

enhancement factor taking into account the activity change with concentration to bring the diffusion equation to semi-Fick's form. The modified diffusion coefficient, $D_c = D_0 L$, is called the *chemical diffusion coefficient* and L is the *enhancement factor* (see details in Section 2.1.3.2). All solid-state diffusion coefficients treated in this chapter are chemical diffusion coefficients even if not explicitly stated.

The dE/dc dependence on SOC of battery materials is also significantly different from Nernstian but is often well described by the Frumkin isotherm, which takes into account attractive or repulsive interactions of adsorbed species, as reviewed by Levi and Aurbach [1999]. The actual dE/dc in the case of any particular material can be obtained by discharge/relaxation experiments, and knowledge of its value can significantly assist quantitative analysis of impedance spectra, as will be shown in the section on battery-specific improvement in impedance spectra fitting.

It is important to note that even if the experimental dE/dc dependence is used in Eqs. (11) and (21)–(25), the estimated diffusion coefficient will still be the *chemical diffusion coefficient*. However, Levi and Aurbach [1999] have shown that analysis of experimental dE/dX (where X is degree of occupation of intercalation sites) allows one to obtain a concentration-independent diffusion coefficient through calculation of the enhancement factor explicitly, as shown as follows:

$$L = \frac{e}{k \cdot T} \cdot X \cdot \frac{dE}{dX} \quad (28)$$

or, in terms of the Frumkin isotherm,

$$L = \frac{1 + g \cdot (1 - X) \cdot X}{1 - X} \quad (29)$$

Here g is the measure of interaction between intercalation sites in the Frumkin isotherm, and X is the degree of occupation of intercalation sites. X can be expressed from the charge Q passed during intercalation as $X = Q/Q_{\max}$, where Q_{\max} is the maximum charge stored by the particular intercalation phase. In many cases, such as intercalation into graphite, multiple phases are present, and therefore the entire intercalation region must be subdivided into subregions for analysis.

Other deviations from Fick's diffusion relationships can be caused by the kinetics of new phase formation, which appears as a secondary reaction reducing the concentration of the diffusing specie. This effect not only alters the apparent diffusion coefficient but also actually changes the shape of the impedance spectrum, introducing deviation from $\sqrt{\omega}$ dependence at low frequencies below 1 mHz. The impedance spectra of Li-ion intercalation anodes exhibiting this effect were analyzed by Barsoukov *et al.* [2000]. It is convenient to express the needed modification of the impedance equations at the equivalent circuit level, as in Figure 4.5.3. In parallel with a diffusion pseudocapacitance, C_d^* , we can add a resistor R_p in series with the capacitor C_p , which represents an additional activated-concentration-reducing process due to new phase formation along the diffusion patch. This will modify Eqs. (11), (21), and (25) so that the diffusion pseudocapacitor admittance $C_d^* s$ is replaced by the admittance of the new parallel circuit, $1/(R_p + 1/C_p^* s) + C_d^* s$, for example, for planar diffusion:

$$Z(s) = \sqrt{\frac{R_d}{1/(R_p + 1/(C_p^* s)) + C_d^* s}} \cdot \tanh \left[\sqrt{R_d \cdot \left(1 / \left(R_p + \frac{1}{C_p^* s} \right) + C_d^* s \right)} \right] \quad (30)$$

A detailed treatment for spherical particles of cathode intercalation material is given by Barsoukov *et al.* [2003].

Porous Electrode. Most battery electrodes comprise an open structure consisting of small particles compressed together, as shown in Figure 4.5.7. This structure does not have well-defined pores (such as cylindrical) but rather an irregular network of interconnected space between particles filled with electrolyte. The absence of well-defined pores complicates ab initio deduction of electrolyte impedance; however the frequency dependence of the impedance of porous materials is well described by the ladder

network approach originally proposed by de Levie [1963] for cylindrical pores. See also Section 2.1.6 for treatment of various geometries of PE.

Different from porous metallic electrodes, where metal-particle resistance is often low and can be neglected, for battery electrodes both the electronic resistance of particles and the ionic resistances of the electrolyte in pores are important. A theoretical treatment of the impedance of PE using ladder networks with both ionic and electronic conductivity considered is given by Paasch *et al.* [1993] by direct solution of the relevant differential equations and by Fletcher [1992] using the formalism developed for chain-connected two ports. Both approaches allow one to modify the equations in order to consider arbitrary impedance functions of particle surface. Unfortunately, analysis of actual experimental data from electrode-electrolyte impedance spectra measurements by nonlinear fitting does not allow one to distinguish between contributions of the ionic and electronic components or even to estimate the two separate conductivities. The effect of the presence of the two conductivities is manifested mostly in a shift of the high-frequency limit of the impedance spectrum, where the imaginary part goes to zero. However, in an actual experimental setup, this limit (series resistance) can make an unknown contribution and obscure the effect of the two separate conductivities. A combination of electrode-electrode and electrolyte-electrolyte measurement across a PE can still allow one to measure separate conductivities (see Popkirov *et al.* [1995], Wang *et al.* [2001b]), but for the usual electrode-electrolyte setup, it is only possible to obtain a combined ionic-electronic conductivity for the PE.

Despite the inability to distinguish between ionic and electronic contributions, information about the combined specific resistance of a PE is often useful because it defines the battery impedance dependence on electrode thickness, as investigated by Barsoukov *et al.* [1999a]. Since PE resistance is a dominant contributor to the total electrode impedance, it is also critical for battery modeling, as shown by Doyle and Newman [1995]. Such information can be obtained by analyzing experimental data using a transmission line model as in Figure 4.5.3, which results in Eq. (14) when reflective boundary conditions are assumed. For a PE, Z_{trans} will represent the combined ionic and electronic specific resistance, ρ_m , and Z_{cross} will be the specific impedance of particles themselves, as defined by the charge transfer and diffusion processes described in previous chapters.

Bringing It All Together. As shown in previous chapter, the transmission line model may be used to analyze the impedance spectra of porous battery electrodes. A simple substitution of the expressions for surface and impedance diffusion discussed earlier, scaled accordingly to particle size, for Z_{cross} transforms Eq. (14) to an equation for entire battery electrode impedance. Such a complete model of battery electrode behavior, valid in the wide frequency range from 10 kHz down to 100 μ Hz, has been applied to Li-ion electrode situation by Barsoukov *et al.* [2000] for flake-type particles and in [2003] for spherical particles. The model can also be used without modification for other intercalation-type battery electrodes, particularly $\text{Ni(OH)}_2\text{O}$ cathodes used in NiMH and NiCd batteries, and metal hydride anodes. It can be applied to even more exotic cases such as slurry electrodes, because they can be seen as static PE for the duration of measurement. Detailed treatment of slurry electrode impedance using transmission line approach is given by Petek *et al.* [2016].

The equivalent circuit for this model is basically the same as that in Figure 4.5.3, except for Z_{cross} being replaced by the surface and diffusion impedance, as shown in Figure 4.5.10.

The frequency dependence of the impedance of this equivalent circuit is obtained by replacing Z_{cross} in Eq. (14) by the impedances of R_{ct} , C_{dl} , and the Z_d circuit and is given by Eq. (30):

$$Z(s) = \sqrt{\frac{R_m}{s \cdot C_{\text{dl}} + 1/(R_{\text{ct}} + Z_d)(s)}} \cdot \coth \left[\sqrt{R_m \cdot \left[s \cdot C_{\text{dl}} + \frac{1}{R_{\text{ct}} + Z_d}(s) \right]} \right] \quad (31)$$

For spherical particles, the diffusion impedance $Z_d(s)$ is given by Eq. (22). To include the kinetics of new crystalline phase formation, this equation must be modified by replacing the admittance of the pseudocapacitance of the diffusion process, $C_d \cdot s$, with the admittance of a circuit including both

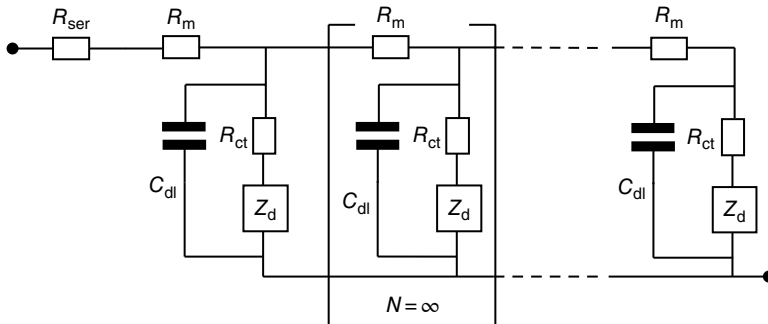


FIGURE 4.5.10 Equivalent circuit of a battery insertion electrode. Here R_m is the distributed resistance of the transmission line representing electronic and ionic resistance of the layer of active material, the charge transfer resistance and passivation layer resistance of the particle interface R_{ct} , and the double-layer capacitance C_{dl} . Z_d is the impedance of diffusion and charge storage processes inside the particles.

non-activated charge storage, C_d , and the activated charge storage due to new phase formation: C_p and R_p . This results in the following modified equation:

$$Z_d(s) = \frac{\tanh \left[\sqrt{3 \cdot R_d \left(s \cdot c_d + \frac{1}{R_p + 1/(C_p \cdot s)} \right)} \right]}{\sqrt{3 \cdot \left(s \cdot c_d + \frac{1}{R_p + 1/(C_p \cdot s)} \right) / r_d - \frac{1}{R_d} \cdot \left[\sqrt{3 \cdot \left(s \cdot c_d + \frac{1}{R_p + 1/(C_p \cdot s)} \right)} \right]}} \quad (32)$$

Experimental data and fits by the aforementioned functions (Barsoukov *et al.* [2003]) are shown in Figure 4.5.11. The spectrum of Li-intercalation cathodes has a depressed semicircle in the high-frequency region, whose size and frequency dependence are determined by R_{ct} and C_{dl} . Combined electronic and ionic resistance of the porous material R_m contributes to its “stretching” along the x -axis. In the lower-frequency region between 0.1 Hz and 1 mHz, the 45° inclination, characteristic for diffusion processes, can be seen. It then starts to approach a vertical line typical for finite-length reflective diffusion. However, this line never becomes perfectly vertical even at 200 μ Hz. It can be seen that including the kinetics of phase formation as in Eq. (31) considerably improves the fit in the low-frequency region where such kinetics significantly influence the spectrum.

Equations (31) and (32) can be used to analyze impedance spectra without knowledge of structural electrode parameters (thickness, density, etc). However, we need this information in order to transform the ohmic parameters obtained by a fit into specific electrochemical parameters. In particular, this information can be used to calculate the effective surface area of the particles. Particles used in practical batteries can usually be treated either as thin plates (Levi and Aurbach [1997]) or as pseudospherical in shape (Barsoukov *et al.* [2003]). In the following, treatment is given for the case of constant particle size since they usually have a narrow size distribution due to sieving. For more complex treatment of battery impedance spectra where wide distribution of particle sizes exists, see Huang *et al.* [2006].

Particle size values are provided by material manufacturers. The number of particles in a given volume can be estimated from the ratio of their crystallographic density of particles, σ_p , to the density of the composite-electrode film, σ . This allows one to calculate the electrochemically active surface area for a composite electrode for thin-plate particles as $S = xAd\sigma/[l\sigma_p]$ and for spherical particles as $S = 3xAd\sigma/[r\sigma_p]$. Here x is the fraction of active material in the composite, A is the geometric area of the electrode, d is

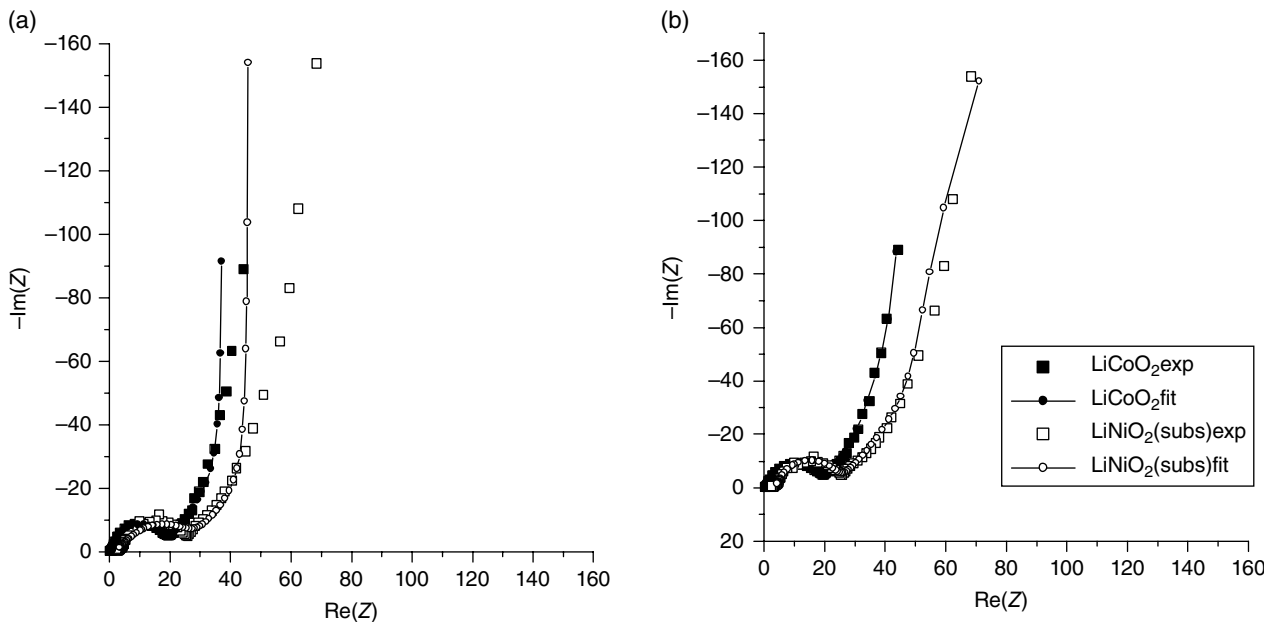


FIGURE 4.5.11 Experimental impedance spectra of Li–cobalt oxide (RC-41) and substituted Li–nickel oxide [FL-2] cathodes in the fully charged state and in the frequency range from 10 kHz to 200 μ Hz obtained by multifrequency FFT impedance measurement. Solid lines indicate the fit by Eqs. (29) and (21) (a), and the fit with inclusion of the kinetics of phase formation by Eqs. (29) and (30) is presented in part (b).

the thickness of the composite electrode, σ is the density of the composite electrode, σ_p is the true density of particles, and l and r are the thickness of the plate and radius of spherical particles, respectively.

Using knowledge of the particle area S , the charge transfer resistance, expressed as the ohmic parameter R_{ct} (Ω), can be used to obtain the specific charge resistance R_{ct}^s (Ωm^2) as $R_{ct} = R_{ct}^s/S$. Correspondingly, C_{dl} (Farad) can be transformed into the specific double-layer capacitance C_{ct}^s (Farad/ m^2) as $C_{dl} = C_{ct}^s S$. The combined ionic and electronic resistance of mesoporous material R_m (Ω) is given by $\rho d/A$ where ρ (Ωm) is the specific resistance of the active material (sum of ionic and electronic resistances), A is the geometric surface area of the electrode (m^2), and d is the thickness of the layer of active material (m).

Estimates of the diffusion parameters R_d and capacitance C_d obtained from data fitting can be used to calculate the chemical diffusion coefficient D (cm^2/s), if the particle radius is known, as $D = r^2/(3C_d R_d)$. The diffusion pseudocapacitance C_d is related to the emf relation of the material so dE/dc ($\text{volt}\cdot\text{cm}^3/\text{mole}$) can be obtained from C_d as $dE/dc = 4Fz\pi r^3 S/(3C_d)$. All these specific parameters can be used as sample-independent characteristics of a particular intercalation material and allow one to predict the change of impedance spectra (and battery performance) with changing active layer particle size or thickness (Barsoukov *et al.* [2000]).

Battery-Specific Improvements Possible in Impedance Spectra Fitting. Ultra-low-frequency (<1 mHz) behavior of batteries is of principal importance for evaluation of their performance, as batteries are mostly used in devices with constant or slightly variable load. Unfortunately, low-frequency impedance measurements take a long time and can be often distorted by system change during the measurement as well as by voltage drift inherent in the components of the measurement system. The good news is that part of the information defining the impedance spectrum at low frequencies can be obtained from dc measurement and integrated with impedance spectrum data analysis. All battery equivalent circuits discussed in the previous chapter, and particularly those defining finite-length diffusion, can be simplified at frequencies approaching zero to a limiting equivalent circuit comprising a resistor in series with capacitor (exemplified by Figure 4.5.1). Ho *et al.* [1980] have shown that the value of this limiting

capacitor at different SOC of the battery can be obtained by differentiation of the open-circuit voltage dependence on passed charge, $C_s = 1/(dE/dq)$. The $E(q)$ dependence can be obtained by discharging the battery at a very low rate, such as 1/20 C rate (full discharge in 20 h), by applying a low-rate voltage ramp, or by applying current pulses followed by relaxation periods with variable duration terminated when dV/dt is below a predefined value (1 μ V/s or less).

The capacity information obtained can be used to increase confidence in the parameters obtained by fitting a finite-length diffusion model to the impedance data measured at a given depth of discharge (DOD). For example, the capacity obtained by differentiation of the aforementioned $V(\text{DOD})$ dependence at DOD = 0 (as in Figure 4.5.12b) can be assigned to C_d in Eq. (10) and used as fixed parameter in the fit of the impedance spectrum measured at this DOD. In this case, one's confidence in the estimation of other low-frequency parameters (R_d) will be significantly increased. R_d cannot be determined at all if the frequency range of the spectrum is not sufficient to include the "bend" point from 45° to vertical dependence in the complex plot. However, when C_d information is available, R_d determination becomes possible even if only the 45° part of the spectrum is available. This approach can be repeated with C_s values at other DODs by analyzing a series of impedance spectra measured at different discharge levels of the battery.

Knowledge of the limiting capacitance is useful also in the analysis of more complex models, where several capacitive elements occur in parallel (such as in Eq. (31)). At the zero-frequency limit, this circuit will be simplified to one series resistor and a series capacitor, which will be a sum of all parallel capacitors that have no resistors in parallel with them. In this case the sum of all parallel capacitive elements can be fixed in the fit as equal to C_s , again reducing the degrees of freedom of the fit and improving the estimated standard deviations of all the parameters. An obvious way to do this would be to define one parallel capacitance through another as $C_1 = C_s - C_2$, and fit only C_2 . However, the previous definition can result in C_1 becoming negative although an impedance fitting program such as LEVM allows restricting the fit parameters to physically meaningful positive values. A better method of estimating the summary capacitance is that of fitting the ratio between the parameters ($r = C_1/C_2$) while expressing the parameters themselves as $C_1 = C_s r / (1 + r)$ and $C_2 = C_s / (1 + r)$. This way, both C_1 and C_2 are guaranteed to remain positive with their sum equal to C_s . The same method can be used to limit the sum of any number of parallel capacitances. This approach to analyze impedance spectra in conjunction with

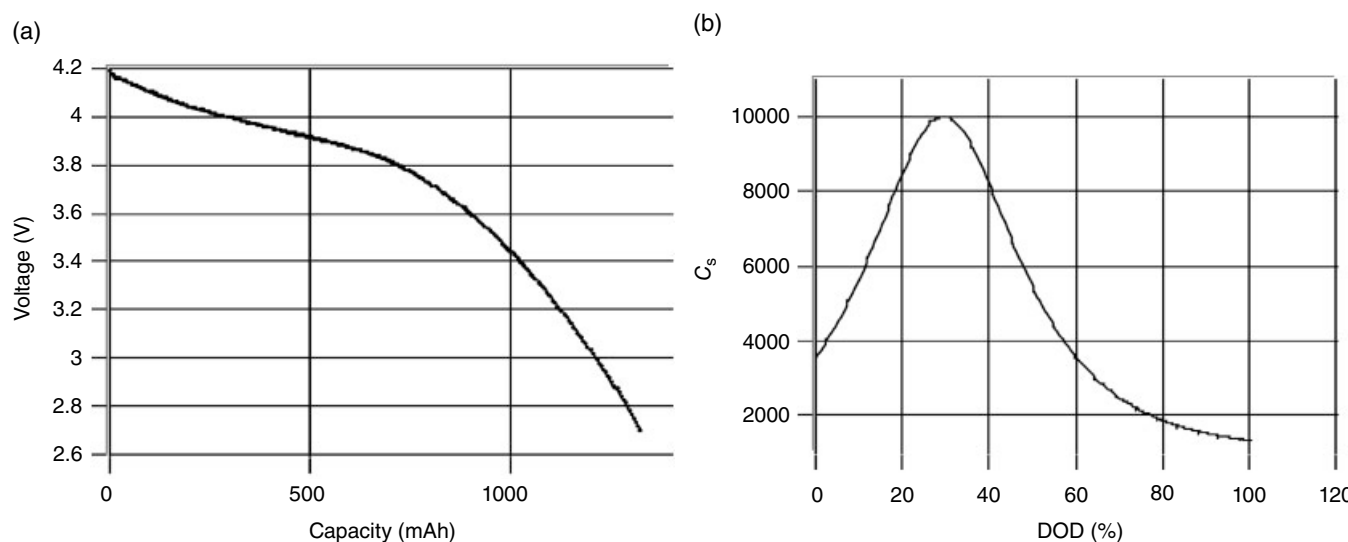


FIGURE 4.5.12 (a) Voltage dependence on discharge capacity of Sony Li-ion battery. (b) Limiting capacitance, C_s (Farad), calculated by differentiation the dependence in (a) versus depth of discharge (DOD).

open-circuit voltage curve has been implemented in impedance analysis software MEISP (Kumho Petrochemical Inc. [2002]).

Parameter Correlation for Quality Control, State, and Health Monitoring. Apart from using IS to analyze specific kinetic properties of battery materials, it can be used to evaluate certain aggregate behavioral properties of a battery such as SOC, degree of degradation, and production faults. Once a wide-frequency-range impedance spectrum is analyzed in the boundaries of the relevant model, it provides a set of parameter estimates that reflect all aspects of battery operation. In the ideal case where the model captures all aspects of the impedance spectra, the set of model parameter values represents the optimum data compression and noise reduction possible for the spectral data. For this reason it is much better to use parameters of the model rather than raw impedance data for correlation with target properties.

Then since battery kinetics is fully determined by the estimated parameters, in most cases some of these parameters would have significant correlation with a particular property of the battery we are interested in. It is sometimes possible to decide which parameter would be likely to have the best correlation with a particular property based on *a priori* knowledge of the mechanism of that particular property. For example, charge transfer resistance R_{ct} is likely to be correlated with the SOC, as suggested by the BV equation. An overview of approaches for determining the charge state by impedance correlation is given by Rodrigues *et al.* [2000]. However, in more complex cases, statistical analysis will be needed to find parameters with best correlation (Yoon *et al.* [2001]). In some cases, no single parameter will exhibit significant correlation, but the combination of several parameters analyzed using multivariate regression techniques such as locally weighted regression (Cleveland and Grosse [1990]) will show useful predictive ability for a particular property. A review of multivariate statistical methods applied to battery research has been published by Hagan and Fellowes [2003], and a particular application to Li-ion batteries appears in Kim *et al.* [1999].

The choice of a model to analyze spectral data should involve a compromise between the complete capture of all kinetic features and the lowest possible standard deviation for parameters that show promising correlation. Indeed, the standard deviations of parameters, as estimated from the spectrum fit, define the lower limit of uncertainty of the target property correlated with them. For example, if R_{ct} is correlated with SOC of a battery linearly as $SOC = R_{ct}^*a + b$, the uncertainty of the SOC estimation will be at least $\delta R_{ct}a$ where δR_{ct} is the absolute value of the standard deviation from the impedance fit. Of course correlation itself is never perfect, so additional error terms will be introduced from a and b . To minimize the standard deviation of critical parameters, the model should be as simple as possible even if it leads to a worse fit in frequency areas weakly influenced by parameters of interest. These frequency areas should preferably be excluded from the fit in order to prevent distortion of the parameters of interest and increase of their uncertainties. However, if making a model more physically relevant leads to a better fit in spectral areas defining the parameters of interest, a more complex model might actually decrease the standard deviations of the relevant parameters, despite having more parameters in the fit. For example, the Li-ion battery impedance spectrum from 1 kHz to 0.1 Hz in Figure 4.5.13 appears as two depressed semicircles in a complex plot. It can be fitted to two serially connected parallel RC elements representing surface insulating layer R_l and C_l , charge transfer resistance R_{ct} , and double-layer capacitance C_{dl} , as in Figure 4.5.9.

The relative standard deviations for R_{ct} and C_{dl} are then 1.8 and 3.8%, respectively. However, it can be seen from Figure 4.5.13a that this fit does not adequately reflect the depression of the semicircles. Recognition that the electrode is porous suggests using a transmission line model as in Figure 4.5.3 where Z_{trans} will be the impedance of the particle surface as in Figure 4.5.9. This model is more complex since it adds the additional parameter—resistance of the porous layer, ρ . It can be seen from Figure 4.5.13b that it leads to a better fit of the experimental data. Despite the increased complexity of the model, the relative standard deviations of the parameters of interest, R_{ct} and C_{dl} , decreased to 1.7 and 2.8%. Moreover, the more physically relevant model is more likely to yield parameter estimates that better reflect the nature of observed process and therefore involve a better correlation with the target properties. In addition, the additional information represented by the parameter ρ can also be used for correlation.

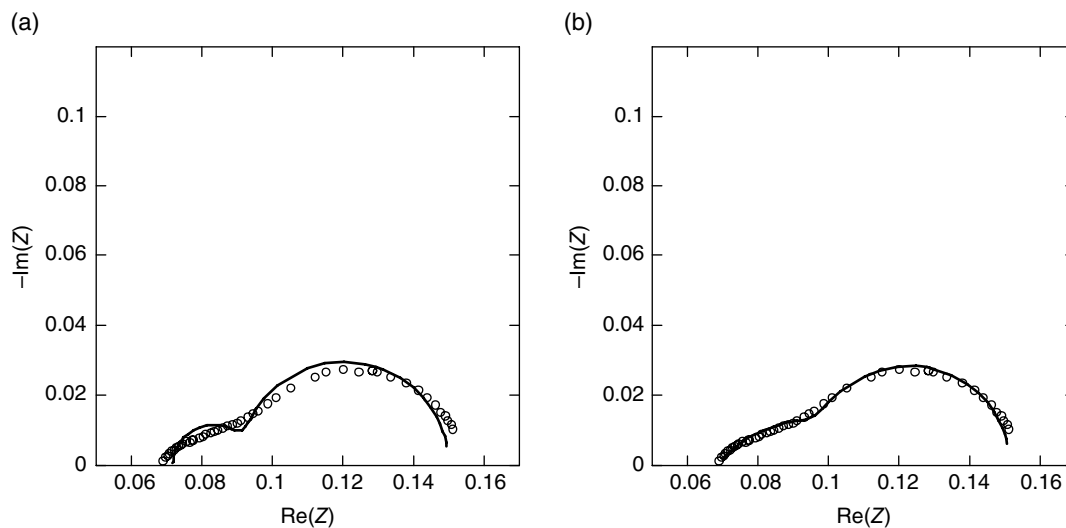


FIGURE 4.5.13 Impedance spectra of Li-ion battery in fully charged state from 1 kHz to 0.1 Hz.
 (a) Fit with 2RC model and (b) fit with distributed 2RC model.

4.5.2.2 Lead-Acid Batteries

While an exhaustive overview of aspects of impedance investigation of a particular battery chemistry is outside the scope of this work, the present generic approach may be exemplified for each particular chemistry by looking separately at the impedance of the electrolyte, the material surface, effects of diffusion and porosity, and the combination of all boundary effects in one model. Subsequently, the model can be simplified for purposes of correlation or discretized and made nonlinear if time-domain simulation is required.

The electrolyte in a lead-acid battery is a highly conductive, concentrated H_2SO_4 solution. Its ionic resistance is always negligible and makes a small contribution to the series resistance of the battery, which depends on SOC. Unique to lead-acid batteries is the fact that the charge reaction produces and discharge captures SO_4^{2-} ions, and therefore the electrolyte concentration is changing during charge and discharge. This involves reflective boundary conditions for diffusion through the electrolyte (Mauracher and Karden [1997]), resulting in pseudocapacitive behavior conforming to Eq. (10), which is, however, apparent only at very low frequencies below 100 μHz .

A typical simulated impedance spectrum of a lead-acid battery is given in Figure 4.5.14.

The impedance of a Pb/PbSO_4 anode surface can be represented quite well by the Randles equivalent circuit, as in Figure 4.5.8. It appears as a small semicircle at the high-frequency side of the battery impedance spectrum (Armstrong and Bladen [1976]) and constitutes a rather small contribution to the overall impedance.

Cathode material, on the other hand, dominates the impedance spectrum and involves a depressed semicircle ranging from 1 Hz to 1 mHz. This semicircle may also be interpreted as caused by diffusion through a porous layer (Mauracher and Karden [1997]); however a greater than 5 times change of this impedance with bias current, observed by the aforementioned authors, and weak dependence on temperature, demonstrated by Hawkins and Barling [1995], both indicate a strong contribution of faradaic charge transfer resistance in this part of the spectrum. Very high pseudocapacitance of this material (Maja and Penazzi [1985]) indicates the presence of an activated adsorption mechanism typical of supercapacitors rather than that involving simple double-layer capacitance. These results explain the significant nonlinear dependence of the associated resistance on current. It is also known that porous PbO_2 is formed during charging and has high conductivity for a metal oxide, and yet much lower conductivity than a metal, which explains the high impedance of the cathode. To take into consideration the combined specific resistance of porous material and electrolyte in pores, as well as the surface impedance

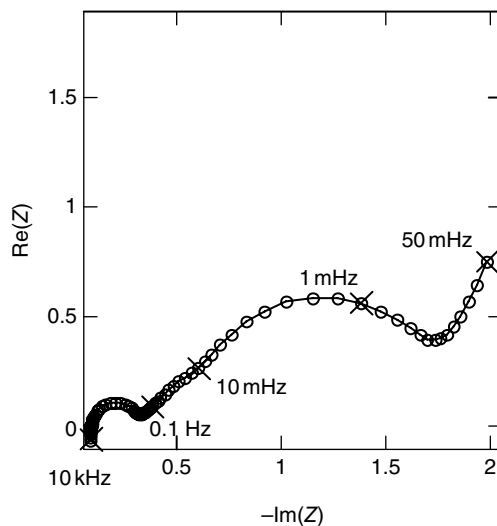


FIGURE 4.5.14 Typical impedance spectrum of a lead–acid battery from 10 kHz to 50 μ Hz.
Source: Mauracher 1997. Reproduced with permission of Elsevier.

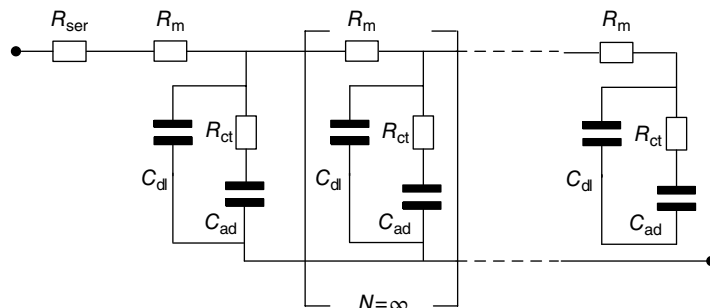


FIGURE 4.5.15 Porous electrode with activated adsorption on particles' surface.

of particles, the transmission line model of Figure 4.5.3 can be used, where Z_{cross} will be the impedance of the surface of the PbO_2 particles. An equivalent circuit taking into account activated adsorption, C_{ad} , is shown in Figure 4.5.15.

The function describing the frequency dependence of such an impedance element is equivalent to that of diffusion in Eq. (29), but the meaning of the parameters must be redefined as $R_d = R_m$, $R_p = R_{ct}$, $C_d = C_{dl}$, and $C_p = C_{ad}$. A complete equivalent circuit of the lead–acid battery will involve serially connected elements described in previous paragraphs for the electrolyte and anode and cathode, with the addition of series resistance and inductance.

The dependence on SOC of a lead–acid battery has been investigated by Hawkins and Barling [1995]. Discharge results in an impedance increase at most frequencies, but specially in the low-frequency region dominated by the PbO_2 porous layer. A significant increase in impedance takes place also on overcharge (floating) cells, probably due to passivation of the positive electrode. Increased impedance starts already at 83% SOC, as shown by Salkind *et al.* [2001]. The use of impedance data for determining the SOC of lead–acid batteries is reviewed by Rodrigues *et al.* [2000].

4.5.2.3 Nickel-Cadmium Batteries

The electrolyte and separator in Ni–Cd batteries do not contribute significantly to overall impedance due to the use in such batteries of highly conductive, concentrated KOH/LiOH solution. The effect of electrolyte and current collector resistance adds to the serial resistance of the cell.

Typical impedance spectra of a Ni–Cd battery are shown in Figure 4.5.16.

It can be seen that the impedance decreases from the fully charged state until it decreases to about 75% SOC and stays mostly unchanged until almost end of discharge, where it slightly increases again. Detailed investigation of SOC dependence of anode and cathode separately was performed by Hammouche *et al.* [2004].

The anode of a Ni–Cd battery typically consists of a mix of Cd and CdO powders with the addition of a conductive additive (acetylene black). The impedance of the anode-particle surface is determined by the activated adsorption of OH[−] anions first on metal surface with subsequent conversion into Cd(OH)₂ and hydrated CdO layers (Duhirel *et al.* [1992]). Reaction products are also present in a partly dissolved Cd(OH)₃[−] state. The activated adsorption mechanism of the anode reaction, as well as porous structure of the electrode, makes it appropriate to use for its analysis the equivalent circuit shown in Figure 4.5.15. It was shown by Xiong *et al.* [1996] by separate impedance measurements on the anode and cathode that most of the impedance decrease during discharge is due to the anode, as the initial formation of a Cd(OH)_{ad}[−] monolayer is the rate-limiting step of the reaction. The consumption of Cd also increases the surface roughness and therefore the active surface area, contributing to the impedance decrease. However, the slight increase of impedance near the end of the discharge may be due to exhaustion of active cathode material in NiO(OH) form, which indicates that the impedance of the cathode is a significant part of the overall impedance.

The cathode of a modern Ni–Cd battery consists of controlled particle size spherical NiO(OH)₂ particles, mixed with a conductive additive (Zn or acetylene black) and binder and pressed onto a Ni-foam current collector. Nickel hydroxide cathode kinetics is determined by a solid-state proton insertion reaction (Huggins *et al.* [1994]). Its impedance can therefore be treated as that of intercalation material, for example, considering H⁺ diffusion toward the center of solid-state particles and specific conductivity of

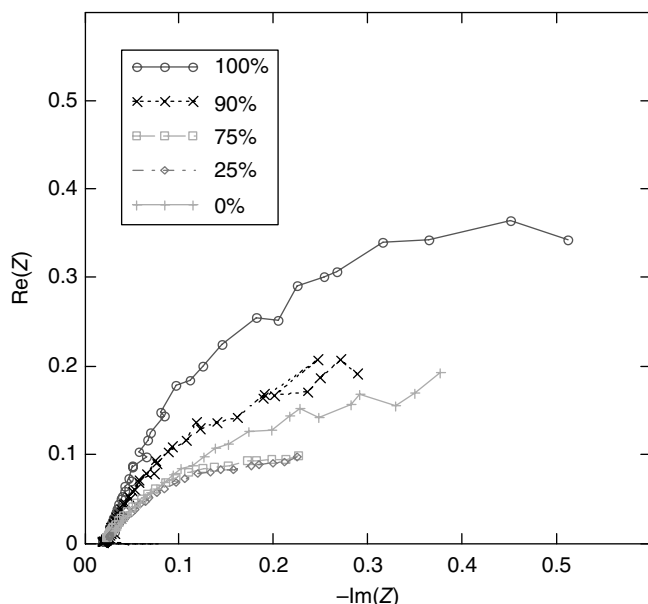


FIGURE 4.5.16 Impedance spectra of a cylindrical AA-size Ni–Cd battery at states of charge (SOC) of 100, 90, 75, 25, and 0%, measured using a multi-wave FFT impedance spectrometer covering the frequency range from 1 kHz to 1 mHz.

the porous material itself. The porous nature of the electrode can be accounted for by using the transmission line model (Macdonald *et al.* [1990]). The equivalent circuit considering both diffusion within particles and layer porosity is given in Figure 4.5.10. Using the diffusion equations derived for spherical boundary conditions, as in Eq. (30), appears most appropriate.

Because the Ni–Cd battery impedance spectrum does not show a gradual change with SOC, single parameter correlation in order to determine SOC appears unfeasible (Reid [1990]). However, multivariate correlation has been successfully used (Rodrigues *et al.* [2000]), and the frequency where $\text{Im}(Z)$ changes sign from negative to positive was found by Hammouche *et al.* [2004] to be a good predictor of SOC. On the other hand, Ni–Cd battery degradation with cycling is accompanied by a significant impedance increase, especially at low frequencies (Haak *et al.* [1984]). The impedance spectra have therefore been widely used for estimating the state of health of Ni–Cd batteries. The reason for the impedance increase at the cathode side was found by Macdonald *et al.* [1990] to involve a decrease of the pore size and an increase of interparticle resistance of the porous layer.

4.5.2.4 Nickel–Metal Hydride Batteries

The electrolyte and cathode material of Ni–MH batteries are identical to those discussed in the Ni–Cd section. The impedance contributions of the anode and cathode are typically similar in magnitude, as shown by Reid [1990]. Most of the differences between these battery types are due to the metal hydride anode, using several different alloy types. Most common alloys have been investigated by IS-type AB_5 ($\text{LaNi}_{4.7}\text{Al}_{0.3}$) by Kuriyama *et al.* [1996] and Cheng *et al.* [1999], more modern ($\text{MmNi}_{3.6}\text{Co}_{0.7}\text{Al}_{0.3}\text{Mn}_{0.4}$) by Lia *et al.* [2004], type AB_2 (e.g., $\text{ZrCr}_m\text{Fe}_n\text{Co}_p\text{V}_o$ where $m + n + p + o = 2$ by Rajalakshmi *et al.* [2001]), Mg_2Ni type (e.g., $\text{Mg}_{1.95}\text{Y}_{0.05}\text{Ni}_{0.92}\text{Al}_{0.08}$ investigated by Cui and Luo [2000]), and other types, especially those containing vanadium. The AB_5 type currently exhibits the best cycle ability and is most commonly used in commercial batteries, while others show higher capacity and are being developed to improve cycle ability.

Typically, the anode consists of small particles of hydride-building alloy held together by a binder and conductive additive (acetylene black) and pressed onto a Ni-foam current collector. The impedance of the particle surface is determined by the charge transfer resistance of hydrogen reduction, double-layer capacitance, and the impedance of subsequent solid-state diffusion into the bulk of the particle. To take into account electronic resistance between the particles and ionic resistance of electrolyte in pores, as well as the impedance of the particle surface, we can use the transmission line model of Figure 4.5.10. Because particle shape is best approximated as a sphere, diffusion with spherical boundary conditions, as in Eq. (30), can be used for Z_d .

The dependence of a NiMH battery on its SOC is mostly defined by an increase of anode impedance with discharge, except for the fully discharged state where increasing cathode impedance becomes pronounced. Some typical impedance spectra measured using the FFT multi-sine method after repeated discharge/relaxation at different DODs on a Hitachi AA-size NiMH battery are shown in Figure 4.5.17 as a perspective complex plot.

A gradual impedance increase in the areas associated with charge transfer and diffusion behavior is apparent, while the series resistance mostly associated with the electrolyte and separators remains unchanged. Bundy *et al.* [1998] used multivariate correlation in order to predict the SOC based on impedance spectra for a large set of commercial NiMH cells and found that despite cell-to-cell variations it was possible to achieve a 7% average error in prediction if a few abnormal cells were removed. Hammouche *et al.* [2004] found that frequency where $\text{Im}(Z)$ changes sign from negative to positive has a good correlation with SOC.

The impedance of a metal hydride anode typically decreases during the first few charge/discharge cycles, apparently because of an increase of the active surface. A similar increase can be produced by pretreatment with a base and reducing agent (Cheng *et al.* [1999]). In the case of battery deterioration with subsequent cycling, both series resistance increase and overall “stretching” of the impedance spectra can indicate depletion of the electrolyte both in the separator and in the pores of the anode and cathode material. Replenishment of the electrolyte decreases the impedance to its original state. Further degradation is associated with corrosion and fracturing of anode material, which also results in an

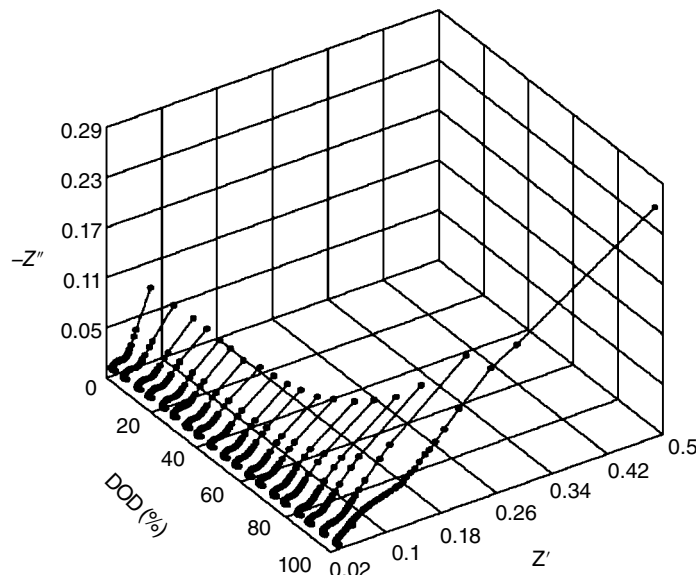


FIGURE 4.5.17 Impedance spectra measured using the FFT multi-sine method after repeated discharge/relaxation at different DOD on a Hitachi AA Ni–MH. The frequency range extends from 1 kHz to 1 mHz.

increase of interparticle resistance and eventually leads to irreversible loss of active surface (Cheng *et al.* [1998]).

4.5.2.5 Li-ion Batteries

The Li-ion battery is the most actively investigated battery of modern times. Its basic design consists of a cathode and anode with an open crystalline structure capable of repeatedly intercalating Li-ions and a high-stability electrolyte and separator. Research of Li-metal anode-based batteries largely overlaps with Li-ion battery research.

A Li-ion battery uses an aprotic (no mobile hydrogen atoms) electrolyte, quite different from other batteries. The need for such electrolyte arises because of the high cell voltage of the battery (4.2 V), which exceeds the water stability region both on the cathode and on the anode side. Electrolytes used can be subdivided into inorganic solid (Bates *et al.* [2000]), solid polymer (Armand [1983], Aihara *et al.* [2003]), plasticized (Rajendran *et al.* [2001]), gelled (Krok *et al.* [1999], Saito *et al.* [2001]), and liquid (Blomgren [2003]). All of these electrolytes have been the subject of investigations using IS; however only liquid and to some extent gel electrolytes are currently of widespread commercial use because of their superior power capability.

The impedance spectrum of polymer and gel electrolyte appears as a depressed semicircle in the frequency region between 100 kHz and 0.1 Hz, which can be analyzed using the Cole and Cole [1941] approach, as described in Section 2.1.2.3. Typically, polymeric, plasticized, and gel Li-ion conductors show abnormally low conductivity as compared with that expected from self-diffusion coefficients calculated using other methods such as PMFG-NMR (Clericuzio *et al.* [1995]). In addition to the usual attribution of this effect to ion association, the incomplete removal of the electrode impedance effect during analysis can contribute to an apparent increase in the electrolyte resistance.

Impedance is typically measured in a two-electrode configuration where the electrolyte is compressed between two blocking (steel, platinum) or non-blocking Li electrodes (Qian *et al.* [2002]). Analysis of electrolyte impedance in the presence of electrode impedance is complicated and usually assumes that the electrolyte is responsible for the highest-frequency region of the spectrum, about 1 kHz. To improve confidence in the conductivity estimation, measurements with several layer thicknesses should be performed. To remove the effect of the electrode impedance in a test setup,

four-electrode measurements have also been proposed (Bruce *et al.* [1988]). Typically two pseudo-RE made of Li-foil stripes are pressed through a cavity in the middle of circular main electrodes to the surface of the polymer electrolyte under test.

Because of the inherent reactivity of the electrolyte with intercalated Li, the choice of solvent/conductive salt is based on a compromise between its conductivity over a wide temperature range and its ability to build a passivating layer on the intercalating host surface. Initially, a propylene carbonate (PC)/ethylene carbonate (EC) combination was widely used because of the high conductivity of the first and the good passivating properties of the second. Presently, more complicated mixtures of multiple solvents (Plichta *et al.* [2001]) and passivation-enhancing additives such as vinylene carbonate (Aurbach *et al.* [2002a]) are used to improve cycle ability and low-temperature performance. Impedance investigations of solvent conductivity dependent on temperature and conductive salt (Jow *et al.* [2003]) are common and can use the standard treatment for conductivity calculation (see Section 2.1.2.3).

The separator in a Li-ion battery is typically a thin (15 µm) microporous polypropylene film. It prevents the electrodes from shorting directly or through Li microdendrite growth on overcharge, and it also serves as a thermal shutdown safety device. When heated above 150°C (e.g., due to an internal short in a cell), the separator melts and its pores close, thus preventing current flow and thermal runaway. It is common to investigate the shutdown behavior of separators by measurement of cell impedance at selected frequencies, such as 1 kHz, dependent on temperature (Uchida *et al.* [2003]).

Separate impedance investigation of electrodes is possible using a three-electrode configuration, where the electrode of interest (anode or cathode) is typically paired with a Li-metal CE and a Li-metal RE. The electrodes are sandwiched with a separator, compressed together in a holding arrangement and immersed in electrolyte. An example of such arrangement, used by Barsoukov *et al.* (1999a), is shown in Figure 4.5.18.

In this case, electrodes are compressed between two glass plates with a spring. Placement of the RE through a hole in the CE provides the most symmetric position, important for measurement reproducibility and for preventing inductive artifacts often associated with a conductive path to the RE coinciding with that of the current flow between the main electrodes. A detailed discussion of three-electrode measurement is given in Dolle *et al.* [2001].

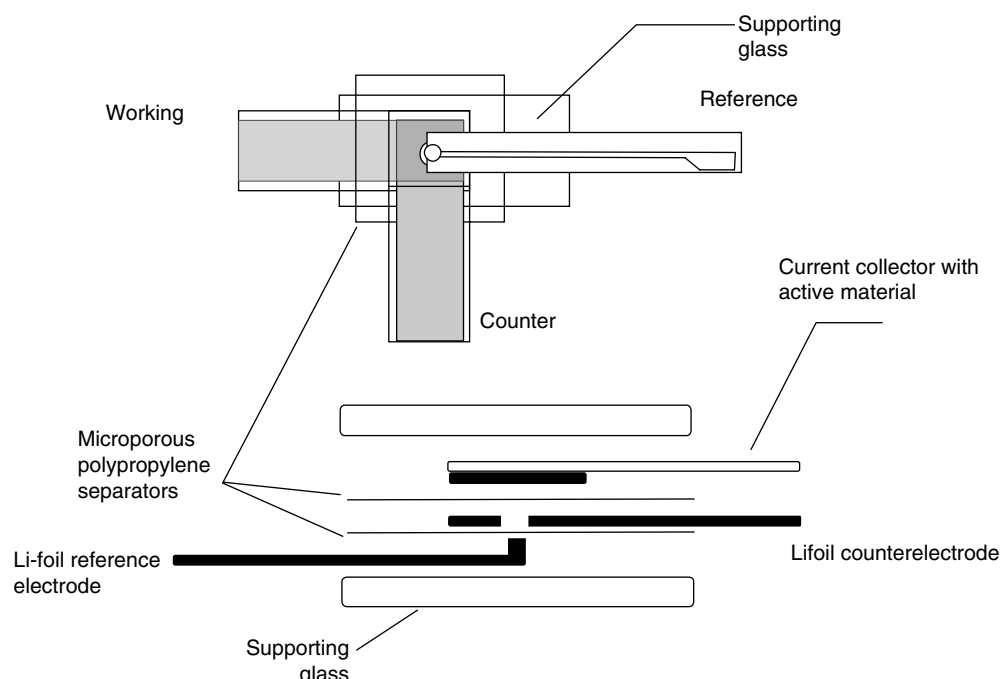


FIGURE 4.5.18 Three-electrode arrangement for impedance measurement on Li-intercalation electrode in battery-like conditions.

Anode Most common intercalation anodes are based on natural graphite and hard carbon graphitized to different degrees, with the degree of graphitization significantly influencing the capacity, kinetics, and first cycle irreversible capacity loss (Dahn *et al.* [1993]). Popular are pre-shaped carbons such as MCMB with spherical particles and cylindrical carbon fibers (Sawai *et al.* [1994]). A well-defined particle surface allows one to reduce the specific area of an electrode and therefore the self-discharge and first cycle capacity loss. The surface impedance of a carbon anode is determined by two factors—the resistance and capacitance of the passivating layer and the charge transfer resistance of the intercalation reaction—followed by solid-state diffusion toward the center of the particles, which can be formalized in terms of the equivalent circuit shown in Figure 4.5.19.

IS was first applied to the investigation of SEI on lithium metal by J. Thevenin [1985]. For PE, both factors have been investigated on MCMB by Barsoukov *et al.* [1998] by studying EIS during the growth of the passivation layer. Typical impedance spectra measured during the growth of the passivation layer are shown in Figure 4.5.20.

It can be seen that a high-frequency semicircle corresponding to the passivation layer grows noticeably at room temperature and is almost unchanged at low temperature, indicating a different character

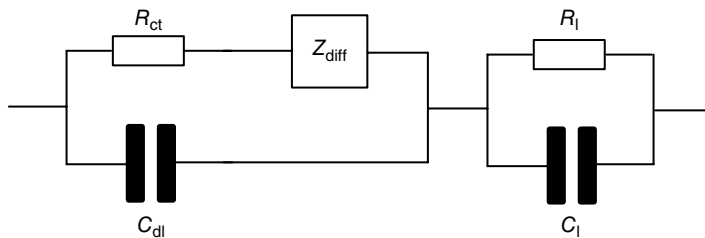


FIGURE 4.5.19 Equivalent circuit of the particle surface of a Li-intercalation anode.

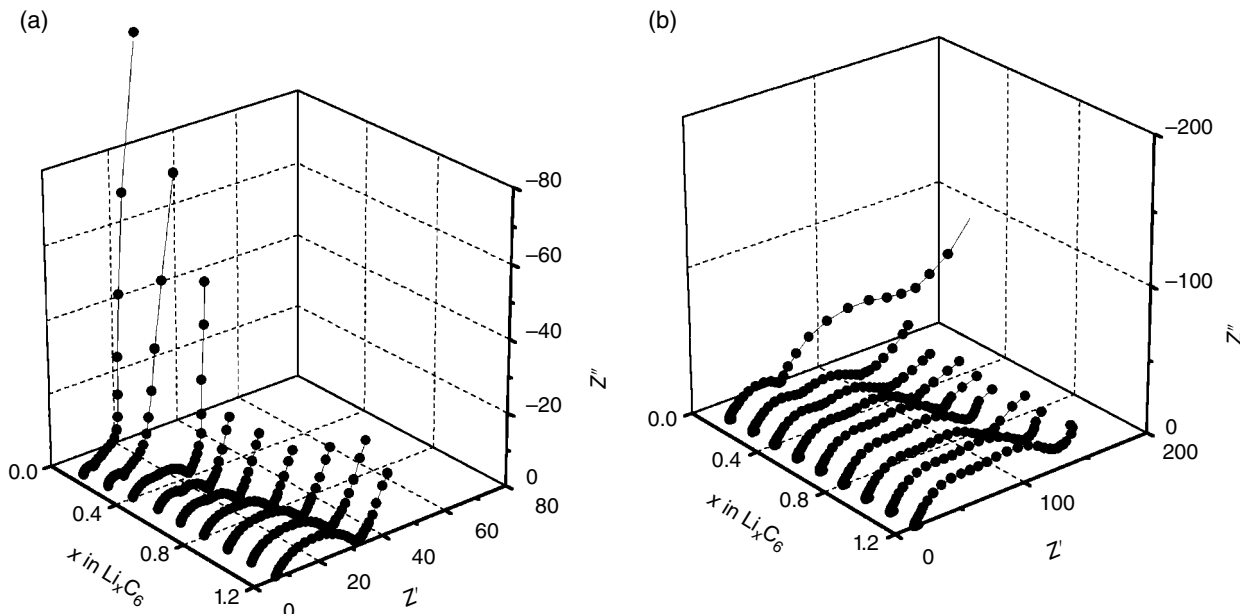


FIGURE 4.5.20 Impedance spectra measured using a multi-sine FFT impedance spectrometer in the range from 10 kHz to 1 mHz in a three-electrode configuration on a hard-carbon anode during first charge at room temperature (a) and at -20°C (b).

of the formed layer. Quantitative analysis of the surface characteristics is only possible by using a model that considers the porosity of the active layer because the influence of the ionic and electronic resistance of the active layer is important in all frequency ranges. The transmission line model in Figure 4.5.3, where impedance is Z_{cross} is given by the equivalent circuit in Figure 4.5.19, can be used to analyze the aforementioned impedance spectra.

The diffusion impedance Z_{diff} should be expressed differently depending on the predominant shape of the particles: Eq. (10) for planar and Eq. (22) for spherical particles. Planar particles are rarely found in commercial batteries, but ultrathin carbon films can be a good model system for studying intercalation kinetics, as demonstrated by Levi and Aurbach [1997]. At very low frequencies the impedance spectrum starts to deviate from the shape expected due to diffusion alone. It was suggested by Barsoukov *et al.* [1999a] that new-phase-formation kinetics starts to influence the solid-state concentration of the free Li^+ ions. Modified diffusion equations that take this effect into consideration have been derived for the planar (Barsoukov *et al.* [1999b]) and the spherical case (Barsoukov *et al.* [2003]) [Eq. (31)]. A correct description of phase formation effects allows one to investigate processes with longtime constants critical for the dc performance of intercalation materials. See also section “Bringing It All Together” for more details. A dependence of carbon-anode impedance on SOC has been reported by Barsoukov *et al.* [1999a], and a typical spectrum development is shown on the perspective complex plot in Figure 4.5.21.

It can be seen that changes in the charge transfer resistance (high-frequency depressed semicircle) and in the chemical diffusion coefficients defining the low-frequency dependence involve Li-intercalation phase changes. The resistance R_{ct} and diffusion hindrance increase in areas where change from one phase to the next occurs. The value of impedance spectra for correlation with SOC is problematic for the Li-ion battery because impedance increases and decreases in the course of discharge several

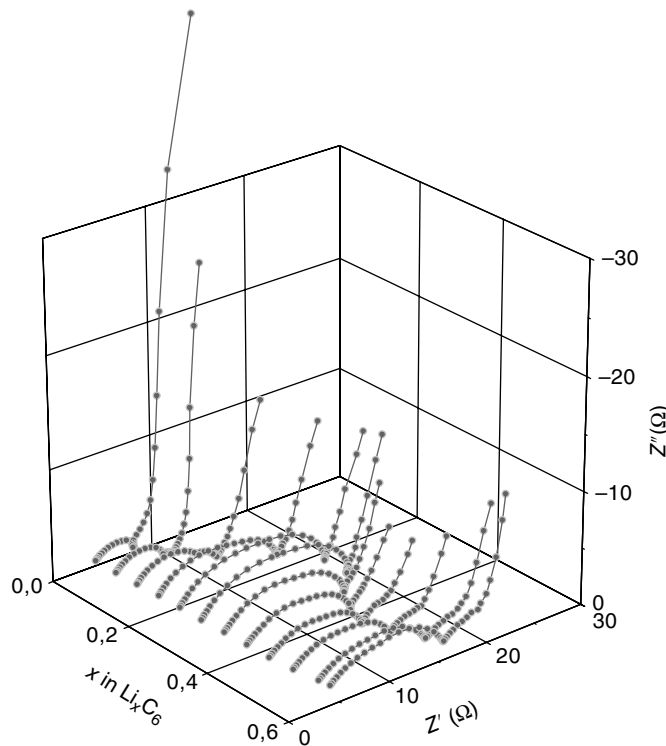


FIGURE 4.5.21 Impedance spectra measured using a multi-sine FFT impedance spectrometer in the range from 10 kHz to 1 mHz in a three-electrode configuration on a hard-carbon anode during discharge/relaxation sequence at different states of charge.

times. Only multivariate correlation using information from multiple frequencies or multiple model parameters can allow confident estimation (Yoon *et al.* [2001]).

A few other materials have been investigated as lithium-intercalation anodes, in particular amorphous Sn, SnO, and SnO₂. Impedance analysis can be performed using similar models as with carbon-based electrodes (Li *et al.* [1999]). The increase in the specific resistance of a PE due to the growth of Sn particle size and the resulting electrical disconnection of particles in line with an increase of the percolation threshold for larger particle size was found to be the main reason for fast capacity fade. Doping elements and manufacturing of glass-like materials allowed improvement of the originally poor cycle ability in addition to their excellent capacity (Miyasaka [1998]). Unfortunately, the champion of this idea, the Fuji Corporation, dropped the project for financial reasons, and since then commercial interest in novel, but hardly economical anode materials, when compared with carbons, remains low. A still promising application for these materials involves all-solid RF sputtering of deposited thin-film batteries (Strømme Mattsson *et al.* [1996a]) because of their ease of deposition compared with carbon.

More recently Si has emerged as the most promising contender for replacing carbon in Li-intercalation anodes. It has huge theoretical capacity of 4200 mAh/g; however, Si particles tend to break apart during cycling due to very large volume expansion. Extensive research is ongoing to stabilize cycling of Si through nanoengineering such as use of Si nanowires and nanoencapsulation of Si in yolk–shell structures or external matrix. Investigation of such electrodes is often performed using IS, where the previously described transmission line model of PE is applicable. For example, it was used by Ruffo *et al.* [2009] to analyze Si-nanowire electrodes behavior.

Cathode. LiCoO₂ (Ozawa [1994]) has been a cathode of choice since the inception of the Li-ion battery, with LiMn₂O₄ (Kim and Pyun [2002]) being investigated because of its fast kinetics and higher capacity; nevertheless it has not been of wide commercial use due to fast degradation above 60°C (Amatucci *et al.* [1999]). Research is continuing on finding doping ions that stabilize spinel structure (Sun *et al.* [1999]).

Typical impedance spectra for LiCoO₂ and LiNiO₂ cathodes are shown in Figure 4.5.11. The surface impedance of Li-intercalation cathode materials is similar to that of anodes and is dominated by surface film impedance and by charge transfer resistance. Because of the relatively low conductivity of the cathode material, 5–15% of conductive additive (carbon black) is added to the material. Still the high material resistance is a major contributor to the overall electrode impedance and can be treated by the transmission line model similar to that discussed for anodes. Capacity fading is also largely attributed to an increase of material resistance due to the growth of insulating layers on particle surfaces and the resulting particle disconnection (Aurbach *et al.* [2002b]). Solid-state diffusion in intercalation cathodes can only be analyzed as part of an overall impedance model because the material resistance of the PE can lead to a 45° angle in the complex plot, which can be mistaken for diffusion effect. Nonlinear fitting to a model that includes both diffusion and material resistance factors (Section 4.5.2.1) allows one to separate their effects because the diffusion effect is expressed only in the low-frequency area but material resistance influences all frequency regions.

The dependence of wide-frequency-range impedance spectra of LiCoO₂ on SOC has been investigated by Barsoukov *et al.* [2000]. Typical impedance spectra are shown in the perspective complex plot of Figure 4.5.22.

It can be seen that although most changes occur in the charge transfer resistance of the material, changes in diffusion hindrance are also significant.

LiNiO₂ higher capacity was not benefited from because it is considered unsafe due of low thermal runaway temperature. However, its derivatives that are replacing part of Ni for Co (especially LiNi_{0.8}–Co_{0.2}O₂) improved its thermal stability and are already widely used in the field due to lower cost of Ni and Mn compared with Co, as well as higher capacity. Lower voltage at high DOD is still preventing the use of such materials in single-cell applications such as smartphones, but multicell notebook, power tools, and automotive applications, which are less sensitive to single-cell voltage cutoff, are embracing these materials. Initial issues with rate capability of such materials have been addressed through adding small amounts of doping ions, as demonstrated through EIS by Barsoukov *et al.* [2003] for LiTi_{0.05}Mg_{0.05}Ni_{0.7}Co_{0.2}O₂.

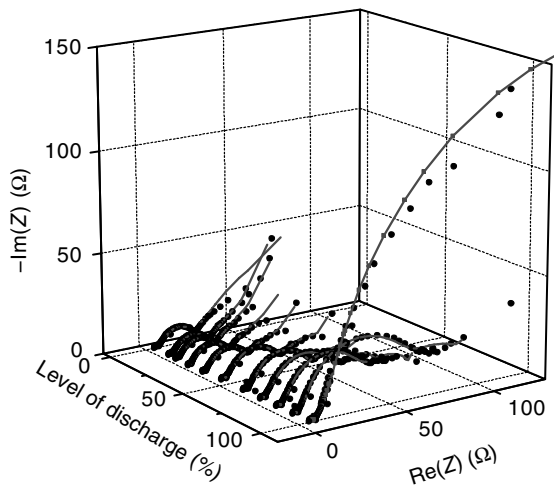


FIGURE 4.5.22 Impedance spectra measured at various levels of discharge on LiCoO_2 -based composite cathode in the frequency range 10 kHz to 1 mHz (markers) and the results of nonlinear fits to the model in Figure 4.5.3 (lines, markers).

Still in research phase is investigation of another promising class of layered Li-rich oxide materials (often abbreviated as OLO), which combine traditional metals in +3 oxidation state with metals in +4 oxidation state (e.g., $\text{Li}[\text{Li}_{0.23}\text{Ni}_{0.15}\text{Mn}_{0.62}]\text{O}_2$ investigated through IS by Gu *et al.* [2015]) providing for higher voltage and capacity. These materials are adding capacity all the way to 4.7 V versus Li, but it has been shown that charge transfer resistance is drastically increasing at voltages approaching 4.7 V. Note that as used by authors simple equivalent circuit using CPE does not allow to differentiate between contributions of R_{ct} and resistance of porous material itself, so these findings could also be attributed to a decrease of electronic conductivity. Diffusion coefficients have been also estimated by authors to be much lower than in traditional materials like LiCoO_2 , but this needs to be taken with caution because solid-state diffusion estimates that do not use actual particle size are only strictly correct for infinitely thick layers of material. Analysis of impedance spectra for porous materials with well-defined particles can be done much more accurately using spherical particle models as given in section “Bringing It All Together.”

A new class of phosphate materials, particularly LiFePO_4 (Prosini *et al.* [2002]) and $\text{Li}_3\text{V}_2(\text{PO}_4)_3$ (Saïd *et al.* [2003]), involving a simple synthetic route including carbonization to improve electronic conductivity has recently led to a promising alternative material with similar capacity and price but highly increased thermal runaway temperature.

Research into new cathode materials with higher capacity and higher voltage range than LiCoO_2 continues.

Impedance spectra of materials like LiFePO_4 where two phases coexist during charging will deviate from simple spherical diffusion behavior but can be modeled using shale-core model, as described in detail by Gambhire *et al.* [2014].

Several non-intercalation cathodes are also being investigated due to much larger theoretical capacities. Most promising (with highest theoretically possible energy density) is air cathode, where Li is reducing oxygen to LiO_2 and further into Li_2O_2 compounds. Due to insolubility and electrically insulating properties of these products, charge/discharge of such cathodes requires very high surface area electrodes, possibly using nanomaterials. An analysis of impedance spectra of Li-air batteries is given by Mehta *et al.* [2013]. Another promising cathode material under active research is sulfur. While offering twice lower energy density compared with oxygen, it is still 5 times higher than present cathode materials like LiCoO_2 . A variety of problems ranging from sulfur’s electrically insulating properties, low

solubility in organic solvents, and tendency to drift to the side of anode in form of polysulfides results in values for pure cycleability and energy density that are very far from theoretical values. Impedance spectra of Li/sulfur batteries measured during charge/discharge and cycling have been reported by Deng *et al.* [2013]. While chosen equivalent circuit model using CPEs did not allow to derive physical properties of the electrodes, the shape of the spectra indicates that use of transmission line model would be justified.

4.5.3 Nonideal Behavior Developed in Porous Electrode Supercapacitors

4.5.3.1 Introduction

The history of the concept of the double layer at interfaces with liquid electrolyte solutions or ionic solids, and at colloids, goes back to early work on colloids and electrode interfaces in the nineteenth century and through the twentieth but is beyond the scope of the present article. However, general reference sources are Adam [1941], Adamson [1982], and Conway [1999].

Double layers of charges, negative and positive, separated by a solvent layer of some 0.3 nm in thickness, arise at electrode and colloid interfaces with electrolyte solutions. Such a configuration of charges, for example, electrons or electron deficiency at electrode interfaces and conjugate ionic charges in a solution in contact with the electrode, has the nature of a “parallel plate” capacitor (model of von Helmholtz [1853]). The capacitance, C , of such a distribution of charges is given in classical electrostatics by

$$C = \frac{A\epsilon\epsilon_0}{d} \quad (33)$$

for an area $A \text{ cm}^{-2}$, with plates separated by a distance d with a dielectric between the plates having dielectric permittivity ϵ , with ϵ_0 being the permittivity of free space, equal to $8.84 \times 10^{-14} \text{ F/cm}$. For a distance $d = 0.3 \text{ nm}$ and an effective dielectric permittivity of the interphasial solution layer at an electrode equal to ca. 6–10 for water at a charged interface, C per cm^2 would have a large value on the order of $20 \mu\text{F}/\text{cm}^2$ as found, for example, at Hg or Au electrodes in aqueous H_2SO_4 or HClO_4 solutions.

Of principal significance is that, per cm^2 , interfacial double-layer capacitance values are very large in comparison with that of hardware capacitors of the same, 1 cm^2 area where values are on the order of picofarads. For comparison, a hardware vacuum ($\epsilon = 1$) capacitor having $d = 0.01 \text{ cm}$, say, would have to have an area some 10^5 times larger to provide a specific capacitance comparable with that, per cm^2 , of the double-layer capacitor. Even with bulk water as the dielectric, the area would need to be some 10^3 times larger! Interfacial double layers thus provide high capacitance density and correspondingly large specific charge storage densities.

Electrochemical capacitors, now often referred to as “supercapacitors” (Conway [1999]), are a relatively recent development in the technology of electric charge storage and delivery devices, though an early original patent (Becker [1957]) describes charge storage by the double-layer capacitance of high-specific-area carbon material. These devices are of significance for practical development as a variety of carbon materials (powders, fibers and aerogels, nanotubes) can be prepared or obtained with specific real areas up to $1000\text{--}2000 \text{ m}^2/\text{g}$. Thus, an electrode made from carbon powder or fibers having real accessible area of $1000 \text{ m}^2/\text{g}$ and interfacial double-layer capacitance at the electrode surface in the range $10\text{--}30 \mu\text{F}/\text{cm}^2$, say, $20 \mu\text{F}/\text{cm}$ (Stern [1924], Grahame [1947], Parsons [1954], Becker [1957]) has an overall electrode capacitance of 200 F/g .

Note (cf. Conway [1999]) that a practical electrochemical double-layer capacitor device always requires, of course, two electrodes per cell, with one electrode interface being charged against the other by opposite directions of polarization. Each electrode has, however, its own characteristic impedance spectrum that is not necessarily the same for the two interfaces due to asymmetry of cation/anion adsorption (Grahame [1947]). Each of the individual electrode impedances can be evaluated in a suitable 2- or 3-electrode configuration, or the overall cell impedance can be evaluated in a 2-terminal configuration. The capacitances of the two interfaces are measured reciprocally in series, and the overall

capacitance is formally half that of each electrode in the symmetrical case, but practically less than such a value.

Contrary to what was naively believed in the early stages of development of electrochemical capacitors, that is, that very high power densities would be achieved in their use because of their capacitive nature (supposedly like that of Figure 4.5.23a), electrochemical supercapacitors do have intrinsic limitations on their power delivery. This arises for two reasons: (i) due to the usual “*iR*” loss when a significant equivalent series resistance (ESR) or real series resistance exists in the electrical configuration of the capacitance element and (ii) on account of the internal distributed resistance in multiple series/parallel (see Figure 4.5.23) connections (de Levie [1963, 1964], Keiser *et al.* [1976]) representing a high-area porous carbon, double-layer electrochemical capacitance. This causes a dispersion of measured capacitance with increasing frequency in ac IS, due to an attenuation of amplitude of the addressing alternating voltage (AV) down the pores of a PE matrix that has been referred to as the “penetration effect” (de Levie [1963, 1964]) or “porous electrode factor.” Note that the “penetration effect” applies, in principle, to any

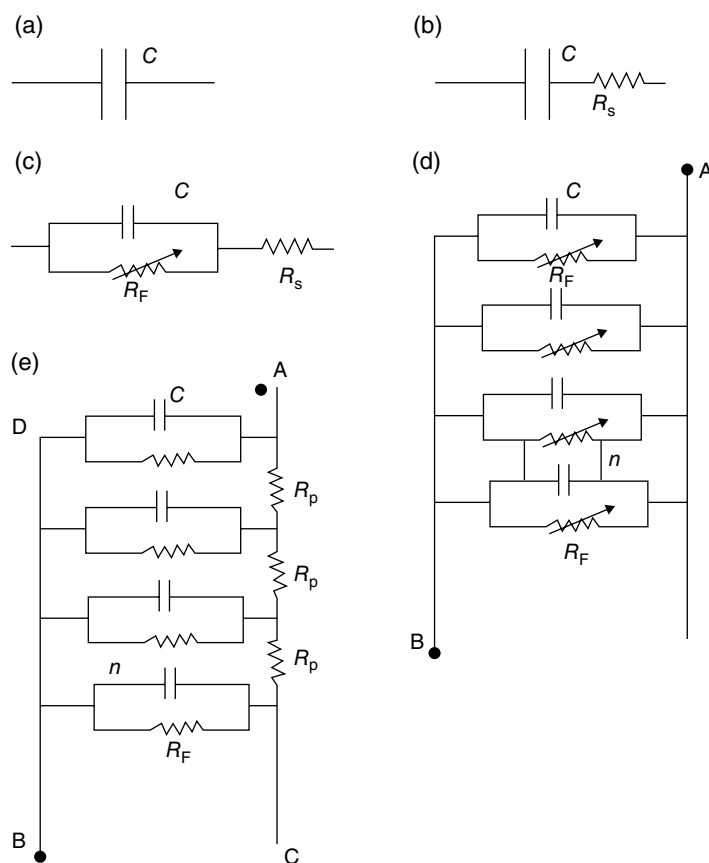


FIGURE 4.5.23 Hierarchy of equivalent circuits for capacitor/resistor combinations, including that for a porous electrode.
 (a) Simple capacitor. (b) Capacitor with equivalent or real series resistance. (c) Capacitor with series resistance and potential-dependent faradaic leakage resistance, R_F . (d) Parallel combination of n C and R_F leakage elements. Overall “ RC ” constants is $R_F/n \times nC \equiv R_F C$ for single element. (e) Series/parallel C , R_F elements connected with pore—resistance elements, R_p (related to transmission line and constant phase element but with R_F leakage pathways).

form of modulation signal such as linear-sweep voltammetry and potential-step chronoamperometry as well as to AV modulation.

The origin of this behavior is fundamental to the understanding of the difference of capacitance response to a modulating signal when the capacitance is developed in a PE matrix in comparison with that of an isolated electrolytic capacitor (Figure 4.5.23a) or at a solid plane electrode of the same (e.g., carbon) material for which a circuit of type shown in Figure 4.5.23b applies. It can be understood in terms of the hierarchy of equivalent circuits (illustrated in Figure 4.5.23) representing the electrical behavior of a pure capacitance (vacuum “dielectric”) without series or parallel resistance elements through to that complex circuit for PE (Figure 4.5.23e).

In terms of the relationship between voltage V across the plates of any capacitor (Figure 4.5.23a) and the stored charge density q per cm^2 , the capacitance, C , is given by the fundamental equation in electrostatics:

$$C = \frac{q}{V} \quad (34)$$

or, differentially,

$$C = \frac{dq}{dV} \quad (35)$$

when the capacity, C , is not constant with charging V , as is often experimentally found. q and V are fundamental and conjugate variables in any study of capacitive devices, especially by means of modulation procedures such as IS (Macdonald [1987a], Lasia [1999]) (modulation of voltage by a sinusoidal AV at various frequencies, ω) and linear-sweep voltammetry (linear modulation of voltage at various sweep rates, $\pm dV/dt$).

These two complementary procedures have provided major instrumental methods for study of electrochemical systems especially for examination of the behavior of the double layer and its capacitance at metal electrodes and semiconductors. Further, they can offer insight into application limitations (Taberna *et al.* [2003]) and causes of device degradation (German *et al.* [2014]).

A capacitor either stores incoming charge or delivers charge. The extent of charge delivery or acceptance (discharging or charging processes) for electrochemical capacitors is time dependent. In any capacitor device having a real material dielectric, the capacitance is effectively connected in series with a real or an ESR. The admission of charge is displaced with respect to potential in the range of overall applied potential, so that the capacitance is apparently “dispersed.” This effect is not to be confused with the -90° phase angle between current and voltage inherent in the charging of any pure capacitance. Porous double-layer capacitor characterization is further complicated in that charge stored and accessible electrochemical area are modulated and dependent on pore structure including both size and shape (Keiser *et al.* [1976]).

The time scale of admission or delivery of charge to or from a capacitance in series with a real or equivalent resistance, R , is characterized by the time constant RC , the product of C and R . The behavior of such an RC combination can be treated in terms of a generalized *reduced* time scale, t/RC . The quantity t/RC enters into any time-based response of a capacitor to change of voltage or admission or delivery of charge and appears in ac impedance studies as a reciprocal time variable, the frequency f (Hz) or the circular frequency, $\omega = 2\pi f$. If RC is small, the response time scale is correspondingly short, while if RC is large, it is long. Systems with large RC require low frequency to be significantly AV modulated, while for smaller RC s they can be modulated by and respond to higher f values.

The “time factor” in charging and discharging capacitors is a prime factor in their applications as it determines attainable *rates* of those processes. This is of special importance in optimizing performance of capacitor devices such as double-layer supercapacitors (Conway [1999]) and pseudocapacitors designed for load leveling and hybridizing with battery or fuel cell systems in electric vehicles and as hybrid electrode systems (faradaic combined with non-faradaic capacitive electrodes). In this respect, the “time factor” therefore determines the power levels at which an electrochemical capacitor device can be operated

and consequently the forms of Ragone plots (Ragone [1968], Pell and Conway [1996], Conway [1999]) representing operating energy densities as a function of achievable power densities on discharge or recharge.

4.5.3.2 Equivalent Circuits and Representation of Electrochemical Capacitor Behavior

The representation of impedance spectra of electrochemical systems in terms of the ac response behavior of equivalent circuits has become a common practice in the field. A physically reasonable circuit is chosen, and values of its C , R , and L components are selected to give the best fit to the observed frequency spectral response over a wide range of frequencies. It should be noted, however, that a particular selected circuit model may not uniquely represent the impedance behavior of the system and that often the models themselves give little or no direct information about the physical significance of the circuit elements themselves (Robinson and Kayinamura [2009]); nevertheless, the circuit modeling approach is widely used, aided by special computer programs.

An alternative but related procedure is to make a purely analytical treatment of impedance of an electrochemical system, as was usefully carried out by Armstrong and Henderson [1972].

While treatment of the impedance spectrum of a unit capacitor is simple, if not trivial, the impedance response of the double-layer capacitance at the interface of a high-specific-area matrix, for example, of carbon powder, felt, or aerogel, becomes very complex owing to the distributed series/parallel RC configurations throughout the electrode matrix, not to mention some usual contribution of 5–10% from faradaic pseudocapacitance due to reactive functionalities at the extended carbon surface.

A seminal treatment of the electrical behavior of a PE was first given in detail in a series of classic papers by de Levie [1963, 1964] with important extensions to pores of various specific shapes by Keiser *et al.* [1976]. These works provided the essential bases for much of the then future basic work on electrochemical supercapacitors and the special effects that arise when a series/parallel distributed network of C and R elements is involved.

A very convenient and informative way of representing the impedance behavior of “ RC ” circuits is by plotting the imaginary (Z'') versus the real (Z') components of the impedance vector (Z) for a range of frequencies, ω , in a so-called Nyquist or Argand diagram drawn in the “complex plane.” This procedure originated in the works of Cole and Cole [1941] on the behavior of dielectrics where real (ϵ') and imaginary (ϵ'') components of the dielectric constant (ϵ) of a material medium can be distinguished and measured over a range of frequencies (Smyth [1938], Frölich [1949], Böttcher [1952]). The Cole–Cole plot for a lossy dielectric is in the form of a semicircle, intercepting the axis of real (ϵ') values at two critical points (Böttcher [1952]). The dispersion of dielectric constant with frequency arises from a phase difference between the dielectric displacement vector, D , and the field vector, E , causing the displacement of the electric polarization, P . The phase difference is due to three factors: (i) electric resistivity, leading to a response component in phase with E ; (ii) relaxation effects in permanent dipole orientation in the dielectric medium associated with the dipole polarization component of P ; and (iii) high-frequency resonance effects arising from electronic and atomic polarization (Böttcher [1952]).

Dielectric loss in capacitors is in most cases related to the dissipative energies associated with the requirement of periodic (at the frequency f) orientation and reorientation of permanent and induced dipoles in the molecular-dielectric material, and their mutual interactions in that material, especially in the case of liquids.

It is useful to illustrate the complexity of electrochemical capacitor EIS by showing a hierarchy of equivalent RC circuits that can be developed, from which an ultimate model of a PE CR device can be constructed. Note that the behavior of an “electrochemical capacitor” device is, electrically, far from that of a pure capacitor in its ac response spectrum to AV modulation; this is primarily due to the complexity of the distributed internal “connections” within the matrix, associated with resistivity of electrolyte channels and the intrinsic resistance of the C microparticles or fibrils and their interparticle contact resistances that usually depend on the pressure applied during fabrication of electrode structures.

In the simplest analysis, the circuit of Figure 4.5.23b represents the electrical configurations encountered in measurement and interpretation of experimental impedance spectroscopic behavior of the double layer at electrode interfaces.

Analogous to two resistors in series, the respective impedances Z_R and Z_C of a series R-C circuit add up linearly:

$$Z_{RC} = Z_R + Z_C \quad (36)$$

However, Z_C is frequency dependent and has to be written as an imaginary quantity, introducing the imaginary factor $j = \sqrt{-1}$. Then, since $Z_R = R_s$ and $Z_C = 1/j\omega C = -j/\omega C$ at frequency ω ,

$$Z_{RC} = R_s - j/\omega C \quad (37)$$

Note, for $\omega \rightarrow \infty$ ($1/\omega \rightarrow 0$) or for very large C , $Z_{RC} \rightarrow R_s$. This is commonly identified on a Nyquist complex plane plot as the intercept on the Z_R axis ($\equiv Z'$ in complex plane plot notation) as $\omega \rightarrow \infty$, $Z_C \rightarrow 0$ (Figure 4.5.24). The low-frequency limit, $\omega \rightarrow 0$, on the other hand can be used to estimate the double-layer capacitance of the system (Taberna *et al.* [2003]); however, this measurement tends to underestimate the capacitance measured either at slow rate cyclic voltammetry or galvanostatic charge/discharge conditions (Wang and Pilon [2012]).

Experimental Nyquist plots for interfacial double layer at an Au electrode in aqueous 0.5 M H₂SO₄ (Germain *et al.* [2004]) (Figure 4.5.25) can be modeled by the equivalent circuit shown in Figure 4.5.23b.

Measured impedance response often results in Nyquist plots of the form shown in Figure 4.5.26, corresponding to the equivalent circuit shown in Figure 4.5.23c. The impedance of the solution resistance, R_s , and parallel arrangement of the double-layer capacitance and faradaic leakage resistance again add up linearly:

$$Z_{\text{total}} = Z_{R_s} + Z_{RC} = R_s + Z_{RC} \quad (38)$$

where Z_{RC} results from the parallel arrangement of a double-layer capacitance, Z_C , and a faradaic leakage resistance, Z_{RF} :

$$\frac{1}{Z_{RC}} = \frac{1}{Z_R} + \frac{1}{Z_C} \quad (39)$$

Introducing the frequency dependence of Z_C and $Z_R \equiv R_f$, Eq. (39) becomes

$$\frac{1}{Z_{RC}} = \frac{1}{R_f} + j\omega C \quad (40)$$

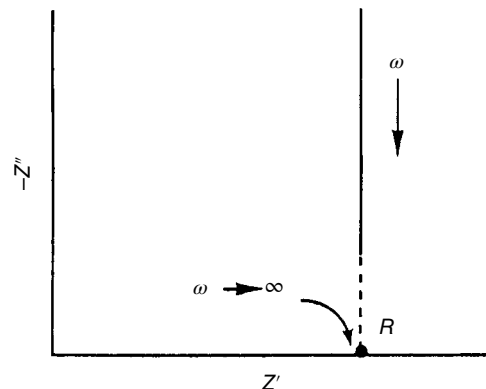


FIGURE 4.5.24 Complex plane or Nyquist plot for the impedance spectrum of a simple series R-C circuit.

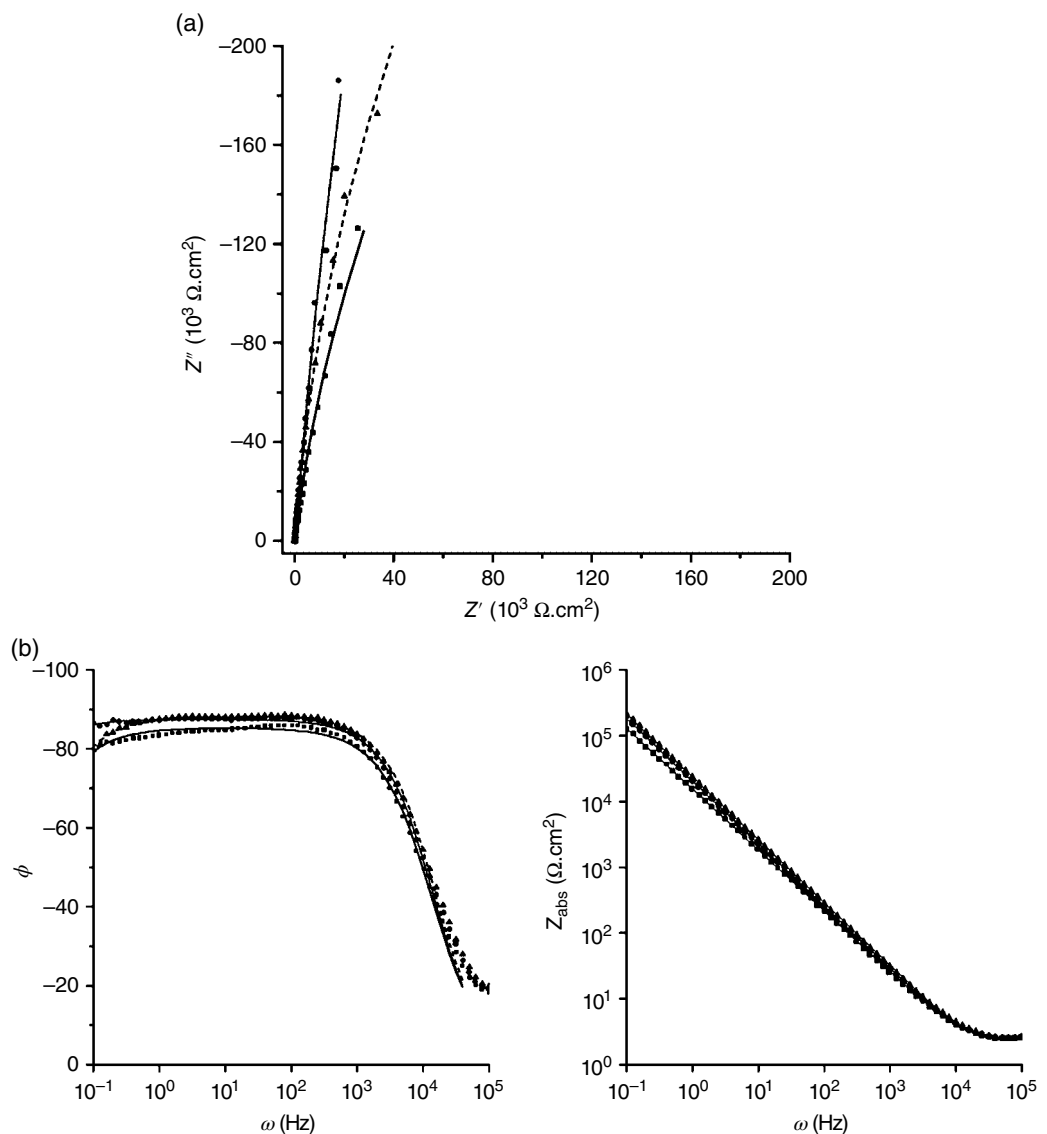


FIGURE 4.5.25 Nyquist (a) and Bode (b) diagrams for the impedance behavior of the double layer at an oxidized gold electrode. Oxide films were formed potentiostatically at 2.20 V for 30 s in 0.5 M HClO_4 at 1.75 V (\blacktriangle), 1.55 V (\bullet), and 1.35 V (\blacksquare). Fitted data to measurements at 1.75 V (---), 1.55 V (···), and 1.35 V (—) are also shown on the figure.

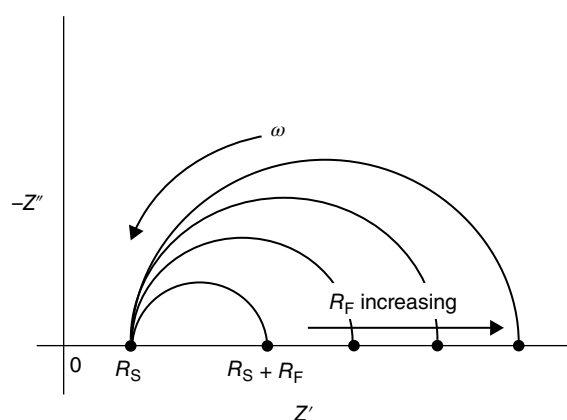


FIGURE 4.5.26 Complex plane or Nyquist plots for the impedance spectrum of a double-layer capacitance in parallel with a potential-dependent (f_v) faradaic resistance, R_f .

$$= \frac{1 + j\omega R_f C}{R_f} \quad (41)$$

In order to separate the real and imaginary components of impedance in this equation, the numerator and denominator are multiplied by the rationalizing complex conjugate of $1 + j\omega R_f C$, namely, $j\omega R_f C - 1$, giving

$$\frac{1}{Z_{RC}} = -\frac{\omega^2 R_f^2 C^2 + 1}{R_f(j\omega R_f C - 1)} \quad (42)$$

so that

$$Z_{RC} = -\frac{j\omega R_f^2 C - R_f}{\omega^2 R_f^2 C^2 + 1} \quad (43)$$

or expanded as

$$Z_{RC} = -\frac{R_f}{\omega^2 R_f^2 C^2 + 1} + \frac{j\omega R_f^2 C}{\omega^2 R_f^2 C^2 + 1} \quad (44)$$

The impedance for the equivalent circuit including solution resistance, R_S , is

$$Z_{total} = \left(R_S + \frac{R_f}{\omega^2 R_f^2 C^2 + 1} \right) - \frac{j\omega R_f^2 C}{\omega^2 R_f^2 C^2 + 1} \quad (45)$$

The first term in parenthesis of Eq. (45) is the real component of impedance, and the second is the imaginary part that is thus separated as a $f(\omega)$ as Z' and Z'' , respectively; these can be plotted against each other in a Nyquist diagram for various values of ω , as shown in Figure 4.5.26. The high-frequency limit of Eq. (45) is R_S and the low-frequency limit is $R_S + R_f$.

The final circuit of the series shown is that in Figure 4.5.23e; its characteristics are that (i) the external capacitor element is directly accessible for input or delivery of charge (except for a possible ESR), that is, it has a small time constant and good localized power density, and (ii) that inner surface regions have double-layer capacitance elements that are accessible only through progressively increasing cumulative resistance down the pores, that is, further into the 3-D porous structure of the electrode. Of course, the real electrical complexity of a PE will depend on the pore size and particle size distributions of the carbon material, a difficult situation to model in a reliable way.

Miller [1992] has been able to model the impedance spectrum and power density (related to the distribution of RC time-constant values) of practical carbon double-layer capacitor devices by a 5-element ladder circuit of C and R elements as illustrated in Figure 4.5.27. The resulting impedance behavior is exemplified in Figure 4.5.28.

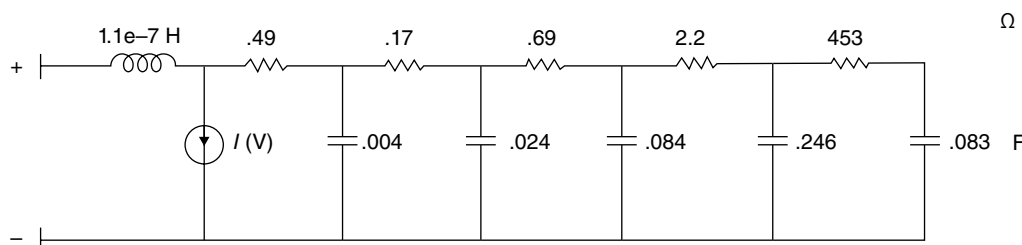


FIGURE 4.5.27 Five-element ladder RC circuit modeling the impedance behavior of a porous, electrochemical capacitor, designed for memory backup. Source: From Miller 1992.

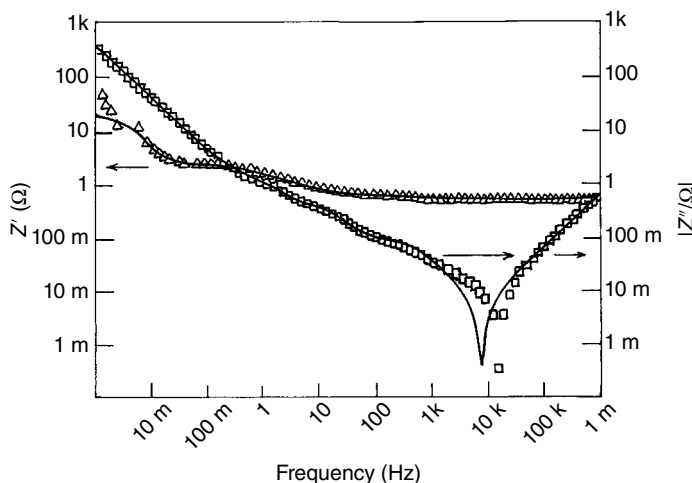


FIGURE 4.5.28 Impedance behavior of the five-element circuit of Figure 4.5.27. Source: From Miller 1992.

Pell *et al.* [1999] examined the behavior of a 5-element circuit made up with series/parallel connections of *hardware* capacitor and resistor elements. They were able to directly demonstrate the nonuniformity of charging of such a network in time (corresponding to the signal “penetration effect” of de Levie [1963, 1964]) and also an interesting internal redistribution of charging of the capacitor elements in time, following a single voltage pulse of short duration. Being a hardware model circuit, potentials at all connections down the ladder circuit could be directly measured as a function of time during the charging pulse and during subsequent open-circuit relaxation (Figure 4.5.29).

The impedance spectra of porous carbon supercapacitor electrodes have a characteristic inflected form (often referred to as a knee) as shown typically in Figure 4.5.30. Three regions can be distinguished in this type of complex plane plot. At relatively high frequencies, a linear relation between $-Z''$ and Z' initially arises having a near 45° slope (for $-Z''$ plotted with the same scale sensitivity as that of Z'), which is characteristic (at such frequencies) of transmission line behavior in distinction to a Warburg 45° phase-angle plot that arises only at low frequencies when a diffusion-controlled process is determining the impedance spectrum. Note that the high-frequency 45° line extrapolates (first region) with respect to $-Z'' \rightarrow 0$ to an intercept on the Z' axis that gives the resistance R_s (ESR) in series with the capacitor device. In well-designed devices including conducting solutions, ESR values for double-layer supercapacitor electrodes can be as low as fractions of milliohms.

Progressing to lower frequencies (second region) in Figure 4.5.30, a knee or smooth inflection arises, going into a (ideal) vertical third region of the complex plane plot in which almost pure capacitive behavior is manifested ($-Z''$ simply increasing according to $1/j\omega C$). Extrapolating the vertical section of the plot in Figure 4.5.30 to zero $-Z''$ gives another intercept on the Z' axis equal to $R_s + \Omega$, where Ω represents an effective internal resistance of the distributed RC network of the PE. Ω is often appreciably larger than the ESR, R_s , and determines, with R_s , the time response and power spectrum of the distributed RC network and thus practical aspects of device performance. Ω can have values up to tens of $m\Omega$ depending on the type of PE material and the electrolyte used in the device. The shape of Figure 4.5.30 was reproduced in the calculated complex plane plots of Keiser *et al.* [1976] for various values of the form factor representing different shapes of pores (Figure 4.5.31).

In some cases, in addition to the classic PE behavior as shown as in Figure 4.5.30, a high-frequency semicircle is observed. This has been attributed to poor electrical contact at the current collector (Fernandez *et al.* [2012], Rangom *et al.* [2015]). Fic *et al.* [2012] showed that impedance studies could offer significant insight into electrolyte selection and optimization of neutral electrolytes for double-layer capacitor devices. The range of frequencies over which electrolyte diffusion-limited capacitor performance was found, not surprisingly, to depend on both concentration and electrolyte identity and rate performance metrics was identified (Fic *et al.* [2012]).

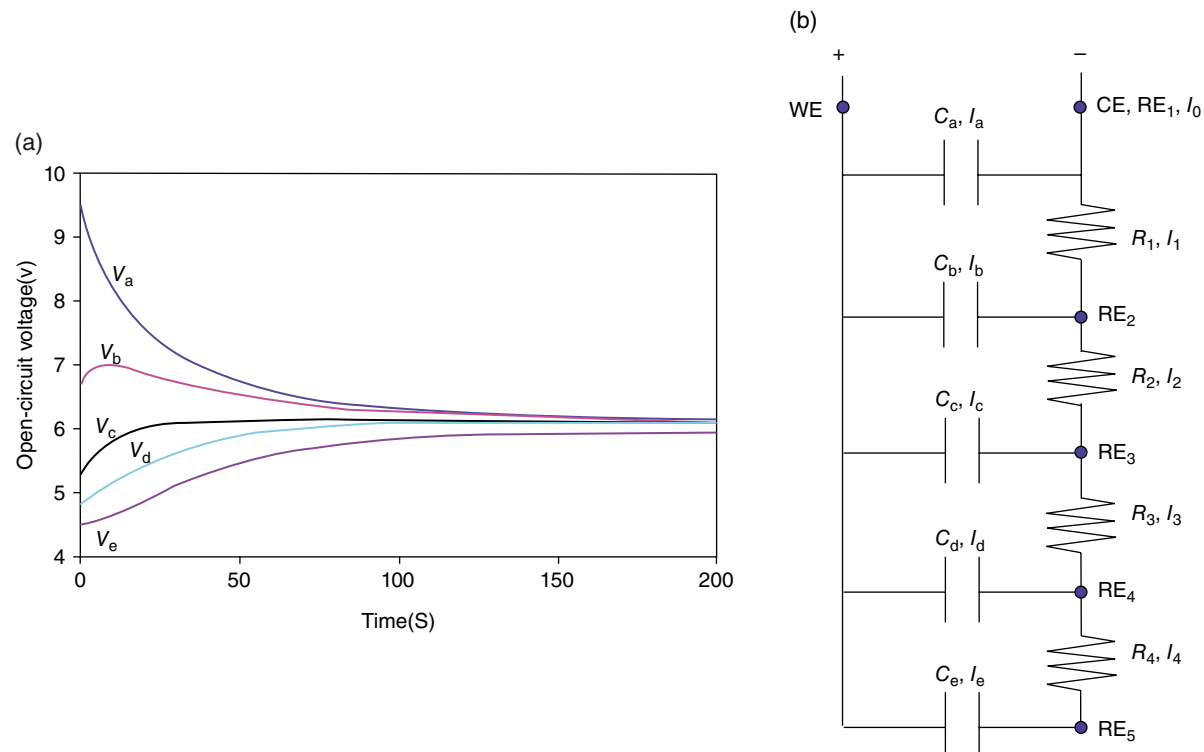


FIGURE 4.5.29 (a) Time-dependent, open-circuit potential (V) behavior of a five-element hardware RC ladder circuit following charging. Source: Pell 1999. Reproduced with permission of Elsevier. (b) Hardware ladder circuit of capacitors C_a , C_b , etc. and resistors R_1 , R_2 , etc. Component currents, I , as indicated. CE, counter electrode; WE, working electrode.

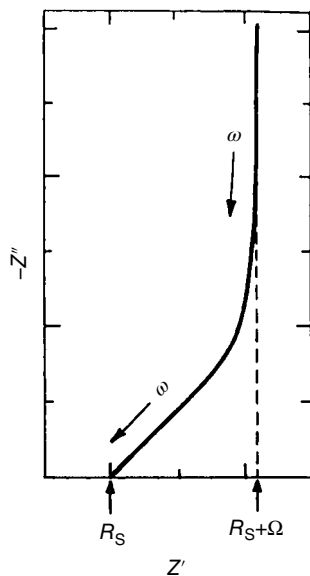


FIGURE 4.5.30 Characteristic form of a complex plane impedance plot for a porous capacitor electrode with series resistance R_s (intercept at $\omega \rightarrow \infty$) and cumulative distributed resistance, Ω .

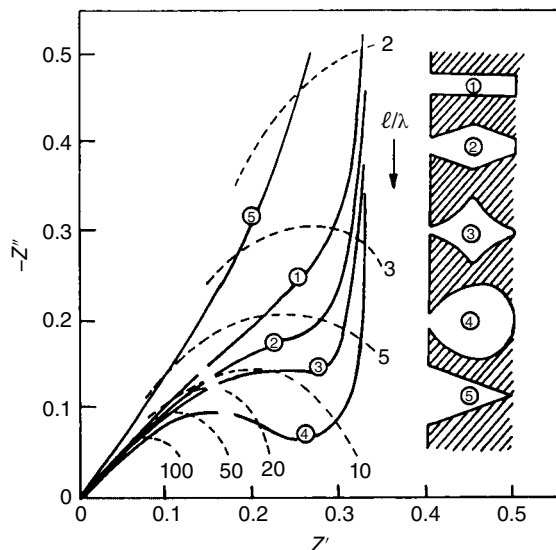


FIGURE 4.5.31 Impedance behavior for a series of pore shapes, as shown in a porous electrode. l is pore length and λ is a form factor. Source: Keiser 1976. Reproduced with permission of Elsevier.

Any discussion of electrochemical capacitors must also address the characterization of capacitors based on pseudocapacitance rather than (or in addition to) double-layer capacitance. Formally, pseudocapacitance of an electrode is recognized when the accepted or delivered charge, q , is faradaic and is a function of potential, V . Then there is a derivative dq/dV , which is a capacitance quantity and can be measured as such, except that the charge originates from a *faradaic* electron transfer process involving a potential-dependent change of oxidation state and sometimes of chemical phase of the surface of the electrode material. In contrast, double-layer capacitor devices involve mainly *non-faradaic* accumulation of charge difference across an interface that is electrostatic (Grahame [1947]), rather than electrochemical, in origin.

Pseudocapacitance can arise in several distinguishable ways that can be summarized as follows:

- From potential dependence of surface coverage by faradaically deposited (i.e., by electrosorption) atomic or radical species, for example, H, OH, or O, at electrode surfaces such as Pt, Rh, Pd, Ru, and Ni. The electrochemical formation of monolayers of H or OH and O requires specific charges of ca. $220 \mu\text{C}/\text{cm}^2$ for H at polycrystalline Pt or $440 \mu\text{C}/\text{cm}^2$ for O species that are passed over potential ranges of ca. 0.35–0.5 V, respectively. This gives average capacitances of ca. $700 \mu\text{F}/\text{cm}^2$ for H or ca. $800 \mu\text{F}/\text{cm}^2$ for O species, for example, at Pt or Au. For H, however, the electrosorption takes place in several peaks, as measured by means of cyclic voltammetry (Will and Knorr [1960]) at polycrystalline Pt and in different specific ways at single-crystal principal index planes. These adsorption pseudocapacitance values are on the order of 10–30 times the double-layer capacity at Pt over the oxide-free and H-free surfaces of Pt. Note, however, that any pseudocapacitance is in parallel configuration to a double-layer capacitance that is always significant at any electrode/solution interface, though it is usually much smaller.
- From potential dependence of the state of oxidation/reduction of redox-electroactive oxide films, for example, at Ru, as RuO_2 , and at other transition metal oxides. The development of redox pseudocapacitance follows formally the same equations as for pseudocapacitance of (Langmuir) chemisorption processes (see Table 4.5.1 for comparative equations). The same

TABLE 4.5.1 Correlation of Types of Systems Giving Rise to Pseudocapacitance with Application to Impedance of Supercapacitors

System type	Essential relations
(a) Redox system $\text{Ox} + ze \rightleftharpoons \text{red}$	$E = E_o + \frac{RT}{zF} \ln \mathfrak{R} / (1 - \mathfrak{R})$ $\mathfrak{R} = [\text{Ox}/([\text{Ox}] + [\text{Red}])]$
(b) Intercalation system Li^+ into "MA ₂ "	$E = E_o + \frac{RT}{zF} \ln X / (1 - X)$ $X = \text{occupancy fraction of layer lattice sites (e.g., for Li}^+ \text{ in TiS}_2\text{)}$
(c) Underpotential deposition $\text{M}^{z+} + \text{S} + ze \rightleftharpoons \text{S.M}$ ($\text{S} \equiv$ surface lattice sites)	$E = E_o + \frac{RT}{zF} \ln \theta / (1 - \theta)$ $\theta = \text{two-dimensional site occupancy fraction}$

Note: (b) and (c) can be regarded as mixing of occupied (X or θ) sites with unoccupied sites, $(1 - \theta)$ or $(1 - X)$, respectively. Also $\theta + (1 - \theta) = 1$ or $X + (1 - X) = 1$.

equations apply to the notional pseudocapacitance arising in a Nernst-type redox reaction in solution, for example, the $[\text{Fe}(\text{CN})_6]^{4-}/[\text{Fe}(\text{CN})_6]^{3-}$ couple at an inert Au electrode where state of oxidation in the couple (\equiv charge) is a thermodynamic function of potential.

- c. From the potential dependence of extents, X , of intercalation of Li into Li-battery layer-oxide or sulfide hosts where pseudocapacitance arises (like for the case of 2-D chemisorption [UPD] referred to earlier) because of potential dependence of extents of quasi-2-D Li^+ ion intercalation into layer lattice host electrode materials. Again, large pseudocapacitances can arise, but, for such systems, the distinction between "battery" and "supercapacitor" behavior becomes nebulous (see Conway [1991] for discussion of this transition situation).
- d. A fourth type of pseudocapacitance behavior arises in the charging and discharging of conducting polymers such as polypyrrole, polythiophene, polyaniline, and their derivatives as reported in much recent literature (e.g., see Gholamian *et al.* [1987], D'Aprano and Leclerc [1993], Rudge *et al.* [1994a, b], Conway [1999]). The charging process can be regarded as a Lewis acid/base oxidation reaction (on positive charge), the extents of which change with potential giving rise to a large pseudocapacitance like that for other surface redox systems. Because the polymer chains acquire electronic conductivity due to conjugation upon charging and then behave as molecular wires, their electrochemical charging behavior has been referred to as equivalent to that of a 1-D double layer with induction of charge analogous to doping of a semiconductor material.

Supercapacitors based on pseudocapacitance suffer "nonideality" of their capacitive behavior, like that of double-layer capacitors, but for two reasons: (i) from the PE effect associated with a distributed resistance/capacitance networks in their equivalent circuits and (ii) because the pseudocapacitance is charged or discharged through a series potential-dependent faradaic reaction resistance, subject to Tafel polarization (cf. Gileadi and Conway [1963]), as illustrated in the equivalent circuit diagram of Figure 4.5.32. Additionally, in the case of adsorption capacitance of anions (Frumkin and Melik-Gaykazyan [1951]), a Warburg diffusional element (Randles [1947, 1952]) (also in series with the pseudocapacitance element) may be required in the case of fast adsorption kinetics, for example, as studied by Kerner and Pajkossy [2002].

The faradaic resistance is associated with finite rates of charging the pseudocapacitance and arises from slowness of the electrochemical changes (e.g., of chemical redox state of transition metal oxides or of deposition of adsorbed H at, say, Pt). Hence there can be a dispersion of the pseudocapacitance with frequency of a modulation signal or of duration of a potentiostatic pulse. Figure 4.5.33 shows the broad range of dispersion of the redox pseudocapacitance of an RuO₂ electrode in aqueous H₂SO₄ at 298 K with AV frequency.

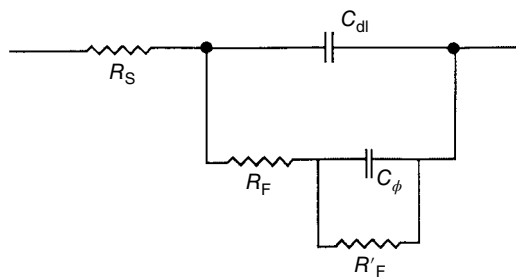


FIGURE 4.5.32 Equivalent circuit for a pseudocapacitance in parallel with a double-layer capacitance through a faradaic resistance, R_F , and a possible leakage resistance, R'_F . R_s is equivalent series resistance.

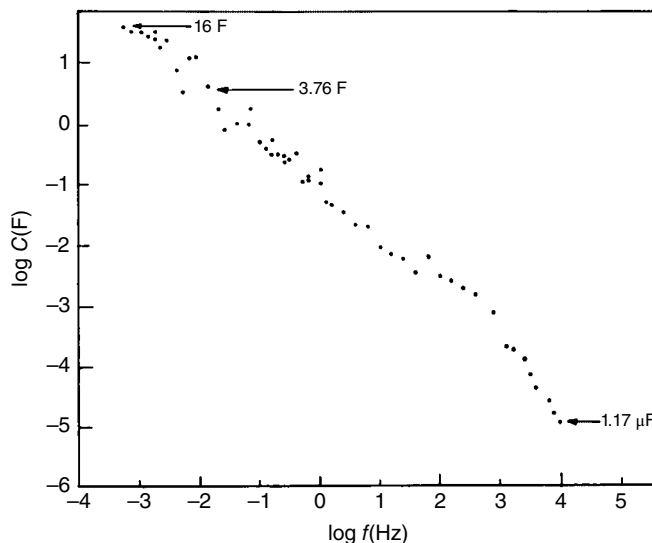


FIGURE 4.5.33 Broad range of dispersion of pseudocapacitance of a porous RuO₂ electrode with frequency. Source: From Miller 1992.

Since the pseudocapacitance element in pseudocapacitor charge storage devices is always in parallel (through the faradaic resistance; Figure 4.5.33) with an interfacial double-layer capacitance, the latter is also subject to the “nonideality effects” associated with electrode interface inhomogeneity and anion adsorption. However, the apparent dispersion associated with finite rates of charging the pseudocapacitance element will usually be much more apparent than that of the double layer itself represented by a CPE. In the case of pseudocapacitance associated with H electrosorption, Frumkin *et al.* [1940a] treated the behavior of Pt electrodes in terms of heterogeneity by considering the electrosorptive charging as taking place through parallel reaction channels having distributed rate constants. The resulting behavior is manifested as a dispersion of measured overall capacitance with frequency.

4.5.3.3 Impedance and Voltammetry Behavior of Brush Electrode Models of Porous Electrodes

Perhaps the most interesting and practically significant aspect of the impedance spectrum of a ladder CR circuit, like that shown in Figure 4.5.23e, is that it exhibits a linear relation between its $-Z''$ and Z'

components with a -45° phase angle at all frequencies. This is the characteristic behavior of a transmission line and was experimentally demonstrated by de Levie [1963, 1964] using a model PE made up, as a brush, from a large number of fine wires in parallel configuration, constrained within a cylindrical tube. This model has anticylindrical, parallel pores and demonstrates (de Levie [1963, 1964]) experimentally a -45° phase-angle behavior over an appreciable range of frequencies (see Figure 4.5.34). Of course, the model pores are linear and of anticylindrical cross section, while pores in a real powder electrode, or an electrode made from unoriented carbon fibers, are of random size and geometry.

Pell and Conway [2001] carried out linear-sweep voltammetry studies at various sweep rates on brush electrodes made from multiple wires of Ag and Au in an inactive electrolyte in order to relate the effects to those of increasing frequency in the de Levie experiments. The purpose of this work was to compare the cyclic voltammetry current response behavior of a brush electrode made from 50 linear and parallel wires (de Levie [1963, 1964]) with that of a free *single* wire of the same metal (Ag) and length over the same range of modulation sweep rates. For the purpose of comparison, the response current profile (for a given sweep rate) was normalized to that of the single wire by dividing by the number (50) of wires in the brush. The resulting comparison is shown in Figure 4.5.35 in which it is clearly seen that the normalized response current profile for a brush electrode is appreciably distorted from the (expected) more rectangular profile observable for the double-layer capacitance at the wire. The distortion has the form, typical in cyclic voltammetry, for the influence of a series iR-drop. In the AV modulation experiment of de Levie [1963, 1964], the distortion effect of progressive iR-drop down the pores of the brush electrode is manifested by transmission line behavior with a 45° phase angle between imaginary and real components of the impedance at all frequencies, resulting in a linear relation in the complex plane plot (Figure 4.5.34). This figure shows plots for three concentrations of the supporting electrolyte, KCl, with intercepts on the Z' axis corresponding to their solution resistances.

The "porous electrode" effects, both in AV and in linear-sweep voltammetry, arise from attenuation of the amplitude of modulation signals down pores having finite resistance, hence progressively increasing iR-drop down the pores. This was referred to by de Levie [1963, 1964] in terms of attenuated "penetration" of the signal down pores, as illustrated for sinusoidal modulation in Figure 4.5.36 in which a reduced scale is used. Closely similar attenuation of the addressing signal amplitude arises in linear-sweep modulation of potential as applied to the brush electrodes in the experiments of Pell and Conway [2001].

A general schematic of Bode-plot type of representation of dispersion of phase angle with frequency for PE impedance is shown in Figure 4.5.37 (de Levie [1963, 1964]). Note the 45° phase-angle values that

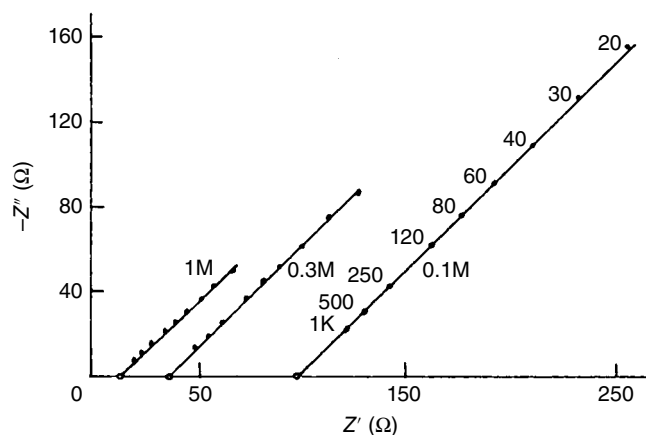


FIGURE 4.5.34 Impedance behavior of the de Levie brush electrode in the complex plane as a function of frequency for three-electrolyte (KCl) concentrations. Source: de Levie 1963, 1964. Reproduced with permission of Elsevier.

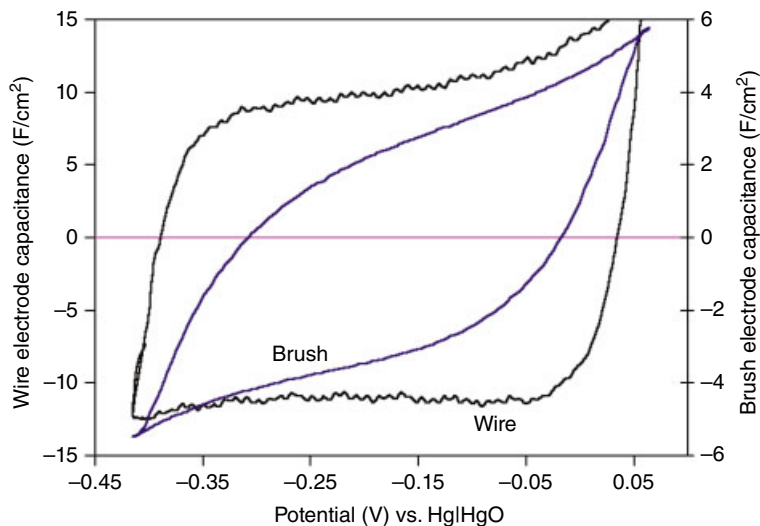


FIGURE 4.5.35 Cyclic voltammogram for a gold-wire brush electrode at 20 mV/s in comparison with that for a single gold-wire electrode on a normalized identical current response scale. Source: Pell 2001. Reproduced with permission of Elsevier.

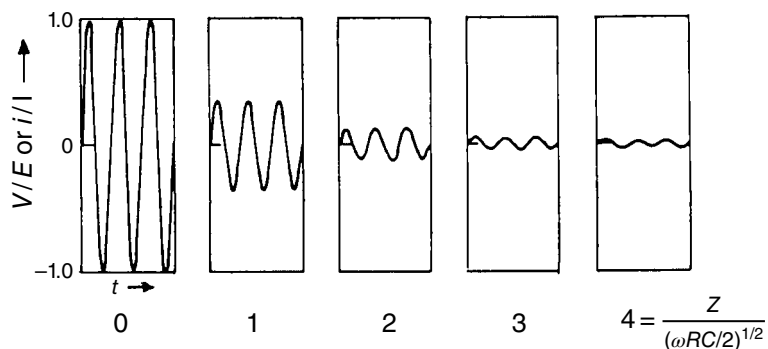


FIGURE 4.5.36 Attenuation of a sinusoidal signal down a pore due to the de Levie signal penetration effect. Dispersions shown for five values of the reduced distance, z , down the pore. Source: de Levie 1963, 1964. Reproduced with permission of Elsevier.

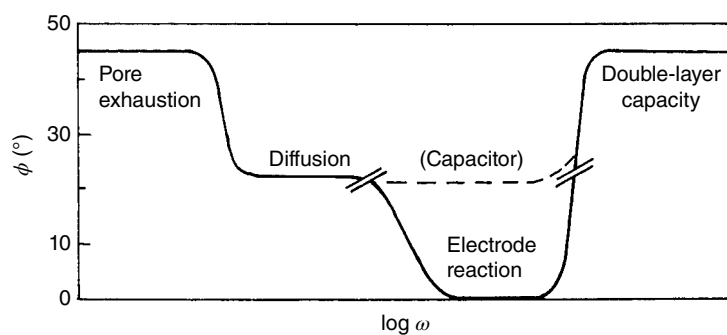


FIGURE 4.5.37 Illustrating dispersion of phase angle of impedance of a porous electrode over a wide range of frequencies, ω , covering various dispersion mechanisms, as indicated, with increasing ω . Source: de Levie 1963, 1964. Reproduced with permission of Elsevier.

arise due to pore exhaustion at low $\log \omega$ and the phase angle of 45° for double-layer capacitance at sufficiently high $\log \omega$.

At this point, it is of interest to relate the current responses that arise in modulation of the double-layer capacitance by liner-sweep voltammetry (cyclic voltammetry) at a sweep rate $s = \pm dV/dt$ comparatively with that by AV.

For voltammetry applied at a capacitance, C , the response current, i , is given by

$$i = \frac{CdV}{dt} \equiv Cs \quad (46)$$

where C may itself be a function of potential V as arises at most metal electrodes and high-specific-area carbon materials. The derived C is i/s and has the nature of a differential capacitance (Grahame [1947]), and s is constant over the selected range of potentials applied with constant *linear variation* in time. In the case of AV modulation, the addressing signal is of course $V = V_o \sin \omega t$ where V_o is the amplitude of the sinusoidal signal. Since, for any capacitance element, the response current to modulation is that given by Eq. (46), then

$$\begin{aligned} i(\text{AV}) &= \frac{Cd(V_o \sin \omega t)}{dt} \\ &= CV_o \omega \cos \omega t \end{aligned} \quad (47)$$

so that $i(\text{AV})$ is out of phase with $V(\text{AV})$ by -90° (Figure 4.5.38). The time-dependent modulation variable is here the frequency ω , which is the analog (Schultze and Koppitz [1976b]) of sweep rate s , and V_o , which is the analog of the potential range of voltage sweep in cyclic voltammetry. Note, of course, that unlike in voltammetry where s is constant (in any one direction of sweep), the sign and magnitude of $\pm dV/dt$ are continuously varying in AV modulation through the half-cycle from 0 to maxima at $\cos \omega t = 1$, that is, twice in the *complete* cycle at 0 and π in the 2π angular cycle.

These types of experiments demonstrate the fundamentally different types of signal response behavior in the impedance of a model or real porous matrix electrode from that of a plane electrode of the same material. Practically, a double-layer type of electrochemical capacitor, based on a high-specific-area carbon material, therefore exhibits a *power spectrum* so that, unlike a plane electrode double-layer capacitance, it exhibits high power performance only for a small fraction of the chargeable area when addressed by short-period pulses or by elevated frequency sinusoidal signals, while a bigger

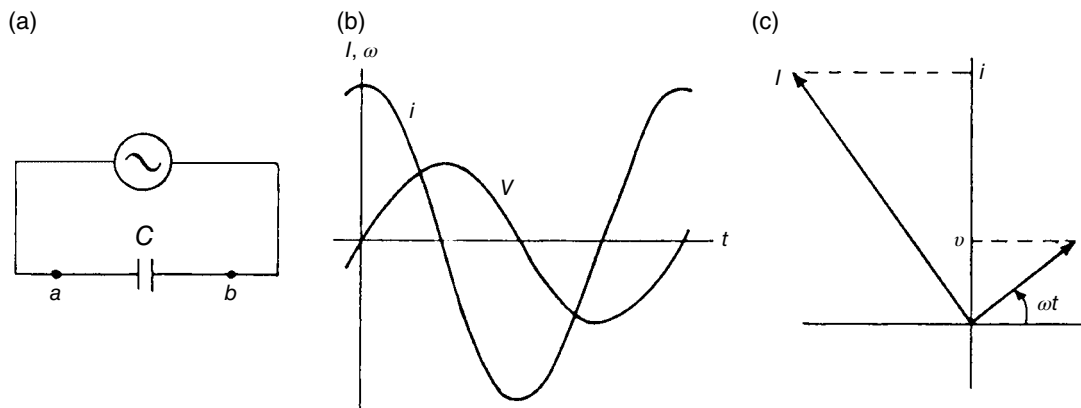


FIGURE 4.5.38 Phase relation between current and voltage for a sinusoidal voltage signal addressed to a simple capacitance element, C , at phase angle -90° . (a) Sinusoidal voltage source. (b) Current, i , versus voltage, V , relation as a function of time, t . (c) Vector diagram for phase relation between i and V .

fraction of the total pore area (inner regions of the electrode matrix) becomes available for charging under longer time pulse modulation or by low-frequency AV. In the dc limit, all of the potential interfacial double-layer capacitance is ultimately available for charging or discharging.

This situation is the origin of the early misapprehension that double-layer supercapacitor devices were capable of operation at very high power densities, like that for a regular capacitor; in fact, it is only some fraction of the rated dc capacitance that is available for rapid charging, therefore at high power densities. This situation is of great importance for performance specifications that have to include data on the operating power spectrum of the device, which will also usually depend on temperature since internal electrolytic resistance is rather sensitive to changes of ambient temperature.

4.5.3.4 Deviations from Ideality

Contrary to the situation at Hg, which provides the ideal smooth electrode surface (notwithstanding thermal fluctuations on the sub-nanoscale), IS studies on the double-layer capacitance at solid electrodes usually (but depending on conditions) show deviations from ideal behavior. Such effects are manifested as a frequency dependence of the capacitance that, on a Nyquist plot, is exhibited by deviations from the expected vertical linear plot of $-Z''$ versus Z' corresponding to frequency dependence of $-Z''$ being simply $1/j\omega C$ (Figure 4.5.30). Such plots, for solid electrodes, show typically a significant slope of $<90^\circ$ from the Z' axis, that is, a systematic deviation from a Z' -independent vertical line; in some cases this deviation shows some curvature away from the $-Z''$ axis in the Nyquist plot. Note that, in earlier years, for example, in the work on double-layer capacitance at Hg in various electrolytes by Grahame [1947], only a single modulation frequency of 1000 Hz was usually employed. This is satisfactory for Hg where little or no dispersion of capacitance arises with frequency but, at other electrodes, a range of frequencies is desirable to characterize the impedance behavior, especially at solid electrodes.

The deviations referred to here and in the literature (Brug *et al.* [1984], Pajkossy [1994]) are mainly of interest in fundamental aspects of electrode interfacial behavior and do not materially influence the performance specifications (and their interpretation) of electrochemical capacitors.

Impedance behavior, corresponding to anomalous capacitance dispersion requiring representation by a CPE, has been examined with respect to a specific form of irregularity or roughness, namely, a surface having fractal, that is, self-similar geometry on various scales, and was treated by Mulder *et al.* [1990] and by Pajkossy [1991].

One of the first observations that ideal capacitance behavior, like that at Hg, is not observed at solid electrodes was given in an analysis by Brug *et al.* [1984]. The anomalous dispersion behavior of capacitance in such cases is manifested as a sloping line, that is, not vertical, in the complex plane plot for the impedance of a series RC situation and a related depression of Nyquist-plot semicircles for a faradaic process involving a reaction kinetic resistance in parallel with the double-layer capacitance element. The deviation from ideal capacitance behavior corresponds to a frequency-dependent phase angle, and the nonideal behavior can be represented by a so-called constant phase element, that is, a complex impedance having the special property that its phase angle is independent of frequency. Such a characteristic behavior seems to have been noted for the first time by Fricke [1932] a long time ago.

This capacitance dispersion at solid electrodes depends strongly on the state of the electrode's surface, for example, its roughness and degree of polycrystallinity, and also importantly on anion adsorption.

The deviations from ideal capacitive behavior can be empirically represented by the so-called constant phase element having the following dependence on frequency and containing the double-layer capacitance quantity, T :

$$Z(\text{CPE}) = \frac{1}{T(j\omega)^\varphi} \quad (48)$$

from which the double-layer capacitance (C_{dl}) itself can be extracted as

$$C_{dl} = \sqrt[\varphi]{\frac{T}{R_s^{(\varphi-1)}}} \quad (49)$$

The parameter φ is related to the phase angle ϕ by $\phi = \varphi(\pi/2)$. The exponent, φ , is <1 , usually in the range 0.9–0.99 depending on the electrode material, its surface preparation, and whether or not adsorbable anions are present in the electrolyte. $\phi \rightarrow 1$ obviously corresponds to true capacitance behavior.

Significantly, Brug *et al.* [1984] noted that the observable nonideal double-layer capacitance, represented by a CPE, is due to inhomogeneity of the electrode surface in such a way that only the value of the capacitance is distributed *along* the electrode surface. Then, it is concluded that the equivalent circuit for the aforementioned situation, with the interface in contact with a homogeneous electrolyte solution, should be represented by a parallel *ladder network* of series C–R elements but not of the kind proposed by de Levie [1963, 1964]] for a 3-D PE having progressively increasing resistance down pores connected cumulatively with C elements (Figure 4.5.23).

The significance of the CPE element and its properties has been definitively and thoroughly discussed in the important papers of Pajkossy [1991, 1994] and of Brug *et al.* [1984]. The smoother and cleaner is the electrode, the closer is the parameter φ to unity.

The deviations from ideal capacitive behavior of the double layer at solid electrodes also become apparent in the IS behavior of electrode reactions at such electrodes where a faradaic resistance is coupled with the capacitance; then, instead of regular semicircular complex plane plots, the Nyquist plots are arcs of semicircles, that is, with centers depressed below the Z' axis.

Physical interpretation of the significance of a required CPE in the response of an RC circuit has been controversial, as explained in Pajkossy [1994]. Theoretical attempts to rationalize capacitance dispersion, as empirically represented by a CPE, can be divided into two groups: (a) the most common explanation, originating from Frumkin's works, is that the dispersion effect originates from microscopic (or nanoscopic) roughness of the electrode metal's surface. Current-density inhomogeneities then arise across the surface so that effects of solution bulk resistance and interfacial capacitance become mutually obscured, leading to inability of the Z' and Z'' components of impedance to be separated. Thus, owing to various forms of roughness, the effective local solution resistance varies along the surface. A related effect in (a) is due to surface inhomogeneity arising from polycrystallinity and resultant faceting.

A second possible explanation (b) is that the capacitance dispersion is entirely of interfacial origin, not involving bulk solution resistance. This effect is associated with anion adsorption, probably coupled with complexity of anion adsorption kinetics (cf. Frumkin and Melik-Gaykazyan [1951], Pajkossy [1994]), at a roughened surface. This conclusion arises because it is found that at a deliberately roughened Pt surface, as studied by Pajkossy [1994], almost ideally capacitive behavior can, in fact, be observed; this is obviously a critical result indicating that it is not inseparable coupling between solution resistance and capacitance at a roughened (Pt) electrode surface (Pajkossy [1994]) that is the origin of dispersion effects. This led (Pajkossy [1994]) to the conclusion that it is ion (anion) adsorption that plays a crucial role in capacitance dispersion, because of frequency-dependent adsorption pseudocapacitance associated with anion chemisorption and associated kinetics of that process (Pajkossy [1994], Pajkossy *et al.* [1996]).

In regard to electrode-roughness effects, it is interesting that Borisova and Ershler [1950] found that capacitance dispersion could be noticeably decreased if the electrode material, Tl, Cd, or Pb, had been melted and allowed to cool down into the form of a droplet, prior to measurements. Thus, Conway *et al.* [1956] found that lead melted in H_2 and allowed to form a drop in a thin glass bulb appeared to be specularly reflective, like Hg.

The results of Scheider [1975] at Au in Cl^- solutions had the form of CPE behavior but were attributed to roughness due to the R–C coupling at the surface. However, it seems that the Cl^- adsorption effect was dominant because of coupling to the roughness factor.

It is to be noted (cf. Brug *et al.* [1984], Pajkossy [1994]) that the roughness-factor effect is really a limiting case of the de Levie PE effect. The impedance spectrum for such systems can have a part that can be approximately modeled by a CPE having the φ parameter equal to 0.5.

From the results of Pajkossy [1994] at Pt in the presence of Cl^- ion, it seems clear that dispersion of the double-layer capacitance is a direct result of Cl^- anion adsorption effects. Similar conclusions arise in the case of Cl^- ion-containing solutions at Au (Pajkossy [1994], Germain *et al.* [2004]). Also to be noted is the fact that in the *oxide region* at Pt, no anomalous dispersion behavior arises despite the possibility of roughness of the oxide film itself. In the presence of extensively formed, anodic oxide films at Pt or Au, Cl^- ion chemisorption (as well as that of HSO_4^- ion) is much diminished although at low O coverages, the surface oxidation of Pt and Au is competitively inhibited (Conway and Novak [1981]).

Interestingly, the capacitance in Cl^- -containing solutions is smaller than in SO_4^{2-} solutions alone and smaller, also, than that for the oxide-film region (Pajkossy [1994]). This is not explicable (cf. Pajkossy [1994]) in terms of simple specific adsorption effects since theories predict an *increase*, rather than a decrease, of capacitance. In these cases, it seems that the double-layer and adsorption pseudocapacitance are coupled in an inseparable way as argued by Delahay [1966] and as pointed out in the studies by Germain *et al.* [2004] in our laboratory in work at Au (cf. Cahan *et al.* [1991]).

Anion adsorption rates have been measured by IS at Au (111) for SO_4^{2-} , Cl^- , Br^- , and I^- . Cl^- ion adsorption is very fast, so the equivalent circuit for the process not only has to include a faradaic pseudocapacitance and its corresponding reaction resistance but also a Warburg element for the anion diffusion (Kerner and Pajkossy [2002]). The interfacial capacitance is then plotted in the Nyquist plane as real versus imaginary capacitance components, C' and C'' , having the form of a semicircle or depressed semicircle, depending on whether (relatively) the diffusion is fast or slow (Pajkossy *et al.* [1996]).

An important conclusion from the paper by Brug *et al.* [1984] is that involvement of a CPE at solid electrodes used for studies of the impedance of faradaic reactions can severely influence the frequency dispersion of interfacial admittance, leading to large errors in the determined faradaic rate parameters. However, those authors note that it is feasible to account for the CPE effect correctly and to check the results of impedance analysis with respect to their internal consistency. The latter can be checked by a KK analysis (cf. Lasia [1999]) that requires, however, detailed frequency-response data. Their approach was supported by experimental impedance studies on proton reduction at single and polycrystalline Au electrodes and on reduction of tris-oxalato-Fe(III) (Brug *et al.* [1984]).

A useful procedure, complementary to plotting real and imaginary components of impedance in the complex plane, is the use of so-called Bode plots (Lasia [1999]). In such representations, the overall impedance vector, Z , in rotating vector diagrams, is related to the corresponding phase angle, ϕ .

The phase angle is the angle between the directions of the real and imaginary components of Z at a given frequency, ω . For a pure capacitor, ϕ is -90° , while for a resistor it is zero. For an RC circuit, it will have some values in between, depending on ω . For a capacitor, in terms of a rotor diagram, the voltage, V_C , *lags behind* the response current by 90° .

Bode plots represent Z and ϕ plotted versus ω , usually over a wide range of ω values, on a logarithmic scale. An advantage of Bode plots, but not to the exclusion of Nyquist plots, is that the impedance behavior at high frequencies is shown with equal weight, along the plot, to that at low frequencies, whereas, in Nyquist plots, high-frequency data tend to become bunched together toward the $\omega \rightarrow \infty$ intercept on the Z' axis. In the phase-angle plot, an approach to pure capacitive behavior at low ω can usually be identified by $\phi \rightarrow -90^\circ$. Deviations from such limiting behavior indicate that the AV response is not purely capacitive so that the behavior has to be modeled in terms of a CPE.

Examples of Bode plots for Z and ϕ are shown in Figure 4.5.25 for interfacial double-layer behavior at an Au electrode in aq. 0.5 M H_2SO_4 (Germain *et al.* [2004]).

Impedance experiments in the case of nonideal behavior have been used as a method for comparison of rate capabilities and performance metrics (Basnayaka *et al.* [2012], Rangom *et al.* [2015]) as well as for evaluating the effects of device aging (German *et al.* [2014]) and temperature (Kotz *et al.* [2006]).

Acknowledgment

Acknowledgment is also made to the Natural Sciences and Engineering Research Council of Canada for support of that work that has led to the present contribution.

4.5.4 Fuel Cells

4.5.4.1 Introduction

General Aspects and Classification of Fuel Cell Systems. Despite their relatively long history, discovered by C. F. Schönbein and invented by W. R. Grove in 1839, as reported by Bossel [2000], fuel cells have attracted much interest during the past 45 years. The need for an efficient, nonpolluting power source for vehicles in urban environments, emphasized by legislative initiatives, has resulted in increased attention to the option of fuel cell-powered vehicles of high efficiency and low emissions. In 2015 Toyota launched the first purchasable fuel cell vehicle (Toyota [2015]). Recently, fuel cells are also used in a variety of new applications like portable devices (e.g., radio communications, mobiles, laptop, etc.), residential applications (combined heat and power generation), and other transport applications (e.g., submarines, ships, rail-guided vehicles, etc.).

Fuel cells can continuously convert the chemical energy of a fuel (hydrogen, methanol, methane, etc.) and an oxidant into electrical energy at up to 70% efficiency with very low pollutant emissions. Depending on the type of electrolyte used in a fuel cell, one can distinguish five main types. The main types of fuel cells are:

- Alkaline fuel cell (AFC)
- Polymer electrolyte membrane fuel cell (PEFC or PEMFC)—also called solid polymer fuel cell (SPFC)
- Phosphoric acid fuel cell (PAFC)
- Molten carbonate fuel cell (MCFC)
- Solid oxide fuel cell (SOFC)

Schematics of these fuel cells are shown in Figure 4.5.39. The two electrodes, cathode and anode, of a fuel cell are porous electrodes in order to increase the reaction area and therefore the current generated. The key technical problems common to all types of fuel cell are the optimal design and stability of these PE and the necessity to increase the three-phase interface between the electrolyte, the gaseous (liquid) reactant, and the electronically conducting catalyst in the electrode. Other research and development (R&D) challenges are the investigation of the reaction mechanism and kinetic at each electrode—

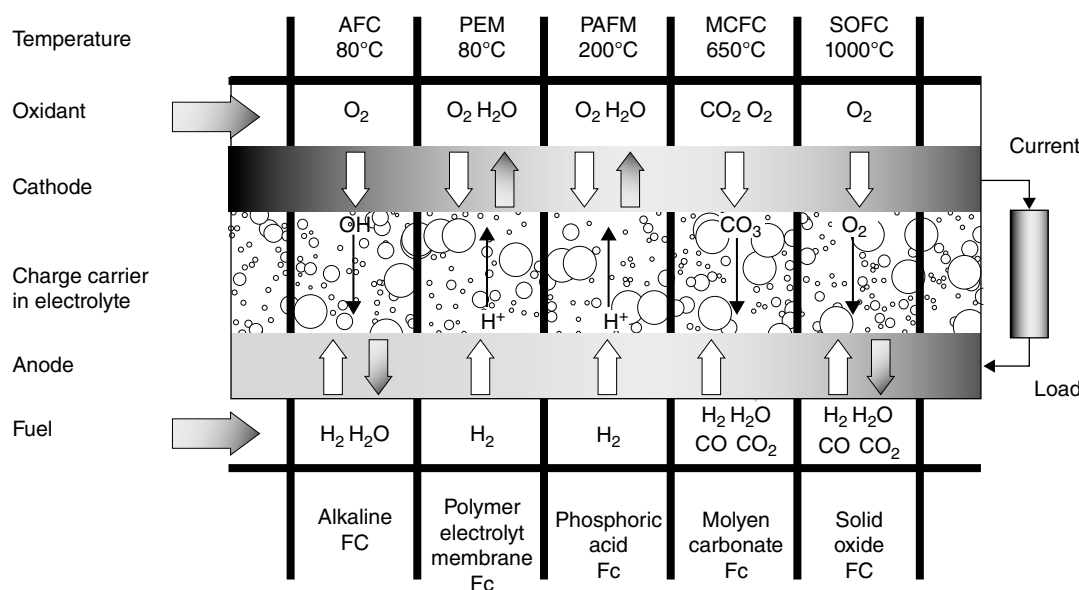


FIGURE 4.5.39 Schematics of main types of fuel cell.

electrolyte interface, determination of degradation (poisoning) mechanism, production of cheap and efficient electrodes with low catalyst loading, development of suitable catalysts, long-term stability, and so on. In order to improve the efficiency of the fuel cell systematically, a better understanding of the electrochemical reactions and mass transport in the fuel cell is essential. Moreover, quality control and understanding of degradation require new nondestructive methods and a better understanding of experimental results based on modeling and simulation. However, EIS is such an *in situ* investigation method and is increasingly applied in fuel cell R&D.

Detailed descriptions of fuel cell technology are extensively presented in several recent monographs by Appleby and Foulkes [1993], Blumen and Mugerwa [1993], Kordesch and Simader [1996], Vielstich *et al.* [2003], Kurzweil [2003], and O’Hayre *et al.* [2009], and a brief description of the main types will be given in Sections 4.5.4.2–4.5.4.4.

Electrochemical Characterization of Fuel Cells: Correlation Between EIS and Current–Voltage Characteristic of Fuel Cells. The performance of a fuel cell depends not only on electrochemical properties of the electrode–electrolyte interfaces and electrolyte but also on the construction of its components such as the gas leads and the gas distributor.

One way to characterize the performance of a fuel cell consists in measuring a steady-state current/potential curve. From such a graph, one obtains information about the entire fuel cell comprising the sum of the electrochemical behavior of the electrode–electrolyte interfaces, conductivity of the electrolyte, the influences of the gas supply, and the electrical contacts between the individual components.

In order to determine current/potential curves, one either scans the whole potential range continuously, beginning from the open-circuit potential (OCP) to full load, with a constant voltage scan rate lying between 0.1 and 10 mV/s and records the resulting current, or gradually alters the potential and the steady-state current being recorded after a definite time period.

One problem with this method is the criteria by which one defines the steady state. Either a distinct time period is fixed after one guesses the principle of the stationarity (second to minute range), or one allows the current to alter over a distinct range in a time unit that should not exceed (e.g., 2 mA in 120 s).

Depending on the criterion used, one gets distinctly different results. If the boundary conditions during the measurement of a steady-state current/potential curve are not known, a comparable statement is not possible. Furthermore, one must consider that a current/potential curve normally is measured beginning from the OCP or full load and then the potential increases or decreases. One switches from a continuous operation point of 500 mV or 700 mV, for instance, to a starting potential of about 1000 mV or 100 mV. Hence it follows that the whole system is suddenly altered after the jump, especially the moisture content of the electrolyte and electrodes. This conditioning potential, different from the potential at which the measurement is made, has a decisive influence on the current/potential curve and the performance of the fuel cell.

Another method to characterize the performance of fuel cells is EIS. EIS was initially applied by Grahame [1947] and later by Delahay [1965] to study the double-layer capacitance and also applied in ac polarography to separate the double-layer charging current from the total current and is now applied to characterize electrode processes and complex interfaces; a review is given by Lasia [1999]. The analysis of the system response yields information about the reactivity and structure of the interface, also about the electrochemical reactions and mass transport limitations taking place there. Its importance recently increased due the modern computer-controlled devices and the corresponding analytical software. With the help of the EIS, it is possible to take measurements without all the external influences, directly *in situ* in a running cell, up to a current of 1000 A (e.g., using the electronic load EL1000 from Zahner-elektrik, Germany). Even after the measurement, the cell can work at the same operation point. The ac response of the fuel cell provides additional information on the investigated system. By the analysis of the impedance spectra, one tries to describe the system-specific physical parameters of the electrochemical setup with an equivalent circuit. Ideally, it is then possible to separate the individual voltage losses of the single components, namely, of the anode, cathode, and electrolyte, and perhaps even to identify diffusion processes to draw conclusions about the limiting processes that determine the performance of the fuel cell.

This powerful technique was first used by Mund [1975] to obtain information about the rate process in the PE of an AFC containing Raney nickel or porous silver and is widely used for the investigation of the reaction kinetic and diffusion phenomena. Springer *et al.* [1996] used a combination of models and experiments to describe the effect of different operation points and cell components on the impedance spectrum and to attribute the lower catalytic activity of the cathode, the conductivity of the catalytic layer, and the decrease of the conductivity of the electrolyte to the low humidity of the airstream.

Furthermore, the individual reaction steps (e.g., oxygen reduction reaction (ORR) and hydrogen oxidation reaction (HOR)) in a fuel cell still were investigated. Arico *et al.* [1996] as well as Holze and Vielstich [1984] used this technique to investigate the ORR in H_2SO_4 in addition to neutral and alkaline environments and concluded that the cathodic overpotential is primarily due to the slow diffusion of oxygen and its reaction products. With measurements over the entire performance range of hydrogen/oxygen, one tries to separate the single contributions to the performance loss of a fuel cell during load or even at OCP.

Theory of the Conversion of Resistance to an Overpotential. The correlation between impedance measurements and current/potential curve was first described by Wagner [2002] and is represented schematically in Figures 4.5.40 and 4.5.41.

The polarization resistance of the cell measured at U_n corresponds to the tangent to the current/potential curve at that potential. The polarization resistance of the cell (R_{Cell}) is the impedance at frequencies near 0 Hz where only ohmic parts attract attention. To obtain the polarization resistance of the cell, one have to extrapolate the simulated impedance (model) at very low frequency (e.g., 1 nHz) or summing up the individual resistances, obtained after fitting the measured spectra with an equivalent circuit.

Assuming that the current/potential curve can be expressed by an Eq. (50) of second order and the resistance is defined by Eq. (51), then the parameters a_n , b_n , and c_n from Eq. (50) are given by Eqs. (52)–(54):

$$U_n = a_n I_n^2 + b_n I_n + c_n \quad (50)$$

$$R_n = \frac{\partial U}{\partial I} \Big|_n \quad (51)$$

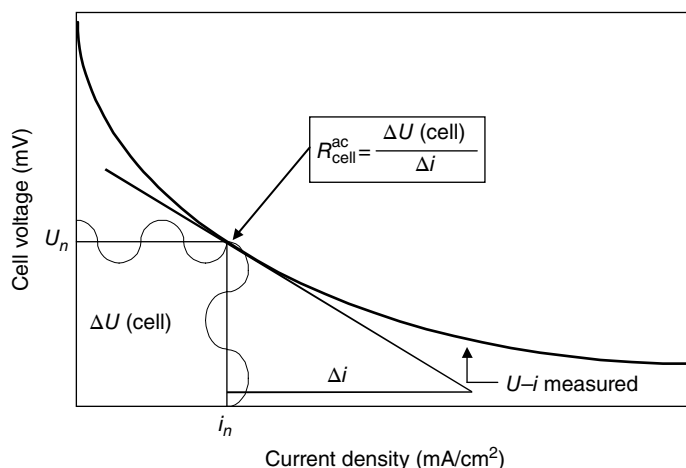


FIGURE 4.5.40 Schematic representation of the correlation between impedance of fuel cell and current–voltage curve.
Source: Wagner 2002. Reprinted with permission of Springer.

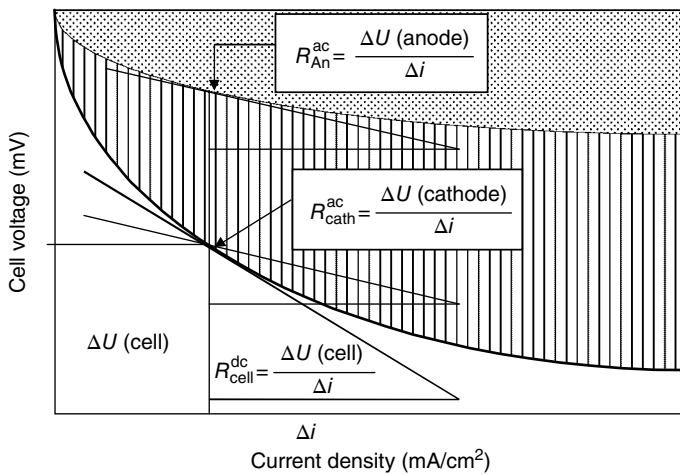


FIGURE 4.5.41 Schematic representation of the correlation between polarization resistances (anode, cathode, and cell) of fuel cell and current–voltage curve.

with

$$a_n = \frac{R_{n+1} - R_n}{2(I_{n+1} - I_n)} \quad (52)$$

$$b_n = R_{n+1} - 2a_n I_{n+1} \quad (53)$$

$$c_n = U_{n-1} - a_n I_{n-1}^2 - b_n I_{n-1} \quad (54)$$

This method was applied successfully to determine the different individual contributions—representing different reaction steps—to the overall overvoltage in the case of a PEFC. An example is given in Section 4.5.4.3.

Theory of Time-Resolved Electrochemical Impedance Spectroscopy (TREIS). A prerequisite for the development and the improvement of fuel cells is the knowledge of the mechanistic processes that take place during operation. The understanding of the kinetic behavior of the fuel cells requires the variation of different experimental parameters. Often, the variation of distinct parameters causes situations where steady-state conditions are no longer fulfilled. In practice EIS analysis often suffers from the fact that the steady-state condition is violated due to time instability of the examined systems. While an EIS measurement is running, the examined system should not change its dynamic behavior. Unfortunately, the violation of steady-state conditions complicates the evaluation of experimentally obtained impedance spectra because all relevant physical models for the interpretation of the data are based on steady-state conditions. The time- and frequency-dependent relationship between current and voltage of an electrochemical system is often called “two-pole impedance transfer function” (TTF). All properties, which are influencing the current–voltage dependence, must be stable in this time interval. Otherwise the TTF will be falsified in a way that is equivalent to a violation of causality.

Nevertheless it is possible to investigate such “drifting” systems and to obtain relevant data for the development of fuel cells using EIS. Enhanced numerical procedures are required to compensate or to eliminate the drift effects of systems with states that change with time.

Causal Transfer Functions. Valid transfer functions H in accordance to the causality rule are complex functions of the angular frequency ω and may be separated into real and imaginary components $R(\omega)$ and $X(\omega)$:

$$H(j\omega) = R(\omega) + jX(\omega) \quad (55)$$

If the transfer function H is in accordance with the causality rule, the components R and X are no longer independent of each other. Causality in the meaning of systems theory forces couplings between the real and imaginary part, which are known as KK relations (KKT) or Hilbert relations (HT); for details see Section 3.1.2.9 (the use of KKT).

These relations offer the possibility to examine measured transfer functions (impedance spectra) on errors caused by time instability or time drift. KK-checking techniques have fundamental problems in their application on practical measurements. Therefore many attempts have been made to overcome these limitations by means of different interpolation procedures. An attempt is the Z-HIT approximation, applied by Schiller *et al.* [2001], Agarwal *et al.* [1995], and Ehm *et al.* [2000], an approximation formula for the calculation of the impedance modulus course from the phase angle by integration.

During operation of fuel cells different time-dependent effects can occur, depending on the type of fuel cell and experimental conditions like gas flow rates (flooding of the electrode, changing of the gas composition), temperature (corrosion or sintering), impurities in the hydrogen (CO) leading to poisoning of the anode in the case of PEFC, degradation of the electrodes during long time of operation, and so on.

One has to assume that the system changes its state not only between two measurements but also during the recording of a single spectrum. The latter fact causes problems for the evaluation of the spectrum, because the recording of an impedance spectrum one frequency after each other requires a finite time, while the measurement at high frequencies requires less time than the measurement at low frequencies. Due to the fact that the recording of a single spectrum in the frequency range, for example, from 10 kHz to 50 mHz, requires about 20 min, the influence of the changed state on the measured spectrum is not negligible. For this reason, one of the fundamental prerequisites for the evaluation of impedance measurements is violated. Nevertheless it is possible to reconstruct "quasi-steady-state" (and therefore "quasi-causal") spectra from drift-affected impedance data using *improved evaluation techniques* that are denoted as the real-time drift compensation, the time course interpolation, and the Z-HIT refinement. These techniques were applied successfully to the interpretation of time-dependent impedance spectra of a fuel cell that exhibits non-steady-state behavior (Figure 4.5.42).

Real-Time Drift Compensation. During recording of an impedance spectrum, a potential drift due to changing of the state of the system can occur. The magnitude of drift is frequency dependent and should be compensated by software during the measurement.

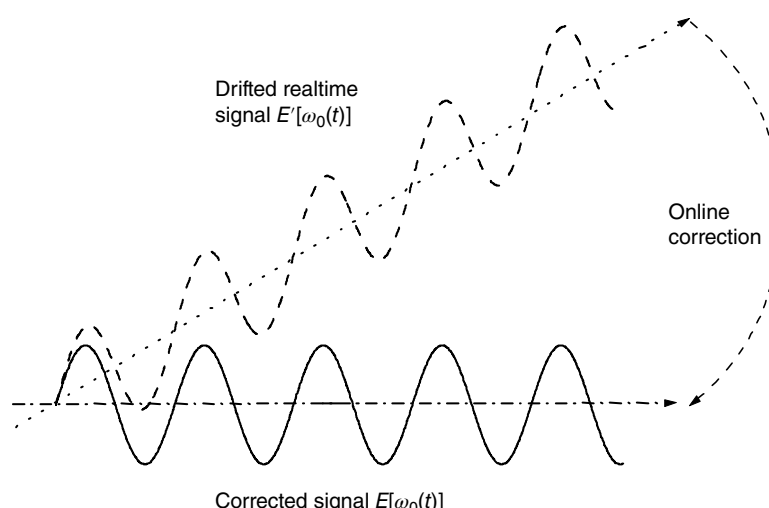


FIGURE 4.5.42 Schematic representation of real-time drift compensation during impedance spectrum measurement.

Time Course Interpolation. Recording an impedance spectrum one frequency after each other requires a finite time, while the measurement at high frequencies requires less time than the measurement at low frequencies. As a consequence, the system at the start is in another state than at the end if the system changes the state during the impedance measurement.

It is impossible to eliminate the drift that is caused by the finite measuring time, performing only a single spectrum. Especially the data recorded at low frequencies are affected, and a mathematical procedure has to be applied to check the data with respect of causality and linearity (Z-HIT) to avoid erroneous interpretations resulting from a fit of the drift-affected data.

According to the idea of Savova-Stoynov and Stoynov [1985, 1992] and Stoynov [1990], recording of a series of impedance measurements at distinct time intervals offers the possibility to eliminate the drift and therefore to reconstruct an impedance spectrum that is acquired in an “infinite” short time. The time course interpolation procedure is schematically depicted in Figure 4.5.43 and outlined in the following. In Figure 4.5.43, the primarily recorded impedance data as well as the reconstructed set of different measurements of the series are plotted against the frequency. Additionally, the elapsed time of the experiment is involved as a third parameter. As mentioned earlier, the measurement at lower frequencies requires a longer time for the registration, and therefore, the measured curve is shifted to the back along the time axes. It should be noted that the absolute value of the shift is frequency dependent because the acquisition time for each measured frequency is different. As indicated in Figure 4.5.43 for the lowest frequency, a single impedance spectrum can be reconstructed by interpolating the impedance value from the time course of the series using an appropriate smoothing function at the time of the start of this distinct measurement. The interpolation procedure is repeated for each measured frequency, resulting in a data set where the effect of finite measurement time is significantly reduced or even eliminated for each recorded spectrum of the series.

Applying all three techniques to time drifting systems, quasi-steady-state impedance spectra at defined times can be obtained, TREIS. In Figure 4.5.44, for illustration, an EIS recorded at the PEFC with flooded cathode, after 4450 s of “dead-end” operation at 2 A, is given (for details see Section 4.5.4.3).

Cylindrical Porous Electrode Model. In electrocatalysis, in catalysis general, there is a great interest in increasing the real surface area, especially the electrochemical active area of electrodes. In such cases PE are used. First investigations of PE with EIS were applied by de Levie (for details see Section 2.1.6.2), presenting a model describing the pores of a PE as essentially circular cylindrical channels of uniform

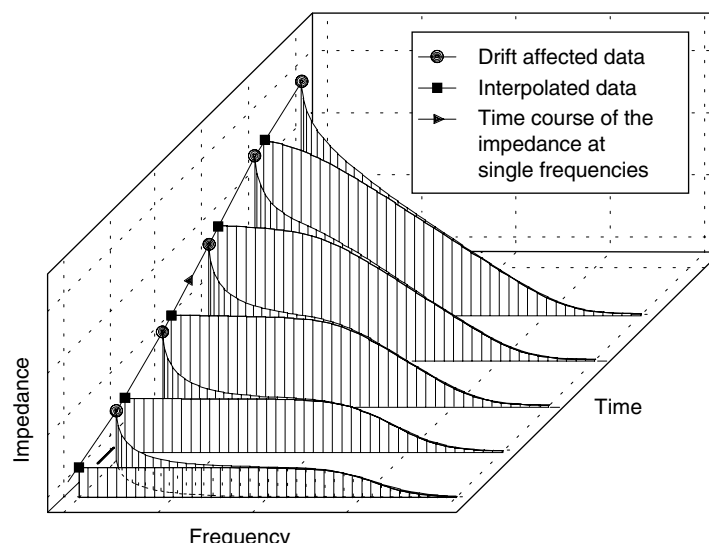


FIGURE 4.5.43 Schematic representation of time course interpolation.

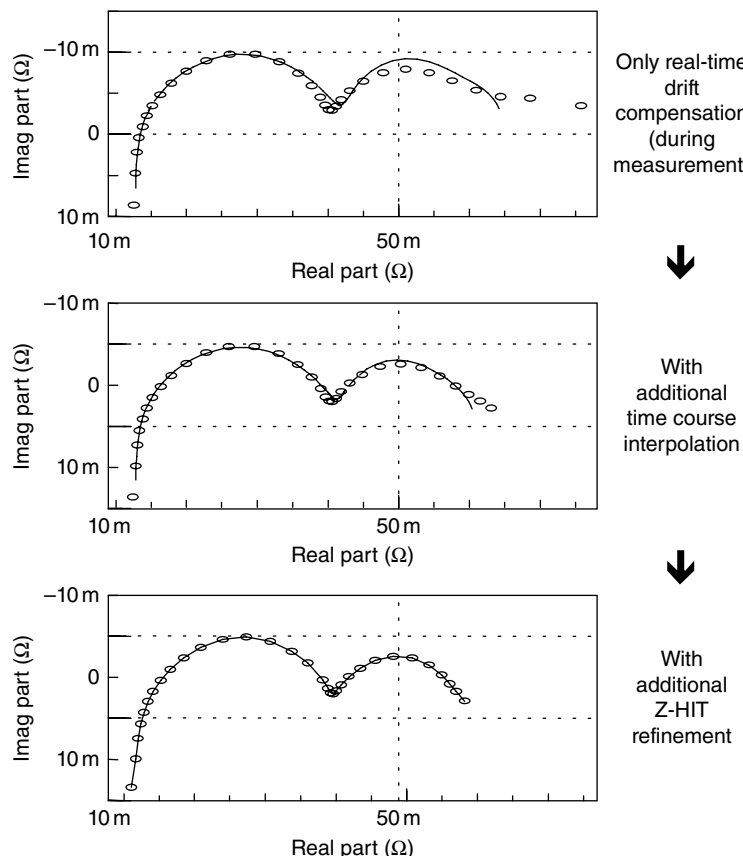


FIGURE 4.5.44 Nyquist plot of a representative example of the series, recorded during flooding the cathode of a PEFC, after 4450 s of “dead-end” galvanostatic operation at 2 A.

diameter and of semi-infinite length. Based on ac impedance measurements, applied for the investigation of porous lead electrodes in sulfuric acid, Göhr *et al.* [1983] and Göhr [1997] proposed another model of the PE. This model, schematically represented in Figure 4.5.45, is integrated in the simulation and evaluation program Thales (Zahner-elektrik, Kronach, Germany). In this model the cylindrical pore is considered as a transmission line made of a large number of infinitesimally thin sections, with impedance elements of pore’s ground surface (Z_n), pore’s electrolyte (Z_p), pore’s wall surface (Z_q), porous layer (Z_s), and surface layer (Z_o). The basic equations for the impedance of a PE are given in Table 4.5.2.

A review describing gas diffusion electrodes (GDE) and flooded electrodes is given by Szpak [1991]. The great number of very interesting publications, regarding ac impedance measurements on PE and model electrodes—not referred here—known in the literature, shows the importance and wide applications of the method, from porous layers to fuel cell electrodes.

Impedance Spectra with Inductive Behavior at Low Frequencies (Relaxation Impedance). Based on the concept of impedance elements, Göhr and Schiller [1986] described the faradaic impedances as connections of impedance elements, each of which is associated with a single process. One of such an impedance element is the relaxation impedance describing the surface relaxation of the interface and explains the development of the pseudo-inductive behavior in the low-frequency range (frequency < 3 Hz) in the impedance spectra of the fuel cell. This behavior was first found by Müller *et al.* [1999b] during poisoning of the anode of a PEFC with a mixture of H₂/CO and will be discussed in detail in Section 4.5.4.3. The surface relaxation impedance represents a faradaic impedance (Z_F) at nonequilibrium potential with a

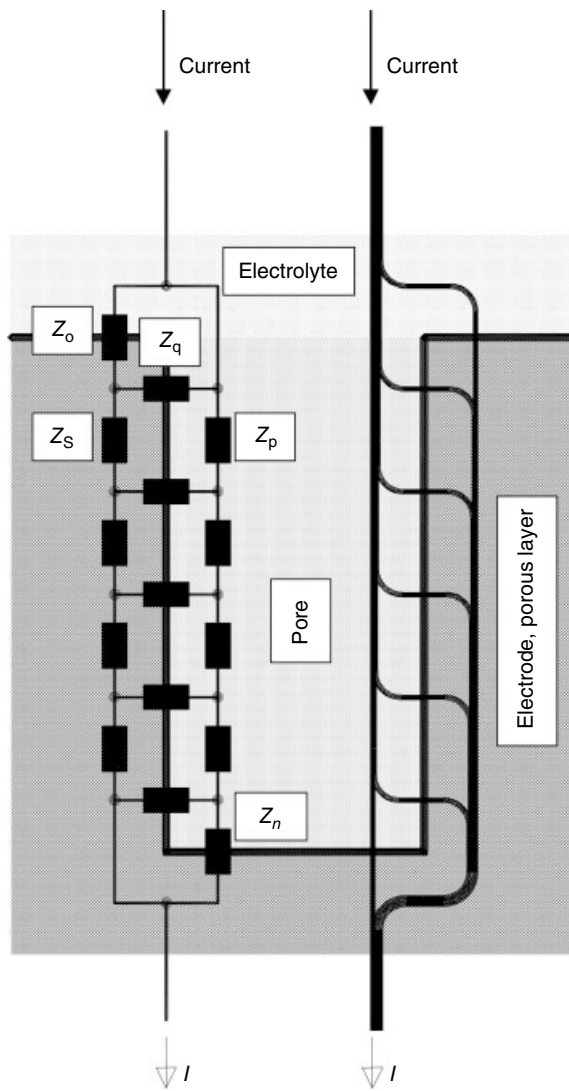


FIGURE 4.5.45 One-dimensional network distributed homogeneous cylindrical porous electrode model after Gehr [1997].

TABLE 4.5.2 Basic Equations for the Impedance Z of a Porous Electrode with Cylindrical Pores

$Z^* = \sqrt{(Z_p + Z_s) \cdot Z_q}$	$Z = \frac{Z_p \cdot Z_s}{(Z_p + Z_s)}$
$C = \cosh\left(\frac{Z_p + Z_s}{Z^*}\right)$	$S = \sinh\left(\frac{Z_p + Z_s}{Z^*}\right)$
$p = \frac{Z_p}{Z_p + Z_s}$	$q_o = \frac{Z^*}{Z_o}$
$q_n = \frac{Z^*}{Z_n}$	$s = \frac{Z_s}{Z_p + Z_s} = 1 - p$
$Z = Z + Z^* \cdot \frac{C + (1-C) \cdot 2 \cdot p \cdot s + S \cdot (p^2 \cdot q_n + s^2 \cdot q_o)}{S \cdot (1 + q_n \cdot q_o) + C \cdot (q_n + q_o)}$	

Source: Gehr 1997. Reproduced with permission of Zahner Scientific Instruments.

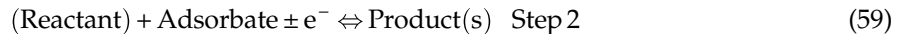
potential-dependent transfer reaction rate, $k = k(\varepsilon)$, and its time-dependent relaxation according to Eqs. (56) and (57):

$$Z_F = \frac{R_{ct}}{1 + (R_{ct}/Z_K)} \quad (56)$$

$$Z_K = \frac{1 + j\omega\tau_K}{I_F \cdot (d \ln k / d\varepsilon)} \text{ with} \\ R_K = \frac{1}{I_F \cdot (d \ln k / d\varepsilon)} \text{ and } X_K = j\omega\tau_K \cdot R_K = j\omega \cdot L_K \quad (57)$$

In Eq. (56) R_{ct} denotes the charge transfer resistance, and Z_K is defined as the relaxation impedance and is schematically shown as series combination of R_K and L_K as well as the box surrounding R_{ct} in Figure 4.5.46, according to Eq. (57), where I_F denotes the Faraday current, τ_K is the time constant of relaxation, and the expression $d \ln k / d\varepsilon$ is the first derivative of the logarithm of the reciprocal relaxation time constant ($k = 1 / \tau_K$) against the potential ε . According to its frequency dependence, Z_K can be split up into the relaxation resistance R_K and the relaxation inductivity X_K , with the pseudo-inductance $L_K = \tau_K - R_K$, which is proportional to the relaxation time constant τ_K (Figure 4.5.46).

Inductive behavior in the low-frequency range of impedance spectra was also observed in systems in which a reaction consisting of two successive electron transfer steps proceed by an adsorbed intermediate species:



This mechanism was proposed by Diard *et al.* [1992] to evaluate EIS for cathodic production of hydrogen by the metallic electrodeposition reaction and anodic oxidation reaction of metals (e.g., iron) close to their corrosion potentials. A similar mechanism was found by Rerolle and Wiart [1996] studying the oxygen evolution during zinc electrowinning (Figure 4.5.47).

Impedance of Fuel Cell Stacks. Given by the more stringent regulations on emissions and fuel economy, global warming, and constraints on energy resources, fuel cells have attracted more and more attention by automakers, governments, and customers. In the last years R&D efforts have been focused on developing novel concepts and low-cost systems on technology readiness level (TRL) higher than 5 (technology development) including fuel cell stacks and subsystems for different applications like electric vehicles and stationary applications (primary and backup power). Fuel cell technology is moving now closer to a commercial breakthrough; methods to measure the “state of health” of operating stacks are becoming of increasing interest. This requires application of advanced methods for detailed electrical and electrochemical characterization during operation. One of the most promising and appropriate method is EIS. There are two ways to increase the power output of a stack: one way is to increase the cell surface (current) and the other is to increase the number of cells (voltage), the repeating units

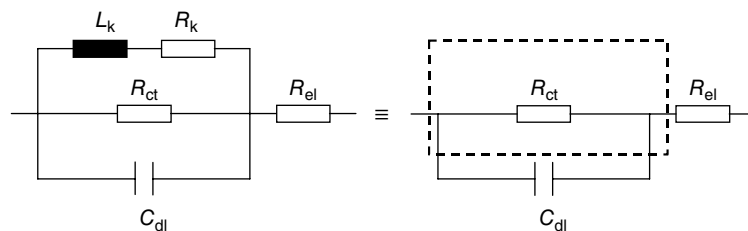


FIGURE 4.5.46 Equivalent circuit with relaxation impedance (Z_K).

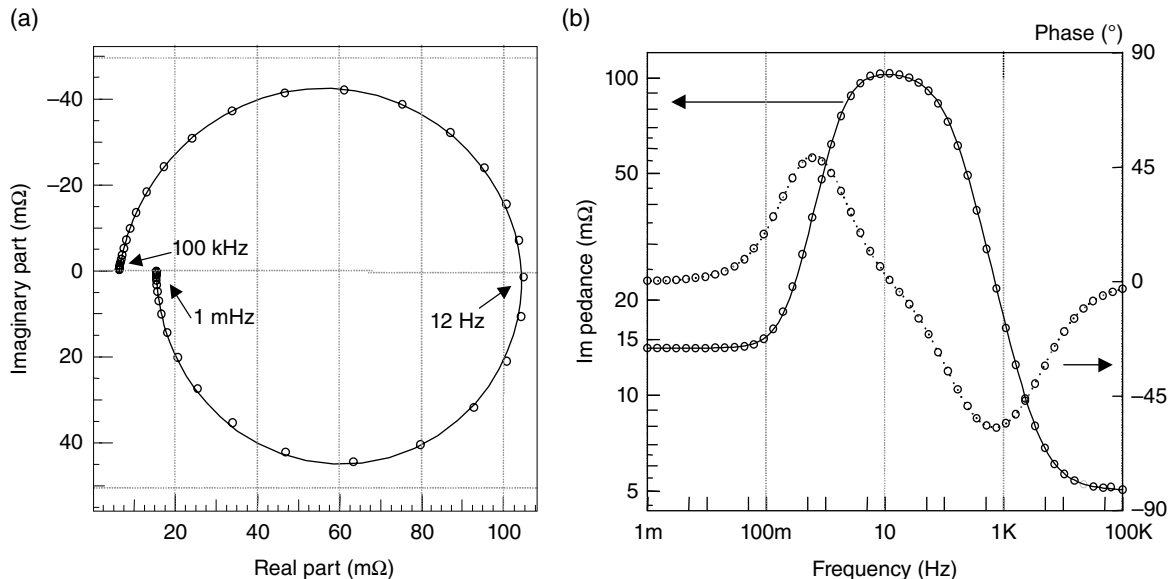


FIGURE 4.5.47 Impedance spectrum simulated with equivalent circuit from Figure 4.5.46. $\tau_K = 1$ s, $R_K = 10$ mΩ, $R_{ct} = 100$ mΩ, $C_{dl} = 10$ mF and $R_{el} = 5$ mΩ, represented as (a) Nyquist plot and as (b) Bode plot.

of the stack. These increases lead to gradients (current density distribution) on cell (surface) and stack level, both inducing an accelerated degradation of the stack. The current density distribution can be measured using a segmented cell, as proposed by Knöri and Wagner [2004] using a system consisting of an electronic current sink and an electrochemical workstation fitted with a device that enables the determination of 16 partial impedances or current densities within the overall system. The anodic flow field of the fuel cell is divided into an array of 4×4 square segments (1.54 cm^2 for each segment), while the cathodic one is not segmented and can have any design. First spatially resolved impedance measurements using a segmented cell with 7×7 segments were shown by Hogarth *et al.* [2007]. Spatially resolved (local) EIS or EIS measurements of single cells in a fuel cell can be done, depending on the used cell and measurement setup in two ways: *the sequential* way measures one segment or one cell from the stack one after one and has the advantage of unsophisticated equipment shown schematically in Figure 4.5.48 but is time consuming, in particular for EIS down to low frequencies. The fuel cell assembly is kept under load using a power potentiostat (PP), which can manage a total current of up to ± 40 A. The electrical connection between the PP and the fuel cell is realized by a multiplexer (PMUX—bottom), which divides the current feeding and sensing lines into 16 individual parallel segments. In addition, the PMUX enables the electrical switching off of an individual segment from the PP as well as it performs an electrical connection of this segment to an impedance measurement. The long measuring time can be inopportune for fuel cells with time changing state, for example, during fuel starvation, poisoning of anode, or water flooding of PEFC cathode. A sequential EIS setup using a homemade rotary switch unit was published by Yuan *et al.* [2006].

The second way is the *parallel* way where EIS measurements are performed simultaneously. This mode of operation is much faster as shown schematically in Figure 4.5.49; the measuring time corresponds to the measuring time of one spectra but requires a more sophisticated measurement equipment, for example, using FRA with multichannel extensions or parallel analog-digital (PAD) converter implemented by Zahner [2015] and schematically shown in Figure 4.5.50.

The synchronous parallel approach was used for EIS measurements on an SOFC short stack with five cells. The impedance response of the five individual cells is represented in Figure 4.5.51. From this figure one can see that the impedance response of the individual cells is different; the greatest difference is found at the first and last cell of the stack (cell 1 and cell 5). This finding emphasizes the need of local

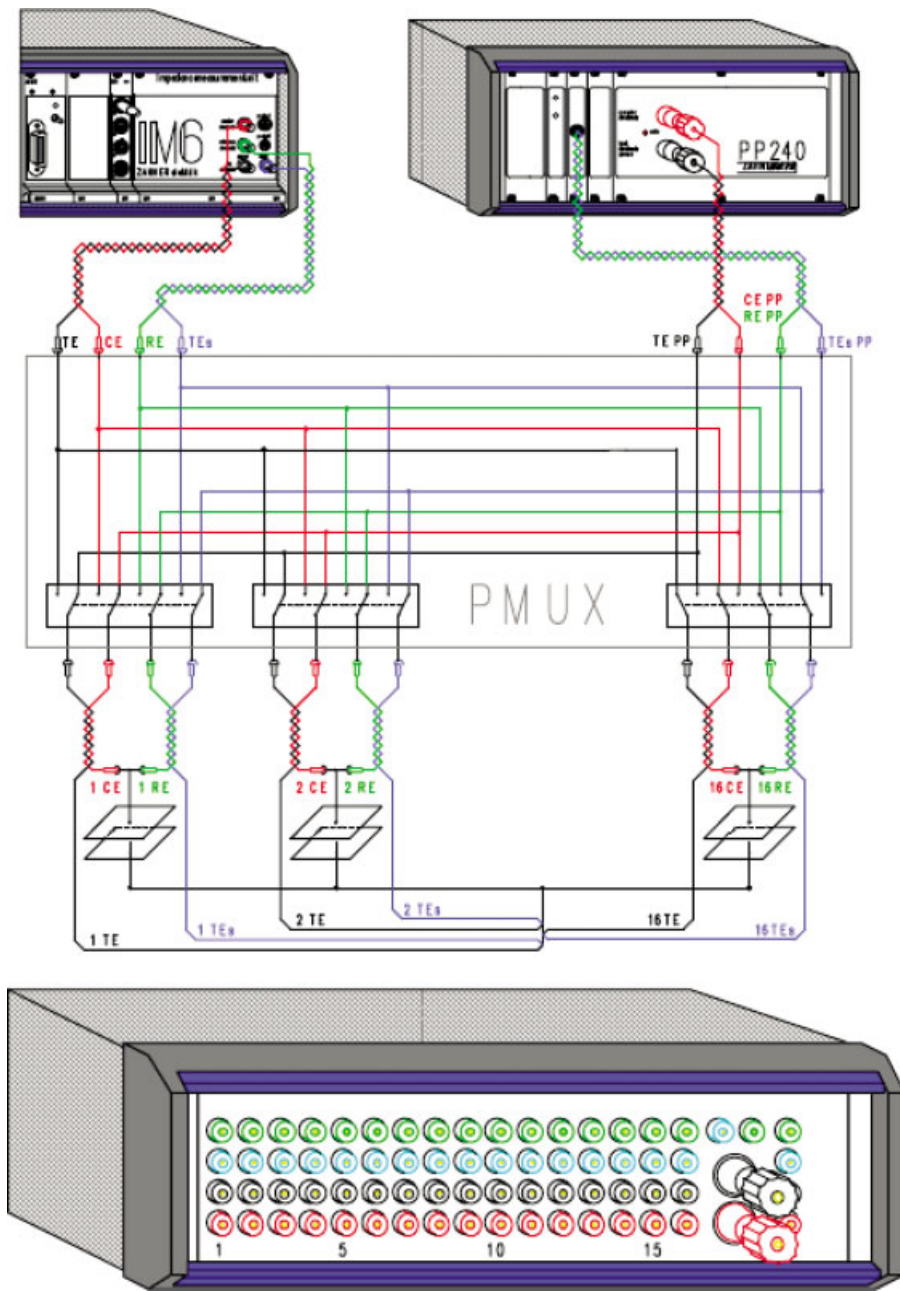


FIGURE 4.5.48 Equipment for the investigation of the local impedance distribution of a fuel cell in the sequential mode using a power multiplexer (PMUX).

resolved and individual cell EIS measurements of a fuel cell stack. These measurements can be used to establish the optimal operation condition (temperature, fuel concentration, humidification, flow rate, etc.), configuration, and design of cell hardware (electrode area, number of cells, geometry of flow field, position of cooling/heating units, etc.).

A detailed comparison of the two measurement principles applied for SOFC stack characterization is given by Mosbaek [2014]. He used a sequential and a parallel measurement setup for acquisition of impedance measurements. From the sequential to the parallel measurement setup, the acquisition time was cut down significantly, and it was demonstrated that the parallel acquisition of 16 repeating units

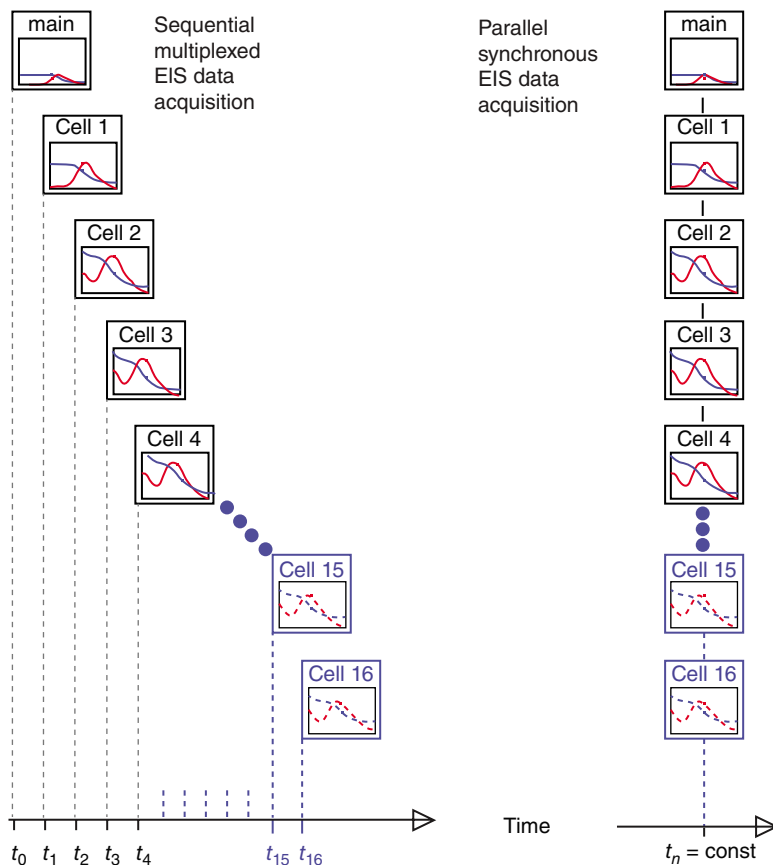


FIGURE 4.5.49 Comparison of the sequential measurement principle for impedance spectra data acquisition (on the left) with the synchronous parallel approach (on the right).

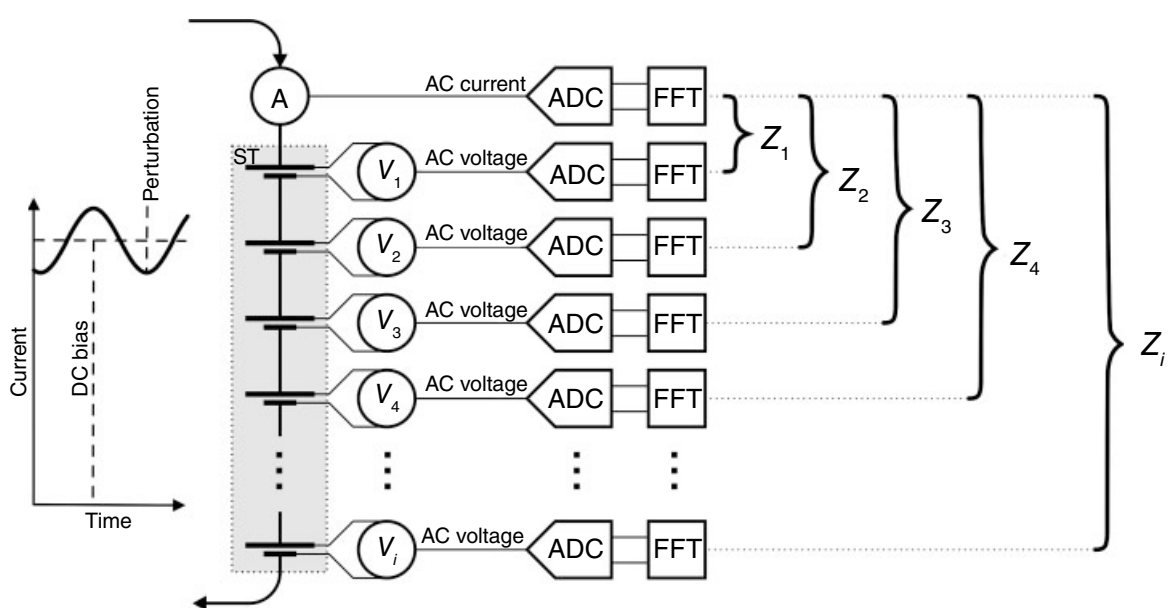


FIGURE 4.5.50 Schematic representation of the experimental equipment and signal processing for the synchronous parallel measurement of the local impedance distribution of a fuel cell stack. A , current sense amplifier and conditioner; V_i , voltage sense amplifier and conditioner; ADC, fast 18-bit analog-to-digital converter; FFT, fast Fourier transformation; Z_i , single-cell impedance; ST, fuel cell stack. (Courtesy of C.A. Schiller, Zahner-Elektrik.)

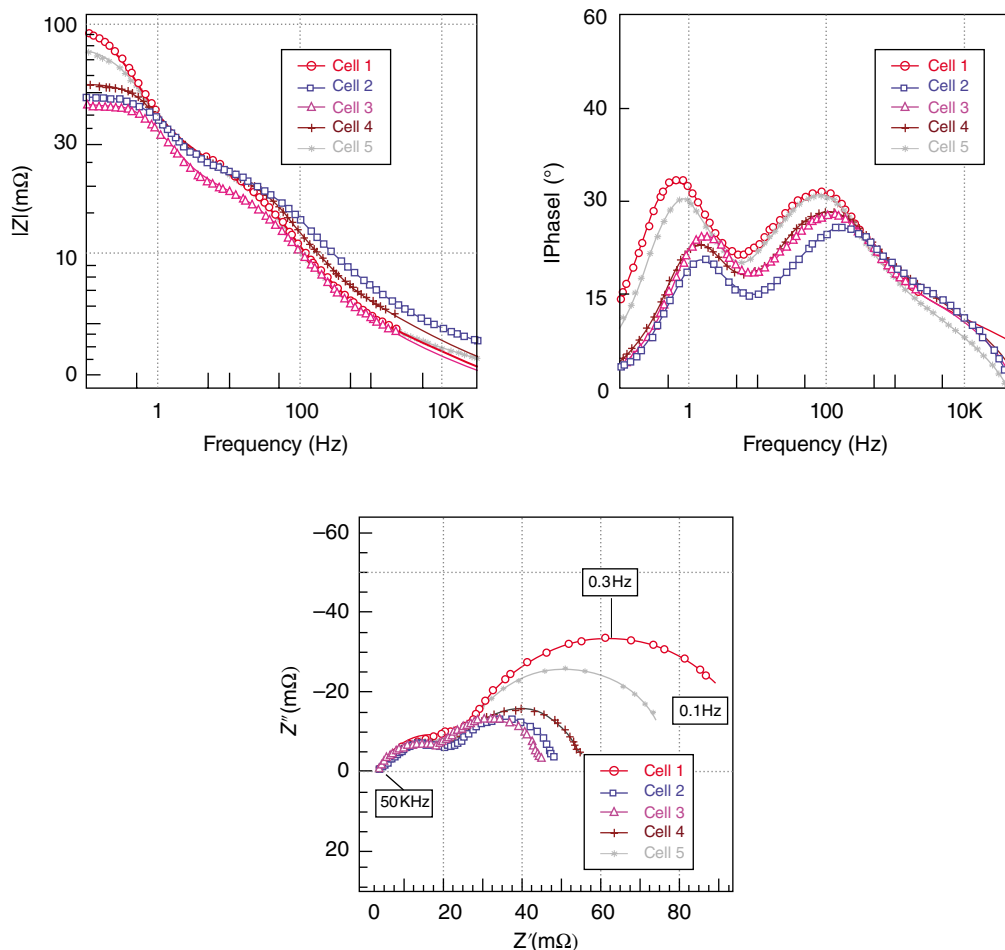


FIGURE 4.5.51 Bode and Nyquist impedance diagram of the five individual cells within the SOFC short stack at OCP (1.19 V). Operation under dry fuel gas (50% H₂ + 50% N₂, no H₂O) and air at 750°C. Symbols, measurement data; solid lines, model fit (see Section 4.5.4.4).

(cells) and the total stack impedance could be made fully automated. The performance and degradation of a 13-cell cross-flow stack was monitored for more than 2500 h at steady operating conditions using the sequential impedance measurement setup. Impedance measurements were used to examine the long-term behavior and monitor the evolution of the series and polarization resistances for four out of the 13 repeating units during the first 1400 h of operation. The SOFC stack was tested galvanostatically with 50% steam in the hydrogen fuel gas supplied to the stack. Parallel acquisition using EIS can be used to detect possible minor differences in the supply of gas to the individual cells, which is important when going to high fuel utilizations. The fuel flow distribution was determined and provides important information about the operating limits of the stack when high electrical efficiency is required.

One setup for integral measurements of 2 kW PEMFC stack from Hydrogenics with 20 cells and active area of each cell of 270 cm² is reported by Yan *et al.* [2007]. But integral measurements of the whole stack do not include information about single cells, so the new setup concepts discussed before were applied for measuring single cells or cell groups of the stack. Hakenjos *et al.* [2006] presented a measurement setup for impedance measurements containing a multichannel FRA system that allows the measurements of impedance spectra of single cells in a fuel cell stack simultaneously. As a proof of reliability, the sum of the impedances of the single cells is compared with the measured impedance of the whole stack. A good correlation was found.

4.5.4.2 Alkaline Fuel Cells (AFCs)

Electrochemical Impedance Studies of AFC Cathodes. A review of the state of the art of AFC is given by McLean *et al.* [2002]. The electrolyte in AFC is a concentrated KOH solution, 25–50 wt %, when operated at 120°C or below, and in older AFC systems, operated at 250°C, a 85 w/o KOH solution was used. The AFC was first fuel cell developed to technical maturity, based on the fundamental research of Bacon [1952] and has been employed extensively in the NASA space programs: Apollo program (1960–1965) and Space Shuttle program (since 1981).

However, for technical use of AFC, the long-term behavior of AFC components is important, especially that of the electrodes. Nickel can be used for the HOR (catalyst in the anode) and on the cathode silver can be used as catalyst (see next section). No expensive noble metal (platinum) is necessary, because the ORR kinetics are more rapid in alkaline electrolytes than in acids and the alkaline electrochemical environment in AFC is less corrosive compared with acid fuel cell conditions. Both catalysts and electrolyte represent a big cost advantage. The advantages of AFC are not restricted only to the cheaper components, as shown by GÜLZOW [1996].

The lifetime of fuel cells is a decisive factor for their commercialization. Therefore, the degradation of fuel cell components is under increased interest and investigation. For AFCs several studies of degradation processes exist—GÜLZOW *et al.* [2002a], Kirov and Schwartz [2000], Rahman *et al.* [1997], and Wagner *et al.* [1996], which are all focused on the degradation of electrodes, because the electrolyte in AFCs can be easily exchanged and regenerated. In the case of using a silver GDE in a complete AFC, the solubility of silver can lead in certain circumstances to a transfer of silver to the anode, and the resulting plating-out feature may damage the catalysts (usually Raney nickel) of the anode. On open-circuit standing the oxidation of silver may occur. Especially carbon-containing cathodes are suffering from oxidation at higher temperatures. Shutdown and restarting procedures can lead to damages as well.

Another important feature of AFC PE is the control of the location and extent of the TPB. This can be achieved by adding a hydrophobing agent such as PTFE (powder or suspension). Alternatively, a dual-porosity structure or as proposed recently by Kaz and Wagner [2002] a dual-composition structure can be used.

The Oxygen Reduction Reaction (ORR). Oxygen reduction electrocatalysis is of special importance for fuel cells and metal-air batteries (Li-air, Zn-air, Al-air, etc.) and as described by Moussallem *et al.* [2012] for industrial chlorine-alkali electrolysis as well. Silver is a known electrocatalyst for the reduction of oxygen in AFC cathodes. To enhance his catalytic activity, silver is used in a form with high specific area such as PE where the silver particles are dispersed in the porous matrix. The porous PTFE-bonded GDE can be prepared by a cold rolling process, first described by Winsel [1985]. The electrodes consist of the electrocatalytic powder (silver, Raney silver, silver-covered PTFE particles, or silver oxide), the organic binding agent (PTFE), pore-forming material (e.g., NaHCO₃), and a metal wire gauze to stabilize mechanically the electrode and to collect the current. In GDE hydrophobic and hydrophilic pore systems are required. In AFC the hydrophilic system allows the penetration of the electrolyte into the electrode and the transport of the ions to or from the reaction zone; the hydrophobic pore system is required for the transport of the oxygen to the reaction zone. In addition, to provide the mechanical stability, the PTFE in the electrodes forms a hydrophobic pore system, whereby the spider web of PTFE fiber in and on the electrode is formed during preparation (high-speed milling). Details of electrode preparation, activation (silver oxide reduction), and experimental setup are given by GÜLZOW *et al.* [2003].

Making use of the fact that the electrolyte is a liquid, the use of a RE (Hg/HgO) is possible, and the two electrodes of a fuel cell, namely, anode and cathode, can be investigated independent from each other, in half-cell configuration. Since the kinetics of the ORR is much slower than the kinetics of the HOR, the performance loss of the fuel cell will be determined mainly by the cathode, and therefore the ORR was intensively investigated with different steady-state and potential-step techniques on smooth and porous electrodes. Hoare [1968] found that the reduction process has been found to follow two reaction pathways: the direct 4e⁻ path and the 2e⁻ path (generally referred to as the sequential path) involving the formation of peroxide as an intermediate product.

To elucidate the reaction mechanism and to obtain the kinetic parameters for oxygen reduction on PTFE-bonded gas diffusion silver electrodes in alkaline solution, the ac impedance method was applied by several investigators: Mund [1975], Holze and Vielstich [1984], and Wagner and Friedrich [2009].

In order to analyze the kinetics of the ORR on silver GDE, EIS were measured at different potentials. The measured impedance spectra are represented as Bode plots, where the logarithm of impedance magnitude $|Z|$ and the phase shift (α) are plotted versus the logarithm of the frequency (f). Impedance spectra have been measured at 18°C in the potential range from OCP (91 mV) to -230 mV versus Hg/HgO (Figures 4.5.52 and 4.5.53). These potential-depending spectra can be classified into two different groups, with a transition potential range between 40 and 50 mV. The first group of impedance spectra exhibits two maxima in the phase shift (two time constants), one maximum at low frequencies ($f < 10$ mHz) and another one in the frequency range 100 mHz $< f < 1$ Hz. The low-frequency phase-shift maximum disappears at potentials more cathodic than 50 mV, while the other phase-shift maximum moves

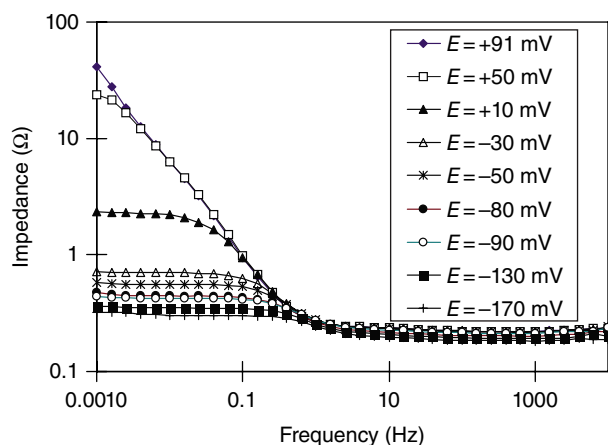


FIGURE 4.5.52 Bode diagram ($\log |Z|$ vs. $\log f$) of the impedance spectra measured in the potential range from OCP (91 mV) to -170 mV during ORR on a Ag GDE in 25 wt % KOH at 18°C, $p_{O_2} = 1$ bar.

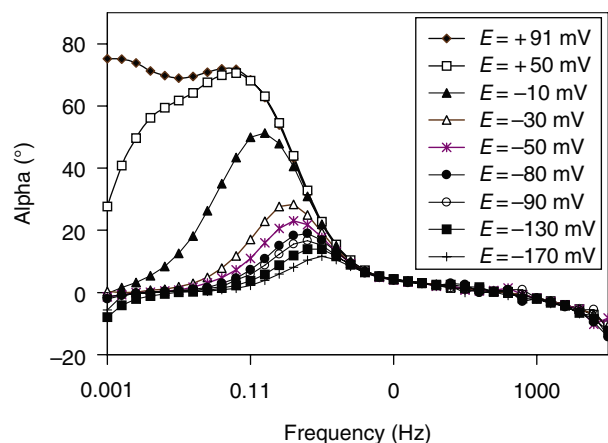


FIGURE 4.5.53 Bode diagram (phase shift vs. $\log f$) of the impedance spectra measured in the potential range from OCP to -170 mV during ORR on a Ag GDE in 25 wt % KOH at 18°C, $p_{O_2} = 1$ bar.

toward higher frequencies when the cathodic polarization is increased. The second group of impedance spectra shows only one phase-shift maximum (one time constant).

The impedance magnitude at the low-frequency end of the measured frequency range decreases with increasing cathodic polarization. The impedance magnitude at frequencies $f > 100$ Hz (R_{el}) is constant in the potential range from OCP to -90 mV, and at more cathodic potentials the electrolyte resistance gets smaller.

In order to evaluate the measured impedance spectra and to obtain kinetic data of the ORR, the reaction steps can be translated into an appropriate equivalent circuit that contains various impedance elements representing the involved reaction steps. These elements are generally represented as ohmic, capacitive, or inductive components with particular dependencies of their complex impedance upon the frequency of the ac signal. The particular linking of these impedance elements described by an equivalent circuit is based upon the relationship between the processes represented by these elements. Subsequently occurring steps are represented by a series connection of the elements, while steps occurring simultaneously are represented by a connection in parallel. In the case of PE, the connection of the elements is more complicated.

The main features of the impedance measurements can be explained using the cylindrical-pore model (see Figure 4.5.45) proposed by Göhr [1997] where the impedance elements of the pore's wall surface (Z_q) are the double-layer capacity (C_{dl}), charge transfer resistance (R_{ct}), and impedance elements of oxygen adsorption or heterogeneous surface reaction ($R_{ad/het}$ and $C_{ad/het}$).

The adsorption/heterogeneous impedance ($Z_{ad/het}$) is given according to Pilla [1970]:

$$Z_{ad/het} = \frac{RT(k - \omega i)}{n^2 F^2 c_s A (k^2 + \omega^2)} \quad (60)$$

with A being the electrode surface, k the first-order reaction rate constant, F the Faraday constant, c_s the surface concentration of reacting species, and i the imaginary quantity and $\omega = 2\pi f$.

As shown by Holze *et al.* [1986], this can be separated into an ohmic and a capacitive part connected in parallel:

$$R_{ad/het} = \frac{RT}{n^2 F^2 c_s A k} \quad (61)$$

$$C_{ad/het} = \frac{n^2 F^2 c_s A}{RT} \quad (62)$$

The numerical values of the impedance parameters, as a function of the applied potential obtained with the CNLS fit program, using for the pore's wall surface the equivalent circuit from Figure 4.5.54, are given in Table 4.5.3 with the corresponding accuracy of the fit.

There is a good agreement between experiment and the results of the fit. The standard deviation of the phase shift, which is more sensitive to the fitting parameters, was found to be in the range of 0.1–0.3°.

The most potential sensitive impedance elements are $R_{ad/het}$ and R_{ct} . The double-layer capacity (C_{dl}) is approximately constant in the measured potential range, and the high value (170 mF/cm 2) indicates a high electrochemical active surface. Assuming that the double-layer capacity for polished silver electrodes measured at the same experimental conditions is about 40 μ F/cm 2 , a surface factor ($C_{dl\text{-porous}}/C_{dl\text{-polished}}$) of 4250 is obtained.

Long-Term Investigation of AFC Electrodes During Oxygen Reduction. In order to analyze in detail the degradation (aging) process of silver electrodes during oxygen reduction, EIS has been performed by Wagner *et al.* [2004]. The PTFE-bonded gas diffusion silver electrodes has been operated galvanostatically at 100 mA/cm 2 over 1400 h, and impedance spectra were recorded at the OCP, daily at the beginning and after 2 weeks of operation in 48 and 72 h intervals, respectively. In the impedance spectra, represented as Bode plots (Figure 4.5.55) or as Nyquist plots (Figure 4.5.56), a change during operation at 100 mA/cm 2 is observed. During the measurement period of each impedance spectrum at OCP, the

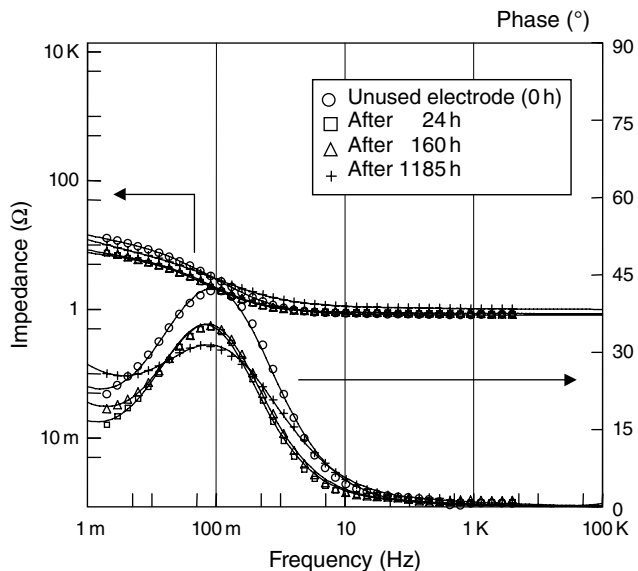


FIGURE 4.5.54 Equivalent circuits for the pore's wall surface.

TABLE 4.5.3 Numerical Values of the Impedance Elements as a Function of the Applied Potential

Potential (mV)	Impedance elements of pore's wall surface (Z_q)					
	$R_{ad/het}$ (Ωcm^2)	$C_{ad/het}$ (mF/cm^2)	R_{ct} (Ωcm^2)	C_{dl} (mF/cm^2)	Z_p ($\text{m}\Omega$)	R_{el} ($\text{m}\Omega\text{cm}^2$)
91	1734 ± 72	251 ± 6	115 ± 5	166 ± 2	46 ± 4	1313 ± 62
50	105 ± 3	435 ± 18	79 ± 16	163 ± 4	45 ± 4	1309 ± 64
10	2.4 ± 0.5	492 ± 24	10 ± 1	179 ± 2	49 ± 4	1307 ± 56
-30	0.5 ± 0.0	590 ± 100	2.3 ± 1	167 ± 1	45 ± 6	1298 ± 77
-50	0.4 ± 0.1	605 ± 106	1.6 ± 0.1	169 ± 5	43 ± 11	1300 ± 148
-70	0.3 ± 0.1	624 ± 135	1.2 ± 0.1	168 ± 8	45 ± 7	1285 ± 37
-90	0.3 ± 0.1	639 ± 102	1 ± 0.1	171 ± 4	42 ± 4	1264 ± 95
-80	0.3 ± 0.1	283 ± 94	1 ± 0.1	159 ± 5	50 ± 9	1194 ± 68
-130	0.2 ± 0.2	303 ± 25	0.6 ± 0.3	162 ± 8	49 ± 3	1134 ± 38
-170	0.2 ± 0.2	312 ± 212	0.5 ± 0.5	162 ± 25	48 ± 5	1080 ± 24
-200	0.1 ± 0.2	321 ± 31	0.3 ± 0.1	167 ± 10	30 ± 2	1007 ± 99

electrode state stays constant; the electrode degrades only during operation at 100 mA/cm^2 . First spectrum (0 h), recorded prior to the beginning of the long-term operation, differs from the EIS recorded after loading. During load, at first, the electrode is activated (second spectrum recorded after 24 h), and a slight change with operation time can be observed.

The main features of the impedance measurements can be explained using the cylindrical-pore model proposed by Göhr [1997]. Taking into account only the pore electrolyte resistance (R_{por}) and the pore wall impedance, then the PE model and pore impedance can be simplified. The spectra can be simulated by an equivalent circuit (Figure 4.5.57) consisting of a series combination of uncompensated electrolyte resistance (R_{el}) and pore impedance. The impedance of the pore wall surface is given by the charge transfer resistance (R_{ct}), Warburg impedance (W), and double-layer capacity (C_{dl}).

The most time-sensitive impedance elements are the double-layer capacity, the Warburg impedance (W), and the charge transfer resistance. The Warburg impedance is related to a diffusion process, as

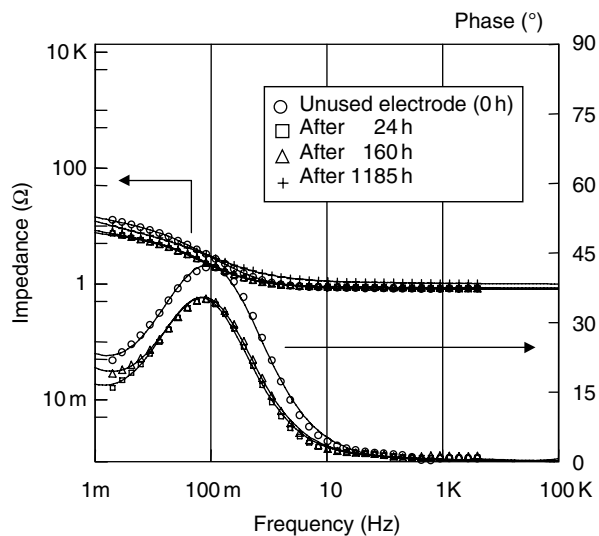


FIGURE 4.5.55 Bode diagram of the impedance spectra of the silver GDE measured at OCP, 70°C, in 30 wt % KOH during oxygen reduction at different times of operation at 100 mA/cm².

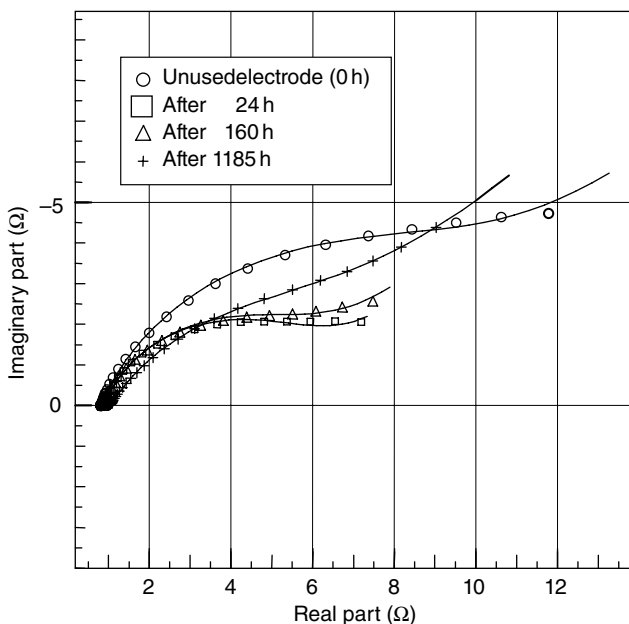


FIGURE 4.5.56 Nyquist diagram of the impedance spectra of the silver GDE measured at OCP, 70°C, in 30 wt % KOH during oxygen reduction at different times of operation at 100 mA/cm².

derived in Section 2.2.2.2. From the time dependency of the impedance parameters, the aging effects can be related to the decrease of the double-layer capacity (Figure 4.5.58), a change of the porous structure and catalyst activity (Figure 4.5.59), and an increase of the Warburg impedance (Figure 4.5.60). The decrease of the capacity is given by a decrease of the electrochemically active surface. The increase of

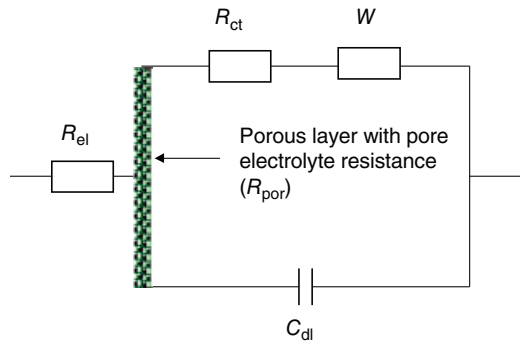


FIGURE 4.5.57 Equivalent circuit (porous electrode model) for the evaluation of the impedance spectra of the silver GDE measured during ORR at different times of operation at 100 mA/cm^2 .

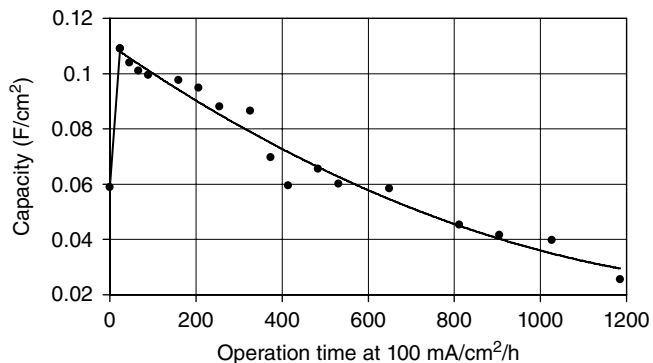


FIGURE 4.5.58 Time dependency of double-layer capacity (C_{dl}) obtained with a least squares fit of the measured impedance spectra at open-circuit potential.

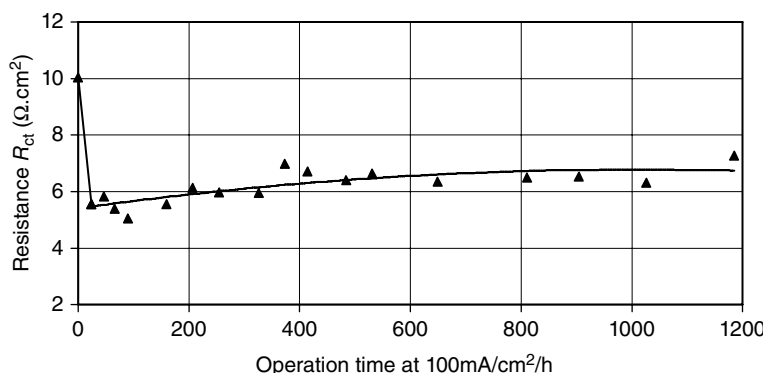


FIGURE 4.5.59 Time course of charge transfer resistance R_{ct} obtained with a least squares fit of the measured impedance spectra at open-circuit potential.

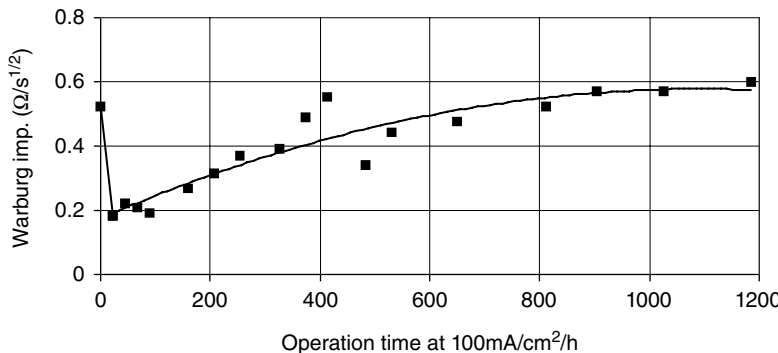


FIGURE 4.5.60 Time course of Warburg impedance obtained with a least squares fit of the measured impedance spectra at open-circuit potential.

the Warburg impedance indicates that the diffusion of reacting gas is hindered. In the Nyquist diagram, one can observe the infinite diffusion as a straight line with a slope of 1 (real part = imaginary part) in the low-frequency range of the spectra. In the Bode diagram due to the logarithmic scale of the impedance, the diffusion cannot be seen so clearly.

The aging effect is also observed by scanning electron microscopy (SEM) and X-ray photoelectron spectroscopy (XPS). Consequently, the combination of electrochemical and physical methods is very helpful for the study of degradation processes as shown by Wagner *et al.* [2004].

The Hydrogen Oxidation Reaction (HOR). The kinetics of hydrogen reduction/oxidation reaction was first investigated by Gerischer and Mehl [1955] using an ac bridge. First ac impedance measurements on porous nickel (Raney nickel) electrodes during HOR in alkaline solution were reported by Mund [1975] and Mund and v. Sturm [1975], respectively. They proposed an equivalent circuit identical with the equivalent circuit shown in Figure 4.5.54; only $R_{\text{ad/het}}$ (indicated with R_2) and $C_{\text{ad/het}}$ (indicated with C_2) have a different meaning. They found for $\omega \rightarrow 0$

$$R_2 = \alpha R_{\text{ct}} \coth \alpha \quad (63)$$

$$C_2 = (R_{\text{ct}} b)^{-1} \left\{ 1 + \frac{(\alpha - 3 \sinh \alpha \cosh \alpha)}{2 a \cosh^2 \alpha} \right\} \quad (64)$$

$$\text{with } \alpha = l \left(\frac{b}{D} \right)^{1/2} \quad (65)$$

$$b = \frac{2i_0}{nF(r_p c_{v0} + 2c_{s0})} \quad (66)$$

where l represents the pore length (cm), D is the effective diffusion coefficient (cm^2/s), i_0 is the exchange current density (A/cm^2) of the charge transfer reaction, r_p is the pore radius (cm), c_{v0} is the saturation concentration of H_2 in the solution (mol/cm^3), and c_{s0} is the saturation concentration of H_2 on the electrode surface (mol/cm^2).

Latest publications regarding HOR in alkaline solution are given by Lasia [1998] and a remarkable overview by Conway and Tilak [2002].

4.5.4.3 Polymer Electrolyte Fuel Cells (PEFCs)

Electrochemical Impedance Studies of Polymer Electrolyte Fuel Cells (PEFCs). Given by the low temperature of operation, CO_2 tolerance by the electrolyte, combination of high power density with high

energy conversion efficiency, and modular construction, PEFCs are considered as one of the most promising options for powering future cars and small combined power units. As shown by Gottesfeld and Zawodzinski [1997] during the last years, a lot of key barriers for the development of PEFC for terrestrial applications have been successfully overcome. However, there is still need for further R&D effort: an important goal is to increase the efficiency and to produce efficient, cheap electrodes and membrane electrode assemblies (MEAs) with low noble metal catalyst loading, optimized electrode composition investigated by Wagner *et al.* [2008], high CO tolerance, and long lifetime. Actually, the R&D efforts are focused on the development of nanodispersed catalysts and non-noble metal catalyst, production techniques that allows production of MEAs with low noble metal catalyst loading and suitable for mass production as proposed by Bevers *et al.* [1998] or Gülvzow *et al.* [1999], the development of high-temperature membranes to enhance the kinetics and to lower the CO influence (up to 200°C), and the integration of the MEA into a fuel cell system with humidifier, gas conditioner, bipolar plate, fuel storage systems, and so on. Another important issue during PEMFC operation in particular for mobile application is the performance of the fuel cell with different residual water amount frozen at subzero temperature as shown by Hou *et al.* [2007] and degradation behavior investigated by Schulze *et al.* [2007] combining EIS and surface analysis investigations.

The main difference between the AFC and PAFC is the gastight solid polymer electrolyte membrane, a solid proton exchange membrane that has its main function the transport of protons from anode to cathode.

To investigate the physical and electrochemical origins of the performance loss in PEFC, operated at different conditions like high current densities, fuel composition (neat H₂, H₂ + 100 ppm CO, H₂O), flow rates, temperature, air or pure oxygen, and so on, electrochemical impedance studies on different PEFC systems with different electrodes and membranes were performed, as mentioned in Section 4.5.4.1.

First impedance measurements and interpretation of EIS performed to characterize PEFC were reported by Srinivasan *et al.* [1988], Fletcher [1992], Wilson *et al.* [1993], and Poltarzewski *et al.* [1992]. With increasing R&D effort to improve the PEFC performance and availability of suitable instrumentation, the number of publications also increased. Comprehensive reviews of the application of EIS for PEMFC characterization are given by Yuan *et al.* [2006] and Niya and Hoofar [2013].

Determination of Performance Losses in PEFC: EIS Measured at Different Cell Voltage (Current Load).

Applying a classical three-electrode cell with one RE is extremely difficult for the investigation of electrochemical systems with solid electrolytes. Therefore, first the anode and cathode transfer functions at OCP can be determined independently without an RE using a symmetrical gas supply of hydrogen and oxygen at the two electrodes of the cell. Thus, cathode and anode impedance at OCP can be determined directly with two independent experiments, like published by Wagner [2002] and shown in Figure 4.5.61 as Bode diagram. From the charge transfer resistance R_{ct} at open cell voltage, an apparent exchange current density i_0 according to $R_{ct} = RT/zF i_0$ can be determined.

The preliminary impedance spectrum (Figure 4.5.61) measured at open cell voltage with symmetrical gas supply (H₂/H₂ and O₂/O₂) at 80°C with impregnated (1 mg/cm² Nafion suspension, Aldrich Chemie) E-TEK-electrodes (20% Pt/C, 0.4 mg/cm², thickness 200 µm, geometric surface of 23 cm²) has shown that the impedance in the low-frequency range is much higher when operated symmetrically with oxygen (symmetrical cathode arrangement) than the impedance when the fuel cell is operated symmetrically with hydrogen (symmetrical anode arrangement).

Furthermore, by varying other experimental conditions such as current load, temperature, gas composition, and as recently shown by Andreaus *et al.* [2002] hydrogen humidification and membrane thickness, measured cell impedance can be split up into anode impedance, cathode impedance, and electrolyte resistance without using RE. These results were used to derive appropriate equivalent circuits for the analysis of impedance spectra measured on fuel cells operating with H₂/O₂, H₂/air, and H₂ + 100 ppm CO/O₂. The variation of the experimental conditions is also a useful method to confirm the accuracy of the equivalent circuit.

For illustration, in Figure 4.5.62 impedance spectra measured over the whole performance range of a PEFC from open circuit to full load were presented. The nature of the impedance spectra varied with cell

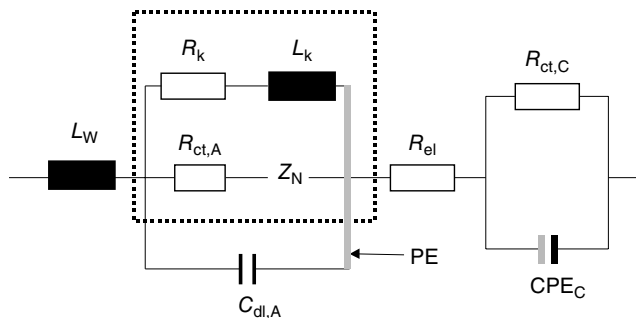


FIGURE 4.5.61 Bode diagram of the measured impedance spectra, PEFC (Nafion-impregnated electrodes) at 80°C, at pH₂ and p_{O_2} = 2 bar absolute, symmetrical gas supply, at open cell potential.

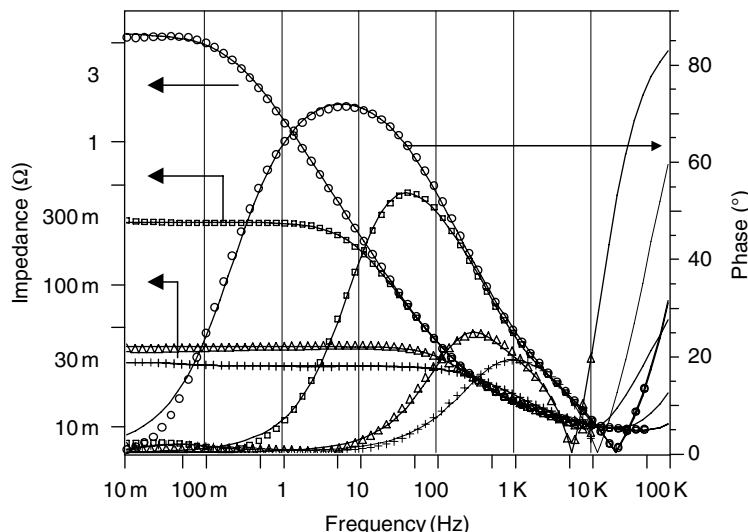


FIGURE 4.5.62 Bode diagram of the measured impedance spectra, PEFC (hot-pressed, Nafion-impregnated E-TEK electrodes) at 80°C, at different cell voltages: (○) OCV (1024 mV), (□) 900 mV, (Δ) 800 mV, (+) 700 mV.

potential; between OCP (1024 mV) and 840 mV, an exponential potential dependency of the impedance due to the high activation energy of the ORR is observed in the low-frequency range ($f < 1$ Hz).

With further increasing current density, an increase in the cell impedance is observed (Figure 4.5.63a) and an additional phase-shift maximum at 75 mHz occurs. From this increase in the cell impedance, one can deduce that at higher load of the cell, an additional overvoltage occurs. This additional process is related to a mass transport process (diffusion). The impedance related to the diffusion is usually found in the lowest-frequency region. Therefore, the impedance has to be measured over a wide frequency range, down to 10 mHz, or even lower.

To identify and separate the different diffusion processes, it is useful to represent the measured impedance spectra also as the Nyquist diagram (Figure 4.5.63b). In the Nyquist diagram, one can observe the finite diffusion as an additional loop at the lowest part of the frequency range and the infinite diffusion as a straight line with a slope of 1 (real part = imaginary part). In the Bode diagram (Figure 4.5.63a), the difference between the two kinds of diffusion cannot be seen so clearly due to

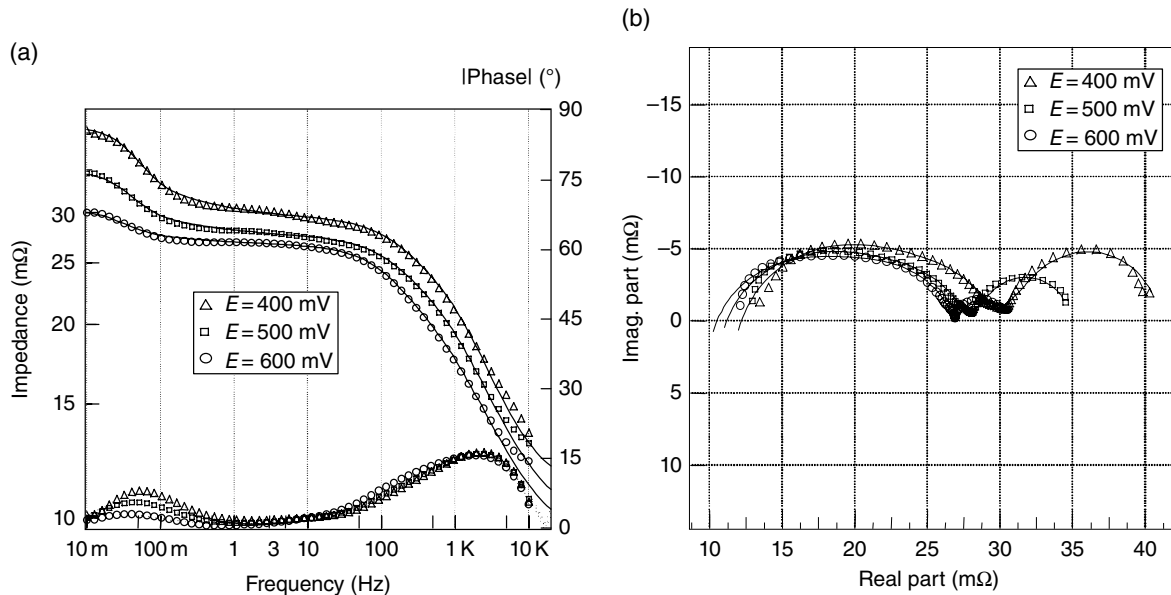


FIGURE 4.5.63 (a) Bode and (b) Nyquist diagram of the measured impedance spectra, PEFC (hot-pressed, Nafion-impregnated E-TEK electrodes) at 80°C, at different cell voltages: (○) 600 mV, (□) 500 mV, (△) 400 mV.

the logarithmic scale. In general, the Bode plot provides a clearer description of the electrochemical system's frequency-dependent behavior than the Nyquist plot, in which frequency values are implicit.

Starting with EIS measured with symmetrical gas supply, an equivalent circuit for the complete PEFC can be applied for the simulation of the measured impedance spectra of the PEFC. Besides a series resistance (electrolyte or membrane resistance R_{el}), the equivalent circuit (Figure 4.5.64b) contains three time constants of parallel R/C . In the simulation the capacitance (C) was replaced by CPE due to the porous structure of the electrodes. The cathode can be described using a time constant for the charge transfer through the double layer ($R_{ct(C)}/CPE_{dl(C)}$), the exponent of the CPE is around 0.85, for an exponent of 1 the CPE is equal with the capacitance), a time constant for the finite diffusion of water with a Nernst impedance-like behavior ($R_{(N)}/CPE_{(N)}$, the exponent of the CPE is around 0.95), and finally the time constant of the anode ($R_{ct(A)}/CPE_{dl(A)}$, the exponent of the CPE is around 0.80). Anode and cathode can be also simulated with the PE model (Figure 4.5.64c).

Applying Eqs. (50)–(54) and using the current density dependency of the resistances (R_N , $R_{ct,A}$, R_{el} , and $R_{ct,C}$) represented in Figure 4.5.65, gained from the simulation with the equivalent circuit from Figure 4.5.64c, the individual performance losses (overpotentials) can be determined (Figure 4.5.66).

At low current densities, the cell overpotential is given mainly by the cathodic overpotential. At higher current densities ($i > 400 \text{ mA/cm}^2$), an additional diffusion overpotential becomes noticeable. The increase in the anodic overpotential with increasing current density can be explained by assuming a partially dry-out of the interface membrane/anode with simultaneous increase of the water content depending on the electrolyte resistance inside the pore ($Z_p \equiv R_{pore}$)—applicable only in the case of impregnated electrodes or electrodes with electrolyte powder inside the electrode—and can be minimized by appropriate water management. Therefore, a further refinement of the equivalent circuit is useful and can be made if one uses the PE model, presented in Section 4.5.4.1. If one assumes that the impedance of the PE is determined only by the resistance (R_{pore}) of the electrolyte inside the pore and the pore's wall surface (R_{ct}), then one can simplify the expression for the impedance of the PE after Göhr [1997]:

$$R_p = \frac{(R_{pore} \cdot R_{ct})^{\frac{1}{2}}}{\tanh \left\{ (R_{pore}/R_{ct})^{\frac{1}{2}} \right\}} \quad (67)$$

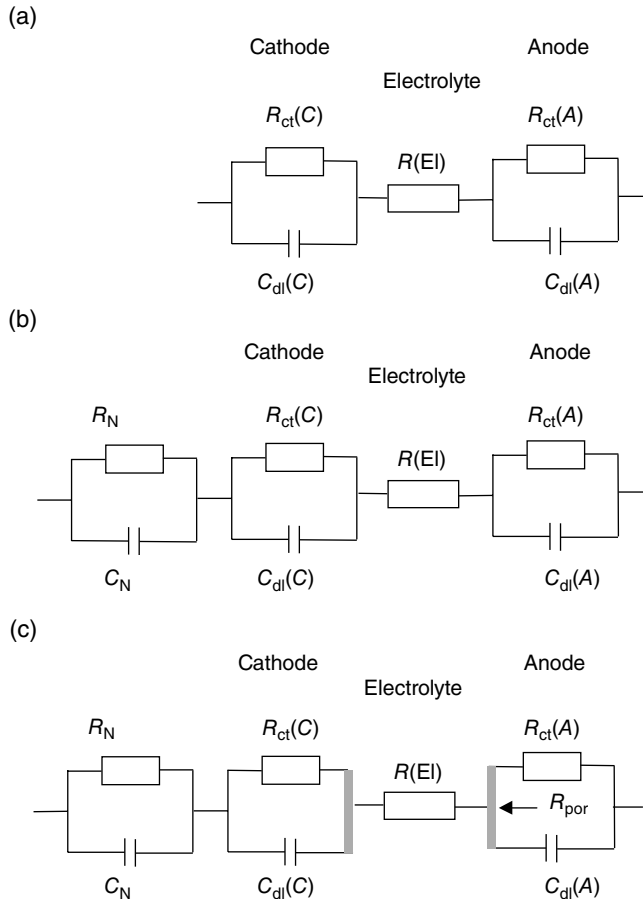


FIGURE 4.5.64 (a) Equivalent circuit (EC) of the PEFC with O₂/H₂ gas supply for low current densities. (b) Equivalent circuit of the PEFC with O₂/H₂ gas supply for high current densities with an additional diffusion step (Nernst impedance). (c) Equivalent circuit of the PEFC with O₂/H₂ gas supply with Nernst impedance and porous electrode model.

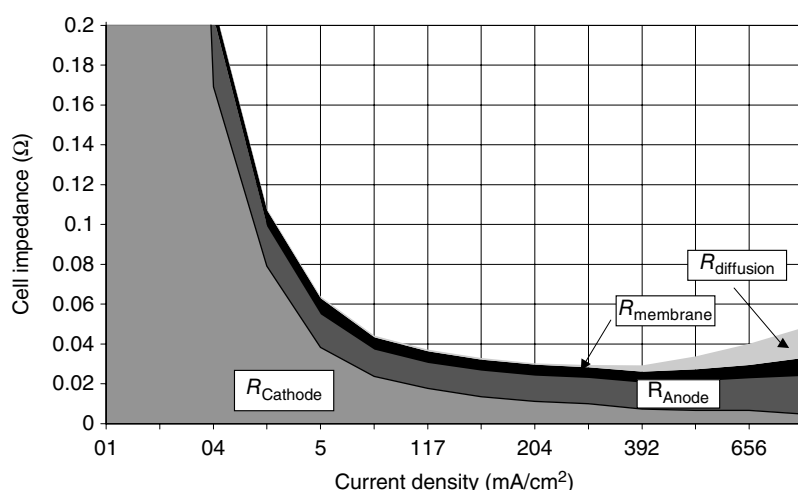


FIGURE 4.5.65 Current density dependency of the resistances after evaluation of the impedance spectra evaluated with EC from Figure 4.5.64.

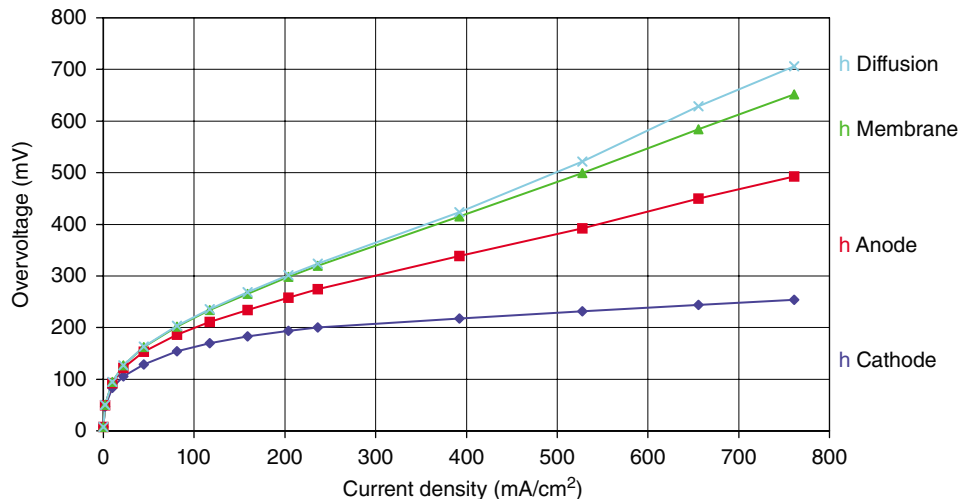


FIGURE 4.5.66 Cell voltage and individual performance losses of the PEFC (hot-pressed, Nafion-impregnated E-TEK electrodes) at 80°C in function of current density, calculated by integration of the individual resistances at different current densities.

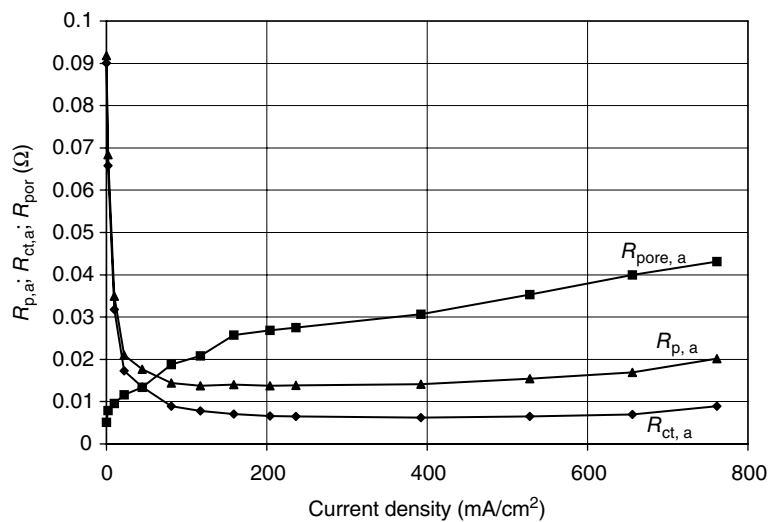


FIGURE 4.5.67 Porous anode resistance ($\blacktriangle R_{p,a}$), charge transfer resistance ($\blacklozenge R_{ct,a}$), and electrolyte resistance ($\blacksquare R_{pore,a}$) in function of the current density.

The impedance of the anode can be split up, according to Eq. (67), and the current density dependency is shown in Figure 4.5.67.

To validate the proposed equivalent circuit other, additional EIS has been performed, for example, flooding the cathode in the “dead-end” mode of operation of the cathode. The fuel cell was operated over 8 h in the galvanostatic mode of operation at constant load, so that one can assume that the impedance change with time can be attributed to the change of and in the cathode, as shown by Schiller *et al.* [2001].

Time-Resolved Electrochemical Impedance Spectra During CO Poisoning of the Pt and Pt/Ru Anodes in a PEFC. As mentioned in the Introduction, due to the high energy conversion rate and the harmless emission products, PEFCs receive more and more attention especially in the case for powering electric

vehicles. The highest performance is achieved with hydrogen (H_2), which is the preferred fuel for low-temperature fuel cells. However, H_2 has several limitations. The storage systems for liquid or compressed H_2 are heavy and bulky. Furthermore, H_2 refueling is costly and takes time. An additional obstacle is actually the lack of an infrastructure to distribute H_2 to the consumer, as shown, for example, by Cleghorn *et al.* [1997].

An alternative to the use of H_2 as fuel is methanol, which is a liquid fuel easy to handle. This can be directly transformed to electrical current in a direct methanol fuel cell (DMFC). The DMFC allows a simple system design. However, presently achieved performance data of DMFC is not satisfying and material costs are too high. As another alternative, methanol or hydrocarbons (e.g., natural gas, biogas) can be transformed to hydrogen on board of the electric vehicle by a reformation reaction. This allows to use the H_2 -PEFC cell, which has a higher level of development. The reformate feed gas may contain up to 2.5% carbon monoxide (CO) by volume, which can be reduced to about 50 ppm CO using a selective oxidizer, after Wilkinson and Thompsett [1997].

The performance of platinum that is known as one of the most effective catalysts for hydrogen oxidation in polymer membrane fuel cells is influenced even by traces of carbon monoxide: compared with the use of pure hydrogen, the maximum power density is more than halved in the presence of only 5 ppm carbon monoxide. One possible explanation for the decrease of the fuel cell performance is that the carbon monoxide blocks or limits the active sites of the platinum catalyst due to adsorption, which leads to an inhibition of the HOR. In the last two decades intensive work has been devoted finding electrocatalysts that are tolerant to CO in hydrogen at operating temperatures below 100°C. This system has been object to numerous studies using electrochemical methods like potentiostatic measurement, potentiodynamic measurement, and stripping voltammetry. Detailed kinetic studies were performed, for example, by Vogel *et al.* [1975], Schmidt *et al.* [1998], and Koper *et al.* [2001].

First *in situ* impedance measurements were reported by Müller *et al.* [1999b] who reported the time dependence of impedance spectra in galvanostatic conditions for CO poisoning Pt anodes. Other publications with detailed kinetic data were published by Ciureanu and Wang [1999, 2000], Wang *et al.* [2001b], Leng *et al.* [2002], Kim *et al.* [2001a, b], and recently Wagner and Gültzow [2004].

For the development of improved electrocatalysts that are less sensitive with respect to the presence of carbon monoxide, a mechanistically understanding of the poisoning process of the anode is desirable. The progressive poisoning with carbon monoxide of a fuel cell can be monitored using TREIS.

As shown in detail by Wagner and Schulze [2003], the CO poisoning of the Pt and PtRu anode during galvanostatic mode of operation with $H_2 + 100$ ppm CO causes a change of the state of the fuel cell, which is reflected in decrease of the cell voltage during operation (Figure 4.5.68) and in time dependency of the recorded impedance spectra. Besides an increase of the total impedance of the fuel cell, in the case

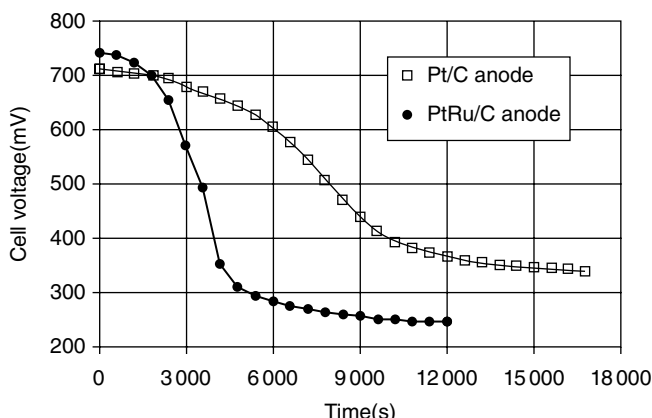


FIGURE 4.5.68 Evolution of cell voltage during CO poisoning of Pt/C (●) and PtRu/C (□) anodes in galvanostatic mode of fuel cell operation at 217 mA/cm², 80°C.

of galvanostatic mode of operation, the occurrence and the increase of a pseudo-inductive behavior at frequencies lower than 3 Hz is observed. It is useful to operate the fuel cell in the galvanostatic mode of operation because at constant current density, the impedance of the cathode and the membrane resistance can be assumed to be constant during the course of impedance measurements and the changes in the impedance spectra during poisoning the anode with CO can be attributed exclusively to the impedance of the anode.

Representative time-dependent impedance spectra of the series, that is, time-resolved impedance spectra, are depicted in Figure 4.5.69 for the fuel cell with Pt anode and in Figure 4.5.70 for the fuel cell with PtRu anode as Nyquist plots whereby the experimental data are represented by dots and the solid lines in the figures represent the modeled curves after fitting the experimental data with the equivalent circuit from Figure 4.5.71.

In series to both half-cells, the resistance of the membrane itself—denoted as the electrolyte resistance (R_{el})—as well as a parasitic wiring inductance (L_w) due to the mutual induction effect has to be taken into account. The impedance of the cathodic half-cell (oxygen reduction) is approximated using a charge transfer resistance ($R_{ct,C}$) in parallel to a CPE (CPE_C). This simple equivalent circuit describes the partial impedance of the cathodic half-cell with sufficient accuracy. In contrast, the impedance of the anode (hydrogen oxidation) is more complicated due to the carbon monoxide poisoning and appearance of an inductive loop in the low-frequency range of the impedance spectra. The impedance of the anode is modeled using a PE in series to a double-layer capacity ($C_{dl,A}$), which is in parallel to the faradaic impedance (Z_F) that contains a surface relaxation impedance Z_K (see Section 4.5.4.1) parallel to the charge transfer resistance ($R_{ct,A}$) in series with a finite diffusion impedance element (Nernst impedance, Z_N) so that the expression for the faradaic impedance from Eq. (56) is extended and is given by Eq. (68):

$$Z_F = \frac{R_{ct} + Z_N}{1 + (R_{ct}/Z_K)} \quad (68)$$

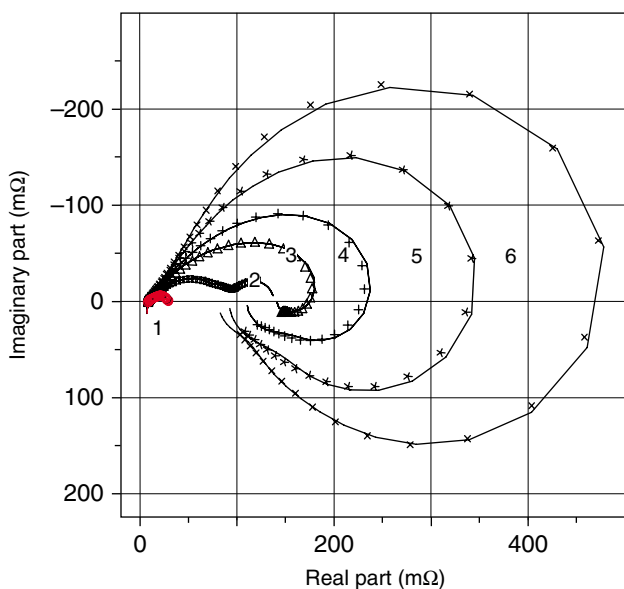


FIGURE 4.5.69 Nyquist plot of EIS measured at (1) 0 s, (2) 3601 s, (3) 5402 s, (4) 7204 s, (5) 9605 s, and (6) 11404 s during CO poisoning of Pt/C anode during galvanostatic mode of operation with $H_2 + 100$ ppm CO (anode), at 5 A (cell surface = 23 cm²), 80°C and oxygen (cathode).

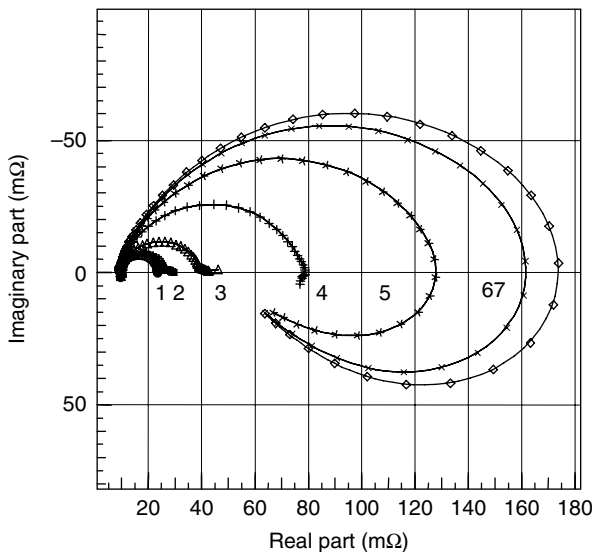


FIGURE 4.5.70 Nyquist plot of EIS measured at (1) 0 s, (2) 3 000 s, (3) 6 000 s, (4) 9 000 s, (5) 12 000 s, (6) 15 000 s, and (7) 16 800 s during CO poisoning of PtRu/C anode during galvanostatic mode of operation with $\text{H}_2 + 100 \text{ ppm CO}$ (anode), at 5 A (cell surface = 23 cm^2), 80°C and oxygen (cathode).

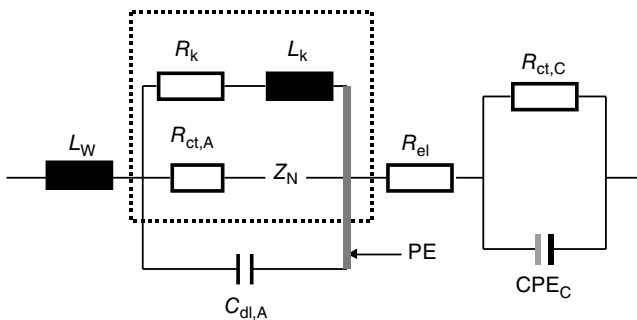


FIGURE 4.5.71 Equivalent circuit used for evaluation of interpolated (time-dependent) impedance spectra during hydrogen oxidation and CO poisoning of the anode and oxygen reduction at the fuel cell cathode.

On the basis of this model and equivalent circuit shown in Figure 4.5.71, the changes and differences, depending on the used anode in the fuel cell (Pt/C or PtRu/C) in the impedance spectra during the experiment, are dominated by the changes of the charge transfer resistance of the anode ($R_{ct,A}$), the surface relaxation impedance (R_K , τ_K), and the finite diffusion impedance Z_N .

The evolution of the charge transfer resistance of the anodes is shown in Figure 4.5.72 (Pt/C anode (●) and PtRu/C anode (□)) as a function of the elapsed time. The Nernst impedance (Z_N) represented in Figure 4.5.73 shows the greatest difference between the two anodes. The Nernst impedance Z_N contains two parameters: the Warburg parameter W ("diffusion resistance" at low frequencies) and a diffusion

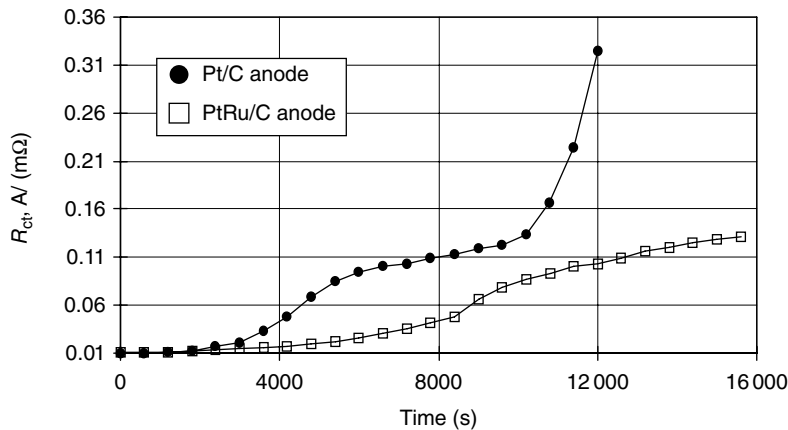


FIGURE 4.5.72 Time elapsed of the charge transfer resistance of the (●) Pt/C and (◻) PtRu/C anodes after evaluation of the time-dependent impedance spectra with the equivalent from Figure 4.5.71.

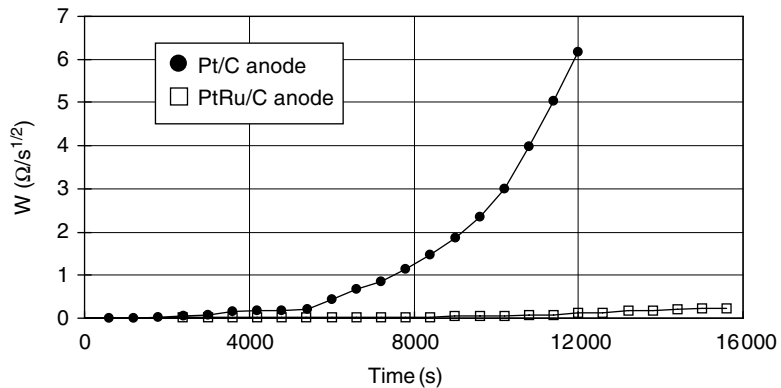


FIGURE 4.5.73 Time elapsed of the Warburg parameter W from the Nernst impedance (Eq. (69)) for the (●) Pt/C and (◻) PtRu/C anodes after evaluation of the time-dependent impedance spectra with the equivalent from Figure 4.5.71.

time constant (k_N), determined by the constant of diffusion (D_k) and diffusion layer thickness (d_N). The Nernst impedance is calculated by Eq. (69):

$$Z_N = \frac{W}{\sqrt{j\omega}} \tanh \sqrt{\frac{j\omega}{k_N}} \quad (69)$$

with

$$k_N = \frac{D_k}{d_N^2} \quad (70)$$

Electrochemical Impedance Studies of Direct Methanol Fuel Cells (DMFC). The DMFC is investigated since more than 50 years and is recently being discussed as an interesting option for a fuel cell-based

mobile power supply system. A more historical overview is given by McNicol *et al.* [1999], and Lamy *et al.* [2002] discussed advances in the development of direct alcohol fuel cells (DAFC). However, methanol is the most promising organic fuel. Other alcohols have also been considered for use in a fuel cell, but until now the most advanced system is the DMFC. The DMFC uses liquid methanol/water solution as fuel, which is, compared with hydrogen, easy to handle and to distribute. But the DMFC has some particular disadvantages, like low electrocatalytic activity of the catalyst regarding methanol oxidation, anode poisoning by strongly adsorbed intermediates, and methanol crossover through the proton exchange membrane, leading to limited performances of the DMFC. At the time, research is focused to overcome the mentioned problems by developing new membranes, as presented by Jörissen *et al.* [2002], applicable at higher temperatures. A review and state of the art of membranes with low methanol crossover and high ionic conductivity is given by Savadogo [2004]. New electrocatalysts for methanol oxidation were found by Burstein *et al.* [1997], Wasmus and Küver [1999], Wang *et al.* [2007], and Yuan *et al.* [2009]. Methanol-tolerant oxygen reduction catalysts were studied by Reeve *et al.* [2000]. Lizcano-Valbuena *et al.* [2003] proposed new production steps to increase the electrocatalytic activity of the catalysts. Finally Gültzow *et al.* [2002b] developed a method to increase the utilization degree of the catalyst by improving the coating technique during MEA production.

Till now there are only a few EIS studies published, with first studies of DMFC being reported by Müller *et al.* [1999a]. They separated the anode and cathode impedance using different fuel cell configurations: the impedance of the anode was measured by eliminating the contribution of the cathode through operating the cathode as dynamic hydrogen electrode (DHE) without oxygen, so that instead of oxygen reduction, protons are reduced and hydrogen was evolved. DMFC cathode impedance spectra were obtained after subtracting the anode impedance from the complete cell impedance. For the modeling of the faradaic impedance of DMFC anodes, Müller *et al.* [1999a] used the same equivalent circuit as proposed by Göhr and Schiller [1986] and used by Müller *et al.* [1999a] for modeling the PEFC anode during CO poisoning.

The model (equivalent circuit) and notations used by Müller *et al.* [1999a] were first derived by Harrington and Conway [1987] for the formulation of the kinetic of hydrogen evolution reaction and were shown in Figure 4.5.74.

Assuming for the methanol oxidation a reaction mechanism with intermediate adsorbed CO,

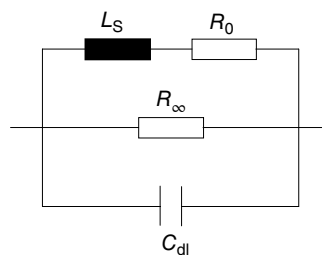
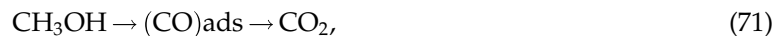


FIGURE 4.5.74 Equivalent circuit for modeling the faradaic impedance of DMFC anodes (for single-adsorbate mechanisms without diffusion control, proposed by Harrington and Conway [1987]. Source: Harrington 1987. Reproduced with permission of Elsevier.

then the Faradaic impedance (Z_F) can be expressed by

$$Z_F = \frac{j\omega + C}{A + B} = \left(\frac{1}{R_\infty} + \frac{1}{R_0 + j\omega L_S} \right)^{-1} \quad (72)$$

where

$$R_\infty = \frac{1}{A}; \quad R_0 = \frac{C}{B} \quad \text{and} \quad L_S = \frac{1}{B}$$

The parameters A , B , and C are defined by Müller *et al.* [1999a] by

$$A = F \left(\frac{\partial r_e}{\partial E} \right)_\Theta; \quad B = \frac{F^2}{q_{CO}} \left(\frac{\partial r_e}{\partial \Theta} \right)_E \left(\frac{\partial r_{CO}}{\partial E} \right)_\Theta; \quad C = \frac{-F}{q_{CO}} \left(\frac{\partial r_{CO}}{\partial \Theta} \right)_E$$

where r_e is the net rate of production of electrons, r_{CO} the net rate of $(CO)_{ads}$, Θ the fractional surface coverage of CO, and q_{CO} the charge required for adsorption of CO to complete surface coverage.

Liu *et al.* [2003] and Zhao *et al.* [2005] studied the impedance behavior of methanol oxidation on a Pt-Ru and unsupported Pt-black anode with different electrolyte (Nafion) content and catalyst loading in the anode and found also an inductive loop in the low-frequency range of the EIS.

4.5.4.4 The Solid Oxide Fuel Cells (SOFCs)

As pictured in Figure 4.5.75, SOFC uses a ceramic (solid oxide) electrolyte. The ionic conductivity (O^{2-} ion conduction) requirement for the ceramic electrolyte necessitates high operating temperatures (600–1000°C). Such high operating temperatures promote fast reaction kinetics, even with non-noble metal electrocatalysts, and allow reforming of hydrocarbon (CO, CH_4 , gasoline, etc.) fuels within the fuel cell. But high operating temperature demands high requirements on materials and requires a very

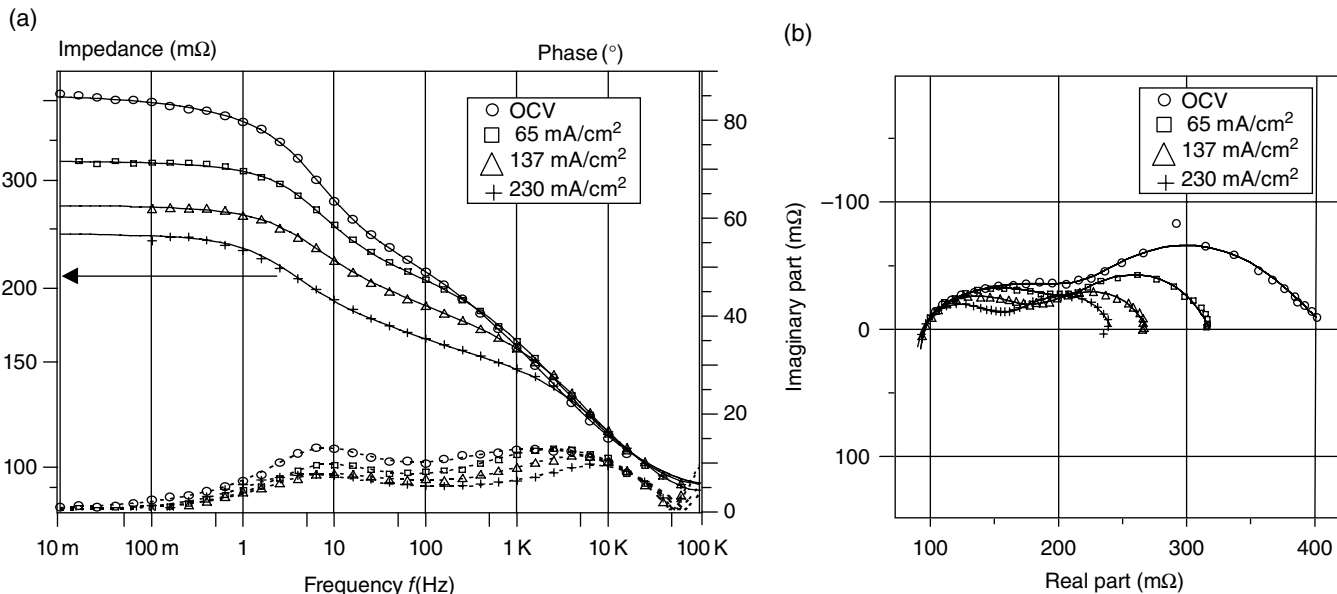


FIGURE 4.5.75 (a) Bode plot of impedance spectra, SOFC cell (ZrO_2 -Ni/YSZ/(La,Sr)MnO₃, geometric surface 5 cm²) measured at 950°C and different current densities. (b) Nyquist plot of impedance spectra, SOFC cell (ZrO_2 -Ni/YSZ/(La,Sr)MnO₃, geometric surface 5 cm²) measured at 950°C and different current densities.

careful selection of components with matching thermomechanical properties. A comprehensive treatise on both the fundamental and technological aspects of SOFC is given by Minh and Takahashi [1995].

First electrochemical impedance measurements were used mainly to determine the conductivity of SOFC components (electrolyte and electrode materials). According to Verkerk and Burggraaf [1983], the equivalent circuit describing the Pt/yttria-stabilized ZrO_2 (YSZ) interface consists of a parallel combination of the double-layer capacity and charge transfer resistance in parallel with a Warburg impedance related to the diffusion of oxygen atoms on the electrode surface and a second Warburg impedance in series. The same equivalent circuit was used by Nicoloso *et al.* [1988] for the study of the effect of impurities on YSZ conductivity. Given by the low conductivity of YSZ, research is focused on finding new materials with higher conductivity, even at lower temperatures as reported by Van Herle *et al.* [1994], or using anode-supported SOFCs with thin gastight electrolyte films by dc sputtering as reported by Wanzenberg *et al.* [2003] and Leonide *et al.* [2008], or vacuum plasma spraying as applied by Schiller *et al.* [2000]. As shown by Wanzenberg *et al.* [2003] and reported by Bossel [1993] and Fleig and Maier [1996], the electrode contact area has some influence on impedance (conductivity) measurements. To increase the electrochemical active surface composite, electrodes containing active catalyst and electrolyte can be used like presented by Barbucci *et al.* [2006] or using mixed ionic-electronic conductive materials (LSCF) as recently shown by Endler-Schuck *et al.* [2015].

Boukamp *et al.* [1991] investigated the kinetic of the ORR and the cathodic reaction in the SOFC, which are important for the determination of the oxygen concentration in oxygen gas sensors (car exhaust).

EIS Measured at SOFC at Different Experimental Conditions: EIS at Different Current Densities. EIS was applied by van Heuveln [1993] to determine the electrical losses in the SOFC. Further refinements have been made by Richter [1997] to represent the porous structure of the electrode using the PE model proposed by Göhr [1997].

Electrochemical impedance spectra of single SOFCs were reported by Wagner *et al.* [1998]. They investigated SOFC with cermet anode (ZrO_2 30% Ni, 30 μm thick) produced by vacuum plasma spraying at DLR (details are given by Lang *et al.* [2002]) deposited onto 640 μm thick YSZ electrolyte substrates (ZrO_2 8 mol % Y_2O_3 , Kerafol GmbH, Germany), and screen printed layers of $(La,Sr)MnO_3$ (40 μm thick, Siemens AG, Germany) were used as cathode.

Due to the high operating temperature of the SOFC, the charge transfer resistance of the anode and the cathode is in the same order of magnitude. Therefore the contribution of the anode cannot be neglected. Even at OCV (1234 mV) and at lower cell voltage (higher current density), in addition to the charge transfer resistances (R_{ct}) and double-layer capacities (C_{dl}) of the electrodes, a phase-shift maximum in the low-frequency range of the spectra (at 10 Hz) with a Nernst impedance-like behavior is observed, as indicated in the impedance spectra represented in Figure 4.5.75a as Bode plot and Figure 4.5.75b as Nyquist plot. The relaxation at 10 Hz is attributed to gas diffusion along the gas supply channels on the anode side caused by inefficient flushing similar to the mechanism proposed by Geyer *et al.* [1997]. Primdahl and Mogensen [1997, 1998] also found this behavior. They call it "gas conversion impedance," which is related to the change of atmosphere composition over the anode or "nonuniform diffusion impedance," as denoted by Van Herle *et al.* [1994].

The same equivalent circuit used to evaluate the PEFC impedance spectra (Figure 4.5.64) can be applied for the simulation of the measured impedance spectra of the SOFC. The time constant of the cathode ($R_{ct(C)}/C_{dl(C)}$) is given by the charge transfer through the double layer of the cathode. The time constants due to anode and cathode respectively are determined by variation of the gas supply, as shown by Lang *et al.* [2002]. From a least squares fit, one obtains a set of impedance parameters. Using these impedance parameters, as shown in the PEFC section (Eqs. (50)–(54)), one can calculate the voltage losses at the components of an SOFC. In the case of a linear current–voltage characteristic, these voltage losses can also be calculated from the product of the impedance parameters magnitude ($R_{ct(A)}, R_{ct(C)}, R_{(N)}$, and R_{EI}) and the current densities (Figure 4.5.76). The calculated cell voltage is in good agreement with the cell voltage, which was measured in an independent second experiment with an external load.

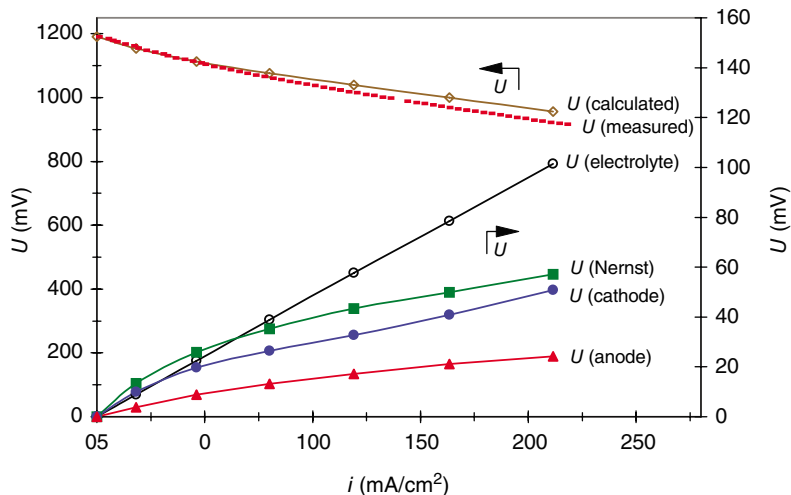


FIGURE 4.5.76 Cell voltage (measured and calculated) and calculated voltage losses at the SOFC (Ni-cermet/YSZ/(La,Sr)MnO₃) measured at 950°C at different current densities.

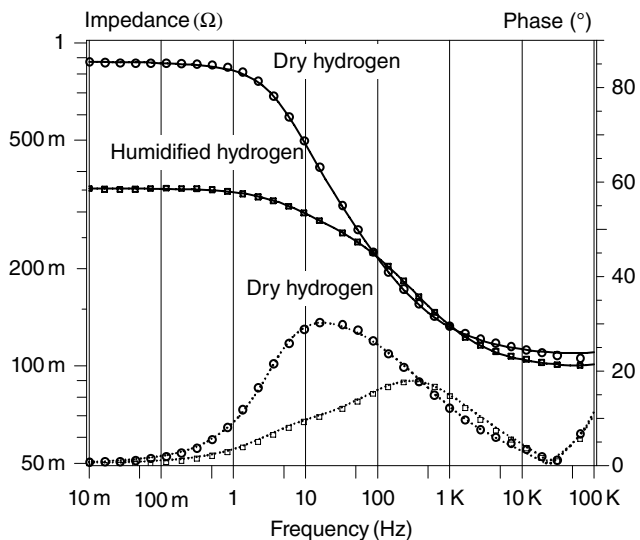


FIGURE 4.5.77 Bode plot of the measured impedance spectra, SOFC (ZrO₂-Ni/YSZ/(La,Sr)MnO₃) at 950°C, measured at different OCV- with dry hydrogen (○) at OCV (1234 mV) and humidified. (□) at OCV (1114 mV).

EIS Measured at SOFC: Anode Supplied with Dry and Moistened Hydrogen. The water vapor content of the fuel gas fed to the SOFC anode has a strong effect on the electrochemical characteristics of the cell. In “dry” hydrogen, a small amount of water has hydrogen due to water production at exchange current density (i_0). In the case of insufficient badly sealed cells, chemically produced water also reduce the OCV below 1000 mV. Therefore the value of the OCV can be used as an indication for the quality, for example, the sealing of the cell. In Figure 4.5.77 impedance spectra measured at open-circuit voltage with dry hydrogen and with humidified hydrogen, obtained after passage of hydrogen through a bubbling bottle at room temperature, are shown.

In order to explain the water vapor influence, one has to refer to the following equations. According to Geyer *et al.* [1997], the dependence of the anodic charge transfer resistance ($R_{ct,A}$ in the equivalent circuit used) on the mole fraction of water vapor (X) in the gas can be explained by assuming a BV kinetic where the exchange current density (i_0) is proportional to powers of the concentrations of the reactants (hydrogen and water vapor):

$$\frac{RT}{2Fi_0} = R_{ct,A}(X) \propto \frac{1}{X^\alpha(1-X)^{(1-\alpha)}} \quad (73)$$

where α is the charge transfer coefficient, R the gas constant, and T the absolute temperature.

Another effect due to the presence of water vapor in the fuel gas is observed in the open cell voltage. The observed differences of the open cell voltage depending of the water vapor content in hydrogen can be explained by the Nernst equation. The gas diffusion overvoltage (η_N) is given by the Nernst equation:

$$\eta_N = \frac{RT}{2F} \ln \frac{X}{(1-X)\sqrt{p_{O_2}}} \quad (74)$$

This diffusion overvoltage leads to the Nernst impedance. Operating the fuel cell with oxygen ($p_{O_2} = 1$), no diffusion overvoltage for $X = 0.5$ occurs.

Therefore, the open cell voltage, given by Eq. (75), is very sensitive to the water vapor content in the fuel gas and can be used to determine the water vapor in the fuel gas quantitatively:

$$OCV = E_{0,\text{th}} + |\eta_N| \quad (75)$$

where $E_{0,\text{th}}$ is the standard cell potential at operating temperature. $E_{0,\text{th}}$ can be calculated using Eq. (76):

$$\Delta_f G_T^0 = -zFE_{0,\text{th}} \quad (76)$$

where $\Delta_f G_T^0$ is the standard molar Gibbs energy change of formation of water vapor at the temperature T in kJ/mol and z the number of transferred during the overall reaction.

From Lide [1997] for $T = 950^\circ\text{C}$ (1223 K), we found $\Delta_f G_T^0 = -180.152$ kJ/mol. Using Eq. (76) one calculate $E_{0,\text{th}} = 934$ mV.

The mole fraction of water vapor (X) in the gas can be calculated with the semiempirical Antoine equation, as shown by Baehr [1988]:

$$\log p_{H_2O}^{\text{sat}} = A - \frac{B}{C + (T - 273.15)} \quad (77)$$

where $A = 8.0732991$, $B = 1656.39$, $C = 226.86$, and $p_{H_2O}^{\text{sat}}$ in mbar.

$$X = \frac{p_{H_2O}^{\text{sat}}}{p} \quad (78)$$

Using Eqs. (77) and (78), for $T = 298.15$ K and $p = 1014$ mbar, the calculated mole fraction of water vapor content (X) reaches 3 mol %. Inserting $X = 0.03$ in Eq. (75) and combining it with Eq. (75), one obtains an open-circuit voltage of 1117 mV. This is in very good agreement with the measured OCV of 1114 mV.

Temperature Dependency of EIS Measured at SOFC at Open Cell Voltage. In order to determine the activation energy of the ORR at the cathode and HOR at the anode and ionic conduction (O^{2-}) in the ceramic (solid oxide) electrolyte, impedance spectra at OCV and different temperature have to be

measured. From the evaluation of the impedance spectra measured at different temperatures (Figure 4.5.78) by applying the proposed equivalent circuit, a set of resistances (charge transfer and electrolyte resistance) are calculated, and using an Arrhenius approach, the activation energy for each process can be calculated, as shown in Figure 4.5.79.

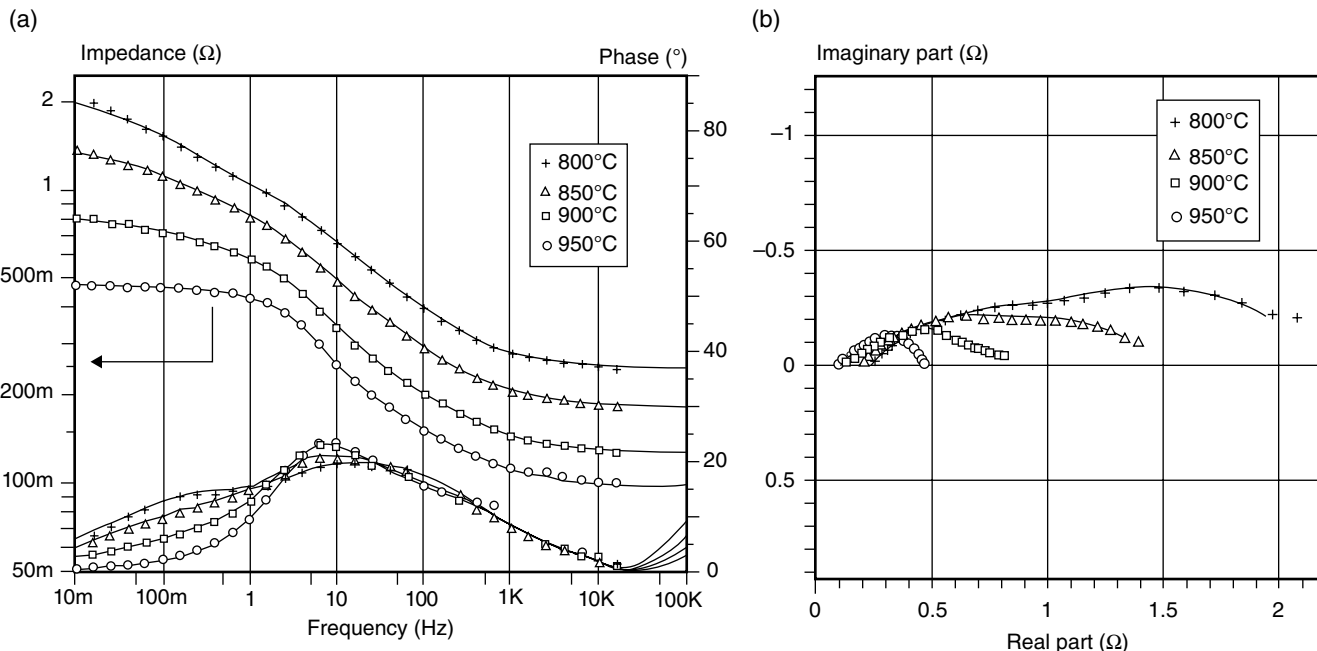


FIGURE 4.5.78 (a) Bode plot of impedance spectra, SOFC cell ($\text{ZrO}_2\text{-Ni/YSZ/(La,Sr)MnO}_3$, geometric surface 5 cm^2) measured at different cell temperatures. (b) Nyquist plot of impedance spectra, SOFC cell measured at different temperatures.

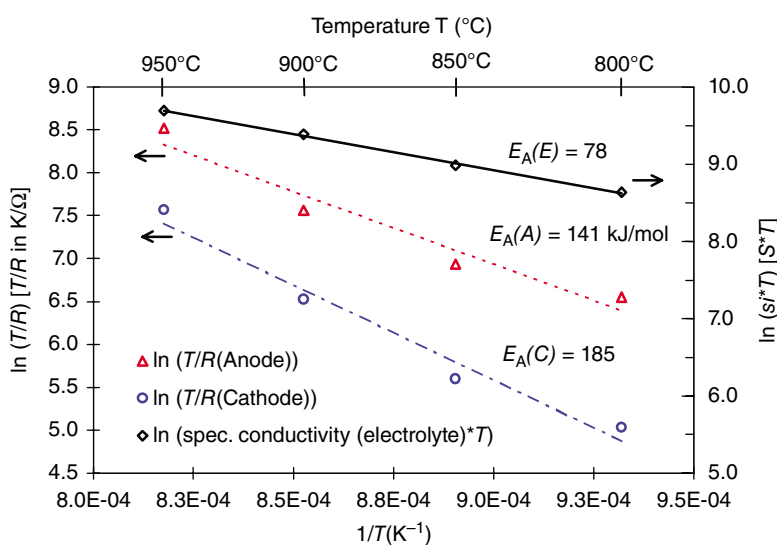


FIGURE 4.5.79 Arrhenius plot for the determination of activation energies of SOFC processes after evaluation of EIS measured at different temperatures at OCV.

4.6 DIELECTRIC RELAXATION SPECTROSCOPY

C. M. Roland

Naval Research Lab, Washington, DC, USA

4.6.1 Introduction

Impedance spectroscopy and dielectric relaxation measurements yield the same information; however, their purpose and analysis methods differ. Impedance spectroscopy is typically used to probe electrochemical processes, while dielectric relaxation data, almost invariably expressed in the complex permittivity representation, provide information on dynamical processes, typically the rate of molecular or polymer chain reorientation. Moreover, the features of interest in an impedance measurement, such as the transport and adsorption of charges, are an unwanted contribution to dielectric relaxation spectra, and thus are either ignored or removed from the latter. (Occasionally, the impedance function representation is used to eliminate interferences with relaxation measurements.) Since the objective of dielectric spectroscopy is to characterize the dynamics, models of molecular motion are the basis for interpretation; equivalent circuits, prominent in impedance spectroscopy studies, are not employed to analyze relaxation spectra. However, since relaxation spectra can be described formally as a distribution of exponential relaxation processes (Lindsey and Patterson [1980], Berberan-Santos *et al.* [2005]), an equivalent circuit diagram can be constructed (Figure 4.6.1) (see Kremer and Schonhals [2003a]). Such a description is phenomenological (a mathematical convenience), and its underlying premise, that the observed peak shape reflects a distribution of exponential decays, is problematic, as shown by Richert [1994].

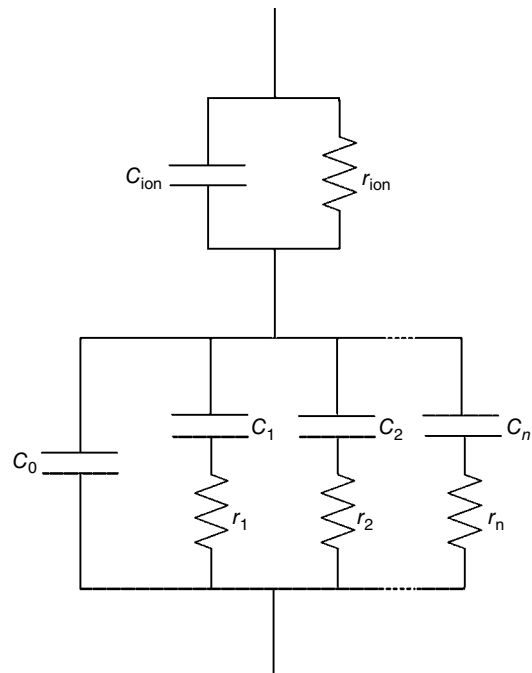


FIGURE 4.6.1 Equivalent circuit diagram for a viscoelastic response characterized by a distribution of n exponential decays, along with a contribution from mobile ions.

TABLE 4.6.1 Comparison of Typical Impedance and Dielectric Experiments

Spectroscopy	Impedance	Dielectric
Primary focus	Electrochemical (conduction mechanisms and interfacial processes)	Reorientation dynamics of molecular dipoles
Sample	Material-electrode system (conductive)	Bulk material (capacitive)
ac voltage	$\leq 10^{-3}$ V	≤ 10 V
dc voltage	Common	Rare
Typical analysis	Equivalent circuits	Relaxation models

and Roland [2011]. Table 4.6.1 summarizes the distinct aspects of impedance and dielectric relaxation spectroscopies.

4.6.2 Dielectric Relaxation

The use of dielectric spectroscopy to probe the motion of molecules requires the latter to have a nonzero dipole moment, μ . However, with modern instrumentation capable of attofarad resolution, this is not a restrictive requirement. Even conventional dielectric bridges can measure polymers with very small dipole moments ($\mu < 0.1$ D), for example, atactic polypropylene, which has a dielectric strength less than 0.01 (Work *et al.* [1964], Kessairi *et al.* [2007]). In the usual relaxation measurement, a weak electric field is applied, with the linear response regime defined by two (equivalent) conditions:

1. The dielectric permittivity does not vary with the electric field, E ; this means that the polarization is proportional to E :

$$P = (\epsilon^* - 1)\epsilon_0 E \quad (1)$$

where ϵ^* is the complex dielectric permittivity of the material and ϵ_0 the dielectric permittivity of vacuum (= 8.854 pF/m).

2. The polarization energy, associated with dipole orientation, is less than the thermal energy, that is, $\mu E \ll kT$. This means there is no net polarization, as orientation of the dipoles is overcome by thermal agitation and the sample remains isotropic.

Since the motions prevailing at equilibrium enable the molecular dipoles to remain unoriented on average, the measured time-dependent fluctuations of the polarization correspond to the equilibrium dynamics. For small molecules (simple liquids), dielectric relaxation spectroscopy probes the molecular reorientations. For most polymers the dipole moment is transverse to the chain, so that the dielectric experiment probes the local segmental dynamics. For those few polymers having a dipole moment component parallel to the backbone (which means their repeat unit structure lacks a symmetric center), dielectric relaxation can measure more global dynamics, as discussed below. Expressing Eq. (1) for the dynamics gives

$$P(t) = P_\infty + \epsilon_0 \int_{-\infty}^t \epsilon(t-t') \frac{dE(t')}{dt'} dt' \quad (2)$$

in which P_∞ accounts for induced polarization (e.g., distortion of the electron cloud) and the second term describes the orientation polarization. The usual experiment applies a time-dependent electric field, with the complex permittivity obtained as

$$\epsilon^*(\omega) = \epsilon'(\omega) - i\epsilon''(\omega) = \epsilon_\infty - \int_0^\infty \frac{d\epsilon(t)}{dt} \exp(-i\omega t) dt \quad (3)$$

The relationship to the impedance is

$$\epsilon^*(\omega) = \frac{1}{i\omega Z^*(\omega)C_0} \quad (4)$$

where C_0 is the vacuum capacitance. In Eq. (3) ϵ_∞ is the constant value of the dielectric permittivity exhibited by materials at sufficiently high frequencies.

The structural relaxation peak (α -process) of liquids and polymers is invariably broader than the Debye function (for which the peak has a width at the half intensity points of 1.14 decades):

$$\epsilon^*(\omega) = \epsilon_\infty + \frac{\Delta\epsilon}{1 + i\omega\tau_D} \quad (5)$$

where τ_D is the Debye relaxation time and $\Delta\epsilon$ the dielectric strength ($= \epsilon_s - \epsilon_\infty$ where ϵ_s is the static or low-frequency permittivity). Structural relaxation spectra are usually fit to either the Havriliak–Negami (H–N) equation (Kremer and Schonhals [2003b])

$$\epsilon^*(\omega) = \Delta\epsilon[1 + (i\omega\tau_{HN})^a]^{-b} \quad (6)$$

where τ_{HN} , a , and b are constants or the KWW function (Kremer and Schonhals [2003b])

$$\epsilon^*(\omega) = \Delta\epsilon \hat{L}_{i\omega} \left[-\frac{d\varphi(t)}{dt} \right] \quad (7)$$

$$\varphi(t) = \exp \left[-\left(\frac{t}{\tau_K} \right)^{\beta_K} \right] \quad (8)$$

with τ_K and β_K constants and $\hat{L}_{i\omega}$ denotes the Laplace transform. Equation (6) is empirical, its popularity deriving from the ability to fit experimental $\epsilon''(\omega)$ peaks. Equation (8), which has one less adjustable parameter than the H–N equation, can be arrived at in various ways: from models based on free volume (Cohen and Grest [1981]), hierachal constraints (Palmer *et al.* [1984]), defect diffusion (Bendler and Shlesinger [1985]), defect distances (Klafter and Blumen [1985]), random free energy (De Dominicis *et al.* [1985]), intermolecular cooperativity (Ngai *et al.* [1986], Kubat *et al.* [1999]), or molecular weight polydispersity (de Gennes [2002]). The KWW function can also be obtained by employing a particular distribution of exponential decay functions (Lindsey and Patterson [1980], Berberan-Santos *et al.* [2005]), illustrated by the equivalent circuit in Figure 4.6.1. Secondary relaxations, which fall at higher frequencies, can be described by Eq. (6) or the symmetric Cole–Cole function (Kremer and Schonhals [2003b])

$$\epsilon^*(\omega) = \frac{\Delta\epsilon}{1 + (i\omega\tau_{CC})^{1-\gamma}} \quad (9)$$

where γ and τ_{CC} are constants. Equation (9) corresponds to the H–N function with $b = 1$ and reduces to the Debye function for $\gamma = 0$. The peak in the dielectric loss spectrum occurs at a frequency corresponding to that of the underlying molecular motions (e.g., rotations of small molecules or the local segmental dynamics of polymers for their α -relaxation peak). Thus, the inverse of the α -peak frequency defines a model-independent relaxation time, τ_α . Reflecting the stretching of the spectrum toward longer frequencies, $\tau_\alpha > \tau_K$, while the relative magnitudes of τ_K and τ_{HN} depend on the shape parameters, a , b , and β_K .

Figure 4.6.2 shows the dielectric relaxation spectrum of polymethyl methacrylate (PMMA), which has an unusually prominent secondary relaxation. If the latter is well separated from the α -peak, the two dispersions can be fit with the assumption that the processes are additive in the frequency domain. If the respective τ are close, this assumption breaks down, and an equation due to Williams [1979] is used:

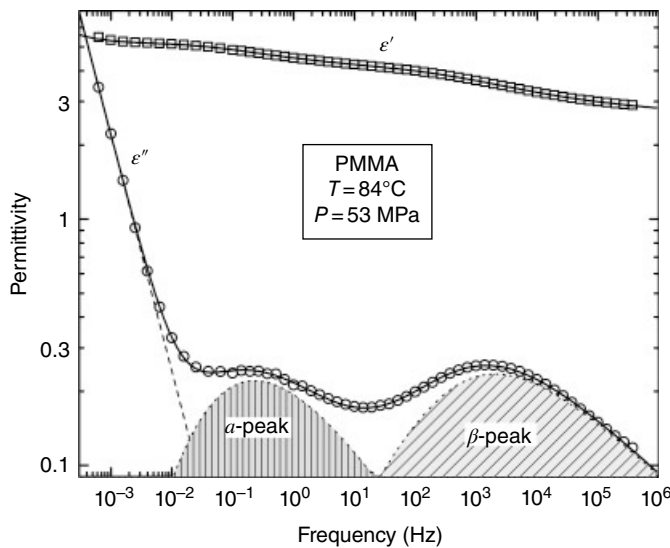


FIGURE 4.6.2 Dielectric spectrum of polymethyl methacrylate, along with the fits of Eqs. (7) and (8) to the local segmental dynamics and Eq. (6) for the secondary relaxation, at respective low and high frequencies. The rise in the loss below approximately 0.01 Hz is due to ionic conduction, fit with Eq. (14) using $j = 1$.

$$\epsilon(t) = f_\alpha \epsilon_\alpha(t) + (1-f_\alpha) \epsilon_\beta(t) \quad (10)$$

Equation (10) assumes the two relaxations are independent, except that the β process takes place in an environment that is rearranging on the time scale of the α -process. The fits of Eqs. (6)–(8), using Eq. (10), to the PMMA dielectric constant and loss spectra are shown in the Figure 4.6.2. Note that the dielectric loss exhibits power-law behavior at low frequencies, a consequence of mobile ions; this dc conductivity is discussed below.

The main features of the dielectric spectra of polymers are the α -relaxation peak due to the local segmental dynamics and various higher-frequency secondary relaxations due to restricted torsional motions of the chain and any side group dynamics. However, polymers having a dipole moment parallel to the chain contour (e.g., 1,4-polyisoprene, polypropylene glycol (PPG), polylactide) exhibit a so-called normal mode peak due to fluctuations of the chain end-to-end vector (Adachi and Kotaka [1993]). Spectra are shown in Figure 4.6.3 for PPG and polyoxybutylene (POB) (Casalini and Roland [2005]), both polymers having dielectrically active normal modes. Sometimes referred to as the global or terminal relaxation, the normal mode peak falls at lower frequencies than the local segmental dispersion by an amount nonlinear in the polymer molecular weight (Roland [2011]). At high temperatures the two relaxation processes have equivalent T -dependences, whereas at temperatures approaching the glass transition, the normal mode relaxation time is less sensitive to temperature than the more local α -process (Roland *et al.* [2001]).

4.6.2.1 Ion Conductivity

Liquids and polymers invariably contain mobile ions, often electrolytic impurities, whose diffusion gives rise to dc conductivity, σ_{dc} (see Figure 4.6.2). In a material that is inherently conducting, σ_{dc} may correspond to translocation of intrinsic ions across sites on a polymer chain, such as protons along hydrogen bonds. This conduction is distinct from the higher-frequency ac conductivity, which in addition to ion diffusion can arise from nonrelaxing, subdiffusive processes, such as local excursions and

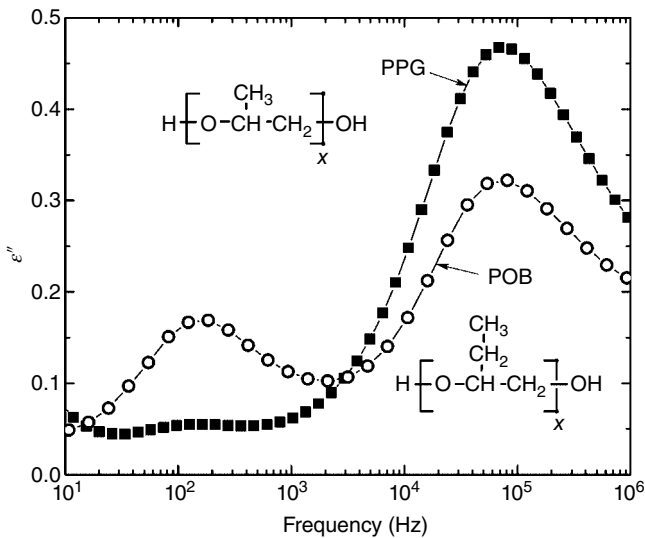


FIGURE 4.6.3 Dielectric loss spectra of POB and PPG having the same number of repeat units (=67), measured at $T = 20^\circ\text{C}$ and $P = 616 \text{ MPa}$ (PPG) and $T = 24^\circ\text{C}$ and $P = 351 \text{ MPa}$ (POB). The peak frequencies of the respective segmental and normal mode relaxations were 71 kHz and 143 Hz for PPG and 99 kHz and 211 Hz for POB.

vibrations of ions within a cage of the host molecules. Whereas a common purpose of impedance spectroscopy is to characterize ion diffusion, for relaxation studies σ_{dc} is usually unwanted because it can mask the relaxation peaks in the loss spectrum. The Nernst equation relates the dc conductivity to the concentration of ions, c , having charge q (Johari and Andersson [2006]):

$$\sigma_{dc} = \frac{cq^2 D}{k_B T} \quad (11)$$

where D is the ion diffusion constant and k_B the Boltzmann constant. For a frequency-dependent diffusion constant, $D^*(\omega)$, the conductivity is complex and yields a term in the permittivity:

$$\epsilon^*(\omega) = \frac{\sigma^*(\omega)}{i\omega\epsilon_0} \quad (12)$$

The usual power-law behavior gives

$$\epsilon^*(\omega) = \frac{\sigma_{dc}}{\epsilon_0(i\omega)^j} \quad (13)$$

with j a constant (≤ 1), equal to unity for free conduction of electrons or ions. This conductivity contribution to the dielectric loss can be described by

$$\epsilon''_{dc}(\omega) = \frac{\sigma_{dc}}{\epsilon_0\omega^j} \quad (14)$$

Provided there is some separation from the relaxation peaks, Eq. (14) can be included in fitting spectra to account for the conductivity.

Ionic conductivity is coupled to reorientational relaxation, since motion of the host molecules or segments provides diffusive pathways. This leads to a relation between ion conductivity and the α -relaxation time (Corezzi *et al.* [1999]):

$$\sigma_{dc}\tau_\alpha^j = \text{const} \quad (15)$$

Equation (15) is an empirical variation of the Debye–Stokes–Einstein (DSE) equation (Stickel *et al.* [1996]):

$$\frac{\sigma_{dc}\tau_\alpha T}{c} = \text{const} \quad (16)$$

Generally, c and T change little over the range of dielectric measurements, so that σ_{dc} is plotted versus τ_α on double logarithmic scales, to yield a power law having a slope equal to $-j$. Results are shown in Figure 4.6.4 for propylene glycol monomer, dimer, and trimer. The exponent ($j = 0.84 \pm 0.02$) is the same for the three liquids, although the magnitude of the ion conductivity decreases with increasing molecular weight.

The conductivity behavior described by the fractional DSE equation (15) can have two origins. Any change in the ion population due to polyelectrolytic dissociation or the formation of ion pairs is usually neglected in analysis of data (i.e., c is assumed constant). And since the effect of temperature and pressure on ion population is usually very different from their influence on ion mobility, the result can be deviations from proportionality of σ_{dc} to the inverse relaxation time. The other cause of departures from Eq. (16) is more general: as temperature is reduced below approximately $1.2T_g$, a reduction in the coupling between translational and rotational dynamics is observed (Ediger [2000]). This is manifested in the T -dependence of translational diffusion becoming weaker than that of the viscosity or the rotational

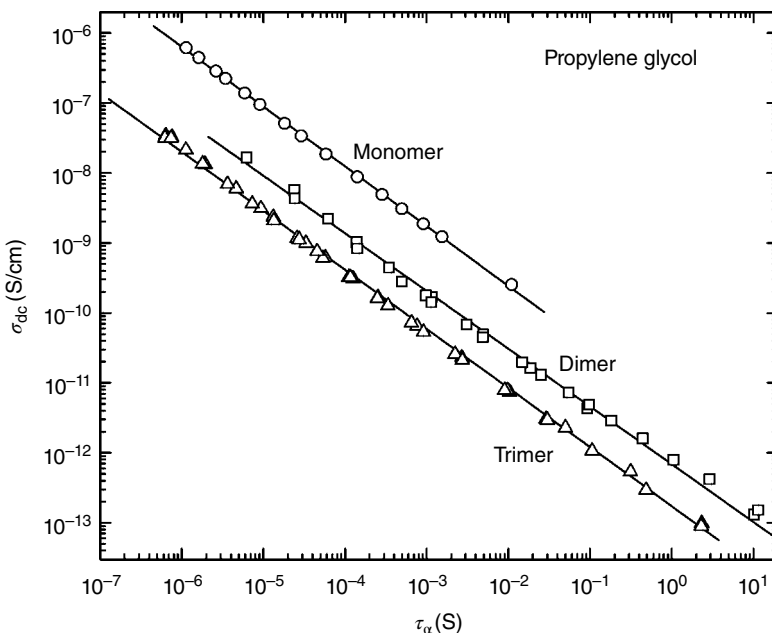


FIGURE 4.6.4 Conductivity versus α -relaxation time for propylene glycol monomer (circles), dimer (squares), and trimer (triangles) at various temperatures and pressures. Lines are fits yielding $j = 0.84 \pm 0.02$ for all three liquids.

dynamics, causing a violation of the DSE equation (Figure 4.6.5, adapted from Roland *et al.* [2001]). The mechanism underlying this decoupling is not well understood.

Although dc conductivity sometimes interferes with characterization of molecular relaxation, the dependence of ion diffusion on the α -dynamics can be exploited to obtain information about structural relaxation of a glass. By definition, the glassy state corresponds to conditions for which molecular diffusion and rotation (or local segmental motion of a polymer) transpire more slowly than the observable time scale; that is, their loss peaks are at frequencies lower than measured by dielectric spectroscopy ($<10^{-4}$ Hz). However, the cessation of these motions retards, but does not preclude, ion diffusion. Thus, below the glass transition ion conduction continues, although the sensitivity of σ_{dc} to temperature (i.e., the activation energy) and to pressure (the activation volume) both decrease. The reduced activation energy below T_g is illustrated in Figure 4.6.6 in a plot of the conductivity relaxation time (defined below) for an ionic liquid versus temperature (Wojnarowska *et al.* [2012]). Physical aging (very gradual densification) of the glass slows the ion diffusion; the time constant describing this effect corresponds to a structural relaxation time, which is too large for direct measurement (below T_g τ_α in Figure 4.6.6 exceeds 8 h).

An obvious method to minimize the conductivity contribution to the spectrum is to reduce the ion concentration. This can be done by successive dissolution–precipitation of the polymer or by application of an electric field to the sample *in situ* to cause accumulation of the ions at the electrode interfaces for subsequent removal (Gainaru *et al.* [2010]). From the Kramers-Kronig relation for the case of $j = 1$ [Eq. (16)],

$$\epsilon'(\omega) = \epsilon_\infty + \frac{2}{\pi} \int_0^\infty \epsilon''(\omega_0) \frac{\omega_0}{\omega_0^2 - \omega^2} d\omega_0 \quad (17)$$

$$\epsilon''(\omega) = \frac{\sigma_{dc}}{\epsilon_0 \omega} + \frac{2}{\pi} \int_0^\infty \epsilon'(\omega_0) \frac{\omega_0}{\omega_0^2 - \omega^2} d\omega_0 \quad (18)$$

it is seen that the dc conductivity makes no contribution to the real part of the permittivity; thus, the measured $\epsilon'(\omega)$ can be converted via Eq. (18) to a dielectric loss spectrum without interference from σ_{dc} . This is illustrated in Figure 4.6.7 (Wubbenhorst and van Turnhout [2002]), showing the measured and calculated dielectric loss for a liquid with a substantial conductivity.

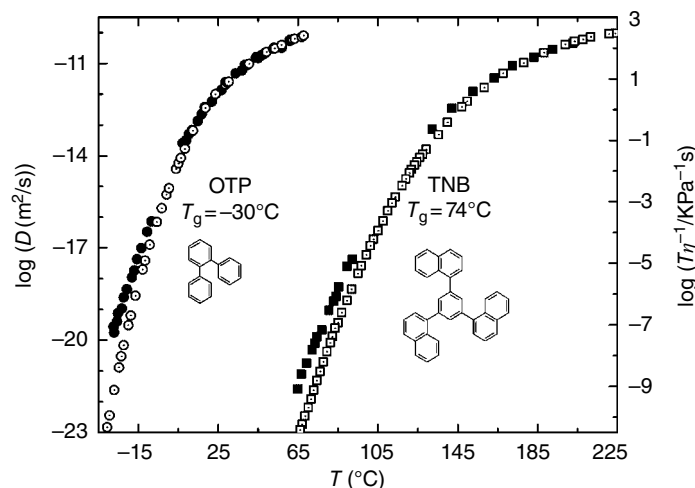


FIGURE 4.6.5 Self-diffusion coefficients of o-terphenyl (filled circles) and tris-naphthylbenzene (filled squares—values shifted upward by 0.16) compared to the ratio of temperature to the viscosity (corresponding open symbols). The right ordinate was adjusted to give superposition with the diffusion coefficients at high T , illustrating the enhancement of translational diffusion close to T_g . Chemical structures are shown.

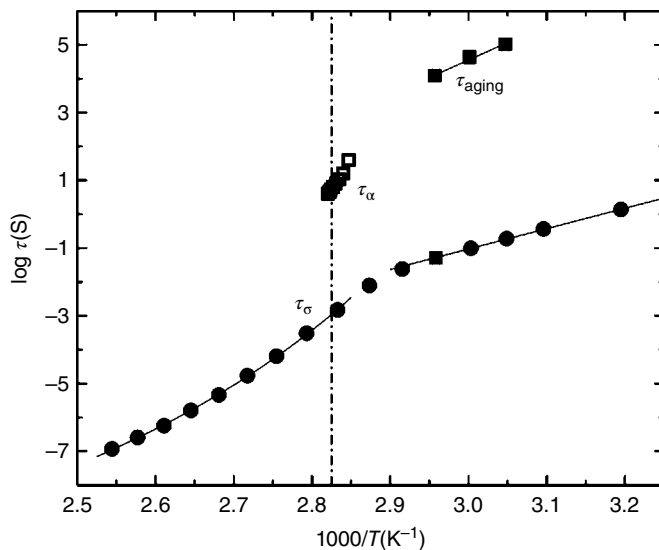


FIGURE 4.6.6 Conductivity relaxation times for carvedilol phosphate (circles), showing the weaker temperature sensitivity below the glass transition (indicated by the vertical dashed line). Also shown (filled squares) are the time constants obtained from the change in permittivity with physical aging; these correspond to the structural relaxation time in the glass, measured directly by calorimetry near T_g (open squares).

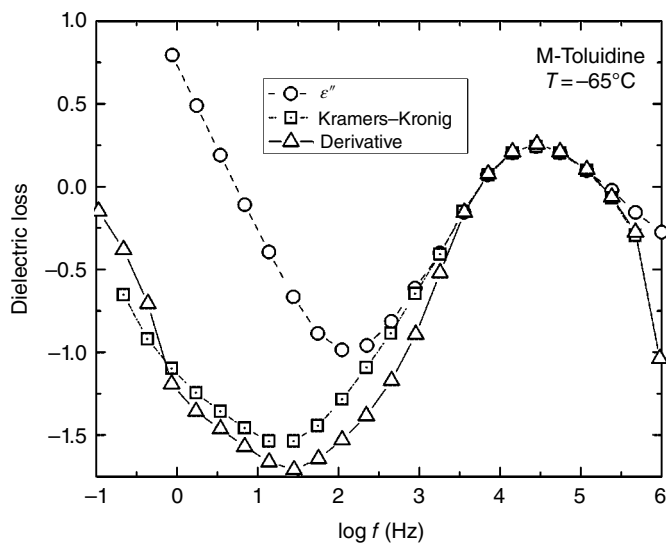


FIGURE 4.6.7 Dielectric loss of 3-amino toluidine as measured (circles), calculated from $\epsilon'(\omega)$ using the Kramers-Kronig relation (squares), and represented by the derivative of the real part of the permittivity (triangles). The last two methods suppress the ionic conduction, seen as the power law at low frequencies, having a slope, $-j = 1$.

For broad relaxation peaks an approximation to the KK formula can be used (Wubbenhorst and Turnhout [2002]):

$$\epsilon''(\omega) \approx -\frac{\pi}{2} \frac{\partial \epsilon'(\omega)}{\partial \ln \omega} \quad (19)$$

The dc conductivity is absent from this calculated dielectric loss. An example of the application of Eq. (19) is included in Figure 4.6.7; it can be seen that the α -peak in the derivative spectrum is artificially narrower than in the directly measured $\epsilon''(\omega)$, although the frequencies of the maxima, and thus the τ_α coincide. This derivative analysis can also be employed to shift the effect of electrode polarization toward lower frequencies, away from the main relaxation (Jimenez *et al.* [2002]). Electrode polarization refers to blocking of charge exchange at the sample/electrode interface, due to the existence of a potential barrier. Mainly arising in more conductive systems, electrode polarization causes the measured dielectric constant at low frequency to be much larger (in the range 10^2 – 10^6) than the actual value for the sample.

4.6.2.2 Dielectric Modulus

The dielectric function $\epsilon^*(\omega)$ is a compliance, the ratio of the electric displacement to the field. Analogous to the mechanical compliance and modulus, a dielectric modulus ("reciprocal permittivity") can be defined as

$$\begin{aligned} M^*(\omega) &= \frac{1}{\epsilon^*(\omega)} \\ M'(\omega) &= \frac{\epsilon'}{\epsilon'^2 + \epsilon''^2} \\ M''(\omega) &= \frac{\epsilon''}{\epsilon'^2 + \epsilon''^2} \end{aligned} \quad (20)$$

The permittivity describes the polarization at constant field, and $M^*(\omega)$ the polarization at constant charge. Of course, the modulus representation contains no information not present in the dielectric permittivity; however, the dc conductivity is manifested in the imaginary component, $M''(\omega)$, as a peak, and the α -relaxation is shifted to higher frequency; thus, the latter is more separated from σ_{dc} than in the permittivity representation. The amount of this shift of the α -peak depends on the dielectric strength of the relaxation; for a Debye process [Eq. (5)], $\tau_{\alpha,\epsilon''} = \frac{\epsilon_s}{\epsilon_\infty} \tau_{\alpha,M''}$. This effect and the presence of a conductivity peak in $M''(\omega)$ are shown in Figure 4.6.8.

The conductivity relaxation time, τ_σ , is defined as the inverse of the frequency of the maximum of the $M''(\omega)$ conductivity peak. This relaxation time differs from the microscopic correlation time, τ_{ion} , describing ion movement (e.g., hopping). From a model of random movement of ions in a disordered medium, a relation can be obtained between the two quantities (Ngai and Leon [1999]):

$$\frac{\tau_{ion}}{\tau_\sigma} = \frac{cq^2 r^2}{6k_B T \epsilon_0 \epsilon_\infty} \quad (21)$$

where r is the mean hopping displacement of the ions.

4.6.2.3 Use of Impedance Function in Dielectric Relaxation Experiments

Dielectric relaxation measurements to determine the dynamics of polymers and liquids analyze the permittivity, ignoring the impedance. However, when measurements are extended to high frequencies (which for a typical dielectric relaxation experiment is defined as frequencies beyond *ca.* 10^6 Hz), the

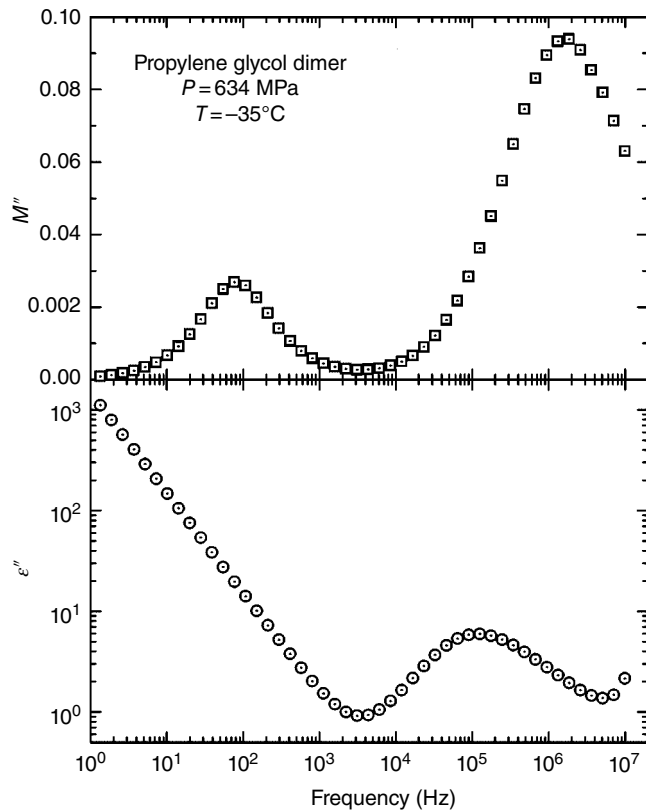


FIGURE 4.6.8 Imaginary component of permittivity (lower) and modulus (upper) of propylene glycol dimer. Ion conductivity is manifested in the former as a power law at lower frequencies and in the latter as a peak at approximately 100 Hz. Note the α -peak shifts about one decade higher frequency in the modulus representation.

complex impedance may be utilized to remove the effects of the resistance and inductance of electrical cables used to connect the sample electrodes to the analyzer. The relevant equation for the resistance R is

$$\lim_{\omega \rightarrow \infty} z'(\omega) = R \quad (22)$$

and for the inductance L (resistance due to current changes in the cable)

$$z''(\omega) = \frac{d}{\omega} - \omega L \quad (23)$$

where d is a constant. The measured impedance functions are then corrected to yield spectra free from these effects of the cables:

$$z'_{\text{corr}}(\omega) = z'(\omega) - R \quad (24)$$

and

$$z''_{\text{corr}}(\omega) = \omega L z''(\omega) \quad (25)$$

In turn, the permittivity is calculated from the corrected impedances using Eq. (4).

To apply Eqs. (22) and (23) requires dielectric measurements that are free from relaxation peaks, that is, any capacitance changes due to the sample. This can be done by measurements at temperatures well below T_g , as illustrated in Figure 4.6.9 for a cross-linked polyvinylethylene (PVE). The fit to the real and imaginary impedance functions yields R and L for the cable assembly, respectively. Equations (24) and (25) are used to calculate the corrected impedance functions, from which the permittivity is obtained. Figure 4.6.10 illustrates this method to remove the interference from the cables in measurements on the PVE network, enabling determination of the actual material response (Casalini and Roland [2010]). Because of the low polarity of PVE, cable contributions become apparent at relatively low frequencies, *ca.* 2 kHz. More typically, corrections for cable effects are required only for measurements beyond *ca.* 10⁶ Hz.

Another use of the impedance function in dielectric spectroscopy is to remove the effects of electrode polarization, that is, charge buildup under low-frequency fields at the electrode/sample interface. This phenomenon is an example of the Maxwell–Wagner–Sillars (MWS) effect, which is a general term for polarization, including at an external electrode or at internal boundary layers within an inhomogeneous sample. For the case of an insulating layer covering the electrode, the layer and sample impedances are in series, with the measured impedance equal to the sum of the values for the sample, z_{sam} , and layer, z_{ins} :

$$z_{\text{meas}}^* = z_{\text{sam}}^* + z_{\text{ins}}^* \quad (26)$$

From Eq. (4)

$$\epsilon_{\text{meas}}^* = \frac{(l_{\text{sam}} + l_{\text{ins}})\epsilon_{\text{sam}}^*\epsilon_{\text{ins}}^*}{l_{\text{ins}}\epsilon_{\text{sam}}^* + l_{\text{sam}}\epsilon_{\text{ins}}^*} \quad (27)$$

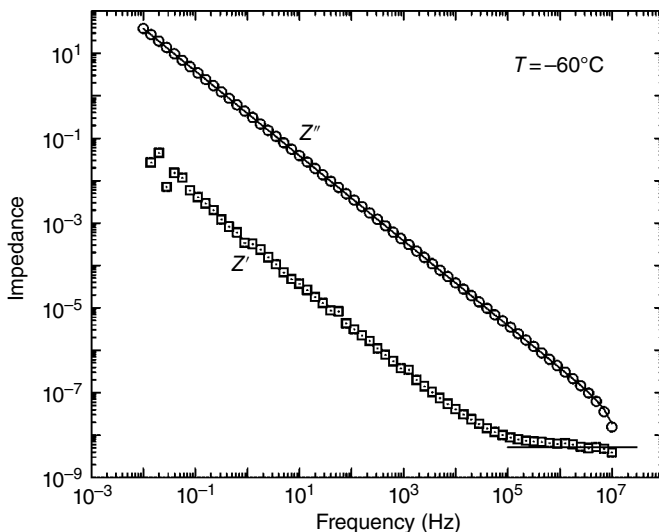


FIGURE 4.6.9 Real and imaginary permittivity measured for a cross-linked PVE at a temperature sufficiently low that no relaxation processes are present in the spectra. The solid lines are the fits of Eq. (22) to z' at high frequencies and of Eq. (23) to z'' .

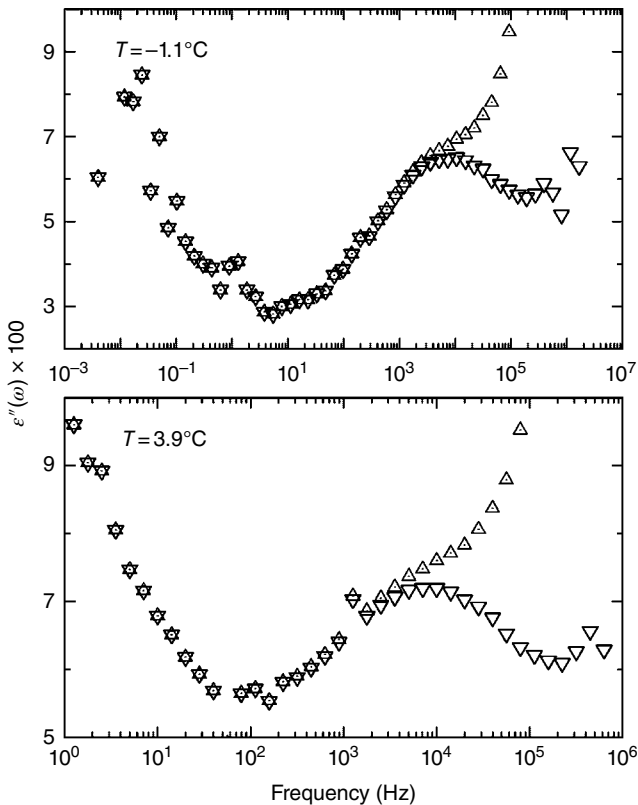


FIGURE 4.6.10 Dielectric loss of PVE networks at two temperatures below T_g ($=9.0^\circ\text{C}$). The rise at high frequencies in the measured spectra (triangles) is due to the cables; after correction (inverted triangles) the actual loss peak is obtained.

in which l_{sam} and l_{ins} represent the respective thicknesses of the sample and insulating layers. If the sample has significant conductivity, it will give rise to a peak due to the interfacial polarization at a frequency, f_{MWS} , given by

$$f_{\text{MWS}} = \frac{\sigma_{\text{sam}}}{2\pi\epsilon_0(\epsilon'_{\text{sam}} + (l_{\text{sam}}/l_{\text{ins}})\epsilon'_{\text{ins}})} \quad (28)$$

Electrode polarization can be exploited to separate the contributions of ion concentration and ion mobility to the conductivity (Klein *et al.* [2006]), although in most relaxation measurements it is an unwanted artifact.

To suppress dc conductivity in a dielectric loss spectrum, use is sometimes made of a “blocking electrode,” which refers to an insulator film placed between the sample and one of the electrodes. Although this method removes the prominent manifestation of σ_{dc} in the response, the steep rise in $\epsilon''(\omega)$ at lower frequencies [Eq. (14)], it does not eliminate the effect of conductivity on the relaxation spectrum. This is shown in Figure 4.6.11 in the dielectric spectrum of xylitol. Introduction of an insulating film causes the conductivity contribution to appear as a loss peak that still masks features of the spectrum in that frequency range.

Dielectric discontinuities within a sample can also give rise to spurious MWS peaks. Figure 4.6.12 shows spectra for glycerol (Casalini and Roland [2011]), in which at frequencies lower than the α -process there is a strong σ_{dc} contribution, manifested as a power law in $\epsilon''(\omega)$ and a rise at lower frequencies in

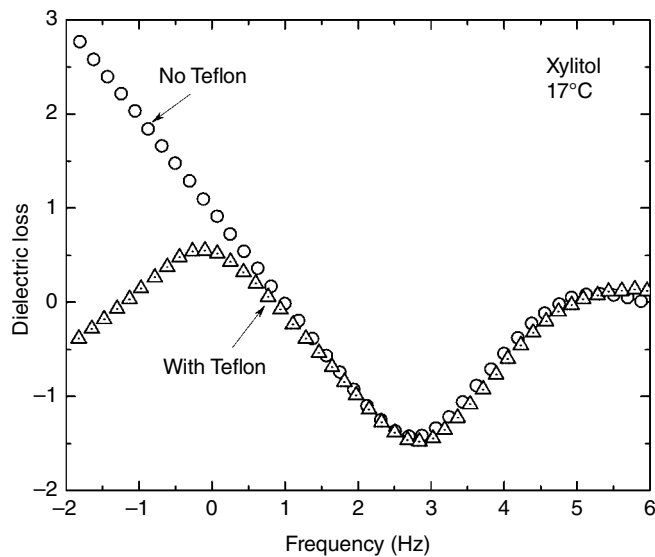


FIGURE 4.6.11 Dielectric loss of a polyalcohol with (triangles) and without (circles) a 5 μm Teflon film between the sample and one electrode. The σ_{dc} manifested in a power law at low frequencies becomes a peak around 1 Hz when the Teflon is present. The α -peak is seen at higher frequencies.

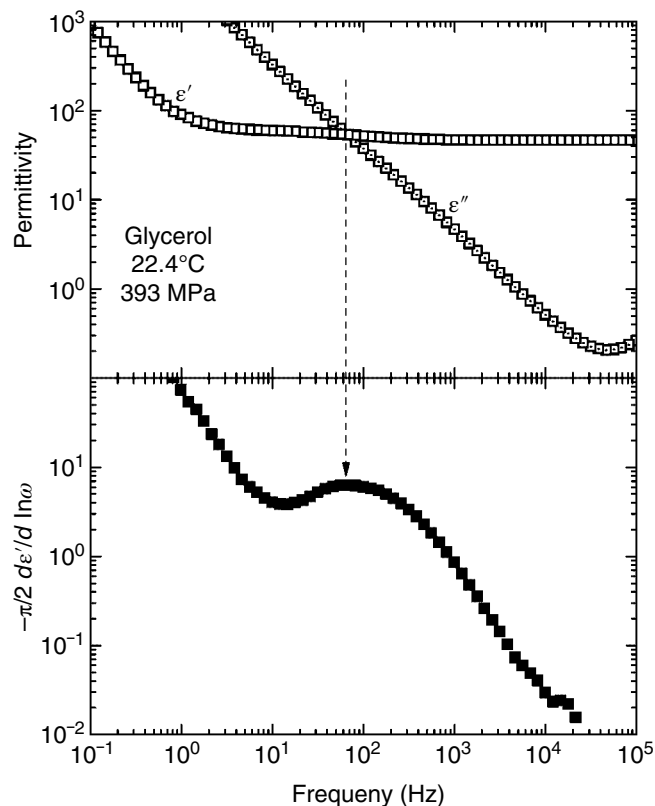


FIGURE 4.6.12 (top) Real (squares) and imaginary (dotted squares) components of permittivity of glycerol, showing the dominant dc conductivity in the loss, which causes electrode polarization seen as a rise in ϵ' at frequencies below 1 Hz. (bottom) Derivative function [Eq. (19)] in which σ_{dc} is manifested as a peak near the frequency at which $\epsilon' = \epsilon''$.

$\epsilon'(\omega)$ due to electrode polarization. Using the derivative of the real part to obtain the loss spectrum *sans* σ_{dc} reveals a weak MWS peak. The latter can be identified, *inter alia*, by its occurrence at frequencies for which $\epsilon' \sim \epsilon''$ (Richert *et al.* [2011]). Teflon and other polymeric insulators are also commonly used in the form of an annular ring to contain liquid samples or as a spacer (ring or fibers) to maintain a constant sample thickness. Since the insulators have a finite capacitance, their presence in parallel with the sample can cause a background loss that is additive in the permittivity. This can alter $\Delta\epsilon$ and shift the frequency of the peaks in the spectrum; typically these errors become significant when the area of the spacer is more than about 0.1% of the sample area (Johari [2012]).

4.6.2.4 Summary

Impedance spectroscopy and dielectric relaxation measurements employ similar instrumentation but are used for different purposes. In dielectric spectroscopy the usual objective is determination of the dipole reorientation dynamics that underlies, for example, structural relaxation of liquids and polymers. Contributions to the spectra from dc conductivity interfere with the measurement of relaxation peaks. This means that the spectral features that comprise the main interest of impedance spectroscopic experiments (e.g., bulk ion conduction, grain boundary and electrode/sample interfacial resistances) must be eliminated in relaxation studies. In this chapter the basics of dipole relaxation measurements have been outlined, along with a summary of methods used to remove conductivity effects from the spectra.

Acknowledgment

This work was supported by the Office of Naval Research. We thank D.M. Fragiadakis for carefully reading the manuscript.

4.7 ELECTRICAL STRUCTURE OF BIOLOGICAL CELLS AND TISSUES: IMPEDANCE SPECTROSCOPY, STEREOLOGY, AND SINGULAR PERTURBATION THEORY

Robert S. Eisenberg

Department of Molecular Biophysics & Physiology, Rush University, Chicago, IL, USA

Impedance spectroscopy is a technique with exquisite resolution since it resolves linear electrical properties into uncorrelated variables as a function of frequency. This separation is robust and most useful when the system being studied is linear. (If the system is significantly nonlinear, the meaning of the parameters is not clear, and they are likely to vary substantially with conditions, making models badly posed.) Impedance spectroscopy can be combined with appropriate structural knowledge (qualitative and quantitative) based on the actual anatomy of the system being studied. The combination provides biologically useful insight into the pathways for current flow in a number of cells and tissues, with more success than other methods.

Biological applications of impedance spectroscopy are often unable to take advantage of the strengths of impedance spectroscopy since so much of biology is strongly nonlinear in its essential features and impedance spectroscopy is fundamentally a linear analysis. There is an important special case, however, present in all cells and tissues in plants and animals, the cell membrane and its capacitance, where bioelectric properties are both linear and important to cell function. Here we take advantage of the ideal properties of membrane capacitance to make impedance spectroscopy a most useful tool for determining the electrical structure of cells and tissues (Eisenberg and Mathias [1980]).

The capacitance of cell membranes is close to perfect, with 90° phase angle as close as can be measured in the entire biologically relevant frequency range of dc to, say, 10^4 or even 10^5 Hz (Hanai *et al.* [1965a, b], Everitt and Haydon [1968], Fettiplace *et al.* [1971], Haydon *et al.* [1980]). Impedance spectroscopy is a useful tool for studying cell membranes then, because linear analysis is appropriate. Cell membranes define every cell in animals and plants, and so impedance spectroscopy is a tool that can be used throughout biology, exploiting the linear electrical properties of this structure. Cell membranes determine a wide range of biological function, and the organization of these membranes into folded and more complex structures is a general motif in biology. Indeed, a glance at the structure of a cell in any cell biology or histology textbook shows that membranes inside cells are extensively folded and organized as well. Impedance spectroscopy can help provide insight into membrane structure and function throughout biology.

Cells are not simple spheres or cylinders. Rather, they include complex membrane structures that channel electrical current to the regions of interest. These structures are important in epithelia that form the kidney and gallbladder and secretory cells (Clausen *et al.* [1979]). These structures are crucial in muscle fibers, skeletal and cardiac, where electrical signals across membranes coordinate contraction. Without coordination, skeletal muscle cannot provide useful force (Ríos and Pizarro [1991], Fill and Copello [2002]). Without coordination the heart cannot pump blood (Bers [2002]). Thus, the arrangement of membranes in skeletal muscle, and some cardiac muscle, includes tubules that are invaginations of the outer cell membrane (Russell [1995]). The outer membrane is a cylinder (roughly speaking) that sprouts tubular invaginations that bring current flow and electrical signals into the interior of the muscle fiber. These signals, like *all* biological signals, are voltages *across membranes*. They allow communication of the propagating action potential of the surface membrane to the depths of the muscle fiber (Eisenberg and Costantin [1971]).

The tubular system of muscle has an interior accessible to the solutions outside of cells. Markers diffuse quickly into the T-system as it is called. Extracellular solutions are derived from salt water and have simple linear electrical properties. Thus, the electrical properties of the T-system are roughly those of a resistor (of the extracellular solution, more or less) in series with a membrane capacitance, both actually resembling the linear electrical circuit elements used to represent them. The capacitance is of course distributed along the series resistance of the resistance. The T-system capacitance is distributed along the T-system luminal resistance.

The resistive properties of membranes in biology are hardly ever linear (Hodgkin [1992], Huxley [1992, 1999, 2002]). Even worse, it is the nonlinearities that are interesting. Specialized proteins called ion channels, with a hole down their middle, carry current (Sakmann and Neher [1995], Neher [1997]). The channels open and close in response to stimuli, and so the currents through the ensemble of channels in a cell membrane perform complex biological functions and are anything but linear. Thus, studies of linear electrical properties of cells and tissues, including muscle and its T-system, choose experimental conditions in which the number of channels open remains fixed and the resistive properties of cell membranes are linear. Fortunately, such conditions are easy to find and enforce. If perturbing potentials are chosen that make the interior of the cell more negative than its normal resting potential (of, say, -80 mv, inside minus outside), and not more than, say, 10 mv in amplitude, the resistance of membranes is constant and the membrane system (of resistor and capacitor in parallel) is a linear circuit element that can be well analyzed by impedance spectroscopy (Eisenberg *et al.* [1977], Eisenberg [1980, 1983a, 1987], Eisenberg and Mathias [1980], Mathias [1984]).

The linear properties of cells of course depend on the layout of the membranes and how they are distributed along resistances (Eisenberg and Mathias [1980]). Thus, to understand linear properties in physical terms, one must know the anatomy of the membranes, and one must know it quantitatively. How much membrane is there? What are the dimensions of the T-tubules? How much outer membrane is there? How much membrane is in the T-system? Without quantitative anatomy, one can only measure effective phenomenological parameters of equivalent circuits. Equivalent circuits are equivalent to useful representations only in the minds of physical scientists. Biologists want to know actual circuits with parameters of definite structures and amounts of membrane. Neglect of anatomy, particularly anatomical measurements, is a sad characteristic of many impedance measurements of biological systems.

Anatomical measurements cannot be used in an electrical circuit however without a theory. To put it baldly, the units are wrong! One must have a theory to connect the structures and their amounts and sizes to the electrical measurements made by impedance spectroscopy. A theory is needed to describe current flow and the role of structure. We see then that

4.7.1 Impedance Spectroscopy of Biological Structures Is a Platform Resting on Four Pillars

The pillars of the platform are:

1. Impedance measurements themselves (with their technical requirements discussed in the succeeding text)
2. Anatomical observations and measurements that provide quantitative information describing the amount of membranes and their connections to each other
3. A theory (field theory or circuit theory or both) linking the electrical properties of tiny pieces of membrane (differential elements, to be precise) and extra- and intracellular space with the anatomy of the system to the impedance measurements themselves
4. Estimation procedures that allow the impedance measurements, anatomical observations, and theories to evaluate properties of individual membrane systems

This book discusses those pillars in the context of work done long ago. It is meant to explain and illustrate this use of impedance spectroscopy. It is a guide (I hope) to how the impedance spectroscopy has been successfully applied to determine the electrical structure of several biological systems of importance (Eisenberg and Mathias [1980]). I apologize to the many more recent workers whom I have slighted out of ignorance and hope that they nonetheless can find this story useful.

4.7.1.1 Anatomical Measurements

The qualitative understanding of anatomical structures underlies any quantitative measurements of those structures and any electrical models and theories tying those structures to impedance measurements. Humans are visual animals, so the unconscious visualization of structure is natural for all of us, particularly for the subset who are visually gifted. Anatomy is an ancient subject for that reason, and only rarely is our (unconscious) visualization qualitatively incorrect, and then usually when dealing with sectioned (i.e., sliced) material. When a three-dimensional structure is sliced into thin sections, reconstruction into the three-dimensional structure can (and has) occasionally confuse spheres and cylinders because they are both circles in slices. But in general we begin with the presumption that the qualitative anatomy of the system is known through the centuries of effort of anatomists and histologists, who are anatomists on a smaller scale, and cell and structural biologists, who are anatomists on a still smaller scale, reaching nowadays to the atoms that make up the structure of membranes, channels, and proteins in general.

The obvious way to measure an anatomical structure has been used “forever.” Slice it into sections, trace out the structure, and measure the tracing. This approach is fraught with danger. As is obvious, the tissue must be fixed and embedded in a hard sliceable material before it can be sectioned, and those steps must be controlled to have minimal artifact. All this is the stuff of classical histology and is more or less under control (Eisenberg and Mobley [1975]). All of this can be improved or replaced by more modern three-dimensional imaging techniques, if those are used to make *quantitative* calibrated measurements of membrane area.

What is often overlooked is that the statistical sampling methods called stereology provide far less biased estimates of crucial membrane parameters (e.g., membrane area) than tracing methods. These stereological methods are of course not the subject of this article, but their existence is so often overlooked over the years that I must point them out (Eisenberg [1979, 1983a, b]). It is easy to show in experiments on computer-generated images that stereological methods are fast and accurate, whereas tracing

methods are slow and badly biased: slow because errors abound, while biased because humans and machines trace in ways that seem natural but are in fact deterministically skewed.

Stereology depends on the projection of an image onto a grid (usually rectangular) of *low* resolution with spacing between lines much larger than one might guess and very much larger than that necessary to resolve the details of the membranes or even their location. Resolution has to be enough only—I repeat *only*—to allow identification of the grid point: is it inside or is it outside the structure? The loss of information in any one image is very large. *But a large number* (say, 500) of images of sections are needed *in any case* to sample the three-dimensional structure successfully. When the low resolution sampling is done of these number of images, the resulting ensemble estimates in fact have (more than) acceptable variance. And most importantly they have much less bias than tracing methods. It might be thought that making this number of observations is unacceptably tedious, but in fact the experience of many investigators show the tedium and work involved is much less than in, say, typical experiments of biophysics or molecular biology.

There are many modern visualization methods that allow direct measurement of tiny membrane structures, including the tubular systems of muscle, in unfixed material. These measurements are very much more reliable than measurements made in fixed and sliced material, because the fixation process introduces large, unknown, and irreproducible changes in volume.

However, the stereological methods developed long ago remain very good and probably the best method to measure membrane area. Membrane area is not disturbed by fixation; membranes and their area cannot be directly visualized by high-resolution microscopy. Of course, methods that tag membranes uniformly and observe the density of the tag in high-resolution microscopy would be better yet.

4.7.1.2 Impedance Measurements

Impedance measurements in biology are most helpful when the impedance being measured is of a system of direct biological importance. When current is applied outside cells, to a whole tissue or to a suspension of cells, the impedance measured is mostly that of the extracellular space. Properties of the extracellular space are not central to most biological function although of course they can be useful assays of malfunction (in clinical medicine) and useful adjuncts to more meaningful measurements.

Impedance measurements discussed here force the applied current to flow across membranes through membrane capacitance and ion channels that form a conductive pathway in parallel with the membrane capacitance (Falk and Fatt [1964], Eisenberg [1967], Schneider [1970], Valdiosera *et al.* [1974a, b, c], Mathias *et al.* [1977]). Current is forced to flow in these paths because current is applied to a tiny probe inserted into a cell, in classical experiments, or in current applied inside cells by the patch clamp method (Hamill *et al.* [1981]). The current flows out of the probe through the cytoplasm of the cell, across the cell membrane, which is by far the largest impedance to flow, through specialized structures just outside the membrane, and then into the extracellular space and the electrode in the extracellular space, the bath electrode, which forms the other side of the current injection circuit.

With care (and some luck) probes can be inserted into most cells larger than, say, 10^{-5} m in diameter, and that includes most cardiac and skeletal muscle, although many cells do not fall into this category. The damage and perturbation produced by one probe can be assessed by inserting one probe for recording and assessment and then inserting another probe. These errors are kept well below 2% in the successful experiments discussed here.

Measurements of impedance are made in the biologically relevant frequency range of, say, 0.1–10 000 Hz where most biological function occurs. Originally, measurements were made using sinusoids, and indeed much impedance spectroscopy is still done that way. Reading the engineering literature (Otnes and Enochson [1972], Bendat and Piersol [2011]) showed clearly, however, that measurements could be made much more quickly if the sum of sinusoids was used as the perturbing signal (Mathias [1984]). Since biological cells impaled with probes are dying preparations (typically lasting only an hour or so), it is important to make measurements as rapidly as possible. The rule of thumb in the engineering literature (which is easy to verify with simulations or breadboard experiments) is that the time to take a broadband measurement with the optimal sum of sinusoids is determined by the lowest-frequency

sinusoid. The higher-frequency measurements come for free, in the sense that they do not take (significant) extra time, although of course the equipment to perform such measurements is anything but free!

This is not the place to derive or justify these statements. They have been textbook material for more than 50 years (Otnes and Enochson [1972], Bendat and Piersol [2011]), even if not widely known outside electrical engineering. The sum of sinusoids mentioned previously is made with random phase (to keep the amplitude of the sum under control), and so the signals are stochastic requiring some knowledge of stochastic signal processing. This is knowledge that is not widespread or trivial to master, so it is understandable that stochastic signals have not been widely used. They have great advantages nonetheless (Mathias [1984]).

One should point out a particular artifact that is easy to make in stochastic analysis. It is tempting, even seductive, to estimate a transfer function by taking a numerical estimate of a Fourier transform of the output of a system and dividing it (in the complex domain) by a numerical estimate of the Fourier transform of the input. This estimate however is so gravely flawed that it is not usable, in the presence of essentially any nonlinearity or contaminating noise, as explained in great detail in the books of Otnes and Enochson (Otnes and Enochson [1972], Eisenberg [1983a], Bendat and Piersol [2011]). If this estimation procedure is tried on a mock circuit, with added noise, one will find that the mean value of the estimate changes with the noise level, but the variance of the estimate does not. The mock circuit of course does not change with the level of added noise, so the qualitative properties of the estimate are wrong. If one fails to check the procedure on a mock circuit, the error can be overlooked because most workers look for variance as a sign of noise contamination, and in this case the sign of noise contamination is a bias in the mean value without an increase in noise.

4.7.1.3 Measurement Difficulties

Probes small enough to insert into cells with acceptable damage and reproducibility are small and have high impedance even if they are micropipettes filled with nearly saturated salt (e.g., 3 M KCl). At frequencies of 10^4 Hz, stray capacitances of even 0.1 pF are important. Thus great care must be taken in the construction of setups, analysis and treatment of errors, and calibration. This process was begun in Falk and Fatt [1964], Eisenberg [1967], Schneider [1970] and extended dramatically in Valdiosera *et al.* [1974a, b, c], Mathias *et al.* (1977), where attention to detail and use of a new recording amplifier allowed a calibrated bandwidth of at least 10^5 Hz, as checked in an actual setup making biological recording. The key was the use of an inverting amplifier circuit in which the current through the micropipette is measured as a replica of the potential within the cell. The resistance of the micropipette is quite pure (because it is lumped in a tiny part of the micropipette, just a few micrometers long). This circuit has optimal noise performance as well, which was later recognized and exploited brilliantly by Neher and Sigworth (Sigworth and Neher [1980], Sigworth [1995]), in the electronics that Neher used in his patch clamp work.

Calibration was performed by injection of current through an *air* capacitor: a physical capacitor proved unreliable because even fingerprints seriously changed the phase angle of current through it (because of the parallel conductance of finger grease). These realities proved to be the key to the later development of the integrating head stage, which has provided the optimal electronics for recording the picoamps of current through single channels in the Axopatch amplifier (Rae *et al.* [1988], Levis and Rae [1992, 1995, 1998], Rae and Levis [1992]), still the leading amplifier in 2015 after nearly 30 years on the market, now sold by Molecular Devices, Inc.

4.7.1.4 Future Measurements

The much lower impedance (by a factor of at least 5 times, without further fiddling) of patch pipettes should allow much wider bandwidth recording that might or might not prove to lead to more biological insight. One cannot be sure until one addresses biological questions specific to a particular cell, tissues, and preparation.

4.7.1.5 Interpreting Impedance Spectroscopy

The results just mentioned all depend on the interpretation of the impedance spectrum. This interpretation requires a specific theory linking the measurement to the structure of the system in question, including the experimental setup and artifacts in the theory, and measurements of the anatomical parameters of the structures involved.

These requirements are often “swept under the rug” because they require extensive work to fulfill by using an “equivalent circuit” to replace the theory. The equivalent circuit is an essential part of the analysis to be sure, and the insight required to understand its simplifications proves to be most useful, but it is not enough to allow the full use of the wonderful resolution of impedance measurements.

The first step in extending the equivalent circuit analysis is the understanding of how the equivalent circuit approximates the electrodynamics of the biological structure and recording apparatus. The artifacts of the recording apparatus have been discussed previously and enumerated and analyzed definitively (it seems to me in my prejudiced opinion) in the literature and so will not be discussed further here (Eisenberg [1967], Valdiosera *et al.* [1974a]).

The relation of the equivalent circuit to the electrodynamics of the system was studied by solving Poisson’s equation by several authors, but the simplification to the usual equivalent circuit only became apparent when series expansions of the solution of Poisson’s equation, and Poisson’s equation itself, were developed (Eisenberg [1967], Eisenberg and Johnson [1970], Barcilon *et al.* [1971], Peskoff and Eisenberg [1973, 1975], Peskoff and Ramirez [1975], Peskoff *et al.* [1976], Kevorkian and Cole [1996]).

These expansions provided wonderful insight (Peskoff and Eisenberg [1973]): the usual equivalent circuit (of a uniform potential for a finite cell, like a sphere, or of a transmission line for a long cylinder) arose as a separate term from the point source effects (i.e., the terms that vary with angular coordinates). Indeed, the beauty and power of the analysis (e.g., by matched asymptotic expansions) led applied mathematicians to use this work as a teaching example of the power of singular perturbation theory.

4.7.1.6 Fitting Data

Once the impedance spectroscopy data is available (e.g., as plots of amplitude and phase vs. frequency), it is necessary to extract the parameters of the model that fits the data. The least squares fitting procedure proved robust and fast, even with ancient computers of the 1970s, and able to do the job. In fact, fitting to biological data was one of the first applications of the Brown–Dennis version of the Levenberg–Marquardt minimization technique, now widely used and enshrined in MATLAB, thanks to the help of many coworkers.

Just as important as fitting the data is determining the significance of the parameter estimates. The issue is not just what is the statistical variance of a parameter estimate. Here there is an additional problem because of the correlation between parameter estimates. Perhaps changing two parameters (or more) might produce a fit nearly as good as the one chosen. This issue can be addressed by fixing one parameter at a different value from its optimal, and then comparing the quality of fit, using the F-variance ratio test (which is quite robust) in, for example, the form of the R-test used widely in crystallography.

4.7.1.7 Results

Measurements proved straightforward in skeletal muscle, cardiac muscle, tendon regions of skeletal muscle, and lens of the eye (Falk and Fatt [1964], Eisenberg [1967], Schneider [1970], Valdiosera *et al.* [1974a, b, c], Mathias *et al.* [1977, 1979, 1981], Clausen *et al.* [1979], Eisenberg and Mathias [1980], Rae *et al.* [1982a], Levis *et al.* [1983], Mathias [1983], Ebihara and Mathias [1985], Milton *et al.* [1985]). In each case the measurements of impedance provided useful information concerning the tissue. In skeletal muscle, measurements provided the best estimates of the predominant (cell) membrane system that dominates electrical properties. In cardiac muscle, measurements showed definitively that classical microelectrode voltage clamp could not control the potential of the predominant membranes, which were in the tubular system separated from the extracellular space by substantial distributed resistance.

In the tendon regions of skeletal muscle, electrical properties needed to interpret extensive voltage clamp analysis of the Cambridge (UK) group were measured (Adrian *et al.* [1966]). In the lens of the eye, impedance spectroscopy changed the basis of all recording and interpretation of electrical measurements and laid the basis for Rae and Mathias' extensive later experimental work (Eisenberg *et al.* [1977], Mathias *et al.* [1979, 1981, 1985, 1997], Rae [1979], Rae *et al.* [1982a, b, 1988, 1996], Mathias and Rae [1985], Pasquale *et al.* [1990], Baldo and Mathias [1992]).

Many tissues are riddled with extracellular space as clefts and tubules, for example, cardiac muscle, the lens of the eye, most epithelia, and of course frog muscle. These tissues are best analyzed with a bi-domain theory (Eisenberg *et al.* [1979], Mathias *et al.* [1979, 1981]) that arose from the work on electrical structure described here. There has been a great deal of work since then on the bi-domain model admirably reviewed in Mori [2015], and this represents the most important contribution to biology of the analysis of electrical structure in my view.

4.7.1.8 Future Perspectives

Science is subject to fashions like all human behavior. The electrical structure of cells and tissues is out of fashion as biologists move to understand the ion channels so important for biological function. These channels function in a biological environment determined in large measure by the electrical structure of the tissues in which they are found. Computational tools are available to compute the properties of channels in the electrical structures in which they are found. Impedance spectroscopy will come back into fashion as scientists realize there are few other techniques with the resolution necessary to determine the electrical structure and how it modulates the current flows driven by ion channels.

Acronym and Model Definitions

BNN	Barton–Nakajima–Namikawa response Section 4.2, Eq. (5)
CK0	The combination of a capacitance in parallel with the K0 response model
CK1	The combination of a capacitance in parallel with the K1 response model
CK1EL	The CK1 model with a four-parameter electrode-effect model in series
CK1S	The CK1 model with a CPE, the SCPE, in series with it
CMF	The corrected modulus formalism response model (see text)
CNLS	Complex nonlinear least squares
CPE	The constant phase distributed response element
CSD	Conductive-system dispersion
DCE	Distributed circuit element
DEC	Conductive-system DE
DED	Dielectric-system DE
DRTs	Distribution of relaxation times
DSD	Dielectric-system dispersion
EL	An electrode-response model that includes the SCPE
EM	Effective medium
K0	The Kohlrausch frequency-response model directly associated with stretched-exponential temporal response
K1	The Kohlrausch frequency-response model derived from the K0 model (see Section 4.2, Eq. (1) with $\epsilon_Z = \epsilon_{C1\infty}$, Eq. (3), and Eq. (4)). Some composite models are the CK0, CK1, PK1, CK0S, CK1S, EMK1, CK1EL, and CPK1. Parallel elements appear on the left side of K0 or K1 and series ones on the right. C denotes a parallel capacitance or dielectric constant
NCL	Nearly constant loss: $\epsilon''(\omega)$ nearly independent of frequency over a finite range
OMF	The original modulus formalism response model; Section 4.2, Eq. (1) with $\epsilon_Z = \epsilon_\infty$, Eq. (2), and Eq. (3)
PCPE	A CPE in parallel with other response; denoted in a composite model by P
SCPE	A CPE in series with other response; denoted in a composite model by S
ZARC	Another name for the ZC response model
ZC	A complex-power-law response model: Cole–Cole response at the impedance level

References

- H. Abe, M. Esashi, and T. Matsuo [1979] ISFET's Using Inorganic Gate Thin Films, *IEEE Trans. Electron Devices* **ED-26**, 1939–1944.
- P. Abélard and J. F. Baumard [1982] Study of the D.C. and A.C. Electrical Properties of an Yttria-Stabilized Zirconia Single Crystal [(ZrO₂)_{0.88} – (Y₂O₃)_{0.12}], *Phys. Rev. B* **26**, 1005–1017.
- P. Abélard and J. F. Baumard [1984] Dielectric Relaxation in Alkali Silicate Glasses: A New Interpretation, *Solid State Ionics* **14**, 61–65.
- M. Abramowitz and I. A. Stegun [1965] *Handbook of Mathematical Functions*, NBS Publication, Vol. 55, United States National Bureau of Standards (NBS), Washington, DC, p. 376.
- K. Adachi and T. Kotaka [1993] Dielectric Normal Mode Relaxation, *Prog. Polym. Sci.* **18**, 585–622.
- N. K. Adam [1941] *The Physics and Chemistry of Surfaces*, 3rd Edition, Oxford University Press, London, UK.
- G. Adam and J. H. Gibbs [1965] On the Temperature Dependence of Cooperative Relaxation Properties in Glass-Forming Liquids, *J. Chem. Phys.* **43**, 139–146.
- A. W. Adamson [1982] *Physical Chemistry of Surfaces*, 4th Edition, John Wiley & Sons, Inc., New York.
- S. B. Adler [2002] Reference Electrode Placement in Thin Solid Electrolytes, *J. Electrochem. Soc.* **149**(5), E166–E172.
- R. H. Adrian, W. K. Chandler, and A. L. Hodgkin [1966] Voltage Clamp Experiments in Skeletal Muscle Fibres, *J. Physiol.* **186**(2), 51P–52P.
- R. R. Adzic, F. C. Anson, and K. Kinoshita, (eds.) [1996] *Proceedings of the Symposium on Oxygen Electrochemistry*, The Electrochemical Society, Pennington, NJ.
- P. Agarwal, M. E. Orazem, and L. H. Garcia-Rubio [1995] Application of Measurement Models to Impedance Spectroscopy. III. Evaluation of Consistency with the Kramers-Kronig Relations, *J. Electrochem. Soc.* **142**, 4159–4168.
- J. Agrisuelas, J. J. Garcia-Jareno, D. Gimenez-Romero, and F. Vicente [2009] Innovative Combination of Three Alternating Current Relaxation Techniques: Electrical Charge, Mass, and Color Impedance Spectroscopy. Part I: The Tool, *J. Phys. Chem. C* **113**, 8430–8437.
- S. Ahn, H. Kwon, and D. D. Macdonald [2005] Role of Chloride Ion in Passivity Breakdown on Iron and Nickel, *J. Electrochem. Soc.* **152**, B482–B490.
- J. Ai, Y. Chen, D. D. Macdonald, and M. Urquidi-Macdonald [2008] Electrochemical Impedance Spectroscopic Study of Passive Zirconium, *J. Nucl. Mater.* **379**(1–3), 162–168.
- Y. Aihara, J. Kuratomi, T. Bando, T. Iguchi, H. Yoshida, T. Ono, and K. Kuwana [2003] Investigation on Solvent-Free Solid Polymer Electrolytes for Advanced Lithium Batteries and their Performance, *J. Power Sources* **114**(1), 96–104.
- S. Alexander, J. Bernasconi, W. R. Schneider, and R. Orbach [1981] Excitation Dynamics in Random One-Dimensional Systems, *Rev. Mod. Phys.* **53**, 175–198.
- R. C. Alkire, M. W. Balmas, D. D. Macdonald, and E. Sikora [1996] The Photo-Inhibition of Localized Corrosion on Stainless Steel in Neutral Chloride Solution, *Corros. Sci.* **38**(1), 97–103.
- D. P. Almond and A. R. West [1981] Measurement of Mechanical and Electrical Relaxations in Beta-Alumina, *Solid State Ionics* **3**(4), 73–77.
- D. P. Almond and A. R. West [1983a] Mobile Ion Concentrations in Solid Electrolytes from an Analysis of AC Conductivity, *Solid State Ionics* **9–10**, 277–282.
- D. P. Almond and A. R. West [1983b] Impedance and Modulus Spectroscopy of "Real" Dispersive Conductors, *Solid State Ionics* **11**, 57–64.
- D. P. Almond, A. R. West, and R. J. Grant [1982] Temperature Dependence of the A. C. Conductivity of Na Beta-Alumina, *Solid State Commun.* **44**, 1277–1280.
- D. P. Almond, G. K. Duncan, and A. R. West [1983] The Determination of Hopping Rates and Carrier Concentrations in Ionic Conductors by a New Analysis of AC Conductivity, *Solid State Ionics* **8**, 159–164.
- D. P. Almond, C. C. Hunter, and A. R. West [1984] The Extraction of Ionic Conductivities and Hopping Rates from A. C. Conductivity Data, *J. Mater. Sci.* **19**, 3236–3248.
- G. Amatucci, A. D. Pasquier, A. Blyr, T. Zheng, and J.-M. Tarascon [1999] The Elevated Temperature Performance of the LiMn₂O₄/C System: Failure and Solutions, *Electrochim. Acta* **45**(1–2), 255–271.
- B. Andreaus, A. J. McEvoy, and G. G. Scherer [2002] Analysis of Performance Losses in Polymer Electrolyte Fuel Cells at High Current Densities by Impedance Spectroscopy, *Electrochim. Acta* **47**, 2223–2229.

- C. A. Angell [1985] Strong and Fragile Liquids, in *Relaxations in Complex Systems*, ed. K. L. Ngai and G. B. Wright, NRL, Washington, DC, p. 3.
- C. A. Angell [1997] Landscapes with Megabasins: Polymorphism in Liquids and Biopolymers and the Role of Nucleation in Folding and Unfolding Diseases, *Phys. D Nonlinear Phenomena* **107**(2), 122–142.
- C. R. Angell, J. Wong, and W. F. Edgell [1969] Far-Infrared Spectra of Inorganic Nitrate and Chloride Glasses, Liquids, and Crystals: Complex Ions or Optical Phonons? *J. Chem. Phys.* **51**(10), 4519–4530.
- A. Appleby and F. R. Foulkes [1993] *Fuel Cell Handbook*, Krieger Publishing Co., Malabar, FL.
- W. I. Archer and R. D. Armstrong [1980] The Application of A. C. Impedance Methods to Solid Electrolytes, in *Electrochemistry*, Chemical Society Specialist Periodical Reports, Vol. 7, Royal Society of Chemistry, London, UK, 157–202.
- A. Arico, P. Creti, H. Kim, R. Mantegna, N. Giordano, and V. Antonucci [1996] Analysis of the Electrochemical Characteristics of a Direct Methanol Fuel Cell Based on a Pt-Ru/C Anode Catalyst, *J. Electrochem. Soc.* **143**, 3950–3959.
- M. Armand [1983] Polymer Solid Electrolytes: An Overview, *Solid State Ionics* **9–10**(2), 745–754.
- R. D. Armstrong [1974] The Metal Solid Electrolyte Interphase, *J. Electroanal. Chem.* **52**, 413–419.
- R. D. Armstrong and K. L. Bladen [1976] The Anodic Dissolution of Lead in Oxygenated and Deoxygenated Sulphuric Acid Solutions, *J. Appl. Electrochem.* **7**, 345.
- R. D. Armstrong and K. Edmondson [1973] The Impedance of Metals in the Passive and Transpassive Regions, *Electrochim. Acta* **18**, 937–943.
- R. D. Armstrong and M. Henderson [1972] Impedance Plane Display of a Reaction with an Adsorbed Intermediate, *J. Electroanal. Chem.* **39**, 81–90.
- R. D. Armstrong and R. Mason [1973] Double Layer Capacity Measurement Involving Solid Electrolytes, *J. Electroanal. Chem.* **41**, 231–241.
- R. D. Armstrong, W. P. Race, and H. R. Thirsk [1968] Determination of Electrode Impedance over an Extended Frequency Range by Alternating-Current Bridge Methods, *Electrochim. Acta* **13**, 215.
- R. D. Armstrong, T. Dickinson, and J. Turner [1973] Impedance of the Sodium β -Alumina Interphase, *J. Electroanal. Chem.* **44**, 157–167.
- R. D. Armstrong, T. Dickinson, and P. M. Willis [1974] The A. C. Impedance of Powdered and Sintered Solid Ionic Conductors, *J. Electroanal. Chem.* **53**, 389–405.
- R. D. Armstrong, M. F. Bell, and A. A. Metcalfe [1977] The Anodic Dissolution of Molybdenum in Alkaline Solutions. Electrochemical Measurements, *J. Electroanal. Chem.* **84**, 61.
- R. D. Armstrong, M. F. Bell, and A. A. Metcalfe [1978] The AC Impedance of Complex Electrochemical Reactions, in *Electrochemistry*, Chemical Society Specialist Periodical Reports, Vol. 6, Royal Society of Chemistry, London, UK, pp. 98–127.
- F. Artuso, F. Bonino, F. Decker, A. Lourenco, and E. Masetti [2002] Study of Lithium Diffusion in RF Sputtered Nickel-Vanadium Mixed Oxides Thin Films, *Electrochim. Acta* **47**, 2231–2238.
- M. Atanasov, C. Daul, J.-L. Barras, L. Benco, and E. Deiss [1999] Polarizable Continuum Model for Lithium Interface Transitions Between a Liquid Electrolyte and an Intercalation Electrode, *Solid State Ionics* **121**, 165–174.
- S. Atlung and T. Jacobsen [1976] On the AC-Impedance of Electroactive Powers: γ -Manganese Dioxide, *Electrochim. Acta* **21**, 575–584.
- D. Aurbach, J. S. Gnanaraj, M. D. Levi, E. A. Levi, J. E. Fischer, and A. Claye [2001] On the Correlation Among Surface Chemistry, 3D Structure, Morphology, Electrochemical and Impedance Behavior of Various Lithiated Carbon Electrodes, *J. Power Sources* **97–98**, 92–96.
- D. Aurbach, K. Gamolsky, B. Markovsky, Y. Gofer, M. Schmidt, and U. Heider [2002] On the Use of Vinylene Carbonate (VC) as an Additive to Electrolyte Solutions for Li-Ion Batteries, *Electrochim. Acta* **47**(9), 1423–1439.
- D. Aurbach, B. Markovsky, A. Rodkin, E. Levi, Y. S. Cohen, H. J. Kim, and M. Schmidt [2002] On the Capacity Fading of LiCoO₂ Intercalation Electrodes: The Effect of Cycling, Storage, Temperature, and Surface Film Forming Additives, *Electrochim. Acta* **47**(27), 4291–4306.
- E. Avendano [2002] *Electrochromic Properties of Nickel Based Oxide Films*, Licentiate thesis, UPTEC 02 009, Uppsala University.
- E. Avendaño, A. Azens, J. Isidorsson, R. Karmhag, G. A. Niklasson, and C. G. Granqvist [2003b] Optimized Nickel-Oxide-Based Electrochromic Thin Films, *Solid State Ionics* **165**, 169–173.
- E. Avendano, A. Azens, G. A. Niklasson, and C. G. Granqvist [2005] Proton Diffusion and Electrochromism Inhydrated NiO_y and Ni_{1-x}V_xO_y Thin Films, *J. Electrochem. Soc.* **152**, F203–F212.
- A. Azens and C. G. Granqvist [2003a] Electrochromic Smart Windows: Energy Efficiency and Device Aspects, *J. Solid State Electrochem.* **7**, 64–68.
- U. Bach, D. Lupo, P. Comte, J. E. Moser, F. Weissortel, J. Salbeck, H. Spreitzer, and M. Grätzel [1998] Solid-State Dye-Sensitized Mesoporous TiO₂ Solar Cells with High Photon-to-Current Conversion Efficiencies, *Nature* **395**, 583–585.
- J. Backholm, Georén, P., and G. A. Niklasson [2008] Determination of Solid Phase Chemical Diffusion Coefficient and Density of States by Electrochemical Methods: Application to Iridium Oxide-Based Thin Films, *J. Appl. Phys.* **103**, 023702.
- F. T. Bacon [1952] *Improvements Relating to Galvanic Cells and Batteries*, Patent GB 667298.
- S. P. S. Badwal [1983] New Electrode Materials for Low Temperature Oxygen Sensors, *J. Electroanal. Chem.* **146**, 425–429.
- S. P. S. Badwal [1984] Kinetics of the Oxygen Transfer Reaction at the (Cu_{0.5}Sc_{0.5})O_{2+x}/YSZ Interface by Impedance Spectroscopy, *J. Electroanal. Chem.* **161**, 75–91.

- S. P. S. Badwal and H. J. de Bruin [1978] Polarization at the $(U_{0.7}Y_{0.3})O_{2+x}/YSZ$ Interface by Impedance Dispersion Analysis, *Aust. J. Chem.* **31**, 2337–2347.
- S. P. S. Badwal, M. J. Bannister, and M. J. Murray [1984] Non-Stoichiometric Oxide Electrodes for Solid State Electrochemical Devices, *J. Electroanal. Chem.* **168**, 363–382.
- J.-S. Bae and S.-I. Pyun [1995] Electrochemical Lithium Intercalation Reaction of Anodic Vanadium Oxide Film, *J. Alloys Compounds* **217**, 52–58.
- H. D. Baehr [1988] *Thermodynamik*, Springer Verlag, New York, p. 212.
- G. J. Baldo and R. T. Mathias [1992] Spatial Variations in Membrane Properties in the Intact Rat Lens, *Biophys. J.* **63**(2), 518–529.
- P. R. Barabash and R. S. C. Cobbold [1982] Dependence on Interface State Properties of Electrolyte: Silicon Dioxide-Silicon Structures, *IEEE Trans. Electron. Devices* **ED-29**, 102–108.
- G. Barbero and A. L. Alexe-Ionescu [2005] Role of the Diffuse Layer of the Ionic Charge on the Impedance Spectroscopy of a Cell of Liquid, *Liq. Cryst.* **32**, 7.
- A. Barbucci, M. Viviani, D. Vladikova, and Z. Stoynov [2006] Impedance Analysis of Oxygen Reduction in SOFC Composite Electrodes, *Electrochim. Acta* **51**, 1641–1650.
- V. Barcilon, J. Cole, and R. S. Eisenberg [1971] A Singular Perturbation Analysis of Induced Electric Fields in Nerve Cells, *SIAM J. Appl. Math.* **21**(2), 339–354.
- A. J. Bard and L. R. Faulkner [1980] *Electrochemical Methods: Fundamentals and Applications*, John Wiley & Sons, Inc., New York.
- G. Barker [1958] Square-Wave Polarography. III. Single Drop Polarography, *Anal. Chim. Acta* **18**, 118.
- G. Barker [1969] Noise Connected with Electrode Processes, *J. Electroanal. Chem.* **21**, 127.
- G. Barker [1975] Large Signal Aperiodic Equivalent Electrical Circuits for Diffusion and Faradaic Impedances, *J. Electroanal. Chem. Interfacial Electrochem.* **58**(1), 5–18.
- G. Barker, R. Faircloth, and A. Gardner [1958] Use of Faradaic Rectification for the Study of Rapid Electrode Processes, IV. Theoretical Aspects of Square Wave Polarography, *Nature* **181**, 247–248.
- E. Barsoukov [1996] *Investigations of the Redox Kinetics of Conducting Polymers*, Ph.D. thesis, DOI:10.13140/RG.2.1.1246.6161, <https://www.researchgate.net/publication/305465965> (accessed on November 3, 2017).
- E. Barsoukov and J. R. Macdonald [2012] Electrochemical Impedance Spectroscopy, in *Characterization of Materials*, 2nd Edition, ed. E. N. Kaufmann, John Wiley & Sons, Inc., Hoboken, NJ.
- E. Barsoukov, J. H. Kim, J. Hun Kim, C. O. Yoon, and H. Lee [1998] Effect of Low-Temperature Conditions on Passive Layer Growth on Li Intercalation Materials: In Situ Impedance Study, *J. Electrochem. Soc.* **145**(8), 2711–2717.
- E. Barsoukov, J. H. Kim, C. O. Yoon, and H. Lee [1999a] Kinetics of Lithium Intercalation into Carbon Anodes: In Situ Impedance Investigation of Thickness and Potential Dependence, *Solid State Ionics* **116**, 249–261.
- E. Barsoukov, J. H. Kim, C. O. Yoon, and H. Lee [1999b] Universal Battery Parameterization to Yield a Non-Linear Equivalent Circuit Valid for Battery Simulation at Arbitrary Load, *J. Power Sources* **83**, 61–70.
- E. Barsoukov, J. H. Kim, D. H. Kim, K. S. Hwang, C. O. Yoon, and H. Lee [2000] Parametric Analysis Using Impedance Spectroscopy: Relationship Between Material Properties and Battery Performance, *J. New Mater. Electrochem. Syst.* **3**, 301–308.
- E. Barsoukov, S. H. Ryu, and H. Lee [2002] A Novel Impedance Spectrometer based on Carrier Function Laplace Transform of the Response to Arbitrary Excitation, *J. Electroanal. Chem.* **536**, 109–122.
- E. Barsoukov, D. H. Kim, H.-S. Lee, H. Lee, M. Yakovleva, Y. Gao, and J. F. Engel [2003] Comparison of Kinetic Properties of $LiCoO_2$ and $LiTi_{0.05}Mg_{0.05}Ni_{0.7}Co_{0.2}O_2$ by Impedance Spectroscopy, *Solid State Ionics* **161**(1), 19.
- J. L. Barton [1966] La relaxation diélectrique de quelques verres ternaires silice oxyde alcalin oxyde alcalino-terreux, *Verres et Refr.* **20**, 328–324.
- P. A. Basnayaka, M. K. Ram, L. Stefanakos, and A. Kumar [2012] Graphene/Polypyrrole Nanocomposite as Electrochemical Supercapacitor Electrode: Electrochemical Impedance Studies, *Graphene* **2**, 81–87.
- H. Bässler [1993] Charge Transport in Disordered Organic Photoconductors, *Phys. Status Solidi B* **175**, 15–56.
- J. B. Bates, N. J. Dudney, B. Neudecker, A. Ueda, and C. D. Evans [2000] Thin-Film Lithium and Lithium-Ion Batteries, *Solid State Ionics* **135**(1–4), 33–45.
- H. H. Bauer [1964] Theory of Faradaic Distortion: Equation for the 2nd-Harmonic Current, *Aust. J. Chem.* **17**, 715.
- J. E. Bauerle [1969] Study of Solid Electrolyte Polarization by a Complex Admittance Method, *J. Phys. Chem. Solids* **30**, 2657–2670.
- J. E. Bauerle [1976] Correlation Between Impedance, Microstructure, and Compositions of Calcia-Stabilized Zirconia, *Electrochim. Acta* **21**, 303–310.
- I. Bayrak Pehlivan, R. Marsal, P. Georén, C. G. Granqvist, and G. A. Niklasson [2010] Ionic Relaxation in Polyethylenimine-Lithium Bis(trifluoromethylsulfonyl)imide Polymer Electrolytes, *J. Appl. Phys.* **108**, 074102.
- H. E. Becker [1957] US Patent 2,800,616 (7,23,57) to GM Co.
- L. K. H. van Beek [1965] Dielectric Behaviour of Heterogeneous System, in *Progress in Dielectrics*, Vol. 7, eds. T. van Dijk and A. J. Burggraaf; [1965] Dielectric Behaviour of Heterogeneous System, in *Progress in Dielectrics*, Vol. 7, ed. J. B. Birks, Heywood Press, London, pp. 69–114.
- N. M. Beekmans and L. Heyne [1976] Correlation Between Impedance, Microstructure, and Compositions of Calcia-Stabilized Zirconia, *Electrochim. Acta* **21**, 303–310.
- J. S. Bendat and A. G. Piersol [2011] *Random Data: Analysis and Measurement Procedures*, John Wiley & Sons, Inc., Hoboken, NJ.

- J. T. Bendler and M. F. Shlesinger [1985] Derivation of the Kohlrausch–Williams–Watts Decay Law from Activation-Energy Dispersion, *Macromolecules* **18**, 591–592.
- U. Bengtzelius, W. Gotze, and A. Sjolander [1984] Dynamics of Supercooled Liquids and the Glass Transition, *J. Phys. C* **17** (33), 5915.
- M. N. Berberan-Santos, E. N. Bodunov, and B. Valeur [2005] Mathematical Functions for the Analysis of Luminescence Decays with Underlying Distributions 1. Kohlrausch Decay Function (Stretched Exponential), *Chem. Phys.* **315**, 171–182.
- J. G. Berberian and R. H. Cole [1969] Null Instrument for Three- and Four-Terminal Admittance Measurements at Ultra-low Frequencies, *Rev. Sci. Instrum.* **40**, 811.
- P. Bergveld [1970] Development of an Ion-Sensitive Solid State Device for Neurophysiological Measurements, *IEEE Trans. Biomed. Eng.* **BME-17**, 70–71.
- P. Bergveld and N. F. De Rooij [1981] History of Chemically Sensitive Semiconductor Devices, *Sensors Actuators* **1**, 5–15.
- L. E. A. Berlouis [1979] An Impedance Study of Flow-Through Porous Electrodes, Ph.D. thesis, the University of Southampton, Southampton, England.
- H. Bernard [1981] *Microstructure et Conductivité de la Zircone Stabilisée Frittée*, Report CEA-R-5090, Commissariat à l'Energie Atomique, CEN-Saclay, France.
- J. Bernasconi, H. U. Beyeler, S. Strassler, and S. Alexander [1979] Anomalous Frequency-Dependent Conductivity in Disordered One-Dimensional System, *Phys. Rev. Lett.* **42**, 819–822.
- D. M. Bers [2002] Cardiac Excitation-Contraction Coupling, *Nature* **415**(6868), 198–205.
- U. Bertocci [1979] AC Induced Corrosion: The Effect of an Alternating Voltage on Electrodes Under Charge Transfer Control, *Corrosion* **35**, 211–215.
- U. Bertocci and J. L. Mullen [1981] Effect of Large Voltage Modulations on Electrodes Under Charge Transfer Control, in *Electrochemical Corrosion Testing*, eds. F. Mansfeld and U. Bertocci, American Society of Testing and Materials, San Francisco, CA, pp. 365–380.
- I. Betova, M. Bojinov, P. Kinnunen, T. Laitinen, P. Pohjanne, and T. Saario [2002] Mechanism of Transpassive Dissolution of Nickel-Based Alloys Studied by Impedance Spectroscopy and Rotating Ring-Disc Voltammetry, *Electrochim. Acta* **47**, 2093–2107.
- I. Betova, M. Bojinov, and T. Tzvetkoff [2004] Oxidative Dissolution and Anion-Assisted Solubilization in the Transpassive State of Nickel-Chromium Alloys, *Electrochim. Acta* **49**, 2295–2306.
- D. Bevers, N. Wagner, and M. von Bradke [1998] Innovative Production Procedure for Low Cost PEFC Electrodes and Electrode Membrane Structures, *Int. J. Hydrogen Energy* **23**, 57–63.
- P. Bindra, M. Fleischmann, J. W. Oldham, and D. Singleton [1973] Nucleation, *Faraday Discuss. Chem. Soc.* **56**, 180.
- R. L. Birke [1971] Operational Admittance of an Electrode Process where an A Priori Dependence of Rate Constant on Potential Is Not Assumed, *J. Electroanal. Chem.* **33**, 201–207, ed. J. B. Birks, Heywood Press, London, pp. 69–114.
- J. Bisquert [2002] Analysis of the Kinetics of Ion Intercalation: Ion Trapping Approach to Solid-State Relaxation Processes, *Electrochim. Acta* **47**, 2435–2449.
- J. Bisquert [2003a] Chemical Capacitance of Nanostructured Semiconductors: Its Origin and Significance for Nanocomposite Solar Cells, *Phys. Chem. Chem. Phys.* **5**, 5360–5364.
- J. Bisquert [2003b] Fractional Diffusion in the Multiple-Trapping Regime and Revision of the Equivalence with the Continuous-Time Random Walk, *Phys. Rev. Lett.* **91**, 010602.
- J. Bisquert and A. Compte [2001] Theory of the Electrochemical Impedance of Anomalous Diffusion, *J. Electroanal. Chem.* **399**, 112–120.
- J. Bisquert and V. S. Vikhrenko [2002] Analysis of the Kinetics of Ion Intercalation. Two State Model Describing the Coupling of Solid State Ion Diffusion and Ion Binding Processes, *Electrochim. Acta* **47**, 3977–3988.
- J. Bisquert, G. Garcia-Belmonte, F. Bueno, E. Longo, and L. O. S. Bulhões [1998] Impedance of Constant Phase Element (CPE)-Blocked Diffusion in Film Electrodes, *J. Electroanal. Chem.* **452**, 229–234.
- K. L. Bladen [1977] The Anodic Dissolution of Lead in Oxygenated and Deoxygenated Sulphuric Acid Solutions, *J. Appl. Electrochem.* **7**, 345.
- G. Blanc, C. Gabrielli, and N. Keddam [1975] Measurement of the Electrochemical Noise by a Cross Correlation Method, *Electrochim. Acta* **20**, 687.
- G. E. Blomgren [2003] Liquid Electrolytes for Lithium and Lithium-Ion Batteries, *J. Power Sources* **119–121**, 326–329.
- L. J. Blumen and M. N. Mugerwa, (eds.) [1993] *Fuel Cell Systems*, Plenum Press, New York.
- L. Bobics, L. Sziraki, and G. G. Lang [2008] The Impedance Related to the Electrochemical Hydrogen Insertion into WO_3 Films: On the Applicability of the Diffusion-Trapping Model, *Electrochim. Commun.* **10**, 283–287.
- R. Boddy [1965] The Structure of the Semiconductor-Electrolyte Interface, *J. Electroanal. Chem.* **10**, 199–244.
- H. W. Bode [1945] Relations Between Real and Imaginary Components of Network Functions, in *Network Analysis and Feedback Amplifier Design*, Van Nostrand, New York.
- R. Bohmer, K. L. Ngai, C. A. Angell, and D. J. Plazek [1993] Nonexponential Relaxations in Strong and Fragile Glass Formers, *J. Chem. Phys.* **99**(5), 4201–4209.
- E. V. Bohn [1963] *The Transform Analysis of Linear Systems*, Addison-Wesley, Reading, MA.
- O. Bohnke and Cl. Bohnke [1988] Comparative Study of the Electrochromic Properties of WO_3 Thin Films, *Displays* **9**, 199–206.
- Cl. Bohnke and O. Bohnke [1990] Impedance Analysis of Amorphous WO_3 Thin Films in Hydrated LiClO_4 -Propylene Carbonate Electrolytes, *Solid State Ionics* **39**, 195–204.

- C1. Bohnke, O. Bohnke, and B. Vuillemin [1993] Constant Phase Angle Behavior of SnO_2/WO_3 Thin Film Electrodes in Anhydrous LiClO_4 -Propylene Carbonate Electrolyte, *Electrochim. Acta* **38**, 1935–1940.
- M. Bojinov, G. Fabricius, T. Laitinen, T. Saario, and G. Sundholm [2000] Coupling Between Ionic Defect Structure and Electronic Conduction in Passive Films on Iron, Chromium and Iron-Chromium Alloys, *Electrochim. Acta* **45**, 2029–2048.
- M. Bojinov, I. Betova, M. Bojinov, T. Laitinen, K. Makela, P. Pohjanne, and T. Saario [2002] The Transpassive Dissolution Mechanism of Highly Alloyed Stainless Steels I. Experimental Results and Modelling Procedure, *Corros. Sci.* **44**, 2675–2697.
- M. Bojinov, S. Cattarin, M. Musiani, and B. Tribollet [2003] Evidence of Coupling Between Film Growth and Metal Dissolution in Passivation Processes, *Electrochim. Acta* **48**, 4107–4117.
- N. Bonanos [1989] High Oxide Ion Conductivity in Bismuth Uranate, Bi_2UO_6 , *Mater. Res. Bull.* **24**, 1531–1540.
- N. Bonanos and E. P. Butler [1985] Ionic Conductivity of Monoclinic and Tetragonal Yttria-Zirconia Single Crystals, *J. Mater. Sci. Lett.* **4**, 561–564.
- N. Bonanos and E. Lilley [1980] Ionic Conductivity of Suzuki Phases, *Solid State Ionics* **1**, 223–230.
- N. Bonanos and E. Lilley [1981] Conductivity Relaxations in Single Crystals of Sodium Chloride Containing Suzuki Phase Precipitates, *J. Phys. Chem. Solids* **42**, 943–952.
- N. Bonanos, R. K. Slotwinski, B. C. H. Steele, and E. P. Butler [1984a] Electrical Conductivity/Microstructural Relationships in Aged CaO and $\text{CaO} + \text{MgO}$ Partially Stabilized Zirconia, *J. Mater. Sci.* **19**, 785–793.
- N. Bonanos, R. K. Slotwinski, B. C. H. Steele, and E. P. Butler [1984b] High Ionic Conductivity in Polycrystalline Tetragonal $\text{Y}_2\text{O}_3\text{-ZrO}_2$, *J. Mater. Sci. Lett.* **3**, 245–248.
- N. Bonanos, R. K. Slotwinski, J. Drennan, E. P. Butler, and B. C. H. Steele [1985] Characterisation of Grain Boundaries in Ceramic Ionic Conductors Using A.C. Electrical techniques, *Silic. Ind.* **9**(10), 127–132.
- N. Bonanos, P. Holtappels, and M. J. Jørgensen [2002] Electrochemical Evaluation of Functionally Graded SOFC Cathodes, *Proceedings of the Fifth European SOFC Forum, Science and Engineering of SOFC*, July 1–5, 2002, Luzern, Switzerland.
- N. Bonanos, P. Pissis, and J. R. Macdonald [2012] Impedance Spectroscopy of Dielectrics and Electronic Conductors, in *Characterization of Materials 1, 14*, ed. E. N. Kaufmann, John Wiley & Sons, Inc., Hoboken, NJ.
- A. Bonnel, F. Dabosi, C. Deslouis, M. Duprat, M. Keddam, and B. Tribollet [1983] Corrosion Study of a Carbon Steel in Neutral Chloride Solution by Impedance Techniques, *J. Electrochem. Soc.* **130**, 753–761.
- C. de Boor [1978] *A Practical Guide to Splines*, Springer-Verlag, New York, pp. 249.
- P. Bordewijk [1975] Defect-Diffusion Models of Dielectric Relaxation, *Chem. Phys. Lett.* **32**, 592–596.
- T. I. Borisova and B. V. Ershler [1950] Determination of the Zero Voltage Points of Solid Metals from Measurements of the Capacity of the Double Layer, *Zh. Fiz. Khim.* **24**, 337–344.
- G. Boschloo and A. Hagfeldt [2001] Spectroelectrochemistry of Nanostructured NiO , *J. Phys. Chem. B* **105**, 3039–3044.
- U. G. Bossel [1993] Effects of Current Collection, Contacting and Wiring on PEN Characterization, *Proceedings of the Solid Oxide Workshop*, Chexbres, Switzerland, pp. 59–61.
- U. Bossel [2000] *The Birth of the Fuel Cell*, The European Fuel Cell Forum.
- C. J. F. Böttcher [1952] *Theory of Electric Polarization*, Elsevier, Amsterdam, the Netherlands.
- C. J. F. Böttcher and P. Bordewijk [1978] *Theory of Electric Polarization, Dielectrics in Time-Dependent Fields*, Vol. II, Elsevier, Amsterdam, the Netherlands.
- P. H. Bottelberghs and G. H. J. Broers [1976] Interfacial Impedance Behavior of Polished and Paint Platinum Electrodes at $\text{Na}_2\text{WO}_4\text{-Na}_2\text{MoO}_4$ Solid Electrolytes, *J. Electroanal. Chem.* **67**, 155–167.
- B. A. Boukamp [1989] *Equivcrt*, University of Twente, the Netherlands.
- B. A. Boukamp and H. J. M. Bouwmeester [2003] Interpretation of the Gerischer Impedance in Solid State Ionics, *Solid State Ionics* **157**(1–4), 29–33.
- B. A. Boukamp, B. A. van Hassel, and A. J. Burggraaf [1991] The Use of Impedance Spectroscopy and NLLS-Fit Data Analysis in the Study of Oxygen Electrode Kinetics, *Proceedings of the Electrochemical Society (Symposium on High Temperature Electrode Materials and Characterization, Washington, DC, October 5, 1991)*, 44–55.
- L. Bousse [1982] Ph.D. thesis, Twente University of Technology, the Netherlands.
- L. Bousse and P. Bergveld [1983] On the Impedance of the Silicon Dioxide/Electrolyte Interface, *J. Electroanal. Chem.* **152**, 25–39.
- F. P. Bowden and E. K. Rideal [1928] The Electrolytic Behavior of Thin Films. II. The Areas of Catalytically Active Surfaces, *Proc. R. Soc. Lond. A* **120**, 80–89.
- A. D. Brailsford and D. K. Hohnke [1983] The Electrical Characterization of Ceramic Oxides, *Solid State Ionics* **11**, 133–142.
- B. Breslin, D. D. Macdonald, J. Sikora, and E. Sikora [1997a] Influence of UV Light on the Passive Behaviour of SS316-Effect of Prior Illumination, *Electrochim. Acta* **42**(1), 127–136.
- C. Breslin, D. D. Macdonald, E. Sikora, and J. Sikora [1997b] Photo-Inhibition of Pitting Corrosion on Types 304 and 316 Stainless Steels in Chloride-Containing Solution, *Electrochim. Acta* **42**(1), 137–144.
- P. M. M. C. Bressers and E. A. Meulenkamp [1998] The Electrochromic Behavior of Indium Tin Oxide in Propylene Carbonate Solutions, *J. Electrochem. Soc.* **145**, 2225–2230.
- B. Breyer and H. H. Bauer [1964] *Alternating Current Polarography and Tensammetry*, Interscience, New York.

- R. Brown, D. E. Smith, and G. Booman [1968] Operational Amplifier Circuits Employing Positive Feedback for IR Compensation. I. Theoretical Analysis of Stability and Bandpass Characteristics, *Anal. Chem.* **40**, 1411.
- P. G. Bruce [1987] Electrical Measurements on Polymer Electrolytes, in *Polymer Electrolyte Reviews I*, eds. J. R. MacCallum and C. A. Vincent, Elsevier, London, UK.
- P. G. Bruce and A. R. West [1983] The A. C. Conductivity of Polycrystalline LISICON $\text{Li}_{2+2x}\text{Zn}_{1-x}\text{GeO}_4$ and a Model for Intergranular Constriction Resistances, *J. Electrochem. Soc.* **130**, 662–669.
- P. G. Bruce, A. R. West, and D. P. Almond [1982] A New Analysis of ac Conductivity Data in Single Crystal Beta-Alumina, *Solid State Ionics* **7**, 57–60.
- P. G. Bruce, J. Evans, and C. A. Vincent [1988] Conductivity and Transference Number Measurements on Polymer Electrolytes, *Solid State Ionics* **28–30**(2), 918–922.
- G. J. Brug, A. Van den Eeden, M. Sluyters-Rehbach, and J. H. Sluyters [1984] The Analysis of Electrode Impedances Complicated by the Presence of a Constant Phase Element, *J. Electroanal. Chem.* **176**, 275–295.
- D. Bruggeman [1935] Berechnung verschiedener physikalischer Konstanten von heterogenen Substanzen, I. Dielektrizitätskonstanten und Leitfähigkeiten der Mischkörper aus isotropen Substanzen, *Annalen der Physik, Series 5* **24**, 636–679.
- T. R. Brumleve and R. P. Buck [1978] Numerical Solution of the Nernst-Planck and Poisson Equation System with Applications to Membrane Electrochemistry and Solid State Physics, *J. Electroanal. Chem. Interfacial Electrochem.* **90**(1), 1–31.
- R. Bube [1992] *Electrons in Solids: An Introductory Survey*, 3rd Edition, Elsevier, Cambridge, MA.
- U. Buchenau, Y. M. Galperin, V. L. Gurevich, D. A. Parshin, M. A. Ramos, and H. R. Schober [1992] Interaction of Soft Modes and Sound Waves in Glasses, *Phys. Rev. B* **46**(5), 2798–2808.
- R. P. Buck [1980] Impedance Diagrams Applied to the Investigation of Ion-Selective Electrodes, *Hungarian Sci. Instr.* **49**, 7–23.
- R. P. Buck [1982] The Impedance Method Applied to the Investigation of Ion-Selective Electrodes, *Ion Select. Electr. Rev.* **4**, 3–74.
- P. R. Bueno, C. Gabrielli, and H. Perrot [2008] Coloring Ionic Trapping States in WO_3 and Nb_2O_5 Electrochromic Materials, *Electrochim. Acta* **53**, 5533–5539.
- A. Bunde, P. Maass, and M. D. Ingram [1991] Diffusion Limited Percolation: A Model for Transport in Ionic Glasses, *Ber. Bunsenges. Phys. Chem.* **95**, 977–983.
- K. Bundy, M. Karlsson, G. Lindbergh, and A. Lundqvist [1998] An Electrochemical Impedance Spectroscopy Method for Prediction of the State of Charge of a Nickel-Metal Hydride Battery at Open Circuit and During Discharge, *J. Power Sources* **72**, 118–125.
- M. S. Burdis, J. R. Siddle, R. A. Batchelor, and J. M. Gallego [1998] $\text{V}_{0.50}\text{Ti}_{0.50}\text{O}_x$ Thin Films as Counterelectrodes for Electrochromic Devices, *Sol. Energy Mater. Sol. Cells* **54**, 93–98.
- A. J. Burggraaf, M. van Hemert, D. Scholten, and A. J. A. Winnebust [1985] Chemical Composition of Oxidic Interfaces in Relation with Electric and Electrochemical Properties, *Mater. Sci. Monogr.* **28B**(Reactivity of Solids), 797–802.
- G. T. Burstein, C. J. Barnett, A. R. Kucernak, and K. R. Williams [1997] Aspects of the Anodic Oxidation of Methanol, *Catal. Today* **38**, 425–437.
- E. P. Butler and N. Bonanos [1985] The Characterization of Zirconia Engineering Ceramics by A.C. Impedance Spectroscopy, *Mater. Sci. Eng.* **71**, 49–56.
- C. Solartron Instrumentation Group [1977] *1170 Series Frequency Response Analyzers: Operation Manual*, Farnborough, Hampshire, UK.
- N. Cabrera and N. F. Mott [1948] Theory of the Oxidation of Metals, *Rep. Progr. Phys.* **12**, 163–184.
- B. D. Cahan and C.-T. Chen [1982] The Nature of the Passive Film on Iron. II. AC Impedance Studies, *J. Electrochem. Soc.* **129**, 474–480.
- B. D. Cahan, H. M. Villulas, and E. B. Yeager [1991] The Effects of Trace Anions on the Voltammetry of Single Crystal Gold Surfaces, *J. Electroanal. Chem.* **306**, 213–238.
- L. M. Callow, J. A. Richardson, and J. L. Dawson [1976] Corrosion Monitoring Using Polarization Resistance Measurements, Parts I and II, *Br. Corros. J.* **11**, 123–132.
- R. Calvert [1948] A New Technique in Bridge Measurements, *Electron. Eng.* **20**, 28–29.
- S. Capaccioli, K. L. Ngai, M. S. Thayyil, and D. Prevosto [2015] Coupling of Caged Molecule Dynamics to JG β -Relaxation: I, *J. Phys. Chem. B* **119**, 8800–8808.
- H. S. Carslaw and J. C. Jaeger [1959] *Conduction of Heat in Solids*, 2nd Edition, Clarendon Press, Oxford, UK.
- C. W. Carter [1925] Impedance of Networks Containing Resistances and Two Reactances, *Bell Sys. Tech. J.* **4**, 387–401.
- R. Casalini and C. M. Roland [2005] Temperature and Density Effects on the Local Segmental and Global Chain Dynamics of Poly(Oxybutylene), *Macromolecules* **38**, 1779–1788.
- R. Casalini and C. M. Roland [2010] Effect of Crosslinking on the Secondary Relaxation in Polyvinylethylene, *J. Polym. Sci. Polym. Phys. Ed.* **48**, 582–587.
- R. Casalini and C. M. Roland [2011] On the Low Frequency Peak in the Dielectric Spectrum of Glycerol, *J. Chem. Phys.* **135**, 094502.
- M. Casciola and D. Fabiani [1983] Ionic Conduction and Dielectric Properties of Anhydrous Alkali Metal Salt Forms of Zirconium Phosphide, *Solid State Ionics* **11**, 31–38.
- E. B. Castro [1994] Analysis of the Impedance Response of Passive Iron, *Electrochim. Acta* **39**, 2117–2123.
- H. Chang and G. Jaffé [1952] Polarization in Electrolytic Solutions, Part I, Theory, *J. Chem. Phys.* **20**, 1071–1077.
- G. W. Chantry and H. A. Gebbie [1965] Submillimeter Wave Spectra of Polar Liquids, *Nature* **208**, 378.

- C. Y. Chao, L. F. Lin, and D. D. Macdonald [1981] A Point Defect Model for Anodic Passive Films: (I) Film Growth Kinetics, *J. Electrochem. Soc.* **128**(6), 1187–1194.
- C. Y. Chao, L. F. Lin, and D. D. Macdonald [1982] A Point Defect Model for Anodic Passive Films: (III) Impedance Response, *J. Electrochem. Soc.* **129**(9), 1874–1879, <http://www.wavemetrics.com/products/igorpro/igorpro.htm> (accessed on November 3, 2017).
- C. C. Chen [2013] Characterization of Porous WO₃ Electrochromic Device by Electrochemical Impedance Spectroscopy, *J. Nanomater.* **2013**, 785023.
- S. Cheng, J. Zhang, H. Liu, Y.-J. Leng, A. Yuan and C. Cao [1998] Study of Early Cycling Deterioration of a Ni/MH battery by Electrochemical Impedance Spectroscopy, *J. Power Sources* **74**(1), 155–157.
- S. Cheng, J. Zhang, M. Zhaob, and C. Caoa [1999] Electrochemical Impedance Spectroscopy Study of Ni/MH Batteries, *J. Alloys Compounds* **293–295**, 814–820.
- D.-T. Chin and S. Venkatesh [1979] A Study of Alternating Voltage Modulation on the Polarization of Mild Steel, *J. Electrochem. Soc.* **126**, 1908–1913.
- H. Chung [1983] *Transient Crack Growth in AISI 4340 Steel in Sodium Chloride Solution*, Ph.D. thesis, Ohio State University.
- H. Chung and D. D. Macdonald [1981] *Corrosion and Corrosion Cracking of Materials for Water Cooled Reactors*, Report to the Electric Power Research Institute, Palo Alto, CA, Project RP1166-1.
- F. Ciuchi, A. Mazzulla, N. Scaramuzza, E. K. Lenzi, and L. R. Evangelista [2012] Fractional Diffusion Equation and the Electrical Impedance: Experimental Evidence in Liquid-Crystalline Cells, *J. Phys. Chem. C* **116**(15), 8773–8777.
- M. Ciureanu and H. Wang [1999] Electrochemical Impedance Study of Electrode-Membrane Assemblies in PEM Fuel Cells. I. Electro-Oxidation of H₂ and H₂/CO Mixtures on Pt-Based Gas-Diffusion Electrodes, *J. Electrochem. Soc.* **146**, 4031–4040.
- M. Ciureanu and H. Wang [2000] Electrochemical Impedance Study of Anode CO-Poisoning in PEM Fuel Cells, *J. New Mater. Electrochem. Syst.* **3**, 107–119.
- C. Clausen, S. A. Lewis, and J. M. Diamond [1979] Impedance Analysis of a Tight Epithelium Using a Distributed Resistance Model, *Biophys. J.* **26**(2), 291–317.
- S. J. C. Cleghorn, T. E. Springer, M. S. Wilson, C. Zawodzinski, T. A. Zawodzinski, and S. Gottesfeld [1997] PEM Fuel Cells for Transportation and Stationary Power Generation Applications, *Int. J. Hydrogen Energy* **22**, 1137–1144.
- M. Clericuzio, W. O. Parker, Jr., M. Soprani, and M. Andrei [1995] Ionic Diffusivity and Conductivity of Plasticized Polymer Electrolytes: PMFG-NMR and Complex Impedance Studies, *Solid State Ionics* **82**, 179–192.
- W. Cleveland and E. Grosse [1990] *Fortran Routines for Locally-Weighted Regression, LOESS Program Source and Documentation*, www.netlib.org (accessed on November 3, 2017).
- J. H. Clint [1992] *Surfactant Aggregation*, Blackie & Son, Glasgow, Scotland.
- W. T. Coffey, P. M. Corcoran, and J. K. Vij [1987] On the Role of Inertial Effects and Dipole-Dipole Coupling in the Theory of the Debye and Far-Infrared Absorption of Polar Fluids. II. Comparison with Experimental Observations, *Proc. R. Soc. Lond. A* **412**(1843), 339–388.
- M. H. Cohen and G. S. Grest [1981] Dispersion of Relaxation Rates in Dense Liquids and Glasses, *Phys. Rev. B* **24**, 4091–4094.
- K. S. Cole [1972] *Membranes, Ions, and Impulses*, University of California Press, Berkeley, CA.
- K. S. Cole and R. H. Cole [1941] Dispersion and Absorption in Dielectrics. I. Alternating-Current Characteristics, *J. Chem. Phys.* **9**, 341–351.
- R. H. Cole and E. Tombari [1991] Analysis of Electric Relaxation in Sodium Trisilicate and Lithium Fluoroborate Glasses from 102 to 109 Hz and 25 to 300°C, *J. Non-Cryst. Solids* **131–133**(Part 2), 969–972.
- M. Colloms [1983] *Computer Controlled Testing and Instrumentation*, Pentech Press, London, UK.
- P. Colonemos and R. G. Gordon [1979] Bounded Error Analyses of Experimental Distributions of Relaxation Times, *J. Chem. Phys.* **71**, 1159–1166.
- B. E. Conway [1991] Transition from “Supercapacitor” to “Battery” Behavior in Electrochemical Energy Storage, *J. Electrochem. Soc.* **138**, 1539–1548.
- B. E. Conway [1999] *Electrochemical Supercapacitors: Scientific Fundamentals and Technological Applications*, Kluwer Academic, Plenum Publishing Co., New York.
- B. E. Conway and E. Gileadi [1962] Kinetic Theory of Pseudo-Capacitance and Electrode Reactions at Appreciable Surface Coverage, *Trans. Faraday Soc.* **58**, 2493–2509.
- B. E. Conway and D. M. Novak [1981] Competitive Adsorption and State of Charge of Halide-Ions in Monolayer Oxide Film Growth-Processes at Pt Anodes, *J. Chem. Soc. Faraday Trans. I* **77**, 2341–2359.
- B. E. Conway and W. G. Pell [2002] Power Limitations of Supercapacitor Operation Associated with Resistance and Capacitance Distribution in Porous Electrode Devices, *J. Power Sources* **105**(2), 169–181.
- B. E. Conway and B. V. Tilak [2002] Interfacial Processes Involving Electrocatalytic Evolution and Oxidation of H₂, and the role of Chemisorbed H, *Electrochim. Acta* **47**, 3571–3594.
- B. E. Conway, J. O'. M. Bockris, and W. Mehl [1956] Preparation and Maintenance of Spherical Metal Electrodes in Hydrogen, *J. Sci. Instr.* **33**, 400.
- B. E. Conway, H. A. Kozlowska, and E. Gileadi [1965] Significance of Nonsteady State A.C. and D.C. Measurements in Electrochemical Adsorption Kinetics. Applications to Galvanostatic and Voltage Sweep Methods, *J. Electrochem. Soc.* **112**, 341–349.
- B. E. Conway, K. Tellefsen, and S. Marshall [1984] Lattice Models, Interactions, and Solvent Effects in Electrochemical Monolayer Formation, in *The Chemistry and Physics of Electrocatalysis*, eds. J. D. E. McIntyre, M. J. Weaver, and E. B.

- Yaeger, The Electrochemical Society Inc., Pennington, NJ, pp. 15–33.
- J. W. Cooley and J. W. Tukey [1965] An Algorithm for the Machine Computation of Complex Fourier Series, *Math. Comput.* **19**, 297.
- S. Cordoba-Torresi, A. Hugot-Le Goff, and H. Takenouti [1990] Electrochromism in Metal Oxide Films Studied by Raman Spectroscopy and A.C. Techniques: Charge Insertion Mechanism, *Proc. SPIE* **1272**, 152–161.
- S. Corezzi, E. Campani, P. A. Rolla, S. Capaccioli, and D. Fioretto [1999] Change in Dynamics of Supercooled Systems Revealed by Dielectric Spectroscopy, *J. Chem. Phys.* **111**, 9343–9351.
- P. Costamagna, P. Costa, and V. Antonucci [1998] Micro-Modelling of Solid Oxide Fuel Cell Electrodes, *Electrochim. Acta* **43**, 375–394.
- R. T. Coverdale, E. J. Garboczi, and H. M. Jennings [1995] An Improved Model for Simulating Impedance Spectroscopy, *Comput. Mater. Sci.* **3**, 465.
- E. J. Crain [1970] *Laplace and Fourier Transforms for Electrical Engineers*, Holt, Rinehart and Winston, New York.
- C. Cramer, K. Funke, M. Buscher, A. Happe, and T. Saatkamp [1995] Ion Dynamics in Glass-Forming Systems: II. Conductivity Spectra Above the Glass Transformation Temperature, *Philos. Mag. B* **71**(4), 713–719.
- C. Cramer, K. Funke, and T. Saatkamp [1995] Ion Dynamics in Glass-Forming Systems: I. Conductivity Spectra below the Glass Transformation Temperature, *Philos. Mag. B* **71**(4), 701–711.
- S. C. Creason and D. E. Smith [1972] Fourier Transform Faradaic Admittance Measurements: Demonstration of the Applicability of Random and Pseudo-Random Noise as Applied Potential Signals, *J. Electroanal. Chem.* **36**, 1.
- S. C. Creason and D. E. Smith [1973] Fourier Transform Faradic Admittance Measurements: On the Use of High-Precision Data for Characterization of Very Rapid Electrode Process Kinetic Parameters, *J. Electroanal. Chem.* **47**, 9.
- N. Cui and J. L. Luo [2000] An AC Impedance Study of Self-Discharge Mechanism of Nickel-Metal Hydride (Ni-MH) Battery Using Mg₂Ni-type Hydrogen Storage Alloy Anode, *Electrochim. Acta* **45**(24), 3973–3981.
- G. D'Aprano and M. Leclerc [1993] Steric and Electronic Effects in Methyl and Methoxy Substituted Polyanilines, *J. Electroanal. Chem.* **351**, 145–148.
- J. R. Dahn, A. K. Sleigh, H. Shi, J. N. Reimers, Q. Zhong, and B. M. Way [1993] Dependence of the Electrochemical Intercalation of Lithium in Carbons on the Crystal Structure of the Carbon, *Electrochim. Acta* **38**(9), 1179–1191.
- L. S. Darken [1948] Diffusion, Mobility, and their Interrelation through Free Energy in Binary Metallic Systems, *Trans. AIME* **175**, 184–201.
- D. W. Davidson [1961] Dielectric Relaxation in Liquids. I. The Representation of Relaxation Behavior, *Can. J. Chem.* **39**, 571–594.
- D. W. Davidson and R. H. Cole [1951] Dielectric Relaxation in Glycerol, Propylene Glycol, and *n*-Propanol, *J. Chem. Phys.* **19**, 1484–1490.
- C. De Dominicis, H. Orland, and F. Lainee [1985] Stretched Exponential Relaxation in Systems with Random Free-Energies, *J. Phys. Lett.* **46**, L463–L466.
- L. C. De Jonghe [1979] Grain Boundaries and Ionic Conduction in Sodium Beta-Alumina, *J. Mater. Sci.* **14**, 33–48.
- S. K. Deb [1969] A Novel Electrophotographic System, *Appl. Opt. Suppl.* **3**, 192–195.
- P. G. Debenedetti and F. H. Stillinger [2001] Supercooled Liquids and the Glass Transition, *Nature* **410**, 259–267.
- P. Debye [1929] *Polar Molecules*, Chemical Catalogue Company, New York, p. 94.
- P. Debye and H. Falkenhagen [1928] Dispersion of the Conductivity and Dielectric Constants of Strong Electrolytes, *Phys. Z.* **29**(121–132), 401–426.
- F. Decker, S. Passerini, R. Pileggi, and B. Scrosati [1992] The Electrochromic Process in Non-Stoichiometric Nickel Oxide Thin Film Electrodes, *Electrochim. Acta* **37**, 1033–1038.
- P. Delahay [1954] *New Instrumental Methods in Electrochemistry*, Interscience, New York.
- P. Delahay [1965] *Double Layer and Electrode Kinetics*, Wiley-Interscience, New York.
- P. Delahay [1966] The Theory of the Electrolytic Double-Layer, *J. Phys. Chem.* **70**, 2373–2379.
- P. Delahay, M. Senda, and C. H. Weis [1960] Faradaic Rectification and Electrode Processes, *J. Phys. Chem.* **64**, 960.
- Z. Deng, Z. Zhang, Y. Lai, J. Liu, J. Li, and Y. Liu [2013] Electrochemical Impedance Spectroscopy Study of a Lithium/Sulfur Battery: Modeling and Analysis of Capacity Fading, *J. Electrochem. Soc.* **160**(4), A553–A558.
- C. Deslouis, C. Gabrielli, Ph. Sainte-Rose Franchine, and B. Tribollet [1980] Relationship Between the Electrochemical Impedance and the Electrohydrodynamical Impedance Measured Using a Rotating Disk Electrode, *J. Electroanal. Chem.* **107**, 193–195.
- C. Deslouis, C. Gabrielli, Ph. Sainte-Rose Franchine, and B. Tribollet [1982] Electrohydrodynamical Impedance on a Rotating Disk Electrode, *J. Electrochem. Soc.* **129**, 107–118.
- J. Devay and L. Meszaros [1980] Study of the Rate of Corrosion of Metals by a Faradaic Distortion Method. II. Effect of the Ohmic Resistance and Capacity of the Double Layer on the Measurement of the Harmonic Components of the Faradaic Currents, *Acta Chim. Acad. Sci. Hung.* **104**, 311.
- J. Devay and L. Meszaros [1982] Study of the Rate of Corrosion of Metals by a Faradaic Distortion Method. IV. Application of the Method for the Case of Reversible Charge Transfer, *Acta Chim. Acad. Sci. Hung.* **104**, 311.
- J. P. Diard and B. LeGorrec [1979] Use of a New Generator with Negative Impedance for Studying the Anodic Behaviour of Zinc in an Alkaline Medium, *Electroanal. Chem.* **103**, 363–374.

- J.-P. Diard and C. Montella [2003] Diffusion-Trapping Impedance Under Restricted Linear Diffusion Conditions, *J. Electroanal. Chem.* **557**, 19–36.
- J.-P. Diard, B. Le Gorrec, and C. Montella [1992] Calculation, Simulation and Interpretation of Electrochemical Impedances. Part 3. Conditions for Observations of Low Frequency Inductive Diagrams for a Two-Step Electron Transfer Reaction with an Adsorbed Intermediate Species, *J. Electroanal. Chem.* **326**, 13–36.
- T. van Dijk and A. J. Burggraaf [1981] Grain Boundary Effects on Ionic Conductivity in Ceramic $\text{Gd}_x\text{Zr}_{1-x}\text{O}_{2-(x/2)}$ Solid Solutions, *Phys. Stat. Sol. (a)* **63**, 229–240.
- J. L. Diot, J. Joseph, J. R. Matin, and P. Clechet [1985] pH Dependence of the Si/SiO₂ Interface State Density for EOS Systems, *Electroanal. Chem.* **193**, 75–88.
- P. K. Dixon, L. Wu, S. R. Nagel, B. D. Williams, and J. P. Carini [1990] Scaling in the Relaxation of Supercooled Liquids, *Phys. Rev. Lett.* **65**, 1108–1111.
- K. Doblhofer and A. A. Pilla [1971] LaPlace Plane Analysis of the Faradaic and Non-Faradaic Impedance of the Mercury Electrode, *J. Electroanal. Chem.* **39**, 91.
- M. Dolle, F. Orsini, A. S. Gozdz, and J.-M. Tarascon [2001] Development of Reliable Three-Electrode Impedance Measurements in Plastic Li-Ion Batteries, *J. Electrochem. Soc.* **148** (8), A851–A857.
- K. Donovan and T. Kreouzis [2000] Deconvolution of Time of Flight Photocurrent Transients and Electronic Response Time in Columnar Crystals, *J. Appl. Phys.* **88**, 918–923.
- M. Doyle and J. Newman [1995] Modeling the Performance of Rechargeable Lithium-Based Cells: Design Correlations for Limiting Cases, *J. Power Sources* **54**(1), 46–51.
- J. Drennan and E. P. Butler [1982] Does Alumina Act as a Grain Boundary Scavenger in Zirconia? *J. Am. Ceram. Soc.* **65**(11), 194–195.
- W. M. Du, G. Li, H. Z. Cummins, M. Fuchs, J. Toulouse, and L. A. Knauss [1994] Light-Scattering Study of the Liquid-Glass Transition in Propylene Carbonate, *Phys. Rev. E* **49**, 2192–2205.
- Y. Duhirel, B. Beden, J.-M. Leger, and C. Lamy [1992] Passivation du cadmium en milieu basique: etude mecanistique par voltammetrie cyclique, *Electrochim. Acta* **37**(4), 665–671.
- S. S. Dukhin and V. N. Shilov [1974] *Dielectric Phenomena and the Double Layer in Disperse Systems and Polyelectrolytes* (English Translation), Keter, Jerusalem, Israel.
- E. C. Dutoit, R. L. Van Meirhaeghe, F. Cardon, and W. P. Gomes [1975] Investigation on the Frequency-Dependence of the Impedance of the Nearly Ideally Polarizable Semiconductor Electrodes CdSe, CdS, and TiO₂, *Ber. Bunsen Gesell.* **79**, 1206–1213.
- J. C. Dyre [1988] The Random Free Energy Barrier Model for AC Conduction in Disordered Solids, *J. Appl. Phys.* **64**, 2456–2468.
- J. C. Dyre and T. B. Schröder [2000] Universality of AC Conduction in Disordered Solids, *Rev. Mod. Phys.* **72**(3), 873–892.
- L. Ebihara and R. T. Mathias [1985] Linear Impedance Studies of Voltage-Dependent Conductances in Tissue Cultured Chick Heart Cells, *Biophys. J.* **48**(3), 449–460.
- M. D. Ediger [2000] Spatially Heterogeneous Dynamics in Supercooled Liquids, *Annu. Rev. Phys. Chem.* **51**, 99–128.
- W. Ehm, H. Göhr, R. Kaus, B. Röseler, and C. A. Schiller [2000] The Evaluation of Electrochemical Impedance Spectra Using a Modified Logarithmic Hilbert Transform, *ACH Models Chem.* **137**, 145–157.
- L. E. Eiselstein, M. C. H. McKubre, and R. D. Caligiuri [1983] *Prediction of Crack Growth in Aqueous Environments*, First Annual Report by SRI to the Office of Naval Research, N00014-82-K-0343, SRI International, Menlo Park, CA.
- L. E. Eiselstein, M. C. H. McKubre, and R. D. Caligiuri [1985] *Electrical and Mechanical Impedance Studies of Crack Growth*, Final Report by SRI to the Office of Naval Research.
- R. S. Eisenberg [1967] The Equivalent Circuit of Single Crab Muscle Fibers as Determined by Impedance Measurements with Intracellular Electrodes, *J. Gen. Physiol.* **50**(6), 1785–1806.
- B. R. Eisenberg [1979] Skeletal Muscle Fibers: Stereology Applied to Anisotropic and Periodic Structures, in *Stereological Methods: Practical Methods for Biological Morphometry*, Vol. 1, ed. E. Weibel, Academic Press, London, UK, pp. 274–284.
- R. S. Eisenberg [1980] Structural Complexity, Circuit Models, and Ion Accumulation, *Fed. Proc.* **39**(5), 1540–1543.
- R. S. Eisenberg [1983] Impedance Measurement of the Electrical Structure of Skeletal Muscle, in *Handbook of Physiology, Section 10: Skeletal Muscle*, ed. L. D. Peachey, American Physiological Society, Washington, DC, pp. 301–323.
- B. R. Eisenberg [1983] Quantitative Ultrastructure of Mammalian Skeletal Muscle, in *Handbook of Physiology*, Vol. 10, eds. L. D. Peachey and R. H. Adrian, American Physiological Society, Bethesda, MD, pp. 73–112.
- R. S. Eisenberg [1987] Impedance Measurements as Estimators of the Properties of the Extracellular Space, *Ann. N. Y. Acad. Sci.* **481**, 116–122.
- R. S. Eisenberg and L. L. Costantin [1971] The Radial Variation of Potential in the Transverse Tubular System of Skeletal Muscle, *J. Gen. Physiol.* **58**(6), 700–701.
- R. S. Eisenberg and E. A. Johnson [1970] Three Dimensional Electrical Field Problem in Physiology, *Prog. Biophys. Mol. Biol.* **20**, 1–65.
- R. S. Eisenberg and R. T. Mathias [1980] Structural Analysis of Electrical Properties, *Crit. Rev. Bioeng.* **4**, 203–232.
- B. R. Eisenberg and B. A. Mobley [1975] Size Changes in Single Muscle Fibers During Fixation and Embedding, *Tissue Cell* **7**, 383–387.
- R. S. Eisenberg, R. T. Mathias, and J. S. Rae [1977] Measurement, Modeling, and Analysis of the Linear Electrical Properties of Cells, *Ann. N. Y. Acad. Sci.* **303**, 342–354.
- R. S. Eisenberg, V. Barcilon, and R. T. Mathias [1979] Electrical Properties of Spherical Syncytia, *Biophys. J.* **25**(1), 151–180.

- K. El Adham and A. Hammou [1983] "Grain Boundary Effect" on Ceria-Based Solid Solutions, *Solid State Ionics* **9–10**, 905–912.
- S. R. Elliott [1992] A Unified Model for the Low-Energy Vibrational Behavior of Amorphous Solids, *Europhys. Lett.* **19**, 201.
- C. Endler-Schuck, J. Joos, A. Weber, and E. Ivers-Tiffée [2015] The Chemical Oxygen Surface Exchange and Bulk Diffusion Coefficient Determined by Impedance Spectroscopy of Porous $\text{La}_{0.58}\text{Sr}_{0.4}\text{Co}_{0.2}\text{Fe}_{0.8}\text{O}_{3-\delta}$ (LSCF) Cathodes, *Solid State Ionics* **269**, 67–79.
- G. R. Engelhardt, R. P. Case, and D. D. Macdonald [2016] Electrochemical Impedance Spectroscopy Optimization on Passive Metals, *J. Electrochem. Soc.* **163**(8), C470–C476.
- H. Engstrom and J. C. Wang [1980] Automatic Multifrequency Measurements of the Complex Impedance of Fast Ion Conductors, *Solid State Ionics* **1**, 441–459.
- I. Epelboin and M. Keddam [1970] Faradaic Impedances: Diffusion Impedance and Reaction Impedance, *J. Electrochem. Soc.* **117**, 1052–1056.
- I. Epelboin, C. Gabrielli, M. Keddam, J.-C. Lestrade, and H. Takenouti [1972] Passivation of Iron in Sulfuric Acid Medium, *J. Electrochem. Soc.* **119**, 1631–1637.
- I. Epelboin, C. Gabrielli, M. Keddam, and H. Takenouti [1975] A Model of the Anodic Behaviour of Iron in Sulphuric Acid Medium, *Electrochim. Acta* **20**, 913–916.
- A. Eucken and B. Weblus [1951] Adsorption of Hydrogen on Platinum According to Measurements of the Capacity of Polarization, *Zeit. Elektrochem.* **55**, 114–119.
- L. R. Evangelista, E. K. Lenzi, and G. Barbero [2011] Anomalous Diffusion and Memory Effects on the Impedance Spectroscopy for Finite-Length Situations, *J. Phys. Condens. Matter* **23**, 485005–485009.
- L. R. Evangelista, E. K. Lenzi, G. Barbero, and J. R. Macdonald [2013] On the Equivalence Between Specific Adsorption and Kinetic Equation Descriptions of the Admittance Response in Electrolytic Cells, *J. Chem. Phys.* **138**, 114702–114706.
- C. T. Everitt and D. A. Haydon [1968] Electrical Capacitance of a Lipid Membrane Separating Two Aqueous Phases, *J. Theor. Biol.* **18**(3), 371–379.
- F. Fabregat-Santiago, G. Garcia-Belmonte, J. Bisquert, E. Ferriols, N. S. Bueno, P. R. Longo, J. S. Anton, and S. Castro-Garcia [2001] Dynamic Processes in the Coloration of WO_3 by Lithium Insertion, *J. Electrochem. Soc.* **148**, E302–E309.
- G. Falk and P. Fatt [1964] Linear Electrical Properties of Striated Muscle Fibres Observed with Intracellular Electrodes, *Proc. R. Soc. Lond. B Biol. Sci.* **160**, 69–123.
- B. W. Faughnan, R. S. Crandall, and P. M. Heyman [1975] Electrochromism in WO_3 Amorphous Films, *RCA Rev.* **36**, 177–197.
- P. S. Fernandez, A. Arenillas, E. G. Calvo, J. A. Menendze, and M. E. Martins [2012] Carbon Xerogels as Electrochemical Supercapacitors. Relation Between Impedance Physicochemical Parameters and Electrochemical Behaviour, *Int. J. Hydrogen Energy* **37**, 10249–10255.
- R. Fettiplace, D. M. Andrews, and D. A. Haydon [1971] The Thickness, Composition and Structure of Some Lipid Bilayers and Natural Membranes, *J. Membr. Biol.* **5**(3), 277–296.
- K. Fic, G. Lota, M. Meller, and E. Frackowiak [2012] Novel Insight into Neutral Medium as Electrolyte for High-Voltage Supercapacitors, *Energy Environ. Sci.* **5**, 5842–5850.
- M. Fill and J. A. Copello [2002] Ryanodine Receptor Calcium Release Channels, *Phys. Rev.* **82**(4), 893–922.
- E. W. Fischer [1993] Light Scattering and Dielectric Studies on Glass Forming Liquids, *Phys. A* **201**(1–3), 183–206.
- J. Fleig [2000] The Influence of Non-Ideal Microstructures on the Analysis of Grain Boundary Impedances, *Solid State Ionics* **131**, 117–127.
- J. Fleig [2002] The Grain Boundary Impedance of random Microstructures, Numerical Simulations and Implications for the Analysis of Experimental Data, *Solid State Ionics* **150**, 181–193.
- J. Fleig and J. Maier [1996] The Impedance of Imperfect Electrode Contacts on Solid Electrolytes, *Solid State Ionics* **85**, 17–24.
- J. Fleig and J. Maier [1997] Rough Electrodes in Solid and Liquid Electrochemistry: Impact of Morphology on the Impedance, *Solid State Ionics* **94**(1–4), 199–207.
- J. Fleig and J. Maier [1998] A Finite Element Study of the Grain Boundary Impedance of Different Microstructures, *J. Electrochem. Soc.* **145**, 2081–2089.
- S. Fletcher [1992] An Electrical Model Circuit that Reproduces the Behaviour of Conducting Polymer Electrodes in Electrolyte Solutions, *J. Electroanal. Chem.* **337**, 127–145.
- D. R. Franceschetti [1981] Small-Signal A. C. Response Theory for Systems Exhibiting Impurity Oxygen Transport, *Solid State Ionics* **5**, 613–616.
- D. R. Franceschetti [1982] *Physics of Electrochemical Systems*, Lecture Notes, State University, Utrecht, the Netherlands, January, pp. 1–165.
- D. R. Franceschetti [1984] Small-Signal AC Response Theory for Systems Exhibiting Diffusion and Trapping of an Electroactive Species, *J. Electroanal. Chem.* **178**, 1–9.
- D. R. Franceschetti [1987] Small-Signal AC Response of Supported Thin-Layer Electrochemical Cells, *J. Chem. Phys.* **86**, 6495.
- D. R. Franceschetti and J. R. Macdonald [1977] Electrode Kinetics, Equivalent Circuits, and System Characterization: Small-Signal Conditions, *J. Electroanal. Chem.* **82**, 271–301.
- D. R. Franceschetti and J. R. Macdonald [1979a] Numerical Analysis of Electrical Response: Statics and Dynamics of Space-Charge Regions at Blocking Electrodes, *J. Appl. Phys.* **50**, 291–302.
- D. R. Franceschetti and J. R. Macdonald [1979b] Numerical Analysis of Electrical Response: Biased Small-Signal A. C. Response for Systems with One or Two Blocking Electrodes, *J. Electroanal. Chem.* **100**, 583–605.

- D. R. Franceschetti and J. R. Macdonald [1979c] Diffusion of Neutral and Charged Species Under Small-Signal A. C. Conditions, *J. Electroanal. Chem.* **101**, 307–316.
- D. R. Franceschetti and J. R. Macdonald [1980] Coupling of Electrode Kinetics and Space Charge Dynamics in Unsupported Systems, in *Proceedings of the Third Symposium on Electrode Processes*, the Electrochemical Society, 1980 Proceedings 80-3, eds. S. Bruckenstein, J. D. McIntyre, B. Miller, and E. Yeager, Electrochemical Society, Princeton, NJ, pp. 94–114.
- D. R. Franceschetti and J. R. Macdonald [1982]. Small-Signal A-C Response Theory for Electrochromic Thin Films. *J. Electrochem. Soc.* **129**, 1754–1756.
- D. R. Franceschetti and A. P. Ross [1989] Impedance Characteristics of Three-Phase Electrodes on Solid Electrolytes, *Appl. Phys. A* **49**(1), 111–116.
- D. R. Franceschetti and P. C. Shipe [1984] Bulk Conductivity and Polarization of Ionic Crystals Exhibiting Defect Exchange Between Inequivalent Sites, *Solid State Ionics* **11**, 285–291.
- D. R. Franceschetti, J. R. Macdonald, and R. P. Buck [1991] Interpretation of Finite-Length-Warburg-Type Impedances in Supported and Unsupported Electrochemical Cells with Kinetically Reversible Electrodes, *J. Electrochem. Soc.* **138**, 1368–1371.
- A. D. Franklin [1975] Electrode Effects in the Measurement of Ionic Conductivity, *J. Am. Ceram. Soc.* **58**, 465–473.
- A. D. Franklin and H. J. de Bruin [1983] The Fourier Analysis of Impedance Spectra of Electroded Solid Electrolytes, *Phys. Stat. Sol. (a)* **75**, 647–656.
- G. Frenning and M. Strømme [2001] Theoretical Derivation of the Isothermal Transient Ionic Current in an Ion Conductor: Migration, Diffusion and Space-Charge Effects, *J. Appl. Phys.* **90**, 5570–5575.
- G. Frenning, M. Nilsson, J. Westlinder, G. A. Niklasson and M. Strømme Mattsson [2001] Dielectric and Li Transport Properties of Electron Conducting and Non-Conducting Sputtered Amorphous Ta₂O₅ Films, *Electrochim. Acta* **46**, 2041–2046.
- G. Frenning, A. K. Jonsson, A. L. Larsson, and M. Strømme [2003] Theoretical Investigation of Ion Conduction in Three-Layered Ion-Conductor Systems: Derivation of the Isothermal Transient Ionic Current and Frequency-Dependent Impedance, *J. Appl. Phys.* **94**, 1629–1638.
- R. J. Friauf [1954] Polarization Effects in the Ionic Conductivity of Silver Bromide, *J. Chem. Phys.* **22**, 1329–1338.
- H. Fricke [1932] The Theory of Electrolytic Polarization, *Philos. Mag.* **14**, 310–318.
- H. Fricke [1953] The Maxwell-Wagner Dispersion in a Suspension of Ellipsoids, *J. Phys. Chem.* **57**, 934–937.
- K. Friestad, G. Hagen, S. Panero, and B. Scrosati [1997] Transmission Spectra and Electrochemical Impedance Analysis of Polyaniline, Prussian Blue and Tungsten Oxide with Incorporated Nickel in Electrochromic Windows, *Electrochem. Soc. Proc.* **96-24**, 353–368.
- H. Frölich [1949] *Theory of Dielectrics*, Oxford University Press, Oxford, UK.
- A. Fromhold and E. L. Cook [1967] Diffusion Currents in Large Electric Fields for Discrete Lattices, *J. Appl. Phys.* **38**, 1546–1553.
- A. N. Frumkin and V. I. Melik-Gaykazyan [1951] Determination of the Kinetics of Adsorption of Organic Substances by A.C. Measurements of the Capacity and the Conductivity at the Boundary: Electrode-Solution, *Dokl. Acad. Nauk.* **77**, 855–858.
- A. N. Frumkin, P. Dolin, and B. V. Ershler [1940a] Kinetics of Processes on the Platinum Electrode. II. The Rate of Discharge of H-Ions and the Rate of the Over-All Process of Hydrogen Evolution on Platinum, *Acta Physicochim. URSS* **13**, 779–792.
- A. N. Frumkin, P. Dolin, and B. V. Ershler [1940b] Kinetics of Processes on the Platinum Electrode. III. The Influence of the Diffusion of Molecular Hydrogen on the Capacity of the Platinum Electrode, *Acta Physicochim. URSS* **13**, 793–802.
- G. S. Fulcher [1925] Analysis of Recent Measurements of Viscosity of Glasses, *J. Am. Ceram. Soc.* **8**(6), 339–355.
- K. Funke [1986] Debye-Hückel-Type Relaxation Processes in Solid Ionic Conductors: The Model, *Solid State Ionics* **18–19**, 183–190.
- K. Funke [1998] A Modified Jump Relaxation Model for Fragile Glass-Forming Ionic Melts, *Z. Phys. Chem.* **206**, 101–116.
- K. Funke and R. D. Banhatti [2004] Modelling Frequency-Dependent Conductivities and Permittivities in the Framework of the Migration Concept, *Solid State Ionics* **169**(1–4), 1–8.
- K. Funke, S. Bruckner, C. Cramer, and D. Wilmer [2002] Dynamics of Mobile Ions in Solid Electrolytes: Conductivity Spectra and the Concept of Mismatch and Relaxation, *J. Non-Cryst. Solids* **307–310**, 921–929.
- R. M. Fuoss and J. G. Kirkwood [1941] Electrical Properties of Solids. VIII. Dipole Moments in Polyvinyl Chloride-Diphenyl Systems, *J. Am. Chem. Soc.* **63**, 385–394.
- C. Gabrielli [1981] *Identification of Electrochemical Processes by Frequency Response Analysis*, Monograph Reference 004/83, Solartron Instrumentation Group, Farnsborough, UK.
- C. Gabrielli and M. Keddam [1974] Recent Progress in the Measurement of Electrochemical Impedances in a Sinusoidal System, *Electrochim. Acta* **19**, 355.
- C. Gabrielli, M. Keddam, H. Perrot, and R. Torresi [1994] Lithium Insertion in WO₃ Studied by Simultaneous Measurements of Impedance, Electrogravimetric and Electro-Optical Transfer Functions, *J. Electroanal. Chem.* **378**, 85–92.
- C. Gainaru, R. Bohmer, and G. Williams [2010] Ion Sweeping in Conducting Dielectric Materials, *Eur. Phys. J.* **75**, 209–216.
- P. Gambhire, K. S. Hariharan, A. Khandelwal, V. S. Kumar, S. M. Kolake, D. Oh, and S. Doo [2014] Impedance Response Model of a Lithium Ion Cell with a Phase Change Electrode, *J. Electrochem. Soc.* **161**(1), A183–A193.

- G. Garcia-Belmonte, P. R. Bueno, F. Fabregat-Santiago, and J. Bisquert [2004] Relaxation Processes in the Coloration of Amorphous WO_3 Thin Films Studied by Combined Impedance and Electro-Optical Measurements, *J. Appl. Phys.* **96**, 853–859.
- J. Garcia-Canadas, F. Fabregat-Santiago, I. Porqueras, C. Person, J. Bisquert, and G. Garcia-Belmonte [2004] Charging and Diffusional Aspects of Li^+ Insertion in Electrochromic a- WO_3 , *Solid State Ionics* **75**, 521–525.
- R. Garnsey [1979] Boiler Corrosion and the Requirement for Feed- and Boiler-Water Chemistry Control in Nuclear Steam Generators, *Nucl. Energy* **18**, 117.
- W. Gärtner [1959] Depletion-Layer Photoeffects in Semiconductors, *Phys. Rev.* **116**, 84–87.
- R. C. Garvie, R. H. Hannink, and R. T. Pascoe [1975] Ceramic Steel? *Nature* **258**, 703–704.
- Y. Gefen, A. Aharony, and S. Alexander [1983] Anomalous Diffusion on Percolating Clusters, *Phys. Rev. Lett.* **50**, 77–80.
- P.-G. de Gennes [2002] Relaxation Anomalies in Linear Polymer Melts, *Macromolecules* **35**, 3785–3786.
- H. Gerischer [1951] Theory of AC Electrochemistry (Max Planck Inst. Phys. Chem. Göttingen, 1951) “Alternating-Current Polarization of Electrodes with a Potential-Determining Step for Equilibrium Potential”, *Z. Physik. Chem.* **198**, 286–313.
- H. Gerischer and W. Mehl [1955] Zum Mechanismus der kathodischen Wasserstoffabscheidung an Quecksilber, Silber und Kupfer, *Z. Elektrochem.* **59**, 1049–1059.
- P. S. Germain, W. G. Pell, and B. E. Conway [2004] Evaluation and Origins of the Difference Between Double-Layer Capacitance Behaviour at Au-Metal and Oxidized Au Surfaces, *Electrochim. Acta* **49**(11), 1775–1788.
- R. German, P. Venet, A. Sari, O. Briat, and J.-M. Vinassa [2014] Improved Supercapacitor Floating Ageing Interpretation Through Multipole Impedance Model Parameters Evolution, *IEEE Trans. Power Electron.* **29**, 3669–3678.
- J. Geyer, H. Kohlmüller and H. Landes R. Stübner [1997] Investigations into the Kinetics of the Ni-YSZ-Cermet-Anode of a Solid Oxide Fuel Cell, in *Proceedings of the Fifth International Symposium on SOFC*, Proceedings The Electrochemical Society, Vol. 97–40, Electrochemical Society, Pennington, NJ, pp. 585–594.
- M. Gholamian, J. Sundaram, and A. Q. Contractor [1987] Oxidation of Formic Acid at Polyaniline-Coated and Modified-Polyaniline-Coated Electrodes, *Langmuir* **3**, 741–744.
- J. H. Gibbs and E. A. DiMarzio [1958a] Nature of the Glass Transition and the Glassy State, *J. Chem. Phys.* **28**, 373–383.
- J. H. Gibbs and E. A. DiMarzio [1958b] Chain Stiffness and the Lattice Theory of Polymer Phases, *J. Chem. Phys.* **28**, 807.
- E. Gileadi and B. E. Conway [1963] Kinetic Theory of Adsorption of Intermediates in Electrochemical Catalysis, *J. Chem. Phys.* **39**, 3420–3430.
- J. S. Gill, L. M. Callow, and J. D. Scantlebury [1983] Corrosion Measurements Derived from Small Perturbation Nonlinearity. I. Harmonic Analysis, *Corrosion* **39**, 61–66.
- S. H. Glarum [1960] Dielectric Relaxation of Isoamyl Bromide, *J. Chem. Phys.* **33**, 639–643.
- S. H. Glarum and J. H. Marshall [1980] The A-C Response of Iridium Oxide Films, *J. Electrochem. Soc.* **127**, 1467–1474.
- H. Göhr [1997] Impedance Modelling of Porous Electrodes, *Electrochem. Appl.* **1**, 2–3, <http://www.zahner.de> (accessed on November 3, 2017).
- H. Göhr and C. A. Schiller [1986] Faraday-Impedanz als Verknüpfung von Impedanzelementen, *Z. Phys. Chemie Neue Folge* **148**, 105–124.
- H. Göhr, J. Söllner, and H. Weinzierl [1983] Kinetic Properties of Smooth and Porous Lead/Lead Sulfate Electrodes in Sulfuric Acid During Charging and Discharging, *Proceedings of the 34th ISE Meeting*, Erlangen, Germany, September 1983, poster 0715.
- S. Goldman [1950] *Transformation Calculus and Electrical Transients*, Prentice-Hall, Englewood Cliffs, NJ.
- A. Gorenstein, F. Decker, W. Estrada, C. Esteves, A. Andersson, S. Passerini, S. Pantaloni, and B. Scrosati [1990] Electrochromic NiO_xH_y Hydrated Thin Films: Cyclic Voltammetry and AC Impedance Spectroscopy in Aqueous Electrolyte, *J. Electroanal. Chem.* **277**, 277–290.
- S. Gottesfeld and T. A. Zawodzinski [1997] Polymer Electrolyte Fuel Cells, in *Advances in Electrochemical Science and Engineering*, Vol. 5, eds. R. C. Alkire, H. Gerischer, D. M. Kolb, and C. W. Tobias, Wiley-VCH, Weinheim, Germany, pp. 196–301.
- S. Gottesfeld, J. D. E. McIntyre, G. Beni, and J. L. Shay [1978] Electrochromism in Anodic Iridium Oxide Films, *Appl. Phys. Lett.* **33**, 208–210.
- W. Götze [1985] Properties of the Glass Instability Treated Within a Mode Coupling Theory, *Z. Phys. B* **60**, 195–203.
- W. Götze and L. Sjogren [1992] Relaxation Processes in Supercooled Liquids, *Rep. Prog. Phys.* **55**, 241.
- D. C. Grahame [1947] The Electrical Double Layer and the Theory of Electro-Capillarity, *Chem. Rev.* **41**, 441–501.
- D. C. Grahame [1952] Mathematical Theory of the Faradaic Admittance, *J. Electrochem. Soc.* **99**, 370c–385c.
- C. G. Granqvist [1995] *Handbook of Inorganic Electrochromic Materials*, Elsevier, Amsterdam, the Netherlands.
- C. G. Granqvist [2000] Electrochromic Tungsten Oxide Films: Review of Progress 1993–1998, *Sol. Energy Mater. Sol. Cells* **60**, 201–262.
- C. G. Granqvist [2014] Electrochromics for Smart Windows: Oxide-Based Thin Films and Devices, *Thin Solid Films* **564**, 1–38.
- J. Gråsjö, K. Welch, and M. Strømme [2008] Determining the Static Dielectric Permittivity of Ion Conducting Materials when Obscured by Electrode Polarization, *Appl. Phys. Lett.* **93**, 092901.
- M. Grätzel [2000] Properties and Applications of Nanocrystalline Electronic Junctions, in *Handbook of Nanostructured Materials and Nanotechnology*, Electrical Properties, Vol. 3, ed. H. S. Nalwa, Elsevier, Cambridge, MA.

- M. Green [1992] *Solar Cells: Operating Principles, Technology, and System Applications*, University of New South Wales, Kensington, Australia.
- M. Green, G. Greeuw, and J. F. Verway [1984] The Mobility of Na^+ , Li^+ , and K^+ Ions in Thermally Grown SiO_2 Films, *J. Appl. Phys.* **56**, 2218–2224.
- S. V. Green, E. Pehlivan, C. G. Granqvist, and G. A. Niklasson [2012] Electrochromism in Sputter Deposited Nickel-Containing Tungsten Oxide Films, *Sol. Energy Mater. Sol. Cells* **99**, 339–344.
- S. Greenbaum, J. J. Wilson, M. C. Wintersgill, and J. J. Fontanelli [1990] Dielectric Relaxation Studies on Polymer Electrolytes, in *Second International Symposium on Polymer Electrolytes*, ed. B. Scrosati, Elsevier, London, UK.
- G. Greeuw and B. J. Hoenders [1984] Theoretical Solution of the Transient Current Equation for Mobile Ions in a Dielectric Film Under the Influence of a Constant Electric Field, *J. Appl. Phys.* **55**, 3371–3375.
- R. M. Gu, S. Y. Yan, S. Sun, C. Y. Wang, and M. W. Li [2015] Electrochemical Behavior of Lithium-Rich Layered Oxide $\text{Li}[\text{Li}_{0.23}\text{Ni}_{0.15}\text{Mn}_{0.62}]\text{O}_2$ Cathode Material for Lithium-Ion Battery, *J. Solid State Electrochem.* **19**, 1659–1669.
- A. Guerrero, E. P. Butler, and P. L. Pratt [1979] The Suzuki Phase in $\text{NaCl}:\text{Cd}^{2+}$ and $\text{NaCl}:\text{Mg}^{2+}$, *J. Phys. Colloque* **7**, C6/363–366.
- E. GÜLZOW [1996] Alkaline Fuel Cells: A Critical View, *J. Power Sources* **61**, 99–104.
- E. GÜLZOW, M. SCHULZE, N. WAGNER, T. KAZ, A. SCHNEIDER, and R. REISSNER [1999] New Dry Preparation Technique for Membrane Electrode Assemblies for PEM Fuel Cells, *Fuel Cells Bull.* **15**, 8–12.
- E. GÜLZOW, M. SCHULZE, and G. STEINHILBER [2002a] Investigations of the Degradation of Different Nickel Anode Types for Alkaline Fuel Cells (AFC), *J. Power Sources* **106**, 126–135.
- E. GÜLZOW, R. REISSNER, S. WEISSHAAR, and T. KAZ [2002b] Progress in DMFC Development Using the Dry Spraying Preparation Technique, *Fuel Cells* **3**, 48–51.
- E. GÜLZOW, N. WAGNER, and M. SCHULZE [2003] Preparation of Gas Diffusion Electrodes with Silver Catalysts for Alkaline Fuel Cells, *Fuel Cells* **3**, 67–72.
- T. K. GUPTA, J. H. BECHTOLD, R. C. KUZNICKI, L. H. KADOFF, and B. R. ROSSING [1977] Stabilization of Tetragonal Phase in Polycrystalline Zirconia, *J. Mater. Sci.* **12**, 2421–2426.
- R. HAAK and D. TENCH [1984] Electrochemical Photocapacitance Spectroscopy Method for Characterization of Deep Levels and Interface States in Semiconductor Materials, *J. Electrochem. Soc.* **131**, 275–283.
- R. HAAK, C. OGDEN, and D. TENCH [1982] Electrochemical Photocapacitance Spectroscopy: A New Method for Characterization of Deep Levels in Semiconductors, *J. Electrochem. Soc.* **129**, 891–893.
- R. HAAK, C. OGDEN, and D. TENCH [1984] Degradation in Nickel–Cadmium Cells Studied by Impedance Measurements, *J. Power Sources* **12**(3–4), 289–303.
- P. HAGAN and D. FELLOWES [2003] Multivariate Statistical Methods in Battery Research, *J. Power Sources* **122**(1), 77–84.
- S. HAGEMAN [1993] Berkeley SPICE, EDV 38/22 117, EECS Department of the University of California, Berkeley, CA.
- A. HAGFELDT and M. GRÄTZEL [1995] Light-Induced Redox Reactions in Nanocrystalline Systems, *Chem. Rev.* **95**, 49–68.
- B. HAGUE [1957] *AC Bridge Methods*, Pitman, London, UK.
- A. HAKENJOS, M. ZOBEL, J. CLAUSNITZER, and C. HEBLING [2006] Simultaneous Electrochemical Impedance Spectroscopy of Single Cells in a PEM Fuel Cell Stack, *J. Power Sources* **154**, 360–363.
- O. P. HAMILL, A. MARTY, E. NEHER, B. SAKMANN, and F. J. SIGNWORTH [1981] Improved Patch-Clamp Techniques for High-Resolution Current Recording from Cells and Cell-Free Membrane Patches, *Pflugers Arch.* **391**(2), 85–100.
- A. HAMMOUCHE, E. KARDEN, and R. W. DE DONCKER [2004] Monitoring State-of-Charge of Ni–MH and Ni–Cd Batteries Using Impedance Spectroscopy, *J. Power Sources* **127**, 105–111.
- T. HANAI, D. A. HAYDON, and J. TAYLOR [1965] The Influence of Lipid Composition and of Some Adsorbed Proteins on the Capacitance of Black Hydrocarbon Membranes, *J. Theor. Biol.* **9**(3), 422–432.
- T. HANAI, D. A. HAYDON, and J. TAYLOR [1965] The Variation of Capacitance and Conductance of Bimolecular Lipid Membranes with Area, *J. Theor. Biol.* **9**(3), 433–443.
- D. A. HARRINGTON and B. E. CONWAY [1987] AC Impedance of Faradaic Reactions Involving Electrosorbed Intermediates – I. Kinetic Theory, *Electrochim. Acta* **32**, 1703–1712.
- J. W. HARTWELL [1971] A Procedure for Implementing the Fast Fourier Transform on Small Computers, *IBM J. Res. Develop.* **15**, 355–363.
- J. M. HAWKINS and L. O. BARLING [1995] Some Aspects of Battery Impedance Characteristics, *Proceedings of the 17th IEEE International Telecommunications Energy Conference INTELEC'95 Meeting*, October 29–November 1, 1995, IEEE.
- D. A. HAYDON, J. REQUENA, and B. W. URBAN [1980] Some Effects of Aliphatic Hydrocarbons on the Electrical Capacity and Ionic Currents of the Squid Giant Axon Membrane, *J. Physiol.* **309**, 229–245.
- E. HELGREN, N. P. ARMITAGE, and G. GRÜNER [2002] Electrodynamic of a Coulomb Glass in n-Type Silicon, *Phys. Rev. Lett.* **89**(4), 246601.
- H. HELMHOLTZ [1853] Ueber einige Gesetze der Vertheilung elektrischer Ströme in körperlichen Leitern mit Anwendung auf die theirisch-elektrischen Versuche, *Ann. Phys. (Leipzig)* **89**, 211–233.
- F. H. VAN HEUVELN [1993] Some Remarks Considering the Determination of Electrical Losses in Fuel Cell Systems, *Proceedings of Solid Oxide Workshop*, Chexbres, Switzerland, pp. 47–52.
- L. HEYNE [1983] Interfacial Effects in Mass Transport in Ionic Solids, in *Mass Transport in Solids*, eds. F. Beniere and C. R. A. Catlow, Plenum Press, New York, pp. 425–456.

- D. Hilberman [1968] Synthesis of Rational Transfer and Admittance Matrices with Active RC Common-ground Networks. Containing. Unity-gain. Voltage. Amplifiers, *IEEE Trans. CT-15*, 431.
- N. E. Hill [1963] A Possible Second Dielectric Dispersion Region in Polar Liquids, *Proc. Phys. Soc.* **82**(5), 723.
- L. Hladky, L. M. Callow, and J. L. Dawson [1980] Corrosion Rates from Impedance Measurements: An Introduction, *Br. Corrosion J.* **13**(1), 20.
- C. Ho [1980] *Application of AC Techniques to Kinetic Studies of Electrochemical Systems*, Ph.D. thesis, Stanford University, Stanford CA.
- C. Ho, I. D. Raistrick, and R. A. Huggins [1980] Application of A-C Techniques to the Study of Lithium Diffusion in Tungsten Trioxide Thin Films, *J. Electrochem. Soc.* **127**, 343–350.
- J. P. Hoare [1968] *The Electrochemistry of Oxygen*, Interscience, New York.
- I. M. Hodge, M. D. Ingram, and A. R. West [1975] A New Method for Analyzing the A.C. Behavior of Polycrystalline Solid Electrolytes, *J. Electroanal. Chem.* **58**, 429–432.
- I. M. Hodge, M. D. Ingram, and A. R. West [1976] Impedance and Modulus Spectroscopy of Polycrystalline Solid Electrolytes, *J. Electroanal. Chem.* **74**, 125–143.
- A. L. Hodgkin [1992] *Chance and Design*, Cambridge University Press, New York.
- W. H. J. Hogarth, J. Steiner, J. B. Benziger, and A. Hakenjos [2007] Spatially-Resolved Current and Impedance Analysis of a Stirred Tank Reactor and Serpentine Fuel Cell Flow-Field at Low Relative Humidity, *J. Power Sources* **164**, 464–471.
- P. Holtappels and C. Bagger [2002] Fabrication and Performance of Advanced Multi-Layer SOFC Cathodes, *J. Eur. Ceram. Soc.* **22**, 41–48.
- P. Holtappels, M. J. Jørgensen, S. Primdahl, M. Mogensen, and C. Bagger [1998] Electrochemical Performance and Structure of Composite $(La_{0.85}Sr_{0.15})_0.9MnO_3/YSZ$ Cathodes, in *Proceedings of the Third European SOFC Forum*, June 2–5, France, ed. P. Stevens, p. 311.
- K. Holub, G. Tessari, and P. Delahay [1967] Electrode Impedance Without a Priori Separation of Double-Layer Charging and Faradaic Process, *J. Phys. Chem.* **71**, 2612–2618.
- R. Holze [1983] *Impedanzmessungen an porösen Elektroden*, Thesis, Bonn, Germany.
- R. Holze and W. Vielstich [1984] The Kinetics of Oxygen Reduction at Porous Teflon-Bonded Fuel Cell Electrodes, *J. Electrochem. Soc.* **131**, 2298–2303.
- R. Holze, I. Vogel, and W. Vielstich [1986] New Oxygen Cathodes for Fuel Cells with Organic Fuels, *J. Electroanal. Chem.* **210**, 277–286.
- A. Hooper [1977] A Study of the Electrical Properties of Single Crystal and Polycrystalline β -Alumina Using Complex Plane Analysis, *J. Phys. D. Appl. Phys.* **10**, 1487–1497.
- J. Hou, W. Song, H. Yu, Y. Fu, Z. Shao, and B. Yi [2007] Electrochemical Impedance Investigation of Proton Exchange Membrane Fuel Cells Experienced Subzero Temperature, *J. Power Sources* **171**, 610–616.
- G. Hsieh, S. J. Ford, T. O. Mason, and L. R. Pederson [1996a] Experimental Limitations in Impedance Spectroscopy: Part I, Simulation of Reference Electrode Artifacts in Three-Point Measurements, *Solid State Ionics* **91**, 191–201.
- G. Hsieh, T. O. Mason, and L. R. Pederson [1996b] Experimental Limitations in Impedance Spectroscopy: Part II, Electrode Artifacts in Three-Point Measurements on Pt/YSZ, *Solid State Ionics* **91**, 203–212.
- G. Hsieh, T. O. Mason, E. J. Garboczi, and L. R. Pederson [1997] Experimental Limitations in Impedance Spectroscopy: Part III, Effect of Reference Electrode Geometry/Position, *Solid State Ionics* **96**, 153–172.
- R. W. J. M. Huang, F. Chung, and E. M. Kelder [2006] Impedance Simulation of a Li-Ion Battery with Porous Electrodes and Spherical Li⁺ Intercalation Particles, *J. Electrochem. Soc.* **153**(8), A1459–A1465.
- R. A. Huggins, H. Prinz, M. Wohlfahrt-Mehrens, L. Jörissen, and W. Witschel [1994] Proton Insertion Reactions in Layered Transition Metal Oxides, *Solid State Ionics* **70–71**(1), 417–424.
- B. D. Hughes, M. F. Shlesinger, and E. W. Montroll [1981] Random Walks with Self Similar Clusters, *Proc. Natl. Acad. Sci.* **78**, 3287–3291.
- A. Hunt [1992] Transport in Ionic Conducting Glasses: II. Scaling Relations and Approximate Power Law Behavior, *J. Phys. Condens. Matter* **4**, 5371–5381.
- A. F. Huxley [1992] Kenneth Stewart Cole, *Biogr. Mem. Fellows R. Soc.* **38**, 98–110, <http://books.nap.edu/html/biomems/kcole.pdf> (accessed on November 3, 2017).
- A. F. Huxley [1999] Hodgkin Obituary. *The Independent*, January 4, 1999 <http://www.independent.co.uk/arts-entertainment/obituaries-professor-sir-alan-hodgkin-1044924.html> (accessed on November 3, 2017).
- A. F. Huxley [2002] From Overshoot to Voltage Clamp, *Trends Neurosci.* **25**(11), 553–558.
- I. Iami and P. Delahay [1962] Faradaic Rectification and Electrode Processes. III. Experimental Methods for High Frequencies and Application to the Discharge of Mercurous Ion, *J. Phys. Chem.* **66**, 1108–1113.
- N. Ibl [1983a] Fundamentals of Transport Phenomena, in *Comprehensive Treatise of Electrochemistry*, Vol. 6, eds. E. Yaeger, J. O'M. Bockris, B. E. Conway, and S. Sarangapani, Plenum Press, New York, pp. 1–63.
- N. Ibl [1983b] Current Distribution, in *Comprehensive Treatise of Electrochemistry*, Electrodics: Transport, Vol. 6, eds. E. Yaeger, J. O'M. Bockris, B. E. Conway, and S. Sarangapani, Plenum Press, New York, p. 239.
- T. Iijima, K. Suzuki, and Y. Matsuda [1995] Electrode Characteristics of Various Carbon Materials for Lithium Rechargeable Batteries, *Synth. Met.* **73/1**, 9–20.
- T. Jacobsen and K. West [1995] Diffusion Impedance in Planar, Cylindrical and Spherical Symmetry, *Electrochim. Acta* **40**(2), 255–262.

- G. Jaffé [1952] Theory of Conductivity of Semiconductors, *Phys. Rev.* **85**, 354–363.
- H. Jain and S. Krishnaswami [1998] Composition Dependence of Frequency Power Law of Ionic Conductivity of Glasses, *Solid State Ionics* **105**, 129–137.
- J. Jamnik [2003] Impedance Spectroscopy of Mixed Conductors with Semi-Blocking Boundaries, *Solid State Ionics* **157**, 19–28.
- J. Jamnik and J. Maier [2001] Generalised Equivalent Circuits for Mass and Charge Transport: Chemical Capacitance and its Applications, *Phys. Chem. Chem. Phys.* **3**, 1668–1678.
- J. Jamnik, J. Maier, and S. Pejovnik [1999] A Powerful Electrical Network Model for the Impedance of Mixed Conductors, *Electrochim. Acta* **44**(24), 4139–4145.
- J. Janata and R. J. Huber, (eds.) [1985] *Solid State Chemical Sensors*, Academic Press, New York.
- W. Jenseit, O. Böhme, F. U. Leidich, and H. Wendt [1993] Impedance Spectroscopy: A Method for In Situ Characterization of Experimental Fuel Cells, *Electrochim. Acta* **38**, 2115–2120.
- M. L. Jimenez, F. J. Arroyo, J. van Turnhout, and A. V. Delgado [2002] Analysis of the Dielectric Permittivity of Suspensions by Means of the Logarithmic Derivative of its Real Part, *J. Colloid Interface Sci.* **249**, 327–335.
- G. P. Johari [2000a] Contributions to the Entropy of a Glass and Liquid, and the Dielectric Relaxation Time, *J. Chem. Phys.* **112**, 7518–7523.
- G. P. Johari [2000b] An Equilibrium Supercooled Liquid's Entropy and Enthalpy in the Kauzmann and the Third Law Extrapolations, and a Proposed Experimental Resolution, *J. Chem. Phys.* **113**, 751–761.
- G. P. Johari [2012] Electrode-Spacer and Other Effects on the Validity of the Kramers–Kronig Relations and the Fittings to the Permittivity and Electrical Modulus Spectra, *Thermochim. Acta* **547**, 47–52.
- G. P. Johari and O. Andersson [2006] On the Nonlinear Variation of DC Conductivity with Dielectric Relaxation Time, *J. Chem. Phys.* **125**, 124501.
- H. B. Johnson and W. L. Worrell [1982] Lithium and Sodium Intercalated Dichalcogenides: Properties and Electrode Applications, *Synth. Met.* **4**, 225–248.
- W. B. Johnson, N. J. Tolar, G. R. Miller, and I. B. Cutler [1969] Electrical and Mechanical Relaxation in CaF₂ Doped with NaF, *J. Phys. Chem. Solids* **30**, 31–42.
- A. K. Jonscher [1974] Hopping Losses in Polarisable Dielectric Media, *Nature* **250**, 191–193.
- A. K. Jonscher [1975a] Physical Basis of Dielectric Loss, *Nature* **253**, 717–719.
- A. K. Jonscher [1975b] The Interpretation of Non-Ideal Dielectric Admittance and Impedance Diagrams, *Phys. Stat. Sol. (a)* **32**, 665–676.
- A. K. Jonscher [1975c] New Interpretation of Dielectric Loss Peaks, *Nature* **256**, 566–568.
- A. K. Jonscher [1977] The ‘Universal’ Dielectric Response, *Nature* **267**, 673–679.
- A. K. Jonscher [1980] The Universal Dielectric Response: A Review of Data and their New Interpretation, *Phys. Thin Films* **11**, 205–317.
- A. K. Jonscher [1983] *Dielectric Relaxations in Solids*, Chelsea Dielectrics, London, UK.
- A. K. Jonscher and J.-M. Reau [1978] Analysis of the Complex Impedance Data for Beta-PbF₂, *J. Mater. Sci.* **13**, 563–570.
- A. K. Jonsson, M. Strømme Mattsson, and G. A. Niklasson [1999] Li Intercalation in Zirconium Dioxide Films, *Defect Diffusion Forum* **177–178**, 51–58.
- A. K. Jonsson, M. Furlani, and G. A. Niklasson [2004] Isothermal Transient Ionic Current Study of Laminated Electrochromic Devices for Smart Window Applications, *Sol. Energy Mater. Sol. Cells* **84**, 361–367.
- M. Jönsson, K. Welch, S. Hamp, and M. Strømme [2006] Bacteria Counting with Impedance Spectroscopy in a Micro Probe Station, *J. Phys. Chem. B* **110**, 10165–10169.
- M. J. Jørgensen and M. Mogensen [2001] Impedance of Solid Oxide Fuel Cell LSM/YSZ Composite Cathodes, *J. Electrochem. Soc.* **148**, A433–A442.
- L. Jörissen, V. Gogel, J Kerres, and J. Garche [2002] New Membranes for Direct Methanol Fuel Cells, *J. Power Sources* **105**, 267–273.
- T. R. Jow, M. S. Dinga, K. Xu, S. S. Zhang, J. L. Allen, K. Amine, and G. L. Henriksen [2003] Nonaqueous Electrolytes for Wide-Temperature-Range Operation of Li-Ion Cells, *J. Power Sources* **119–121**, 343–348.
- M. Juhl, S. Primdahl, C. Manon, and M. Mogensen [1996] Performance/Structure Correlations for Composite SOFC Cathodes, *J. Power Sources* **61**, 173.
- V. G. Karpov, M. I. Klinger, and F. N. Inganatiev [1983] Atomic Tunneling States and Low-Temperature Anomalies of Thermal Properties in Amorphous Materials, *Sov. Phys. JETP* **57**, 439.
- T. Katsube, M. Hara, T. Yaji, S. Kobayashi, K. Suzuki, and Y. Nakagawa [1986] Electrical Characterization of a Complementary Electrochromic Device, *Jpn. Display* **86**, 376–379.
- W. Kauzmann [1942] Dielectric Relaxation as a Chemical Rate Process, *Rev. Mod. Phys.* **14**(1), 12–44.
- W. Kauzmann [1948] The Nature of the Glassy State and the Behavior of Liquids at Low Temperatures, *Chem. Rev.* **43**(2), 219–256.
- T. Kaz and N. Wagner [2002] *Method for Production of Multi-Layer Electrode or Electrode Assembly and Gaseous Diffusion Electrode*, US Patent 2002,150,812 A1.
- M. Keddam, O. R. Mattos, and H. J. Takenouti [1981] Reaction Model for Iron Dissolution Studied by Electrode Impedance. Determination of the Reaction Model, *J. Electrochem. Soc.* **128**, 257–274.
- M. Keddam, J.-F. Lizée, C. Pallotta, and H. J. Takenouti [1984] Electrochemical Behaviour of Passive Iron in Acid Medium, *J. Electrochem. Soc.* **131**, 2016–2024.
- H. Keiser, K. D. Beccu, and M. A. Gutjahr [1976] Estimation of the Pore Structure of Porous Electrodes by Impedance Measurements, *Electrochim. Acta* **21**, 539–543.

- H. Keister, K. D. Beccu, and M. A. Gutjahr [1976] Abschätzung der Porenstruktur von Porösen Elektroden aus Impedanzmessung, *Electrochim. Acta* **21**, 539–543.
- T. Kenjo, S. Osawa, and K. Fujikawa [1991] High Temperature Air Cathodes Containing Ion Conductive Oxides, *J. Electrochem. Soc.* **138**, 349–355.
- Z. Kerner and T. Pajkossy [2002] Measurement of Adsorption Rates of Anions on Au(111) Electrodes by Impedance Spectroscopy, *Electrochim. Acta* **47**, 2055–2063.
- K. Kessairi, S. Napolitano, S. Capaccioli, P. Rolla, and M. Wubbenhorst [2007] Molecular Dynamics of Atactic Poly(propylene) Investigated by Broadband Dielectric Spectroscopy, *Macromolecules* **40**, 1786–1788.
- J. Kevorkian and J. D. Cole [1996] *Multiple Scale and Singular Perturbation Methods*, Springer-Verlag, New York.
- S. W. Kim and S. I. Pyun [2002] Analysis of Cell Impedance Measured on the LiMn₂O₄ Film Electrode by PITT and EIS with Monte Carlo Simulation, *J. Electroanal. Chem.* **528** (1–2), 114–120.
- J. J. Kim, D. A. Tryk, T. Amemiya, K. Hashimoto, and A. Fujishima [1997] Color Impedance and Electrochemical Impedance Studies of WO₃ Thin Films: H⁺ and Li⁺ Transport, *J. Electroanal. Chem.* **435**, 31–38.
- D. H. Kim, S. H. Ryu, and H. S. Lee [1999] Method for Evaluating Capacity of Secondary Battery Using Mathematical Calculation of Specific Resistance Components of Equivalent Circuit Model Fitted from Impedance Spectrum, US Patent 2004,0006,440.
- J.-D. Kim, Y.-I. Park, K. Kobayashi, and M. Nagai [2001a] Effect of CO Gas and Anode-Metal Loading on H₂ Oxidation in Proton Exchange Membrane Fuel Cell. *J. Power Sources*, **103**, 127–133.
- J.-D. Kim, Y.-I. Park, K. Kobayashi, M. Nagai, and M. Kunimatsu [2001b] Characterization of CO Tolerance of PEMFC by AC Impedance Spectroscopy, *Solid State Ionics* **140**, 313–325.
- S. W. Kim, J. Fleig, and J. Maier [2003] Space Charge Conduction: Simple Analytical Solutions for Ionic and Mixed Conductors and Application to Nanocrystalline Ceria, *Phys. Chem. Chem. Phys.* **5**(11), 2268.
- M. Kimura, T. Osaki, and S. Toshima [1975] Interfacial Capacity Between a Silver Bromide Solid Electrolyte and a Blocking Electrode, *Bull. Chem. Soc. Jpn.* **48**, 830–834.
- R. Kirchheim [1987] Growth Kinetics of Passive Films, *Electrochim. Acta* **32**, 1619–1629.
- S. Kirkpatrick [1973] Percolation and Conduction, *Rev. Mod. Phys.* **45**(4), 574–588.
- J. G. Kirkwood and R. M. Fuoss [1941] Anomalous Dispersion and Dielectric Loss in Polar Polymers, *J. Chem. Phys.* **9**, 329–340.
- Y. Kiros and S. Schwartz [2000] Long-Term Hydrogen Oxidation Catalysts in Alkaline Fuel Cells, *J. Power Sources* **87**, 101–105.
- J. Klafter and A. Blumen [1985] Models for Dynamically Controlled Relaxation, *Chem. Phys. Lett.* **119**, 377–382.
- R. J. Klein, S. Zhang, S. Dou, B. H. Jones, R. H. Colby, and J. Runt [2006] Modeling Electrode Polarization in Dielectric Spectroscopy: Ion Mobility and Mobile Ion Concentration of Single-Ion Polymer Electrolytes, *J. Chem. Phys.* **124**, 144903 (8 pages).
- M. Kleitz and J. H. Kennedy [1979] Resolution of Multicomponent Impedance Diagrams, in *Fast Ion Transport in Solids*, eds. P. Vashishta, J. N. Mundy, and G. K. Shenoy, North-Holland, Amsterdam, the Netherlands, pp. 185–188.
- M. Kleitz, H. Bernard, E. Fernandez, and E. J. L. Schouler [1981] Impedance Spectroscopy and Electrical Resistance Measurements on Stabilized Zirconia, in *Advances in Ceramics*, Vol. 3, eds. A. H. Heuer and L. W. Hobbs, American Ceramic Society, Columbus, OH, pp. 310–336.
- T. Knöri and N. Wagner [2004] Locally Resolved Electrochemical Impedance Spectroscopy in Polymer Electrolyte Fuel Cells (PEFC), Poster presented at the *Sixth International Symposium on Electrochemical Impedance Spectroscopy*, May 16–21, 2004, Cocoa Beach, FL.
- K. Kobayashi, H. Kayajima, and T. Masaki [1981] Phase Change and Mechanical Properties of Zirconia-Yttria Solid Electrolyte After Aging, *Solid State Ionics* **3**(4), 489–493.
- R. Kohlrausch [1854] Theorie des Elektrischen Rückstandes in der Leidener Flasche, *Ann. Phys. Chem.* **91**, 179–214.
- M. T. M. Koper, T. J. Schmidt, N. M. Markovic, and P. N. Ross [2001] Potential Oscillations and S-Shaped Polarization Curve in the Continuous Electro-Oxidation of CO on Platinum Single-Crystal Electrodes, *J. Phys. Chem. B* **105**, 8381–8386.
- A. K. Kordesch and G. Simader [1996] *Fuel Cells and Their Application*, Wiley VCH, Weinheim, Germany.
- A. Kornyshev, W. Schmickler, and M. Vorotyntsev [1982] Non-local Electrostatic Approach to the Problem of a Double Layer at a Metal-Electrolyte Interface, *Phys. Rev. B* **25**, 5244–5256.
- R. Kotz, M. Hahn, and R. Gallay [2006] Temperature Behavior and Impedance Fundamentals of Supercapacitors, *J. Power Sources* **154**, 550–555.
- H. A. Kramers [1929a] Die Dispersion und Absorption von Röntgenstrahlen, *Z. Phys.* **30**, 521.
- H. A. Kramers [1929b] Theory of Dispersion in the X-Ray Region, *Phys. Z.* **30**, 52.
- F. Kremer and A. Schönhals [2003a] The Scaling of the Dynamics of Glasses and Supercooled Liquids, in *Broadband Dielectric Spectroscopy*, eds. F. Kremer and A. Schönhals, Springer Verlag, Berlin/Heidelberg, Germany.
- F. Kremer and A. Schönhals, (eds.) [2003b] *Broadband Dielectric Spectroscopy*, Springer-Verlag, Berlin, Germany.
- F. Krok, J. R. Dygas, B. Misztal-Faraj, Z. Florjacyk, and W. Bzducha [1999] Impedance and Polarisation Studies of New Lithium Polyelectrolyte Gels, *J. Power Sources* **81–82**, 766–771.
- R. de L. Kronig [1926] The Theory of Dispersion of X-Rays, *J. Opt. Soc. Am.* **12**, 547.

- F. Kruger [1903] Theorie der Polarisationskapazität, *Z. Phys. Chem.* **45**, 1.
- M. M. Kubat, P. Riha, R. W. Rychwalski, and S. Uggla [1999] A Kohlrausch Type Equation Based on a Simplified Cooperative Model, *Mech. Time Depend. Mater.* **3**, 31–47.
- A. Kudlik, T. Blochowicz, S. Benkhof, and E. Rossler [1996] Reply to Comment on ‘Spectral Shape of the α -Process in Supercooled Liquids Revisited’, *Europhys. Lett.* **36** (6), 475.
- A. Kudlik, S. Benkhof, T. Blochowicz, C. Tschirwitz, and E. Rössler [1999] The Dielectric Response of Simple Organic Glass Formers, *J. Mol. Struct.* **479**, 201–218.
- Kumho Petrochemical Inc. [2002] MEISP Multiple EIS Parameterization Software, <http://impedance0.tripod.com/#3> (accessed on November 3, 2017).
- N. Kuriyamaa, T. Sakaia, H. Miyamuraa, H. Tanakaa, I. Ueharaa, F. Melib, and L. Schlapbachb [1996] Surface Treatment of a LaNi₅-type Metal-Hydride Electrode with an Alkaline Solution Dissolving Cobalt(II) Hydroxide, *J. Alloys Compounds* **238**(1–2), 128–140.
- P. Kurzweil [2003] *Brennstoffzellentechnik*, Vieweg Verlag, Wiesbaden, Germany.
- R. B. Laibowitz and Y. Gefen [1984] Dynamic Scaling near the Percolation Threshold in Thin Au Films, *Phys. Rev. Lett.* **53**, 380–383.
- C. M. Lampert [2003] Large-Area Smart Glass and Integrated Photovoltaics, *Sol. Energy Mater. Sol. Cells* **76**, 489–499.
- C. M. Lampert [2004] Chromogenic Smart Materials, *Materials Today* March 2004, p. 28–35.
- C. Lamy, A. Lima, V. LeRhun, F. Delime, C. Coutanceau, and J.-M. Léger [2002] Recent Advances in the Development of Direct Alcohol Fuel Cells (DAFC), *J. Power Sources* **105**, 283–296.
- R. Landauer [1978] Electrical Conductivity in Inhomogeneous Media, in *Electrical Transport and Optical Properties of Inhomogeneous Media*, eds. J. C. Garland and D. B. Tanner, American Institute of Physics, New York, pp. 2–43.
- M. Lang, T. Franco, G. Schiller, and N. Wagner [2002] Electrochemical Characterization of Vacuum Plasma Sprayed Thin-Film Solid Oxide Fuel Cells (SOFC) for Reduced Operating Temperatures, *J. Appl. Electrochem.* **32**, 871–874.
- V. Lanteri, A. H. Heuer, and T. E. Mitchell [1983] Tetragonal Precipitation in the System Y₂O₃-ZrO₂, in *Proceedings of the 41st Annual Meeting of the Electron Microscopy Society of America*, ed. G. W. Bailey, San Francisco Press, San Francisco, CA, pp. 58–59.
- S. Lányi [1975] Polarization of Ionic Crystals with Incompletely Blocking Electrodes, *J. Phys. Chem. Solids* **36**, 775–781.
- A.-L. Larsson, B. E. Sernelius, and G. A. Niklasson [2003] Optical Absorption of Li-Intercalated Polycrystalline Tungsten Oxide Films: Comparison to Large Polaron Theory, *Solid State Ionics* **165**, 35–41.
- A. Lasia [1998] Hydrogen Evolution/Oxidation Reaction on Porous Electrodes, *J. Electroanal. Chem.* **454**, 117–123.
- A. Lasia [1999] Electrochemical Impedance Spectroscopy and Its Applications, in *Modern Aspects of Electrochemistry*, Vol. 32, eds. B. E. Conway, J. Bockris, and R. E. White, Kluwer Academic/Plenum Publishers, New York, pp. 143–248.
- I. R. Lauks and J. N. Zemel [1979] The Silicon Nitride/Silicon Ion Sensitive Semiconductor Electrode, *IEEE Trans. Electron Devices* **ED-26**, 1959–1964.
- E. Laviron [1972] Effect of the Adsorption of the Depolarizing Agent or an Electrochemical Reaction Product on Polarographic Currents. XVI. Theoretical Voltammetric Study with Linear Voltage Variation, of the Surface Reaction, *J. Electroanal. Chem.* **34**, 463–473.
- C. G. Law and J. J. S. Newman [1979] A Model for the Anodic Dissolution of Iron in Sulfuric Acid, *J. Electrochem. Soc.* **126**, 2150–2155.
- A. Le Mehaute [1984] Transfer Processes in Fractal Media, *J. Stat. Phys.* **36**, 665–676.
- A. Le Mehaute and G. Crepy [1983] Introduction to Transfer and Motion in Fractal Media: The Geometry of Kinetics, *Solid State Ionics* **9–10**, 17–30.
- M. Le Stanguennec and S. R. Elliott [1994] Frequency-Dependent Ionic Conductivity in AgI-AgPO₃ Glasses, *Solid State Ionics* **73**(3–4), 199–208.
- M. Lee and M. L. Stutzmann [2001] Microwave AC Conductivity Spectrum of a Coulomb Glass, *Phys. Rev. Lett.* **87**, 056402.
- W. K. Lee, J. F. Liu, and A. S. Nowick [1991] Limiting Behavior of AC Conductivity in Ionically Conducting Crystals and Glasses: A New Universality, *Phys. Rev. Lett.* **67**, 1559.
- S.-H. Lee, H. M. Cheong, C. E. Tracy, R. P. Mascarenhas, G. Jorgensen, and S. K. Deb [2000] Alternating Current Impedance and Raman Spectroscopic Study of Electrochromic A-WO₃ films, *Appl. Phys. Lett.* **76**, 3908–3910.
- S.-H. Lee, H. M. Cheong, C. E. Tracy, A. Mascarenhas, J. R. Pitts, G. Jorgensen, and S. K. Deb [2001] Influence of Microstructure on the Chemical Diffusion of Lithium Ions in Amorphous Lithiated Tungsten Oxide Films, *Electrochim. Acta* **46**, 3415–3419.
- R. L. Leheny and S. R. Nagel [1997] High-Frequency Asymptotic Shape of the Primary Relaxation in Supercooled Liquids, *Europhys. Lett.* **39**, 447.
- R. L. Leheny, N. Menon, and S. R. Nagel [1996] Comment on ‘Spectral Shape of the α -Process in Supercooled Liquids Revisited’, *Europhys. Lett.* **36**(6), 473.
- I. Lelidis and G. Barbero [2005] Effect of Different Anionic and Cationic Mobilities on the Impedance Spectroscopy Measurements, *Phys. Lett. A* **343**, 440–445.
- Y.-J. Leng, X. Wang, and I.-M. Hsing [2002] Assessment of CO-Tolerance for Different Pt-Alloy Anode Catalysts in a Polymer Electrolyte Fuel Cell Using AC Impedance Spectroscopy, *J. Electroanal. Chem.* **528**, 145–152.
- S. J. Lenhart, D. D. Macdonald, and B. G. Pound [1984] Restructuring of Porous Nickel Electrodes, *Proceedings of the 19th Intersociety Energy Conversion Engineering Conference (IECEC)*, San Francisco, CA, August 19–24, 1984, p. 875.

- S. J. Lenhart, D. D. Macdonald, and M. Urquidi-Macdonald [1987] Photo-Inhibition of Passivity Breakdown on Nickel, *Electrochim. Acta* **32**, 1739–1741.
- E. K. Lenzi, P. R. G. Fernandes, T. Petrucci, H. Mukai, and H. V. Ribeiro [2011] Anomalous-Diffusion Approach Applied to the Electrical Response of Water, *Phys. Rev. E* **84**, 041128.
- C. León, J. Santamaría, M. A. Paris, J. Sanz, J. Ibarra, and A. Varez [1998] Non-Debye Conductivity Relaxation in the non-Arrhenius Fast Ionic Conductor. A Nuclear Magnetic Resonance and Complex Impedance Study, *J. Non-Cryst. Solids* **235–237**, 753–760.
- C. León, A. Rivera, A. Varez, J. Sanz, J. Santamaría, and K. L. Ngai [2001] Origin of Constant Loss in Ionic Conductors, *Phys. Rev. Lett.* **86**, 1279–1282.
- A. Leonide, V. Sonn, A. Weber, and E. Ivers-Tiffée [2008] Evaluation and Modeling of the Cell Resistance in Anode-Supported Solid Oxide Fuel Cells, *J. Electrochem. Soc.* **155**, B36–B41.
- F. Leroy, P. Gareil, and R. Rosset [1982] Gas and Ion Selective Field Effect Transistor Electrodes, *Analysis* **10**, 351–366.
- E. Leutheuser [1984] Dynamical Model of the Liquid–Glass Transition, *Phys. Rev. A* **29**(5), 2765–2773.
- V. Levi and D. Aurbach [1997] Simultaneous Measurements and Modeling of the Electrochemical Impedance and the Cyclic Voltammetric Characteristics of Graphite Electrodes Doped with Lithium, *J. Phys. Chem. B* **101**(23), 4630–4640.
- M. Levi and D. Aurbach [1999] Frumkin Intercalation Isotherm – A Tool for the Description of Lithium Insertion into Host Materials: A Review, *Electrochim. Acta* **45**(1), 167–185.
- R. de Levie [1963] Porous Electrodes in Electrolyte Solutions, I, *Electrochim. Acta* **8**, 751.
- R. de Levie [1964] On Porous Electrodes in Electrolyte Solutions, II, *Electrochim. Acta* **9**, 1231–1245.
- R. de Levie [1965] The Influence of Surface Roughness of Solid Electrodes on Electrochemical Measurements, *Electrochim. Acta* **10**, 113–130.
- R. de Levie [1967] Electrochemical Response of Porous and Rough Electrodes, in *Advances in Electrochemistry and Electrochemical Engineering*, Vol. 6, eds. P. Delahay and C. W. Tobias, Interscience, New York, pp. 329–397.
- R. de Levie and D. Vukadin [1975] Dipicrylamine Transport Across Ultrathin Phosphatidylethanolamine Membrane, *J. Electroanal. Chem.* **62**, 95–109.
- L. M. Levinson [1981] Grain Boundary Phenomena in Electronic Ceramics, in *Advances in Ceramics*, Vol. 1, ed. L. M. Levinson, American Ceramic Society, Columbus, OH.
- R. A. Levis and J. L. Rae [1992] Constructing a Patch Clamp Setup, in *Methods in Enzymology*, Vol. 207, eds. L. Iverson and B. Rudy, Academic Press, New York, pp. 66–92.
- R. A. Levis and J. L. Rae [1995] Technology of Patch Clamp Recording Electrodes, in *Patch-Clamp Applications and Protocols*, eds. W. Walz, A. Boulton, and G. Baker, Humana Press, Totowa, NJ.
- R. A. Levis and J. L. Rae [1998] Low-Noise Patch-Clamp Techniques, *Methods Enzymol.* **293**, 218–266.
- R. A. Levis, R. T. Mathias, and R. S. Eisenberg [1983] Electrical Properties of Sheep Purkinje Strands. Electrical and Chemical Potentials in the Clefts, *Biophys. J.* **44**(2), 225–248.
- W.-J. Li and Z.-W. Fu [2010] Nanostructured WO_3 Thin Film as a New Anode Material for Lithium-Ion Batteries, *Appl. Surf. Sci.* **256**, 2447–2452.
- H. Li, X. Huang, and L. Chen [1999] Electrochemical Impedance Spectroscopy Study of SnO and Nano- SnO Anodes in Lithium Rechargeable Batteries, *J. Power Sources* **81–82**, 340–345.
- S. Lia, G. L. Panb, X. P. Gao, J. Q. Qua, F. Wu, and D. Y. Songa [2004] The Electrochemical Properties of $\text{MmNi}_{3.6}\text{Co}_{0.7}\text{Al}_{0.3}\text{Mn}_{0.4}$ Alloy Modified with Carbon Nanomaterials by Ball Milling, *J. Alloys Compounds* **364**(1–2), 250–256.
- R. Liang, B. G. Pound, and D. D. Macdonald [1984] Impedance Analysis of Passive Films on Single Crystal Nickel, *Ext. Abst. Electrochem. Soc.* **84–2**, 356.
- D. R. Lide, (ed.) [1997] *CRC Handbook of Chemistry and Physics*, 77th Edition, CRC Press, Boca Raton, FL.
- E. Lilley and J. E. Strutt [1979] Bulk and Grain Boundary Ionic Conductivity in Polycrystalline β'' -Alumina, *Phys. Stat. Sol. (a)* **54**, 639–650.
- L. F. Lin, C. Y. Chao, and D. D. Macdonald [1981] A Point Defect Model for Anodic Passive Films – (II) Chemical Breakdown and Pit Initiation, *J. Electrochem. Soc.* **128**(6), 1194–1198.
- C. P. Lindsey and G. D. Patterson [1980] Detailed Comparison of the William-Watts and Cole-Davidson Functions, *J. Chem. Phys.* **73**, 3348–3357.
- Y. Ling, M. Taylor, S. Sharifi-Asl, and D. D. Macdonald [2013] The Semiconducting Properties and Impedance Analysis of Passive Films on Copper in Anoxic Sulfide-Containing Solutions from the Viewpoint of the Point Defect Model, *ECS Trans.* **50**(31), 53–67.
- S. H. Liu [1985] Fractal Model for the ac Response of a Rough Interface, *Phys. Rev. Lett.* **55**, 529–532.
- C. Liu and C. A. Angell [1990] Mid- and Far-Infrared Absorption of Alkali Borate Glasses and the Limit of Supersonic Conductivity, *J. Chem. Phys.* **93**(10), 7378–7386.
- Y.-C. Liu, X.-P. Qiu, W.-T. Zhu, and G.-S. Wu [2003] Impedance Studies on Mesocarbon Microbeads Supported Pt-Ru Catalytic Anode, *J. Power Sources* **114**, 10–14.
- W. H. Lizcano-Valbuena, V. A. Paganin, C. A. P. Leite, F. Galembek, and E. R. Gonzalez [2003] Catalysts for DMFC: Relation Between Morphology and Electrochemical Performance, *Electrochim. Acta* **48**, 3869–3878.
- J. Llopis and F. Colom [1958] Study of the Impedance of a Platinum Electrode Acting as Anode, *Proceedings of the Eighth Meeting of the CITCE*, Madrid, 1956, Butterworths, London, pp. 414–427.
- W. Lorenz [1954] Zeitschrift für Naturforschung A, *Kristallisationsüberspannungen* **9**(9).
- W. Lorenz and G. Salié [1961a] Reaction Steps of the Electrochemical Phase-Boundary Reaction, *Zeit. Phys. Chem. N. F.* **29**, 390–396.

- W. Lorenz and G. Salié [1961b] Potential Dependence and Charge Transition Coefficients of the Tl/Tl+ Reaction, *Zeit. Phys. Chem. N. F.* **29**, 408–412.
- S. W. Lovesey [1984] *Theory of Neutron Scattering from Condensed Matter*, Vol. 1, Clarendon Press, Oxford, UK, p. 301.
- Z. Lu, S. Sharifi-Asl, and D. D. Macdonald [2013] In-Situ Spectroscopic Ellipsometry and Electrochemical Studies of the Barrier Layer on Iron in Borate Buffer Solutions, *ECS Trans.* **50**(31), 251–266.
- P. Lu, D. Kursten, and D. D. Macdonald [2014] Deconvolution of the Partial Anodic and Cathodic Processes During the Corrosion of Carbon Steel in Concrete Pore Solution Under Simulated Anoxic Conditions, *Electrochim. Acta* **143**, 312–323.
- P. Lunkenheimer and A. Loidl [2003a] Response of Disordered Matter to Electromagnetic Fields, *Phys. Rev. Lett.* **91**(20), 207601.
- P. Lunkenheimer and A. Loidl [2003b] Glass Dynamics Beyond the α -Relaxation, in *Broadband Dielectric Spectroscopy*, eds. F. Kremer and A. Schönhals, Springer Verlag, Berlin/Heidelberg, Germany.
- P. Lunkenheimer, A. Pimenov, M. Dressel, Y. G. Goncharov, R. Böhmer, and A. Loidl [1996] Fast Dynamics of Glass-Forming Glycerol Studied by Dielectric Spectroscopy, *Phys. Rev. Lett.* **77**(2), 318–321.
- P. Lunkenheimer, A. Pimenov, and A. Loidl [1997] Fast Dynamics in CKN and CRN Investigated by Dielectric Spectroscopy, *Phys. Rev. Lett.* **78**(15), 2995–2998.
- P. Lunkenheimer, U. Schneider, R. Brand, and A. Loidl [1999] Broadband Dielectric Response of Glycerol and Propylene Carbonate: A Comparison, in *Slow Dynamics in Complex Systems, 8th Tohwa University International Symposium*, AIP Conference Proceedings, Vol. 469, eds. M. Tokuyama and I. Oppenheim, AIP, New York, p. 433.
- P. Lunkenheimer, U. Schneider, R. Brand, and A. Loidl [2000] Glassy Dynamics, *Contemp. Phys.* **41**, 15.
- P. Lunkenheimer, V. Bobnar, A. V. Pronin, A. I. Ritus, A. A. Volkov, and A. Loidl [2002] Origin of Apparent Colossal Dielectric Constants, *Phys. Rev. B* **66**, 052105.
- J. R. Macdonald [1953] Theory of AC Space-Charge Polarization Effects in Photoconductors, Semiconductors, and Electrolytes, *Phys. Rev.* **92**, 4–17.
- J. R. Macdonald [1954] Static Space-Charge Effects in the Diffuse Double Layer, *J. Chem. Phys.* **22**, 1317–1322.
- J. R. Macdonald [1955] Capacitance and Conductance Effects in Photoconducting Alkali Halide Crystals, *J. Chem. Phys.* **23**, 275–295.
- J. R. Macdonald [1962] Restriction on the Form of Relaxation-Time Distribution Functions for a Thermally Activated Process, *J. Chem. Phys.* **36**, 345–349.
- J. R. Macdonald [1963] Transient and Temperature Response of a Distributed, Thermally Activated Process, *J. Appl. Phys.* **34**, 538–552.
- J. R. Macdonald [1971a] Electrical Response of Materials Containing Space Charge with Discharge at the Electrodes, *J. Chem. Phys.* **54**, 2026–2050.
- J. R. Macdonald [1971b] The Impedance of a Galvanic Cell with Two Plane-Parallel Electrodes at a Short Distance, *J. Electroanal. Chem.* **32**, 317–328.
- J. R. Macdonald [1974a] Simplified Impedance/Frequency-Response Results for Intrinsically Conducting Solids and Liquids, *J. Chem. Phys.* **61**, 3977–3996.
- J. R. Macdonald [1974b] Binary Electrolyte Small-Signal Frequency Response, *J. Electroanal. Chem. Interfacial Electrochem.* **53**, 1–55.
- J. R. Macdonald [1974c] Theory of Space-Charge Polarization and Electrode-Discharge Effects, *J. Chem. Phys.* **58**, 4982–5001; [1974] **60**, 343 (correction).
- J. R. Macdonald [1976a] Complex Rate Constant for an Electrochemical System Involving an Adsorbed Intermediate, *J. Electroanal. Chem.* **70**, 17–26.
- J. R. Macdonald [1976b] Interpretation of AC Impedance Measurements in Solids, in *Superionic Conductors*, eds. G. D. Mahan and W. L. Roth, Plenum Press, New York, pp. 81–97.
- D. D. Macdonald [1977] *Transient Techniques in Electrochemistry*, Plenum Press, New York.
- D. D. Macdonald [1978a] An Impedance Interpretation of Small Amplitude Cyclic Voltammetry. I. Theoretical Analysis for a Resistive-Capacitive System, *J. Electrochem. Soc.* **125**, 1443–1449.
- D. D. Macdonald [1978b] An Impedance Interpretation of Small Amplitude Cyclic Voltammetry. II. Theoretical Analysis of Systems that Exhibit Pseudoinductive Behavior, *J. Electrochem. Soc.* **125**, 1977–1981.
- D. D. Macdonald [1978c] A Method for Estimating Impedance Parameters for Electrochemical Systems That Exhibit Pseudoinductance, *J. Electrochem. Soc.* **125**, 2062–2064.
- J. R. Macdonald [1979] Optoisolator Initializes Signal-Averaging Circuit, *Electronics* **52**, 121.
- J. R. Macdonald [1984] Note on the Parameterization of the Constant-Phase Admittance Element, *Solid State Ionics* **13**, 147–149.
- J. R. Macdonald [1985a] Ambiguity in Models of Small-Signal Response of Dielectric and Conducting Systems and a New Umbrella Model, *Bull. Am. Phys. Soc.* **30**, 587.
- J. R. Macdonald [1985b] New Aspects of Some Small-Signal AC Frequency Response Functions, *Solid State Ionics* **15**, 159–161.
- J. R. Macdonald [1985c] Frequency Response of Unified Dielectric and Conductive Systems Involving an Exponential Distribution of Activation Energies, *J. Appl. Phys.* **58**, 1955–1970.
- J. R. Macdonald [1985d] Generalizations of “Universal Dielectric Response” and a General Distribution-of-Activation-Energies Model for Dielectric and Conducting Systems, *J. Appl. Phys.* **58**, 1971–1978.
- J. R. Macdonald [1987a] Relaxation in Systems with Exponential or Gaussian Distributions of Activation Energies, *J. Appl. Phys.* **61**, 700–713.
- J. R. Macdonald [1987b] *Impedance Spectroscopy: Emphasizing Solid Materials and Systems*, John Wiley & Sons, Inc., New York.

- D. D. Macdonald [1992] The Point Defect Model for the Passive State, *J. Electrochem. Soc.* **139**(12), 3434–3449.
- J. R. Macdonald [1993] Some New Directions in Impedance Spectroscopy Data Analysis, *Electrochim. Acta* **38**(14), 1883–1890.
- J. R. Macdonald [1995] Exact and Approximate Nonlinear Least Squares Inversion of Dielectric Relaxation Spectra, *J. Chem. Phys.* **102**, 6241–6250.
- J. R. Macdonald [1996] Analysis of Dispersed, Conducting-System frequency-Response Data, *J. Non-Cryst. Solids* **197**, 83–110.
- J. R. Macdonald [1997a] Accurate Fitting of Immittance Spectroscopy Frequency-Response Data Using the Stretched Exponential Model, *J. Non-Cryst. Solids* **212**, 95–116.
- J. R. Macdonald [1997b] Limiting Electrical Response of Conductive and Dielectric Systems, Stretched-Exponential Behavior, and Discrimination Between Fitting Models, *J. Appl. Phys.* **82**, 3962–3971.
- J. R. Macdonald [1998] The Ngai Coupling Model of Relaxation: Generalizations, Alternatives, and Their Use in the Analysis of Non-Arrhenius Conductivity in Glassy Fast-Ionic Materials, *J. Appl. Phys.* **84**, 812–827.
- D. D. Macdonald [1999a] Passivity: The Key to Our Metals-Based Civilization, *Pure Appl. Chem.* **71**(6), 951–978.
- J. R. Macdonald [1999b] Dispersed Electrical-Relaxation: Discrimination Between Conductive and Dielectric Properties, *Braz. J. Phys.* **29**, 332–346.
- J. R. Macdonald [1999c] Critical Examination of the Mismatch-and Relaxation Frequency-Response Model for Dispersive Materials, *Solid State Ionics* **124**, 1–19.
- J. R. Macdonald [2000a] Comparison of Parametric and Non-parametric Methods for the Analysis and Inversion of Immittance Data: Critique of Earlier Work, *J. Comput. Phys.* **157**, 280–301.
- J. R. Macdonald [2000b] Comparison of the Universal Dynamic Response Power-Law Fitting Model for Conducting Systems with Superior Alternative Models, *Solid State Ionics* **133**, 79–97.
- J. R. Macdonald [2000c] On Relaxation-Spectrum Estimation for Decades of Data: Accuracy and Sampling-Localization Considerations, *Inverse Problems* **16**, 1561–1583.
- J. R. Macdonald [2001a] Nearly Constant Loss or Constant Loss in Ionically Conducting Glasses: A Physically Realizable Approach, *J. Chem. Phys.* **115**, 6192–6199.
- J. R. Macdonald [2001b] Assessing Some Sacred Cows: Strengths and Weaknesses of Some Dispersive Relaxation-Response Models for Thermally Activated Conductive Systems, Talk presented at the 4th International Discussion Meeting on Relaxations in Complex Systems, Crete, Greece, June 18.
- J. R. Macdonald [2001c] Scaling and Modeling in the Analysis of Dispersive Relaxation of Ionic Materials, *J. Appl. Phys.* **90**, 153–161.
- J. R. Macdonald [2002a] New Model for Nearly Constant Dielectric Loss in Conductive Systems: Temperature and Concentration Dependencies, *J. Chem. Phys.* **116**, 3401–3409.
- J. R. Macdonald [2002b] Discrimination Between Series and Parallel Fitting Models for Nearly Constant Loss Effects in Dispersive Ionic Conductors, *J. Non-Cryst. Solids* **307–310**, 913–920.
- J. R. Macdonald [2002c] Some Alternate Models for Nearly Constant Loss in Conductive Systems, *Phys. Rev. B* **66**, 064305.
- J. R. Macdonald [2002d] Resolution of Conflicting Views Concerning Frequency-Response Models for Conducting Materials with Dispersive Relaxation, and Isomorphism of Macroscopic and Microscopic Models, *Solid State Ionics* **150**, 263–279.
- J. R. Macdonald [2003a] Comparison and Evaluation of Several Models for Fitting the Frequency Response of Dispersive Systems, *J. Chem. Phys.* **118**, 3258–3267.
- J. R. Macdonald [2003b] Effective-Medium Model for Nearly Constant Loss in Ionic Conductors, *J. Appl. Phys.* **94**, 558–565.
- J. R. Macdonald [2004] On Two Incompatible Models for Dispersion in Ionic Conductors, *J. Appl. Phys.* **95**, 1849–1853.
- J. R. Macdonald [2005a] Universality, the Barton, Nakajima, and Namikawa Relation, and Scaling for Dispersive Ionic Materials, *Phys. Rev. B* **71**, 184307–184319
- J. R. Macdonald [2005b] Impedance Spectroscopy: Models, Data Fitting, and Analysis, *Solid State Ionics* **176**(25), 1961–1969.
- D. D. Macdonald [2006] Reflections on the History of Electrochemical Impedance Spectroscopy, *Electrochim. Acta* **51**, 1376–1388.
- J. R. Macdonald [2009] Comments on the Electric Modulus Formalism Model and Superior Alternatives to It for the Analysis of the Frequency Response of Ionic Conductors, *J. Phys. Chem. Solids* **70**, 546–554.
- J. R. Macdonald [2010] Utility of Continuum Diffusion Models for Analyzing Mobile-Ion Immittance Data: Electrode Polarization, Bulk, and Generation-Recombination Effects, *J. Phys. Condens. Matter* **22**, 495101–495115.
- J. R. Macdonald [2011] Effects of Various Boundary Conditions on the Response of Poisson–Nernst–Planck Impedance Spectroscopy Analysis Models and Comparison with a Continuous-Time Random-Walk Model, *J. Phys. Chem. A* **115**, 13370–13380.
- D. D. Macdonald [2012a] Some Personal Adventures in Passivity: A Review of the Point Defect Model for Film Growth, *Russ. J. Electrochem.* **48**(3), 235–258.
- J. R. Macdonald [2012b] Three to Six Ambiguities in Immittance Spectroscopy Data Fitting, *J. Phys. Condens. Matter* **24**, 175004–175015.
- J. R. Macdonald [2013] Utility and Importance of Poisson–Nernst–Planck Immittance-Spectroscopy Fitting Models, *J. Phys. Chem. C* **117**, 23433–23450.
- J. R. Macdonald and M. M. Ahmad [2007] Slopes, Nearly Constant Loss, Universality, and Hopping Rates for Dispersive Ionic Conduction, *J. Phys. Condens. Matter* **19**, 046215–046227.

- J. R. Macdonald and C. A. Barlow, Jr. [1963] Relaxation, Retardation, and Superposition, *Rev. Mod. Phys.* **35**, 940–946.
- J. R. Macdonald and M. K. Brachman [1956] Linear System Integral Transform Relations, *Rev. Mod. Phys.* **28**, 393–422.
- J. R. Macdonald and G. B. Cook [1984] Analysis of Impedance Data for Single Crystal Na Beta-Alumina at Low Temperatures, *J. Electroanal. Chem.* **168**, 335–354. Also presented at a Meeting of the South-eastern Section of the American Physical Society, November 1983, and at the Sixth Australian Electrochemistry Conference, Geelong, February, 1984.
- J. R. Macdonald and G. B. Cook [1985] Reply to Comments by Almond and West on Na β -Alumina Immittance Data Analysis, *J. Electroanal. Chem.* **193**, 57–74.
- D. D. Macdonald and G. R. Engelhardt [2010] The Point Defect Model for Bi-Layer Passive Films, *ECS Trans.* **28**(24), 123–144.
- J. R. Macdonald and D. R. Franceschetti [1978] Theory of Small-Signal A-C Response of Solids and Liquids with Recombining Mobile Charge, *J. Chem. Phys.* **68**, 1614–1637.
- J. R. Macdonald and D. R. Franceschetti [1979a] Compact and Diffuse Double Layer Interaction in Unsupported System Small-Signal Response, *J. Electroanal. Chem.* **99**, 283–298.
- J. R. Macdonald and D. R. Franceschetti [1979b] A Method for Estimating Impedance Parameters for Electrochemical Systems That Exhibit Pseudoinductance, *J. Electrochem. Soc.* **126**, 1082–1083.
- J. R. Macdonald and D. R. Franceschetti [1991] Precision of Impedance Spectroscopy Estimates of Bulk, Reaction Rate, and Diffusion Parameters, *J. Electroanal. Chem.* **307**, 1–11.
- J. R. Macdonald and J. A. Garber [1977] Analysis of Impedance and Admittance Data for Solids and Liquids, *J. Electrochem. Soc.* **124**, 1022–1030.
- J. R. Macdonald and C. A. Hull [1984] Pseudo Reaction Rate in the AC Response of an Electrolytic Cell, *J. Electroanal. Chem.* **165**, 9–20.
- J. R. Macdonald and R. L. Hurt [1986] Analysis of Dielectric or Conductive System Frequency Response Data Using the Williams-Watts Function, *J. Chem. Phys.* **84**, 496–502.
- J. R. Macdonald and S. W. Kenkel [1985] Comparison of Two Recent Approaches Towards a Unified Theory of the Electrical Double Layer, *Electrochim. Acta* **30**, 823–826.
- D. D. Macdonald and M. C. H. McKubre [1981] Electrochemical Impedance Techniques in Corrosion Science, in *Electrochemical Corrosion Testing*, eds. F. Mansfield and U. Bertocci, STP 727, ASTM, Philadelphia, PA.
- D. D. Macdonald and M. C. H. McKubre [1982] Impedance Measurements in Electrochemical Systems, in *Modern Aspects of Electrochemistry*, Vol. 14, eds. J. O'M. Bockris, B. E. Conway, and R. E. White, Plenum Press, New York.
- J. R. Macdonald and J. C. Phillips [2004] In Homogeneous Glasses, Stretched-Exponential Relaxation Is Purely Topological, *Phys. Rev. Lett.*
- J. R. Macdonald and L. D. Potter, Jr. [1987] A Flexible Procedure for Analyzing Impedance Spectroscopy Results: Description and Illustrations, *Solid State Ionics* **24**, 61–79.
- D. D. Macdonald and S. I. Smedley [1990] An Electrochemical Impedance Analysis of Passive Films on Nickel (111) in Phosphate Buffer Solutions, *Electrochim. Acta* **35**(11/12), 1949–1956.
- J. R. Macdonald and Solartron Inc. [2003] The Current MS-DOS and Windows Versions of the LEVM CNLS Fitting and Inversion Program, <http://www.physics.unc.edu/~macd> (accessed on November 3, 2017).
- D. D. Macdonald and M. Urquidi-Macdonald [1985] Application of Kramers-Kronig Transforms in the Analysis of Electrochemical Systems I. Polarization Resistance, *J. Electrochem. Soc.* **132**, 2316–2319.
- D. D. Macdonald and M. Urquidi-Macdonald [1986] Distribution Functions for the Breakdown of Passive Films, *Electrochim. Acta* **31**, 1079–1086.
- J. R. Macdonald, D. R. Franceschetti, and R. Meaudre [1977] Electrical Response of Materials with Recombining Space Charge, *J. Phys. C Solid State Phys.* **10**, 1459–1471.
- J. R. Macdonald, D. R. Franceschetti, and A. P. Lehnens [1980a] Interfacial Space Charge and Capacitance in Ionic Crystals: Intrinsic Conductors, *J. Chem. Phys.* **73**, 5272–5293.
- J. R. Macdonald, J. Schoonman, A. Wolfert, and D. R. Franceschetti [1980b] Interfacial Phenomena of Beta-PbF₂, in *Reactivity in Solids*, Wageningen, the Netherlands, January 14–15; 12–13(A).
- J. R. Macdonald, J. Schoonman, and A. P. Lehnens [1981] Three Dimensional Perspective Plotting and Fitting of Immittance Data, *Solid State Ionics* **5**, 137–140.
- J. R. Macdonald, A. Hooper, and A. P. Lehnens [1982a] Analysis of Hydrogen-Doped Lithium Nitride Admittance Data, *Solid State Ionics* **6**, 65–77.
- J. R. Macdonald, J. Schoonman, and A. P. Lehnens [1982b] The Applicability and Power of Complex Nonlinear Least Squares for the Analyses of Impedance and Admittance Data, *J. Electroanal. Chem.* **131**, 77–95.
- D. D. Macdonald, S. Real, and M. Urquidi-Macdonald [1986] Application of Kramers-Kronig Transforms in the Analysis of Electrochemical Impedance Data. II. Transformations in the Complex Plane, *J. Electrochem. Soc.* **133**(10), 2018–2024.
- D. D. Macdonald, B. G. Pound, and S. J. Lenhart [1990] The Application of Electrochemical Impedance Spectroscopy for Characterizing the Degradation of Ni(OH)₂/NiOOH Electrodes, *J. Power Sources* **29**(3–4), 477–502.
- D. D. Macdonald, M. Al Rafaie, and G. R. Engelhardt [2001] New Rate Laws for the Growth and Reduction of Passive Films, *J. Electrochem. Soc.* **148**, B343–B347.
- D. Macdonald, A. Sun, N. Priyantha, and P. Jayaweera [2004] An Electrochemical Impedance Study of Alloy-22 in NaCl Brine at Elevated Temperature: II. Reaction Mechanism Analysis, *J. Electroanal. Chem.* **572**(2), 421–431.
- J. R. Macdonald, L. R. Evangelista, E. K. Lenzi, and G. Barbero [2011] Comparison of Impedance Spectroscopy Expressions and Responses of Alternate Anomalous Poisson-Nernst-Planck Diffusion Equations for Finite-Length Situations, *J. Phys. Chem. C* **115**, 7648–7655.

- D. D. Macdonald, S. Sharifi-Asl, A. Almarzooqi, G. R. Engelhardt, and B. Kursten [2013] Electrochemical Impedance Modeling of the Passivity of Carbon Steel in Simulated Concrete Pore Water, *ECS Trans.* **50**(30), 41–56.
- P. B. Macedo, R. Bose, V. Provenzano, and T. A. Litowitz [1972] in *Amorphous Materials*, eds. R. W. Douglas and B. Ellis, Interscience, London, UK, p. 251.
- P. B. Macedo, C. T. Moynihan, and R. Bose [1972] The Role of Ionic Diffusion in Polarization in Vitreous Ionic Conductors, *Phys. Chem. Glasses* **13**, 171–179.
- S. Mafe, J. Pellicer, and V. M. Aguilera [1986] Ionic Transport and Space Charge Density in Electrolytic Solutions as Described by Nernst–Planck and Poisson Equations, *J. Phys. Chem.* **90**, 6045–6950.
- J. Maier [1986] On the Conductivity of Polycrystalline Materials, *Ber. Bunsenges. Phys. Chem.* **90**, 26–33.
- J. Maier [1996] Interface Effects in Mixed Conductors, in *High Temperature Electrochemistry, Ceramics and Metals, Proceedings of the 17th Risø International Symposium on Materials Science, September 2–6, 1996*, eds. F. W. Poulsen, N. Bonanos, S. Linderoth, M. Mogensen, and B. Zachau-Christiansen, Risø National Laboratory, Roskilde, Denmark, pp. 678–676.
- J. Maier [2004] *Physical Chemistry of Ionic Materials: Ions and Electrons in Solids*, John Wiley & Sons, Inc., Hoboken, NJ.
- J. Maier, J. Jamnik, and M. Leonhardt [2000] Kinetics of Oxygen Stoichiometry Changes, *Solid State Ionics* **129**(1–4), 25–32.
- M. Maja and N. Penazzi [1985] AC Behaviour of Lead Dioxide Electrode: Antimony Effect, *Electrochim. Acta* **30**, 773–778.
- V. K. Malinovsky, V. N. Novikov, and A. P. Sokolov [1987] Investigation of Structural Correlations in Disordered Materials by Raman Scattering Measurements, *J. Non-Cryst. Solids* **90**(1–3), 485–488.
- B. Mandelbrot [1983] *The Fractal Geometry of Nature*, Freeman, New York.
- F. Mansfeld [1976] Electrochemical Monitoring of Atmospheric Corrosion Phenomena, *Adv. Corros. Sci. Tech.* **6**, 163.
- F. Mansfeld, M. W. Kendig, and S. Tsai [1982] Evaluation of Organic Coating Metal Systems by AC Impedance Techniques, *Corrosion* **38**, 478–485.
- S. W. Martin and C. A. Angell [1986] D. C. and A. C. Conductivity in Wide Composition Range Li₂O-P₂O₅ Glasses, *J. Non-Cryst. Solids* **83**, 185–207.
- R. T. Mathias [1983] Effect of Tortuous Extracellular Pathways on Resistance Measurements, *Biophys. J.* **42**(1), 55–59.
- R. T. Mathias [1984] Analysis of Membrane Properties Using Extrinsic Noise, in *Membranes, Channels, and Noise*, eds. R. Eisenberg, M. Frank, and C. Stevens, Springer, Berlin, Germany, pp. 49–116.
- R. T. Mathias and J. L. Rae [1985] Transport Properties of the Lens, *Am. J. Physiol.* **249**(3 Pt 1), C181–C190.
- R. T. Mathias, R. S. Eisenberg, and R. Valdiosera [1977] Electrical Properties of Frog Skeletal Muscle Fibers Interpreted with a Mesh Model of the Tubular System, *Biophys. J.* **17**(1), 57–93.
- R. T. Mathias, J. L. Rae, and R. S. Eisenberg [1979] Electrical Properties of Structural Components of the Crystalline Lens, *Biophys. J.* **25**(1), 181–201.
- R. T. Mathias, J. L. Rae, and R. S. Eisenberg [1981] The Lens as a Nonuniform Spherical Syncytium, *Biophys. J.* **34**(1), 61–83.
- R. T. Mathias, J. L. Rae, L. Ebihara, and R. T. McCarthy [1985] The Localization of Transport Properties in the Frog Lens, *Biophys. J.* **48**(3), 423–434.
- R. T. Mathias, J. L. Rae, and G. J. Baldo [1997] Physiological Properties of the Normal Lens, *Physiol. Rev.* **77**(1), 21–50.
- N. Matsui [1981] Complex-Impedance Analysis for the Development of Zirconia Oxygen Sensors, *Solid State Ionics* **3**(4), 525–529.
- A. Matsumoto and K. Higasi [1962] Dielectric Relaxation of Nonrigid Molecules at Lower Temperature, *J. Chem. Phys.* **36**, 1776–1780.
- P. Mauracher and E. Karden [1997] Dynamic Modelling of Lead/Acid Batteries Using Impedance Spectroscopy for Parameter Identification, *J. Power Sources* **67**, 69–84.
- J. C. Maxwell [1881] *A Treatise on Electricity and Magnetism*, 2nd Edition, Clarendon Press, Oxford, UK.
- J. C. Maxwell Garnett [1904] Colours in Metal Glasses and Metal Films, *Trans. R. Soc. CCIII*, 385–420.
- J. F. McCann and S. P. S. Badwal [1982] Equivalent Circuit Analysis of the Impedance Response of Semiconductor/Electrolyte/Counterelectrode Cells, *J. Electrochem. Soc.* **129**, 551–559.
- N. G. McCrum, B. E. Read, and G. Williams [1967] *Anelastic and Dielectric Effects in Polymeric Solids*, John Wiley & Sons, Ltd, London, UK, p. 111.
- M. C. H. McKubre [1976] *An Impedance Study of the Membrane Polarization Effect in Simulated Rock Systems*, Ph.D. thesis, Victoria University, Wellington, New Zealand.
- M. C. H. McKubre [1981] The Use of Harmonic Analysis to Determine Corrosion Rates, Paper Number 135 in *the 160th meeting of the Electrochemical Society*, Denver, Colorado.
- M. C. H. McKubre [1983] *The Electrochemical Measurement of Corrosion Rates in Cathodically Protected Systems*, EPRI Report CS-2858 on Project 1689-7, SRI International, Menlo Park, CA.
- M. C. H. McKubre and D. D. Macdonald [1984] Electronic Instrumentation for Electrochemical Studies, in *A Comprehensive Treatise of Electrochemistry*, eds. J. O'M. Bockris, B. E. Conway, and E. Yeager, Plenum Press, New York, pp. 1–98.
- M. C. H. McKubre and H. B. Sierra-Alcazar [1985] *Sulfur Side Supporting Studies for the Sodium Sulfur Battery*, Interim Report on EPRI Contract 128-2, SRI International, Menlo Park, CA.
- M. C. H. McKubre and B. C. Syrett [1986] Harmonic Impedance Spectroscopy for the Determination of Corrosion Rates in Cathodically Protected Systems, in *Corrosion Monitoring in Industrial Plants Using Nondestructive Testing and Electrochemical Methods*, ASTM STP, Vol. 908, eds. G. C. Moran and

- P. Labine, American Society for Testing and Materials, Philadelphia, PA, pp. 433–458.
- D. S. McLachlan, M. Blaszkiewicz, and R. E. Newnham [1990] Electrical Resistivity of Composites, *J. Am. Ceram. Soc.* **73**(8), 2187–2203.
- G. F. McLean, T. Niet, S. Prince-Richard, and N. Djilali [2002] An Assessment of Alkaline Fuel Cell Technology, *Int. J. Hydrogen Energy* **27**, 507–526.
- B. D. McNicol, D. A. J. Rand and K. R. Williams [1999] Direct Methanol: Air Fuel Cells for Road Transportation, *J. Power Sources* **83**, 15–31.
- M. Mehta, G. Mixon, J. P. Zheng, and P. Andreia [2013] Analytical Electrochemical Impedance Modeling of Li-Air Batteries Under D.C Discharge, *J. Electrochem. Soc.* **160**(11), A2033–A2045.
- N. Menon and S. R. Nagel [1991, 1993] Comment on Scaling of the α Relaxation in Low-Molecular-Weight Glass-Forming Liquids and Polymers, *Phys. Rev. Lett.* **71**, 4095.
- N. Menon and S. R. Nagel [1995] Evidence for a Divergent Susceptibility at the Glass Transition, *Phys. Rev. Lett.* **74**(7), 1230.
- R. E. Meredith and C. W. Tobias [1962] Conduction in Heterogeneous Systems, in *Advances in Electrochemistry and Electrochemical Engineering*, Vol. 2, ed. C. W. Tobias, Interscience, New York, p. 15.
- L. Meszaros and J. Devay [1982] Study of the Rate of Corrosion by a Faradaic Distortion Method, IV, Application of the Method for the Case of Reversible Charge Transfer Reaction, *Acta Chim. Acad. Sci. Hungaria* **109**, 241–244.
- A. Metcalfe [1977] The Anodic Dissolution of Silver into Silver Rubidium Iodide-Impedance Measurements, *J. Electroanal. Chem.* **88**, 187–192.
- M. Mihelicic, A. Surca Vuk, I. Jerman, B. Orel, F. Svegl, H. Moulki, C. Faure, G. Campet, and A. Rougier [2014] Comparison of Electrochromic Properties of Ni_{1-x}O in Lithium and Lithium-Free Aprotic Electrolytes: From Ni_{1-x}O Pigment Coatings to Flexible Electrochromic Devices, *Sol. Energy Mater. Sol. Cells* **120**, 116–130.
- J. R. Miller [1992] Performance of Mixed Metal Oxide Pseudocapacitors: Comparison with Carbon Double Layer Capacitors, in *Proceedings of the Second International Symposium on Electrochemical Capacitors and Similar Energy Storage Devices*, eds. S. P. Wolsky and N. Marinicic, Florida Educational Seminars Inc., Boca Raton, FL.
- R. L. Milton, R. T. Mathias, and R. S. Eisenberg [1985] Electrical Properties of the Myotendon Region of Frog Twitch Muscle Fibers Measured in the Frequency Domain, *Biophys. J.* **48**(2), 253–267.
- N. Q. Minh and T. Takahashi [1995] *Science and Technology of Ceramic Fuel Cells*, Elsevier, Amsterdam, the Netherlands.
- S. P. Mitoff [1968] Properties Calculations for Heterogeneous Systems, in *Advances in Materials Research*, Vol. 3, ed. H. Herman, Wiley-Interscience, New York, pp. 305–329.
- T. Miyasaka [1998] US Patent 6,416,902.
- J. Mizusaki, K. Amano, S. Yamuchi, and K. Fueki [1983] *Response and Electrode Reaction of Zirconia Oxygen Gas Sensor*, Analytical Chemistry Symposium Series, Vol. 17, Elsevier, New York, pp. 279–284.
- T. P. Moffat and R. M. Latanision [1992] Electrochemical and X-Ray Photoelectron Spectroscopy Study of the Passive State of Chromium, *J. Electrochem. Soc.* **139**, 1869–1879.
- P. M. S. Monk [1999] Charge Movement Through Electrochromic Thin Film Tungsten Trioxide, *Crit. Rev. Solid State Mater. Sci.* **24**, 193–226.
- E. W. Montroll and J. T. Benders [1984] On the Levy (or Stable) Distribution and the Williams-Watts Model of Dielectric Relaxation, *J. Stat. Phys.* **34**, 129–162.
- E. W. Montroll and M. F. Shlesinger [1984] On the Wonderful World of Random Walks, in *Non-Equilibrium Phenomena. II. From Statistics to Hydrodynamics*, eds. J. L. Lebowitz and E. W. Montroll, Elsevier, New York, pp. 1–121.
- E. W. Montroll and G. H. Weiss [1965] Random Walks on Lattices, II, *J. Math. Phys.* **6**, 167–181.
- C. I. Mooring and H. L. Kies [1977] AC Voltammetry at Large Amplitudes: A Simplified Theoretical Approach, *J. Electroanal. Chem.* **78**, 219.
- Y. Mori [2015] A Multidomain Model for Ionic Electrodifusion and Osmosis with an Application to Cortical Spreading Depression, *Phys D Nonlinear Phenomena* **308**, 94–108.
- C. T. Morse [1974] A Computer Controlled Apparatus for Measuring AC Properties of Materials over the Frequency Range 10^{-5} to 10^{-5} Hz, *J. Phys. E* **7**, 657–662.
- R. R. Mosbæk [2014] *Solid Oxide Fuel Cell Stack Diagnostics*, Ph. D. thesis, Technical University of Denmark, Kongens Lyngby, Denmark.
- N. F. Mott [1939] Copper-Cuprous Oxide Photocells, *Proc. R. Soc. Lond.* **A171**, 281–285.
- I. Moussallem, S. Pinnow, N. Wagner, and T. Turek [2012] Development of High-Performance Silver-Based Gas-Diffusion Electrodes for Chlor-Alkali Electrolysis with Oxygen Depolarized Cathodes, *Chem. Eng. Process.* **52**, 125–131.
- C. T. Moynihan, L. P. Boesch, and N. L. Laberge [1973] Decay Function for the Electric Field Relaxation in Vitreous Ionic Conductors, *Phys. Chem. Glasses* **14**, 122–125.
- J. T. Mueller and P. M. Urban [1998] Characterization of Direct Methanol Fuel Cells by AC Impedance Spectroscopy, *J. Power Sources* **75**, 139–143.
- W. H. Mulder, J. H. Sluyters, T. Pajkossy, and L. Nyikos [1990] Tafel Current at Fractal Electrodes. Connection with Admittance Spectra, *J. Electroanal. Chem.* **285**, 103–115.
- J. T. Müller, P. M. Urban, and W. F. Hölderich [1999] Impedance Studies on Direct Methanol Fuel Cell Anodes, *J. Power Sources* **84**, 157–160.
- B. Müller, N. Wagner, and W. Schnurnberger [1999] Change of Electrochemical Impedance Spectra (EIS) with Time during CO-Poisoning of the Pt-Anode in a Membrane Fuel Cell, in *Proton Conducting Membrane Fuel Cells II*, Electrochemical Society Proceedings, Vol. 98–27, eds. S. Gottesfeld and T. F.

- Fuller, The Electrochemical Society, Pennington, NJ, pp. 187–199.
- K. Mund [1975] Impedanzmessungen an porösen gestützten Raney-Nickel-Elektroden für alkalische Brennstoffzellen, *Siemens Forsch. Entwickl. Ber.* **4**, 68.
- K. Mund and F. v. Sturm [1975] Degree of Utilization and Specific Effective Surface Area of Electrocatalysts in Porous Electrodes, *Electrochim. Acta* **20**, 463–467.
- H. Näge [1984] Ionic Conductivity of ThO_2 - and ZrO_2 -Based Electrolytes Between 300 and 2000 K, *Solid State Ionics* **13**, 255–263.
- J. Nagai, T. Kamimori, and M. Mizuhanshi [1986] Electrochromism in Amorphous Lithium Tungsten Oxide Films, *Sol. Energy Mater.* **13**, 279–295.
- T. Nakajima [1972] Correlations Between Electrical Conduction and Dielectric Polarization in Inorganic Glasses, in *1971 Annual Report, Conference on Electrical Insulation and Dielectric Phenomena*, National Academy of Sciences, Washington, DC, pp. 168–176.
- H. Namikawa [1975] Characterization of the Diffusion Process in Oxide Glasses Based on the Correlation Between Electric Conduction and Dielectric Relaxation, *J. Non-Cryst. Solids* **18**, 173–195.
- E. Neher [1997] Ion Channels for Communication Between and Within Cells Nobel Lecture, December 9, 1991, in *Nobel Lectures, Physiology or Medicine 1991–1995*, ed. N. Ringertz, World Scientific Publishing Co., Singapore, pp. 10–25.
- J. S. Newman [1973] *Electrochemical Systems*, Prentice-Hall, Englewood Cliffs, NJ.
- K. L. Ngai [1979] Universality of Low-frequency Fluctuation, Dissipation, and Relaxation Properties of Condensed Matter. I. Comments, *Solid State Phys.* **9**, 127–140.
- K. L. Ngai [1980] Universality of Low-Frequency Fluctuation, Dissipation, and Relaxation Properties of Condensed Matter. II. Comments, *Solid State Phys.* **9**, 141–155.
- K. L. Ngai [1998] Evidence of Interaction Between Oxygen Ions from Conductivity Relaxation and Quasielastic Light Scattering Data of Yttria-Stabilized Zirconia, *Philos. Mag. B* **77**, 187–195.
- K. L. Ngai [1999] Properties of the Constant Loss in Ionically Conducting Glasses, Melts, and Crystals, *J. Chem. Phys.* **110**, 10576–10584.
- K. L. Ngai and C. Leon [1999] Relating Macroscopic Electrical Relaxation to Microscopic Movements of the Ions in Ionically Conducting Materials by Theory and Experiment, *Phys. Rev. B* **60**, 9396–9405.
- K. L. Ngai and C. León [2002] Cage Decay, Near Constant Loss, and Crossover to Cooperative Ion Motion in Ionic Conductors: Insight from Experimental Data, *Phys. Rev. B* **66**, 064308.
- K. L. Ngai and C. T. White [1979] Frequency Dependence of Dielectric Loss in Condensed Matter, *Phys. Rev. B* **20**, 2475–2486.
- K. L. Ngai, A. K. Jonscher, and C. T. White [1979] On the Origin of the Universal Dielectric Response in Condensed Matter, *Nature* **277**, 185–189.
- K. L. Ngai, R. W. Rendell, A. K. Rajagopal, and S. Teitler [1986] Three Coupled Relations for Relaxations in Complex Systems, *Ann. N. Y. Acad. Sci.* **484**, 150–184.
- K. L. Ngai, S. Capaccioli, D. Prevosto, and L.-M. Wang [2015a] Coupling of Caged Molecule Dynamics to JG β -Relaxation II: Polymers, *J. Phys. Chem. B* **119**, 12502–12518.
- K. L. Ngai, S. Capaccioli, D. Prevosto, and L.-M. Wang [2015b] Coupling of Caged Molecule Dynamics to JG β -Relaxation III: van der Waals Glasses, *J. Phys. Chem. B* **119**, 12519–12525.
- E. H. Nicollian and J. R. Brew [1982] *MOS (Metal Oxide Semiconductor Technology) Physics and Technology*, John Wiley & Sons, Inc., New York.
- E. H. Nicollian and A. Goetzberger [1967] The Si-SiO₂ Interface: Electrical Properties as Determined by the Metal-Insulator-Silicon Conductance Technique, *Bell Syst. Tech. J.* **46**, 1055–1133.
- N. Nicoloso, W. Kernler, B. Leibold, A. Löbert, and W. Weppner [1988] Electrical Response of Oxygen Sensing TiO₂ Surfaces and Fractal Pt/YSZ-Interfaces, *Solid State Ionics* **28–30**, 1637–1643.
- G. A. Niklasson [2008] Proton Diffusion in Polyethylene Oxide: Relevance to Electrochromic Device Design, *Sol. Energy Mater. Sol. Cells* **92**, 1293–1297.
- G. A. Niklasson and C. G. Granqvist [2007] Electrochromics for Smart Windows: Thin Films of Tungsten Oxide and Nickel Oxide, and Devices Based on These, *J. Mater. Chem.* **17**, 127–156.
- G. A. Niklasson, R. Ahuja, and M. Stromme [2006] Electronic States in Intercalation Materials Studied by Electrochemical Techniques, *Mod. Phys. Lett.* **20**, 863–875.
- G. A. Niklasson, S. Malmgren, S. Green, and J. Backholm [2010] Determination of Electronic Structure by Impedance Spectroscopy, *J. Non-Cryst. Solids* **365**, 705–709.
- S. M. R. Niya and M. Hoorfar [2013] Study of Proton Exchange Membrane Fuel Cells Using Electrochemical Impedance Spectroscopy Technique: A Review, *J. Power Sources* **240**, 281–293.
- I. M. Novoseleskii, N. N. Gudina, and Y. I. Fetistov [1972] Identical Equivalent Impedance Circuits, *Sov. Electrochem.* **8**, 546–548.
- A. S. Nowick, A. V. Vaysleyb, and W. Liu [1998] Identification of Distinctive Regimes of Behavior in the AC Electrical Response of Glasses, *Solid State Ionics* **105**, 121–128.
- N. A. O'Brien, J. Gordon, H. Mathew, and B. P. Hichwa [1999] Electrochromic Coatings: Applications and Manufacturing Issues, *Thin Solid Films* **345**, 312–318.
- R. O'Hayre, S.-W. Cha, W. Colella, and F. B. Prinz [2009] *Fuel Cell Fundamentals*, 2nd Edition, John Wiley & Sons, Inc., New York.
- B. O'Regan and M. Grätzel [1991] A Low-Cost, High-Efficiency Solar Cell Based on Dye-Sensitized Colloidal TiO₂ Films, *Nature* **353**, 737–740.
- T. Odagaki and M. Lax [1980] AC Hopping Conductivity of a One-dimensional Bond-Percolation Model, *Phys. Rev. Lett.* **10**, 847–850.

- H. Oheda [1981] Phase-Shift Analysis of Modulated Photocurrents: Its Application to the Determination of the Energetic Distribution of Gap States, *J. Appl. Phys.* **52**, 6693–6700.
- K. B. Oldham [1957] Faradaic Rectification: Theory and Application to the Hg^{++}/Hg Electrode, *Trans. Faraday Soc.* **53**, 80–90.
- L. Onsager [1926] Theory of Electrolytes, I, *Phys. Z.* **27**, 388–392.
- L. Onsager [1927] Theory of Electrolytes, II, *Phys. Z.* **28**, 277–298.
- M. E. Orazem and B. Trbolet [2008] *Electrochemical Impedance Spectroscopy*, John Wiley & Sons, Inc., Hoboken, NJ.
- R. K. Otnes and L. Enochson [1972] *Digital Time Series Analysis*, John Wiley & Sons, Inc., New York.
- K. Ozawa [1994] Lithium-Ion Rechargeable Batteries with LiCoO_2 and Carbon Electrodes: The LiCoO_2/C System, *Solid State Ionics* **69**(3–4), 212–221.
- G. Paasch, K. Micka, and P. Gersdorf [1993] Theory of the Electrochemical Impedance of Macrohomogeneous Porous Electrodes, *Electrochim. Acta* **38**(18), 2653–2662.
- T. Pajkossy [1991] Electrochemistry at Fractal Surfaces, *J. Electroanal. Chem.* **300**, 1–11.
- T. Pajkossy [1994] Impedance of Rough Capacitive Electrodes, *J. Electroanal. Chem.* **364**, 111–124.
- T. Pajkossy, T. Wandlowski, and D. M. Kolb [1996] Impedance Aspects of Anion Adsorption on Gold Single Crystal Electrodes, *J. Electroanal. Chem.* **414**, 209–220.
- R. G. Palmer, D. L. Stein, E. Abrahams, and P. W. Anderson [1984] Models of Hierarchically Constrained Dynamics for Glassy Relaxation, *Phys. Rev. Lett.* **53**, 958–961.
- J. R. Park [1983] *The Mechanism of the Fast Growth of Magnetite on Carbon Steel Under PWR Crevice Conditions*, Ph.D. thesis, Ohio State University, Columbus, OH.
- J. R. Park and D. D. Macdonald [1983] Impedance Studies of the Growth of Porous Magnetite Films on Carbon Steel in High Temperature Aqueous systems, *Corros. Sci.* **23**, 295.
- R. Parsons [1954] in *Modern Aspects of Electrochemistry*, Vol. 1, eds. J. O'M. Bockris and B. E. Conway, Butterworths, London, UK, p. 103.
- L. R. Pasquale, R. T. Mathias, L. R. Austin, P. R. Brink, and M. Ciunga [1990] Electrostatic Properties of Fiber Cell Membranes from the Frog Lens, *Biophys. J.* **58**(4), 939–945.
- A. Patkowski, T. Thurn-Albrecht, E. Banachowicz, W. Steffen, P. T. Bösecke, T. Narayanan, and E. W. Fischer [2000] Long-Range Density Fluctuations in Orthoterphenyl as Studied by Means of Ultrasmall-Angle X-Ray Scattering, *Phys. Rev. E* **61**(6), 6909–6913.
- J. L. de Paula, J. A. da Cruz, E. K. Lenzi, and L. R. Evangelista [2012] Immittance Response of an Electrolytic Cell in the Presence of Adsorption, Generation, and Recombination of Ions, *J. Electroanal. Chem.* **682**, 116–120.
- T. Pauporté and R. Durand [2000] Impedance Spectroscopy Study of Electrochromism in Sputtered Iridium Oxide Films, *J. Appl. Electrochem.* **30**, 35–41.
- E. Pehlivan, G. A. Niklasson, C. G. Granqvist, and P. Georén [2010] Ageing of Electrochromic WO_3 Coatings Characterized by Electrochemical Impedance Spectroscopy, *Phys. Status Solidi A* **207**, 1772–1776.
- E. Peled [1983] Film Forming Reaction at the Lithium/Electrolyte Interface, *J. Power Sources* **9/3**, 253–266.
- W. G. Pell and B. E. Conway [1996] Quantitative Modeling of Factors Determining Ragone Plots for Batteries and Electrochemical Capacitors, *J. Power Sources* **63**, 255–266.
- W. G. Pell and B. E. Conway [2001] Voltammetry at a de Levie Brush Electrode as a Model for Electrochemical Supercapacitor Behavior, *J. Electroanal. Chem.* **500**, 121–133.
- W. G. Pell, B. E. Conway, W. A. Adams, and J. de Oliveria [1999] Electrochemical Efficiency in Multiple Discharge/Recharge Cycling of Supercapacitors in Hybrid EV Applications, *J. Power Sources* **80**, 134–141.
- O. Pensado-Rodríguez, M. Urquidi-Macdonald, and D. D. Macdonald [1999a] Electrochemical Behavior of Lithium in Alkaline Aqueous Electrolytes. I. Thermodynamics, *J. Electrochem. Soc.* **146**, 1318–1325.
- O. Pensado-Rodríguez, J. Flores, M. Urquidi-Macdonald, and D. D. Macdonald [1999b] Electrochemical Behavior of Lithium in Alkaline Aqueous Electrolytes. II. Point Defect Model, *J. Electrochem. Soc.* **146**, 1326–1335.
- O. Pensado-Rodríguez, J. Flores, M. Urquidi-Macdonald, and D. D. Macdonald [2001] The Electrochemistry of Lithium in Alkaline Aqueous Electrolytes. Part III: Impedance Model, *J. Electrochem. Soc.* **148**, B386–B399.
- T. S. Perova and J. K. Vij [1996] Low Frequency Vibrational Spectroscopy of Highly Viscous and Highly Polar Liquids, *J. Mol. Liq.* **69**, 1–17.
- T. S. Perova, J. K. Vij, D. H. Christensen, and O. F. Nielsen [1999] A Comparison of the Far-infrared and Low-frequency Raman Spectra of Glass-Forming Liquids, *J. Mol. Struct.* **479**(2–3), 111–122.
- A. Peskoff and R. S. Eisenberg [1973] Interpretation of Some Microelectrode Measurements of Electrical Properties of Cells, *Annu. Rev. Biophys. Bioeng.* **2**, 65–79.
- A. Peskoff and R. S. Eisenberg [1975] The Time-Dependent Potential in a Spherical Cell Using Matched Asymptotic Expansions, *J. Math. Biol.* **2**, 277–300.
- A. Peskoff and D. M. Ramirez [1975] Potential Induced in a Spherical Cell by an Intracellular Point Source and an Extracellular Point Sink, *J. Math. Biol.* **2**(4), 301–316.
- A. Peskoff, R. S. Eisenberg, and J. D. Cole [1976] Matched Asymptotic Expansions of the Green's Function for the Electric Potential in an Infinite Cylindrical Cell, *SIAM J. Appl. Math.* **30**(2), 222–239.
- T. J. Petek, N. C. Hoyt, R. F. Savinell, and J. S. Wainright [2016] Characterizing Slurry Electrodes Using Electrochemical Impedance Spectroscopy, *J. Electrochem. Soc.* **163**(1), A5001–A5009.
- L. Peter [1990] Dynamic Aspects of Semiconductor Photoelectrochemistry, *Chem. Rev.* **90**, 753–769.

- W. Petry and J. Wuttke [1995] Quasielastic Neutron Scattering in Glass Forming Viscous Liquids, *Transp. Theory Stat. Phys.* **24**(6–8), 1075–1095.
- G. Pfister and H. Scher [1978] Dispersive (Non-Gaussian) Transient Transport in Disordered Solids, *Adv. Phys.* **27**, 747–798.
- J. C. Phillips [1994] Microscopic Theory of the Kohlrausch Constant, *J. Non-Cryst. Solids* **172–174**, 98–103.
- A. A. Pilla [1970] Transient Impedance Technique for the Study of Electrode Kinetics: Application to Potentiostatic Methods, *J. Electrochem. Soc.* **117**, 467.
- A. A. Pilla [1972] Electrochemistry, in *Computers in Chemistry and Instrumentation*, Vol. 2, eds. J. S. Mattson, H. B. Mark, Jr., and H. C. Macdonald, Jr., Marcel Dekker, New York, p. 139.
- A. A. Pilla [1975] Introduction to Laplace Plane Analysis, in *Information Chemistry*, eds. S. Fujiwara and H. B. Mark, Japan Science Society, Tokyo, Japan, pp. 181–193.
- M. Pittaluga [2014] Electrochromic Glazing and Walls for Reducing Building Cooling Needs, in *Eco-Efficient Materials for Mitigating Building Cooling Needs: Design, Properties and Applications*, eds. F. Pacheco-Torgal, J. Labrincha, L. F. Cabeza, and C. G. Granqvist, Woodhead, Cambridge, UK.
- E. J. Plichta, M. Hendrickson, R. Thompson, G. Au, W. K. Behl, M. C. Smart, B. V. Ratnakumar, and S. Surampudi [2001] Development of Low Temperature Li-ion Electrolytes for NASA and DoD Applications, *J. Power Sources* **94**(2), 160–162.
- I. Pochard, S. Frykstrand, O. Ahlström, J. Forsgren, and M. Strømme [2014] Water and Ion Transport in Ultra-Adsorbing Porous Magnesium Carbonate Studied by Dielectric Spectroscopy, *J. Appl. Phys.* **115**, 044306.
- E. A. A. Pogna, C. Rodríguez-Tinoco, G. Cerullo, C. Ferrante, J. Rodríguez-Viejo, and T. Scopigno [2015] Probing Equilibrium Glass Flow Up To Exapoise Viscosities, *Proc. Natl. Acad. Sci. U. S. A.* **112**(8), 2331–2336.
- J. P. Poley [1955] Microwave Dispersion of Some Polar Liquids, *Appl. Sci. Res. B* **4**, 337–387.
- Z. Poltarzewski, P. Staiti, V. Alderucci, W. Wieczorek, and N. Giordano [1992] Nafion Distribution in Gas Diffusion Electrodes for Solid-Polymer-Electrolyte-Fuel-Cell Applications, *J. Electrochem. Soc.* **139**, 761–765.
- G. Popkirov and R. N. Schindler [1992] A New Impedance Spectrometer for the Investigation of Electrochemical Systems, *Rev. Sci. Instrum.* **63**(11), 5366–5372.
- G. Popkirov and R. N. Schindler [1994] A New Approach to the Problem of “Good” and “Bad” Impedance Data in Electrochemical Impedance Spectroscopy, *Electrochim. Acta* **39**(13), 2025.
- G. Popkirov, E. Barsoukov, and R. N. Schindler [1995] Electrochemical Impedance Spectroscopy of Twin Working Electrodes Bridged with Conducting Polymer Layer, *Electrochim. Acta* **40**(12), 1857–1862.
- G. Popkirov, E. Barsoukov, and R. N. Schindler [1997] Investigation of Conducting Polymer Electrodes by Impedance Spectroscopy During Electropolymerization Under Galvanostatic Conditions, *J. Electroanal. Chem.* **425**, 209–216.
- M. Porto, P. Maass, M. Meyer, A. Bunde, and W. Dieterich [2000] Hopping Transport in the Presence of Site Energy Disorder: Temperature and Concentration Scaling of Conductivity Spectra, *Phys. Rev. B* **61**, 6057–6062.
- E. C. Potter and G. M. W. Mann [1965] The Fast Linear Growth of Magnetite on Mild Steel in High Temperature Aqueous Conditions, *Corros. J.* **1**, 26.
- B. G. Pound and D. D. Macdonald [1985] *Development of Noise Impedance Techniques for the Measurement of Corrosion Rates*, Final Report by SRI International on Sohio Contract NT-MEM-2219, August.
- R. W. Powers [1984] The Separability of Inter- and Intragranular Resistivities in Sodium Beta-Alumina Type Ceramics, *J. Mater. Sci.* **19**, 753–760.
- R. W. Powers and S. P. Mitoff [1975] Analysis of the Impedance of Polycrystalline Beta-alumina, *J. Electrochem. Soc.* **122**, 226–231.
- W. H. Press, S. A. Teukolsky, W. T. Vetterling, and B. P. Flannery [1992] *Numerical Recipes in Fortran 77*, Cambridge University Press, New York.
- S. Primdahl and P. V. Hendriksen [1996] Pitfalls in Solid Electrode Characterisation, in *High Temperature Electrochemistry, Ceramics and Metals, Proceedings of the 17th Risø International Symposium on Materials Science, September 2–6, 1996*, eds. F. W. Poulsen, N. Bonanos, S. Linderoth, M. Mogensen, and B. Zachau-Christiansen, Risø National Laboratory, Roskilde, Denmark, pp. 403–410.
- S. Primdahl and M. Mogensen [1997] Gas Conversion Impedance: SOFC Anodes in H₂/H₂O Atmospheres, in *Proceedings of the Fifth International Symposium on SOFC, Aachen, Germany, June 2–5, 1997*, Vol. 97–40, The Electrochemical Society, Pennington, NJ, pp. 530–539.
- S. Primdahl and M. Mogensen [1998] Gas Conversion Impedance: A Test Geometry Effect in Characterization of Solid Oxide Fuel Cell Anodes, *J. Electrochem. Soc.* **145**, 2431–2438.
- P. P. Prosini, M. Lisi, D. Zanec, and M. Pasquali [2002] Determination of the Chemical Diffusion Coefficient of Lithium in LiFePO₄, *Solid State Ionics* **148**(1–2), 45–51.
- M. Proskurnin and A. N. Frumkin [1935] Determination of the Capacity of the Electric Double Layer, *Trans. Faraday Soc.* **31**, 110–115.
- S. W. Provencher [1976] An Eigenfunction Expansion Method for the Analysis of Exponential Decay Curves, *J. Chem. Phys.* **64**, 2772, <http://s-provencher.com/pages/discrete.shtml> (accessed on November 3, 2017).
- S.-I. Pyun and J.-S. Bae [1996] Lithium Ion Transport in R.F.-Magnetron Sputtered WO₃ Film as a Function of Lithium Content, *J. Alloys Compounds* **245**, L1–L4.
- S.-I. Pyun, D.-J. Kim, and J.-S. Bae [1996] Hydrogen Transport Through R.-F. Magnetron Sputtered Amorphous and Crystalline WO₃ Films, *J. Alloys Compounds* **244**, 19–22.
- X. Qian, N. Gu, Z. Cheng, X. Yang, E. Wang, and S. Dong [2002] Plasticizer Effect on the Ionic Conductivity of PEO-Based Polymer Electrolyte, *Mater. Chem. Phys.* **74**, 98–103.
- J. L. Rae [1979] The Electrophysiology of the Crystalline Lens, *Curr. Top. Eye Res.* **1**, 37–90.

- J. L. Rae and R. A. Levis [1992] A Method for Exceptionally Low Noise Single Channel Recordings, *Pflugers Arch.* **420** (5–6), 618–620.
- J. L. Rae, R. T. Mathias, and R. S. Eisenberg [1982] Physiological Role of the Membranes and Extracellular Space with the Ocular Lens, *Exp. Eye Res.* **35**(5), 471–489.
- J. L. Rae, R. D. Thomson, and R. S. Eisenberg [1982] The Effect of 2-4 Dinitrophenol on Cell to Cell Communication in the Frog Lens, *Exp. Eye Res.* **35**(6), 597–609.
- J. L. Rae, R. A. Levis, and R. S. Eisenberg [1988] Ionic Channels in Ocular Epithelia, in *Ion Channels*, Vol. 1, ed. T. Narahashi, Plenum, New York, pp. 283–327.
- J. L. Rae, C. Bartling, J. Rae, and R. T. Mathias [1996] Dye Transfer Between Cells of the Lens, *J. Membr. Biol.* **150**(1), 89–103.
- D. V. Ragone [1968] Review of Battery Systems for Electrically Powered Vehicles, in *Proceedings of the Society of Automotive Engineers Conference on Review of Battery Systems for Electric Vehicles*, Detroit, MI, Society of Automotive Engineers, Warrendale, PA.
- S.-U. Rahman, M. A. Al-Saleh, A. S. Al-Zakri, and S. Gultekin [1997] Preparation of Raney-Ni Gas Diffusion Electrode by Filtration Method for Alkaline Fuel Cells, *J. Appl. Electrochem.* **27**, 215–220.
- I. D. Raistrick [1983] Lithium Insertion Reactions in Tungsten and Vanadium Oxide Bronzes, *Solid State Ionics* **9**(10), 425–430.
- I. D. Raistrick, C. Ho, and R. A. Huggins [1976] Ionic Conductivity of Some Lithium Silicates and Aluminosilicates, *J. Electrochem. Soc.* **123**, 1469–1476.
- I. D. Raistrick, C. Ho, Y.-W. Hu, and R. A. Huggins [1977] Ionic Conductivity and Electrode Effects on β -PbF₂, *J. Electroanal. Chem.* **77**, 319–337.
- N. Rajalakshmi, K. S. Dhathathreyana, and S. Ramaprabhub [2001] Electrochemical Investigations of ZrCrmFenCopVo ($m+n+o+p=2$) Electrode for Ni-MH Battery Applications, *Int. J. Hydrogen Energy* **26**(10), 1097–1102.
- S. Rajendran, R. Kannan, and O. Mahendran [2001] Study on Li ion Conduction Behaviour of the Plasticized Polymer Electrolytes Based on Poly Acrylonitrile, *Mater. Lett.* **48**(6), 331–335.
- D. O. Raleigh [1976] The Electrochemical Double Layer in Solid Electrolytes, in *Electrode Processes in Solid State Ionics*, eds. M. Kleitz and J. Dupuy, Reidel, Dordrecht, the Netherlands/Boston, MA, pp. 119–147.
- A. C. Ramamurthy and S. K. Rangarajan [1977] Fournier Polarography Revisited, *J. Electroanal. Chem.* **77**, 267–286.
- J.-P. Randin and R. Viennet [1982] Proton Diffusion in Tungsten Trioxide Thin Films, *J. Electrochem. Soc.* **129**, 2349–2354.
- J. E. B. Randles [1947] Kinetics of Rapid Electrode Reactions, *Disc. Faraday Soc.* **1**, 11–19.
- J. E. B. Randles [1952] Kinetics of Rapid Electrode Reactions. II. Rate Constants and Activation Energies of Electrode Reactions, *Trans. Faraday Soc.* **48**, 828–832.
- J. E. B. Randles and K. W. Somerton [1952] Kinetics of Rapid Electrode Reactions, Parts 3 and 4, *Trans. Farad. Soc.* **48** (937–950), 951–955.
- S. K. Rangarajan [1974] A Simplified Approach to Linear Electrochemical Systems. I. The Formalism; II. Phenomenological Coupling; III. The Hierarchy of Special Cases; IV. Electron Transfer Through Adsorbed Modes, *J. Electroanal. Chem.* **55**, 297–327, 329–335, 337–361, 363–374.
- S. K. Rangarajan [1975] Non Linear Relaxation Methods. III. Current Controlled Perturbations, *J. Electroanal. Chem.* **62**, 31–41.
- Y. Rangom, X. Tang, and L. F. Nazar [2015] Carbon Nanotube-Based Supercapacitors with Excellent AC Line Filtering and Rate Capability via Improved Interfacial Impedance, *ACS Nano* **9**(7), 7248–7255.
- G. P. Rao and A. K. Mishra [1977] Some AC Techniques to Evaluate the Kinetics of Corrosion Kinetics, *J. Electroanal. Chem.* **77**, 121.
- D. Ravaine and J.-L. Souquet [1973] Application du Trace des Diagrammes D'Impedance Complex de la Determination de la Conductivité Electrique des Verres Silice-Oxyde Alcalin, *Compt. Rend. Acad. Sci. (Paris)* **277**C, 489–492.
- R. W. Reeve, P. A. Christensen, A. J. Dickinson, A. Hamnett, and K. Scott [2000] Methanol-Tolerant Oxygen Reduction Catalysts Based on Transition Metal Sulfides and Their Application to the Study of Methanol Permeation, *Electrochim. Acta* **45**, 4237–4250.
- L. E. Reichl [1977] *Fast Fourier Transform Module: Product Guide*, Reticon Model R5601. The Reticon Corporation, Sunnyvale, CA.
- L. E. Reichl [1980] *A Modern Course in Statistical Physics*, University of Texas Press, Austin, TX, Tex. Reticon Corporation.
- M. A. Reid [1990] Impedance Studies of Nickel/Cadmium and Nickel/Hydrogen Cells Using the Cell Case as a Reference Electrode, *J. Power Sources* **29**(3–4), 467–476.
- G. Reinhardt and W. Göpel [1998] Electrode Reactions at Solid Electrolytes: Finite Difference Calculations to Describe Geometric and Electrical Properties of Planar Devices, *Proceedings of the Electrochemical Society*.
- C. Rerolle and R. Wiart [1996] Kinetics of Oxygen Evolution on Pb and Pb-Ag Anodes During Zinc Electrowinning, *Electrochim. Acta* **41**, 1063–1069.
- E. Rhoderick and R. H. Williams [1988] *Metal-Semiconductor Contacts*, 2nd Edition, Oxford Science Publications, Oxford, UK.
- R. Richert [1994] Homogeneous Dispersion of Dielectric Responses in a Simple Glass, *J. Non-Cryst. Sol.* **172–174**, 209–213.
- R. Richert and A. Blumen, (eds.) [1994] *Disorder Effects on Relaxational Processes: Glasses, Polymers, Proteins*, Springer-Verlag, Berlin/Heidelberg, Germany.
- R. Richert, A. Agapov, and A. P. Sokolov [2011] Appearance of a Debye Peak at the Conductivity Relaxation Frequency of a Viscous Liquid, *J. Chem. Phys.* **134**, 104508.

- F. Richter [1997] Impedance Measurements Under High Current for Development and Quality Control of Solid Oxide Fuel Cells (SOFCs), *Electrochim. Appl.* **1**, 3–7, <http://www.zahner.de> (accessed on November 3, 2017).
- E. Ríos and G. Pizarro [1991] Voltage Sensor of Excitation-Contraction Coupling in Skeletal Muscle, *Phys. Rev.* **71**(3), 849–908.
- A. Rivera, C. León, J. Sanz, J. Santamaría, C. T. Moynihan, and K. L. Ngai [2002] Crossover of Near-Constant Loss to Ion Hopping Relaxation in Ionically Conducting Materials: Experimental Evidences and Theoretical Interpretation, *J. Non-Cryst. Solids* **305**, 88–95.
- J. F. Robinson and Y. P. Kayinamura [2009] Charge Transport in Conducting Polymers: Insights from Impedance Spectroscopy, *Chem. Soc. Rev.* **38**, 3339–3347.
- S. Rodrigues, N. Munichandraiah, and A. K. Shukla [2000] A Review of State-of-Charge Indication of Batteries by Means of A.C. Impedance Measurements, *J. Power Sources* **87**, 12–20.
- C. M. Roland [2011] *Viscoelastic Behavior of Rubbery Materials*, Oxford University Press, Oxford, UK.
- C. M. Roland, K. L. Ngai, P. G. Santangelo, X. H. Qiu, M. D. Ediger, and D. J. Plazek [2001] Temperature Dependence of Segmental and Terminal Relaxation in Atactic Polypropylene, *Macromolecules* **34**, 6159–6160.
- B. Roling, C. Martiny, and S. Murugavel [2001] Ionic Conduction in Glass: New Information on the Interrelation Between the “Jonscher Behavior” and the “Nearly Constant-Loss Behavior” from Broadband Conductivity Spectra, *Phys. Rev. Lett.* **87**, 085901-1–085901-4.
- A. Roos, D. R. Franceschetti, and J. Schoonman [1984] The Small Signal AC Response of $\text{La}_{1-x}\text{Ba}_x\text{F}_{3-x}$ Solid Solutions, *Solid State Ionics* **12**, 485–491.
- E. Rössler, V. N. Novikov, and A. P. Sokolov [1997] Toward a General Description of the Dynamics of Glass Formers, *Phase Transit.* **63**(1–4), 201–233.
- P. R. Roth [1970] Digital Fourier Analysis. Some of the Theoretical and Practical Aspects of Measurements Involving Fourier Analysis by Digital Instrumentation, *Hewlett Packard J.* **21**, 2.
- J. Rouxel [1979] Recent Progress in Intercalation Chemistry: Alkali Metal in Chalcogenide Hosts, *Rev. Inorg. Chem.* **1**, 245–279.
- A. Rudge, J. Davey, I. D. Raistrick, and S. Gottesfeld [1994] Conducting Polymers as Active Materials in Electrochemical Capacitors, *J. Power Sources* **47**, 89–107.
- A. Rudge, I. D. Raistrick, S. Gottesfeld, and J. P. Ferraris [1994] A Study of the Electrochemical Properties of Conducting Polymers for Application in Electrochemical Capacitors, *Electrochim. Acta* **39**, 273–287.
- R. Ruffo, S. S. Hong, C. K. Chan, R. A. Huggins, and Y. Cui [2009] Impedance Analysis of Silicon Nanowire Lithium Ion Battery Anodes, *J. Phys. Chem. C* **113**(26), 11390–11398.
- B. Russell [1995] Striated Muscle, in *Gray's Anatomy*, Churchill Livingstone, London, UK.
- C. T. Sah [1970] The Equivalent Circuit Model in Solid-State Electronics—III: Conduction and Displacement Currents, *Solid State Electron.* **13**(12), 1547–1575.
- M. Y. Saïd, J. Barker, H. Huang, J. L. Swoyer, and G. Adamson [2003] Performance Characteristics of Lithium Vanadium Phosphate as a Cathode Material for Lithium-Ion Batteries, *J. Power Sources* **119**–**121**, 266–272.
- Y. Saito, H. Kataoka, T. Sakai, and S. Deki [2001] Conduction Properties of Lithium Gel Electrolytes Investigated by Impedance Spectroscopy and Pulsed-Field Gradient NMR with Electric Field, *Electrochim. Acta* **46**(10–11), 1747–1751.
- B. Sakmann and E. Neher [1995] *Single Channel Recording*, Plenum, New York.
- A. Salkind, T. Atwater, P. Singh, S. Nalatryk, S. Damodar, C. Fennie, Jr., and D. Raisner [2001] Dynamic Characterization of Small Lead-Acid Cells, *J. Power Sources* **96**, 151–159.
- R. P. Sallen and E. L. Key [1955] A Practical Method of Designing RC Active Filters, *IEEE Trans. CT-2*, 74.
- J. R. Sandifer and R. P. Buck [1974] Impedance Characteristics of Ion Selective Glass Electrodes, *J. Electroanal. Chem.* **56**, 385–398.
- P. A. Santoro, J. L. de Paula, E. K. Lenzi, and L. R. Evangelista [2011] Anomalous Diffusion Governed by a Fractional Diffusion Equation and the Electrical Response of an Electrolytic Cell, *J. Chem. Phys.* **135**, 114704.
- N. Sato [1978] in *Passivity of Metals*, eds. R. P. Frankenthal and J. Kruger, The Electrochemical Society, Pennington, NJ, p. 29.
- N. Sato and M. Cohen [1964] Kinetics of Anodic Oxidation of Iron in Neutral Solution, *J. Electrochem. Soc.* **111**, 512–522.
- O. Savadogo [2004] Emerging Membranes for Electrochemical Systems Part II. High Temperature Composite Membranes for Polymer Electrolyte Fuel Cells, *J. Power Sources* **127**, 135–161.
- B. Savova-Stoynov and Z. Stoynov [1985] Computer Analysis of Non-Stationary Impedance Data, in *Proceedings of the Symposium on Computer Aided Acquisition and Analysis of Corrosion Data*, Vol. 85-3, eds. M. W. Kendig, U. Bertocci, and J. E. Strutt, Electrochemical Society Inc., Pennington, NJ, pp. 152–158.
- B. Savova-Stoynov and Z. B. Stoynov [1992] Four-Dimensional Estimation of the Instantaneous Impedance, *Electrochim. Acta* **37**, 2353–2355.
- K. Sawai, Y. Iwakoshi, and T. Ohzuku [1994] Carbon Materials for Lithium-Ion (Shuttlecock) Cells, *Solid State Ionics* **69** (3/4), 273.
- D. F. Schanne and E. Ruiz-Ceretti [1978] *Impedance Measurements in Biological Cells*, John Wiley & Sons, Inc., New York.
- W. Scheider [1975] Theory of the Frequency Dispersion of Electrode Polarization: Topology of Networks with Fractional Power Frequency Dependence, *J. Phys. Chem.* **79**, 127–136.
- H. Scher and M. Lax [1973a] Stochastic Transport in Disordered Solids. I. Theory, *Phys. Rev. B* **7**, 4491–4502.

- H. Scher and M. Lax [1973b] Stochastic Transport in Disordered Solids. II. Impurity Conduction, *Phys. Rev. B* **7**, 4502–4519.
- H. Scher and E. W. Montroll [1975] Anomalous Transit-Time Dispersion in Amorphous Solids, *Phys. Rev. B* **12**, 2455–2477.
- G. Schiller, R. H. Henne, M. Lang, R. Ruckdäschel, and S. Schaper [2000] Development of Vacuum Plasma Sprayed Thin-Film SOFC for Reduced Operating Temperature, *Fuel Cells Bull.* **21**, 7–12.
- C. A. Schiller, F. Richter, E. Gützow, and N. Wagner [2001] Validation and Evaluation of Electrochemical Impedance Spectra of Systems with States That Change with Time, *J. Phys. Chem. Chem. Phys.* **3**, 374–378.
- W. Schirmacher, G. Diezemann, and C. Ganter [1998] Harmonic Vibrational Excitations in Disordered Solids and the "Boson Peak", *Phys. Rev. Lett.* **81**(1), 136–139.
- M. F. Schlesinger [1984] Williams-Watts Dielectric Relaxation: A Fractal Time Stochastic Process, *J. Stat. Phys.* **36**, 639–648.
- M. F. Schlesinger and E. W. Montroll [1984] On the Williams-Watts Function of Dielectric Relaxation, *Proc. Natl. Acad. Sci.* **81**, 1280–1283.
- T. J. Schmidt, H. A. Gasteiger, G. D. Stäb, P. M. Urban, D. M. Kolb, and R. J. Behm [1998] Characterization of High-Surface-Area Electrocatalysts Using a Rotating Disk Electrode Configuration, *J. Electrochem. Soc.* **145**, 2354–2358.
- M. F. Schneider [1970] Linear Electrical Properties of the Transverse Tubules and Surface Membrane of Skeletal Muscle Fibers, *J. Gen. Physiol.* **56**(5), 640–671.
- U. Schneider, P. Lunkenheimer, R. Brand, and A. Loidl [1998] Dielectric and Far-Infrared Spectroscopy of Glycerol, *J. Non-Cryst. Solids* **235–237**, 173–179.
- U. Schneider, P. Lunkenheimer, R. Brand, and A. Loidl [1999] Broadband Dielectric Spectroscopy on Glass-Forming Propylene Carbonate, *Phys. Rev. E* **59**(6), 6924.
- U. Schneider, R. Brand, P. Lunkenheimer, and A. Loidl [2000] Excess Wing in the Dielectric Loss of Glass Formers: A Johari-Goldstein β Relaxation? *Phys. Rev. Lett.* **84**(24), 5560–5563.
- A. Schönhals, F. Kremer, and E. Schlosser [1991, 1993] Scaling of the α Relaxation in Low-Molecular-Weight Glass-Forming Liquids and Polymers, *Phys. Rev. Lett.* **67**, 999.
- A. Schönhals, F. Kremer, and F. Stickel [1993] Schönhals, Kremer, and Stickel Reply, *Phys. Rev. Lett.* **71**, 4096.
- W. Schottky [1939] Zur Halbeitertheorie der Sperrschiene- und Spitzengleichrichter, *Z. Phys.* **113**, 367–414.
- W. Schottky [1942] Vereinfachte und erweiterte Theorie der Randschichtegleichrichter, *Z. Phys.* **118**, 539–592.
- J. Schoukens, R. Pintelon, Y. Rolain, and T. Dobrowiecki [2001] Frequency Response Function Measurements in the Presence of Nonlinear Distortions, *Automatica* **37**(6), 939–946.
- E. J. L. Schouler [1979] *Etude des Cellules à Oxyde Electrolyte Solide par la Méthode des Impédances Complexes: Applications à la Mesure Precise de la Conductivité et à l'Etude de la Réaction d'Electrode à Oxygène*, Ph.D. thesis, Institut National Polytechnique de Grenoble, France.
- E. J. L. Schouler, G. Giroud, and M. Kleitz [1973] Application selon Bauerle du Tracé des Diagrammes d'Admittance Complexes en Électrochimie des Solides, *J. Chim. Phys.* **70**, 1309–1316.
- E. J. L. Schouler, M. Kleitz, E. Forest, E. Fernandez, and P. Fabry [1981] Overpotential of $\text{H}_2\text{-H}_2\text{O}/\text{YSZ}$ Electrodes in Steam Electrolyzers, *Solid State Ionics* **5**, 559–562.
- E. J. L. Schouler, N. Mesbahi, and G. Vitter [1983] In Situ Study of the Sintering Process of Yttria Stabilized Zirconia by Impedance Spectroscopy, *Solid State Ionics* **9–10**, 989–996.
- J. Schrama [1957] On the Phenomenological Theory of Linear Relaxation Processes, Ph.D. thesis, University of Leiden, Leiden, the Netherlands.
- D. Schroder [1998] *Semiconductor Material and Device Characterization*, 2nd Edition, Wiley-Interscience, New York.
- J. W. Schultze and F. D. Koppitz [1976a] Bond Formation in Electrosorbates. I. Correlation Between the Electrosorption Valency and Pauling's Electronegativity for Aqueous Solutions, *Electrochim. Acta* **21**, 327–336.
- J. W. Schultze and F. D. Koppitz [1976b] Bond Formation in Electrosorbates. II. Electrosorption and Double Layer Properties in Nonaqueous Solvents, *Electrochim. Acta* **21**, 337–343.
- M. Schulze, N. Wagner, T. Kaz, and K. A. Friedrich [2007] Combined Electrochemical and Surface Analysis Investigation of Degradation Processes in Polymer Electrolyte Membrane Fuel Cells, *Electrochim. Acta* **52**, 2328–2336.
- H. J. Schütt and E. Gerdes [1992a] Space-Charge Relaxation in Ionically Conducting Oxide Glasses. I. Model and Frequency Response, *J. Non-Cryst. Solids* **144**, 1–13.
- H. J. Schütt and E. Gerdes [1992b] Space-Charge Relaxation in Ionically Conducting Oxide Glasses. II. Free Carrier Concentration and Mobility, *J. Non-Cryst. Solids* **144**, 14–20.
- H. G. Scott [1975] Phase Relationships in the Zirconia-Yttria System, *J. Mater. Sci.* **10**, 1527–1535.
- B. Scrosati [1981] Non Aqueous Lithium Cells, *Electrochim. Acta* **26**, 1559–1567.
- M. Seralathan and R. de Levie [1987] On the Electrode Admittance of Complex Electrode Reactions, in *Electro-Analytical Chemistry*, ed. A. J. Bard, Marcel Dekker, New York.
- A. Serghei, M. Tress, J. R. Sangoro, and F. Kremer [2009] Electrode Polarization and Charge Transport at Solid Interfaces, *Phys. Rev. B* **80**, 184301.
- S. Sharifi-Asl, D. D. Macdonald, A. Almarzooqi, B. Kursten, and G. R. Engelhardt [2013] A Comprehensive Electrochemical Impedance Spectroscopic Study of Passive Carbon Steel in Concrete Pore Water Solution, *J. Electrochem. Soc.* **160**(8), C316–C325.
- S. Sharifi-Asl, M. L. Taylor, Z. Lu, G. R. Engelhardt, B. Kursten, and D. D. Macdonald [2013] Modeling of the Electrochemical Impedance Spectroscopic Behavior of Passive Iron Using a Genetic Algorithm Approach, *Electrochim. Acta* **102**, 161–173.

- N. Sharma, M., Deepa, and S. A. Agnihotry [2002] Impedance Studies of Li Inserted Sol-Gel Derived WO_3 Films, *Solid State Ionics* **152–153**, 873–875.
- W.-M. Shen, W. Siripala, and M. Tomkiewicz [1986] Electrolyte Electroreflectance Study of Surface Optimization of n-CuInSe₂ in Photoelectrochemical Solar Cells, *J. Electrochem. Soc.* **133**, 107–111.
- W.-M. Shen, M. Tomkiewicz, and D. Cahen [1986] Impedance Study of Surface Optimization of n-CuInSe₂ in Photoelectrochemical Solar Cells, *J. Electrochem. Soc.* **133**, 112–116.
- J. Sibik and J. A. Zeitler [2016] Study of Disordered Materials by Terahertz Spectroscopy, in *Disordered Pharmaceutical Materials*, 1st Edition, ed. M. Descamps, Wiley-Interscience, New York, pp. 393–425.
- D. L. Sidebottom [1999] Universal Approach for Scaling the AC Conductivity in Ionic Glasses, *Phys. Rev. Lett.* **82**, 3653–3656.
- D. L. Sidebottom, P. F. Green, and R. K. Brow [1995] Two Contributions to the AC Conductivity of Alkali Oxide Glasses, *Phys. Rev. Lett.* **74**(25), 5068–5071.
- H. B. Sierra-Alcazar [1976] The Electrodeposition of Zinc, Ph. D. thesis, University of Newcastle-upon-Tyne, England.
- H. B. Sierra-Alcazar, A. N. Fleming, and J. A. Harrison [1977] A Rapid On-Line Method for Electrochemical Investigations, *Surface Technol.* **6**, 61.
- F. Sigworth [1995] Electronic Design of Patch Clamp, in *Single Channel Recording*, eds. B. Sakmann and E. Neher, Plenum, New York, pp. 95–128.
- F. J. Sigworth and E. Neher [1980] Single Na⁺ Channel Currents Observed in Cultured Rat Muscle Cells, *Nature* **287** (5781), 447–449.
- A. Sihvola [1999] *Electromagnetic Mixing Formulas and Applications*, IEE Electromagnetic Waves Series, Vol. 47, eds. P. J. B. Clarricoats and E. V. Jull, The Institute of Electrical Engineers, London, UK.
- S. Silverman, G. Cagnolino, and D. D. Macdonald [1982] An Ellipsometric Investigation of Passive Films Formed on Fe-25 Ni-xCr Alloys in Boric Buffer Solution, *J. Electrochem. Soc.* **129**, 2419–2424.
- W. M. Siu and R. S. C. Cobbald [1979] Basic Properties of the Electrolyte-Silicon Dioxide-Silicon System: Physical and Theoretical Aspects, *IEEE Trans. Electron Devices* **ED-26**, 1805–1815.
- R. K. Slotwinski, N. Bonanos, and E. P. Butler [1985] Electrical Properties of MgO + Y₂O₃ and CaO + Y₂O₃ Partially Stabilized Zirconias, *J. Mater. Sci. Lett.* **4**, 641–644.
- J. H. Sluyters [1960] On the Impedance of Galvanic Cells, I, *Recl. Trav. Chim.* **79**, 1092–1100.
- J. H. Sluyters [1963] On the Impedance of Galvanic Cells. V. The Impedance of a Galvanic Cell with Two Plane Parallel Electrodes at a Short Distance, *Recl. Trav. Chim.* **82**, 100–109.
- J. H. Sluyters and J. J. C. Oomen [1960] On the Impedance of Galvanic Cells. II. Experimental Verification, *Recl. Trav. Chim.* **79**, 1101–1110.
- M. Sluyters-Rehbach and J. H. Sluyters [1964a] On the Impedance of Galvanic Cells. IX. The Double Layer Capacity of the Mercury-M HClO₄ Interface at High Direct Current Potentials, *Recl. Trav. Chim. Pays Bas* **83**, 217–222.
- M. Sluyters-Rehbach and J. H. Sluyters [1964b] Impedance of Galvanic Cells. X. The Impedance of the H⁺/H₂(Hg)-Electrode in 1M Perchloric Acid, *Recl. Trav. Chim. Pays Bas* **83**, 581–586.
- M. Sluyters-Rehbach and J. H. Sluyters [1964c] The Impedance of Galvanic Cells. XI. The Impedance of the Hg-Hg²⁺⁺ Electrode in 1M and 0.1M HClO₄, *Recl. Trav. Chim. Pays Bas* **83**, 967–975.
- M. Sluyters-Rehbach and J. H. Sluyters [1970] Sine Wave Methods in the Study of Electrode Processes, in *Electroanalytical Chemistry*, Vol. 4, ed. A. J. Bard, Marcel Dekker, New York, pp. 1–127.
- M. Sluyters-Rehbach and J. H. Sluyters [1984] AC Techniques, in *Comprehensive Treatise of Electrochemistry*, Vol. 9, eds. E. Yaeger, J. O'M. Bockris, B. E. Conway, and S. Sarangapani, Plenum Press, New York.
- P. H. Smith [1939] Transmission Line Calculator, *Electronics* **12**, 29–31.
- P. H. Smith [1944] An Improved Transmission Line Calculator, *Electronics* **17**(130–133), 318–325.
- D. E. Smith [1966] AC Polarography and Related Techniques: Theory and Practice, in *Electroanalytical Chemistry*, Vol. 1, ed. A. J. Bard, Marcel Dekker, New York, pp. 1–155.
- D. E. Smith [1971] Computers in Chemical Instrumentation: Application of On-Line Digital Computers to Chemical Instrumentation, *CRC Crit. Rev. Anal. Chem.* **2**, 248.
- D. E. Smith [1976] The Acquisition of Electrochemical Response Spectra by On-Line Fast Fourier Transform: Data Processing in Electrochemistry, *Anal. Chem.* **48**, 221A.
- W. Smyrl [1985] Digital Impedance for Faradaic Analysis. III. Copper Corrosion in Oxygenated 0.1 N HCl, *J. Electrochem. Soc.* **132**, 1563–1567.
- W. Smyrl [1985a] Digital Impedance for Faradaic Analysis. I. Introduction to Digital Signal Analysis and Impedance Measurements for Electrochemical and Corrosion Systems, *J. Electrochem. Soc.* **132**, 1551–1555.
- W. Smyrl and L. L. Stephenson [1985] Digital Impedance for Faradaic Analysis. II. Electrodissolution of Cu in HCl, *J. Electrochem. Soc.* **132**, 1555–1562.
- C. P. Smyth [1938] *Dielectric Behavior and Structure*, McGraw Hill, New York.
- L. Solymar and D. Walsh [1999] *Electrical Properties of Materials*, 6th Edition, Oxford Science Publications, Oxford, UK.
- I. Sorar, E. Pehlivan, G. A. Niklasson, and C. G. Granqvist [2013] Electrochromism of DC Magnetron Sputtered TiO₂ Thin Films: Role of Deposition Parameters, *Sol. Energy Mater. Sol. Cells* **115**, 172–180.
- P. R. Sorensen and T. Jacobsen [1982] Conductivity Charge Transfer and Transport Number: An Investigation of the Polymer Electrolyte LiSCN-Poly(Ethylene Oxide), *Electrochim. Acta* **27**, 1671–1675.

- T. E. Springer, T. A. Zawodzinski, M. S. Wilson, and S. Gottesfeld [1996] Characterisation of Polymer Electrolyte Fuel Cells Using AC Impedance Spectroscopy, *J. Electrochem. Soc.* **143**, 587–599.
- S. Srinivasan, E. A. Ticianelli, C. R. Derouin, and A. Redondo [1988] Advances in Solid Polymer Electrolyte Fuel Cell Technology with Low Platinum Loading Electrodes, *J. Power Sources* **22**, 359–375.
- U. Staudt and G. Schön [1981] Automatic Spectroscopy of Solids in the Low Frequency Range, *Solid State Ionics* **2**, 175–183.
- B. C. H. Steele [1976] High Temperature Fuel Cells and Electrolysers, in *Electrode Processes in Solid State Ionics*, eds. M. Kleitz and J. Dupuy, Reidel, Dordrecht/Boston, MA, pp. 368–384.
- B. C. H. Steele and E. P. Butler [1985] Electrical Behaviour of Grain Boundaries in Zirconia and Related Ceramic Electrolytes, *Br. Ceram. Proc.* **36**, 45–55.
- B. C. H. Steele, J. Drennan, R. K. Slotwinski, N. Bonanos, and E. P. Butler [1981] Factors Affecting the Performance of Oxygen Monitors, in *Advances in Ceramics*, Vol. 3, eds. A. H. Heuer and L. W. Hobbs, American Ceramic Society, Columbus, OH, pp. 286–309.
- O. Stern [1924] The Theory of the Electrolytic Double-Layer, *Zeit. Elektrochem.* **30**, 508–516.
- M. Stern and A. L. Geary [1957] Electrochemical Polarization. I. Shape of Polarization Curves, *J. Electrochem. Soc.* **104**, 56.
- F. Stickel, E. W. Fischer, and R. Richert [1996] Dynamics of Glass-Forming Liquids. II. Detailed Comparison of Dielectric Relaxation, DC-Conductivity, and Viscosity Data, *J. Chem. Phys.* **104**, 2043–2055.
- F. H. Stillinger [1995] A Topographic View of Supercooled Liquids and Glass Formation, *Science* **267**(5206), 1935–1939.
- Z. Stoynov [1990] Impedance Modelling and Data Processing: Structural and Parametrical Estimation, *Electrochim. Acta* **35**, 1493–1499.
- U. Strom and P. C. Taylor [1977] Temperature and Frequency Dependences of the Far-Infrared and Microwave Optical Absorption in Amorphous Materials, *Phys. Rev. B* **16**(12), 5512–5522.
- U. Strom, J. R. Hendrickson, R. J. Wagner, and P. C. Taylor [1974] Disorder-Induced Far Infrared Absorption in Amorphous Materials, *Solid State Commun.* **15**, 1871–1875.
- M. Strømme Mattsson [2000] Li Insertion into WO_3 : Introduction of a New Electrochemical Analysis Method and Comparison with Impedance Spectroscopy and the Galvanostatic Intermittent Titration Technique, *Solid State Ionics* **131**, 261–273.
- M. Strømme Mattsson and G. A. Niklasson [1999] Isothermal Transient Ionic Current as a Characterization Technique for Ion Transport in Ta_2O_5 , *J. Appl. Phys.* **85**, 8199–8204.
- M. Strømme Mattsson, G. A. Niklasson, and C. G. Granqvist [1996a] Fractal Dimension of Li Insertion Electrodes Studied by Diffusion-Controlled Voltammetry and Impedance Spectroscopy, *Phys. Rev. B* **54**, 2968–2971.
- M. Strømme Mattsson, G. A. Niklasson, and A. G. Granqvist [1996c] Li Diffusion in Ti Oxyfluoride Films: Thermal Activation Energy and Jump Length Derived from Impedance Spectroscopy, *J. Appl. Phys.* **80**, 2169–2174.
- M. Strømme Mattsson, G. A. Niklasson, and C. G. Granqvist [1997] Diffusion of Li, Na and K in Fluorinated Ti Dioxide Films: Applicability of the Anderson-Stuart Model, *J. Appl. Phys.* **81**, 2167–2172.
- M. Strømme Mattsson, G. A. Niklasson, K. Forsgren, and A. Härsta [1999a] A Frequency Response and Transient Current Study of $\beta\text{-Ta}_2\text{O}_5$: Methods of Estimating the Dielectric Constant, DC Conductivity and Ion Mobility, *J. Appl. Phys.* **85**, 2185–2191.
- M. Strømme Mattsson, J. Isidorsson, and T. Lindström [1999b] A Theoretical Analysis of Chronoamperometric Electrochemical Ion Intercalation, *J. Electrochem. Soc.* **146**, 2613–2615.
- M. Strømme, A. Gutarra, G. A. Niklasson, and C. G. Granqvist [1996b] Impedance Spectroscopy on Lithiated Ti Oxide and Ti Oxyfluoride Thin Films, *J. Appl. Phys.* **79**, 3749–3757.
- M. Strømme, J. Isidorsson, G. A. Niklasson, and C. G. Granqvist [1996] Impedance Studies on Li Insertion Electrodes of Sn Oxide and Oxyfluoride, *J. Appl. Phys.* **80**(1), 233–241.
- M. Strømme, R. Ahuja, and G. A. Niklasson [2004] New Probe of the Electronic Structure of Amorphous Materials, *Phys. Rev. Lett.* **93**, 206403.
- J. E. Strutt, M. W. Weightman, and E. Lilley [1976] A Versatile Cell for the Measurement of Ionic Thermo-Currents (ITC), *J. Phys. E9*, 683–685.
- E. C. Subbarao [1981] Zirconia: An Overview, in *Advances in Ceramics*, Vol. 3, eds. A. H. Heuer and L. W. Hobbs, American Ceramic Society, Columbus, OH, pp. 1–24.
- E. C. Subbarao and H. S. Maiti [1984] Solid Electrolytes with Oxygen Ion Conductivity, *Solid State Ionics* **11**, 317–338.
- Y.-K. Sun, D.-W. Kim, and Y.-M. Choi [1999] Synthesis and Characterization of Spinel $\text{LiMn}_{2-x}\text{Ni}_x\text{O}_4$ for Lithium/Polymer Battery Applications, *J. Power Sources* **79**(2), 231–237.
- S. Sunde [1996a] Monte Carlo Simulations of Conductivity of Composite Electrodes for Solid Oxide Fuel Cells, *J. Electrochem. Soc.* **143**, 1123–1132.
- S. Sunde [1996b] Monte Carlo Simulations of Polarisation Resistance of Composite Electrodes for Solid Oxide Fuel Cells, *J. Electrochem. Soc.* **143**, 1930–1939.
- S. Sunde [1997] Calculations of Impedance of Composite Anodes for Solid Oxide Fuel Cells, *Electrochim. Acta* **42**, 2637–2648.
- S. Sunde [2000] Simulations of Composite Electrodes in Fuel Cells, *J. Electroceramics* **5**, 153–182.
- J. S. E. M. Svensson and C. G. Granqvist [1986] Electrochromic Hydrated Nickel Oxide Coatings for Energy Efficient Windows: Optical Properties and Coloration Mechanism, *Appl. Phys. Lett.* **49**, 1566–1568.

- B. C. Syrett and D. D. Macdonald [1979] The Validity of Electrochemical Methods for Measuring Corrosion Rates of Copper-Nickel Alloys in Seawater, *Corrosion* **35**, 505–508.
- S. M. Sze [1981] *Physics of Semiconductor Devices*, 2nd Edition, Wiley-Interscience, New York.
- S. M. Sze [1985] *Semiconductor Devices, Physics, and Technology*, John Wiley & Sons, Inc., New York.
- L. Sziraki and L. Bobics [2002] Impedance Study of Electrochromism in Anodic Ir Oxide Films, *Electrochim. Acta* **47**, 2189–2197.
- S. Szpak [1991] Experimental Simulation of Porous Electrodes, in *Techniques for Characterization of Electrodes and Electrochemical Processes*, eds. R. Varma and J. R. Selman, Wiley-Interscience, New York, pp. 677–716.
- P. L. Taberna, P. Simon, and J. F. Fauvarque [2003] Electrochemical Characteristics and Impedance Spectroscopic Studies of Carbon-Carbon Supercapacitors, *J. Electrochem. Soc.* **150**, A292–2300.
- I. Takashi, K. Suzuki, and Y. Matsuda [1995] Electrode Characteristics of Various Carbon Materials for Lithium Rechargeable Batteries, *Synth. Met.* **73**(1), 9–20.
- G. Tammann and W. Hesse [1926] Die Abhängigkeit der Viscosität von der Temperatur bei unterkühlten Flüssigkeiten, *Z. Anorg. Allg. Chem.* **156**(1), 245–257.
- B. Tanner [1995] *Introduction to the Physics of Electrons in Solids*, Cambridge University Press, Cambridge, UK.
- M. L. Taylor, S. Sharifi, and D. D. Macdonald [2013] Optimization of Impedance Models with Differential Evolution, *ECS Trans.* **50**(31), 131–139.
- A. J. Terezo, J. Bisquert, E. C. Pereira, and G. Garcia-Belmonte [2001] Separation of Transport, Charge Storage and Reaction Processes of Porous Electrocatalytic IrO_2 and $\text{IrO}_2/\text{Nb}_2\text{O}_5$ Electrodes, *J. Electroanal. Chem.* **508**, 59–69.
- J. Thevenin [1985] Passivating Films on Lithium Electrodes. An Approach by Means of Electrode Impedance Spectroscopy, *J. Power Sources* **14**(1–3), 45–52.
- B. V. Tilak, C. P. Chen, and S. K. Rangarajan [1992] A Model to Characterize the Impedance of Electrochemical Capacitors Arising from Reactions of the Type $\text{O ad} + n \text{ e}^- \rightleftharpoons \text{R ad}$, *J. Electroanal. Chem.* **324**, 405–414.
- B. V. Tilak, C. P. Chen, and S. K. Rangarajan [1993] A Model to Characterize the Impedance of Electrochemical Capacitors Arising from Reactions of the Type $\text{O ad} + n \text{ e}^- \rightleftharpoons \text{R ad}$, *J. Electroanal. Chem.* **356**, 319–321.
- M. Tomkiewicz [1979] Relaxation Spectrum Analysis of Semiconductor-Electrolyte Interface- TiO_2 , *J. Electrochem. Soc.* **126**, 2220–2225.
- Toyota [2015] 2017 Toyota Mirai Fuel Cell Vehicle, <http://www.toyota.com/mirai/fcv.html> (accessed on October 31, 2017).
- Y.-T. Tsai and D. W. Whitmore [1982] Nonlinear Least-Squares Analysis of Complex Impedance and Admittance Data, *Solid State Ionics* **7**, 129–139.
- Y. Tsividis and J. Milios [2013] A Detailed Look at Electrical Equivalents of Uniform Electrochemical Diffusion Using Nonuniform Resistance-Capacitance Ladders, *J. Electroanal. Chem.* **707**, 156–165.
- E. Tuncer, S. M. Gubański, and B. Nettelblad [2001] Dielectric Relaxation in Dielectric Mixtures: Application of the Finite Element Method and Its Comparison with Dielectric Mixture Formulas, *J. Appl. Phys.* **89**(12), 8092–8100.
- E. Tuncer, Y. V. Serdyuk, and S. M. Gubański [2002] Dielectric Mixtures: Electrical Properties and Modeling, *IEEE Trans. Dielectr. Electr. Insul.* **9**(5), 809–828.
- V. A. Tyagai and G. Y. Kolbasov [1972] Use of Kramers-Kronig Relations for the Analysis of Low Frequency Impedance, *Elektrokhimiya* **8**, 59.
- I. Uchida, H. Ishikawa, M. Mohamedi, and M. Umeda [2003] AC-Impedance Measurements During Thermal Runaway Process in Several Lithium/Polymer Batteries, *J. Power Sources* **119–121**, 821–825.
- H. H. Uhlig [1978] in *Passivity of Metals*, eds. R. P. Frankenthal and J. Kruger, The Electrochemical Society, Pennington, NJ, p. 1.
- M. Urquidi-Macdonald, and D. D. Macdonald [1985] Solute/Vacancy Interaction Model for the Effect of Minor Alloying Elements on the Breakdown of Passive Films, *J. Electrochem. Soc.* **85**-1, 29–30.
- M. Urquidi-Macdonald, and D. D. Macdonald [1989] Theoretical Analysis of the Effects of Alloying Elements on Distribution Functions of Passivity Breakdown, *J. Electrochem. Soc.* **136**(4), 961–967.
- M. Urquidi-Macdonald, S. Real, and D. D. Macdonald [1986] Application of Kramers-Kronig Transforms in the Analysis of Electrochemical Impedance Data, II, Transformations in the Complex Plane, *J. Electrochem. Soc.* **133**, 2018–2024.
- M. Urquidi-Macdonald, S. Real, and D. D. Macdonald [1986] Application of Kramers-Kronig Transforms in the Analysis of Electrochemical Impedance Data, II, Transformations in the Complex Plane, *J. Electrochem. Soc.* **133**, 2018–2024.
- M. Urquidi-Macdonald, S. Real, and D. D. Macdonald [1986] Application of Kramers-Kronig Transforms in the Analysis of Electrochemical Impedance Data, II, Transformations in the Complex Plane, *J. Electrochem. Soc.* **133**, 2018–2024.
- M. Urquidi-Macdonald, S. Real, and D. D. Macdonald [1986] Application of Kramers-Kronig Transforms in the Analysis of Electrochemical Impedance Data, II, Transformations in the Complex Plane, *J. Electrochem. Soc.* **133**, 2018–2024.
- R. Valdiosera, C. Clausen, and R. S. Eisenberg [1974a] Measurement of the Impedance of Frog Skeletal Muscle Fibers, *Biophys. J.* **14**, 295–314.
- R. Valdiosera, C. Clausen, and R. S. Eisenberg [1974b] Impedance of Frog Skeletal Muscle Fibers in Various Solutions, *J. Gen. Physiol.* **63**(4), 460–491.
- R. Valdiosera, C. Clausen, and R. S. Eisenberg [1974c] Circuit Models of the Passive Electrical Properties of Frog Skeletal Muscle Fibers, *J. Gen. Physiol.* **63**, 432–459.

- J. Van Herle, A. J. McEvoy, and K. R. Thampi [1994] Conductivity Measurements of Various Yttria-Stabilized Zirconia Samples, *J. Mater. Sci.* **29**, 3691–3701.
- R. L. Van Meirhaeghe, E. C. Dutoit, F. Cardon, and W. P. Gomes [1976] On the Application of the Kramers–Kronig Relations to Problems Concerning the Frequency Dependence of Electrode Impedance, *Electrochim. Acta* **21**, 39–43.
- R. Vannier, O. Théry, C. Kinowski, M. Huvé, C. van Tendeloo, E. Stuart, and F. Abraham [1999] Zr Substituted Bismuth Uranate, *J. Mater. Chem.* **9**, 435–443.
- M. J. Verkerk and A. J. Burggraaf [1983] Oxygen Transfer on Substituted ZrO_2 , Bi_2O_3 , and CeO_2 Electrolytes with Platinum Electrodes II. AC Impedance Study, *J. Electrochem. Soc.* **130**, 78–84.
- M. J. Verkerk, B. J. Middlehuis, and A. J. Burggraaf [1982] Effect of Grain Boundaries on the Conductivity of High-Purity Zirconium Oxide-Yttrium Oxide Ceramics, *Solid State Ionics* **6**, 159–170.
- E. J. W. Verwey [1935] Electrolytic Conduction of a Solid Insulator at High Fields: The Formation of the Anodic Oxide Film on Aluminium, *Physica* **2**, 1059–1063.
- M. Veszelei, M. Strømme Mattsson, L. Kullman, A. Azens, and C. G. Granqvist [1999] Zr-Ce oxides as Candidates for Optically Passive Counter Electrodes, *Sol. Energy Mater. Sol. Cells* **56**, 223–230.
- K. J. Vetter [1967] *Electrochemical Kinetics*, Academic Press, New York.
- K. J. Vetter and F. Gorn [1973] Kinetics of Layer Formation and Corrosion Processes of Passive Iron in Acid Solutions, *Electrochim. Acta* **18**, 321–326.
- W. Vielstich, A. Lamm, and H. Gasteiger, (eds.) [2003] *Handbook of Fuel Cells: Fundamentals, Technology, Applications*, John Wiley & Sons, Inc., New York.
- J. K. Vij and F. Hufnagel [1985] Advances in Microwave and Submillimeter Wave Dielectric Spectroscopic Techniques and Their Applications, in *Dynamical Processes in Condensed Matter*, ed. M. W. Evans, John Wiley & Sons, Inc., New York, p. 775.
- H. Vogel [1921] The Law of the Relationship Between Viscosity of Liquids and the Temperature, *Phys. Z.* **22**, 645–646.
- W. Vogel, J. Lundquist, P. Ross, and P. Stonehart [1975] Reaction Pathways and Poisons-II. The Rate Controlling Step for Electrochemical Oxidation of Hydrogen on Pt in Acid and Poisoning of the Reaction by CO, *Electrochim. Acta* **20**, 79–93.
- J. Volger [1960] Dielectric Properties of Solids in Relation to Imperfections, in *Progress in Semiconductors*, Vol. 4, eds. A. F. Gibson, F. A. Kröger, and R. E. Burgess, Heywood, London, UK, pp. 205–236.
- K. W. Wagner [1914] Explanation of the Dielectric Fatigue Phenomenon on the Basis of Maxwell's Concept, in *Arkiv für Electrotechnik*, ed. H. Schering, Springer-Verlag, Berlin, Germany.
- C. Wagner [1933] Über die Natur des Elektrischen Leitvermögens von a Silbersulfide, *Z. Phys. Chem.* **B21**, 42–52.
- C. Wagner [1953] Investigation on Silver Sulfide, *J. Chem. Phys.* **21**, 1819–1827.
- N. Wagner [2002] Characterization of Membrane Electrode Assemblies in Polymer Electrolyte Fuel Cells Using A.C. Impedance Spectroscopy, *J. Appl. Electrochem.* **32**, 859–863.
- N. Wagner and K. A. Friedrich [2009] Application of Electrochemical Impedance Spectroscopy for Fuel Cell Characterization: PEMFC and Oxygen Reduction Reaction in Alkaline Solution, *Fuel Cells* **9**, 237–246.
- N. Wagner and E. Gülgow [2004] Change of Electrochemical Impedance Spectra (EIS) with Time During CO-Poisoning of the Pt-Anode in a Membrane Fuel Cell, *J. Power Sources* **127**, 341–347.
- N. Wagner and M. Schulze [2003] Change of Electrochemical Impedance Spectra (EIS) During CO-Poisoning of the Pt and Pt-Ru-Anodes in a Membrane Fuel Cell (PEFC), *Electrochim. Acta* **48**, 3899–3907.
- N. Wagner, E. Gülgow, M. Schulze, and W. Schnurnberger [1996] Gas Diffusion Electrodes for Alkaline Fuel Cells, in *Solar Hydrogen Energy, German-Saudi Joint Program on Solar Hydrogen Production and Utilization Phase II 1992–1995*, eds. H. Steeb and H. Aba Oud, Deutsches Zentrum für Luft- und Raumfahrt, Stuttgart, Germany.
- N. Wagner, W. Schnurnberger, B. Müller, and M. Lang [1998] Electrochemical Impedance Spectra of Solid-Oxide Fuel Cells and Polymer Membrane Fuel Cells, *Electrochim. Acta* **43**, 3785–3793.
- N. Wagner, M. Schulze, and E. Gülgow [2004] Long Term Investigations of Silver Cathodes for Alkaline Fuel Cells, *J. Power Sources* **127**(2004), 264–272.
- N. Wagner, T. Kaz, and K. A. Friedrich [2008] Investigation of Electrode Composition of Polymer Fuel Cells by Electrochemical Impedance Spectroscopy, *Electrochim. Acta* **53**, 7475–7482.
- J. Wang and J. M. Bell [1999] The Kinetic Behaviour of Ion Injection in WO_3 Based Films Produced by Sputter and Sol-Gel Deposition: Part II. Diffusion Coefficients, *Sol. Energy Mater. Sol. Cells* **58**, 411–429.
- D. Y. Wang and A. S. Nowick [1979] Cathodic and Anodic Polarization Phenomena at Platinum Electrodes with Doped CeO_{2} as Electrolyte, *J. Electrochem. Soc.* **126** (7), 1166.
- H. Wang and L. Pilon [2012] Intrinsic Limitations of Impedance Measurements in Determining Electric Double Layer Capacitance, *Electrochim. Acta* **63**, 55–63.
- X. Wang, I.-M. Hsing, Y.-J. Leng, and P.-L. Yue [2001] Model Interpretation of Electrochemical Impedance Spectroscopy and Polarization Behavior of H_2/CO Mixture Oxidation in Polymer Electrolyte Fuel Cells, *Electrochim. Acta* **46**, 4397–4405.
- C. Wang, A. J. Appleby, and F. E. Little [2001] Comparison of the Electrochemical Impedance Spectroscopy Characteristics of Insertion Electrode Materials Used in Secondary Metal Hydride and Lithium-Ion Electrodes, *J. Electrochem. Soc.* **148**(7), A762–A767.

- Z.-B. Wang, G.-P. Yin, Y.-Y. Shao, B.-Q. Yang, P.-F. Shi, and P.-X. Feng [2007] Electrochemical Impedance Studies on Carbon Supported PtRuNi and PtRu Anode Catalysts in Acid Medium for Direct Methanol Fuel Cell, *J. Power Sources* **165**, 9–15.
- E. Wanzenberg, F. Tietz, D. Kek, P. Panjan, and D. Stöver [2003] Influence of Electrode Contacts on Conductivity Measurements of Thin YSZ Electrolyte Films and the Impact on Solid Oxide Fuel Cells, *Solid State Ionics* **164**, 121–129.
- K. E. D. Wapenaar and J. Schoonman [1981] Small Signal AC Response of $\text{Ba}_{1-x}\text{La}_x\text{F}_{2+x}$ Crystals, *Solid State Ionics* **2**, 253–263.
- K. E. D. Wapenaar, H. G. Koekkoek, and J. van Turnhout [1982] Low-Temperature Ionic Conductivity and Dielectric Relaxation Phenomena in Fluorite-Type Solid Solutions, *Solid State Ionics* **7**, 225–242.
- E. Warburg [1899] Über das Verhalten sogenannter unpolarisierbarer Elektroden gegen Wechselstrom, *Ann. Phys. Chem.* **67**, 493–499.
- R. M. Waser [1989] Electrochemical Boundary Conditions for Resistance Degradation of Doped Alkaline Earth Titanates, *J. Am. Ceram. Soc.*, **72**(12), 2234–2240.
- S. Wasmus and A. Küver [1999] Methanol Oxidation and Direct Methanol Fuel Cells: A Selective Review, *J. Electroanal. Chem.* **461**, 14–31.
- M. Watanabe, S. K. Rikukawa, and N. Ogata [1985] Evaluation of Ionic Mobility and Transference Number in a Polymeric Solid Electrolyte by Isothermal Transient Ionic Current Method, *J. Appl. Phys.* **58**, 736–740.
- G. H. Weiss and R. J. Rubin [1983] Random Walks: Theory and Selected Applications, *Adv. Chem. Phys.* **52**, 363–505.
- W. van Weperen, B. P. M. Lenting, E. J. Bijrank, and H. W. der Hartog [1977] Effect of the Ce^{3+} Concentration on the Reorientation of Dipoles in $\text{SrF}_2:\text{Ce}^{3+}$, *Phys. Rev.* **B16**, 1953–2958.
- W. Weppner and R. A. Huggins [1977] Determination of the Kinetic Parameters of Mixed Conducting Electrodes and Application to the System Li_3Sb , *J. Electrochem. Soc.* **124**, 1569–1578.
- D. White, S. Ramdas, J. L. Hutchinson, and P. D. Billyard [1989] Surface Profile Imaging of a Bismuth Uranium Oxide, Bi_2UO_6 , *Ultramicroscopy* **31**, 124–131.
- S. Whittingham [1978] Chemistry of Intercalation Compounds: Metal Guests in Chalcogenide Hosts, *Prog. Solid State Chem.* **12**, 41–49.
- M. S. Whittingham and R. A. Huggins [1971] Measurement of Sodium Ion Transport in β -Alumina Using Reversible Solid Electrodes, *J. Chem. Phys.* **54**, 414–416.
- D. P. Wilkinson and D. Thompsett [1997] Materials and Approaches for CO and CO_2 Tolerance for Polymer Electrolyte Fuel Cells, in *Proceedings of the Second National Symposium on New Materials for Fuel Cell and Modern Battery Systems*, Montreal, Quebec, Canada, eds. O. Savadogo and P. R. Roberge, p. 268.
- F. G. Will and C. A. Knorr [1960] Investigation of Formation and Removal of Hydrogen and Oxygen Coverage on Platinum by a New, Nonstationary Method, *Zeit. Elektrochem.* **64**, 258–259.
- G. Williams [1979] Molecular Aspects of Multiple Dielectric Relaxation Processes in Solid Polymers, *Adv. Polym. Sci.* **33**, 59–92.
- G. Williams and D. C. Watts [1970] Non-Symmetrical Dielectric Relaxation Behavior Arising from a Simple Empirical Decay Function, *Trans. Faraday Soc.* **66**, 80–85.
- G. Williams, D. C. Watts, S. B. Dev, and A. M. North [1970] Further Considerations of Non-Symmetrical Dielectric Relaxation Behavior Arising from a Simple Empirical Decay Functions, *Trans. Faraday Soc.* **67**, 1323–1335.
- M. S. Wilson, F. H. Garzon, K. E. Sickafus, and S. Gottesfeld [1993] Surface Area Loss of Supported Platinum in Polymer Electrolyte Fuel Cells, *J. Electrochem. Soc.* **140**, 2872–2877.
- J. M. Wimmer, H. C. Graham, and N. M. Tallan [1974] Microstructural and Polyphase Effects, in *Electrical Conduction in Ceramics and Glasses, Part B*, ed. N. M. Tallan, Marcel Dekker, New York, pp. 619–652.
- J. Winkler, P. V. Hendriksen, N. Bonanos, and M. Mogensen [1998] Geometric Requirements of Solid Electrolyte Cells with a Reference Electrode, *J. Electrochem. Soc.* **145**(4), 1184–1192.
- A. Winsel [1985] *Poröse Gaselektroden*, German Patent, DE 3342969.
- Z. Wojnarowska, C. M. Roland, K. Kolodziejczyk, A. Swiety-Pospiech, K. Grzybowska, and M. Paluch [2012] Quantifying the Structural Dynamics of Pharmaceuticals in the Glassy State, *J. Phys. Chem. Lett.* **3**, 1238–1241.
- J. Wong and C. A. Angell [1976] *Glass: Structure by Spectroscopy*, Dekker, New York.
- T. Wong and M. Brodwin [1980] Dielectric Relaxation Phenomena Associated with Hopping Ionic Conduction, *Solid State Commun.* **36**, 503–508.
- R. N. Work, R. D. McCammon, and R. G. Saba [1964] Effective Dipole Moment of Polypropylene, *J. Chem. Phys.* **41**, 2950.
- Z. Wu and M. Liu [1997] Modelling of Ambipolar Transport Properties of Composite Mixed Ionic-Electronic Conductors, *Solid State Ionics* **93**, 65–84.
- Y. G. Wu, G. M. Wu, X. Y. Ni, and X. Wu [2000] Ion Transport in Electrochromic Nickel Oxide Thin Films, *Sol. Energy Mater. Sol. Cells* **63**, 217–226.
- M. Wubbenhorst and J. van Turnhout [2002] Analysis of Complex Dielectric Spectra. I. One-Dimensional Derivative Techniques and Three-Dimensional Modelling, *J. Non-Cryst. Sol.* **305**, 40–49.
- J. Wuttke, J. Hernandez, G. Lee, G. Coddens, H. Z. Cummins, F. Fujara, W. Petry, and H. Sillescu [1994] Neutron and Light Scattering Study of Supercooled Glycerol. *Phys. Rev. Lett.* **72**(19), 3052–3055.
- J. Wuttke, M. Ohl, M. Goldammer, S. Roth, U. Schneider, P. Lunkenheimer, R. Kahn, B. Rufflé, R. Lechner, and M. A. Berg [2000] Propylene Carbonate Reexamined: Mode-Coupling β Scaling without Factorization? *Phys. Rev. E* **61**, 2730.

- X. Y. Xiong, H. V. Poorten, and M. Crappe [1996] Impedance Parameters of Ni/Cd Batteries: Individual Electrode Characteristics, *Electrochim. Acta* **41**(7/8), 1267–1275.
- X. Yan, M. Hou, L. Sun, D. Liang, Q. Shen, H. Xu, P. Ming, and B. Yi 2007] AC Impedance Characteristics of a 2 kW PEM Fuel Cell Stack Under Different Operating Conditions and Load Changes, *Int. J. Hydrogen Energy* **32**, 4358–4364.
- C. Yoon, Y. Barsukov, and J. H. Kim [2001] Method of and Apparatus for Measuring Battery Capacity by Impedance Spectrum Analysis, US Patent 6,208,147.
- S. Yoon, S.-G. Woo, K.-N. Jung, and H. Song [2014] Conductive Surface Modification of Cauliflower-like WO_3 and its Electrochemical Properties for Lithium-Ion Batteries, *J. Alloys Compounds* **613**, 187–192.
- N. Yoshiike, M. Ayusawa, and S. Kondo [1984] Electrochemical Properties of $\text{WO}_3 \cdot x\text{H}_2\text{O}$. III. Complex Plane Analysis of the Film on SnO_2 , *J. Electrochem. Soc.* **131**, 2600–2605.
- L. Young [1961] *Anodic Oxide Films*, Academic Press, New York.
- X. Yuan, J. C. Sun, H. Wang, and J. Zhang [2006] AC Impedance Diagnosis of a 500 W PEM Fuel Cell Stack: Part II: Individual Cell Impedance, *J. Power Sources* **161**, 929–937.
- Z. H. Yuan, D. Guo, X. Qiu, W. Zhu, and L. Chen [2009] Influence of Metal Oxides on Pt Catalysts for Methanol Electrooxidation Using Electrochemical Impedance Spectroscopy, *J. Power Sources* **188**, 8–13.
- X.-Z. Yuan, C. Song, H. Wang, and J. Zhang [2010] *Electrochemical Impedance Spectroscopy in PEM Fuel Cells*, Springer, London, UK.
- Zahner [2015] PAD4 Parallel AD Converter Plug'n Play Card for Synchronous Parallel Measurements, <http://www.zahner.de/products/addon-cards/pad4.html> (accessed on November 3, 2017).
- R. Zallen [1983] *The Physics of Amorphous Solids*, John Wiley & Sons, Inc., New York.
- J. Zarzycki [1991] *Glasses and the Vitreous State*, Cambridge Solid State Science Series, Cambridge University Press, Cambridge, UK.
- T. Zeuthen [1978] Potentials and Small-Signal Impedance of Platinum Micro-Electrodes in vivo and Vitro, *Med. Biol. Eng. Comput.* **16**, 483–488.
- L. Zhang and D. D. Macdonald [1998] On the Transport of Point Defects in Passive Films, *Electrochim. Acta* **43**, 679–691.
- X. Zhao, X. Fan, S. Wang, S. Yang, B. Yi, Q. Xin, and G. Sun [2005] Determination of Ionic Resibookstance and Optimal Composition in the Anodic Catalyst Layers of DMFC Using AC Impedance, *Int. J. Hydrogen Energy* **30**, 1003–1010.
- O. Zinke and A. Vlcek [1987] *Lehrbuch der Hochfrequenztechnik*, Vols. 1, 3 Springer-Verlag, Berlin, Germany, pp. 60–64.

Index

- Ac analysis, 2, 3, 6, 7, 8, 9, 13, 14, 15, 16, 19
Activation energy(ies), 61, 223, 276, 277, 278, 465
 distribution of, 32, 41, 42
 electrodes, 38, 44, 62, 197, 212, 445
 polarization resistance, 62, 197
 solid electrolytes, 39, 62, 225
Active-passive transition, 308, 310, 311, 312
Admittance, 12, 72, 204, 328, 378
 conductivity determination for solid
 electrolytes, 7, 19
 electrochemical-mechanical, 204, 372
Adsorption, 55, 86, 89, 94, 95, 242, 422, 423
 reaction, 3, 10, 12, 55, 56, 60, 79, 85, 86, 87, 88
 specific, 55, 90, 242, 243
Air cell, 110, 147, 159, 198, 199, 221, 243, 255, 258, 259, 263
Aliasing, 136, 151, 385
Alkaline fuel cell (AFC)
 degradation process, 437
 α -relaxation, 282, 283, 284, 286, 291
Ambiguous circuits
 relations, 75, 78
Analog/digital filtering, 151
Analog-to-digital (A/D) conversion (ADC),
 129, 130
 successive approximation, 130
 tracking, 130
 voltage-to-frequency, 129, 130
Analytical treatment of impedance, 409
Anatomical measurements, 474
Anion chemisorption, 56, 416, 417, 421, 422, 423
Anisotropy, 61, 210, 215
Anode/cathode measurement, 153, 391, 398, 400,
 401, 425, 430, 433, 444, 450, 455
Anode, SOFC, 424, 456, 458
Anomalous diffusion, 265, 268, 271, 272, 273
Anticorrosion coatings, 147
Aqueous electrochemistry
 first complex plane analysis, 16
 supporting electrolyte, 45, 49
Arcs, 13, 73, 74, 75, 76, 98, 166, 209, 221, 222
Argand diagram, 5, 409
Armstrong
 rate equation, 59
Arrhenius, 282, 284, 285
Arrhenius plots, 207, 208, 212, 223
Artifacts, 153, 156, 358, 401, 477
Autoclave, 156, 358
Auxiliary electrode, 153, 154
Averaging, 118, 119, 131, 132, 137, 139, 149,
 166, 226
Bad cells, 154
Bandwidth, 121, 127, 147, 148, 304, 476
Barrier layer, 325, 326, 333, 347, 351, 352, 355
Battery, 381, 386, 389, 391, 393, 395, 396,
 399, 400
 common kinetic steps, 376, 386
 generic modeling, 142
 lead acid, 383, 396, 397, 416
 Lithium-ion, 404
 Nickel-metal hydride, 399
 typical impedance spectrum, 152, 381, 392, 396,
 399, 400, 403
Battery electrode
 equivalent circuit of, 381, 383, 388, 391, 393, 397,
 398, 399, 403, 408, 416
Bauerle, 60, 61, 180, 204
Bessel-functions, 64, 72, 300, 389
Beta-alumina, 39
 β -relaxation, 282, 283, 284, 286, 288
Bias, DC, 79, 83, 85, 95, 240, 247
Bilayer passive film, 325
Blocking
 coefficient, 86, 209, 244, 269, 400
 electrodes, 96, 173, 233, 470
 of ions, 80, 95, 280, 467
Bode plots, 336, 365, 366, 368, 411, 423, 438, 439
Boson peak, 282, 283, 286, 289, 290
Breakdown potential, 157

- Bridge
 audio-frequency, 108, 109, 112
 Berberian–Cole, 112, 113, 114, 115, 123
 transformer ratio arm, 110, 111, 112, 115
- Bruggeman, 187, 189, 190, 191
- Brush electrode, 417, 418, 419
- Bulk dielectric constant, 174, 225, 226
- Butler–Volmer
 boundary conditions, 85, 94, 95, 96, 241
 equation, 58, 80, 85, 94, 95, 96, 241
- Cable errors, 159
- Cable impedance, 144
- Calculation
 of dC_0i/dU , 329
 of $dCLv/dU$, 331
 of passive film admittance, 329
- Calibrated reference, 159
- Capacitance, 54, 159, 249, 267, 406, 408, 415, 416, 421, 422
- bulk (geometrical), 11, 82
- cell membranes, 473
- diffuse double layer, 7, 53, 54, 81
- Gouy–Chapman, 54, 83
- interface, 54, 56, 63, 159, 249, 251, 261, 268, 406
- muscle fiber, 473
- stray, 109, 111, 140, 141, 144, 161, 198
- Capacitive samples, 139, 150
- Carbon anode
 equivalent circuit, 402, 403
 impedance spectra, 402, 403
 state of charge dependence, 403, 404
- Carbon fibers, 402, 418
- Carvedilol phosphate, 466
- Causality, 4, 126, 138, 293, 303, 337, 427, 428, 429
- Cell
 membranes, 473, 474
 planar, 54, 201, 202
- Ceramic(s), 182, 191, 203, 204, 206, 207, 208, 210
 aging of, 182, 216
 polyphase, 191, 216, 218
 zirconia, 191, 204, 206, 207, 210
- Cerium oxide, 266
- Chain-connected network, 380
- Characterization example, 7, 8, 16, 25, 139, 158, 173, 201, 215, 258, 389
- Charge/discharge cycling, 154, 399, 406
- Charge transfer resistance, 267, 271, 272, 276, 278, 371, 381, 395, 404, 440, 450, 451, 455
- Charging of a capacitance, 52, 59, 64, 66, 373, 394, 396, 408, 416, 417, 421
- Chemical capacitance, 267, 269, 273, 274
- Chemical diffusion coefficient, 49, 50, 266, 275, 276, 390, 393
- Chromium, 319
- Circuit
 ambiguous, 21, 47, 78, 108, 243
 equivalent, 7, 8, 60, 67, 90, 169, 172, 176, 178, 179, 180, 204, 208, 360, 409, 417, 477
 ladder network, 77, 89, 90, 391, 422
 Randles, 10, 267
- Circuit elements
 capacitors, 10, 69, 384, 409
 diffusion-related, 10, 76, 233, 267, 440
 distributed elements, 8, 10, 239
 inductances, 10, 69
 lumped constant, 6, 8, 10, 69, 97, 170
 resistors, 10, 69, 384
- Clipping, 118, 151
- CNLS fitting, 102, 166, 167
- Coatings, 144, 147, 150, 264, 265, 365–366
- Coherence, 138
- Cole and Cole, 6, 73
- Cole–Cole
 dispersion, 29, 39, 68, 112, 233, 244, 409, 461
 distribution, 10, 13, 29, 30, 31, 32, 33, 34, 39, 72, 73
 plot, 6, 13, 29, 30, 34, 74, 75, 99, 166, 233, 243
- Coloration, 264, 265, 280, 281
- Color impedance, 281
- Comparison of simplified model with experiment, 355
- Complex dielectric constant, 6, 10, 25, 67, 68, 69, 74, 76, 225, 227
- Complex frequency, 24, 27, 46, 68, 86, 136, 375
- Complex nonlinear least squares (CNLS) fitting, 7, 15, 167, 168, 225
- Complex plane, 6, 7, 12, 13, 18, 103, 162, 321, 410, 413
- Complex plane impedance diagrams for film/solution interface, 323
- Complex-plane plots, 6, 7, 11, 12, 13, 30, 95, 99, 102, 162, 163
- Composite electrode, 191, 192, 193, 194, 220, 389, 392, 393
- Composite model, 226, 227, 228, 232, 233, 239, 241, 244, 247
- Conducting polymers, 270, 381
- Conductive-system
 dispersion, 225, 244
 dispersion response, 68, 225, 233, 244
 response, 101, 241
- Conductivity, 38, 39, 43, 44, 194, 210, 455, 464, 465, 470
 complex, 3, 22, 40, 176, 184, 186, 187, 227, 380
 dc, 462, 463, 464, 465, 467, 470
 frequency dependent, 44, 62

- hopping, 22, 38, 39, 41, 100, 226, 227, 467
Constant phase element (CPE), 8, 10, 27, 61, 72, 76, 99, 228, 256, 267, 344, 407, 417, 421, 422, 423
Contact resistance, 192
Copper–nickel alloys, 295
Correlation
 auto, 137, 138, 404, 436
 cross, 137, 148, 149, 230, 403, 436
 with impedance function parameters, 75, 138, 427
Corrosion, 292, 293, 298, 300, 301, 302, 324, 362, 365, 366, 367
 ac, 292, 293, 298, 300, 301, 324, 362, 365, 367
 coating, 147, 150
 denting, 362
 mechanisms, 292, 293, 306
 rate, 298, 362
Counter electrode (CE), 49, 50, 80, 81, 110, 112, 134, 201, 218, 277, 370, 414
Coupling model, 230
CPE, 72, 73, 75, 97, 268, 359, 422, 446
C powder, 437
Crest factor, 149
Cross-talk, 155
Cryostat, 160, 161, 194
Crystal tests, 157, 344
Current collector, 191, 220, 221, 373, 398, 399, 401, 413
Current distribution
 definition 28, 227
 frequency dependent, 62
 primary, 62, 63
 secondary, 63
Current interrupt, 223, 385
Current measurement, 140–141, 142, 143, 144, 146, 161, 275, 276
Current-to-voltage converter, 158, 196
Cylindrical porous electrode model
 impedance of, 63, 391, 418, 430, 439

Dag, 60, 200, 226
Data analysis methods
 CNLS, 14, 15, 166, 167, 168, 172
 simple, 2, 13, 14, 15, 167, 168, 172, 270, 395
Data anomalies, 2, 164, 166
Data fit, 75, 225, 226, 231, 232
Data fitting examples, 281
Data fitting results, 7, 15, 21, 75, 93, 94, 97, 102, 103, 104, 105
Davidson–Cole distribution, 32, 33, 34, 101
DC bias, 83, 85, 95, 114, 115, 194, 220, 240, 247
DC conductivity, 462, 465, 467
Debye
 dispersion relation, 25, 27
 expression, 25, 33, 39, 83, 181, 241
function, 26, 27, 32, 162, 461
length, 53, 83, 87, 180, 240, 241, 244, 269, 270
response, 27, 101, 162, 241, 269, 270
Debye–Stokes–Einstein, 464, 465
Deconvolution, 169, 170
Defect annihilation, 325, 336, 359
Defect diffusivity, 348
Defect generation, 325, 336, 349
Defect generation and annihilation reactions, 326
Definition of the rate constants, 350
De Levie, 63, 64, 77, 80, 97, 112, 361, 391, 407, 409, 413, 418, 419, 422
Density of states
 electrochemical, 266, 267, 273, 274
 electronic, 264, 266
Dielectric
 breakdown, 160
 constant, 6, 10, 23, 67, 68, 194, 228, 461, 467
 dispersion, 68, 225, 233, 244
 loss, 22, 25, 162, 409, 462, 465, 470, 472
 modulus, 467
 permittivity, 6, 225, 270, 279, 281, 287, 406, 460, 461, 467, 469, 471
 relaxation, 22, 25, 27, 194, 225, 459, 460, 461, 462, 467
 relaxation time, 10, 22, 27, 44, 69, 162, 225, 461, 465, 467
Dielectric constant, 6, 10, 23, 53, 67, 68, 194, 225, 409
 complex, 6, 10, 68, 225, 409
 high frequency, 194, 250
 static, 10, 23, 69, 194
Differential voltage, 146
Diffusion, 36, 49, 70, 83, 268, 275, 276, 378, 390
 chemical, 276, 281, 376, 389
 coefficient, 36, 49, 275, 276, 390
 controlled process, 413
 cylindrical geometry, 389
 finite length, 70, 240, 430
 Gaussian, 36
 impedance in terms of electric parameters, 21, 72, 298, 376, 377, 380, 383, 389
 length, 47, 70, 71, 83, 97, 240, 267, 268, 269, 381
 limiting equivalent capacitance, 10, 70, 71, 239, 277, 281, 376, 377, 378, 393, 423
 limiting equivalent resistance, 10, 70, 71, 239, 277, 376, 377, 378, 393, 423
 non-uniform, 10, 66, 97, 455
 open circuited, 71
 resistance, 268, 374, 376, 381, 386, 388, 391, 393, 399, 404
 semi-infinite, 46, 47, 48, 57, 58, 70, 72, 83, 86, 97, 240
 shorted, 71
 spherical geometry, 389

- Diffusion (*cont'd*)
 toward center of the particle, 389, 399, 402
- Diffusion coefficient, 36, 275, 276, 390
 chemical, 49, 264, 268, 275, 276, 390
 component, 21, 35, 36, 43, 49, 266, 393
 frequency dependent, 3, 22, 40, 41, 43, 70, 85, 86,
 269, 276, 277
 ionic, 264, 269, 275, 276, 278
- Diffusion control, 18, 453
- Diffusion effects, 83, 95, 243, 386
- Diffusion impedance, 267
- Diffusion layer, Nernst, 70, 84, 269, 416, 446, 450,
 452, 455
- Digital signal processor (DSP), 149
- Dihydrogenated tallow dimethylammonium
 chloride (DHTDMAC), 219
- Dipole–dipole interactions, 29, 39, 55, 232, 409
- Dipole reorientation, 473
- Direct methanol fuel cell (DMFC), equivalent
 circuit, 453
- Discretization, 379, 380
 of transmission line, 380
- Dispersion of dielectric constant, 409
- Dispersion response, 68
- Dispersive materials, 159
- Displacement, electric, 13, 23, 43, 96, 228, 372,
 409, 467
- Display technology, 263
- Dissolution, active, 308, 312, 389
- Distributed circuit elements, 10, 239
 constant phase (CPE), 8, 10, 76, 99
 for dielectric liquids, 10
 physical interpretation, 10
 summary, 233
- Distributed elements, discretization, 380
- Distribution
 of activation energies (DAE), 101, 102, 237
 of conductivity relaxation times, 44
 Gaussian, 29, 36, 37, 38, 40, 41, 43, 261
 of jump distance, 38, 40, 42, 43
 of jump frequencies, 38, 40, 43
 of relaxation times (DRT), 27, 225, 227
 of waiting (residence) times, 41
- Distribution function
 Cole–Cole, 29, 30, 31, 32, 33, 34, 72, 74, 75, 97
 Davidson–Cole, 32, 33, 34
 Gaussian (normal), 29, 37, 40
 Kirkwood–Fuoss, 27, 32
 Levy, 43
 lognormal (Wagner), 29, 30
 Williams–Watts, 33, 34, 42, 45, 227
- Distribution of activation energies
 exponential, 32, 41, 102, 225, 237
- Gaussian, 29, 38, 40, 41
- Double injection model, 96
- Double layer, 59, 406, 415, 421, 423, 439
 capacitance, 54, 92, 116, 267, 276, 406, 407, 410, 415,
 417, 421, 422, 423
 capacitor, 408, 423
 diffuse, 7, 53, 54, 81, 388
- Double structure of the barrier layer, 352
- Driven shield, 155
- Dynamic range, 126, 150, 151, 281
- Easy paths, 180, 182, 183, 208, 212
- Effective medium models, 176, 184, 185, 191,
 218, 232
- Electrical double layer, 1
- Electrical interference, 155
- Electric modulus, 44, 467
- Electrochemical capacitors, 406, 408, 415, 421
- Electrochemical cell, 148, 197
- Electrochemical impedance, 152
- Electrochemical potential, 35, 52, 80, 96
- Electrochromic device, 49, 263, 264, 265, 266, 280
- Electrochromic material, 263, 264, 265, 266,
 267, 268, 270, 275, 277, 280
- Electrochromism, 263, 264
 aging, 280
 devices, 264, 280
- Electrode
 alignment, 201
 blocking, 79, 80, 240, 241, 244
 clusters in, 191, 192, 194
 composite, 191, 192, 193, 194, 220, 221, 392
 counter (CE), 49, 50, 80, 81, 110, 112, 134, 201,
 218, 401, 414
 parent atom, 80, 85, 91, 400, 477
 placement, 202, 203, 372, 409, 467
 polarizable, 52, 80
 polarization, 19, 467
 porous, 63, 220, 391, 401, 407, 430, 437
 preparation, 19, 200, 203, 256, 258, 271, 276,
 422, 437, 475
 reaction, 7, 52, 80, 83, 85, 86, 243, 256
 redox, 9, 80, 81, 83, 84, 258, 367, 415, 416
 reference (RE), 1, 2, 3, 5, 6, 7, 8, 9, 10, 11, 12
 reversible, 38, 50, 51, 52, 80, 81, 388, 400, 402
 rough, 22, 63, 161, 386, 401, 404, 417, 422
 surface roughness, 97, 112, 279, 398
 working (WE), 2, 46, 109, 110, 113, 116, 201,
 386, 414
- Electrolyte
 impedance, 220, 248, 249, 386, 387, 391, 396,
 399, 400, 443
 solid, 1, 2, 7, 9, 54, 81, 204

- supported, 9, 70, 79, 81, 82, 83, 84, 92, 386
thin, 53, 82, 96, 112, 203, 220, 264, 280
unsupported, 9, 79, 81, 92
- Electrolyte–insulator–semiconductor (EIS)
 sensors, 248
 inversion layer, 248
 overview, 248
 surface potential, 248
- Electrometer, 148, 155
- Electron diffusion, 3, 21, 22, 34, 36, 40, 41, 45, 46, 49, 50
- Electron drift, 393, 406
- Electroneutrality, 34, 36, 46, 50, 62, 81, 83, 85, 87, 96
- Ellipsoids, 186, 187, 188, 189, 216
- Empty cell, 6, 159, 198
- Energy-efficient windows, 263
- Equilibrium potential, 58, 266, 271, 276, 277, 280, 333, 430
- Equipotential lines, 201, 202
- Equivalent circuit, 7, 8, 67, 81, 169, 453, 459, 460, 477
 analysis, 7, 8, 172, 372, 381, 444, 477
 Randles-type, 10, 81, 82, 267, 280, 416
- Equivalent circuits, 90, 379
- Equivalent electrical circuit describing the total impedance of the iron-concrete pore water interface, 338
- Equivalent series resistance, 407, 408, 412, 413
- ESR, 407, 408, 412, 413
- Exchange current, 52, 58, 83, 388, 443, 444, 456, 457
- Exponential distribution of activation energies, 237
- External reference, 159
- Extraction of PDM parameters from EIS data, 343
- Fabric conditioner, 219
- Faradaic admittance, 351, 359
- Faradaically deposited species, 415
- Faradaic impedance expressions for the barrier layer due to different point defects, 354
- Faradaic resistance, 349, 353, 355, 358, 410, 411, 416, 417, 422
- Faraday cage, 155, 158, 159
- Faradic reaction rates, 13
- Fast Fourier transform (FFT), 3, 129, 435
- Fast measurement, 149
- Ferroelectric, 157, 158, 194
- FFT speed, 149, 150, 151
- Film/solution interface, 319
- Finite length, 70, 136, 232, 240, 430
- Five-element ladder circuit, 412, 413, 414
- Floating measurement, 156
- Form factors, 186, 187, 188, 217
- Fourier
 discrete, 4, 43, 129, 136, 294
 fast (FFT), 3, 129, 435
 analysis, 2, 3, 107, 128, 135, 136, 137, 228, 298, 476
 synthesis, 107, 294
 transform, 2, 3, 4, 43, 128, 129, 135, 136, 476
- Fractal
 dimension, 267
 interface, 66, 75, 267, 268
 space processes, 42
 time processes, 42
- Fractional exponent, 13, 14, 33, 73, 75, 99, 101, 240, 241
 estimation, 241
- Frequency
 accuracy, 147
 relaxation, 22, 39, 42, 194, 225, 269, 286, 461, 462
 resolution, 146
 response analysis, 148
 sweep, 147, 149, 159
- Frequency response analyzer (FRA), 119, 121, 151, 157, 158, 195, 196
- Fricke, 72, 184, 186, 187, 188, 189, 216, 421
- Fringing errors, 161
- Frumkin isotherm, 384, 390
- Fuel cell, 424, 425, 427, 432, 433, 437, 444, 449
 ac response, 425
- Furnace, 134, 160, 161, 194, 199
- Galvanostat, 197, 201, 366, 368, 449, 450
- Galvanostatic, 366, 368, 449, 450
- Genetic algorithms for optimizing reaction mechanisms on experimental EIS data, 336
- Gerischer impedance, 72, 193
- GHz-THz-region, 281, 289
- Gibbs-DiMarzio model, 282
- Gigahertz, 281
- Glass, 281, 282, 292
 formers, 286
 glass-forming, 282, 286, 289
 transition, 282, 284, 292
 wide frequency, 285
- Glycerol, 470, 471
- Gouy–Chapman diffuse layer, 54, 83
- Grahame, 60, 406, 415, 420, 421
- Grain
 shape, 179, 182, 183, 186, 204, 207, 210, 215, 217
 size, 179, 183
- Grain boundary, 179, 180, 182, 186, 206, 207, 209, 210, 212
 activation energy, 61, 62, 212

- Grain boundary (*cont'd*)
 characterization of, 204
 conduction, 20, 62, 178, 180, 182, 183, 210, 212, 213, 472
 impedance, 62, 179, 182, 186, 210, 211, 218, 219
 phases, 184, 206, 207, 209, 215, 218
 resistance, 20, 61, 62, 179, 180, 206, 207, 218, 220, 256, 472
 thickness, 176, 177, 179, 185, 200, 206, 208, 209, 220, 472
- Ground
 loops, 156
 virtual, 2, 112, 123, 142, 144, 156, 195
- Grounded measurement, 156
- Guard electrodes, 161
- Guard ring, 161
- Hard carbon, 402
- Harmonic distortion, 109, 110, 138, 149, 150
- Harmonic measurement, 5, 109, 122, 138, 139, 149, 150, 156, 301, 351
- Harmonic tests, 132, 156
- Havriliak–Negami equation, 461
- Heaviside function, 4, 375
- Heterogeneous electrode reaction, 1, 52, 56, 439
- Heterogeneous media
 electrical properties of, 175
- Hierarchical response, 90, 98
- High impedance, 144, 158
 materials, 157, 158
- High specific-area materials, 67, 225, 247, 281, 388, 404, 406, 420
- High temperature impedance measurement, 2, 9, 11, 19, 39, 62, 72, 81, 82, 147, 155
- High voltage amplifiers, 157, 160
- High voltage tests, 159
- Hilbert relation (HT), 5, 428
- Ideal capacitor, 60, 72, 74, 75, 98, 159, 232
- IEEE-488
 bus, 133
 FRA, 135, 152
 interface, 125, 126, 133, 134, 152
 oscillator, 125, 126
 potentiostat, 125, 134, 135, 152
- Igor Pro, 335
- Immittance, 6, 68, 226, 233, 240, 243, 245, 246
 response function, 68, 75
 spectroscopy, 6, 225
- Impedance, 4, 5, 112, 157, 158, 195, 396, 398, 430, 440
 adaptor, 195, 196, 197
- adsorption-reaction, 3, 10, 12, 56, 60, 79, 87, 88, 89, 90, 94
- analyzers, 126, 128, 157, 158, 195, 196, 197
- artifacts, 153
- definition, 2, 5, 13, 49, 74, 94, 128, 221, 394
- electrochemical mechanical, 293, 366, 372, 373
- faradic, 56, 59, 300, 307
- finite length Warburg, 70, 71, 72, 76, 81, 83, 90, 91, 92, 96, 97
- indicial, 2
- lumped elements, 8
- modulus, 6, 177, 185, 186, 191, 468
- of nickel in phosphate buffer solution, 317
- parameters, 128, 138, 439, 441, 455
- phase angle, 355, 418, 421, 423
- rate dependency, 1, 445
- relation with Fourier transformation, 2, 4, 5, 135, 137, 375
- spectra for carbon steel in sat. $\text{Ca}(\text{OH})_2 + \text{NaOH}$, 337
- Warburg, 64, 90, 440
- Impedance of fuel cell, overpotential, 426
- Impedance function, low and high frequency limits, 126, 194
- Impedance measurement, suitable for power sources, 385
- Impedance spectroscopy (IS), 1, 276, 459, 472, 473, 474
- background, 39, 472
- biological applications, 472
- devices, 1, 175
- electrical stimuli, 473
- frequency domain response, 6, 225
- frequency range, 39, 213, 225, 273, 281, 292, 443, 473, 475
- ion conductors, 1, 39, 225, 281
- measurements, 6, 39, 225, 276, 443, 459, 469, 472, 473, 474, 475
- parameters derived from, 473
- selected applications, 271
- simple RC circuits, 21, 460, 473
- Impedance spectrum, 186, 218, 396, 428, 429
 battery, 393, 395, 396
- IMPS, 290
- Instrumentation errors, 145, 159, 472
- Insulator, 144, 158, 248, 249, 251, 252, 253, 254, 472
- Interaction between intercalation sites, 390
- Intercalation, 416
 of Li, 265
- Interface(s), 1, 2, 3, 7, 9, 10, 16, 17, 18, 19, 20
 capacitance, 3, 7, 10, 16, 18, 20, 21, 52, 53, 54, 55

- electrochemical, 1, 2, 3, 7, 16, 17, 19, 20, 21, 22, 23
Ethernet, 152
 film-solution, 3, 312, 313, 314, 318, 319, 320, 322, 323, 325, 336
 fractal, 66, 75, 267, 268
 importance of, 3, 7, 16, 62, 112, 133, 197, 247, 263, 264, 323
 irreversible, 52, 325, 333, 349
 metal-film, 22, 264, 266, 281, 312, 313, 325, 333, 336, 337, 365
 physical properties of, 1, 7, 10, 20, 21, 34, 218, 263, 264, 293, 406
 reversible, 50, 51, 52, 80, 81, 325, 333, 349
RS232, 152
 states, 52, 157, 249, 251, 253, 254, 258, 259, 261, 263, 264
USB, 152
Interfacial capacitance, 13, 21, 63, 193, 422, 423
Interference, 139, 155, 156, 158, 159, 302, 459, 465, 469
Internal reference, 159
Ion channels, 473
Ion concentration, 269, 270, 279
Ion conductor, 200, 264, 266, 280
Ion density, 266, 269, 270
Ion diffusion, 264, 265, 277, 463, 465
Ion/electron extraction, 264
Ion/electron insertion, 264, 265
Ionic hopping model, 39, 100, 101, 226, 229, 231, 232
Iridium oxide, 96, 265, 277, 278, 280
IR loss, 465
Iron, 306, 343, 347, 348, 355, 362
Isotherm
 Frumkin, 55, 384, 390
 Langmuir, 55, 56, 306
 Temkin, 56
Kauzmann paradox, 282
Kirkwood–Fuoss distribution, 27, 32
Kohlrausch, 99, 101, 227
Kohlrausch–Williams–Watts (KWW), 99, 101, 227 function, 461
Kramers–Kronig (KK), 465, 466, 467 transforms, 124, 125, 126, 303, 304, 305, 336, 337, 338
Ladder
 circuit, 412, 413, 414, 417, 422
 network, 77, 89, 90, 391, 422
Lanthanum strontium manganite (LSM), 191
Laplace
 equation, 34, 46, 62, 315, 374, 375, 376
 frequency, 46, 128, 135, 293, 369, 375
 transform, 24, 46, 128, 135, 293, 369, 374, 375, 376, 385
Laplace current, 375
Laplace transform
 differential equations, 374, 375, 376, 379
 inverse, 28, 34, 47, 375, 376, 384, 385, 461
 of the excitation signal, 107, 128, 129, 135, 137, 384
 relationship with impedance, 135, 297, 375, 384, 461
Layer models, 177, 183, 184
Lead acid battery, 383, 396, 397, 416 equivalent circuit, 383, 397, 416 impedance spectrum, 396, 397
Levenberg–Marquardt, 477
LEVM, 102, 228, 233, 234, 241, 244
Limiting capacitance, 71, 277, 377, 394 measurement of, 71, 108, 116, 386, 393, 422, 425 use in fitting, 71, 228, 239, 281, 376, 377, 393, 394
Limiting resistance, 376, 377, 378
Linearity, 138, 150, 381, 383
Linear regime, 5, 149, 150, 153, 220
Linear response, 460
Linear-sweep voltammetry, 408, 418
Liposomes, 219
Liquid crystal, 157, 219, 243, 244
Liquid materials, 1, 2, 7, 22, 29, 34, 54, 73, 75, 79, 95
Lithium, 49, 50, 266 -ion battery, 404 trifluoromethanesulfonate, 280
Lognormal distribution, 30, 44
Loss angle, 162
Low cable capacitance, 53, 83, 112, 140, 141, 143, 144, 155, 158, 159, 167
Low impedance, 145, 146, 147, 151, 152, 155, 157, 158, 160, 196 cell measurement, 2, 6, 7, 8, 11, 19, 39, 81, 82, 92, 109
Luminous transmittance, 263
Lunkenheimer-Loidl plot, 281, 282
Mass impedance, 281
Materials
 disordered, 22, 26, 40, 41, 85, 224, 281, 292
 glasses, 22, 26, 40, 41, 44, 224, 231
 impedance measurement, 161
 interface, 1, 2, 3, 7, 21, 22, 23, 27, 34, 40, 54
 polycrystalline, 1, 60, 61
Maxwell element, 35, 77, 78, 90, 97, 176, 183, 186, 190
Maxwell–Wagner model, 183, 184, 186, 187, 189, 190, 216
MCMB, 402
Measurement
 constant load, 384
 current interrupt, 385

- Measurement (*cont'd*)
 errors due to cables, 159
 FFT, 148, 153, 156, 384
 noise, 109, 117, 118, 126, 131, 137, 138, 139, 145, 146, 148
 2-/3-/4-terminal, 6, 112, 113, 114, 123, 125, 139, 144, 145, 374, 384
 MEISP, 395
 Membrane, impedance, 444, 446, 450, 453, 472, 473, 474, 475, 477
 Metal/film interface, 313
 Metal oxide semiconductor (MOS), 248, 249, 250, 254, 261
 capacitor, 248, 249
 field effect transistor (MOSFET), 248
 impedance characteristics, 249
 inversion layer, 248, 249
 reference electrode, 249, 250
 surface states, 254, 261
 Microstructure, 175, 176, 177, 182, 184, 215, 220
 Migration, 45, 46, 351, 352, 386
 Miller, 412, 413, 417
 Mixed conductor, 79, 96, 190, 265
 Mixed conductor model, 2, 49, 79, 96, 190, 191, 265, 280, 281, 355
 Mixed oxides, 266
 Mobility, 35, 36, 93, 242, 243, 269, 270, 279
 drift, 37
 ionic, 269, 270, 279
 ratio, 85, 93, 240, 242
 Mode-coupling theory (MCT), 282, 284, 285, 289, 290
 Model
 brick layer, 177, 179, 180, 182, 183, 184, 208, 224
 Bruggeman asymmetric, 187, 190
 Bruggeman symmetric, 190, 191
 composite, 191, 193, 226, 227, 228, 232
 easy path, 180, 182, 183, 208
 effective medium, 176, 183, 184, 185, 190, 191, 216, 218, 232, 240
 finite element, 62, 182, 183, 190, 202, 215
 ionic hopping, 100, 101, 226
 nearly constant loss, 226
 optimization, 335, 336, 347, 349, 359, 413
 variable-slope, 227
 Modeling, time domain, 376, 378, 381, 383
 Model parameters, expressing in electrical terms, 176, 376
 Modulus
 function, 6, 44
 spectroscopy, 6, 162, 225
 spectrum, 177, 179, 185, 187, 188, 189, 190, 216
 Molecular reorientation, 460
 Monte Carlo method, 193
 Mott–Schottky plot, 261, 262
 Mullite, 206
 Multichannel measurement, 157, 433, 436
 Multiplexed measurement, 157, 435
 Nagel scaling, 286
 Na-alumina, 39, 61, 75, 163, 164, 165, 175, 197, 198, 206, 210
 Nearly constant loss, 226
 Negative impedance converters (NICs), 311
 Nernst equation, 58, 457, 463
 Nernst impedance, 446, 447, 450, 451, 452, 455, 457
 Nernst–Planck–Poisson equation, 36, 37, 45, 91, 96, 97, 239, 240, 334
 Network models, 67, 96, 97, 374, 409
 New phase formation, 390, 392
 impedance of, 390, 392
 Nickel, 191, 265, 277, 280, 316, 318, 357, 398, 443
 Nickel–metal hydride battery, 399
 impedance spectra, 399
 Nickel oxide, 191, 265, 277, 280, 393
 Nitrogen/helium systems, 160
 Noise, 3, 137, 149, 476
 Noise/harmonic rejection, 132, 149
 Nonlinear, 5, 138, 167, 168, 298, 300, 379, 383, 384
 cell, 5, 7, 12, 95, 109, 110, 120, 122, 148, 149, 150
 least squares, 7, 15, 100, 167, 168, 225
 Non-linearity, in corrosion response, 150, 298
 Normalization, dimensionless, 67, 75
 Normal mode, 462, 463
 Nyquist diagram, 6, 412, 441, 443, 445, 446
 Nyquist plot, 410, 421, 423, 450
 Ohmic resistances due to interfacial reactions, 354
 Oils, 157, 270, 361
 Optical properties, 184, 263, 264, 265, 292
 Optimized parameters for the corrosion of carbon steel in borate buffer solution, 356
 Original modulus formalism (OMF), 225
 Oscillator, 282
 harmonic, 283
 o-terphenyl, 465
 Pajkossy, 416, 421, 422, 423
 Parallel load resistance, 374, 376, 378, 381, 408, 455
 Parallel measurement, 157, 434, 435
 Parallel RC circuit, 2, 6, 7, 10, 11, 12, 44, 59, 60, 64, 70
 Parameter Values as a Function of pH and Potential from EIS Data for Iron in 0.3M H₃BO₃ + 0.075M Na₂B₄O₇ + 0.001M EDTA, 346
 Particle surface
 equivalent circuit, 388, 391, 398, 399, 402
 impedance, 388, 389, 391, 395, 398, 399, 402, 404

- Passivating layer, equivalent circuit, 388, 402
Passive
 film, 312, 318, 319, 323
 state, 308, 311, 324, 325, 336, 349, 359
Passivity, 312
Pell and Conway, 409, 418
Penetration effect, 407, 413, 419
Percolation, 43, 184, 190, 194, 218, 404
Permittivity, 6, 406, 460, 467, 469
Pharmaceutical, 157
Phase angle, 66, 337, 355, 418, 420, 421, 423
Phase-sensitive detector (PSD), 109, 110, 114, 118, 137
Photoelectrochemical solar cells, 258
 description, 258
 general response, 258
 impedance response, 258
 surface states, 258
Physical aging, 465, 466
Piezoelectric, 147, 157
Plot
 Arrhenius, 282
 Bode, 163, 336, 339, 344, 365, 366, 368, 411, 418, 423, 433
 Mott–Schottky, 261, 262
 Randles plane, 6, 7, 271, 277, 316, 317
 3-D, 162
Point defect model, 313, 314, 324
Poisoning, of catalyst, 425, 449, 453
Poisson equation, 91, 96, 240, 242
Polar form, 5, 163, 169
Polarizability, 79, 333, 335, 336, 346, 354
Polarization, 23, 51, 201, 202, 294, 460, 467
 concentration, 23, 51
 electric, 23, 44, 51, 269, 362, 409, 460, 467, 469, 470
 electrode, 201, 202, 409, 467
 resistance, 124, 193, 202, 294, 304, 362, 426
Polarography, 3, 129, 295, 300, 425
Polyaniline, 280, 416
Polyethylene glycol, 280
Polyisoprene, 462
Polylactide, 462
Polymer, 266, 270, 400, 424, 460, 462
 conductive, 416
 electrolyte, 266, 269, 270, 280, 401, 424, 444
Polymer Membrane Fuel Cell (PEFC)
 CO poisoning of Pt/C anode, 449
 CO poisoning of PtRu/C anode, 449
 equivalent circuit, 444
 performance loss, 444
Polymethyl methacrylate, 461, 462
Polyoxybutylene, 462, 463
Polypropylene, 460
 glycol, 462
Polyvinylethylene, 469, 470
Porosity, 63, 97, 175, 186, 220, 365, 396, 399, 403, 437
Porous electrodes, 20, 22, 406, 407, 408, 424, 437
 effects, 20, 22, 63, 80, 255, 386, 417, 418, 441
 specific conductivity, 380
 surface area, 373, 392, 393, 395, 398, 399, 406, 429, 455
Potentiostat, 115, 116, 147, 152, 155, 156, 157
Potentiostatic, 115, 366
Potentiostatic control, 113, 114, 115, 125, 311
Power-densities, 407, 409, 412, 421, 433, 444, 448
Power law, 286, 289
Power loss, 39, 231, 232, 281, 286, 289, 373, 374, 379, 400, 407
Power spectrum, 29, 137, 138, 413, 420, 421
Prediction of defect distributions, 334
Propylene glycol, 464, 468
Prussian blue, 280
Pseudocapacitance, 409, 415, 416, 417, 422, 423
Pseudocapacitor, 408, 417
PTCR materials, 191
Quality control, 3, 7, 280, 425
Radio frequency analyzers, 127
Ragone plots, 409
Randles, 416
 circuit, 82, 265, 267, 268, 271, 275, 276, 277, 278, 280, 281, 388
 equivalent circuit, 265, 280, 388
Random noise, 137
Random walk, 22, 34, 38, 40, 41, 43, 45
 continuous time (CTRW), 41
 discrete time, 38, 40, 43
Rate constants, 59, 80, 86, 326, 343, 347
 complex, 86
 frequency dependent, 3, 5, 12, 19, 29, 40, 68, 69, 70, 73, 86
RC time constant, 10
Reactance, 1, 6, 81, 96, 112, 114, 294
Reaction
 charge-transfer, 2, 7, 16, 17, 18, 50, 52, 56, 57, 59, 60
 charge-transfer resistance, 2, 7, 16, 57, 59, 60, 81, 83, 256, 278, 302
 redox, 9, 80, 81, 83, 258, 323, 367, 416
Reaction-diffusion sequence, 86, 87, 90, 191
Reaction mechanism analysis of passive metals, 324
Recombination, 93, 94, 243, 262
Rectification, faradic, 299, 300
Redox pseudocapacitance, 415, 416
Reference electrode (RE), 1, 2, 3, 5, 6, 7, 8, 9, 10, 11, 12
Reference measurement technique, 144
Relative standard deviation, 169, 227, 395
Relaxation frequency, 183, 194, 212, 220

- Relaxation impedance
theory of, 23, 60, 97, 162, 269, 292, 333, 360
equivalent circuit, 450, 451
- Relaxation time(s), 1, 10, 11, 13, 22, 23, 24, 26, 27, 28, 30
conductivity, 1, 10, 13, 22, 23, 34, 39, 40, 42, 44, 60
distribution of, 1, 10, 13, 22, 26, 27, 28, 30, 31, 32, 33
single, 11, 13, 22, 23, 24, 27, 28, 40, 42, 44, 60
- Resistance
bulk, 10, 386
charge-transfer, 2, 7, 16, 21, 57, 58, 59, 60, 81, 83, 91
distributed, 407, 409, 413, 414, 416
polarization, 202, 294, 304, 362, 426
- Response
constant phase, 66, 72, 99, 228, 256
Debye, 87, 101, 225, 243
harmonic, 119, 120, 150, 297, 298, 299, 300, 301, 302
hierarchical, 90, 98
linear, 5, 150, 298, 299, 300, 384
Warburg, 18, 50, 59, 66, 70, 71, 72, 90, 93, 96, 97
- Rotating vector diagrams, 423
- Roughness factor, 422
- Sample contamination, 160
- Sample holders, 157, 161
- Sample oxidation, 2, 160, 260, 261, 262
- Sample rate, 129, 151
- Secondary relaxation, 461, 462
- Segmental
dispersion, 462
dynamics, 460, 461, 462
motion, 465
relaxation, 463
- Segmented fuel cell, 433
- Semiconductors, 40, 41, 96, 157, 194, 218, 224, 258, 259, 408
- Sensitivity analysis, 339
- Sensors
electrolyte-insulator-semiconductor (EIS), 248, 254
oxygen, 2, 7, 255, 257, 258, 455
semiconductor-insulator-electrolyte, 247, 248, 254
solid electrolyte chemical, 247
zirconia-based, 255
- Sequential measurement, 435
- Series and parallel RC circuits, 6, 7, 74, 75, 90, 98, 189, 196, 378, 407, 408
- Series RC circuit, 6, 7, 10, 18, 39, 63, 64, 65, 70, 71, 74
- Simplified method for expressing the impedance of a stationary barrier layer, 349
- Simultaneous measurement, 153
- Single sine analysis, 148, 149, 151
- Single sine correlation, 148, 149
- Sintering, 7, 182, 200, 203, 206, 210, 255, 256, 257, 428
- Smith–Chart impedance diagram, 6
- SnO, 6, 404
- Solar transmittance, 263
- Solid electrolyte chemical sensors, 247
applications, 247
electrode materials, 1, 2, 7, 225, 247, 258
electrode preparation, 258
impedance spectra, 247
oxygen, 2, 7, 258
- Solid electrolytes, 9, 60, 81, 93, 225, 386
- Solid materials, 73, 95, 157
- Solid oxide fuel cells (SOFC), 175, 424
equivalent circuit, 457
Nernst impedance, 457
- Solid state batteries, 1, 247, 381, 386, 387, 388, 389, 393, 398, 399, 403
- Solid state devices, 1, 2, 157, 175, 247, 248, 254, 258, 280, 393, 421
advantages and limitations, 247
ion selective membranes, 247
secondary batteries, 247
semiconductor-insulator-electrolyte sensors, 247, 248
solid electrolyte chemical sensors, 1, 2, 247, 248, 258
steam electrolyzers, 247
- Space charge, 62, 81, 83, 180, 182, 183, 218, 314
- Space charge region, 182
capacitance, 10, 70, 83, 95, 218, 219, 248, 249, 263, 281, 390
- Space-charge effects, 269
- Space-charge relaxation, 269, 279
- Specific adsorption, 10, 12, 55, 85, 86, 90, 242, 423
- Specific conductivity
electronic, 399
ionic, 399
porous electrode, 380
- Spectroscopy, modulus, 6, 162, 225
- Spectrum analyzers, 146, 152
dynamic, 126, 127, 128
parallel filter, 127
swept filter, 127
- Spectrum, admittance, 25, 204, 205, 378, 390, 391
- Spherical particles, impedance function, 391
- SPICE, 379, 384
- Stability, 153, 155, 324, 400
- Standard rate constants, 335, 336
- State of health, 399, 432
- Statistical sampling, biological structures, 474
- Stefan–Maxwell equation, 35
- Step/pulse waveforms, 148

- Stereology, 474
 Stern–Geary equation, 293
 Stray capacitance, 111, 161, 198
 Sublinear-superlinear power-law (SLPL), 281
 Supercapacitors, 381, 406, 407, 408, 409, 416
 Supported electrolyte, 7, 50, 70, 80, 81, 83, 386
 Supported situations, 9, 72, 82, 84, 85
 Surface
 impedance in series with diffusion, 10, 56, 64, 220, 221, 267, 379, 386, 388, 389, 391
 inhomogeneity, 422
 potential, 55, 251, 259, 261, 310, 415, 439
 states, 253, 258, 261, 263
 Susceptance, 6
 Suzuki phase, 215
 Symmetry factor, 80, 216,
- Tafel
 coefficients, 293, 298, 301, 302
 constants, 58, 293, 298, 301
 Tantalum oxide, 266, 279, 280
 Tantalum pentoxide, 279
 Teflon, 471, 472
 Temperature control, 160, 197
 Temperature dependence, of impedance in SOFC, 457
 Temperature tests, 155, 160, 161
 Terahertz, 281
 Test circuits, 69, 115, 139, 147, 155, 260, 379, 384
 Tetragonal zirconia polycrystals (TZP), 204
 The Film, 314
 Theoretical Complex Plane Impedance Diagrams for a Passive Film, 324
 Thermal activation, 10, 28, 197, 207, 225, 229, 277, 278
 Thermodynamic enhancement factor, 50
 Three-dimensional (3-D) perspective plotting, 12, 162
 Three-phase boundary (TPB), 191
 Time course interpolation, 428, 429, 430
 Time domain analysis, 2, 3, 6, 107, 126, 128, 135, 136, 137, 148, 158
 Time domain response
 capacitor, 129, 225, 375, 378, 383
 inductor, 375
 Time drift, real time-drift compensation, 428, 430
 Time variant systems, 2, 5, 67, 69, 150
 Time-domain modelling, non-linear, 376, 378, 381, 383
 Tin oxides, 49, 50, 203, 264, 265, 266, 270, 281, 318, 319, 415
 Titanium dioxide, 265
 Titanium oxide, 265, 276, 277
 Top-point, 64, 139, 236, 475
 Transfer function, 107, 121, 137, 293
 fracture (FTF), 366
 Transference number, 50, 51
 Transforms
 Fourier, 135
 Laplace, 135
 Transient current, 270, 275, 276, 279, 280
 measurement, 270, 276, 280
 Transmission electron microscopy (TEM), 207
 Transmission line, 63, 64, 96, 267, 383, 407, 413, 418
 branched, 64, 65
 characteristic impedance, 406
 coefficient, 48, 49, 66, 70, 268, 365, 380, 403
 de Levie, 63
 diffusion, 267, 268
 discretization, 380
 equivalent circuit, 268
 finite, 47, 48, 63, 65, 70, 71, 72, 96, 267, 380
 finite length, 70, 430
 impedance, 48, 63, 64, 71, 267, 383
 Nernst–Planck–Poisson equation system, 91, 96, 97, 239
 non-uniform, 63, 66, 96, 97
 random, 42, 418
 RC, 47, 48, 63, 64, 65, 66, 71, 96, 361, 383
 semi infinite, 47, 48, 70, 72, 96, 97, 267, 366, 430
 semi infinite length, 47, 48, 70, 72, 96, 97, 267, 430
 Transmittance modulation, 281
 Transparent conductor, 263, 264, 265
 Trapping, 265, 267, 268, 274, 275, 281
 Tris-naphthylbenzene, 465
 T-system, 473
 Tungsten oxide, 264, 265, 266, 270, 271, 272, 273, 274, 275, 280
 Two-electrode configuration, 213, 400, 401, 402, 406, 407, 409, 434, 437
 Type 304SS Passivated in 0.1N Na₂HPO₄
 Solution, 319
 Ultra-capacitors, 145
 Underpotential deposition, 416
 Universal dielectric response, 281
 Unsupported situations, 9, 84, 85
 Vanadium oxide, 266, 278
 Variable-slope model, 227
 Virtual earth current measurement, 112, 139, 141, 142, 143, 144, 156, 158, 159, 161
 Vogel–Fulcher
 temperature, 286
 Vogel–Fulcher–Tammann (VFT), 282

- Voigt element, 176, 178
Voltage follower, 115, 123, 155
Voltammetry behavior, 21, 408, 415, 417, 418, 420
- Wagner
distribution, 29, 30, 45, 183, 186, 433
ground (earth), 109
- Warburg, 413, 416, 423
Warburg diffusion impedance, 267
Warburg diffusional element, 416
Waveguide techniques, 158
Weighting
P, 103, 104, 168, 169, 172, 179, 234, 238
unity (unweighted), 168
What to fit, 7, 8, 69, 72, 75, 76, 93, 97, 101, 103, 164
Williams-Watts distribution, 33, 34, 42, 45, 101, 227
- Wing, 282, 283, 286, 288, 289
Working electrode (WE), 2, 46, 109, 110, 113, 116, 201, 361, 386, 401, 414
- YARC, 73, 75, 76
- ZARC, 13, 73, 75, 97, 98, 221
Zirconia
bulk electrolyte behavior, 19
ceramics, 191, 204, 206, 207, 210
cubic, 194, 203, 204, 206, 208, 209, 216
dielectric constant of, 194
intergranular resistance, 207
monoclinic, 203, 209, 210, 211
single crystal, 209, 210, 216
tetragonal, 203, 204, 206, 207, 208, 209, 210, 211, 216
- Zirconium oxide, 266, 280